

MOLECULAR GELS

Materials with Self-Assembled
Fibrillar Networks

Edited by
Richard G. Weiss and Pierre Terech



 Springer

MOLECULAR GELS

Molecular Gels

Materials with Self-Assembled Fibrillar Networks

Edited by

RICHARD G. WEISS

*Department of Chemistry, Georgetown University,
Washington, DC, U.S.A.*

and

PIERRE TERECH

*CNRS-Atomic Energy Center-Grenoble University,
Grenoble, France*

A C.I.P. Catalogue record for this book is available from the Library of Congress.

ISBN-10 1-4020-3352-4 (HB)
ISBN-13 978-1-4020-3352-0 (HB)
ISBN-10 1-4020-3689-2 (e-book)
ISBN-13 978-1-4020-3689-7 (e-book)

Published by Springer,
P.O. Box 17, 3300 AA Dordrecht, The Netherlands.

www.springeronline.com

Printed on acid-free paper

All Rights Reserved

© 2006 Springer

No part of this work may be reproduced, stored in a retrieval system, or transmitted in any form or by any means, electronic, mechanical, photocopying, microfilming, recording or otherwise, without written permission from the Publisher, with the exception of any material supplied specifically for the purpose of being entered and executed on a computer system, for exclusive use by the purchaser of the work.

Printed in the Netherlands.

Dedication

For Jeanne and Inna, our human serendipity

TABLE OF CONTENTS

List of Contributors	xi
Introduction <i>Richard G. Weiss and Pierre Térech</i>	1
THEORY	
1 Theory of Molecular Association and Thermoreversible Gelation <i>Fumihiko Tanaka</i>	17
2 Growth and Chirality Amplification in Helical Supramolecular Polymers <i>Jeroen van Gestel, Paul van der Schoot and M.A.J. Michels</i>	79
3 Self-Assembling Peptide Gels <i>A. Aggeli, N. Boden, L.M. Carrick, T.C.B. Mcleish, I.A. Nyrkova and A.N. Semenov</i>	99
4 Kinetics of Nucleation, Aggregation and Ageing <i>Jörn W.P. Schmelzer</i>	131
5 Soft Glassy Rheology <i>Peter Sollich</i>	161

6		
Rheological Chaos in Wormlike Micelles and Nematic Hydrodynamics		193
<i>Moumita Das, Ranjini Bandyopadhyay, Buddhapriya Chakrabarti, Sriram Ramaswamy, Chandan Dasgupta and A.K. Sood</i>		
7		
Wetting of Fibers		223
<i>Elise Lorenceau, Tim Senden and David Quéré</i>		
TECHNIQUES		
8		
Gel Formation: Phase Diagrams Using Tabletop Rheology and Calorimetry		241
<i>Srinivasa R. Raghavan and Bani H. Cipriano</i>		
9		
Direct-Imaging and Freeze-Fracture Cryo-Transmission Electron Microscopy of Molecular Gels		253
<i>Dganit Danino and Yeshayahu Talmon</i>		
10		
Molecular Gels and Small-Angle Scattering		275
<i>Pierre Térech</i>		
11		
X-Ray Diffraction of Poorly Organized Systems and Molecular Gels		325
<i>Michel Anne</i>		
12		
Optical Spectroscopic Methods as Tools to Investigate Gel Structures		363
<i>Henri Bouas-Laurent and Jean-Pierre Desvergne</i>		
13		
Circular Dichroism for Studying Gel-Like Phases		431
<i>Giovanni Gottarelli, Gian Piero Spada and Ettore Castiglioni</i>		

SYSTEMS – ORGANOGELS**14****Low Molecular-Mass Organic Gelators** **449***Mathew George and Richard G. Weiss***15****Design and Function of Low Molecular-Mass Organic Gelators (LMOGs) Bearing Steroid and Sugar Groups** **553***Norifumi Fujita and Seiji Shinkai***16****Safin Gels With Amphiphilic Molecules** **577***Reiko Oda***SYSTEMS – HYDROGELS****17****Advances in Molecular Hydrogels** **613***Santanu Bhattacharya, Uday Maitra, Samrat Mukhopadhyay and Aasheesh Srivastava***18****Aqueous Gels Made of Chiral Lipid- and Porphyrin-Amphiphiles** **649***Jürgen-Hinrich Fuhrhop, Tianyu Wang, Sheshanath Bhosale, Sidhanath Bhosale and Matthias Lauer***ANALYSES OF SPECIFIC SYSTEMS****19****Rheology of Wormlike Micelles: Equilibrium Properties and Shear Banding Transitions** **667***Jean-François Berret***20****Cryo-Tem, X-Ray Diffraction and Modeling of an Organic Hydrogel** **721***Lara A. Estroff and Andrew D. Hamilton*

21		
Gelation of a Liquid-Crystalline L_α Phase Induced by the Proliferation of Topological Defects		743
<i>Patrick Davidson</i>		
APPLICATIONS		
22		
Gels of Liquid Crystals and Ion-Conducting Fluids		773
<i>Rifat A.M Hikmet</i>		
23		
Electron Conducting and Magneto-Sensitive Gels		793
<i>Frédéric Fages</i>		
24		
Photoresponsive Gels		817
<i>André Del Guerzo and Jean-Luc Pozzo</i>		
25		
Gels of Low Molecular-Mass Organic Gelators as Templates for Transcription		857
<i>Arianna Friggeri, Kjeld J.C. van Bommel and Seiji Shinkai</i>		
26		
Responsive Molecular Gels		895
<i>Jaap J.D. de Jong, Ben L. Feringa and Jan van Esch</i>		
27		
Gels as Cleaning Agents in Cultural Heritage Conservation		929
<i>Emiliano Carretti and Luigi Dei</i>		
Color Section		941
Index		000

LIST OF CONTRIBUTORS

Amalia Aggeli

Centre for Self-Organising Molecular
Systems *and* School of Chemistry,
University of Leeds LS2 9JT,
United Kingdom
a.aggeli@chemistry.leeds.ac.uk

Michel Anne

Laboratoire de Cristallographie, CNRS,
25 avenue des Martyrs, BP166,
38042 Grenoble, Cedex09, France
michel.anne@grenoble.cnrs.fr

Ranjini Bandyopadhyay

Department of Physics and Astronomy,
The Johns Hopkins University,
Baltimore, MD 21218, USA

Jean-François Berret

Matière et Systèmes Complexes,
UMR CNRS n° 7057, Université Denis
Diderot, 140 rue de Lourmel, 75015
Paris, France
Jean-Francois.Berret@ccr.jussieu.fr

Santanu Bhattacharya

Department of Organic Chemistry,
Indian Institute of Science,
Bangalore 560 012, India
sb@orgchem.iisc.ernet.in

Sheshanath Bhosale

Freie Universität Berlin, FB Biologie,
Chemie, Pharmazie, Institut für
Chemie/Organische Chemie, Takustr. 3,
D-14195 Berlin, Germany

Sidhanath Bhosale

Freie Universität Berlin, FB Biologie,
Chemie, Pharmazie, Institut für
Chemie/Organische Chemie, Takustr. 3,
D-14195 Berlin, Germany

Neville Boden

Centre for Self-Organising Molecular
Systems and School of Chemistry,
University of Leeds LS2 9JT,
United Kingdom
nevb@chem.leeds.ac.uk

Kjeld J. C. van Bommel

BiOMaDe Technology Foundation,
Nijenborgh 4, 9747 AG Groningen,
The Netherlands
van.Bommel@biomade.nl

Henri Bouas-Laurent

Laboratoire de Chimie Organique et
Organométallique, UMR 5802, CNRS
Université Bordeaux 1, 33405
TALENCE Cedex, France
h.bouaslaurent@lcoo.u-bordeaux1.fr

Emiliano Carretti

Department of Chemistry & CSGI
Consortium, University of Florence, via
della Lastruccia, 3, I-50019 Sesto
Fiorentino, Italy
carretti@csgi.unifi.it

Lisa M. Carrick

Centre for Self-Organising Molecular
Systems, University of Leeds LS2 9JT,
United Kingdom

Ettore Castiglioni

JASCO EUROPE srl, via Confalonieri 25,
23894 Cremella, Italy

Buddhapriya Chakrabarti

Department of Physics, University of
Massachusetts, Amherst, MA 01003,
USA

buddho@physics.umass.edu

Bani H. Cipriano

Department of Chemical Engineering,
University of Maryland, College Park,
MD 20742, USA

Moumita Das

Department of Physics, Indian Institute of
Science, Bangalore 560 012, India
moumita@physics.iisc.ernet.in.

Chandan Dasgupta

Department of Physics, Indian Institute of
Science, Bangalore 560 012,
India
cdgupta@physics.iisc.ernet.in

Patrick Davidson

Laboratoire de Physique des Solides, Bât.
510, UMR 8502 CNRS, Université
Paris-Sud 91405 Orsay Cedex, France
davidson@lps.u-psud.fr

Luigi Dei

Department of Chemistry & CSGI
Consortium, University of Florence, via
della Lastruccia, 3, I-50019 Sesto
Fiorentino, (Florence) Italy
dei@apple.csgi.unifi.it

André Del Guerzo

Photochemistry for Nanoscience, CNRS
UMR 5802, Université Bordeaux 1, 351
cours de la Libération, 33405 Talence,
France

Jean-Pierre Desvergne

Laboratoire de Chimie Organique et
Organométallique, UMR 5802, CNRS
Université Bordeaux 1, 33405
TALENCE Cedex, France
jp.desvergne@lcoo.u-bordeaux1.fr

Dganit Danino

Department of Biotechnology and Food
Engineering, Technion-Israel Institute
of Technology, Haifa 32000, Israel
dganitd@technix.technion.ac.il

Jan H. van Esch

Organic and Molecular Inorganic
Chemistry, Stratingh Institute,
University of Groningen Nijenborgh 4,
9747 AG Groningen, The Netherlands
J.van.Esch@chem.rug.nl

Lara A. Estroff

Department of Chemistry, Yale University,
PO Box 208107, New Haven,
CT 06520-8107, USA
lestroff@gmwgroup.harvard.edu

Frédéric Fages

UMR CNRS 6114, Université de la
Méditerranée, Faculté des Sciences de
Luminy, 13288 Marseille Cedex 9,
France
fages@luminy.univ-mrs.fr

Ben L. Feringa

Organic and Molecular Inorganic
Chemistry, Stratingh Institute,
University of Groningen Nijenborgh 4,
9747 AG Groningen, The Netherlands
b.l.feringa@rug.nl

Arianna Friggeri

BiOMaDe Technology Foundation,
Nijenborgh 4, 9747 AG Groningen,
The Netherlands
A.Friggeri@chem.rug.nl

Jürgen-Hinrich Fuhrhop

Freie Universität Berlin, FB Biologie,
Chemie, Pharmazie, Institut für
Chemie/Organische Chemie, Takustr. 3,
D-14195 Berlin, Germany
fuhrhop@chemie.fu-berlin.de

Norifumi Fujita

Department of Chemistry and
Biochemistry, Graduate School of
Engineering, Kyushu University 6-10-1
Hakozaki, Higashi-ku, Fukuoka
812-8581, Japan
nftjctm@mbbox.nc.kyushu-u.ac.jp

Mathew George

Department of Chemistry, Georgetown
University, Washington, D.C.
20057-1227, USA
mg49@georgetown.edu

Jeroen van Gestel

Eindhoven Polymer Laboratories,
Eindhoven University of Technology,
PO Box 513, 5600 MB Eindhoven,
The Netherlands
jvggestel@home.nl

Giovanni Gottarelli

Alma Mater Studiorum – Università di
Bologna, Dipartimento di Chimica
Organica “A. Mangini”, Via San
Giacomo 11-40126 Bologna, Italy
gottarel@alma.unibo.it

Andrew D. Hamilton

Department of Chemistry, Yale University,
PO Box 208107, New Haven,
CT 06520-8107, USA
Andrew.Hamilton@yale.edu

Rifat A.M. Hikmet

Philips Research, Prof. Holstlaan 4,
5656 AA, Eindhoven, The Netherlands
rifat.hikmet@philips.com

Jaap J.D. de Jong

Organic and Molecular Inorganic
Chemistry, Stratingh Institute,
University of Groningen Nijenborgh 4,
9747 AG Groningen, The Netherlands
J.J.D.de.Jong@chem.rug.nl

Matthias Lauer

Freie Universität Berlin, FB Biologie,
Chemie, Pharmazie, Institut für
Chemie/Organische Chemie, Takustr. 3,
D-14195 Berlin, Germany

T.C.B. Mcleish

Centre for Self-Organising Molecular
Systems, Department of Physics and
Astronomy, and School of Chemistry,
University of Leeds LS2 9JT, United
Kingdom

Elise Lorenceau

Laboratoire de Physique de la Matière
Condensée, URA 7125 du CNRS,
Collège de France, 75231
Paris Cedex 05, France
elise.lorenceau@univ-mlv.fr

Uday Maitra

Department of Organic Chemistry, Indian
Institute of Science, Bangalore 560 012,
India
maitra@orgchem.iisc.ernet.in

M.A.J. Michels

Eindhoven Polymer Laboratories,
Eindhoven University of Technology,
PO Box 513, 5600 MB Eindhoven,
The Netherlands

Samrat Mukhopadhyay

Department of Organic Chemistry, Indian
Institute of Science, Bangalore 560 012,
India
samrat@tifr.res.in

I.A. Nyrkova

Institute Charles Sadron, 67083 Strasbourg,
France

Reiko Oda

Institut Européen de Chimie et Biologie,
UMR CNRS 5144 Molécules,
Biomolécules et Objets
Supramoléculaires (MOBIOS), 2 rue
Robert Escarpit – 33607 PESSAC
Cedex, France
r.oda@iecb.u-bordeaux.fr

Jean-Luc Pozzo

Photochemistry for Nanoscience, CNRS
UMR 5802, Université Bordeaux 1, 351
cours de la Libération, 33405 Talence,
France
jl.pozzo@lcoo.u-bordeaux1.fr

David Quere

Laboratoire de Physique de la Matière
Condensée, URA 7125 du CNRS,
Collège de France, 75231
Paris Cedex 05, France
quere@ext.jussieu.fr

Srinivasan R. Raghavan

Department of Chemical Engineering,
University of Maryland, College Park,
MD 20742, USA
sraghava@eng.umd.edu

Sriram Ramaswamy

Department of Physics, Indian Institute of
Science, Bangalore 560 012, India
sriram@physics.iisc.ernet.in

Jörn W.P. Schmelzer

Rostock University, Universitätsplatz,
18051 Rostock, Germany
juern-w.schmelzer@physik.uni-rostock.de

Paul van der Schoot

Eindhoven Polymer Laboratories,
Eindhoven University of Technology,
PO Box 513, 5600 MB Eindhoven,
The Netherlands
p.p.a.m.v.d.schoot@tue.nl

A.N. Semenov

Institute Charles Sadron, 67083 Strasbourg,
France

Tim Senden

Department of Applied Mathematics,
Research School of Physical Sciences
and Engineering, The Australian
National University, Canberra, ACT
0200 Australia
tim.senden@anu.edu.au

Seiji Shinkai

Department of Chemistry and
Biochemistry, Graduate School of
Engineering, Kyushu University 6-10-1
Hakozaki, Higashi-ku, Fukuoka
812-8581, Japan
seijitcm@mbox.nc.kyushu-u.ac.jp

Peter Sollich

Department of Mathematics, King's
College London Strand, London WC2R
2LS, United Kingdom
peter.sollich@kcl.ac.uk

Ajay K. Sood

Department of Physics, Indian Institute of
Science, Bangalore 560 012, India
asood@physics.iisc.ernet.in

Gian Piero Spada

Alma Mater Studiorum – Università di
Bologna, Dipartimento di Chimica
Organica “A. Mangini”, Via San
Giacomo 11-40126 Bologna, Italy
GianPiero.Spada@unibo.it

Aasheesh Srivastava

Department of Organic Chemistry, Indian
Institute of Science, Bangalore 560 012,
India

Yeshayahu Talmon

Department of Chemical Engineering,
Technion-Israel Institute of Technology,
Haifa 32000, Israel
ishi@technix.technion.ac.il

Fumihiko Tanaka

Department of Polymer Chemistry, Kyoto
University, Katsura, Nishikyo-ku,
Kyoto, 615-8510, Japan
ftanaka@phys.polym.kyoto-u.ac.jp

Pierre Terech

UMR5819, CEA-Grenoble,
DRFMC-SI3M-PCM, 17, rue des
Martyrs, 38054, Grenoble Cedex 9,
France
pterech@cea.fr

Richard G. Weiss

Department of Chemistry, Georgetown
University, Washington, D.C.
20057-1227, USA
weissr@georgetown.edu

Tianyu Wang

Freie Universität Berlin, FB Biologie,
Chemie, Pharmazie, Institut für
Chemie/Organische Chemie, Takustr. 3,
D-14195 Berlin, Germany

INTRODUCTION

Richard G. Weiss¹ and Pierre Térech²

¹*Department of Chemistry, Georgetown University, Washington, DC 20057-1227, USA*

²*UMR5819 CEA-CNRS-Université J. Fourier, DRFMC-SI3M-PCM, CEA-Grenoble 17, rue des Martyrs, 38054 Grenoble Cedex 9, France*

It has been eight years since the editors of this book decided to review the state of the art in a burgeoning field, “molecular gels” and their “self-assembled fibrillar networks” (SAFINs) in which the agents for gelation, low molecular-mass organic gelators (LMOGs), are differentiated from molecules which polymerize during gelation and lead to mostly inorganic networks (e.g., sol-gel glasses) [1]. The rapid growth of interest in “molecular gels” since 1990 is indicated by Figure 1 in which the number published articles in the Web of Science[®] that use the term “organogel” or “hydrogel” in their titles, keywords, or abstracts is plotted by year. The plot of the “organogel” data alone is included to demonstrate that its rate of rise surpasses that of even hydrogels. An analogous plot, demonstrating the rise in interest in “molecular hydrogelators” over a much longer period, is included as Figure 1 of Chapter 17. The actual number of publications per year dealing with “organogels” and “hydrogels” is much larger than shown because many articles devoted to the subject do not use either of these terms, and “molecular gels” are referred to by several other names. More importantly, the numbers do not provide an assessment of the enormous advances in our understanding of the subject that has occurred during the intervening years. Regardless, the increased attention paid to molecular gels and SAFINs is apparent, and the pace of discovery shows no signs of slowing. Although many books have been written about gels and their properties, virtually all are devoted to aqueous or organic polymeric gels and their applications, mostly in the food, cosmetic, and pharmaceutical industries [2], and we have been able to find no book devoted to molecular gels or SAFINs. The rise in interest in the field and its rapid development make this a propitious moment to bring together the vast amounts of information that have been accumulating. In this book, we attempt to place that information in

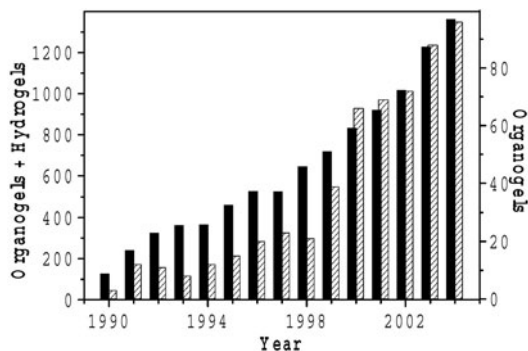


Figure 1. Number of articles per year found in “The Web of Science” in which “organogel” or “hydrogel” (solid columns) or only “organogel” (shaded columns) appears in the title, key word index, or abstract.

a framework that will be useful as a reference for scientists already active in the field and as a guide for those interested in learning about it.

Initial attempts to develop an outline for the book confirmed what others and we have known for some time – to present a comprehensive picture of molecular gels and SAFINs, or even to attempt to do so – requires inputs from scientists in diverse fields. The authors of the chapters are a testimonial to this assertion. They include chemists, engineers, spectroscopists, physicists, biologists, theoreticians, and material scientists; the editors are a physicist and a chemist. The subject, molecular gels, has given us a common forum to discuss the complex issues dealing with them from a myriad of perspectives; Mother Nature defines the problems and we work piece-meal to find the solutions. We have tried to integrate those pieces as much as possible so that the interdisciplinary nature of the approaches to studying and understanding molecular gels and SAFINs is apparent to the reader. The parable about the blind men and the elephant may be an applicable analogy.

The different aspects of molecular gels and SAFINs – their theory, techniques for investigating them, their different types, and their applications – are treated by sections in the order shown. Each chapter delves into one or more aspects of one of the topics in a didactic way. By design, and as a logical consequence of the multi-disciplinary approaches needed to study molecular gels, several topics are treated in more than one chapter, but from different perspectives. Our objective is to present methodologies and perspectives rather than reviews. The chapter authors have been selected carefully for their expertise in the areas they treat and for their ability to relate them to the “total picture”; we wish to reveal the true nature of “the elephant” for all to see and admire.

Before proceeding further, we address a fundamental, but not simple, question: “What is a molecular gel?” To start, we will try to answer the broader

question, “What is a gel?”, and then narrow the classification eventually to “molecular gels”. Gels are very diverse systems chemically and they are not easily defined in a few words. In 1861, Thomas Graham tried to describe gels: “While the rigidity of the crystalline structure shuts out external expressions, the softness of the gelatinous colloid partakes of fluidity, and enables the colloid to become a medium for liquid diffusion, like water itself” [3]. He continued, “The colloid possesses *ENERGIA*. It may be looked upon as the probable primary source of the force appearing in the phenomena of vitality.” [3] Given the analytical tools at his disposition, Graham had no recourse except to use descriptive and macro-structural terms; as “Master of the Mint” at the time, he may have felt entitled to a bit of speculation about *ENERGIA*. One may assume that he was referring to the ability of a colloidal suspension to undergo structural changes when it is not at equilibrium, or he may have had more metaphysical ideas in mind! Sixty-five years later, Dr. Dorothy Jordon Lloyd wrote, “The colloid condition, the “gel,” is one which is easier to recognize than to define.” [4] Then, she went on to state, “Only one rule seems to hold for all gels, and that is that they must be built up from two components, one of which is a liquid at the temperature under consideration, and the other of which, the gelling substance proper, often spoken of as the gelator, is a solid. The gel itself has the mechanical properties of a solid, i.e., it can maintain its form under the stress of its own weight, and under any mechanical stress, it shows the phenomenon of strain.” The latter definition addresses structural aspects of gels *and* comments on their viscoelastic properties. The former definition is an enigmatic dictum, but when adopted by an experimentalist looking for a quick determination of what is and what is not a gel, it is very useful even though it is inaccurate, of course – not all gels are colloidal and not all colloids are gels! [5]. All of these definitions reflect the continued limited ability of scientists of the era to analyze complex materials. By 1949, our understanding of gels had progressed to the point where Hermans maintained that gels: “(a) . . . are coherent colloid disperse systems of at least two components, (b) . . . exhibit mechanical properties characteristic of the solid state. . .,” and “(c) both the dispersed component and the dispersion medium extend themselves continuously throughout the whole system.” [6] Still, Ferry recognized that the complexity of gels and gel types might obviate the utility of a detailed encompassing definition. Thus, he offered a less rigorous and more descriptive one: “[A gel] is a substantially diluted system which exhibits no steady state flow.” [7] In a sense, this definition is a “retreat,” a capitulation to the realization gleaned from detailed structural and rheological investigations that gels are just diverse and complex! Finally, Webster’s Third New International Dictionary defines a gel as “a colloidal in a more solid form than a sol: as **a**: a semisolid apparently homogeneous substance that may be elastic and jelly-like (as gelatin) or more or less rigid (as silica gel) and that is formed by coagulation of a sol in various ways. . . .” [8] This definition is not intended to describe molecular gels! Several other definitions of gels which

have appeared in the literature are much more sophisticated, but their complexity makes them difficult to apply in daily practice. For screening purposes, at least one of the editors of this book ascribes to the Lloyd philosophy: “... if it looks like ‘Jell-O’, it must be a gel!” [1]

Each of the more sophisticated definitions attempts to link the microscopic and macroscopic properties of a gel [9–11]. Based on these definitions, one can classify a substance as a gel if it (1) has a continuous microscopic structure with macroscopic dimensions that is permanent on the time scale of an analytical experiment and (2) is solid-like in its rheological behavior despite being mostly liquid. Much more precise and detailed explanations of what is a gel and, especially, what is a molecular gel, will be provided within the chapters of this book. There are several subclasses of gels, and each meets both of these basic criteria. Flory suggested four different types of gels [10, 12]:

1. Those with well-ordered lamellar structures. Some of these are lyotropic liquid-crystalline phases.
2. Those with cross-linked polymeric networks swollen with solvent. In these phases, the polymer chains are disordered.
3. Those with polymer networks in which the chain-chain interactions are physical. The chains may be predominantly disordered, but regions of local order (especially where inter-chain interactions occur) may also exist.
4. Those with particulate disordered structures. They include materials in which the gel networks are comprised of fibrils and are the focus of this book.

For instance, polymer gels are “... cross-linked networks of polymers swollen with a liquid,” [2d] and sol-gel glasses are 3-dimensional matrices of crystalline or amorphous solids with honey-combed channels. As such, their microscopic networks are present at all times and at all temperatures (below those at which irreversible decomposition occurs). Especially for polymers in which interchain attractions are based on electrostatic (N.B., polyelectrolytes) or H-bonding (N.B., poly-*N*-alkylacrylamides) interactions, network (and, therefore, gel) stability can depend on temperature, pH, the nature of the liquid, and even the history of the material. However, bonding within the polymer chains does not; such systems start with one dimension of molecular assembly, the covalent linkage of monomers within each polymer chain.

In molecular gels, supramolecular aggregation and corresponding SAFIN formation usually occur when a solution or sol (i.e., “a fluid colloidal system: as **a**: a dispersion of solid particles in a liquid colloid solution ...” [8]) of a low concentration of gelator molecules (frequently $\lesssim 2$ wt. %, representing the percolation concentration threshold of the fibrillar species) in an appropriate liquid is cooled below its characteristic gelation temperature (T_g). In this

super-saturated concentration regime, microscopic phase separation occurs, rather than the macroscopic phase separation common to crystallization processes (where a bulk solid and liquid are visible to the naked eye). Instead, the gelator molecules self-assemble in stochastic nucleation events involving highly specific interactions that allow preferential one-dimensional growth, usually to form fibers that are frequently crystal-like; they serve the function of the polymer chains in polymer gels. The “junction zones” [13] between fibers, whose shapes may be in the form of strands, tapes, chiral ribbons, tubules or other aggregates with very large aspect ratios (see Chapters 2, 3, 14, 16, and 22), provide rigidity to the microstructure. They are the “glue” that distinguishes the three-dimensional networks of gels from an aggregate of one-dimensional fibrillar objects that do not interact. The resulting network of microscopic or nanoscopic objects with high aspect ratios (and, in many cases, mono-disperse cross-sections) interact to form the three-dimensional porous lattice that permeates the volume of the sample, encapsulating the liquid component and inhibiting its flow. Thus, solids or other aggregates (N.B., giant worm-like micelles; see Chapters 6 and 19) in these gels differ from common crystals, for which the ratio of dimensions of small and large crystals is usually nearly constant. In addition, crystalline morphs in the fibrils may be the same as or different from those in the single crystals of the constituent LMOG molecules (see Chapter 11). Fortunately, the rod-like species can be characterized by techniques in real space (see Chapter 9) or reciprocal space (see Chapter 10).

The interactions holding together individual strands as well as the junction zones that link different strands of most SAFINs are non-covalent and considerably weaker than covalent bonds. The natures of these secondary interactions depend mainly on the structure of the gelator molecules, but they can run the gamut from hydrogen bonds to weaker London dispersion forces, and the liquid part of the gel can be instrumental by either promoting or discouraging interactions among SAFINs (see Chapters 1 and 7). As mentioned above, gelators can be organic or inorganic. When they are inorganic, the SAFINs frequently (but certainly not always; N.B., laponite gels) are formed irreversibly because aggregation is accompanied in those cases by new covalent bonds. Non-covalent interactions among constituent low molecular-mass organic gelators (for the purpose of this book, molecules of $\lesssim 2000$ Daltons that are basically organic in their structures) are more common (see Chapter 14). They lead to SAFINs that can be repeatedly disassembled upon heating the gels and reassembled upon cooling their solutions (or sols). The relationships between the molecular structure of the LMOG and the ability to form rod-like structures are still topics of active investigation and speculation. They involve very subtle balances between opposing parameters, such as those controlling the solubility in a given liquid and those that trigger the epitaxial growth into axially symmetric elongated aggregates (see Chapter 4). At a larger length scale, the attractiveness

of the potential between the rod-like species will influence the relative amounts of SAFIN bundles and ends as well as the degree of homogeneity of the mesh size.

In a few cases, the network appears to consist of branches in the fibrillar assembly that provides a self-similar pattern, enabling the use of fractal descriptions (see Chapter 9). Also, some static or semi-static properties of worm-like aggregates formed by LMOGs can exhibit very specific rheological (in the linear and non-linear regimes) and structural features that appear like those of polymers, especially breakable “equilibrium polymers” (see Chapter 19). The concepts that have been invoked to explain surfactant interactions and discrete polymer domains are also applicable when considering theoretical frameworks to derive phase diagrams that start from a conventional lattice description to a refined cascade theory of gelation (see Chapter 1).

The nature of a SAFIN and the manner in which its constituent LMOG molecules aggregate are very sensitive to the properties of the liquid being gelled (see Chapters 7 and 14). The liquid may be aqueous (resulting in a *hydrogel*; see Chapters 16 and 17) or organic (resulting in an *organogel*; see Chapter 14). Due to the nature of the non-covalent interactions responsible for the stabilization of the SAFINs, both types of molecular gels are classified as physical, and LMOGs that gelate both organic and aqueous media are termed “amphiphilic” (see Chapters 15–17). Liquid is trapped within the SAFIN network, essentially stopping macroscopic flow (see Chapter 7). However, it has been recognized for nearly a century that the vast preponderance of the liquid molecules are able to diffuse, in some cases, as though the gel network is not present [4, 14]. When heated to temperatures exceeding T_g , the networks of the reversibly-formed gels disassemble and the sample becomes free-flowing again. In some cases, the liquid component of a molecular gel can be removed without disassembling the SAFIN structures. Lyophilization, slow evaporation, and careful liquid replacement (with a very volatile species, such as supercritical CO_2) are examples of strategies that have been employed to isolate a SAFIN. The network so obtained may or may not be the same structurally and morphologically as the one within the gel. Many LMOGs are polymorphous and can undergo a phase transition during removal of the liquid from the gel. In addition, the network may collapse onto itself in the absence of liquid, resulting in a *xerogel*. If the network does not collapse, an *aerogel* is obtained.

A wide variety of rheological behaviors and structures has already been found in these physical gels, and they range from those associated with soft viscoelastic solids to “equilibrium polymers” (see Chapters 5, 6, and 19) and nematic-like gels (see Chapters 3, 6, 19, and 21). Each presents a spectrum of degrees of ordering in the basic units and/or junction zones of the SAFINs (see Chapter 9). Under certain circumstances, a rheological chaos in sheared systems is also found to be spatio-temporally dependent (see Chapter 6). Although a great deal of attention has been paid to the structures and rheological properties

of gels, very little attention has been paid to the dynamics of assembly of SAFINs in gels. Two noteworthy approaches to express the dimensionality and kinetics of growth employ the Avrami equation or are related to it [15], and a fractal model that is closely related in form to the Avrami equation [16] (see Chapter 4).

Some forms of fibrils can be stabilized by twisting individual supramolecular aggregates of rod-like chiral species. The competition between opposing interaction energies may restrict the growth of the fibrils to finite cross-sectional dimensions (see Chapter 3). Bending and twisting mechanisms are opposing packing constraints and contribute to the existence of a hierarchical self-aggregation process. The relation and the reversible tunability between molecular and supramolecular chirality is of fundamental and applied importance (see Chapters 15–17) [17]. In this regard, chiral molecules can self-assemble into chiral membranes (see Chapters 2 and 3). Variations in the direction of molecular tilt and in the curvature can induce the formation of helical ribbons that behave as unstable intermediate states along a protracted process leading to tubules. In turn, gels with tubular morphologies may have specific orientations and flow characteristics.

Despite the crystalline natures of many SAFIN fibers, they are able to bend somewhat as a result of their very large aspect ratios! These assemblies *on the micro- and nano-scales* have the same mechanical properties designed by architects and engineers [18] to protect skyscrapers from crumbling during earthquakes. The link between this characteristic at different size scales has been recognized and discussed in general terms for many centuries [19, 20]. Of course, Mother Nature has exploited SAFIN-like structures to impart unique properties to many macrobiological systems. Examples include fibrous actin [21] and clathrin [22], tubulin [23], keratin [24], insulin [25], collagen gels [26], silk processing by insects and spiders [27], amyloid fibrils that have been implicated in Alzheimer's and other neurodegenerative diseases [28], sickle cell anemia hemoglobin in its deoxy state [29], and fibrinogen, the blood clotting factor [23a, 30]. One can envision that, one day, SAFIN structures of molecular gels will be designed to direct and use the work done by biological "motors" such as kinesin and myosin [31].

The specific properties of a gel may depend upon its history and method of formation, the temperature at which it is kept, its age (because many molecular gels are not thermodynamically stable and undergo phase separation or SAFIN changes with time), LMOG concentration, and liquid type (see Chapter 4). The compromise between attractive and repulsive interactions in SAFINs is subtle and key to the metastability of the molecular gels. This issue is also very important in determining the nature of the gel obtained since the organized structures in molecular gels are observed only after having moved the system far from equilibrium. Although these perturbations are accomplished usually by heating the system, they can be effected mechanically (as in the

case of thixotropic gels; *vide infra*), by irradiation, or by addition of a chemical agent. It is amazing then that gelation follows a supercritical entropy export that directs the self-assembly process into well-organized structures on the nanoscale.

For these reasons, the stability of a gel is difficult to define as well because several criteria may be used, depending on one's perspective and interests:

- (1) T_g is a popular stability criterion when temperature is most important.
- (2) The lifetime of a gel at room temperature may be featured when long-term applications are sought. Some gels are stable for a few hours while others are stable for at least several decades.
- (3) The critical gelator concentration (cgc; that is, the lowest concentration of an LMOG providing a gel at room temperature) is a useful monitor when maximizing the liquid content is important.
- (4) Rheological criteria involving the magnitudes and ratios of the elastic (G') and loss (G'') moduli and viscosity are probably the most useful and physically quantifiable criteria (see Chapter 8). They allow a differentiation between a "true" gel and a jelly. However, analyses of the relations between the strain and stress tensors in such systems reveal that the choice of the most appropriate theoretical context to describe the mechanical properties is still not clear and depends upon the type of SAFIN that is generated from a specific gelator/liquid mixture. Thus, SAFINs have rheological behaviors that can be described as cellular solids, fractal or colloidal systems, or soft glassy materials (see Chapter 5).

In addition to the above considerations, many other physical properties have not yet been explored extensively and certainly deserve close scrutiny. For instance, the hindered dynamics of probes or non-connected components in SAFINs, the "mapping" of heterogeneities and domains in SAFINs, the reversibility of the properties in sol-gel transitions, and the control of the tunability of some structural features are additional avenues of future investigation to gain deeper scientific insights about the stabilities and properties of molecular gels.

Thixotropic gels become flowing liquids if mechanically disturbed by stirring or shaking and then return to their non-flowing gel state again if allowed to stand undisturbed [32]. An early and interesting example of a thixotropic molecular gel is comprised of <5.5 wt% cholesterol as the LMOG and isopropyl alcohol as the liquid [33]. Subsequent studies with substituted steroids have led to discovery of many diverse gels and SAFIN structures (see Chapters 14 and 15). We know of no thixotropic gels that exhibit *rheopexy* (i.e., the accelerated gelation of a thixotropic sol brought about by jarring the containing vessel, by slow stirring, or by pouring" [8]). However, many exhibit syneresis

or Ostwald ripening (i.e., some shrinkage that expels a bit of liquid with time as the population of smaller aggregates decreases and larger aggregates grow).

Different forms of gels, including molecular gels, are common in everyday life. Their applications range from personal care products (toothpaste, shampoo, deodorants, etc.) to foodstuffs (puddings, syrups, etc.) to electronic devices to drug delivery and tissue engineering [34]. Many of these will be discussed in the *Applications* section of the book and others can be found in the books listed in Ref. 2. Perhaps the extremes are represented, on the one hand, by the delicate application of gels to the surfaces of oil paintings in art restoration (see Chapter 27) or the weaving of a spider's web [35] and the massive pumping of gels into oil wells to increase the efficiency of crude oil recovery [36] on the other. In some cases, gels have been used for destructive purposes, as in the gelation of gasoline to make napalm [37]. Vision in animals depends on two hydrogels, the vitreous humor (the transparent, mass in front of the retina that fills the eyeball) and stroma (the thickest layer of tissue in the cornea) of eyes [38]. A wonderful "bubble" tea is made from the gelled seeds of *Hyptis suaveolens* (L.) Poir, an herbal medicine whose common Chinese name, *san-fan-yuan*, translates as "mountain powder ball" [39]. It is used as a treatment for colds, diarrhea, cuts, etc. The chemicals in the plant include friedelin, lupeol, lupeolacetate, hentriacontane, hentriacotanone, urs-12-en-3 β -ol-29-oic acid, hyptadienic acid, 1,19a-dihydroxy-urs-2(3),12-dien-28-oic acid, amyirin, 3 β -hydroxylup-12-en-28-oic acid, 3p-hydroxylup-20(29)-en-27-oic acid, ursolic acid, betulic acid, sitosterol- β -D-glucoside, heptacosanone, campesterol, β -caryophyllene, and myrcene. Some rather popular gastronomic collagen-based gels include the aforementioned "Jell-O" [40] (eaten by the US editor) and aspic (consumed by the French editor).

Finally, we end this introduction with a short and somewhat biased history of gels [41]. Perhaps the first formal scientific molecular hydrogel "sighting" dates from 1841 when Lipowitz reported the gelation of aqueous solutions by lithium urate [42]. Thixotropic hydrogels have been implicated in a much earlier and more controversial and bloody application dating from the 14th century [43]. An early (if not the first) scientific study of thixotropy was part of a larger investigation of the magneto-optical properties of colloidal ferric hydroxide systems [44]. Thomas Graham's account of the gel and jelly states of aqueous (and alcoholic) mixtures of silicic acid and several other metallo acids in 1864 [45] is a classic precursor of the now well-established sol-gel chemistry.

In 1871, in a letter to the *British Journal of Photography* entitled, "An Experiment with Gelatino Bromide," Richard Leach Maddox, an English physician, introduced the concept of "dry" gelatin plates with silver salts for photography [46]. The plates increased the sensitivity of the salts to light (lowering light exposure times) and avoided the necessity of immediate development after

exposure. Subsequently, George Eastman coated silver halide dispersions in gelatin onto cellulose nitrate rolls of film, and placed the film in a camera [47]. His product, the Kodak system, permitted 100 photographs to be recorded before the film was developed and printed at the Rochester, NY factory. Thus began photochemistry for the masses! Raphael Liesegang also investigated hydrogels of gelatin and other substances for many years, and, as early as 1896, reported on reactions of molecules, as well as their diffusion and crystallization, in gels [48].

An early 20th century account describes the gelation of aqueous and alcoholic liquids by fatty acid salts, and notes that this phenomenon was known in the 19th century [49]. This paper, one published contemporaneously by Hatschek [50], and another published by Hardy more than a decade before [51] are noteworthy for several reasons. One is the inclusion and/or discussion of microscopic images of the networks of several gels. Another yet earlier publication by Hardy describes a separation by gel electrophoresis! [52] Even in that period, the definition of a gel was controversial and somewhat contentious [53]. Organogels using camphoryl thioisemicarbazide as the LMOG were made in 1907 by Foster and Jackson [54] and characterized later by Hatschek [50]. In the late 19th century, Meunier discovered gels of 1,3:2,4-di-O-benzylidene-D-sorbitol, a widely used LMOG today [55]. Hardy reported the properties of thermally-reversible LMOG gels in 1912 [56].

As the field of colloids and gels became somewhat established, several books that attempted to collect and categorize the many observations were published. One of the earliest was “The Chemistry of Colloids” by Zsigmondy and Spear [57]. More recently, cross-linked hydrogels of polymethacrylic acid were observed to expand and contract as a function of pH. The article in which the properties of these hydrogels appeared [58] contains a prophetic remark given the interest today in artificial muscles: “. . . it is possible to realize on a macroscopic scale the stretching and coiling of charged macromolecules, and that it is possible by means of these systems, to transform chemical energy into mechanical energy.” Subsequent developments have led to several different gel systems, most of which are based on polymeric gellants, that respond mechanically, physically, or electronically to a variety of stimuli (see Chapters 23, 24 and 26).

Serious attempts to formulate a theoretical basis for how rod-shaped objects aggregate into colloids and, in some cases, result in gels were made perhaps initially by von Weimarn [59] and Hardy [60], starting in the first decade of the 20th century. They were expanded upon in the 1930’s and 1940’s by Langmuir and Onsager, amongst others [61]. Those efforts are ongoing [62], as witnessed by the expositions in the section of the book entitled *Theory*, and will be in the foreseeable future!

References

- [1] Terech, P.; Weiss, R.G. *Chem. Rev.*, **1997**, *97*, 3133–3159.
- [2] For some of the more recent examples, see: (a) Osada, Y.; Kajiwara, K., Eds., *Gels Handbook*, San Diego: Academic Press, 2001+, vols 1–4. (b) Bohidar, H.B.; Dubin, P.; Osada, Y.; Eds., *Polymer gels: fundamentals and applications* (ACS Symposium Series #833); Washington, DC: American Chemical Society, **2003**. (c) Russo, P.R., Ed., *Reversible polymeric gels and related systems* (ACS Symposium Series #350), Washington, DC: American Chemical Society, **1987**. (d) Dusek, K., Ed., *Responsive gels: volume transitions* (*Adv. Polym. Sci. series*); New York: Springer-Verlag, **1993**, vols 109,110. (e) Dickinson, E., Ed., *Food polymers, gels and colloids* Cambridge: Royal Society of Chemistry, **1991**. (f) Henisch, H.K.; *Crystals in gels and Liesegang rings: in vitro veritas*; University Park: Cambridge University Press, **1970**. (g) K. te, Nijenhuis, *Thermoreversible networks: viscoelastic properties and structure of gels*; New York: Springer, **1997**. (i) Peppas, N.A., Ed.; *Hydrogels in medicine and pharmacy*; Boca Raton, Fla.: CRC Press, **1986–1987**, vols 1–3.
- [3] Graham, T. *Phil. Trans. Roy. Soc.*, **1861**, *151*, 183–224.
- [4] Jordan Lloyd, D. In *Colloid Chemistry*; Alexander, J., Ed., New York: The Chemical Catalog Co., **1926**; vol 1, p. 767–782.
- [5] In a somewhat dated but rather descriptive definition, Dean stated [5a], “Colloid chemistry deals with particles which are so small that they behave in some respects like molecules, and with molecules that are so large that they behave in some respects like particles.” (a) Dean, R.B. *Modern Colloids*; New York: D. Van Nostrand Co., **1948**, p. 2.
- [6] Hermans, P.H. In *Colloid Science*; vol II; Kruyt, H.R., Ed., Amsterdam: Elsevier, **1949**, Chapter XII (p. 484).
- [7] Ferry, J.D. *Viscoelastic Properties of Polymers*, New York: Wiley, **1961**, p 391.
- [8] *Webster’s Third New International Dictionary* (Unabridged), Springfield, MA: Merriam-Webster, Inc., **1993**.
- [9] Ref 6, p. 483.
- [10] Flory, P. J. *Discuss Faraday Soc.*, **1974**, *57*, 7–18.
- [11] Gelbart, W.M.; Ben-Shaul, A. *J. Phys. Chem.*, **1996**, *100*, 13169–13189.
- [12] Twenty-five years earlier than Flory, four slightly different types of gel network structures, based on colloidal concepts, were suggested by Kruyt [12a] and Hermans [6]. (a) Kruyt, H.R. in *Colloid Science*; Vol I; Kruyt, H.R., Ed., Amsterdam: Elsevier, **1952**, Chapter I.
- [13] Terech, P.; Furman, I.; Weiss, R.G. *J. Phys. Chem.*, **1995**, *99*, 9558–9566.
- [14] Bechhold, H.; Ziegler, A.Z. *physik. Chem.*, **1906**, *56*, 105–121.
- [15] (a) Terech, P. *J. Colloid and Interface Science*, **1985**, *107*, 244–245. (b) Huang, X.; Terech, P.; Raghavan, S.R.; Weiss, R.G. *J. Am. Chem. Soc.*, **2005**, *127*, 4336–4344.
- [16] (a) Liu, X.Y.; Sawant, P.D. *Appl. Phys. Lett.*, **2001**, *79*, 3518–3520. (b) Liu, X.Y.; Sawant, P.D. *Adv. Mater.*, **2002**, *14*, 421–425.
- [17] Spector, M.S.; Selinger, J.V.; Schnur, J.M. in *Materials-Chirality (Topics in Stereochemistry*; vol 24); Green, M.M.; Nolte, R.J.M.; Meijer, E.W., Eds.; Hoboken: Wiley **2003**, pp. 281–372.
- [18] See for instance the architecture and sculpture art of Buckminster Fuller and Kenneth Snelson for applications of the concept of “tensegrity” [19].
- [19] Ingber, D.E. *Sci. Amer.*, **1998**, *278*, 48–57.
- [20] Thompson, D.W. (Bonner, J.T., Ed.) *On Growth and Form*; London: Cambridge University Press, **1961**, and references cited therein to treatises by Galileo, amongst others.

- [21] Greer, S.C. *Ann. Rev. Phys. Chem.*, **2002**, *53*, 173–200.
- [22] Kirchhausen, T. *Ann. Rev. Biochem.*, **2000**, *69*, 699–727.
- [23] (a) Tuszyński, J.A.; Brown, J.A.; Sept, D.J. *Biol. Phys.*, **2003**, *29*, 401–428. (b) Oakley, B.R.; Akkari, Y.N. *Cell Struct. Funct.*, **1999**, *24*, 365–372.
- [24] (a) Fuchs, E. *Ann. Rev. Cell Dev. Biol.*, **1995**, *11*, 123–153. (b) Smack, D.P.; Korge, B.P.; James, W.D. *J. Am. Acad. Dermatol.*, **1994**, *30*, 85–102.
- [25] (a) Waugh, D.F. *J. Am. Chem. Soc.*, **1946**, *68*, 247–250. (b) Jimenez, J.L.; Nettleton, E.J.; Bouchard, M.; Robinson, C.V.; Dobson, C.M. *Proc. Natl. Acad. Sci. USA*, **2002**, *99*, 9196–9201.
- [26] (a) Caria, A.; Bixio, L.; Kostyuk, O.; Ruggiero, C. *IEEE Trans. Nanobiosci.*, **2004**, *3*, 85–89. (b) Wallace, D.G.; Rosenblatt, J. *Adv. Drug Deliv. Revs.*, **2003**, *55*, 1631–1639.
- [27] (a) Jin, H.-J.; Kaplan, D.L. *Nature* **2003**, *424*, 1057–1061. (b) Valluzzi, R.; Jin, H.-J.; Park, J. *PCT Int. Appl. WO 2004 41,845* (Cl. C07K), 21 May 2004.
- [28] (a) Jimenez, J.L.; Nettleton, E.J.; Bouchard, M.; Robinson, C.V.; Dobson, C.M.; Saibil, H.R. *Proc. Natl. Acad. Sci. USA*, **2002**, *99*, 9196–9201. (b) Liu, W.; Prausnitz, J.M.; Blanch, H.W. *Biomacromol.* **2004**, *5*, 1818–1823. (c) Nilson, M.R. *Methods* **2004**, *34*, 151–160. Waterhouse, S.H.; Gerrard, J.A. *Aust. J. Chem.*, **2004**, *57*, 519–523.
- [29] Galkin, O.; Vekilov, P.G. *J. Mol. Biol.*, **2004**, *336*, 43–59.
- [30] (a) Drukman, S.; Kavallaris, M. *Intern. J. Oncol.*, **2002**, *21*, 621–628. (b) Reinhart, W.H. *Biorheol.*, **2001**, *38*, 203–212.
- [31] (a) Yildiz, A.; Tomishige, M.; Vale, R.D.; Selvin, P.R.; *Science*, **2004**, *303*, 676–678. (b) Yildiz, A.; Forkey, J.N.; McKinney, S.A.; Ha, T.; Goldman, Y.E.; Selvin, P.R.; *Science*, **2003**, *300*, 2061–2065.
- [32] (a) Barnes, H.A.J. *Non-Newtonian Fluid Mech.*, **1997**, *70*, 1–33. (b) According to webster’s Dictionary, thixotropy is “. . . the property exhibited by various gels (as bentonite or paint containing pigments) of becoming fluid when shaken, stirred, or otherwise disturbed and of setting again to gel when allowed to stand: a reversible gel-sol transformation under isothermal shearing stress followed by rest.”
- [33] Acree, W.E., Jr.; Bertrand, G.L. *Nature*, **1977**, *269*, 450.
- [34] Wallace, D.G.; Rosenblatt, J. *Adv. Drug Deliv. Revs.*, **2003**, *55*, 1631–1649.
- [35] (a) Jin, H.-J.; Kaplan, D.L. *Nature*, **2003**, *424*, 1057–1061. (b) Valluzzi, R.; Jin, H.-J. *PCT Int. Appl. WO 2004 41, 845* ((Cl. C07K), 21 May 2004.
- [36] The first patent for this application: Clark, J.B. *Treatment of Wells*; U.S. Patent 2,596,844; May 13, 1952.
- [37] Fieser, L.P.; Harris, G.C.; Hershberg, E.B.; Morgana, M.; Novello, F.C.; Putnam, S.T. *Ind. Eng. Chem.*, **1946**, *38*, 768–773.
- [38] (a) Hogan, M.J.; Alvarado, J.A.; Weddell, J.E. *Histology of the human eye; an atlas and textbook*; Philadelphia: Saunders, **1971**. (b) Land, M.F.; Nilsson, D.-E. *Animal eyes*; Oxford University Press: New York, **2002**.
- [39] Readers of the Chinese language may consult http://hulu.com.tw/tfd/Hyptis_1H.htm for additional information.
- [40] For an interesting history of Jell-O, see: www.jellomuseum.com.
- [41] For different historical treatises, see Refs 6, 12a, and 40a and various chapters in the book cited in Ref 4. (a) Bungenberg de Jong, H.G. In *Colloid Science*; Vol II; Kruyt, H.R.; Ed., Elsevier: Amsterdam, **1949**, Chapter I.
- [42] Von Lipowitz, A. *Liebigs Ann. Chem. Pharm.*, **1841**, *38*, 348–355.
- [43] See the controversy concerning the Naples, Italy ceremony purportedly involving the blood of St. Januarius [43a]. It exhibits thixotropic properties. (a) Garlaschelli, L.; Ramaccini, F.; Della Sala, S. *Nature*, **1991**, *353*, 507.
- [44] Cotton, A.; Mouton, H. *Ann. Chim. Phys.*, **1907**, *11* (8th series), 145–203 (see p. 186).

- [45] Graham, T. J. *Chem. Soc.*, **1864**, 17, 318–327.
- [46] Maddox, R.L. *British J. Photogr.*, **1871**, 18, 422–423.
- [47] Eastman, G. *US Pat.* 388,850, 4 Sept. 1888.
- [48] (a) Liesegang, R.E. *Naturwiss. Wochenschr.*, **1896**, IX, 353–362 and articles cited in Chapter 1 of Ref 2f. (b) Liesegang, R.E. *Chemische Reaktionen in Gallerten*; Düsseldorf: Ed. Liesegang's Verlag, 1898.
- [49] Zsigmondy, R.; Batchmann, W. *Z. Chem. Ind. Koll.*, **1912**, 11, 145–157.
- [50] Hatschek, F. *Z. Chem. Ind. Koll.*, **1912**, 11, 158–165.
- [51] Hardy, W.B. *Proc. Roy. Soc. London*, **1900**, 66, 95–109.
- [52] Hardy, W.B. *J. Chem. Ind. Koll.*, **1912**, 11, 158–165.
- [53] Zsigmondy, R.; Bachmann, W. *Z. Chem. Ind. Koll.*, **1913**, 12, 16–18.
- [54] Foster, M.O.; Jackson, T. *Trans. Chem. Soc.*, **1907**, 91, 1877–1890.
- [55] Meunier, M.J. *Ann. Chim. Phys.*, **1891**, 22, 412.
- [56] Hardy, W.B. *Proc. Roy. Soc. London (A)*, **1912**, 87, 29–37.
- [57] Zsigmondy, R.; Spear, E.B. *The Chemistry of Colloids*, New York: John Wiley, **1917**.
- [58] Kuhn, W.; Hargitay, B.; Katchalsky, A.; Eisenberg, H. *Nature*, **1950**, 165, 514–516.
- [59] Von Weimarn, P.P. In *Colloid Chemistry*, Alexander, J., Ed., New York: The Chemical Catalog Co., **1926**, vol 1, p. 27–101.
- [60] Hardy, W.B. *Proc. Roy. Soc. London (A)*, **1912**, 87, 601–610.
- [61] Onsager, L. *Ann. New York Acad. Sci.*, **1949**, 51, 627–659, and refs cited therein.
- [62] See for instance: (a) *Adv. Mater.*, **2000**, 15, special issue 5. (b) Gránásy, L.; Pusztai, T.; Börzsönyi, T.; Warren, J.A.; Douglas, J.F. *Nature: Materials*, **2004**, 3, 645–650 and Refs cited therein.

THEORY

Chapter 1

THEORY OF MOLECULAR ASSOCIATION AND THERMOREVERSIBLE GELATION

Fumihiko Tanaka

Department of Polymer Chemistry

Kyoto University, Katsura, Nishikyo-Ku, Kyoto, 615-8510, Japan

1.	Thermodynamic Theory of Network-Forming Liquid Mixtures	18
1.1.	Models of Associating Mixtures	18
1.2.	Free Energy and Distribution Function of Aggregates	20
1.3.	Phase Separation, Stability Limit and Other Solution Properties	26
2.	Some Important Examples of Non-Gelling Associating Mixtures	27
2.1.	Dimer Formation	28
2.2.	Linear Association and Ring Formation	31
2.3.	Side-Chain Association	34
2.4.	Hydration in Aqueous Polymer Solutions and Closed-Loop Miscibility Gap	39
2.5.	Hydrogen-Bonded Liquid-Crystalline Supramolecules	41
3.	Gelling Solutions and Mixtures	44
3.1.	Micellization and Gelation	44
3.2.	Gelation by Pairwise Association	48
3.3.	Multiple Association	58
3.4.	Structure of the Networks with Multiple Junctions	63
3.5.	Mixtures of Associative Molecules – Gelation with Co-Networks	69
4.	Conclusions and Perspectives for the Future	74

1. Thermodynamic Theory of Network-Forming Liquid Mixtures

This chapter presents a general theoretical framework for deriving phase diagrams of multi-component liquid mixtures of low molecular-weight molecules, as well as high molecular weight polymers, in which molecules associate with each other by strongly attractive forces such as hydrogen bonds, hydrophobic force, etc. We treat association from the viewpoint of reversible chemical reactions forming molecular complexes by such associative forces. We first present a general theory for studying molecular weight distribution function of aggregates and phase transitions induced by association. These transitions include macro- and microphase separation, micellization, hydration, thermoreversible gelation and liquid-crystallization. To stress the unique feature of gelation, we classify this type of association into non-gelating and gelating ones. In non-gelling mixtures, oligomers or clusters of finite size are stabilized, while in gelling ones, aggregates grow to macroscopic scales. The theoretical treatments of these two cases are fundamentally different. Several possible applications of the theory to non-gelling systems are presented, followed by a detailed study of thermoreversible gelation with multiple cross-link junctions with special attention to the multiplicity and sequence length of the network junctions. Then, the theory is applied to more complex thermoreversible gels, such as binary networks (interpenetrating networks, alternating networks and randomly mixed networks). Potential applications to hydrated networks with high-temperature gelation, to polymer-surfactant interaction etc. are suggested.

1.1. Models of Associating Mixtures

As a model system, we consider a binary mixture of linear polymers $R\{A_f\}$ and $R\{B_g\}$. The number of statistical units on a chain (referred to as degree of polymerization, DP) is assumed to be n_A for $R\{A_f\}$ chains and n_B for $R\{B_g\}$ chains. Although we use the word “polymer” for the primary molecule forming complexes, we may apply our theory to low molecular weight molecules equally well by simply fixing n_A and/or n_B at small values. These polymers are assumed to be reactive and carry a fixed number f of reactive groups indicated by A for $R\{A_f\}$ and a number g of reactive groups B for $R\{B_g\}$, both are capable of forming reversible bonds that can thermally break and recombine. Hydrogen bonds, hydrophobic interaction, electrostatic interaction etc. are important examples of such associative forces. The type of associative interaction need not be specified at this stage, but it will be in each of the following applications. We symbolically write this model system as $R\{A_f\}/R\{B_g\}$. In the experiments,

various types of solvents are commonly used, so that we should consider a mixture $R\{A_f\}/R\{B_g\}/S$, where S denotes the solvent. Extension of the following theoretical consideration to such ternary systems is straightforward. Therefore, for simplicity, we confine this article to binary systems. Forces working among associative groups form intermolecular clusters covering a wide range of aggregation number. If either of the functionalities f or g exceeds the critical value (3 for pairwise association, but it can be 2 for multiple association), a cluster grows to macroscopic dimensions as soon as a threshold temperature or composition (concentration) is reached. Above such a threshold, three-dimensional networks, most generally comprized of the two components, are formed [1–5]; see also Chapter 19.

To describe such reversible network formation in associating mixtures, we take the simplest theoretical view, and start from a conventional lattice theoretical picture of polymer solutions [6–9] with an attempt to include association [10–12] in the form of reaction equilibrium. Let us first divide the total volume V of the system into small cells of size a of the monomeric unit on a chain [6]. We have a total number $\Omega \equiv V/a^3$ of microscopic cells. We first specify the part of the system containing only clusters of finite size, which will be referred to as *sol*. Let $N_{l,m}$ be the number of connected clusters consisting of the number l of $R\{A_f\}$ molecules (referred to as A-chains) and m of $R\{B_g\}$ molecules (B-chains). We introduce the symbol (l, m) to specify such a cluster. The total volume fraction of A-chains in the sol is given by:

$$\phi_A^S = n_A \sum_{l,m} l v_{l,m} \quad (1)$$

$v_{l,m} \equiv N_{l,m}/\Omega$ is the number of clusters per lattice cell. Similarly, the total volume fraction of B-chains in the sol is given by:

$$\phi_B^S = n_B \sum_{l,m} m v_{l,m} \quad (2)$$

The total volume fraction of the sol in the system is given by $\phi^S = \phi_A^S + \phi_B^S$. This should be equal to unity for non-gelling systems, or in the *pregel regime* of gelling systems, but can be smaller than unity as soon as an infinite network (referred to as *gel*) appears (i.e., in the *postgel regime* of the gelling systems). In the postgel regime, the volume fraction of the chains of species i in the gel network is given by $\phi_i^G = \phi_i - \phi_i^S$ for $i = A, B$, where ϕ_i is the total volume fraction of the species i that is fixed at the preparatory stage of the experiments. The number density v_i^G of the species i in the gel is then given by $v_i^G \equiv \phi_i^G/n_i = N_i^G/\Omega$ for $i = A, B$, where N_i^G is the number of i -chains in the gel. Such decomposition into a sol and a gel parts automatically takes place in accordance with thermodynamic principles. Since we have the identity $\phi_A + \phi_B = 1$, in what follows we can take ϕ_A as an independent variable and write it simply as ϕ . The volume fraction of B is then given by $\phi_B = 1 - \phi$.

1.2. Free Energy and Distribution Function of Aggregates

In order to study thermodynamic properties, we start from the *standard reference state* in which unconnected A-chains and B-chains are prepared separately in a hypothetical crystalline state [6, 8]. We first consider the free energy change ΔF_{rea} to bring the system from the reference state to a fictitious intermediate state in which chains are disoriented and connected in such a way that the cluster distribution is exactly the same as the real one [12–14]. It is given by:

$$\beta \Delta F_{\text{rea}} / \Omega = \sum_{l,m} \Delta_{l,m} v_{l,m} + \delta_A v_A^G + \delta_B v_B^G \quad (3)$$

$\Delta_{l,m}$ is the free energy produced when a single (l, m) cluster is formed from l of A-chains and m of B-chains in the reference state. We call this the *free energy of reaction*. Let $\mu_{l,m}^\circ$ be the internal free energy of an (l, m) cluster. The free energy difference $\Delta_{l,m}$ is then given by:

$$\Delta_{l,m} = \beta(\mu_{l,m}^\circ - l\mu_{1,0}^\circ - m\mu_{0,1}^\circ) \quad (4)$$

Under a constant pressure, $\mu_{l,m}^\circ$ is equivalent to the internal free energy produced by combination, configurational change, and bond formation of the constitutional primary molecules. Specific forms of these contributions will be considered in each of the following systems studied. Similarly, the δ_i ($i = A, B$) are the free energy changes produced when an isolated chain of species i is connected to the gel network: $\delta_A = \beta(\mu_A^{\circ G} - \mu_{1,0}^\circ)$ and $\delta_B = \beta(\mu_B^{\circ G} - \mu_{0,1}^\circ)$, where $\mu_i^{\circ G}$ is the internal free energy of an i -chain in the gel network. The two last terms in Eq. (3) are necessary in the postgel regime because the number of molecules contained in the gel part becomes macroscopic and reaches a finite fraction of the total number of molecules in the system. In the second step, we mix these clusters with each other to get to the real mixture studied. According to the conventional lattice theory of polydisperse polymer mixtures [8, 9], the mixing free energy ΔF_{mix} in this process is given by:

$$\beta F_{\text{mix}} / \Omega = \sum_{l,m} v_{l,m} \ln \phi_{l,m} + \chi \phi (1 - \phi) \quad (5)$$

$\phi_{l,m} \equiv (n_A l + n_B m) v_{l,m}$ is the volume fraction occupied by the (l, m) -clusters, and χ is Flory's χ -parameter which specifies the strength of van der Waals type contact interaction between monomers of different species. The first term gives the mixing entropy of the clusters. Since clusters formed by association are generally polydisperse, and have largely different volumes, a mixing entropy of the Flory-Huggins type must be used even if the primary molecules are low molecular-weight molecules. Macroscopically connected clusters, such as gel networks (i.e., SAFINs), infinitely long linear aggregates, do not give the mixing entropy since their centers of mass lose a translational degree of

freedom. The χ -parameter varies with temperature, but is assumed to be independent of the composition, as in the conventional theory. The number of contacts between the two species may change by molecular association, and hence the mixing enthalpy (the last term of Eq. (5)) may be modified. We assume here, however, that the same form remains valid after association except when the modification is significant due to polymer conformational change etc. We modify this term whenever necessary. The total free energy from which our theory starts is given by the sum of the above two parts (Figure 1):

$$\Delta F = \Delta F_{\text{rea}} + \Delta F_{\text{mix}}. \quad (6)$$

We next derive the chemical potentials of the clusters to study the solution properties. By the thermodynamic definition of the chemical potential $\Delta\mu_{lm} \equiv (\partial\Delta F/\partial N_{lm})_{T, N_{l'm'} \dots}$ for clusters of the size (l, m) , we find:

$$\begin{aligned} \beta\Delta\mu_{lm} = & 1 + \Delta_{lm} + \ln\phi_{lm} - (n_A l + n_B m)\nu^S \\ & + \chi\{n_A l(1 - \phi) + n_B m\phi - (n_A l + n_B m)\phi(1 - \phi)\} \\ & + [n_A l(1 - \phi) - n_B m\phi][\delta'_A(\phi)\nu_A^G - \delta'_B(\phi)\nu_B^G] \end{aligned} \quad (7)$$

where

$$\nu^S \equiv \sum_{l,m} v_{lm} \quad (8)$$

is the total number of finite clusters (per lattice cell) in the mixture. This number gives the total number of molecules and clusters that possess a translational degree of freedom. Within the ideal solution approximation, they equally contribute to the osmotic pressure. Obviously, the gel part is excluded from ν^S because it is macroscopic, and its center of mass is localized. The ratio defined by Eq. (9) gives the *number-average cluster size*, or *number-average aggregation number* of clusters.

$$P_n \equiv [\phi/n_A + (1 - \phi)/n_B]/\nu^S \quad (9)$$

In particular, we have for molecules that remain unassociated:

$$\begin{aligned} \frac{\beta\Delta\mu_{10}}{n_A} = & \frac{1 + \ln\phi_{10}}{n_A} - \nu^S + \chi(1 - \phi)^2 \\ & + [\delta'_A(\phi)\nu_A^G - \delta'_B(\phi)\nu_B^G](1 - \phi) \end{aligned} \quad (10a)$$

$$\frac{\beta\Delta\mu_{01}}{n_B} = \frac{1 + \ln\phi_{01}}{n_B} - \nu^S + \chi\phi^2 - [\delta'_A(\phi)\nu_A^G - \delta'_B(\phi)\nu_B^G]\phi \quad (10b)$$

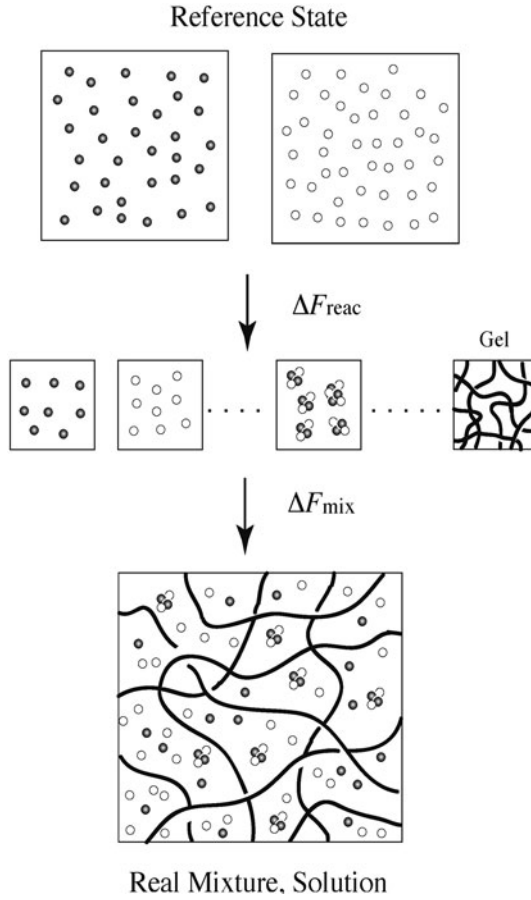


Figure 1. Construction of the free energy of associating mixtures. The total free energy is given by the sum of the free energy of reaction and that of mixing. The standard reference state is chosen in such a way that each species of molecules is regularly placed on a hypothetical crystalline lattice with a reference intramolecular conformation (a straight rod in the case of polymers).

Similarly, chemical potentials of the polymer chains in the gel part are given by:

$$\beta \Delta \mu_A^G / n_A = \delta_A / n_A - v^S + \chi(1 - \phi)^2 + (1 - \phi) \left[\delta'_A(\phi) v_A^G - \delta'_B(\phi) v_B^G \right] \quad (11a)$$

$$\beta \Delta \mu_B^G / n_B = \delta_B / n_B - v^S + \chi \phi^2 - \phi \left[\delta'_A(\phi) v_A^G - \delta'_B(\phi) v_B^G \right] \quad (11b)$$

To find the equilibrium distribution of clusters, we impose the *multiple chemical equilibrium conditions* in Eq. (12) for all possible combinations of the integers (l, m) .

$$\Delta\mu_{l,m} = l\Delta\mu_{1,0} + m\Delta\mu_{0,1} \quad (12)$$

Upon substitution of the specific forms of the chemical potentials, we find that the volume fractions of the clusters are given by:

$$\phi_{l,m} = K_{l,m}x^l y^m \quad (13)$$

For simplicity, we have written as x and y for the concentrations $\phi_{1,0}$ and $\phi_{0,1}$ of unassociated molecules. These unassociated molecules in the solution are sometimes called *unimers* to avoid confusion with monomers. The new constant $K_{l,m}$ (*equilibrium constant*) is defined by Eq. (14) which depends only on the temperature through $\Delta_{l,m}$.

$$K_{l,m} \equiv \exp(l + m - 1 - \Delta_{l,m}) \quad (14)$$

Similarly, the number density of clusters is given by:

$$\nu_{l,m} = \frac{K_{l,m}}{n_A l + n_B m} x^l y^m \quad (15)$$

The total volume fraction ϕ^S and the total number ν^S of clusters in the sol part as functions of x and y are then found by the infinite sum:

$$\phi^S(x, y) = \sum_{l,m} K_{l,m} x^l y^m \quad (16)$$

and

$$\nu^S(x, y) = \sum_{l,m} \frac{K_{l,m}}{n_A l + n_B m} x^l y^m \quad (17)$$

1.2.1. Pregel regime

In non-gelling mixtures, or pregel regime of gelling ones, the total volume fraction should be given by Eq. (18) since all clusters are included in the summation.

$$\phi^S(x, y) = 1 \quad (18)$$

The volume fraction of each species is then given by:

$$\phi = n_A \sum_{l,m} l \nu_{l,m} \quad (19a)$$

$$1 - \phi = n_B \sum_{l,m} m \nu_{l,m} \quad (19b)$$

These equations are transformed into the coupled equations, Eq. (20), for unknown variables x and y .

$$\phi = n_A x \frac{\partial v^S}{\partial x} \quad (20a)$$

$$1 - \phi = n_B y \frac{\partial v^S}{\partial y} \quad (20b)$$

We solve them with respect to x and y , and substitute the result into the physical quantities considered. For instance, the number-average numbers of A-chains and B-chains in the finite clusters are given by:

$$\langle l \rangle_n = \frac{\partial \ln v^S(x, y)}{\partial \ln x} \quad \text{and} \quad \langle m \rangle_n = \frac{\partial \ln v^S(x, y)}{\partial \ln y} \quad (21)$$

The average symbol shows the number average of the quantity $Q_{l,m}$. Eq. (22).

$$\langle Q_{l,m} \rangle_n \equiv \frac{\sum Q_{l,m} v_{lm}}{\sum v_{lm}} \quad (22)$$

Similarly, the weight-average is defined by:

$$\langle Q_{l,m} \rangle_w \equiv \frac{\sum Q_{l,m} \phi_{lm}}{\sum \phi_{lm}} \quad (23)$$

The weight-averages of the aggregation numbers l and m in the clusters are then given by:

$$\langle l \rangle_w = \frac{\partial \ln \phi^S(x, y)}{\partial \ln x} \quad \text{and} \quad \langle m \rangle_w = \frac{\partial \ln \phi^S(x, y)}{\partial \ln y} \quad (24)$$

The weight-average degree of polymerization (DP) of the clusters is thus given by the sum:

$$\begin{aligned} \bar{M}_w &\equiv \frac{\sum (n_A l + n_B m) \phi_{lm}}{\sum \phi_{lm}} = n_A \langle l \rangle_w + n_B \langle m \rangle_w \\ &= \left(n_A \frac{\partial}{\partial \ln x} + n_B \frac{\partial}{\partial \ln y} \right) \ln \phi^S(x, y) \end{aligned} \quad (25)$$

1.2.2. Sol/gel transition and postgel regime

Thus far we have tacitly assumed that the infinite double summation in ϕ^S (and hence in v^S) converges. These are double power series with positive coefficients, so that they are monotonically increasing functions. For mixtures capable of gelling, a borderline exists which separates the unit square on the (x, y) plane into a convergent and a divergent region. Exactly on the boundary line, the sol composition ϕ^S takes a finite value, but it diverges outside this line. Since the radius of convergence generally depends on the composition, let us

express the boundary by a parametric form $(x^*(\phi), y^*(\phi))$ for $0 \leq \phi \leq 1$. The value $\phi^S(x^*, y^*)$ can become smaller than unity for a certain region of the composition and the temperature because the sum *does not include* contributions from the infinite clusters appearing in the postgel regime. Hence, we can find the sol/gel transition line by mapping the condition $\phi^S(x^*, y^*) = 1$ onto the original temperature-concentration plane.

In the postgel regime, a chain participating in the gel network must be in chemical equilibrium with an unassociated chain of the same species. This imposes the additional conditions:

$$\Delta\mu_{1,0} = \Delta\mu_A^G \quad \text{and} \quad \Delta\mu_{0,1} = \Delta\mu_B^G \quad (26)$$

Hence, we find that x and y become functions of the concentration in the form of Eq. (27) for the gelating component in the postgel regime.

$$x^* = \exp[\delta_A(\phi) - 1] \quad \text{and} \quad y^* = \exp[\delta_B(\phi) - 1] \quad (27)$$

Asterisks indicate quantities beyond the gel point. The chemical potentials of each species take a uniform value in the solution, so that we can write them as $\Delta\mu_A$ and $\Delta\mu_B$.

We now substitute all relations obtained by such equilibrium conditions back into the original free energy Eq. (6), or equivalently, we use the Gibbs-Dühem relation $\Delta F/\Omega = \Delta\mu_A\phi/n_A + \Delta\mu_B(1-\phi)/n_B$, and find that the free energy is simply given by:

$$\beta\Delta F/\Omega = \frac{1 + \ln x}{n_A}\phi + \frac{1 + \ln y}{n_B}(1 - \phi) - \nu^S + \chi\phi(1 - \phi) \quad (28)$$

(The concentrations x and y should be replaced by x^* and y^* in the postgel regime.) This free energy can be separated into two parts as:

$$\beta\Delta F/\Omega = f_{\text{FH}}(\phi) + f_{\text{AS}}(\phi) \quad (29)$$

The part in Eq. (30) is the conventional Flory-Huggins free energy of the non-associative counterpart.

$$f_{\text{FH}}(\phi) \equiv \frac{\phi}{n_A} \ln \phi + \frac{(1 - \phi)}{n_B} \ln(1 - \phi) + \chi\phi(1 - \phi) \quad (30)$$

$$f_{\text{AS}}(\phi) \equiv \frac{\phi}{n_A} \ln\left(\frac{x}{\phi}\right) + \frac{1 - \phi}{n_B} \ln\left(\frac{y}{1 - \phi}\right) + \frac{\phi}{n_A} + \frac{1 - \phi}{n_B} - \nu^S \quad (31)$$

The part in Eq. (31) gives the effect of association. It can also be regarded as a *renormalization* of Flory's χ -parameter and produces a shift from χ to $\chi + \Delta\chi$, where:

$$\Delta\chi \equiv f_{\text{AS}}(\phi)/\phi(1 - \phi) \quad (32)$$

The short-range associative interaction energy originally introduced in the reaction terms is now interpreted as a composition-dependent modification of the χ -parameter.

1.3. Phase Separation, Stability Limit and Other Solution Properties

Some important physical quantities characterizing the mixture are defined now.

(1) *Osmotic pressure.* The osmotic pressure π of the A component is essentially the chemical potential of the B species with opposite sign, and it given by:

$$\beta\pi/n_B a^3 = -(1 + \ln y)/n_B + v^S(x, y) - \chi\phi^2 + [\delta'_A(\phi)v_A^G - \delta'_B(\phi)v_B^G]\phi \quad (33)$$

In a polymer solution in which the B component is a low molecular weight non-associative solvent ($n_B = 1$ and $\delta_B(\phi) = 0$), this definition reduces to the osmotic pressure in the conventional meaning. If this pressure is expanded in powers of the concentration with $n_B = 1$, we have the virial series:

$$\pi a^3/k_B T = \phi/n_A + A_2\phi^2 + A_3\phi^3 + \dots \quad (34)$$

$A_2 = 1/2 - \chi - \Delta A_2$ with ΔA_2 being a positive temperature-dependent constant. Hence, the second virial coefficient has a reduction ΔA_2 from $1/2 - \chi$ due to the associative interaction. At higher concentrations across the gel point, the osmotic compressibility $K_T \equiv (\partial\phi/\partial\pi)_T/\phi$, or its higher derivatives, may have a discontinuity due to the appearance of the gel part.

(2) *Phase separation.* The two-phase equilibrium conditions, or a *binodal* line can be found by equating the chemical potential of each component [8, 9]:

$$\Delta\mu_A(\phi', T) = \Delta\mu_A(\phi'', T) \quad (35)$$

$$\Delta\mu_B(\phi', T) = \Delta\mu_B(\phi'', T) \quad (36)$$

ϕ' and ϕ'' are the compositions of the dilute phase and concentrated A phase, respectively. If either or both phases, lie inside the postgel regime, the chemical potentials must be replaced by their postgel forms, $\Delta\mu_A^*(\phi'', T)$ and $\Delta\mu_B^*(\phi'', T)$.

(3) *Stability limit.* The thermodynamic stability limit or a *spinodal* line can be found for the binary system by the single condition $(\partial\Delta\mu_A/\partial\phi)_T = 0$, or equivalently, $\partial(\Delta\mu_A/n_A - \Delta\mu_B/n_B)/\partial\phi = 0$. Then, Eq. (37) obtains in which the new functions are defined by Eq. (38).

$$\frac{\kappa_A(\phi)}{n_A\phi} + \frac{\kappa_B(\phi)}{n_B(1-\phi)} - 2\chi = 0 \quad (37)$$

$$\kappa_A(\phi) \equiv \phi \frac{d}{d\phi} \left(1 + \phi_A^G \frac{d}{d\phi} \right) \ln x \quad (38a)$$

$$\kappa_B(\phi) \equiv -(1-\phi) \frac{d}{d\phi} \left(1 - \phi_B^G \frac{d}{d\phi} \right) \ln y \quad (38b)$$

In the pregel regime, these equations are related to the weight-average aggregation number of clusters. For homopolymer association where only A-chains are associated, for instance, κ_A reduces to the reciprocal of the weight-average cluster size as in conventional polydisperse polymer solutions [9, 15]. In heteropolymer association, however, κ 's are related to the average cluster sizes in a more complicated way.

2. Some Important Examples of Non-Gelling Associating Mixtures

We first show some results for non-gelling mixtures. Throughout this section, pairwise association of reactive groups is assumed. The strength of association can be expressed in terms of the three *association constants* defined by Eq. (38) for three combinations of pairs [16], where Δf is the free energy change upon forming a bond of the specified pair.

$$\lambda_{AA} \equiv \exp(-\beta \Delta f_{AA}), \lambda_{BB} \equiv \exp(-\beta \Delta f_{BB}), \lambda_{AB} \equiv \exp(-\beta \Delta f_{AB}) \quad (39)$$

To prevent gelation, we assume that the functionalities of either or both species of polymers are less than or equal to two in this section.

The general theory presented above is applied and the main results are summarized in the form of phase diagrams. For the numerical calculation, we introduce the reduced temperature deviation:

$$\tau \equiv 1 - \Theta/T \quad (40)$$

The unperturbed theta temperature Θ is defined by the equation, $\chi(\Theta) = 1/2n_B$. The unrenormalized second virial coefficient of the osmotic pressure in the generalized sense defined by Eq. (34) vanishes at this temperature. We then assume Shultz-Flory's form [8, 17] in Eq. (41) for the *bare* interaction parameter, where ψ_1 is a dimensionless material parameter of order unity.

$$\chi(T) = 1/2n_B - \psi_1 \tau \quad (41)$$

Since the binding free energy can be split into an energy and an entropy part as $\Delta f = \Delta\epsilon - T\Delta s$ for all pairs, the association constant $\lambda(T)$ can be rewritten:

$$\lambda(T) = \lambda_0 \exp[\gamma(1 - \tau)] \quad (42)$$

The dimensionless binding energy is given by Eq. (43) and the entropy-related constant $\lambda_0 \equiv \exp(\Delta s/k_B)$ [10, 12].

$$\gamma \equiv |\Delta\epsilon|/k_B\Theta \quad (43)$$

2.1. Dimer Formation

The first system studied is a mixture of $R\{A_1\}$ and $R\{B_1\}$ chains, each carrying a functional group A or B at its one end. Diblock copolymers are formed by the end-to-end association (*hetero-dimerization*) [18]. End groups A and B are assumed to be capable of forming a pairwise bond A-B by thermoreversible hetero-association. A hydrogen bond between an acid and base pair is the most important example of this category. For such mixtures, we have $f = g = 1$. A composite chain formed is a diblock copolymer $R\{A_1\}$ -*block*- $R\{B_1\}$ with a temporal junction (Figure 2). The system is made up of a mixture of diblock copolymers, (1,1), and unassociated homopolymers of each species, (1,0) and (0,1). It is apparently the same as a mixture of chemically connected diblock copolymers dissolved in their homopolymer counterparts [19, 20], but its phase behavior is much more complex because the population of the block copolymers varies with both temperature and composition. Let $n \equiv n_A + n_B$ be the total number of the statistical units on a block copolymer chain, and let $a \equiv n_A/n$ ($b \equiv n_B/n$) be the fraction of A part (B part). The relation, $a + b = 1$, holds by definition. Our starting free energy is given by:

$$\begin{aligned} \beta \Delta F / \Omega = & \Delta \cdot v_{11} + v_{10} \ln \phi_{10} + v_{01} \ln \phi_{01} \\ & + v_{11} \ln \phi_{11} + \chi \phi (1 - \phi) \end{aligned} \quad (44)$$

$\Delta \equiv \beta(\mu_{A-B}^\circ - \mu_A^\circ - \mu_B^\circ)$ is the free energy of dimer formation. By differentiation, the chemical potential of each component is:

$$\beta \Delta \mu_{10} = \ln x + 1 - n_A v^S + \chi n_A (1 - \phi)^2 \quad (45a)$$

$$\beta \Delta \mu_{01} = \ln y + 1 - n_B v^S + \chi n_B \phi^2 \quad (45b)$$

$$\beta \Delta \mu_{11} = \Delta + \ln z + 1 - n v^S + \chi \{n_A (1 - \phi)^2 + n_B \phi^2\} \quad (45c)$$

$v^S \equiv v_{10} + v_{01} + v_{11}$ is the total number of molecules that possess a translational degree of freedom, and $x \equiv \phi_{1,0}$, $y \equiv \phi_{0,1}$, $z \equiv \phi_{1,1}$.

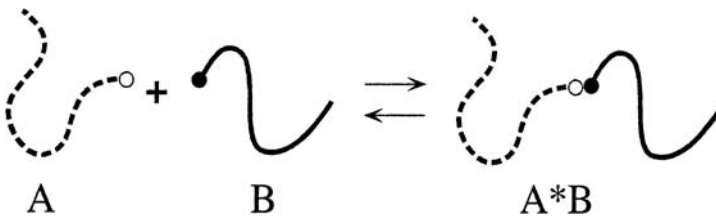


Figure 2. Block copolymer formed by reversible association of a pair of end-functional polymers $R\{A_1\}$ and $R\{B_1\}$. The system becomes a mixture of block copolymers $R\{A_1\}$ -*block*- $R\{B_1\}$ and their homopolymers whose population distribution is thermally controlled.

The association equilibrium condition in Eq. (12) then leads to Eq. (46) for the volume fraction z of the block copolymers, where $K \equiv \exp(1 - \Delta)$ is the temperature-dependent association constant.

$$z = Kxy \quad (46)$$

Because of the non-gelling nature, we have an identity:

$$\phi^S = x + y + Kxy \equiv 1 \quad (47)$$

The number density of clusters is given by:

$$\nu^S = \nu = \frac{1}{n} \left(\frac{x}{a} + \frac{y}{b} + Kxy \right) \quad (48)$$

Solving the coupled Eq. (20):

$$x(\phi) = \left\{ \phi - a - K^{-1} + \sqrt{D(\phi)} \right\} / 2b \quad (49a)$$

$$y(\phi) = \left\{ a - \phi - K^{-1} + \sqrt{D(\phi)} \right\} / 2a \quad (49b)$$

Here, $D(\phi) \equiv [a(1 - \phi) + b\phi + K^{-1}]^2 - 4ab\phi(1 - \phi)$.

We now split Δ into conformation and bonding parts as $\Delta = \beta\Delta f_{\text{conf}} + \beta\Delta f_{\text{bond}}$. The conformational free energy appears because the entropy of disorientation is reduced when two chains are combined. Using the lattice-theoretical entropy of disorientation [6, 8] in Eq. (50) for a linear chain of n statistical units (ζ being the lattice coordination number, σ the symmetry factor), yields Eq. (51) for the entropy change, and the free energy is given by $\Delta f_{\text{conf}} = -T\Delta S_{\text{dis}}$.

$$S_{\text{dis}}(n) = k_B \ln \left\{ \frac{n\zeta(\zeta - 1)^{n-2}}{\sigma e^{n-1}} \right\} \quad (50)$$

$$\Delta S_{\text{dis}} \equiv S_{\text{dis}}(n_A + n_B) - S_{\text{dis}}(n_A) - S_{\text{dis}}(n_B) = k_B \ln \left\{ \frac{\sigma(\zeta - 1)^2}{\zeta enab} \right\} \quad (51)$$

Combining the free energy of bonding $\Delta f_{\text{bond}} = \Delta\epsilon - T\Delta s$, the equilibrium constant is given by $K = \lambda_0 e^{-\beta\Delta\epsilon}$, where $\lambda_0 \equiv \sigma(\zeta - 1)^2 e^{\Delta s/k_B} / \zeta enab$ is a temperature independent constant. The volume fraction of the diblock copolymers z can then be calculated using the general theoretical scheme given above.

It is well known that diblock copolymers form a variety of microscopically ordered phases [21, 22]. To study their microphase separation transitions (MST), one should calculate the correlation function $S(\mathbf{q})$ of the concentration

fluctuation as a function of the wave vector \mathbf{q} (and temperature, concentration). Details of the calculation using the random phase approximation (RPA) can be found in references [21, 22]. When it is divergent at a certain finite wave number q , it is the precursor of the instability against the fluctuation whose spatial variations are characterized by the length q^{-1} . Hence, it leads to the formation of an ordered state with periodicity q^{-1} . In the case of block copolymers, q^{-1} is of the order of the radius of gyration of a single polymer chain. Divergence of $S(\mathbf{q})$ thus suggests periodic microdomain formation. We can, therefore, find the MST boundary by the condition:

$$S(\mathbf{q})^{-1} = 0. \quad (52)$$

From the same standpoint, the macroscopic stability limit (or spinodal condition) can also be found from the condition $S^{-1}(\mathbf{q} = 0) = 0$ using the same scattering function. This condition is equivalent to the divergence condition (Eq. (37)) of the osmotic compressibility. The general theoretical scheme developed by Leibler [21] has been applied and the correlation function has been calculated [18] for the associating diblock mixture. In this way, the MST boundaries for thermoreversible dimers were found.

Figure 3 shows a theoretical calculation of the phase diagram for a symmetric blend involved both chains have the same length [18]. The solid line shows the binodal, the broken line shows the MST line, and dotted lines show the spinodal. The MST and spinodal intersect at the two symmetric points

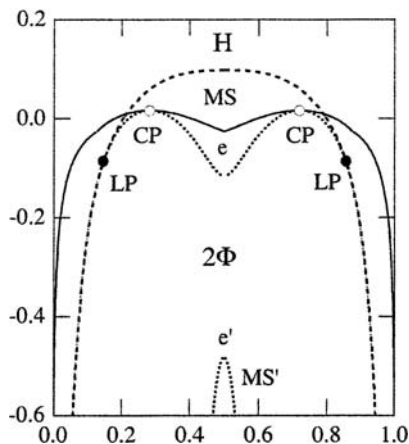


Figure 3. A typical phase diagram of associating diblock copolymers in which macrophase and microphase separation compete. Binodal (solid), spinodal (dotted) and MST (broken lines) are drawn. Critical points are indicated by CP. At the crossing of spinodal and MST lines, Lifshitz points (LP) appear. At the stoichiometric composition where the number of A groups equals that of B groups, an eutectic point (e) appears. (Reprinted with permission from [14]. Copyright (2002) Japanese Society for Polymer Science)

(indicated by LP) at which the two conditions in Eqs. (37) and (52) reduce to a single one. They are examples of the *Lifshitz point* – the point where an order parameter with finite wave number starts to appear [19, 23].

The whole plane is divided into several regions, each characterized by the capital letters in it. The region with the letter H has a homogeneously mixed fluid phase. Those shown by MS and MS' exhibit microscopically ordered phases where microdomains are regularly ordered. The region with the letters 2Φ in the figure is a biphasic region (or *miscibility gap*) where two distinct phases coexist. The point indicated by the letter e in the middle of the phase diagram is an *eutectic point* where the single microphase melts into the two coexisting homogeneously mixed fluids when the temperature is lowered. At extremely low temperature, the miscibility gap splits again at the point e' in the center of the concentration axis, and a new homogeneous microphase (shown by MS') is stabilized in the region between. Such a low-temperature microphase (a *reentrant microphase*) is stabilized because the population of block copolymers becomes so large in this low-temperature region that they homogenize the two demixed fluid phases into a single phase.

Experimentally, hydrogen bonds are expected to lead to a thermoreversible MST if they are strong compared to the repulsive interaction between the polymer segments but still weak enough to be broken by temperature. In this respect, a single hydrogen bond is not sufficiently strong, but reversible lamellar formation was confirmed to be possible for semi-crystalline block copolymers, (i.e., a blend of one-end-aminated polystyrene and one-end-carboxylated polyethylene glycol) [24–26]. By contrast, a variety of liquid-crystalline ordered phases induced by *multiple hydrogen* bonds have been the focus of recent interest [27–29].

2.2. Linear Association and Ring Formation

In this section, we consider the association of polymers $R\{A_2\}$ carrying two functional groups at their ends (*telechelic polymers*) in a solution. We consider only pairwise association, so that the polymers $R\{A_2\}$ form either linear chains or rings (*Chain/Ring Equilibrium*) [30]. In the case of a low molecular mass organic gelator (LMOG) [38] carrying two complementary hydrogen-bonding groups, the molecular weight n_A should be a small number, and no ring formation is possible due to the stiffness of fibrous aggregates. The more general case of multiple association, where polymer networks with micellar junctions are formed, will be treated as a gelling case later. Let N_m^C be the number of m -mer open chains, and let N_m^R be the number of m -mer rings in the system. The total number of primary polymer chains ($n_A \equiv n$) is then given by:

$$N = \sum_{m=1}^{\infty} m(N_m^C + N_m^R) \quad (53)$$

If N_0 is the number of solvent molecules ($n_B \equiv 1$), the number of cells is $\Omega = N_0 + nN$. Let $\phi_m^C \equiv nmN_m^C/\Omega$ and $\phi_m^R \equiv nmN_m^R/\Omega$ be the volume fraction of chains and rings. The volume fraction of polymers is then given by:

$$\phi = \sum_{m=1}^{\infty} (\phi_m^C + \phi_m^R) = 1 - \phi_0 \quad (54)$$

ϕ_0 is the volume fraction of the solvent. The fraction of rings among the total polymers is given by:

$$\rho \equiv \sum_{m=1}^{\infty} \phi_m^R / \phi. \quad (55)$$

We follow the general strategy given above, and start with the free energy of the solution:

$$\begin{aligned} \beta \Delta F = & \sum_{m \geq 1} \{ \Delta_m^C N_m^C + \Delta_m^R N_m^R \} + N_0 \ln \phi_0 \\ & + \sum_{m \geq 1} \{ N_m^C \ln \phi_m^C + N_m^R \ln \phi_m^R \} + \chi \phi (1 - \phi) \Omega \end{aligned} \quad (56)$$

The Δ are free energies of reaction defined by Eqs. (57) and (58) for chains and rings measured from those of the primary polymers.

$$\Delta_m^C \equiv \beta (\mu_m^{C^\circ} - m\mu_1^\circ) \quad (57)$$

$$\Delta_m^R \equiv \beta (\mu_m^{R^\circ} - m\mu_1^\circ) \quad (58)$$

We first consider open chains. The number of different ways to connect m identical polymers into a linear array is 2^m , but since the connected chain is symmetric, we have to divide it by the symmetry number $\sigma_C = 2$, and hence, 2^{m-1} is the combinatorial factor. The conformational term is the difference, $\Delta S_{\text{conf}}(m) = S_{\text{dis}}(mn) - mS_{\text{dis}}(n)$, as before. The bonding free energy is assumed to be Δf_0 for each bond. Hence, Eq. (59) is the equilibrium constant of the chains, where $\lambda(T) \equiv [\sigma_C(\zeta - 1)^2/\zeta]e^{-\beta\Delta f_0}$ is the association constant.

$$K_m^C = 2^{m-1} m \left[\frac{\sigma_C(\zeta - 1)^2}{n\zeta} \right]^{m-1} (e^{-\beta\Delta f_0})^{m-1} \equiv m \left(\frac{2\lambda}{n} \right)^{m-1} \quad (59)$$

Thus, Eq. (60) is the volume fraction of chains, where $x \equiv 2\lambda\phi_1^C/n$ is the number density of associating groups on the unassociated chains.

$$\frac{2\lambda}{n} \phi_m^C = mx^m \quad (60)$$

On the contrary, the equilibrium constant for the rings includes extra factor of the probability to form a ring. This factor is proportional to $(mn)^{-3/2}$ for a

Gaussian chain of length mn , but again we have to divide it by the symmetry factor $\sigma_R = m$ for a ring because a chain may close at any one of m bonds to form a ring. We thus have Eq. (61) for rings, where $B \equiv B_0 e^{-\beta \Delta f_0}$ is a temperature dependent constant.

$$\begin{aligned} K_m^R &= 2^{m-1} \cdot m \left[\frac{\sigma_C (\zeta - 1)^2}{n \zeta} \right]^{m-1} (e^{-\beta \Delta f_0})^{m-1} \cdot \frac{B_0}{m^{5/2}} \\ &= m \left(\frac{2\lambda}{n} \right)^{m-1} \frac{B}{m^{5/2}} \end{aligned} \quad (61)$$

The volume fraction of rings is given by:

$$\frac{2\lambda}{n} \phi_m^R = m \cdot \frac{B}{m^{5/2}} x^m. \quad (62)$$

The total volume fraction of polymers is the sum of the two:

$$\begin{aligned} \frac{2\lambda}{n} \phi &= \frac{2\lambda}{n} (\phi^C + \phi^R) = \sum_{m \geq 1} m x^m + B \sum_{m \geq 1} \frac{x^m}{m^{3/2}} \\ &= \frac{x}{(1-x)^2} + B \Phi(x:3/2) \end{aligned} \quad (63)$$

The new function Φ is defined by the infinite sum:

$$\Phi(x:\alpha) \equiv \sum_{m \geq 1} \frac{x^m}{m^\alpha} \quad (64)$$

Although the upper limit of the summation is the maximum possible aggregation number and should not exceed the total number N of polymers, we have taken the thermodynamic limit and let N go to infinity. The total number of clusters and molecules is similarly given by:

$$\begin{aligned} \lambda v^S &= \lambda(1 - \phi) + \sum_{m \geq 1} x^m + B \sum_{m \geq 1} \frac{x^m}{m^{5/2}} \\ &= \lambda(1 - \phi) + \frac{x}{1-x} + B \Phi(x:5/2) \end{aligned} \quad (65)$$

Solving Eq. (63) with respect to x and substituting the result into (65), we complete our general procedure, and can find the equilibrium solution properties. The functions $\Phi(x:\alpha)$ with $\alpha = 3/2, 5/2$ appear in the study of Bose-Einstein condensation of ideal quantum particles [31] that obey Bose-Einstein statistics. Their mathematical properties were studied by Truesdell [32] in detail, so that it is called *Truesdell function*. Their radius of convergence is given by $x = 1$. Both function $\Phi(x:3/2)$ and $\Phi(x:5/2)$ remain at a finite value at $x = 1$, but diverge as soon as x exceeds unity. Jacobson and Stockmayer [30] showed the fraction of chains and rings on the temperature-concentration phase plane, and

found very interesting phenomena that are analogous to Bose-Einstein condensation (i.e., when the parameter B exceeds a certain critical value, 100% rings are formed below a critical concentration of polymers). Such a transition originates in the singularity in Truesdell functions, and hence loop entropy, and serves as an interesting example of Bose-Einstein condensation in classical statistical mechanics.

Another singular property of this model is the divergence of the weight-average molecular weight at the point $x = 1$. The condition gives the *thermal polymerization* line when mapped onto the temperature-concentration plane because the average chain length goes to infinity at this point. Application of our theory gives essentially the same results as those originally found by Scott *et al.* [33], and later refined by Wheeler *et al.* [34–36]. More recently, Dudowicz *et al.* [37] studied living polymerization theoretically as well as thermal polymerization of sulfur using a similar approach.

In a similar way the mixed linear association of $R\{A_2\}$ and $R\{B_2\}$ molecules can be studied. The sequence distribution along an associated chain can be either alternative, sequential, or statistically random, depending upon the strength of association constants. All these associated chains, or rings, are block copolymers if the primary molecules are polymers, so that they undergo a microphase separation transition as well as macroscopic phase separation. The problem of competing micro- and macrophase separation in associating polymers remains an unsolved important problem.

In the case of linear association of low molecular-weight rigid molecules, the problem is related to fibrillar association of bifunctional molecules by (multiple) hydrogen bonds, such as occurs in hydrogen-bonded supramolecular liquid crystals [27–29] and LMOGs [38]. Equilibrium properties and phase diagrams of other systems can be studied within the theoretical framework presented here. Orientational ordering of the associated mesogens in hydrogen-bonded liquid crystals will be considered in the following sections.

2.3. Side-Chain Association

The next system studied is a mixture of high molecular weight polymers $R\{A_f\}$ ($DP \equiv n_A$) bearing a number f of associative A groups and low molecular weight monofunctional molecules $R\{B_1\}$ ($DP \equiv n_B$) [39, 40], or solvent molecules S ($DP \equiv 1$) [41]. We assume that a B group, or solvent molecule, can be attached to an A group from a side of the polymer chains. Adsorption of surfactant molecules onto polymer backbones by hydrogen bonds (Figure 4) is an important example of the former, and hydration of water molecules in an aqueous polymer solution (Figure 5) is an important example of the latter. To simplify the theoretical description, we write the DP of molecules as $n_A \equiv na$ and $n_B \equiv nb$ by using $n \equiv n_A + n_B$. The type of clusters formed is specified

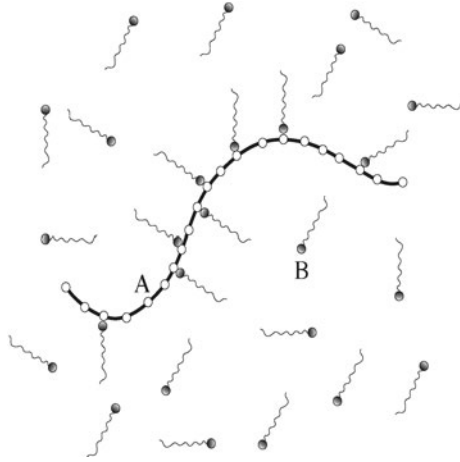


Figure 4. Association of end-functional low molecular-weight molecules $R\{B_1\}$ from the side of a long polymer chain $R\{A_f\}$. Comb like block copolymers are formed.

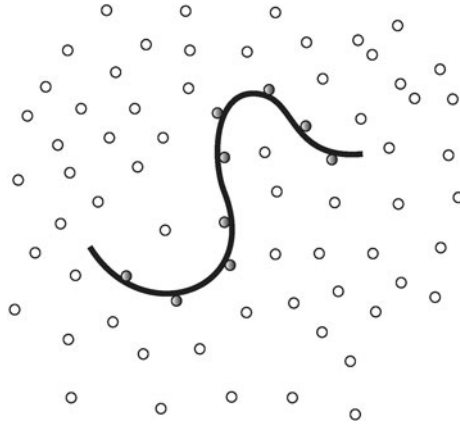


Figure 5. Hydration of water-soluble polymers. Water molecules S are hydrogen bonded to a polymer chain $R\{A_f\}$, so that they appear compatible with the surrounding solvent molecules.

by $(1, m)$ with $m = 0, 1, 2, \dots$, while the unassociated $R\{B_1\}$ molecule is indicated by $(0, 1)$. As in the general scheme, we start with the free energy of the mixture:

$$\beta \Delta F = \sum_{m=1}^f \Delta_m N_{1m} + N_{01} \ln \phi_{01} + \sum_{m=0}^f N_{1m} \ln \phi_{1m} + \Omega \chi \phi (1 - \phi) \quad (66)$$

The volume fraction of $R\{A_f\}$ molecules is given by:

$$\phi \equiv \sum_{m=0}^f \frac{a}{a + mb} \phi_{1m} \quad (67)$$

The free energy required to form a $(1, m)$ -mer from the primary molecules in the reference state is given by:

$$\Delta_m \equiv \beta(\mu_{1m}^\circ - \mu_{10}^\circ - m\mu_{01}^\circ) \quad (68)$$

Chemical equilibrium conditions in Eq. (69) then lead to the distribution function of the clusters in Eq. (70).

$$\Delta\mu_{1m} = \Delta\mu_{10} + m\Delta\mu_{01} \quad (69)$$

$$\phi_{1m} = K_m \phi_{10} \phi_{01}^m, \quad (70)$$

$K_m \equiv \exp(m - \Delta_m)$ is the equilibrium constant. As usual, we split the free energy Δ_m into combinatorial, conformational and bonding terms:

$$\Delta_m = -\frac{1}{k_B} (\Delta S_{\text{comb}} + \Delta S_{\text{conf}}) + m\beta\Delta f_0 \quad (71)$$

The combinatorial entropy is given in terms of the number ${}_f C_m$ of different ways to attach m molecules onto f available sites on a polymer as Eq. (72) if the attaching process occurs *independently*.

$$\Delta S_{\text{comb}} = k_B \ln({}_f C_m) \quad (72)$$

When there is strong attractive interaction between the attached $R\{B_1\}$ molecules located next to each other along the chain, they are adsorbed in sequences (i.e., sequences with varied length of $R\{B_1\}$ molecules distribute along the polymer chain). These sequences may induce *helical order* on the main chain due to the steric hindrance of neighboring adsorbed molecules. The combinatorial factor changes to the number of different ways to select the specified sequences from the finite total length n . Such a *correlated adsorption* was recently studied in detail in relation to helix formation on polymers by adsorption of chiral molecules [40].

The conformational entropy is given by Eq. (73) by using the entropy of disorientation as before.

$$\begin{aligned} \Delta S_{\text{conf}}(m) &= S_{\text{dis}}(n_A + mn_B) - S_{\text{dis}}(n_A) - mS_{\text{dis}}(n_B) \\ &= k_B \ln \left[\frac{a + bm}{a} \left\{ \frac{\sigma(\zeta - 1)^2}{n_B \zeta e} \right\}^m \right] \end{aligned} \quad (73)$$

Putting the results together, we find

$$K_m = \frac{a + bm}{a} {}_f C_m \left[\frac{\lambda(T)}{n_B} \right]^m \quad (74)$$

for the equilibrium constant, where $\lambda(T) \equiv [\sigma(\zeta - 1)^2/e\zeta] \exp(-\beta\Delta f_0)$ is the association constant. The cluster distribution function takes the form:

$$f\lambda v_{1m} = {}_f C_m x y^m \quad (75)$$

The two unknown variables are defined by

$$x \equiv f\lambda(T)\phi_{10}/n_A \quad \text{and} \quad y \equiv \lambda(T)\phi_{01}/n_B \quad (76)$$

These give the number density of A and B groups on the molecules that remain unassociated in the solution. They are always accompanied by the association constant λ , so that the concentration can be scaled by this factor. The association constant therefore behaves as a *temperature shift factor* of the concentration. By counting the number of molecules and clusters moving together, the total number density is:

$$\lambda v^S(x, y) = y + \frac{x}{f}(1 + y)^f \quad (77)$$

The coupled Eq. (20) becomes:

$$x(1 + y)^f = f\lambda\phi/n_A \quad (78a)$$

$$y + xy(1 + y)^{f-1} = \lambda(1 - \phi)/n_B \quad (78b)$$

Since the concentrations appear together with the association constant in the right hand side of these equations, we introduce the new variables $c_A \equiv \lambda f\phi/n_A$ and $c_B \equiv \lambda(1 - \phi)/n_B$ to describe concentrations. These variables give the total number density of A and B groups. Solving these equations with respect to x and y , we find:

$$x(\phi) = c_A/(1 + y(\phi))^f \quad (79a)$$

$$y(\phi) = \left[c_B - c_A - 1 + \sqrt{D(\phi)} \right] / 2 \quad (79b)$$

Substituting these results into physical properties, in particular into $v^S(x, y)$, expresses them as functions of the temperature and concentration. For instance, the average number $\langle m \rangle$ of B groups that attach to a polymer chain is given by:

$$\langle m \rangle \equiv \sum_{m=0}^f m v_{1m} = xy(1 + y)^{f-1}/\lambda. \quad (80)$$

The spinodal condition becomes:

$$\frac{\kappa_A(\phi)}{na\phi} + \frac{\kappa_B(\phi)}{nb(1 - \phi)} - 2\chi = 0 \quad (81)$$

In this equation, $\kappa_A(\phi)$ and $\kappa_B(\phi)$ are now functions of ϕ through c_A and c_B .

$$\kappa_A(\phi) = 1 - f\phi y'(\phi)/(1 + y(\phi)) \quad (82a)$$

$$\kappa_B(\phi) = (1 - \phi)y'(\phi)/y(\phi) \quad (82b)$$

We first show theoretical phase diagrams of hydrogen-bonded comb copolymers. Ruokolainen and co-workers [42–46] have recently observed a microphase separation transition (MST) in the mixture of poly(4-vinylpyridine) (P4VP) and the surfactant 3-pentadecylphenol (PDP). In this system, the hydrogen bonds between the hydroxyl group of PDP and the basic amino nitrogen in the pyridine group lead to the formation of combshaped block copolymers with densely grafted short side chains (called a *molecular bottlebrush* [45]). They observed lamellar structures at low temperature. The lamellar period L decrease in proportion to the reciprocal of x , the fraction of surfactant molecules per pyridine group in P4VP, and the MST temperature is a minimum value (easiest MST) near the stoichiometric concentration $x = 1$. Our theory can readily be applied to study such side-chain associations [39]. An example of the phase diagram for associating comb polymers is shown in Figure 6. The structures of possible mesophases inside the MS region were recently studied by Angerman *et al.* [47] by constructing random phase approximation (RPA) free energies of non-uniform systems.

Helix induction on a polymer chain by association of hydrogen-bonding chiral molecules provides another important application of our theory. Chiral

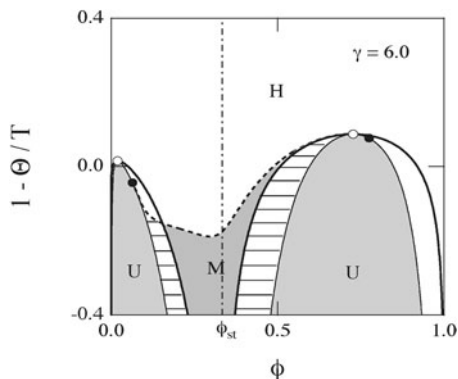


Figure 6. Phase diagram in which macro- and microphase separation compete by comb-shaped low-mass side-chain association. $n_A = 1000$, $f = 200$, $n_B = 10$, $\lambda_0 = 1.0$, $\gamma = 6.0$. Homogeneous liquid phase (H), microphase separated region (M), and unstable region (U) are shown. MST is easiest at the stoichiometric composition indicated by ϕ_{st} . Critical solution point (white circle) and Lifshitz point (black circle) are indicated. Metastable regions inside M region are indicated by horizontal thin lines. (Reprinted with permission from [39]. Copyright (1997) American Chemical Society)

centers attached to a chain often induce helical structures along the polymer chain as a consequence of the tendency of hydrogen bonds to grow in sequence. The small difference in physical interaction is non-linearly amplified by the cooperative nature of the bonds, such that formation of a new bond becomes easier in the nearest-neighbor position of the already formed bond. Cooperative helix induction and chiral ordering in polymers with hydrogen-bonding side groups was reported by Yashima *et al.* [48]. A series of experiments [48–51] with poly((4-carboxyphenyl)acetylene) revealed that, in the presence of chiral and achiral amines and amino alcohols in dimethyl sulfoxide (DMSO) as solvent, the optical activity measured by circular dichroism (CD) responds sharply to a slight excess of the R enantiomers the (*majority effect*). It was also found that the optical activity sharply responds to small concentrations of chiral groups when achiral molecules are added. Chiral groups are therefore called “sergeants” and achiral groups “soldiers” (*sergeants-and-soldiers effect*). We attempted [40] to describe theoretically such cooperative chiral ordering in polymers carrying hydrogen-bonded pendant groups by directly analyzing the sequence selection process when chiral molecules are attached to the polymer backbone. See also Chapter 2.

2.4. Hydration in Aqueous Polymer Solutions and Closed-Loop Miscibility Gap

We next present phase diagrams for aqueous polymer solutions in which water molecules are hydrogen-bonded onto polymer chains [41]. The solvent molecule are regarded as $R\{B_1\}$, and fix $n_B = 1$. The DP of polymers is given by $n_A = n$. Figure 7 shows a possible phase diagram in which $\lambda_0 = 0.002$, and $\gamma = 3.5$ (from the measured strength of the hydrogen bond in a solution) for a typical example. The number of the statistical units on a polymer chain is varied from curve to curve. The number f of attaching sites on a polymer chain is assumed to be equal to n because each monomer carries one hydrogen-bonding oxygen. The open circles show critical solution points. The solid curves show binodals, and the dashed curves spinodals. For such a small value of λ_0 , there are two miscibility gaps for low molecular-weight polymers: one ordinary miscibility dome and one closed loop above the dome (see $n = 10^2$ curve). The closed loop [9, 52–55] has one *upper critical solution temperature* (UCST) at the top and one *lower critical solution temperature* (LCST) at the bottom. The dome has an ordinary UCST. As the molecular weight is increased, the LCST and the UCST of the dome become closer, and for a certain value of n (1670 for the parameters given in this figure) the two points merge into a higher order critical point (called the *double critical point* [56]). For a molecular weight higher than this critical value, the two gaps merge into a single *hourglass*

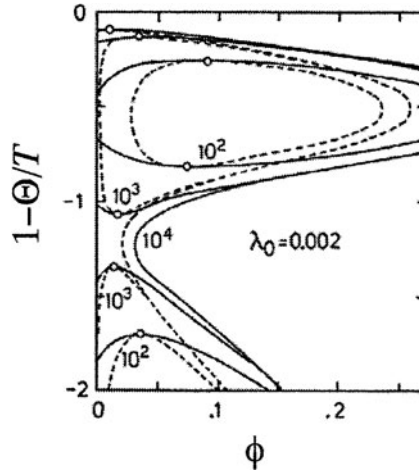


Figure 7. Phase diagram of hydrated polymer solutions. The segment number n is varied from curve to curve. Binodals (solid lines) and spinodals (broken lines) are drawn. The critical solution points are indicated by open circles. The LCST and UCST approach and eventually merge into an hourglass upon increasing the polymer molecular weight. The phase separation loop vanishes by decreasing the polymer molecular weight. (Reprinted with permission from [41]. Copyright (1990) The American Physical Society)

shape. The miscibility loop shrinks with decrease in the molecular weight, and eventually vanishes at a certain critical molecular weight ($n = 37$ in Figure 7). This vanishing loop is called the *hypercritical point*. For a slightly higher value of λ_0 , however, it was found that the two gaps remain separated no matter how large the molecular weight may become [41]. There are three θ temperatures under such a condition to which each critical point approaches in the limit of infinite molecular weight. For a still larger value of λ_0 , the closed loop does not appear, and we are left with an ordinary miscibility dome only. Since the parameter λ_0 is small if the entropy loss during the bond formation is large, there must be a strong orientational or configurational constraint in the local geometry for the appearance of an hourglass.

Figure 8 shows a comparison [41] of the theoretical calculation and the observed phase diagram [57, 58] for polyethylene oxide (PEO) in water. The number-average molecular weight in the experiment covers the range $2.17 \times 10^3 - 1.02 \times 10^6$. The solid curves show the calculated binodals. The number n of statistical units on a chain is varied from curve to curve. Parameters used for fitting are: $\psi_1 = 1$, $\Theta = 730K$, $\gamma = 6$, and $\lambda_0 = 1.66 \times 10^{-5}$. Fitting is made mainly by adjusting the unknown parameter λ_0 . The agreement is very good. The calculation of PEO/water phase diagrams was later examined by taking into account the hydrogen-bond networks in water [59]. The effect

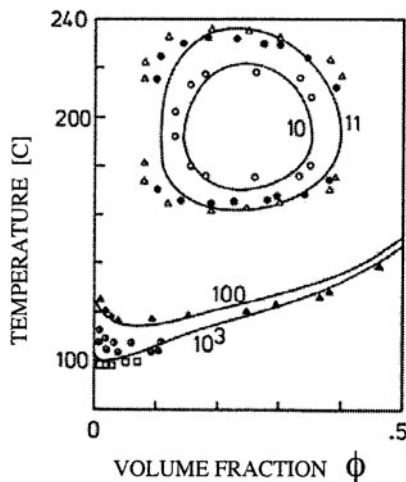


Figure 8. Phase diagram of aqueous poly(ethylene oxide) (PEO) showing closed-loop miscibility gap. Theoretical curves are fitted to the experimental data of the cloud points measured by Saeki *et al.* The miscibility loop expands with increase in the molecular weight. The UCST phase separation expected at low temperature cannot be observed due to crystallization of PEO. (Reprinted with permission from [41]. Copyright (1990) The American Physical Society)

of pressure on the miscibility loop was studied to derive temperature-pressure phase diagrams [60].

2.5. Hydrogen-Bonded Liquid-Crystalline Supramolecules

Some rigid molecules are known to become liquid crystalline when hydrogen-bonded to each other. For a binary mixture of low-mass molecules, as well as polymers, $R\{A\}$ and $R\{B\}$ (each carrying at least one rigid part A and B that form a mesogenic core when associated), dimer, trimer, main-chain, side-chain, combined, and network types are known [29, 61]. They are called *hydrogen-bonded supramolecular liquid crystals*. For example, aromatic acid derivatives with alkoxy or alkyl terminal groups form dimers due to hydrogen bonds between their carboxylic acid groups and show mesomorphism [62–65]. Association between different species of molecules also induces the isotropic/anisotropic phase transition [29, 66, 67]. The most remarkable case is that of non-mesogenic molecules forming compounds with mesogenic cores when hydrogen-bonded. In such combinations, isotropic materials become liquid crystallize by simple mixing.

To describe liquid crystallinity by association, we introduce the orientational free energy in addition to the free energy of reaction and mixing. Assume that an $R\{A_f\}$ molecule carries a number f of linear rigid associative groups A

of length n_A^* , and an $R\{B_g\}$ molecule carries a number g of rigid groups B of length n_B^* . The total DPs are $n_A = n'_A + fn_A^*$ and $n_B = n'_B + gn_B^*$. For the orientational free energy, we employ the conventional molecular field theory of Maier and Saupe [68], or its extension by McMillan [69] that includes both orientational ordering of the mesogenic cores and translational ordering of their center of mass. It is given by:

$$\beta \Delta F_{\text{ori}} = \{(-\ln Z) + \frac{1}{2}\zeta(\eta^2 + \alpha\sigma^2)v_M\}N_M \quad (83)$$

N_M is the total number of mesogenic cores formed in the system, and $v_M \equiv N_M/\Omega$ is their number density. In contrast to conventional liquid crystals, they are variables that depend on the temperature and composition, and should be determined by the equilibrium condition. The symbol η expresses the nematic order parameter defined by:

$$\eta \equiv \langle P_2(\cos\theta) \rangle \quad (84)$$

Similarly, σ is the smectic order parameter.

$$\sigma \equiv \langle P_2(\cos\theta) \cos(2\pi z/d) \rangle \quad (85)$$

(The function $P_2(x) \equiv (3x^2 - 1)/2$ is the Legendre polynomial of degree 2.) The coupling constant ζ (Maier-Saupe's interaction parameter) is the nematic interaction parameter, and α is McMillan's smectic interaction parameter. The averages refer to the statistical weight for orientation of each mesogenic core whose partition function Z is defined by:

$$Z(\eta, \sigma) \equiv \frac{1}{d} \int_0^d dz \int_0^1 d \cos\theta \exp\{\zeta[\eta + \alpha\sigma \cos(2\pi z/d)]\} \\ \times P_2(\cos\theta)v_M, \quad (86)$$

d is the distance between the neighboring planes in the smectic A structure on which the centers of mass of mesogenic cores are located (layer thickness). The symbol θ shows the angle of the longitudinal axis of each mesogenic core measured from the preferential orientational axis. By using this statistical weight, the definitions in Eqs. (84) and (85) become self-consistent coupled equations to find the order parameters. First, these equations are solved with equilibrium conditions for v_M , and then, by substitution, the chemical potential of each component as functions of the temperature and composition is found. An example of the phase diagram calculated by this theoretical framework in the case of dimer formation has been reported [70]. Figure 9 shows a phase diagram of a symmetric mixture with $n_A = n_B = 10$, and $n_A^* = n_B^* = 1$ (small rigid head groups carrying short aliphatic flexible tails). The temperature is measured

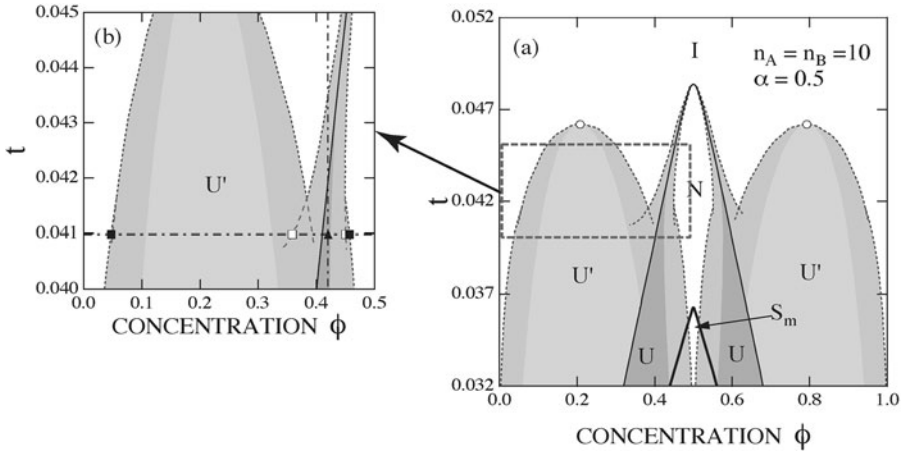


Figure 9. Phase diagram of a dimer-forming hydrogen-bonded supramolecular liquid crystal, and its partial magnification. Parameters are fixed at $n_A = n_B = 10$, $n_A^* = n_B^* = 1$, $\lambda_0 = 30.0$, $C = 0.3$, $C_1 = -0.5$, $C_2 = -0.05$, and $\alpha = 0.5$. (Reprinted with permission from [70]. Copyright (2002) American Chemical Society)

by $t \equiv T/T_{NI}$ in the unit of the nematic/isotropic transition temperature T_{NI} . We have assumed that Flory's χ -parameter takes the form $\chi \equiv C_1 + C_2/t$ using the reduced temperature t with C_1 and C_2 constants specified by the combination of molecular species. They are fixed at $C_1 = -0.5$ and $C_2 = 0.05$. The association constant is assumed to take the form $\lambda(T) = \lambda_0 \exp(C/t)$, where $C \equiv |\Delta\epsilon|/k_B T_{NI}$ is the dimensionless energy of the hydrogen bond. We have fixed λ_0 at 30.0 and $C = 0.3$. The inset magnifies the important part in the figure. The thin solid line is for the I/N transition, and the thick solid line the N/ S_m transition. Letters I, N, and S_m represent the state whose free energy is lowest in the area. Dotted lines limiting the hatched metastable region are binodals. The dark gray area indicated by U is the unstable region that is hidden inside the coexistence region, whereas the light gray area with U' is the conventional unstable region due to demixing. Open circles represent critical solution points. An unstable region hidden in a two-phase coexistence region due to the first order nature is well known in metallurgy as a metastable phase boundary [71]. Recently the existence of the spinodal curve hidden in a metastable region has been the focus of a study on crystallization of polymers [72, 73]. These hidden unstable regions usually accompany first-order phase transitions, and lie in the region where the liquid state has the lowest free energy.

At high temperature, the coexistence regions, caused by first order I/N phase transition, and by demixing the two different species of molecules, appear. Depending upon the composition, the mixture separates into either two I phases

by the effect of mixing enthalpy or I phase and N phase by the I/N transition. At intermediate temperature, the two coexistence regions merge, but the U region and the U' region remain separated. From such a phase diagram, two-step spinodal decomposition is possible; the mixture first separates into two metastable I phases or metastable I and N phases, and then into stable I and N phases. For example, when the mixture is quenched to the black triangle point from a high temperature shown in Figure 9(b), it separates temporarily into metastable I and N phases (open square) by the driving force based on the I/N transition, and eventually into stable I and N phases (black square) by cooperative driving force due to the I/N transition and the usual demixing. It is, however, also possible that larger fluctuations in spinodal decomposition lead to direct separation into stable I and N phases. At lower temperature, the two unstable regions U and U' also merge, so that the mixture separates directly into stable I and N phases, or into stable I and S_m phases by the cooperative driving force. If we divide the phase diagram into two at the middle and consider the left half, it is similar to the theoretical phase diagram of a lyotropic liquid crystal first derived by Flory [74], and later confirmed experimentally by Miller *et al.* [75]. The narrow I/N coexisting region extending from the macroscopic phase separation region is called a miscibility *chimney*. In lyotropic liquid crystals, the chimney goes straight up to high temperature, but our results show that there is a limiting temperature (the top of N phase) to which the chimney approaches, because the number of mesogenic cores decreases with increasing temperature.

3. Gelling Solutions and Mixtures

We consider now solutions that form gels. We first study simple pairwise association of functional groups, and then generalize the theory to multiple association. Finally, complex mixtures, where networks are formed by more than one species of polymers, are treated.

3.1. Micellization and Gelation

We start with a simple model binary mixture [12–14] in which solute molecules $R\{A_f\}$ of molecular weight $n_A \equiv n$, each carrying f identical functional groups A, are mixed with low molecular weight ($n_B = 1$) solvent molecules S . The solute molecules can be low molecular-weight functional molecules as well as polymers carrying functional groups. Pairwise association between A groups only is assumed ($\lambda_{AA} > 0, \lambda_{AB} = \lambda_{BB} = 0$). In the equilibrium state, solvent (0, 1) and l -mers ($l, 0$), where $l = 1, 2, 3$, etc. exist.

To simplify the symbols, the double suffies are contracted into single ones, and l is written for an l -mer and 0 for a solvent. The starting free energy is given by:

$$\beta \Delta F = \sum_{l \geq 1} N_l \ln \phi_l + N_0 \ln \phi_0 + \chi \phi (1 - \phi) \Omega + \sum_{l \geq 1} \Delta_l N_l + \delta(\phi) N^G \quad (87)$$

$\phi_0 \equiv 1 - \phi$ is the volume fraction of the solvent, and N^G is the number of $R\{A_f\}$ molecules in the macroscopic cluster if it exists. In general, such a macroscopic cluster can be any structure as long as its molecular weight is infinite; it can be a three dimensional branched network, a worm-like micelle, an infinitely long string, etc. But, in what follows, we mainly treat networks (i.e., SAFINs). Let us first find a simple criterion for gelation with regard to the size of the aggregate clusters.

By differentiation, the chemical potentials are:

$$\beta \Delta \mu_l = \Delta_l + 1 + \ln \phi_l - nlv^S + \chi nl(1 - \phi)^2 + nl\delta'(\phi)v^G(1 - \phi) \quad (88a)$$

$$\beta \Delta \mu_0 = 1 + \ln(1 - \phi) - v^S + \chi \phi^2 - \delta'(\phi)v^G \phi \quad (88b)$$

The general procedure developed above for chemical equilibrium leads to the volume fraction of the clusters:

$$\phi_l = K_l \phi_1^l \quad (89)$$

ϕ_1 is the volume fraction of the unassociated molecules, and the equilibrium constant is given by:

$$K_l = \exp(l - 1 - \Delta_l) \quad (90)$$

We then consider the total amount of materials in the sol:

$$\phi^S(x, y) = y + \sum_{l=1}^{\infty} K_l x^l \quad (91)$$

$x \equiv \phi_1$ for the solute molecules and $y \equiv 1 - \phi$ for the solvent. To study convergence of the infinite summation in this equation, we define the free energy gain $\delta_l \equiv \Delta_l/l$ produced when a single chain participates in a cluster of the size l . Application of the Cauchy-Hadamard's theorem [76] gives the convergence radius x^* of the power series in the form of Eq. (92) where the least upper bound of the limit has been indicated by a bar.

$$1/x^* = \overline{\lim}_{l \rightarrow \infty} (K_l)^{1/l} = e^{1-\delta_\infty} \quad (92)$$

The quantity $\delta_\infty \equiv \lim_{l \rightarrow \infty} \delta_l$ is defined by the limiting value of δ_l as $l \rightarrow \infty$. In the present special case of self assembly, there is a linear boundary in the

unit square on the (x, y) plane which is parallel to the y -axis. Within the radius of convergence, the normalization condition $\phi^S(x, y) = 1$ gives a one-to-one relationship between ϕ and x . Formation of several different spatial structures can be seen from the behavior of δ_l . Figure 10 schematically shows the exponent $\delta_l + 1/l - 1$ in the equilibrium constant $K_l^{-1/l}$ as a function of l . This function may either be a minimum at a certain finite l (curve (I) and (III) of Figure 10) or it may decrease monotonically to a finite value $\delta_\infty - 1$ (curve (II)). l_0 is defined as the value of l at which the curve reaches the minimum (including $l_0 = \infty$ for the monotonic case). The cluster size l for which the volume fraction ϕ_l becomes largest is:

$$\partial \Delta_l / \partial l = 1 + \ln x \quad (93)$$

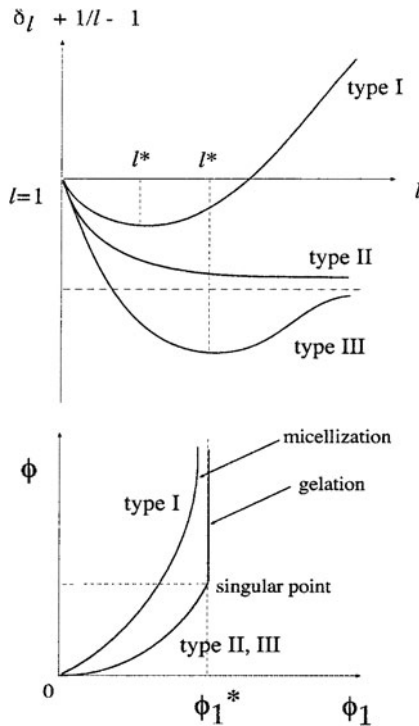


Figure 10. (Top) The binding free energy per molecule as a function of the aggregation number. (Bottom) Total volume fraction as a function of the unimer concentration. Type I leads to micellization with a finite aggregation number. Type II and Type III lead to macroscopic aggregates, such as infinitely long cylindrical micelles and three dimensional networks. In the latter case, the volume fraction ϕ_1 of the molecules that remain unassociated in the solution as a function of the total volume fraction ϕ of the molecules shows a singularity at the point where the weight average molecular weight of aggregates becomes infinite.

l^* is defined as the solution of this equation for the value of x at the convergence radius x^* . In the case where l^* is finite, the total concentration corresponding to the upper bound x^* is called the *critical micelle concentration* (cmc), since the volume fraction of the clusters with aggregation number l^* goes to a finite fraction at this value of the total volume fraction [77]. The Sharpness in their appearance is controlled by the curvature of the function $\delta_l + 1/l - 1$ around l^* . At the cmc, $l_0 = l^*$.

In the case where l^* is infinite, a macroscopic cluster appears as soon as x exceeds the critical value $x^* \equiv \exp(\delta^* - 1)$. The macroscopic clusters can be branched networks (SAFIN gels) [4, 5], infinitely long polymers [33], or wormlike micelles [78–80]. For brevity, we call the former case *gelation* and the latter case *polymerization* (including worm-like micellization) (Precisely, worm-like micelles formed by hydrophobic association fall in the category of multiple association described below. Here, we roughly call a one-dimensional self-assembled object a worm-like micelle; see also Chapter 19.) The total concentration ϕ^* obtained from x^* gives the concentration at which this transition takes place. It depends on temperature through δ_∞ . For ϕ above ϕ^* , the sum in, $\phi^S(x, y)$, cannot reach ϕ . The amount of shortage; $\phi - \sum \phi_i$; condenses into the macroscopic clusters.

When molecules form a linear array as in Figure 11(a), the internal free energy of an aggregate is $\mu_l^\circ = -(l - 1)\alpha k_B T$, where $\alpha k_B T$ is the free energy of a bond. We have Eq. (94) with $p = 1$.

$$\delta_l + 1/l - 1 = -(1 - \alpha) + \alpha/l^p + 1/l \quad (94)$$

For two-dimensional, disk-like aggregates, as in Figure 11(b), we have the same equation with $p = 1/2$, because the aggregation number l is proportional to the area πR^2 , and there are no bonds from outside along the edge. Similarly, $p = 1/3$ for three dimensional aggregates as in Figure 11(c). All these examples give monotonically decreasing curves of type II, and, hence, $(\phi_1)_{\text{cmc}} = \exp[-(1 + \alpha)]$ for the critical micelle concentration. Above the cmc,

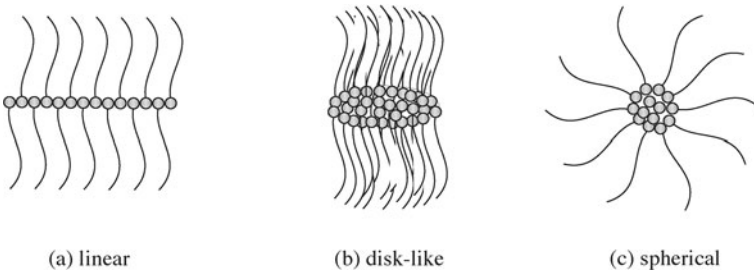


Figure 11. Micellization of end-associative polymer chains. (a) linear association, (b) two-dimensional discotic association and (c) three-dimensional spherical association.

the unimer concentration is nearly constant at this value, and the volume fraction of aggregates with a specified number is given by $\phi_l \simeq \exp[-(1 + \alpha l^{1-p})]$, or:

$$\phi_l \simeq \begin{cases} e^{-\alpha} & (p = 1) \\ e^{-\alpha l^{1/2}} \ll 1 & (p = 1/2) \\ e^{-\alpha l^{2/3}} \ll 1 & (p = 1/3) \end{cases} \quad (95)$$

Therefore, a widely polydisperse distribution for linear aggregates is expected because ϕ_l is almost constant. For two- and three-dimensional aggregates, the distribution function decays quickly with the aggregation number, and since the total concentration is a given variable, aggregates of infinite size easily appear.

Next, consider the type I and type III, where stable micelles of finite size are formed. The binding free energy is expanded around l^* :

$$1 - \delta_l - \frac{1}{l} \cong a - b(l - l^*)^2 + \dots \quad (96)$$

a and b are positive constants. Since the volume fraction of l -mers is:

$$\phi_l = e^{-bl(\Delta l)^2} (e^a \phi_1)^l \quad (97)$$

The cmc is determined from the condition:

$$(\phi_1)_{\text{cmc}} = e^{-a} \quad (98)$$

Hence, we have Eq. (99) near $l = l^*$ (i.e., the distribution function of micelles becomes Gaussian with mean value l^* and variance $1/\sqrt{2l^*b}$).

$$\phi_l \cong e^{-l^*b(\Delta l)^2} \quad (99)$$

3.2. Gelation by Pairwise Association

Consider the simplest gelling binary mixture in which primary functional molecules form networks in a solvent [10–12]. In order to derive the equilibrium constants in an analytical form, a simple model for the internal structure of clusters is introduced. Clusters are assumed to take a tree structure with no internal loops (called a *Cayley tree*). Cycle formation within a cluster is neglected. This is a crude approximation, based on the classical theory of gelation [8, 81, 82], but it is known to work very well before the gel point is reached.

The general theoretical scheme gives the chemical potentials of the clusters and solvent:

$$\beta \Delta \mu_l = \Delta_l - l + 1 + \ln \phi_l - nlv^S + \chi nl(1 - \phi)^2 + nl\delta'(\phi)v^G(1 - \phi) \quad (100a)$$

$$\beta \Delta \mu_0 = 1 + \ln(1 - \phi) - v^S + \chi \phi^2 - \delta'(\phi)v^G\phi \quad (100b)$$

Eq. (101) gives the total number of molecules and clusters having translational degree of freedom.

$$v^S \equiv \sum v_l + 1 - \phi \quad (101)$$

As usual, the free energy is split into three parts:

$$\Delta_l = \Delta_l^{\text{comb}} + \Delta_l^{\text{conf}} + \Delta_l^{\text{bond}} \quad (102)$$

To find the combinatorial part, we employ the entropy change on combining l identical f -functional molecules to form a single Cayley tree. The classical tree statistics [82] gives:

$$\Delta S_l^{\text{comb}} = k_B \ln[f^l \omega_l] \quad (103)$$

Eq. (104) is Stockmayer's combinatorial factor [82].

$$\omega_l \equiv \frac{(fl - l)!}{l(fl - 2l + 2)!} \quad (104)$$

The free energy is given by $\Delta_l^{\text{comb}} = -\Delta S_l^{\text{comb}}/k_B$.

For the conformational free energy, we again employ the lattice theoretical entropy of disorientation (Eq. (50)), and find:

$$\Delta S_l^{\text{conf}} = S_{\text{dis}}(ln) - lS_{\text{dis}}(n) = k_B \ln \left[\left(\frac{\sigma(\zeta - 1)^2}{\zeta en} \right)^{l-1} l \right] \quad (105)$$

Finally, free energy of bonding is given by Eq. (106) because there are $l - 1$ bonds in a tree of l molecules, where Δf_0 is the free energy change on forming a single bond.

$$\Delta_l^{\text{bond}} = (l - 1)\beta\Delta f_0 \quad (106)$$

Combining these results, we find Eq. (107) for the equilibrium constant.

$$K_l = fl\omega_l \left(\frac{f\lambda}{n} \right)^{l-1} \quad (107)$$

Also, $\lambda(T)$ is the association constant.

$$\lambda(T) \equiv [\sigma(\zeta - 1)^2/\zeta e] \exp(-\beta\Delta f_0) \quad (108)$$

The distribution of clusters (Eq. (89)) then gives Eq. (109) for the number density.

$$\lambda v_l = \omega_l x^l \quad (109)$$

The independent variable x here is defined in Eq. (110).

$$x \equiv f\lambda\phi_1/n = f\lambda v_1 \quad (110)$$

It gives the number of functional groups $f\phi_1/n$ carried by the unassociated polymer chains in the solution, multiplied by the association constant $\lambda(T)$ as a temperature shift factor. From this distribution function, we can obtain average values of physical quantities. First, the total number concentration of the finite clusters is given by:

$$\lambda \sum_{l \geq 1} v_l = S_0(x) \quad (111)$$

Their volume fraction is:

$$\frac{\lambda}{n} \sum_{l \geq 1} \phi_l = S_1(x) \quad (112)$$

Therefore, the number average of the cluster size is given by:

$$\bar{l}_n \equiv \sum l v_l / \sum v_l = S_1(x) / S_0(x) \quad (113)$$

The weight average is:

$$\bar{l}_w \equiv \sum l^2 v_l / \sum l v_l = S_2(x) / S_1(x) \quad (114)$$

These are written in terms of the moments of Stockmayer's distribution function defined by:

$$S_k(x) \equiv \sum_{l=1}^{\infty} l^k \omega_l x^l \quad (k = 0, 1, 2, \dots) \quad (115)$$

These moments are explicitly written in terms of the extent α of reaction:

$$x \equiv \alpha(1 - \alpha)^{f-2} \quad (116)$$

For instance:

$$S_0(x) = \alpha(1 - f\alpha/2)/f(1 - \alpha)^2 \quad (117a)$$

$$S_1(x) = \alpha/f(1 - \alpha)^2 \quad (117b)$$

$$S_2(x) = \alpha(1 + \alpha)/f[1 - (f - 1)\alpha](1 - \alpha)^2 \quad (117c)$$

To understand the physical meaning of α , the probability for a randomly chosen functional group to be associated is calculated. Since an l -mer includes a total of fl groups, among which $2(l - 1)$ are associated, the probability of association (extent of reaction) is:

$$2[S_1(x) - S_0(x)]/f S_1(x) = \alpha \quad (118)$$

Thus, α gives the extent of association.

By using α , the average cluster sizes are:

$$\bar{l}_n = 1/(1 - f\alpha/2) \equiv P_n(\alpha) \quad (119a)$$

$$\bar{l}_w = (1 + \alpha)/[1 - (f - 1)\alpha] \equiv P_w(\alpha) \quad (119b)$$

3.2.1. Pregel regime

The weight average diverges at $\alpha = 1/(f - 1)$. This suggests that $\alpha = \alpha^* \equiv 1/(f - 1)$ is the gel point. The number average also diverges at $\alpha = 2/f$, but since $2/f > 1/(f - 1)$, the postgel regime must be studied to examine its behavior. In the pregel regime, where $\alpha < \alpha^*$, the volume fraction ϕ^S occupied by the polymer chains belonging to the sol must always be equal to the total polymer volume fraction ϕ since no gel network exists. Thus, the total polymer volume fraction ϕ and the extent of association α satisfy the relation:

$$\frac{f\lambda}{n}\phi = \frac{\alpha}{(1 - \alpha)^2} \quad (120)$$

This equation can be solved for α (as in Eq. (121) in terms of the number concentration of the functional groups (with the temperature shift factor of the association constant) (Eq. (122))).

$$\alpha = \frac{1}{2c} \{1 + 2c - \sqrt{1 + 4c}\} \quad (121)$$

$$c \equiv \frac{f\lambda(T)}{n}\phi \quad (122)$$

All physical quantities directly can be expressed then in terms of c . For instance, the total free energy per lattice cell is:

$$\frac{\beta\Delta F}{\Omega} = \frac{\phi}{n} \left\{ (f - 2)\ln(1 - \alpha) + \ln\alpha + \frac{1}{2}f\alpha \right\} + (1 - \phi)\ln(1 - \phi) + \chi\phi(1 - \phi) \quad (123)$$

Hence, the renormalization of the χ -parameter by association becomes:

$$\Delta\chi(\phi) = \left[(f - 2)\ln(1 - \alpha) + \ln\alpha + \frac{1}{2}f\alpha - \ln\phi \right] / n(1 - \phi) \quad (124)$$

We thus find the molecular origin of the concentration dependence of the χ -parameter in associating polymer solutions. In a similar way, the spinodal condition is:

$$\frac{\kappa(\phi)}{n\phi} + \frac{1}{1 - \phi} - 2\chi = 0 \quad (125)$$

Here, a new function κ is defined by Eq. (126) with α given by Eq. (121).

$$\kappa(\phi) = \frac{1 - (f - 1)\alpha}{1 + \alpha} = \frac{1}{P_w(\alpha)} \quad (126)$$

It is the reciprocal of the weight-average cluster size.

3.2.2. Gel point

Next, we find the sol/gel transition point. The free energy change δ_l per molecule is a steadily decreasing function of l , approaching the limiting value $\delta_\infty = 1 - (f - 1)\ln(f - 1) + (f - 2)\ln(f - 2) - \ln\lambda(T)$. This model therefore falls within category II in Figure 10. This limit for the convergence radius of the series given by Eq. (125):

$$\phi_1^* = \exp(\delta_\infty - 1)$$

or, equivalently,

$$x^* = (f - 2)^{f-2}/(f - 1)^{f-1} \quad (127)$$

in terms of x , and $\alpha^* = 1/(f - 1)$ in terms of the extent of association as was expected from the divergence of \bar{l}_w . The volume fraction of polymers at the gel point is then:

$$\frac{\lambda(T)}{n}\phi^* = \frac{f - 1}{f(f - 2)^2} \quad (128)$$

This gives the sol/gel transition line on the temperature-concentration plane.

3.2.3. Postgel regime

In the postgel regime, where $\phi > \phi^*$ and $\alpha > \alpha^*$, there is an additional condition of equating the chemical potential of a polymer chain in the sol part and one in the gel part [83]. This equilibrium condition $\Delta\mu_1 = \Delta\mu^G$ gives:

$$\ln x = \delta(\phi) - 1 \quad (129)$$

Here, the free energy $\delta(\phi)$ produced on binding a chain onto the gel network should depend upon the concentration because the structure of the gel changes. It starts with the initial value δ_∞ at the gel point, (i.e., $\delta(\phi^*) = \delta_\infty$). Thus, the volume fraction of the unreacted chains is related to the binding free energy.

Since the conversion in the sol can in general be different from that in the gel, the former is written as α' and the latter as α'' . The average conversion α of the solution as a whole is:

$$\alpha = \alpha'w^S + \alpha''w^G \quad (130)$$

The volume fraction ϕ^S of polymers belonging to the sol is consequently expressed by Eq. (131) in the postgel regime, so that it is different from the total ϕ that is in terms of α .

$$\lambda\phi^S/n = S_1(\alpha') \quad (131)$$

The sol fraction w^S is:

$$w^S \equiv \phi^S/\phi = S_1(\alpha')/S_1(\alpha) \quad (132)$$

Hence, the gel fraction is:

$$w^G = 1 - S_1(\alpha')/S_1(\alpha). \quad (133)$$

The number ν^S of total clusters in the chemical potentials must also be replaced by Eq. (134) since it must give the number of molecules and clusters that have a translational degree of freedom.

$$\nu^S = S_0(\alpha')/\lambda + 1 - \phi \quad (134)$$

The gel network spans the entire solution and loses translational motion. By using this ν^S , the chemical potentials are:

$$\frac{\beta \Delta \mu_1^*}{n} = \frac{1 + \ln x}{n} - \nu^S + \chi(1 - \phi)^2 + \delta'(\phi)(1 - \phi)\nu^G \quad (135a)$$

$$\beta \Delta \mu_0^* = 1 + \ln(1 - \phi) - \nu^S + \chi\phi^2 - \delta'(\phi)\phi\nu^G \quad (135b)$$

The function κ in the spinodal condition takes the form of Eq. (136) which is different from the one in the pregel regime.

$$\kappa(\phi) = \frac{d}{d \ln \phi} \left(1 + w^G \frac{d}{d \ln \phi} \right) \ln x(\alpha') \quad (136)$$

Explicitly, it becomes:

$$\kappa(\phi) = \left[1 + w^S \left(1 - \frac{P_w(\alpha')}{P_w(\alpha)} \right) \right] \frac{1}{P_w(\alpha)} + w^G \frac{d}{d \ln \phi} \left(\frac{1}{P_w(\alpha)} \right) \quad (137)$$

(1) *Flory's treatment.* By the definition of α in Eq. (116), x takes a maximum value $x^* = (f - 2)^{f-2}/(f - 1)^{f-1}$ at $\alpha = 1/(f - 1)$. Therefore, two values of α can be found for a given value of x . Consider the postgel regime, $\alpha > \alpha^*$. For a given α , the value of x is fixed by the relation $x \equiv \alpha(1 - \alpha)^{f-2}$. Flory postulated [8] that another root α' , lying below α^* of this equation for a given value of x , gives the extent of reaction in the sol. The larger valued α , lying above α^* , applies to all functional groups in the system. The volume fraction ϕ^S of polymers in the sol is then:

$$\frac{\lambda}{n} \phi^S = \frac{\alpha'}{f(1 - \alpha')^2} \quad (138)$$

Also, the gel fraction is:

$$w^G = 1 - w^S = 1 - (1 - \alpha)^2 \alpha' / (1 - \alpha')^2 \alpha \quad (139)$$

Hence, the gel fraction reaches unity only at the limit of complete reaction, $\alpha = 1$. The extent of association α'' in the gel can be obtained from Eq. (130). Explicitly, it gives:

$$\alpha'' = [(1 - \alpha')^2 \alpha^2 - (1 - \alpha)^2 \alpha'^2] / [(1 - \alpha')^2 \alpha - (1 - \alpha)^2 \alpha'] \quad (140)$$

This value is larger than that given by the infinite limit in the tree approximation (Eq. (141)) so that, in Flory's picture, cycle formation is allowed within the gel network.

$$\lim_{l \rightarrow \infty} [(f - 2)l + 2] / fl = 2/f \quad (141)$$

The binding free energy $\delta(\phi)$ of a chain onto the gel network is then:

$$\delta(c) = 1 - (f - 1) \ln c + f \ln[(\sqrt{1 + 4c} - 1)/2] \quad (142)$$

As shown in Figure 12, the absolute value of the binding free energy is a monotonically increasing function of the concentration. With increase in the concentration, the network structure becomes tighter, so that binding of a polymer chain becomes stronger. The main results obtained by Flory's picture are summarized in Figure 13.

(2) *Stockmayer's treatment.* However, Stockmayer [82] later remarked that Flory's result in the postgel regime is inconsistent with the tree assumption, since the treatment permits cycle formation in the gel network. To remove this inconsistency, he proposed another treatment for the postgel regime. He introduced a different assumption, that the extent of reaction of functional groups in the finite clusters remains at the critical value $1/(f - 1)$ throughout the postgel regime. He also proposed that in the postgel regime the extent

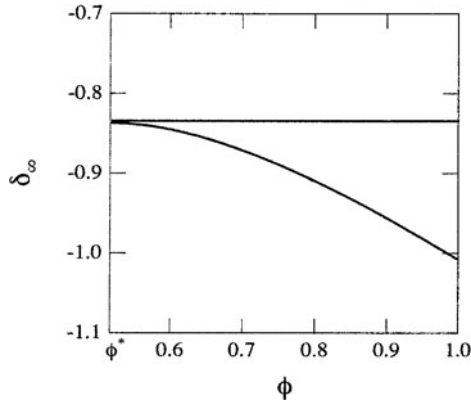


Figure 12. The dimensionless binding free energy in the postgel regime in two treatments. In Flory's treatment, the absolute value of the binding free energy increases with the concentration because the number of junctions on a chain increases on average.

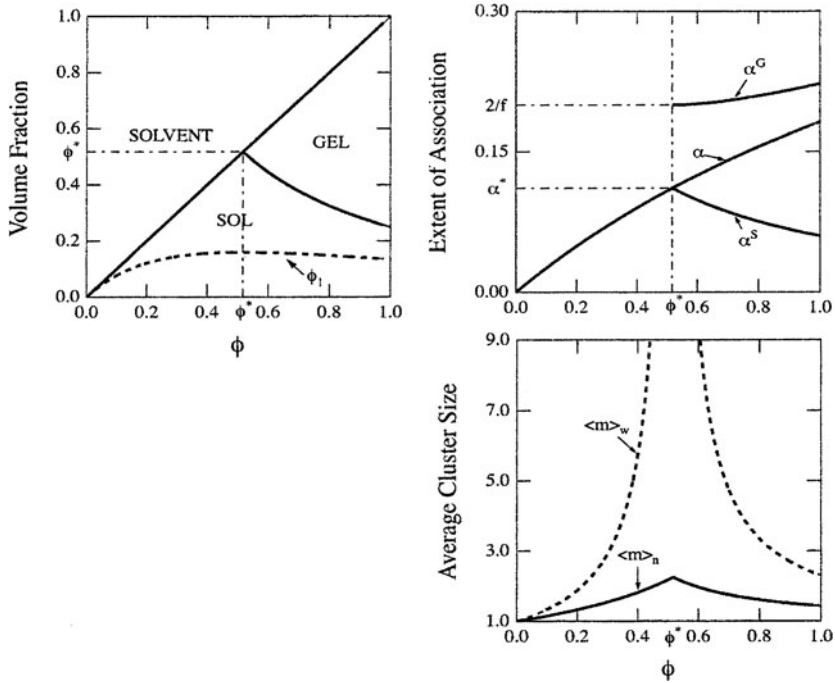


Figure 13. The gel fraction, the extent of association, and the average molecular weight calculated on the basis of Flory's postgel picture. The number average has discontinuous slope across the gel point, while the weight average diverges.

of association in the gel network takes the value $\alpha'' = 2/f$ appropriate to an infinite tree structure without cycles. The weight fraction w^G of the gel then takes the form:

$$w^G = \frac{(f-1)\alpha - 1}{1 - 2/f} \quad (143)$$

$\alpha (> \alpha^*)$ is the extent of reaction including all functional groups. It is a linear function of α , and reaches unity at $\alpha = 2/f$ before reaction is completed. The volume fraction of the sol ϕ^S remains constant at $\phi^S = \phi^*$. The number average DP remains constant at $\bar{l}_n = (f-2)/2(f-1)$, while the weight average is divergent ($\bar{l}_w = \infty$) in the postgel regime. The binding free energy is fixed at δ_∞ . From a physical viewpoint, Flory's model is closer to reality since intramolecular connection is an essential feature of the network structure. The main results obtained by Stockmayer's picture are summarized in Figure 14.

Figure 15 compares phase diagrams calculated by the two different treatments of the postgel regime [83]. Binodals and spinodals appear in different positions. For the same association constant, Stockmayer's treatment gives a

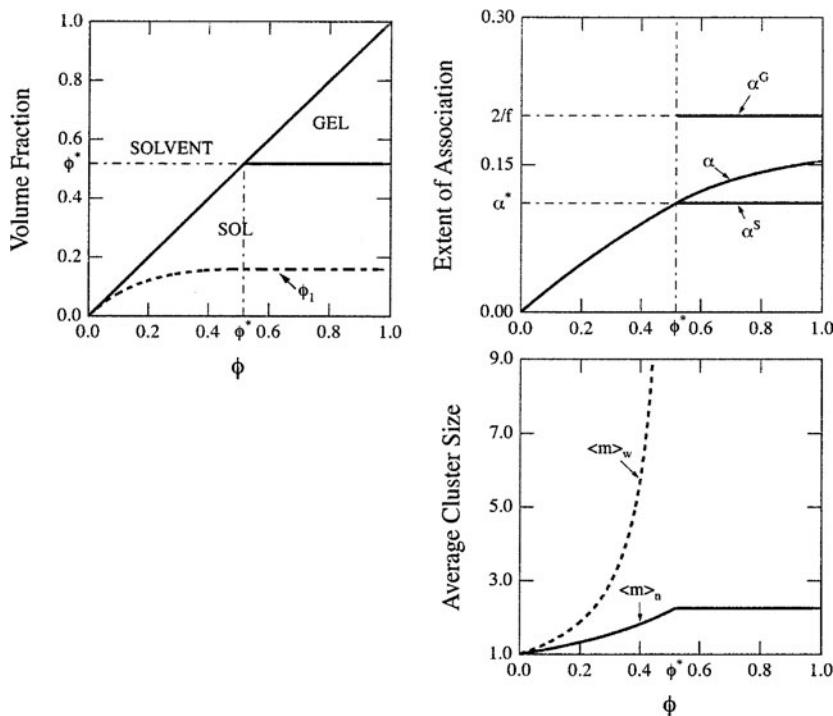


Figure 14. The gel fraction, the extent of association, and the average molecular weight calculated on the basis of Stockmayer's postgel picture. The number average has again a discontinuous slope across the gel point while the weight average remains divergent in the postgel regime.

tricritical point (TCP) [84, 85] at the crossing of sol/gel transition line and binodal (spinodal), while Flory's treatment gives a critical endpoint (CEP) [85] at the shoulder of the binodal and a critical point (CP) in the postgel regime. This is possible because Flory's treatment allows cycle formation within the gel network. Existence of a CP in the postgel regime suggests that phase separation between dilute gel (with only a few cycles) and concentrated gel (with many cycles) in the postgel regime is possible.

Figure 16 presents a comparison of the experimental and theoretical phase diagrams of atactic polystyrene (at-PS) solution in carbon disulfide (CS_2) [86–88]. This solution shows a TCP type phase diagram, but CEP types were also reported for at-PS in different solvents [87]. Here, we attempted to fit the data by simple pairwise crosslinking in Stockmayer's picture. The molecular origin of cross-linking has been the subject of a great deal of investigation [4, 87, 89, 90], but divergent opinions still remain. One series of studies postulates [89] the existence of short, crystallizable, stereoregular segment sequences on polymer chains (even if they are atactic) that are responsible for

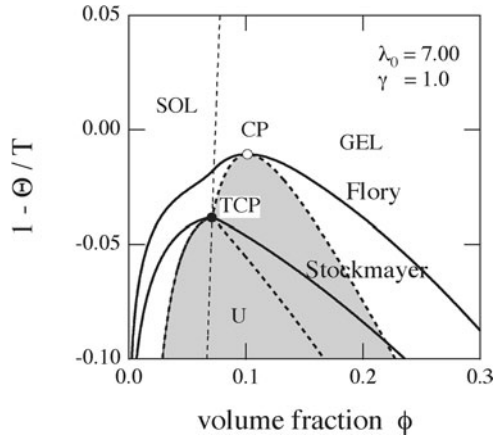


Figure 15. Comparison of the theoretical phase diagrams for low molecular-weight ($n = 1$) trifunctional ($f = 3$) molecules calculated by Flory's treatment (upper lines) and Stockmayer's treatment (lower lines) of the postgel regime for the same association constant. Flory's treatment allows cycle formation within the gel network, so that phase separation of dilute gel with only a few cycles and concentrated gel with many cycles with a critical solution point (white circle indicated by CP) is possible in the postgel regime. (Reprinted with permission from [14]. Copyright (2002) Japanese Society for Polymer Science)

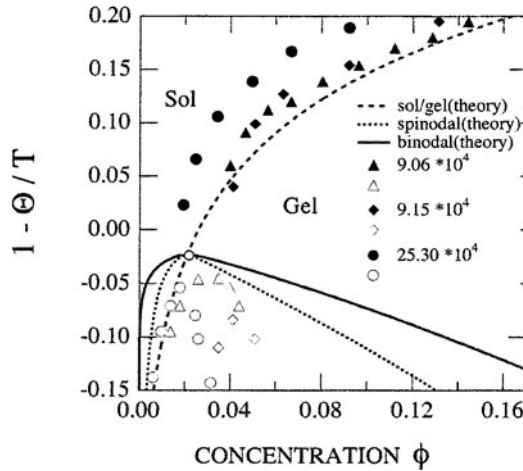


Figure 16. Phase diagram of atactic polystyrene in carbon disulfide. Thermoreversible gelation coexists with phase separation. Theoretical sol/gel transitions (broken line), binodal (solid line) and spinodal (dotted line) are drawn. The reduced temperature is $\tau \equiv 1 - \Theta/T$, with the theta temperature $\Theta = -70^\circ \text{C}$. Experimental data of the gel points (black symbols) and cloud points (white symbols) are shown for three different molecular weights of at-PS. The calculation is fitted to the data for $M = 9.06 \times 10^4$. (Reprinted with permission from [14]. Copyright (2002) Japanese Society for Polymer Science)

the formation of microcrystalline junctions. Another study [4, 90] proposes that cross-linking takes place by specific interactions, such as formation of stoichiometric compounds involving solvent molecules. If such complex formation were the mechanism of cross-linking, the gelation temperature should not show steadily increase with increasing polymer concentration, but should show a maximum at a certain concentration [90]. The existence of specific interactions was later indicated by a light scattering study of a dilute at-PS solution in toluene-CS₂ mixtures [91].

3.3. Multiple Association

Most thermoreversible gels of polymers and biopolymers have crosslink junctions connecting polymer segments belonging to several distinct chains (*multiple junctions*). For instance, gelation by micro-crystallization of chain segments by ionic aggregation and by hydrophobic association of special groups attached on the polymer chains belong to this important category [4, 5]. In some biopolymer gels, triple helices serve as extended cross-link junctions.

Among these, *associating polymers* (AP) are very important because they form ultra-weak networks in water. Associating polymers are water-soluble polymers carrying hydrophobic groups on the backbone or on the chain side [13, 92]. Typical model APs that have recently been the focus of study are partially modified by hydrophobic groups. One series of APs are based on poly(ethylene oxide) chains (PEO), modified by short alkyl chains [93–99], propylene oxide (or butylene oxide) chains [100] and fluorocarbon chains [101–104]. Hydrophobes are either periodically or randomly attached on a polymer chain. The simplest one is a telechelic polymer carrying two hydrophobes at the chain ends. Another series of APs are based on cellulose derivatives. Some examples are ethyl hydroxyethyl cellulose (EHEC) [105–107] and hydroxypropyl methyl cellulose (HPMC) [108, 109]. Polyelectrolytes partially modified by hydrophobic groups have also been intensely studied [110–114].

In this section, we attempt to extend our theory from pairwise association to the more general multiple association. As a model solution, consider a mixture of associative molecules in a solvent. Molecules are distinguished by the number f of associative groups they bear, each group being capable of taking part in the junctions with variable multiplicity which may bind together any number k of such groups [115–117]. We include $k = 1$ for unassociated groups. Junctions of all multiplicities are allowed to coexist in proportions determined by the thermodynamic equilibrium conditions. In order to incorporate polydispersity in the functionality, the number f of associative groups is allowed to vary. Such polydispersity in the functionality of polymers is essential when

associative groups are activated by the conformational transition of polymers as in biopolymer gels. In such cases, the functionality f is not a fixed number but changes depending upon temperature, concentration, and other environmental parameters.

Let n_f be the number of statistical segments on an f -functional primary molecule, and let N_f be the total number of molecules in the solution. The weight fraction w_f of the associative groups carried by the molecules with specified f relative to the total number of associative groups is:

$$w_f = f N_f / \sum f N_f \quad (144)$$

The number- and weight-average functionality of the primary molecules are then:

$$f_n \equiv \left(\sum w_f / f \right)^{-1} \quad (145a)$$

$$f_w \equiv \sum f w_f \quad (145b)$$

The volume fraction of f -functional molecules is $\phi_f = n_f v_f$, where $v_f \equiv N_f / \Omega$ is their number density, and the total volume fraction by $\phi = \sum_f \phi_f$.

In thermal equilibrium, the solution has a distribution of clusters with the population distribution fixed by the equilibrium conditions. Following the notation used by Fukui and Yamabe [115], we define a cluster of type $(\mathbf{j}; \mathbf{l})$ to consist of j_k junctions of multiplicity k ($k = 1, 2, 3, \dots$) and l_f molecules of functionality f ($f = 1, 2, 3, \dots$). The bold letters $\mathbf{j} \equiv \{j_1, j_2, j_3, \dots\}$ and $\mathbf{l} \equiv \{l_1, l_2, l_3, \dots\}$ denote the sets of indices (Figure 17). An isolated molecule of functionality f , for instance, is indicated by $\mathbf{j}_{0f} \equiv \{f, 0, 0, \dots\}$, and $\mathbf{l}_{0f} \equiv \{0, \dots, 1, 0, \dots\}$. (The f -th number is unity; others are zero.)

Let $N(\mathbf{j}; \mathbf{l})$ be the number of $(\mathbf{j}; \mathbf{l})$ -clusters in the system. Then their number density is given by $\nu(\mathbf{j}; \mathbf{l}) = N(\mathbf{j}; \mathbf{l}) / \Omega$, and their volume fraction is:

$$\phi(\mathbf{j}; \mathbf{l}) = \left(\sum_{f \geq 1} n_f l_f \right) \nu(\mathbf{j}; \mathbf{l}) \quad (146)$$

The total volume fraction of the polymer component in the sol part is the sum over all possible cluster types:

$$\phi = \sum_{\mathbf{j}, \mathbf{l}} \phi(\mathbf{j}; \mathbf{l}) \quad (147)$$

As in the preceding sections, we start from the standard reference state (polymers and solvent molecules being separated in hypothetical crystalline states). The free energy change on passing from this reference state to the final



Figure 17. A cluster formed by multiple association. It is characterized by a set of vectorial indices \mathbf{j} specifying the type of junctions and \mathbf{l} specifying the type of molecules.

solution, at equilibrium with respect to cluster formation, is [116]:

$$\beta \Delta F / \Omega = \phi_0 \ln \phi_0 + \sum_{\mathbf{j}, \mathbf{l}} \nu(\mathbf{j}; \mathbf{l}) [\Delta(\mathbf{j}; \mathbf{l}) + \ln \phi(\mathbf{j}; \mathbf{l})] + \chi \phi_0 \phi + \sum_f \nu_f^G \delta_f(\phi) \quad (148)$$

Here, the free energy change $\Delta(\mathbf{j}; \mathbf{l})$ accompanying the formation of a $(\mathbf{j}; \mathbf{l})$ -cluster in a hypothetical undiluted amorphous state from the separate primary molecules in their standard states is:

$$\Delta(\mathbf{j}; \mathbf{l}) \equiv \beta \left\{ \mu^\circ(\mathbf{j}; \mathbf{l}) - \sum_f l_f \mu^\circ(\mathbf{j}_{0f}; \mathbf{l}_{0f}) \right\} \quad (149)$$

In the postgel regime where a cluster grows to a macroscopic network, the last term for the gel part in the free energy is necessary [12, 116].

Following the general strategy, we first derive chemical potentials of the clusters and solvent, and pose chemical equilibrium conditions (Eq. (150)) to find the cluster size distribution function written in terms of the volume fraction of the polymer chains that remain unassociated.

$$\Delta \mu(\mathbf{j}; \mathbf{l}) = \sum_f l_f \Delta \mu(\mathbf{j}_{0f}; \mathbf{l}_{0f}) \quad (150)$$

Substituting the result back into the starting free energy (Eq. (148)), yields Eq. (29), where the association part is:

$$f_{AS}(\{\phi\}) = \sum_f \frac{\phi_f}{n_f} \ln \left(\frac{\phi_{0f}}{\phi_f} \right) + 1 - \phi + \sum_f \frac{\phi_f}{n_f} - \nu^S \quad (151)$$

Here, $\phi_{0f} \equiv \phi(\mathbf{j}_{0f}; \mathbf{l}_{0f})$ is the volume fraction of f -molecules that remain unassociated in the solution. The number of molecules and clusters possessing translational degree of freedom takes the form:

$$v^S = \left(\sum_f \frac{\phi_f}{n_f} \right) / \bar{l}_n + 1 - \phi \quad (152)$$

To derive \bar{l}_n (the number average DP of the clusters), we again apply classical tree statistics, but now augmented to account for multiple association. We have recently presented a systematic method [118, 119] to calculate number- and weight-average DP of condensate polymers (aggregates) based on the application of a cascade process [120] to the polycondensation of functional molecules. Derivation of the main result is straightforward but tedious, so that only the outline of the multiple cascade theory is described here.

First, the probability p_k for a randomly chosen associative group to be in the junction of multiplicity k is introduced. The total extent α of reaction is:

$$\alpha \equiv \sum_{k \geq 2} p_k \quad (153)$$

Then, $p_1 \equiv 1 - \alpha$ is the probability for an associative group to remain unassociated. This is equivalent to the normalization condition, $\sum p_k = 1$. The cascade theory then uses the function $u(x)$ with regard to the junction. This function (referred to as the *junction function*) is:

$$u(x) \equiv \sum_{k \geq 1} p_k x^{k-1}. \quad (154)$$

The number- and weight-average multiplicity of the junctions are:

$$\bar{\mu}_n \equiv \left(\sum_k p_k / k \right)^{-1} \quad (155a)$$

$$\bar{\mu}_w \equiv \sum_k k p_k \quad (155b)$$

The cascade theory of multiple association [118, 119] then gives for the number- and weight-average DP of polymer aggregates:

$$\bar{l}_n^{-1} = 1 - f_n \int_0^1 x u'(x) dx = 1 - f_n (1 - 1/\bar{\mu}_n) \quad (156a)$$

$$\bar{l}_w = 1 + \frac{f_n (\bar{\mu}_w - 1)}{1 - (f_w - 1)(\bar{\mu}_w - 1)} \quad (156b)$$

From the weight average, the gel point is defined by the condition:

$$(f_w - 1)(\bar{\mu}_w - 1) = 1 \quad (157)$$

In the case of the thermoreversible reaction we now consider that the probability p_k obeys the reaction equilibrium condition:

$$\psi p_k / (\psi p_1)^k = K_k \quad (158)$$

$\psi \equiv \sum f N_f / \Omega$ is the number density of functional groups. Hence, p_k is:

$$p_k = K_k \psi^{k-1} p_1^k \quad (159)$$

Then, the form $K_k = \lambda(T)^{k-1} \gamma_k$ is assumed, where $\lambda(T) = \exp(-\Delta f_0 / k_B T)$ is the association constant (Δf_0 being the binding free energy), and γ_k includes the free energy due to the existence of the surface on the micellar junction. Substituting this form of p_k into the normalization condition, we find:

$$\lambda(T) \psi = z \tilde{u}(z) \quad (160)$$

The function $\tilde{u}(z)$ to be used to characterize the junctions is defined by Eq. (161) by using the parameter z defined in Eq. (162).

$$\tilde{u}(z) \equiv \sum_{k \geq 1} \gamma_k z^{k-1}, \quad (161)$$

$$z \equiv \lambda(T) \psi p_1 = \lambda(T) \psi (1 - \alpha) \quad (162)$$

The parameter z gives the concentration of the associative groups that remain unassociated in the solution (multiplied by the association constant). From Eq. (160), that relates the parameter z (and hence reactivity α) with given polymer concentration ϕ , $\bar{\mu}_n$ and $\bar{\mu}_w$ can be found as functions of the temperature and concentration. Hence, the free energy is obtained. The gel point condition (Eq. (157)) is transformed into the equation:

$$(f_w - 1) z \tilde{u}'(z) / \tilde{u}(z) = 1 \quad (163)$$

The multiplicity of the junctions is, in principle, determined automatically by the equilibrium requirement for a given associative interaction. In the case of hydrophobic interactions, the chain length of a hydrophobe, the strength of the water-hydrophobe interaction, the geometric form of an aggregate, and other factors determine the association constant $\lambda(T)$ and the junction multiplicity k . For practical treatment, we avoid this complexity in finding the precise form of the coefficients γ_k , and, hence, the distribution of the multiplicity. Instead, model junctions are introduced [116].

In one of the practical models in common use, multiplicities lying in a certain range, covering $k = k_{\min}$ to k_{\max} , are equally allowed (*mini-max junction*). We have:

$$k = 1(\text{free}), k = k_{\min}, k_{\min} + 1, \dots, k_{\max}(\text{associated}) \quad (164)$$

The junction function takes the form:

$$\tilde{u}(z) = 1 + \sum_{k=k_{\min}}^{k_{\max}} z^{k-1} = 1 + (z^{k_{\min}-1} - z^{k_{\max}})/(1 - z) \quad (165)$$

Such an assumption of limited range can be, to some extent, justified in the case of micelles of hydrophobic chains [117].

When only a single value is allowed (i.e., $k_{\min} = k_{\max} \equiv k$), the so-called *fixed multiplicity model* is applied. Thus, for $k = 2$, the fixed multiplicity model reduces to pair-wise association. The above normalization relation for the fixed multiplicity model of monodisperse polymers (f and n definite) is given by Eq. (166) in terms of the extent α of association to the (scaled) polymer concentration.

$$\lambda(T)\phi/n = \alpha^{1/(k-1)}/f(1 - \alpha)^{k/(k-1)}, \quad (166)$$

The gel point condition Eq. (163), gives $(f - 1)(k - 1)\alpha = 1$ and, hence:

$$\alpha^* \equiv 1/(f - 1)(k - 1) \quad (167)$$

This leads to the critical concentration:

$$\lambda(T)\phi^*/n = (f - 1)(k - 1)/f[(f - 1)(k - 1) - 1]^{k/(k-1)} \quad (168)$$

ϕ^* is the volume fraction of the polymer at the gel point.

Figure 18 plots the reduced concentration $\lambda(T)\phi^*/n$ at the gel point as a function of the junction multiplicity. The functionality is changed from curve to curve. For bifunctional molecules ($f = 2$), at least multiplicity 3 is necessary for gelation. The gelation concentration monotonically decreases with multiplicity. For functionality higher than 2, however, there is an optimal multiplicity for which gelation is easiest. In such cases, growth of the networks becomes difficult with an increasing number of branches at the junctions.

Figure 19 shows the shift of phase diagrams with increasing multiplicity for bifunctional molecules. The sol/gel transition (thick broken), binodals (thin broken) and spinodals (solid) lines are drawn for a fixed multiplicity within Flory's postgel treatment. Above a certain critical multiplicity ($k = 5$ in the figure) the two critical solution points merge into one, and the phase diagram changes from CEP type to TCP type.

3.4. Structure of the Networks with Multiple Junctions

On passing the gel point, networks appear and coexist with finite clusters. The structure of a network can be studied from two different viewpoints: the local and the global viewpoint. The local structure of a network focuses on the structure of each network junction, including its multiplicity, sequence length,

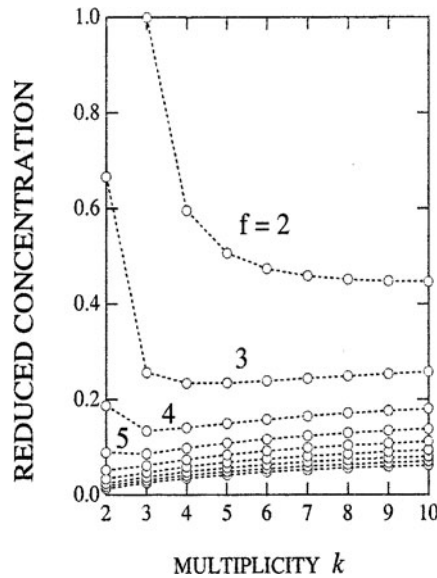


Figure 18. The reduced concentration $\lambda(T)\phi^*/n$ at the gel point plotted against the junction multiplicity. The functionality is varied from curve to curve. For the bifunctional case of $f = 2$, it is a monotonically decreasing function, while for f larger or equal to 3, it has a minimum at a certain multiplicity, where gelation becomes easiest.

degree of chain packing, etc., while the global structure treats topological connectivity of the network as a whole, paying special attention to the *cycle rank* (number of independent loops), number of *elastically effective chains*, number of *dangling ends*, average *path number* of junctions, etc. Studies from such different viewpoints are complementary, and both are necessary.

3.4.1. Local structure of networks – augmented Eldridge-Ferry method

When an associative group on a chain involves ζ sequential repeat units, we can write the standard free energy change as $\Delta f_0 = \zeta(\Delta h - T\Delta s)$. By taking the logarithm of the gelation concentration (Eq. (168)), the important relation is obtained:

$$\ln \phi^* = \zeta \frac{\Delta h}{k_B T} + \ln \left[\frac{(f-1)(k-1)n}{f\{(f-1)(k-1)-1\}^{k/(k-1)}} \right] - \zeta \frac{\Delta s}{k_B} \quad (169)$$

We can find the multiplicity k and sequence length ζ by comparing this relation with the experimental sol/gel transition concentration (see Figure 20) [121]. For the hydrophobes on associating polymers, the enthalpy Δh of a cross-link is found because ζ is known from the number of carbon atoms in a hydrophobe. For the fringed micellar micro-crystalline junction formed by homopolymers,

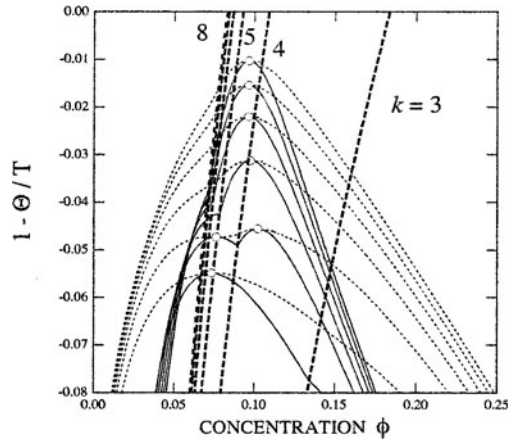


Figure 19. Sol/gel transition lines (thick broken lines), binodals (thin broken lines) and spinodal lines (solid lines) of bifunctional ($f = 2$) polymers with $n = 100$, $\lambda_0 = 10.0$ for association with fixed multiplicity ($k_{\min} = k_{\max} \equiv k$). Multiplicity k is changed from 3 to 8. The transition line shifts to high temperature and low concentration regions with the multiplicity. Gelation is easier for larger multiplicity. (Reprinted with permission from [14]. Copyright (2002) Japanese Society Polymer Science)

each ζ sequence of repeat units along a chain serves as a functional group for cross-linking. In such a case, a polymer chain is regarded as carrying roughly $f = n/\zeta$ functional groups. Since n is large, and hence f is large, we can neglect 1 compared to n or f . This leads to Eq. (170) for micro-crystalline gels.

$$\ln c^* = \zeta \frac{\Delta h}{k_B T} - \frac{1}{k-1} \ln M + \text{constant} \quad (170)$$

Here, the weight concentration c^* has been substituted for the volume fraction. This equation allows ζ and k to be calculated independently. For the special case of pair-wise association ($k = 2$), this equation reduces to the conventional Eldridge-Ferry equation [122] (see also Chapter 8).

From a plot of $\ln c^*$ against $10^3/T + \ln M$, the slope $-B$ of the line at constant T gives $-1/(k-1)$, while the slope $-A$ of the line at constant M gives:

$$\zeta = \frac{10^3 k_B}{|\Delta h|} A = \frac{10^3 R}{|(\Delta h)_{\text{mol}}|} A \quad (171)$$

$(\Delta h)_{\text{mol}}$ is the enthalpy of bonding per mole of repeat units, and R is the gas constant. This method has been applied to experimental data on the gel melting curves of several thermoreversible gels [123, 124].

For example, Figure 21 presents the result for the gelation of poly(vinyl alcohol) (PVA) in water [123]. PVA is a typical crystalline polymer, but it also forms

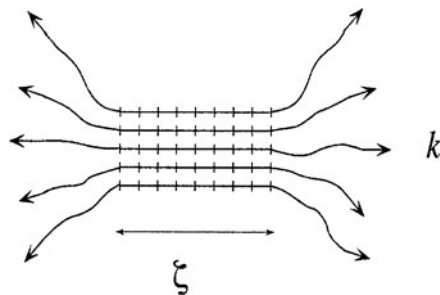


Figure 20. Micellar junction consisting of k chains combined together by the monomer sequences of length ζ .

gels in aqueous solution under large supercooling. There are several pieces of experimental evidence that the cross-links are formed by partial crystallization of the polymer segments in which syndiotactic sequence dominates, while subchains connecting the junctions consist mainly of atactic non-crystalline sequences on PVA chains. The micro-crystals at the junctions are thought to be stabilized by hydrogen bonds between the hydroxy groups. The gel melting temperature (for a given concentration) found from differential scanning calorimetry (DSC) are plotted against visco-elastic measurements for PVA with different molecular weights, covering the range from 2×10^4 to 8×10^5 , in various concentrations [124]. The gel melting temperature T_m is estimated from the temperature at which the DSC heating curve shows an endotherm peak. The slope of the solid lines in Figure 21 with constant molecular weight gives $A = 13.43$; it is almost independent of molecular weight. Hence $\zeta = 26.7$ kcal/mol/ $|\Delta h|_{\text{mol}}$. If we use the heat of fusion $(\Delta h)_{\text{mol}} = 1.64$ kcal/mol in the bulk crystal, $\zeta = 16.3$. On the other hand, the slope of the dotted lines with constant temperature depends on the temperature. At the highest temperature, $T = 91^\circ\text{C}$, of the measurement, it is -0.38 , while it gives a larger value, -0.9 , at $T = 71^\circ\text{C}$. The multiplicity is estimated to decrease from 3.6 for high-temperature melting to 2.1 for low-temperature melting, suggesting a very thin junction structure. From the thermodynamic stability of the junctions, it is natural that a gel which melts at lower temperature has thinner junctions.

3.4.2. Global structure of networks – elastically effective chains

To study visco-elastic properties of networks, we next find the number ν_{eff} of elastically effective chains [8, 125]. The elastically effective chains are those that transmit stress when the network is deformed by an external force. They are related to the topological structure of the network. First, the type of junctions

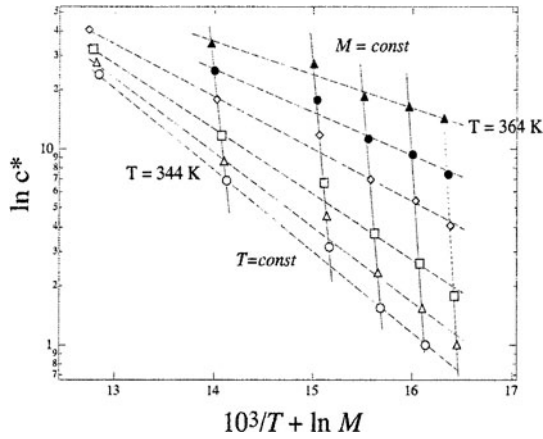


Figure 21. Augmented Eldridge-Ferry plot applied to the gel melting concentration of poly(vinyl alcohol)/water mixtures. Dotted lines show the gel melting concentration at constant temperature, while thin straight lines show those at constant molecular weight of polymer. (▲)91° C; (●)87° C; (◇)83° C; (□)78° C; (△)74° C; (○)71° C. (Reprinted with permission from [123]. Copyright (1996) American Chemical Society)

from their connection paths to the network matrix is specified [121]. A junction of multiplicity k that is connected to the network matrix through i paths is referred to as an (i, k) -junction. Let $\mu_{i,k}$ be the number of junctions in the network specified by the type (i, k) for $0 \leq i \leq 2k$ and for $k = 1, 2, 3, 4, \dots$. The total number of junctions with multiplicity k is:

$$\mu_k = \sum_{i=0}^{2k} \mu_{i,k} \quad (172)$$

To find the number of elastically effective chains, the criterion introduced by Scanlan [126] and Case [127] is employed. It assumes that only subchains connected at both ends to junctions carrying at least *three paths* to the gel are elastically effective. Thus, $i, i' \geq 3$ for an effective chain. A junction with one path ($i = 1$) to the gel unites a group of subchains dangling from the network matrix whose conformations are not affected by an applied stress. A junction with two paths ($i = 2$) to the gel merely extends the length of an effective subchain. A junction with $i \geq 3$ is called an *elastically effective junction*. An effective chain is defined as a chain connecting two effective junctions at both ends. We thus find Eq. (173) for the number of elastically effective junctions, and Eq. (174) for the number of elastically effective chains.

$$\mu_{\text{eff}} = \sum_{k=2}^{\infty} \sum_{i=3}^{2k} \mu_{i,k} \quad (173)$$

$$\nu_{\text{eff}} = \frac{1}{2} \sum_{k=2}^{\infty} \sum_{i=3}^{2k} i \mu_{i,k} \quad (174)$$

These numbers can be explicitly written in terms of the cascade junction function $u(x)$ defined by Eq. (154). Specifically for monodisperse polymer chains with a fixed functionality f , the number of elastically effective chains in a unit volume of the solution takes the form:

$$\nu_{\text{eff}} = \frac{1}{2} (f \nu \alpha) [(\zeta_1 + 2\zeta_2)(1 - \theta(\zeta_0)) - \zeta_1^2 \theta'(\zeta_0)] \quad (175)$$

ν is the total number density of chains, α the extent of association (Eq. (153)), the function $\theta(x)$ is the associated part of the junction function defined by the equation $u(x) \equiv 1 - \alpha + \alpha\theta(x)$, and ζ_i is the probability for a randomly chosen unassociated functional group to be connected to the matrix of the gel network through the number i of paths [121]. These probabilities are written in terms of the solution ζ_0 of the algebraic equation (Eq. (176)) that is smaller than unity; see reference [121] for details.

$$x = u(x)^{f-1} \quad (176)$$

These topological relations hold for arbitrary networks. Their advantage lies in the fact that, by combinatorial counting, we can actually find $\mu_{i,k}$ as a function of the degree α of association [128]. Thus, the degree α is found as a function of the temperature and concentration through Eq. (160), so that all topological numbers described above can be calculated as functions of the temperature and concentration [121]. These curves can be compared with the experimental data on the high frequency dynamic modulus measured by Annable *et al.* [93]. Their experimental data for HEUR C16/35K (PEO end-capped with C₁₆H₃₃, molecular weight 35,000) are compared with the theoretical calculation [121] for $f = 2$ in Figure 22. The value $c^* = 1.0\%$ has been chosen for the weight concentration at gelation. With this gel concentration, the scaling power at the critical region gives $t = 1.6$, close to the percolation value [129]. However, since this power depends sensitively on the way c^* is chosen, more detailed experimental examination in the critical region is clearly required. In fitting the data, we have horizontally shifted the experimental data because of the temperature pre-factor $\lambda(T)$ and also because of the difference in the units of polymer concentration. Although fitting by a single theoretical curve is impossible due to the existence of polydispersity in the multiplicity, the theory produces a good result over a wide range of concentration with multiplicity ranging from 6 to 8. It turns out that about 60% of the chains are elastically effective in the limit of high concentration.

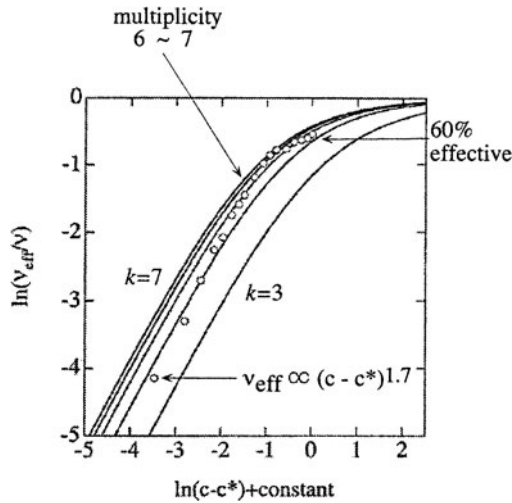


Figure 22. The number of elastically effective chains as a function of the polymer concentration. Experimental data of the HEUR 16C/35K are compared with calculations. In the calculation, the junction multiplicity k is changed from curve to curve. (Reprinted with permission from [121]. Copyright (1996) American Chemical Society)

3.5. Mixtures of Associative Molecules – Gelation with Co-Networks

In biological and medical science, thermoreversible gels consisting of more than two species of molecules or polymers are very important for controlling the cross-link structure. For example, it has been suggested that the repeated sol/gel transition of actin, controlled by the actin-binding protein (ABP), drives motions of individual biological cells [130]. In this ternary system (actin, ABP and water), ABP works as a cross-linker of the actin filaments. In the food industry, biopolymer mixtures in which either single or multiple ingredients form networks have many important applications, and have been the focus of intensive experimental study [131, 132].

To study thermoreversible formation of mixed networks (see also Chapter 21), we first consider a model mixture of reactive molecules $R\{A_f\}$ and $R\{B_g\}$, each carrying the number f of A-groups and g of B-groups. Another important case where each molecule carries both species A and B (*co-associating polymer*) has recently been studied [118, 133]. We allow multiple association of both groups, but first consider the simpler case of pairwise association [16, 134]. The strength of the bonds can be expressed by the three association constants in Eq. (38). By the relative strength of these

constants, now we can place the types of association into three fundamental categories [16]:

- (i) *Interpenetrating Polymer Networks (IPN)* – Reactive groups A and B form bonds within the same species, but do not form between different species (i.e., $\lambda_{AB} = 0$). We refer to this case as A·A/B·B.
- (ii) *Alternating Polymer Networks (APN)* – Bonds are allowed only between different species (i.e., $\lambda_{AA} = \lambda_{BB} = 0$). We refer to this case as A·B. Because the clusters (of finite or infinite size) formed are in general multi-block copolymers, the system may undergo microphase separation. Hence, macrophase separation, microphase separation, and gelation interfere with each other.
- (iii) *Randomly Mixed Networks (RMN)* – If the strengths of associative forces in all three combinations are of the same order, cluster formation progresses randomly. The resultant networks can be regarded as macroscopic random block-copolymers.

We now extend this classification to suit multiple association. For multiple association, it is convenient to classify from the mixing properties *inside* the junctions. To specify a multiple junction precisely, a set of integers (k_1, k_2) is introduced, where k_1 is the number of A groups contained, and k_2 is the number of B groups [118, 119]. The cascade junction functions then take the form in Eq. (177) for the junction which an arbitrarily chosen A-group (and B-group) enters.

$$u_A(x, y) = \sum_{k_1 \geq 1, k_2 \geq 0} p_{k_1, k_2} x^{k_1-1} y^{k_2} \quad (177a)$$

$$u_B(x, y) = \sum_{k_1 \geq 0, k_2 \geq 1} q_{k_1, k_2} x^{k_1} y^{k_2-1} \quad (177b)$$

p_{k_1, k_2} is the probability for a randomly chosen A-group to be in the junction specified by the number (k_1, k_2) , and q_{k_1, k_2} is the same for the B-group. The number density ν^S of clusters and molecules that possess a translational degree of freedom is:

$$\nu^S = \frac{\phi}{n_A} \left\{ 1 - f \int_0^1 x u'_A(x) dx \right\} + \frac{1 - \phi}{n_B} \left\{ 1 - g \int_0^1 y u'_B(y) dy \right\} \quad (178)$$

Abbreviated notations $u_A(x) \equiv u_A(x, x)$ etc. for the diagonal elements have been used.

This result can be intuitively derived by stoichiometric consideration. Within the tree approximation, the number of connected clusters is the same as

the number of primary molecules minus the total number of connecting bonds. The integral in Eq. (178) gives:

$$\int_0^1 x u'_A(x) dx = \sum \frac{k_1 + k_2 - 1}{k_1 + k_2} p_{k_1, k_2} = 1 - \frac{1}{\bar{\mu}_A} \quad (179)$$

Hence,

$$v^S = \frac{\phi}{n_A} \left\{ 1 - f \left(1 - \frac{1}{\bar{\mu}_A} \right) \right\} + \frac{1 - \phi}{n_B} \left\{ 1 - g \left(1 - \frac{1}{\bar{\mu}_B} \right) \right\} \quad (180)$$

Here, the average multiplicity $\bar{\mu}_A$ and $\bar{\mu}_B$ of the mixed junctions are defined by:

$$\bar{\mu}_A^{-1} \equiv \sum p_{k_1, k_2} / (k_1 + k_2), \quad \text{and} \quad \bar{\mu}_B^{-1} \equiv \sum q_{k_1, k_2} / (k_1 + k_2) \quad (181)$$

Since the number of unreacted A-groups and B-groups are given by $\psi_A p_{1,0}$, and $\psi_B q_{0,1}$, the reaction equilibrium condition for an A-group joining in a (k_1, k_2) junction, is:

$$\frac{\psi_A p_{k_1, k_2}}{(\psi_A p_{1,0})^{k_1} (\psi_B q_{0,1})^{k_2}} = K_{k_1, k_2}^{(A)} \quad (182)$$

$K_{k_1, k_2}^{(A)}$ is the reaction equilibrium constant. A similar relation holds for the B-groups. Now, we assume as usual that the equilibrium constant takes the form:

$$K_{k_1, k_2}^{(A)} = \gamma_{k_1, k_2}^{(A)} \lambda_A(T)^{k_1-1} \lambda_B(T)^{k_2} \quad (183)$$

In Eq. (183), $\lambda_\alpha(T)$ are the association constants written in terms of the free energy Δf_α required for binding a reactive group of the type α into the junction.

$$\lambda_\alpha(T) = \exp(-\Delta f_\alpha / k_B T), \quad \text{for } \alpha = A, B \quad (184)$$

The coefficient $\gamma_{k_1, k_2}^{(A)}$ gives a correction due to the existence of the surface of micellar junction [116]. Similar formulae for $K_{k_1, k_2}^{(B)}$ are assumed.

Substituting the results into the cascade junction functions, we find Eq. (185) by using new variables $z_A \equiv \lambda_A \psi_A p_{1,0}$ and $z_B \equiv \lambda_B \psi_B q_{0,1}$.

$$u_A(x, y) = p_{1,0} \sum_{k_1 \geq 1, k_2 \geq 0} \gamma_{k_1, k_2}^{(A)} (z_A x)^{k_1-1} (z_B y)^{k_2} \quad (185)$$

These z parameters are the number densities of reactive groups (times association constant) that remain unassociated in the system. We next define a \tilde{u} function by the sum in Eq. (185) as in Eq. (186), and there is a similar equation for \tilde{u}_B .

$$\tilde{u}_A(x, y) \equiv \sum_{k_1 \geq 1, k_2 \geq 0} \gamma_{k_1, k_2}^{(A)} x^{k_1-1} y^{k_2} \quad (186)$$

Since $u_A(1, 1) = 1$, the parameters z_A and z_B satisfy the coupled equations:

$$\lambda_A \psi_A = z_A \tilde{u}_A(z_A, z_B) \quad (187a)$$

$$\lambda_B \psi_B = z_B \tilde{u}_B(z_A, z_B) \quad (187b)$$

By solving these equations with respect to z 's, we find them as functions of a given total number of reactive groups in a unit volume. Solution properties, the gel point, etc. can be studied by substituting the result into the chemical potentials, the weight-average molecular weight, etc.

For pair-wise association, we have only to assume $p_{1,0} = 1 - (\alpha + p)$, $p_{1,1} = p$, $p_{2,0} = \alpha$ and $q_{0,1} = 1 - (\beta + q)$, $q_{1,1} = q$, $q_{0,2} = \beta$, where α is the reaction probability of an A-group with an A-group, p is that with a B-group, while β is the reaction probability of a B-group with B-group, q is that with A-group. Figure 23(a),(b) shows typical phase diagrams [10] of alternately cross-linked networks in a symmetric case ($n_A = n_B = 10$, $f = g = 3$, $\lambda_0 = 1.0$). The dimensionless binding energy γ (Eq. (43)) between the functional

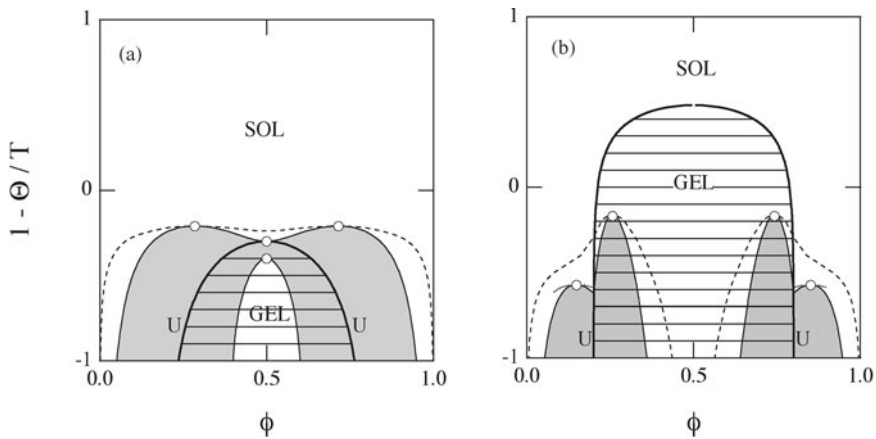


Figure 23. Phase diagrams of an alternately cross-linked network in a mixture of low molecular-weight trifunctional molecules (Flory's treatment); $n_A = n_B = 10$, $f = g = 3$, $\lambda_0 = 1.0$. The Association constant γ is changed with other parameters being fixed: (a) $\gamma = 1.9926$, (b) $\gamma = 5.0$. The sol/gel transition (thick solid lines), binodal (thin dashed) and spinodal (thin solid) lines are shown. The postgel region is indicated by thin horizontal lines. The shaded parts indicated by the letter U, are unstable regions. The open circles show critical solution points. The gel region lies inside the spinodal for small values of the association constant as in (a), but in the case of strong association as shown in (b), the miscibility gap splits into two separate pieces, and the gel region is stabilized. The alternating network works as the solubilizer in this case due to its amphiphilic nature. The critical points remain inside the gel region so that phase separation into two gels with different concentrations, and hence different cross-link densities, is possible. (Reprinted with permission from [16]. Copyright (1999) American Chemical Society)

groups on A-chains and B-chains is different. Thick solid lines show the sol/gel transition, thin dashed lines are for binodal, thin solid lines are for spinodal, and white circles show the critical solution point. The gel region is indicated by the horizontal lines, and the unstable region (U) is shaded. For small γ , the gel region lies inside the unstable region, so that a stable homogeneous gel is not expected. In Figure 23(a), the population of hetero-clusters becomes so large at low temperatures that a reentrant homogeneous phase appears, and, as a result, a new critical solution point lies on the sol/gel transition line. With a slight increase in γ , the two critical solution points lying at $\phi = 0.5$ merge into a single point. Upon further increase in γ , the gel region grows and the miscibility gap is completely separated around the stoichiometric concentration ($\phi = 0.5$) (in the symmetric case) by the existence of mixed clusters.

For mixed networks with multiple junctions, Clark *et al.* [131], for instance, studied composite aqueous gels consisting of thermoreversible cold-setting gelating components such as agarose and gelatin by electron and optical microscopy. They reported micrographs that appeared quite similar to those observed for a number of synthetic interpenetrating networks [135, 136], and showed phase separation into two polymer networks with possible phase inversion at a certain mixture composition. Durrani *et al.* [137, 138] derived a phase diagram for the ternary amylopectin-gelatin-D₂O mixture in the sol state by the use of Fourier transformed infrared spectroscopy.

Formation of mixed networks may also be used to modify the rheological properties of aqueous polymer solutions. For instance, it was found [139] that the viscosity of mixtures of two species of polymers, poly(*N*-isopropylacrylamide) and hydrophobically modified poly(sodium acrylate), in aqueous solution becomes several orders of magnitude higher than is achieved without hydrophobic modification. A possible mechanism of heteropolymer cross-linking between the hydrophobes on the different species, followed by network formation by the hydrophobic aggregation of molecules, was proposed [139].

The theory presented in this section for treating binary mixtures with heteromolecular association is directly applicable to other important systems. For instance, when polymer-polymer association and polymer-water association coexist, as seen in aqueous biopolymer solutions, there is a mixture of $R\{A_f\}$ and $R\{B_1\}$ with A·A and A·B bonds, and competition between hydration and cross-linking takes place. As a result, the solution gels at high temperature (*inverted gelation*). Interaction of hydrophobically modified water-soluble polymers with added surfactant molecules is another important example. In this case, the hydrophobes of the surfactant molecules strongly interact with those on the polymers, and form mixed micelles. The polymer network is modified by the concentration of the added surfactant, leading to interesting rheological behavior. Other potential applications to complex associating polymer solutions of industrial importance are apparent.

4. Conclusions and Perspectives for the Future

We have presented an outline of a theoretical scheme to study molecular association and thermoreversible gelation in polymer solutions and mixtures. The effects of the thermodynamic nature of the sol/gel transition, interference with phase separation, structure of the network junctions, path connectivity in the network have been studied on the basis of the multiple tree statistics combined with classical lattice-theoretical polymer solutions. This chapter has focused mainly on the gelation of water-soluble associating polymers driven by hydrophobic aggregation, but applications to other many types of gels, such as those driven by hydrogen bonds, micro-crystallization, helix formation, etc. are possible. We close in hoping that, after reading this chapter, readers will try to find phase diagrams of their own systems in the framework of this theory.

References

- [1] Clark, A.H.; Ross-Murphy, S.B. *Ad. Polym. Sci.*, **1987**, 83, 57.
- [2] Russo, P.S. *Reversible Polymeric Gels and Related Systems*, **1987**, ACS Symposium Series, 350.
- [3] Kramer, O. *Biological and Synthetic Polymer Networks*, London and New York: Elsevier Applied Science, **1988**.
- [4] Guenet, J. M. *Thermoreversible Gelation of Polymers and Biopolymers*, London: Academic Press, **1992**.
- [5] te Nijenhuis, K. *Ad. Polym. Sci.*, **1997**, 130, 1.
- [6] Flory, P.J. *J. Chem. Phys.*, **1944**, 12, 425.
- [7] Huggins, M.L. *J. Chem. Phys.*, **1942**, 46, 151.
- [8] Flory, P.J. *Principles of Polymer Chemistry*, Ithaca: Cornell University Press, **1953**.
- [9] Koningsveld, R.; Stockmayer, W.H. Nies, E. *Polymer Phase Diagrams*, Oxford: Oxford University Press, **2001**.
- [10] Tanaka, F. *Macromolecules*, **1989**, 22, 1988.
- [11] Tanaka, F.; Matsuyama, A. *Phys. Rev. Lett.*, **1989**, 62, 2759.
- [12] Tanaka, F. *Macromolecules*, **1990**, 23, 3784; 3790.
- [13] Tanaka, F.; Koga, T. *Bull. Chem. Soc. Jpn*, **2001**, 74, 201.
- [14] Tanaka, F. *Polym. J.*, **2002**, 74, 479.
- [15] Šolc, K. *Macromolecules*, **1970**, 3, 665.
- [16] Tanaka, F.; Ishida, M. *Macromolecules*, **1999**, 32, 1271.
- [17] Shultz, A.R.; Flory, P.J. *J. Am. Chem. Soc.*, **1953**, 75, 3888; 5631.
- [18] Tanaka, F.; Ishida, M.; Matsuyama, A. *Macromolecules*, **1991**, 24, 5582.
- [19] Kielhorn, L.; Muthukumar, M. *J. Chem. Phys.*, **1997**, 107, 5588.
- [20] Tanaka, H.; Hashimoto, T. *Macromolecules*, **1991**, 24, 5398; 5713.
- [21] Leibler, L. *Macromolecules*, **1980**, 13, 1602.
- [22] Bates, F.S.; Fredrickson, G.H. *Ann. Rev. Phys. Chem.*, **1990**, 41, 525.
- [23] Hornreich, R.M.; Luban M.; Shtrikman, S. *Phys. Rev. Lett.*, **1975**, 35, 1678.
- [24] Haraguchi, M.; Nakagawa, T.; Nose, T. *Polymer*, **1995**, 36, 2567.
- [25] Haraguchi, M.; Inomata, K.; Nose, T. *Polymer*, **1996**, 37, 3611.
- [26] Inomata, K.; Haraguchi, M.; Nose, T. *Polymer*, **1996**, 37, 4223.

- [27] Lehn, J.-M. *Supramolecular Chemistry – Concepts and Perspectives*, New York: VCH **1995**.
- [28] Ciferri, A., Ed. *Supramolecular Polymers*, New York: Marcel Dekker **2000**.
- [29] Kato, T. *Structure and Bonding*, **2000**, 96, 95.
- [30] Jacobson, H.; Stochmayer, W. H. *J. Chem. Phys.*, **1950**, 18, 1600; **1950**, 18, 1607.
- [31] Mayer, J. E.; Mayer, M.G. *Statistical Mechanics*, New York: John Wiley & Sons, Chap. 16, **1940**.
- [32] Truesdell, C. *Ann. Math.*, **1945**, 46, 144.
- [33] Scott, R.L. *J. Phys. Chem.*, **1967**, 69, 261; **1965**, 71, 352.
- [34] Wheeler, J.C.; Pfeuty, P. *Phys. Rev. Lett.*, **1981**, 46, 1409.
- [35] Wheeler, J.C.; Pfeuty, P. *Phys. Rev.*, **1981**, A24, 1050.
- [36] Wheeler, J.C.; Pfeuty, P. *J. Chem. Phys.*, **1981**, 74, 6415.
- [37] Dudowicz, J.; Freed, K.; Douglas, J.F. *J. Chem. Phys.*, **1999**, 111, 7116; **1999**, 112, 1002.
- [38] Terech, P.; Weiss, R.G. *Chem. Rev.*, **1997**, 97, 3133.
- [39] Tanaka, F.; Ishida, M. *Macromolecules*, **1997**, 30, 1836.
- [40] Tanaka, F. *Macromolecules*, **2004**, 37, 605; Toda, M.; Tanaka, F. *Ibid*, **2005**, 38, 561.
- [41] Matsuyama A.; Tanaka, F. *Phys. Rev. Lett.*, **1990**, 65, 341.
- [42] Ruokolainen, J.; ten Brinke, G.; Ikkala, O.; Torkkeli, M.; Serimaa, R. *Macromolecules*, **1996**, 29, 3409.
- [43] Ruokolainen, J.; Torkkeli, M.; Serimaa, R.; Vahvaselkä, S.; Saariaho, M.; ten Brinke, G.; Ikkala, O. *Macromolecules*, **1996**, 29, 6621.
- [44] ten Brinke, G.; Ruokolainen, J.; Ikkala, O.; *Europhys. Lett.*, **1996**, 35, 91.
- [45] ten Brinke, G.; Ikkala, O. *Trends Polym. Sci.*, **1997**, 5, 213.
- [46] Ruokolainen, J.; Torkkeli, M.; Serimaa, R.; Komanschek, B.E.; Ikkala, O.; ten Brinke, G. *Phys. Rev. E.*, **1996**, 54, 6646.
- [47] Angerman, H.J.; ten Brinke, G.; *Macromolecules*, **1999**, 32, 6813.
- [48] Yashima, E.; Matsushima, T.; Okamoto, Y. *J. Amer. Chem. Soc.*, **1997**, 119, 6345.
- [49] Yashima, E.; Maeda, K.; Okamoto, Y. *Nature*, **1999**, 399, 449.
- [50] Maeda, K.; Okada, S.; Yashima, E.; Okamoto, Y. *J. Polym. Sci. Part A, Polym. Chem.*, **2001**, 39, 3180.
- [51] Morino, K.; Maeda, K.; Okamoto, Y.; Yashima E.; Sato, T. *Chem. Eur. J.*, **2002**, 8, 5112.
- [52] Anderson G.R.; Wheeler, J.C. *J. Chem. Phys.*, **1980**, 73, 5778.
- [53] Walker, J.S.; Vause, C.A. *Phys. Lett.*, **1980**, 79A, 421.
- [54] Goldstein, R.E.; Walker, J.S. *J. Chem. Phys.*, **1983**, 78, 1942.
- [55] Walker, J.S.; Vause, C.A. *Sci. Am.*, **1987**, 256, 90.
- [56] Narayanan, T.; Kumar, A. *Phys. Rep.*, **1994**, 249, 135.
- [57] Saeki, S.; Kuwahara, N.; Konno, S.; Kaneko, M.; *Macromolecules*, **1975**, 6, 247; **1973**, 8, 799.
- [58] Saeki, S.; Kuwahara, N.; Nakata, M.; Kaneko, M. *Polymer*, **1976**, 17, 685.
- [59] Dormidontova, E.E. *Macromolecules*, **2002**, 35, 987.
- [60] Bekiranov, S.; Bruinsma, R.; Pincus, P. *Phys. Rev. E*, **1997**, 55, 577.
- [61] Bazuin, C.G. In *Mechanical and Thermophysical Properties of Polymer Liquid Crystals*, W. Brostow, Eds., London: Chapman & Hall, Chap. 3, **1998**.
- [62] Bradfield, A.E.; Jones, B. *J. Chem. Soc.*, **1929**, 2660.
- [63] Jones, B. *J. Chem. Soc.*, **1935**, 1874.
- [64] Weygand, C.; Gabler, R. *Z. Phys. Chem.*, **1940**, B46, 270.
- [65] Gray, G.W.; Jones, B. *J. Chem. Soc.*, **1953**, 4179.

- [66] Brienne, M.-J.; Gabard, J.; Lehnand, J.-M.; Stibor, I. *J. Chem. Soc. Chem. Comm.*, **1989**, 1868.
- [67] Kato, T.; Fréchet, J.M.J. *Macromolecules*, **1989**, *22*, 3818.
- [68] Maier, W.; Saupe, A. *Z. Naturforsch.*, **1958**, *13a*, 564; **1959**, *14a*, 882; **1960**, *15a*, 287.
- [69] McMillan, W.L. *Phys. Rev.*, **1971**, *A4*, 1238.
- [70] Shoji, M.; Tanaka, F. *Macromolecules*, **2002**, *35*, 7460.
- [71] Cahn, J.W. *Trans. Metall. Soc. AIME*, **1968**, *242*, 166.
- [72] Martin, J.W.; Doherty, R.D.; Cantor, B. *Stability of Microstructures in Metallic Systems*, Cambridge: Cambridge University Press, **1997**, Sec. 3.2.
- [73] Olmsted, P.D.; Poon, W.C.K.; McLeish, T.C.B.; Terrill, N.J.; Ryan, A.J. *Phys. Rev. Lett.*, **1998**, *81*, 373.
- [74] Flory, P.J. *Proc. Roy. Soc., London*, **1956**, *A234*, 73.
- [75] Miller, W.G.; Kou, L.; Tohyama, K.; Voltaggio, V. *J. Polym. Sci.: Polym. Symp.*, **1978**, *65*, 91.
- [76] Whittaker, E.T.; Watson, G.N. *A Course of Modern Analysis*, Cambridge: Cambridge University Press, Chap. 2, **1969**.
- [77] Tanford, C. *The Hydrophobic Effect*, New York: Wiley Chap. 7, **1980**.
- [78] Candau, S.J.; Hirsch E.; Zana, R. *J. Phys. France*, **1984**, *45*, 1263.
- [79] Shikata, T.; Hirata, H.; Kotaka, T. *Langmuir*, **1987**, *3*, 1081; **1988**, *4*, 354.
- [80] Hofmann, H.; Rehage, H. *Mol. Phys.*, **1989**, *5*, 1225.
- [81] Flory, P.J. *J. Am. Chem. Soc.*, **1941**, *63*, 3091; **1941**, *63*, 3096.
- [82] Stockmayer, W.H. *J. Chem. Phys.*, **1943**, *11*, 45; **1944**, *12*, 125.
- [83] Ishida, M.; Tanaka, F. *Macromolecules*, **1997**, *30*, 3900.
- [84] Knobler, C.M.; Scott, R.L. In *Phase Transitions and Critical Phenomena*, 9, New York: Academic Press, **1984**.
- [85] Pynn R.; Skjeltorp, A. *Multicritical Phenomena*, New York: Plenum Press, **1984**.
- [86] Wellinghoff, S.; Shaw, J.; Baer, E. *Macromolecules*, **1979**, *12*, 932.
- [87] Tan, H.M.; Moet, A.; Hiltner, A.; Baer, E. *Macromolecules*, **1983**, *16*, 28.
- [88] Boyer, R.F.; Baer, E.; Hiltner, A. *Macromolecules*, **1985**, *18*, 427.
- [89] Domszy, R.C.; Alamo, C.; Edwards, O.; Mandelkern, L. *Macromolecules*, **1986**, *19*, 310.
- [90] Gan, J.Y.S.; Francois, J.; Guenet, J.M. *Macromolecules*, **1986**, *19*, 173.
- [91] Chen, S.-J.; Berry, G.C.; Plazek, D.J. *Macromolecules*, **1995**, *28*, 6539.
- [92] Winnik, M.A. *Curr. Opin. Colloid Interface Sci.*, **1997**, *2*, 424.
- [93] Annable, T.; Buscall, R.; Ettelaie, R.; Whittlestone, D. *J. Rheol.*, **1993**, *37*, 695.
- [94] Annable, T.; Buscall, R.; Ettelaie, R.; Shepherd, P.; Whittlestone, D. *Langmuir*, **1994**, *10*, 1060.
- [95] Rao, B.; Uemura, Y.; Dyke, L.; Macdonald, P.M. *Macromolecules*, **1995**, *28*, 531.
- [96] Alami, E.; Almgren, M.; Brown, W.; Francois, J. *Macromolecules*, **1996**, *29*, 2229.
- [97] Alami, E.; Almgren, M.; Brown, W. *Macromolecules*, **1996**, *29*, 5026.
- [98] Xu, B.; Yekta A.; Winnik, M.A. *Langmuir*, **1997**, *13*, 6903.
- [99] Tam, K.C.; Jenkins, R.D.; Winnik, M.A.; Bassett, D.R. *Macromolecules*, **1998**, *31*, 4149.
- [100] Zhou, Z.; Yang, Y.-W.; Booth, C.; Chu, B. *Macromolecules*, **1996**, *29*, 8357.
- [101] Amis, E.J.; Hu, N.; Seery, T.A.P.; Hogen-Esch, T. E.; Yassini, T.E.M.; Hwang, F. In *Hydrophobic Polymers: Performance with Environmental Acceptance*, E. Glass, Ed., Washington: American Chemical Society **1996**, p. 279.
- [102] Hwang, F.S.; Hogen-Esch, T.E. *Macromolecules*, **1995**, *28*, 3328.
- [103] Xie, X.; Hogen-Esch, T.E. *Macromolecules*, **1996**, *29*, 1734.

- [104] Zhang, H.; Pan, J.; Hogen-Esch, T.E. *Macromolecules*, **1998**, *31*, 2815.
- [105] Nilsson, S. *Macromolecules*, **1995**, *28*, 7837.
- [106] Nyström, B.; Thuresson, K.; Lindman, B. *Langmuir*, **1995**, *11*, 1994.
- [107] Nyström, B.; Walderhaug, H.; Hansen F.K.; Lindman, B.; *Langmuir*, **1995**, *11*, 750.
- [108] Sarkar, N. *J. Appl. Polym. Sci.*, **1979**, *24*, 1073.
- [109] Kobayashi, K.; Huang, C.; Lodge, T.P. *Macromolecules*, **1999**, *32*, 7070.
- [110] Morishima, Y. *Trends in Polym. Sci.*, **1994**, *2*, 31.
- [111] Morishima, Y.; Nomura, S.; Ikeda, T.; Seki, M.; Kamachi, M. *Macromolecules*, **1995**, *28*, 2874.
- [112] Petit, F.; Iliopoulos, I.; Audebert, R.; Szonyi, S. *Langmuir*, **1997**, *13*, 4229.
- [113] Bokias, G.; Hourdet, D.; Iliopoulos, I.; Staikos, G.; Audebert, R. *Macromolecules*, **1997**, *30*, 8293.
- [114] Bokias, G.; Hourdet, D.; Iliopoulos, I. *Macromolecules*, **2000**, *33*, 2929.
- [115] Fukui, K.; Yamabe, T. *Bull. Chem. Soc. Jpn*, **1967**, *40*, 2052.
- [116] Tanaka, F.; Stockmayer, W.H. *Macromolecules*, **1994**, *27*, 3943.
- [117] Tanaka, F.; Koga, T. *Comp. Theor. Polym. Sci.*, **2000**, *10*, 259.
- [118] Tanaka, F.J. *Polym. Sci., Part B: Polym. Phys.*, **2003**, *41*, 2405.
- [119] Tanaka, F.J. *Polym. Sci., Part B: Polym. Phys.*, **2003**, *41*, 2413.
- [120] Gordon, M. *Proc. Roy. Soc. (London)*, **1962**, A268, 240.
- [121] Tanaka, F.; Ishida, M. *Macromolecules*, **1996**, *29*, 7571.
- [122] Eldridge, J.E.; Ferry, J.D. *J. Phys. Chem.*, **1954**, *58*, 992.
- [123] Tanaka, F.; Nishinari, K. *Macromolecules*, **1996**, *29*, 3625.
- [124] Nishinari, K.; Tanaka, F. *J. Chim. Phys.*, **1996**, *93*, 880.
- [125] Flory, P.J. *Proc. R. Soc. London, Ser.A*, **1976**, *351*, 351.
- [126] Scanlan, J. *J. Polym. Sci.*, **1960**, *43*, 501.
- [127] Case, L.C. *J. Polym. Sci.*, **1960**, *45*, 397.
- [128] Pearson, D.S.; Graessley, W.W. *Macromolecules*, **1978**, *11*, 528.
- [129] Stauffer, D. *Introduction to Percolation Theory*, Chap. 2, London: Taylor & Francis, **1985**.
- [130] Stossel, T.P. *Sci. Am.*, **1994**, *265*, 40.
- [131] Clark, A.H.; Richardson, R.K.; Ross-Murphy, S.; Stubbs, J.M. *Macromolecules*, **1983**, *16*, 1367.
- [132] Nishinari, K.; Doi, E. *Food Hydrocolloids: Structures, Properties, and Functions*, New York: Plenum Press, **1994**.
- [133] Indei, T.; Tanaka, F. *J. Rheology*, **2004**, *48*, 641.
- [134] Stockmayer, W.H.; *J. Polym. Sci.*, **1952**, *9*, 69.
- [135] Sperling, L.H. *Interpenetrating Polymer Networks and Related Materials*, New York: Plenum Press, **1981**.
- [136] Utracki, L.A. *Multiphase Polymers: Blends and Ionomers*, 395, ACS Symposium Series, New York: Plenum Press, **1988**.
- [137] Durrani, C.M.; Prystupa, D.A.; Donald, A.M.; Clark, A.H. *Macromolecules*, **1993**, *26*, 981.
- [138] Durrani, C.M.; Donald, A.M. *Macromolecules*, **1994**, *27*, 110.
- [139] Bokias, G.; Hourdet, D.; Iliopoulos, I.; Staikos, G.; Audebert, R. *Macromolecules*, **1997**, *30*, 8293.

Chapter 2

GROWTH AND CHIRALITY AMPLIFICATION IN HELICAL SUPRAMOLECULAR POLYMERS

Jeroen van Gestel*, Paul van der Schoot, and M.A.J. Michels

*Eindhoven Polymer Laboratories, Technische Universiteit Eindhoven,
P.O. Box 513, 5600 MB Eindhoven, The Netherlands*

1. Introduction	79
2. Helical Aggregation	80
3. Discotics	82
4. Linear Self-Assembly	83
5. A Two-State Model	85
6. Aggregate Ends	86
7. Chirality Amplification	90
8. Sergeants and Soldiers	91
9. Conclusions and Perspectives for the Future	94

1. Introduction

Helical self-assembled, supramolecular polymers have been known to exist in nature for some time [1–6]. It is well-established that aggregates such as f-actin [3, 4], tobacco mosaic virus [6] and β -sheet ribbons formed by certain oligopeptides [7] are helical. Recently, many different molecules have been synthesized that also self-assemble into helical conformations [8–16].

Helical self-assembly [17] can be a one-state or a two-state process, depending on the physical conditions. In the latter case, polymerization into non-helical aggregates precedes a conformational transition of the assemblies to a helical state. Both the helical transition and the polymerization can be triggered by

*Current address: Physical Chemistry and Molecular Thermodynamics Group, DelftChemTech, Julianalaan 136, 2628 BL, Delft, The Netherlands.

changes in concentration or temperature [18, 19]. Neither of the two are phase transitions in the true sense of the word, but more or less gradual crossovers. However, the helical transition in particular can be fairly sharp due to cooperative effects, leading to a remarkable temperature sensitivity. Because of this, it is possible to define the transition temperatures. See below.

Several of the known helical self-assembled systems seem to display a gel-like phase at high enough concentrations, which is presumably linked with the helical transition [3, 8, 10, 20]. The reason is that helical polymers are typically more rigid (i.e., have a larger radius of gyration) than non-helical ones, and that the helical transition is accompanied by a strong increase in the mean aggregate size and ultimately, when sufficiently long, entanglements.

2. Helical Aggregation

In order to understand the mechanisms driving the helical aggregation, a host of experimental and theoretical work has been done [3, 8–16, 21–23]. The most well-known theory in this context, is the Oosawa-Kasai treatment for the helical assembly of f-actin fibers from the g-actin protein [3, 23]. Due to their molecular architecture, the actin units are thought to be able to attach themselves to each other in two ways, one of which results in a non-helical assembly, and one in a helical one (see Figure 1). Oosawa and co-workers assign one equilibrium constant to each process (K and K_h). This means that their model is in essence an all-or-nothing model: partially helical polymers are completely suppressed. Similar models are still in use (see [24] and references cited therein).

In the Oosawa-Kasai model it is also possible for a non-helical chain to become helical or vice versa. This introduces another (generalized) equilibrium constant $\gamma(K_h/K)^{N-3}$ with $N > 2$ the number of monomers in the aggregate, possibly linked to a conformational switching of the protein molecules. In this

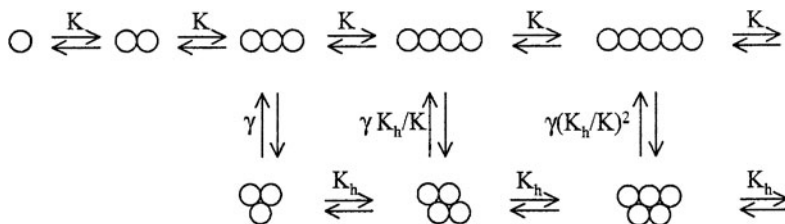


Figure 1. Schematic depiction of the Oosawa-Kasai multi-equilibrium model. K is the equilibrium constant for the addition of a monomer in a non-helical conformation, K_h is that for the addition in a helical conformation, and γ is the nucleation parameter for a helical trimer [3].

picture, not every aggregate can undergo the transition from a non-helical to a helical state; for f-actin it is surmised that a critical nucleus of three monomeric units is necessary for helix formation. The model predicts that helical or non-helical polymers form, dependent on the values of the three equilibrium constants. For $K_h \gg K$ and $\gamma \rightarrow 0$, a critical concentration for the formation of helical aggregates is required. All excess monomers above this concentration are absorbed into helical polymers that co-exist with the free monomers and with short non-helical polymers.

The theory of Oosawa and Kasai is easy to implement and can be expected to accurately describe systems requiring a nucleation step and which display a large co-operativity of the helical transition, because then the polymers become fully helical or fully non-helical. Indeed, the model seems to accurately describe the helical polymerization of f-actin [25]. However, when compared to experimental measurements on helical aggregates of disc-shaped monomers (discotics) [9, 21, 22], shown in Figure 2, the agreement is poor. See Figure 5, to be discussed in more detail below. Therefore, a different theoretical treatment is needed if we wish to describe helical supramolecular systems in general.

Here, we outline a recent extension [21, 22, 26] of the theory of Oosawa and Kasai to polymers that need not be fully helical or non-helical. The well-known Zimm-Bragg model for the helix-coil transition in polypeptides [27] is a similar improvement on the all-or-nothing model for this conformational transition in conventional polymers [18]. Our treatment accurately describes the conformational state of aggregates of the discotic molecules of Figure 2. The treatment is fairly general, however, and can, in principle, be applied to

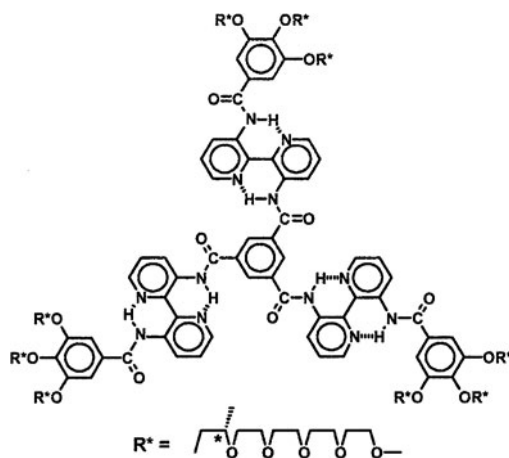


Figure 2. Chemical formula of the chiral discotic molecules used by Brunsveld and co-workers in their helical-assembly experiments [9]. The chemical name of the molecule is N,N',N''-tris{3[3'-(3,4,5-tris{(2S)-2-(2-[2-(2-methoxyethoxy)-ethoxy]-ethoxy)-ethoxy)-propyloxy]-benzoylamino]-2,2'-bipyridyl}benzene-1,3,5-tricarboxamide.

any type of supramolecular polymer that displays a transition between a helical and a non-helical state.

Because the helical transition is accompanied by a sharp increase in the mean molecular weight of the supramolecular assemblies and that in their bending stiffness, the solution viscosity should also dramatically increase. Indeed, as is well known [28], the intrinsic viscosity of stiff, rod-like polymers grows with their molecular weight to the second power in dilute solution, and with a sixth power in semi-dilute solution when the rods overlap. This means that a tenfold increase in the molecular weight upon crossing the helical transition temperature could lead to a million-fold increase of the viscosity within a few degrees of temperature change. It is for this reason, that we believe that helical supramolecular polymers are promising candidates as gelating agents.

3. Discotics

The molecules we focus on in our comparison to experiment have a large aromatic core and nine flexible, polar, side chains (see Figure 2). This allows them to be dissolved in polar solvents, such as water and n-butanol. Since the core of the molecules is solvophobic, the monomers form stacks in solution [9]. From the experiments, it becomes clear that the monomers can form disordered linear aggregates, as well as helical aggregates with a relatively high degree of order (depending on the temperature and the concentration) [9, 29]. This can be explained microscopically by the propeller-like shape of the monomers, which allows for a stronger interaction if they take on a helical conformation by rotating the side groups out of the plane of the center of the monomer (see Figure 3) [9, 21]. Phenomenologically, this corresponds to the situation we presumably have in actin assembly, in that both monomers have a molecular

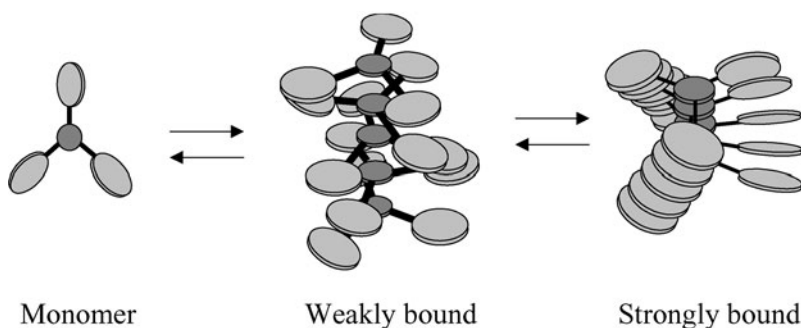


Figure 3. Cartoon of the linear and helical aggregation of propeller-shaped discotic molecules. The molecules self-assemble into disordered stacks, in which they are more or less free to rotate. These stacks then undergo a transition to a more strongly bound, helical state, under the right conditions.

architecture that accommodates two types of binding, and can therefore undergo a helical transition.

As shown in Figure 2, the discotics have a stereocenter in each of their side chains. In the experiments of Brunsveld and co-workers [9] only one of the enantiomers was used, which causes a bias for the formation of one helical screw sense. Such a bias may also follow from, e.g., the use of a homochiral solvent or homochiral counterions in ionic systems. If a racemic mixture of the enantiomers had been used, or an achiral discotic, equal amounts of right-handed and left-handed helices would form [30], and the conformational state of the polymers could not be determined by spectroscopic methods such as circular-dichroism (CD) spectroscopy. CD spectroscopy allows one to gauge the overall chirality in a solution, but it so happens that for the material in hand, it can be used to determine the helical state of the stacks because the individual monomers do not display a Cotton effect. See Chapter 13 for experimental details.

The disordered (non-helical) aggregates form due to the effects of mass action, whereby the monomers gain binding energy, but lose translational entropy relative to the free monomeric state. Upon lowering the temperature, the bound monomers decrease their configurational entropy further by taking on a helical conformation. This increases the binding enthalpy due to increased proximity between the monomers (see Figure 3). The addition of a non-helical bond to a helical aggregate or vice versa is unfavorable on steric grounds, as this would ultimately lead to a frustrated conformational state. Nonetheless, unfavorable or not, such thermally excited states would form for entropic reasons, and are the reason why the theory of Oosawa and Kasai needs to be amended.

4. Linear Self-Assembly

Let us first focus on the theory of linear self-assembly (i.e., the self-assembly of monomeric units into polymer-like chains) in which these monomers are connected to each other by physical, reversible bonds [24, 31–37]. There are many ways to theoretically deal with linear self-assembly [36, 38–47]. In the simplest Ansatz, the aggregation depends solely on a single energetic parameter, describing the free energy expended to break an aggregate into two. This free energy cost is assumed to be independent of the point along the polymer where the break is introduced [48, 49]. It is known in the field of giant micelles [48] as the scission energy or the end-cap energy. For supramolecular polymers which can undergo a helical transition, a single free-energy parameter does not necessarily suffice, because the aggregate ends can have two different conformations, and hence different energies [22, 26]. Also, and perhaps more importantly, the chain becomes subject to conformational fluctuations that cannot be described by a scission energy alone.

Generally, the dimensionless grand potential density Ω of a solution of non-interacting aggregates can be written as:

$$\Omega = \sum_{N=1}^{\infty} \rho(N) [\ln \rho(N) - 1 - \mu N - \ln \Xi(N)] \quad (1)$$

with $\rho(N)$ the (dimensionless) number density of aggregates of degree of polymerization N , μ the chemical potential of the monomers, and $\Xi(N)$ the generalized partition function of an individual aggregate. Note that all energies are given here in units $k_B T$, with k_B Boltzmann's constant and T the absolute temperature, unless otherwise specified. By setting $\delta\Omega/\delta\rho(N) = 0$, we find for the equilibrium size distribution:

$$\rho(N) = \Xi(N) \exp \mu N \quad (2)$$

It is obvious from Eq. (2) that any terms in the free energy $-\ln \Xi(N)$ of a single chain, that are extensive (i.e., proportional to N) can simply be absorbed into the chemical potential [48, 50]. This means that non-extensive terms in $\ln \Xi(N)$, which are often ignored altogether in the context of conventional polymers, are crucial to the description of equilibrium polymers and in fact explain the emergence of the scission energy alluded to in the beginning of this section. We cannot neglect them here as they couple directly to the size distribution of the equilibrium polymers.

We can fix the chemical potential, μ , by invoking conservation of mass (Eq. (3)).

$$\phi = \sum_{N=1}^{\infty} N \rho(N) \quad (3)$$

Here, ϕ is the volume fraction of self-assembling material in the solution. The mean size of the aggregates may be found from Eq. (4).

$$\langle N \rangle \equiv \frac{\phi}{\sum_{N=1}^{\infty} \rho(N)} \quad (4)$$

The crucial ingredient in the theory that contains all the information about the conformational state of the aggregates is the partition function $\Xi(N)$. It follows from Eq. (2) that the size distribution of the aggregates and their conformational state are closely linked. If only one type of bond is formed, the partition function effectively takes the form $\Xi(N) = \exp(N - 1)E$, with $-E$ the free energy of the formation of a bond. (This is true irrespective of the chain model; it holds for rods and flexible chains alike.) The mean aggregate size is then expressed by Eq. (5).

$$\langle N \rangle = \frac{1}{2} + \frac{1}{2} \sqrt{1 + 4\phi \exp E} \quad (5)$$

If two types of bonds are allowed, the situation is slightly more involved, as is detailed in the next section.

5. A Two-State Model

While the conformational state of polymers depends on many factors, such as the molecular architecture and the solvent composition, the helix-coil transition of polypeptides and other helix-forming polymers can be accurately described in terms of a simple quasi one-dimensional model known as the Zimm-Bragg model [18, 27]. It concerns a two-state model that can be mapped onto the Ising chain [18, 51–53]. “Interfaces” between helical and non-helical regions along the aggregate axis are attributed a free-energy penalty denoted R that is related to the coupling constant in the Ising model.

Within a slight modification of the Zimm-Bragg theory, necessary to apply it to equilibrium polymers, the partition function becomes Eq. (6) [21, 22, 27].

$$\Xi(N) = \left[x\lambda_+^{N-2} + y\lambda_-^{N-2} \right] \exp E(N-1) \quad (6)$$

Here, $-E$ is the free energy of a non-helical bond between two neighboring monomers, and the weights x and y represent non-extensive contributions to the free energy that depend on the boundary conditions imposed on the aggregate ends (see below) [26]. The quantities λ_+ and λ_- are the eigenvalues of the so-called transfer matrix of the Ising chain [54]. For a detailed description of the transfer matrix method we refer to the book of Poland and Scheraga [18]. From the Zimm-Bragg theory we have Eq. (7).

$$\lambda_{\pm} = \frac{1}{2} + \frac{1}{2}s \pm \frac{1}{2}\sqrt{(1-s)^2 + 4\sigma s} \quad (7)$$

$s \equiv \exp -P$, where P denoted the excess free energy of a helical bond over a non-helical one, and $\sigma \equiv \exp -2R$ the square of the Boltzmann factor of the free energy penalty R imposed on an interface between a helical and non-helical part of the chain. The latter is often seen as a co-operativity parameter, because the larger R becomes, the fewer interfaces form, and the longer the helical and non-helical regions become [27, 55]. This implies a large co-operativity for small values of σ .

Since λ_- is always smaller than λ_+ , the second term of Eq. (6) is usually neglected in the limit where $N \gg 1$; this is the so-called ground-state approximation. It corresponds to the earlier-mentioned treatment of ideal linear aggregates, albeit with a renormalized scission energy. Often, however, the aggregates turn out to be too small to be accurately described with a ground-state theory, and the full description as in Eq. (6) is required, a fact underappreciated by workers in the field of giant micelles.

Note that Eq. (6) is only valid for $N \geq 3$. For monomers we set $\Xi(1) = 1$, whereas for dimers, the partition function depends on the boundary conditions we enforce and becomes $\Xi(2) = x + y$. The importance of the choice of boundary conditions is discussed in more detail in the next section.

The mean fraction of helical bonds in a single aggregate can be calculated from Eq. (8).

$$\langle \theta(N) \rangle \equiv \frac{1}{(N-1)} \cdot \frac{\partial \ln \Xi(N)}{\partial \ln s} \quad (8)$$

In the limit $N \rightarrow \infty$ we have $\langle \theta(N) \rangle \sim \frac{1}{2} + \frac{1}{2}(s-1)/2\sqrt{(s-1)^2 + 4s\sigma}$. At the helical-transition temperature, T_{**} , we require that half the bonds are helical, so that $\langle \theta(N) \rangle = 1/2$, i.e., for infinitely long chains it is given by $s = 1$. If we average over all aggregate sizes, we get Eq. (9).

$$\langle \theta \rangle \equiv \frac{1}{\phi - \rho(1)} \sum_{N=2}^{\infty} N \rho(N) \langle \theta(N) \rangle \quad (9)$$

6. Aggregate Ends

It seems reasonable to suggest that the conformational state of monomers near the ends of the chains are different from those in the center, because the local environments of the monomers are different. Some care must be taken in the description of the ends of the aggregates, because they have a large impact on the self-assembly of the chains, as noted in Section (4) [26]. To account for this, we define the Boltzmann factors a , b , c and d for helical and non-helical bonds at either aggregate end, where a and c represent a non-helical end, and b and d a helical one. (Note that the ends of an aggregate need not be identical since the helix is an object with an inherent direction.) The prefactors of Eq. (6) then become Eqs. (10) and (11).

$$x = \frac{(a\sqrt{\sigma} + b\lambda_+ - b)(c - c\lambda_- + ds\sqrt{\sigma})}{\sqrt{\sigma}(\lambda_+ - \lambda_-)} \quad (10)$$

$$y = \frac{(a\sqrt{\sigma} + b\lambda_- - b)(c\lambda_+ - c - ds\sqrt{\sigma})}{\sqrt{\sigma}(\lambda_+ - \lambda_-)} \quad (11)$$

Even in the ground-state approximation, the aggregate ends influence the scission energy, which becomes $E + 2 \ln \lambda_+ - \ln x$, and not E . Interestingly, depending on the properties of the aggregate ends, the polymerization may in fact require a nucleation step. For instance, if we consider the case that one of the aggregate ends must be non-helical (so $a = b = c = 1$, $d = 0$), we must automatically assume that all dimers are also non-helical [26]. If we are in the regime where the helical bond is more favorable than the non-helical one

($s > 1$), the aggregates become helical as they grow. This means that the non-helical short chains represent a nucleation barrier, since, in order to form a long helical chain, a non-helical (less energetically favorable) nucleus must first be formed. This recalls the cases of actin polymerization and β -sheet tape formation, in which nucleation is also believed to be required [3, 7].

Since the state of the ends couples strongly to the self-assembly, and since the self-assembly couples to the helical state of the assemblies, the ends in fact influence the nature of the helical transition in a non-trivial way. This is shown in Figure 4. We obtain good fits to experimental data only if we let at least one of the ends be helical. The figure also shows that the transition from a non-helical aggregate to a helical one must be highly cooperative, since the curve is quite steep at the transition temperature T_{**} . From the steepness of the curve at this point, the Boltzmann factor for the formation of an “interface”, $\sqrt{\sigma}$, may be obtained, as in Eq. (12), provided the enthalpy Δh for the helical transition is known [21].

$$\sqrt{\sigma} \Delta h = 4T_{**} \left. \frac{\partial \langle \theta \rangle}{\partial T} \right|_{T_{**}} \quad (12)$$

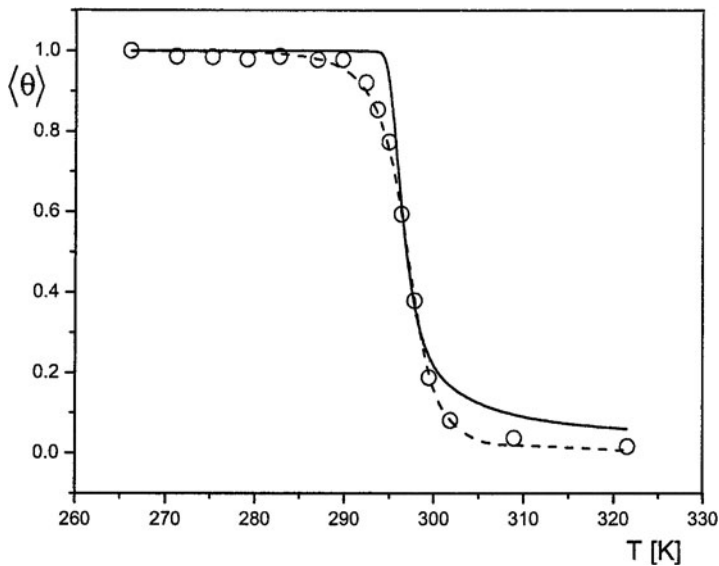


Figure 4. The fraction of helical bonds as a function of temperature. The symbols indicate experimental circular-dichroism data on solutions in n-butanol of the discotics of Figure 2, at a volume fraction of monomers of $2.55 \cdot 10^{-4}$ [9]. The lines give the best theoretical agreement with experiment, given the boundary conditions imposed. Drawn line: boundary conditions one end helical. Dashed line: one end non-helical. The helical-transition temperature, T_{**} (where $\langle \theta \rangle = 1/2$) is approximately equal to 296 K.

For the material of Figure 2 dissolved in n-butanol, we find a value of the Zimm-Bragg parameter $\sigma = 0.0015$ (indicating a relatively high cooperativity, comparable to that in some covalently bound helical polymers [18]) when we insert the value for the excess helical-bonding enthalpy of $-27(k_B T)$, obtained by differential scanning calorimetry measurements [9].

A comparison between experimental data and theoretical predictions on the concentration dependence of the helical-transition temperature is shown in Figure 5, highlighting again the importance of a careful description of the ends. We find that the experimental system at hand can be well-described by the limiting case conditions where we presume one or both ends to be non-helical ($a = b = c = 1, d = 0$). Both the Oosawa-Kasai model and our model with both ends free (as well as those with one or both ends helical – results not shown) describe the experimental results poorly. For the latter set of boundary conditions, this is because a helicity of one-half can always be attained, irrespective of the size of the aggregates, whereas with the other boundary conditions the dimers (and trimers) can never have a different conformation than that enforced by the boundary conditions.

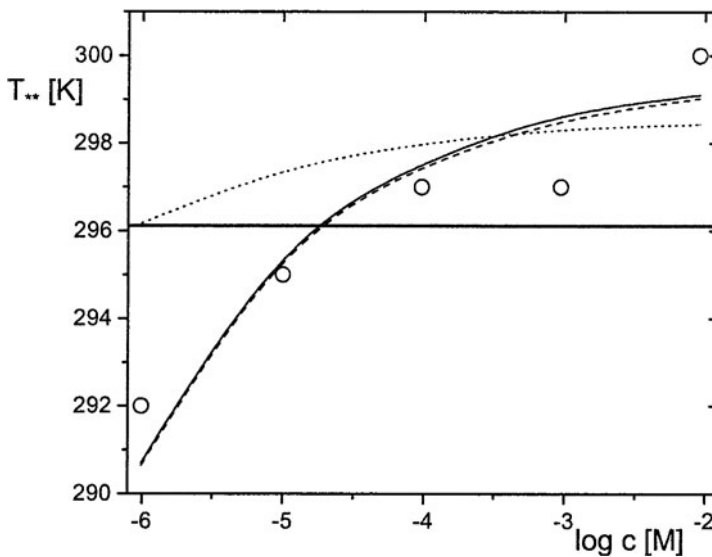


Figure 5. The helical-transition temperature T_{**} in K versus the concentration in M of the discotic compound of Figure 2 in n-butanol [9]. The symbols represent the experimentally found values, the curves give the theoretical results for different limiting boundary conditions: the dashed curve gives the results of the case with one end free and one fixed non-helical ($a = b = c = 1, d = 0$), the drawn curve that for the case with both ends non-helical ($a = c = 1, b = d = 0$), and the thick (horizontal) line that for the case where both ends are left free ($a = b = c = d = 1$). The dotted curve is a fit to the Oosawa-Kasai model [3, 23].

Focusing on the imposed boundary conditions that best describe the experimental data (i.e., with one end non-helical), we compare small angle neutron scattering (SANS) measurements to the mean aggregate size in Figure 6, and obtain reasonable agreement. If the temperature drops below the helical-transition temperature (indicated by an arrow in Figure 6), the mean size of the aggregates exhibits a growth spurt. It shows that there is a strong coupling between the internal conformational state of the polymers and their growth. Unfortunately, given the experimental data of Figure 6, we cannot distinguish between the only two boundary conditions that describe the helical transition in the discotics well, although in principle it should be possible to distinguish them by means of the mean aggregate size measured for a larger temperature range (see the inset of Figure 6).

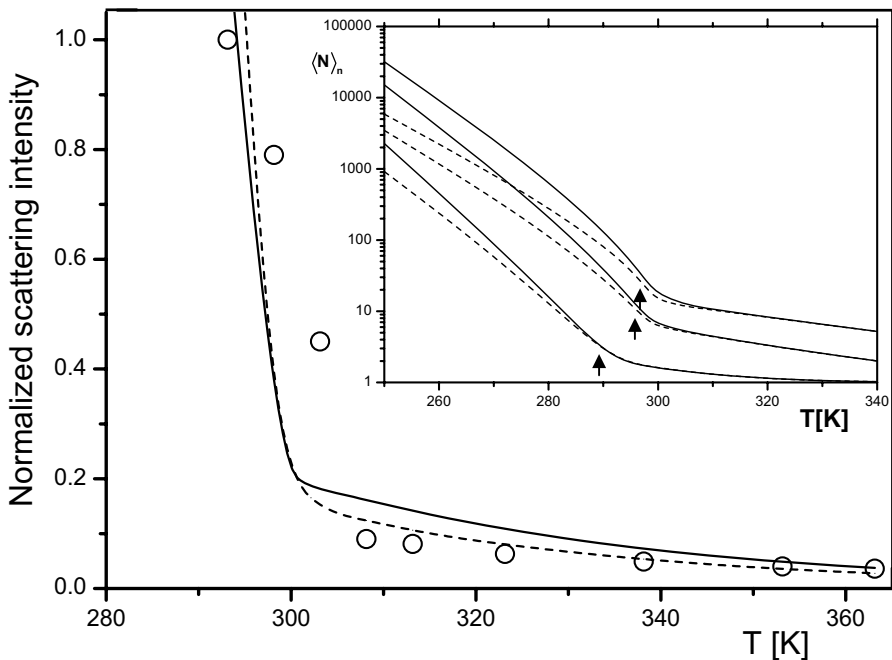


Figure 6. Theoretical fits to the results of SANS measurements on the system of the discotic molecules depicted in Figure 2 in n-butanol at a concentration of $2.39 \cdot 10^{-3}$ M. On the vertical axis is the normalised scattering intensity (which is a measure for the mean aggregate size), on the horizontal axis the temperature in K. The drawn line gives the weight-averaged aggregate size as a function of the temperature, rescaled to give the best possible fit, for the limiting case with one end free and one non-helical ($a = b = c = 1, d = 0$). The dashed line gives the same for the case with both ends non-helical ($a = c = 1, b = d = 0$). In the inset is the mean aggregate size as a function of the temperature, for the concentrations (from top to bottom) $9.21 \cdot 10^{-3}$ M, $9.64 \cdot 10^{-5}$ M and $9.89 \cdot 10^{-7}$ M, with the dashed line the case with one end non-helical and the drawn line that with both ends fixed to be non-helical [21].

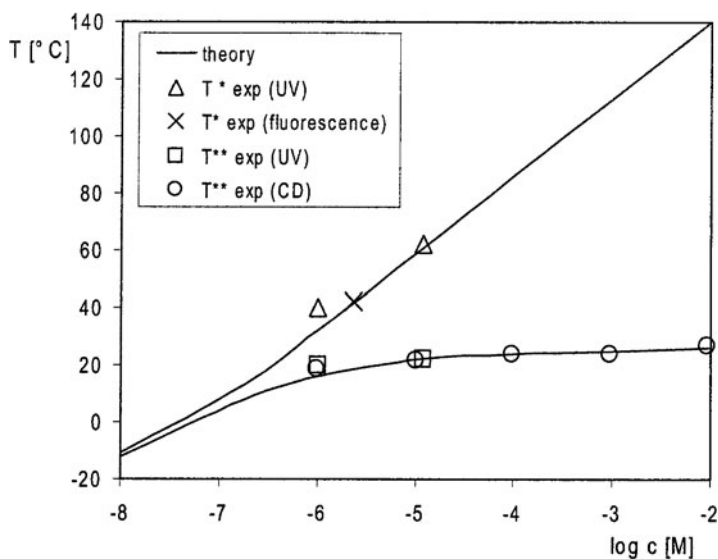


Figure 7. Diagram of aggregated states of the discotic monomers (see Figure 2) in n-butanol in terms of the temperature in °C and solute concentration in M. The symbols indicate experimental results obtained with different techniques, such as circular-dichroism spectroscopy (CD), time-resolved fluorescence spectroscopy, and UV spectroscopy, as indicated. The lines indicate the temperatures where the theory predicts the helical (bottom, T_{**}) and polymerization (top, T_*) transitions to take place. At T_{**} half the bonds are helical, at T_* half the dissolved material is absorbed into aggregates [9]. Hence, the regime at the bottom of the Figure is the helical-chain regime, in between the two curves non-helical chains dominate, and the top regime is the monomeric regime.

In Figure 7 we summarise our results with a diagram of states. It would seem that our model captures the essential physics of the problem at hand. We conclude that there are two regimes, one where the polymerization and helical transitions are far apart, and one where they practically coincide. Here, the crossover from one to the other is regulated by the concentration of aggregating material. A similar shift may be induced by a change in solvent [9, 56, 57].

7. Chirality Amplification

Another phenomenon of interest observed in supramolecular polymers is chirality amplification [30, 58–61]. It is linked with the presence of both left- and right-handed helical conformations, either in different assemblies or within a single assembly; if the monomers are achiral, or if racemic mixtures of chiral ones are present in the solution, both helical screw senses are formed in equal amounts. The two forms are mirror images of each other, and one can therefore

say that the formation of a helix introduces a macromolecular chirality into the system [62]. Clearly, macromolecular (or in this case, supramolecular) chirality cannot easily be detected if there is no net molecular chirality. Symmetry can be broken by polymerizing homochiral material, leading to a bias for one of the helical screw senses.

Often, however, the copolymerization of only a small amount of chiral material suffices to introduce a bias for one of the helical screw senses, a phenomenon referred to in the field as chirality amplification. Two types of chirality amplification can be distinguished: the “sergeants-and-soldiers” type [58–60, 63], and the “majority-rules” type [61, 64]. The former occurs if a small amount of homochiral material is mixed with a large amount of achiral monomers. A large number of bonds with the screw sense preferred by the chiral monomers is then formed. The majority-rules principle is similar, except that the monomers used are the enantiomeric forms of the (chiral) monomers. A slight majority of one of the enantiomers produces a disproportionately large preference for one screw sense.

8. Sergeants and Soldiers

Experimentally, chirality amplification of the sergeants-and-soldiers type has been observed in solutions of mixtures of chiral and achiral discotics [60, 65, 66]. Again, two regimes are found, one where the effect is independent of the concentration of dissolved material, and one where this is not so. That a treatment quite similar to that of the Zimm-Bragg theory described in Section 5, is able to fit the experimental data in both regimes can be clearly seen from Figures 8 and 9 [67, 68]. Perhaps the most striking feature of the Figures is the maximum that occurs. How we deal with this feature theoretically is described in some detail below. (For a similar treatment on the majority-rules principle the reader is referred to the literature [69].)

The adaptation of the theory of Section 5 to model supramolecular chirality amplification is fairly straightforward, with right-handed and left-handed helical bonds replacing the helical and non-helical bonds. This means that s now gives the Boltzmann factor of a right-handed helical bond over a left-handed one, and σ is the square of the Boltzmann factor of a helix reversal [67]. The analogy is not exact, however, since in chirality amplification two types of monomer are present (chiral and achiral in the sergeants-and-soldiers experiment and left-handed and right-handed for the majority-rules principle), requiring an additional chemical potential. Another (obvious) small difference is in the interpretation of experimental results, where the measured optical effect corresponds to the difference between the fractions of right- and left-handed helical bonds, rather than the bare number of helical bonds. This means we study a mean net helicity $\eta \equiv 2 \langle \theta \rangle - 1$ rather than the mean bare helicity $\langle \theta \rangle$.

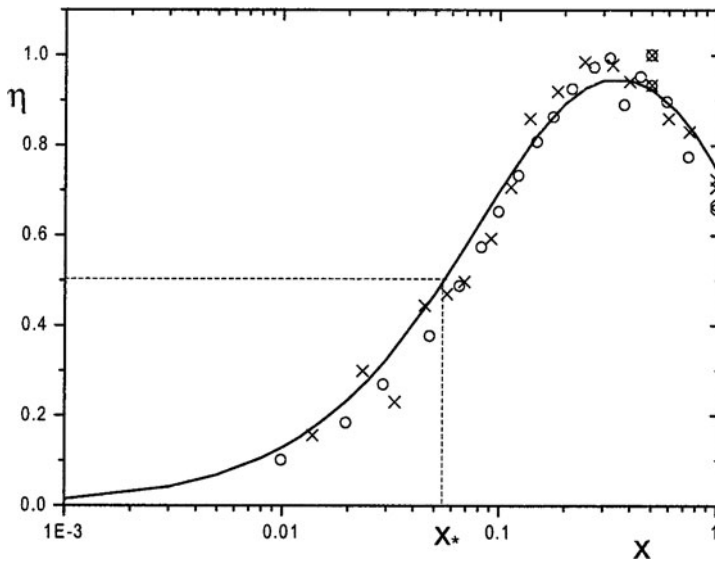


Figure 8. Sergeants-and-soldiers experiment. The net helicity η versus the fraction of chiral material x (line). Symbols: experimental data of Brunsveld *et al.* in water at two concentrations [65]. (Circles: 10^{-5} M, crosses 10^{-4} M). Line: fitted theoretical curve.

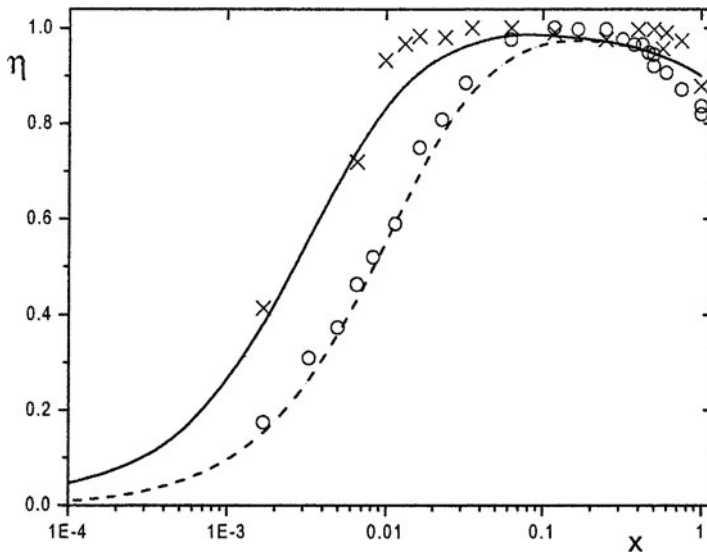


Figure 9. Fit of the theoretical net helicity η versus x to experimental data of Brunsveld *et al.* [66] in n-butanol at two concentrations. Circles: 10^{-5} M, crosses 10^{-4} M. Dashed line: fit for 10^{-5} M. Solid line: fit for 10^{-4} M.

To account for the extra component, the Boltzmann weight s of Section 5 has to be replaced by $1 + z$, with z the excess fugacity of the chiral monomers over the achiral ones. Note that there is no *a priori* preference for left- or right-handed helical bonds in achiral aggregates. In order to keep the number of free parameters to a bare minimum, we insist that a bond following a chiral monomer must always be right-handed helical, mimicking an absolute preference of the chiral units for a certain screw sense.

That our treatment is reasonable is shown in Figure 8, where we compare theoretical and experimental values for the net helicity η versus the fraction of homochiral monomers x , and obtain very good agreement. In the limit of large cooperativity (where the Boltzmann factor of a helix reversal, $\sqrt{\sigma}$, is much smaller than unity) we find that the point x_* at which the net helicity is one-half of its maximum value (Eq. (13)).

$$x_* \approx \frac{1}{2} \sqrt{3\sigma} \quad (13)$$

It provides an easy way to determine the helix-reversal penalty from experiment. A qualitative argument that immediately gives Eq. (13) is that one in principle only needs one chiral monomer per correlation length to get a fully right-handed helical chain, and that the correlation length scales with $\sigma^{-1/2}$. (This follows from the Ising model.) Note that both Eq. (13) and Figure 8 are independent of the concentration of dissolved material.

In Figure 9, we give results similar to those in Figure 8, except that the chirality amplification now does depend on the concentration. We interpret the concentration dependence as an aggregate-size dependence, since in self-assembly the concentration and aggregate size are well known to be linked (see Eq. (5)). This means that we can describe the concentration-independent results of Figure 8 by assuming long chains (and implementing the ground-state approximation). In this case, the size of the aggregates is not an important factor, and the conformational state of the aggregates can be described in terms of the free energy of a helix reversal. Conversely, in the concentration-dependent (short-chain) regime of Figure 9, the aggregates are too short to contain many helix reversals, and in this case the average size of the aggregates determines how many bonds a single chiral monomer influences. The amount of chiral material needed to fully bias the handedness of an average chain is given by the number of chains in the solution. A crude estimate for x_* is therefore given by Eq. (14) where $\langle N \rangle$ is given by Eq. (5).

$$x_* \approx \frac{1}{2 \langle N \rangle} \quad (14)$$

On average half the chains then have a fixed handedness. The full theory gives a somewhat better estimate than Eq. (14), but needs to be evaluated numerically.

To fit the theory to the concentration-independent case (Figure 8) we extract an estimate of the parameter σ at the point x_* using Eq. (13), and fix it at

$\sigma = 0.0064$. We describe the maximum in the optical activity by taking into account the possibility of different contributions to the overall optical effect of chiral and achiral monomers. This may be due to imperfect stacking, as suggested by Brunsveld and co-workers [65, 67], since the chiral discotic has an extra methyl group in each of its side chains and therefore potentially attains a less perfect helix than the achiral monomer. This means that the optical rotation per monomer may vary between the species. We assume that the chiral monomers have a lower contribution to the overall optical effect than the achiral ones, and so obtain a maximum in the curve. A detailed discussion of this is beyond the scope of this chapter. We therefore refer to earlier work [67, 68].

For the concentration-dependent data of Figure 9, we perform a fit with the parameter $\phi \exp E$ to fix x_* using Eq. (14) (see Section 4). We obtain good agreement with the experimental results at the higher concentration for a value of this parameter of 60 000. The bottom curve corresponds to a concentration of a factor ten lower than the top one, and as such should give good agreement for $\phi \exp E = 6000$. This is indeed the case, demonstrating that our model takes the concentration dependence into account in a proper way (see Figure 9). Note that the chirality amplification becomes independent of σ in this regime.

9. Conclusions and Perspectives for the Future

The complex behaviour of monomeric units that can undergo helical self-assembly can be captured by a relatively simple theory. It allows for the (quantitative) prediction of such quantities as the fraction of helical bonds (observable by circular-dichroism spectroscopy) and the mean aggregate size (measurable by radiation scattering techniques). We find that the aggregate ends have a large influence on the conformational state of the monomers inside the aggregates, and that it can be determined what boundary conditions apply to a specific system by comparing our theory to the experimental results.

Experiment and theory point at the presence of two regimes: one where the helical transition and the polymerization are two separate transitions, and one where they coincide. Which regime a system finds itself in depends on the concentration of monomers and on the solvent type. As is also the case in many helix-forming covalently-bound polymers, the helical transition is strongly cooperative and an aggregate can become helical due to a change in temperature of only a few degrees. Furthermore, it appears (experimentally and theoretically) that the polymerization and the helical transition are coupled; the polymers exhibit a growth spurt below the helical-transition temperature.

With some modifications, our model can also be used to describe chirality amplification in self-assembled helical polymers. Here, too, we find two regimes, in accord with experiments. In one regime, the strength of the chirality amplification depends on the concentration of self-assembling material, and

in the other it does not. In each regime a different control parameter dictates the conformational state of the polymers. In the concentration-independent (long-chain) regime, this is the free energy of a helix reversal along the chain, in the concentration-dependent (short-chain) regime, it is the mean aggregate size.

Extensions of our treatment to cases where the aggregates interact, form liquid-crystalline phases or require an activation step before self-assembly seem worthwhile. Work on applying our model to the majority-rules type of chirality amplification and comparison to experimental results is in progress [69, 70].

References

- [1] Friedhoff, P.; von Bergen, M.; Mandelkow, E.-M.; Davies, P.; Mandelkow, E. *Proc. Natl. Acad. Sci. USA*, **1998**, *95*, 15712.
- [2] Watts, N.R.; Misra, M.; Wingfield, P.T.; Stahl, S.J.; Cheng, N.; Trus, B.L.; Steven, A.C.; Williams, R.W. *J. Struct. Biol.*, **1998**, *121*, 41.
- [3] Oosawa, F.; Asakura, S. *Thermodynamics of the Polymerization of Protein*, 1st edition, London: Academic Press, **1975**.
- [4] Oosawa, F. *Biophys. Chem.*, **1993**, *47*, 101.
- [5] Korn, E.D. *Physiol. Rev.*, **1982**, *62*, 672.
- [6] Klug, A. *Angew. Chem. Int. Ed. Engl.*, **1983**, *22*, 565.
- [7] Aggeli, A.; Nyrkova, I.A.; Bell, M.; Harding, R.; Carrick, L.; McLeish, T.C.; Semenov, A.N.; Boden, N. *Proc. Natl. Acad. Sci. USA*, **2001**, *98*, 11857.
- [8] Brunsveld, L.; Folmer, B.J.B.; Meijer, E.W. *MRS Bulletin*, **2000**, *25*, 49.
- [9] Brunsveld, L.; Zhang, H.; Glasbeek, M.; Vekemans, J.A.J.M.; Meijer, E.W. *J. Am. Chem. Soc.*, **2000**, *122*, 6175.
- [10] Hirschberg, J.H.K.K.; Brunsveld, L.; Ramzi, A.; Vekemans, J.A.J.M.; Sijbesma, R.P.; Meijer, E.W. *Nature*, **2000**, *407*, 167.
- [11] Van Nostrum, C.F.; Bosman, A.W.; Gelinck, G.H.; Schouten, P.G.; Warman, J.M.; Kentgens, A.P.M.; Devillers, M.A.C.; Meijerink, A.; Picken, S.J.; Sohling, U.; Schouten, A.-J.; Nolte, R.J.M. *Chem. Eur. J.*, **1995**, *1*, 171.
- [12] Yoshida, N.; Harata, K.; Inoue, T.; Ito, N.; Ichikawa, K. *Supramol. Chem.*, **1998**, *10*, 63.
- [13] Gallivan, J.P.; Schuster, G.B. *J. Org. Chem.*, **1995**, *60*, 2423.
- [14] Lovinger, A.J.; Nuckolls, C.; Katz, T.J. *J. Am. Chem. Soc.*, **1998**, *120*, 264.
- [15] Fenniri, H.; Mathivanan, P.; Vidale, K.L.; Sherman, D.M.; Hallenga, K.; Wood, K.V.; Stowell, J.G. *J. Am. Chem. Soc.*, **2001**, *123*, 3854.
- [16] Engelkamp, H.; Middelbeek, S.; Nolte, R.J.M. *Science*, **1999**, *284*, 785.
- [17] van Gestel, J. *PhD thesis*, Technische Universiteit Eindhoven, **2003**.
- [18] Poland, D.; Scheraga, H.A. *Theory of Helix-Coil Transitions in Biopolymers*, New York: Academic Press, **1970**.
- [19] Bloomfield, V.A. *Am. J. Phys.*, **1999**, *67*, 1212.
- [20] MacKintosh, F.C.; Janmey, P.A. *Curr. Opin. Solid State Mater. Sci.*, **1997**, *2*, 350.
- [21] van der Schoot, P.; Michels, M.A.J.; Brunsveld, L.; Sijbesma, R.P.; Ramzi, A. *Langmuir*, **2000**, *16*, 10076.
- [22] van Gestel, J.; van der Schoot, P.; Michels, M.A.J. *J. Phys. Chem. B*, **2001**, *105*, 10691.
- [23] Oosawa, F.; Kasai, M. *J. Mol. Biol.*, **1962**, *4*, 10.
- [24] Greer, S.C. *Annu. Rev. Phys. Chem.*, **2002**, *53*, 173.

- [25] Niranjan, P.S.; Forbes, J.G.; Greer, S.C.; Dudowicz, J.; Freed, K.F.; Douglas, J.F. *J. Chem. Phys.*, **2001**, *114*, 10573.
- [26] van Gestel, J.; van der Schoot, P.; Michels, M.A.J. *Langmuir*, **2003**, *19*, 1375.
- [27] Zimm, B.H.; Bragg, J.K. *J. Chem. Phys.*, **1959**, *31*, 526.
- [28] Doi, M.; Edwards, S.F. *The Theory of Polymer Dynamics*, 10th edition, (2003); New York: Oxford Science Publications, **1986**.
- [29] Palmans, A.R.A.; Vekemans, J.A.J.M.; Fischer, H.; Hikmet, R.A.; Meijer, E.W. *Chem. Eur. J.*, **1997**, *3*, 300.
- [30] Green, M.M.; Park, J.-W.; Sato, T.; Teramoto, A.; Lifson, S.; Selinger, R.L.B.; Selinger, J.V. *Angew. Chem. Int. Ed. Engl.*, **1999**, *38*, 3138.
- [31] Ciferri, A. *Prog. Polym. Sci.*, **1995**, *20*, 1081.
- [32] Moore, J.S. *Curr. Opin. Colloid Interface Sci.*, **1999**, *4*, 108.
- [33] Lawrence, D.S.; Jiang, T.; Levett, M. *Chem. Rev.*, **1995**, *95*, 2229.
- [34] Reinhoudt, D.N.; Crego-Calama, M. *Science*, **2002**, *295*, 2403.
- [35] Lehn, J.-M. *Supramolecular Chemistry: Concepts and Perspectives*, Weinheim: VCH, **1995**.
- [36] Ben-Shaul, A.; Gelbart, W.M. In *Micelles, Membranes, Microemulsions, and Monolayers*, W.M. Gelbart, A. Ben-Shaul and D. Roux, Eds., New York: Springer Verlag, **1994**.
- [37] Ciferri, A. Ed., *Supramolecular Polymers*, New York: Marcel Dekker Inc, **2000**.
- [38] Scott, R.L. *J. Phys. Chem.*, **1965**, *69*, 261.
- [39] Tobolsky, A.V.; Eisenberg, A. *J. Am. Chem. Soc.*, **1960**, *82*, 289.
- [40] Missel, P.J.; Mazer, N.A.; Benedek, G.B.; Young, C.Y.; Carey, M.C. *J. Phys. Chem.*, **1980**, *84*, 1044.
- [41] Wheeler, J.C.; Pfeuty, P. *Phys. Rev. A*, **1981**, *24*, 1050.
- [42] van der Schoot, P. *Europhys. Lett.*, **1997**, *39*, 25.
- [43] Henderson, J.R. *Phys. Rev. E*, **1997**, *55*, 5731.
- [44] Schäfer, L. *Phys. Rev. B*, **1992**, *46*, 6061.
- [45] Wittmer, J.P.; Milchev, A.; Cates, M.E. *J. Chem. Phys.*, **1998**, *109*, 834.
- [46] Wang, Z.-G.; Costas, M.E.; Gelbart, W.M. *J. Phys. Chem.*, **1993**, *97*, 1237.
- [47] Dudowicz, J.; Freed, K.F.; Douglas, J.F. *J. Chem. Phys.*, **1999**, *111*, 7116.
- [48] Cates, M.E.; Candau, S.J. *J. Phys.: Condens. Matt.*, **1990**, *2*, 6869.
- [49] Taylor, M.P.; Herzfeld, J. *J. Phys.: Condens. Matt.*, **1993**, *5*, 2651.
- [50] Odijk, T. *Curr. Opin. Colloid Interface Sci.*, **1996**, *1*, 337.
- [51] Cabani, S.; Paci, A.; Rizzo, V. *Biopolymers*, **1976**, *15*, 113.
- [52] Qian, H.; Schellman, J.A. *J. Phys. Chem.*, **1992**, *96*, 3987.
- [53] Ising, E. *Z. Phys.*, **1925**, *31*, 253.
- [54] Kramers, H.A.; Wannier, G.H. *Phys. Rev.*, **1941**, *60*, 252.
- [55] Applequist, J. *J. Chem. Phys.*, **1963**, *38*, 934.
- [56] Palmans, A.R.A.; Vekemans, J.A.J.M.; Havinga, E.E.; Meijer, E.W. *Angew. Chem. Int. Ed. Engl.*, **1997**, *36*, 2648.
- [57] Brunsveld, L. *private communication*.
- [58] Teramoto, A. *Prog. Polym. Sci.*, **2001**, *26*, 667.
- [59] Carlini, C.; Ciardelli, F.; Pino, P. *Makromol. Chem.*, **1968**, *119*, 244.
- [60] Green, M.M.; Reidy, M.P.; Johnson, R.J.; Darling, G.; O'Leary, D.J.; Willson, G. *J. Am. Chem. Soc.*, **1989**, *111*, 6452.
- [61] Green, M.M.; Garetz, B.A.; Munoz, B.; Chang, H.; Hoke, S.; Cooks, R.G. *J. Am. Chem. Soc.*, **1995**, *117*, 4181.
- [62] Goodby, J.W. *J. Mater. Chem.*, **1991**, *1*, 307.
- [63] Selinger, J.V.; Selinger, R.L.B. *Phys. Rev. E*, **1997**, *55*, 1728.

- [64] Selinger, J.V.; Selinger, R.L.B. *Phys. Rev. Lett.*, **1996**, 76, 58.
- [65] Brunsveld, L.; Lohmeijer, B.G.G.; Vekemans, J.A.J.M.; Meijer, E.W. *Chem. Commun.*, **2000**, 2305.
- [66] Brunsveld, L.; Lohmeijer, B.G.G.; Vekemans, J.A.J.M.; Meijer, E.W. *J. Incl. Phenom. Macrocycl. Chem.*, **2001**, 41, 61.
- [67] van Gestel, J.; van der Schoot, P.; Michels, M.A.J. *Macromolecules*, **2003**, 36, 6668.
- [68] van Gestel, J.; van der Schoot, P.; Michels, M.A.J. *J. Chem. Phys.*, **2004**, 120, 8253.
- [69] van Gestel, J. *Macromolecules*, **2004**, 37, 3894.
- [70] van Gestel, J.; Palmans, A.R.A.; Titulaer, B.; Vekremans, J.A.J.M.; Meijer, E.W. *J. Am. Chem. Soc.*, **2005**, 127, 5490.

Chapter 3

SELF-ASSEMBLING PEPTIDE GELS

A. Aggeli^{1,3}, N. Boden^{1,3}, L.M. Carrick¹, T.C.B. Mcleish^{1,2}, I.A. Nyrkova⁴,
and A.N. Semenov⁴

¹*Centre for Self-Organising Molecular Systems, University of Leeds LS2 9JT, UK*

²*Department of Physics and Astronomy, University of Leeds LS2 9JT, UK and*

³*School of Chemistry, University of Leeds LS2 9JT, UK*

⁴*Institute Charles Sadron, 67083 Strasbourg, France*

1. Introduction	99
2. Theoretical Model of Self-Assembling Chiral Rod-Like Units	100
3. Experiments Illustrating Predictions of the Model	105
3.1. P ₁₁ -1: CH ₃ CO-Gln-Gln-Arg-Gln-Gln-Gln-Gln-Gln-Glu-Gln-Gln-NH ₂	105
3.2. P ₁₁ -2: CH ₃ CO-Gln-Gln-Arg-Phe-Gln-Trp-Gln-Phe-Glu-Gln-Gln-NH ₂	108
4. Stabilization by Twist	112
5. Wider Implications of the Model	114
6. Peptide Gels are Nematic Hydrogels	117
7. Prospects for Engineering Functional Hydrogels	119
8. Conclusions and Perspectives for the Future	127

1. Introduction

In this chapter, we examine the formation, structure and properties of gels formed by simple peptides that have an intrinsic propensity to undergo one-dimensional self-assembly into long tape-like structures having a cross- β structure. The motivation for this work derives from an emerging interest in exploiting biological-like self-assembly as a route to novel nanostructured materials [1, 2]. We [3–11] and others [12] are focusing on exploiting protein-like self-assembly to this end with the view of being able to incorporate protein-like responsivity into the nanostructure to provide for control

of properties by external triggers. At the heart of this exercise lies the need to harness one or more of the structural motifs that occur in natural proteins. Arguably, the simplest is the cross- β structure as this involves one-dimensional self-assembly which can be treated analytically. At the outset simple tapes were expected to be produced in this way [5], but a hierarchy of structures obtain: helical tapes (single molecule thick), twisted ribbons (double tapes), fibrils (twisted stacks of ribbons), and fibers (entwined fibrils) are formed successively with increasing concentration in water [3]. Tapes are quite flexible and can become topologically entangled at concentrations of ca. 0.001 v/v [5, 6]. In contrast, fibrils are semi-rigid and can form nematic fluids at concentrations of ca. 0.001 v/v. At higher concentrations, fiber formation sets in and gives rise to networks comprised of fibrils linked at fiber-like junctions creating nematic hydrogels [3]. This behavior has been shown to stem from the chirality of the peptide molecule which, in turn, originates from the intrinsic chirality of the constituent amino acids (L in the case of naturally occurring ones). We believe this to be a generic principle. It follows that any chiral molecule able to undergo one-dimensional self-assembly may form fibrils and fibers and, consequently, networks leading to gelation of the solvent (see Chapters 2 and 18). A rich variety of synthetic self-assembling chiral molecules appear to behave in this way and give rise to what are generally termed “organogels” or “hydrogels” [13]. The terminology “Self-Assembling Fibrillar Networks” (SAFINs), proposed by Terech [14] is therefore a highly appropriate descriptor of this novel class of supra-molecular, soft-solid-like materials.

The theoretical model is outlined in Section 2, its predictions are compared with detailed experiments on model peptides in Section 3, the issue of stabilization of aggregate structures by twist is discussed in Section 4, the wider applicability of the model is reviewed in Section 5, properties of nematic fluids and gels are the focus of Section 6, and, finally, we consider the opportunities for controlling properties by external pH triggers and the production of polyelectrolyte complexes in Section 7.

2. Theoretical Model of Self-Assembling Chiral Rod-Like Units

Consider a peptide in a β -strand conformation as a chiral rod-like unit, with complementary donor and acceptor groups aligned on opposing sides, and having chemically different upper and lower surfaces (Figure 1a). In common with many successful approaches in statistical soft-matter physics, this represents a single step of coarse-graining from atomic detail to the nanoscale. The chiral unit is able to undergo one-dimensional self-assembly in solution and to form the hierarchical set of structures depicted in Figure 1 at concentrations depending on the values of a small set of coarse-grained interaction

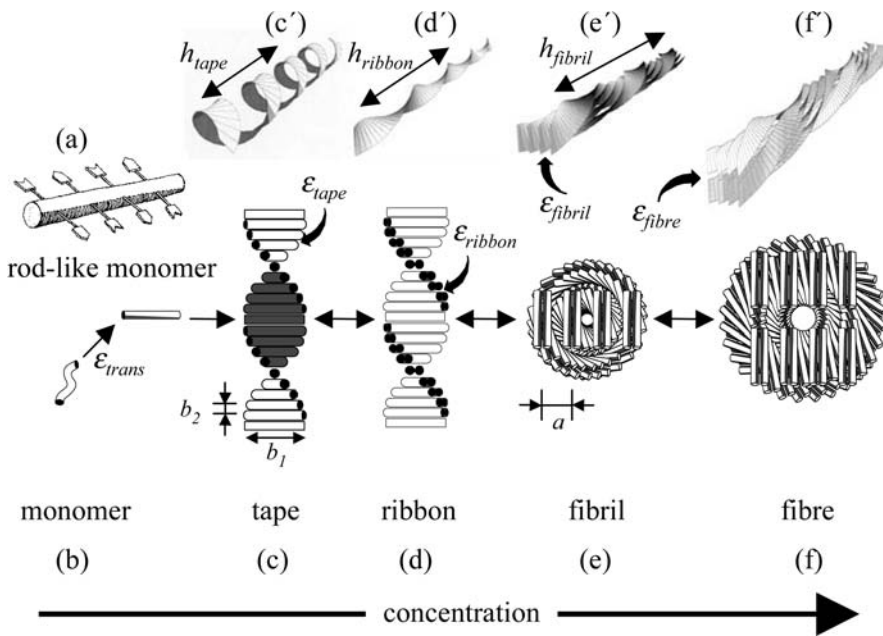


Figure 1. Model of hierarchical self-assembly of chiral rod-like units: Local arrangements (c-f) and the corresponding global equilibrium conformations (c' – f') for the hierarchical self-assembling structures formed in solutions of chiral molecules (a), which have complementary donor and acceptor groups, shown by arrows, via which they interact and align to form tapes (c). The black and the white surfaces of the rod (a) are reflected in the sides of the helical tape (c) which is chosen to curl towards the black side (c'). The outer sides of the twisted ribbon (d), of the fibril (e) and of the fiber (f) are all white. One of the fibrils in the fiber (f') is drawn with darker shade for clarity. (e) and (f) show the front views of the edges of fibrils and fibers, respectively. Geometrical sizes (the numbers in parentheses show the values of the corresponding geometric sizes for P_{11-1} and P_{11-2} peptides, based on X-ray diffraction data and molecular modeling): inter-rod separation in a tape b_2 ($b_2 = 0.47$ nm); tape width, equal to the length of a rod, b_1 ($b_1 \approx 4$ nm); inter-ribbon distance in the fibril, α ($\alpha \approx 1.6$ – 2 nm for P_{11-1} , and $\alpha \approx 2$ – 2.4 nm for P_{11-2}) [3]. Copyright (2001) National Academy of Sciences, USA.

energies ϵ_j . Generally, an isolated monomer in solution will be in a different conformation (Figure 1b), with lower free energy than in the rod-like state: the corresponding conformational free energy change is ϵ_{trans} . The rod-like “monomers” self-assemble via intermolecular recognition between multiple interacting groups to form long twisted tapes (Figure 1c): the association free energy change is ϵ_{tape} per inter-monomer bond. The tape twist stems from the chirality of the monomers (Figure 1a; e.g., right-handed in the case of peptides, due to the L-chirality of naturally-occurring amino acids), which gives rise to a left-handed twist around the long axis of the tape (Figure 1c). The differences in the chemical structures of the two faces of the tape and in their affinity to the solvent give rise to a cylindrical curvature, causing the tape to

curl into a helical configuration (Figure 1c'), with helical pitch h_{tape} and radius r_{tape} given by:

$$h_{\text{tape}} = b_2 \left(\frac{2\pi}{\gamma_\theta} \right) \left(1 + \left(\frac{\gamma_v}{\gamma_\theta} \right)^2 \right)^{-1} \quad (1)$$

and

$$r_{\text{tape}} = b_2 \left(\frac{\gamma_v}{\gamma_\theta^2} \right) \left(1 + \left(\frac{\gamma_v}{\gamma_\theta} \right)^2 \right)^{-1} \quad (2)$$

γ_v and γ_θ are, respectively, the tape bend and twist angles (in radians) per monomer rod, along the tape and b_2 is the distance between adjacent rods in the tape.

One face of the tape (colored black in Figure 1c) is expected to be less soluble than the other (i.e., black is more hydrophobic if the solvent is water). This chemical anisotropy results in inter-tape attraction which leads to double tape (ribbon, Figure 1d) formation (energy $\varepsilon_{\text{ribbon}}^{\text{attr}}$ per peptide). Both faces of the ribbon are identical (white in Figure 1d), and are characterized by a saddle curvature. Hence, the ribbon does not bend, and its axis is straight at equilibrium (Figure 1d'). The white sides of the ribbons are, in turn, mutually attractive leading to stacking of ribbons into fibrils (Figure 1e). Furthermore, the ends of the rods decorating the edges of the fibrils can also be mutually attractive, causing fibrils to entwine into fibers (Figure 1f), stabilized by an attraction energy per pair of interacting peptides, $\varepsilon_{\text{fiber}}^{\text{attr}}$.

All of the self-assembling structures in Figure 1 are left-handed twisted due to chirality of the rod-like monomer. If the ribbons were not twisted, an unlimited growth of fibril and fiber widths would be expected. Instead, when twisted ribbons aggregate into stacks, fibrils with well-defined widths are formed. Fibers are formed in a similar way from twisted fibrils, but again to well-defined widths. Indeed, to aggregate, twisted objects must bend and adjust their twist in response to the packing constraints imposed by its twisted neighbors. Hence, there is an elastic energy cost $\varepsilon_{\text{elast}}$ which must be compensated for by the gain in attraction energy (coming from $\varepsilon_{\text{ribbon}}^{\text{attr}}$, $\varepsilon_{\text{fibril}}^{\text{attr}}$ and $\varepsilon_{\text{fiber}}^{\text{attr}}$) upon stacking. The distortion energy $\varepsilon_{\text{elast}}$ is higher for thicker stacks. This serves to stabilize the widths of fibrils and fibers. Thus, the fibril width is determined by a balance between the gain in attraction energy (coming from $\varepsilon_{\text{fibril}}^{\text{attr}}$) associated with ribbon stacking and the elastic cost on the ribbons associated with fibril formation. Assuming that the ribbon contour length is fixed and the deformations are weak, from symmetry arguments we find that this cost per unit length of each ribbon in the fibril is given by Eq. (3):

$$\varepsilon_{\text{elast}} = \frac{1}{2} \kappa_{\text{bend}} (\nu - \nu_0)^2 + \frac{1}{2} \kappa_{\text{twist}} (\theta - \theta_0)^2 \quad (3)$$

where ν and θ are the local curvature and the local twist strength of the ribbon within a fibril, $\theta_0 = 2\pi/h_{\text{ribbon}}$ is the equilibrium value of twist strength of an isolated ribbon, while its bend strength is zero ($\nu_0 = 0$), and κ_{bend} and κ_{twist} are the ribbon elastic constants [4a]. For a ribbon a distance p from the central axis of a fibril, it is straightforward to show that $\nu = \gamma^2\rho/(1 + \gamma^2\rho^2)$, $\theta = \gamma/(1 + \gamma^2\rho^2)$, where $\gamma = 2\pi/h_{\text{fibril}}$ and h_{fibril} is the fibril's helical pitch. The thicker is the fibril, the larger are the typical ρ , and hence, the higher the cost $\varepsilon_{\text{elast}}$. The net energy gain $\varepsilon_{\text{fibril}}$ per peptide in a fibril (Eq. (4)) has a maximum at some p ; p is the number of ribbons in the fibril. Hence, a well-defined width of fibrils arises, corresponding to this optimal p [4a].

$$\varepsilon_{\text{fibril}} = \frac{p-1}{2p} \varepsilon_{\text{fibril}}^{\text{attr}} - \varepsilon_{\text{fibril}}^{\text{elast}}, \quad (4)$$

The ‘‘state diagram’’ of possible aggregate structures calculated by using this model, and seeking its structure of minimum free energy in each case, is shown in Figure 2. Fibrils with finite diameter are seen to be stable for a wide range of values of $\varepsilon_{\text{fibril}}^{\text{attr}}$ provided that the intrinsic pitch h_{ribbon} of the lone ribbon strongly exceeds the inter-ribbon gap a in the fibril. For low $\varepsilon_{\text{fibril}}^{\text{attr}}$, the ribbons do not stack into fibrils. For high $\varepsilon_{\text{fibril}}^{\text{attr}}$, the ribbons form infinite aggregates (sheet-like crystallites) in which the ribbons are completely untwisted. The optimum number p of stacked ribbons per fibril, and hence the fibril diameter, increases with h_{ribbon} and $\varepsilon_{\text{fibril}}^{\text{attr}}$. This is usually accompanied by an increase in h_{fibril} .

The concentration ranges over which the various self-assembled structures are observable, their contour lengths, and abruptness of inter-structure transformations with concentration are determined by the energy parameters ε_j . For example, if $\varepsilon_{\text{trans}}$ is high enough ($\varepsilon_{\text{trans}} > 4$, all energies here are measured in $\kappa_B T$ units) and $\varepsilon_{\text{ribbon}}$ is small (≤ 1), the single tapes emerge abruptly at:

$$c_{\text{cr}}^{\text{tape}} \cong \nu_{\text{tape}}^{-1} \exp(-\varepsilon_{\text{tape}} + \varepsilon_{\text{trans}}) \quad (5)$$

and their typical aggregation number is:

$$\langle m_{\text{tape}} \rangle \cong [(c/c_{\text{cr}}^{\text{tape}}) - 1]^{1/2} \exp(\varepsilon_{\text{trans}}/2), \quad (6)$$

if $c_{\text{cr}}^{\text{tape}} < c < c_{\text{cr}}^{\text{tape}}$; c is the total peptide concentration and ν_{tape} is the ‘freedom’ volume of the bonds forming the tape. Next, given that the tape bend and twist are not very high (i.e., $\varepsilon_{\text{elast}}$ (cf. Eq. (3)) is small enough), the net ribbon energy (Eq. (7)) is positive.

$$\varepsilon_{\text{ribbon}} = \frac{1}{2} \varepsilon_{\text{ribbon}}^{\text{attr}} - \varepsilon_{\text{ribbon}}^{\text{elast}} \quad (7)$$

Hence, at concentration:

$$c_{\text{cr}}^{\text{ribbon}} \cong c_{\text{cr}}^{\text{tape}} + c_{\text{tape}}^{\text{max}}, \quad c_{\text{tape}}^{\text{max}} \cong \nu_{\text{tape}}^{-1} \varepsilon_{\text{ribbon}}^{-2} \exp(-\varepsilon_{\text{tape}}) \quad (8)$$

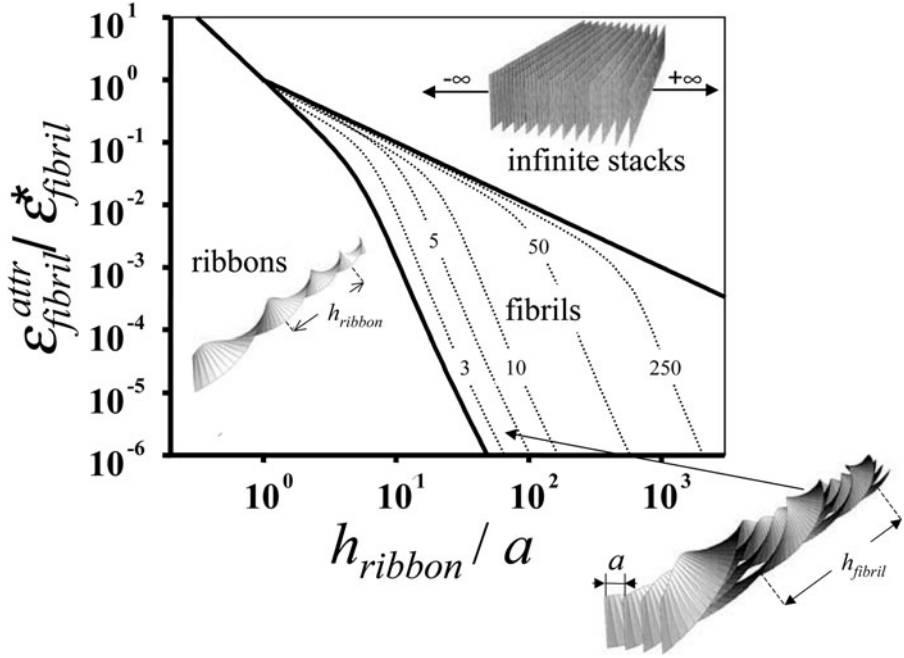


Figure 2. Phase diagram of a solution of twisted ribbons which form fibrils. The scaled variables are: relative helix pitch of isolated ribbons h_{ribbon}/a , and relative side-by-side attraction energy between ribbons $\epsilon_{\text{fibril}}^{\text{attr}}/\epsilon_{\text{fibril}}^*$ ($\epsilon_{\text{fibril}}^* \equiv (2\pi^2 b_2/a^2)\kappa_{\text{twist}}$; see the text and Figure 1d,e' for notations). The areas divided by the thick lines reveal the conditions where ribbons, fibrils and infinite stacks of completely untwisted ribbons are stable. The dotted lines are lines of stability for fibrils containing p ribbons (p is written on the lines); $\kappa_{\text{bend}}/\kappa_{\text{twist}} = 0.1$ [3]. Copyright (2001) National Academy of Sciences, USA.

the ribbons emerge; above $c_{\text{cr}}^{\text{ribbon}}$, the population of peptide in single tapes saturates at $c_{\text{tape}}^{\text{max}}$ and all extra peptide goes into ribbons; simultaneously, the average aggregation number of ribbons grows as:

$$\langle m_{\text{ribbon}} \rangle \approx [(c/c_{\text{cr}}^{\text{ribbon}}) - 1]^{1/2} \epsilon_{\text{ribbon}}^2 \exp((\epsilon_{\text{trans}} + \epsilon_{\text{tape}})/2) \quad (9)$$

whereas the length of tapes saturates at:

$$\langle m_{\text{tape}} \rangle \cong \epsilon_{\text{ribbon}}^{-1} \quad (10)$$

The formulae (Eqs. (5), (6), (8), (9) and (10)) are asymptotic.

To realize sequentially the entire hierarchy of structures in Figure 1 with increasing monomer concentration, it is essential that $\epsilon_{\text{tape}} \gg \kappa_B T \gg \epsilon_{\text{ribbon}} \gg \epsilon_{\text{fibril}} \gg \epsilon_{\text{fiber}}$. Otherwise, some structures may not appear. These are the net energies gained per one peptide inside the corresponding structures as compared to a peptide inside the structure of the previous level.

3. Experiments Illustrating Predictions of the Model

3.1. P₁₁-1: CH₃CO-Gln-Gln-Arg-Gln-Gln-Gln-Gln-Gln-Glu-Gln-Gln-NH₂

The structure is based on a sequence of glutamine (Gln) residues whose side-chains are believed to interact strongly in water [34], presumably via hydrophobic and complementary hydrogen bonding interactions. Arginine (Arg) and glutamate (Glu) residues have been placed in positions 3 and 9, to provide molecular recognition between adjacent antiparallel β -strand peptides in tape-like aggregates, in order to prevent random peptide association. These favorable intermolecular side-chain interactions, coupled with co-operative intermolecular hydrogen bonding between peptide backbones, results in high scission energy $\varepsilon_{\text{tape}}$, thus promoting β -sheet tape formation (Figure 1c). Furthermore, one side (“black”) of the tape is lined by the CONH₂ groups of the Gln residues, while its other side (“white”) is lined by the CONH₂, the guanido, and the COOH groups of the Gln, Arg and Glu, respectively. At low pH in particular, there is also a net positive charge per peptide. The high hydrophilicity of both surfaces of the tape, combined with the electrostatic repulsion between positively charged surfaces, results in very small $\varepsilon_{\text{ribbon}}^{\text{attr}}$ and $\varepsilon_{\text{fibril}}^{\text{attr}}$ energies compared to $\kappa_B T$, thus promoting predominantly single tape formation for low enough peptide concentration in acidic solutions.

At very low concentrations, P₁₁-1 is predominantly in a monomeric random coil conformation (Figures 1b and 3a), whereas at higher concentrations ($c \geq 0.01$ mM), it forms semi-flexible tapes (Figure 3b) with a width $W \approx 4$ nm, equal to the expected length of an 11-residue peptide in a β -strand conformation, and persistence length ($\tilde{l} < 0.3$ μm). The different chemical nature of the two sides of the tape seems to cause it to bend and twist simultaneously, resulting in curly tapes with a left-handed twist, a helical pitch ($h_{\text{tape}} \approx (30 \pm 15)$ nm), and a radius ($r_{\text{tape}} \approx 5$ nm) (Figure 3b). At $c \geq 1$ mM, loose ribbons are also observed, with $\tilde{l} \sim 0.3 - 1$ μm , and $h_{\text{ribbon}} \approx (50 \pm 20)$ nm. These values, in conjunction with the theoretical model, were used to derive the magnitudes of the bend ($\gamma_\nu = 3^\circ$) and twist ($\gamma_\theta = 3^\circ$) angles for the single tapes and the ribbons (Table 1).

FTIR spectra of aqueous solutions of P₁₁-1 tapes exhibit absorption maxima in amide I' at 1630 and 1690 cm^{-1} , demonstrative of a predominantly antiparallel β -sheet structure. They also exhibit characteristic β -sheet circular dichroism (CD) spectra [16] (see Chapter 13) with minimum and maximum ellipticities at 218 nm and 195 nm, respectively (Figure 3a).

The fraction of the peptide in β -sheet tapes starts to grow abruptly at a critical concentration, $c_{\text{cr}}^{\text{tape}} \approx 0.008$ mM (Figure 3c). The two-state transition from random-coil to β -sheet with increasing concentration has an isodichroic

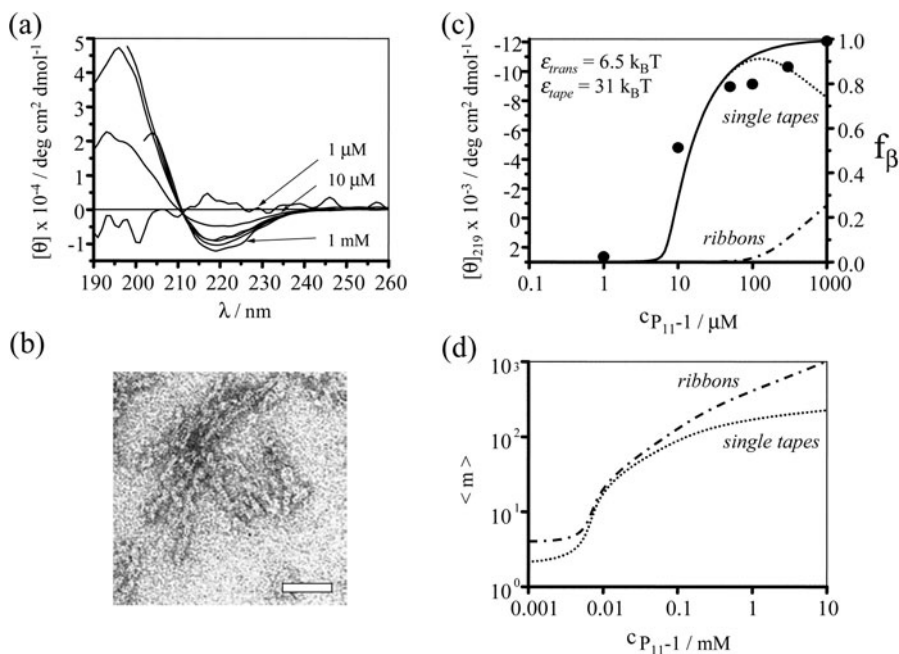


Figure 3. Self-assembly of P₁₁-1. (a) Far-UV CD spectra as a function of peptide concentration. The solutions were prepared by mixing the dry peptide with the required volume of water adjusted to pH = 2 with phosphoric acid. Data were collected with one-month old solutions stored at 20° C. For interpretation of the CD spectra, see the text and legend of Figure 5(a) and (b). (b) Negatively-stained TEM image of single “curly” tapes, reminiscent of Figure 1c’; the scale bar corresponds to 50 nm. (c) Plot of the β -sheet fraction in solution (black circles) as a function of total peptide concentration, based on the CD data (the mean residue ellipticity $[\theta]$ at 219 nm is taken as a linear function of the β -sheet fraction in solution). The solid line is the fit of the data with the single tape theory. The best-fit values of the energetic parameters, ϵ_{trans} and ϵ_{tape} , which were chosen to comply with the concentration dependence of the CD data and with the observed lengths of tapes at $c = 5$ mM, are shown in the panel. (d) Theoretical concentration dependence of the average number $\langle m \rangle$ of peptides per single tape (dotted line) and in ribbons (dash-dot line), based on the energetic parameters derived from the fit (c). Minimum number of peptides in tapes is 2, and in ribbons is 4. The predicted lengths of tapes and ribbons are in agreement with the observed lengths in the TEM pictures for the same peptide concentration [3]. Copyright (2001) National Academy of Sciences, USA.

point at 211 nm (Figure 3a). Using ϵ_{trans} and ϵ_{tape} as fitting parameters, the growth of the β -sheet CD band with concentration (solid line in Figure 3c) could be described. The best-fit energy values are in Figure 2c. The ϵ_{trans} energy results in the nucleated growth of tapes, manifested by a “sudden” onset of β -sheet tape formation at $c_{\text{cr}}^{\text{tape}}$. Using these values of energetic parameters, this single tape model predicts a mean tape contour length for a given peptide concentration which agrees well with the observed range of contour lengths

Table 1. Comparative molecular parameters and macroscopic properties of aqueous solutions of the *de novo* designed self-assembling β -tape forming peptides, P₁₁₋₁ and P₁₁₋₂ [3].

	P ₁₁₋₁			P ₁₁₋₂		
	β -Tapes	Ribbons	Fibrils	β -Tapes	Ribbons	Fibrils
$c_{cr}/\mu\text{M}$	8*	1000*	$c < 25000^*$	$< 90^*$	90*	$700 \pm 200^*$
$\varepsilon_{trans}/K_B T$		6.5 ± 1.5			3 ± 1	
$\varepsilon_{tape}/K_B T$	31.0 ± 1.5			24.5 ± 1.0		
$\varepsilon_{ribbon}/K_B T$		$(3.5 \pm 1.5)10^{-3}$			0.6 ± 0.3	
$\varepsilon_{fibril}/K_B T$			$< 10^{-3}$			
Pitch h/nm	$30 \pm 15^*$	$50 \pm 20^*$			160 ± 40	$(2.0 \pm 0.3)10^{-4}$
Twist angle $Y_{\theta}/^\circ$	3*	3*		1	1	1^*
Bend angle $Y_{\nu}/^\circ$	3*	0*			0*	0*
$l/\mu\text{m}$	$< 0.3^*$	$0.6 \pm 0.2^*$			$1.0 \pm 0.3^*$	$20-70^*$
$L/\mu\text{m}$ ($c = 6 \text{ mM}$)	10^{-1}	$10^{-1} - 10^0$		10^{-3}	10^0	10^{17}
Properties of aq. solution		Isotropic fluid ($c < 13 \text{ mM}$) Nematic fluid/gel ($c > 13 \text{ mM}$)			Isotropic fluid ($c < 0.9 \text{ mM}$) Nematic fluid ($c \approx 0.9 - 6 \text{ mM}$) Nematic gel ($c > 6 \text{ mM}$)	

in the TEM images for the same concentration. At $c_{\text{cr}}^{\text{ribbon}} \approx 1$ mM, loose ribbons start appearing, implying a weak attraction between tapes. This attraction may be mediated by multiple, co-operative, complementary hydrogen bonding between the $-\text{CONH}_2$ groups of glutamine side-chains which line completely one of the two polar sides of the tapes. van der Waals forces are likely to be involved, too. From the value of $c_{\text{cr}}^{\text{ribbon}}$, the ribbons are estimated to be stabilized by $\varepsilon_{\text{ribbon}} = (0.0035 \pm 0.0015)\kappa_B T$. Fibrils (Figure 1e') are not observed up to $c = 25$ mM. Hence, $\varepsilon_{\text{fibril}} < 10^{-3}\kappa_B T$, and $\varepsilon_{\text{fibril}}^{\text{attr}} = 0.1\kappa_B T$.

3.2. P₁₁-2: CH₃CO-Gln-Gln-Arg-Phe-Gln-Trp-Gln-Phe-Glu-Gln-Gln-NH₂

To increase the tendency of the peptide to associate into ribbons, the magnitude of $\varepsilon_{\text{ribbon}}$ must be increased either by decreasing $\varepsilon_{\text{ribbon}}^{\text{elast}}$ or by increasing $\varepsilon_{\text{ribbon}}^{\text{attr}}$. The latter can be achieved by addition of salts or of appropriate cosolvents, but more elegantly by replacing the glutamines at positions 4, 6 and 8 by phenylalanine, tryptophan and phenylalanine, respectively. This peptide, P₁₁-2, forms β -sheet tapes with a hydrophobic ‘‘adhesive’’ strip running along one side of the tape that promotes their association into ribbons in water. At $c \geq 0.1$ mM in water, P₁₁-2 forms long, stable semi-flexible β -sheet ribbons with a width of 2–4 nm, which fits with the expected cross section of $\approx 2 \times 4$ nm² of these ribbons, and a persistence length $\tilde{l} \approx 1$ μm (Figure 4a). At $c \geq 0.6$ mM, a second transition from ribbons to fairly rigid fibrils is observed (Figure 4b and c). The fibrils have a well-defined screw-like structures with typical minimum and maximum widths of $W_1 \approx 4$ nm and $W_2 \approx 8$ nm. At even higher concentrations, a third structural transition takes place and fibers are detected. Typically, they are comprised of two entwined fibrils (Figure 4d). The sequence of these structural transitions is also supported by distinctive far- and near-UV CD spectra, corresponding to P₁₁-2 monomers, ribbons and fibrils (Figure 5a and b).

Focusing on the behavior at low concentrations, it is seen that P₁₁-2 is predominantly in the monomeric random coil conformation (Figure 1b), whereas the fraction of peptide in β -sheet structures starts to grow abruptly at $c \approx 0.07$ mM (Figure 5a and c).

By treating $\varepsilon_{\text{trans}}$ and $\varepsilon_{\text{tape}}$ as fitting parameters, the growth of the β -sheet CD band with concentration could be described well. However, this single tape model yields a mean tape length of about 20 nm at $c = 0.2$ mM (Figure 5d), much shorter than the observed length ≥ 500 nm (Figure 4a). It is possible, however, to describe the CD data (solid line in Figure 5c) and simultaneously to predict the occurrence of these long aggregates (Figure 4a) by inclusion of a third energetic parameter associated with $\varepsilon_{\text{ribbon}}$ (double tape) formation (Figure 1d). These long aggregates are double tapes rather than single ones (Figure 5c and d). The CD spectra as a function of concentration have no

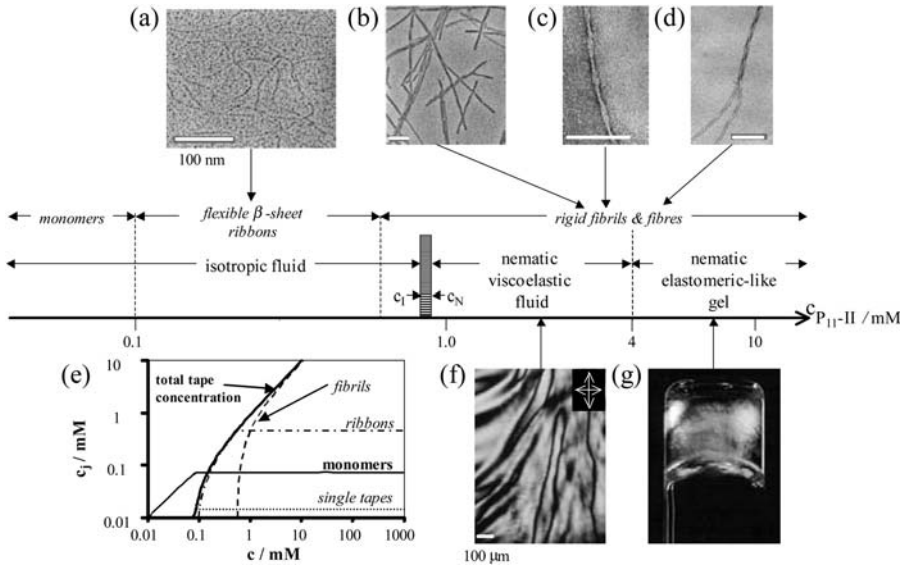


Figure 4. Aggregate structures and liquid crystalline phase behavior observed in solutions of P₁₁-2 in water with increasing peptide concentration c (log scale). The electron micrographs (a) of ribbons ($c = 0.2$ mM), and (b) of fibrils ($c = 6.2$ mM) were obtained with a four month old solution after platinum rotary shadowing. The observed micrometer-long contour length may be limited by multiple ruptures of the fibrils during preparation of the samples for TEM imaging. Higher resolution TEM images of the fibrils were also obtained using negatively stained samples (data not shown). Micrographs (c) ($c = 6.2$ mM) and (d) ($c = 6.2$ mM) were obtained with a one-month-old solution after uranyl acetate negative staining. CD and FTIR have confirmed that the fibrils are made of β -sheet structures. X-ray diffraction data have also shown arcs corresponding to 0.47 nm periodicity, consistent with the expected interstrand distance in a β -sheet (unpublished data). The TEM micrographs show the principle aggregate structures whose populations $c_j = f_j c$ (f_j is the fraction of peptides incorporated in the j -th structure) change with peptide concentration, as depicted in (e). The curves in (e) were calculated with the generalized model described in the text (see also Figure 5d). The aggregation behavior of the peptide, probed using time-resolved fluorescence anisotropy and CD of filtered solutions, is fully consistent with the model (data not shown). The polarizing optical micrograph (f) shows the thick thread-like texture observed for a solution with $c = 3.7$ mM in a 0.2 mm pathlength microslide. (g) shows a self-supporting birefringent gel ($c = 6.2$ mM) in an inverted 10 mm o.d. glass tube, viewed between crossed polarizers. The scale bars in a, b, c and d correspond to 100 nm and in f to 100 μ m [3]. Copyright (2001) National Academy of Sciences, USA.

isodichroic point (Figure 5a), further supporting that more than two states (i.e., peptide monomers, β -tapes and ribbons) are involved in the conformational transition. The best-fit energy values obtained are: $\varepsilon_{\text{trans}} = (3 \pm 1)\kappa_B T$, $\varepsilon_{\text{tape}} = (24.5 \pm 1.0)\kappa_B T$ and $\varepsilon_{\text{ribbon}} = (0.6 \pm 0.3)\kappa_B T$.

It is instructive to compare the energy parameters obtained for the two peptides in the context of the proposed arrangements of peptide molecules in

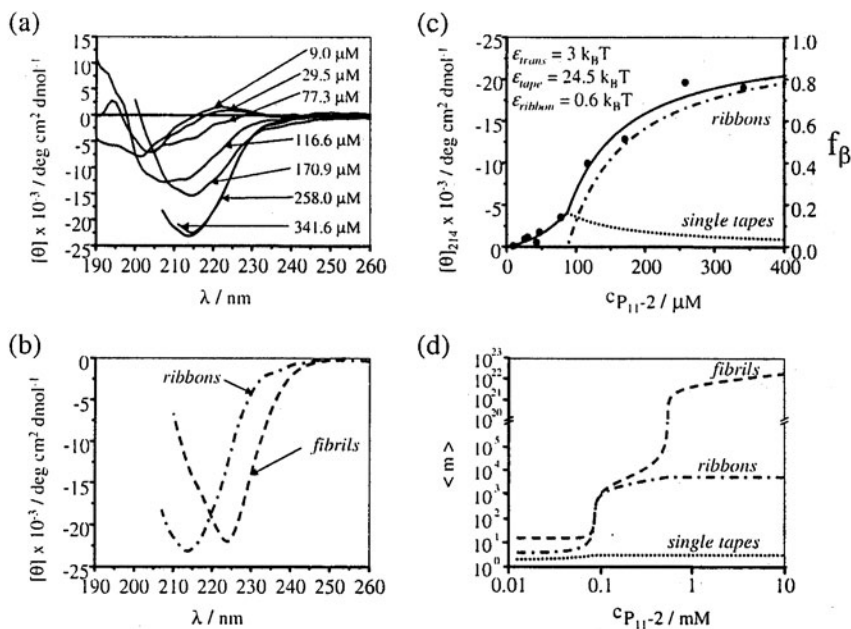


Figure 5. Self-assembly of P₁₁₋₂. (a) and (b) far-UV CD spectra in water at 20°C. (a) Solutions were prepared by dilution (within 15 min) of a freshly prepared isotropic fluid (3.1 mM), and incubated for 3 days. The spectra were unchanged 10 days later. The negative ellipticity at ca. 200 nm and a positive ellipticity at ca. 222 nm in spectra for $c < 50 \mu\text{M}$ is characteristic of random coil monomeric peptide, whereas the negative CD band at ca. 214 nm and the positive band below ca. 195 nm, at $150 \mu\text{M} < c < 400 \mu\text{M}$ is typical of a β -sheet conformation [16]. (b) Comparison of the CD spectra of isotropic solutions of P₁₁₋₂ ribbons and of fibrils at $c = 0.3 \text{ mM}$. The solution for the ribbon spectrum was prepared as in (a), while the solution for the fibrils was prepared by dilution of a nematic gel ($c = 3.1 \text{ mM}$). The fibril spectrum reveals a red-shifted negative band (centred at 224 nm, compared to 214 nm for ribbons). The red shift accompanying formation of fibrils is thought to arise partly from the superposition of a strong aromatic CD band on the classical β -sheet CD spectrum. The appearance of the aromatic CD band suggests a change in the packing of tryptophan side chains [17], which are in a more constrained chiral environment in fibrils than in ribbons. The ribbons and the fibrils produce distinct near-UV CD spectra, which further supports a change of packing of aromatic side-chains (unpublished data). (c) Fit of the theoretical model (solid line) for the self-assembly of peptides into single and double β -sheet tapes, to the measured concentration dependence of the mean residue ellipticity $[\theta]$ of the negative CD band at $\lambda = 214 \text{ nm}$. $[\theta]_{214}$ is taken to be a linear function of the fraction f_β of peptides in β -sheet tapes. The fractions of peptides involved in single and double tapes are represented with dotted and dash-dot lines, respectively. (d) Theoretical concentration dependencies of the average number $\langle m \rangle$ of peptides in single tapes (dotted line) and in ribbons (dash-dot line) and in fibrils made of $p = 4$ ribbons (dashed line) [3]. Copyright (2001) National Academy of Sciences, USA.

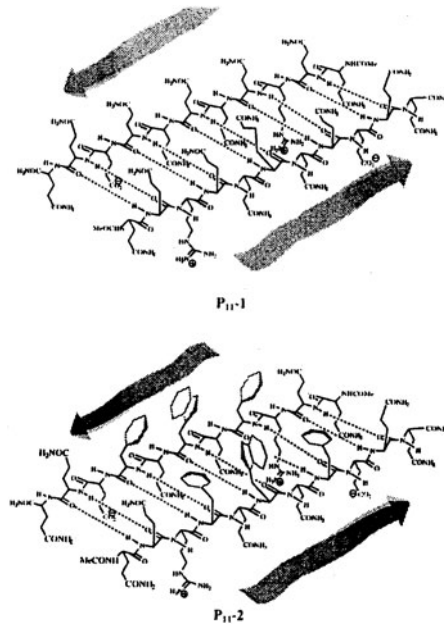


Figure 6. Molecular arrangements in dimeric P₁₁-1 and P₁₁-2 cross- β tapes showing details of hydrogen bonding and side-chain orientations. Reprinted with permission from [9]. Copyright (2003) American Chemical Society.

the tape-like substructures depicted in Figure 6. The estimated ϵ_{trans} is higher for P₁₁-1 than for P₁₁-2 (Table 1).

Although both peptides have the same length, they may have a different propensity to form a random coil in the monomeric state. This difference may account for the difference in ϵ_{trans} . The magnitude of ϵ_{tape} is also higher for P₁₁-1 than for P₁₁-2, indicating that the inter-peptide glutamine side-chain interactions between P₁₁-1 peptides are more efficient at promoting self-assembly than intermolecular aromatic side-chain interactions between P₁₁-2 peptides (Figure 6). ϵ_{ribbon} is at least two orders of magnitude lower for P₁₁-1 than for P₁₁-2, as predicted by peptide design. This difference explains the shorter (by one order of magnitude) length of P₁₁-1 ribbons than the P₁₁-2 ones (Table 1). It also accounts for the one order of magnitude difference in critical concentrations for ribbon formation between the two peptides. As a result, single, curly β -tapes are stable over a wide range of P₁₁-1 concentrations. In contrast, P₁₁-2 tapes are not observed because they convert to ribbons as soon as they are 3–4 peptides long, at very low concentration.

The formation of fibrils (Figure 4b) at higher concentrations of P₁₁-2, implies the presence of a weaker attraction between the polar sides of P₁₁-2 ribbons ($\epsilon_{\text{fibril}}^{\text{attr}}$, Figure 1e'). From the concentration at which they appear, we calculate

$\varepsilon_{\text{fibril}} = (2.0 \pm 0.3) \cdot 10^{-4} \kappa_B T$. Despite this attraction, the fibril dispersions are stable and the fibril diameter is finite (rather than growing indefinitely). Furthermore, the fibril width W_1 corresponds to the expected length of an 11-residue β -strand, while W_2 corresponds to roughly 4 ribbons (i.e., 8 single tapes, each tape with a thickness of ca. 1 nm) per fibril, and is concentration independent (at least from 0.6 to 7 mM). The energy required to break such a fibril, scission energy ε_{sc} , is $\varepsilon_{\text{sc}} = 8\varepsilon_{\text{tape}} \sim 200\kappa_B T$ (comparable to covalent bond energies), and is much higher than that of a single ribbon, $\varepsilon_{\text{sc}} = 2\varepsilon_{\text{tape}} \sim 50\kappa_B T$. This results in fibrils whose equilibrium average lengths are predicted to be very long: $L_{\text{fibril}} \sim 10^8$ km compared to $L_{\text{ribbon}} \sim 1 \mu\text{m}$, for $c = 6$ mM.

4. Stabilization by Twist

Thus, the general behaviors of P₁₁-1 and P₁₁-2 are consistent with the predictions of the model outlined in Section 1. Tapes, ribbons, fibrils and fibers all have an intrinsically left-handed twist. This twist and its handedness is a result of the presence of the L-amino acid residues comprising the peptide precursors, and is reminiscent of the left-handed twisting of β -sheet regions in natural proteins [18]. This is demonstrated in Figure 7 which shows how fibrils of P₁₁-2 derived from D-amino acids have a right-handed twist.

Ribbons stack to form twisted fibrils, the structural characteristics of which are also predicted by the model. Within a fibril, the degree of twist associated with each of the ribbon sub-units is necessarily reduced as a geometric requirement in order for multiples of these objects to be stacked together. The magnitude of this untwisting becomes greater as the number of ribbons within the fibril is increased (Figure 2). This “flattening” of the ribbon structures from their equilibrium twisted state is compensated for by the energy gained from the interacting faces of the ribbons upon stacking inside the fibrils. In the case of P₁₁-2, beyond a total of four stacked ribbons per fibril, the energy cost of further untwisting of ribbons becomes greater than the energy gained from inter-ribbon face-to-face interactions. Thus, according to the model, this subtle energy balance determines the equilibrium dimensions of the fibril; h_{fibril} is ca. 120–200 nm (Figure 4c). From the observed geometrical characteristics of P₁₁-2 ribbons and of fibrils, the theory estimates $h_{\text{ribbon}} \sim 120\text{--}200$ nm, elastic constants κ_{bend} and κ_{twist} , and twist angle $\gamma_{\theta} = 1^\circ$ for isolated P₁₁-2 ribbons and $\varepsilon_{\text{fibril}}^{\text{attr}} \sim 0.015\kappa_B T$ for fibrils (Table 1).

That P₁₁-1 ribbons do not associate into fibrils up to at least $c = 25$ mM while P₁₁-2 forms fibrils at $c < 1$ mM is at first sight surprising because the magnitude of $\varepsilon_{\text{fibril}}^{\text{attr}}$ is expected to be similar for both peptides in view of the identity of their outer (“white”) polar sides (Figure 6). This behavior can again be traced to the role of twist as gleaned from molecular dynamics-generated structures [9] (Figure 8). That P₁₁-1 and P₁₁-2 tapes have similar degrees of twisting about

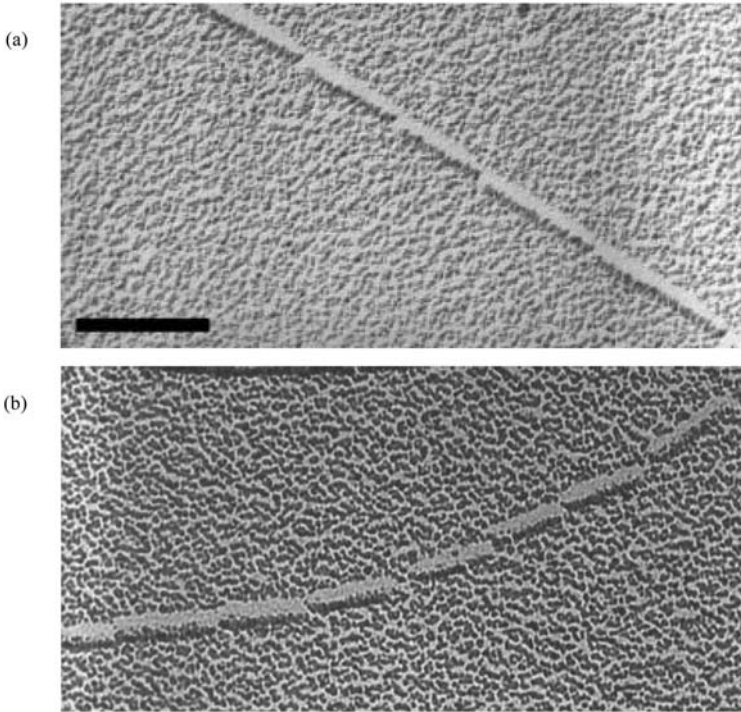


Figure 7. Uniaxial shadowed TEM of (a) L-P₁₁-2 and (b) D-P₁₁-2 at 20 μ M in HPLC water. Observe the opposite fibril handedness. Scale bar = 100 nm. [A.Beevers, M.Bell, L.M.Carrick, C.W.G. Fishwick, A. Aggeli, and N.Boden.]

their axes is not surprising in view of the similar overall amino acid sequences of the two peptides. The greater bend in P₁₁-2 tapes stems from the greater chemical asymmetry of its outer surfaces. For the ribbons, the twist is 3-4 times weaker for P₁₁-2 than for P₁₁-1, indicating much stronger cross-tape attractive forces in the case of the former. This is reflected in molecular dynamics based estimates for the adhesion energies, 26.86 kcal/mol and 12.44 kcal/mol per peptide molecule, for P₁₁-2 and P₁₁-1 ribbons, respectively. The much greater adhesion between the inner tape-like faces within P₁₁-2 ribbons stems from hydrophobic forces arising from substitution of glutamines at positions 4, 6, and 8 by phenylalanine, tryptophan, and phenylalanine, respectively (Figure 6). Adhesion increases as contact between the two faces increases, and becomes a maximum when the ribbon is flat. Opposing this is the tendency for the tape-like faces to twist away from planarity in order to optimize side-chain interactions within the tape-like sub-structures. The resulting twist of the ribbon is therefore a compromise between these two opposing factors; strong inter-tape attractive forces tend to flatten the ribbon, as in the case of P₁₁-2.

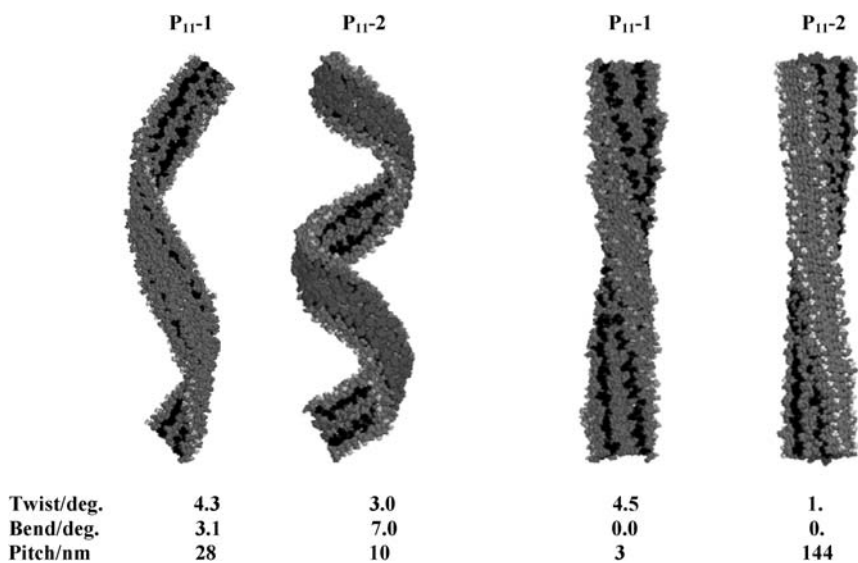


Figure 8. Molecular dynamics generated structures of tapes (left) and ribbons (right) for peptides P₁₁-1 and P₁₁-2 [9]. Reprinted in part with permission from [9]. Copyright (2003) American Chemical Society. [A color version of this figure may be found on page 941.]

5. Wider Implications of the Model

The scheme in Figure 1 is expected to apply to any chiral molecule able to undergo one-dimensional self-assembly, although only rod-like molecules are expected to form tapes. The formation of fibrils and fibers, and, consequently, SAFINS [14] is expected to be quite general. Here, three examples, chosen because of their topical interest, but typifying the generic nature of the phenomena, are discussed.

Natural proteins – amyloid fibrils. The core structures of the pathological amyloid fibrils associated with many degenerative diseases, such as Alzheimer's, have been shown by X-ray diffraction and ¹³C NMR [19] to be comprised of several (typically 6 to 8) tapes having a cross- β structure, stacked one atop the other, and a full twist pitch of ca. 100–200 nm [20–26]. Protein and peptide molecules that are not implicated with amyloid pathologies [28–30], as well as polyamino acids [31], have also been found to self-assemble into amyloid-like fibrils. Interestingly, it has recently been suggested [32] that the tendency to self-assemble into β -sheet tapes and, in turn, fibrils is an intrinsic property of many natural proteins. A number of design motifs appear to have evolved to suppress this tendency for spontaneous aggregation [33]. One is to decorate the leading and trailing edges of the β -sheet domain with flexible domains, rendering ϵ_{tape} unfavorable. An alternative way of achieving the same end is to incorporate electrostatically repelling, charged side-chains. Another

control strategy is to regulate the term $\varepsilon_{\text{trans}}$ in Eq. (5). Clearly, if $\varepsilon_{\text{trans}}$ is large, the critical tape concentration will lie above the ambient protein concentration, and the tendency towards self-assembly is suppressed. However, $\varepsilon_{\text{trans}}$ is dramatically attenuated if the polypeptide chain is able to form a cross- β hairpin, thereby changing the critical tape concentration to a value well below the ambient protein concentration. Huntington's protein is one well-known example where this mechanism is evident. The disease develops when a pathological threshold of about 41 glutamine residues is exceeded [34]. Cross-strand hydrogen bonding between glutamines promotes hairpin formation. The folding of poly(L-glutamine) into a hairpin configuration as a prerequisite for cross- β assembly was first pointed out by Perutz [35] in 1994. The occurrence of a nucleation step in the self-assembly of the Alzheimer's peptide is also explicable in terms of Eq. (5) [36].

Designer Peptides. The designed peptides considered in the previous sections have a random coil configuration in solution as the starting point for self-assembly into tapes. The free energy $\varepsilon_{\text{trans}}$ associated with the transformation from random coil to rod-like β -strand plays a key role in determining the critical tape concentration via Eq. (5). Other peptides have been observed to assemble into fibrils from alternate distinctive starting configurations. These include: α -helices [37, 38], β -hairpins [39], 12-16 amino acid residue long β -strands flanked by nonstructured octapeptide sequences [40], β -sheet proteins comprised of amphiphilic β -strands connected by appropriate turns [41], the *de novo* β -sandwich protein betabellin 15 D [42] and self-assembling peptide-PEG block copolymers [43]. $\varepsilon_{\text{trans}}$ in Eq. (5) then takes on a different significance accordingly. In this way the critical tape concentration can be dramatically changed; it is usually perceived as a way of controlling assembly of β -sheets. However, as we have seen in the case of proteins, it is a matter of degree rather than of substance.

Chiral organics. A wide variety of synthetic chiral "molecules" also exhibits this kind of behavior. They are normally described as "LMOGs" (see Chapters 14–18). Typical examples include complementary associating derivatives of tartaric acid [44], or of chiral 1,2-diaminocyclohexane with (S,S)1,2-cyclohexanol [45], substituted porphyrins and phthalocyanines [13a], derivatives of carbohydrates [45] and cholesterol [13a, 46], lithium salts of D (or L)-12-hydroxystearic acid [27], N-n-octyl-D-gluconamide [45, 47], copper β -diketonates [13a] and chiral cyclohexanediamides [48], oligoheterocyclic pyridine-pyridazine molecular strands [49], amphiphilic porphyrin bearing four β -D-galactopyranoside groups [50], L-glutamic acid modified bolaamphiphilic diacetylene lipids [51], bis[(alkoxy)benzoylsemicarbazides] [52], pyrene-based [53], and bis-urea-based LMOGs [54]. They form fibrils with well-defined helicity and dimensions and which have the propensity to form SAFINs, gels and liquid crystals.

Figure 9 compares the mesoscopic structures of fibrils formed by representatives of the three classes of chiral molecules. Strikingly, they are essentially

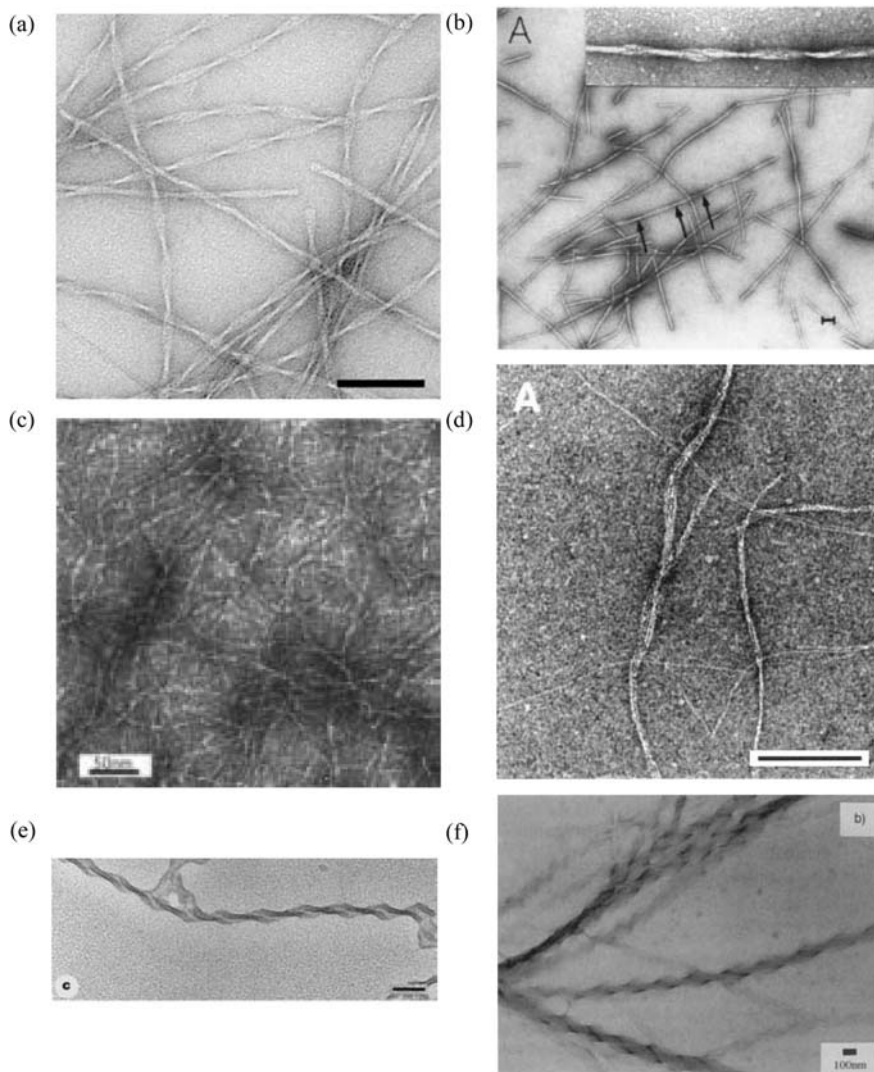


Figure 9. TEM images of fibrils of (a) P₁₁-2 in water [3], (b) Alzheimer's amyloid β -protein (β _{34–42}) Reprinted with permission of the Biophysical Society [20]. (c) designed amphiphilic β -sheet protein [41]. Copyright (1996) National Academy of Sciences, USA. (d) β -sandwich protein betabellin. Reprinted with permission from [42]. Copyright (2000) Elsevier. (e) cationic gemini surfactant with L-tartrate anion [27]. Reprinted with permission of Nature. (f) alkylamide derivative of *trans*-1,2-diaminocyclohexane [13b]. Reprinted with permission from [13b]. Copyright (2003) Wiley-VCH. Scale bars 100 nm except (c) where it is 50 nm.

the same; at the length scales of fibrils and also of the macroscopic gels, the detailed chemical structures of the constituent molecules are not deterministic. Thus, we conclude that the aggregate structures depicted in Figure 1 provide an insight into the way in which chirality is expressed in the mesoscopic structures of one-dimensional chiral aggregates. This, in turn, governs the macroscopic structures and properties of these materials.

In contrast, the energetics that govern fibril formation depend on the exact chemical nature of the monomeric unit and the experimental conditions. The magnitude of $\varepsilon_{\text{trans}}$ depends on the starting (monomeric) and final (self-assembled) conformations of the LMOGs as well as on the solution conditions. $\varepsilon_{\text{tape}}$ or an analogous molecular energy governs the formation of the individual thin self-assembled strands which are the subunits of the fibrils. $\varepsilon_{\text{ribbon}}$ and $\varepsilon_{\text{fibril}}$ can be different or the same in nature and magnitude depending on whether the self-assembling molecule is uniaxial or biaxial. The competition between $\varepsilon_{\text{trans}}$ and $\varepsilon_{\text{tape}}$ is expected to define the magnitude of the critical concentration $c_{\text{cr}}^{\text{tape}}$ above which the nucleated self-assembly of the fibrils starts.

For example, we find that peptide self-assembly into β -sheet tapes and fibrils starts at much lower concentrations in polar organic solvents, such as methanol, than in water as a result of the lower relative dielectric constant of the former. This causes a significant increase of the strength of the numerous intermolecular hydrogen bonds that bind adjacent peptides in the tape, thus increasing significantly the magnitude of $\varepsilon_{\text{tape}}$ and lowering $c_{\text{cr}}^{\text{tape}}$ in polar organic solvents, $\varepsilon_{\text{tape}}$ can also be modulated by changing the solution pH when the peptide contains acidic or basic side-chains. pH responsivity will be discussed in Section 7.

The magnitude of $\varepsilon_{\text{tape}}$ is expected to change significantly depending on the chemical nature of the self-assembling objects (e.g., peptide, protein or synthetic organic molecule). Unfortunately, there is very little quantitative work available in the literature that allows comparisons of the magnitudes of the energetic parameters of different systems. The application of the model in Section 2 to a wide range of chemically distinct systems will provide insight into the relationship between energetic parameters and molecular structure as well as solvent properties. *Such information will lead to the establishment of the requisite protocols for designing molecular gels.*

6. Peptide Gels are Nematic Hydrogels

The rigidity of the fibrils/fibers results in a nematic phase at $c \geq 0.9$ mM (0.001 v/v) for P₁₁-2. The texture in the optical micrograph in Figure 4f and its dependence on flow are characteristic of viscoelastic nematic fluids of semi-rigid polymers [55]. The isotropic-to-nematic phase separation gap is narrow: $0.8 \text{ mM} < c_I < c_N < 0.9 \text{ mM}$ (relative gap width, $w \equiv c_N/c_I - 1 < 0.13$), and is

insensitive to temperature variations from room temperature to at least 60° C. Polydisperse *rigid-rod* solutions have much wider phase separation gaps $w \sim 2$ [56]. The fibrils behave more like typical semi-rigid (worm-like) chains with hard-core excluded volume interactions, for which $w \sim 0.09$ [56]. The isotropic-to-nematic transition of such chains with rectangular cross-section, $W_1 \times W_2$, is predicted [56] to occur at volume fractions, $\Phi_{IN} \approx 5.5W/\tilde{l}_{\text{fibril}}$ (where $W \approx 2W_1W_2/(W_1 + W_2)$), provided that $L \geq \tilde{l}_{\text{fibril}}$; this yields for P₁₁-2, $\Phi_{IN} \approx 0.0004 - 0.0015$ v/v (corresponding to $c_{IN} \approx 0.4 - 1.5$ mM), in agreement with our observations. $\tilde{l}_{\text{ribbon}}$ for P₁₁-1 is one to two orders of magnitude shorter than $\tilde{l}_{\text{ribbon}}$ of P₁₁-2. The isotropic-to-nematic transition of solutions of semi-flexible ribbons of P₁₁-1 is predicted to occur at $\Phi_{IN} \approx 0.015 - 0.05$ v/v (corresponding to 15–50 mM). Indeed P₁₁-1 forms a nematic phase at $c \sim 13$ mM (Table 1).

At $c \geq 4$ mM, the birefringent solution of P₁₁-2 becomes a self-supporting birefringent gel (Figure 4g). Dynamic and steady-state rheological measurements show that fibril-based gels are brittle and do not relax even after days, behavior reminiscent of permanent gels of semi-rigid polymers [10]. Gelation is associated with the onset of fiber formation (Figure 4) which leads to the perception that in the gels, fibrils in the SAFINs are linked by fiber-like junctions (Figure 10). In contrast, tape-based gels are more extendable [5] and relax slowly with time, behavior indicative of transient gels of semi-flexible polymers. We conclude that the type of polymer (tape, ribbon or fibril, each associated with its own characteristic flexibility, contour length and cross-linking mechanism) determines the liquid crystalline and gelation properties of its solution.

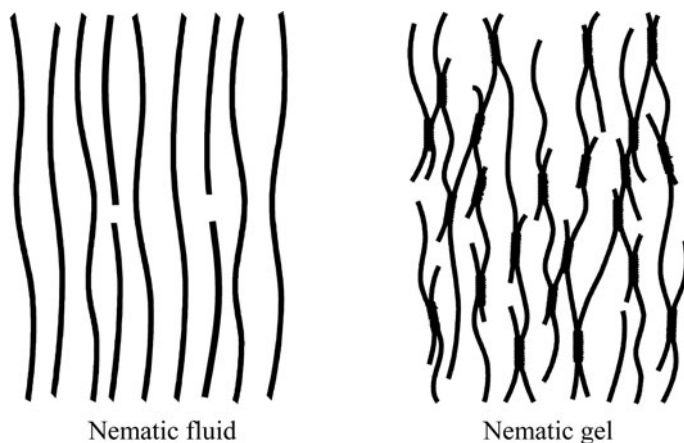


Figure 10. Schematic showing global arrangement of fibrils in nematic fluids (a), and the fiber-like junctions in nematic gel states (b). (Reprinted with permission from [7]. Copyright (2003) American Chemical Society.)

At concentrations of ca. 0.001 v/v, tapes themselves become entangled to form SAFINs and viscoelastic gels [5, 6]. The formation, structures and rheological properties of these gels fall outside the scope of this article, and the reader is referred to the above references for further information.

7. Prospects for Engineering Functional Hydrogels

Up to this point, the focus has been on exposing the structural characteristics and properties of peptide hydrogels. In this section, the prospects for their applications are addressed. This will of course, depend on the functional properties that can be built into these materials. A wide variety of peptides could be designed to assemble into chiral tape-like or fibrillar macromolecular structures which may persist as nematic fluids or gels. Moreover, by appropriate peptide design, a combination of desirable properties, such as biological-like functionality, chemical stability or responsiveness to external triggers (such as solvent polarity, temperature, pH, light or ionic strength) can be incorporated, making the new materials much more versatile than existing peptidic biomaterials such as collagen [57]. This unique combination of properties would make these materials well suited for use in biomedical and other applications, such as for the production of scaffolds to control the shape and alignment of cells for tissue engineering, new suture materials, templates for growth of inorganic helical nanotubes [58], and matrices for separation of chiral molecules.

By way of demonstration, how responsivity to pH can be readily incorporated by relatively minor changes in the chemical structure of the peptide P₁₁-2 will be outlined. The peptides in Table 2 exploit the fact that amino acid side chains terminated with -COOH or -NH₃⁺ groups can be in either a protonated or deprotonated state at pH values when they are, respectively, below or above their nominal *pK* values. The side chains can, by design, be specifically located on the peptide to modulate the electrostatic interactions between neighboring peptides and, thereby, to control ϵ_{tape} . For example, substituting glutamic acid residues for glutamine residues in positions 5 and 7 of P₁₁-2 gives P₁₁-4 (Table 2).

We expected the γ -carboxyl groups to be uncharged at low pH and stable dispersions of fibrils to obtain. At higher pH, all three carboxyl groups

Table 2. Peptide primary structures.

P ₁₁ -1:	CH ₃ CO-Gln-Gln-Arg-Gln-Gln-Gln-Gln-Gln-Glu-Gln-Gln-NH ₂
P ₁₁ -2:	CH ₃ CO-Gln-Gln-Arg-Phe-Gln-Trp-Gln-Phe-Glu-Gln-Gln-NH ₂
P ₁₁ -3:	CH ₃ CO-Gln-Gln-Arg-Phe-Gln-Trp-Gln-Phe-Gln-Gln-Gln-NH ₂
P ₁₁ -4:	CH ₃ CO-Gln-Gln-Arg-Phe-Glu-Trp-Glu-Phe-Glu-Gln-Gln-NH ₂
P ₁₁ -5:	CH ₃ CO-Gln-Gln-Orn-Phe-Orn-Trp-Orn-Phe-Gln-Gln-Gln-NH ₂

were expected to be deprotonated (negatively charged), resulting in electrostatically repulsive forces between adjacent $\gamma\text{-COO}^-$ groups in neighboring peptides, and severely attenuating the magnitude of ϵ_{tape} , and leading to fibril-to-monomer dissociation (Figure 11).

In practice, more complex behavior was observed (Figure 12(a)): for $c = 6.3$ mM, self-supporting birefringent gels were obtained between $2.0 < \text{pH} < 3.2$ (region I); between $3.2 < \text{pH} < 5.0$, flocculation occurs (region II); between $5.0 < \text{pH} < 7.0$ viscous birefringent nematic fluids prevail (region III). Nematic gels were obtained only at $c \geq 12.6$ mM in the pH range $5.0 < \text{pH} < 7.0$. At $\text{pH} > 7.2$, optically isotropic Newtonian fluids were observed (region IV). The nematic-to-isotropic fluid transition occurs within the pH range 6.8–7.2, approximately three pH units higher than the pK (4.1) of free glutamic acid. This complex behavior can be understood in the context of the results of a titration of a nematic gel of P₁₁-4 (pH 2) against 0.25 M NaOH solution (Figure 13). The dissociation of protons occurs over a wide band of pH values from 2 to 8, reminiscent of the titration behavior of proteins and linear polyacids [59–61]. Proton dissociation from the glutamic acids embedded in fibrils is influenced by extensive electrostatic forces between $\gamma\text{-COO}^-$ of Glu, and also the δ -guanidinium⁺ groups of Arg in the tape-like substructure. Attractive forces essentially lower the acid pK to below that of the free peptide (ca. 4.1), while repulsive ones raise it to higher values [62]. It is usually more appropriate to consider the Gibbs free energy change ΔG^0 as a function of degree of dissociation (Figure 13b). Flocculation in region II is associated with electrical neutrality of the fibril: the negative charge on the single ionized $\gamma\text{-COO}^-$ of Glu is balanced by the single positive charge on the δ -guanidinium⁺ of Arg in the tape-like substructure. Fibrils seem to require roughly one net positive or negative charge per

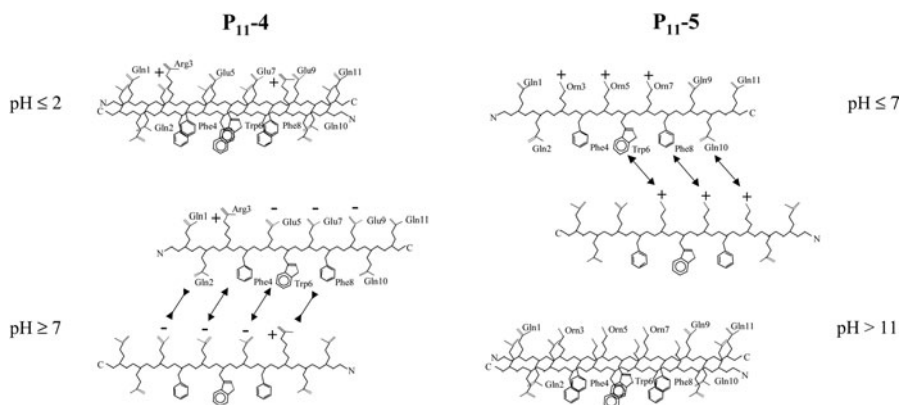


Figure 11. Ionization states of P₁₁-4 and P₁₁-5 at low and high pH values showing the side-by-side organization of peptides in tape-like substructures and in their dissociated monomeric states. (Reprinted with permission from [7]. Copyright (2003) American Chemical Society.)

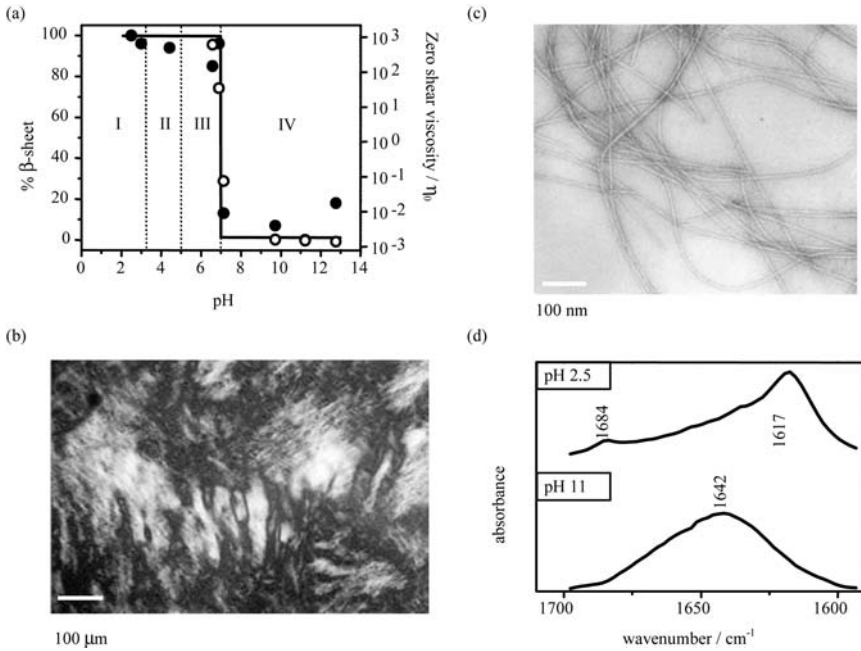


Figure 12. (a) Phase behavior of P₁₁-4 ($c = 6.3$ mM) as a function of pH (DCI/NaOD): I = nematic gel, II = floculate, III = nematic fluid, IV = isotropic fluid. \circ = zero shear viscosity, and \bullet = % β -sheet determined using FTIR spectroscopy: the continuous line denotes the proportion of peptide in fibrils. The broken vertical lines separating regions I, II and III denote approximate boundaries between different macroscopic fibrillar states, while that separating regions III and IV denotes a first order nematic-to-isotropic transition. (b) Polarizing optical micrograph of a P₁₁-4 gel in water ($c = 6.3$ mM, pH = 3) showing a typical thick thread-like viscoelastic nematic texture (Pathlength = 0.2 mM). (c) Transmission electron micrograph of a P₁₁-4 gel in water ($c = 6.3$ mM, pH = 3) showing semi-rigid fibrils and fibers. Micrographs were obtained after dilution to 20 μ M and negative staining with uranyl acetate. (d) FTIR spectrum of amide I' (mainly C=O stretching absorption) bands showing β -sheet conformation of P₁₁-4 nematic gel ($c = 6.3$ mM) in DCI at pH 2.5 (upper trace), and random coil state of P₁₁-4 isotropic fluid ($c = 6.3$ mM) in NaOD at pH 11 (lower trace). (Reprinted with permission from [7]. Copyright (2003) American Chemical Society.)

peptide molecule to stabilize the dispersions against flocculation. This must involve electrical double layer repulsive forces and explains why dispersions of P₁₁-2 are only stable at pH < 5, while P₁₁-3 (in which substitution Glu \rightarrow Gln at position 9 leaves a single ionizable arginine side chain which is expected to remain positively charged up to its pK (pH 12.5)), forms stable fibrillar dispersions over a wide pH range (Figure 14). In region III, the electrostatic repulsion between negatively charged P₁₁-4 fibrils becomes sufficient to cause any fiber-like junctions to dissociate, resulting in fluid nematic phases.

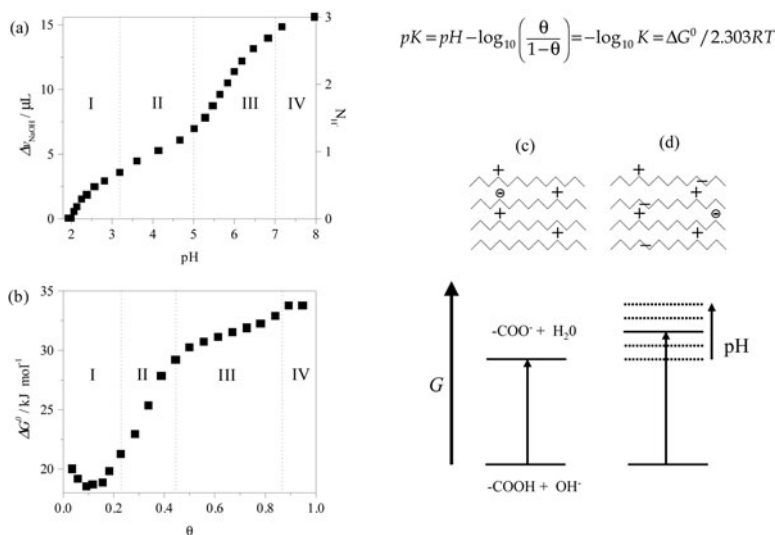


Figure 13. Titration of P₁₁-4: (a) The volume of 250 mM NaOH required to titrate glutamic acid side chains in 200 μ L of 6.3 mM peptide solution as a function of pH. The corresponding number of dissociated protons N_{H^+} is given on the right hand axis. I, II, III and IV denote the regions corresponding, respectively, to nematic gel, flocculate, fluid nematic and isotropic solution states; (b) the Gibbs free energy change ΔG^0 as a function of the degree of acid dissociation θ ; (c) deprotonation of the first glutamic acid at pH = 2.0, the resulting charge distribution [$+ = \text{Arg}^+$; $- = \text{Glu}^-$] along the peptide backbone is also illustrated; (d) depicts the effect of increasing electrostatic repulsion on ΔG^0 resulting from raising the pH value above 2.0 (region I). (Reprinted with permission from [7]. Copyright (2003) American Chemical Society.)

The isotropic-to-nematic transition observed on lowering the pH of a 6.3 mM solution of P₁₁-4 is distinctly different in its nature from that observed with increasing concentration of P₁₁-2 in acid solution. IR experiments have established that in the isotropic fluid state, the peptide is a monomeric species, while in the nematic state, it is in elongated fibrils. Here, the isotropic-to-nematic transition is governed by the reversible association of monomeric peptide molecules into fibrils, a simple two-state transition. The width of the nematic/isotropic co-existence region is determined by the pH interval of this transition. It is quite narrow, between pH 6.8 and 7.2, according to rheology measurements. Optical microscopy (Figure 15b) reveals a similar isotropic-to-nematic coexistence interval for P₁₁-5. Single domain proteins undergo highly cooperative reversible unfolding transitions over comparable pH intervals [63]. The highly cooperative dissociation of fibrils observed here stems from the regular crystal-like structure of the fibrils: they are comprised of stacks of twisted tapes. Within each tape, the peptide molecules are arranged linearly and the peptide-peptide interaction

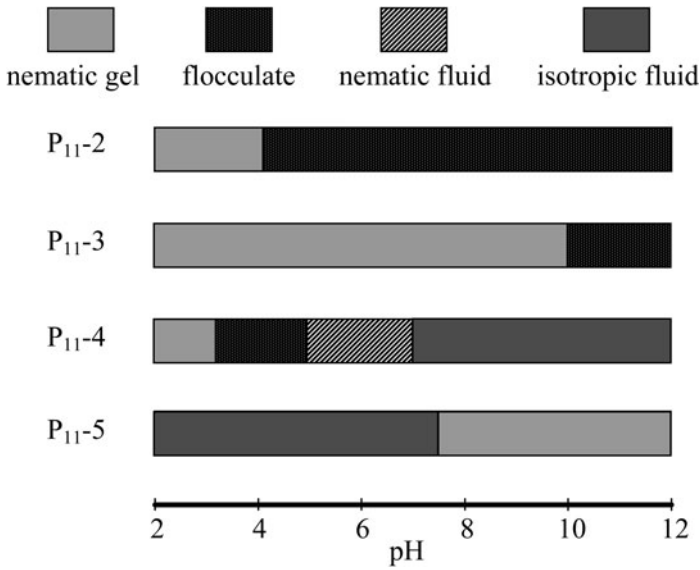
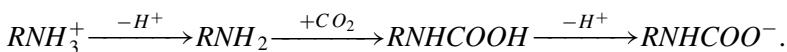


Figure 14. Summary of phase behavior of 11 amino acid peptides in aqueous solution as a function of pH. For P₁₁-2, P₁₁-3 and P₁₁-4 $c = 6.3$ mM, for P₁₁-5 $c = 13.1$ mM. (Reprinted with permission from [7]. Copyright (2003) American Chemical Society.)

free energy $\varepsilon_{\text{tape}}$ contains contributions stemming from long-range electrostatic forces between charged side-chain groups. The deprotonation at a single Glu will therefore trigger long range perturbations of $\varepsilon_{\text{tape}}$, and it is responsible for the cooperativity of the transition and also its extreme sensitivity to additions of very small aliquots of base/acid. Thus, repetitive and rapid reversal of the transition can be achieved by addition of either acid or base.

The converse switching process, between nematic gel at high pH and isotropic fluid at low pH, can be accomplished by designing a complementary peptide P₁₁-5. It needs to be in the monomeric state in acid solutions and in fibrillar aggregates in basic solutions (Figure 14). To achieve this, residues at positions 3, 5 and 7 in P₁₁-2 were changed to ornithine (Arg3 \rightarrow Orn, Gln5 \rightarrow Orn, Gln7 \rightarrow Orn), and the glutamic acid at position 9 to glutamine (Glu9 \rightarrow Gln) (Table 7). It is unnecessary to incorporate a residue that will be negatively charged at pH values greater than the apparent pK of Orn to prevent flocculation of fibrils at very high pH values because, conveniently, the reaction of CO₂ with the amino groups on deprotonated Orn at high pH values leads to formation of carbamate [64]:



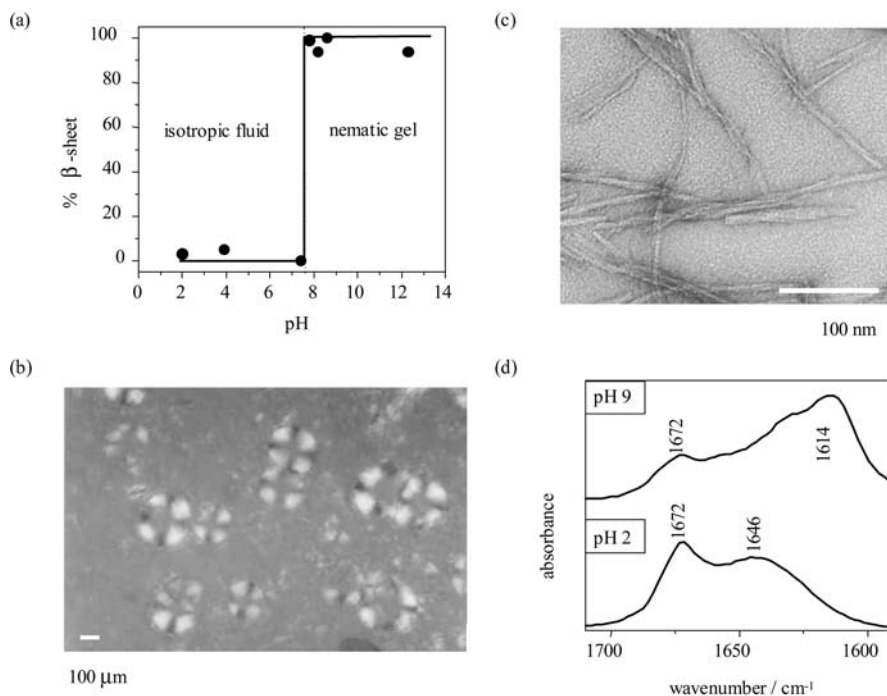


Figure 15. (a) Phase behavior of P_{11-5} ($c = 13.1$ mM) as a function of pH (DCI/NaOD), showing the sharp transition from isotropic fluid to nematic gel states at pH 7.5. (b) Polarizing optical micrograph showing nematic droplets with a radial director distribution (Maltese cross) dispersed in an isotropic fluid phase. (c) Transmission electron micrograph of a gel (pH 9, $c = 13.1$ mM) showing semi-rigid fibrils. (d) FTIR spectrum of amide I' bands showing β -sheet conformation of P_{11-5} in the nematic gel state ($c = 13.1$ mM, pH 9 – NaOD) - upper trace, and the random coil conformation in the isotropic fluid state ($c = 13.1$ mM, pH 2 – DCI) - lower trace. (Reprinted with permission from [7]. Copyright (2003) American Chemical Society.)

Repulsion between negatively charged carbamate groups provides stabilization of fibrillar dispersions.

Acidic solutions are Newtonian fluids of monomeric peptide, Above pH 7.8, fluid nematic phases occur at concentrations in excess of 0.9 mM and nematic gels appear above 6.6 mM (comparable to the behavior of P_{11-4}). The pH dependence of a 13.1 mM solution of P_{11-5} is summarized in Figure 15a. The isotropic-to-nematic transition occurs within the pH interval 7.4–7.8, some 3 pH units below the pH observed for deprotonation of ornithine in peptide monomers [65]. A solution of pH = 7.6 displays nematic droplets with a radial director distribution (Maltese cross when viewed between crossed polarizers; diameter $\sim 300 \mu\text{m}$) dispersed in an isotropic fluid phase, indicative of the biphasic nature of the transition (Figure 15b). At pH ≤ 7.4 , the peptide is in an unstructured state in solution (Figure 15d (lower trace)), while at higher pH

values it is incorporated in semi-rigid fibrils (Figure 15c) in an anti-parallel crossed- β configuration (Figure 15d (upper trace)). The maximum “diameter” of the fibrils is typically 8–12 nm, corresponding to 8 to 12 stacked tapes.

In the pH window $7.2 < \text{pH} < 7.4$, both P₁₁-4 (A- denoting anionic) and P₁₁-5 (B-denoting cationic) are in their monomeric states (Figure 16a). The three

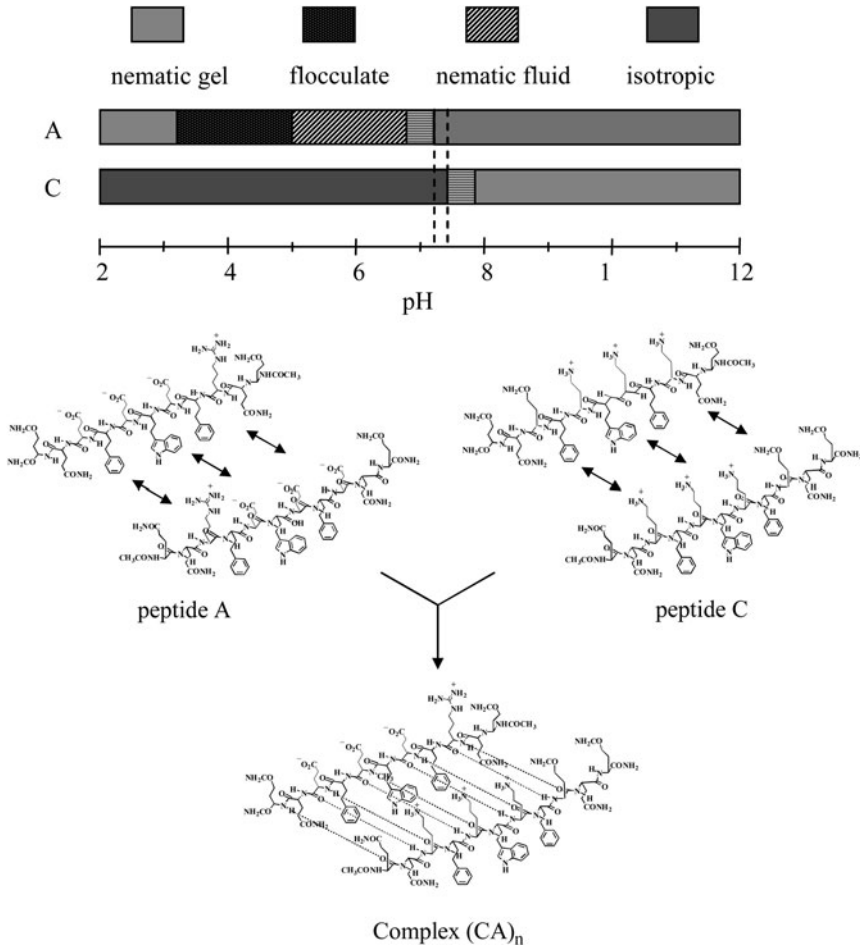


Figure 16. (a) Phase behavior of 6.3 mM aqueous solutions of peptides A and C as a function of pH. The nematic-to-isotropic biphasic region of A extends from pH 6.8 to 7.2 and for C from 7.4 to 7.8, defining the pH interval 7.2 to 7.4 for mixing of A and C. The termini of the horizontal lines spanning the biphasic intervals denote pH values of co-existing nematic and isotropic phases. (b) Molecular structures of A, C and the complex CA, respectively, showing the electrostatic charge distributions at pH 7.3. (Reprinted with permission from [8]. Copyright (2003) Wiley-VCH.)

Glu ($-\text{CH}_2\text{CH}_2\text{COOH}$) residues in A at positions 5, 7, and 9 are in their deprotonated states giving the peptide a net two units of negative charge (Figure 16b). The resultant Coulombic repulsion keeps the peptides apart and suppresses self-assembly. Similarly, for peptide C, the three Orn ($-\text{CH}_2\text{CH}_2\text{CH}_2\text{NH}_2$) in positions 3, 5, and 7 are positively charged and give the peptide three units of net charge (Figure 16b). When equal quantities of these two solutions at $\text{pH} = 7.3$ are mixed, a self-supporting, turbid gel is obtained instantaneously. The gel is birefringent when viewed between crossed polarizers and the optical micrograph (Figure 17a) is characteristic of a nematic gel. The fibrils have

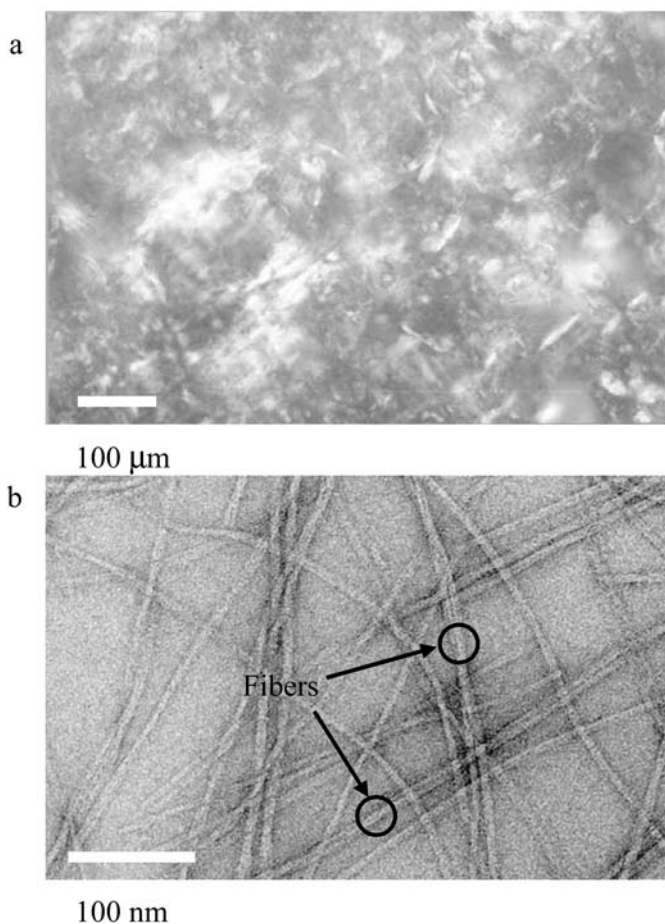


Figure 17. (a) Polarizing optical micrograph of the gel ($c = 6.3 \text{ mM}$) formed after mixing aqueous solutions of monomeric peptides A and C at $\text{pH} 7.3$ showing a typical nematic texture [55]. (b) Transmission electron micrograph showing mainly fibrils and a few fibers (having twice the diameter of the fibrils) in the nematic gel ($c = 6.3 \text{ mM}$). (Reprinted with permission from [8]. Copyright (2003) Wiley-VCH.)

cross-sections of 8×4 nm and are comprised of 4 ribbons (Figure 17b), just like those of pure A and B. Spectroscopic measurements are consistent with the fibrils being a 1:1 complex of A and C, arranged alternately in an antiparallel cross- β structure within the tape-like fibrillar substructure. Being salts, these complexes are stable over wide pH windows (1–12). They may be likened to the polyelectrolyte complexes formed on mixing oppositely charged polymeric polyelectrolytes [66], and are accordingly termed *Peptide Polyelectrolyte β -sheet Complexes*. The two residues employed here can be inserted into almost any basic β -sheet tape forming peptide structure to create such complexes, as long as the other functional properties have already been incorporated into the structure. That is, functional properties can be incorporated additively to a first approximation.

8. Conclusions and Perspectives for the Future

It is possible to exploit the intrinsic one-dimensional self-assembling propensities of peptides to form cross- β structures [3] in order to produce a hierarchy of structures: helical tapes (single molecule thick), twisted ribbons (double tapes), fibrils (twisted stacks of ribbons), and fibers (entwined fibrils) with increasing concentration in water [3, 4]. The fibrils are semi-rigid and can form viscoelastic nematic fluids at concentrations of ca. 0.001 v/v. At higher concentrations, fiber formation occurs and gives rise to networks comprised of fibrils linked at fiber-like junctions (i.e., SAFINs) creating elastomeric nematic hydrogels [3]. Single tapes can also become topologically entangled to form viscoelastic gels. Organogels can readily be produced by appropriate peptide design and using polar organic solvents. The stability of the gels is governed by electrical double layer forces between tapes or fibrils accordingly. This requires the peptides to have a net positive or negative residual charge. The charge on peptides can be readily controlled by changes in pH values. pH can be used, in turn, to control the self-assembly behavior and the macroscopic properties of the solution. This self-assembly also leads to peptide polyelectrolyte β -sheet complexes which are relatively insensitive to pH changes. pH switching provides a way for the direct and controlled production of gels from solid peptides, avoiding any structural traps. Potential applications envisaged for these hydrogels are, for example, encapsulation, immobilization and separation of cells, proteins, antibodies, or enzymes, and as templates for growing nanostructured inorganic materials.

The self-assembly behavior of β -sheet-forming peptides has been shown to be explicable in terms of a generic model for the self-assembly of chiral rod-like molecules. The model is also applicable to the behavior of any chiral molecule

that can undergo one-dimensional self-assembly. Since many LMOGs are chiral, this model provides a generic insight into the formation of the corresponding “hydrogels” or “organogels” which are comprised of SAFINs.

References

- [1] *Self-Assembling Peptide Systems in Biology, Medicine and Engineering*, A. Aggeli, N. Boden, and S. Zhang, Eds., Dordrecht: Kluwer Academic Publishers, **2001**.
- [2] Spector, M.S.; Selinger, J.V.; Schnur, J.M. In *Materials - Chirality: A Special Volume in the Topics in Stereochemistry Series*, M.M. Green, R.J.M. Nolte, and E.W. Meijer, Eds., New York: John Wiley and Sons Inc., **2003**, Chapter 5, pp. 281–372.
- [3] Aggeli, A.; Nyrkova, I.A.; Bell, M.; Harding, R.; Carrick, L.; McLeish, T.C.B.; Semenov, A.N.; Boden, N. *Proc. Nat. Acad. Sci. (USA)*, **2001**, *98*, 11857–11862.
- [4] (a) Nyrkova, I.; Semenov, A.; Aggeli, A.; Boden, N. *Eur. Phys. J. B*, **2000**, *17*, 481–497. (b) Nyrkova, I.; Semenov, A.N.; Aggeli, A.; Bell, M.; Boden, N.; McLeish, T.C.B. *Eur. Phys. J. B*, **2000**, *17*, 499–513.
- [5] Aggeli, A.; Bell, M.; Boden, N.; Keen, J.N.; Knowles, P.F.; McLeish, T.C.B.; Pitkeathly, M.; Radford, S.E. *Nature*, **1997**, *386*, 259–262.
- [6] Aggeli, A.; Bell, M.; Boden, N.; Keen, J.N.; McLeish, T.C.B.; Nyrkova, I.A.; Radford, S.E.; Semenov, A.N. *J. Mat. Chem.*, **1997**, *7*, 1135–1145.
- [7] Aggeli, A.; Bell, M.; Carrick, L.M.; Fishwick, C.W.G.; Harding, R.; Mawer, P.J.; Radford, S.E.; Strong, A.E.; Boden, N. *J. Am. Chem. Soc.*, **2003**, *125*, 9619–9628.
- [8] Aggeli, A.; Bell, M.; Boden, N.; Carrick, L.M.; Strong, A.E. *Angew. Chem. Int. Ed.*, **2003**, *42*, 5603–5606.
- [9] Fishwick, C.W.G.; Beevers, A.J.; Carrick, L.M.; Whitehouse, C.D.; Aggeli, A.; Boden, N. *Nano Lett.*, **2003**, *14*, 1475–1479.
- [10] Mawer, P.J.; Waigh, T.A.; Harding, R.; McLeish, T.C.B.; King, S.M.; Bell, M.; Boden, N. *Langmuir*, **2003**, *19*, 4940–4949.
- [11] Aggeli, A.; Fytas, G.; Vlassopoulos, D.; McLeish, T.C.B.; Mawer, P.J.; Boden, N. *Biomacromolecules*, **2001**, *2*, 378–388.
- [12] (a) Collier, J.H.; Hu, B.H.; Ruberti, J.W.; Zhang, J.; Shum, P.; Thompson, D.H.; Messersmith, P.B. *J. Am. Chem. Soc.*, **2001**, *123*, 9463–9464. (b) Marini, D.M.; Hwang, W.; Lauffenburger, D.A.; Zhang, S.; Kamm, R.D. *Nano Lett.*, **2002**, *2*, 295–299. (c) Lashuel, H.A.; LaBrenz, S.R.; Woo, L.; Serpell, L.C.; Kelly, J.W. *J. Am. Chem. Soc.*, **2000**, *122*, 5262–5277. (d) Yamada, N.; Ariga, K.; Naito, M.; Matsubara, K.; Koyama, E. *J. Am. Chem. Soc.*, **1998**, *120*, 12192–12199. (e) Burkoth, T.S.; Benzinger, T.L.S.; Jones, D.N.M.; Hallenga, K.; Meredith, S.C.; Lynn, D.G. *J. Am. Chem. Soc.*, **1998**, *120*, 7655–7656. (f) Qu, Y.; Payne, S.C.; Apkarian, R.P.; Conticello, V.P.; *J. Am. Chem. Soc.*, **2000**, *122*, 5014–5015.
- [13] (a) Terech, P.; Weiss, R.G. *Chem. Rev.*, **1997**, *97*, 3133–3159; (b) Hanabusa, K.; Yamada, M.; Kimura, M.; Shirai, H. *Angew. Chem. Int. Ed.*, **1996**, *35*, 1949–1951; (c) Gronwald, O.; Snip, E.; Shinkai, S. *Curr. Opin. Colloid Interface Sci.*, **2002**, *7*, 148–156; (d) de Loos, M.; van Esch, J.; Kellogg, R.M.; Feringa, B.L. *Angew. Chem. Int. Ed.*, **2001**, *40*, 613–616.
- [14] Terech, P. *Proceedings of Euroconference on Self-Assembling Fibrillar Networks*, Autrans, France, November **2001**.
- [15] Perutz, M.F.; Johnson, T.; Suzuki, M.; Finch, J.T. *Proc. Natl. Acad. Sci. (USA)*, **1994**, *91*, 5355–5358.

- [16] Manning, M.C.; Illangasekare, M.; Woody, R.W. *Biophys. Chem.*, **1988**, *31*, 77–86.
- [17] Grishina, I.B.; Woody, R.W. *Faraday Discussions*, **1994**, *99*, 245–262.
- [18] Chothia, C. *J. Mol. Biol.*, **1973**, *75*, 295–302.
- [19] Benzinger, T.L.S.; Gregory, D.M.; Burkoth, T.S.; Miller-Auer, H.; Lynn, D.G.; Botto, R.E.; Meredith, S.C. *Proc. Nat. Acad. Sci. (USA)*, **1998**, *95*, 13407–13412.
- [20] Halverson, K.; Fraser, P.A.; Kirschner, D.A.; Lansbury, P.T. *Biochemistry*, **1990**, *29*, 2639–2644.
- [21] Burkoth, T.S.; Benzinger, T.L.S.; Urban, V.; Morgan, D.M.; Gregory, D.M.; Thiya-garajan, P.; Botto, R.E.; Meredith, S.C.; Lynn, D.G. *J. Am. Chem. Soc.*, **2000**, *122*, 7883–7889.
- [22] Ionescu-Zanetti, C.; Khurana, R.; Gillespie, J.R.; Petrick, J.S.; Trabachino, L.C.; Minert, L.J.; Carter, S.A.; Fink, A.L. *Proc. Nat. Acad. Sci. (USA)*, **1999**, *96*, 13175–13179.
- [23] Sikorski, P.; Atkins, E.D.T.; Serpell, L.C. *Structure*, **2003**, *11*, 915–926.
- [24] Rechtes, M.; Porat, Y.; Gazit, E. *J. Biol. Chem.*, **2002**, *277*, 35475–35480.
- [25] Kad, N.M.; Myers, S.L.; Smith, D.P.; Smith, D.A.; Radford, S.E.; Thomson, N.H. *J. Mol. Biol.*, **2003**, *330*, 785–797.
- [26] Kayed, R.; Bernhagen, J.; Greenfield, N.; Sweimeh, K.; Brunner, H.; Voelter, W.; Kapurniotu, A. *J. Mol. Biol.*, **1999**, *287*, 781–796.
- [27] Oda, R.; Huc, I.; Schmutz, M.; Candau, S.J.; MacKintosh, F.C. *Nature*, **1999**, *399*, 566–569.
- [28] de la Paz, M.L.; Serrano, L. *Proc. Nat. Acad. Sci. (USA)*, **2004**, *101*, 87–92.
- [29] Luckey, M.; Hernandez, J.F.; Arlaud, G.; Forsyth, V.T.; Ruigrok, R.W.H.; Mitraki, A. *FEBS Letters*, **2000**, *468*, 23–27.
- [30] Hamodrakas, S.J.; Hoenger, A.; Iconomidou, V.A. *J. Str. Biol.*, **2004**, *145*, 226–235.
- [31] Fandrich, M.; Dobson, C.M. *EMBO J.*, **2002**, *21*, 5682–5690.
- [32] Fandrich, M.; Fletcher, M.A.; Dobson, C.M. *Nature*, **2001**, *410*, 165–166.
- [33] Richardson, J.S.; Richardson, D.C. *Proc. Nat. Acad. Sci. (USA)*, **2002**, *99*, 2754–2759.
- [34] (a) Perutz, M.F. *Trends In Biochem. Sci.*, **1999**, *24*, 58–63. (b) Perutz, M.F. *Curr. Opin. Struc. Biol.*, **1996**, *6*, 848–858.
- [35] Perutz, M.F.; Johnson, T.; Suzuki, M.; Finch, J.T. *Proc. Nat. Acad. Sci. (USA)*, **1994**, *12*, 5355–5358.
- [36] (a) Terzi, E.; Holzemann, G.; Seelig, J. *Biochemistry*, **1994**, *33*, 1345–1350. (b) Terzi, E.; Holzemann, G.; Seelig, J. *J. Mol. Biol.*, **1995**, *252*, 633–642.
- [37] Altman, M.; Lee, P.; Rich, A.; Zhang, S.G. *Protein Sci.*, **2002**, *9*, 1095–1105.
- [38] Takahashi, Y.; Ueno, A.; Mihara, H. *Struct. Fold. Des.*, **2000**, *8*, 915–925.
- [39] Choo, D.W.; Schneider, J.P.; Graciani, N.R.; Kelly, J.W. *Macromolecules*, **1996**, *29*, 355–366.
- [40] Janek, K.; Behlke, J.; Zipper, J.; Fabian, H.; Georgalis, Y.; Beyermann, M.; Bienert, M.; Krause, E. *Biochemistry*, **1999**, *38*, 8246–8252.
- [41] West, M.W.; Wang, W.X.; Patterson, J.; Mancias, J.D.; Beasley, J.R.; Hecht, M.H. *Proc. Nat. Acad. Sci. (USA)*, **1999**, *96*, 11211–11216.
- [42] Lim, A.; Makhov, A.M.; Bond, J.; Inouye, H.; Connors, L.H.; Griffith, J.D.; Erickson, B.W.; Kirschner, D.A.; Costello, C.E.A. *J. Struc. Biol.*, **2000**, *130*, 363–370.
- [43] Collier, J.H.; Messersmith, P.B. *Adv. Mater.*, **2004**, *16*, 907–910.
- [44] Gulik-Krzywicki, E.T.; Fouquey, C.; Lehn, J.M. *Proc. Natl. Acad. Sci. USA*, **1993**, *90*, 163–167.
- [45] Rowan, A.E.; Nolte, R.J.M. *Angew. Chem. Int. Ed.*, **1998**, *37*, 63–68.
- [46] Murata, K.; Aoki, M.; Suzuku, T.; Harada, T.; Kawabata, H. *J. Am. Chem. Soc.*, **1994**, *116*, 6664–6676.

- [47] Fuhrhop, J.H.; Helfrich, W. *Chem. Rev.*, **1993**, *93*, 1565–1582.
- [48] Hanabusa, K.; Yamada, M.; Kimura, M.; Shirai, H. *Angew. Chem. Int. Ed.*, **1996**, *35*, 1949–1951.
- [49] Cuccia, L.A.; Lehn, J.M.; Homo, J.C.; Schmutz, M. *Angew. Chem. Int. Ed.*, **2000**, *39*, 233–236.
- [50] Tamaru, S.; Nakamura, M.; Takeuchi, M.; Shinkai, S. *Org. Lett.*, **2001**, *3*, 3631–3634.
- [51] Song, J.; Cisar, J.S.; Bertozzi, C.R. *J. Am. Chem. Soc.*, **2004**, *126*, 8459–8465.
- [52] Beginn, U.; Tartsch, B. *Chem. Comm.*, **2001**, *19*, 1924–1925.
- [53] Maitra, U.; Potluri, V.K.; Sangeetha, N.M.; Babu, P.; Raju, A.R. *Tetrahedron: Asymmetry*, **2001**, *12*, 477–480.
- [54] Brinksma, J.; Feringa, B.L.; Kellogg, R.M.; Vreeker, R.; van Esch, J. *Langmuir*, **2000**, *16*, 9249–9255.
- [55] Dobb, M.G.; Johnson, D.J.; Saville, B.P. *J. Polym. Sci.*, **1977**, *15*, 2201–2211.
- [56] Semenov, A.N.; Khokhlov, A.R. *Sov. Phys. Usp.*, **1988**, *31*, 988.
- [57] Byrom, D. *Biomaterials: Novel Materials from Biological Sources*, Basingstoke: Macmillan Academic and Professional, **1991**, Chapters 1 and 2, pp. 1–123.
- [58] Meegan, J.E.; Aggeli, A.; Boden, N.; Brydson, R.; Brown, A.P.; Carrick, L.; Brough, A.R.; Hussain, A.; Ansell, R.J. *Adv. Funct. Mater.*, **2004**, *14*, 31–37.
- [59] Nagasawa, M.; Holtzer, A. *J. Am. Chem. Soc.*, **1964**, *86*, 531–538.
- [60] Olander, D.S.; Holtzer, A. *J. Am. Chem. Soc.*, **1968**, *90*, 4549.
- [61] Ullner, M.; Woodward, C.E. *Macromolecules*, **2000**, *33*, 7144–7156.
- [62] Edsall, J.T.; Gutfreund, H. *Biothermodynamics: The Study of Biochemical Processes at Equilibrium*, Chichester: John Wiley and Sons Inc., **1983**, Chapter 5, pp. 157–209.
- [63] Creighton, T.E. *Proteins – Structures and Molecular Properties*, 2nd edition, New York: W.H. Freeman, **1993**, Chapter 7, pp. 287–291.
- [64] (a) Schimming, V.; Hoelger, C.G.; Buntkowsky, G.; Sack, I.; Fuhrhop, J.H.; Rocchetti, S.; Limbach, H.H. *J. Am. Chem. Soc.*, **1999**, *121*, 4892–4893. (b) Edsall, J.T.; Wyman, J. *Biophysical Chemistry, Volume 1*, New York: Academic Press, **1958**, Chapter 10, pp. 550–590.
- [65] Greenstein, J.P.; Winitz, M. *Chemistry of the Amino Acids*, New York: John Wiley and Sons Inc., **1961**, Chapter 4, p. 486.
- [66] Tsuchida, E.; Abe, K. *Adv. Polym. Sci.*, **1982**, *45*, 1–119.

Chapter 4

KINETICS OF NUCLEATION, AGGREGATION AND AGEING

Jörn W.P. Schmelzer

*Fachbereich Physik der Universität Rostock Universitätsplatz,
18051 Rostock, Germany*

1. Introduction	131
2. Some Basic Thermodynamic Concepts	132
3. Basic Concepts of the Theory of Nucleation and Cluster Growth	134
3.1. The Origin of Metastability: Critical Clusters	134
3.2. The Steady-State Nucleation Rate	137
3.3. Methods of Determination of the Work of Critical Cluster Formation	140
3.4. Nucleation and Simultaneous Growth: The Kolmogorov-Avrami Equation	151
3.5. Depletion Effects and the Overall Course of First-Order Phase Transitions	153
4. Spinodal Decomposition	154
5. Secondary Aggregation, Coarsening and Ageing	158
6. Overview	160

1. Introduction

Phase formation processes, in general, and processes of structure formation in non-crystalline materials, represent a particularly interesting field of the universal phenomenon of self-structuring of matter. Such processes of ordering cannot be, as a rule, influenced directly. They may be governed by choosing appropriate initial and boundary conditions. For this reason, the knowledge of

the dependence of these processes on the conditions under which they may proceed, are of essential importance for their appropriate control.

The processes of phase formation and their further evolution may be described frequently via three basic theoretical models, the nucleation-growth model, the model of spinodal decomposition and aggregation (coagulation) model. Here, we give a brief overview of the respective methods, focusing on the main ideas and results. Details can be found in extended overviews [1–4] and in the other references.

2. Some Basic Thermodynamic Concepts

Basic concepts of the theoretical description of first-order phase transitions may be introduced quite easily via the consideration of the thermal equation of state of the van der Waals fluid. In the pressure – volume diagram and reduced variables ($\Pi = p/p_c$ (p : pressure), $\omega = v/v_c$ (v : volume), $\theta = T/T_c$ (T : temperature); the subscript (c) refers here to the values of the respective thermodynamic parameters at the critical point), the isotherms of the van der Waals fluid, and the location of the binodal and spinodal curves have a form as shown in Figure 1. The spinodal curve (dotted curve) connects (in the framework of the mean-field approach underlying the derivation of the van der Waals equation of state) the extrema of the isotherms, and the position of the binodal curve (full curve) may be determined via the Maxwell rule (e.g. [1]).

A similar picture is observed for segregation processes in solutions. Here we consider, for illustration purposes, the simple cases of a binary regular solution.

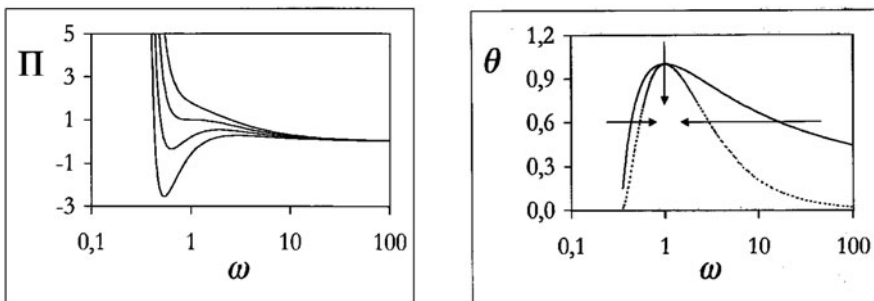


Figure 1. Left: Isotherms of the van der Waals fluid. Right: Binodal (full) and spinodal (dotted) curves of the van der Waals fluid. The arrows on the right hand side illustrate possible paths of penetration of the system into metastable or unstable initial states.

The chemical potentials of both components may be expressed for binary regular solutions via the molar fraction of the second component, x , in the form:

$$\mu_1(p, T, x) = \mu_1^*(p, T) + k_B T \ln(1 - x) + \omega x^2 \quad (1)$$

$$\mu_2(p, T, x) = \mu_2^*(p, T) + k_B T \ln(x) + \omega(1 - x)^2 \quad (2)$$

The coordinates of the critical solution point and the location of binodal and spinodal curves in this system are given by (cf. also Figure 2):

$$T_c = \frac{\omega}{2k_B}, \quad x_c = \frac{1}{2} \quad (3)$$

$$\ln\left(\frac{1-x}{x}\right) = 2\left(\frac{T_c}{T}\right)(1-2x), \quad x(1-x) = \frac{T}{4T_c} \quad (4)$$

The position of the binodal curve is thermodynamically well-defined. It can be determined via measurements of the state parameters of the respective two-phase system in equilibrium. The location of the spinodal curve is determined here from the theoretical model of the respective systems. This procedure is connected with some uncertainty due to the limits of validity of mean-field approaches in the determination of the equations of state. However, as shown in [5] for the case of bubble formation in liquids, the location of the spinodal can be determined experimentally by an extrapolation of thermodynamic data obtained for metastable states of the system to higher supersaturations.

Homogeneous states in between binodal and spinodal curves are metastable states, they are small and unstable with respect to fluctuations exceeding a well-defined finite size. These may act as “embryos” of the new phase (i.e., as aggregates, capable to a further deterministic growth). This is the range of initial states in the space of thermodynamic variables, where the model of nucleation

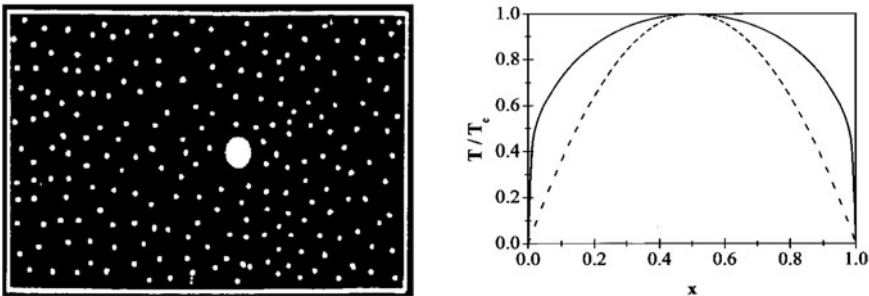


Figure 2. Left: Model system considered in the analysis: formation of a cluster in a binary solution. Right: Phase diagram of a binary regular solution with critical point (T_c, x_c) , binodal curve (full curve) and spinodal (dotted) curve.

and growth is appropriate for the description of the transition of the system into the new phase.

The spinodal curve encloses the region of thermodynamically unstable states. In this range of homogeneous initial states, fluctuations of a particular type exist (long wave-length fluctuations with an initially small amplitude), which may grow spontaneously. Here, it is not required that the amplitudes of the fluctuations exceed critical size. For thermodynamically unstable initial states, the description of the evolution of the new phase can be performed via the model of spinodal decomposition describing the process of formation and growth of such types of fluctuations.

In the analysis of phase formation, the concept of supersaturation is of basic importance. As measures of supersaturation, different parameters may be introduced describing the degree of penetration of the system into the two-phase region (i.e., the distance from the binodal curve) in the course of the variation of the thermodynamic state parameters. For the particular example of a van der Waals fluid, one could define as supersaturation the deviations of the pressure or the specific volume per particle in the homogeneous initial state from the respective values at the binodal curves (referring to a stable equilibrium co-existence of both phases at planar interfaces). Possible ways of increasing the supersaturation in the system are marked in Figure 1 by arrows. Similarly, for segregation processes in binary solutions, the deviation of the concentration from the value at the binodal curve determines the degree of supersaturation of the system.

For the description of phase formation in solids, the difference of the chemical potentials, $\Delta\mu$, per mole or particle in both considered phases is a more convenient measure of the supersaturation [2]. The thermodynamically stable phase corresponds – according to the general evolution criteria of classical thermodynamics – to the minimum Gibbs free energy G . The difference between the values of G in both phases can be considered, therefore, as the driving force of the transformation, $\Delta\mu$, or as the supersaturation (generalizations for multi-component systems can be formulated in all mentioned cases under certain conditions straightforwardly [2, 4]).

3. Basic Concepts of the Theory of Nucleation and Cluster Growth

3.1. The Origin of Metastability: Critical Clusters

According to the thermodynamic evolution criteria, any spontaneous process in a thermodynamic system is accompanied by a monotonic increase (e.g., entropy at constant energy, volume and particle numbers in the system) or decrease (e.g., the Gibbs and Helmholtz free energies at the appropriate

boundary conditions) of the characteristic thermodynamic functions. Thus, the questions arise: why, in the course of variation of pressure or temperature, the evolution to the new phase does not start immediately after the system has entered the range of parameters where the new phase corresponds to lower values of the respective thermodynamic potential, and why are the respective states stable with respect to small and unstable with respect to sufficiently large fluctuations (i.e., why so-called metastable states exist)?

As explained in detail for the first time by Gibbs, the origin for the existence of metastable states consists in the necessity of formation of a phase boundary in the course of evolution of a critically-sized aggregate, an embryo of the new phase, in the initially homogeneous ambient phase. A surface or interfacial tension, σ , may be assigned to the interfacial region with the surface area A , too. The change of the thermodynamic potential (at constant external pressure and temperature; this is the Gibbs free energy), due to the formation of an aggregate of the newly evolving phase, may be expressed approximately as [2, 4] in Eq. (5). We assume here that the cluster is incompressible with some given density c_α and, at least, approximately of spherical shape with a radius R .

$$\Delta G = -n_\alpha \Delta\mu + \sigma A \quad (5)$$

Here, n_α is the number of particles in the cluster of the newly evolving phase.

The dependence $\Delta G = \Delta G(R)$ is illustrated at the left side of Figure 3. For clusters with a radius $R < R_c$, the thermodynamic evolution criteria lead to the conclusion that the respective aggregates will dissolve as a rule, again. In contrast, clusters with a size $R > R_c$ will grow, in general, spontaneously up to macroscopic dimensions.

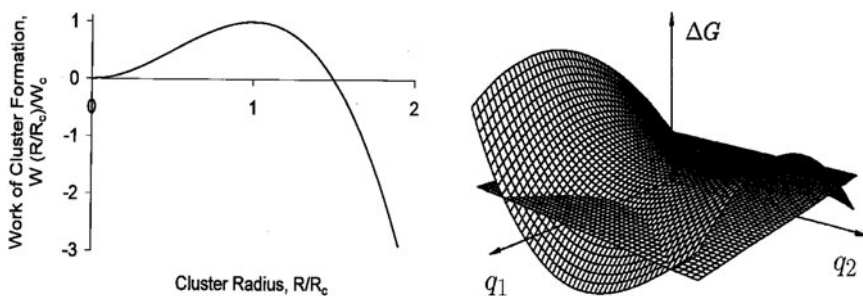


Figure 3. Left: Change of the thermodynamic potential ΔG (or the work of cluster formation, W) in the course of formation of a cluster of the newly evolving phase. The variable state parameters of the cluster (its size) are specified here by the radius, R (the respective dependence is given in dimensionless terms $W(R/R_c)$ vs R/R_c). Right: Qualitative shape of the Gibbs free energy surface if several parameters (here q_1 and q_2) are required for the specification of the state of the clusters of the newly evolving phase.

The critical cluster size, R_c , corresponds here to a maximum of ΔG . R_c and $\Delta G_c = \Delta G(R = R_c)$ may be determined approximately [2, 4] via the relations in Eqs. (6a) and (6b).

$$R_c = \frac{2\sigma}{c_\alpha \Delta\mu} \quad (6a)$$

$$\Delta G_c = W_c = \frac{16\pi}{3} \frac{\sigma^3}{(c_\alpha \Delta\mu)^2} \quad (6b)$$

In general, one parameter of state is not sufficient in order to describe the properties of the aggregates of the newly evolving phase and, in particular, the properties of the critical clusters. In addition to the size, the density of the clusters may change and, for multi-component systems, their composition. In addition, for application to crystal formation, structure parameters have to be introduced into the description. In more general cases, the critical cluster does not correspond to a maximum but to a saddle point of the free energy surface. The maximum is reached with respect to variations of the size, while with respect to a change of the state parameters of the cluster phase, the critical cluster refers to a minimum of G . This situation is illustrated on the right hand side of Figure 3.

The change of the thermodynamic potential, due to the formation of a cluster of critical size, is also denoted commonly as work of critical cluster formation, W_c ; it equals the minimum work on the system needed in a reversible process to generate the same change of the state. The work of W_c represents the barrier for the transition of the system into the new phase. For this reason, the work of critical cluster formation is required to tend to zero for initial metastable states in the immediate vicinity of the spinodal curve.

The values of the work of critical cluster formation may be reduced considerably if heterogeneous centers of nucleation are present in the system. Commonly, the work of critical cluster formation in the presence of heterogeneous nucleation cores, $W_c^{(het)}$, can be expressed via the respective value for homogeneous nucleation, $W_c^{(hom)}$, multiplied by a factor $\varphi \leq 1$:

$$W_c^{(het)} = W_c^{(hom)}\varphi, \quad \varphi \leq 1 \quad (7)$$

The value of φ is determined by specific properties of the heterogeneous nucleation cores considered [2].

Similar effects may occur if sufficiently large structures of the ambient phase are present which may catalyze the process of nucleation in the same way as heterogeneous foreign particles. As possible examples, one could note holes in a polymeric network (which could favor, eventually, bubble formation)

or specific short-range order structures in glass-forming melts allowing easier crystallization. In contrast to heterogeneous nucleation cores, such centers (which are also denoted as active homogeneous nucleation sites) cannot be eliminated totally. However, the path of transfer of the system into the considered initial state can have a significant effect on their activity.

On the other hand, not all foreign particles and internal structures are active with respect to nucleation. Much more work remains to be done in the future until a satisfactory understanding of these effects will be reached.

3.2. The Steady-State Nucleation Rate

In accordance with the above given considerations, the formation of critical and supercritical clusters is a fluctuative process. The rate of formation of such clusters is determined as a rule by the lowest value of the barrier a cluster has to surpass in its evolution to the new phase (or in other words, by the work of critical cluster formation). This statement is reflected in the expression for the steady-state nucleation rate, J , given generally by Eq. (8).

$$J = J_0 \exp\left(-\frac{\Delta G_c}{k_B T}\right) \quad (8)$$

J is the number of critical clusters formed per unit time in a unit volume of the ambient phase [2, 4], k_B is the Boltzmann constant and T is the absolute temperature. In accordance with Eq. (8), thermodynamic aspects of the phase transformation are described mainly by the work of ΔG_c . Specific features of the kinetics of the process are incorporated into the description via the pre-exponential factor, J_0 .

For one-component systems, we may write, for example [2, 4]:

$$J_0 = cw^{(+)}(n_c)\Gamma^{(Z)} \quad (9)$$

Here, c is the number of possible centers of the nucleation process. For homogeneous nucleation, it equals the number of particles in the considered one-component system. $\Gamma^{(Z)}$ is a thermodynamic correction factor (the Zeldovich factor). The type of kinetics of aggregation and dissolution is specified by the parameter $w^{(+)}(n_c)$. It is the number of particles of the new phase which are incorporated in unit time into a cluster of critical size.

For processes of condensation of gases, boiling in liquids or segregation processes in solutions, this parameter depends often only weakly on the values of the thermodynamic state variables (such as pressure and temperature). In these cases, the dependence of the steady-state nucleation rate as a function of the supersaturation is determined basically by the exponential term in Eq. (8).

For small supersaturations, the nucleation rate is practically equal to zero. Only after a certain critical value of the supersaturation is reached may intensive nucleation processes be observed in the system. With a further even moderate increase of the supersaturation, the nucleation rate increases dramatically by many orders of magnitude. As one consequence, the possibility of existence of metastable states is re-established. It follows further that such systems cannot be transferred, as a rule, into unstable homogeneous initial states (where spinodal decomposition determines the transformation) along the paths shown in Figure 1 by horizontal arrows. Here, spinodal decomposition may be of relevance only if the system is transferred into unstable states by passing the vicinity of the critical point (e.g., the path described by a vertical arrow in Figure 1). Consequently, for systems of such type, phase formation processes will proceed as a rule via nucleation and growth.

Figure 4 (left hand side) illustrates also the significant dependence of the work of critical cluster formation and, consequently, of the steady-state nucleation rate on the value of the surface or interfacial tension. If the value of the surface tension is increased, intensive nucleation occurs at higher supersaturations only.

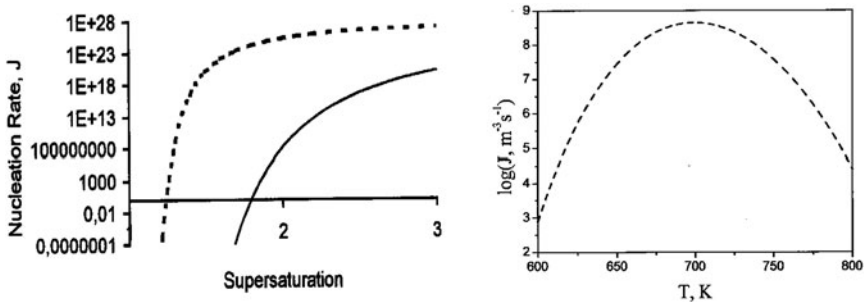


Figure 4. Dependence of the nucleation rate on supersaturation for different typical situations. *Left:* For segregation processes in solutions (taken here for example), the dependence of the nucleation rate on supersaturation (here determined via changes in the molar fraction of the second component as compared with the respective value at the binodal curve) is determined basically by changes in the work of critical cluster formation. After a certain value of the supersaturation is reached, its further moderate increase results then in a dramatic monotonic increase of the nucleation rate. The curves are shown for two different values of σ (σ (full curve) and 0.5σ (dashed curve)). *Right:* Typical dependence of the nucleation rate as a function of supersaturation in crystallization processes (shown here for a lithium disilicate glass [6]). The increase of the supersaturation (connected here with the decrease of temperature) and the resulting decrease of the work of critical cluster formation are compensated partly or totally by the drastic decrease of the kinetic coefficients (or an increase of viscosity) with a decrease of temperature.

For the description of phase transformations in solids or, for example, in glass-forming melts, the aggregation coefficients $w^{(+)}(n_c)$ may be expressed either via characteristic jump or oscillation times around (temporary) equilibrium positions, τ , via diffusion- or self-diffusion coefficients, D , or applying the so-called Stokes-Einstein relation (see, e.g., [2]), via the Newtonian viscosity, η [2] as in Eq. (10).

$$w^{(+)}(n_c) \propto \frac{1}{\tau} \quad (10a)$$

$$w^{(+)}(n_c) \propto D \quad (10b)$$

$$w^{(+)}(n_c) \propto \frac{1}{\eta} \quad (10c)$$

In this case, the dependence of the nucleation process on temperature is governed by two equivalent importance factors acting against each other: the increase of the thermodynamic driving force of the transformation (due to the decrease of temperature) is compensated partly or totally by the decrease in the values of the kinetic coefficients governing the rates of the aggregation processes. As a result, a non-monotonous dependence of the nucleation rate on temperature is found with a maximum located, in general, at temperatures near the temperature of vitrification, T_v . With a further decrease of temperature, the kinetic processes become widely frozen-in and the undercooled liquid is transformed into a glass (see Figure 4, right).

Different aspects of the dynamics of molecular motions in liquids have been discussed with a renewed interest during the last decade. In this connection, concepts like heterogeneous dynamics of the molecular motion, limits of validity of the Stokes-Einstein equation, decoupling of diffusion and relaxation etc. have been advanced. New insights for the understanding of the specific features of the molecular motion in liquids should be forthcoming, with new consequences in application to the theoretical understanding of nucleation. As shown recently, decoupling of diffusion and relaxation in the vicinity and below the temperature of vitrification results in changes of the kinetic prefactor and other parts in the expression describing the steady-state nucleation rate. More importantly, the expression for the work of critical cluster formation has to be modified as well, taking into account the evolution of elastic stresses in crystallization [6].

A general theory of nucleation in viscoelastic materials, where both stress evolution and stress relaxation are considered, has been developed recently. Its application to particular systems is being carried out presently. It is believed that the incorporation of elastic stresses into the theoretical description of phase formation in glass-forming melts will resolve a number of puzzles in the interpretation of experimental results on nucleation which have not found a satisfactory explanation so far. Such stresses are expected to have

an important impact at different stages in the evolution of molecular gels as well.

Similar equations to those discussed here for phase formation in one-component systems may be derived for nucleation processes in multi-component systems if the new phase has a given stoichiometric composition independent of cluster size [4]. In this case, both the number of centers of aggregation and the aggregation coefficients become functions of the thermodynamic and kinetic parameters of all components, both in the ambient and the newly evolving phases. However, in general, the state of the clusters depends on their sizes and additional analyses have to be performed in order to determine the dependence.

3.3. Methods of Determination of the Work of Critical Cluster Formation

Accurate knowledge of the work of critical cluster formation and its dependence on the state parameters of the homogeneous initial state are very important for the correct determination of the steady-state nucleation rate. For this reason, we summarize briefly the basic different methods for determination of this quantity.

3.3.1. Gibbs' classical method

In the framework of Gibbs' method of description of heterogeneous systems, the real inhomogeneous system is replaced by an idealized model system. This idealized model system consists of two homogeneous phases that are divided by a mathematical dividing surface. All extensive thermodynamic properties of the real system are written, then, as the sum of the contributions of the two homogeneous phases supplemented by a correction term. The correction terms can be interpreted formally as properties of the mathematical dividing surface. However this approach can lead to difficulties since correction terms to the mole or particle numbers of the different components may be negative, for example.

Here we outline briefly Gibbs' approach for the case in which a cluster of the newly evolving phase is formed in the initially homogeneous ambient phase. The parameters of the ambient phase will be specified in general, by the subscript (β), the parameters of the cluster phase by (α), and the correction terms by (σ). Generally, for the description of a particular two-phase system, we are interested in:

$$\Phi = \Phi_{\alpha} + \Phi_{\beta} + \Phi_{\sigma} \quad (11)$$

In the framework of Gibbs' method, the answers to two questions must be addressed at this point: (a) How is the position of the dividing surface defined? (b) Which properties should be assigned to the both homogeneous bulk phases in Gibbs' model system?

One of the possible definitions of the dividing surface consists for one-component systems in the choice of the equimolecular dividing surface, R_e . This dividing surface is defined in Eq. (12).

$$n = n_\alpha + n_\beta + n_\sigma \text{ where } n_\sigma = 0 \quad (12)$$

Generalizations for multi-component systems are possible (e.g., $n_{i\sigma} = 0$, where the subscript i one specifies of the components).

In most applications (in particular, those employing the theory for the determination of the work of critical cluster formation), an alternative definition is preferred. The so-called *surface of tension*, $R = R_s$, is chosen as the dividing surface. Its location is defined theoretically in Gibbs' theory via the expression for the pressure equilibrium:

$$p_\alpha - p_\beta = \frac{2\sigma}{R} + \left[\frac{d\sigma}{dR} \right] \text{ where } \left[\frac{d\sigma}{dR} \right] = 0 \text{ for } R = R_s \quad (13)$$

The surface of tension refers to $[d\sigma/dR] = 0$. The derivative $[d\sigma/dR]$ is denoted commonly as a notional derivative that describes the variation of the surface tension with a change of the position of the dividing surface while the physical state of the system is unchanged.

Note that the surface of tension according to its definition cannot be determined directly via computer simulations or in experimental investigations. Its location can be calculated via Gibbs' theory if other characteristics of the critical clusters are known.

In Gibbs' theory, parameters such as the size of clusters and surface tension depend significantly (in particular, for high supersaturations) on the choice of the dividing surface. Only for planar interfaces do the respective quantities coincide widely. In subsequent analyses, the surface of tension will be used as the dividing surface.

The second problem in the application of Gibbs' theory to nucleation processes consists in the choice of the reference states for the description of the bulk properties of the cluster phase. Note that Gibbs restricts his analysis to equilibrium states, and in particular, to the analysis of phase coexistence of different types at thermodynamic equilibrium. Critical clusters obey the necessary thermodynamic equilibrium conditions and can be treated by Gibbs' method. However, even equations such as $\Delta G = -n_\alpha + \sigma A$ (cf. Eq. (5)) represent non-trivial generalizations of Gibbs' method. They may be derived under certain (somewhat drastic) simplifying assumptions [4] which restrict considerably the field of possible applications. We will return to this point later.

In line with Gibbs' original method, the properties of the reference states for the description of the bulk contributions of the cluster phase to the thermodynamic functions are determined via a subset of Gibbs' equilibrium conditions, which can be written as shown in Eq. (14).

$$\begin{aligned} \mu_{j\alpha}(T_\alpha, p_\alpha, \{x_{j\alpha}\}) &= \mu_{j\beta}(T_\beta, p_\beta, \{x_{j\beta}\}), \text{ where } j = 1, 2, \dots, k, \text{ and} \\ T_\alpha &= T_\beta \\ &\Downarrow \\ (T_\beta, p_\beta, \{x_{j\beta}\}) &\implies (T_\alpha, p_\alpha, \{x_{j\alpha}\}) \end{aligned} \quad (14)$$

Equation (14) determines uniquely the state parameters of the cluster phase, if the state parameters of the ambient phase and the dependencies of the chemical potentials of both phases on the state parameters ($\{\mu_{j\alpha}(T_\alpha, p_\alpha, \{x_{i\alpha}\})\}$ and $\{\mu_{j\beta}(T_\beta, p_\beta, \{x_{i\beta}\})\}$) are known. Note that the determination of these reference states is performed in Gibbs' theory independent of the choice of the dividing surface.

Moreover, the choice of the reference states for the bulk contributions of the cluster phase is performed without reference to the actual state of the cluster (which is not known in most cases). The reference states for the cluster phase as determined via Gibbs' original method resemble widely the macroscopic properties of the newly evolving phases (with modifications due to the Young-Laplace equation Eq. (13); i.e., the difference in the mechanical equilibrium conditions for phase coexistence at planar and curved interfaces). This approach is applicable, in principle, for any arbitrary values of the thermodynamic parameters of the ambient phase, including the region near the spinodal curve. However, one must be very careful in correlating Gibbs' results for the cluster properties with the properties of the actual evolving critically sized clusters.

Provided the surface of tension is utilized as the dividing surface, Eq. (13) allows determination of the ratio σ_s/R_s . Then, σ_s must be known in order to determine R_s or vice versa.

Alternatively, one may calculate also the work of critical cluster formation. In the framework of Gibbs' method, one obtains without any further approximations Eq. (15) for the work of cluster formation for clusters of spherical sizes [4].

$$W_c = \Delta G_c = \frac{1}{3} \sigma A_c \quad (15a)$$

$$A_c = 4\pi R_c^2 \quad (15b)$$

$$R_c = \frac{2\sigma}{p_\alpha - p_\beta} \quad (15c)$$

In this case, the new phase can be considered as incompressible, the substitution $p_\alpha - p_\beta \Rightarrow \Delta\mu$ may be performed, and we obtain approximately and as a particular special case Eq. (6) [2, 4] that is employed widely in the analysis of phase formation in solids.

Similar to previous considerations, we can conclude: if σ is known, it is possible to calculate W_c , or if W_c is known as a function of the supersaturation, we can determine σ and R as a function of supersaturation as well. Without having at ones disposal such additional knowledge, one cannot calculate via Gibbs' method the parameters of the critical clusters. The same situation is found in thermodynamic computations.

In the framework of the classical theory of nucleation, this problem is solved by assuming that the surface tension of clusters of critical sizes is equal to the respective values for the equilibrium coexistence of both phase at planar interfaces: $\sigma = \sigma_\infty$ (capillarity approximation). This approach has advantages, such as: (i) it is relatively simple in its application (i.e., cluster properties may be determined from knowledge of the properties of the respective macrophases); (ii) it is correct for small supersaturations (large sizes of the critical clusters). The disadvantage is that the results are as a rule quantitatively incorrect, and for large supersaturations, even qualitatively wrong; they lead, for example, to finite values of the work of critical cluster formation near the spinodal curve (e.g., Figure 5).

A detailed analysis shows that the origin of these problems is connected basically to Gibbs' choice of the reference states for the critical clusters. For high supersaturations, the bulk properties of the critical clusters differ considerably

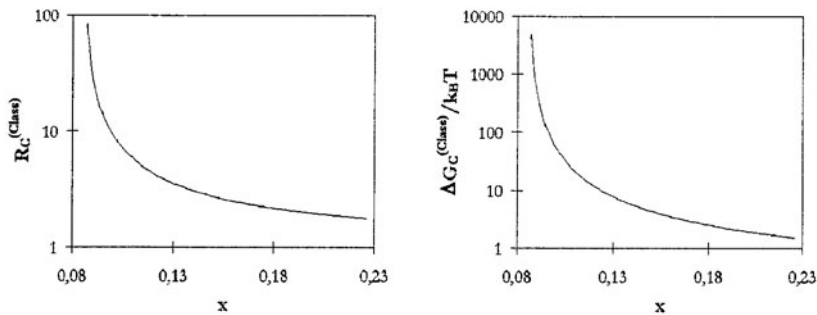


Figure 5. Dependence of the radius of the critical clusters $R_c^{(Class)}$ (referred to the surface of tension) and work of critical cluster formation, $\Delta G_c^{(Class)}/k_B T$ (both as determined via Gibbs' classical approach) on the initial supersaturation (expressed by the molar fraction of the solute, x , of a binary regular solution). In the determination of this quantity, the capillarity approximation is employed. The temperature is chosen equal to $T = 0.7T_c$.

(as far as they may be determined uniquely at all) from the properties of the newly evolving macrophases. Gibbs' method of determination of the reference states is, especially in this range of supersaturations, not adequate to describe the real situation.

This problem is, however, not fatal for Gibbs' theory. In the analysis with the determination of the steady-state nucleation rate, one may always correct the model by assuming a suitable form of a curvature dependence of the surface tension. Indeed, for any arbitrary dependence of the work of critical cluster formation, one can always find a dependence of σ on the state parameters of the ambient phase which fulfils Eq. (16).

$$W_c = \Delta G_c = \frac{16\pi}{3} \frac{\sigma^3}{(p_\alpha - p_\beta)^2} \quad (16)$$

Once the state parameters of the ambient phase, including p_β , are known, p_α can be determined uniquely via the equilibrium conditions using Eq. (14). Then, one can determine the critical cluster (referred to the surface of tension) and the dependence $\sigma = \sigma(R)$. In such an interpretation, the surface tension σ loses its original physical meaning but becomes a fitting parameter compensating the inappropriate choice of the reference state for the bulk contributions of the cluster phase.

In even more general terms and independent of the shape and the properties of the real critical cluster, one can always construct a spherical Gibbs' model cluster resulting in the same values of the work of critical cluster formation as found for the real one provided the work of critical cluster formation is known in dependence on supersaturation. However, the real critical cluster and the Gibbs model cluster will differ, of course, in their detailed characteristics and usually by a large amount.

3.3.2. *Density-functional approaches: van der Waals, Cahn & Hilliard, Skripov, Baidakov, Oxtoby, ...*

The qualitative and quantitative defects of the classical theory, employing the additional assumptions described, may be overcome by employing an approach developed for the first time by van der Waals at the end of the 19th century and about sixty years later by Cahn and Hilliard, applied to phase formation in regular solutions. According to this approach, the volume density of the Gibbs' free energy \tilde{g} of a binary solution has to be considered in the simplest case as a function not only of pressure, temperature and concentration of one of the components, c , but also of the spatial variation of the density or

concentration. These dependencies can be expressed in the simplest case via a dependence of \tilde{g} on the gradient ∇c :

$$\tilde{g}(p, T, c) \Rightarrow \tilde{g}(p, T, c, \nabla c) \quad (17)$$

By a Taylor expansion of \tilde{g} with respect to the gradient terms, one obtains Eq. (18) in a first approximation:

$$G = \int_V \tilde{g}(p, T, c, \nabla c) dV \cong \int_V [\tilde{g}(p, T, c) + \kappa(\nabla c)^2] dV + \dots \quad (18)$$

The problem consists now in the determination of those density or concentration profiles $c(\vec{r})$, which result in an extremum (saddle point) of the Gibbs free energy. The properties of the critical clusters (and similar to the classical Gibbs' approach, only of the critical clusters) can be determined via density functional calculations utilizing basic results of the Gibbs' theory as outlined above.

In order to perform the respective calculations, one has to have the following information on the system of interest:

- Bulk properties of the systems under consideration, $\tilde{g}(p, T, c)$. They can be obtained from experiments or theoretical model studies (e.g., regular solution model, van der Waals' or improved equations of state, etc.);
- Values of the interfacial or surface tension for planar interfaces (experiment or theoretical models) for the determination of the influence coefficient κ .

As the result of such calculations, Cahn and Hilliard came to the conclusion for regular solutions that the work of critical cluster formation vanishes at the spinodal and that the characteristic size of the critical clusters diverges there. In more detail, one finds:

- (i) The characteristic size of the critical clusters, expressed via the radius of the equimolecular dividing surface, R_e , and the value of the surface tension, σ_e , referred to this particular dividing surface, behave in the vicinity of the spinodal curve ($c \cong c^{(s)}$) as:

$$R_e \propto (c - c^{(s)})^{-1/6} \quad (19a)$$

$$\sigma_e \propto (c - c^{(s)})^{-1/6} \quad (19b)$$

- (ii) The work of critical cluster formation tends to zero in the vicinity of the spinodal curve:

$$W \propto (c - c^{(s)})^{3/2} \quad (20)$$

- (iii) The surface tension σ_s and the radius R_s of the surface of tension behave near the spinodal curve as:

$$\sigma_s \propto (c - c^{(s)})^{1/2} \quad (21a)$$

$$R_s \propto (c - c^{(s)})^{1/2} \quad (21b)$$

It follows as one consequence that notations like critical cluster size and surface tension have a definite meaning only as far as the dividing surface is specified.

There are advantages and disadvantages of the van der Waals and Cahn-Hilliard approach. The method allows the direct and, at least, qualitatively correct determination of the work of critical cluster formation based on the knowledge of *macroscopic properties* of the systems under consideration in the whole range of metastable states, including in the vicinity of the spinodal curve. Problems of this approach are, among others, the limits of validity of the square gradient approximation in Eq. (18), in the effect of higher order terms in the expansion, the method of determination of the coefficients κ_{ij} for multi-component systems, the applicability to crystal nucleation, etc.

The van der Waals and Cahn-Hilliard approach may be formulated in an alternative, microscopically-based form by introducing the interaction potentials between the particles of the system. Following, for example, the approach of Evans, Oxtoby and others, the Gibbs free energy may be expressed via a contribution corresponding to a system of hard spheres (hs) supplemented by a second term reflecting the contribution of attractive forces (i.e., their potentials V_{attr}) on the thermodynamics of the system:

$$G = \int d\vec{r} g_{hs}(c(\vec{r})) + \iint d\vec{r} d\vec{r}' V_{\text{attr}}(|\vec{r} - \vec{r}'|) c(\vec{r}) c(\vec{r}') \quad (22)$$

Again, the density profile has to be determined corresponding to the extremum or saddle point of the Gibbs free energy. The general qualitative result is (following Oxtoby): *... the surface free energy should depend on curvature and the nucleation barrier should vanish at the spinodal. ...*

This and alternative density functional theories allow a qualitative analysis of the properties of critical clusters to be performed. This is of importance, in particular, for high supersaturations. It turns out that the properties of the critical clusters deviate, in general, significantly from the properties of the newly evolving macroscopic phases.

From a quantitative point of view, the results depend significantly on the assumptions employed in the theoretical analysis (e.g., choice of the interaction potentials, the radius of action of the forces etc.). As a result, quantitatively correct calculations for real systems are outside the scope of current capabilities. For this reason, an alternative approach outlined below, combining the simplicity of the classical Gibbs' approach with the advantages of density functional calculations seems highly promising.

3.3.3. A new approach: basic ideas and consequences

Our recently developed approach to the determination of the work of cluster formation represents a modification or generalization of Gibbs' theory ([4, 7, 8] and the cited references). It has the following features:

- Its application is as simple and straight-forward as Gibbs' classical approach.
- The results are in agreement with the above mentioned approaches for the determination of the work of critical cluster formation for small supersaturations.
- For high supersaturations, where the classical Gibbs' approach (involving the capillarity approximation) fails, the results are, at least, qualitatively as correct as those obtained via density functional computations.
- The method is applicable not only for the determination of the work of critical cluster formation, but for the calculation of the change of the thermodynamic potentials in cluster formation for clusters of any size. Such quantities are required, for example, to model the evolution of cluster size distributions during the whole course of the nucleation-growth process [4, 7, 8].

The method is based on Gibbs' original approach but differs in the choice of the reference states for the specification of the bulk contributions of the clusters. The state of the cluster phase was determined originally by an additional postulate, denoted as the *Generalized Ostwald's Rule of Stages* [4]. According to this principle, the reference state of the cluster phase is selected as follows: *The intensive state parameters of the critical clusters will differ as a rule from the respective parameters of the newly evolving macroscopic phase. Those critical clusters will determine the process of nucleation, which correspond to a minimum of the work of critical cluster formation as compared with all other allowed states of the cluster.*

For segregation in binary regular solutions, we arrive again at Eqs. (23)–(25) for the determination of the critical cluster size and the work of critical cluster formation [2, 4].

$$\frac{\Delta G_c}{k_B T} = \Omega_1 \frac{g^3(x, x_\alpha)}{f^2(x, x_\alpha)} \quad (23a)$$

$$R_c = -\Omega_2 \frac{g(x, x_\alpha)}{f(x, x_\alpha)} \quad (23b)$$

$$g(x, x_\alpha) = (x - x_\alpha)^2 \quad (24a)$$

$$\Delta\mu(p, T, x, x_\alpha) = -k_B T f(x, x_\alpha) \quad (24b)$$

$$f(x, x_\alpha) = -(1 - x_\alpha) \left[\ln \left(\frac{1 - x_\alpha}{1 - x} \right) + 2 \left(\frac{T_c}{T} \right) (x_\alpha^2 - x^2) \right] - x_\alpha \left\{ \ln \left(\frac{x_\alpha}{x} \right) + 2 \left(\frac{T_c}{T} \right) [(1 - x_\alpha)^2 - (1 - x)^2] \right\} \quad (25)$$

Here, Ω_1 and Ω_2 are combinations of (constant) parameters of the system. For the computations leading to Figures 5 and 7 they are both set equal to one.

For the specification of the value of the interfacial tension, an equation derived by Becker (1938) from statistical model considerations is employed. For the case of planar coexistence of two phases with the compositions x_1 and x_2 at planar interfaces, Becker obtained Eq. (26).

$$\sigma_\infty = \tilde{\sigma} \left(\frac{T}{T_c} \right) g(x_1, x_2) \quad \text{where } g(x_1, x_2) = (x_1 - x_2)^2 \quad (26)$$

According to above given relations, both the surface tension and the thermodynamic driving force of the process of phase formation depend on the *composition of the ambient phase* x , as well as on the *composition of the newly evolving cluster phase*, x_α . According to the classical approach to nucleation, one has to assume:

- The critical cluster has bulk properties widely equivalent to the respective properties of the newly evolving macrophase (i.e., $x_\alpha \cong x_{\text{binodal}}^{(\text{right})}$) as a result of Gibbs' equilibrium conditions;
- The surface tension equals the respective value for the equilibrium coexistence of both phases at a planar interface (capillarity approximation).

The classical results of the computation dependence of the work of critical cluster formation and the radius of the cluster (referred to as the surface of tension) on x (in the range between the values of x from the right hand side binodal curve to the right hand side spinodal $x_{\text{binodal}}^{(\text{left})} \leq x \leq x_{\text{spinodal}}^{(\text{left})}$) are shown in Figure 5, employing the additional assumption that $\Omega_1 = \Omega_2 = 1$. The work of critical cluster formation and the radius of the critical cluster, referred to the surface of tension, decrease monotonously with increasing supersaturation; they remain, however, finite at the spinodal curve.

As mentioned, the work of critical cluster formation should tend to zero near the spinodal curve. Consequently, the result from the classical approach to nucleation is qualitatively incorrect (as are, for example, analyses by other approaches of condensation and boiling in a van der Waals fluid [4]).

For regular solutions, the state of the critical cluster is determined from its composition, x_α . The dependence of the value of x_α on supersaturation can be determined in the newly developed approach using the generalized Ostwald's

rule of stages by searching, for any given value of x , for the minimum of ΔG_c as a function of x_α . The result is shown in Figure 6.

Having at our disposal the dependence $x_\alpha = x_\alpha(x)$, we can calculate dependence of the work of critical cluster formation and the size of the critical cluster on supersaturation. (Figure 7). They are qualitatively and, even quantitatively equivalent to the results of density functional computations.

The method is not restricted in its applicability to systems with one state parameter. For segregation processes in multi-component systems, the work of critical cluster formation is, in general, a function of $(k - 1)$ independent molar

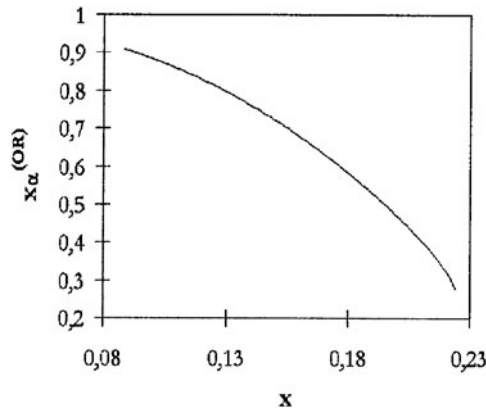


Figure 6. Dependence of composition of the critical cluster, x_α , on supersaturation in the system, x , for segregation processes in binary regular solutions. For the determination of the composition of the cluster, x_α , the generalized Ostwald's rule of stages is employed as formulated in the text.

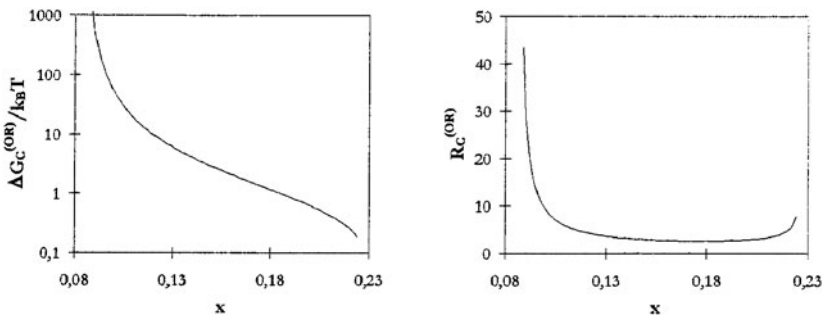


Figure 7. Dependence of the work of critical cluster formation and cluster size on supersaturation calculated by utilizing the generalized Ostwald's rule of stages for the specification of the state of the critical clusters.

fractions of the different components. The work of critical cluster formation can be written then in the form:

$$W_c \propto \frac{\sigma^3(p, T, x_{1\alpha}, x_{2\alpha}, \dots, x_{k-1,\alpha}; x_{1\beta}, x_{2\beta}, \dots, x_{k-1,\beta})}{[\Delta\mu(p, T, x_{1\alpha}, x_{2\alpha}, \dots, x_{k-1,\alpha}; x_{1\beta}, x_{2\beta}, \dots, x_{k-1,\beta})]^2} \quad (27)$$

The composition of the critical cluster is determined in this case via the set of equations:

$$\left. \frac{\partial W_c}{\partial x_{i\alpha}} \right|_{\{x_\beta\}} = 0, \quad i = 1, 2, \dots, k - 1 \quad (28)$$

In addition to the consideration of segregation in solutions, the method of determination of the work of critical cluster formation has been applied successfully to analyses of condensation and boiling [4, 7]. First attempts to apply the method to experimental results on crystallization show that the properties of the crystallites of critical and near-critical sizes will differ, as a rule, significantly from the macroscopic properties of the newly evolving phases. The application of the method to such type of processes will be ongoing.

3.3.4. Discussion

A detailed comparison of the basic assumptions underlying the classical Gibbs' approach and the new modification is given in [4, 7, 8]. Here we stress one very important point, again. Gibbs' theory is restricted to the analysis of equilibrium states, including two-phase and multi-phase equilibria. The respective equations are developed only for such states. For quasi-stationary variations of the state of the respective two-phase systems, Gibbs' adsorption equation, for example, leads to the conclusion that the surface tension depends on the state parameters of one of the coexisting phases only.

However, in general, in order to find the extremum of some function, one must formulate it for any reasonable states of the system, including those non-equilibrium states which may be treated by the respective theory. Only afterwards, having the functional dependencies, is it possible to search for the extrema or saddle points. This is the methodology followed in any of the density functional approaches discussed earlier.

First, the work of critical cluster formation is calculated for clusters of arbitrary sizes (under certain assumptions applying thermodynamic methods). Also, how the surface tension should behave as a function of the state parameters of both phases is specified. As a next step, the extremum conditions are applied. This thermodynamic approach is equivalent to the results obtained via the generalized Ostwald's rule of stages. For this reason, it is really a direct consequence of the modification of Gibbs' approach.

Summarizing the analysis, the newly developed method represents a generally applicable tool to the interpretation of experimental results on phase formation processes. It can supplement or even replace employed methods of determination of the work of critical cluster formation. Moreover, since it is not restricted to equilibrium states, it should allow study of the evolution of the state of a cluster from its initial formation up to the macroscopic phase.

3.4. Nucleation and Simultaneous Growth: The Kolmogorov-Avrami Equation

In addition to the determination of the number of aggregates of the newly evolving phase, the time evolution of the total mass or volume fraction of the newly evolving phase has been studied extensively as well. In order to describe the evolution of the total amount of the newly evolving phase, one has to combine the description of nucleation and subsequent growth of the already formed supercritical clusters.

We assume the nucleation process proceeds with some given rate $J(t')$ starting at some moment of time $t = 0$. The number of supercritical clusters formed in the time interval $t', t' + dt'$, is given then by Eq. (29).

$$dN(t') = J(t') dt' \quad (29)$$

The clusters, once formed, grow and give a contribution $dV(t, t')$ at time t .

$$dV(t, t') = v(t, t') dN(t') \quad (30)$$

to the total volume $V(t)$ of the newly evolving phase. $v(t, t')$ is the volume of a cluster at time t which was formed originally at time t' . It is assumed commonly that this quantity is determined mainly by the time of growth, $t - t'$.

G_R , the growth rate of the linear dimensions of the aggregates of the newly evolving phase, and ω_n , a geometrical shape factor, determine $v(t, t')$.

$$v(t, t') = \omega_n \left\{ \int_{t'}^t G_R(t'' - t') dt'' \right\}^n \quad (31)$$

The parameter n specifies the number of independent directions of cluster growth in space in Eq. (31).

Substituting the variable $x = t'' - t'$, we obtain Eq. (32).

$$v(t, t') = \omega_n \left\{ \int_0^{t-t'} G_R(x) dx \right\}^n \quad (32)$$

and Eq. (33) follows.

$$V(t) = \omega_n \int_0^t J(t') dt' \left\{ \int_0^{t-t'} G_R(t'') dt'' \right\}^n \quad (33)$$

For spherical clusters and three-dimensional phase formation and kinetic limited growth:

$$\frac{dR}{dt} = \gamma_1 \quad \text{where } \gamma_1 = \text{constant} \quad \text{and} \quad G_R(t) = \gamma_1 \quad (34)$$

When growth is diffusion limited:

$$\frac{dR}{dt} = \frac{\gamma_2}{2R} \quad \text{where } \gamma_2 = \text{constant} \quad \text{and} \quad G_R(t) = \frac{\sqrt{\gamma_2}}{2t^{1/2}} \quad (35)$$

Assuming, in addition, constancy of the nucleation rate, we arrive at Eq. (36) for kinetic limited growth and Eq. (37) for diffusion limited growth:

$$V(t) = \Gamma_1 J t^{n+1} \quad \text{where } \Gamma_1 = \frac{\omega_n \gamma_1^n}{(n+1)} \quad (36)$$

$$V(t) = \Gamma_2 J t^{(n+2)/2} \quad \text{where } \Gamma_2 = \left(\frac{2}{n+2} \right) \omega_n \gamma_2^{n/2} \quad (37)$$

From knowledge of the value of the exponent of the time variable t , one can derive conclusions concerning the mechanism of nucleation and growth; for more details, see [2].

The degree of overall crystallization or the degree of completion of the transformation, $\alpha(t)$, at time t is defined as the ratio in Eq. (38), where $V(t)$ is the volume crystallized at time t and V_0 is the initial volume of the melt.

$$\alpha_n(t) = \frac{V(t)}{V_0} \quad (38)$$

The main difficulty in solving the problem of overall crystallization kinetics in the finite volume of an undercooled melt is to account adequately for the possibility of contact of different crystallites and the resulting inhibition of growth when two or more growing crystallites meet. Another point is the decrease of the ratio of the volume in the course of the transformation where further nucleation may take place. Such a depletion of the volume open to nucleation has to be taken into account in the analysis of overall crystallization.

In the derivation of an equation for $\alpha(t)$, as proposed by Avrami, it is assumed that the change of the degree of crystallization with time depends on the ratio of still non-crystallized volume in the form of Eq. (39).

$$d\alpha(t) = (1 - \alpha(t)) dV(t) \quad (39)$$

This equation may be integrated to give Eq. (40).

$$\alpha(t) = 1 - \exp[-V(t)] \quad (40)$$

The dependence of α on t has the typical *s*-shaped course. As mentioned, conclusions about the type of nucleation and growth kinetics involved in the transformation can be obtained if the form of the dependence of α on t is known.

3.5. Depletion Effects and the Overall Course of First-Order Phase Transitions

A more detailed analysis of the course of nucleation-growth processes can be obtained by formulating and solving numerically a set of kinetic equations for the cluster size distribution function [2, 3]. This set of equations can be transformed into a Fokker-Planck equation, the so-called Frenkel-Zeldovich equation. The latter equation can be analyzed analytically to derive further important conclusions concerning the overall course of first-order phase transitions and basic characteristics of this process.

In fact, steady-state conditions are established in the system only after a certain time-interval has passed. This time-interval is denoted as the time-lag in nucleation. Thereafter, steady-state nucleation and simultaneous growth of the clusters is followed for some characteristic nucleation time. Due to nucleation and growth of the already formed supercritical clusters, the concentration of single particles is decreased and the nucleation rate is decreased significantly as well.

As the consequence, the stage of nucleation and growth is followed by a stage of independent growth of the supercritical clusters, their number being nearly constant. In the course of this process of independent growth, the supersaturation is decreased to values near zero. Once this state is reached, a further growth of the largest clusters is possible only if smaller clusters are dissolved. This late stage of the transformation is usually denoted as coarsening or Ostwald ripening.

A detailed analysis of the first stages of the nucleation-growth process, including an analytical derivation of their basic characteristics, is given in [3, 4]. An illustration is presented in the left-hand side of Figure 8. In the first stages of the process, monotonically decreasing distributions are continuously transformed in the further evolution into a bimodal distribution. Arrows indicate the actual value of the critical cluster size. On the right hand side, the behavior in the late stages of the process (in the course of Ostwald ripening) is shown. In this late state of the evolution, the critical cluster radius behaves for diffusion-limited growth as $R_c^3 \propto t'$, and a time-independent shape of the distribution function $\varphi(u)$ develops as predicted first by Lifshitz and Slezov.

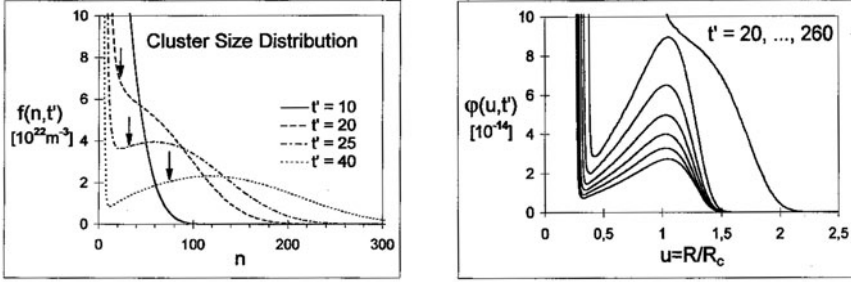


Figure 8. Left: Different stages in the evolution of the cluster size distribution, $f(n, t)$, if the condition of conservation of the total number of monomers is taken into account. Right: Cluster size distribution function $\varphi(u, t')$ in reduced variables $u = (R/R_c)$ for different moments of time (with $\varphi(u, t') = \frac{1}{N(t')} f(R, t') R_c$, where N is the total number of clusters of the new phase at time t').

4. Spinodal Decomposition

Spinodal decomposition is another important mechanism by which first-order phase transformations may proceed. In contrast to nucleation, it is characterized by a continuous diffusional amplification of initially small variations of density or concentration in the system (*up-hill diffusion*).

A theoretical description of this process was developed first by Hillert, Cahn and Hilliard based on the van der Waals theory of interfacial effects [3]. The theory was extended by Filipovich and Cook among others, to include the influence of stochastic fluctuations into the theory and by Langer, Bar-on and Miller to account for non-linear terms in spinodal decomposition.

Following van der Waals, Cahn and Hilliard, the free enthalpy G of a binary inhomogeneous solution can be written in a first approximation in the form of Eq. (18). If the deviations from the initial homogeneous concentration c_0 are relatively small, a Taylor expansion of Eq. (18) results in Eq. (41), an expression for the change of the free enthalpy caused by the evolution of the concentration field $c(\vec{r}, t)$.

$$\Delta G = \int \left[\frac{1}{2} \left(\frac{\partial^2 \tilde{g}}{\partial c^2} \right)_{c_0, T} (c - c_0)^2 + \kappa (\nabla c)^2 \right] dV \quad (41)$$

In agreement with the thermodynamic stability conditions, a spontaneous growth of the density fluctuations takes place only for $\tilde{g}''(c_0, T) < 0$, since only in this case may the amplification of the density profile be accompanied by a decrease of the free enthalpy of the system. This mechanism of decomposition works for initial states inside the spinodal curves.

In the framework of the Cahn-Hilliard-Cook theory, the kinetics of the decomposition process is described by a generalized diffusion equation

connecting the variations in the thermodynamic potential G with the kinetics of the decomposition process. It follows from Eqs. (42) and (43) and has the form of Eq. (44).

$$\frac{\partial c}{\partial t} + \text{div} \vec{j} = 0 \quad \text{where } \vec{j} = \vec{j}_D + \vec{j}_A \quad (42)$$

$$\vec{j}_D = -M \nabla \frac{\delta G}{\delta c} \quad (43a)$$

$$\vec{j}_A = -\nabla A(\vec{r}, t) \quad (43b)$$

$$\frac{\partial c(\vec{r}, t)}{\partial t} = M \tilde{g}''(c_0, T) \nabla^2 c(\vec{r}, t) - 2M\kappa \nabla^4 c(\vec{r}, t) + \nabla^2 A(\vec{r}, t) \quad (44)$$

Here \vec{j}_D is the vector describing the deterministic density of fluxes of particles, and \vec{j}_A represents the flow connected with the fluctuating scalar field $A(\vec{r}, t)$ superimposed on the deterministic flow. M is a mobility coefficient.

To solve this equation, the $c(\vec{r}, t)$ and $A(\vec{r}, t)$ fields are expressed through Fourier expansions in Eqs. (45)–(48).

$$c(\vec{r}, t) = c_0 + \sum_{-\infty}^{\infty} S(\vec{k}_n, t) \exp(i\vec{k}_n \vec{r}) d\vec{r} \quad (45)$$

$$S(\vec{k}_n, t) = \frac{1}{V} \int [c(\vec{r}, t) - c_0] \exp(-i\vec{k}_n \vec{r}) d\vec{r} \quad (46)$$

$$A(\vec{r}, t) = \sum_{-\infty}^{\infty} B(\vec{k}_n, t) \exp(i\vec{k}_n \vec{r}) d\vec{r} \quad (47)$$

$$B(\vec{k}_n, t) = \frac{1}{V} \int A(\vec{r}, t) \exp(-i\vec{k}_n \vec{r}) d\vec{r} \quad (48)$$

V is the volume of the system.

Equations (42)–(48) result in the following differential equation for the spectral function $S(\vec{k}_n, t)$:

$$\frac{\partial S(\vec{k}, t)}{\partial t} = R(\vec{k}, t) S(\vec{k}, t) - \kappa^2 B(\vec{k}, t) \quad (49)$$

The amplification factor $R(\vec{k}, t)$ is determined by:

$$R(\vec{k}, t) = -M\vec{k}^2 \left[\tilde{g}''(c_0, T) + 2\kappa \vec{k}^2 \right] \quad (50)$$

The subscript n in \vec{k}_n is omitted here and subsequently for simplicity of the notations.

Based on Eq. (50) and in analogy to the critical cluster size in nucleation (cf. Eq. (6)), a critical wave number k_c may be introduced. It is defined by the condition that the deterministic amplification rate $R(k_c, t)$ is equal to zero. This condition yields:

$$\vec{k}_c^2 = -\frac{1}{2\kappa} \tilde{g}''(c_0, T) \quad (51)$$

Concentration waves in the Fourier spectrum with wave numbers $k > k_c$ decay while the modes with $k < k_c$ grow. The value of the wave number corresponding to the highest amplification rate is given by Eq. (52).

$$k_{\max} = \frac{1}{\sqrt{2}} k_c \quad (52)$$

Moreover, in experimental studies of phase transformation processes, a quantity proportional to the average of the square of the spectral function $\langle S^2 \rangle = \langle SS^* \rangle$, rather than the spectral function itself, is of relevance. Assuming that, on average, the concentration fluctuations are equal to zero and uncorrelated (Eq. (53)), one obtains Eqs. (54) and (55).

$$\langle A(t) \rangle = 0 \quad (53a)$$

$$\langle A(\xi)A(\chi) \rangle = Q(\vec{k})\delta(\xi - \chi) \quad (53b)$$

$$\frac{\partial \langle S^2(\vec{k}, t) \rangle}{\partial t} = 2R(\vec{k}, t)\langle S^2(\vec{k}, t) \rangle + \vec{k}^4 Q(\vec{k}) \quad (54)$$

$$Q(\vec{k}) = \frac{2Mk_B T}{V} \frac{1}{k^2} \quad (55)$$

Finally, from Eq. (51) and by introducing dimensionless wave numbers \tilde{k} and a dimensionless time scale \tilde{t} (Eq. (56)), Eq. (57) is obtained.

$$\tilde{k} = ak \quad (56a)$$

$$\tilde{t} = \frac{4\kappa M}{a^4} t \quad (56b)$$

$$\frac{\partial \langle S^2(\tilde{k}, \tilde{t}) \rangle}{\partial \tilde{t}} = \tilde{k}^2 \left\{ \left[\tilde{k}_c^2 - \tilde{k}^2 \right] \langle S^2(\tilde{k}, \tilde{t}) \rangle + \frac{k_B T a^2}{2\kappa V} \right\} \quad (57)$$

The parameter a is a measure of the intermolecular distance in the solution.

Numerical solutions of Eq. (57) predict that after a relatively short initial period, determined by the stochastic generation of the initial distribution (left part in Figure 9), the typical features of the Cahn-Hilliard scenario of spinodal decomposition (i.e., constant values of the critical wave number and the wave number of highest amplification rates) are found (central part of Figure 9).

However, in real systems and also in Monte-Carlo simulations of spinodal decomposition, the situation is different. Both the critical wave number as well as the wave number of highest amplification rate are shifted in the course of time to lower values of k . Such effects may be accounted for by the introduction of non-linear terms in the respective kinetic equation. In our simulations, such linearities are accounted for already by the linear Cahn-Hilliard-Cook equation, since the system is supposed to be in an adiabatic enclosure. Temperature changes during the course of the decomposition process lead, then, to depletion effects and to results similar to those in nucleation-growth processes.

Indeed, taking into account such non-linearities, the whole course of the transition may be divided into several different stages (see Figure 10). In the first stages of generation of the density fluctuations by fluctuations and the subsequent

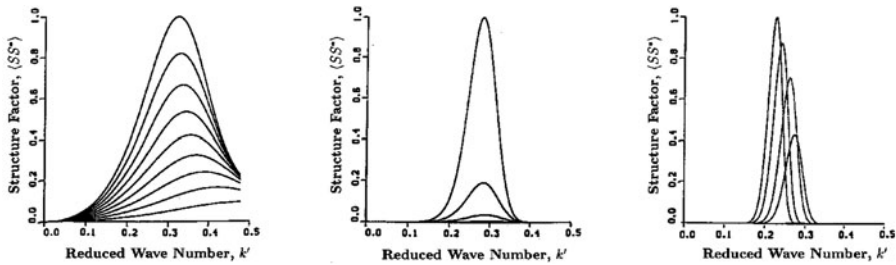


Figure 9. Time evolution of the spectral function: *Left*: Initial stage of stochastic generation of the density fluctuations ($t' = 30, 60, 90, 120, 150, 180, 210, 240, 270$); *Middle*: Cahn-Hilliard deterministic amplification of the density fluctuations ($t' = 300, 600, 900, 1200, 1500$); *Right*: Late stages, where non-linear effects become of importance ($t' = 3000, 4000, 5000, 7000, 9000$).

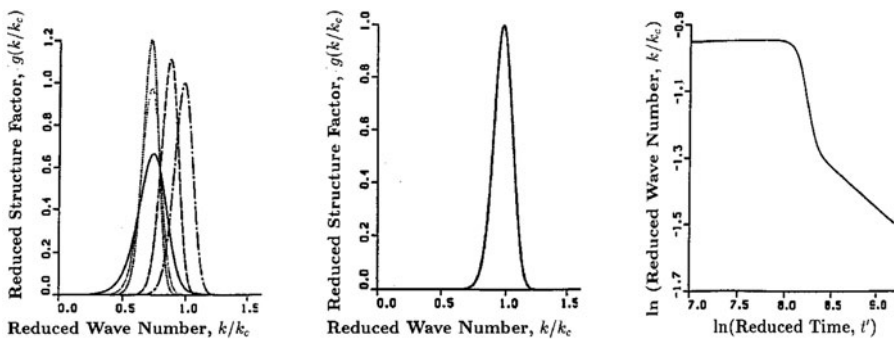


Figure 10. *Left*: Time evolution of the scaled spectral function, $g(k/k_c)$: $t' = 1000$ (full curve), $t' = 2000$ (dotted), $t' = 3000$ (dashed), $t' = 4000$ (dashed-dotted), $t' = 5000$ (double dashed). *Middle*: Similar curves for $t' = 5000$ and $t' = 9000$. As evident, the shape of the function does not change with time in this stage. *Right*: Critical wave number as a function of time. The late stage is characterised by the power law $k_c \propto t'^{1/4}$.

Cahn-Hilliard stage of evolution, the critical wave number remains nearly constant. Non-linearities due to temperature changes lead then to a stage of evolution where the critical wave number increases rapidly followed by a stage of slow evolution characterized by self-similarity and scaling laws. Indeed, similar to the stage of Ostwald ripening in nucleation-growth processes, we may express then the spectral function in the form of Eq. (58).

$$\langle S^2(k', t') \rangle = f(t') g\left(\frac{k}{k_c}\right) \quad \text{with} \quad \int_0^{\infty} g(u) du = 1 \quad (58)$$

As evident from Figure 10 and verified analytically [3], $k_c \propto t'^{1/4}$ holds and $g(u)$ becomes independent of time in the late stage.

5. Secondary Aggregation, Coarsening and Ageing

In the kinetic description of nucleation processes, it is commonly assumed that clusters of the new phase grow and decay by emission or incorporation of atoms or molecules, only. This assumption represents, in a variety of cases, a quite reasonable approximation. It allows frequently a description not only of nucleation, but also of the stages of independent growth and coarsening.

However, in the more general case, one has to take into account other mechanisms of cluster growth as well. One of them consists of the aggregation of clusters of different sizes or the decay of clusters into smaller sized clusters. A kinetic equation for the description of coagulation processes was formulated for the first time by Smoluchowski. In the simplest case, for one-component closed systems, it reads:

$$\frac{dN(n, t)}{dt} = \sum_{k=1}^{n_{\max}} [w_{k,n}(t)N(k, t) - w_{n,k}(t)N(n, t)] \quad (59)$$

$N(n, t)$ is the number of clusters consisting of n particles, $w_{k,n}(t)$ is the frequency of transition of a cluster of size k into a cluster of size n .

The kinetics of the aggregation process is thus fully determined by the values of the kinetic coefficients. Many articles are devoted to analyses of the kinetics of coagulation in diverse systems. In the case where emission and aggregation of only single particles is allowed, the equations above give a kinetic description of nucleation and growth processes.

Eq. (59) includes an assumption that for any value of n , the clusters transform to an equilibrium shape in time scales that are small compared with the characteristic aggregation times. However, once one is dealing with the description of processes of gelation, this assumption is invalid.

The variety of structures which may evolve once this assumption is removed has been indicated in the last decades by a large number of computer simulations

(e.g., [9]). One of the widely employed models is the Witten-Sander model. It assumes reactions exclusively between a cluster and single monomers. However, in contrast to the assumptions in the above theory, the further reorganization of the resulting cluster is widely or partially hindered by the strength of the bonds. An example of the variety of different types of structures that may be obtained is shown in Figure 11.

A second model approach incorporates cluster-cluster collision and the resulting aggregation processes. Here, again, depending on the conditions of aggregation, quite different structures may evolve. One such example is shown in Figure 11.

Once formed, such clusters may form complete networks leading to gelation. However, even at such a stage, they may rearrange their local configurations further. These processes result in changes of the properties of the gels denoted as ageing. In addition, the gel structure may serve as a more or less rigid matrix affecting the processes of aggregation of a possible second component of the system. In this case, aggregation, growth and coarsening in porous media

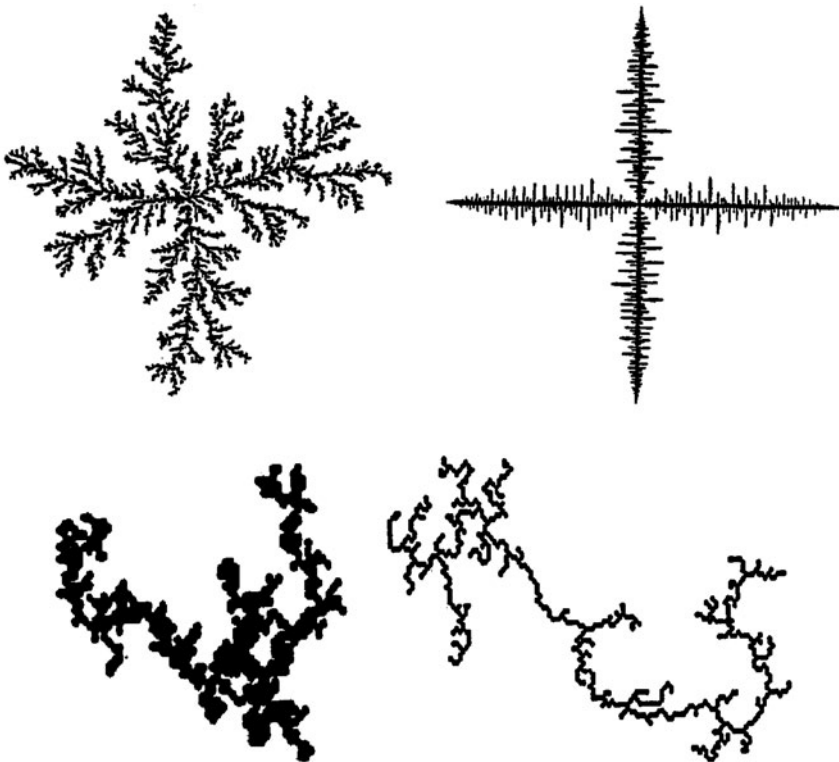


Figure 11. Top: Witten-Sander cluster (on lattice) with (left) and without (right) noise reduction. Bottom: Results of cluster-cluster aggregation with different numbers of blocked bonds [10].

with some given pore size distribution must be considered. A theory of such processes has been developed in the last decade. An overview of the results is given in [3].

6. Overview

An overview of different approaches which can be employed in the analysis of cluster formation and growth processes has been presented. Hopefully, it will find use for the analysis of the very complicated and different problem encountered in the analysis of processes of molecular gels [11].

References

- [1] Schmelzer, J.W.P. "Phases, phase transitions, and nucleation", In *Encyclopedia of Surface and Colloid Science*, A. Hubbard, Ed., New York: Marcel Dekker, **2002**, pp. 4017–4029.
- [2] Gutzow, I.; Schmelzer, J. *The Vitreous State: Thermodynamics, Structure, Rheology, and Crystallization*. Berlin: Springer, **1995**.
- [3] Schmelzer, J.W.P.; Röpke, G.; Mahnke, R. *Aggregation Phenomena in Complex Systems*. Weinheim: Wiley-VCH, **1999**.
- [4] Schmelzer, J.W.P.; Röpke, G.; Priezhev, V.B. *Nucleation Theory and Applications*, Dubna, Russia, Joint Institute for Nuclear Research Publishing House, **1999, 2002**.
- [5] Baidakov, V.G. "Thermodynamic Properties of Superheated Liquids". In *Thermal Physics Reviews*, A.E. Scheindlin and V.E. Fortov, Eds., New York: Harwood Publishers, **1994**.
- [6] Schmelzer, J.W.P.; Potapov, O.V.; Fokin, V.M.; Müller, R.; Reinsch, S. *J. Non-Crystalline Solids*, **2004**, 333, 150.
- [7] Schmelzer, J.W.P.; Baidakov, V.G.; Boltachev, G.Sh. *J. Chem. Phys.*, **2003**, 119, 6166.
- [8] Schmelzer, J.W.P.; Gokhman, A.R.; Fokin, V.M. *J. Colloid Interface Science*, **2004**, 272, 109.
- [9] Feder, J. *Fractals*, New York and London: Plenum Press, **1988**.
- [10] Tietze, H. *Fractal Aggregation Processes: An Analysis of Gelation in Silica Solutions*, PhD thesis, University of Rostock, Germany, **1992**.
- [11] Terech, P.; Weiss, R.G. *Chem. Rev.*, **1997**, 97, 3133.

Chapter 5

SOFT GLASSY RHEOLOGY

Peter Sollich

*Department of Mathematics, King's College London Strand,
London WC2R 2LS, U.K.*

1. Introduction	162
2. Rheology	163
2.1. Constitutive Properties	163
2.2. Step Strain	164
2.3. Linearity	164
2.4. Behaviour of the Linear Response Function	165
2.5. Creep Compliance	165
2.6. Viscoelastic Spectra	165
2.7. Steady State Response: The Flow Curve	167
2.8. Ageing	168
3. The SGR Model	170
3.1. Constitutive Equation	173
3.2. Tensorial SGR Model	174
3.3. Rheological Properties Without Ageing	175
4. Rheological Ageing: Imposed Strain	176
4.1. Linear Response	177
4.2. Nonlinear Response	182
5. Rheological Ageing: Imposed Stress	184
5.1. Linear Response	184
5.2. Nonlinear Response	186
6. Conclusions and Perspectives for the Future	188

1. Introduction

This chapter describes a theoretical model developed to rationalize the rheology of a large class of soft materials. The members of this class, which include foams, dense emulsions, pastes slurries, among others, display intriguing features in their low frequency shear rheology. In oscillatory shear, for example, their viscoelastic storage and loss moduli, $G'(\omega)$ and $G''(\omega)$, are often weak power laws of shear frequency [1–7], while their nonlinear stress response σ to shear strain of constant rate $\dot{\gamma}$ is often fit to the form $\sigma = A + B\dot{\gamma}^n$ (known as the Herschel-Bulkley equation, or when $A = 0$, the power-law fluid) [8–10]. The fact that such a broad family of soft materials exhibits similar rheological anomalies is suggestive of a common cause, and it has been argued that these anomalies are symptomatic of the generic presence in such materials of slow, glassy dynamics [11, 12]. Indeed, all the above materials share features of structural disorder and metastability: large energy barriers impede reorganization into states of lower free energy because this would require rearrangement of local structural units, such as the droplets in a dense emulsion (see Chapter 7). The term “soft glassy materials” (SGMs) has therefore been proposed to describe such materials [11, 12]. A prime manifestation of glassy dynamics is rheological *ageing*, where the elastic modulus increases as time goes by, while the loss modulus decreases. Effects of this type can be rather complicated, with the rate of ageing depending on stress [13]. Rheological ageing effects have seen intense experimental interest recently [13–18], stimulated (we may hope) at least in part by the theoretical developments that will be reviewed below.

We will focus in this chapter on the “soft glassy rheology” (SGR) model which has been developed over the last few years to describe the rheology of soft glasses [11, 12, 19, 20]. As will be clear from the above introduction, this model was designed for what can be termed *repulsive glasses*, in which metastability arises because the particles (or droplets, etc.) that make up the material are too compressed to easily move past each other and rearrange. Gels, on the other hand, can be thought of as *attractive glasses*, where particles form tenuous networks but are held together by bonds that are sufficiently strong to again hinder rearrangements [21]. This aspect is not captured by the SGR model. The model also does not incorporate structural changes during ageing. This is appropriate for repulsive glasses: in a compressed assembly of colloidal particles, only very weak changes in the overall structure are expected while the material ages by local rearrangements which bring particles into energetically more favourable positions. For gels, on the other hand, structural changes during ageing are surely important, with characteristic lengthscales of network structures growing in time. A final deficiency of the SGM model is that it assumes local elastic properties to be essentially homogeneous, whereas in gels strong inhomogeneities must be expected.

In spite of these shortcomings, the present chapter will describe the SGM model “as is”, without modifications that could be contemplated to make it more appropriate for gels. It is hoped that the approach presented, which attempts to capture complex rheological phenomena using minimal models, will nevertheless prove useful. One key advantage of the SGR model is its simplicity, which allows for a full study of a broad range of non-trivial rheological effects including ageing. Confronting the resulting predictions with experiment for verification or falsification should help to stimulate the development of more sophisticated models, both for the “traditional” soft glasses and for gels.

We begin in Section 2 by briefly introducing rheology and ageing. Then in Section 3 we review the SGR model and its recent generalization to a tensorial description of stress and strain, and review its rheological predictions under non-ageing conditions. Section 4 begins with a discussion of the origin of the SGR model’s glass transition and the nature of the glass phase, and then describes the predicted rheological ageing phenomena for conditions of controlled strain. The corresponding results for imposed stress are given in Section 5. We close in Section 6 by summarizing and discussing our results; a brief comparison with related rheological models that have recently been developed is also provided.

2. Rheology

Here we review the basic definitions of rheology. Unlike most in the literature, our formulation [19] does not assume time translational invariance (TTI). The formalism allows in principle an arbitrary dependence of the material properties on time; we defer to Section 2.8 a discussion of what form this dependence might take in materials which exhibit ageing effects, rather than other, more trivial time dependencies.

2.1. Constitutive Properties

In general, deformation can comprise volume changes, extensional strain, and shear strain; here we consider incompressible materials and assume that only shear strains arise. A system’s shear stress $\sigma(t)$ then depends functionally on its strain rate history $\dot{\gamma}(t' < t)$, where $\dot{\gamma}$ is the strain rate. Conversely, $\gamma(t)$ can be expressed as a functional of the preceding stress history. A specification of either type is referred to as a *constitutive equation*. In general, of course, the constitutive equation is a relationship between stress and strain *tensors*; see, for example, Doi and Edwards [22] for an introduction. We mainly ignore the tensorial aspects here, because the original SGR model is too simple to include them. A recent tensorial generalization [20] will be described in Section 3.

2.2. Step Strain

A standard rheological test consists of suddenly straining a previously undeformed material by an amount γ_0 . Suppose this to be done at time t_w : then $\gamma(t) = \gamma_0 \Theta(t - t_w)$, where Θ is the usual step function. For the moment, t_w is an arbitrary time label, but later we will take it as the time that the strain is applied, relative to the preparation of the sample in some prescribed state, at time zero. The subsequent stress can be written as Eq. (1), thereby defining the step strain response, $G(t - t_w, t_w; \gamma_0)$.

$$\sigma(t) = \gamma_0 G(t - t_w, t_w; \gamma_0) \quad (1)$$

2.3. Linearity

In the small deformation limit ($\gamma_0 \rightarrow 0$), a regime may exist for which σ is linearly related to γ_0 :

$$\lim_{\gamma_0 \rightarrow 0} G(t - t_w, t_w; \gamma_0) = G(t - t_w, t_w) \quad (2)$$

In this linear regime, by decomposing the applied strain $\gamma(t)$ into a series of infinitesimal steps, one finds that:

$$\sigma(t) = \int_{-\infty}^t G(t - t', t') \dot{\gamma}(t') dt' \quad (3)$$

Eq. (3) represents the most general (non-tensorial) linearized constitutive equation. Note that there is no unique extension of this to the nonlinear case: the response to an arbitrary flow cannot in general be written solely in terms of $G(t - t_w, t_w; \gamma_0)$, although this is assumed for certain constitutive models [23].

If the material exhibits TTI, then $G(t - t_w, t_w; \gamma_0)$ can be written as $G(t - t_w; \gamma_0)$ – it depends only on the elapsed time since the step strain was imposed. Only by assuming *both* linearity and TTI do we obtain:

$$\sigma(t) = \int_{-\infty}^t G(t - t') \dot{\gamma}(t') dt' \quad (4)$$

where $G(t - t_w)$ is the linear step-strain response as usually defined. In the steady state (constant $\dot{\gamma}$) one recovers:

$$\sigma = \dot{\gamma} \int_0^{\infty} G(t'') dt'' \quad (5)$$

The integral, whenever it exists, defines the material's zero-shear viscosity η . For many soft materials, however, $G(t)$ decays to zero so slowly that the integral diverges. In this case, there can be no regime of linear response in steady shear flow, although there may be a linear regime in, say, oscillatory shear.

2.4. Behaviour of the Linear Response Function

The principle of causality demands that the response function $G(t - t_w, t_w)$ is zero for times $t < t_w$. At $t = t_w$, G typically increases very rapidly (in effect discontinuously) to a value G_0 , the instantaneous elastic modulus. Thereafter, $G(t - t_w, t_w)$ is (almost always) a decaying function of its first argument. Specializing to the TTI case, we recall that for a purely Newtonian liquid of viscosity η , the function $G(t)$ approaches a delta function $\eta\delta(t)$, whereas an ideally Hookean elastic solid has $G(t) = G_0$.

Most real materials display intermediate behaviour and are thus *viscoelastic*; for the soft materials of interest here, the timescale of the viscoelasticity is readily observable in rheological experiments. The simplest (TTI) example is the Maxwell fluid (see Chapter 19), which is solid-like at short times and liquid at longer ones, with a simple exponential response function $G(t) = G_0 \exp(-t/\tau)$ connecting the two (so that $\eta = G_0\tau$). This behavior is seen in a few experimental systems [24], but $G(t)$ is usually not an exponential.

2.5. Creep Compliance

Arguing along parallel lines to those developed above, we can write the strain response to a step stress $\sigma(t) = \sigma_0 \Theta(t - t_w)$ as:

$$\gamma(t) = \sigma_0 J(t - t_w, t_w; \sigma_0) \quad (6)$$

The linear creep compliance $J(t - t_w, t_w)$ is then found by letting $\sigma_0 \rightarrow 0$ (assuming this limit exists).

For a system exhibiting TTI, the linear compliance reduces to a function of elapsed time, $J(t - t_w)$. For a viscous liquid, an elastic solid, and a Maxwell material we have $J(t) = t/\eta$, $J(t) = 1/G_0$, and $J(t) = 1/G_0 + t/\eta$, respectively. The zero-shear viscosity η can then be defined as the limiting ratio of stress to strain rate long after application of an infinitesimal step stress; it therefore obeys $\eta^{-1} = \lim_{t \rightarrow \infty} dJ(t)/dt$, which may be shown to be equivalent to Eq. (5) whenever the required limit exists; see also Section 2.7 below.

2.6. Viscoelastic Spectra

A common experiment is to apply a steady oscillatory strain and measure the resulting stress, or vice versa. For example, suppose that a sample is prepared in a known state at time zero. The choice (Eq. (7)) describes an oscillatory flow started at time t_s after sample preparation, and continued up to (at least) the time t at which the stress is measured.

$$\gamma(t) = \Theta(t - t_s) \text{Re} \left[\gamma_0 e^{i(\phi + \omega t)} \right] \quad (7)$$

For small enough γ_0 , we can use the linear constitutive Eq. (3) to obtain:

$$\begin{aligned}\sigma(t) &= \text{Re} \left[\gamma_0 i \omega \int_{t_s}^t e^{i(\phi + \omega t')} G(t - t', t') dt' + \gamma_0 e^{i(\phi + \omega t_s)} G(t - t_s, t_s) \right] \\ &\equiv \text{Re} \left[\gamma_0 e^{i(\phi + \omega t)} G^*(\omega, t, t_s) \right]\end{aligned}\quad (8)$$

where the second term in Eq. (8) accounts for any step strain arising at the switch-on time t_s . This procedure defines a *time-varying* viscoelastic spectrum as:

$$G^*(\omega, t, t_s) = i\omega \int_{t_s}^t e^{-i\omega(t-t')} G(t - t', t') dt' + e^{-i\omega(t-t_s)} G(t - t_s, t_s) \quad (9)$$

A similar compliance spectrum, $J^*(\omega, t, t_s)$ can be defined by exchanging stress and strain in this protocol.

Note that, in principle, to identify by experiment the real and imaginary parts of G^* for given ω, t, t_s one would require the experiment to be repeated for two different phases ϕ (e.g., pure sine and cosine deformations). A more common procedure for TTI systems is to maintain the oscillatory strain over many cycles and record the “steady state” amplitude and phase response of the stress. However, in systems without TTI this will only give a unique result when material properties vary slowly enough; whenever it does, it will coincide with Eq. (9).

Since it depends on two time arguments as well as frequency, $G^*(\omega, t, t_s)$ is a cumbersome object. However, simplifications arise in the limit $\omega(t - t_s) \gg 1$. In the TTI case, where $G^*(\omega, t, t_s)$ depends only on the time interval $t - t_s$, the further condition $\omega(t - t_s) \gg 1$ can be used to eliminate simple transients. The stress then settles to a simple harmonic function of time and we can write $\sigma(t) = \text{Re}[G^*(\omega)\gamma(t)]$ where:

$$G^*(\omega) = i\omega \int_0^\infty e^{-i\omega t} G(t) dt \quad (10)$$

Traditionally one writes $G^*(\omega) = G'(\omega) + iG''(\omega)$ where G' and G'' , the storage and loss moduli, give the in-phase (elastic) and out-of-phase (dissipative) response to an applied strain.

Clearly one can reach an identical steady state by applying a small amplitude oscillatory stress and measuring the resulting strain. This defines, for the TTI case, a complex compliance $J^*(\omega)$ via $\gamma(t) = \text{Re}[J^*(\omega)\sigma(t)]$, which is just the reciprocal of $G^*(\omega)$. But by an argument similar to that given above for Eq. (10) one also has $J^*(\omega) = i\omega \int_0^\infty e^{-i\omega t} J(t) dt$. Hence, within the linear response regime of a system with TTI, knowledge of any one of $G(t)$, $J(t)$, $G^*(\omega)$, $J^*(\omega)$ is enough to determine the other three.

A similar set of simplifications are certainly not guaranteed in the absence of TTI. However, the transient dependence on t_s may become negligible when $\omega(t - t_s) \gg 1$. In this case we have Eq. (11).

$$G^*(\omega, t, t_s) \rightarrow G^*(\omega, t) \quad (11)$$

It gives a viscoelastic spectrum that depends only on the measurement time t . If, in addition, the time evolution of the underlying material properties is negligible on the timescale of one oscillation, then $G^*(\omega, t)$ may obey the relation:

$$G^*(\omega, t) = i\omega \int_0^\infty e^{-i\omega t'} G(t', t) dt' \quad (12)$$

Similar statements apply to the compliance spectrum $J^*(\omega, t, t_s)$. Finally, $G^*(\omega, t)$ and $J^*(\omega, t)$ may obey the usual reciprocal relation $G^*(\omega, t) = 1/J^*(\omega, t)$. Indeed, we shall find that all the above simplifying relationships are true for the SGR model (subject to an additional requirement that $\omega t_s \gg 1$; see below). As discussed by Fielding *et al.* [19], they may also hold more generally for systems with “weak long term memory”, but there is no general proof of this that we are aware of. The above simplifications cannot therefore be assumed for all non-TTI systems, and should be verified for each system studied. This *prima facie* breakdown of conventional linear viscoelastic relationships in ageing systems was emphasized by Struik [25] though he argued that they are recovered in sufficiently ‘short-time’ measurements. It does not (as Struik seems to suggest) extend necessarily to breakdown of linear superposition itself, which survives in the form of Eq. (3). In fact, breakdown of TTI is a quite separate issue from nonlinearity; neither implies the other.

2.7. Steady State Response: The Flow Curve

Consider now the ultimate state of a material, with TTI, long after an infinitesimal step stress of amplitude σ_0 has been applied. The ultimate deformation may involve a limiting strain $\gamma = \sigma_0 J(t \rightarrow \infty)$, in which case the steady state elastic modulus is $G_\infty = \sigma_0/\gamma$. Alternatively, it may involve a limiting strain rate, in which case the zero-shear viscosity is $\eta = \sigma_0/\dot{\gamma}$. However, neither outcome need occur. If, for example, one has “power law creep”, i.e., $J(t) \sim t^y$ with $0 < y < 1$, the material has both zero modulus (infinite compliance) and infinite viscosity in steady state.

What if the stress amplitude is larger than infinitesimal? The ultimate steady state can again be that of a solid, a liquid, or something in between. When a liquid-like response is recovered, it is conventional to measure the “flow curve”, or steady state relationship between stress and strain rate: $\sigma_{ss} = \sigma(\dot{\gamma})$. In many materials, the limit in Eq. (13), called the yield stress, is non-zero.

$$\sigma(\dot{\gamma} \rightarrow 0) = \sigma_y \quad (13)$$

The experimental existence of a true yield stress, in this sense, is debatable [10], though behaviour closely approaching it is often reported.

The presence of non-zero yield stress does not necessarily imply a finite Hookean modulus G_∞ : for $\sigma < \sigma_y$, the material could creep forever, but at an ever decreasing rate. Alternatively, it could reach a steady strain γ that is not linear in σ even as $\sigma \rightarrow 0$. Nor does the *absence* of a finite yield stress imply a finite viscosity; a counterexample is the power law fluid, for which $\sigma \sim \dot{\gamma}^p$. This has $\sigma_y = 0$ but, for $p < 1$, infinite viscosity $\eta = \lim_{\dot{\gamma} \rightarrow 0} \sigma(\dot{\gamma})/\dot{\gamma}$.

What is the flow curve for materials without TTI? For these, no meaningful definition of “steady state response” exists in general. However, in the SGR model considered below, TTI is restored for non-zero $\dot{\gamma}$ [11, 12], and this may be generic for certain types of ageing [11, 12, 26, 27]. If so, the flow curve, including the value of the yield stress σ_y (but *not* the behavior for $\sigma < \sigma_y$) remains well-defined.

2.8. Ageing

Ageing has been intensively studied in the context of both spin glasses [26, 28–30] and structural glasses [31]. Some of the earliest experimental investigations of ageing in fact involved rheological studies of glassy polymers [25]. Nevertheless, in much of the rheological literature ageing effects have traditionally been regarded as unwanted obstacles to observing the “real” behavior of the system, and not in themselves worthy of study. But this may be illusory: ageing, when present, can form an integral part of a sample’s rheological response. For example, the literature contains many reports of viscoelastic spectra in which the loss modulus $G''(\omega)$, while remaining less than the (almost constant) storage modulus $G'(\omega)$ in a measured frequency window, appears to be increasing as frequency is lowered (see Figure 1, bold lines). The usual explanation [32] is that some unspecified relaxation process is occurring at a lower frequency still, giving a loss peak (dashed), whose true nature could be elucidated if only the frequency window was extended. This may often be the case, but an alternative explanation, based on explicit calculations for the SGR model, is shown by the thin solid lines in Figure 1, representing subsequent observations in a wider frequency window. No oscillatory measurement can probe a frequency far below the reciprocal of the sample’s age; yet in ageing materials, it is typically the age itself which sets the relaxation time of whatever slow relaxations are present. Accordingly, the putative loss “peak” can never be observed and is, in fact, a complete figment of the imagination. Instead, a rising curve in $G''(\omega)$ at low frequencies will *always* be seen, but with an amplitude that decreases as the system gets older (typically ensuring that $G''(\omega)$ never exceeds $G'(\omega)$).

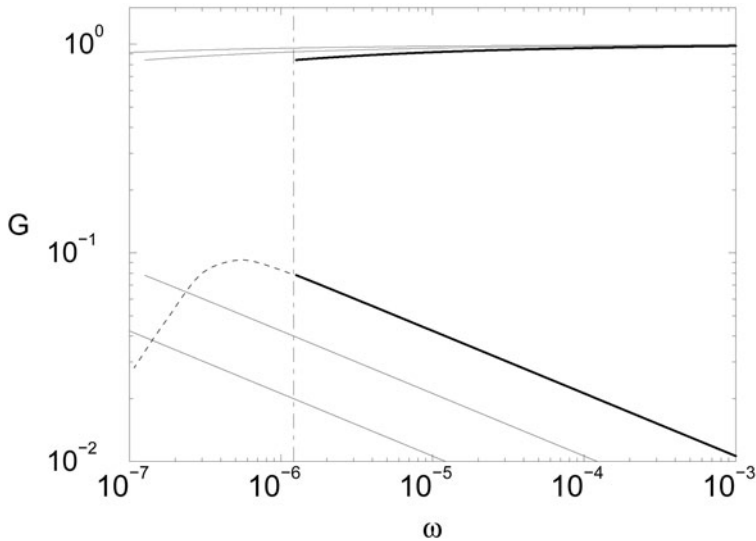


Figure 1. Sketch of ageing scenario for dynamic moduli G' (top) and G'' (bottom). Thick and thin solid lines: initial spectrum and two subsequent ones. Dashed: putative loss peak. Dot-dashed: limit to frequency window set initially by sample age. (In fact, the solid lines are calculated from the SGR model at noise temperature $x = 0.7$; see Section 4.) (Reprinted with permission from [19]. Copyright (2000) The Society of Rheology.)

In the previous section, we set up a general framework for describing the rheological properties of systems without TTI. Time translation invariance can be broken, in a trivial sense, by the transients that any system exhibits during equilibration. We now consider how such transients can be distinguished from ageing proper, considering by way of example the linear step strain response function $G(t - t_w, t_w)$. Ageing can then be defined [19] as the property that *a significant part of the stress relaxation takes place on timescales that grow with the age t_w of the system*. If ageing is present, then in order to see the full stress relaxation we need to allow the time t at which we observe the stress to be much larger than the time t_w at which the step strain has been applied. On the other hand, if there is no ageing, then the full stress relaxation is “visible” on finite timescales: as long as $\Delta t = t - t_w$ is large enough, we observe the full stress relaxation whatever the age t_w of the system at the time when the strain was applied. Mathematically, this means that the limits $\Delta t \rightarrow \infty$ and $t_w \rightarrow \infty$ can be interchanged. We will refer to deviations from TTI in non-ageing systems (for which all significant relaxation processes can essentially be observed on finite timescales) as *transients*; see also the discussion, in the context of the SGR model, in Section 4 below.

In the simplest case, there is only one growing timescale, t_w , proportional to the age of the system itself. The (ageing part of the) stress relaxation then

becomes a function of the scaled time difference $(t - t_w)/t_w$. We will encounter such simple ageing behaviour in the glass phase of the SGR model. More complicated ageing scenarios are possible, however: There may be several timescales that grow differently with the age of the system. This can be represented as:

$$G(t - t_w, t_w) = \sum_i \mathcal{G}_i [h_i(t)/h_i(t_w)] = \sum_i \tilde{\mathcal{G}}_i [\xi_i(t) - \xi_i(t_w)] \quad (14)$$

The functions $h_i(t)$ define the different diverging timescales and $\xi_i = \ln h_i$, $\tilde{\mathcal{G}}_i(\ln h) = \mathcal{G}_i(h)$. If there is only a single term in the sum, with $h(t) = t$, then the simplest ageing scenario is recovered. But Eq. (14) also includes TTI and intermediate ageing scenarios: for $\xi(t) = t/\tau_0$, corresponding to $h(t) = \exp(t/\tau_0)$ (where τ_0 is a microscopic time), one has TTI. More generally, $\xi(t) = (1 - \mu)^{-1}(t/\tau_0)^{1-\mu}$ interpolates between TTI for $\mu = 0$ and simple ageing for $\mu \rightarrow 1$. In the regime of short time differences ($t - t_w \ll t_w$), one then finds that the response function depends on $\xi(t) - \xi(t_w) = (t - t_w)/(t_w^\mu \tau_0^{1-\mu})$, thus recovering Struik's general 'time waiting-time superposition principle' [25].

3. The SGR Model

The phenomenological SGR model captures many of the observed rheological properties of soft metastable materials, such as foams, emulsions, slurries and pastes [1–7]. It is based upon Bouchaud's trap model of glassy dynamics, with the addition of strain degrees of freedom, and the replacement of the thermodynamic temperature by an effective (noise) temperature. It incorporates only those characteristics deemed common to all soft glassy materials (SGMs), namely structural disorder and metastability. We now review its essential features.

We conceptually divide a macroscopic sample of SGM into many mesoscopic elements. By mesoscopic we mean large enough such that the continuum variables of strain and stress still apply for deformations on the elemental scale, and small enough that any macroscopic sample contains enough elements to allow the computation of meaningful "averages over elements". We then assign to each element a local strain l , and corresponding stress kl , which describe deformation away from some local position of unstressed equilibrium relative to neighbouring elements. The macroscopic stress of the sample as a whole is defined to be $\langle kl \rangle$, where $\langle \rangle$ denotes averaging over elements.

For a newly prepared, undeformed sample, we make the simplest assumption that $l = 0$ for each element. Physically, of course, $\langle l \rangle = 0$ would be sufficient and is indeed more plausible. The subsequent application of a macroscopic strain at rate $\dot{\gamma}$ causes each element to strain relative to its local equilibrium state and acquire a non-zero l . For a given element, this continues up to some

maximal strain l_y , at which point that element yields, and rearranges into a new configuration of local equilibrium with local strain $l = 0$. This ignores possible “frustration” effects: an element may not be able to relax to a fully unstrained equilibrium position due to interactions with neighbouring elements. Such effects can be incorporated into the model, but are not expected to affect the results in a qualitative way [12]. Under continued macroscopic straining, the yielded element now strains relative to its new equilibrium, until it yields again; its local strain (and stress) therefore exhibits a saw-tooth dependence upon time.

The simplest assumption to make for the behaviour between yields is that $\dot{\gamma} = \dot{l}$: the material deformation is locally affine [22]. Yield events apart, therefore, the SGR model behaves as an elastic solid of spring constant k . Yields confer a degree of liquidity by providing a mechanism of stress relaxation.

Although we have introduced yielding as a purely strain-induced phenomenon, we in fact model it as an “activated” process [11, 12]. We assume that an element of yield energy $E = \frac{1}{2}kl_y^2$, strained by an amount l , has a certain probability for yielding in a unit time interval. We write this rate as τ^{-1} , where the characteristic yield time (Eq. (15)) is taken to be the product of an attempt time and an activation factor which is thermal in form.

$$\tau = \tau_0 \exp \left[\left(E - \frac{1}{2}kl^2 \right) / x \right] \quad (15)$$

This captures the strain-induced processes described above since any element strained beyond its yield point will yield exponentially quickly; but it also allows even totally unstrained elements to yield by a process of activation over the energy barrier E . These activation events mimic, within our simplified model, non-linear couplings to other elements. A more complete model would treat these couplings explicitly. However, in the SGR model, which does not, x is regarded as an effective “noise” temperature to model the process. Alternatively, we can think of x as the typical *energy* available for an activated processes. We use units in which the Boltzmann constant $k_B = 1$ throughout, so there is no need to distinguish between these two interpretations of x as either a temperature or an energy. Because the energy barriers are for typical foams, emulsions, etc. large compared to the thermal energy $k_B T$, so are the energy changes caused by these nonlinear couplings, and so to mimic these, one expects to need x of order the mean barrier height $\langle E \rangle$. Whether it is fully consistent to have a noise temperature $x \gg k_B T$ is a debatable feature of the model [11, 12]. However, similar “macroscopic” effective temperatures, which remain nonzero even for $k_B T \rightarrow 0$, have been found in other theories of out-of-equilibrium systems with slow dynamics [27, 33].

The disorder inherent to SGMs is captured by assuming that each element of a macroscopic sample has a different yield energy: a freshly yielded element is assigned a new yield energy selected at random from a “prior”

distribution $\rho(E)$. This suggests the following alternative view of the dynamics: each material element of a SGM can be likened to a particle moving in a landscape of quadratic potential wells or “traps” of depth E . The depths of different traps are uncorrelated with each other and distributed according to $\rho(E)$. The bottom of each trap corresponds to the unstrained state $l = 0$; in straining an element by an amount l , we then effectively drag its representative particle a distance $\frac{1}{2}kl^2$ up the sides of the trap, and reduce the effective yield barrier height ($E \rightarrow E - \frac{1}{2}kl^2$). Once the particle has got sufficiently close to the top of its trap ($E - \frac{1}{2}kl^2 \approx x$), it can hop by activated dynamics to the bottom of another one. This process corresponds to the yielding of the associated material element.

A specific choice of $\rho(E)$ is now made: $\rho(E) = (1/x_g) \exp(-E/x_g)$, where $x_g = \langle E \rangle$ is the mean height of a barrier chosen from the prior distribution $\rho(E)$. As shown by Bouchaud [34], the exponential distribution, combined with the assumed thermal form for the activated hopping, is sufficient to give a glass transition in the model. The transition is at $x = x_g$ and divides the glass phase ($x \leq x_g$), in which “weak ergodicity breaking” [34] occurs, from a more normal phase ($x > x_g$). In the glass phase, the Boltzmann distribution (which is the only possible steady state for activated hopping dynamics, in the absence of strain), $P_{\text{eq}}(E) \propto \rho(E) \exp(E/x)$ is not normalizable: thus there is no steady state, and the system must age with time. The converse applies for $x > x_g$: there is then a unique equilibrium state, which is approached at long times. Apart from our use of an effective temperature x , the only modification to Bouchaud’s original model of glasses lies in our introduction of dynamics within traps coupled to strain.

It may appear suspicious that, to obtain a glass transition at all, an exponential form of $\rho(E)$ is required. In reality the glass transition is certainly a collective phenomenon: the remarkable achievement of Bouchaud’s model is to represent this transition within what is, essentially, a single-particle description. Thus, the chosen “activated” form for the particle hopping rates, and the exponential form of the trap depth distribution, should not be seen as two independent (and doubtful) physical assumptions, but viewed jointly as a tactic that allows glassy dynamics to be modelled in the simplest possible way [11, 12].

From now on, without loss of generality, we choose units so that both $x_g = k = 1$. This means that the strain variable l is defined such that an element, drawn at random from the prior distribution, will yield at strains of order one. Since the actual value of the strain variable can be rescaled within the model (the difference being absorbed in a shift of k), this is purely a matter of convention. Our choice should nevertheless be borne in mind when interpreting the results: where strains “of order unity” arise, these are in fact of order some yield strain l_y , which may in reality be a few percent or less. In addition we choose by convention $\tau_0 = 1$; the timescale in the SGR model is scaled by the mesoscopic

“attempt time” for the activated dynamics. The low frequency limit, which is the main regime of interest, is then defined by $\omega\tau_0 = \omega \ll 1$. Note that, with our choice of units, $\langle E \rangle = 1$ so that we expect the interesting physics to involve $x \simeq 1$.

3.1. Constitutive Equation

The SGR model is exactly solved by two coupled constitutive equations [12], the first of which expresses strain as an integral over stress history, while the second embodies the conservation of probability. We assume that the sample is prepared (in a known initial state of zero stress and strain) at time zero and that a time dependent macroscopic strain $\gamma(t)$ is applied thereafter, so $\gamma(t) = 0$ for $t \leq 0$. The constitutive equations are then:

$$\sigma(t) = \gamma(t)G_0(Z(t, 0)) + \int_0^t [\gamma(t) - \gamma(t')] Y(t') G_\rho(Z(t, t')) dt' \quad (16)$$

$$1 = G_0(Z(t, 0)) + \int_0^t Y(t') G_\rho(Z(t, t')) dt' \quad (17)$$

In these equations,

$$Z(t, t') = \int_{t'}^t \exp([\gamma(t'') - \gamma(t')]^2 / 2x) dt'' \quad (18)$$

while $Y(t')$ is the average yield rate at time t' . The functions $G_\rho(Z)$ and $G_0(Z)$ obey:

$$G_\rho(Z) = \int_0^\infty \rho(E) \exp(-Ze^{-E/x}) dE \quad (19)$$

$$G_0(Z) = \int_0^\infty P_0(E) \exp(-Ze^{-E/x}) dE \quad (20)$$

$P_0(E)$ is the probability distribution for the yield energies (or trap depths) in the initial state of preparation of the sample at time $t = 0$.

These equations can be understood by viewing yielding as a “birth and death” process: each time an element yields it dies and is reborn with zero stress, and with a yield energy selected randomly from the prior distribution $\rho(E)$. The (average) yield rate rate at time t' is $Y(t')$; the birth rate at time t' of elements of yield energy E is therefore $Y(t')\rho(E)$. The proportion of these which survive without yielding until time t is found as $\exp[-Z(t, t')/\tau(E)]$ where $\tau(E) = \exp(E/x)$ is the (mean) lifetime that an unstrained element of yield energy E would have. The Eq. (18) for $Z(t, t')$ reflects the fact that an element that last yielded at time t' and has a yield energy E will have a yield rate of $\tau(E)^{-1} \exp([\gamma(t'') - \gamma(t')]^2 / 2x)$ at time t'' . Here the exponential factor

accounts for the lowering of the yield barrier by strain applied since the element last yielded. Eq. (16) is then obtained by multiplying the contribution from each element by the strain (and hence stress) $\gamma(t) - \gamma(t')$ acquired since it was last “born”, and integrating over t' . The additional first term arises from elements that have never yielded since time 0. Eq. (17), which is an integral equation for $Y(t)$, is obtained similarly from the conservation of the total number of elements.

Under conditions where the local strain is everywhere negligible, one has $Z(t, t') \rightarrow t - t'$. More generally, $Z(t, t')$ can be thought of as an effective time interval measured on an “internal clock” within an element, which allows for the effect of local strain on its yield rate, by speeding up the clock. This speeding up effect, which describes strain-induced yielding, is the only source of non-linearity within the (scalar) SGR model; additional non-linearities arise in the tensorial version discussed next.

3.2. Tensorial SGR Model

Although we focus in the rest of this chapter on the scalar SGR model as described above, it is worth outlining briefly how the model can be extended to account fully for the tensorial nature of stress and strain [20]. It turns out that the modifications required are in fact rather minimal. Instead of the shear $\gamma(t)$, one now needs a tensorial quantity to describe the deformation history of the material. This is furnished by $\mathbf{E}_{tt'}$, the deformation tensor between times t' and t : a small vector $\delta \mathbf{r}$ embedded in the material is transformed to $\mathbf{E}_{tt'} \cdot \delta \mathbf{r}$ during this time interval. $\mathbf{E}_{tt'}$ thus replaces $\gamma(t) - \gamma(t')$. We can now assume as before that the deformation of a local mesoscopic element follows the macroscopic deformation between yield events, and that elements are “reborn” in an unstrained state after a yield event. The constitutive Eq. (16) is then replaced by Eq. (21) while Eq. (17) remains as before except for the modified definition of $Z(t, t')$, as shown in Eq. (22).

$$\boldsymbol{\sigma}(t) = \mathbf{Q}(\mathbf{E}_{t,0})G_0(Z(t, 0)) + \int_0^t \mathbf{Q}(\mathbf{E}_{tt'})Y(t')G_\rho(Z(t, t'))dt' \quad (21)$$

$$Z(t, t') = \int_{t'}^t \exp[R(\mathbf{E}_{t''t'})/x]dt'' \quad (22)$$

Here, $\boldsymbol{\sigma}$ is the overall stress tensor, and \mathbf{Q} and R are tensor and scalar functions of \mathbf{E} that can in principle be freely chosen. $\mathbf{Q}(\mathbf{E})$ gives the stress contributed by an element that has been deformed by \mathbf{E} , generalizing our earlier simple linear relation between local strain l and local stress kl . $R(\mathbf{E})$ is the corresponding increase in internal energy of the element which lowers the yield barrier and

generalizes the earlier $kl^2/2$. All other quantities have the same meaning as for the scalar model.

Suitable choices for \mathbf{Q} and R are described in detail by Cates and Sollich [20] with particular attention to the case of foams and emulsions. This paper also discusses the predictions of the tensorial SGR model for a range of rheological quantities and scenarios that cannot be addressed within the scalar model, including normal stress differences and extensional flows.

3.3. Rheological Properties Without Ageing

We now return to the scalar SGR model and review briefly its predictions in the non-ageing regime where TTI applies. Solution of the constitutive Eqs. (16) and (17) is then relatively straightforward [11, 12]. Only the linear spectra and the flow curve are discussed below; predictions for more complicated experiments such as large-amplitude oscillatory shear are detailed by Sollich [12].

A regime of **linear rheological response** arises whenever the effect of strain on the effective time interval $Z(t, t')$ is small. This requires that the local strains in each element remain small; in oscillatory shear, where $\gamma(t) = \gamma_0 e^{i\omega t}$, this is satisfied at low enough strain amplitudes γ_0 for any finite frequency ω . The same is not true in steady shear flow; see below. The elements' lifetimes are then, to order γ_0 , strain-independent, and in the constitutive equations $Z(t, t')$ can then be replaced by $t - t'$.

As described in Section 2.6 above, the conventional definition of the linear viscoelastic spectra $G'(\omega)$, $G''(\omega)$ Eq. (10), requires not only linearity but also TTI. Thus, they are well-defined only for an equilibrium state; in the SGR model, the latter exists only for $x > 1$. But even at $x > 1$ these spectra show interesting power law dependencies at low frequency; these are summarized as follows (prefactors [11, 12] are omitted):

$$\begin{aligned} G'' &\propto \omega & \text{for } 2 < x, & \quad \propto \omega^{x-1} & \text{for } 1 < x < 2 \\ G' &\propto \omega^2 & \text{for } 3 < x, & \quad \propto \omega^{x-1} & \text{for } 1 < x < 3 \end{aligned} \quad (23)$$

Here and throughout, “low frequency” in the SGR model means $\omega \ll 1$, that is, frequencies small compared to the mesoscopic attempt rate for activated hopping $\tau_0^{-1} = 1$ (in our units).

The **flow curve** was defined in Section 2.7 as the nonlinear stress response $\sigma(\dot{\gamma})$ to a steady strain rate $\dot{\gamma}$. For the SGR model, it shows the following scalings for $\dot{\gamma} \ll 1$:

$$\begin{aligned} \sigma &\propto \dot{\gamma} & \text{for } x > 2 \\ \sigma &\propto \dot{\gamma}^{x-1} & \text{for } 1 < x < 2 \\ \sigma - \sigma_y &\propto \dot{\gamma}^{1-x} & \text{for } x < 1 \end{aligned} \quad (24)$$

These results exhibit two interesting features which are explored more fully in Section 5.2. Firstly, for $x < 1$ there is a yield stress $\sigma_y(x)$. A linear response regime exists at $\sigma \ll \sigma_y$; ageing can occur for all $\sigma < \sigma_y$. For $\sigma > \sigma_y$ the system achieves a steady state, and ageing no longer occurs. This is because any finite flow rate, however small, causes strain-induced yielding of elements even in the deepest traps; the time required to yield, with a steady flow present, is only power law, rather than exponential in E . Thus the ageing process is curtailed or “interrupted” by flow [11, 12, 19]; the flow curve is well-defined even in the glass phase. The second interesting feature is that, for $1 < x < 2$ (where ageing is absent) there is no linear response regime at all in steady shear: however small the applied stress, the behaviour is dominated by strain-induced yielding. There is an anomalous (power law) relation between stress and strain rate, and an infinite zero-shear viscosity (cf., Section 2.7 above). This also shows up in Eq. (23), where $\eta = \lim_{\omega \rightarrow 0} G''(\omega)/\omega$ is likewise infinite. More recently, it has been argued [35] that alternative methods of averaging the contributions to the viscosity of the local elements can give a finite zero-shear viscosity for $1 < x < 2$. This then diverges strongly as $x = 1$ is approached.

It is worth mentioning that the flow curves produced by the SGR model are all shear-thinning, with $\sigma/\dot{\gamma}$ and $d\sigma/d\dot{\gamma}$ both decreasing as $\dot{\gamma}$ is increased. The model can be modified, however, to account for shear-thickening effects. This also leads to interesting rheological instabilities and even chaotic behaviour [36, 37].

4. Rheological Ageing: Imposed Strain

Before giving the results for ageing under imposed strain, it is useful to discuss some general features of ageing in the SGR model. These will provide a basis for an intuitive understanding of the predicted behavior.

As noted above, to solve the constitutive Eqs. (16) and (17) the initial distribution $P_0(E)$ of yield energies at time zero must be specified. For simplicity, we choose the case where $P_0(E) = \rho(E)$; this is equivalent to suddenly “quenching” the noise temperature x , at time zero, from a very large value ($x \gg 1$) to a value within the range of interest. The effects of other initial conditions are discussed in detail in [19].

Following a quench, the system will age, and this will be reflected within the SGR model in the evolution of the distribution of lifetimes (or equivalently particle hopping rates). We ignore the presence of a strain, so that the discussion applies when there is no flow, and in the linear response regime, where strain-induced hops can be ignored. Under such conditions, the hopping rate $Y(t)$ is a strain-independent function of time, and is readily found from Eq. (17) by Laplace transform [19]: for $x > 1$, $Y(t) \rightarrow \text{const.}$ for $t \rightarrow \infty$, while for $x < 1$, $Y(t) \sim t^{x-1}$. From this, the distribution of yield energies

$P(E, t)$ can be deduced. By “birth-death” arguments similar to those above, it is given by:

$$P(E, t) = P_0(E) \exp[-t/\tau(E)] + \int_0^t Y(t') \rho(E) \exp[-(t - t')/\tau(E)] dt' \quad (25)$$

$\tau(E) = \exp(E/x)$ as before. Equivalently, one can consider the lifetime distribution $P(\tau, t)$. As pointed out above, in the absence of strain, the only candidate for a steady state distribution of yield energies $P_{\text{eq}}(E)$ is the Boltzmann distribution: $P_{\text{eq}}(E) \propto \rho(E) \exp(E/x)$, which translates to $P_{\text{eq}}(\tau) = P_{\text{eq}}(E) dE/d\tau \propto \tau^{-x}$. In either language, the distribution is not normalizable for $x < 1$, leading to broken TTI in the model [34]: the probability distribution probability distribution of trap lifetimes $P(\tau, t_w)$ evolves as a function of the waiting time t_w elapsed since sample preparation. The initial lifetime distribution is obtained from $P(E, 0) = \rho(E)$ as $P(\tau, 0) \propto \rho(E) dE/d\tau \propto \tau^{-(1+x)}$. Thereafter, by changing variable from E to τ in Eq. (24), we find the following approximate expressions for $P(\tau, t_w)$:

$$\begin{aligned} P(\tau, t_w) &\simeq xY(t_w)\tau\rho(\tau) & \text{for } \tau \ll t_w & \text{ and } t_w \gg 1 \\ P(\tau, t_w) &\simeq xY(t_w)t_w\rho(\tau) & \text{for } \tau \gg t_w & \text{ and } t_w \gg 1 \end{aligned} \quad (26)$$

For a quench “temperature” above the glass point ($x > 1$), $P(\tau, t_w)$ exhibits a transient decay; as $t_w \rightarrow \infty$, $P(\tau, t) \rightarrow P_{\text{eq}}(\tau) = (1 - x)\tau^{-x}$, as expected. The nature of the approach to the long time limit is illustrated schematically in Figure 2(a); the final distribution has most of its weight at $\tau = O(1)$. For $x < 1$, in contrast, $P(\tau, t_w)$ evolves as in Figure 2(b). Since $Y(t_w) \sim t_w^{x-1} \rightarrow 0$ at long times, the limit of $P(\tau, t_w)$ is zero for any finite τ as $t_w \rightarrow \infty$. Thus, the proportion of elements having yield time of order unity tends to zero as $t_w \rightarrow \infty$; the bulk of the distribution’s weight is at $\tau \simeq t_w$. This is consistent with the idea that, in a system undergoing ageing, the characteristic relaxation time is typically of the order of the age of the system itself.

We are now ready to presented the predictions of the SGR model in the ageing regime. Because the constitutive Eqs. (16) and (17) are more readily solved to find the stress response to an imposed strain, rather than vice-versa, we discuss first strain-controlled experiments and defer the stress-controlled case to Section 5.

4.1. Linear Response

As described in Section 3.3 above, when local strains are negligible, the SGR model displays a linear response regime, with the effective time interval $Z(t, t')$ becoming the actual time interval $t - t'$, and the hopping rate $Y(t')$ a

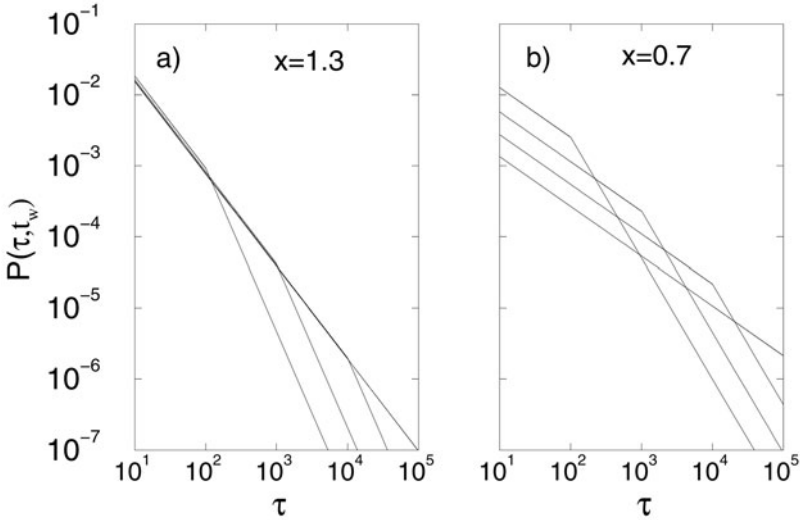


Figure 2. Schematic evolution of the relaxation time distribution (a) above the glass transition; (b) below it. The first shows a transient decay onto a steady state, the second shows ageing behaviour. The curves lie in order of increasing t_w at the bottom of each figure. (Reprinted with permission from [19]. Copyright (2000) The Society of Rheology.)

strain-independent function of time. The stress response to any strain history then follows directly from Eq. (16).

For a **step strain**, the amplitude γ_0 gives the maximum local strain experienced by any element, making the condition for linearity $\gamma_0 \ll 1$. The linearized step strain response, defined in Eq. (2), can be found in the SGR model by rewriting the constitutive Eq. (16) as:

$$G(t - t_w, t_w) = 1 - \int_{t_w}^t Y(t') G_\rho(t - t') dt' \quad (27)$$

Limiting analytic forms for $G(t - t_w, t_w)$ can be obtained when experimental timescales are large on the scale of the mesoscopic attempt time $\tau_0 = 1$, so that $t - t_w \gg 1$ and $t_w \gg 1$. We then identify two distinct regimes: a short time interval regime $t - t_w \ll t_w$ and long time interval regime $t - t_w \gg t_w$ (where the measure of “short” and “long” is not now τ_0 but t_w itself). The limiting forms in each case depend on the value of x . For $x > 1$, one has $G \sim (t - t_w)^{1-x}$ for short time intervals and $G \sim t_w(t - t_w)^{-x}$ for long ones; here and in the following we omit all numerical prefactors. In the glass phase ($x < 1$), on the other hand, one has $G \sim 1 - [(t - t_w)/t_w]^{1-x}$ and $G \sim [(t - t_w)/t_w]^{-x}$, respectively. These results can be motivated physically by recognizing that $G(t - t_w, t_w)$ just measures the fraction of elements that have not yielded between t_w and t . To a good approximation, this is the fraction of elements that

have a lifetime $\tau > t - t_w$ at time t_w , $\int_{t-t_w}^{\infty} P(\tau, t_w) d\tau$. Inserting the approximate forms Eq. (26) for P one then indeed recovers the predicted scalings of G .

Numerical results for $G(t - t_w, t_w)$ are shown in Figure 3. For $x > 1$, one has no ageing and only transients, as displayed in the left panel: the curves coincide at short time intervals $t - t_w \ll t_w$. At large t_w , this regime accounts for more and more of the decay of G ; the remaining t_w -dependence is only through an unimportant tail. For $t_w \rightarrow \infty$, the “short time” regime extends to all finite values of $t - t_w$; one recovers the equilibrium response which decays to zero on a t_w -independent timescale. Equivalently, if we assume that $G(t - t_w, t_w)$ can be measured reliably only as long as it remains greater than some specified value (a small fraction ϵ of its initial value $G(0, t_w) = 1$, for example), then the results will become t_w -independent for sufficiently large t_w .

For $x < 1$, on the other hand, one has ageing proper as illustrated in the right panel of Figure 3: the major part of the decay of G occurs on a timescale of order t_w itself, with unimportant corrections to this scaling at early times. We note that in this regime, the SGR model shows the simplest kind of ageing, with only a single ageing timescale that is directly proportional to t_w , and no

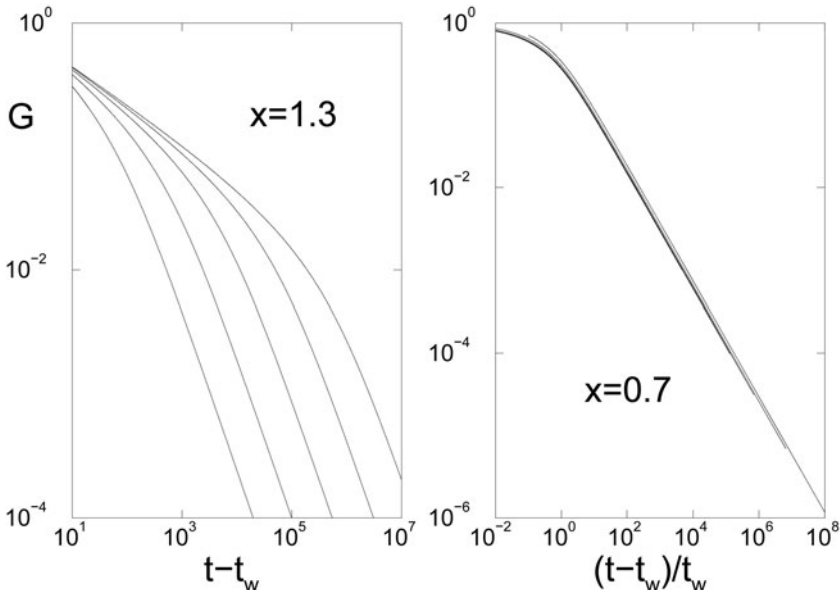


Figure 3. Stress relaxation modulus $G(t - t_w, t_w)$, for $x = 1.3$ against $t - t_w$ (left) and for $x = 0.7$ against the scaled time interval $(t - t_w)/t_w$ (right). Shown are data for waiting times $t_w = 10^2, 10^3, \dots, 10^6$ (left to right in left panel, right to left in right panel). (Reprinted with permission from [19]. Copyright (2000) The Society of Rheology.)

separate TTI part of the stress relaxation which would take place for $t - t_w$ of $O(1)$.

Next we consider **oscillatory strain**, for which the stress response is determined by the spectrum Eq. (9). In principle, this quantity depends on t_s , the time when the oscillatory strain was started. However, when the experimental timescales become large, one finds [19] that this dependence on t_s is weak. In fact, within the SGR model, the conditions needed to make G^* negligibly dependent on t_s (for low frequencies, $\omega \ll 1$) are that $\omega(t - t_s) \gg 1$ and $\omega t_s \gg 1$. The first signifies merely that many cycles of oscillatory strain are performed before the stress is measured; the second ensures that transient contributions from the initial sample preparation stage (the quench at $t = 0$) are negligible. The fact that these criteria are sufficient even in the glass phase is far from obvious physically, and requires a careful discussion [19]. Broadly speaking, they are satisfied in any experiment that would reliably measure a conventional $G^*(\omega)$ spectrum for systems with TTI.

For the purposes of such experiments, we can therefore drop the t_s argument and define a time-dependent spectrum $G^*(\omega, t)$. For long times ($t \gg 1$) this is found to behave as [19]:

$$\begin{aligned} G^*(\omega, t) &\sim (i\omega)^{x-1} && \text{for } 1 < x < 2 \\ G^*(\omega, t) &\approx 1 - (i\omega t)^{x-1} && \text{for } x < 1 \end{aligned} \quad (28)$$

These results are easily understood. By measuring $G^*(\omega, t)$ we are directly probing the properties of the system at the time of measurement, t . In the ergodic phase ($x > 1$), $G^*(\omega, t)$ will reach a t -independent value within a time of $O(1/\omega)$ after the quench, as the relevant traps will then have attained their equilibrium population. The relaxation time is then also of $O(1)$ and the response $G^*(\omega, t)$ is a function only of ω . In contrast, below the glass point the characteristic relaxation time at the epoch of measurement is of order t , and the response is a function only of the product ωt . Since, the losses in an oscillatory measurement arise from traps with lifetimes less than about $1/\omega$ (elements in deeper traps respond elastically), the overall response becomes more elastic as the system ages into traps with $\tau > 1/\omega$.

Numerical results for the viscoelastic spectrum $G^*(\omega, t)$ are shown in Figure 4. The spectra become increasingly flat as the glass point $x = 1$ is approached from above, with G' and G'' being of comparable order of magnitude; such flat spectra are seen experimentally in many materials; compare the discussion in the introduction section of this chapter. In the glass phase, the storage modulus at low frequencies evolves upwards, and the loss modulus downwards as expected [11, 12]. If plotted against ω rather than ωt , the data for $x = 0.7$ would resemble Figure 1. Each spectrum terminates at frequencies of order $\omega t \simeq 1$. This is because one cannot measure a true oscillatory response for periods *beyond* the age of the system. Therefore, the rise at low frequencies in G'' -spectra like Figure 1 represents the ultimate rheological behaviour.

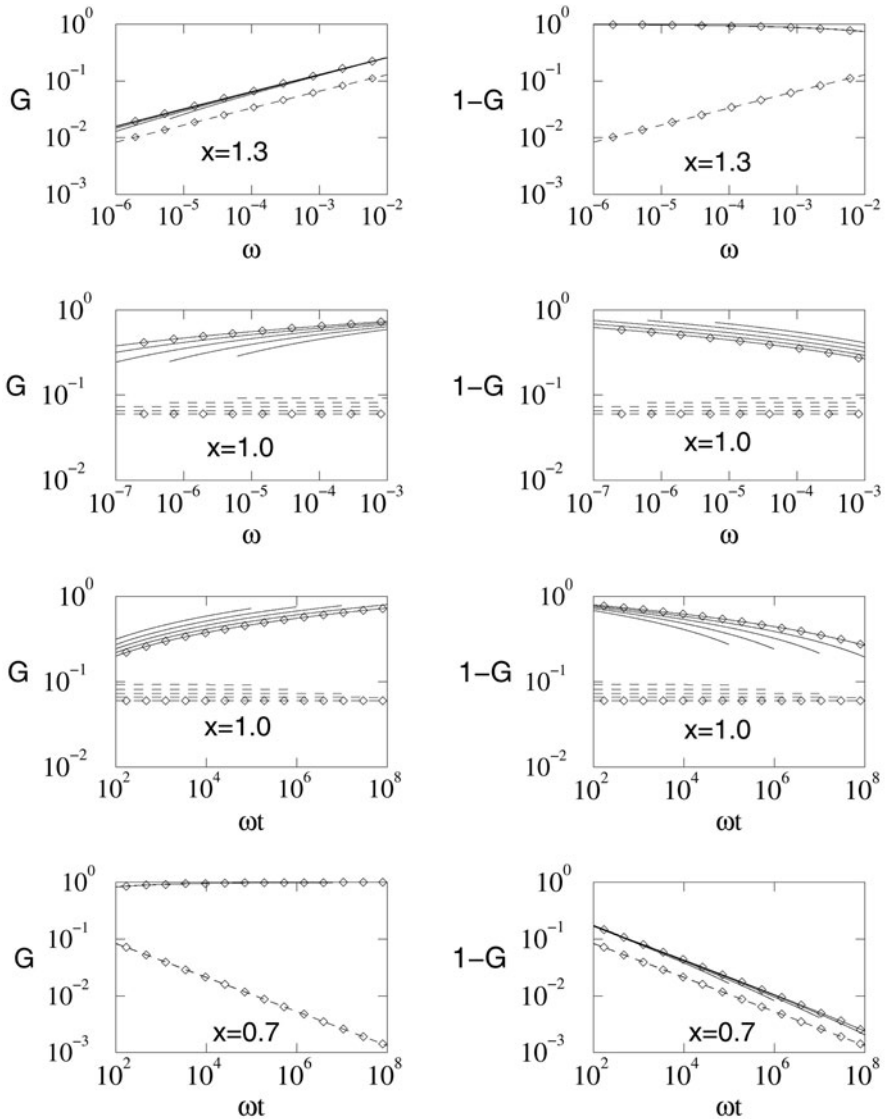


Figure 4. Left column: viscoelastic spectra $G'(\omega)$ (solid lines) and $G''(\omega)$ (dashed lines) versus frequency, ω (for $x \geq 1$) or scaled frequency ωt (for $x \leq 1$). Right column: frequency-dependent corrections to Hookean elasticity, $1 - G'$ (solid lines), G'' (dashed lines). Data are shown for systems aged $t = 10^7, 10^8, \dots, 10^{11}$. At any fixed ω the curves lie in order of age; data on the oldest system is marked by the symbols. (Reprinted with permission from [19]. Copyright (2000) The Society of Rheology.)

(The middle rows of Figure 4 illustrate that at $x = 1$ itself, logarithmic corrections cause G' and G'' to scale neither with ω nor with ωt .)

One can show [19] that the insensitivity of $G^*(\omega, t, t_s)$ to t_s in practical measurements of the viscoelastic spectrum (where an oscillatory strain is maintained over many cycles) arises because the most recently executed strain cycles dominate the stress response at time t . This “forgetfulness” of strain cycles in the distant past also means that, in the SGR model, the Fourier relationship Eq. (12) between oscillatory and step strain responses is recovered to a good approximation.

We mention briefly, at this stage, that the SGR model has recently also been used to analyse so-called “over-ageing” effects [16, 17]. These occur experimentally if one applies a large-amplitude oscillatory strain to an ageing system, for some finite duration, then lets the system evolve and eventually measures its viscoelastic spectrum with a small oscillatory probe-strain. Naively, one might suspect that the large-amplitude oscillatory strain would tend to “reset” the ageing process, reducing the effective age t . However, the situation is more subtle: Viasnoff and Lequeux [16], Viasnoff *et al.* [17] the large-amplitude strain leaves elements with large yield energies E unaffected. Elements with moderate E are forced to yield, and will be reborn with small E (as directly after a quench). The population of yield energies is thus depleted in an intermediate range of E , and increased for small E . During the subsequent evolution and continued ageing, the new population of small- E elements yields quickly and acquires progressively larger E . The depletion of the intermediate E -values then eventually becomes important, and the viscoelastic spectrum has a *larger* contribution from deep traps. The overall effect is that the sample can behave as if it the large oscillatory strain had made it *older* (hence the name over-ageing) rather than younger.

Finally, consider a **startup** experiment in which a steady shear of rate $\dot{\gamma} \ll 1$ begins at time t_w . So long as we restrict attention to times short enough that the total strain remains small ($\dot{\gamma}(t - t_w) \ll 1$) the system exhibits linear response; the crossover to the nonlinear regime is discussed in Section 4.2. One finds [19] for long times and in the linear response regime that $\sigma(t) \sim \dot{\gamma}(t - t_w)$ for $x < 1$ (which is purely elastic behavior), $\sigma(t) \sim \dot{\gamma}(t - t_w)^{2-x}$ for $1 < x < 2$ (which is an anomalous power law), and $\sigma(x) \sim \dot{\gamma}$ for $x > 2$. Except for prefactors, these scalings are independent of whether $t - t_w \ll t_w$ or $\gg t_w$, so that *linear* startup experiments are not a useful probe of ageing dynamics.

4.2. Nonlinear Response

We now turn to the non-linear behavior of the SGR model under imposed strain. For **step strain** of amplitude γ_0 , the effective time interval $Z(t, t')$ is

increased by a factor $\exp(\gamma_0^2/2x)$ for times above t_w , and this translates into the simple relation:

$$G(t - t_w, t_w; \gamma_0) = G\left((t - t_w) \exp\left(\gamma_0^2/2x\right), t_w\right) \quad (29)$$

This result generalizes that of [12] for the non-ageing case ($x > 1$). It can be understood as follows. Within the SGR model, instantaneous response to a step strain at t_w is always elastic (that is, $G(0, t_w, \gamma_0) = 1$); the fraction of stress remaining at time $t > t_w$ is the fraction of elements which have survived from t_w to t without yielding (see above). The stress decay is therefore determined entirely by the distribution of relaxation times in the system just after the strain is applied at time t_w . The effect of a finite strain is solely to modify the distribution of barrier heights, and hence to modify this distribution of relaxation times τ ; in fact (within the scalar model) nonlinear strain reduces the yield time of every element by an identical factor of $\exp(\gamma_0^2/2x)$ [12].

In Section 4.1, we discussed the response to **startup of steady shear** (with $\dot{\gamma} \ll 1$) at time t_w , assuming linear response. Now consider the effect of strain-induced yield events, which cause nonlinearity. For $x > 2$ (where the SGR model predicts Newtonian fluid behaviour for $\dot{\gamma} \ll 1$), one can show that the stress response remains linear at all times, including the steady state limit [19]. For $x < 2$, on the other hand, one finds [19] that the linear period ends at $t \simeq \dot{\gamma}^{-1}$ (within logarithmic terms, discussed below); at later times, the main stress-bearing elements will, during their lifetimes, become strongly strained. Indeed, at strain rate $\dot{\gamma}$, an element with yield energy E will be strained to the top of its yield barrier in a time $t_{\text{int}} \simeq E^{1/2}/\dot{\gamma} \simeq (\ln \tau)^{1/2}/\dot{\gamma}$. The tendency of the distribution of local stresses to evolve toward deeper and deeper traps is thereby *interrupted*: the lifetime of a deep trap is converted from τ to a much smaller value, of order $(\ln \tau)^{1/2}/\dot{\gamma}$ [11, 12]. This truncation of the lifetime distribution is enough to ensure that these distributions are never dominated by the deep traps, and a steady state is recovered; accordingly, there are no ageing effects at late enough times. Ageing is also absent during the initial linear regime (Section 4.1), so any nontrivial effects must be confined to an intermediate time regime. There, at the end of the linear regime, the stress can be *higher* than the steady state value, leading to an overshoot in the startup curve [12]. This overshoot region, unlike the two asymptotes, shows a significant dependence on the system age t_w , as shown in Figure 5. The physics of this is clear: the extent of the linear regime gets progressively larger as t_w is increased, because the system has aged into deeper traps (and because the scalar SGR model assumes that within each trap the relation between stress and strain is linear). Thus the strain at which strong yielding sets in increases (roughly logarithmically) with t_w ; the height of the overshoot is accordingly increased before dropping onto the same, t_w -independent, steady-shear plateau.

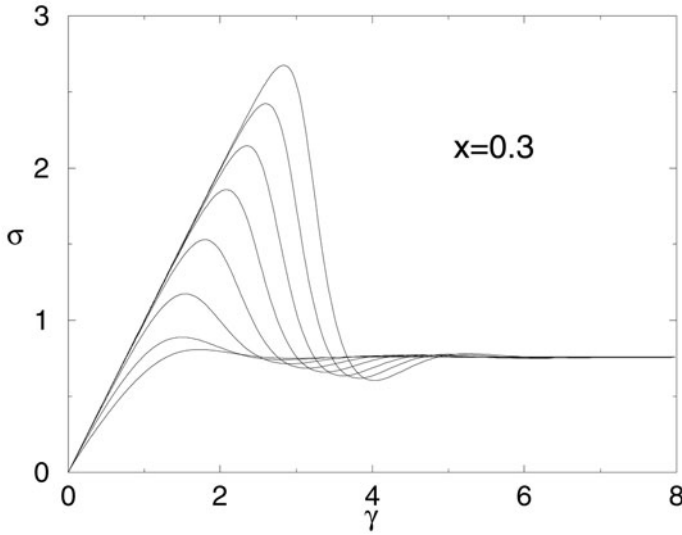


Figure 5. Stress response σ , in shear startup, vs strain γ at noise temperature $x = 0.3$ and strain rate $\dot{\gamma} = 0.001$. Curves from bottom to top correspond to increasing ages $t_w = 10^2, 10^3, \dots, 10^9$ at time of startup. (Reprinted with permission from [19]. Copyright (2000) The Society of Rheology.)

5. Rheological Ageing: Imposed Stress

We now review the SGR model's predictions for various stress-controlled rheological experiments; these are mostly obtained by numerical solution of the constitutive equations [19].

5.1. Linear Response

In **step stress**, the SGR model predicts that there will be an instantaneously elastic response. Elements then progressively yield and reset their local stresses to zero; thus we must apply progressively more strain to maintain the macroscopic stress at a constant value. Potentially, therefore, individual elements can acquire large local strains and linearity of the response need not be maintained at late times. As for shear startup, it is therefore sensible to first assume that the response *is* linear and then to consider *a posteriori* up to what time t the linear results remain valid.

In the linear regime the step stress response is described by the creep compliance $J(t - t_w, t_w)$, defined in Section 2.5. One finds that J scales

as $t - t_w$ for $x > 2$ and as $(t - t_w)^{x-1}$ for $1 < x < 2$. These results apply both for $t - t_w \ll t_w$ and $t - t_w \gg t_w$, though with different prefactors. The non-Newtonian behavior for $1 < x < 2$ reflects the low-shear rate power-law behavior of the flow curve. In the glass phase ($x < 1$), finally, one finds $J \sim \ln(t - t_w/t_w)$ for $t - t_w \gg t_w$. This exhibits the expected ageing effects, but being logarithmic these are rather weak; see Figure 6. Such behavior is intuitively reasonable: the strain response at time t to step stress is *not* determined purely by the relaxation spectrum at t_w (as was the case in step strain), but by the dynamics of the system over the entire interval between t_w and t . This decreases the sensitivity to the time t_w at which the perturbation was switched on.

For **oscillatory stress**, one finds results very similar to those for the case of oscillatory strain (Section 4.1). Although unsurprising, this does require explicit confirmation in a system exhibiting rheological ageing; see Section 2.6. One confirms numerically that the reciprocity relation $J^*(\omega, t) = 1/G^*(\omega, t)$ is obeyed to good accuracy, so that the linear responses to imposed oscillatory strain and stress contain essentially the same information.

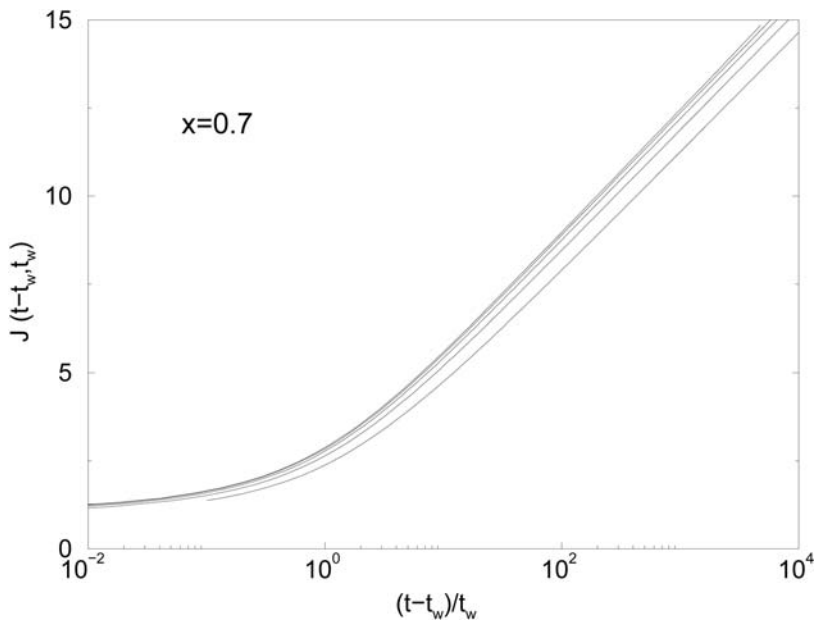


Figure 6. Linear creep compliance $J(t - t_w, t_w)$ against scaled time interval $(t - t_w)/t_w$ for noise temperature $x = 0.7$. Curves from bottom to top correspond to increasing times $t_w = 10^2, 10^3, \dots, 10^6$ of stress onset. Note the approach to a limiting scaling form as t_w becomes very large compared with the microscopic time $\tau_0 = 1$. (Reprinted with permission from [19]. Copyright (2000) The Society of Rheology.)

5.2. Nonlinear Response

Within the SGR model, application of a **step stress** of size $\sigma_0 \ll 1$ induces a strain response $\gamma(t)$ which increases over time, but remains linear in σ_0 for at least as long as the linearized constitutive equations predict $\gamma(t) \ll 1$. This is because $\gamma(t)$ provides an upper bound on the local strain of each element. Although sufficient to ensure linearity, this is not always necessary; one requires only that the characteristic strain of *those elements which dominate the stress* is small. For $x > 2$ (the Newtonian regime), the dominant elements have lifetimes $O(1)$ and so the response is linear to indefinite times so long as $\sigma_0 \ll 1$ (ensuring $\dot{\gamma}(t) \ll 1$ for all times t). But, whenever $x < 2$, the linear analysis sketched above [19] indicates that the dominant elements have lifetimes of order $t - t_w$; so a self-consistently linear response is maintained only provided that $\dot{\gamma}(t)(t - t_w) \ll 1$, just as in startup of steady shear (see Section 4.2. For $1 < x < 2$ this condition translates into $t - t_w \ll (1/\sigma_0)^{1/(x-1)}$ [19]. Figure 7 indeed shows a linear regime of the expected temporal extent, followed by a crossover into a nonlinear steady-state flow regime, in which $\gamma(t) \propto \sigma_0^{1/(x-1)} t$. The latter is in agreement with the flow curve Eq. (24).

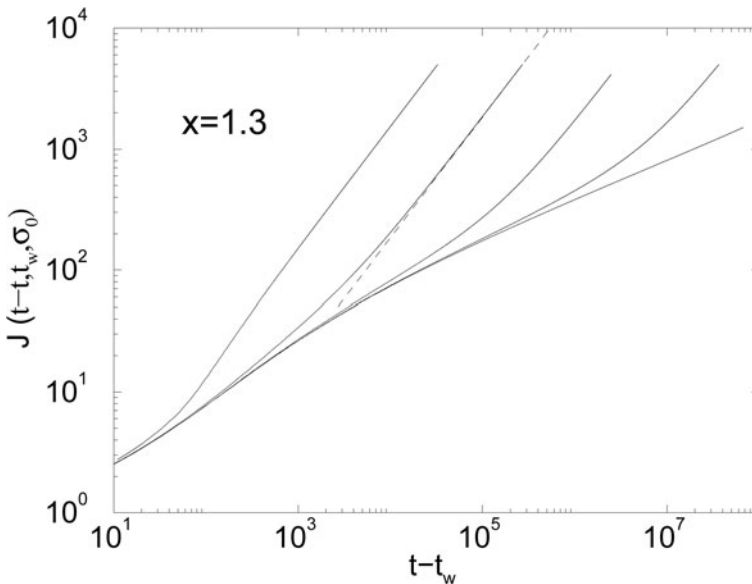


Figure 7. Nonlinear creep compliance $J(t - t_w, t_w, \sigma_0)$ as a function of time interval $t - t_w$, for a step stress of size σ_0 applied at time t_w . The noise temperature is $x = 1.3$. Solid lines, bottom to top: $\sigma_0 = 10^{-3}, 10^{-2.5}, 10^{-2}, 10^{-1.5}, 10^{-1}$. Over the time intervals shown, the curve for $\sigma_0 = 10^{-3}$ is indistinguishable from the linear compliance (not shown). Dotted line: final flow behavior predicted from steady state flow curve for $\sigma_0 = 10^{-1.5}$. (Reprinted with permission from [19]. Copyright (2000) The Society of Rheology.)

In the glass phase, $x < 1$, for which the flow curve shows a finite yield stress, $\sigma_y(x)$, the behavior is rather more complicated. As expected, the numerical results for step stress of very small amplitude $\sigma_0 \ll \sigma_y$ show no crossover to a steady flow regime at late times. Instead, the system continues to creep logarithmically, according to the linear creep result for $J(t - t_w, t_w)$. When σ_0 is not small but less than the yield stress σ_y the creep is still logarithmic to a good approximation, but now with a nonlinear dependence of its amplitude on stress. Very close to the yield stress, $\gamma(t)$ grows more quickly in time, but with a strain rate $\dot{\gamma}(t)$ that still decreases to zero at long times. Finally, as expected from the flow curve, only for stress amplitudes exceeding the yield stress σ_y does one see an eventual crossover from logarithmic creep to steady flow at long times which recovers numerically the flow-curve result, $\gamma(t) \propto (\sigma_0 - \sigma_y)^{1/(1-x)}(t - t_w)$. Figure 8 illustrates these various behaviors. Comparison of the curves for the two different waiting times for $\sigma_0/\sigma_y = 1.2$ shows that before the crossover into flow, the response scales with $(t - t_w)/t_w$; once ergodicity has been restored and the system flows, on the other hand, scaling with $t - t_w$ is recovered.

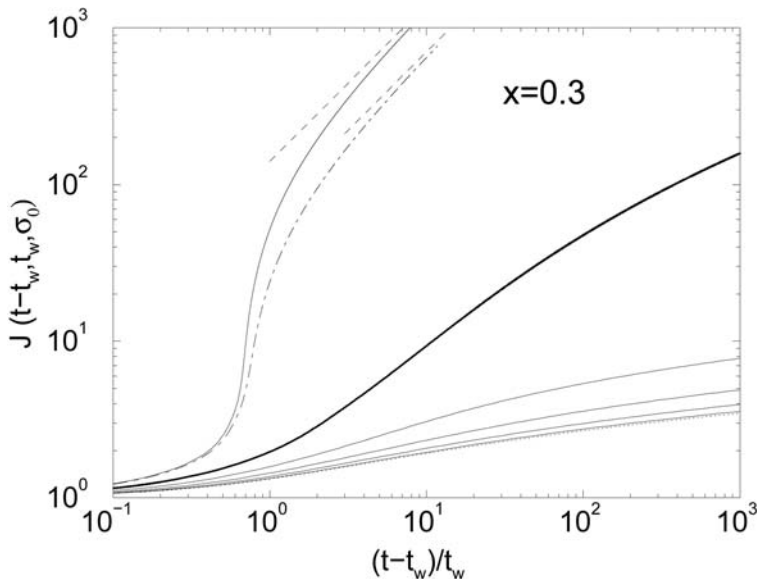


Figure 8. Nonlinear creep compliance $J(t - t_w, t_w, \sigma_0)$ as a function of scaled time interval $(t - t_w)/t_w$, for a step stress of size σ_0 applied at time t_w . The noise temperature is $x = 0.3$. Solid curves, bottom to top: $\sigma_0/\sigma_y = 0.2, 0.4, \dots, 1.2$, all for $t_w = 100$. The case $\sigma_0 = \sigma_y$ is shown in bold; the dotted curve is the linear response result ($\sigma_0 \rightarrow 0$). The dot-dashed curve shows the effect of decreasing the waiting time to $t_w = 50$, for $\sigma_0/\sigma_y = 1.2$. The dashed lines are the predictions for final flow behavior (for the stress above yield) from the steady state flow curve. (Reprinted with permission from [19]. Copyright (2000) The Society of Rheology.)

6. Conclusions and Perspectives for the Future

In this chapter, we have reviewed the soft glassy rheology (SGR) model. Taking into account only the shared features of disorder and metastability that are present in many soft glasses, the model essentially adds strain degrees to Bouchaud's trap model. In the original formulation only shear strain and stress are considered, but we have also outlined a recent generalization which properly accounts for the tensorial nature of stress and strain. In either version, the model can be solved to give an explicit constitutive equation.

One of the hallmarks of glassy systems is the occurrence of ageing, where time-translation invariance is lost, and the SGR model indeed predicts such ageing effects in the rheology of soft glasses. We outlined in Section 2 a general formulation of the linear and nonlinear rheological response functions suited to ageing materials, and also distinguished ageing from ordinary transients that occur during equilibration. This conceptual framework is independent of the SGR model and should be of wider relevance, not least to the analysis of gel rheology.

The SGR model and its simple rheological properties were reviewed in Section 3, while Sections 4 and 5 cover the more complicated rheological ageing effects. These occur mainly in the glass phase of the model ($x < 1$), where the elastic elements that it describes evolve forever towards higher yield thresholds (deeper traps), causing a progression toward more elastic and less lossy behavior. Within this glass phase, there is a yield stress σ_y , and genuine ageing arises for applied stresses less than this. For step strains and stresses, we showed that the nature of the ageing is relatively simple: both the linear stress relaxation function $G(t - t_w, t)$ and the linear creep compliance $J(t - t_w, t_w)$ become functions of the scaled time interval $(t - t_w)/t_w$ only. The time-dependent viscoelastic spectra $G'(\omega, t)$ and $G''(\omega, t)$ have the characteristic ageing behavior shown in Figure 1: a loss modulus that rises as frequency is *lowered*, but falls with age t , in such a way that it always remains less than $G'(\omega, t)$ (which is almost constant by comparison). For $x < 1$ such spectra collapse to a single curve (see Figure 4) if ωt , rather than ω , is used as the independent variable.

Significant ageing was also found for nonlinear rheological responses of the SGR model. For example the nonlinear step-strain relaxation follows the same ageing scenario as the linear one, except that all relaxation rates are speeded up by a single strain-dependent factor Eq. (29). This form of nonlinearity is a characteristic simplification of the SGR model, and extends to its tensorial generalization [20]. Another interesting case was startup of steady shear; here there is no significant ageing in either the initial (elastic) or the ultimate (steady flow) regime; yet, as shown in Figure 5, the intermediate region shows an overshoot that increases with sample age. Finally we found that the nonlinear creep compliance (Figure 8) shows interesting dependence on both the stress

level and the age of the sample. For small stresses one has logarithmic creep. As the yield stress is approached this crosses over to a more rapid creep that nonetheless has zero strain rate in the long time limit, and then finally to steady flow above the yield stress.

There are, of course, many open issues with the model; these are discussed in detail elsewhere [12]. One of these concerns the interpretation of the noise temperature x and whether or not this should depend on flow history: we have assumed throughout that it does not. Also, the rheological ageing predictions of the model, though surprisingly rich as we have shown, do not include all those found experimentally [13–15]. As a model for *gel* rheology, the SGR model has further drawbacks. As explained in the introduction, it was designed for (soft) repulsive glasses, whereas gels are more akin to attractive glasses. It also neglects the possibility of significant structural change during ageing, and assumes that the local elastic properties are homogeneous. Nonetheless, the model certainly represents a useful step towards understanding the rheology of soft glassy materials, in particular in regimes where their behavior is not time-translation invariant [19].

We conclude by mentioning some recent approaches related to the SGR model, which may provide inspiration for the development of improved models in the future. Lequeux and co-workers proposed a model which is not dissimilar from the SGR model but attempts to make explicit that the effective noise in the system arises from yield events [38, 39]. Starting from the SGR picture, their model can be obtained by the following modifications: (1) All elements have the same yield energy E ; (2) the yield rate, rather than being activated, is zero for $kl^2/2 < E$ and a constant $1/\tau_0$ for larger $|l|$; (3) yield events are assumed to lead to random changes and thus to an effective diffusion of the local strain l . The self-consistent nature of the model comes in through the postulate that the relevant diffusion constant D is proportional to the overall yielding rate, $D = \alpha Y$. The constant α governs the behavior of the model: in the absence of shear ($\dot{\gamma} = 0$), the system has nonzero Y and D only for $\alpha > \alpha_c = 1/2$, while for $\alpha \leq \alpha_c$ it is completely frozen. This occurrence of a glass-like phase is reflected in the flow curve: for $\alpha < \alpha_c$ there is a nonzero yield stress, while for $\alpha > \alpha_c$ Newtonian behavior is predicted. Precisely at the transition, a power-law flow curve $\sigma \sim \dot{\gamma}^{1/5}$ is predicted; this also governs the behavior for α close to α_c and intermediate $\dot{\gamma}$. It is arguable whether such a fixed power-law exponent can be expected to reflect the behavior of a wide range of soft glasses. The behavior under small oscillatory strain is also unusual: in the glass phase, the stress response is always nonlinear, with G'' exhibiting a peak at a frequency scaling linearly with the strain amplitude γ_0 . The linear response limit $\gamma_0 \rightarrow 0$ therefore gives purely elastic behavior.

We mention here that one could similarly make the effective temperature in the SGR model self-consistent, for example by assuming that it is proportional

to the overall yield rate, $x = \alpha Y$. The consequences of this remain to be fully explored but appear to include interesting effects such as flow curves with metastable and unstable branches.

To simplify their analysis yet further, Derec, Ajdari and Lequeux later suggested a model with only two fundamental variables: the (shear) stress σ and a “mobility” D [40, 41]. The dynamic equation for σ is $d\sigma/dt = -D\sigma + k\dot{\gamma}$ so that for $D = 0$ one gets purely elastic behavior; viscous effects require $D > 0$. For the time evolution of D , the assumption is that dD/dt can, by loose analogy with a Landau expansion, be expanded in powers of D for small D . The coefficients are then taken to depend on stress σ and the imposed shear rate $\dot{\gamma}$. Depending on whether D evolves to zero in the quiescent state ($\dot{\gamma} = 0$) or not, one then again finds glass and liquid states. An interesting result is that, for appropriate choices of the exponents in the Landau-like expansion, the model predicts sub-ageing, where the typical relaxation timescale grows not as t_w but as t_w^μ with $\mu < 1$. Some caveats apply, however: for example, some of the parameter settings considered by Derec *et al.* [40, 41] give a well-defined response to oscillatory strain but produce divergences for step strain. An even simpler one-parameter model involving only the “degree of jamming” (essentially the inverse of D) has also recently been proposed [42].

Finally, it is important to mention the so-called shear-transformation zone (STZ) theory, developed by Falk and Langer [43] around the same time as the SGR model. Inspired by numerical simulations, STZ theory postulates that plastic deformations in a sheared amorphous material take place in local elements that have bistable configurations. The defining equations of motion then govern the evolution of the populations of the two kinds of configurations as they are transformed into one another, created or destroyed. This model has been very influential, and continues to be developed further [44–46].

It will be clear from the above brief survey that there are by now a number of simple models designed to describe the rheology of soft glasses, with the predictions of the SGR and STZ models having been explored in most detail. Much further work needs to be done, in particular in making the models more realistic without losing the important advantage of being able to extract predictions analytically rather than by simulation. There is even more scope in modifying and extending models of this type to make them applicable to gels in particular.

Acknowledgments

I am indebted to my collaborators Michael Cates, Suzanne Fielding, Pascal Hébraud and François Lequeux, much of whose work on the development and analysis of the SGR model is described in this chapter.

References

- [1] Mackley, M.R.; Marshall, R.T.J.; Smeulders, J.B.A.F.; Zhao, F.D. “The rheological characterization of polymeric and colloidal fluids”, *Chem. Engin. Sci.*, **1994**, *49*, 2551–2565.
- [2] Ketz, R.J.; Prud’homme, R.K.; Graessley, W.W. “Rheology of concentrated microgel solutions”, *Rheol. Acta*, **1988**, *27*, 531–539.
- [3] Khan, S.A.; Schnepper, C.A.; Armstrong, R.C. “Foam rheology. 3: Measurement of shear-flow properties”, *J. Rheol.*, **1988**, *32*, 69–92.
- [4] Mason, T.G.; Bibette, J.; Weitz, D.A. “Elasticity of compressed emulsions”, *Phys. Rev. Lett.*, **1995**, *75*, 2051–2054.
- [5] Panizza, P.; Roux, D.; Vuillaume, V.; Lu, C.Y.D.; Cates, M.E. “Viscoelasticity of the onion phase”, *Langmuir*, **1996**, *12*, 248–252.
- [6] Hoffmann, H.; Rauscher, A. “Aggregating systems with a yield stress value”, *Coll. Polymer Sci.*, **1993**, *271*, 390–395.
- [7] Mason, T.G.; Weitz, D.A. “Linear viscoelasticity of colloidal hardsphere suspensions near the glass-transition”, *Phys. Rev. Lett.*, **1995**, *75*, 2770–2773.
- [8] Holdsworth, S.D. “Rheological models used for the prediction of the flow properties of food products”, *Trans. Inst. Eng.*, **1993**, *71*, 139–179.
- [9] Dickinson, E. *An Introduction to Food Colloids*, Oxford: Oxford University Press, **1992**.
- [10] Barnes, H.A.; Hutton, J.F.; Walters, K. *An Introduction to Rheology*, Amsterdam: Elsevier, **1989**.
- [11] Sollich, P.; Lequeux, F.; Hébraud, P.; Cates, M.E. “Rheology of soft glassy materials”, *Phys. Rev. Lett.*, **1997**, *78*, 2020–2023.
- [12] Sollich, P. “Rheological constitutive equation for a model of soft glassy materials”, *Phys. Rev. E*, **1998**, *58*, 738–759.
- [13] Cloître, M.; Borrega, R.; Leibler, L. “Rheological ageing and rejuvenation in microgel pastes”, *Phys. Rev. Lett.*, **2000**, *85*, 4819–4822.
- [14] Höhler, R.; Cohen-Addad, S.; Asnacios, A. “Rheological memory effect in aqueous foam”, *Europhys. Lett.*, **1999**, *48*, 93–98.
- [15] Cohen-Addad, S.; Höhler, R. “Bubble dynamic relaxation in aqueous foam probed by multispeckle diffusing-wave spectroscopy”, *Phys. Rev. Lett.*, **2001**, *86*, 4700–4703.
- [16] Viasnoff, V.; Lequeux, F. “Rejuvenation and overaging in a colloidal glass under shear”, *Phys. Rev. Lett.*, **2002**, *89*, 065701.
- [17] Viasnoff, V.; Jurine, S.; Lequeux, F. “How colloidal suspensions that age are rejuvenated by strain application”, *Faraday Discussions*, **2003**, *123*, 253–266.
- [18] Cloître, M.; Borrega, R.; Monti, F.; Leibler, L. “Glassy dynamics and flow properties of soft colloidal pastes”, *Phys. Rev. Lett.*, **2003**, *90*, 068303.
- [19] Fielding, S.M.; Sollich, P.; Cates, M.E. “Ageing and rheology in soft materials”, *J. Rheol.*, **2000**, *44*, 323–369.
- [20] Cates, M.E.; Sollich, P. “Tensorial constitutive models for disordered foams, dense emulsions, and other soft nonergodic materials”, *J. Rheol.*, **2004**, *48*, 193–207.
- [21] Dawson, K.A. “The glass paradigm for colloidal glasses, gels, and other arrested states driven by attractive interactions”, *Curr. Opin. Colloid Interface Sci.*, **2002**, *7*, 218–227.
- [22] Doi, M.; Edwards, S.F. *The Theory of Polymer Dynamics*, Oxford: Clarendon Press, **1986**.
- [23] Bernstein, B.; Kearsley, E.A.; Zapas, L.J. “A study of stress relaxation with finite strain”, *Trans. Soc. Rheol.*, **1963**, *7*, 391–410.

- [24] Cates, M.E.; Candau, S.J. “Statics and dynamic of wormlike surfactant micelles”, *J. Phys. Cond. Matt.*, **1990**, 2, 6869–6892.
- [25] Struik, L.C.E. *Physical ageing in amorphous polymers and other materials*, Houston: Elsevier, **1978**.
- [26] Bouchaud, J.P.; Dean, D.S. “Ageing on Parisi’s tree”, *J. Phys. (France) I*, **1995**, 5, 265–286.
- [27] Kurchan, J. “Rheology, and how to stop ageing”, *Jamming and Rheology: constrained dynamics on microscopic and macroscopic scales*, A.J. Liu, S.R. Nagel, Eds., London: Taylor and Fransis, 2001.
- [28] Cugliandolo, L.F.; Kurchan, J. “Weak ergodicity breaking in meanfield spin-glass models”, *Phil. Mag. B*, **1995**, 71, 501–514.
- [29] Cugliandolo, L.F.; Kurchan, J.; Le Doussal, P.; Peliti, L. “Glassy behaviour in disordered systems with nonrelaxational dynamics”, *Phys. Rev. Lett.*, **1997**, 78, 350–353.
- [30] Bouchaud, J.P.; Cugliandolo, L.F.; Kurchan, J.; Mézard, M. “Out of equilibrium dynamics in spin-glasses and other glassy systems”, In *Spin glasses and random fields*, A.P. young, Ed., Singapore: World Scientific, **1998**, pp. 161–223.
- [31] Scherer, G.W. *Relaxation in glass and composites*, New York: Wiley, **1986**.
- [32] Kossuth, M.B.; Morse, D.C.; Bates, F.S. “Viscoelastic behavior of cubic phases in block copolymer melts”, *J. Rheol.*, **1999**, 43, 167–196.
- [33] Cugliandolo, L.F.; Kurchan, J.; Peliti, L. “Energy flow, partial equilibration, and effective temperatures in systems with slow dynamics”, *Phys. Rev. E*, **1997**, 55, 3898–3914.
- [34] Bouchaud, J.P. “Weak ergodicity breaking and ageing in disordered systems”, *J. Phys. (France) I*, **1992**, 2, 1705–1713.
- [35] Lequeux, F.; Ajdari, A. “Averaging rheological quantities in descriptions of soft glassy materials”, *Phys. Rev. E*, **2001**, 63, 030502.
- [36] Head, D.A.; Ajdari, A.; Cates, M.E. “Jamming, hysteresis, and oscillation in scalar models for shear thickening”, *Phys. Rev. E*, **2001**, 64, 061509.
- [37] Head, D.A.; Ajdari, A.; Cates, M.E. “Rheological instability in a simple shear-thickening model”, *EuroPhys. Lett.*, **2002**, 57, 120–126.
- [38] Hébraud, P.; Lequeux, F. “Mode-coupling theory for the pasty rheology of soft glassy materials”, *Phys. Rev. Lett.*, **1998**, 81, 2934–2937.
- [39] Derec, C.; Ajdari, A.; Lequeux, F. “Mechanics near a jamming transition: a minimalist model”, *Faraday Discuss.*, **1999**, 112, 195–207.
- [40] Derec, C.; Ajdari, A.; Ducouret, G.; Lequeux, F. “Rheological characterization of ageing in a concentrated colloidal suspension”, *C. R. Acad. Sci. Ser. IV-Phys. Astrophys.*, **2000**, 1, 1115–1119.
- [41] Derec, C.; Ajdari, A.; Lequeux, F. “Rheology and ageing: a simple approach”, *Eur. Phys. J. E*, **2001**, 4, 355–361.
- [42] Coussot, P.; Nguyen, Q.D.; Huyunh, H.T.; Bonn, D. “Avalanche behavior in yield stress fluids”, *Phys. Rev. Lett.*, **2002**, 88, 175501.
- [43] Falk, M.L.; Langer, J.S. “Dynamics of viscoplastic deformation in amorphous solids”, *Phys. Rev. E*, **1998**, 57, 7192–7205.
- [44] Langer, J.S. “Microstructural shear localization in plastic deformation of amorphous solids”, *Phys. Rev. E*, **2001**, 64, 011504.
- [45] Lemaitre, A. “Rearrangements and dilatancy for sheared dense materials”, *Phys. Rev. Lett.*, **2002**, 89, 195503.
- [46] Eastgate, L.O.; Langer, J.S.; Pechenik, L. “Dynamics of large-scale plastic deformation and the necking instability in amorphous solids”, *Phys. Rev. Lett.*, **2003**, 90, 045506.

Chapter 6

RHEOLOGICAL CHAOS IN WORMLIKE MICELLES AND NEMATIC HYDRODYNAMICS

Moumita Das¹, Ranjini Bandyopadhyay², Buddhapriya Chakrabarti³, Sriram Ramaswamy¹, Chandan Dasgupta¹, and A.K. Sood¹

¹*Department of Physics, Indian Institute of Science, Bangalore 560012, INDIA*

²*Department of Physics and Astronomy, The Johns Hopkins University, Baltimore, MD 21218-2686, USA*

³*Department of Physics, University of Massachusetts, Amherst, MA 01003, USA*

1. Introduction	193
2. Deterministic Chaos in Viscoelastic Materials in Shear Flow	195
2.1. Experiments	195
2.2. Theories	202
3. Spatio-temporal Rheological Oscillations and Chaotic Dynamics	210
3.1. Theoretical Investigations of Spatio-temporal Rheochaos	210
4. Proposed Experiments	218

1. Introduction

The rheological properties of viscoelastic gels formed by the entanglement of wormlike micelles have been the subject of a large number of experimental and theoretical studies in recent years [1, 2]. Wormlike micelles are very long and semi-flexible cylindrical micelles which act like “living polymers” in aqueous media and self-assemble to form long-chain molecules even after they are broken to pieces by a strong flow (see Chapter 19). They typically have radii $\sim 20\text{--}25 \text{ \AA}$ and persistence lengths $\sim 150 \text{ \AA}$ while the average lengths

can be several microns. Further, though the static and quasistatic properties of these solutions are very similar to those of conventional polymeric systems, wormlike micelles, unlike covalently bonded polymers, can reversibly break and rejoin, with profound consequences for stress relaxation and flow behavior. In fact, it was found that while in steady shear, the rheological properties of these systems are like those of entangled flexible polymers [3], the application of large stresses and strains on wormlike micellar solutions can result in a wealth of complex phenomena. It has been observed that many dilute solutions of wormlike micelles exhibit a dramatic shear thickening behavior when sheared above a certain threshold rate, often followed by the onset of a flow instability [4–6]. Other experiments report shear-banded flow in wormlike micellar solutions with formation of bands or slip layers of different microstructures having very different rheological properties [7–10]. Of particular interest are observations suggesting shear-banding in transient organogels with organometallic monomolecular wires and fibers [11].

Rheochaos or rheological chaos in surfactant solutions was first observed in experimental investigations of the rheology of such a gel formed in the dilute aqueous solutions of cetyltrimethylammonium tosylate, a surfactant (CTAT) [12–15], which shows many intriguing features. In the non-linear regime, the shear stress σ shows a plateau as a function of the shear rate $\dot{\gamma}$ above a certain cutoff shear rate $\dot{\gamma}_c$. Under controlled shear rate conditions in the plateau regime, the shear stress and the first normal stress difference show oscillatory and more complicated irregular time-dependence. The analysis of the measured time series of shear stress and normal stress shows the existence of a finite correlation dimension and a positive Lyapunov exponent, unambiguously implying the presence of low-dimensional deterministic chaos.

Subsequently, the presence of sustained rheological oscillations have been reported in some other experiments on complex fluids in shear flow. Roux *et al.* [16] have studied sustained oscillations of the viscosity of a complex fluid near an out of equilibrium transition, namely the layering transition to the “onion” state in a lyotropic lamellar system. The system under consideration is a close-compact assembly of soft elastic spheres [16, 17]. The presence of oscillations in the viscosity are due to structural changes in the fluid. It has been conjectured that the oscillations in this particular system arise as a competition between an ordering mechanism that is driven by stress and a slow textural evolution which destroys the stress-induced ordered state.

Also noteworthy is the observation by Ramamohan *et al.* [18] of rheochaos in numerical studies of sheared hard-sphere Stokesian suspensions, with fluctuations that seem not to decrease significantly with increasing system size.

2. Deterministic Chaos in Viscoelastic Materials in Shear Flow

2.1. Experiments

2.1.1. Chaotic dynamics of sheared wormlike micelles – dilute aqueous solutions of cetyltrimethylammonium tosylate (CTAT)

We summarize the experimental observations on the rheological behavior of CTAT [12, 14]. The linear and non-linear rheology of dilute aqueous solutions of this surfactant system at 25° C has been well studied [14]. Above concentrations of 0.04 wt. % and temperatures of 23° C [19], CTAT self-assembles to form cylindrical wormlike micelles which become entangled at concentrations >0.9 wt. %. The lengths of these wormlike micelles depend on the concentrations of the surfactant and the added salt, the temperature and the energy of scission of the micelles. In these systems, stress relaxation occurs by reptation on a time scale τ_{rep} (the curvilinear diffusion of a micelle through an imaginary tube segment), as for conventional polymers, and by the reversible scission (breakdown and recombination of micelles) with a time scale τ_b [20]. The time scales τ_{rep} and τ_b may or may not be comparable and depend on the surfactant concentration, presence of counterions in the solution and the temperature. The frequency response of the system in the experiment of Bandyopadhyay *et al.* [12] was measured using a rheometer with temperature control and software for strain-rate control to measure the elastic and viscous responses of 1.35 wt. % CTAT between the angular frequency range of 0.03 rad/sec and 10 rad/sec. The rheometer used was equipped with four strain gauge transducers capable of measuring the normal force with an accuracy of 10^{-4} N. Linear response measurements show that at the lowest frequencies CTAT behaves like a viscous material, whereas in higher frequency runs, the behavior is found to be predominantly elastic. The crossover occurred at 0.3 rad/sec, which corresponds to a relaxation time τ_R of 3 secs. It has been shown by Cates *et al.* [21] that for a system of wormlike micelles, like cetylpyridinium chloride-NaCl (CPyCl-NaCl) (where $\tau_b \ll \tau_{\text{rep}}$), $G'(\omega)$ and $G''(\omega)$ are given by the Maxwell model (Eqs. (1) and (2)) where $\tau_R = (\tau_b \tau_{\text{rep}})^{1/2}$.

$$G'(\omega) = G_0 \frac{\omega^2 \tau_R^2}{1 + \omega^2 \tau_R^2} \quad (1)$$

$$G''(\omega) = G_0 \frac{\omega \tau_R}{1 + \omega^2 \tau_R^2} \quad (2)$$

Some molecular gels (e.g., organic solutions of thin monomolecular organometallic threads [22] which are sufficiently breakable) indeed exhibit

a mechanical relaxation close to Maxwellian behavior. This is a rare example of such behavior in apolar fluids and the rheological properties of this system are strongly reminiscent of breakable giant entangled micelles.

However, for wormlike micelles of CTAT [12] at concentration 1.35 wt. %, the fit to the Maxwell model is very poor [23]. Further, the Cole-Cole plot deviates from the semi-circular behavior expected in Maxwellian systems and shows an upturn at high frequencies. This deviation from Maxwellian behavior is possibly due to the comparable values of τ_{rep} and τ_b in this system, unlike in other wormlike micellar systems where the differences in the time scales lead to a “motional averaging” effect [21]. The behavior is also very different from the Doi-Edwards model or the model proposed by Hess *et al.* [19]. The nonlinear rheological studies of CTAT reveal yet another surprising feature. It has been observed that the shear stress and the first normal stress difference show chaotic oscillations in the plateau region of the flow curve [12].

Studies of the nonlinear rheology of CTAT involve measurement of the flow curve of the system. The measurements done under conditions of controlled stress showed that the flow curve saturates almost to a constant stress value ($\sigma\alpha\dot{\gamma}^\alpha$, where $\alpha = 0.06 \pm 0.004$) above a critical shear rate $\dot{\gamma}_c$, while the first normal stress difference is found to increase linearly with shear rate [24]. The plateau of the shear stress at high shear rates in CPyCl-sodium salicylate (CPyCl-NaSal) has been interpreted [24] as a characteristic feature of the flow curves of complex fluids that gives rise to a dynamical instability of the nature of shear banding [20]. Shear banding results in the formation of bands of high and low viscosities in the sample, supporting low and high shear rates respectively. However, the same phenomenon observed in cetyltrimethylammonium bromide-NaSal (CTAB-NaSal) at a higher concentration has been explained by Berret *et al.* [25] as due to the coexistence of stable thermodynamic phases, namely isotropic and nematic, in the sheared sample. Studies on the stress relaxation in the sample after subjecting it to a step strain rate show very novel features [12]. At 25° C, on applying controlled shear rates whose values lie in the plateau region of the flow curve, instead of decaying to a steady state, the stress is found to oscillate in time. The relaxation of the stress as a function of the shear rate and temperature is indicated in Figure 1. It is observed that for low shear rates, $\dot{\gamma} \leq 22\text{ s}^{-1}$, relaxes monotonically to a steady state value in a few seconds. At higher values of the shear rate, the stress oscillates in time, as shown in Figure 1(a–e) for a few typical values of applied shear rates. Figure 1(f) shows the oscillations in the normal stress measured along with the shear stress (curve c) at $\dot{\gamma} = 100\text{ s}^{-1}$. As the temperature is increased, we observe a decrease in the amplitude of oscillations in the stress relaxation, the oscillations finally disappearing completely at a temperature of 35° C Figure 1(g). This may be because of a decrease in the width of the stress plateau in the flow curve with increasing temperatures [26]. A spectral analysis reveals that more and more frequencies emerge as the value of the shear rate is increased. This might be

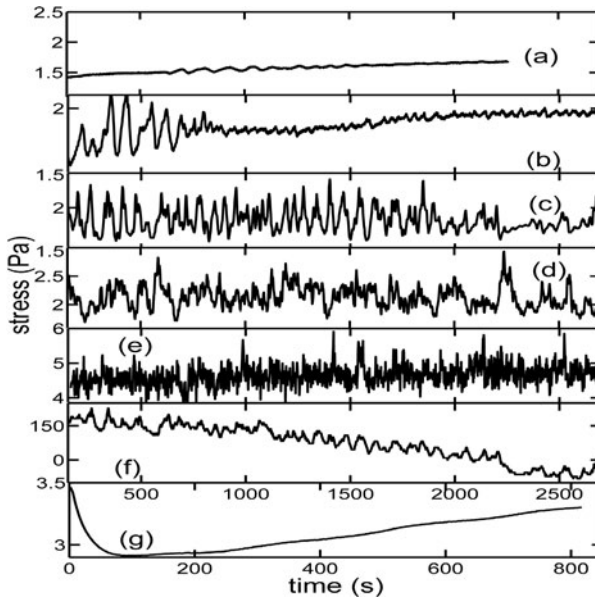


Figure 1. Shear stress relaxation in CTAT 1.35% on subjecting the sample to step shear rates of (a) 22.5 s^{-1} , (b) 75 s^{-1} , (c) 100 s^{-1} , (d) 138 s^{-1} , (e) 175 s^{-1} at 25°C . Panel (f) shows the time-dependent decay of the normal stress on application of $\dot{\gamma} = 100 \text{ s}^{-1}$, also at 25°C . Panel (g) shows the disappearance of the time-dependent oscillations at 35°C at $\dot{\gamma} = 100 \text{ s}^{-1}$. (Reprinted with permission from [12]. Copyright (2000) The American Physical Society)

understood in light of realignment of macro-domains which form as a result of shear banding. Stick-slip between these domains due to the application of shear can result in the observed time-dependent behavior. A careful analysis of these oscillations reveals signatures of low dimensional chaos [12].

Chaotic time-series data have often been observed in experiments on fluid dynamics [27]. Liquid crystalline polymers show a wagging regime on the application of suitable shear rates, where the director fluctuates periodically between limiting values. Time resolved measurements of the linear conservative dichroism in this regime [28] show irregular response at intermediate shear rates which may have its origin in chaotic dynamics. Noronha *et al.* [29] have reported the existence of chaotic dynamics in the jerky flow of some metal alloys undergoing plastic deformation. These systems also exhibit non-monotonic flow curves. As the name suggests the most obvious feature of a chaotic data train is the lack of periodicity. Traditionally, therefore, a spectral analysis is first done on a given data train to bring out hidden periodicities that might explain the source of signal variability. Further, deterministic chaos represents the apparently irregular behavior of dynamical systems that arises from strictly deterministic laws in the absence of any external stochasticity.

Thus, it is essential to look for signatures expected in a deterministic chaotic system which would distinguish it from a stochastic one. Chaotic dynamics in physical systems is characterized by an exponentially sensitive dependence on initial conditions, as a result of which long-term predictability of the dynamics of these systems is impossible. In other words, phase space trajectories that have nearly identical initial states separate from each other at an exponentially increasing rate. The *Lyapunov exponent* provides a quantitative measure of this sensitivity. If we consider two neighboring points in phase space at the start of the dynamics (i.e., $t = 0$) and if their separation along the i th direction is $\|\delta x_i(0)\|$, and $\|\delta x_i(t)\|$ at times 0 and t , then the Lyapunov exponent is defined by the average growth rate λ of the initial distance:

$$\lambda = \lim_{t \rightarrow \infty} \frac{1}{t} \log_2 \frac{\|\delta x_i(t)\|}{\|\delta x_i(0)\|} \quad (3)$$

Chaotic time series may be characterized by certain invariants, metric and dynamical, such as the various fractal dimensions, the largest Lyapunov exponent and the sum of positive Lyapunov exponents. A chaotic time series is characterized by a positive Lyapunov exponent, which is a direct consequence of the sensitivity of its trajectories in phase space to small changes in the initial conditions and describes the divergence of neighboring trajectories [27]. A unique feature of strange attractors is their stretching and folding dynamics, which in contrast to stochastic dynamics, prevents the orbits from filling the entire local subspace and gives rise to a unique self-similar geometrical structure – a fractal. A common and efficient way to characterize the fractal geometry or the boundedness of attractors is the so-called correlation dimension ν [30, 31].

We now describe the analysis of the time-dependent data for shear stress σ and normal stress difference Z to establish the presence of chaotic dynamics in the sheared CTAT solution. The time series analysis was performed by using the method of state space construction by embedding time delay vectors [32]. In doing so, it is crucial to determine the optimal embedding dimension m_o , because at $m < m_o$, one is not looking at the real dynamics, but at its projection. The optimum value of embedding dimension for the experimental time series described here was found to be 5. The calculated value of the correlation dimension ν of the attractors corresponding to the dynamics of stress relaxation is found to be >2 above a shear rate of 75 s^{-1} (e.g., it is 2.8 at a shear rate of 100 s^{-1} ; Figure 2(a)). Figure 2(b) shows the correlation dimensions ν as a function of the shear rate. ν is found to increase monotonically with the control parameter (shear rate), similar to that observed in the weakly turbulent Couette-Taylor flow exhibited by orange oil [33], where the Rayleigh number was the control parameter. The largest Lyapunov exponent was calculated for the time series of the viscoelastic stresses (using the method proposed by

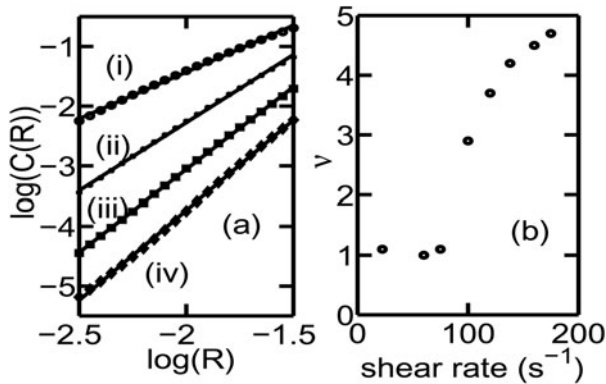


Figure 2. Panel (a) shows the plot of $\log(C(R))$ vs. $\log(R)$ [58] of the stress trajectories at $\dot{\gamma} = 100\text{s}^{-1}$ for $m = 2$ to 5 ((i)–(iv)). The slopes of the plots give the following values of ν : (i) $\nu = 1.6$ for $m = 2$, (ii) $\nu = 2.3$ for $m = 3$, (iii) $\nu = 2.8$ for $m = 4$ and (iv) $\nu = 2.8$ for $m = 5$. Panel (b) shows the correlation dimensions calculated as a function of shear rate $\dot{\gamma}$. (Reprinted with permission from [12]. Copyright (2000) The American Physical Society)

Gao and Zheng [31]), and was also found to increase monotonically with shear rate [12].

The existence of a finite correlation dimension, $\nu > 2$, and a positive largest Lyapunov exponent λ indicates the presence of deterministic chaos in the dynamics of stress relaxation in CTAT. This occurs only when the shear rates are high enough and lie in the plateau region of the flow curve. Because the volume fraction of CTAT in the experiment described is very small, the possibility of an isotropic-nematic phase transition was ruled out as the cause of the observed instabilities. We conclude that the observed chaotic dynamics is a natural consequence of a mechanical instability.

Many dilute solutions of wormlike micelles exhibit shear-thickening above a certain threshold shear rate, characterized by a large increase in the time-dependent values of the viscosity and the first normal stress difference (i.e., a flow curve $\sigma(\dot{\gamma})$ with upward curvature). The flow behavior of shear-thickening materials [34, 35] can be complex. Rheological and neutron scattering studies of shear-thickening solutions of CTAT [36] have shown the coexistence of a highly viscoelastic shear-induced phase (SIP) with a viscous regime made up of short aggregates. Subsequently, experiments [14] have found deterministic chaos in the stress relaxation of dilute CTAT solutions in the shear thickening regimes which can be possibly attributed to a stick-slip process between the shear induced structures (SIS) and the co-existing dilute phases. This is followed by an increase in the complexity of the dynamics of stress relaxation at still higher values of the shear rate, due to the percolation and fracture of the SIS, together with the formation of large vortices in the sheared solution. This

suggests that the occurrence of co-existing phases, rather than a plateau in the flow curve, is a prerequisite for the existence of complex dynamical behavior in stress relaxation of a sheared surfactant solution.

2.1.2. Sustained rheological oscillations in a dense lamellar phase

Lyotropic lamellar phases have shown a richness of behavior under shear flow [16]. Shear controls the texture of these systems and the spatial orientation of the lamellae changes as a function of the rate of shear. Roux *et al.* [16] studied the temporal behavior of rheological properties in a lyotropic lamellar phase (prepared with sodium dodecyl sulphate, octanol and water, salted with sodium chloride). This system shows several instabilities among which is a transition between two states of multilamellar spherulites or onions – (a) a disordered state in which the spherulites show only short range correlations, such as in liquids or glassy states, and (b) an ordered state where the onions are organized in hexagonal planes that flow over each other and exhibit long range orientational order under shear (which is conserved and leads to long-range positional order once the shear is stopped). This transition, also called the “layering transition”, can be characterized using rheology. Taking into account only stationary states, the stress/shear rate curve shows a jump in shear rate above a critical stress σ_c which is controlled by both the temperature and the composition of the sample. A constant shear stress is imposed and shear rate is recorded as a function of time while the shear stress is varied as adiabatically as possible. In the vicinity of the layering transition, the appearance of complex time-dependent behavior, which includes sustained finite amplitude regular oscillations of the shear rate (where the maximum of the shear rate corresponds to the “ordered state” and the minimum to the “disordered state”) is observed. A complex signal which can possibly be seen as chaotic is also detected. It is hypothesized that there is a coupling between temporal behavior and spatial instabilities involving a finite but small number of cells. The oscillations may be the result of a competition between an ordering of the disordered state driven by the stress (mechanical ordering) and slow textural evolution which destroys the stress-induced ordered state. These two effects may take place on different time scales and may produce oscillating behavior.

2.1.3. Elastic turbulence in polymer solution flow

Yet another example of flow instability in non-Newtonian fluids at very low Reynolds number, Re , where non-linearity of mechanical properties of the fluid can give rise to irregular flow, is the so-called phenomenon of “elastic turbulence” in highly elastic polymer solutions [37]. A characteristic feature

of turbulence is that fluid motion is excited in a broad range of spatial and temporal scales, so that many degrees of freedom are excited in the system. More than a century ago, since Osborne Reynolds discovered that turbulence in fluid flow is controlled by the inertia or momentum of the fluid. Groisman and Steinberg [37] found that flow of a polymer solution with large enough elasticity can become quite turbulent even at low velocity, high viscosity and in a small tank. The experiments were done on a swirling flow between two plates with a wide gap. They showed that the transition to this flow occurs as a result of an instability associated with polymer elastic stresses and hence the name “elastic turbulence”.

They conjecture the scenario of development of elastic turbulence as follows: The presence of polymers can change the stability of a laminar flow, and polymers with large elasticity (i.e., large relaxation times) can be stretched even by a weak primary shear flow, producing elastic instabilities which causes irregular secondary flow. This flow further stretches the polymer molecules, thereby increasing the elastic stresses further. Because of this feedback mechanism, turbulence increases until a kind of saturated dynamic state is reached. The resulting increase of the elastic stresses can reach two orders of magnitude. Also, while the Re may be arbitrarily low, the observed flow has all the main features of developed turbulence, and can be compared to turbulent flow in a pipe at an $Re \simeq 10^5$ [37].

2.1.4. Director turbulence in nematic liquid crystals

Another prime example of a phenomenon characterized by temporal fluctuations and spatial irregularities seen in experiments on viscoelastic materials is “director turbulence” in a nematic liquid crystal in shear flow [38, 39]. In the experiments of [38, 39], a sequence of instabilities was found to occur with increasing shear as the system cascades from one stationary state (for the director) to another, finally leading to a turbulent state. The parameter which governs the type of transitions observed in nematics at low shear rates is the Ericksen number. It measures the effect of the shear on the director field and is given by the ratio of the strength of distortional elasticity and viscous effects. At very small values of the Ericksen number, the director first rotates towards the vorticity direction, followed by the appearance of roll cells and birefringent stripes, both oriented in the flow direction. With an increase in the Ericksen number, this roll-cell structure becomes progressively fine scale, with a decrease in roll spacing. At still higher values of the Ericksen number, the observed striped pattern becomes so irregular that no single dominant stripe width can be derived from experimental observations. The director field now becomes spatially irregular and time-dependent with disclination threads generated in abundance and director turbulence sets in [38, 39].

2.2. Theories

2.2.1. Early work: Chaos in rheology of slender-body suspensions

One of the first theoretical investigations of chaos in rheological parameters involved the demonstration of chaotic dynamics in dilute suspensions of slender bodies in simple shear flow by Ramamohan *et al.* [40] They showed that the orientation of periodically forced slender rods and spheroids in simple shear flow varies chaotically for a certain range of the values of the parameter corresponding to the external periodic force. They studied the effect of these chaotic orientation evolution equations on rheological quantities such as the viscometric material functions.

Ramamohan *et al.* have derived the evolution equations of the slender rods in simple shear flow following the analysis of Berry and Russel [41]. The undisturbed velocity profile is chosen as $v_o = \dot{\gamma} y \hat{x}$ where $\dot{\gamma}$ is the shear rate, y is the y coordinate and \hat{x} is the unit vector in the x direction. A typical slender body in the suspension is modelled as a rigid rod of length $2l$. The particles are assumed to be sufficiently small such that the boundaries of the physical apparatus containing the suspension do not significantly affect the rheology of the bulk of the suspension. It is found that in the presence of periodic forcing (externally induced torque upon a slender rigid rod), the orientation of the particles evolves chaotically for a certain range of values of the components of the orientation-independent part of the torque due to the external force and initial conditions. Reference [42] also provides numerical evidence for existence of a low-dimensional attractor in the rheological properties. Subsequently, they have demonstrated that the dynamics underlying the fluctuations in stress of Stokesian suspensions under shear flow is deterministic, low-dimensional, and chaotic [18]; the simulations are for shear between plane parallel walls of a suspension of rigid identical spheres in a Newtonian fluid, over a range of particle concentration.

The existence of such complex behavior in this system, which is the simplest of a class of such systems, is indicative of the possibility of existence of chaotic dynamics in rheological properties of a wider variety of systems.

2.2.2. Rheological chaos in a shear thickening model

As discussed earlier, experiments [14] have observed deterministic chaos in the stress relaxation of shear thickening surfactant solutions. Unlike Newtonian fluids where flow instabilities essentially arise from the advection of momentum, rheological instabilities observed in the shear thickening of viscoelastic materials arise from the constitutive behavior of the material, perhaps strongly enhanced by the presence of memory effects. Cates *et al.* [43] propose a simple

phenomenological model for a shear thickening fluid with memory and an underlying tendency to form shear-banded flows, with only one degree of freedom – the shear stress. They show that the simplest constitutive equation for spatially homogenous states of such a system that allows chaotic dynamics has the following retarded and non-linear features: a nonlinear retarded relaxation rate for stress (chosen nonmonotonic) and a linear and retarded relaxation.

$$\dot{\sigma} = \dot{\gamma} - R(\sigma_1) - \lambda\sigma_2 \quad (4)$$

with single exponential kernels:

$$\begin{aligned} \sigma_1 &= \int_0^t \sigma(t') \tau_1^{-1} \exp[-(t-t')/\tau_1] dt' \\ \sigma_2 &= \int_{-\infty}^t \sigma(t') \tau_2^{-1} \exp[-(t-t')/\tau_2] dt' \end{aligned} \quad (5)$$

with $\tau_1 \leq 1 \ll \tau_2$. The essential idea is that even with a nonmonotonic decay rate $R(\sigma_1)$, the monotonicity of the flow curve can be recovered via the retarded contribution coming from σ_2 or σ_1 depending on in which case the relaxation is more retarded. However, if too retarded, the temporal stability is not restored because the system continues to amplify perturbations over short time scales. For a range of parameter values in the unstable region, a period doubling cascade is found to lead to chaos.

Recently Aradian and Cates [44] have studied a spatially inhomogeneous extension of this model, with spatial variation in the vorticity (z) direction. Working at a constant average stress ($\langle\sigma\rangle$), they observe complex spatiotemporal dynamics, most remarkably seen in what they call “flip flop shear bands” – a low and a high unstable shear band separated by an interface and periodically flipping into one another. For a certain choice of parameters they observe irregular (though not chaotic) time-varying behavior.

2.2.3. Temporal chaos in nematogenic fluids

The presence of a shear flow always introduces some form of nematic order in a complex fluid. In addition, wormlike micelles being elongated, will inevitably have a local aligning tendency. Also, the constitutive equation for the Johnson-Segalman model [45] which has generically similar non-monotonic behavior to the reptation-reaction model of wormlike micelles is very similar to the relaxation equation of the alignment tensor of a nematic liquid crystal and is best thought of as arising from the underlying dynamics of an orientational order parameter. We therefore now discuss the relaxation equation of the alignment tensor characterizing the molecular orientation of a nematic liquid crystal in

shear flow [47–49]. Rienaecker *et al.* [50] used these equations to investigate the spatially homogeneous dynamics of nematic liquid crystals in flow. Very recently the same authors have extended their analysis [51, 52] to include biaxially ordered steady and transient states. Their work revealed a transition from a kayaking-tumbling motion to a chaotic one via a sequence of tumbling and wagging states. Both intermittency and period doubling routes to chaos have been found.

Let us consider a nematogenic liquid consisting of N rodlike molecules, with molecular orientation denoted by the unit vectors n_i ($i = 1, N$). The presence of an average preferred direction of these molecules, called the director, is a characteristic feature of a nematic phase and distinguishes it from the isotropic phase, but order in the system is not measured by the director. Since the nematic phase is symmetric under a rotation by π about an axis normal to the director, any vector order parameter constructed by averaging over n will vanish. An appropriate choice for an order parameter to describe the ordering in a nematic is a tensor built from an average over the second moment of the orientational distribution function $P(n)$:

$$\mathbf{Q}_{\alpha\beta}(r) = \frac{1}{N} \sum_{i=1}^N \left\langle \left(n_{\alpha}^i n_{\beta}^i - \frac{1}{3} \delta_{\alpha\beta} \right) \right\rangle \delta(r - r^i) \quad (6)$$

The equation governing the relaxation mechanisms of this alignment tensor is given by:

$$\frac{\partial \mathbf{Q}}{\partial t} = \tau^{-1} \mathbf{G} + (\alpha_0 \boldsymbol{\kappa} + \alpha_1 \boldsymbol{\kappa} \cdot \mathbf{Q})_{ST} + \boldsymbol{\Omega} \cdot \mathbf{Q} - \mathbf{Q} \cdot \boldsymbol{\Omega} \quad (7)$$

The subscript ST denotes symmetrization and trace-removal. \mathbf{I} is the unit tensor, \mathbf{u} is the hydrodynamic velocity field, $\boldsymbol{\kappa} \equiv (1/2)[\nabla \mathbf{u} + (\nabla \mathbf{u})^T]$ and $\boldsymbol{\Omega} \equiv (1/2)[\nabla \mathbf{u} - (\nabla \mathbf{u})^T]$ the shear-rate and vorticity tensors, respectively, τ is a bare relaxation time, and α_0 and α_1 are parameters related to flow alignment. The flow geometry imposed is plane Couette with velocity $\mathbf{u} = y\dot{\gamma}\hat{x}$ in the \hat{x} direction, gradient in the \hat{y} direction and vorticity in the \hat{z} direction.

\mathbf{G} , the molecular field conjugate to \mathbf{Q} , for a Landau-de Gennes [53] free-energy functional F that governs the equilibrium nematic-isotropic transition, is given by:

$$\mathbf{G} \equiv -(\delta F / \delta \mathbf{Q})_{ST} = -[A\mathbf{Q} - \sqrt{6}B(\mathbf{Q} \cdot \mathbf{Q})_{ST} + C\mathbf{Q}\mathbf{Q}:\mathbf{Q}] \quad (8)$$

A, B, C are phenomenological coefficients.

\mathbf{Q} is a traceless and symmetric 2nd rank 3×3 tensor and so has five degrees of freedom. Accordingly, the equations of motion of the alignment tensor

when scaled appropriately, and expressed in the following orthonormalized basis:

$$\begin{aligned}
 \mathbf{Q} &= \sum_i a_i \mathbf{T}_i \\
 \mathbf{T}_0 &= \sqrt{\frac{3}{2}} (\hat{\mathbf{z}}\hat{\mathbf{z}})_{ST} \\
 \mathbf{T}_1 &= \sqrt{\frac{1}{2}} (\hat{\mathbf{x}}\hat{\mathbf{x}} - \hat{\mathbf{y}}\hat{\mathbf{y}}) \\
 \mathbf{T}_2 &= \sqrt{2} (\hat{\mathbf{x}}\hat{\mathbf{y}})_{ST} \\
 \mathbf{T}_3 &= \sqrt{2} (\hat{\mathbf{x}}\hat{\mathbf{z}})_{ST} \\
 \mathbf{T}_4 &= \sqrt{2} (\hat{\mathbf{y}}\hat{\mathbf{z}})_{ST}
 \end{aligned} \tag{9}$$

They yield the equations for the components $a_k, k = 0, 1, \dots, 4$ [51, 52].

In mean-field theory, the isotropic-nematic transition occurs at $A = A_* = 2B^2/9C$. As in [51, 52], we rescale time by the relaxation time τ/A_* at the isotropic-nematic transition, \mathbf{Q} as well by its magnitude at that transition. We choose $A = 0$ and $\alpha_1 = 0$ throughout. $\lambda_k (= -(2/\sqrt{3})\alpha_0)$, which is related to the tumbling coefficient in Leslie-Ericksen theory [51, 52], and $\dot{\gamma}$ are used as the control parameters to study the phase behavior of this system.

Further, the contribution of the alignment tensor to the deviatoric stress [52, 54, 55] is $\sigma^{OP} \propto \alpha_0 \mathbf{G} - \alpha_1 (\mathbf{Q} \cdot \mathbf{G})_{ST}$ where \mathbf{G} , defined in Eq. (8), is the nematic molecular field, and the total deviatoric stress is σ^{OP} plus the bare viscous stress which is a constant within the passive convection approximation. We therefore look at σ^{OP} alone.

We have integrated these equations using Runge-Kutta scheme with a fixed time step ($\Delta t = 0.001$). Depending on the model parameters entering the equations, the order parameter equations can have different characteristic orbits [51, 52]. Possible in-plane states, where as the name suggests, the principal director is in the plane of flow determined by the direction of the flow and its gradient and the order parameter components $a_3, a_4 = 0$ are ‘‘Tumbling’’ (T , in plane tumbling of the alignment tensor), ‘‘Wagging’’ (W , in plane wagging) and ‘‘Aligning’’ (A , in plane flow alignment) states. Out of plane solutions, characterized by non-zero values of a_3 and a_4 , observed are ‘‘Kayaking-tumbling’’ (KT , a periodic orbit with the projection of the main director in the shear plane describing a tumbling motion), ‘‘Kayaking-wagging’’ (KW , a periodic orbit with the projection of the main director in the shear plane describing a wagging motion, to be distinguished from the KT motion by the method adopted by Andrews *et al.* [56]) and finally ‘‘Complex’’ (C) characterized by complicated motion of the alignment tensor. This includes periodic orbits composed of sequences of KT and KW motion and chaotic orbits characterized by a positive largest Lyapunov exponent.

A solution phase diagram based on the various in-plane and out-of-plane states for $A = 0$ and $\alpha_1 = 0$ as given in [52] is shown in Figure 3. It is observed that $\alpha_1 \neq 0$ gives similar results. We focus on the C regime. The dynamics of the components of the order parameter for $\lambda_k = 1.25$, and $\dot{\gamma} = 3.693$ is shown in Figure 4. We now study the time evolution of rheological quantities like

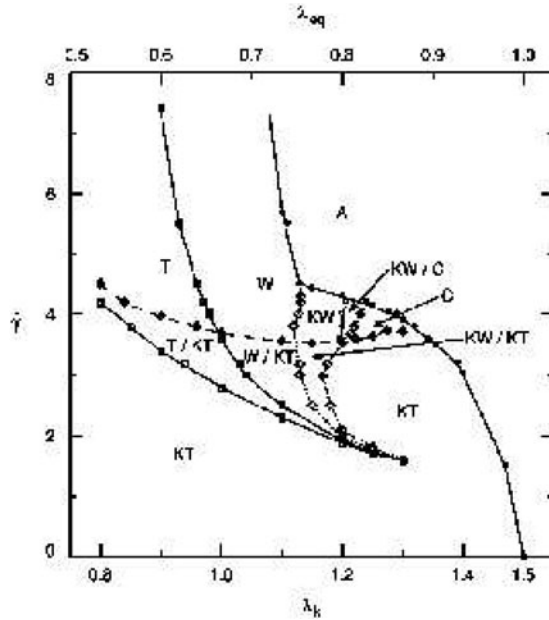


Figure 3. Phase diagram for the spatially uniform model of Rienecker *et al.* (Reprinted with permission from [51]. Copyright (2002) The American Physical Society)

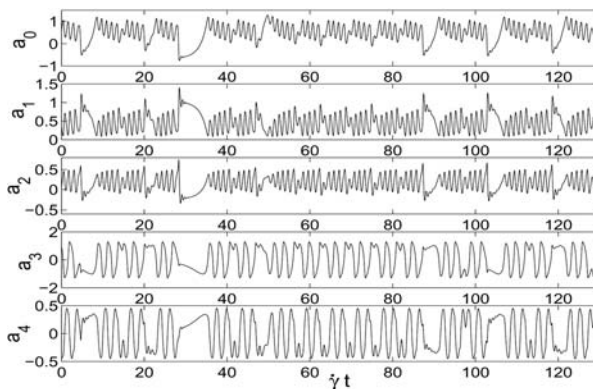


Figure 4. Different components of the order parameter as a function of time t for $\lambda = 1.25$, $\dot{\gamma} = 3.693$ for the spatially uniform case ($\Delta t = 0.001$) (Figure taken from [46]).

the shear stress σ_{xy}^{OP} (henceforth called Σ_{xy} for simplicity) and the first normal stress difference $\sigma_{xx}^{OP} - \sigma_{yy}^{OP}$ (called $\Sigma_{xx} - \Sigma_y$). The time variation of the shear stress shows features similar to the order parameter components. In Figure 5 we show the time variation of shear stress. We have thereafter calculated the time autocorrelation function of this signal and done a spectral analysis (Figure 6). The sharp peak corresponds to a period of $\simeq 45$. A wide range of frequencies is also seen in the plot of the power spectrum which are not in harmonics. This indicates that the signal is aperiodic and probably chaotic. Next we analyze the data train obtained by the numerical integration of the equations of motion described earlier. A surrogate data analysis is first performed on the time series of the shear stress to check for evidence of determinism. In this method,

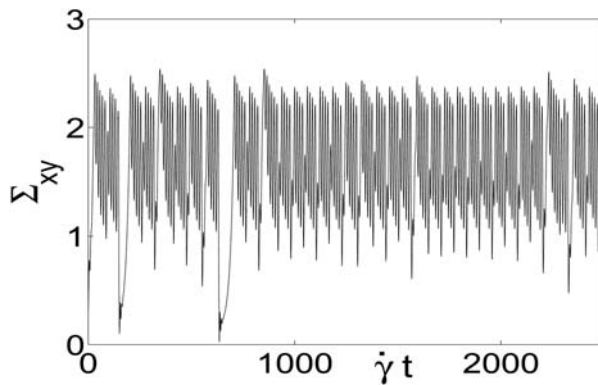


Figure 5. Time variation of the shear stress for $\lambda = 1.25, \dot{\gamma} = 3.693$ for the spatially uniform case. (Figure taken from [46]).

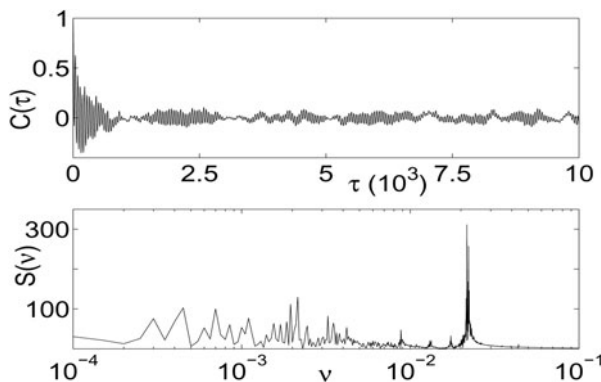


Figure 6. Autocorrelation function (top panel) and power spectrum (bottom panel) for the shear stress at $\lambda = 1.25, \dot{\gamma} = 3.693$ for the spatially uniform case (Figure taken from [46]).

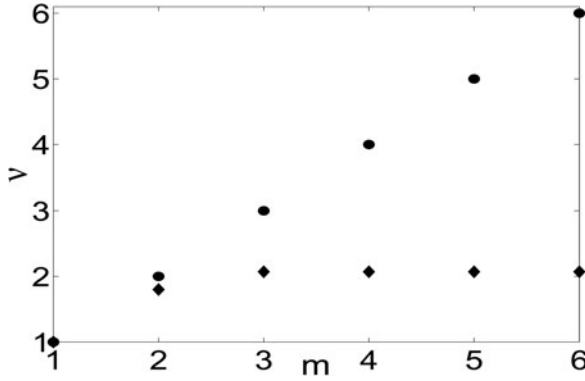


Figure 7. The correlation dimension ν [58] as a function of the embedding dimension m for the data corresponding to the shear stress for $\dot{\gamma} = 3.693$, $\lambda_k = 1.25$, $\alpha_1 = 0$ and $A = 0$ for the original data (diamonds) and surrogate data (circles) (Figure taken from [46]).

stochastic surrogate data are generated that have the same power spectra as the original, but have random phase relationships among the Fourier components. If any numerical procedures for studying chaotic dynamics produce the same results for the surrogates as for the original data, we cannot reject the hypothesis that the observed dynamics is generated by a linear stochastic model rather than representing deterministic chaos. We have plotted the correlation dimension ν as a function of the embedding dimension m for the original time series and the surrogate. It is seen in Figure 7, that ν increases with m for surrogates while for experimental time series, it initially increases and then saturates, thus confirming existence of determinism in the data.

We numerically estimate a few dynamical invariants (maximum Lyapunov exponent Λ_{\max} , the correlation dimension ν , embedding dimension m) to characterize the chaos. We then compare it with the experimental data of rheochaos in wormlike micelles in shear flow [12]. To this end, we use the non-linear time series analysis package (TISEAN) to analyze the chaotic data [57]. As has been pointed out earlier, in a situation where one is dealing with flow data of a single dynamical variable, it is useful to construct m dimensional vectors:

$$\vec{X}_i = (x_i, x_i + L_0, \dots, x_i + L_0(m - 1)), \quad (10)$$

m is the embedding dimension and L_0 is a delay parameter. Using \vec{X}_i , it is possible to calculate the correlation dimension ν [58], which describes the strange attractor on which the trajectories lie in the asymptotic limit [30]. The rate of divergence of neighboring trajectories is provided by the Lyapunov exponent λ which may be calculated using the method proposed by Gao and Zheng [31]. The estimated value of the correlation dimension, for the time-series of the shear stress for parameter values as mentioned in Figure 8 is $\nu \simeq 2.08$. We have

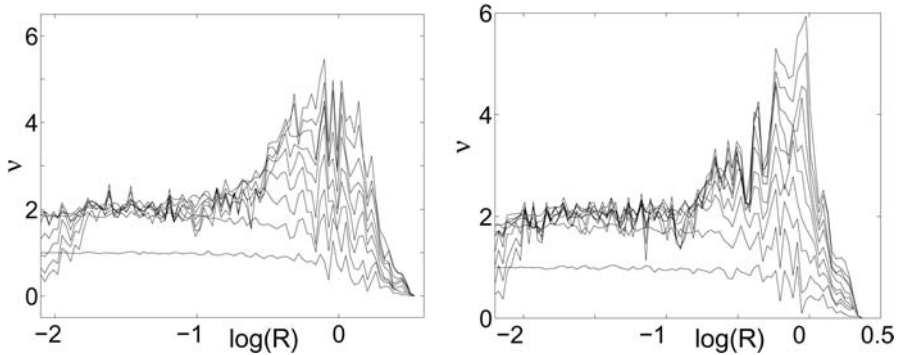


Figure 8. The correlation dimension ν [58] as a function of the average neighborhood for the first normal stress difference $\Sigma_{xx} - \Sigma_{yy}$ (left figure) and Σ_{xy} (right figure) for different embedding dimensions and $\dot{\gamma} = 3.693, \lambda_k = 1.25, \alpha_1 = 0$ and $A = 0$ (Figure taken from [46]).

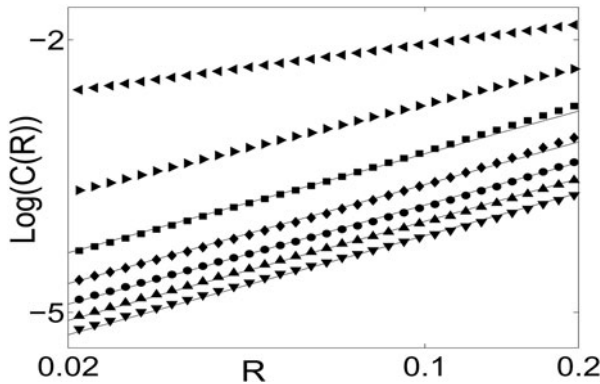


Figure 9. The correlation integral $C(R)$ [58] as a function of the average neighborhood R on a log-log scale for the first normal stress difference $\Sigma_{xx} - \Sigma_{yy}$ for various embedding dimensions for $\dot{\gamma} = 3.693, \lambda_k = 1.25, \alpha_1 = 0$ and $A = 0$. The topmost curve (denoted by left black triangles) corresponds to $m = 1$, and m increases as one moves progressively downward (Figure taken from [46]).

also calculated the largest Lyapunov exponent of the data train using the algorithm of [31] implemented using the TISEAN package [57]. The maximum Lyapunov exponent turns out to be $\simeq 0.0159$. The time series thus shows signatures of low dimensional chaos. The variation of the correlation dimension for the shear stress Σ_{xy} and the first normal stress difference $\Sigma_{xx} - \Sigma_{yy}$ as a function of the shear rate for the uniform problem is shown in Figure 10. It has been seen in experiments [12] that for sufficiently high values of the shear rate the correlation dimension $\nu \sim 2.7$. We have not seen such high values of the correlation dimension in any of our runs. We have also changed the shape

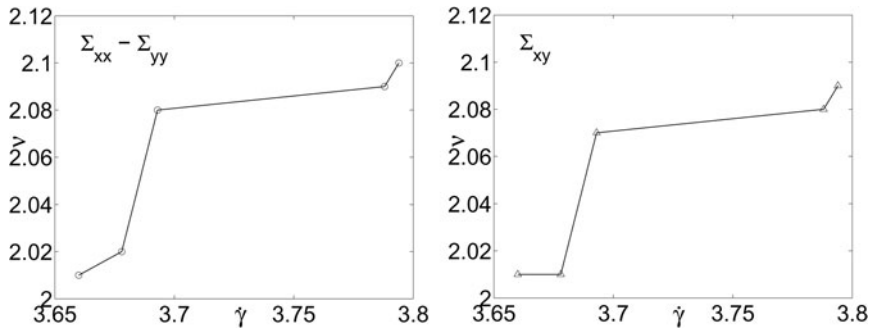


Figure 10. Variation of the correlation dimension ν for the first normal stress difference (left figure) with shear rate $\dot{\gamma}$ and for the shear stress with shear rate (right figure) in the C region of the phase diagram [51, 52], for $\lambda_k = 1.25$, $\alpha_1 = 0$ and $A = 0$ (Figure taken from [46]).

factor to a nonzero value $\alpha_1 = 0.4$ and calculated the dynamical invariants. It is seen that the correlation dimension does not change substantially. We have thereafter incorporated the spatial inhomogeneities in the model and looked for shear banding and spatio-temporal chaos in such a case.

3. Spatio-temporal Rheological Oscillations and Chaotic Dynamics

3.1. Theoretical Investigations of Spatio-temporal Rheochaos

3.1.1. In a shear-banding model with flow-microstructure coupling

Many complex fluids have non-linear rheological constitutive equations that cannot sustain a homogenous steady flow. This material instability occurs when shear versus strain rate curve is non-monotonic in nature, admitting multiple strain rates $\dot{\gamma}$ at a common stress Σ . Particularly for shear flow, it has been shown [59] that homogenous flow is linearly unstable in a region where the incremental shear viscosity is negative (i.e., $d\Sigma/d\dot{\gamma} < 0$). The system then undergoes a separation into two co-existing macroscopic shear bands at different shear rates arranged so as to match the total imposed shear gradient. Systems where the dynamic variables Σ or $\dot{\gamma}$ are coupled to microstructural quantities may admit many other possibilities – the flow may never be rendered steady in time, or it may become spatially inhomogeneous, erratic or both. Fielding and Olmsted studied one such scenario [60] in the context of shear thinning worm-like micelles where the flow is coupled to the mean micellar length n . They

propose a simple model of shear banding governed by the following equations:

$$\Sigma = \sigma + \eta\dot{\gamma} \quad (11)$$

$$\partial_t \sigma = -\frac{\sigma}{\tau(n)} + \frac{g[\dot{\gamma}\tau(n)]}{\tau(n)} + D\partial_y^2 \sigma \quad (12)$$

$$\partial_t n = -\frac{n}{\tau_n} + \frac{N(\dot{\gamma}\tau_n)}{\tau_n} \quad (13)$$

Here $g(x) = (x/1 + x^2)$, $N(x) = (n_0/1 + x^\beta)$, σ is micellar contribution to the shear stress, η is the solvent viscosity and inertia has been ignored. σ has a relaxation time $\tau(n)$ that depends on the mean micellar length n and a homogeneous steady state $\sigma = g[\dot{\gamma}\tau(n)]$ which allows a negative slope in the constitutive curve. τ_n is the relaxation time associated with n itself and can be used as a control parameter for tuning the strength of coupling between the mechanical quantities $(\Sigma, \sigma, \dot{\gamma})$ and microstructure n . They studied the flow between two parallel plates at $y = 0, L$ with boundary condition $\partial_y \Sigma = 0$, and parameter values as described in [60].

Upon thus varying the strength of the instability and the applied shear rate, they found a complex variety of spatio-temporal oscillations and chaotic shear banded flows. At low shear and weak instability, the induced phase pulsates in width while adhering to the wall of the flow cell, or meanders about the cell. For stronger instability, single or multiple high shear pulses are observed ricocheting back and forth across the cell (and also bouncing off each other in the case of multiple pulses). In this regime, once three or more such pulses are present, periodicity gives way to chaotic behavior. For an intermediate range of shear rates, one observes intermittency between these chaotic patterns and more regular oscillations. At high shear rates, regular oscillations of spatially extended bands on either side of a defect are found. In some cases, multiple defects exist and one finds oscillatory bands separated by defects moving across the cell to interact with each other, giving rise once again to erratic banded flow.

3.1.2. In nematic hydrodynamics

The equations for the uniform alignment tensor were analyzed in a previous section. We now study the equations of the traceless symmetric order parameter for a sheared nematic system, allowing for spatial variation [61]. Since nematic fluids possess long-range directional order, there is a penalty associated with the introduction of spatial inhomogeneities. In general, when the variable describing an ordered phase is fluctuating in space, the free energy density will also have terms corresponding to the energy cost in the form of bilinear gradients. So, the derivative of the Landau-deGennes free energy functional

now becomes:

$$\begin{aligned} \mathbf{G} \equiv -(\delta F/\delta \mathbf{Q})_{ST} = & -[A\mathbf{Q} - \sqrt{6}B(\mathbf{Q}\cdot\mathbf{Q})_{ST} + C\mathbf{Q}\mathbf{Q}:\mathbf{Q}] \\ & + \Gamma_1\nabla^2\mathbf{Q} + \Gamma_2(\nabla\nabla\cdot\mathbf{Q})_{ST} \end{aligned} \quad (14)$$

Here, we have considered only bilinears in $\nabla\mathbf{Q}$ in $F[\mathbf{Q}]$, the lowest order terms in such a correction in a series expansion both in powers of ∇ and \mathbf{Q} .

The equations of motion for the alignment tensor in this case are given by:

$$\begin{aligned} \frac{\partial \mathbf{Q}}{\partial t} + \mathbf{u}\cdot\nabla\mathbf{Q} = & \tau^{-1}\mathbf{G} + (\alpha_0\kappa + \alpha_1\kappa\cdot\mathbf{Q})_{ST} \\ & + \Omega\cdot\mathbf{Q} - \mathbf{Q}\cdot\Omega \end{aligned} \quad (15)$$

Hereafter, we express the equations in the same orthonormalized basis as described in the purely temporal study. As in that case, we rescale time by the relaxation time τ/A_* at the isotropic-nematic transition, \mathbf{Q} as well by its magnitude at that transition, and distances by the diffusion length made from Γ_1 and τ/A_* . The ratio Γ_2/Γ_1 of the Frank constants is therefore a free parameter which we have set to 1 in our study. We choose $A = 0$ and $\alpha_1 = 0$ throughout.

The resulting equations are then numerically integrated using a 4th order Runge-Kutta scheme with a fixed time step ($\Delta t = 0.001$). For all the results discussed here, a symmetrized form of the finite difference scheme involving nearest neighbors is used to calculate the gradient terms. The results are not changed if smaller values of Δt are used. The results do not change if the grid spacing is changed and more neighbors to the left and right of a particular site in question are used to calculate the derivative. This provides evidence that the results do reflect the behavior of a continuum theory and are not artifacts of the numerical procedure used. Boundary conditions have the director normal to the walls. With this, the first 6×10^6 time steps were discarded to avoid any possibly transient behavior. The time evolution of the system was monitored for the next 5×10^6 time steps (i.e., $t = 5000$), recording configurations after every 10^3 steps, and system sizes were varied from 100 to 5000. In the time-series analysis for the Lyapunov spectrum, simulation were run until $t = 20,000$, for a spatial system size of 5000, recording data at spatial points at gaps of 10. The space-time evolution of the shear stress (the xy component of the deviatoric stress σ^{OP}), referred to as Σ_{xy} , and the first and second normal stress differences were monitored.

First we address the question of whether the nature of the phase diagram changes upon the incorporation of the spatial degrees of freedom. This issue was addressed by constructing local phase portraits (plotting different components of the order parameter against each other) as a function of the parameters entering into the model, the shear rate $\dot{\gamma}$ and the tumbling parameter λ_k . Shown in Figure 11 are the local phase portraits for a particular point x_0 for various

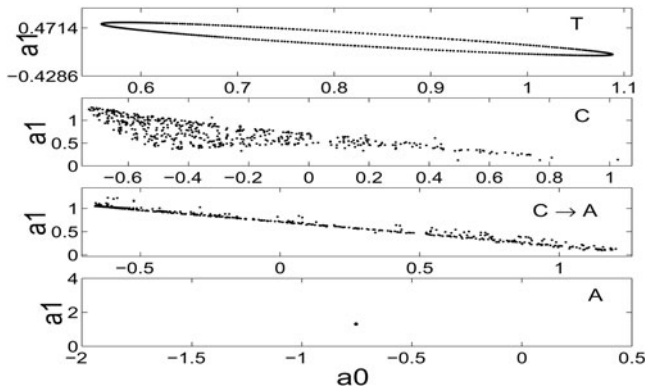


Figure 11. Plots showing $\alpha_1(x_0, t)$ vs $\alpha_0(x_0, t)$ for tumbling (panel T), chaotic (C), onset of aligning (C \rightarrow A) and aligning (A) regimes. (Reprinted with permission from [61]. Copyright (2004) The American Physical Society.)

shear-rates $\dot{\gamma}$, obtained by holding the value of the tumbling parameter fixed at $\lambda_k = 1.25$. The character of the phase portrait (space-filling or otherwise) remains intact upon going from one space point to another although there is no phase coherence between two such portraits. A closed curve corresponding to a limit cycle is seen in the tumbling region of parameter space (denoted by “T”) in the figure, while in the “C” region of the phase space, it is space filling. When one goes away from the “C” region of the phase space to the region where the director aligns with the flow the points reduce to those on a line and, eventually, in the aligning regime where the director has already aligned with the flow, it is represented by a point. This assures us that the local dynamics in the spatially extended case is similar to that of the ODEs of [51, 52].

We now focus at the detailed spatio-temporal structure of the phase diagram of this system. Many interesting phases are encountered, including spatio-temporally chaotic states, states showing periodicity in time and/or space, those showing dynamic shear banding, as well as a flow-aligned phase. Further, there are regions of parameter space where co-existing phases appear. The parameter values at which these are seen, furthermore, correspond well with the phase diagram of [51, 52].

Let us now focus on the parameter region labelled “C” or “Complex” in [51, 52], where spatio-temporal chaos is found. This regime is characterized by dynamic instability of shear bands (Figure 12). It shows several distinct events, such as the persistence, movement, and abrupt disappearance of shear bands. It is found that the typical length scale at which banding occurs is a fraction of the system size. As one moves closer to the phase boundary separating the spatio-temporally chaotic state from stable flow alignment, the bands become more persistent in time and larger in spatial extent (Figure 13).

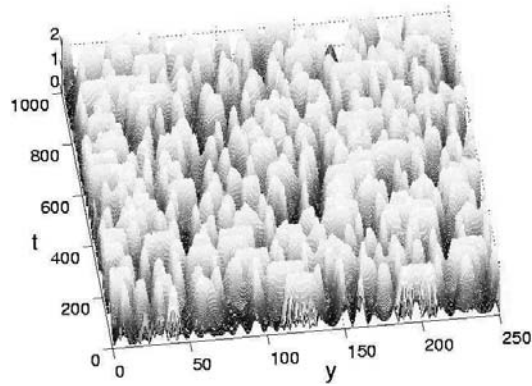


Figure 12. Space-time behavior of the shear stress in the chaotic regime, $\dot{\gamma} = 3.678$ and $\lambda_k = 1.25$. Spatial co-ordinate is along the x-axis, time is along y axis and shear stress along the vertical axis. Slice taken from a system of size 5000.

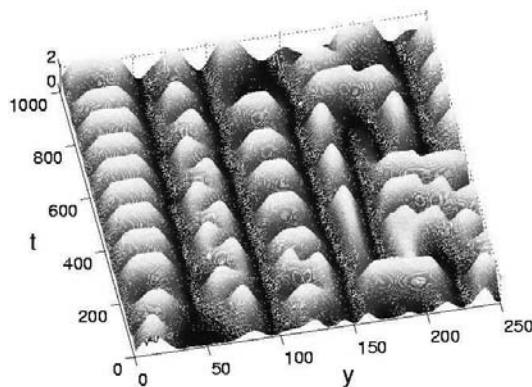


Figure 13. Space-time behavior (surface plots) of the shear stress in the chaotic to aligning regime, $\dot{\gamma} = 4.05$ and $\lambda_k = 1.25$. Slice taken from a system of size 5000.

It would be useful to obtain a better understanding of the disorderly structure of the shear bands in Figure 12 and compare it with the behavior seen close to the phase boundary in Figure 13. It is also essential to rule out any hidden periodicity in Figure 12. To this end, we look at the distribution of band sizes or spatial “stress drops”, and look for the presence of dominant length scales in the system. At a given time (say t_i), we define a threshold Σ_{0xy} , slightly above the global mean $\langle \Sigma_{xy} \rangle_{y,t}$, and map the spatial configuration to a space-time array of ± 1 : $\tilde{\Sigma}_{xy} = \text{sgn}(\Sigma_{xy} - \Sigma_{0xy})$. Figure 14 shows the histogram of the spatial length of intervals corresponding to the +state for the Chaotic and the Chaotic to

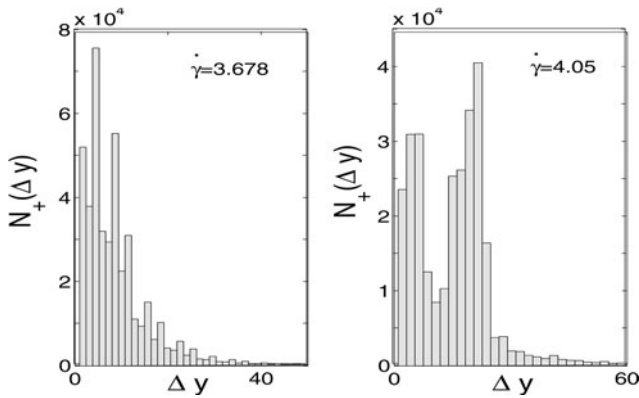


Figure 14. Spatial distribution of “stress drops” (corresponding to residence intervals in which the shear stress is above a threshold $\Sigma_{0xy} = 0.8$) in the Chaotic and $C \rightarrow A$ regimes.

Aligning ($C \rightarrow A$) regimes. We have considered configurations extending over 2500 spatial points, and the statistics is summed over configurations sampled at 5000 times (i.e., $i = 1, 5000$). As expected, the distribution of band lengths in the spatio-temporally chaotic regime is fairly broad and roughly exponential in shape, whereas in the Chaotic-to-Aligning regime, the distribution is peaked about a few dominant lengthscales. Also, note that as one moves away from the chaotic regime and towards the flow aligned regime, the dominant mode in the system grows in size.

We now monitor the approach to the spatio-temporally chaotic state as a function of the tumbling parameter λ_k , for a fixed value of $\dot{\gamma}$ ($= 3.8$). A sequence of states is observed. At low λ_k (1.0), the shear stress is periodic in time and homogeneous in space (Figure 15(a)). As λ_k is increased, states are encountered which are both spatially and temporally disordered (Figures 15(b) and (c)), consisting of patches of plane waves beset with highly irregular local structures and which resemble geometric patterns seen in cellular automata. These states are typical of what is known as “spatio-temporal intermittency” (STI) [62]. In contrast to low dimensional systems where intermittency is restricted to temporal behavior, STI manifests itself as a sustained regime where coherent-regular and disordered-chaotic domains coexist and evolve in space and time, and previous studies suggest a relation to directed percolation [62]. It has been further suggested that in systems showing spatio-temporal chaos, spatio-temporal intermittency should occur in the transition route from regular to chaotic states and indeed Figures 15(b) and (c) show complex irregular structures (high shear stress) intermittently present with more regular low shear regions. A detailed analysis of this route to the rheochaotic regime is presently underway [63]. In Figures 15(d) and (e), the system is in the chaotic regime. On passing from the chaotic towards the aligning regime, more regular structures are seen to

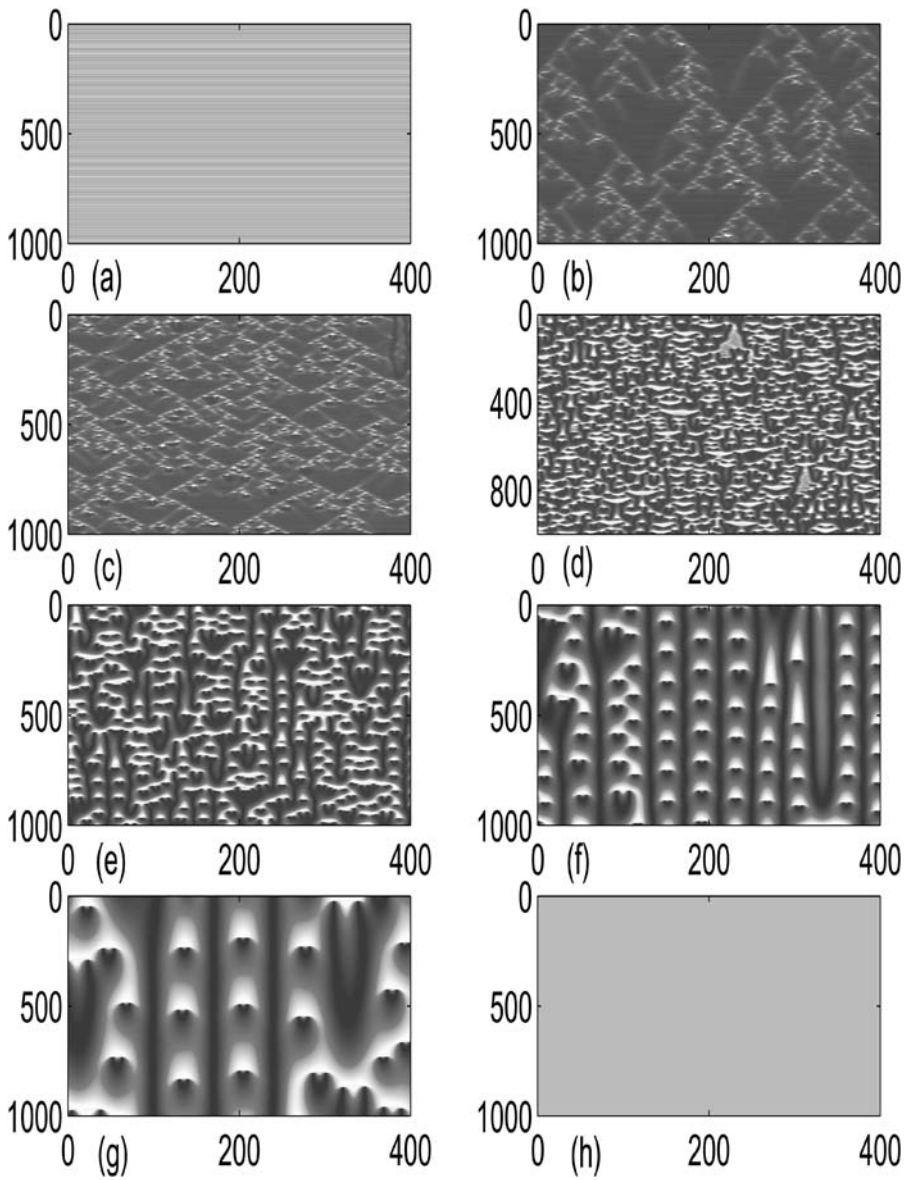


Figure 15. Space-time plots (space along horizontal axis and time along vertical axis) of the shear stress for $\dot{\gamma} = 3.8$ and $\lambda_k = 1.0, 1.115, 1.13, 1.2, 1.27, 1.3, 1.31$ and 1.32 . (Colormap used: “hot”, black (low shear stress) \rightarrow red \rightarrow yellow (high shear stress)). Slices taken from system of size 5000.

evolve (Figures 15(f) and (g)); the shear bands grow in spatial extent and are more long-lived. Figure 15(h) shows a snapshot of the shear stress in the flow aligned regime.

We now try to characterize the chaotic state. In studying dynamics of spatio-temporal systems, one has to establish whether the system is in a spatio-temporally chaotic regime or can be described by a model with only a few (dominant) independent modes. From the multivariate time-series generated by such systems, quantities analogous to the invariant measures used to characterize low dimensional chaos should be computed. However, spatially extended systems often have high dimensional attractors, with dimension growing with the system's spatial extent, and the estimation of invariants such as the correlation dimension can be very difficult. Indeed we find that the chaos that we observe is quite high dimensional (embedding dimension [32, 57] $m \geq 10$). A very long data train is then required for the analysis of the spatially averaged time series to yield a correct value of the correlation dimensions and would require a prohibitively long time to generate.

An alternative approach is to study the Lyapunov spectrum. It has been widely observed that the Lyapunov spectrum for spatio-temporal systems is an extensive measure (i.e., $\lambda_i = F(i/V)$ is a function depending on index i , rescaled by volume of the system V) [64]. Related invariant measures like the Kaplan-Yorke dimension, and number of positive Lyapunov exponents scale extensively with system size [65]. A consequence of the rescaling property of the Lyapunov spectrum is that instead of trying to study the spectrum and related quantities in a large and potentially infinite system of size N , one could confine the analysis to relatively small, more manageable subsystems of size N_s (i.e., at space points j in an interval $i_0 < j < i_0 + N_s - 1$, where i_0 is an arbitrary reference point), and study the scaling of these quantities with subsystem size N_s [57]. Thus, instead of trying to implement the correlation-dimension method for our spatially extended problem, we study the Lyapunov spectrum [57, 66]. Further, instead of studying systems of ever-increasing size, subsystems of size N_s in a given large system of size N are examined. For spatio-temporal chaos, we expect to find that the number of positive Lyapunov exponents grows systematically with N_s , which is what Figure 16 shows. The procedure has been carried out with two different reference points i_0 and essentially the same curves have been found. Furthermore, it has been reported in many studies of spatio-temporally chaotic systems [64] that when calculating the subsystem Lyapunov spectrum for increasing subsystem size N_s , the Lyapunov exponents of two consecutive sizes are interleaved (i.e., the i th Lyapunov exponent λ_i for the sub-system of size N_s lies between the i th and $(i + 1)$ th Lyapunov exponent of the subsystem of size $N_s + 1$). A direct consequence of this property is that with increasing subsystem size N_s , the largest Lyapunov exponent will also increase, asymptotically approaching its value corresponding to the case when the subsystem size \sim system size. This trend is clearly seen in Figure 16 (right).

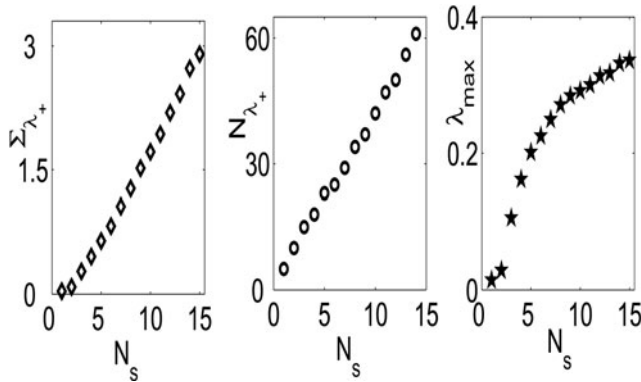


Figure 16. Sum of positive Lyapunov exponents (left panel), number of positive Lyapunov exponents (middle panel) and the largest Lyapunov exponent (right panel) as functions of subsystem size N_s , for $\dot{\gamma} = 3.678$, $\lambda_k = 1.25$, Embedding dimension for the time series of each space point is 10. ($i_0 = 101$, see text).

4. Proposed Experiments

In summary, we have discussed a few examples of viscoelastic systems where chaotic and irregular rheological response has been observed in experiments and in numerical calculations. In particular, the nonlinear relaxation of the order parameter in nematogenic fluids, together with the coupling of nematic order parameter to flow, are the key ingredients for rheological chaos in a variety of problems. The dynamics of the alignment tensor can be studied in rheo-optical experiments on dichroism [28], flow birefringence and rheo-small angle light scattering [67]. Recently, spatio-temporal dynamics of wormlike micelles in shear flow has been studied using high-frequency ultrasonic velocimetry [10], and various dynamical regimes, including slow nucleation and growth of a high-shear band and fast oscillations of the band position, have been observed, although the complex fast behavior reported is not chaotic. We look forward to experiments that measure directly the spatio-temporal structure of rheochaos in micellar and other systems such as self-assembled rod-like species in suspensions or gels formed with low molecular mass organic gelators.

Acknowledgments

MD acknowledges support from CSIR, India, and CD and SR from DST, India through the Centre for Condensed Matter Theory.

References

- [1] Larson, R. *The Structure and Rheology of Complex Fluids*, New York: Oxford University Press, **1999**.
- [2] Israelachvili, J.N. *Intermolecular and Surface Forces: With Applications to Colloidal and Biological Systems*, London: Academic, **1985**.
- [3] Rehage, H.; Hoffmann, H. *Mol. Phys.*, **1991**, *74*, 933.
- [4] Hu, Y.; Boltenhagen, P.; Matthys, E.; Pine, D.J. *J. Rheol.*, **1998**, *42*, 1209.
- [5] Kadoma, I.A.; van Egmond, J.W. *Phys. Rev. Lett.*, **1998**, *80*, 5679.
- [6] Wheeler, E.K.; Fischer, P.; Fuller, G.G. *J. Non-Newtonian Fluid Mech.*, **1998**, *75*, 208.
- [7] Spenley, N.A.; Cates, M.E.; McLeish, T.C.B. *Phys. Rev. Lett.*, **1993**, *71*, 939; Berret, J.F.; Roux, D.C.; Porte, G. *J. Physique II*, **1994**, *4*, 1261; Olmsted, P.D.; Lu, C.-Y.D. *Phys. Rev. E*, **1997**, *56*, R55.
- [8] Larson, R.G. *Rheol. Acta*, **1992**, *31*, 497.
- [9] Mair, R.W.; Calaghan, P.T. *Europhys. Lett.*, **1996**, *36*, 719.
- [10] Becu, L.; Manneville, S.; Colin, A. *Phys. Rev. Lett.*, **2004**, *93*, 018301.
- [11] Terech, P.; Ber. Bunsenges. *Phys. Chem.*, **1998**, *102*, 1630.
- [12] Bandyopadhyay, R.; Basappa, G.; Sood, A.K. *Phys. Rev. Lett.*, **2000**, *84*, 2022.
- [13] Bandyopadhyay, R. and Sood, A.K. *Europhys. Lett.*, **2001**, *56*, 447.
- [14] Bandyopadhyay, R.; Basappa, G.; Sood, A.K. *Pramana*, **1999**, *53*, 223.
- [15] Bandyopadhyay, R. Ph D Thesis, Indian Institute of Science, Bangalore, India, **2000**.
- [16] Salmon, J.-B.; Colin, A.; Roux, D. *Phys. Rev. E*, **2002**, *66*, 031505.
- [17] Wunenburger, A.S.; Colin, A.; Leng, J.; Arneodo, A.; Roux, D. *Phys. Rev. Lett.*, **2001**, *86*, 1374.
- [18] Dasan, J.; Ramamohan, T.R.; Singh, A.; Nott, P.R. *Phys. Rev. E*, **2002**, *66*, 021409.
- [19] Soltero, J.F.A.; Puig, J.E.; Manero, O. *Langmuir*, **1996**, *12*, 2654.
- [20] Spenley, N.A.; Cates, M.E.; McLeish, T.C.B. *Phys. Rev. Lett.*, **1993**, *71*, 939.
- [21] Cates, M.E.; Candau, S.J. *J. Phys. Condens. Matter*, **1990**, *2*, 6869.
- [22] Terech, P.; Coutin, A. *J. Chem. Phys. B*, **2001**, *105*, 5670; Terech, P.; Coutin, A. *Langmuir*, **1999**, *15*, 5513.
- [23] Others [23a] also observe non-Maxwellian behavior in micellar solutions (aqueous solution of the non-ionic surfactant polyoxyethylene sorbitan trioleate) at all frequencies and concentrations except at very low concentrations. [a] Teipel, U.; Heymann, L.; Aksel, N. *Experiments in Fluids* **2001**, *30*, 584.
- [24] Grand, G.; Arrault, J.; Cates, M.E. *J. Phys. II (France)*, **1997**, *7*, 1071.
- [25] Berret, J.-F.; Roux, D.C.; Porte, G. *J. Phys. II (France)*, **1994**, *4*, 1261.
- [26] Porte, G.; Berret, J.-F.; Harden, J.L. *J. Phys. II (France)*, **1997**, *7*, 459.
- [27] Ott, E. *Chaos in Dynamical Systems*, Cambridge: Cambridge University Press, **1993**.
- [28] Mewis, J.; Mortier, M.; Vermant, J.; Moldenaers, P. *Macromol.*, **1997**, *30*, 1323.
- [29] Noronha, S.J.; Ananthakrishna, G.; Quaouire, L.; Fressengeas, C.; Kubin, L.P. *Int. J. of Bifurcation and Chaos*, **1997**, *7*, 2577.
- [30] Grassberger, P.; Procaccia, I. *Phys. Rev. Lett.*, **1983**, *50*, 346; *Physica D*, **1983**, *9*, 189.
- [31] Gao, J.; Zheng, Z. *Phys. Rev. E*, **1994**, *49*, 3807.
- [32] Kennel, M.B.; Brown, R.; Abarbanel, H.D.I. *Phys. Rev. A*, **1992**, *45*, 3403.
- [33] Brandstater, A.; Swinney, H.L. *Phys. Rev. A*, **1987**, *35*, 2207.
- [34] Berret, J.-F.; Gamez-Corrales, R.; Lerouge, S.; Decruppe, J.-P. *Eur. Phys. J. E.*, **2000**, *2*, 343.
- [35] Cates M.E.; Candau, S.J. *Europhys. Lett.*, **2001**, *55*, 887.

- [36] Gamez-Corrales, R.; Berret, J.-F.; Walker, L.M.; Oberdisse, J. *Langmuir*, **1999**, *15*, 6755; Berret, J.-F.; Gamez-Corrales, R.; Oberdisse, J.; Walker, L.M.; Lindner, P., *Europhys. Lett.*, **1998**, *41*, 677.
- [37] Groisman, A.; Steinberg, V. *Nature*, **2000**, *405*, 53.
- [38] Cladis, P.E.; van Saarloos, W. In *Solitons in Liquid Crystals*, L. Lam and J. Prost, Eds., New York: Springer, **1992**, pp. 136–137, find “director turbulence” in nematics in cylindrical Couette flow.
- [39] Manneville, P. *Mol. Cryst. Liq. Cryst.*, **1981**, *70*, 223.
- [40] Satheesh Kumar, K.; Savitri, S.; Ramamohan, T.R. *Jpn. J. Appl. Phys.*, **1996**, *35*, 5901.
- [41] Berry, D.H.; Russel, W.B. *J. Fluid Mech.*, **1987**, *180*, 475.
- [42] Radhakrishnan, K.; Ashokan, K.; Dasan, J.; Chandrasekhara Bhat, C.; Ramamohan, T.R. *Phys. Rev. E*, **1999**, *60*, 6602.
- [43] Cates, M.E.; Head, D.A.; Ajdari, A. *Phys. Rev. E*, **2002**, *66*, 025202.
- [44] Aradian, A.; Cates, M.E. Proceedings of the 3rd International Symposium on Slow Dynamics in Complex Systems AIP Conference Proceedings, Melville, N.Y., T. Tokyama, I. Oppenheim, Eds., **2004**, Vol. 708, p. 87.
- [45] This model predicts damped oscillations in the shear stress in controlled shear rate conditions, however our studies on this model and its variants did not observe any chaotic oscillations [46].
- [46] Chakrabarti, B., Ph.D. Thesis, Indian Institute of Science, Bangalore, India, **2003**.
- [47] Hess, S.; Naturforsch, Z. **1975**, *30a*, 728; Pereira Borgmeyer, C.; Hess, S. *J. Non Equil. Thermodyn.*, **1995**, *20*, 359.
- [48] Forster, D.; Lubensky, T.C.; Martin, P.C.; Swift, J.; Pershan, P.S. *Phys. Rev. Lett.*, **1971**, *26*, 1016.
- [49] Leslie, F.M. *Quart. J. Mech. Appl. Math.*, **1966**, *19*, 357; Ericksen, J.L. *Arch. Ration. Mech. Anal.*, **1960**, *4*, 231; Stephen, M.J. *Phys. Rev. A*, **1970**, *2*, 1558.
- [50] Rieuaecker, G.; Hess, S. *Physica A*, **1999**, *267*, 294.
- [51] Rieuaecker, G.; Kroeger, M.; Hess, S. *Phys. Rev. E*, **2002**, *66*, 040702(R).
- [52] Rieuaecker, G.; Kroeger, M.; Hess, S. *Physica A*, **2002**, *315*, 537.
- [53] De Gennes, P.G.; Prost, J. *The Physics of Liquid Crystals*. Oxford: Clarendon, **1995**.
- [54] Forster, D. *Phys. Rev. Lett.*, **1974**, *32*, 1161; Doi, M. *Polym. J. Sci. Polym. Phys. Ed.*, **1981**, *19*, 229.
- [55] Olmsted, P.D.; Goldbart, P.M. *Phys. Rev. A*, **1990**, *41*, 4578.
- [56] Andrews, N.C.; McHugh, A.J.; Edwards, B.J. *J. Rheol.*, **1996**, *40*, 459.
- [57] Hegger, R.; Kantz, H.; Schreiber, T. *CHAOS*, **1999**, *9*, 413.
- [58] The correlation integral $C(R)$ gives the number of point pairs separated by a distance less than R . For small R , $C(R) \sim R^\nu$, where the *correlation dimension* ν gives us information about the local structure of the attractor. The exponent ν is obtained as a function of $\log R$ from the slopes of the plots of $\log C(R)$ vs $\log(R)$. A plateau in the plot of ν vs $\log R$ gives the correct ν for a chosen embedding dimension m . The value of m at which this saturation sets in is the correct value of the embedding dimension m_o .
- [59] Katz, S.; Shinnar, R. *Chemical Engineering Science*, **1970**, *25*, 1891.
- [60] Fielding, S.M.; Olmsted, P.D. *Phys. Rev. Lett.*, **2004**, *92*, 084502.
- [61] Chakrabarti, B.; Das, M.; Dasgupta, C.; Ramaswamy, S.; Sood, A.K. *Phys. Rev. Lett.*, **2004**, *92*, 055501.
- [62] Chate, H.; Manneville, P. *Physica D*, **1988**, *32*, 409; Kaneko, K. *Progr. Theoret. Phys.*, **1985**, *74*, 1033; van Hecke, M. *Phys. Rev. Lett.*, **1998**, *80*, 1896; Janaki, T.M.; Sinha, S.; Gupte, N. *Phys. Rev. E*, **2003**, *67*, 056218.
- [63] Das, M.; Chakrabarti, B.; Ramaswamy, S.; Dasgupta, C.; Sood, A.K. *Phys. Rev. E*, **2005**, *71*, 021707.

- [64] Carretero-Gonzalez, R.; Orstavik, S.; Stark, J. *Chaos*, **1999**, *9*, 466; Orstavik, S.; Carretero-Gonzalez, R.; Stark, J. *Physica D*, **2000**, *147*, 204; Carretero-Gonzalez, R.; Bunner, M.J., unpublished results.
- [65] Pande, A. Ph.D. Thesis, Indian Institute of Science, explores spatiotemporal chaos in a wide variety of systems, **2000**.
- [66] Sano, M.; Sawada, Y. *Phys. Rev. Lett.*, **1985**, *55*, 1082.
- [67] Berghausen, J.; Fuchs, J.; Richtering, W. *Macromolecules*, **1997**, *30*, 7574.

Chapter 7

WETTING OF FIBERS

Elise Lorenceau¹, Tim Senden², and David Quéré¹

¹*Laboratoire de Physique de la Matière Condensée, UMR 7125 du CNRS, Collège de France, 75231 Paris Cedex 05, France*

²*Department of Applied Mathematics, Research School of Physical Sciences and Engineering, The Australian National University, Canberra, ACT 0200 Australia*

1. Introduction	223
2. The Rayleigh-Plateau Instability	224
3. Drop Shapes	225
3.1. Axisymmetric Shapes	226
3.2. Asymmetric Droplets	227
4. Heterogeneous Fiber	230
5. Invasion of a Network of Fibers	231
6. Conclusions and Perspectives for the Future	236

1. Introduction

The capillary length is defined as the length for which surface tension and gravity balance each other. It is typically of the order of one millimeter for a liquid/air system. For interfaces with dimensions larger than the capillary length, gravity dominates the shape the interface takes. Conversely, for small interfaces, capillary forces dictate the shape. Flow in a confined geometry such as a capillary tube, fiber or fiber networks will therefore be driven by capillary morphology and surface effects. In this chapter, we focus on the behavior of liquids on single fibers and move onto fibrous networks. First, the formation of drops on a fiber is considered, analyzing their shapes, with emphasis on the existence of axisymmetric and asymmetric drops. Next, wetting along conical fibers, and finally within a network of fibers is treated. In both of these systems, the substrate curvature is not homogeneous, and leads to displacement of liquid in order to decrease surface energy.

2. The Rayleigh-Plateau Instability

The most famous effect associated with the wetting of fibers is the Rayleigh-Plateau instability, which takes place when a continuous wetting liquid film is deposited on a fiber. This may be achieved by drawing the fiber out of a bath of liquid, or by the condensation of a vapor. In both cases, the film will generally break into a regular array of droplets, as shown in Figure 1. This instability was first observed by Plateau [1] in a simple liquid jet in which liquid flowing from a nozzle breaks into drops about 50 cm below the nozzle. Such arrays of droplets can be observed on dew-covered spider webs early in the morning. Indeed spiders use this very phenomenon to uniformly space sticky globules along their snare lines.

The driving force of this instability is the interfacial tension between the liquid and the surrounding medium, usually air. That is, the array of drops has a smaller surface area than the cylinder from which they arise. More generally, and provided that the wavelength of the instability is large enough, undulating the surface of the liquid/air interface lowers the overall energy. This is a remarkable feature of a cylindrical geometry and can be understood by considering the Laplace pressure across the liquid interface, given by:

$$\Delta P = \gamma C = \gamma \left(\frac{1}{R_1} + \frac{1}{R_2} \right) \quad (1)$$

Here, γ is the liquid/air interfacial tension with a surface of curvature, C . It can alternatively be stated in terms of the two principal radii of curvature, R_1 and R_2 . The pressure in a cylindrical film is thus constant and equal to γ/R , where R is the radius of that cylinder. Fluctuations, external or thermal in origin, can cause the cylinder of liquid to undulate, in turn modulating the pressure. Provided the wavelength of the instability is large enough, the pressure in a trough becomes larger than in a bump. Thus the trough will continue to empty liquid into the bump, and the instability will grow until separate drops are formed (Figure 1). Note that gravity does not deform the resulting drops. This is understood by examining the balance of pressures in the system. While the



Figure 1. Pattern resulting from the spontaneous destabilization of a film of (wetting) silicone oil deposited on a cylinder of radius $b = 100 \mu\text{m}$.

typical Laplace pressure across the cylinder is γ/R , the difference of hydrostatic pressure between the topside and the bottom of the fiber is $2\rho gR$, where ρ is the liquid density. Hence, gravity can be neglected for cylinders of radius smaller than $\sqrt{\gamma/\rho g}$, the so-called capillary length, which is in the millimeter range for most liquids.

More precisely, the difference in surface energy ΔE between an undulating film and a flat film can be evaluated on a length equal to one wavelength λ :

$$\Delta E = \int_0^\lambda 2\pi(b+t)\gamma ds - 2\pi(b+t_0)\gamma\lambda \quad (2)$$

b is the radius of the fiber, t is the modulated thickness of the film and t_0 is the initial thickness of the film. If the amplitude, ε , of the corrugation is not too large, Eq. (2) becomes Eq. (3):

$$\Delta E = \frac{1}{4}\gamma \frac{\varepsilon^2}{b+t_0} 2\pi\lambda(q^2(b+t_0)^2 - 1) \quad (3)$$

ΔE decreases if the wave number of the corrugation, q , is larger than the inverse of the radius of the cylinder. Hence, if the wavelength of the perturbation is larger than the circumference of the cylinder, a film longer than $2\pi(b+t_0)$ will break spontaneously into several droplets.

Note that this simple analysis does not discriminate between all unstable modes ($\lambda > 2\pi(b+t_0)$). The kinetics of growth of the unstable modes can be calculated, as first done by Lord Rayleigh [2] who found that the fastest mode corresponds to a wavelength of about $10(b+t_0)$, in very good agreement with the experimental observations of Plateau. We will now analyze the shape of the droplets resulting from this instability, and focus on the origins of their asymmetry.

3. Drop Shapes

Because of the fiber curvature, a drop on a fiber has a shape very different from one on a plate, particularly in the limit of complete wetting. A drop spreading on a plate thins until it vanishes, while the same liquid will persist on fibers as drops (see Figure 1). This behavior explains why it is often said that fibers “cannot be wetted” by liquids. Indeed they can, but the wetting film will coexist in general with drops, whose shape is dictated by the existence of two antagonistic curvatures close to the ends of the drop. We will first focus on this symmetric case, and then describe the possible existence of non-axisymmetric drops.

3.1. Axisymmetric Shapes

Droplets observed in Figure 1 are highly axisymmetric. Their shape is deduced from a condition of constant curvature, and found by integrating Eq. (1), as shown by Carroll [3, 4]. Neglecting gravity (i.e., considering a drop of radius much smaller than the capillary length), the two radii of curvature can be written as a function of the polar angle, ϕ , defined in Figure 2:

$$\gamma \left(\cos \phi \frac{d\phi}{dx} + \frac{\sin \phi}{x} \right) = \Delta P \quad (4)$$

This equation can be integrated once, taking into account the boundary conditions at the edge and at the apex of the drop ($x = h$, $\phi = \pi/2$ and $x = b$, $\phi = \theta$, where θ is the contact angle of the drop on the fiber). We deduce the pressure across the drop in Eq. (5) where $n = h/b$ (see Figure 2).

$$\Delta P = \frac{2\gamma}{b} \left(\frac{n - \cos \theta}{n^2 - 1} \right) \quad (5)$$

If the liquid totally wets the fiber ($\theta = 0$), as in Figure 1, then Eq. (5) simplifies to Eq. (6):

$$\Delta P = \frac{2\gamma}{b + h} \quad (6)$$

This formula is consistent with the particular geometry of the fiber: when the volume of the drop tends toward zero ($h \rightarrow b$), ΔP tends to γ/b , the pressure across a cylinder of radius b . In this case, we expect drops to be nearly cylindrical. On the other hand, if the radius of the fiber tends toward zero for a drop of given volume, ΔP is equal to $2\gamma/h$, the pressure across a sphere of radius h . A thin fiber will hardly deform a large drop which becomes nearly spherical [5].

The profile, length, liquid/air surface area and volume of the drop can also be derived analytically as a function of the maximal radius of the drop h , the fiber radius b and the contact angle θ , using Eq. (4) – in which the constant

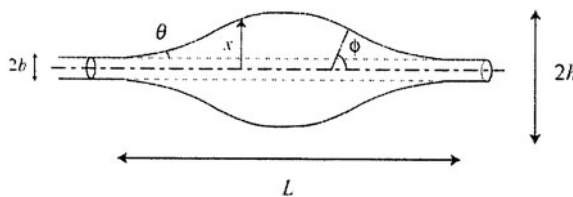


Figure 2. Sketch of a drop of length L , of maximal radius h , deposited on a fiber of radius b . The liquid wets the fiber with a contact angle θ .

ΔP is known and given by Eq. (5). Thus we can describe very accurately the shape of these axisymmetric, so-called unduloidal, drops [3, 5, 6].

Those formulas can be used to calculate the evolution of shape of a drop as a function of the different parameters of the system: volume, fiber radius or contact angle. In Figure 3 the “cylinder-like” and “sphere-like” behaviors described above can be seen as a function of maximal drop volume. The maximal radius of a drop deposited on a fiber of $150\ \mu\text{m}$ radius has been displayed as a function of the volume of the drop. For large volumes, the radius is found to increase with the volume as a power law of exponent $1/3$ – a signature of the sphere-like regime – and for a small volume the maximal radius tends toward a constant value slightly above $150\ \mu\text{m}$ (the fiber radius), which is a characteristic feature of a cylinder-like regime.

3.2. Asymmetric Droplets

There are two main reasons for a drop to be asymmetric (i.e., the influence of partial wetting or gravity). Figure 4 shows what can happen in partial

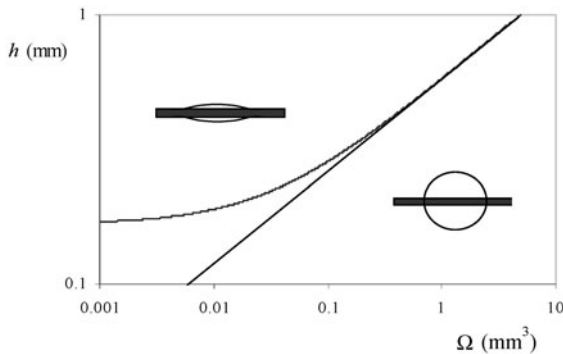


Figure 3. Calculated maximum radius of a drop deposited on a fiber of (given) radius $r = 150\ \mu\text{m}$, as a function of the volume of the drop. The thin line indicates the slope $1/3$.

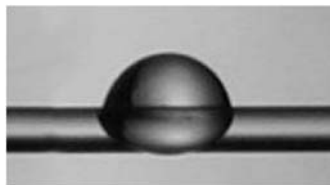


Figure 4. Drop in a partial wetting condition (water on fiber nylon of $100\ \mu\text{m}$ radius) adopting an asymmetric shape. The drop is pointing upward showing that it is not deformed by gravity.

wetting. If the contact angle is large enough, the drop is indeed found to be asymmetric, simply because this conformation is of lower surface energy than an axisymmetric case.

If the contact angle depends on an external parameter (such as an electric field, or adsorption of surfactants), the drop is observed to roll up if the contact angle is larger than some threshold value. This threshold decreases with the drop volume. This process is important in detergency, as noted by Adam [7], since an asymmetric grease drop sticks less to the fiber than a symmetric one and is therefore easier to detach. The value of this critical angle was calculated by Carroll and McHale, who characterized how it depends on the radius of the drop and of the fiber [8–11].

Asymmetric configurations can also be induced by an external field acting on the drop (gravity or electric field). For drops hanging in a gravity field, this effect will be relevant for drops of size comparable to the capillary length $\kappa^{-1} = \sqrt{\gamma/\Delta\rho g}$, where $\Delta\rho$ denotes the density difference between the two fluids. Kumar *et al.* [12] focused on the influence of gravity for drops deposited on a vertical fiber – hence in the limit where the external field and the fiber axis are aligned.

Figure 6 displays photographs of drops of silicon oil in air hanging from a horizontal fiber of radius $b = 12\mu\text{m}$, hence in the limit where gravity is perpendicular to the fiber axis [12]. The drops are of increasing volume from left to right. It can be observed that the shape of the drop changes as its volume increases: the two smallest drops are symmetric (as expected in this wetting situation), but the largest ones are asymmetric. In particular the larger the drop,

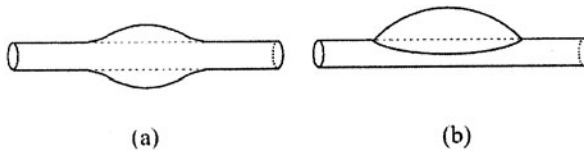


Figure 5. A drop deposited on a fiber can adopt two different conformations (a) axisymmetric or (b) asymmetric.



Figure 6. Drops of silicon oil of various volumes ($\Omega = 0.01, 0.10, 0.23, 0.32$ and 0.52 mm^3 , from left to right) hanging from a horizontal fiber of radius $b = 12\mu\text{m}$.

the lower its centre of mass, which stresses the increasing influence of gravity. The fiber is here much smaller than the capillary length κ^{-1} , which is of order 1.5 mm for silicon oils. However, the largest drops have a diameter of 1000 μm and approach the capillarity limit.

All the drops in Figure 6 are static, which shows that gravity (for large drops) can be balanced by capillary forces. Obviously, this equilibrium cannot hold for very large drops: a capillary force is bounded, while the drop weight increases as R^3 (with R the drop radius) – we thus expect a threshold radius R_M above which a drop will detach. We note the corresponding threshold volume Ω_M (with $\Omega_M = 4\pi R_M^3/3$). Figure 7 shows a sequence of events occurring when the drop size slightly exceeds Ω_M .

This quantity can be measured, and Figure 8 shows how R_M varies as a function of the fiber radius (both quantities are normalized by the capillary length and plotted in logarithmic scales).

It is observed that all the data collapse along the same curve despite the range in capillary lengths. Moreover, we observed that for large fiber radii, R_M saturates at a constant value of $1.6\kappa^{-1}$. Then, the substrate curvature becomes very small and the liquid behaves as if it were hanging from a flat solid surface. The maximal volume Ω_M of such a pendant drop must scale as κ^{-3} , since



Figure 7. Set of pictures showing a drop of silicon oil falling off a fiber of radius $b = 350 \mu\text{m}$. The volume of the drop is just above Ω_M , so that gravity dominates the capillary force: the drop falls (interval between two successive pictures: 1 ms).

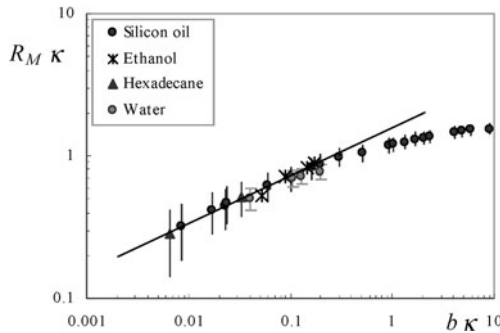


Figure 8. Radius R_M of the largest drop hanging on a fiber, as a function of the fiber radius b . Both quantities are normalized by the capillary length κ^{-1} , and are drawn in logarithmic coordinates.

the capillary length is the only length in the system. Padday [14] numerically calculated this volume and found Ω_M to be equal to about $19 \kappa^{-3}$, which yields $R_M = 1.65 \kappa^{-1}$, in very good agreement with the observations. For thin fibers ($b \ll \kappa^{-1}$), R_M is found to scale as $b^{1/3} \kappa^{-2/3}$. This again is quite logical, since the capillary force and the weight scale as γb and $\rho g R_M^3$, respectively. The balance between these two forces indeed leads to the observed scaling.

4. Heterogeneous Fiber

A drop will be at equilibrium if its pressure (expressed in Eqs. (5) and (6) is constant. If a fiber is not homogeneous in radius, and here we shall consider the simple case of a conical fiber, the pressure in the drop axis will not be constant. Provided that there is no contact angle hysteresis, the axial pressure gradient is likely to induce a motion, as first noticed by Carroll [15].

Such a situation is reported in Figure 9, where a drop of silicone oil is observed to spontaneously move on a conical copper wire (of conicity of about 10^{-2}), towards the region of larger radius. This can be easily understood by considering Eq. (6), which shows that the pressure in a drop depends on the fiber radius: the smaller the radius, the larger the internal pressure – a drop deposited on a conical fiber will indeed move towards large radii, as described [16].

This phenomenon is of particular interest if one considers the impregnation of a heterogeneous cluster of fibers, since a conical fiber can be seen as a model substrate which helps to study the influence of heterogeneity in the curvature substrate. Hence the drops shall always move toward the regions of small curvature which are typically the overlaps in a fiber bed. Moreover, this motion can be exploited for drying a solid, even if forced to be coated with a film (which can be achieved either by a relative motion between the liquid and the solid, or by exposing the latter to a vapor which condenses on it). It can be seen in Figure 10 that films are driven towards regions of large radius, which stresses that such cones could be used as efficient condensers, large surface

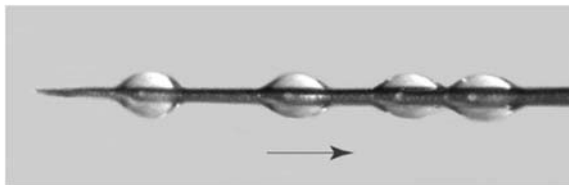


Figure 9. Multi-exposed photograph of a millimetric drop of silicone oil on a tapered copper wire. The time interval between two pictures is 1.6 s, and it is observed that the drop moves towards the region of low curvature. (Reprinted with permission from [16]. Copyright Cambridge University Press.)



Figure 10. Successive snapshots (interval between each picture: 10 s) showing the evolution of a liquid film (thickness between 8 and 25 μm) made of silicone oil ($\eta = 20$ mPa.s and $\gamma = 20$ mN/m) deposited on a conical fiber (of radius between 100 and 300 μm). (Reprinted with permission from [16]. Copyright Cambridge University Press.)

areas being coated and “pumped” towards thicker regions where the liquid can be collected, without the use of any motor.

5. Invasion of a Network of Fibers

In many applications, fibers are gathered together to comprise a structure designed to imbibe liquids. In one extreme this problem can be treated in an academic exercise as an assembly of parallel fibers packed together with hexagonal order. The criterion of wicking in such a porous medium is the same as for a capillary tube: comparing this medium empty and full of liquid, we see that the difference between the two situations is the replacement of a dry surface (of surface energy γ_{SV}) by a wet one (of surface energy γ_{SL}). The surface energy is thus lowered if we have: $\gamma_{\text{SL}} < \gamma_{\text{SV}}$. Using Young’s relation ($\gamma_{\text{SV}} - \gamma_{\text{SL}} = \gamma \cos \theta$), which expresses the link between the different surface tension and the contact angle θ (of the liquid on the solid, with air around), we find that the criterion of wicking can be written equivalently: $\theta < 90^\circ$.

This wetting criterion is much more difficult to define for a random assembly of fibers, as we shall see in the case of paper. Then, supposing that the liquid invades the assembly, the size and shape of the meniscus is not clearly specified, and it is likely to vary along the progression of the liquid. In some regions where the fibers get further from each other, the meniscus radius increases as the liquid progresses, as does the surface energy associated with this meniscus, making the progression less likely. Conversely, as the liquid goes in more confined regions, the meniscus radius gets smaller, making the liquid invasion more favorable in these regions.

We can try to go further by describing flow into such a complex fiber web and show that competition between local capillaries and global interconnectivity results in observed penetration rates. In the process which ultimately forms

the sheet, many factors dictate the interconnectivity within the fiber web. The physical and chemical heterogeneity has a great influence over preferred flow paths. However, one can generalize about the way fibers are associated with their neighbors. Fibers emerge from the refining process as millimeter long hollow tubes of about 20 microns in diameter. These tubes typically collapse during sheet formation so the fibers form flat, but very flexible ribbons less than 10 microns thick. Where fibers overlap they can flatten and bond, which locks the web in place, creating on average 80 fiber overlaps per millimeter of fiber, with over 3000 fibers per mm^2 [17]. The way in which the sheet is formed also aligns the fibers so the plane of the ribbons is largely oriented parallel to the sheet, with a very low degree of cross-over from one layer to the next.

The structure is of course highly porous and, in the maze of fibers, it is difficult to see which course a liquid might take in wetting the sheet. Figure 11 illustrates some of the potential pathways for liquid conduction. The shape a wetting front creates as it moves over an interface is dictated by surface curvature and interfacial energy, and in paper there are four different structures which offer potential flow paths. In order of increasing capillary pressure they are voids or “pores” formed between fibers (Figure 11b), channels formed by overlapping fibers (Figure 11c), surface roughness on individual fibers, and intra-fiber porosity.

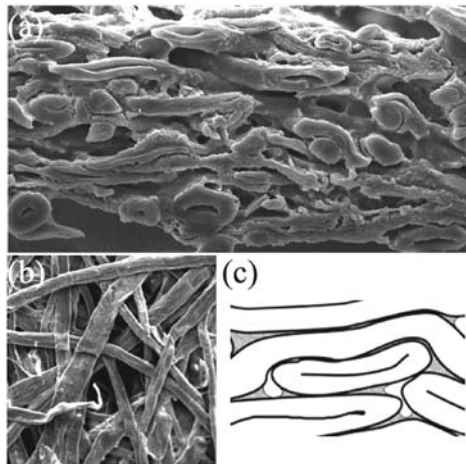


Figure 11. (a) A scanning electron micrographic cross-section through a 100 micron thick sheet of paper showing the complexity of the fiber arrangement. (b) Viewed from above the sheet a surface void, seen center, produced between intersecting fibers gives the impression of a “pore”. (c) A schematic illustrating the concave channels formed between overlapping fibers. Liquid menisci can be seen in the wedge-shaped channels. Fibers also possess surface roughness on the sub-micron scale, see (b), and some intra-fiber micro-porosity. Courtesy of Dr. R. J. Roberts.

The “pores” at the surface of paper generally range from 20–50 microns and have highly irregular cross-sections. Within a few fibers depth they typically diverge into other voids and are characterised by many surface discontinuities. Fluid negotiating these structures is faced with a range of opening diameters in which to span. Small voids may fill, only to be constrained at the openings of larger voids.

The channels formed by overlapping fibers present the next available path flow. Here the wedge-shaped channels typically have included angles of $< 90^\circ$ with a depth of a few microns. From the work of Hasuike *et al.* [17], it is clear that the massive density of fiber overlaps forms a vastly interconnected network. Surface roughness over the fiber and micro-porosity within it contribute to the final pathways, and have structures well below a micron in scale.

While all structures do play some role in the overall wetting profile, only the channels created between overlapping fibers can maintain interconnectedness on the fiber-scale. This conclusion results from the direct microscopic observation of wetting films in paper [18], and is depicted in Figure 12. Here the imbibing front is seen frozen in time, moving from top to bottom. Clearly, the areas of fiber overlap show film flow, which thicken with time allowing voids to fill. The films closest to the drop (top) are clearly thicker than those at the extremities. Note that the tops of the fibers remain dry, which demonstrates that fiber roughness does not contribute significantly to film flow. Here the probability of pinning on top of a convex fiber surface is clearly higher than along the concave channel formed between overlapping fibers. Thus, given the choice, a film finds the path of highest capillary pressure and proceeds.

While it may not be surprising that the advancing front is via film flow, the extent and use of inter-fiber channels is revealing. The language of describing

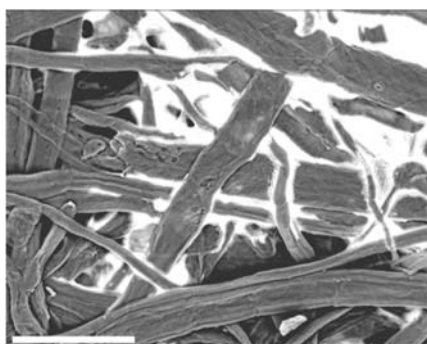


Figure 12. Unsized paper snap-frozen the instant a droplet of water began to wick into the fibers. The wetting front was moving from the top of the image down. See Roberts *et al.* [18] for details of this cryogenic SEM technique. Scale bar = 100 microns. Courtesy of Dr. R. J. Roberts.

flow in interconnected channels was first introduced by Lenormand *et al.* [19] where they investigated the competition between piston-like flow and film flow in model systems. They demonstrated that network connectivity and channel morphology are crucial in determining the overall rate of impregnation. This follows from their observation that surface inhomogeneities pin and delay meniscus advance until films have found a path around the discontinuity. Where films thicken and disconnect an air filled void, they coined the term “snap-off”. This mechanism of pore filling can be a rate limiting process in many porous systems. This delay in local imbibition may ultimately cost the “race” as an adjacent, but competing film can forge ahead depleting the first film. Piston-like flow then occurs as a “rear guard” action behind the advancing films.

Without knowledge of film flow, it has been convenient in the past to consider the voids as the primary wetting path. Misleadingly, these voids have been called “pores,” leading to the broad use of the Lucas-Washburn equation in the literature, which simply models the web as a series of circular non-connected, parallel capillaries. To support this approach, techniques such as mercury porosimetry have provided effective pore size distributions. Being a non-wetting liquid, however, mercury has no opportunity to fill via film flow and gives information only about the large inter-fiber voids. In a highly connected structure like paper the higher propensity to pin on a fiber surface precludes extensive flow paths around single fibers, and greatly restricts piston flow through voids. In the case of spontaneous imbibition, the voids are the final structures to fill, and only have a chance to fill once all pinning has released the wetting film to form an unsupported concave meniscus (“snap-off”) (Figure 13). The smaller the void the better chance it has of filling, but in general this is completely dependant on the local configuration of fibers, and one frequently observes incomplete saturation of paper.

Figure 14 shows a tomographic cross-section through a saturating paper where several unfilled sub-surface voids can be seen.

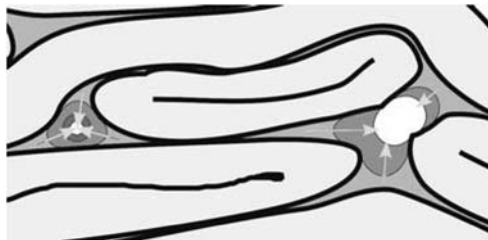


Figure 13. Internal voids may (left) or may not (right) fill depending on propensity to pin the wetting films.



Figure 14. A section through the mid-plane of a paper sheet using X-ray tomography. Again the liquid, flowing from top to bottom, has been snap-frozen during wetting and is seen in light grey, with voids as dark to black. Note the voids shown do not connect with either surface of the sheet and represent trapped air. Scale bar = 350 microns.

It can be very instructive to first consider the impregnation of a single horizontal circular cavity: a capillary tube. The rate of penetration is determined balancing the viscous pressure loss with the driving Laplace pressure that leads to the well-known Lucas-Washburn equation [20]:

$$H = \left(\frac{R\gamma}{2\eta} \right)^{1/2} t^{1/2} \quad (7)$$

Here, t denotes the time, H is the height of liquid in the tube of radius R , and γ and η are the liquid/air surface tension and viscosity, respectively. As examined recently, Washburn does predict the correct scaling of $t^{1/2}$ for impregnation rate of liquid by a paper [21], but it over estimates the observed rate by more than an order of magnitude [18]. This overestimation stems from both the failure to take into account the channel geometry (wedge versus tube), and the network of interconnected channels. The latter has inherent delays built into the way a film must negotiate surface discontinuities [22].

A predictive model for overall rate is not obvious. The problem cannot be posed in terms of very slow wetting which would give rise to uniform film thickness in all channels. Although convenient, since voids would simply fill based on size alone, such a model would be unrealistic. The finite rate of impregnation in channels implies that films are thicker nearest the liquid source, and thin towards the extremities. Even complete knowledge of a network of the channel connectivity would require computer simulation to test the range of solutions possible.

We have not considered here the other components often found in paper, such as filters and sizing agents, or chemical heterogeneity. In reality, these obey the same principals as above, and can be viewed as simply adding to the array of alternative capillary networks within paper. An advancing film continuously determines which of two capillaries is more favorable. Film flow remains the dominant mode of wetting, and interconnectivity a crucial factor.

6. Conclusions and Perspectives for the Future

We have considered the wetting of fibers in different configurations. Firstly, we considered the size and shape of drops supported by a single fiber. We have shown that a cylindrical fiber of arbitrary length can only hold a quantity of liquid that is bound. The volume of liquid is mainly in the drop, therefore gravity eventually overcomes capillary forces. On the contrary, a surface of varying curvature – an infinite conical fiber – can pump the liquid and drain it toward regions of large radius. The amount of liquid that can be sustained by a conical fiber is therefore not limited. Then, we have focused on spontaneous impregnation into paper, where the displacement is assumed to be dominated by capillary forces. The rate of penetration increases with the square root of time as in a diffusive process. A more rigorous treatment of the complex dynamics of frontal displacements requires accounting for film swelling, pore filling and viscous pressure gradients associated with flow through films. The dynamics of film flow, pore filling near and away from the front and the simultaneous filling of multiple pores via films and filled throats ahead of the front can lead to very different behaviors that are only now being considered.

A question of obvious interest in the perspective of molecular gels concerns the possibility of extending the ideas described here to the case of molecules that assemble into nanofibers. Recent experiments performed with nanotubes show that capillary phenomena resist quite well a reduction of the size (the question of the renormalization of the macroscopic quantities such as the surface tension being the subject of active research today). Single wall nanotubes generally form bundles, whose penetration by a wetting liquid should thus compare to what is found with other assemblies of fibers. Nanocapillarity is indeed a very natural extension of research in this field during the next several years.

References

- [1] Plateau, J.A.F. *Statique expérimentale et théorique des liquides soumis aux seules forces moléculaires*, Paris: Gauthier-Villars, **1873**.
- [2] Lord Rayleigh. “On the instability of a cylinder of viscous liquid under capillary force”, *Phil. Mag.*, **1892**, 34, 145.

- [3] Carroll, B.J. “The accurate measurement of contact angle, phase contact areas, drop volume and laplace excess pressure in drop-on-fiber systems”, *J. Colloid Interface Sci.*, **1976**, 57, 488.
- [4] Carroll, B.J. “The equilibrium of liquid drops on smooth and rough circular cylinders”, *J. Colloid Interface Sci.*, **1984**, 97, 195.
- [5] Joanny, J.F. *Le mouillage, quelques problèmes statiques et dynamiques*. PhD Thesis, Université Paris VI, **1985**.
- [6] Bauer, C.; Dietrich, S. “Shapes, contact angles, and line tensions of droplets on cylinders”, *Phys. Rev. E*, **2000**, 62, 2428.
- [7] Adam, N.K. “Detergent action and its relation to wetting and emulsification”, *J. Soc. Dyers Colour*, **1937**, 53, 122.
- [8] Carroll, B.J. “Equilibrium conformations of liquid drops on thin cylinders under forces of capillarity”, *Langmuir*, **1986**, 2, 248.
- [9] McHale, G.; Käb, N.A.; Newton, M.I.; Rowan, S.M. “Wetting of a high-energy fiber surface”, *J. Colloid Interface Sci.*, **1997**, 186, 435.
- [10] McHale, G.; Newton, M.I. “Global geometry and the equilibrium shapes of liquid drops on fibers”, *Colloids and Surfaces A*, **2002**, 206, 79.
- [11] McHale, G.; Newton, M.I.; Carroll, B.J. “The shape and stability of small liquid drops on fibers”, *Oil & Gas Science and Technology*, **2001**, 56, 47.
- [12] Kumar, A.; Hartland, S. “Shape of a drop on a vertical fiber”, *J. Colloid Interface Sci.*, **1988**, 124, 67.
- [13] Lorenceau, E.; Clanet, C.; Quéré, D. “Capturing drops with a thin fiber”, *J. Colloid Interface Sci.*, **2004**, 279, 192.
- [14] Padday, J.F.; Pitt, R.A. “The stability of axisymmetric menisci”, *Phil. Trans. Roy. Soc. Lond.*, **1974**, 275, 489.
- [15] Carroll, B.J. “The equilibrium of liquid drops on smooth and rough circular cylinders”, *J. Colloid Interface Sci.*, **2004**, 97, 195.
- [16] Lorenceau, E.; Quéré, D. “Drops on a conical wire”, *J. Fluid Mech.*, **2004**, 510, 29.
- [17] Hasuike, M.; Kawasaki, T.; Murakami, K. “Evaluation method of 3D geometric structure of paper sheet”, *J. Pulp Paper Sci.*, **1992**, 18, J114.
- [18] Roberts, R.J.; Senden, T.J.; Knackstedt, K.A.; Lyne, M.B. “Spreading of aqueous liquids in unsized papers is by film flow”, *J. Pulp Paper Sci.*, **2003**, 29, 123.
- [19] Lenormand, R.; Zarcone, C.; Sarr, A. “Mechanisms of displacement of one fluid by another in a network of capillary ducts”, *J. Fluid Mech.*, **1983**, 135, 337.
- [20] Washburn, E.W. “The dynamics of capillary flow”, *Phys. Rev.*, **1921**, 17, 273.
- [21] Bico, J.; Quéré, D. “Precursors of impregnation”, *Europhys. Lett.*, **2003**, 61, 348.
- [22] Senden, T.J.; Knackstedt, M.A.; Lyne, B. “Droplet penetration into porous networks: Role of pore morphology”, *Nordic Pulp and Paper Journal*, **2000**, 15, 554.

TECHNIQUES

Chapter 8

GEL FORMATION: PHASE DIAGRAMS USING TABLETOP RHEOLOGY AND CALORIMETRY

Srinivasa R. Raghavan and Bani H. Cipriano

Department of Chemical Engineering, University of Maryland, College Park, MD 20742, USA

1. Introduction	241
2. Detecting the Sol-Gel Transition by Tabletop Rheology	242
2.1. Tube Inversion	243
2.2. Falling of Spheres	245
2.3. Rise of Bubbles	246
2.4. Other Methods	246
3. Thermodynamics of Gelation: Sol-Gel Transition by Calorimetry	247
3.1. First- and Second-Order Phase Transitions	248
3.2. The Question of Gelation	248
3.3. Calorimetry of the Sol-Gel Transition	250
3.4. Gelation Temperature vs. Gelator Concentration	250
4. Conclusions and Perspectives	251

1. Introduction

In previous chapters, we have attempted to define the term “gel” in a consistent and meaningful way, while recognizing that the gel state is often easier to recognize than to define (if it looks like “Jell-O”, feels like “Jell-O”, and responds like “Jell-O”, it must be a gel [1]). This leads us to the theme of the present chapter, the elucidation of phase diagrams and composition maps for molecular gels. Typically, this is the first step in a given study. Other chapters are devoted to detailed analyses of gels and their phase transitions (see Chapters 1–4).

Molecular gel samples are usually prepared by dissolving low molecular-mass organic gelator (LMOG) in a liquid, usually by warming [1]. At this point,

the gelator is unaggregated or in small aggregates and this system is referred to as a *sol*. The sol is then cooled below a transition temperature whereupon it transforms into a *gel*. Typically, the higher the gelator concentration c , the higher is the *sol-gel* transition temperature T_g and a plot of T_g against c constitutes a phase boundary. A phase diagram is a map of T vs. c showing the sol-gel boundaries as well as the boundaries of any multi-phase or lyotropic liquid crystal regions that are also present. Most articles on molecular gels usually have an accompanying phase diagram.

While studying gelators, especially those with novel structures, the focus is on determining the entire phase diagram rapidly and using as little gelator as is practically feasible. Thus, there is a need for simple, reliable, and convenient techniques for phase characterization. Two such techniques fit the bill and are widely used by practitioners for a broad range of molecular gelators:

- (1) **“Tabletop” rheological techniques:** These are techniques such as the tube inversion and falling sphere methods that have a rheological basis. More detailed analyses of rheological properties of gels are found in Chapters 5 and 6.
- (2) **Thermal characterization methods:** In particular, differential scanning calorimetry (DSC).

We will now consider these two techniques systematically in the rest of this chapter. A variety of other techniques that are useful in studying specific types of gelators are discussed in Chapters 9–13.

2. Detecting the Sol-Gel Transition by Tabletop Rheology

The definitive signature of a gel is its elastic rheological response, or more precisely, the presence of a *non-zero equilibrium modulus* G_e [2]. There are two alternative ways of stating the same idea: the gel should *not relax* under a small mechanical stress even if given an infinitely long time; or the gel should *not flow* under the action of a mechanical stress imposed for an infinite period of time. The former condition implies an infinite relaxation time t_R in a linear viscoelastic test while the latter stipulates the existence of a yield stress σ_y below which no flow occurs, i.e., below which the viscosity is infinite. Note that the stipulated conditions do not preclude relaxation or flow occurring at higher (nonlinear) stresses or strains.

The existence of gel-like rheological properties in a sample can be qualitatively diagnosed by simple (“tabletop”) experimental tests without using a rheometer. Such tests, which rely on visual observation and feel, are particularly useful in evaluating the sol-gel boundary. In a typical study, samples are placed in a bath at constant temperature and their physical state (sol or gel) is noted, for instance, by tube inversion. The bath temperature is then varied and

the samples are equilibrated at a new temperature, whereupon their physical state is again recorded. This process is repeated over the temperature range of interest. Alternately, instead of equilibration, a slow heating or cooling rate (e.g. $<1^\circ/\text{min}$) may be imposed. Through these studies, a plot of T_g versus gelator concentration c can be obtained.

We consider below some of the common “tabletop” tests for gelation that have a rheological basis. A discussion of gelation and gel point based on standard rheological measurements (using a rheometer) is given in Chapters 5, 6, and 19.

2.1. Tube Inversion

The most common diagnostic test of gelation is to turn a test-tube or vial containing the sample upside-down and then to note whether the sample flows under its own weight (Figure 1). It is assumed that a sample having a yield stress (gel) will not flow whereas a viscous but inelastic sample (sol) will show appreciable flow [3]. The simplicity of this test makes it the method of choice in phase behavior studies with molecular gels.

Care must be taken in conducting and interpreting tube inversion experiments. It is easy to mistake a viscous sol for a gel and conversely, to misinterpret a gel with a small yield stress to be a sol. To understand why, we will consider the basis for the tube inversion test. Before doing so, it is useful to recall that the yield stress σ_y is given by [3]:

$$\sigma_y = G \cdot \gamma_c \quad (1)$$

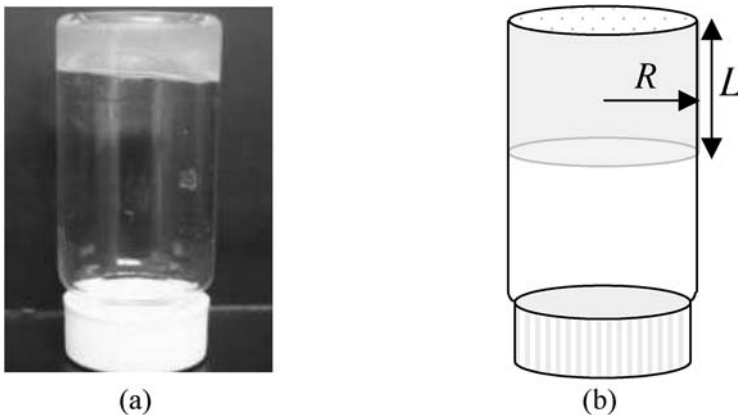


Figure 1. (a) Photograph of a gel from the author’s lab that satisfies the tube inversion test; (b) The test sample is idealized as a cylinder of radius R and length L .

G is the gel modulus and γ_c is the critical strain that marks the linear viscoelastic limit (critical strain at yield). The gel modulus signifies the stiffness or rigidity of the network, while the critical strain denotes the strength of bonds in the network. Thus, for σ_y to be high, both G and γ_c should be high.

In the tube inversion test, consider a sample with yield stress σ_y placed in a cylindrical vial of radius R , with the length of the vertical column of sample being L (Figure 1b). The sample mass is $\pi R^2 L \cdot \rho g$, where ρ is the sample density and g the acceleration due to gravity. The condition for static equilibrium, from the von Mises yield criterion, balances the yield stress with the gravitational stress [4]:

$$\sigma_y \cong \rho g \cdot L \quad (2)$$

It is assumed here that the sample yield coincides with the disruption of the network structure in the gel.

Equation (2) shows that the tube inversion test is dependent on both sample mass and vial size. The column height L is proportional to sample mass and density, and inversely related to vial size for a given mass. When using this test for phase behavior determination, it is therefore crucial to use the *same sample mass and vial type* (geometry, size).

Rheological tests can confirm the approximate yield stress values indicated by tube inversion. For example, Booth *et al.* [5, 6] studied aqueous gels of block copolymers using both tube inversion and conventional rheometry. They used 0.5 g of each sample in tubes of 1 cm internal diameter. Under these conditions, samples of yield stress $\sigma_y \geq 40$ Pa were able to hold their own weight indefinitely. Incidentally, this value is in rough agreement with Eq. (2).

The time of observation can also influence the outcome of tube inversion experiments. To understand this, consider how a highly viscous but inelastic sample would behave in the same inverted geometry as in Figure 1b. In this case, the sample would move (flow) downward by a distance ε over a time t under the action of gravity. An approximate expression for ε is obtained by balancing the gravitational and viscous stresses [4]:

$$\frac{\varepsilon}{t} \cong \frac{\rho g L R}{\eta} \quad (3)$$

Here, it is assumed that the sample viscosity η is invariant with shear-rate. This equation shows that a high viscosity can inhibit motion of the sample. Using a high value of η , say 10^5 Pa · s (a very reasonable value for a pre-gel) together with typical geometry conditions suggests that a sample may move only a few millimeters in a couple of minutes. Thus, based on a short period of observation, the motion detected may be so negligible that one may erroneously classify the sample as a gel. To prevent such mistakes, a sufficiently large observation time must be employed in tube inversion experiments. Experiments with a

test fluid such as honey (a highly viscous but inelastic fluid) may be used to gauge timescales with viscous fluids and thereby to “calibrate” the geometry of choice.

2.2. Falling of Spheres

A second method used for determining the onset of gelation is to examine the motion of small spherical particles suspended in the sample (Figure 2). This method is an adaptation of the Stokes’ law problem to yield stress fluids. A quantitative criterion has been derived by Beris *et al.* [7] assuming that the fluid can be approximated as a Bingham fluid (i.e., no flow till the yield stress; Newtonian flow at higher shear stresses). Their prediction is that a spherical ball of size R_b and density ρ_b will not fall in a fluid of density ρ and yield stress σ_y provided [4, 7]:

$$\sigma_y > 0.095(\rho_b - \rho)g \cdot R_b \quad (4)$$

It is clear from Eq. (4) that the particle size and density dictate the balance between gravitational stress and the yield stress. This intuitive picture is illustrated by Figure 2 where the settling of spheres of different sizes and densities is shown in a range of viscoelastic polymeric fluids [8]. The Xanthan gum and Carbopol[®] samples are physical gels that have appreciable yield stresses and hence are able to suspend dense spherical particles for more than a month [8].

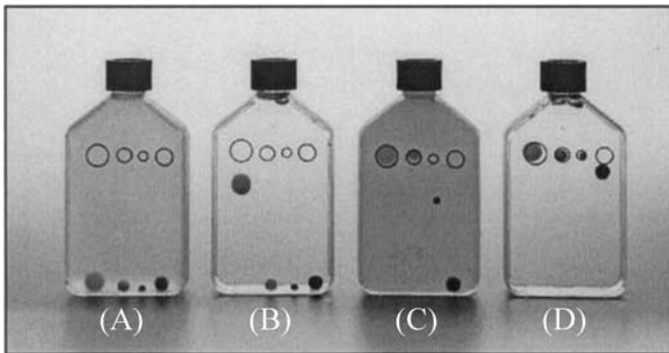


Figure 2. Photograph of the falling sphere test in a series of viscoelastic or gel-like fluids. The circles show the initial position of the test spheres, whereas this photograph was taken after one month of storage. The four spheres in each flask correspond to different sizes and densities: the furthest to the left is a low-density plastic sphere, while that at the rightmost is made of high density steel. The four samples are aqueous solutions of: (A) 2.1% guar gum; (B) 2.3% carboxymethyl cellulose; (C) 6% Xanthan gum; (D) 0.4% Carbopol[®] 940F. (Reproduced with permission from [8]. Copyright Noveon, Inc.)

In using sphere settling for characterizing molecular gels, the ideal scenario is for the sphere to remain immobile in the gel phase, but to rapidly settle in the sol phase. For this, it is preferable to use a dense ball (e.g., of steel or other metal) that is also sufficiently large. An important precaution is that the sample tube or vessel should be much larger than the test sphere – if this is not so, the presence of nearby walls can influence the motion of the sphere [9]. However, eliminating wall effects completely would require an impractically large amount of sample, so a compromise between accuracy and process economics has to be reached. Finally, it is also important that the sphere settle from rest – most gels tend to be shear thinning fluids and if the sphere is dropped into the fluid with a force, the fluid in the local vicinity may be thinned, thus promoting further downward motion of the sphere [9]. A simple way to ensure settling from rest is to place a dense ball *on top* of the gelled material within a sealed vial [10].

2.3. Rise of Bubbles

A third method for evaluating the gel-like nature of a sample is to observe the motion of bubbles in a sample. Bubbles can either be injected specifically for this test or they may remain in the sample after preparation. The essential idea is that bubbles will remain trapped in a gel whereas they will slowly rise to the surface in a viscous fluid [11]. Note that the bubble rise problem is mathematically identical to the settling sphere problem in Newtonian fluids and thus, the rise velocity is expected to inversely scale with the fluid viscosity. Therefore, to distinguish between a viscous sol and a gel requires long periods of observation.

Bubble rise may still be a useful test for certain gels. When a sample is heated, the bubbles tend to rise faster. Thus, for gels that form only upon heating, the trapping of bubbles may provide a stark contrast between sols and gels. Likewise, techniques that are used to remove bubbles can serve as a “quick and dirty” rheological indicator. For example, if gel samples are routinely centrifuged to remove bubbles, then the persistence of bubbles after various extents of centrifuging (speed and duration) may offer a rapid qualitative gauge of both the sol-gel boundary as well as the variation of yield stress or gel modulus among different samples.

2.4. Other Methods

In principle, any method used to measure the yield stress can also be used to devise a rheological criterion for gelation. The rheological literature reports several inexpensive approaches to measure yield stress, most of which are

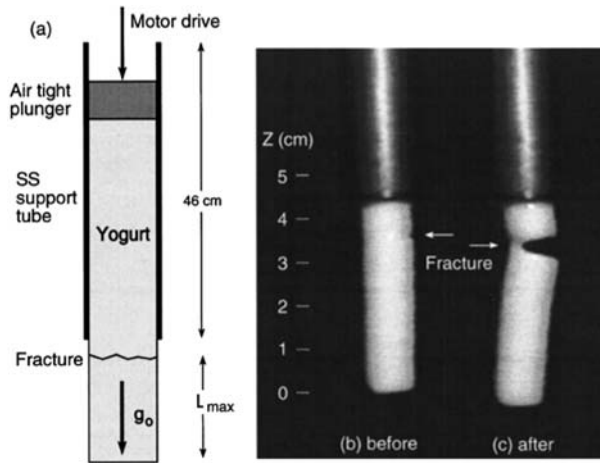


Figure 3. Extrusion of gel (yogurt) cylinders to measure their yield strength. A schematic of the configuration used is shown in (a). When the extruded length exceeds L_{\max} , the gel fractures. Images taken (b) before and (c) after fracture of the sample are also shown. (Reproduced with permission from [4]. Copyright American Institute of Physics.)

variations on the themes explored above. For example, instead of tube inversion, it is also possible to use an inclined plane, with the yield stress correlating with the thickness up to which the sample stays intact on the plane [12].

A further variation on the inverted tube removes the influence of the container walls [4]. Here, a sample is *extruded* through a tube (Figure 3), exposing a piece of gel to gravitational tension. The maximum length L_{\max} at which the gel fractures can be correlated to the yield stress, in a manner analogous to Eq. (2), as long as L_{\max} greatly exceeds the radius of the tube. Figure 3 shows a demonstration of this test with a yogurt gel.

Finally, Boger *et al.* [13] also showed how to develop a “50 c rheometer” by utilizing the **slump test**. This method was originally used to determine the flow properties of fresh concrete. Here, a cylindrical frustum is filled with the sample and then the frustum is lifted off, allowing the sample to collapse under its own weight. The difference between the initial and final heights (i.e., the slump height) is inversely related to the yield stress.

3. Thermodynamics of Gelation: Sol-Gel Transition by Calorimetry

A second approach for constructing gelator phase diagrams is using thermal characterization techniques such as differential scanning calorimetry (DSC).

Before we discuss this topic further, it is useful to briefly review the thermodynamics of gelation. The same topic is discussed in much more detail in Chapter 1.

3.1. First- and Second-Order Phase Transitions

Is the sol-gel transition a first- or second-order process? There have been many conflicting views on this issue, and we mention only the key points here. First, let us distinguish between these two types of transitions [14].

First-order transitions are sharply defined – all molecules undergo the transition in unison, provided there is sufficient thermal energy. Thus, quantities that are first derivatives of the chemical potential μ , such as the enthalpy H and specific volume V , change discontinuously at the transition. Second derivatives of μ like the heat capacity c_p (i.e., dH/dT) show a singularity (i.e., the system has an infinite heat capacity at the transition temperature). First order transitions typically proceed by a *nucleation and growth* mechanism and hence often exhibit metastabilities arising from supercooling or superheating.

Second-order transitions, on the other hand, are “smooth”. The enthalpy H and specific volume V change continuously, while the heat capacity c_p shows a discontinuity. In such transitions, the molecules begin to undergo changes well before the transition temperature. The transition tends to be co-operative (i.e., groups of molecules act in accord). As the transition point is approached, the range of co-operativity increases, and this range or “domain size” diverges at the critical point. Many properties of the system diverge through power laws with respect to the distance from the critical point T_c (i.e., *property* $\sim (T - T_c)^\beta$). Second-order transitions occur by *spinodal decomposition* in the unstable or spinodal region of the phase diagram. Between the binodal and spinodal curves, the system phase separates via nucleation and growth, thus allowing metastabilities to occur.

3.2. The Question of Gelation

In a DSC scan (Figure 4), the process of molecular gelation upon cooling is often associated with an exothermic peak. Conversely, the process of gel melting or dissolution upon heating is associated with an endothermic peak. A *sharp* calorimetric peak indicates a *discontinuous* enthalpy change, implying that the transition is first order. Guenet, in his book on polymer and biopolymer gels [15], states that “in most cases, gel formation proceeds via a first-order transition”. Note that the melting transition alluded to here does not correspond to the melting point of the gelator itself – the latter typically occurs at much higher temperatures.

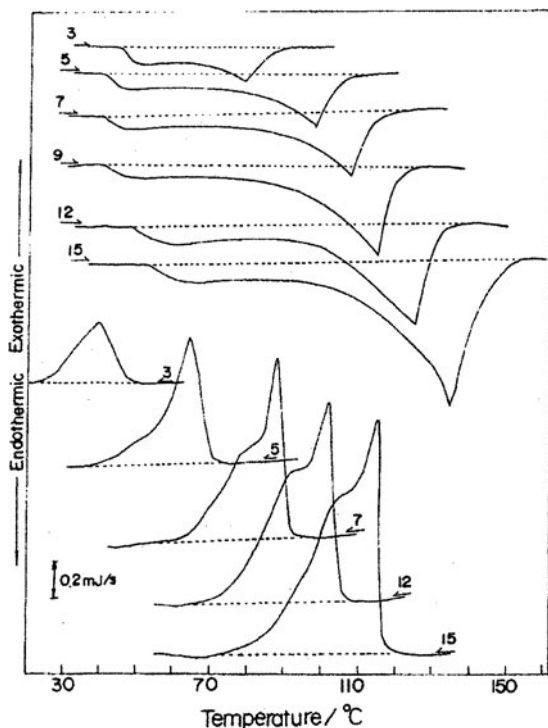


Figure 4. DSC curves (heating, bottom and cooling, top) for the gelator dibenzylidene sorbitol (DBS) in triethylene glycol. The numbers represent the gelator concentration in w/w. The dashed lines are baselines used for the calculation of enthalpies. (Reproduced with permission from [16]. Copyright American Chemical Society.)

The melting peak for gelation, however, is often rather broad [5] or even absent [17], suggesting that the transition may be weakly first-order or possibly second-order. Support for the latter viewpoint arises from the power law dependence of rheological properties in the vicinity of the gel point. Such power laws also lend support to the idea of gelation as a percolative process [1]. Percolation theory assumes that the gelator molecules assemble first into small clusters, which then further assemble into a three-dimensional (3-D) volume-filling network (a SAFIN). Thus, the cluster size or correlation length increases in a power law as the gel point is approached. The divergence of the correlation length is characteristic of a second-order process.

In the case of molecular gels, the experimental data can be rationalized in the following manner [18]. It is assumed that the gelator molecules assemble into fibrils, strands, ropes or other assemblies by a first-order process (i.e., with a discontinuous enthalpy change). These assemblies then further link together

to form clusters and ultimately the SAFIN. The cluster size diverges, as in a second-order transition.

3.3. Calorimetry of the Sol-Gel Transition

In DSC, a sample cell and a reference cell are maintained at the same temperature. The power supplied to raise the temperature of each cell at a constant rate (e.g., $10^\circ\text{C}/\text{min}$) is recorded. This power is converted to a heat capacity vs. temperature curve. The peak temperature in a heating curve corresponds to the gel “melting” point T_g and the area under the peak yields the enthalpy of gelation (melting). Figure 4 shows DSC curves for a sorbitol-based molecular gelator in an organic solvent [16]. As the gelator concentration is increased, both the melting temperature and the enthalpy of melting are observed to increase. Note that there is some hysteresis in the gelation behavior, with the gel-to-sol transition (melting) not coinciding perfectly with the sol-to-gel transition. Also the peak is better defined in cooling curves rather than in heating curves.

3.4. Gelation Temperature vs. Gelator Concentration

Plots of the gelation temperature T_g vs. gelator concentration c are shown in Figure 5a for a sugar-based gelator in two organic solvents [19]. Note that there is an exponential increase of c with T_g . In turn this implies that an Arrhenius plot of $\ln c$ vs. $1/T_g$ will be linear, and this is nicely confirmed by Figure 5b.

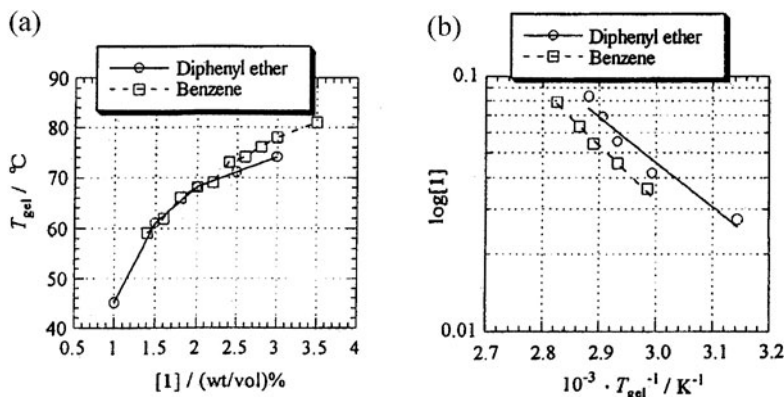


Figure 5. (a) Sol-gel phase boundaries for dibenzylidene sorbitol (DBS) in two organic solvents determined by tube inversion. (b) The same data plotted in an Arrhenius-type plot. (Reproduced with permission from [19]. Copyright Royal Society of Chemistry.)

The above experimental result for T_g vs. c is well established for a wide range of gelators, both molecular as well as polymeric. However, its physical implication is still controversial. There are at least two models that can explain such a relationship. First, the gel-to-sol transition can be interpreted as a melting or dissolution of gelator *crystals* [14]. In that case, the gelator concentration corresponds to the solubility of its crystals in an ideal solution at a temperature T_g and is given by the following equation [1, 19]:

$$\ln c = -\frac{\Delta H_m}{RT_g} + \text{constant} \quad (5)$$

where R is the universal gas constant and ΔH_m is the enthalpy of fusion (melting) of the neat gelator. The above equation has been referred to as Schrader's equation [19] or the Schroeder-van Laar equation [17]. Note that this assumes that the transition is first order. Eliminating the constant from Eq. (5) gives:

$$\ln c = -\frac{\Delta H_m}{R} \left(\frac{1}{T_g} - \frac{1}{T_m} \right) \quad (6)$$

Here T_m is the melting temperature. Values of ΔH_m obtained via Eq. (6) are typically comparable or slightly higher than values from DSC measurements at the melting point of the gelator [19].

An identical form of Eq. (5) can be derived from very different assumptions. Eldridge and Ferry [20] assumed that the gelation of biopolymers, such as gelatin, is controlled by a pairwise crosslinking of biopolymer chains. The crosslinking reaction is exothermic, and therefore one can write:

$$\ln c = \frac{\Delta H_{cr}}{RT_g} + \text{constant} \quad (7)$$

Here, ΔH_{cr} is the heat evolved in the crosslinking reaction. Once again, this equation suggests an Arrhenius relationship from which one can obtain ΔH_{cr} . Note, however, that gelation is considered here to be a second-order process, which is in direct contrast to the assumptions inherent in Eq. (5).

4. Conclusions and Perspectives

In this chapter, we have described how the *phase diagram* for molecular gelators can be obtained using simple, straightforward techniques. The phase diagram is a plot of temperature vs. gelator concentration showing the location of sol-gel boundari(es) as well as any multi-phase or lyotropic regions. The first set of techniques involve application of rheological principles to detect gelation. These include: (a) tube inversion; (b) falling sphere; and (c) rising bubbles. Calorimetry studies are also useful in directly measuring the enthalpy

of gelation (melting). The latter quantity can also be obtained by analyzing an Arrhenius plot of the gelator concentration as a function of the gelation temperature.

Among the rheology-based methods, tube inversion is by far the most popular and convenient, and arguably also the least ambiguous. As a starting point for studying gels, it is preferable to use tube inversion over falling ball or other alternatives. If falling ball must be used, it is important to use a heavy ball and a sufficiently large vessel in order to obtain a clean measurement. Finally, where possible, the simple “tabletop” rheological methods should be benchmarked using data from conventional rheometry.

References

- [1] Terech, P.; Weiss, R.G. *Chem. Rev.*, **1997**, *97*, 3133–3159.
- [2] Winter, H.H. “Gels”, In *Encyclopedia of Polymer Science and Engineering*, H.H. Mark, Ed., New York: Wiley, **1985**, pp. 343.
- [3] Macosko, C.W. *Rheology: Principles, Measurements and Applications*, New York: VCH Publishers, **1994**.
- [4] Dimonte, G.; Nelson, D.; Weaver, S.; Schneider, M.; Flower-Maudlin, E.; Gore, R.; Baumgardner, J.R.; Sahota, M.S. *J. Rheol.*, **1998**, *42*, 727–742.
- [5] Li, H.; Yu, G.E.; Price, C.; Booth, C.; Hecht, E.; Hoffmann, H. *Macromolecules*, **1997**, *30*, 1347–1354.
- [6] Kelarakis, A.; Mingvanish, W.; Daniel, C.; Li, H.; Havredaki, V.; Booth, C.; Hamley, I.W.; Ryan, A. *J. Phys. Chem. Chem. Phys.*, **2000**, *2*, 2755–2763.
- [7] Beris, A.N.; Tsamopoulos, J.A.; Armstrong, R.C.; Brown, R. A. *J. Fluid Mech.*, **1985**, *158*, 219–244.
- [8] Noveon, Inc. <http://www.pharma.noveoninc.com/literature/bulletin/epb12.pdf> “Bulletin 12: Flow and suspension properties”, 2000.
- [9] Gheissary, G.; van den Brule, B.J. *Non-Newtonian. Fluid Mech.*, **1996**, *67*, 1–18.
- [10] van Esch, J.; Schoonbeek, F.; de Loos, M.; Kooijman, H.; Spek, A.L.; Kellogg, R.M.; Feringa, B.L. *Chem.-Eur. J.*, **1999**, *5*, 937–950.
- [11] Stein, S.; Buggisch, H.Z. *Angew. Math. Mech.*, **2000**, *80*, 827–834.
- [12] Coussot, P.; Boyer, S. *Rheol. Acta*, **1995**, *34*, 534–543.
- [13] Pashias, N.; Boger, D.V.; Summers, J.; Glenister, D.J. *J. Rheol.*, **1996**, *40*, 1179–1189.
- [14] Atkins, P.W. *Physical Chemistry*, 5th edition, New York: W.H. Freeman & Co., **1994**.
- [15] Guenet, J.-M., Ed., *Thermoreversible Gelation of Polymers and Biopolymers*, London: Academic Press, **1992**.
- [16] Watase, M.; Nakatani, Y.; Itagaki, H. *J. Phys. Chem. B*, **1999**, *103*, 2366–2373.
- [17] Menger, F.M.; Caran, K.L. *J. Am. Chem. Soc.*, **2000**, *122*, 11679–11691.
- [18] Terech, P.; Rossat, C.; Volino, F. *J. Colloid Interface Sci.*, **2000**, *227*, 363–370.
- [19] Amanokura, N.; Yoza, K.; Shinmori, H.; Shinkai, S.; Reinhoudt, D.N. *J. Chem. Soc. Perkin Trans.*, **1998**, *2*, 2585–2591.
- [20] Eldridge, J.E.; Ferry, J.D. *J. Phys. Chem.*, **1954**, *58*, 992–995.

Chapter 9

DIRECT-IMAGING AND FREEZE-FRACTURE CRYO-TRANSMISSION ELECTRON MICROSCOPY OF MOLECULAR GELS

Dganit Danino¹ and Yeshayahu Talmon²

¹*Department of Biotechnology and Food Engineering and*

²*Department of Chemical Engineering, Technion-Israel Institute of Technology, Haifa 32000, Israel*

1. Introduction	253
2. Cryo-TEM	254
3. Cryo-TEM Investigations of LMOG Gels	258
4. Conclusions and Perspectives for the Future	271

1. Introduction

Full characterization of liquid, semi-liquid, gel, or solid systems requires direct, supramolecular-level information (i.e., images, which show how molecules arrange to form clusters of various sizes and shapes). Cryogenic-temperature transmission electron microscopy (cryo-TEM) is the method of choice for obtaining such direct imaging of liquid or semi-liquid specimens, thermally fixed into a vitreous or quasi-solid state. Cryo-TEM provides high-resolution direct images of the assemblies in the system. Thus, it can elucidate the nature of the basic building blocks that make up the systems, covering a wide range of length scales from few nanometers to several microns. In addition, coexistence of many different assemblies present in the examined systems is quite easily observed in the micrographs. The interpretation of data cryo-TEM produces is usually quite straightforward, not model-dependent. In contrast, experimental interpretation data from “indirect methods”, such as scattering techniques, is model dependent and is complicated when the system contains more than one type of aggregate or a broad size distribution.

In the case of molecular gels, the unique rheological properties are the result of supramolecular aggregates. Those may be regular or irregular, homogenous or very diverse. Thus, cryo-TEM is most useful to image the range of the nanostructures present in those systems. In some cases, direct images provide the only way to prove a suggested or a theoretically predicted model. That was demonstrated for example in the case of the theoretically predicted branched micelles [1], the shape of the “end-caps” of thread-like micelles [2, 3], and the exact nanostructure and mechanism of formation of lithocholate nanotubes [4, 5].

While micrographs are most useful, at the same time one should keep in mind that cryo-TEM is not a strictly quantitative technique. It is the technique of choice to determine the structural building blocks of complex fluid systems, but the quantitative data should be usually provided by other techniques, such as small-angle X-ray scattering (SAXS) (see Chapter 11), small-angle neutron scattering (SANS) (see Chapter 10), or nuclear magnetic resonance (NMR). Another advantage of these scattering techniques is that they probe the bulk of the system, not just a small sample of it; they thus provide a real statistical average. However, in a very heterogeneous system, such an average may be difficult to interpret. In addition, these techniques are “model dependent”; they are not “observer-dependent”. In fact, the best experimental approach is to apply cryo-TEM to collect data on the nature of the nano-building blocks of the system, use that information to construct a physical model that is used to interpret data from the above mentioned “indirect techniques”, and then check whether those latter results agree with cryo-TEM images to rule out possible artifacts.

Below we describe the basic aspects of cryo-TEM. That is followed by a review of the applications of the technique to the study of gel and gel-like systems. The interested reader will find more details about the technique and its application to other systems in references [6, 7].

2. Cryo-TEM

To examine samples that contain high concentrations of liquids in the TEM, it is necessary to lower in the vapor pressure to make them compatible with the high vacuum in the microscope column, lower typically than 10^{-6} Pa. Also, any supramolecular motion must be arrested to prevent blurring of the recorded image. TEM specimens must be thin, not thicker than about 300 nm. Thicker specimens give rise to inelastic electron scattering that deteriorates image quality. However, inelastically scattered electrons may be filtered out by electron microscopes equipped with an in-column or post-column energy filter.

We can reduce vapor pressure and arrest supramolecular motion by either “chemical” or “physical” (thermal) fixation. Chemical fixation involves addition of an alien chemical substance to the sample. Because microstructured

fluids are very sensitive to changes in composition, addition of compounds such as a stain or fixative, followed in some cases by a chemical reaction between the fixative and the specimen, and often by drying the sample, may alter the original microstructure of the studied system. That makes chemical fixation unacceptable for the study of microstructured fluids. Hence, the method of choice is thermal fixation (i.e., ultra-fast cooling of the liquid specimens into a vitrified or quasi-solid state). This is achieved by rapidly plunging the specimen into a suitable cryogen. Because thermal diffusivities are larger than mass diffusivities, thermal fixation is much more rapid than chemical fixation, and, of course, eliminates the addition of an alien compound to the system.

The cooling rate needed for vitrification of water is on the order of 100,000 K/s, as estimated theoretically [8] and measured experimentally in an actual specimen preparation set-up [9]. When cooling is too slow, hexagonal or cubic ice forms in aqueous systems, or other crystalline matrices may form in non-aqueous systems. Such crystalline matrix formation leads to optical artifacts, to mechanical damage to the microstructure, and to redistribution of solutes. Solute are expelled from the growing ice lattice, and are deposited either in the crystal grains or often at grain boundaries.

The high cooling rates needed for vitrification require very large surface area-to-volume ratio. The geometry of choice is a thin film. Thin films (up to 300 nm thick, as stated above) are also required due to the limited penetration power of even high-energy electrons. High-resolution imaging requires thinner samples. It should be emphasized that most direct-imaging vitrified specimens display a wide thickness range. While microscopes operating at 200, 300 and 400 kV, found in many universities and research institutes, are capable of imaging specimens thicker than specified above, image interpretation becomes increasingly more difficult with specimen thickness. It is the high depth-of-focus of the TEM that leads to superposition of information from many layers of thick specimens, all projected on the plane of the detector.

The cryogen needed to successfully vitrify the specimen has to be at a low temperature, and well below its boiling point to avoid formation of a gas film around the specimen during quenching; such a gas film acts as a thermal insulator (the so-called Leidenfrost effect). The cryogen should also have a high thermal conductivity. Liquid nitrogen is a poor cryogen because of the narrow temperature range between its freezing and boiling. In contrast, liquid ethane, cooled to its freezing point (-183°C) by liquid nitrogen, is the best cryogen (its normal boiling point is about 100 K higher).

Another issue is the preservation of the nanostructure at precise conditions of (especially) temperature and concentration. This cannot be achieved unless the specimen is prepared in a controlled environment of the prescribed temperature and atmosphere that prevents loss of volatiles (e.g., water vapor) from the specimen during preparation. This requires a so-called controlled-environment vitrification system (CEVS). Several models are available, especially the relatively

simple but very reliable systems based on that developed by Bellare *et al.* [10] and modified by Talmon and co-workers over the years [9, 11], and the automatic “Vitrobot” of the FEI company that was developed by Frederik and co-workers [12]. The CEVS can be used from -10 to $+70^{\circ}\text{C}$ and with various saturated or unsaturated atmospheres.

Cryo-TEM specimen preparation is performed inside the CEVS, where the atmosphere is closed and controlled, from the outside. A small drop, typically 3 to $5\ \mu\text{L}$, of a pre-equilibrated system is pipetted onto a perforated carbon film supported on a TEM copper grid, held by tweezers and mounted on a spring-loaded plunger. The drop is blotted by filter paper wrapped on a metal strip, thus forming a thin liquid film supported on the perforated carbon film. After blotting, the plunging mechanism is activated, a trap door opens simultaneously, and the specimen is driven into the cryogen and vitrified. Finally, the vitrified sample is transferred under liquid nitrogen to the “working-station” of a cooling holder where it is loaded into the special holder and transferred in it into the microscope. In some cases, a “bare grid” (i.e., a microscope grid not covered by a perforated film) is used. More technical details can be found elsewhere [6, 10].

The blotting of the specimen may be performed in a number of ways. The simplest is wicking most of the liquid by simply touching the filter paper to the edge of the grid carrying the drop. Viscoelastic fluids require blotting with a shearing or “smearing” action. That temporarily reduces the viscosity of a shear-thinning liquid, allowing the formation of a thin enough liquid film on the support. Another way that can be performed either manually or, as in the case of the Vitrobot, automatically, is to press two pieces of blotting paper on the two sides of the specimen. That mode usually produces more uniform films. The blotting process and the confinement of the liquid in a thin specimen may introduce artifacts one should be aware of (see below). In addition to changes of the nature of the nanostructure, distortions of large objects, and alignment of slender “one dimensional” (rods or threads) or large “two-dimensional” (sheets) objects may take place.

While the prepared specimen is still in the liquid form, one can keep it in the controlled environment of the CEVS for some time. This allows the specimen to relax, following shear and elongation it may experience during blotting [13, 14], or to undergo other processes directly on-the-grid. Such processes may be chemical or physical reactions induced by different triggers, such as fast heating [9, 11] or cooling [15], pH jumps [16], or gelation. Those processes may be stopped at any intermediate stage by plunging the specimen into the cryogen. By repeating the experiment a number of times, each time allowing the process to proceed further towards completion, one can obtain a sequence of vitrified specimens that give “time-sectioning” of the process. This protocol is called “time-resolved cryo-TEM”. Several variations of the CEVS have been built to facilitate such experiments [9, 11, 17].

On-the-grid cooling (or, in rare cases, heating) is a straightforward way to produce high-viscosity gel phases on the grid, starting with a low viscosity precursor. An example, described in some detail below, is that of a high viscosity lamellar phase formed upon cooling of a monoglyceride solution in olive oil. Above 50° C, the system is a low viscosity liquid which can be easily made into a thin liquid film in the properly controlled CEVS. The thin film is then cooled in the CEVS to about 40° C, and the formed gel is vitrified. In such cases one should use liquid nitrogen as the cryogen rather than liquid ethane, as the latter is a good solvent for many organic compounds even at its freezing point. Some systems, such as those containing glycerides, branched hydrocarbons or aromatics, do not crystallize readily upon cooling, and thus can be vitrified even in liquid nitrogen [18]. That is also true for aqueous systems containing sufficiently high concentrations of glycols (>20%) [14].

An indirect route to cryo-TEM is freeze-fracture-replication (FFR). This technique involves freezing the specimen (the specimen is larger than that of direct imaging cryo-TEM; thus in most cases vitrification is not accomplished), fracturing the frozen specimen, and preparing a metal replica of the fracture surface by vapor deposition. First, a heavy metal is deposited at an angle of 45° or less to the horizon, to enhance contrast (“shadowing”), and then a carbon layer is added for mechanical stability of the replica. Following replication, the sample is melted, the replica washed, dried, and imaged in the TEM at room temperature. The entire process of fracturing the specimen and replication is carried out in commercially available systems. Fast cooling may be carried out in the CEVS to allow quenching from given, well controlled, conditions [19]. FFR is most useful to examine high viscosity systems, or systems containing large particles that cannot be accommodated in the thin specimens of direct-imaging cryo-TEM; in both cases, direct-imaging cryo-TEM is not practicable. Of course, fine details or fine particles can be imaged by the technique. In fact, one early success in imaging a network structure of molecular organogel was achieved by applying the FFR technique in the study of a steroid/cyclohexane physical gel by Wade *et al.* [20]. While the technique is excellent to complement direct imaging cryo-TEM [4], it has lost popularity in the last two decades and, regrettably, is used in only a few research laboratories.

To prevent warming, which may lead to water crystallization and rearrangement of material, the vitrified specimens must be kept under liquid nitrogen until they are examined in the microscope. In typical cryo work, transfer of specimen into the microscope is carried out in a “cryo-holder”, a special specimen holder that can be cooled by liquid nitrogen to –165° C or lower.

Low inherent contrast of cryo-specimens and their sensitivity to electron-beam radiation-damage make them difficult to image. One has to take these factors into account and optimize the conditions to extract as much information as possible from the specimen. For most applications, an acceleration voltage of 120 to 200 kV is used. The lower acceleration voltage offers better contrast,

while the higher affords better penetration power, and, in some cases, better resolution. Because the cryo-specimen is the coldest spot in the vacuum system and could collect contaminants by condensation, the vacuum system of the microscope must be very clean. An “anti-contaminator”, a device made of large liquid nitrogen-cooled surfaces installed in the microscope column as close as possible above and below the specimen, must be used to trap molecules of residual volatiles, preventing them from condensing on the specimen. Images are recorded by cooled slow-scan CCD cameras. Such cameras offer easy use, with straightforward low-dose operation and immediate post-microscopy image processing. Such features are vital for the study of cryo-specimens. Low electron dose exposure, not more than $10 \text{ e}^-/\text{\AA}^2$, and possibly lower, is applied to minimize electron-beam radiation damage. Phase contrast (equivalent in principle to phase-contrast light microscopy, namely converting phase differences to amplitude differences in image formation) is regularly applied to enhance contrast by defocusing of the microscope objective lens. This must be applied with care to avoid loss of resolution and introduction of imaging artifacts.

The complications induced by the low inherent contrast and sensitivity of most molecular assemblies to electron-beam radiation damage are demonstrated in Figure 1 of a cubic phase of Pluronic127TM (F-127). F-127 is a commercial triblock copolymer, poly(ethyleneoxide)-poly(propyleneoxide)-poly(ethyleneoxide) (PEO-PPO-PEO), that, at low polymer concentrations, forms spheroidal micelles, $\sim 8\text{--}9$ nm in diameter, consisting of a bulky hydrated shell and a fairly dense core. As the concentration is increased ($> 12.5\%$) and the micellar volume fraction grows, the micelles close-pack into a body centered cubic lattice, and gel. In cryo-TEM images of a 15% F-127 sample, no microstructures or texture are observed at regular electron doses ($\sim 10 \text{ e}^-/\text{\AA}^2$) used in examination of cryo-TEM specimens because of the low inherent contrast of the PEO and PPO polymer units (Figure 1, region A). At twice the exposure, the fine texture of the ordered cubic phase emerges (Figure 1, region B). It was confirmed by a fast-Fourier transform (FFT) that was easily applied to the digitally-recorded image. A third exposure of the concentrated sample to the electron beam leads to bubbling and complete distortion of the structure, as seen in the lower right part of the image (region C).

3. Cryo-TEM Investigations of LMOG Gels

In the following sections, we review direct-imaging and FFR studies of various gels formed by self-assembly and interactions between synthetic and natural biopolymers, lipids, and surfactants, manifested, as described below, in rich morphology and structure. Cryo-TEM has not been used extensively yet to study strictly “LMOG gel” and SAFIN systems. However, we feel that

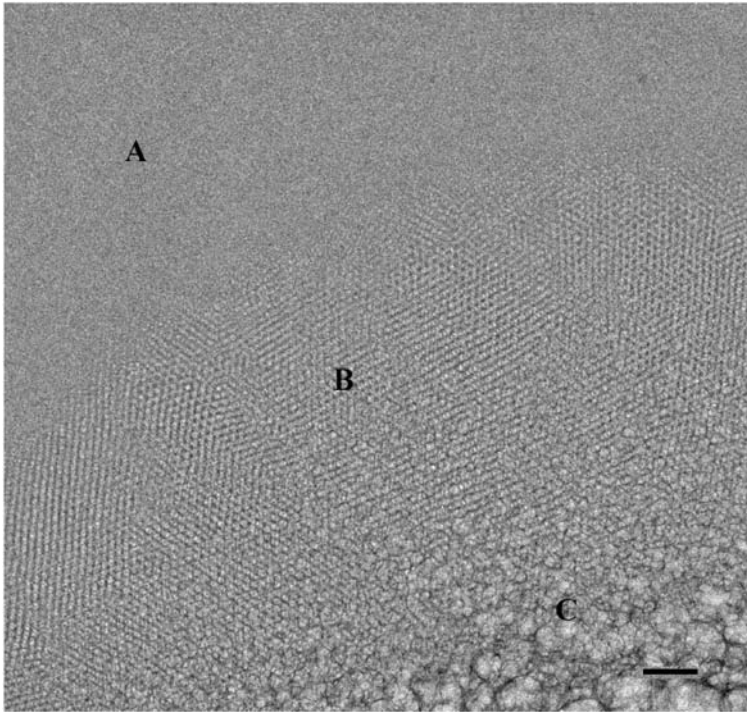


Figure 1. The effect of beam-exposure on the texture of low-contrast cubic mesophase of F-127. At low exposures of $\sim 10 \text{ e}^-/\text{\AA}^2$, no texture is observed (region A). At twice this exposure, the fine texture of the ordered cubic phase appears (region B), and, at 3-times the electron dose, the structure is completely destroyed. Bar = 100 nm.

the examples shown here will be of interest to those who consider applying cryo-TEM. They illustrate potential applications of the technique, the difficulties associated with applying it to high-viscosity systems, and some routes to overcome those obstacles en route to successful direct imaging.

Freeze-fracture and direct-imaging cryo-TEM were used to study the viscous gel and diluted gel solutions of dioctadecyldimethylammonium chloride (DODMAC), which formed upon heating monohydrate crystal slurries to just below the Krafft temperature while stirring [21].

Typically, round liposomes and vesicles of up to several microns in diameter were observed in the diluted samples at 25°C , but some vesicles and small lens-like objects (suspended in solution or encapsulated in vesicles), with sharp corners or cusps, were also found (Figure 2A). Similar structures were seen in FF replicas of the viscous gel phase (Figure 2B). In contrast, mostly lens-like structures and multilamellar angular vesicles were found upon vitrification from 55°C , with a rather uniform spacing between membranes. Upon shearing at room temperature, mainly round and much smaller multilamellar vesicles

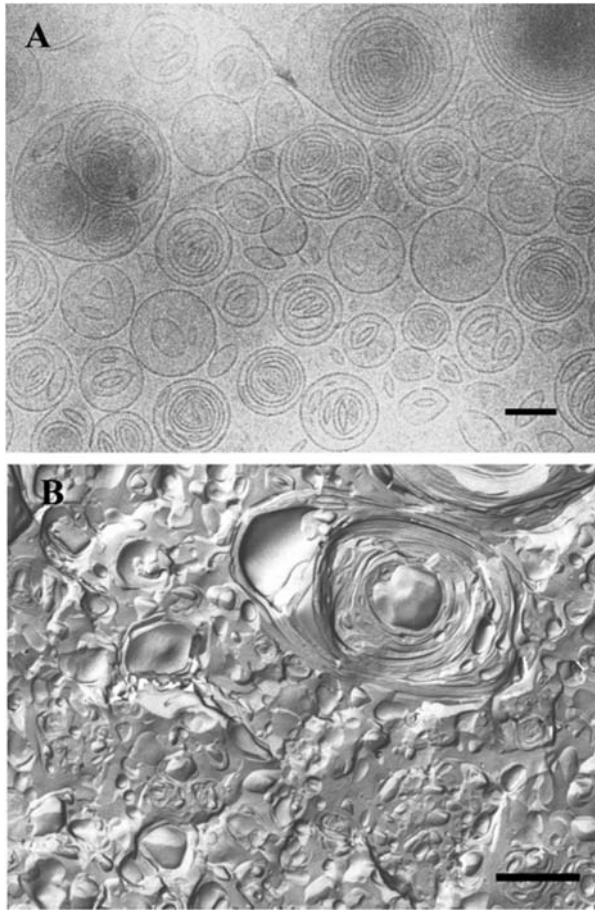


Figure 2. Cryo-TEM images of DODMAC dispersed in water: (A) direct-imaging micrograph of a 2% dispersion sheared at $50,000 \text{ s}^{-1}$ to reduce vesicle size; (B) an FFR image of a 5% gel-like dispersion. Both images show the same building blocks, mainly multilamellar vesicles of a wide size-distribution, although the 2% solution flows freely while the 5% sample is in the gel phase. Bars = 100 nm.

were found, encapsulating both round and lens-shaped structures. The decrease in the vesicle size was coupled to a decrease in the viscosity. Upon aging, the vesicles collapsed to form a flat, layered structure, with an interlayer spacing of about 4 nm.

Vesicular phospholipid gels were also prepared by Kaiser and co-workers [22] for encapsulation and release of anticancer drugs. The gels were formed from mixtures of hydrogenated soy phosphatidylcholine and cholesterol at different compositions by high-pressure homogenization. Small lens-like structures, similar to those seen in the DODMAC system, were found, free

in solution and entrapped within round vesicles. The membrane defects of the small, free lens-like structures (< 40 nm) were used to explain the fast initial drug release.

Maitra and co-workers [23] synthesized tripodal bile acid derivatives that act at low concentrations in the presence of organic cosolvents (such as acetone) to form transparent thermoreversible and thixotropic gels. Cryo-TEM images of the vitrified gel showed a well-developed intertwined network, made of very thin flat ribbons, 2 to 5 nm wide, that formed by one-dimensional growth of the tripodal bile. Twisted ribbons were also identified by cryo-TEM at the early stages of gel formation of hydrogelators of the bis-urea dicarboxylic acids family in the presence of CaCl_2 in Tris buffer [24]. The width of the ribbons ranged from 15 to 40 nm; the periodicity of the twisting was from 120 to 330 nm. The authors suggested that the ribbons are responsible for the gel formation, by becoming entangled, then trapping and immobilizing solvent via surface tension.

Viscoelastic solutions of lithocholic acid (LCA) form in an extended range of concentrations at basic pH. Helical ribbons and several microns long, stiff single-walled nanotubes, ~ 52 nm in diameter and ~ 1.5 nm thick, were identified by cryo-TEM in dilute LCA solutions [5]. Recently, FFR, direct-imaging cryo-TEM, and SAXS studies were performed to elucidate the early structures leading to the formation of the uniform tubes (Figure 3). Direct-imaging cryo-TEM images showed that less than 2 min after initiating the process by

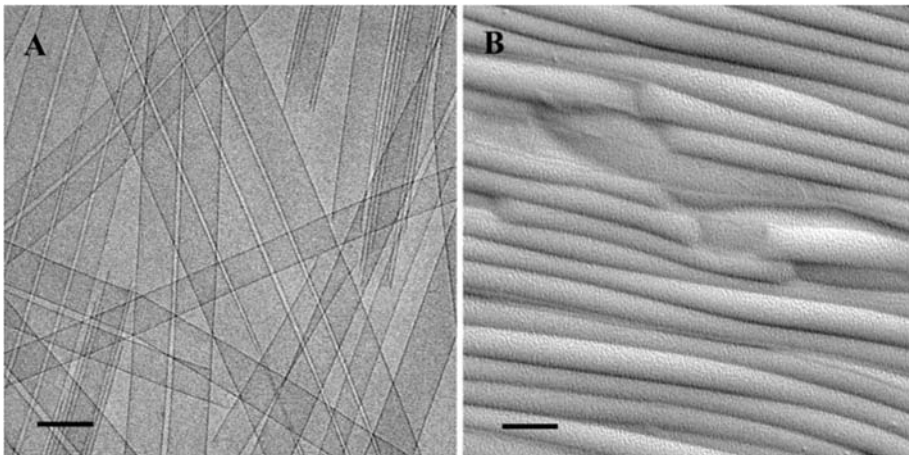


Figure 3. Direct-imaging and FFR images (**A and B, respectively**), of LCA nanotubes. (A) 0.1% LCA in 0.05N NaOH, 6 min 50 s after mixing the components. Long, single- and multi-walled nanotubes are found at the early times of nanotubes formation. (B) 1% LCA in 0.1N NaOH, 6 days after mixing. Notice the similarity in dimensions (diameter and length) in the two images of the complementary cryo-TEM methods. Bars = 100 nm.

mixing LCA powder in aqueous NaOH solution, single- and multi-walled tubules of different diameters were formed [4]. Other intermediates, including helical ribbons and thin long fibers, were also observed within the first 30 min. The multi-wall structures were probably rather short-lived intermediates; after one hour they were no longer observed. Upon heating to 62° C, the tubes disintegrated and fibrillar aggregates, hundreds of micrometers long and resembling some of the intermediates found at the early times of the assembly, were found [25].

A comparative study on the assembly of the chiral amphiphile, N-dodecanoyl-(D- and L-) serine, under reversed polarity conditions was performed by Boettcher and co-workers [26]. Aqueous and toluene solutions were cooled from 110° C to room temperature to give gels, and then vitrified in liquid ethane and nitrogen, respectively. Multilamellar vesicles and tubules of about 1 mm in length, 80 nm in diameter, and inner channels of 25 nm, formed in toluene. Similar tubes but with diameters in the range of 80–139 nm were found in buffered solutions. Interestingly, the curvature did not change upon shifting from toluene to water, but much longer helices of up to 10 mm in length formed in water. In addition, many multilayered twisted ribbons of different widths were observed in water.

A gel-like phase consisting of microns long, overlapping, threadlike micelles was found during solubilization of small, unilamellar vesicles of phosphatidylcholine-phosphatidic acid mixtures with the nonionic detergent dodecyl maltoside (DOM) [27]. Other intermediate structures observed during the solubilization process, prior to the micelles, include open and intact large unilamellar vesicles, and bilayer fragments. Upon solubilization of biological membranes (sarcoplasmic reticulum) by DOM, similar long micelles were seen, but they were less numerous and progressively broke down. In reconstitution studies by detergent removal, a slow transition through the gel-like phase led to the formation of multilamellar liposomes, while homogeneous unilamellar vesicles formed upon rapid transition. Another gel phase was identified upon addition of the bile salt, sodium desoxycholate (NaDOC), to cetyltrimethylammonium chloride (CTAB). This system has been studied by cryo-TEM, but the experiments were limited to the low viscosity conditions within the micellar phase [28]. Various structures were observed including mixed spheroidal micelles, flexible long and interconnected threadlike micelles, and short rod-like structures.

Schneider and co-workers [29], designed a 20-residue peptide that self-assembles in a pH-dependent manner to construct a chemically and mechanically responsive hydrogel. Intermolecular folding of this peptide into a β -hairpin is only permitted in basic aqueous solution (at $\text{pH} \geq 9$), while acidification of the solution results in β -hairpin unfolding, and dissolution of the hydrogel. By cryo-TEM, they showed a network scaffold in the assembled conformation, which resembles the networks found in surfactant

systems. They also studied the gelation behavior of several amphiphilic diblock copolypeptides, 200 amino acids long, of which the poly(L-lysine) or poly(L-glutamic acid) hydrophilic block made up 80 or 90% of the structure, and the hydrophobic block was made of poly(L-leucine) or poly(L-valine). These copolypeptides form gels at low concentrations [30, 31]. The 90:10 mol% hydrophilic:hydrophobic group polypeptide was studied at concentrations up to 5 wt.%. Cryo-TEM images showed a gel scaffold consisting of interpenetrating membranous structures, several hundreds of nanometers long at all the concentrations studied. Within the cellular scaffold, particularly in the more diluted gels (1 and 2%), the lateral distances observed between neighboring cell membrane walls were larger than 100 nm [30]. In the case of the 80:20 polypeptide, a thin film of ~ 100 nm of the hydrogel was pre-formed, and then applied to the grid and vitrified. Cryo-TEM images showed the polypeptide gel was highly porous, made of membranous networks surrounded by significant amounts of water. Based on the appearance of the edges of the hydrogel matrix, it was concluded that the polypeptide associated throughout the sample until there was no free peptide in solution [31]. Hartgerink and co-workers, [32] designed a self-assembling peptide-amphiphile (PA) to prepare a nanostructured composite material that, upon mineralization, recreated the structural orientation between collagen and hydroxyapatite observed in bone. At low pH and concentrations above 2.5 mg/mL, PA formed birefringent gels in water which by cryo-TEM were shown to be a network of fibers about 7.6 nm in diameter and several microns in length.

The globular phosphoglycoprotein ovalbumin unfolds in solution upon heating. During unfolding, part of the hydrophobic regions are exposed, and denaturation is followed by aggregation, and, finally, gelation. At pH 7 and low ionic strength, ovalbumin self-organizes into linear cylindrical structures. The effect of electrostatic interactions on the gelation process at this pH was investigated by Weijers *et al.* [33], but with cryo-TEM they only studied the dilute solution. After heat treatment, long, flexible structures, about 5–7 nm in diameter and containing only very few branch points, were seen at low ionic strength. At higher ionic strength, but still below the gelation concentration, densely branched clusters were found. The authors concluded that the aggregation at this pH was essentially the same at different ionic strength, but branching is inhibited by electrostatic repulsions.

Gelation, precipitation, and re-dispersion may occur in mixed protein-surfactant systems. Khan and co-workers studied the gelation of a similarly charged system composed of lysozyme (a small ellipsoidal protein) and SDS (sodium dodecyl sulfate) [34]. In the absence of surfactant, small globular structures formed at low lysozyme concentrations. In the presence of low SDS concentrations, within the 3-phase region of precipitate, gel, and solution, short flexible aggregates, about 50 nm in diameter, were found to coexist with large sheet-like domains. A variety of other structures were identified at increasing

SDS concentrations near and after full redissolution of the precipitate, and at various total protein concentrations. Those structures included small globular assemblies and long rod-like (10 nm thick and 500–1500 nm long) intercrossing objects, termed star-like structures. No change in structures was observed upon aging for several weeks. Similar phase behavior, namely coexistence of precipitate, gel, and solution over a wide concentration range is exhibited by the system composed of oppositely charged ovalbumin and DOTAC (dodecyltrimethylammonium chloride) at pH above the isoelectric point [34]. In that system, flexible rod-like structures, which may constitute the gel phase, were identified. Sheet-like structures were not seen in the cryo-TEM images, but the authors found indications of large structures by light microscopy, suggesting the large objects may have been expelled from the cryo-TEM specimen during sample preparation (a known phenomenon in cryo-TEM). Similar structures were found in the transparent and bluish phases of the oppositely charged DOTAC-BSA (bovine serum albumin, prolate ellipsoidal structure) system. Neither precipitate nor gel was observed in that system up to very high protein concentrations.

Kappa-carrageenan (KC), a linear sulphated polysaccharide extracted from red algae, is often used in the food industry as a gelling agent. Thermoreversible gelation of KC occurs rapidly upon cooling, possibly as a result of a coil-to-double helix transition. KC may also be gelled isothermally (at constant ionic strength) by dialysis against “gel-inducing” salts such as KCl and CsCl [35]. Early cryo-TEM studies showed stiff microfibers several hundred in nm long and a few nm thick in the presence of KCl [36]. They were interpreted as individual KC helices. In a series of papers, Piculell and co-workers used the isothermal gelation approach to study the structure of intact and ultrasonically degraded KC in solution and towards the gel phase [37–39]. Using mixtures containing NaI and CsI salts at a constant salt concentration of 0.1M, they tuned the helix-helix interactions and the tendency of the helices to aggregate. Below CsI fractions of 0.4, no structures were observed. At higher concentrations where the viscosity increases, short and rigid “super-helical rods”, ~ 300–400 nm long and less than 5 nm thick, were found by cryo-TEM. Those structures, which were arranged in bundles of 2–8 fibers, aggregated into larger bundles and formed clusters and bigger aggregates as the amount of cesium salt was further increased [37, 39]. These findings indicated that the network formation occurs not through the double-helix formation itself, but only through association of helices. Additional experiments were conducted in the presence of locust bean gum (LBG), a plant polysaccharide having a random-coil structure in solution that considerably increases the gel strength of KC and reduces the minimum concentration for gelation. Cryo-TEM images showed thicker, polydispersed, and more flexible fibers in the presence of LBG, suggesting that LBG stabilizes the superhelical rods, and shifts the transition to a lower Cs content [38].

Amylose and amylopectin are the two main components of starch. Amylose is a linear polysaccharide, while amylopectin consists of short, highly branched amylose segments. Aqueous solutions of these two polysaccharides are unstable, and upon cooling or aging tend to gelate, precipitate, or crystallize, depending on their concentration and molecular weight. The mechanism of amylose gelation has been attributed to a transition from random coil configuration to a phase-separated gel-like network with polymer-rich and polymer-deficient regions. Cryo-TEM was used to characterize the behavior of dilute amylose and amylopectin aqueous solutions as a function of time, and to determine the dimensions and shape of the elementary structures constituting the networks at different steps of aggregation and crystallization [40]. Precipitation of amylose appeared as a continuous process involving network clustering of semicrystalline units of 10–15 nm in size into branched networks, followed by slow condensation of the networks into 300–500 nm domains, and later of thick semicrystalline aggregates, roughly composed of polygonal blocks. Amylopectin followed a similar pathway, and formed similar networks made of necklace-like substructures. However, those networks remained stable for several months and did not undergo further aggregation. It was suggested that long-range rearrangement of the crystallites into large aggregates was hindered by the branched configuration of the molecules.

Poly(ethylene glycol) (PEG) grafted with poly(lactic acid-co-glycolic acid), PEG-g-PLGA, was studied as a potential injectable drug delivery system. Low concentration aqueous solutions have low viscosity and flow freely at room temperature, but aqueous solutions with high concentrations of PEG-g-PLGA undergo a temperature dependent sol-to-gel transition [41]. In that study, the authors showed by cryo-TEM that micelles about 9 nm in diameter exist at low polymer concentrations and at 23.7° C.

Gels also formed upon absorption of PEG onto clay particles. At low polymer concentrations, aggregation was inhibited by steric interactions, while at high polymer and clay content the particles bridged to form gels. Recent cryo-TEM studies revealed the polymer-clay gels contain structures on multiple length-scales. Direct-imaging cryo-TEM of dilute pure clay solutions showed individual clay platelets, about 1 nm thick [42]. In the polymer-clay gel, characterized by FF, a fine texture of a network-like structure made of interconnected strings, ~4 nm thick, was observed. These structures were interpreted as complexes consisting of the 1 nm clay objects with absorbed polymer layers of about 1.5 nm on each side, in agreement with values obtained from the dilute solutions and scattering data. Network formation was explained by bridging of neighboring clay particles by the polymer chains. These polymer-clay complexes extend to microns through formation of fibrous polymer-clay bundles, thus forming macroscopically homogeneous, transparent, shear-thinning hydrogels.

Paulsson and Edsman [43] studied the controlled-release of charged drugs from gels by adding surfactants that interact with both the drug and polymer

matrix. They investigated different types of gels, surfactants, and drugs, and characterized the drug-surfactant structures in polymer-free solutions and in gels by cryo-TEM. Unilamellar and oligolamellar vesicles, up to several hundred of nm in diameter, and open membranes, formed at physiological salt conditions in mixtures of oppositely charged diphenylramine and SDS at a 1:2 drug:surfactant ratio. At half the SDS concentration, the system phase-separated, while at double the SDS content the viscosity increased, and long, highly branched threadlike micelles, similar to those found in surfactant/salt systems and forming a bicontinuous structure, were observed. Vesicles were found in mixtures of other drugs with SDS and negatively charged drugs with oppositely charged surfactants. Vesicles of similar sizes were also observed upon mixing 1:2 diphenylramine and SDS in the gel, but they were faceted as a result of interactions with the polymer. Such vesicles were seen for the same solution composition of alprenolol and SDS, but, in the presence of the polymer C1342 (a covalently crossed-linked poly(acrylic acid) hydrogel with lipophilic modification), only very small vesicles, up to 50 nm in diameter, were found.

Mixtures of cationic polyelectrolytes and net negatively charged catanionic vesicles made of SDS and DDAB (didodecyldimethylammonium bromide) also show a wide region of phase separation containing solution and precipitate, and a polymer-rich gel region [44, 45]. Addition of JR-400 to the small catanionic vesicles within the bluish solution region resulted in the formation of huge concentric multilamellar vesicles coexisting with the small unilamellar and bilamellar vesicles. In the vicinity of the precipitation boundary faceted vesicles, open membranes, and disc-like aggregates became dominant, and then precipitation occurred. Addition of LM200 (a hydrophobically modified polymer) induced comparable changes, but at different ratios. Also, the variety of coexisting structures increased in the presence of LM200. Clustering of small vesicles suggested that the hydrophobic side chains of LM200, bearing the charge, anchor to the vesicle bilayer and cross-link them into possibly vesicle-polymer networks, though the polymer chains were not imaged. In the highly viscous polymer-rich phase and the gel phase, where excess of polymer charge existed, open bilayers and large membrane fragments, as well as disc-like structures that became dominant at higher polymer concentrations, were observed. Upon further addition of polymer, small elliptical vesicles reformed. Overall, an increase in the mean curvature was found with increase in the excess of polymer charge.

Mixing the oppositely charged surfactants, SDS and DOTAC, with the non-ionic hydrophobically modified hydroxyethyl cellulose (HMHEC) resulted in the formation of completely different structures [46]. Here, the viscosity increased with increasing DOTAC molar fraction at a constant polymer concentration, reflected structurally in a transition from spheroidal micelles to a structure of discrete micelles that were probably bound to (the invisible)

polymer organized in a repeating cell-like pattern, as shown by cryo-TEM. At high DOTAC concentrations, cell-like structures coexisting with unilamellar and multilamellar vesicles were seen by cryo-TEM; vesicles of up to several microns in diameter were detected by light microscopy.

While the polymer interacts with catanionic vesicles in the SDS/DDAB/JR-400 system discussed above, the interaction is between the polymer and a micelle-forming surfactant in SDS/JR-400 mixtures. Three distinct zones were identified with increase in the surfactant level, including a clear solution at low SDS concentrations and excess of polymer, precipitation and formation of a clear non-viscous solution and a gel-like phase around charge neutralization, and resolubilization at excess SDS, characterized also by a viscosity increase. In the presence of low SDS levels, mainly membranous structures were found, including bilayer fragments, small vesicles and disc-like aggregates [47]. Large aggregates of spheroidal and elongated micellar structures, disc-like structures, and a few vesicles were found in the turbid solution near the precipitation zone. At a 1:1 charge ratio, large globular and elongated flocs were found by both cryo-TEM and light microscopy. No structures were found in the supernatant at the precipitation zone (2:1 surfactant:polymer charge ratio), but a variety of structures were observed after resolubilization, including vesicles, disc-like and thread-like objects that possibly contributed to the increase in the viscosity. When resolubilization was completed, only spheroidal micelles were seen, probably free SDS micelles with only little interaction with the polymer, which was fully neutralized by SDS under those conditions.

In another anionic surfactant/cationic polyelectrolyte system, made of SDS and PDAC (poly(dialkyldimethylammonium chloride)), a variety of nano- and micro-particles were found upon changing the SDS/PDAC molar ratio [48]. Below the critical micellar aggregation of pure SDS in aqueous solutions, large domains of a well-ordered phase, with spacings of ~ 4 nm, were found. Based on the images, and supported by SAXS data, the authors concluded that the ordered regions are of a hexagonal liquid crystalline phase of SDS that formed by screening of electrostatic interactions by the polymer charges. Small spheroidal micelles coexisting with particles of several tens of nm were observed in the solubilization domain. Many particles were faceted, with short threadlike micelles emerging from their surfaces. The size of these complexes decreased, and they became less numerous, as the solubilization process advanced by increasing the SDS/PDAC molar ratio, although complete solubilization was not reached and some (probably metastable) complexes coexisted with spheroidal micelles at all the conditions studied.

Viscous phases often form in surfactant solutions upon increasing the surfactant concentration or temperature, adding salt to charge surfactants, or varying the molar ratio between the components in mixed surfactant systems. In some cases, a sharp rise of several orders of magnitudes in the viscosity was reported, followed by a strong decrease to almost the viscosity of water [49, 50]; in a few

instances, the formation of a second viscosity peak was also found [49]. The viscosity increase was correlated to micellar growth, and the viscosity decrease was explained by a structural transition from linear to branched micelles and saturated networks [51]. These explanations are based primarily on the rheological measurements because direct structural information of such systems is still limited due to difficulties in preparing thin vitrified films of highly-viscous phases.

Early cryo-TEM studies by Clausen *et al.* [52] showed a transition from spheroidal to long, flexible micelles of cetyltrimethylammonium bromide and chloride surfactants at increasing salt concentration. More recently, Bernheim-Groswasser *et al.* [2] showed a gradual transformation from spheroidal micelles, existing at low surfactant concentrations, to long, thread-like micelles and then to elongated branched micelles and a saturated networks in aqueous solutions of the gemini (dimeric) surfactant, 12-2-12 (dimethylene-1,2-bis(dodecyl dimethylammonium bromide), at increasing concentrations. Vesicles were found in the viscous phase of the analogue hybrid fluorocarbon/hydrocarbon gemini surfactant $C_8^F C_4-2-C_8^F C_4$ [53], while saturated stiff networks were observed in the hybrid $C_8^F C_4-2-12$ dimer. It was further shown that after phase separation of $C_8^F C_4-2-C_8^F C_4$ and 12-2-12 mixtures, entangled threadlike micelles existed in the 12-2-12 rich phase (upper phase), while vesicles formed in the lower viscous phase contained mainly $C_8^F C_4-2-C_8^F C_4$. Other intermediates, including ribbons, open bilayers, small rings, and linear micelles, were observed depending on the mixing ratios between the various components [53].

Corce and co-workers [54] investigated the effect of added salt in the EHAC/KCl system, and correlated the microscopy findings to the rheological curve. Cryo-TEM images showed a transition from spheroidal micelles in the absence of salt to linear elongated micelles at low KCl concentrations (below the concentration of the viscosity peak), and to a network consisting of 3-fold junctions of branched micelles at compositions above the concentration of the viscosity peak. Linear and branched micelles were also shown by cryo-TEM in mixtures of $CpClO_3/NaClO_3$ (hexadecylpyridinium chlorate/sodium chlorate) [13]. However, folded and crumpled bilayer fragments were also found frequently in the vitrified samples. They were explained as long-lived intermediate structures that formed on the grid during specimen preparation by the strong shearing forces applied during blotting and formation of the thin films [13].

A peak in the viscosity vs. surfactant molar ratio curve was also reported for a system composed of the surfactant C12 β G1 (*n*-dodecyl- β -D-glucopyranoside) in the presence of increasing SDS concentrations, above 40° C [55]. Our cryo-TEM studies [56] revealed a continuous transformation from a lamellar phase in the absence of SDS, through saturated micellar networks, to a micellar phase of spherical and short threadlike micelles, upon gradual

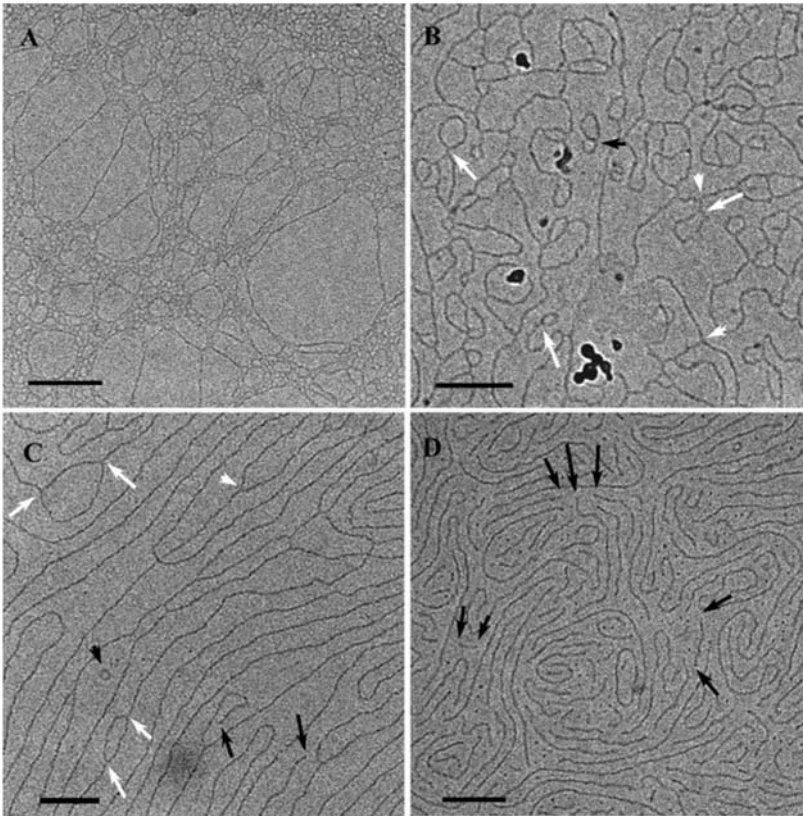


Figure 4. Cryo-TEM images of C12 β G1/SDS mixtures, at a 5% constant total surfactant concentration and increasing SDS fractions equal to 0.07 (A), 0.14 (B) and 0.2 (C). Panels (A) and (B) relate to samples of comparable viscosity found below and above the viscosity peak concentration, respectively. Both images show well-developed networks made of elongated branched segments and closed rings. The network in (A) is saturated, while in (B) some free rings are also observed, but not micellar endcaps. At low viscosities (~ 0.01 Pa S, panel C) micellar endcaps appear, although interconnections between micelles are still frequent. (D) Threadlike and spheroidal micelles coexist at high SDS content. Arrowheads in B and C point to 3-fold junctions (white), and rings (black). Arrows point to micellar segments connected to rings (white), and micellar endcaps (black). Bars = 100 nm.

increase in SDS levels. In this system, however, saturated networks of different topology exist on both sides of the viscosity peak (Figure 4). At low SDS content, and throughout the region of concentrations below the viscosity peak, the network was made of multiple micellar segments that emerge typically from small, closely packed and connected rings (Figure 4A). At concentrations above the viscosity peak, where theoretically linear micelles should exist, a micellar phase of well-developed networks, consisting typically of 3-fold junctions, was found at high and medium viscosities. At high viscosities, the network was

saturated, while at medium viscosities individual rings were observed occasionally, coexisting with the connected micelles (Figure 4B). Upon further addition of charges, the number of junction points decreased and the number of micellar endcaps increased, but connected micelles were observed even at viscosities comparable to those of water (Figure 4C). Eventually, at much higher SDS content, linear thread-like assemblies formed and coexisted with globular micelles (Figure 4D).

Pure olive oil can be transformed into a butter-like spread (i.e., a “gel”) by adding a sufficient amount of a monoglyceride. This is, of course, a phenomenon of interest to the food industry, and is behind the water-free olive-oil spread of the Eger Company of Israel. The product cannot be made into thin liquid films at room temperature and it melts into a low-viscosity liquid above 60° C. To directly image the nanostructure of this gel, we melted it at about 60° C, prepared cryo-specimens in a CEVS kept at the same temperature, cooled the grids to 58° C in the CEVS, and quenched the samples in liquid nitrogen. Olive oil is vitrified even in that rather poor cryogen. Figure 5 shows an example of such cryo-TEM images. Arrows point to stacks of lamellae. They have sufficient contrast only when positioned parallel to the electron beam. When they are positioned perpendicularly to the beam, there is insufficient contrast

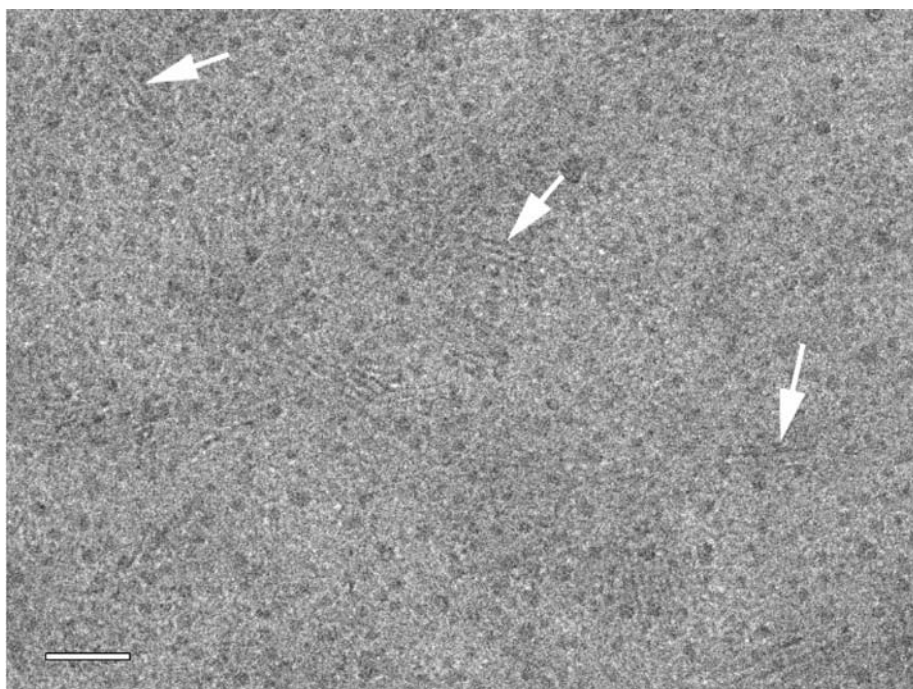


Figure 5. Cryo-TEM image of 7% monoglyceride in olive oil vitrified in the gel phase, from 58° C. Arrows point to stacks of lamellae that are parallel to the electron beam. Bar = 50 nm.

to make them visible; thus, much of the field-of-view does not show lamellae. That the gel phase is indeed made of small liquid crystalline domains was verified by SAXS and by light microscopy [15].

4. Conclusions and Perspectives for the Future

While the applications of direct imaging (“real-space”) methods to elucidate the nanostructure of LMOG gels have been so far rather limited, recent technical development in cryo-TEM make the technique much more applicable for the study of those systems. Perhaps the most important development is the wide availability of reliable cooled-CCD cameras. Those cameras make low-dose imaging, vital for gel systems applications, much easier. Higher format cameras (4 mega-pixel, at least), and lower prices (they are still not cheap, but prices are expected to continue to fall) make them the tool of choice to record high resolution images that can be easily digitally processed. The great challenge when gels are concerned is still specimen preparation. We expect more on-the-grid gelation experiments to be used, applying either “home-built” or commercial CEVS-type systems. FFR, regrettably a “dying art”, should be “revived” and used more for imaging high-viscosity systems.

Scanning probe microscopes, such as the atomic force microscope (AFM), are also potentially very useful. Many can be operated on liquid and semi-liquid systems under controlled temperature and humidity in operation modes that are minimally destructive to labile systems. Thus, we may expect to see clear images of gel systems emerge from these microscopes, too. A key to the success of this direction will depend on development of techniques by a “community” focusing on imaging this class of materials.

References

- [1] Danino, D.; Talmon, Y.; Levy, H.; Beinert, G.; Zana, R.; “Branched thread-like micelles in an aqueous-solution of a trimeric surfactant”, *Science*, **1995**, *269*, 1420–1421.
- [2] Bernheim-Groswasser, A.; Zana, R.; Talmon, Y. “Sphere-to-cylinder transition in aqueous micellar solution of a dimeric (gemini) surfactant”, *J. Phys. Chem. B*, **2000**, *104*, 4005–4009.
- [3] Zheng, Y.; Won, Y.Y.; Bates, F.S.; Davis, H.T.; Scriven, L.E.; Talmon, Y. “Directly resolved core-corona structure of block copolymer micelles by cryo-transmission electron microscopy”, *J. Phys. Chem. B*, **1999**, *103*, 10331–10334.
- [4] Jean, B., Oss-Ronen, L.; Terech, P.; Talmon, Y. “Monodisperse bile salt nanotubes in water: kinetics of formation”, *Adv. Mater.*, **2005**, *17*, 728–731.
- [5] Terech, P.; de Geyer, A.; Struth, B.; Talmon, Y. “Self-assembled monodisperse steroid nanotubes in water”, *Adv. Mater.*, **2002**, *14*, 495–498.
- [6] Talmon, Y. “Cryogenic temperature transmission electron microscopy in the study of surfactant systems”, In *Modern characterization methods of surfactant systems*, B.P. Binks, Ed., New York: Marcel Dekker, **1999**, Chap. 5, pp. 147–178.

- [7] Danino, D.; Bernheim-Groswasser, A.; Talmon, Y. "Digital cryogenic transmission electron microscopy: an advanced tool for direct imaging of complex fluids", *Coll. Surf. A-Physicochem. Eng. Aspects*, **2001**, *183*, 113–122.
- [8] Uhlmann, D.R. "A kinetic treatment of glass formation", *J. Non-cryst. Solids*, **1972**, *7*, 337–348.
- [9] Siegel, D.P.; Green, W.J.; Talmon, Y. "The mechanism of lamellar-to-inverted hexagonal phase-transitions – a study using temperature-jump cryoelectron microscopy", *Biophys. J.*, **1994**, *66*, 402–414.
- [10] Bellare, J.R.; Davis, H.T.; Scriven, L.E.; Talmon, Y. "Controlled environment vitrification system - an improved sample preparation technique", *J. Electron Microsc. Techn.*, **1988**, *10*, 87–111.
- [11] Chestnut, M.H.; Siegel, D.P.; Burns, J.L.; Talmon, Y. "A temperature-jump device for time-resolved cryo-transmission electron-microscopy", *Microsc. Res. Techn.*, **1992**, *20*, 95–101.
- [12] <http://www.vitrobot.com/>.
- [13] Danino, D.; Talmon, Y.; Zana, R. "Cryo-TEM of thread-like micelles: on-the-grid microstructural transformations induced during specimen preparation", *Coll. Surf. A-Physicochem. Eng. Aspects*, **2000**, *169*, 67–73.
- [14] Zheng, Y.; Lin, Z.; Zakin, J.L.; Talmon, Y.; Davis, H.T.; Scriven, L.E. "Cryo-TEM imaging the flow-induced transition from vesicles to threadlike micelles", *J. Phys. Chem. B*, **2000**, *104*, 5263–5271.
- [15] Schmidt, J.; Eger, S.; Talmon, Y. (manuscript in preparation).
- [16] Talmon, Y.; Burns, J.L.; Chestnut, M.H.; Siegel, D.P. "Time-resolved cryotransmission electron-microscopy", *J. Electron Microsc. Techn.*, **1990**, *14*, 6–12.
- [17] Fink, Y.; Talmon, Y., "The Flow Thru Controlled Environment Vitrification System", In *Proc. 13th Int'l Congress on Electron Microsc.*, **1994**, *1*, p. 37.
- [18] Danino, D.; Gupta, R.; Satyavolu, J.; Talmon, Y. "Direct cryogenic-temperature transmission electron microscopy imaging of phospholipid aggregates in soybean oil", *J. Coll. Interface Sci.*, **2002**, *249*, 180–186.
- [19] Burns, J.L.; Talmon, Y. "Freeze-fracture-replication using the controlled environment vitrification system (CEVS)", *J. Electron Microsc. Techn.*, **1988**, *10*, 113–114.
- [20] Wade, R.H.; Terech, P.; Hewat, E.A.; Ramasseul, R.; Volino, F. "The network structure of a steroid/cyclohexane physical gel", *J. Coll. Interface Sci.*, **1986**, *114*, 442–251.
- [21] Laughlin, R.G.; Munyon, R.L.; Burns, J.L.; Coffindaffer, T.W.; Talmon, Y. "Physical science of the dioctadecyldimethylammonium chloride water-system .3. Colloidal aspects", *J. Phys. Chem.*, **1992**, *96*, 374–383.
- [22] Kaiser, N.; Kimpfler, A.; Massing, U.; Burger, A.M.; Fiebig, H.H.; Brandl, M.; Schubert, R. "5-fluorouracil in vesicular phospholipid gels for anticancer treatment: entrapment and release properties", *Int. J. Pharm.*, **2003**, *256*, 123–1231.
- [23] Mukhopadhyay, S.; Maitra, U.; Ira; Krishnamoorthy, G.; Schmidt, J.; Talmon, Y. "Structure and dynamics of a molecular hydrogel derived from a tripodal cholamide", *J. Am. Chem. Soc.*, **2004**, *126*, 15905–15914.
- [24] Estroff, L.A.; Leiserowitz, L.; Addadi, L.; Weiner, S.; Hamilton, A.D.; "Characterization of an organic hydrogel: a cryo-transmission electron microscopy and X-ray diffraction study", *Adv. Mater.*, **2003**, *15*, 38–42.
- [25] Oss-Ronen, L. "Nanosopic characterization of self-assembled nanotubules of lithocholic acid in water", *M.Sc. Thesis, Technion – Israel Institute of Technology, Haifa, Israel*, **2004**.
- [26] Boettcher, C.; Schade, B.; Fuhrhop, J.H. "Comparative cryo-electron microscopy of noncovalent N-dodecanoyl- (D- and L-) serine assemblies in vitreous toluene and water", *Langmuir*, **2001**, *17*, 873–877.

- [27] Lambert, O.; Levy, D.; Ranck, J.L.; Leblanc, G.; Rigaud, J.L. "A new "gel-like" phase in dodecyl maltoside-lipid mixtures: implications in solubilization and reconstitution studies", *Biophys. J.*, **1998**, *74*, 918–930.
- [28] Vethamuthu, M.S.; Almgren, M.; Brown, W.; Mukhtar, E. "Aggregate structure, gelling, and coacervation within the L(1) phase of the quasi-ternary system alkyltrimethylammonium bromide sodium deoxycholate water", *J. Coll. Interface Sci.*, **1995**, *174*, 461–479.
- [29] Schneider, J.P.; Pochan, D.J.; Ozbas, B.; Rajagopal, K.; Pakstis, L.; Kretsinger, J. "Responsive hydrogels from the intramolecular folding and self-assembly of a designed peptide", *J. Am. Chem. Soc.*, **2002**, *124*, 15030–15037.
- [30] Pochan, D.J.; Pakstis, L.; Ozbas, B.; Nowak, A.P.; Deming, T.J. "SANS and Cryo-TEM study of self-assembled diblock copolypeptide hydrogels with rich nano- through microscale morphology", *Macromolecules*, **2002**, *35*, 5358–5360.
- [31] Pakstis, L.M.; Ozbas, B.; Hales, K.D.; Nowak, A.P.; Deming, T.J.; Pochan, D. "Effect of chemistry and morphology on the biofunctionality of self-assembling diblock copolypeptide hydrogels", *Biomacromolecules*, **2004**, *5*, 312–318.
- [32] Hartgerink, J.D.; Beniash, E.; Stupp, S.I. "Self-assembly and mineralization of peptide-amphiphile nanofibers", *Science*, **2001**, *294*, 1684–1688.
- [33] Weijers, M.; Visschers, R.W.; Nicolai, T. "Light scattering study of heat-induced aggregation and gelation of ovalbumin", *Macromolecules*, **2002**, *35*, 4753–4762.
- [34] Moren, A.K.; Regev, O.; Khan, A. "A Cryo-TEM study of protein-surfactant gels and solutions", *J. Coll. Interface Sci.*, **2000**, *222*, 170–178.
- [35] Viebke, C.; Borgstrom, J.; Piculell, L. "Characterization of kappa-carrageenan and iota-carrageenan coils and helices by mALLS/gpc", *Carbohydrate Polym.*, **1995**, *27*, 145–154.
- [36] Sugiyama, J.; Rochas, C.; Turquois, T.; Tarevel, F.; Chanzy, H. "Direct imaging of polysaccharide aggregates in frozen aqueous dilute systems", *Carbohydrate Polym.*, **1994**, *23*, 261–264.
- [37] Borgstrom, J.; Piculell, L.; Viebke, C.; Talmon, Y. "On the structure of aggregated kappa-carrageenan helices. A study by Cryo-TEM, optical rotation and viscometry", *Int. J. Biol. Macromol.*, **1996**, *18*, 223–229.
- [38] Chronakis, I.S.; Borgstrom, J.; Piculell, L. "Conformation and association of kappa-carrageenan in the presence of locust bean gum in mixed NaI/CsI solutions from rheology and cryo-TEM", *Int. J. Biol. Macromol.*, **1999**, *25*, 317–328.
- [39] Piculell, L.; Borgstrom, J.; Chronakis, I.S.; Quist, P.O.; Viebke, C. "Organisation and association of kappa-carrageenan helices under different salt conditions", *Int. J. Biol. Macromol.*, **1997**, *21*, 141–153.
- [40] Putaux, J.L.; Buleon, A.; Chanzy, H. "Network formation in dilute amylose and amylopectin studied by TEM", *Macromolecules*, **2000**, *33*, 6416–6422.
- [41] Jeong, B.; Kibbey, M.R.; Birnbaum, J.C.; Won, Y.Y.; Gutowska, A. "Thermogelling biodegradable polymers with hydrophilic backbones: PEG-g-PLGA", *Macromolecules*, **2000**, *33*, 8317–8322.
- [42] Loizou, E.; Butler, P.; Porcar, P.; Kesselman, E.; Talmon, Y.; Schmidt, G. "Large scale structures in nanocomposite hydrogels", (manuscript in preparation).
- [43] Paulsson, M.; Edsman, K. "Controlled drug release from gels using surfactant aggregates. II. Vesicles formed from mixtures of amphiphilic drugs and oppositely charged surfactants", *Pharma. Res.*, **2001**, *18*, 1586–1592.
- [44] Marques, E.F.; Regev, O.; Khan, A.; Miguel, M.D.; Lindman, B. "Interactions between cationic vesicles and oppositely charged poly electrolytes-phase behavior and phase structure", *Macromolecules*, **1999**, *32*, 6626–6637.

- [45] Regev, O.; Marques, E.F.; Khan, A. "Polymer-induced structural effects on catanionic vesicles: formation of faceted vesicles, disks, and cross-links", *Langmuir*, **1999**, *15*, 642–645.
- [46] Nilsson, S.; Goldraich, M.; Lindman, B.; Talmon, Y. "Novel organized structures in mixtures of a hydrophobically modified polymer and two oppositely charged surfactants", *Langmuir*, **2000**, *16*, 6825–6832.
- [47] Goldraich, M.; Schwartz, J.R.; Burns, J.L.; Talmon, Y. "Microstructures formed in a mixed system of a cationic polymer and an anionic surfactant", *Coll. Surf. A-Physicochem. Engin. Aspects*, **1997**, *125*, 231–244.
- [48] Nizri, G.; Magdassi, G.; Schmidt, J.; Cohen, Y.; Talmon, Y. "Microstructural characterization of micro- and nanoparticles formed by polymer-surfactant interactions", *Langmuir* **2004**, *20*, 4380–4385.
- [49] Hoffmann, H. "Viscoelastic surfactant solutions", In *Structure and Flow in Surfactant Solutions*, ACS Symposium Series 578, C.A. Herb and R. K. Prud'homme, Eds., Washington, DC: The American Chemical Society, **1994**, Chap. 1, pp. 1–31.
- [50] Raghavan, S.R.; Fritz, G.; Kaler, E.W. "Wormlike micelles formed by synergistic self-assembly in mixtures of anionic and cationic surfactants", *Langmuir*, **2002**, *18*, 3797–3803.
- [51] Lequeux, F.; "Reptation of connected wormlike micelles", *Europhys. Lett.*, **1992**, *19*, 675–681.
- [52] Clausen, T.M.; Vinson, P.K.; Minter, J.R.; Davis, H.T.; Talmon, Y.; Miller, W.G. "Viscoelastic micellar solutions - microscopy and rheology", *J. Phys. Chem.*, **1992**, *96*, 474–484.
- [53] Oda, R.; Huc, I.; Danino, D.; Talmon, Y. "Aggregation properties and mixing behavior of hydrocarbon, fluorocarbon, and hybrid hydrocarbon-fluorocarbon cationic dimeric surfactants", *Langmuir*, **2000**, *16*, 9759–9769.
- [54] Croce, V.; Cosgrove, T.; Maitland, G.; Hughes, T.; Karlsson, G. "Rheology, cryogenic transmission electron spectroscopy, and small-angle neutron scattering of highly viscoelastic wormlike micellar solutions", *Langmuir*, **2003**, *19*, pp. 8536–8541.
- [55] Kaler, E.W.; Baser, B. (manuscript in preparation).
- [56] Ziserman, L.; Baser, B.; Kaler, E.W.; Danino, D. (manuscript in preparation).

Chapter 10

MOLECULAR GELS AND SMALL-ANGLE SCATTERING

Pierre Térech

*UMR5819 CEA-CNRS-Université J. Fourier, DRFMC-SI3M-PCM, CEA-Grenoble
17, rue des Martyrs, 38054 Grenoble Cedex 9, France*

1. Foreword	276
2. Introduction	276
3. Basic Principles	279
4. Form-Factors of Rod-Like Scatterers	282
4.1. Plain Fibers	282
4.2. Short Rods	290
5. Semi-Rigid Fibers	292
6. Fibers with Anisometric Sections	293
6.1. Rectangular Sections	294
6.2. Elliptical Cross-Sections	294
7. Tubes	295
8. Helices	298
9. Scattering by the Junction Zones in the Networks	300
9.1. Form-Factor of a Disk	300
9.2. Spherulitic Nodes	302
9.3. Random Nodes: Debye-Büeche Context	302
9.4. Ideally Homogeneous Networks	303
9.5. Fractal Context	304
9.6. Orientation Correlated Domains	305
10. Structure Factor Peak in Poorly Organized Fibrillar Scatterers	307
11. Oriented Fibers	311
11.1. One Dimensional Crystal and Fiber Diffraction Pattern	311
11.2. Shear Alignment	312
12. Real Space Data	316
13. Kinetic Studies	317

14. Useful Hints for a Standard SANS Investigation of Molecular Gels	319
15. Conclusions	321

1. Foreword

The present chapter is not a treatise on neutron scattering but a guide for applying the small angle scattering technique to the original materials that are molecular gels (i.e., mostly those containing low molecular mass organic gelators (LMOGs), although some containing inorganic gelators are also known). All details and rigorous mathematical formalisms will be found in specialized collections. Classical demonstrations are not detailed here except for some basic models, such as the rod-like and helical structures so as to take into account both their academic interest and their high level of occurrence in real systems. Specific hints are also given to prepare a classical experimental program, and guidelines for data analysis are proposed in the context of Self-Assembled Fibrillar Networks (SAFINs) that form the solid-like part of molecular gels. Up to now, examples of structural investigations using the Small Angle Scattering (SAS) technique are more numerous with molecular organogels than with hydrogels. There is growing interest in hydrogels, motivated by their potential biological applications and utility in nanosciences. Selected practical illustrations are presented. Prospective digressions are included for fundamental issues that are usually not treated in detail. Thus, chirality, heterogeneities, kinetics, ionic interactions, and structure factors are aspects for which efforts expected from theoreticians and experimentalists are clearly needed for a satisfactory description of the scattering by molecular gels.

2. Introduction

For more than two decades, the SAS technique has been shown to be a very powerful tool for the investigation of structures of a wide variety of colloidal systems. Photons (from infrared to X-rays), electrons and neutrons can be used to probe the structure of matter. They provide complementary information based on their interaction with matter. The interaction of X-rays with electrons in molecules is electromagnetic while the nature of the interaction of an electron beam is electrostatic. Neutrons interact with atomic nuclei through short-range strong nuclear forces. Both X-rays and neutrons are frequently used to study the molecular gels [1]. Light scattering (SALS) can be used for a few micellar gels with appropriate optical properties. Unfortunately, many SAFIN gels are more or less turbid, depending upon the concentrations, and thus may not be suited for SALS studies. A supplemental interaction (not developed here) is

available with neutrons through the dipole-dipole interaction between the magnetic moment of the neutrons and that of unpaired electron(s) when present in the system. Other techniques to probe the structures at the nanoscopic scale of fragile systems, such as molecular gels, are Transmission Electron Microscopy (TEM) and Atomic Force Microscopy (AFM), for instance. Nevertheless, SAS has the great advantage of using samples as they are and provides immediately a picture in the reciprocal space that is a statistical average over the macroscopic irradiated volume. Relations between reciprocal and real space structural features in molecular gels are presented here.

Standard SAS equipment usually gives access to 3 decades in reciprocal space (0.001 \AA^{-1} – 1 \AA^{-1}), corresponding to ca. 6000–6 \AA sizes of the scatterers in real space. Smaller scattering angles are accessible with special spectrometers (ultra-small angle diffractometer with a Bonse-Hart configuration, for instance) [2]. Larger angles are part of the diffraction techniques from which crystallographic molecular structures are extracted (see Chapter 11). A first question concerns the choice of the most appropriate radiation. Considerations for choosing between X-rays and neutrons are:

1. Penetration depth: short-range nuclear interactions allow a deeper penetration of the beam. This can be useful for systems for which X-ray transmission is not good enough. The thickness of the sample is chosen to optimize the transmission, the potentiality for undesirable multiple scattering and, finally, the signal/noise ratio of the scattered intensity in the experimental Q -range (*vide infra*).

2. Contrast variation: depending on the chemical composition of the systems, it may be advantageous to analyze the scattering data for which the contrast profile has been varied. This is conveniently achieved with neutron scattering by changing the isotopic composition of the solvent (deuterated *versus* protiated). Sometimes, this can also be achieved by changing the isotopic structure of the gelator itself. However, the synthetic challenges associated with this approach are usually difficult. A contrast variation experiment can also be performed by keeping the composition of the system unchanged but changing the nature of the radiation. In particular, if metallic elements and/or protons are present in the gelator, complementary X-ray/neutron scattering experiments can be useful.

3. Solvent type: depending upon the type of liquid in a molecular gel, the corresponding deuterated liquid may or may not be available at a reasonable price.

4. Signal limitation: to extract a pure form-factor contribution in the scattering signal, as dilute systems as possible must be studied in the gel domain of the phase diagram. Under such conditions, the acquisition time to cover the full desired Q -range (by varying the sample to detector distance and possibly the radiation wavelength) is important. Molecular gels can be formed

at concentrations as low as 0.1% v/v. Thus, an equivalent solid quantity of ca. 5 mg gelator (50 μ L) that is irradiated by a neutron beam can be made ca. 50/100 times lower if a capillary is used in a micro-focus synchrotron beam experiment. The flux at the sample position of the most powerful neutron source (i.e., spectrometer D22 at ILL, Institut Laue Langevin, Grenoble, France) is 1.2×10^8 neutrons/($\text{cm}^2 \cdot \text{s}$) while the flux through the sample at the synchrotron source ID2-ESRF (European Synchrotron Radiation Facility (ESRF), Grenoble, France) is 8×10^{12} photons/s. As a result, the counting time is a few seconds at ESRF and a couple of hours at ILL.

5. Radiation damage: intense synchrotron beams may “burn” organic molecules. Radiation damaging usually does not exist with conventional X-ray (rotating anodes) or neutron sources.

6. Q -resolution: the devices for radiation detection are specific for each type of radiation and have their own limitations (N.B., intensity dynamic range, dead time, transfer of data, linearity of the response, correction procedures, intrinsic background). Different options exist mainly for X-ray detection. The Q -resolution needed for a given scattering profile has to be taken into account. If numerous and narrow oscillations and/or Bragg peaks are expected, it is recommended to use X-ray experiments which provide a much larger number of points (ID2, ESRF 1024 \times 1024 points) compared to neutron experiments (usually 64 or 128 points per side of a 96 \times 96 cm^2 detector). The final Q -resolution, including the beam divergence, the λ distribution and the detection condition, is usually better with a synchrotron source.

7. Amplitude of the contrast factor: with large facilities, this parameter is usually not very crucial except if contrast variation experiments are involved.

8. Absolute intensities: the mechanism of formation of molecular gels, starting from individual gelator molecules provides important information, and the molecular weight per unit length of fiber is a determinant parameter. Absolute intensities can also be useful for quantitative models for the determination

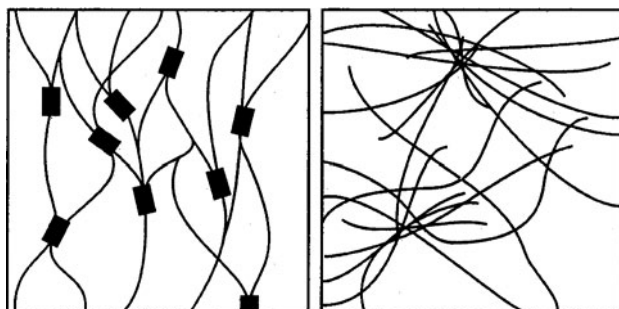


Figure 1. Cartoon representation for two extreme ideal situations in SAFINs. *Left*: crystalline-like network with extended junction zones; *right*: swollen network of entangled semi-rigid fibers.

of the interfacial surface per unit volume of aggregate, etc. Neutron detectors allow an easy calibration of the intensities.

SAFINs are made up of fibers whose interactions may lead to two main classes of networks. Figure 1 shows two situations resulting from interactions that are slightly attractively or repulsively unbalanced potentials between the constitutive fibers. The SAS technique attempts to characterize the structural aspects of such SAFINs.

The following discussions pertain to neutron scattering experiments, and comparisons with X-ray scattering are occasionally given.

3. Basic Principles

Simplified expressions are given in the chapter. Rigorous formalisms are found in original citations [3–5].

A quantum-mechanical context is necessary to deal with basic equations describing the wave functions of neutrons. The Fermi nuclear potential has a range small enough with respect to the neutron wavelength λ (λ is typically 6–15 Å) to consider that the interaction is punctual. Consequently, the neutron scatters isotropically in contrast with X-rays. The scattering of neutrons by matter can affect not only their momentum $m\vec{v}$ ($m\vec{v} = \hbar\vec{k}/2\pi$, where h is Planck's constant, \vec{k} is the neutron wave vector and \vec{v} is its velocity) but also their energy. In a classical scattering experiment, with momentum Q and energy E transfers, an intensity $I(\vec{Q}, E)$ is measured. The intensity depends on time-dependent correlations between positions of pairs (i, j) of atoms in the irradiated system. The relative positions and motions of atoms in the specimen can be related to the intensity of the scattered neutrons using a specific experimental set-up. For instance, inelastic coherent scattering provides information about the collective motion of correlated pairs. The present chapter focuses on the SAS technique, where only elastic scattering is considered.

The inter-relation of momentum transfer and energy during collisions between neutrons and matter leads to relations (Eq. (1)) describing the momentum transfer. In the following, Q is expressed in Å⁻¹, *inc* subscript is for incident while *scat* refers to the scattered beam.

$$h/2\pi(\vec{k}_{inc} - \vec{k}_{scat}) = h/2\pi \vec{Q} \quad (1a)$$

$$Q = 4\pi \sin \theta / \lambda \quad (1b)$$

If the scattering proceeds in elastic conditions, only the direction of the beam is modified by the collisions and not its momentum ($k_{inc} = k_{scat} = 2\pi/\lambda$). Equation (1a) reduces to Eq. (1b) where θ is half the scattering angle. If pairs from different nuclei in the system interfere, the corresponding elastic coherent scattering can provide information about the structure of the matter at equilibrium. The component due to the interaction of the neutron wave with individual

nuclei ($i = j$) is independent (no interferences) and is additive for each nucleus. Such a component is the incoherent scattering and it provides information about atomic diffusion. There is no incoherent scattering for nuclei with a zero nuclear spin (e.g., ^{12}C , ^{16}O , etc.) since they produce no interaction with the neutron spin. The level of incoherent (and coherent) scattering varies strongly with the isotope considered, and it is listed in specialized Tables [6]. An illustration is given for ^1H and ^2H for which the ratio of incoherent cross-sections σ_H/σ_D is ca. 80.26/2.05. For SAS experiments, the incoherent scattering is undesirable and the concentration of elements with high levels of incoherent scattering should be kept to a minimum. The nuclear interaction, defined by the Fermi pseudo-potential, is considered as *punctual* (m_n is the neutron mass) according to Eq. (2):

$$U(\vec{r}) = (h/2\pi)m_n b_i \delta(\vec{r} - \vec{r}_i) \quad (2)$$

b_i is the neutron scattering length of the nucleus i (related to the cross-section $\sigma = 4\pi b^2$ expressed in barns; 1 barn = 10^{-24} cm²) and measures the strength of the nuclear interaction (with a negative sign for a repulsive interaction). The order of magnitude is ca. 10^{-12} cm and is a real number for most nuclei. Complex values of b_i mean that b_i depends upon the energy of the incident beam, and the absorption component is described by the imaginary part of the scattering length. For elastic scattering conditions, the incident plane wave e^{ikr} is scattered as spherical wavefronts $(-b/r)e^{ikr}$ by a scattering center at the origin of the coordinate system. The time dependence, $\exp(-i\omega t)$, does not appear in the expression since the scattering is elastic. The scattering law for a system is expressed from correlations between the positions of pairs of atoms in the system. In the direction \vec{k}_{scat} , the scattered wave has a $\vec{Q} \cdot (\vec{r}_i - \vec{r}_j)$ phase and an amplitude $A(\vec{Q})$ for a given orientation of the vector \vec{Q} (modulus Q):

$$A(\vec{Q}) = (A_0/r) \exp(ikr) \sum_{i,j} b_i \exp(i\vec{Q} \cdot (\vec{r}_i - \vec{r}_j)) \quad (3)$$

The summation in Eq. (3) is extended to all i, j pairs in the scatterer, as assumed for coherent scattering conditions. The contrast between the aggregate and the solvent may present discontinuities based on the distance within the rod-like aggregate (usually radial). Examples of heterogeneous densities of scattering length will be given.

$$\Delta\rho = \frac{1}{V} \int_V \rho(r) d^3r - \rho_s \quad (4)$$

Since SAS operates at low angles (low resolution $2\pi/Q_{\text{max}}$), it is convenient for simplification to assume that the scatterer is locally a continuous medium with a uniform neutron scattering length density (Eq. (4)). The aggregates

with a scattering length density b_{agg} are immersed in a liquid with a uniform scattering length density b_{solv} so that $\rho(\vec{r})$ is no longer r -dependent. $\Delta\rho = (b_{\text{agg}} - b_{\text{solv}})/v$ is the contrast factor; the summation of the b_i elements is done over the aggregate volume v and the same volume of solvent.

$$A(\vec{Q}) = A_0/r \exp(ikr) \Delta\rho \int \exp(i\vec{Q} \cdot \vec{r}_{ij}) d\vec{r} \quad (5)$$

The scattered intensity is the scattered power flux expressed as the average of the squared amplitude ($I(\vec{Q}) = \langle A(\vec{Q}) \cdot A^*(\vec{Q}) \rangle = \langle |A(\vec{Q})|^2 \rangle$) in a summation extended to all i, j pairs defined by $\vec{r}_{ij} = \vec{r}_i - \vec{r}_j$.

$$I(\vec{Q}) = (I_0/r^2) \Delta\rho^2 \left| \int \exp(i\vec{Q} \cdot \vec{r}_{ij}) d\vec{r} \right|^2 \quad (6)$$

Equation (6) is the fundamental equation describing the small-angle elastic and coherent scattering. The integral concerns the irradiated volume V in which large-scale fluctuations of the scattering length density define the individual contours of the aggregates. At $Q \rightarrow 0$, all scattered waves are in-phase and the absolute value of Eq. (6) reduces to:

$$I(Q \rightarrow 0) = (N_{\text{agg}} v \Delta\rho)^2 \quad (7)$$

N_{agg} is the number of single aggregates of volume v ($V = vN_{\text{agg}}$). With SAFINs, V is related to the critical aggregation concentration cac of the gelator. The determination of cac (using fluorescence, ESR, NMR techniques, etc.) is important to estimate all absolute quantities associated to the amount of gelator in the fibrillar aggregates $C = C_0 - cac$, while C_0 is the global gelator concentration. The extraction of any structural information from SANS data requires careful attention to the units used. The flux is expressed as the number of neutrons per unit time and unit area at the sample position. The differential $d\sigma(Q)/d\Omega$ is the number of scattered neutrons per unit time relative to the incident flux per unit solid angle at Q and *per unit volume of sample*. The partial coherent cross-section is $d\sigma_{\text{coh}}/d\Omega$.

Widespread evidence of the prominence of fiber-like morphologies in SAFINs has been collected from electron micrographs, in particular. Coherent scattering is generated by large-scale fluctuations of the neutron scattering length density. These heterogeneities are associated with all kinds of a solid-like aggregates present in the three-dimensional networks. A first basic question is: Why using SAS techniques? It is not *a priori* trivial that working in the reciprocal Q -space is an advantage when dealing with molecular gels. In fact, in most cases, fundamental and practical reasons may account for this choice. Rheologically, molecular gels exhibit significant yield stresses (a few hundreds of Pa for a 1% gel). Thus, molecular gels do not flow and are soft solids with a variety of specific viscoelastic properties [7]. This consistency makes the clotting technique on a copper grid, as

described in different cryo-TEM protocols, difficult to be used. Standard SANS measurements (except with micro-focused synchrotron set-up) do not select specific regions of a specimen, but give a statistical average over ca. 0.1 cm^3 volumes. In addition, neutron scattering offers opportunities to obtain complementary patterns with a varied contrast, so as to emphasize or attenuate different regions of the scatterer. A careful examination of the evolution of the scattering profile as a function of the gelator concentration is a pre-requisite before using any numerical analysis. SAFINs are formed with up to 3 basic components:

- fibrillar interconnected species (the infinite network),
- nodal zones and
- smaller and non-connected species (spherical or elongated micelles).

Each component contributes to the scattering and, depending on the concentration, interference effects may also complicate the pattern. A dilute gel corresponds, in fact, to the semi-dilute regime of concentrations of fibers that are overlapping each other. As a first step in the analysis, conditions are sought for which the scattering is dominated by the form-factor of the fibers (lower limit of the semi-dilute concentration range).

4. Form-Factors of Rod-Like Scatterers

A variety of structures can be found with fibrillar species. Their cross-sections can be anisotropic but can also be more-or-less heterogeneous (radial contrast profile). The axial direction can also be subject to different options: curvilinear fiber axes are found in helical morphologies and periodically axial contrast fluctuations are found with special stacking aggregation mechanisms. In all cases, the determination of the geometrical features of the fibers is helpful to elucidate the mechanism of gel formation.

4.1. Plain Fibers

The calculation of the form-factor of cylindrical particles is the first step for the analysis of the scattering of SAFINs. The amplitude $A(\vec{Q})$ of the scattered waves is first considered for a given orientation of the rod with respect to the vector \vec{Q} . To model the situation of randomly oriented rods, as commonly found in molecular gels, all orientations of \vec{Q} for a given point in the fiber (length $2L$) are considered. Vectors $\vec{r}(r \cos \phi, r \sin \phi, z)$ and $\vec{Q}(Q \sin \theta \cos \psi, Q \sin \theta \sin \psi, Q \cos \theta)$ are given in a cylindrical symmetry with $dv = r dr d\phi dz$ (see, for example, Figure 13). Assuming a uniform neutron

scattering length density over the rods of radius R , the amplitude of the scattered wave for a given orientation of vector \vec{Q} is:

$$A(\vec{Q}) = \Delta\rho \int_0^R \int_0^{2\pi} \int_{-\infty}^{+\infty} \exp i[Qr \sin \theta \cos \psi \cos \phi + Qr \sin \theta \sin \psi \sin \phi + Qz \cos \theta] r \, dr \, d\phi \, dz \quad (8)$$

$$A(\vec{Q}) = \Delta\rho \int_0^R r \, dr \int_0^{2\pi} \exp i[Qr \sin \theta \cos(\psi - \phi)] \, dr \, d\phi \times \int_{-\infty}^{+\infty} \exp i[Qz \cos \theta] \, dz \quad (9)$$

Since $\int_{2\pi} \exp(ix \cos \delta) \, d\delta = 2\pi J_0(x)$, it comes:

$$A(\vec{Q}) = \frac{2\pi \Delta\rho}{iQ \cos \theta} [\exp(iQz \cos \theta)]_{-L}^L \int_0^r r J_0(Qr \sin \theta) \, dr \quad (10)$$

$$A(\vec{Q}) = 4\pi L \Delta\rho \frac{\sin(QL \cos \theta)}{QL \cos \theta} \int_0^r r J_0(Qr \sin \theta) \, dr \quad (11)$$

Averaging over all orientations of vector \vec{Q} defined by angles θ and ϕ requires a summation of the type $\frac{1}{4\pi} \int_0^\pi \sin \theta \, d\theta \int_0^{2\pi} d\phi$ which reduces to $\frac{1}{4\pi} \int_0^\pi \sin \theta \, d\theta$ since the averaging over ϕ has already been made to explicit the Bessel function. With oriented systems, this part of the calculation must be strongly modified,

$$A(\vec{Q}) = L\rho \int_0^\pi \frac{\sin(QL \cos \theta)}{QL \cos \theta} \int_0^r r J_0(Qr \sin \theta) \, dr \sin \theta \, d\theta \quad (12)$$

The specific property of the second integral is such that:

$$A(\vec{Q}) = L \Delta\rho \int_0^\pi \frac{\sin(QL \cos \theta)}{QL \cos \theta} \sin \theta \, d\theta \int_0^r r J_0(Qr) \, dr \quad (13)$$

Knowing that Bessel functions can be generated, as in Eq. (14), the amplitude $A(\vec{Q})$ involves a Bessel function of the first kind J_1 (Eq. (15)).

$$\int J_n(x) x^{n+1} \, dx = x^{n+1} J_{n+1}(x) \quad (14)$$

$$A(\vec{Q}) = Lr^2 \Delta\rho \int_0^\pi \frac{\sin(QL \cos \theta)}{QL \cos \theta} \sin \theta \, d\theta \frac{J_1(Qr)}{Qr} \quad (15)$$

The scattered intensity $I(\vec{Q})$ is then:

$$I(Q) = L^2 r^4 \Delta \rho^2 \left[\int_0^\pi \left(\frac{\sin(QL \cos \theta)}{QL \cos \theta} \right)^2 \sin \theta d\theta \right] \cdot \left[\frac{J_1(Qr)}{Qr} \right]^2 \quad (16)$$

The first term can be reduced to Eq. (18) for large values of L knowing that:

$$\int_{-\infty}^{+\infty} \left(\frac{\sin \pi x}{\pi x} \right)^2 dx = 1 \quad (17)$$

$$I(Q) = \frac{L^2 r^4 \Delta \rho^2 \pi}{QL} \left[\frac{J_1(Qr)}{Qr} \right]^2 \quad (18)$$

The final expression simplifies to:

$$I(Q) = \frac{\phi r^2 \Delta \rho^2}{2Q} \left[\frac{J_1(Qr)}{Qr} \right]^2 \quad (19)$$

Equation (19) is used for long, rigid and isolated rods [8] and is given per unit volume V_{sam} of gel (in $[\text{cm}^{-1}]$ with $\phi = nv/V_{\text{sam}} = V/V_{\text{sam}}$). The assembly of fibers themselves has a total volume V of cylinders assumed to have monodisperse sections. A first consequence is that the signal directly depends on V and the square of the contrast. The first part of Eq. (19) is the axial term exhibiting a typical Q^{-1} low- Q intensity decay. The second part of the scattering function is the cross-sectional term describing the interferences in a circular section. It generates typical oscillations in the large Q domain. The experimental intensity results finally from a convolution with the instrumental resolution function Res according to:

$$I(\langle Q \rangle) = \int Res(\langle Q \rangle, Q) \frac{d\sigma(Q)}{d\Omega} dQ \quad (20)$$

where $d\sigma/d\Omega$ is the scattering differential cross-section.

The differential scattering cross-section $d\Sigma/d\Omega$ per unit sample volume ($\Sigma = \sigma/V_{\text{sam}}$) is expressed in cm^{-1} and is the probability of an incident neutron to be scattered by a volume element of the sample in a solid angle element $d\Omega$ of the detector. Measurements are made with gels with the highest transmissions T ($T = \phi/\phi_0 = \exp(-\Sigma d)$, where ϕ is the flux after crossing the sample of thickness d). The concentrations for a form-factor analysis are such that T of the sample must not be very different from that of the solvent to minimize the undesirable effects of both multiple and incoherent scattering of the protons of the gelator.

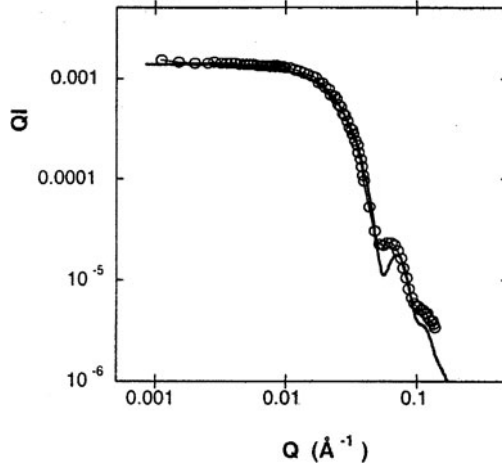


Figure 2. SANS profile of a SAFIN gel of a modified androstanol steroid in deuterated methylcyclohexane [9]. A clear Q^{-1} low- Q decay characterizes the scattering by long and rigid fibers ($r_0 = 77 \text{ \AA}$, $\varepsilon = 0.13$).

Equation (19) can be re-formulated (per unit volume of sample) in terms of L and the section A of the fibers:

$$I(Q) = \frac{\pi L}{Q} \left[A \Delta\rho \frac{2J_1(Qr)}{Qr} \right]^2 \tag{21}$$

Figure 2 shows the axial and cross-sectional contributions in the scattering of a fibrillar system (di-*n*-propyl-17,17-aza-17a-D-homo-5 α -androstanol-3 β steroid (**PAS**) organogel) that can be considered as the first “model” system in the context of scattering studies of molecular gels.

4.1.1. Low- Q asymptotic behavior

Equation (6) can be expanded at low Q values to Eq. (22), knowing that $\exp(x) = 1 + x + \frac{x^2}{2}$.

$$I(Q) = \left\langle \left| \int_V \Delta\rho(r) \left(1 + i\vec{Q} \cdot \vec{r} - \frac{1}{2}(\vec{Q} \cdot \vec{r})^2 + \dots \right) d^3r \right|^2 \right\rangle \tag{22}$$

If the center of gravity of $\Delta\rho(\vec{r})$ is also that for volume v , then:

$$I(Q) = (\Delta\rho v)^2 \left[1 - \frac{1}{3} \frac{Q^2}{\Delta\rho v} \int_v \vec{r}^2 \Delta\rho(\vec{r}) d^3r \right] \tag{23}$$

Eq. (23) includes the definition of the second moment of the distribution of the scattering density [10]:

$$r_g^2 = \frac{1}{\Delta\rho v} \int_v \vec{r}^2 \Delta\rho(\vec{r}) d^3r \quad (24)$$

The analogy with classical mechanics leads to approximate r_g to the radius of gyration:

$$I(Q) = I_0 \left[1 - \frac{Q^2 r_g^2}{3} + \dots \right] \quad (25)$$

corresponding to $I(Q) \cong I_0 \exp -Q^2 r_g^2/3$.

If the form-factor of fibers (Eq. (21)) is considered, the expansion of the Bessel function at $x \rightarrow 0$ is $\left[\frac{2J_1(x)}{x} \right]^2 \rightarrow 1 - \frac{1}{4}x^2$ and gives equivalently:

$$I(Q) = \phi \frac{\pi}{Q} \Delta\rho^2 \pi r^2 \exp(-Q^2 r^2/4) \quad (26a)$$

$$QI(Q) = QI(0) \exp(-r_c^2 Q^2/2) \quad (26b)$$

$$\text{where } QI(0) = (\Delta\rho A)^2 \quad (27)$$

The denominator of the Guinier Eq. (26b) is 2 (3 for a three-dimensional scatterer; Eq. (25)) and the cross-sectional radius of gyration is then for a circular section:

$$r_c = \frac{r_0}{\sqrt{2}} \quad (28)$$

The geometrical radius r is deduced from the slope $r_c^2/2$ of a $\ln(QI)$ vs. Q^2 plot. Depending on the geometrical model used, r_c provides the typical correlation length of the section. A second equation is needed for anisometric sections (e.g., rectangular, elliptical etc.) which can be obtained from the Porod's behavior at large Q [11].

Figure 3 shows "Guinier plots" appropriate for fibers with heterogeneous sections having metallic elements. A variation of the contrast using alternatively X-rays to probe the organometallic core and neutrons to probe the overall section is then very instructive.

4.1.2. Influence of the cross-sectional polydispersity

Fibers in SAFINs exhibit more-or-less monodisperse sections. In addition, a small fraction of fibers in dilute gels is involved in the formation of bundles, acting as nodes in the network. As a result, the apparent radius of fibers,

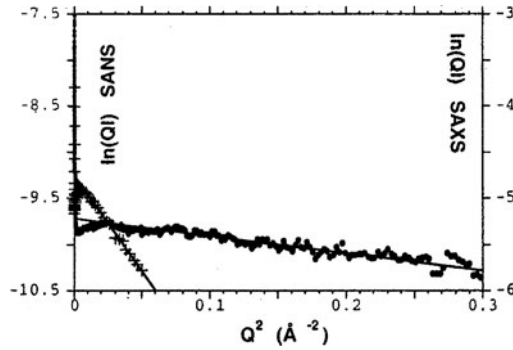


Figure 3. Guinier representation $\ln(QI)$ vs Q^2 for very thin organometallic monomolecular and semi-rigid fibers ($r = 8.8 \text{ \AA}$) in perdeuterated cyclohexane. X-rays (\bullet) and neutrons ($+$) identify the two contrasting shells in the section (radius of the organometallic core = 2.8 \AA probed by SAXS) [12]. (Reprinted with permission from [15]. Copyright (1994) American Chemical Society.)

extracted from the global scattering, can be affected by this fraction of bundles (in addition to thermodynamic shape fluctuations of the sections). For the sake of simplicity and considering the uncertainty of the determination of r ($\pm 5\%$) or M_L ($\pm 20\%$), a radial Gaussian polydispersity $G(r)$ can be included in the calculation.

$$G(r) = \frac{2\sqrt{\ln 2}}{\Delta r_{1/2}\sqrt{\pi}} \exp - (4 \ln 2) \left(\frac{r - r_0}{\Delta r_{1/2}} \right)^2 \quad (29)$$

The resulting scattered intensity is the convolution of Eq. (21) with the normalized distribution of radial distances.

$$QI \propto \frac{1}{\varepsilon} \sqrt{\frac{\ln 2}{\pi}} \int \left(\frac{2J_1(Qr_0x)}{Qr_0x} \right)^2 \exp - \frac{\ln 2}{\varepsilon^2} (x - 1)^2 dx \quad (30)$$

$\Delta r_{1/2}$ is the full width of the Gaussian distribution, $\varepsilon = \frac{\Delta r_{1/2}}{2r_0}$ and $x = r/r_0$.

$$\int_{-\infty}^{+\infty} \exp - \frac{\ln 2}{\varepsilon^2} (x - 1)^2 dx = \varepsilon \sqrt{\frac{\pi}{\ln 2}} \quad (31)$$

The effect of the radial polydispersity on the cross-sectional radius of gyration is illustrated by an equation of the type:

$$QI = QI_0 \exp - Q^2 r_c^2 / 2 \approx QI_0 \left(1 - \frac{r_c^2}{2} Q^2 \right) \quad (32)$$

It becomes:

$$r_c^2 = \frac{1}{\varepsilon} \sqrt{\frac{\ln 2}{\pi}} \frac{r_0^2}{2} \int_{-\infty}^{+\infty} x^2 \exp - \frac{\ln 2}{\varepsilon^2} (x - 1)^2 dx \quad (33)$$

The cross-sectional radius of gyration r_c is then expressed as:

$$r_c^2 = \frac{r_0^2}{2} \left[1 + \varepsilon \frac{2}{\sqrt{\pi \ln 2}} + \varepsilon^2 \frac{1}{2 \ln 2} \right] \quad (34)$$

The distribution will also affect the extrapolation at $Q \rightarrow 0$ of the cross-sectional intensity $QI(Q)$. The number of gelator molecules associated in a section of fiber of unit length is $n_L \propto (QI)_0/C \propto k\pi r^2$ with $C = pC_0 = C_0 - cac$ being the concentration of gelator molecules participating in the self-aggregation process. As already mentioned, p (the corresponding fraction) has to be estimated during the preliminary determination of the phase diagram. The solubility of the molecular gelators is extremely variable, even if frequently weak, but its temperature dependence may affect very significantly the accuracy of n_L values. The average and centered nominal value of n_L is written n_L^0 .

$$n_L^0 = 10^3 N \frac{(QI)_0}{\pi M^2 p C_0 (\bar{b}_g - \bar{b}_s g_s v_g)^2} \quad (35)$$

The effect of the polydispersity is then:

$$n_L = k\pi r_0^2 \left(1 + \varepsilon \frac{2}{\sqrt{\pi \ln 2}} \right) \quad (36)$$

where N is Avogadro's number, M is the molecular weight of the gelator, \bar{b}_s [cm/g] is its specific scattering length density, \bar{b}_s [cm/g] is the specific scattering length density of the solvent, g_s [cm³/g] is the specific volume of the solvent, and v_g [cm³/g] is the specific volume of the gelator. The specific contrast is thus, $\Delta b = \bar{b}_g - \bar{b}_s g_s v_g$ [cm/g].

Similar developments for other sectional morphologies give comparable expressions. For instance, for a tubular structure (with either a cylindrical wall separating the interior and exterior media or core/shell(s) systems), the expression for r_c can be deduced. The radius of the core is identified with subscript co and that of the shell with subscript sh . If the contrast factor is defined by $k = \Delta\rho_{sh}/\Delta\rho_{co}$, $\Delta\rho$ being the scattering length density calculated with respect to the reference level of the solvent ($\Delta\rho_{sh} = \rho_{sh} - \rho_{co}$), then:

$$r_c^2 = \frac{\frac{kr_{sh}^4}{2} - \frac{(k-1)r_{co}^4}{2}}{kr_{sh}^2 - (k-1)r_{co}^2} \quad (37)$$

$k = 1$ is for a plain cylinder $r_{co}^2 = r_{sh}^2/2$ while $r_c^2 = \frac{a^2+b^2}{4}$ is for an elliptical plain section with a, b half axes. $r_c^2 = \frac{a^2+b^2}{3}$ for a rectangular cross-section, $k \rightarrow \infty$ for a tube for which the inner part is identical to the external medium (solvent) $r_c^2 = \frac{(r_{sh}^2+r_{co}^2)}{2}$. The effect of the radial polydispersity is described by

Eq. (38) for rectangular polydisperse sections with identical ε values in the two orthogonal directions.

$$r_c^2 = \frac{a^2 + b^2}{3} \left[1 + \varepsilon \frac{2}{\sqrt{\pi \ln 2}} + \varepsilon^2 \frac{1}{2 \ln 2} \right] \quad (38)$$

For simplicity, the cross-sectional and longitudinal contrasts can be assumed constant over the volume of the rod. Chemical features of the aggregation mechanism are determinant for the estimation of the radial and axial polydispersities. With fibers in hydrogels, the diameter results frequently from associated bimolecules through hydrophobic interactions: weak radial fluctuations are expected. The length or the molecular weight distribution is driven by thermal equilibrium reactions. In a mean-field theory [13], the statistical contour length of micellar fibers with a scission energy E_{sci} is described in the form:

$$\langle L \rangle \sim \phi^{1/2} \exp(E_{sci}/2k_B T) \quad (39)$$

Possible variations of the exponent of the volume fraction are not discussed here. As a result of mass-action effects, lengths are polydisperse and different distribution functions can be used. Expressions developed to describe the distribution of the molecular weight for polymers can be tentatively used. A Flory-Schulz (one-parameter) or Schulz-Zimm (two-parameters) distribution function can conveniently model the length distribution. Using the polymer terminology, the z -average may also describe the scattering function of polydisperse semi-rigid fibers:

$$\langle I(Q, L, l_p) \rangle_z = \frac{\int N(L) L^2 I(Q, L, l_p) dL}{\int N(L) L^2 dL} \quad (40)$$

Here, $N(L)$ is the number distribution of fibers of length $2L$.

Since networks in molecular gels are giant meshes of connected fibers, it is impossible to probe the lengths of individual fibers in SAFINs. Rare examples of ternary suspensions, obtained from dilute gels in which the lengths can be monitored by addition of end-cappers (so as to form rods), are known and they can be discerned by SAXS-SANS scattering data [14]. In this case, the modeling of SAFINs as described above is inadequate.

4.1.3. Asymptotic large- Q behavior

The asymptotic behavior at large- Q can also be used to extract structural parameters of individual fibers since this part of the scattering curve is not sensitive to large-scale interference effects. The correlation function $\gamma(r)$ is

the average of the product of two fluctuations at a distance r . $\gamma(r)$ is obtained by the inverse Fourier transform:

$$\gamma(r) = \frac{1}{V2\pi^2} \int_0^\infty I(Q)Q^2 \frac{\sin Qr}{Qr} dQ \quad (41)$$

The integral INV is a constant (invariant defined by Eq. (42)) and related to the mean square fluctuation of the neutron scattering length density over the volume (where ϕ is the volume fraction).

$$INV = \int_0^\infty Q^2 I(Q) dQ = 2\pi^2 V \gamma(0) = (\Delta\rho)^2 \phi(1 - \phi) 2\pi^2 \quad (42)$$

The final slope at $Q \rightarrow \infty$ of the scattering function of any type of scatterer is given by Eq. (43) (known as Porod's law), S being the total interface of the aggregates.

$$\lim I(Q) = (\Delta\rho)^2 \frac{2\pi}{Q^4} S \quad Q \rightarrow \infty \quad (43)$$

Equation (43) is used to evaluate S assuming absolute intensities are available and the contrast is calculable *a priori*. A combination of Eqs. (42) and (43) leads to Eq. (44) in which no absolute intensity or a preliminary model of the contrast is needed.

$$S/V = \pi \cdot \lim I(Q)Q^4 / INV \quad (44)$$

For long rod-like scatterers, the contribution to the interface by the ends can be neglected and $S/V \neq 2/r$. The large-angle part of the scattering curve (Porod region) can thus be used to estimate a radius of the fibers. A cross-check with values extracted in the low- Q Guinier domain can be supported both by values from a fit of the scattering profile and by M_L values obtained by extrapolation at zero Q . These values should give a consistent pattern to corroborate a structural model. Figure 4 shows a Porod's plot that reveals four form-factor oscillations characteristic of monodisperse sections in a fatty acid organogel system. The asymptotic limit at large Q is identifiable as a plateau, allowing further calculations (in absolute units using Eq. (43) or without any preliminary structural hypothesis using Eq. (44)).

4.2. Short Rods

SAFINs are formed by the self-assembly of LMOGs into various micellar aggregates at thermal equilibrium. *The length polydispersity of fibers is very large*. Still, the presence of non-connected short rods is probable. By chance, the end of the distribution function of lengths may fall within the experimental Q -range. When the concentration is increased, a significant contribution of such short rods to the scattering can thus be observed. Due to the finite length

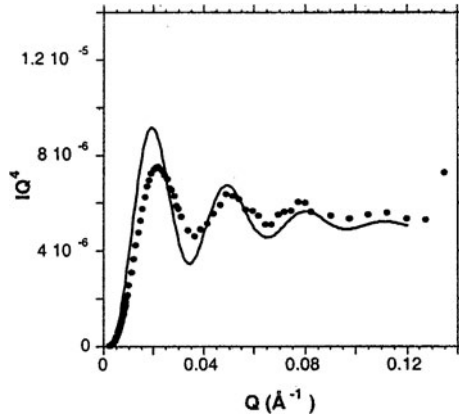


Figure 4. Porod IQ^4 vs Q plot for a 12-hydroxystearic acid organogel in perdeuterated-benzene [15]. Fibers have square sections (210 \AA side). Full line is a theoretical profile obtained from Eq. (49). (Reprinted with permission of EDP Sciences, France, Copyright 1994.)

$2L$ of the rods, the simplification mentioned for Eq. (18) cannot be used and the form-factor is obtained through a numerical integration. For a rod axis oriented at an angle θ with respect to \vec{Q} , the calculation becomes:

$$\begin{aligned} A(\vec{Q}) &= 4\pi L \Delta\rho \frac{\sin(QL \cos\theta)}{QL \cos\theta} \int_0^\infty r J_0(Qr \sin\theta) dr \\ &= 4\pi L r^2 \Delta\rho \frac{\sin(QL \cos\theta)}{QL \cos\theta} \frac{J_1(Qr \sin\theta)}{Qr \sin\theta} \end{aligned} \quad (45)$$

The scattered intensity is obtained after averaging over all rod orientations (random situation):

$$I(Q) = \left| 4\pi L r^2 \Delta\rho \int_0^{\pi/2} \frac{\sin(QL \cos\theta)}{QL \cos\theta} \frac{J_1(Qr \sin\theta)}{Qr \sin\theta} \sin\theta d\theta \right|^2 \quad (46)$$

Experimental evidence for rods with finite lengths is the low-angle cut-off of the Q^{-1} decay. In a Guinier plot $\ln(QI)$ vs Q^2 , the linear part from which r_c is extracted is preceded by a maximum. In SAFINs, long and short rods can coexist and in a QI vs Q plot, a slightly positive slope in this graphic representation transforms the aspect of this Q -domain into a profile having a very broad bump [14]. Figure 5 displays 3 types of “Guinier plots” for rod-like scatterers. Curve 1 is a straight line, curve 2 displays an innermost extra-scattering and curve 3 shows the typical plot for rods with finite lengths ($L < 2\pi/Q_{\min}$). The low- Q extra-scattering (curve 2) suggests an attractive interaction potential between fibers leading to higher order aggregates or heterogeneities.

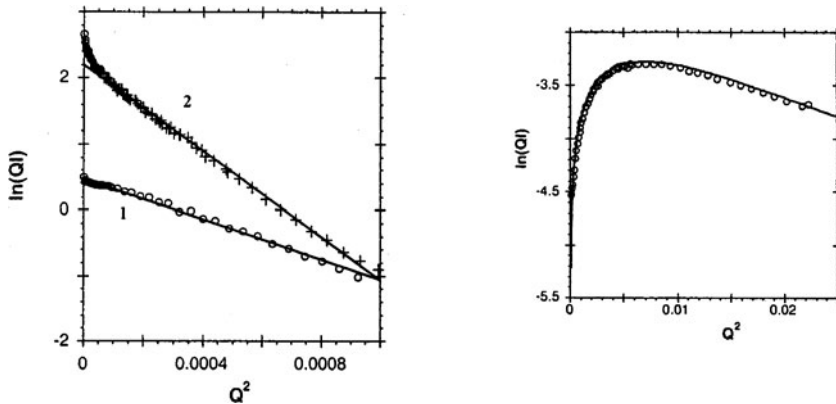


Figure 5. Guinier plots $\ln QI$ vs Q^2 for rod-like scatterers. Left, 1: modified androstanol steroid in D-methyl-cyclohexane (see Figure 1); 2: 12-hydroxystearic acid organogel in D-benzene (square section, $b = 100 \text{ \AA}$) [15]; right: rods formed by adding a pyridine end-capper species to a porphyrinic organogel in perdeuterated-cyclohexane (circular section, $r = 11 \text{ \AA}$, $L/r \sim 3$) [16]. (Reprinted with permission from [16]. Copyright (2003) American Chemical Society.)

5. Semi-Rigid Fibers

Micellar fibers in SAFINs are usually rigid on the length-scale associated with the SAS technique. Nevertheless, electron and optical micrographs frequently show large curvature radii. Rare examples exhibit semi-rigid characteristics (in the polymer terminology) with persistence lengths l_p of the order of a few hundreds of angstroms. For instance, very rare examples in organic media are known of monomolecular fibrils [17] (or slightly thicker fibers) [18] with a low rigidity that also undergo scission/recombinations reactions, depending on the balance between the energy of scission and the thermal energy. In aqueous solutions, a detailed examination is given in Chapter 19. The characterization of the flexibility of micellar fibers can be determined at low concentrations so as to characterize a form-factor feature only. The ability to find the combined existence of a dilute regime of concentrations and long enough rods ($2L > l_p$) is challenging. The complete characterization of the flexibility requires the use of a complementary technique, such as magnetic birefringence measurements [19, 20]. In fact, such a regime has never been found to date with SAFINs. The characterization cannot usually be done in the gel phase since conditions where l_p remains lower than the average mesh size of the network may not be found due to the high rigidity of the fibers and the high gelling ability of the LMOGs. Furthermore, an unequivocal distinction between a low- Q upturn due to a segmental fiber trajectory and due to the structure of the network and its homogeneity is not trivial. The different formalisms

developed for polymeric chains will not be detailed here since it is not evident that SAFIN systems (or the viscous liquid-like suspensions from their ternary mixtures) would lead to a reliable estimation. For instance, the scattering function of semi-rigid chains with excluded volume effects can use the numerical parametrization given by Yamakawa [21–23]. Details are found in references devoted to polymeric solutions or polymer-like micellar solutions.

To summarize, a Q^{-2} low- Q upturn is the expected signature typical of the form-factor of isolated, flexible rod-like aggregates. The flexibility is expressed using the persistence length l_p or Kuhn length b where $b = 2l_p$. Also, for charged systems, an electrostatic contribution to the persistence length is assumed ($l_p = l_{p,e} + l_{p,0}$). Different models have been proposed, mainly in the context of polyelectrolytes [24]. l_p may also depend on the fiber concentration, the counter-ions and added salts. The latter screen the interactions that usually cause electrostatic repulsion and further stretching of the fibers. The electrostatic contribution can be expressed, according to Odijk *et al.* [25], as a function of the Debye screening and Bjerrum lengths and it has an inverse dependence on ionic strength. The Bjerrum ($B_j = e^2/\epsilon_0 kT$) and Debye-Hückel screening lengths are related by:

$$DH^2 = 8\pi B_j C_c \quad (47)$$

C_c is the concentration of counterions and B_j in water is ca. 7.1 Å. The Debye screening length κ^{-1} is given by (I is the ionic strength, ξ the dielectric constant of water, and e the electronic charge):

$$\kappa^{-1} = \left[\frac{8\pi N e^2 I}{1000 \xi k_B T} \right]^{1/2} \quad (48)$$

Recently, significant effects of ionic strength on semi-rigid charged fibers and associated networks of modified bile salt hydrogels have been discovered. Rheology has been used to characterize the induced variations of the network rigidity [26].

6. Fibers with Anisometric Sections

When intermolecular associations contribute to the formation of fibers (through hydrogen bonds in organic media or hydrophobic interactions in aqueous media), rectangular and elliptical cross-sections can be potentially generated. However, they are somewhat rare. Mittelbach calculations [27–29] can then be used to analyze such possibilities.

6.1. Rectangular Sections

The scattering function involves a numerical integration of a trigonometrical expression describing the cross-sectional factor.

$$I(Q) = \left(\frac{2A\phi\Delta\rho^2}{Q} \right) \int_0^{\pi/2} \left[\frac{\sin(Qa \sin \varphi) \sin(Qb \cos \varphi)}{Qa \sin \varphi Qb \cos \varphi} \right]^2 d\varphi \quad (49)$$

a, b are half the sides of the cross-section. The trigonometrical term accounts for differences in the profiles illustrated in Figure 6 whose amplitudes must be carefully evaluated to justify the use of additional parameters describing the anisotropy of the cross-sections.

6.2. Elliptical Cross-Sections

Instead of having sharp angles forming the edges of the cross-sections, it may be more rational to consider elliptical cross-sections. Such a morphology may also provide the possibility for development of an inner host cavity possibly that may be able to accept polar additives in apolar organic media,

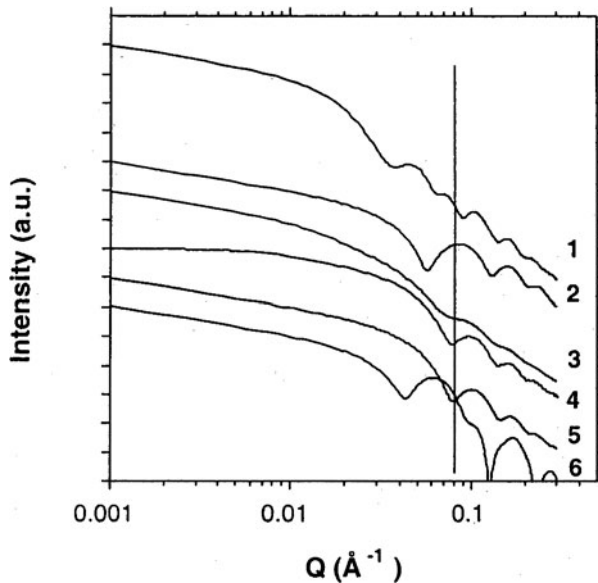


Figure 6. Theoretical scattering profiles for different cross-sections of fibers ($\varepsilon = 0.1$): 1: rectangular, $b = 50 \text{ \AA}$, $b/a = 0.3$; 2: hollow tube, $r = 50 \text{ \AA}$, $r_{\text{core}} = 35 \text{ \AA}$; 3: elliptical, $b = 50 \text{ \AA}$, $b/a = 0.3$; 4: short rod with circular cross-section, $r = 50 \text{ \AA}$, $L/r = 5$; 5: circular, $r = 50 \text{ \AA}$; 6: helix (see Ref. [36, 37]), $r = 50 \text{ \AA}$, $r_{\text{cyl}} = 7 \text{ \AA}$, $\text{pitch} = 150 \text{ \AA}$. Curves have been vertically shifted for clarity.

for instance. The structure can be considered as a precursor for tubular structures. The degree of roundness is expressed by the eccentricity κ , defined as $0 < \kappa = b/a < 1$, where b is half the minor axis and a half the major axis.

$$I(Q) \propto \int_0^\pi \left[\frac{2J_1 \left(Qa \sqrt{\left(\frac{1+\kappa^2}{2}\right) + \left(\frac{1-\kappa^2}{2}\right) \cos \varphi} \right)}{Qa \sqrt{\left(\frac{1+\kappa^2}{2}\right) + \left(\frac{1-\kappa^2}{2}\right)}} \right]^2 d\varphi \quad (50)$$

Figure 6 summarizes the various scattering curves obtained for rod-like aggregates presenting a similar characteristic distance of 100 Å and illustrates the variety of subtle differences between the intensity decays and cross-sectional oscillations for simple form-factors.

The assortment can be compared to experimental profiles encountered with real SAFINs (Figure 16). One parameter κ (and possibly ε_a and/or ε_b for anisotropic cross-sectional polydispersities), is thus needed to describe rectangular and elliptical morphologies. Departures observed in the profile at low- Q and/or large- Q oscillations that cannot be accounted for with a simple model of plain, cylindrical fibers may suggest the use of anisotropic cross-sections (N.B., rectangular and elliptical) in a refined analysis. Indications for such a refined analysis can be either the observation of a low- Q asymptotic slope slightly larger than the expected -1 value (form-factor analysis) or the observation of unfitted large- Q oscillations.

7. Tubes

The tubular structure derives from its homogeneous cylindrical morphology, but it is complicated by a heterogeneous radial contrast profile. The simplest case consists of a solid-like wall separating identical internal and external media. Plain fibers made of two solid-like shells of different contrasts are tubes with a three-step radial contrast profile.

$$QI(Q) = K(\rho_{\text{out}} - \rho_{\text{in}})^2 \times \left[\frac{\rho_{\text{out}} - \rho_{\text{sol}}}{\rho_{\text{out}} - \rho_{\text{in}}} r_{\text{out}}^2 \frac{J_1(Qr_{\text{out}})}{Qr_{\text{out}}} - r_{\text{in}}^2 \frac{J_1(Qr_{\text{in}})}{Qr_{\text{in}}} \right]^2 \quad (51)$$

If the internal and external media are identical, $\rho_{\text{in}} = \rho_{\text{out}}$ and Eq. (50) can be simplified. The formation of hollow tubes in viscoelastic suspensions of self-assembling chiral small molecules is known for a limited number of systems (such as steroids, lipids, etc.) and are of great interest for potential applications in the nanoscience fields. The mechanism of tubule formation is complex

and proceeds through various intermediates (fibrils, ribbons, chiral ribbons) instead of being directly formed from smaller tubular embryos, as proposed by a theoretical description [30, 31]. Because chiral molecules usually stack at an oblique angle with respect to their neighbors, a twist is generated in the aggregates that make a chiral membrane-like morphology folding into helical, twisted ribbons or tubules with a given radius. Helical structures are intermediate states in the tube formation and the driving force is the chirality of the small molecules. The theoretical modeling can be done in a continuum elastic free energy framework [30, 31]. The cylindrical structure is determined by a competition between the curvature and edge energies through bending, twist and chirality factors balancing the free energy. The free energy includes standard isotropic curvature rigidity and a chiral term. The optimum structure exhibits a tilt angle of $\pm 45^\circ$ with respect to the equator of the tube. Refinements of the model [32] are available for situations in which the tilt is non-uniform in the membrane, for instance. Striped modulation in the molecular tilt direction is also a consequence of the molecular chirality that can be experimentally observed. In the different intermediate species experimentally observed, chiral ribbons (with cylindrical curvature) and twisted ribbons (with Gaussian curvature) are associated respectively with a crystalline or fluid-like order within the membrane. In such complex mechanisms of formation, the matching between real and reciprocal-space observations is an efficient approach to extract reliable structural information in the reacting mixture.

To account for the sectional monodispersity in chiral systems, observed in many molecular gels, there is a theoretical description of the stabilization of fibril formation that is supported well by experimental data for aqueous solutions of synthetic *de novo* 11-mer peptides (DN1) self-assembled into ribbons [33, 34]. The primary structure of DN1 is $\text{CH}_3\text{CO-Gln-Gln-Arg-Phe-Gln-Trp-Gln-Phe-Gln-Gln-NH}_2$. Thread-like fibrils are stabilized by face-to-face attractions balanced by distortions of the ribbons (untwisting modes). The fibril aggregation number and its equilibrium twist can be predicted by the theoretical model (see Chapter 3). In this context, small-angle scattering techniques are especially appropriate to estimate the monodispersity of the cross-sections of 1D aggregates since the scattering signal is a statistical average over a large irradiated volume.

Examples of SAFINs in aqueous or organic liquids made up of connected or entangled tubular species are rare. Suspensions of tubes refer usually to the second generic class of networks presented in Figure 1. The frontier between viscoelastic suspensions and gels is not sharp and needs some clarification. Yield stress values measured in rheological experiments can be used to remove the ambiguity. Approximately two orders of magnitude in the elastic shear modulus measured at 1 Hz frequency distinguish the two types of materials. For instance, a suspension of lithocholate tubes at volume fraction $\phi = 1\%$ exhibits $G' < \text{ca. } 100 \text{ Pa}$. The fundamental difference lies mainly in the strength

of the interaction potential between the rod-like species. If the concentration is further increased, the viscoelastic suspensions exhibit the consistency and G' values typical of a gel, and a more refined rheological characterization is then necessary to reveal the specificity of the interactions (through creep-recovery protocols, for instance). The G' , G'' rheological profiles as a function of the frequency of the applied oscillatory stress are then used to discern gels from suspensions or equilibrium-breakable segmental fibrils.

For tubes with elliptical cross-sections, the scattering intensity is given by:

$$QI(Q) \propto \frac{2}{\pi} \int_0^{\pi/2} \left[\begin{aligned} & (\rho_{\text{out}} - \rho_s) \frac{2J_1 \left(Q \sqrt{r_{\text{out}}^2 \sin^2 \theta + \varepsilon^2 r_{\text{out}}^2 \cos^2 \theta} \right)}{Q \sqrt{r_{\text{out}}^2 \sin^2 \theta + \varepsilon^2 r_{\text{out}}^2 \cos^2 \theta}} + \\ & A_{\text{in}}/A_{\text{out}} (\rho_{\text{in}} - \rho_{\text{out}}) \frac{2J_1 \left(Q \sqrt{r_{\text{in}}^2 \sin^2 \theta + \varepsilon^2 r_{\text{in}}^2 \cos^2 \theta} \right)}{Q \sqrt{r_{\text{in}}^2 \sin^2 \theta + \varepsilon^2 r_{\text{in}}^2 \cos^2 \theta}} \end{aligned} \right]^2 d\theta \quad (52)$$

The cross-sections are $A_{\text{in}} = \pi \varepsilon r_{\text{in}}^2$, $A_{\text{out}} = \pi r_{\text{out}}^2$ and ε is the ratio of the axes [35].

Figure 7 shows an example of remarkably monodisperse tubular aggregates in aqueous viscoelastic suspensions of a lithocholate bile salt ($C = 2$ wt.%). Depending on the concentration and pH, suspensions (0.001 wt.% $< C < 1$ wt.%) and gels can be obtained. Due to the subtraction of Bessel functions and depending on the set of r_{in} and r_{out} values, oscillations may be more marked than with a thick fiber of equivalent diameter. The remarkable number of oscillations

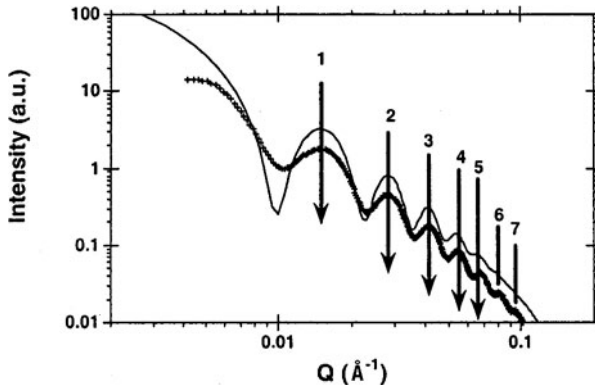


Figure 7. Experimental (+) SAXS profile for an aqueous sodium lithocholate gel-like system. Full line is the theoretical behavior for nanotubes ($D_{\text{ext}} = 520$ Å, $D_{\text{int}} = 490$ Å). The monodispersity of the section accounts for the observation of 7 clearly resolved form-factor oscillations [36].

indicates the high monodispersity of the diameters and wall thicknesses of the structures.

A major challenge for fundamental and applied fields is the discovery of chemical “rules” governing the spontaneous thermoreversible fibrillar aggregation and gelation phenomena. The elucidation of the mechanisms for structural evolution from plain cylinders to fibers with elliptical cross-sections, elliptical tubes and coaxial tubes within a class of gelators would also be of interest for the important issue of “encapsulation” processes.

8. Helices

A large amount of work has already been dedicated to chiral LMOGs. Chirality can be involved at different length scales of the SAFINs. From the molecular to supramolecular length range, chirality may also be present in various intermediate species (twisted *versus* chiral ribbons) or can be generated by various external actions on chiral SAFINs. Thus, external stimuli, such as stresses developed at the migration of a liquid-gas meniscus during the evaporation of the solvent in a gel can produce helical superstructures in SAFINs made up of chiral molecules [37].

The Fourier transform of an infinite continuous helix is non-zero on a set of planes spaced by $2\pi/P$ (P is the pitch of the helix) perpendicular to its axis [8, 38]. The calculation takes into account the fact that the helix shape is generated by a convolution of a single turn with a lattice of points separated by P (one-dimensional periodic crystal structure). The calculation is made for an infinitely long and thin helix. Using cylindrical polar coordinates, vectors \vec{r} and \vec{Q} have respectively the components $(r \cos 2\pi z/P, r \sin 2\pi z/P, z)$ and (α, β, χ) . The Fourier transform becomes:

$$F(\alpha, \beta, \chi) = \int_0^P \exp i[\alpha r \cos(2\pi z/P) + \beta r \sin(2\pi z/P) + \chi z] dz \quad (53)$$

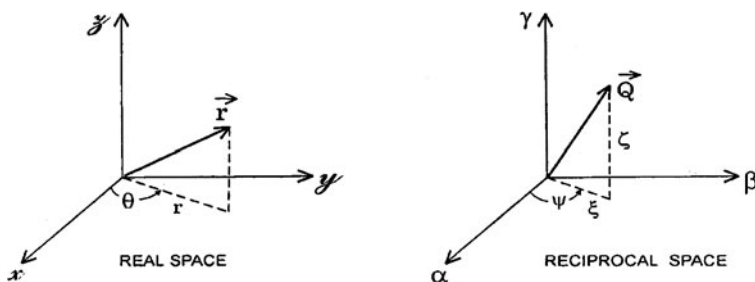


Figure 8. Correspondence between the rectangular and cylindrical polar coordinates in real and reciprocal spaces.

In cylindrical polar coordinates with ψ as the polar angle and ξ the projection in the $\alpha\beta$ plane, it gives:

$$F(\xi, \psi, \chi) = \int_0^P \exp i[\xi r \cos(2\pi z/P - \psi) + \chi z] dz \quad (54)$$

The transform has to be evaluated at $\chi = 2\pi l/P$ (i.e., the l th plane in Q -space). Assuming $Z = z/P$, the equation simplifies to:

$$F(\xi, \psi, l) = \int_0^1 \exp i[\xi r \cos(2\pi Z - \psi)] \exp i[2\pi l Z] dZ \quad (55)$$

The Fourier transform can be re-written as in Eq. (56) with $X = \xi r$ and $\phi = 2\pi Z - \psi$.

$$(1/2\pi) \exp(il\psi) \int_{-\psi}^{2\pi-\psi} \exp(iX \cos \phi) \exp(il\phi) d\phi \quad (56)$$

The integral conveniently corresponds to a definition of the l th order of the Bessel function of the first kind:

$$F(\xi, \psi, l) = \exp il(\psi + \pi/2) J_l(\xi r) \quad (57)$$

The scattered intensity on the l th plane (Q -space) is thus:

$$I(\xi, l) = J_l^2(\xi r) \quad (58)$$

The infinite summation for all l values of the χ axis gives a diagonal cross-like (ξ, χ) , two-dimensional pattern. For n -fold coaxial helices with a n -fold rotation axis (equivalence obtained by a rotation of $2\pi/n$), the repeat distance is reduced from c to c/n . The layer line spacing in Q -space is then increased to $2\pi n/c$. Consequently, some layer lines can be absent and modify the profile of a one-dimensional $I(Q)$ plot.

Other numerical approaches are available to describe the scattering of helical supramolecular organizations. Among them, the Schmidt's model [39, 40] is a numerically convenient one describing a range of different structural possibilities. To simplify the calculations, the cross-section is sketched by sectors extending from the center of the circular section with variable angular and radial extensions. The model covers thus the cases of single, double and hollow helices. The main limitation is that the actual cross-sectional shape of the helical aggregates cannot be idealized as in the Schmidt model. To summarize:

$$QI(Q) = \sum_{n=0}^{\infty} \varepsilon_n \cos^2(n\varphi/2) \frac{\sin^2(n\omega/2)}{(n\omega/2)^2} [g_n(QR, a)]^2 \quad (59a)$$

where R is the external radius of the helix and a the hollow part (if any).

$$g_n(QR, a) = 2R^{-2}(1 - a^2)^{-1} \int_{ar}^r r J_n \left(Qr \sqrt{1 - q_n^2} \right) dr \quad (59b)$$

$$\begin{aligned} \text{with: } b &= 2\pi R/P, q_n = nb/QR \text{ for } QR \geq nb, \\ q_n &= 1 \text{ for } QR \leq nb, \varepsilon_0 = 1 \text{ and } \varepsilon_n = 2 \text{ for } n \geq 1 \end{aligned} \quad (59c)$$

ω is the angular of the sector containing the matter, and φ is the angle between the two sectors or the angle by which the fact that one helix is rotated with respect to the other ($\varphi = 0$ for a single helix). Despite infinite series are involved in the expression, the number of terms is limited since only terms for $n \leq QR/b$ must be considered, an expansion in a power series is easily obtainable. This model has been tested with a steroid organogel [9]. Certainly, the data need a sufficient number of oscillations to justify the use of a model with up to 6 parameters. An extension of such calculations of interest for SAFINs (and related suspensions) would involve helical and twisted ribbon structures.

9. Scattering by the Junction Zones

The merging process of fibers in a network produces “junction zones” whose shape can be rod-like (achiral or helical bundle), platelet-like or disk-like, or even spherulitic-like (see Figure 9). The latter (Figures 4–9) corresponds to heterogeneities grown from a central nucleation site and represents a more-or-less branched network that might also be considered in a fractal (or special epitaxial growth) context. Spheres with appropriate density decay functions can also delimitate the heterogeneities in such a network. Due to their important dimensions (compared to the cross-section), the junction zones mainly contribute to the low- Q part of I vs Q curves through either their structure and/or form factors. The evolution of the signal versus concentration is again crucial to discern the origin of the extra-scattering.

In the following, situations describing the form-factors for simple structures of uncorrelated heterogeneities are considered first before those for correlated “nodal” scatterers.

9.1. Form-Factor of a Disk

Fibers can merge in platelet-like junction zones if interfacial polarities of the genuine fibers differentiate the two orthogonal directions of the cross-section. Similar arguments as those used with rod-like scatterers lead to a decoupling approximation giving a $\sim Q^{-2}$ factor typical of the flatness character (as was the

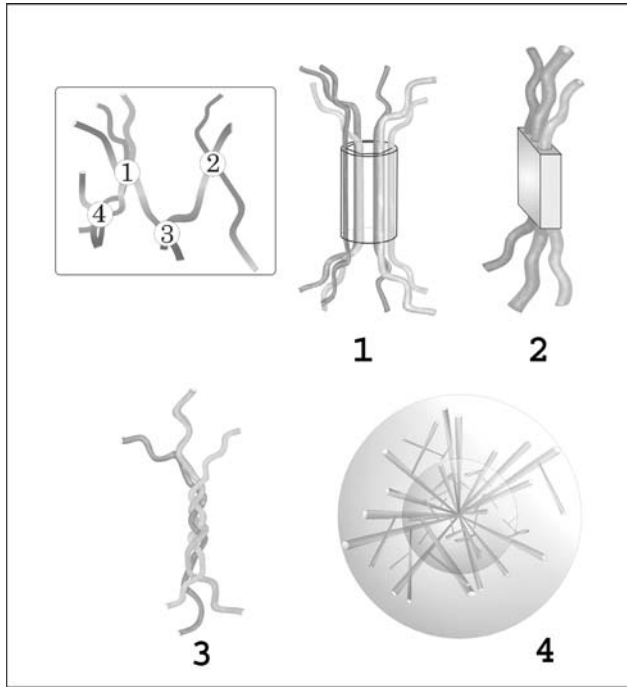


Figure 9. Cartoon representations of the structural modes of fibers merging in junction zones. 1: hexagonal arrangement; 2: platelet-like structure; 3: helical merging; 4: branched germination.

Q^{-1} axial term with fibers) and a “thickness-factor” $I_t(Q)$ (as was the cross-sectional term $J_1(Qr)/Qr$ with fibers). Integration over the large dimensions of the disk gives non-negligible contributions only for \vec{Q} nearly perpendicular to the disk plane, accounting for the separation in two factors that can be independently averaged.

$$I(Q) = A \frac{2\pi}{Q^2} (\Delta\rho)^2 t^2 \left(\frac{\sin(Qt/2)}{Qt/2} \right)^2 \quad (60)$$

At low scattering angles, a “Guinier-type” expression is deduced:

$$I(Q) = A \frac{2\pi}{Q^2} (\Delta\rho)^2 t^2 \exp-(Q^2 t^2 / 12) \quad (61)$$

From the slope s of a Guinier-like plot of $\ln Q^2 I$ vs Q^2 , appropriate for platelets (as was the Guinier-like plot $\ln Q I$ vs Q^2 for rods), the transverse thickness is extracted as $t = (12s)^{1/2}$. Mechanisms of aggregation and growth are different in the two orthogonal directions of the section. For instance, hydrophobic interactions in aqueous systems favor head-to-head bimolecular aggregates

in one direction while H-bonds or any other stacking mode may proceed in the other direction. The latter mechanism leads to an asymmetric degree of spatial extension of the cross-section.

9.2. Spherulitic Nodes

To a certain extent, the high fluctuation of the gelator concentration observed in some branched-like junction zones can be approximated with an overall spherical shape (with possibly shells of decreasing density). For homogeneous spherical scatterers, the corresponding scattering function is:

$$I(Q) = \left[\frac{4\pi}{3} r^3 \frac{3(\sin(Qr) - Qr \cos(Qr))}{(Qr)^3} \right]^2 \quad (62)$$

Variants with core-shell or depleted zone core-shell models are available to describe layers of different contrasts. These models represent the progressive decrease of gelator concentration from the center of the node to its periphery. Naturally, a large polydispersity has to be introduced in the model to account for the random character of the size of the merging-nucleating sites. These options are progressively explored in concentrated SAFINs and compared to other analyses (e.g., the fractal context) [41].

The following section details the most relevant ways to account for the influence of correlated heterogeneities in SAFINs on the low angle scattering signal.

9.3. Random Nodes: Debye-Büeche Context

Large scale fluctuations in a random two-phase distribution can be described by the Debye-Büeche model [42]. The spatial correlations of average length Ξ are damped according to the exponential correlation function $g(r) \cong \exp(-r/\Xi)$. In reciprocal space, the related scattered intensity is:

$$I(Q) \propto \frac{\Xi^3}{(1 + Q^2 \Xi^2)^2} \quad (63)$$

$I(Q)_{Q \rightarrow 0} = 8\pi \Delta\rho^2 \Xi^3 \phi(1 - \phi)$, r is a radial distance, and ϕ is the volume fraction of heterogeneities. Depending upon the value of Ξ with respect to the lowest Q experimentally available, the Q^{-4} decay and possibly part of the upturn before the plateau can be observed, thus allowing the evaluation of Ξ . This is probably an appropriate manner to analyze crystalline-like concentrated SAFINs [43]. A confirmation of Ξ can be searched in the large- Q

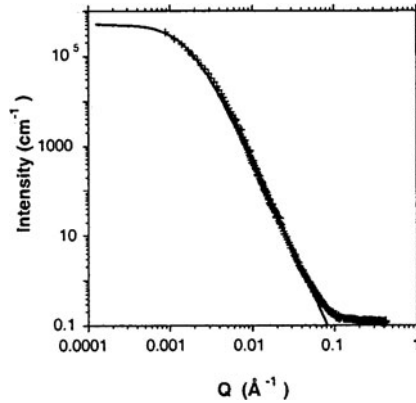


Figure 10. Example of a Debye-Büee analysis attempted for a *N*-alkyl perfluoroalkanamide organogel in perdeuterated benzene ($C = 2\%$ wt) [45]. Full line is a fit using Eq. (63) with $\Xi \sim 600 \text{ \AA}$.

domain by taking advantage of the width of Bragg peaks typical of the internal structure of the heterogeneities. The mean thickness of the microcrystallites along the normal to the Bragg planes is estimated by the Sherrer [44] equation:

$$\Delta(2\theta) = \frac{0.89\lambda}{\Xi \cos\theta_{\text{Bragg}}} \quad (64)$$

$\Delta(2\theta)$ is the full width at half-maximum (FWHM) of a Bragg reflection at θ_{Bragg} . Ξ is the average thickness of the microcrystallites along the normal to the Bragg plane. The Debye-Büee formalism is convenient to model the Q^{-4} low- Q decay in various materials, from molecular gels to ionic polymeric membranes.

Figure 10 shows an example of a SAFIN for which the scattering is overwhelmed by the Q^{-4} decay assigned to the dispersed solid phase, which is amorphous in this case. Figure 17-1 illustrates the complementary situation where the junction zones dominate the scattering and are formed of crystallized domains responsible for an intense and narrow Bragg peak at large Q .

9.4. Ideally Homogeneous Networks

Ideally, a suspension of semi-rigid fibers can entangle in the manner of polymer solutions in good solvents [46]. A solution in the semi-dilute range of concentrations is schematically described as a closely packed system of

blobs of size ξ . Scaling laws of various static and semi-static properties of the networks as a function of the average mesh size can be observed. The field of polymer physics has been very active in this field and can be considered as a reference framework, but few general behaviors and trends can be applied to molecular gels. There are too many fundamental differences between the two classes of systems. It is instructive to observe for instance, how the polymer renormalization group theory for semi-dilute polymer solutions is applied to the so-called “equilibrium polymers” [47] (see also Chapter 19). At higher concentrations, gel phases are, nevertheless, frequently observed.

Also, the osmotic pressure in such ideal systems has a strong dependence on ξ .

$$\Pi \cong \frac{T}{\xi^3} \quad (65)$$

The pair correlation function may follow an Ornstein-Zernike form:

$$g(r) \cong C \frac{\xi}{r} \exp(-r/\xi) \quad (66)$$

$$\text{The Fourier transform of Eq. (66) gives: } g(Q) \cong \frac{c\xi}{Q^2 + \xi^{-2}} \quad (67a)$$

$$\text{It can be presented in a Lorentzian form: } I(Q) = \frac{I_0}{1 + Q^2\xi^2} \quad (67b)$$

The smaller is ξ (dense network), the larger is the scattered signal. In an I vs Q plot, a Q^{-2} low- Q upturn is expected. Despite the applicability of the blob concept, its appropriateness for SAFIN systems has not been demonstrated the presence of crystalline-like heterogeneities certainly severely restricts the observation of a Q^{-2} decay. Still, the model is interesting and addresses the question of the two main classes of networks in Figure 1. The first class is made up of rigid fibers entangled or fused into crystalline-like zones: a Q^{-4} upturn (modeled by the Debye-Büéche context) is then appropriate. The second class consists of semi-rigid fibers with more self-avoiding trajectories in networks with only transient and/or poorly organized zones.

9.5. Fractal Context

As shown in Figure 9, the branching degree of the networks might be envisioned as a fractal feature. A gel may be an arrangement of uncorrelated domains of size ξ and fractal dimension D_f [48, 49]. The characteristic self-similarity property means that the detail of the merging/branching of fibers in junction zones are structurally identical to observations made at different length scales.

In SAFINs, the branching itself can be viewed as resulting from the merging of fibers, from self-epitaxial growth or from crystallographic mismatches [41, 50]. The relation between the mass and the gauge of measurement r_0 introduces the mass fractal exponent D_f .

$$M(R) \approx (R/r_0)^{D_f} \quad (68)$$

The density distribution goes to zero at infinite distances and is expressed:

$$\rho \cong R^{D_f-d} \quad (69)$$

d is the dimension of space in which the fractal system is immersed. The subsequent Fourier transform leads to a convenient relation for SAS characterizations:

$$S(Q) \cong Q^{-D_f} \quad (70)$$

The relation holds in the range $\zeta^{-1} < Q < r_0^{-1}$ where ζ is a cut-off distance at large scales introduced to be compatible with the non-zero density of the sample. The auto-similarity property breaks down at large Q when the form-factor of the individual fibers or the interfacial scattering is probed. In the concentration and Q ranges dominated by $S(Q)$, a simple $\log S(Q)$ vs $\log Q$ plot enables a trivial extraction of the fractal dimension. The relation between D_f and a kinetical mechanism is not evident with fibrous networks for which conditions for diffusion-limited aggregation reactions are expected to be valid. The comparison of fractal exponents obtained in a class of SAFINs should relate to their branching degree, their mesh size and, in turn, their elastic shear modulus G' values. Open fractal-like structures have not yet been clearly characterized by SAS in SAFINs. Usually, dilute gels exhibit a scattering profile dominated by the form-factor of the fibers. On increasing the concentration in crystalline-like gels, frequently, the scattering signal is overwhelmed by a Q^{-4} decay (N.B., the first generic class mentioned above). Intermediate situations can be observed, but the assignment of a power law decay at low- Q to a self-similarity relationship is not clear. Indeed, the complexity of the SAS signal is such that at extremes, a Q^{-4} decay component, Q^{-2} behaviors or contributions from infinitely long and/or short rods (with different dimensions) may lead by chance to non-integer exponents of the intensity decay in a given Q -range.

9.6. Orientation Correlated Domains

Two frameworks can be considered mainly to interpret oscillations (or secondary maxima) in a scattering curve of molecular gels. On the one hand, monodisperse sectional morphologies have been shown to generate oscillations after the Guinier Gaussian decay and are superimposed to a Q^{-4} asymptotic

behavior. On the other hand, a structure factor can imply Bragg or correlation peak(s) whose broadening depends on the size of the crystallites (Sherrer's law) or type of correlation. The crystalline-like molecular ordering in the junction zones can be either of a solid or lyotropic nature. Depending upon the 2d symmetry of the in-plane organization of fibers, the sequence of peaks will differ. Experiments at different concentrations can lead to identification of the symmetry of the ordering and its distinction from form-factor oscillations of thicker aggregates.

For hexagonal symmetry (space group $p6m$), the relation between the positions of peaks in reciprocal space and the distances between the diffracting reticular planes is:

$$Q_{hk} = 2\pi a^*(h^2 + k^2 - hk)^{1/2} \quad (71)$$

$$a = K/(a^* \sin \gamma^*) = K/(a^* \sqrt{3/2}).$$

The sequence of peaks has spacings: $1(Q_{11})$, $\sqrt{3}(Q_{12})$, $2(Q_{22})$, $\sqrt{7}(Q_{31})$, $3(Q_{30})$.

If fibers are hexagonally packed in junction zones with solvent entrapped between the columns, the lyotropic nodal microdomains exhibit modified spacings according to:

$$\left(\frac{d_{\text{rod}}}{d_{\text{swe}}}\right)^2 = \left[1 + \frac{1}{1 + \frac{C_g v_g}{1 - C_g v_s}}\right] \quad (72)$$

C_g is the concentration of gelator, v_g and v_s are the partial volumes of gelator and solvent, respectively, d_{swe} is the lattice parameter of the swollen system (obtained from $Q_{11} = d\sqrt{3/2}$), and d_{rod} is the diameter of the cylinders.

The analysis can be refined by considering the shape of the signal [51]. The ideal situation, where the long axes of fibers are perfectly oriented perpendicular to the incident beam, may represent a local situation in the junction zones. Fibers either in close contact or separated are situations that can be described by introducing the swelling ratio, $\gamma = D/2r$, where D is the cylinder center-to-center distance ($r = d_{\text{rod}}/2$). For a central hexagonal arrangement of seven fibers, the intensity profile is given by Eq. (73) with F^2 being the form-factor intensity of a fiber (see Eq. (19)).

$$I(Q) = \frac{F^2}{49} [7 + 24J_0(2\gamma Qr) + 6J_0(4\gamma Qr) + 12J_0(2\sqrt{3}\gamma Qr)] \quad (73)$$

For a similar system with fibers free to occupy any position in the orthogonal plane, a radial distribution function $g(r)$ is included in the calculation and the intensity is:

$$I(Q) = F^2(Qr) \left[1 - v \int_0^\infty 2\pi r(1 - g(r))J_0(Qr) dr\right] \quad (74)$$

An increase of the correlation between the fibers reduces the intensity. The special case, $g(r) = 0$ for $D_{CA}/2 < r < 0$, illustrates the maximum interference effect on the intensity according to:

$$I(Q) = F^2(Qr) \left[1 - \nu\pi D_{CA}^2 \left(\frac{2J_1(QD_{CA})}{QD_{CA}} \right) \right] \quad (75)$$

D_{CA} is the closest distance of approach and ν is the number density of rod centers in the plane normal to the longitudinal axes.

For rectangular ordering, diffraction conditions at which diffraction peaks are observed become in the cmm space group:

$$Q_{hk} = 2\pi(h^2a^{*2} + k^2b^{*2})^{1/2} \quad \text{with } h + k = 2n \quad (76a)$$

and in the pgg space group:

$$Q_{hk} = 2\pi(h^2a^{*2} + k^2b^{*2})^{1/2} \quad \text{with } h_0 = 2n, 0k = 2n \quad (76b)$$

It is important to emphasize again the importance of a preliminary concentration dependence analysis before attempting any interpretation of the profile and its diffraction singularities. The complex nature of the networks requires that variations of the scattering as a function of pertinent parameters be consistent with the hypotheses used. For instance, if an asymptotic low- Q behavior is assumed to characterize the fibrillar shape, its associated slope should not depend on concentration in the range where the single particle approximation holds. The contrary would support a $S(Q)$ analysis. The problem is that usually this range is limited only to a few percent of gelator. Similarly, if large- Q oscillations are thought to be due to the particular shape of the sections, their position should not depend on the concentration. Conversely, if intensity oscillations are believed to come from lyotropic organization in the network, it is probable that their position should depend on the swelling degree of the gel. It is also helpful to complement SAS data with other techniques. In particular, if lyotropism is suggested, polarizing optical microscopy can provide some insights, as can analysis of the anisotropy of the scattering signals.

10. Structure Factor Peak in Poorly Organized Fibrillar Scatterers

Sections 9 and 10 could have been inserted in Section 8, but their potential importance in SAFINs deserves a separate treatment. Calculation of correlations between orientations and positions of rods in interacting systems is usually not available. It requires a spherical symmetry of the scatterer and associated

interactions. *Only when* it can be assumed that particles have a small anisotropy (and a small polydispersity), can a decoupling approximation be proposed:

$$I(Q) = (\Delta\rho)^2 \left[\left\langle F^2(\vec{Q}, \alpha) \right\rangle_\alpha + \left\langle F(\vec{Q}, \alpha) \right\rangle_\alpha^2 (S(\vec{Q}) - 1) \right] \quad (77)$$

α is the angle between the rod axis and \vec{Q} . Such an approximation normally does not hold for fibers with large aspect ratios in interconnected SAFINs. Nevertheless, a great deal of theoretical and experimental work has been devoted to the description of interferences between fibrillar systems in a variety of charged and uncharged materials. In the context of the random phase approximation developed for stiff polymers, the interactions account for a so-called nematic-like interaction in which segments of the polymers experience not only the external field but also the molecular field interactions [52]. Other models use a hard core repulsion between rods in a second virial approximation [53]. It appears that the description, including the length distribution, is far from simple. $S(Q)$ can also be described using the concept of correlation holes in ionic domains [54] due to the repulsive potential in the region $d < d_{CA}$ expelling other fibers. Considering the complexity and the controversial character of the structure factor in fibrillar systems and the rarity of SAFIN systems presenting clear scattering features of $S(Q)$, this aspect will not be developed further here. Nevertheless, in molecular hydrogels of modified bile salts, evidence for such behavior has been found [26]. In such a case, the spherical symmetry of the spatial distribution and correlation of the globular scatterers allows a simpler formalism:

$$\frac{d\sigma(Q)}{d\Omega} = nV_p^2(\Delta\rho)^2(F(Q))^2S(Q) \quad (78)$$

Here, n is the number density of spherical scatterers per unit volume.

The starting point remains [3] the static structure factor for spherical scatterers of radius R .

$$S(Q) = \left[3 \frac{\sin QR - QR \cos QR}{(QR)^3} \right]^2 \times \left[1 + 4\pi\phi \int_0^\infty r^2(g(r) - 1) \frac{\sin Qr}{Qr} dr \right] \quad (79)$$

$g(r)$ is the associated pair distribution function.

The globules can be assumed to interact through a hard sphere repulsion potential with a closest distance of approach and according to a random distribution. One advantage of such a modeling is to introduce only two parameters, R the size of the pockets and the closest approach distance R_{CA} . Yarusso and Cooper [55, 56] have tentatively described the structure of ionomers with a hard

sphere model (Eq. (80)). A liquid-like degree of order in the relative positions of spherical particles can also be included.

$$S(Q) = \frac{1}{1 + (8V_{CA}/v)\varepsilon F^{sph}(Q, R_{CA})} \quad (80)$$

$\varepsilon \sim 1$ and $F^{sph}(Q, R_{CA})$ is the form-factor for spherical scatterers (Eq. (62)).

Hayter and Penfold have also derived convenient expressions for the structure factor of macro ion solutions [57, 58]. It is assumed that the repulsive screened Coulomb pair potential between the spherical macro ions is a determining factor for the time-averaged structure of the solutions. A mean spherical approximation is used and at a zero charge limit, a Percus-Yevick hard sphere expression is recovered. Expressions to reproduce the maximum of $S(Q)$ can be also found in the work of Pedersen [59]:

$$S(Q) = \frac{1}{1 + 24\phi_p G(2QR_p, \phi_p)/(2QR_p)} \quad (81)$$

R_p is the hard-sphere radius of the particle interactions and G is a function of $x = 2QR_p$:

$$\begin{aligned} G(x, \phi_p) = & \left(\frac{\alpha(\phi_p)}{x^2} \right) [\sin x - x \cos x] \\ & + \left(\frac{\beta(\phi_p)}{x^3} \right) [2x \sin x + (2 - x^2) \cos x - 2] \\ & + \left(\frac{\gamma(\phi_p)}{x^5} \right) [-x^4 \cos x \\ & + 4[(3x^2 - 6) \cos x + (x^3 - 6x) \sin x + 6]] \end{aligned} \quad (82)$$

The coefficients α, β, γ are defined as:

$$\begin{aligned} \alpha &= \frac{(1 + 2\phi_p)^2}{(1 - \phi_p)^4}, \quad \beta = \frac{-6\phi_p(1 + \phi_p/2)^2}{(1 - \phi_p)^4}, \\ \gamma &= (\phi_p/2) \frac{(1 + 2\phi_p)^2}{(1 - \phi_p)^4} \end{aligned} \quad (83)$$

These formalisms must be used cautiously with SAFINs formed in hydrogels and only after identification of the chemical nature of the globular scatterers. Analysis is complicated by scattering contributions from other components, such as fibers, counterions, and rods. A peak position varying with concentration consistently with simple space filling arguments in real-space is a required reasonable first step.

Figure 11 shows a rare example of separated form and structure factor features observable simultaneously for a molecular hydrogel comprised of a tripodal cholestamide LMOG. The low- Q peak is shifted towards large angles

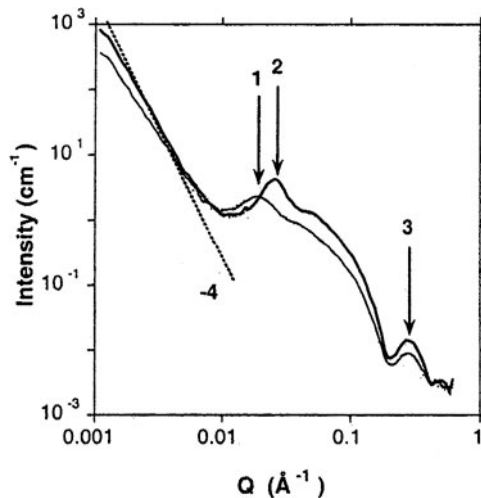


Figure 11. Example of structure and form-factor neutron scattering features in a hydrogel (20:80 perdeuterated mixture of acetic acid:water) with a tripodal cholamine LMOG [26]. $C = 0.02$ (dark line curve) and 0.03 (light line curve) $\text{g} \cdot \text{cm}^{-3}$. The dotted line is a slope = -4 .

when the concentration is increased (features 1, 2) and can be assigned to a $S(Q)$ contribution. The innermost Q^{-4} upturn observed before the $S(Q)$ correlation peak is not predicted by the different models above and can be attributed to a Debye-Büecher contribution of heterogeneities in the system. Simultaneously, the large-angle part of the curve has a profile insensitive to the concentration, as expected for a form-factor assignment. The corresponding Q^{-1} and Q^{-4} intensity decays are observed to precede a sectional form-factor oscillation (feature 3).

The thermodynamic properties of molecular gels could also be approached by the extrapolated value $S(0)$, in the same manner used with light scattering experiments on polymeric gels. No such SAXS/SANS examples are yet available with SAFINs. $S(0)$ is related to the chemical potentials μ . Such analyses are interesting tests of models based on the free energy (μ is the derivative of the free energy) and interaction potentials.

$$S(0) = N^2 \langle n - \langle n \rangle^2 \rangle = N^2 kT \left[\frac{\partial \mu}{\partial \langle n \rangle} \right]^{-1} = N^2 \langle n \rangle kT \left[\frac{\partial \pi}{\partial \rho} \right]^{-1} \quad (84)$$

$\langle n \rangle$ is the mean number of solvent molecules, N is the number of scatterers, π is the osmotic pressure, and ρ is the concentration of scatterers. Depending upon the strength of interactions between the scatterers, the term $(\partial \mu / \partial n)^{-1}$ will vary from $\langle n \rangle / kT$ for no interaction (perfect gas) to 0 for strong interaction, and $S(Q)$ will be strongly affected. Thus, a lower value of $S(0)$ contributes to the observation of a maximum in $S(Q)$.

11. Oriented Fibers

11.1. One Dimensional Crystal and Fiber Diffraction Pattern

It is interesting to examine the effect on diffraction patterns of fiber orientation in one-dimensional SAFIN crystals. The corresponding Fourier transform is the convolution product of the transform of a one-dimensional (1d) lattice and a layer. For an infinite 1d periodic structure, the interference function $S(Q)$ is zero except at Q -regions where:

$$\vec{c} \cdot \vec{Q} = 2\pi l \quad (85)$$

c is the repeat distance along the c -axis.

The Ewald construction (Figure 12) shows that the diffraction pattern is a series of lines formed when the planes l , where the intensity is non-zero, intersect the sphere. The layer line at $l = 0$ is called the equator line while the

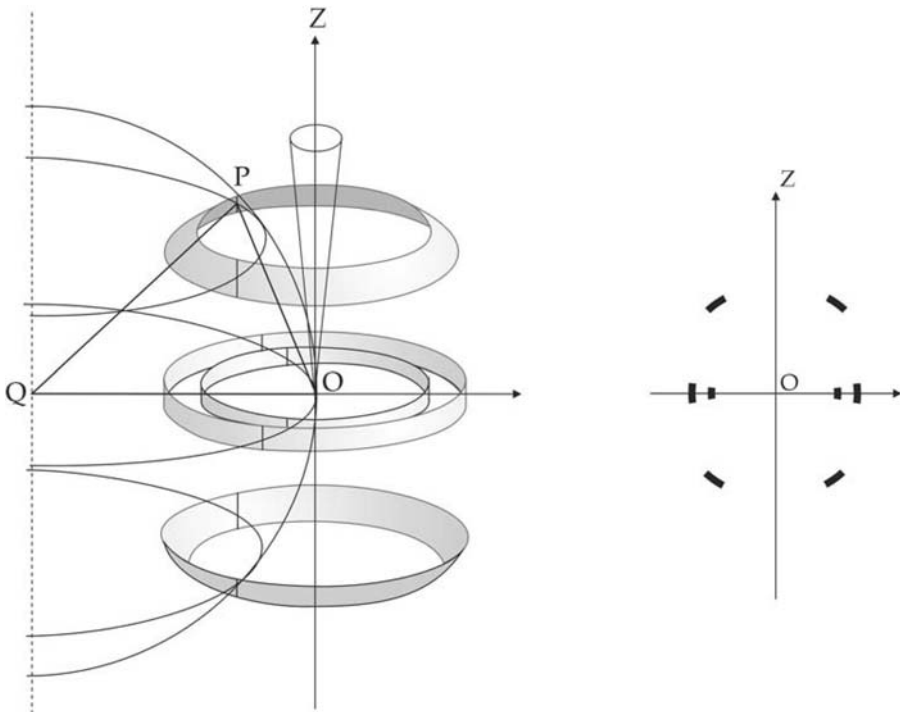


Figure 12. Ewald construction for oriented fibers. Left: left sphere (Ewald sphere of reflection) has a radius QO of length $1/\lambda$. Its intersection with the sphere of position in reciprocal space (right sphere) indicates the direction of diffracted beam (QP) which is also the normal to the set of planes P for which the Bragg relation is fulfilled. Right: corresponding diffraction pattern.

line parallel to the c -axis (and χ -axis) is called the meridian line. The spacing in Q -space is $2\pi l/c$. When the orientation of the c -axis is not the same all over the imperfectly oriented system (or in the case of the existence of a 1d mosaic spread), the structure projected onto a plane perpendicular to the z -axis can be considered similar to a random array of discs. The corresponding diffraction pattern is the intersection of the cylindrically symmetric intensity distribution with the surface of the Ewald sphere. The interference function on the equator line will provide information on the projected structure onto a plane perpendicular to z and can be expressed with a two-dimensional radial distribution function $g(r)$. The cylindrical average about the χ -axis is equivalent to an average over all ψ values. $S(\xi, \chi)$ is independent of ψ if the intensity distribution remains in the cylindrical symmetry. The Fourier transform is:

$$FT = \int_0^\infty 2\pi r \rho(r) J_0(Qr) dr \quad (86)$$

Then, the equatorial intensity distribution is:

$$S(\xi) = 1 + n \int_0^\infty 2\pi [g(r) - 1] J_0(\xi r) dr \quad (87)$$

n is the number of discs per unit area.

Conditions for diffraction of a particular set of planes can be examined with the Ewald sphere construction (Figure 12). The axes orthogonal to the fiber axis are randomly distributed about this axis. In Q -space, on the sphere of position, each scattering point describes a circle around the fiber axis (the diffraction rings from randomly oriented specimens). Since the crystal axes are usually disoriented about the fiber axis, the rings become bands. The disorientation may be sufficient at low Q and large d_z spacing to bring a lattice point on the meridian into a reflecting position. The corresponding fiber diffraction pattern is illustrated on the right part of Figure 12. If the beam is parallel to the fiber axis, equatorial bands are observed while at intermediate orientations, the reflections will be asymmetric along the fiber axis. Practically, it may be useful to characterize the orientation degree of the rods. The evaluation of an orientational distribution function $f(\beta)$ (β being the angle between a rod and a nematic-like director \vec{n}) is of interest to compare the orientations in differently processed samples. The method uses the intensity distribution of the signal in the wide-angle diffuse crescent ring [60, 61] in a direction at polar angle θ .

11.2. Shear Alignment

Due to the high yield stress values (σ^*) measured usually for molecular gels, they can be sheared and oriented only in the disrupted state above σ^* or

during the growth process. Since, in most cases, mechanical failure of a SAFIN is accompanied by solid-liquid phase separation, this type of experiment is frequently not possible. Below σ^* , only minor orientation effects of the fraction of non-connected short rods (if any) or shear-induced bundle formation are possible. By contrast, under conditions where viscoelastic suspensions (low σ^*) exist (as in weak molecular gels or ternary systems with end-cappers), significant orientation effects can be observed. Also-called Couette measuring cell (comprised of rotating concentric cylinders) is frequently used for liquid-like micellar systems, but plate-plate or cone-plate geometries are preferred for gels. Depending upon the type of cell and its specific set-up for scattering measurements, the detection can be achieved either in the $(\vec{v}, \text{neutral axis})$ plane or $(\vec{v}, \nabla \vec{v})$ plane; the neutral axis is parallel to the axis of rotation of the shear device). The calculation for solutions of rods in dilute isotropic systems (non-interacting rods) leads to Eq. (88), an average over all orientations of rods with respect to \vec{Q} .

$$I(Q) = \left\langle \left| F(\vec{Q}) \right|^2 \right\rangle_Q \quad (88)$$

$F(\vec{Q})$ is the form factor of a rod-like scatterer of length $2L$ and radius r_0 at a given orientation defined by the angle γ between the rod axis and \vec{Q} :

$$F(\vec{Q}) = F(Q, \gamma) = 2\Delta\rho V \frac{\sin(QL \cos \gamma)}{(QL \cos \gamma)} \frac{J_1(Qr \sin \gamma)}{Qr \sin \gamma} \quad (89)$$

If rods have the same orientation, the intensity reduces to:

$$I(\vec{Q}) = F^2(\vec{Q}) S_\infty(\vec{Q}) \quad (90)$$

In the ideal situation of suspensions of non-interacting rods, Brownian motion competes with the imposed viscous flow in a shear experiment according to the ratio:

$$\Gamma = \frac{\partial \gamma / \partial t}{D_r} \quad (91)$$

D_r is the rotational diffusion coefficient and $\partial \gamma / \partial t$ is the shear rate produced by the alignment device. Expressions for D_r applicable to various cells are known and show that with common $\partial \gamma / \partial t$ values, full alignment ($\Gamma \gg 1$) is never reached. This statement is correct for networks involving long fibers rigidly interconnected. The scattered intensity depends upon the relative time spent in a given orientation (θ, φ) characterized by a probability function $p(\theta, \varphi, \Gamma)$ [62]. Here, θ is the angle between the rod axis and the Q_\perp axis while φ is the angle between $Q_{//}$ and the projection of rod axis in the plane (neutral axis, $Q_{//}$). Theoretical treatments are available for different micellar systems

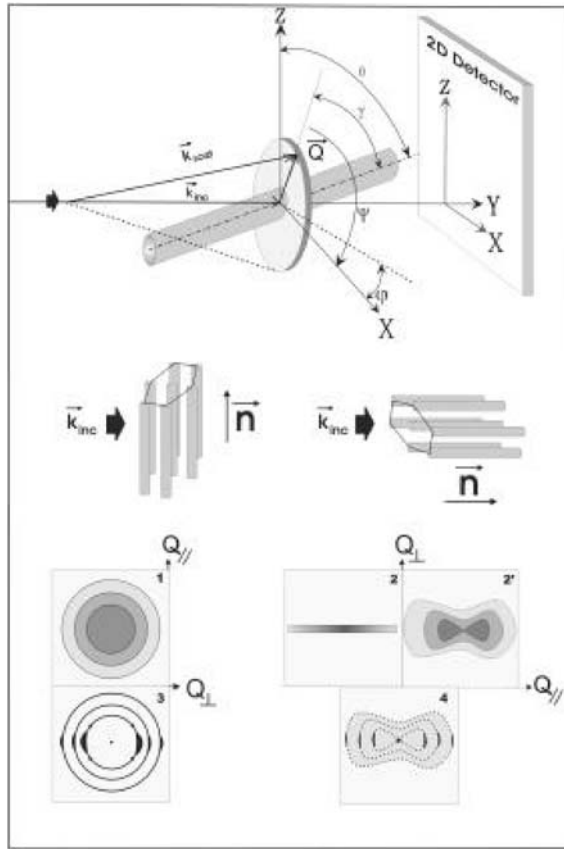


Figure 13. SAS of assemblies of rods. \vec{Q} can rotate over 2π following ψ in the plane (\vec{x}, \vec{z}) . First row: dilute systems. Rods oriented perpendicularly to the direct beam: **1**. Rods oriented parallel to the direct beam: **2, 2'**. Bottom row: concentrated systems: **3, 4**. (Reprinted with permission of Marcel Dekker, from Surfactant Science Series, Vol. 87. Copyright 2002.)

[62–64]. Such equations can describe the anisotropic 2d patterns and/or the deformation of a correlation peak (charged systems) as a function of the shear gradient. The polydispersity and flexibility of the rods can be included in the modeling.

Figure 13 illustrates the relationship between the rod orientation and the scattering anisotropy. The vertical plane of the detector (\vec{x}, \vec{z}) contains \vec{Q} for large sample-detector distances (i.e., low-angle scattering). Rods with lengths much larger than their diameters make a contribution to the scattering only when they lie nearly perpendicular to \vec{Q} . In a random gel, fibers are randomly oriented and there is no dependence of the intensity with the angular position of the sample in (\vec{x}, \vec{z}) . The detector shows isotropic scattering with circular

isointensity contours. Conversely, with oriented systems, rods are position- and/or orientation-correlated, and the scattering is dependent upon the angular position of the sample. Two extreme situations for perfect orientation of the rods are shown. First, if the direction of orientation \vec{n} is orthogonal to the incident beam, Eq. (89) gives non-zero contributions only for $\gamma = \pi/2$. A horizontal line or band is observed (image 2). A real sample is not perfectly oriented and is composed of domains with a distribution of orientations around \vec{n} . The orientation of each rod in a domain is defined in polar coordinates by angles θ and φ and the direction is assumed to coincide with $Q_{//}$ (Q_{\perp} is the orthogonal direction). In a sheared material, $Q_{//}$ is conveniently taken as the direction of shear. The signal evolves to an anisotropic scattering with elliptical isointensity contours (image 2) which reveals, for each ψ value in the (\vec{x}, \vec{z}) plane, the existence of a population of rods which fulfills the orthogonality condition of the \vec{Q} and rod axes. The typical correlation length in the perpendicular axis to the shear is decreased (increased intensity in Q -space) while it is increased along the shear axis (decreased intensity), forming thus an elliptical pattern. Second, the director can be parallel to the incident beam \vec{k}_{inc} (i.e., \vec{n} is orthogonal to the (\vec{x}, \vec{z}) detector plane). An isotropic scattering independent of the \vec{Q} position (\vec{x}, \vec{z}) develops (image 1).

In the semi-dilute ($C > 1/L^3$) and concentrated ($C > 1/2rL^2$) regimes, the long ($L \gg 2r$) rods interact. According to the symmetry of 2-d ordering, the structure factor can add specific diffraction features. Assuming that rods are hexagonally packed, two situations are worthy of note. First, if the directions of \vec{n} and the incident beam are orthogonal, spots separated in a $1:\sqrt{3}:\sqrt{4}:\sqrt{7}$ Q positional sequence, can appear along the horizontal equatorial direction \vec{x} . Due to imperfect ordering, elliptical intensity contours can be superimposed on the spots (image 3). Second, if \vec{n} is parallel to the incident beam, rings appear in a $1:\sqrt{3}:\sqrt{4}:\sqrt{7}$ positional sequence and contain hexagonally located spots. Additional spots along the equator reveal the deviation from perfect ordering (image 4). The angular extension of the crescent-like spots shows the ordering degree described by $p(\theta, \varphi)$, as for the measurement of the nematic order parameter of rod-shaped molecules.

Shearing experiments distinguish between scatterers with a characteristic relaxation or fluctuation time with respect to the typical time for flow ($t = 1/\partial\gamma/\partial t$). If the latter is short enough, the flow may affect the structural organization of the system. Combined shear and scattering experiments can then provide information about the composition of the systems and their relaxation and symmetry/structural modifications under flow. The complexity of SAFINs is important and the structural composition of the network has to be estimated to facilitate the interpretation of anisotropic signals. If non-entangled rods are present in the interstices of the network, if lyotropic junction zones exist, or

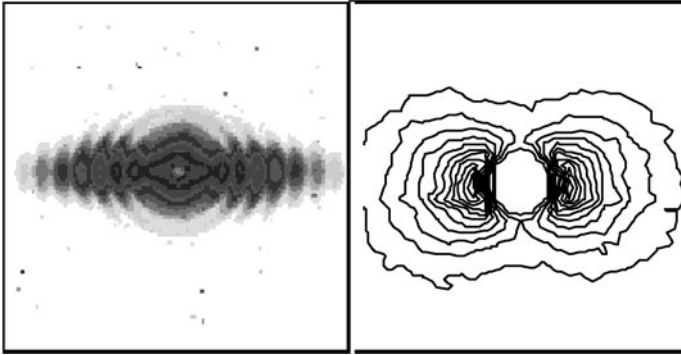


Figure 14. Comparison of the orientation effects in two different systems. Two-dimensional isointensity contour plots for a hydrogel of sodium lithocholate ($C = 8\%$) [36] submitted to an elongational stress as studied by SAXS (left). Flow-induced orientation in an organogel of 4-*tert*-butyl-1-phenylcyclohexenol in perdeuterated-octane at $C = 1.4\%$ can also be observed (right) [43]. (Reprinted with permission from [33]. Copyright (1997) Wiley-VCH.)

if the gel consistency is restricted to short times (Maxwell-like liquid), the anisotropy of the scattering as a function of shear rate will have to be considered accordingly.

Figure 14 shows that significant ordering can be obtained with both LMOG hydrogels and organogels. When submitted to an elongational shear, a hydrogel with a rather weak yield stress value can exhibit highly anisotropic scattering patterns. A strong molecular organogel (i.e., with a high σ^* value) can also exhibit same orientation of its fibers if it is induced by flow during the filling protocol of the sample cell.

12. Real Space Data

Inverse Fourier transforms have been successfully used to extract structural information in real-space with dilute suspensions of finite scatterers (micelles) [4]. In SAFINs, heterogeneities may obscure the extraction. Different methods are available whose applicability is probably restricted to systems presenting a purely form-factor scattered intensity as shown in Figure 15. In particular, the IFT (Inverse Fourier Transform) method [65–67] and variants [68] can be used to reduce the usual constraints of the method since it does not require Q -extrapolations of the experimental data. Corrections for the instrumental smearing effects can also be included.

A Fourier transform of the scattering gives the pair distance distribution function $p(r)$:

$$p(r) = r^2 \gamma(r) \quad (92)$$

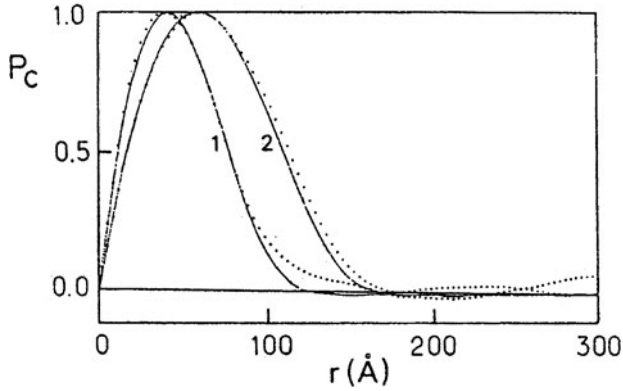


Figure 15. Hankel representation for a paramagnetic steroid (3β -hydroxy-17,17-dipropyl-17a-aza-D-homoandrostanoyl-17a-oxy) organogel [69] (points are experimental, full lines are theoretical curves using Eq. (93)). Curve 1: in perdeuterated-cyclohexane ($C = 2.3 \text{ g cm}^{-3}$), $r = 54 \text{ \AA}$, $\varepsilon = 0.2$. Curve 2: in perdeuterated-methylcyclohexane ($C = 2.1 \text{ g cm}^{-3}$), $r = 72 \text{ \AA}$, $\varepsilon = 0.12$ (ε is the cross-sectional polydispersity of the fibers, see Eqs. (30)–(31)). (Reprinted with permission from [69]. Copyright (1989), EDP Sciences, France.)

$\gamma(r)$ is the correlation function and $4\pi p(r)$ represents the distribution of distances within the homogeneous particle. For large aspect ratio fibers, the Hankel transformation can be used to extract $p(r)$.

$$p_c(r) = \frac{1}{2\pi} \int_0^\infty (QI) J_0(Qr) Qr \, dQ \quad (93)$$

$p_c(r)$ is a distance distribution function within the cross-section of fibers.

For a Q -range large enough for a reliable integration to be conducted, artifacts due to Q -truncation can be limited and the radial neutron scattering length density can be reasonably deduced. The method and its variations are not discussed here further because the conditions required to propose a unique interpretation of $p(r)$ are easier to extract from reciprocal space data.

13. Kinetic Studies

Depending upon the characteristic time scale of the molecular aggregation reactions, the SAS technique can be used to extract the number density of growing rod-like particles in the system *versus* time during the sol-to-gel phase transition. For faster kinetics ($t_{\text{equ}} < 15 \text{ min}$), a synchrotron beam is preferable. To now, a stable sol phase preceding the SAFINs has never been observed by scattering techniques. The heated solutions are unstable in the gel domain of the phase diagram and the excess of material with respect to the solubility

concentration at the equilibrium temperature (or *cac*) is involved in the various aggregates forming the SAFINs. In addition, the SAS technique (that is sensitive to the presence of large-scale aggregates) can be combined with a resonance or other spectroscopic method (that is sensitive to the molecular environment of the probes) to obtain complementary information about the phase diagram. The SAS follows the increase of signal at the sol-to-gel phase transition while the “molecular techniques” provide information about the amount of isolated species in the solution fraction or other aspects of the SAFIN component [70, 71].

During the course of a kinetic investigation, the estimation of the critical threshold t_g (in a percolation sense) at which gelation occurs is a difficult task. The unfavorable enthalpic excess due to the rod extremities is such that the growth of long fibers is fast and their steric overlap concomitant. Three objectives can be sought with SAS kinetic studies. First, the experimental conditions (flux, time resolution of the technical set-up, contrast, kinetic features of the aggregation reaction) allow the accumulation of scattering patterns as a function of time. The morphological changes during the kinetics of aggregation can then be analyzed. Usually, SAFINs made up of plain fibers exhibit embryos that are also rods of the same diameter. A striking example of morphological evolution from fibrils, chiral ribbons to tubules has been observed by SAXS in lithocholate hydrogels and has been confirmed by cryo-TEM measurements [73].

Within a purely form-factor approximation, the total counts of scattered neutrons on the detector *versus* time (corrected by the incoherent signal) can be approximated to the kinetic variation of the number of growing rod-like species, whether or not they are connected. Such data [72] is useful to examine the thermal reversibility of the aggregation phenomenon and its associated kinetic constants. In addition, the dimensionality n (or the fractality) of the colloidal growth can be analyzed since it will affect the mechanical properties of the gels. The Avrami-Mempel heterogeneous kinetic models [74–76] provide a simple approach to the complex relationship among kinetic, structural, and rheological properties [71]. Two asymptotic regimes are distinguished (Eq. (94)), and from trivial graphic representations of the reaction rate $r(t)$, the dimensionality n of the growth can be deduced.

$$\begin{aligned}
 t \rightarrow 0 \quad 1 - r(t) &\cong \exp(-kt^{n+1}) \\
 t > 0 \quad 1 - r(t) &\cong \exp(-kt^n)
 \end{aligned}
 \tag{94}$$

Figure 16 illustrates the type and quality of kinetic data that can be obtained from neutron scattering experiments. With interconnected networks in which bundle formation and other types of heterogeneities are parts of the complex architecture, the appropriate theoretical modeling is unfortunately still lacking despite the availability of models describing the kinetics of nucleation, aggregation and aging (see Chapter 4).

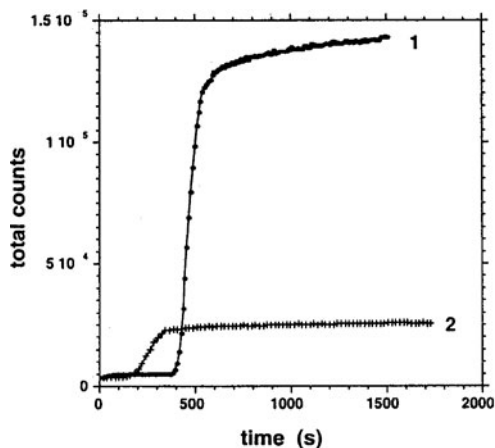


Figure 16. Time-dependence of scattering intensity curves of gel formation with steroid gelators. Variation of the total neutron counts scattered on the D22 ILL detector *versus* time for the solid angle corresponding to the Q -range $3.2 \times 10^{-3} - 7.3 \times 10^{-2} \text{ \AA}^{-1}$. Acquisition time: 10 s. Curve 1: Di-*n*-propyl-17,17-aza-17 α -D-homo (5α) androstanol-3 β steroid organogel in perdeuterated cyclohexane ($C = 4.3\%$) [72]. Curve 2: modified bile salt derivative hydrogel of a cationic bile salt (derived from a 3,12-dihydroxycholane steroid) [26] at $C = 1\%$.

14. Useful Hints for a Standard SANS Investigation of Molecular Gels

The structural characterization of the SAFINs of LMOG gels is a compulsory step in the description of this special gelation phenomenon. A network is composed of fiber-like particles that interact over variable lengths, energy and time scales in the “junction zones” (or interaction zones). The structural information can be gained at different length-scales using complementary techniques operating in reciprocal space (mainly SAS and WAXS) and real space (TEM, AFM, etc.).

The elucidation of “rules” that link the chemical structure of the LMOGs and the structural features in the network is a major challenge for chemists and physicists. Subtle variations in chemical structures of the gelators are known to affect gelation ability, structures of the fibers, and mechanisms of formation and structures of the junction zones. The chemical structure may also have a key role in determining the mechanism of the evolution of the networks as concentration is increased by altering the fibers/junction zones ratio.

The determination of the structures formed in the various aggregates is of invaluable help to propose a molecular mechanism for aggregation. It is also necessary to develop chemical synthesis strategies so as to obtain, by *a priori* design, specific SAFIN structures and gel properties. The ability to predict whether a molecule that is unrelated structurally to a known LMOG will

function effectively to yield hydrogels or organogels (with specified liquids) has not been achieved.

In accordance with the aggregation mechanism to form fibers and junction zones at different length scales, it is important to characterize the flow properties of the gels. Practically, gels are used in many applications because of their consistency and also when manipulation of their nanostructures is advantageous. Knowledge of the sizes of the cross-sections of fibers, as well as the type and structures of the junction zones, is useful to relate to the elastic modulus and yield stress values of the systems. Other mechanical properties, such as creep/recovery behavior, thermal stability, and thixotropy, are certainly associated with structural features extracted from SAS.

When molecular gels are used for special applications such as the elaboration of rigidified replicas, sol-gel switches, conducting systems, etc., their efficiency can be monitored more easily if structures and flowing properties are accurately known.

Other properties of molecular gels such as surface properties [77], wetting aspects, evaporation kinetics and molecular diffusion are also fundamental issues of importance both for the basic understanding of the systems and for their application in the fields of drug control release and processing of gels. Efforts are expected in these directions using specialized techniques, such as reflectivity, grazing incidence X-ray diffraction (GID), and grazing incidence X-ray small-angle scattering (GISAXS).

In most cases, molecular gels are heterogeneous systems, many of whose properties are randomly distributed while some others are rather monodisperse. For instance, a network is made up of fibers that interconnect in junction zones, but the SAFINs may be more complex. Fibers with a given morphology can coexist with other species that may contribute to the thermal equilibria between them (N.B., short rods, ribbons, twisted ribbons, and helices). The number, the shape of the junction zones, and their organization and volume fraction are parameters that may appear as somewhat chaotic variables [78]. With such potential complexity, it is reasonable to focus on non-sophisticated structural parameters that can be extracted with a minimal number of calculation parameters. Data obtained using different methodologies in different Q -regions improve significantly the reliability of proposed structural models. A sequence of operations as on to explore progressively the SAFINs is proposed below as a conclusion and invitation to explore the structural aspects of molecular gels with the SAS techniques:

1. Best choice of gelator/liquid: the solvent should ideally contain no protons (for SANS). Fluorine elements can be easily used (incoherent cross-section is 0.0008 barns for F and $\sigma_{\text{inc}} = 80.26$ barns for H). The gelator should not contain a very large number of H atoms per molecule, and the related incoherent contribution for a dilute system should be subtracted in the analysis

of the scattered intensity. According to the stoichiometry, the examination of the specific values of coherent and incoherent cross-sections will provide information about the feasibility of the scattering experiment. The importance of the absolute value of the contrast is decreased when using modern radiation sources.

2. A range of gel concentrations, typically between 0.1% to 5–10%, should be used to identify features that are not relevant to the form-factor analysis of the constitutive fibers; these include structure factors, form-factor of the junction zones, internal structures, heterogeneities, and ordering effects. The spectrometer is able to cover the range ca. $0.001\text{--}0.6 \text{ \AA}^{-1}$ that usually requires 3 sample-detector distances.

3. The dilute range must be sampled with at least 3 samples to guarantee the reproducibility and validity of the subsequent conclusions. The first objective of the approach is to identify the structural features of the major fibrillar component in the networks. The determination of the radius of the fibers from the Guinier plot must be confirmed at large angles with the so-called Porod analysis. At the end, a fit of the complete scattering curve should be attempted with a simple model, focussing on the most significant Q -regions. The model usually does not account for all parts of the scattering curve. In particular, special treatments should focus on the existence of (i) Bragg peaks at large angles, (ii) a Debye-Büecher component at low angle, or (iii) an interference peak. Importantly, the molecular weight per unit length has to be consistent with the value of the cross-sectional dimensions of the fibers.

15. Conclusions

Scattering techniques offer the advantage of probing unadulterated gel samples. Moreover, they provide a picture that is a statistical average over the irradiated volume of the sample. However, the structural information derived from scattering data is model-driven due to the loss of phase information and requires significant mathematical manipulation. This chapter is not a collection of convenient numerical recipes to extract the structural information, but introduces the most used approaches applied to SAFINs. The examples used represent well the rich complexity of this type of soft-condensed matter. Even if very time consuming, the numerical treatment is not the rate-limiting step for the data analysis. The “state of the art” consists in being able to conduct the appropriate experiments that clearly demonstrate the applicability of the above models and formulas. Being able to distinguish and identify in the scattering profile the asymptotic power laws, the oscillations, the bumps, the broad Bragg peaks, and the curvatures in the intensity decay, and to make the proper (consistent) structural assignments is the core of the technique. Finding unambiguous relationships between variations in the scattering curves and

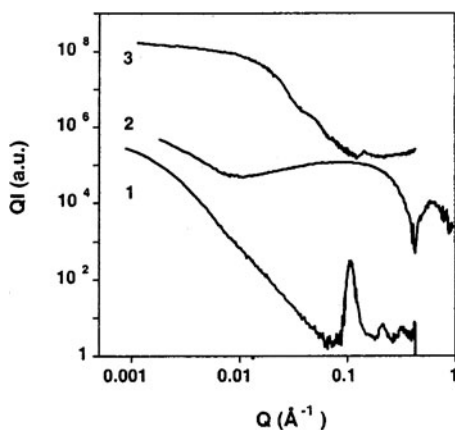


Figure 17. Different scattering QI vs Q profiles observed in SAFINs. 1: N-alkyl perfluoroalkylamide [45] in perdeuterated benzene ($C = 3\%$); 2: bicopper tetracarboxylate ($C = 8\%$) in perdeuterated cyclohexane [14]; 3: 12-hydroxystearic acid ($C = 2\%$) in perdeuterated toluene [15].

experimental parameters (such as concentration, temperature, level of interferences, crystallinity of the network, ionic strength, etc.) is a mandatory corollary. Such “premonitions” require both large amounts of beam time and a significant experience in the data treatment of a variety of scattering signatures of molecular gels. Figure 17 selects different scattering profiles of molecular gels (in addition to those already presented in the chapter) to illustrate the extreme variety of “signatures” that the scientist has to decipher!

The appropriate approaches vary from the Debye-Büeche random two-phase model in a crystalline network (curve 1), the presence of an important proportion of short rods with very monodisperse sections (curve 2) and finally to a model involving long and thick fibers in a swollen network (curve 3).

References

- [1] Terech, P.; Weiss, R.G. *Chem. Rev.*, **1997**, *97*, 3133–3159.
- [2] Lambard, J.; Zemb, T.J. *Appl. Cryst.*, **1991**, *24*, 555–561.
- [3] Guinier, A.; Fournet, G. *Small Angle Scattering of X-rays*, New York: Wiley, **1955**.
- [4] Glatter, O.; Kratky, O. *Small Angle X-ray Scattering*, London: Academic Press, **1982**.
- [5] Higgins, J.S.; Benoit, H.C. *Polymers And Neutron Scattering*, Oxford: Clarendon Press, **1994**.
- [6] *Neutron News*, **1992**, *3*, 29–37.
- [7] Terech, P.; Pasquier, D.; Bordas, V.; Rossat, C. *Langmuir*, **2000**, *16*, 4485–4494.
- [8] Vainshtein, B.K. *Diffraction of X-rays By Chain Molecules*, Amsterdam: Elsevier, **1966**.
- [9] Terech, P.; Ramasseul, R.; Volino, F. *J. Phys. France*, **1985**, *46*, 895–903.

- [10] Jacrot, B. *Rep. Prog. Phys.*, **1976**, *39*, 911–953.
- [11] Bonini, C.; Heux, L.; Cavaille, J.-Y.; Lindner, P.; Dewhurst, C.; Terech, P. *Langmuir*, **2002**, *18*, 331–3314.
- [12] Terech, P. *Il Nuovo Cimento*, **1994**, *16D*, 757–764.
- [13] Cates, M.E.; Candau, S.J. *J. Phys.: Condens. Matter*, **1990**, *2*, 6869–6892.
- [14] Terech, P.; Coutin, A. *Langmuir*, **2000**, *15*, 5516–5525.
- [15] Terech, P.; Rodriguez, V.; Barnes, J.D.; McKenna, G.B. *Langmuir*, **1994**, *10*, 3406–3418.
- [16] Terech, P.; Scherer, C.; Deme, B.; Ramasseul, R. *Langmuir*, **2003**, *19*, 10641–10647.
- [17] Terech, P.; Schaffhauser, V.; Maldivi, P.; Guenet, J.M. *Europhys. Lett.*, **1992**, *17*, 515–521.
- [18] Lortie, F.; Boileau, S.; Bouteiller, L.; Chassenieux, C.; Deme, B.; Ducouret, G.; Jalabert, M.; Laupretre, F.; Terech, P. *Langmuir*, **2002**, *18*, 7218–7222.
- [19] Porte, G.; Appell, J.; Poggi, Y. *J. Phys. Chem.*, **1980**, *84*, 3105–3110.
- [20] Appell, J.; Porte, G.; Poggi, Y. *J. Colloid Interface Sci.*, **1982**, *87*, 492–499.
- [21] Yoshizaki, T.; Yamakawa, H. *Macromolecules*, **1980**, *13*, 1518–1525.
- [22] Yamakawa, H.; Fujii, M. *Macromolecules*, **1974**, *7*, 649–654.
- [23] Muroga, Y.; Tagawa, H.; Hiragi, Y.; Ueki, T.; Kataoka, M.; Izumi, Y.; Amemiya, Y. *Macromolecules*, **1988**, *21*, 2756–2760.
- [24] Nierlich, M.; Boue, F.; Lapp, A.; Oberthur, R. *Coll. Polym. Sci.*, **1985**, *263*, 955–964.
- [25] Odijk, T. *J. Polym. Sci. Ed.*, **1977**, *15*, 477–483.
- [26] Mukhopadhyay, S.; Maitra, U.; Ira; Krishnamoorthy, G.; Schmidt, J.; Talmon, Y. *J. Am. Chem. Soc.*, **2004**, *126*, 15905–15914.
- [27] Mittelbach, P. *Acta Physica Austriaca*, 53–102.
- [28] Mittelbach, P.; Porod, G. *Acta Physica Austriaca*, **1961**, *14*, 185–211.
- [29] Mittelbach, P.; Porod, G. *Acta Physica Austriaca*, **1961**, *14*, 405–493.
- [30] Selinger, J.V.; MacKintosh, F.C.; Schnur, J.M. *Phys. Rev. E*, **1996**, *53*, 3804–3818.
- [31] Selinger, J.V.; Spector, M.S.; Schnur, J.M. *J. Phys. Chem. B*, **2001**, *105*, 7157–7169.
- [32] Spector, M.S.; Selinger, J.V.; Schnur, J.M. “Chiral molecular self-assembly” In *Materials Chirality*, M.M. Green, R.J.M. Nolte, E.W. Meijer, Eds., New York: Wiley, **2002**.
- [33] Nyrkova, I.A.; Semenov, A.N.; Aggeli, A.; Boden, N. *Eur. Phys. J.*, **2000**, *B 17*, 481–497.
- [34] Nyrkova, I.A.; Semenov, A.N.; Aggeli, A.; Bell, M.; Boden, N.; McLeish, T.C.B. *Eur. Phys. J.*, **2000**, *B 17*, 499–513.
- [35] Arleth, L.; Bauer, R.; Ogendal, L.H.; Egelhaaf, S.U.; Schurtenberger, P.; Pedersen, J.S. *Langmuir*, **2003**, *19*, 4096–4104.
- [36] Terech, P.; de Geyer, A.; Struth, B.; Talmon, Y. *Adv. Mat.*, **2002**, *14*, 495–498.
- [37] Terech, P.; Wade, R.H. *J. Colloid Interface Sci.*, **1988**, *1252*, 542–551.
- [38] Hukins, D.W.L. *X-ray Diffraction by Disordered and Ordered Systems.*, Oxford: Pergamon Press, **1981**.
- [39] Pringle, O.A.; Schmidt, P.W. *J. Appl. Cryst.*, **1971**, *4*, 290–293.
- [40] Schmidt, P.W. *J. Appl. Cryst.*, **1970**, *3*, 257–264.
- [41] Liu, X.Y.; Sawant, P.D. *Angew. Chem. Int. Ed.*, **2002**, *41*, 3641–3645.
- [42] Debye, P.; Bueche, A.M. *J. Appl. Phys.*, **1949**, *20*, 518.
- [43] Terech, P.; Coutin, A.; Giroud, A.M. *J. Phys. Chem. B*, **1997**, *101*, 6810–6818.
- [44] Guinier, A. *X-ray Diffraction*, W.H., F., Ed. San Francisco: **1963**.
- [45] George, M.; Snyder, S.I.; Terech, P.; Weiss, R.G.; To appear in *Langmuir*.
- [46] De Gennes, P.G. *Scaling Concepts in Polymer Physics*, Ithaca NY.: Cornell University Press, **1979**.

- [47] Schurtenberger, P.; Cavaco, C. *J. Phys. II France*, **1993**, 3, 1279–1288.
- [48] Teixeira, J. *J. Appl. Cryst.*, **1988**, 21, 781–785.
- [49] Jullien, R. *J. Phys. I France*, **1992**, 2, 759–770.
- [50] Liu, X.Y.; Sawant, P.D. *Appl. Phys. Lett.*, **2001**, 79, 3518–3520.
- [51] Oster, G.; Riley, D.P. *Acta Cryst.*, **1952**, 5, 272–276.
- [52] Shimada, T.; Doi, M.; Okano, K. *J. Chem. Phys.*, **1988**, 88, 2815–2821.
- [53] van der Schoot, P. *Macromolecules*, **1992**, 25, 2923–2927.
- [54] Benmouna, M.; Weill, G.; Benoit, H. *J. Phys. France*, **1982**, 43, 1679–1685.
- [55] Yarusso, D.J.; Cooper, S.L. *Macromolecules*, **1983**, 16, 1871–1880.
- [56] Yarusso, D.J.; Cooper, S.L. *Polymer*, **1985**, 26, 371–378.
- [57] Hayter, J.B.; Zulauf, M. *Colloid Polymer Sci.*, **1982**, 1023–1028.
- [58] Hayter, J.B.; Penfold, J. *Colloid Polym. Sci.*, **1983**, 261, 1022–1030.
- [59] Pedersen, J.S. *Adv. Coll. Interface Sci.*, **1997**, 70, 171–210.
- [60] Leadbetter, A.J.; Norris, E.K. *Mol. Phys.*, **1979**, 38, 669–686.
- [61] Davidson, P.; Petermann, D.; Levelut, A.M. *J. Phys. II France*, **1995**, 113–131.
- [62] Hayter, J.B.; Penfold, J. *J. Phys. Chem.*, **1984**, 88, 4589–4593.
- [63] Kalus, J.; Hoffman, H. *J. Chem. Phys.*, **1987**, 87, 714–722.
- [64] Penfold, J. *J. Appl. Cryst.*, **1988**, 21, 770–776.
- [65] Glatter, O. *J. Appl. Cryst.*, **1977**, 10, 415–421.
- [66] Glatter, O. *J. Appl. Cryst.*, **1979**, 12, 166–175.
- [67] Glatter, O. *J. Appl. Cryst.*, **1980**, 13, 577–584.
- [68] Pedersen, J.S.; Schurtenberger, P. *J. Appl. Cryst.*, **1996**, 29, 646–661.
- [69] Terech, P. *J. Phys. France*, **1989**, 50, 1967–1982.
- [70] Terech, P.; Ramasseul, R.; Volino, F. *J. Colloid Interface Sci.*, **1983**, 91, 280–282.
- [71] Huang, X.; Terech, P.; Raghavan, S.R.; Weiss, R.G. *J. Am. Chem. Soc.*, **2005**, 127, 4336–4344.
- [72] Jean, B.; Oss Ronen, L.; Terech, P.; Talmon, Y. *Adv. Mat.*, **2005**, 17(6), 728–731.
- [73] Jean, B.; Oss Ronen, L.; Smith, J.; Talmon, Y.; Terech, P. To be published.
- [74] Avrami, M. *J. Chem. Phys.*, **1939**, 7, 1103–1112.
- [75] Avrami, M. *J. Chem. Phys.*, **1940**, 8, 212–224.
- [76] Avrami, M. *J. Chem. Phys.*, **1941**, 9, 177–184.
- [77] Struth, B.; Rieutord, F.; Konovalov, O.; Brezesinski, G.; Grubel, G.; Terech, P. *Phys. Rev. Lett.*, **2002**, 88, 025502–4.
- [78] Salmon, J.-B.; Colin, A.; Roux, D. *Phys. Rev. E*, **2002**, 66, 031505–13.

Chapter 11

X-RAY DIFFRACTION OF POORLY ORGANIZED SYSTEMS AND MOLECULAR GELS

Michel Anne

*Laboratoire de Cristallographie, CNRS, 25 avenue des Martyrs, BP166,
38042 Grenoble, Cedex 09, France*

1. Introduction	325
2. Long Range Ordering	327
2.1. Diffraction and Diffuse Scattering	327
2.2. The Crystal Structure	327
3. Single Crystal Diffraction	329
3.1. The Structure Factor	330
3.2. Crystal Structure Solution	331
4. Powder Diffraction	337
4.1. Structure Determination from Powders	338
4.2. Multi-phases and Quantification by Profile Refinement Techniques	344
4.3. Microstructures	345
5. X-Rays and Neutrons	347
6. Applications of Diffraction	348
6.1. Partially Disordered Compounds: Pharmaceutical Molecules	348
6.2. Molecular Gels	353
7. Conclusions	360

1. Introduction

Crystal structure determination by X-ray or neutron (see Chapter 10) diffraction is an important method to understand molecular shapes, the modes of molecular packing, and related physical and chemical properties. Using

proteins, new superconductors, ionic conductors, polymers or ferro-magnetic compounds, fundamental research is laying foundations for applications as varied as microelectronics, metallurgy, fine chemicals, the oil industry, energy storage, building materials, pulp, cosmetics and pharmaceuticals.

Many of the materials pertinent to these fields have complex packing arrangements, such as partially disordered crystalline solids. The disorder can be static or dynamic in origin, one being occasionally the consequence of the other in the same structure. Various solids show some degree of disorder in their periodic arrangement and can be very different in nature, as for instance, ionic conductors and pharmaceuticals. An order-disorder transition initiating disordered vacancies in the former may lead to ion diffusion inside the crystalline solid, inducing high thermal vibrations of atoms in the lattice. In the latter, size and individualistic character of the molecules gives rise to two kinds of structural disorder due to intra- and inter-molecular atomic vibrations. The high frequency internal modes correspond to torsions and distortions inside the molecule, whereas the low frequency external modes describe oscillations of the global molecule and result in larger atomic displacement parameters. The intramolecular vibrations may perturb the long range order of the molecular arrangement.

Nowadays, solving structures from single crystal data has become relatively routine using well-proven modern methods and software packages assisted by more and more powerful computers. Crystal structure determination from powders, a much more recent technique, is less straight-forward. Even so, the same basic principles are applied. The main drawback of this method is the projection of the three-dimensional reciprocal lattice onto a single axis (θ, d, q) which very often produces a severe overlap of the Bragg reflections.

For that reason, it is highly advantageous to work with single crystals when they are available. Unfortunately, it is often difficult or not possible to grow single crystals of disordered molecules due to their intrinsically disorganized character.

In order to overcome these difficulties when determining crystal structures from powders, methods have been developed recently to improve the usual procedures. Simulated crystallographic models can be built from molecular chemistry, local atomic arrangement and structure fragments. The resulting trial structures are calculated and compared to the diffraction data, and some atom parameters are changed in the direct space in order to find the best fit. Besides this, molecular dynamics, statistic genetic algorithms and simulated annealing help to predict the most probable crystallographic structure. The next step of the determination is classical refinements of Rietveld type.

In the following parts, some definitions and principles concerning the crystalline state are given. Then methods for determining and refining a crystal structure are developed. Finally, some typical examples of structure determinations of partially disordered structures are presented.

2. Long Range Ordering

A crystalline compound may be defined as a homogeneous solid having an ordered internal atomic arrangement and a definite overall chemical composition (stoichiometric or not). Beside the classical crystalline materials, other compounds may be described as crystalline because they present some degrees of long-range order over many periods. Such examples include sheet and fibrous substances.

A crystal may be defined as a solid that is crystalline in three dimensions and is bounded by plane faces. A useful distinction is that crystalline compounds exhibit long-range order in three or fewer dimensions, whereas crystals have three-dimensional regularity and plane bounding faces.

2.1. Diffraction and Diffuse Scattering

X-ray (or neutron) scattering by atoms can be separated into two parts. The first part arises from the average periodic structure and the second from fluctuations around and away from the equilibrium positions. The former describes the Bragg scattering and the latter refers to diffuse scattering.

Diffuse scattering is due to inelastic scattering generated by electronic excitations, to thermal diffuse scattering related to atomic motions (TDS), to scattering from disorder, and/or from crystal defects (DDS). Thermal vibrations break down the perfect periodicity of the crystals with fluctuations in the atomic density around the instantaneous positions. Structure factor amplitudes are reduced by such atomic displacement through the Debye-Waller factor.

In solid-state physics, “lattice dynamics” and “lattice vibrations” are used in referring to the collective modes of vibrations of the entire crystal. On the other hand, “diffraction” is sometimes restricted to elastic scattering processes and the measurement of the intensity as a function of direction then constitutes a “diffraction experiment”. Indeed, “diffraction” has a more general sense for any measurement involving the interference of wave trains scattered by different atoms in the crystal. Thus, Bragg scattering, thermal diffuse scattering of X-rays, and the coherent inelastic scattering of slow neutrons by crystals are diffraction processes. Bragg scattering is simply coherent elastic scattering.

2.2. The Crystal Structure

The crystalline state may be defined as a regular repetition in the three-dimensional space of an object made of atoms, molecules or groups of

molecules, extending over a distance corresponding to a very high number of motif units. However, some crystals do not show three-dimensional periodicity, as in defect compounds or in fibrous materials which are ordered only along the fiber axis. Thus, the periodicity can be observed to a lesser extent in crystals, but it is useful to introduce the ideal crystal with perfect periodicity and the symmetry rules determining its formation [1]. Every crystal has a lattice as its geometric basis that is described in relation to three basic translation vectors **a**, **b**, **c** and constituted of an infinite arrangement of points. A unit-cell is defined as the smallest repeat unit for which its delimiting vectors are parallel to important symmetry directions in the lattice. Fourteen three-dimensional lattices, or Bravais lattices, can be built and are unequally distributed among the seven crystal systems: triclinic, monoclinic, orthorhombic, tetragonal, cubic, hexagonal and trigonal (Figure 1).

Inside the unit-cell, atoms may correspond by combined symmetry operations defining a group, namely, rotary axes, mirrors, centers of symmetry and

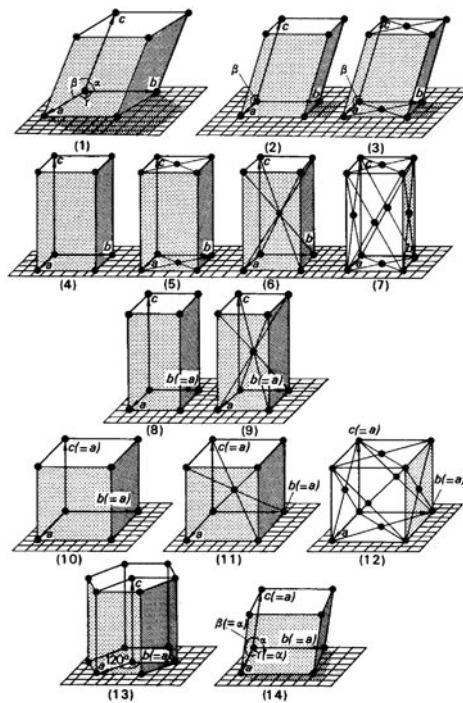


Figure 1. Unit cells of the 14 Bravais lattices; interaxial angles are 90° unless indicated otherwise by a numerical value or symbol: (1) triclinic *P*, (2) monoclinic *P*, (3) monoclinic *C*, (4) orthorhombic *P*, (5) orthorhombic *C*, (6) orthorhombic *I*, (7) orthorhombic *F*, (8) tetragonal *P*, (9) tetragonal *I*, (10) cubic *P*, (11) cubic *I*, (12) cubic *F*, (13) hexagonal *P*, (14) trigonal *R*. (Reprinted with permission from [1]. Copyright (1977) Plenum Press.)

rotary inversion axes. Crystals can be classified in terms of the groups of symmetry operations they are related to. Each of these groups, known as the 32 point groups, represents one of the possible unique combinations of crystallographic symmetry elements. It can be shown rigorously that combining the 32 point groups with the 14 Bravais lattices leads to 230 unique arrangements of points in space. These are the 230 space groups that describe the only ways in which identical atoms of a crystal structure can be arranged in an infinite lattice. Furthermore, knowledge of the symmetry elements between atoms, ions or molecules in a crystal structure facilitates its determination by reducing the number of unique parameters to be adjusted.

3. Single Crystal Diffraction

As it is still not possible to construct a microscope that would enable us to clearly see the structure directly, X-ray (or neutron) diffraction must be performed in order to determine the structure of a crystal. The term diffraction refers to the interference phenomena exhibited by the coherently scattered radiation and, consequently, this imposes the diffraction conditions.

An incident beam is reflected from parallel layers of atoms in a crystal. The angle of incidence is equal to the angle of reflection, so both are designated as θ . Then, for a maximum in the reflected beam, the component beams reflected from adjacent layers must be in phase (that is, they must have a path difference which is an integral number of wavelengths). Hence, it follows that the reflection condition is:

$$n\lambda = 2d \sin \theta$$

n is an integer called the order of the reflection. This is the Bragg equation.

The Reciprocal lattice

From Bragg's law it is seen that $\sin \theta$ is inversely proportional to d , the interplanar spacing in the crystal lattice. Since $\sin \theta$ is a measure of the deviation of the diffracted beam from the direct beam, it follows that structures with large d will have compressed diffraction patterns, and conversely for small d . Thus, the idea is to build a reciprocal lattice based on $1/d$, which varies directly as $\sin \theta$. This concept simplifies virtually all problems of lattice and diffraction geometry.

The crystal lattice is called the direct lattice ($\mathbf{a}_1, \mathbf{a}_2, \mathbf{a}_3$ or $\mathbf{a}, \mathbf{b}, \mathbf{c}$ axes) which is opposed to the reciprocal lattice ($\mathbf{a}_1^*, \mathbf{a}_2^*, \mathbf{a}_3^*$ or $\mathbf{a}^*, \mathbf{b}^*, \mathbf{c}^*$ axes) and they exist in the direct space opposed to the reciprocal space. These axes are determined by the relations:

$$\mathbf{a}_i \cdot \mathbf{a}_j^* = \delta_{ij}$$

where

$$\begin{aligned}\delta_{ij} &= 1 && \text{for } i = j \\ &= 0 && \text{for } i \neq j\end{aligned}$$

This definition of the reciprocal lattice axes requires that \mathbf{a}^* be normal to \mathbf{b} and \mathbf{c} , and so on. Two properties useful for describing diffraction are derived:

- (1) The reciprocal lattice vector

$$\mathbf{S}(hkl) \equiv h\mathbf{a}^* + k\mathbf{b}^* + l\mathbf{c}^*$$

is normal to the family of planes (hkl) in the direct lattice

- (2) The length of the reciprocal lattice vector $\mathbf{S}(hkl)$ is the reciprocal of the interplanar spacing $d(hkl)$ for the planes (hkl)

$$d(hkl) = 1/S(hkl)$$

3.1. The Structure Factor

In a diffraction experiment, the intensities measured for a large number of Bragg reflections are proportional to the squared amplitudes $|F_{hkl}|^2$ of the structure factors F_{hkl} written in the form:

$$F_{hkl} = \sum_{j=1}^n f_j \exp(-W_j) \exp[2\pi i(hx_j + ky_j + lz_j)]$$

The summation is over the n atoms in the unit cell, f_j is the X-ray scattering factor (or alternatively b_j is the coherent neutron scattering length) and x_j, y_j, z_j are the co-ordinates of the j th atom within the cell. The quantity $\exp(-W_j)$ is the Debye-Waller factor which accounts for the lattice vibrations and reduces the intensity of the Bragg reflection. For an isotropically vibrating atom:

$$W_j = B_j \frac{\sin^2 \theta}{\lambda^2}$$

The B -factor is related to the mean-square displacement of atom j in any direction.

Examining the structure factor formula, it is obvious that translational symmetry elements can be detected from systematic absences of Bragg reflections. This is a good aid to determine the space group symmetry, which is mandatory for solving a crystal structure.

3.2. Crystal Structure Solution

Actually, solving the crystal structure of a crystallized compound from diffraction data needs two stages. The first one leads to the determination of a rough model including the main features of the structure. The second is the completion of the structure with the optimization of the original approximate structural description by refining some adjustable parameters.

3.2.1. The phase problem and direct methods

The fundamental difficulty of determining a structure by diffraction is the fact that the crystallographically available data consist only of the structure factor magnitudes and not their phases ($F_{hkl} = |F_{hkl}|e^{i\alpha}$, where α is the unobservable phase). The phase problem arises from the fact that this missing information has to be supplied. There are various methods of obtaining phasing models and the following list is not exhaustive:

- Patterson Methods
- Direct Methods (Inequalities, Fs, Us, and Es, Structure Invariants and Seminvariants, Probability Methods)
- Heavy Atom Methods
- Search Methods (Trial-and-Error Methods, the Rotation Search, the Translation Search, the Superposition Methods)

Once some atoms have been revealed by one or more of these methods, this model is used for the calculation of structure factors (F_c), and these serve as a source of phases for Fourier calculations. We shall only focus our attention here on the two most commonly used techniques, the Patterson and direct methods.

The Patterson function

If the structure factors and phases are known, the distribution of the electron density (or nuclei-related density in the case of neutrons) in the unit cell can be calculated using the general expression:

$$\rho(x, y, z) = \frac{1}{V} \sum_h \sum_k \sum_l F_{hkl} e^{-2\pi i(hx + ky + lz)}$$

This Fourier series corresponds to the Fourier transform of the structure factor F_{hkl} but crystallographic Fourier series can be calculated with any sort of coefficients. One of these is the Patterson or $|F|^2$ function:

$$P(u, v, w) = \frac{1}{V} \sum_h \sum_k \sum_l |F_{hkl}|^2 \cos 2\pi(hu + kv + lw)$$

In this case, the coefficients of the Fourier series are the squares of the observed structure factors $|F_o|$. Since the coefficients are squares, they are phaseless and the Patterson function can be immediately obtained from diffraction data [2].

Whereas the usual Fourier synthesis with F s as coefficients shows the distribution of atoms in the cell, the map calculated with $|F|^2$ gives peaks corresponding to all of the interatomic vectors. Thus a peak at the point uvw in a Patterson map indicates that atoms exist in the crystal at x_1, y_1, z_1 and x_2, y_2, z_2 such that:

$$u = x_1 - x_2$$

$$v = y_1 - y_2$$

$$w = z_1 - z_2$$

For a molecule containing N atoms in a unit cell, the Patterson synthesis will show N^2 peaks, corresponding to the N possible vectors that can be drawn from each of the N atoms (Figure 2). Of these, N will be vectors of zero length from each atom to itself and will be concentrated as a very large peak at the origin. The remaining $N^2 - N$ will be distributed throughout the cell. The weight of a Patterson peak depends on the numbers of electrons (X-rays) or on the scattering lengths (neutrons) of the atoms between which the vector

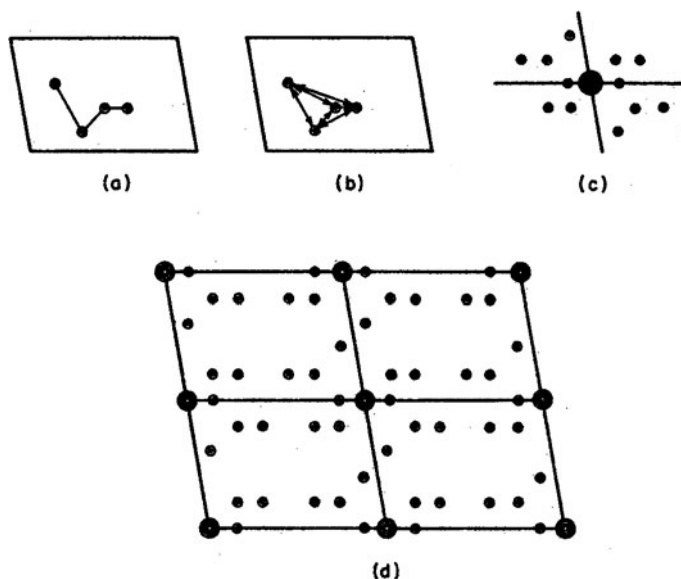


Figure 2. (a) Set of points. (b) Interatomic vectors. (c) Patterson peaks about the origin from one set; (●) origin peak. (d) Patterson peaks in four unit cells. (Reprinted with permission from [2]. Copyright (1989) John Wiley and Sons.)

occurs, and can be shown to be proportional to the products of their atomic numbers or their scattering lengths. It is this fact that allows the heavy atom vectors to be recognized in the Patterson map, usually without difficulty. Concerning the symmetry of the Patterson function, the following rules can be listed:

- All Patterson functions are centrosymmetric.
- Their lattice type (P , C , F , etc.) is the lattice type of the original space group.
- Their space group is derived from the original space group by replacing all translational symmetry elements (screws, glides) by the corresponding non-translational elements (axes, mirrors) and by adding a center of symmetry if it is not already present.

Despite the overlapping problem, structures have been solved from powder data by Patterson techniques and this method seems less sensitive to errors in the intensities than direct methods.

Direct methods

Methods of direct calculation of phases are now widely used and have been automated to the extent that most of the programs work as “black box” techniques in which the raw data go in at one end and the essentially solved structure appears at the other. In fact, this is not really true in powder diffraction which, once again, suffers from the small number of reliable reflections due to overlapping. This situation is strongly improved by high resolution synchrotron X-ray diffraction. Hereafter follows a short description of the methods, but details can be easily found in specialized crystallographic literature.

Expressions relating phases to intensities and resulting from the combination of structure factor expressions with certain classical inequalities, provide the first means of determining the phase of a reflection. These inequalities represent limiting cases of the more general probability relationships and become ineffective for reasonably complex structures. Another approach is the probability methods: in the range of intensities that are too small for inequalities but still relatively large, it is possible to set up “equations” that are probably true, and from these to extract phase information. Thus, in the case of centrosymmetric space groups, it can be shown that, within certain restrictions:

$$F_{hkl} = \Omega_{hkl} \sum_{h'} \sum_{k'} \sum_{l'} F_{h'k'l'} F_{-h',k-k',l-l'}$$

Ω_{hkl} is a scaling term. From this full Sayre equation, some probability equations conditioning the phases have been derived. Equivalent expressions have been obtained for non-centrosymmetric space groups as well.

The practical objective of direct methods is to phase a sufficient number of reflections to give an identifiable Fourier representation of the molecule being studied. Roughly, 10 reflections per atom in the asymmetric unit seem quite satisfactory. Two main procedures are used for the application of direct methods.

Symbolic addition method

In this method, one starts with a very limited number of phases and uses them to pyramid to a number large enough to give a recognizable Fourier representation of the structure. The problem met in practice is that of obtaining some initial phases to work with. Fortunately, a limited number, usually three, can be assigned arbitrary values, subject to certain restrictions. These arbitrarily assigned phases constitute the initial set.

Multiple solution methods

Various programs have been written to carry out symbolic addition by machine, but the standard approach to symbolic addition does not make the best use of computer abilities. On this basis, Woolfson and his collaborators built their direct methods and the program MULTAN [3] which is widely used either directly or in the form of other programs derived from it. This program includes many features, one of them being the introduction of magic integer methods which reduce the number of trial sets.

Once the analysis is completed, the result is a number of possible phase sets and Fourier syntheses are calculated for each of these. The maps are examined in order to determine the most promising structural model.

3.2.2. Real-space method and simulated annealing

Standing aside the direct methods for crystal structure solution are simulated annealing techniques working in the real space [4].

The real-space method solves structures by altering positions, orientations and conformations of the molecule(s) in the unit cell, according to the constraints of space group symmetry, until a good match is obtained between calculated and observed intensities. For powder diffraction data, observed integrated intensities can be extracted by Pawley or Le Bail full pattern refinements. In the case of Pawley analysis, the level of agreement between a trial structure and the experimental diffraction data is quantified by χ^2 , whose formula is:

$$\chi^2 = \sum_h \sum_k \left[(I_h - c|F_h|^2)(V^{-1})_{hk}(I_k - c|F_k|^2) \right]$$

With $I_{h,k}$ = extracted integrated intensity from Pawley refinements, V_{hk} = covariance matrix, c = scale factor, $F_{h,k}$ = calculated structure factor from a trial structure.

The process is a search for a global minimum in multi-dimensional parameter space, the parameters being positions, rotations and torsion angles. This search is performed using a simulated annealing algorithm (i.e., a Monte-Carlo method based on the Metropolis algorithm which implements a weighted random walk through conformational space). A series of structures are generated, and each structure is derived from the previous structure forming a Markov chain. The first structure is chosen as a random position of the molecule(s) in the unit cell. A trial structure generated from structure i is accepted automatically if $\chi_{\text{trial}}^2 - \chi_i^2 \leq 0$; if $\chi_{\text{trial}}^2 - \chi_i^2 > 0$. The trial structure is accepted only with probability $e^{-((\chi_{\text{trial}}^2 - \chi_i^2)/k_B T)}$ and rejected with probability $(1 - e^{-((\chi_{\text{trial}}^2 - \chi_i^2)/k_B T)})$, where k_B is the Boltzmann constant and T a “temperature” that is decreased systematically according to an annealing process. If the trial structure is rejected, structure $i + 1$ is taken to be the same as i . The above procedure is repeated, and each structure is deduced from the previous one through small random displacements until the system reaches a global minimum.

3.2.3. Refinements

The refinement stage of a structure analysis is assumed to begin with a completed trial structure containing all the atoms and, thus, prior to it, the Fourier techniques can help to reveal the missing one. The problem to be solved is the following: given a set of experimental observations $|F_o|$ and a theoretical model which, from trial values of some parameters, generates a set of calculated $|F_c|$ values, find the values of parameters which give the best fit to the data and estimate their accuracy. The observed structure factor moduli $|F_o|$ of the measured Bragg reflections are extracted from the observed integrated intensities $I_0 \propto |F_0|^2$. There are several approaches to solve this problem and the most used is the method of least squares. The principle of this method states that the best values for the optimized parameters are those that minimize the sums of the squares of the properly weighted differences between the observed and calculated values of a linear function for all the observational points. The functional form of the structure factor F_{hkl} is transcendental and so must be approximated by a truncated Taylor series. In diffraction, the quantity most commonly minimized is M over all the observed reflections:

$$M = \sum_{hkl} w_{hkl} (|F_o| - |k F_c|)^2$$

Minimization is achieved by taking the derivative with respect to each of the parameters and equating it to zero; w_{hkl} is the weight to be assigned an observation $|F_o|$, k is a scale factor and $|k F_c|$ is the corresponding calculated value. The weight is equal to the reciprocal of the square of the standard deviation of the observation.

The accuracy of the refinements is evaluated with the conventional crystallographic residual index R , defined as:

$$R = \frac{\sum ||F_o| - |kF_c||}{\sum |F_o|}$$

A useful index often output by least squares refinement programs is the so-called *goodness of fit (gof)*:

$$gof = \left[\frac{\sum w(|F_o| - |kF_c|)^2}{n - m} \right]^{1/2}$$

n is the number of reflections and m is the total number of parameters refined.

3.2.4. Electron or nuclear density maps

The expression of the density distribution of the unit-cell has already been given above. It is the Fourier transform of the structure factor, which means that the coefficients of the crystallographic Fourier series are the F_{hkl} s; this Fourier transform is called “Fourier synthesis.”

The other important Fourier function is the so-called “difference synthesis” or “Fourier difference.” In this case, the coefficients are defined as:

$$\Delta F = F_o - F_c$$

F_o and F_c are the observed and calculated structure factors (Figure 3). The calculation of difference syntheses requires using the phases of the F_c s obtained from the refinements, for both F_o and F_c , the F_o phases being unobservable. The Fourier coefficients are then defined as:

$$\Delta F = (|F_o| - |F_c|)\pi e^{i\alpha_c}$$

$|F_o|$ and $|F_c|$ are the observed and calculated structure factor moduli, and α_c is the F_c phase. The expression for the difference synthesis is:

$$\Delta\rho(X, y, z) = \frac{1}{V} \sum_h \sum_k \sum_l \Delta F e^{-2\pi i(hx+ky+lz)}$$

The units are proportional to differences in density of electrons for X-rays or nuclei related for neutrons. A specific advantage of this difference synthesis arises from the fact that, even when the phases are moderately in error, a difference map is able to show the discrepancies between the proposed structural model and the reality, as missing atoms for example.

Thus, new atoms appearing on the difference map are added to the model to be refined and the procedure is repeated until the structure is complete.

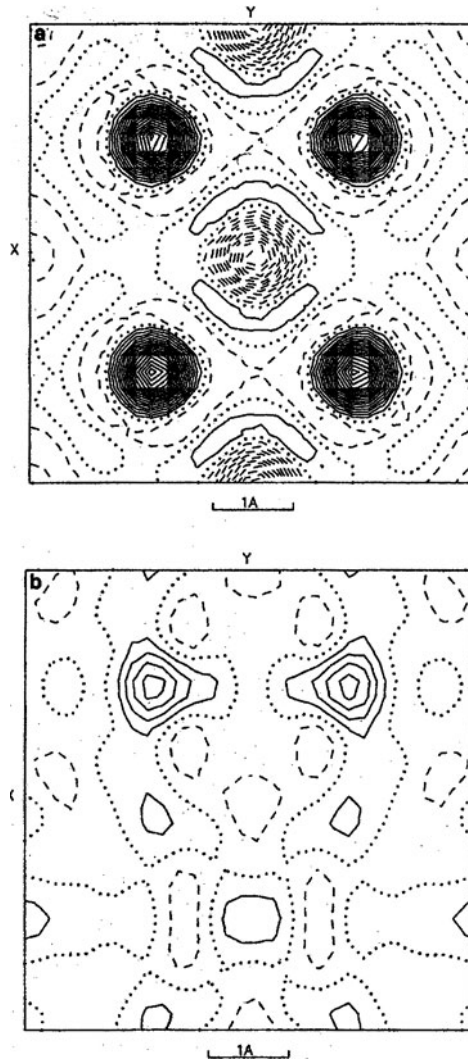


Figure 3. Fourier maps determined from the powder diffraction pattern of sample $\text{Li}_{1.05}\text{Mn}_2\text{O}_{4-\delta}$. (a) Fourier section for $z = 0$; (b) difference map at $z = 0.05$, showing residual density around the oxygen atom position along the z axis.

4. Powder Diffraction

Structure determination of single crystals from X-ray or neutron diffraction data collected on an automatic four-circle diffractometer is very easy to handle for most compounds. The unit cell is obtained from Weissenberg or Buerger precession photographs, or from an automatic peak search, and the

space group deduced from systematic absences. Starting crystallographic models are selected from Patterson techniques or direct method results. Then, the structural parameters are refined and the remaining unknown atoms revealed by difference Fourier techniques.

In the case of powders, one of the main difficulties encountered in interpreting the diffraction pattern is the fact that the three-dimensional reciprocal lattice is reduced to a single axis (θ, d, q defined by $\lambda = 2d \sin \theta$ and $q = (4\pi/\lambda) \sin \theta$). As a consequence of that, there are strong overlaps of reflections with close Bragg angles due to the broadening of the instrumental resolution. Therefore, it is difficult to evaluate with accuracy the contributing intensities in the diffraction pattern, and this leads to an uncertainty at each step of the structure determination. Nevertheless, completely unknown structures have been determined successfully from X-ray and neutron powder diffraction, and the very high resolution which can be obtained with synchrotron X-ray powder diffraction may explain the recently increasing interest observed in powder structure determination.

The Rietveld method is a profile fitting procedure that refines parameters from a structural model which already exists. This is not enough for an “*ab initio*” structure determination where prior knowledge of cell parameters, space group and initial model is needed. The approximate structure can be obtained by Patterson, direct methods as used in single crystal structure determination, and the Fourier techniques can also be employed in the final stage of the refinements. However, it must be kept in mind that peak overlapping is a real drawback, and there are some methods to overcome this difficulty.

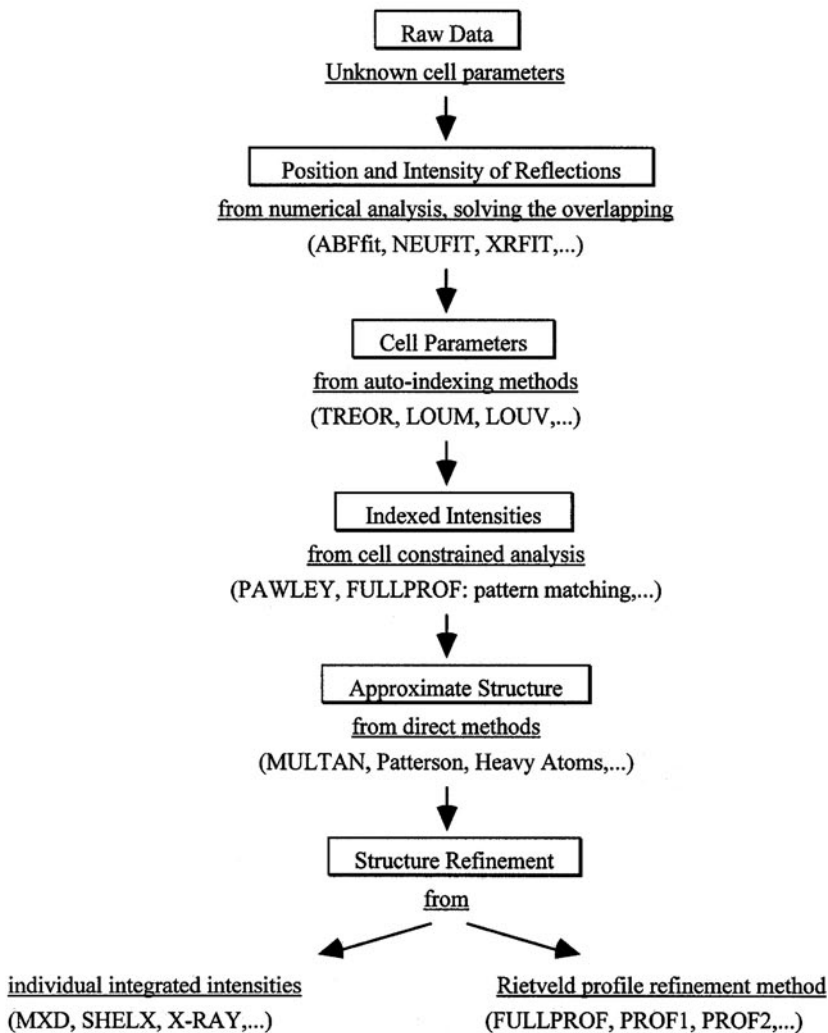
4.1. Structure Determination from Powders

How can a completely unknown structure be resolved from powder diffraction data? When no *a priori* information on the pattern is available (unknown cell parameters), the diffraction data are analyzed numerically. In such a case, the analysis will be restricted to fitting a given line shape above a polynomial background. The pattern is divided into several domains with an angular range as small as possible, depending on the number of reflections and the overlaps in each one, and the positions of the lines will be determined for all the individual reflections which can be separated by this fitting procedure. For an unknown crystalline compound, the next step would normally be the determination of the cell parameters by using an auto-indexing method.

Once the cell parameters are approximately determined, a cell constrained analysis is carried out to extract refined cell parameters and intensities from the powder diffraction patterns (Pawley-type programs or full pattern matching, cell constrained refinement procedures). The next step will be the determination

of the structure by Patterson and/or direct methods, or by a few other procedures. The crystallographic model, very often only partially determined, is optimized and the remaining atoms are then revealed using Fourier difference techniques. The final stage will be the refinement of all the adjustable parameters of the completed structural model.

A path for:
"Ab initio" Structure Determination
from:
Powder Diffraction Patterns



Schematically, structure determination from powder diffraction data can be considered to proceed in five steps:

1. Derivation of the unit cell from measured Bragg peak positions, using auto-indexing methods.
2. Determination of the possible space group symmetry from examination of systematically absent reflections.
3. Least square refinement of the intensities, I_{hkl} , and hence the structure factor magnitudes, $|F_{hkl}|$, of all measured Bragg reflections (N.B., $I_{hkl} \propto |F_{hkl}|^2$).
4. Determination of the structural model to be optimized by application of the Patterson method, direct methods or real-space techniques, using the observed structure factor magnitudes.
5. Least square refinement of the approximate crystal structure obtained from step 4.

4.1.1. Unit cell determination and auto-indexing procedures

Lattice constants can be determined by a variety of techniques (e.g., reference to known structures, electron diffraction, trial-and-error methods and auto-indexing). A number of sophisticated programs exist for the latter purpose, but in general an accurate set of low-angle peak positions is crucial to the success of this approach.

First of all, as mentioned above, individual line positions are extracted from the overlapping intensities of the diffraction pattern; this needs to be done with maximum accuracy and requires the use of powerful computing programs. One of the most efficient and easy to use is WinPLOTR [5]; a given numerical function is fitted to a measured diffraction line or group of lines which have been selected and the estimated positions (and intensities) are adjusted through a least squares or maximum-of-likelihood fitting (several profile shape functions can be chosen: Gaussian, pseudo-Voigt etc.).

Powder indexing means the reconstruction of crystal lattices from d -spacing data without prior knowledge of the unit cell dimensions. The d -spacings are deduced from the peak positions using Bragg's law ($\lambda = 2d_{hkl} \sin \theta$) and indexation of the pattern requires solving the relations:

$$d_{hkl} = f(h, k, l, a, b, c, \alpha, \beta, \gamma)$$

h, k, l are the Miller indices and $a, b, c, \alpha, \beta, \gamma$, the lattice constants to be found.

There are several graphical and simple numerical methods for finding the unit-cell parameters from powder data for compounds with lattices of high symmetry. However, for lattices of low symmetry, reliable indexing is, in most

cases, only possible with the aid of computers and, except in the highest symmetry cases, this can only be easily carried out for single solid phases. Powder indexing methods have developed rapidly over the last fifteen years, in parallel with the increasing interest in quantitative powder diffraction methods. Several excellent auto-indexing programs are available, including ITO, TREOR and DICVOL. They all require very accurate angular positions, but systematic error is much greater and it is desirable to keep the zero-point error in the counter setting below 0.02° of 2θ . This difficulty is overcome by means of a preliminary scan with a well-characterized standard. Aberrations such as those induced by sample displacement and transparency can be avoided by using parallel-beam geometry diffractometers of the type commonly found at synchrotron sources. Clearly, the auto-indexing procedure is greatly facilitated if high resolution data are available.

4.1.2. *Extraction of the Bragg intensities and structure solution*

Once the unit cell is known, it may be possible to identify the structure by comparison with other compounds found in the literature, but in many cases there is no straightforward solution and the structure determination may be a tremendous task. In particular, solving the phase problem is known to be difficult, one of the main reasons being the overlapping of close reflections which introduces ambiguity in the attribution of intensities for some hkl values. The overlapping problem exists for low symmetry structures, where the number of reflections is very high, as well as for high symmetry structures in which there may be superposition of non-equivalent reflections. It seems important at this stage to emphasize the necessity of high quality intensity data to be used in Patterson and direct methods in order to obtain reliable results.

Pattern decomposition

Then, the next step is extracting, with the highest level of accuracy, the maximum number of integrated intensities (I_{hkl}) from the powder diffraction pattern. Two main possibilities are available for this pattern decomposition, individual peak-fitting and whole pattern fitting with cell constrained refinements. The first procedure is the same as was used to determine the line positions during the first step, the adjusted shape model giving also the peak intensity. Contributions from an unknown impurity can be eliminated using this method and the width of each individual peak can be refined, permitting the analysis of anisotropic broadening.

The other approach was first initiated by Pawley and is a process in which no structural model is introduced, but instead, the profile parameters (unit cell, zero-point, peak shape parameters) and integrated intensities I_{hkl} are refined as least squares variables. The advantage of this method is that, at the end of the

refinements, an intensity is assigned to each theoretically existing reflection, even if its value is very small; the result is a complete set of reflections which can be used as input to standard crystallographic programs for *ab initio* structure determinations as well as for structure refinements. Standard deviations of the individual I_{hkl} values take into account the ambiguities arising from the more or less pronounced overlapping. Drawbacks of this method are the time consuming calculations due to the number of refinable parameters and strong correlations existing between intensities in heavily overlapped regions of the pattern, which may affect the quality of the data.

A more efficient algorithm was developed by J. C. Taylor and A. Le Bail in which the profile parameters are refined, but the integrated intensities are no longer considered as variables. Starting values are assigned to the reflections, and re-calculated by iteration at each least squares cycle. This method is more stable and simpler than Pawley's program, but the e.s.d.'s do not include the uncertainties due to partial or complete overlapping.

None of these programs are capable of decomposing the pattern if exact overlapping does occur. However, the use of a maximum entropy algorithm may allow the evaluation of the intensities of overlapping reflections. Indeed, good reconstruction may be retrieved when only 20% of the reflections are well separated.

When the pattern decomposition is completed, observation of the systematic absences of reflections means that one or a small number of possible space groups can be selected and the phase problem encountered in structure determination is solved by the conventional crystallographic methods used in single crystal studies. The main difficulties in applying these methods are the considerably smaller number of reflections retrieved from a powder diffraction pattern and their loss of reliability caused by overlaps.

The Rietveld method

Once the basic crystal structure has been found, Rietveld profile refinements and Fourier syntheses are used to reveal the remaining atoms. First, the profile parameters, the scale factor, the unit-cell, and the background are refined together with the atomic parameters of the partial structure model (with a progressive addition of all these variables as suggested in profile refinements strategy). After convergence of the least-squares procedure, the observed Bragg intensities are calculated with more or less accuracy by the Rietveld program and converted into structure factors which are used to calculate a difference Fourier map in order to localize the missing atoms.

The Rietveld method is nowadays the most common procedure of powder data analysis when the structure of the sample is at least approximately known. The Rietveld algorithm fits the observed diffraction pattern using the instrumental characteristics (resolution curve of the diffractometer) and the structural parameters of the sample material (cell constants, atomic and displacement

parameters) as variables. More specifically, the refinement routine minimizes the function:

$$M = \sum w_i (y_i - y_{ci})^2$$

$w_i = 1/\sigma_i$ is the weight assigned to the individual step intensity y_i (σ_i is the variance assigned to the observation y_i). y_i is the observed intensity at the i th step of the pattern, y_{ci} is the calculated intensity at the i th step of the pattern, and the sum runs over all data points. The calculated intensities are determined by summing the contributions of the overlapping Bragg reflections plus the background:

$$y_{ci} = y_{bi} + \sum_{\phi=1}^{\text{phases}} S_{\phi} \sum_{k=k_1}^{k_2} j_{\phi k} L p_{\phi k} O_{\phi k} |F_{\phi k}|^2 \Omega_{i\phi k}$$

- y_{bi} is the background intensity at position $2\theta_i$
- S_{ϕ} is a scale factor, proportional to the volume fraction of the phase
- $j_{\phi k}$ is the multiplicity factor of the k th reflection
- $L p_{\phi k}$ is the Lorentz factor (including the polarization factor for X-ray scattering)
- $O_{\phi k}$ is a factor intended to describe the effects of preferred orientation (i.e., the departure of the sample from a purely random particle orientation distribution)
- $|F_{\phi k}|$ is the structure factor (including the thermal vibration contribution)
- $\Omega_{i\phi k}$ describes the peak profile function which approximates the effects of both instrumental and, possibly, sample parameters.

The first summation is over all contributing phases ϕ and the second one over all neighboring reflections k_1 to k_2 contributing to a given step i . Background intensity can be estimated either by linear extrapolation between points where no peaks appear to contribute or by refining the parameters of an empirical function.

Because the assessment of a profile refinement is more complicated than for a conventional integrated intensity structure analysis, several residual quantities (R-factors) have been introduced to estimate the agreement between the observations and the model during the course of the refinement. The most useful ones are the profile, weighted profile R factors and the goodness-of-fit χ^2 :

$$R_p = \frac{\sum |y_i - y_{ci}|}{\sum y_i}$$

N and P are the numbers of information (data points) and refined parameters, respectively, and C is the number of constraints, if any. The goodness-of-fit χ^2 would be expected to converge to values close to 1 for a successful refinement; however, much larger values are commonly observed.

For sake of comparison with refinements with the traditional integrated intensity method of structure refinement, it is usual to calculate also the Bragg R factor:

$$R_{\text{Bragg}} = \frac{\sum_k |I_k - I_k^{\text{calc}}|}{\sum_k I_k}$$

I_k is the “observed” integrated intensity of the k^{th} reflection calculated at the end of the refinement after apportioning each individual intensity y_i between the contributing Bragg peaks according to the calculated intensities I^{calc} using the relation:

$$I_k = \sum_i I_k^{\text{calc}} \Omega_{ik} \frac{y_i - y_{bi}}{y_{ci} - y_{bi}}$$

4.2. Multi-phases and Quantification by Profile Refinement Techniques

The intensity diffracted by a crystalline phase is proportional to the amount of irradiated material (not taking into account corrections for absorption effects). As the measurement is a non destructive one, powder diffraction appears like an ideal analytical tool and is, indeed, largely used. The conventional approach is usually based on the use a single reflection which makes the method prone to many systematic errors (e.g., preferred orientation).

As mentioned above, the calculated step intensity for multi-phase patterns is written:

$$y_{ci} = y_{bi} + \sum_{\phi=1}^{\text{phases}} S_{\phi} \sum_{k=k_1}^{k_2} j_{\phi k} L P_{\phi k} O_{\phi k} |F_{\phi k}|^2 \Omega_{i\phi k}$$

The scale factor for each phase is given in Debye-Scherrer geometry by the product:

$$S_{\phi} = C \left(\frac{\rho' V}{\rho V_c^2} \right)_{\phi}$$

The corresponding equation in Bragg-Brentano geometry is written:

$$S_{\phi} = \frac{C'}{\mu} \left(\frac{V}{V_c^2} \right)_{\phi} = \frac{C' \rho'}{\mu'} \left(\frac{V}{\rho V_c^2} \right)_{\phi}$$

ρ and μ are the density and the linear absorption coefficient of the compound and ρ' and μ' are the density and the linear absorption coefficient of the sample.

The terms C and C' contain only experimental constants which apply to all phases contributing to the diffraction pattern. The mass of phase ϕ present in the sample is $m_\phi = (\rho'V)_\phi$, while $(\rho V_c)_\phi$ is the mass of the same compound in the unit-cell. Introducing the mass M_ϕ per formula unit of phase ϕ and Z_ϕ , the number of formula units per unit cell, one obtains:

$$S_\phi = \frac{C m_\phi}{(Z M V_c)_\phi}$$

This shows that the masses m_ϕ of the component phases of a mixture are proportional to the product $S_\phi (Z M V_c)_\phi$ where S_ϕ is the scale factor obtained for phase ϕ in the Rietveld refinement. Constraining to unity the sum of the weight fractions of the phases present in the sample, it follows:

$$W_\phi = \frac{S_\phi (Z_\phi M_\phi V_{c\phi})}{\sum_{i=1}^N S_i (Z_i M_i V_{ci})}$$

- S_ϕ is the scale factor of phase ϕ
- Z_ϕ the number of formula units per unit cell of phase ϕ
- M_ϕ the mass per formula unit of phase ϕ
- $V_{c\phi}$ the unit cell volume of phase ϕ

This relation gives the relative weight of any component and provides an absolute weight fraction if an internal standard is introduced in a known proportion in the mixture.

4.3. Microstructures

When using high resolution diffractometers, the line shapes often depart from the usual Gaussian model and that their widths do not always obey the expected instrumental resolution function as measured, for instance, with a standard sample. This additional line broadening, known as sample broadening, arises from two main effects (Figure 4):

– the *particle-size broadening* which results from the finite extent D of the coherently diffracting domains within the grains (note that this is NOT strictly equivalent to the true particle size as can be observed by optical or electron microscopy). For very small particles the assumption of an infinite lattice no longer holds: the reciprocal lattice points are not Dirac δ -functions anymore, but are all smeared out uniformly to an extent that depends on the average crystallite size. Therefore, all the points are the same size independent of the distance from the origin and $\Delta d^* = \text{constant}$, which implies that $\Delta d/d^2$ is also constant. Using Bragg's law, one derives:

$$\frac{\Delta d}{d^2} = \text{constant} = \frac{-\Delta\theta}{\tan\theta} = \frac{-\Delta 2\theta \cdot \cos\theta}{\lambda}$$

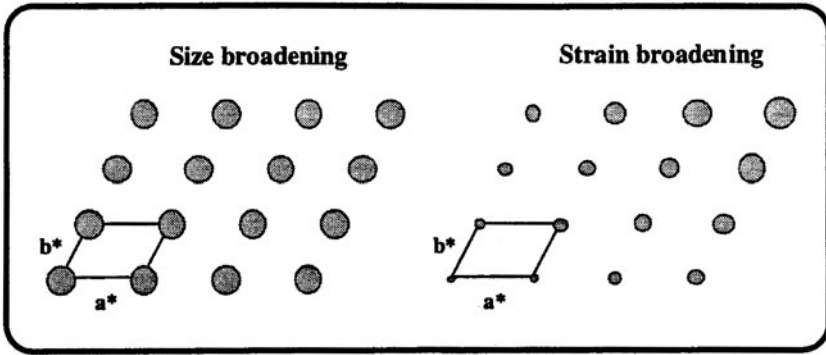


Figure 4. Particle-size and microstrain broadening representation in the reciprocal space.

It shows that particle-size broadening varies inversely with $\cos\theta$ in 2θ space and is larger at large scattering angles:

$$\Delta 2\theta = \frac{k\lambda}{\cos\theta}$$

– the *microstrain broadening* characterized by lattice strain ε that results from local variations Δd of the average d -spacing produced by non-uniform crystalline strains (e.g., lattice defects or distribution of composition in solid solutions). The extent of these d -spacing fluctuations is characterized by $\Delta d/d = \text{constant}$, which implies also that $\Delta d^*/d^*$ is constant in the reciprocal space. Thus, the effect on the reciprocal lattice points increases with distance from the origin. The effect of the strain can be assessed quantitatively by differentiating the Bragg equation:

$$\Delta\lambda = 2\Delta d \cdot \sin\theta + 2d \cdot \Delta(\sin\theta)$$

Then, dividing by the Bragg equation:

$$\frac{\Delta\lambda}{\lambda} = 0 = \frac{\Delta d}{d} + \frac{\Delta(\sin(\theta))}{\sin(\theta)}$$

For small values $2\Delta\theta = \Delta(2\theta)$, which yields:

$$\text{strain broadening} = \Delta(2\theta) = -2 \frac{\Delta d}{d} \tan\theta$$

The variation of the line width with scattering angle is larger than in the previous case.

Both effects can be present in a one material.

Evaluation of crystallite size and lattice strain from diffraction data is not straightforward and quantitative results (e.g., to determine the morphology of anisotropic grains) require an analysis of individual line profiles by Fourier techniques (Warren-Averbach method). However, an elementary procedure, known as the Williamson-Hall plot, allows these two effects to be distinguished and estimated quickly. It is based on the fact mentioned above that the broadening due to lattice strain and that due to size have a different angular dependence:

$$\beta \frac{\cos \theta}{\lambda} = \frac{1}{D} + k \cdot \varepsilon \frac{\sin \theta}{\lambda}$$

β is either the usual FWHM or the integral line breadth corrected for the instrumental resolution and k depends on the measures of breadth and strain used. The intercept and slope of a graph $\beta \cdot \cos \theta$ versus $\sin \theta$ give an indication of the crystallite/domain size D and lattice strain ε , respectively. Note in addition that both D and ε may be anisotropic: this introduces an additional complexity in the analysis of data, but allows determination of the shape of the crystallites in the material sample.

5. X-Rays and Neutrons

The great advantage of X-ray diffraction is clearly the resolution of the information obtained. X-ray powder diffraction is the best method to detect weak lattice distortions which would go unnoticed in a neutron powder pattern. The weak point is the form factor. Its decrease with increasing $\sin \theta / \lambda$ means that the scattered intensity drops rapidly at high scattering angles while its monotonic evolution with atomic number implies that the diffraction pattern is dominated by the heaviest atoms of the structure. This lack of contrast between elements which are neighbors in the periodic table can now be largely overcome by using anomalous scattering with synchrotron X-rays. In favorable cases, this method can even allow to distinguish between different oxidation states of a same element (e.g., $\text{Eu}^{2+} / \text{Eu}^{3+}$) in an ordered mixed valence compound.

The advantages of neutron (as compared to X-ray) diffraction (see Chapter 10) arise from its different interaction with matter. First, neutrons interact with the nuclei and the neutron scattering amplitude varies almost randomly throughout the periodic table (Figure 5). This has the advantage of giving large contrasts between elements with similar atomic numbers, as well as between isotopes of one element (for instance, $b(^1\text{H}) = -0.374 \times 10^{-12}$ and $b(^2\text{H}) = 0.6674 \times 10^{-12}$ cm). A second and unique advantage of neutrons results from the interaction of the neutron spin with the moment of the unpaired electrons of the outer shells of atoms; this interaction gives rise to magnetic

scattering. The main areas of application of neutron powder diffraction besides basic structural work, are:

– *location of hydrogen and light atoms*: this is the traditional application of neutron powder diffraction and it accounts for a large fraction of the beam time used at high resolution neutron powder diffractometers. In general these experiments concern structures that have been partially solved by X-ray diffraction techniques (single-crystal or powders) and neutron diffraction is used only to locate the missing atoms. Note that neutrons “see” equally well oxygen atoms, or other anions, and as heavier cations which, in general, yield more accurate bond distances than X-rays.

– *cation distribution*: a great advantage of neutron diffraction is the extremely variable scattering lengths for the elements. Indeed, whereas adjacent elements in the periodic table have very similar form factors (e.g., Mn and Fe), they can have very different Fermi lengths ($b(\text{Mn}) = -0.373$, $b(\text{Fe}) = 0.954 \times 10^{-12}$ cm). This allows one to determine site compositions with much higher precision.

It has been mentioned that X-ray form factors vary continuously with atomic number, whereas neutron scattering lengths (a property of the nuclei) vary randomly. This means that the contrast between different atoms in a crystal is different in the two techniques. For instance, in oxides of heavy metals, oxygen atoms usually contribute very little to the X-ray diffraction pattern whereas they give the dominant contribution to the neutron powder pattern.

This shows the complementarity of the two radiations for structure determination and refinement. Patterson functions derived from X-ray data are usually simpler to decrypt since they are largely dominated by the heavy atoms of the structure, but neutron data normally provide more accurate atomic positions.

6. Applications of Diffraction

As a result of X-ray diffraction techniques, numerous complex structures have been solved from high resolution powder diffraction data using synchrotron radiation or conventional laboratory diffractometers. Some examples concerning the characterization of various and more or less disordered materials are presented here.

6.1. Partially Disordered Compounds: Pharmaceutical Molecules

Cosmetic recipes in ancient Egypt and modern day therapeutic products

Powder X-ray diffraction was used to elucidate the composition and the elaboration process of the mineral constituents of ancient Egyptian cosmetics.

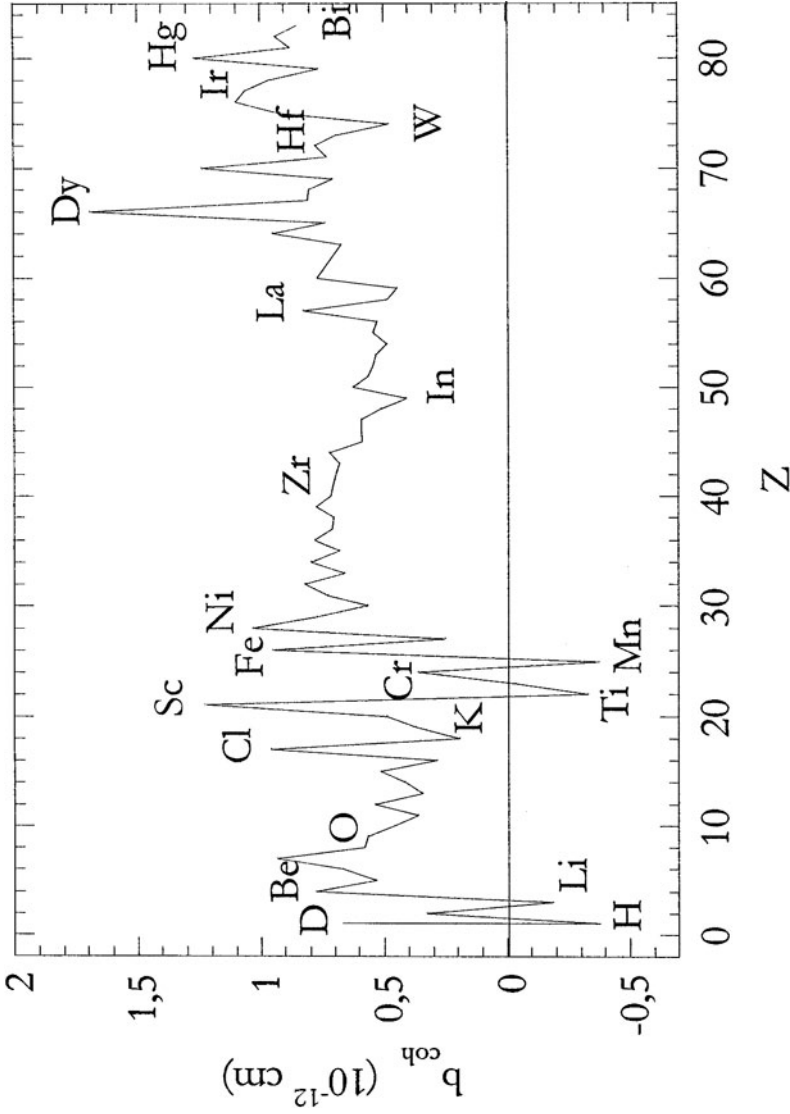


Figure 5. Distribution of the neutron scattering length b with the atomic number Z .

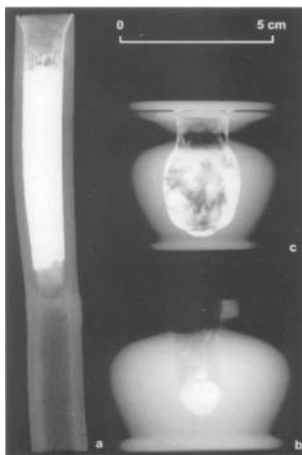


Figure 6. X-ray radiography of different make-up receptacles from the Egyptian collections of the Louvre Museum. The white areas show the distribution of the X-ray absorbing lead powders present in the make-up. (a) reed case, still full of make-up. (b) alabaster recipient with a fabric lid. (c) alabaster recipient and cover. It contains a small amount of make-up attached on the inner wall.

The funerary furniture discovered in Egyptian tombs, dating from between 2000 BC and 1200 BC, provides significant information about the customs of everyday life in Ancient Egypt [6]. Among these objects, there was an abundance of toilet accessories (such as mirrors, hairpins, eyeliner applicators, combs or spatulas, and make-up receptacles), some of which are now preserved in the Egyptian Department of the Louvre Museum (Figure 6). Inside these 3000–4000 year-old containers (made of marble, alabaster, wood or reed) were found cosmetic powders in an exceptionally good state of conservation. In order to decipher their composition and the methods used in their elaboration, the organic fractions were analyzed by chromatographic techniques and the mineral content by scanning electron microscopy, FT-IR spectroscopy and powder X-ray diffraction [7]. Standard laboratory quantitative X-ray diffraction was impeded by several factors: 1) owing to the high archaeological value of the powders, only small quantities can be extracted and analyzed; 2) the cosmetics found are highly absorbing mixtures of lead-based compounds; 3) most mixtures contain as many as 10 phases (i.e., the resulting diffractograms display a complex series of overlapping Bragg lines). The measurements were able to take advantage of the high flux, the high energy and the high resolution of a synchrotron beam line. The Rietveld refinement method (Fullprof software package [8]) was applied to work out the respective crystalline phase mass fractions. Taking into account the anisotropic line profile of some phases, it was possible to significantly improve the fit agreement factors (to less than 10%) and it was possible to detect quantities of minerals as low as 0.5% (see Figure 7).

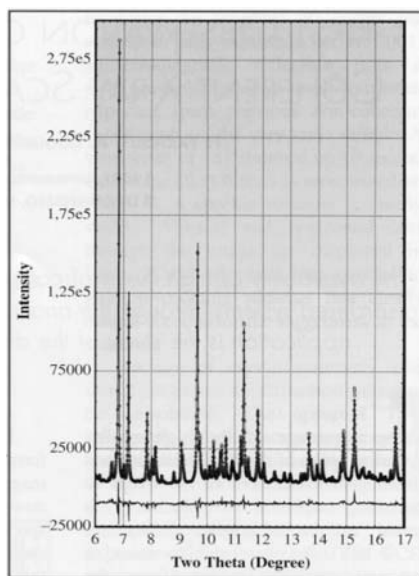


Figure 7. Powder pattern measured on a synchrotron beam ($\lambda = 0.35 \text{ \AA}$) of an archaeological sample dated from the Tutankhamon reign: observed (o), calculated (—) patterns and difference curve.

Two natural compounds bound with some animal grease, crushed ore of black galena (PbS) and cerussite (PbCO_3) were identified. Galena is still the basic constituent of many khols traditionally used in North Africa, Asia and the Middle-East. White cerussite enters the composition of grey-to-white make-up. More surprisingly our analyses revealed the presence of two more white constituents, laurionite (PbOHCl) and phosgenite ($\text{Pb}_2\text{Cl}_2\text{CO}_3$). These products are very rare in nature and could not have been extracted from the mines in sufficient quantities for the preparation of the cosmetics. They may have been formed by chemical alteration and ageing, assuming the original content of the make-up receptacles had been in contact with carbonated and chlorinated waters. However, no clear trace and no evidence of such alteration processes could be found in any of the 49 receptables.

Therefore, one major conclusion of this work is that laurionite and phosgenite were intentionally manufactured by the Egyptians. The text of Pliny the Elder and Dioscorides (first century AD) report on a number of medical recipes. In particular, some of them refer to the use of lead oxide that was ground and diluted into salted and sometimes carbonated (natron) water. The wet process was mimicked in the laboratory. By maintaining the solution at a neutral pH, a slow reaction yields white precipitates of either laurionite or phosgenite. This is the first indication that wet chemistry has been practiced since 2000 BC.

Why should these white lead derivatives PbOHCl and $\text{Pb}_2\text{Cl}_2\text{CO}_3$ be added to black PbS , since white cerussite PbCO_3 was sufficient to vary and tune the cosmetics tint from black to white? Since the earliest periods of Egyptian history, cosmetics have been intensively used not only for aesthetic purposes, but also for their therapeutic and magic or religious properties. The Greco-Roman texts mention that the white precipitates synthesized from PbO are good for eye and skin care. These lead compounds could be used as a bactericide and as a protection for the eye against exposure to the sun's rays.

In addition, the diffraction peak profiles have also been analyzed, comparing strain and crystallite size broadening effects in archaeological, synthetic and natural powders [9]. A preliminary peak breadth analysis combined with SEM observations shows that the PbS ore present in the cosmetics was ground and sorted according to grain size. The resulting granulometry of galena provided the make-up with the expected texture and its metallic brightness. By contrast, the Bragg line broadening of PbOHCl and $\text{Pb}_2\text{Cl}_2\text{CO}_3$ is free from any strain, suggesting that they were synthesized as fine powders and were not prepared by crushing. Thus, X-ray line broadening related to the crystallographic microstructure can help to determine the origin and the process of manufacture of archaeological powders. The microstructure of PbS has been determined in terms of dislocation density, crystallite size, and size distribution [10].

Today, hair grown *in vitro* is used by the L'Oréal company as a model for the study of the influence of nutrients or cosmetics on hair fiber production and the keratinization process. In the field of cosmetics, X-ray micro-diffraction is useful to evaluate and compare the efficacy of different cosmetic treatments, particularly in the field of hair growth treatment and for the development of products for the prevention of hair loss [11].

Pharmaceutical compounds

Many drug substances are administered in the form of polycrystalline powders. In such cases, in addition to the intrinsic pharmacological activity of the drug molecule itself, knowledge of the crystal structure is crucial for fully understanding and optimizing the therapeutic properties.

Polymorphism

A given drug substance administered in different polymorphic forms may lead to very different results. For this reason, knowledge of the crystal structures of pharmaceutical compounds is of considerable importance, and, in many cases, powder diffraction provides the only possible route to this information. In addition, the quest to produce and fully characterize all accessible polymorphs of a given drug substance has become an area of intense activity within the pharmaceutical industry in recent years, motivated by patenting, registration, and litigation issues.

An example from the pharmaceutical field concerns the structure determination of Irbesartan, an antihypertensive agent whose polymorphic structure was already determined on a single crystal [12]. The powder data were collected using a high resolution synchrotron beamline at $T = 90$ K and 300 K ($\lambda = 0.85$ Å). The high resolution of the spectrometer was essential to determine the parameters of the large unit-cell ($V \sim 12000$ Å³), the space group and to solve the structure, including 60 atoms in the asymmetric unit. The diffraction pattern at 90 K is displayed in Figure 8 and enlarged to show how high angular resolution, low noise and good statistics are necessary to get the maximum number of peaks needed for the use of direct methods.

The structure was partially solved by introducing the basic molecule of the polymorphic form as a fragment, and by using direct methods and simulated annealing. Later on, the obtained approximate crystallographic model was confirmed and the structure completed when single crystals of this form were successfully grown.

6.2. Molecular Gels

Androstanol steroid derivatives

Gels are important in medicine, biology, chemistry, polymer science and are used in applications as varied as photography, cosmetics and pharmaceutical steroids. The example presented here concerns gels [13] made from low concentrations of an androstanol steroid derivative in hydrocarbon liquids.

Many techniques have been used (small angle scattering of neutrons [14] and X-rays, electron microscopy [15], EPR, etc.) to investigate the gels. The data derived from them provide a coherent picture of a network constituted of helical fibers fused into microcrystalline domains that act as the nodes of the SAFIN. The structures and the rheological or optical behaviors appear to be dependent upon the solvent type. In order to model the molecular ordering within the fibers as a function of the solvent type, the related molecular structures in different gels and xerogels are needed. High resolution diffraction patterns have been recorded using synchrotron radiation ($\lambda = 1.8$ Å) at 100 K. The molecular structure of the androstanol unit is already known from a crystallographic study previously done [16]. The xerogels give crystal-like patterns superimposed onto a broad component. The corresponding gels have been studied and clearly show that diffraction peaks emerge from the intense broad components of the structure factor of the related organic liquid (Figure 9).

Knowledge of the molecular structures and their evolution from the crystal, the gel and the xerogel states should provide important clues for the understanding of the gelation mechanism of this class of crystalline organogels.

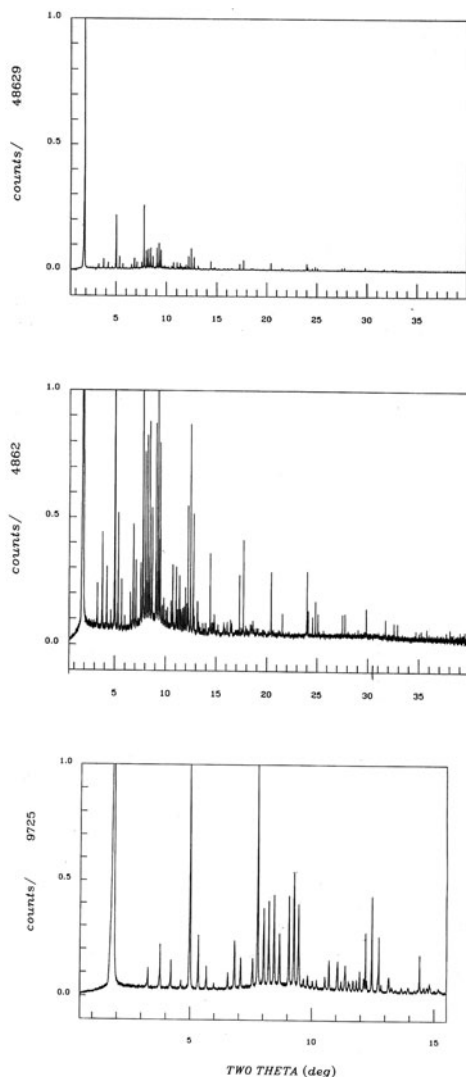


Figure 8. X-ray diffraction pattern of Irbesartan at 90 K (top), and the same diffraction pattern with enlargements (middle and bottom) to show the effects of high resolution, low noise and good statistics.

Cyclic Bis-Urea Compounds as Gelators for Organic Solvents

Simple bis-urea compounds, in which the urea groups are connected by a linear alkyl chain, are able to gelate organic solvents and surprisingly, despite their conformational flexibility, aggregate into well-ordered thin flat fibers with lengths up to several hundred micrometers [17]. Structural studies on these fibers indicate that, in addition to hydrogen bonding between the urea

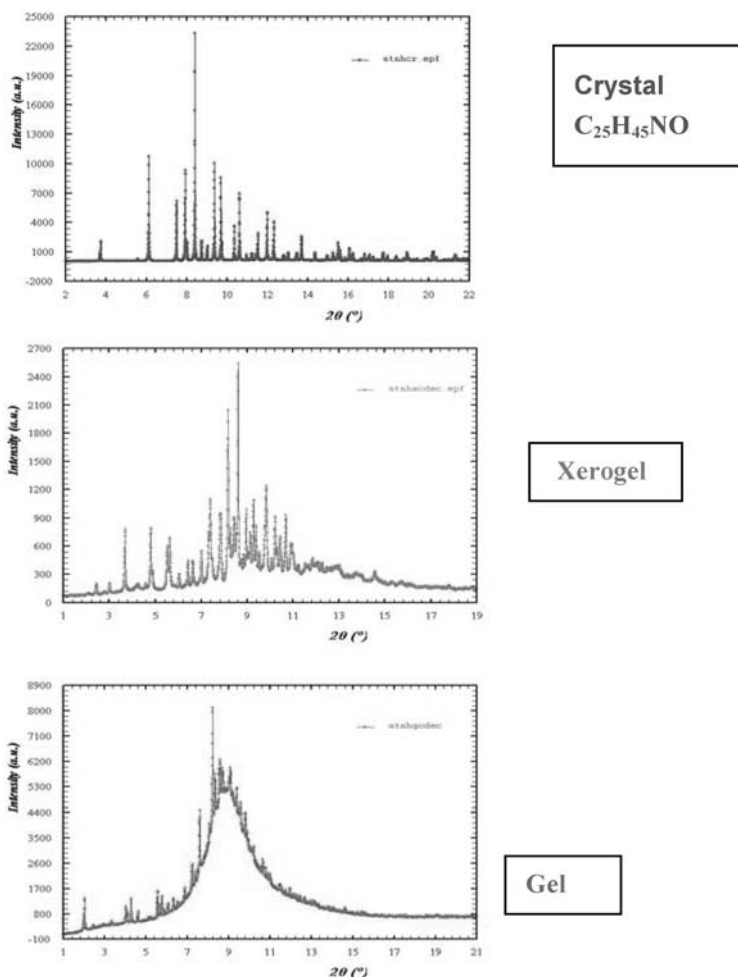


Figure 9. X-ray diffraction patterns for the crystal, the xerogel and the gel.

groups, a regular packing of the alkyl chains causes the formation of these well-ordered structures. When the packing of the alkyl chains is distorted, as in non-symmetric bis-urea compounds ($R_1 \neq R_2$), less regular two-dimensional structures are obtained. This behavior can be related to the conformational flexibility of the linker between the two urea moieties, making it possible for each urea group to aggregate in a particular direction (Figure 10a). In order to enforce aggregation along one direction, the conformational flexibility of the linker should be reduced and the urea groups should have a coplanar orientation (Figure 10b). Molecular modeling studies revealed that this can most easily be achieved by using cyclic compounds that are substituted at adjacent positions with urea moieties as a spacer.

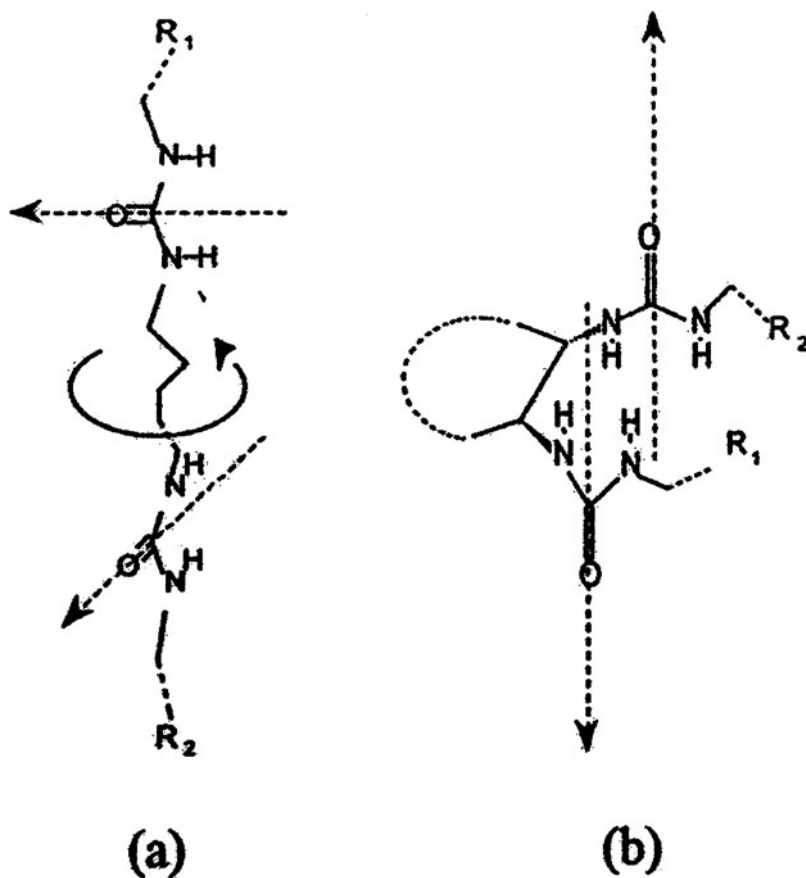


Figure 10. Hydrogen bonding directionality of bis-urea compounds with a flexible linker (a) and with a conformationally constrained linker (b). (Reprinted with permission from [17]. Copyright (1999) Wiley-VCH.)

A single crystal X-ray structure determination of one of the compounds showed that the molecules were assembled into one-dimensional chains which are stabilized by the formation of hydrogen bonds between the urea groups and adjacent molecules. The molecular arrangement in gels is most likely very similar to that in the crystal, but the complete elucidation of the molecular arrangement in gels is complicated because aggregation of these compounds is prone to polymorphism. It is concluded that the very efficient aggregation of these molecules and the elongated shape of the fibers most likely arise from the highly anisotropic hydrogen-bonding properties of these molecules, which is due to the presence of two coplanar oriented urea moieties in a single molecule. These bis-urea compounds are excellent building blocks for the construction of molecular gels.

X-ray Method for In Situ Determination of Gelator Strand Structure

The method described here offers the possibility for determining the molecular packing arrangement of gelator fibers and other compounds of this type *in situ* [18]. Cholesteryl anthraquinone-2-carboxylate (CAQ) and many structurally related molecules form thermotropic liquid-crystalline phases as well as being LMOGs for a variety of organic liquids. The length and thickness of the gelator fibers can be influenced strongly by solvent properties and by the rate of formation of the fiber networks. Using SANS and SAXS data, Terech *et al.* (see Chapter 10) have deduced information about the dimensions of fibers and the types of junctions between them in various gel phases [19]. Additional important structural questions can be answered by relating structural information from powder and single-crystal X-ray diffraction data from different sample phases. The questions are: What is the molecule packing within a fiber and what is the relationship between packing in bulk crystals and gel fibers?

To address these questions, the X-ray powder diffraction pattern of a gel is subtracted from that of the neat liquid component measured under identical conditions. The difference is thus approximately the diffraction from the solid-like fibers that are composed primarily of gelator molecules. If the subtracted diffraction pattern and the powder diffractogram from a crystalline form of the neat gelator are similar, molecular packing in gelator fibers can be related to that in the bulk single-crystals.

The packing arrangement of CAQ molecules in a single-crystal obtained from 1-butanol/toluene was determined by an X-ray structural analysis (Figure 11). Its powder diffraction pattern simulated from the single-crystal packing information is very close to the pattern obtained for CAQ recrystallized from ethyl acetate, and this confirms that the two ways of recrystallisation produce the same dimorph. The molecular packing displays none of the characteristics expected for gelator fibers. There are no apparent strongly attractive interactions and the molecules are not packed in lamellae (see Chapter 14).

Molecular organization of an organic hydrogel

The combined use of cryo-TEM and X-ray diffraction have provided insight into the mechanism of gelation in a family of bis-urea dicarboxylic acid LMOGs leading to hydrogels [20]. The cryo-TEM images reveal the nanoscale structures formed by one of the molecules (**1**) that results in gelation. The homologue **2** is not a gelator of aqueous liquids (see Chapter 20).

In order to obtain molecular-level resolution, the mature gel of that molecule was investigated by X-ray diffraction. However, even at high concentrations, the diffraction from the hydrated gel was weak and, since crystal structures of related molecules can provide information about molecular order in the gelled state, an X-ray diffraction pattern was obtained for crystalline fibers formed by another molecule (**3**). A powdered sample of **3**-Ca²⁺ (precipitated from a

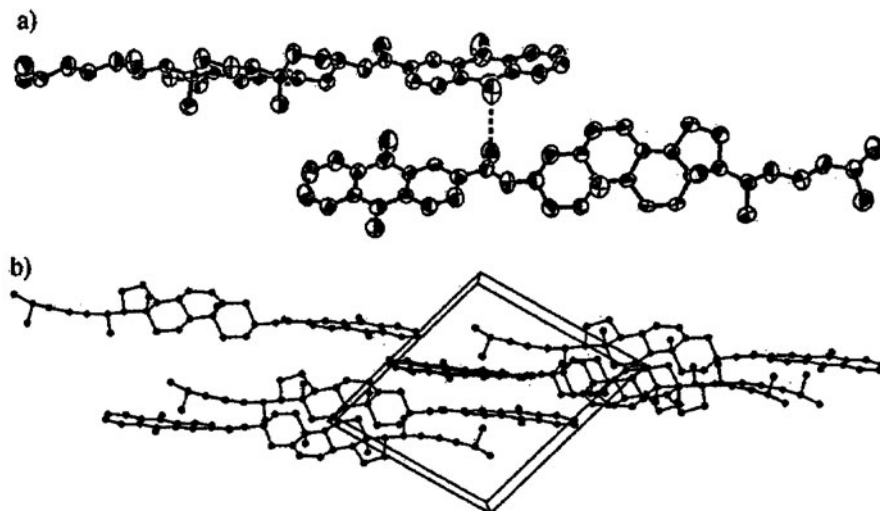


Figure 11. Molecular packing of CAQ in crystals obtained from 1-butanol/toluene. a) ORTEP plot; b) Molecular packing within the unit cell. (Reprinted with permission from [19]. Copyright (1996) VCH Verlag.)

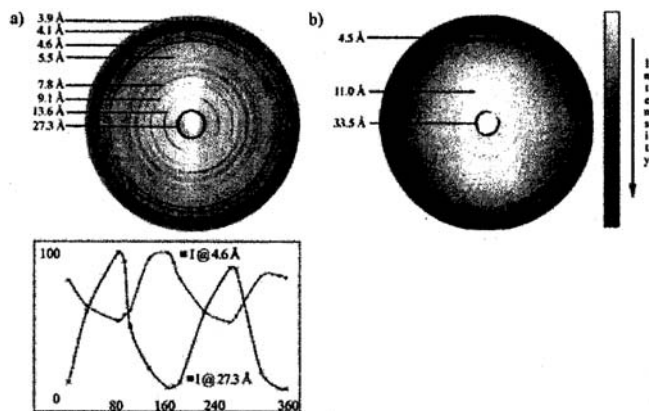
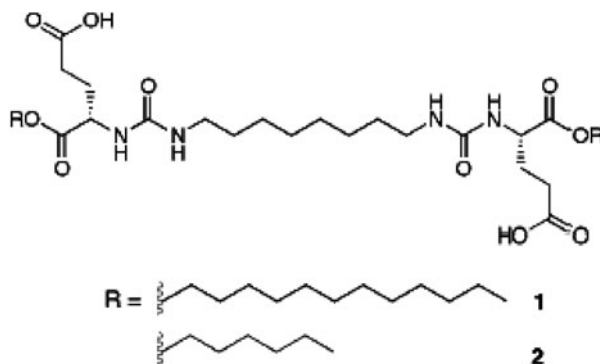


Figure 12. X-ray image plates of a) uncrushed fibers of 3-Ca^{2+} . Inset: Graph of intensity variation with orientation of the diffraction bands. b) 8 mM **2**, 8 mM CaCl_2 , 50 mM Tris, pH 9, oriented pattern. (Reprinted with permission from [20]. Copyright (2003) Wiley-VCH.)

solution of 3 mM **3**, 3 mM CaCl_2 , 50 mM Tris, pH 9) diffracted well to give a two-dimensional pattern with 19 sharp rings (Figure 12a).

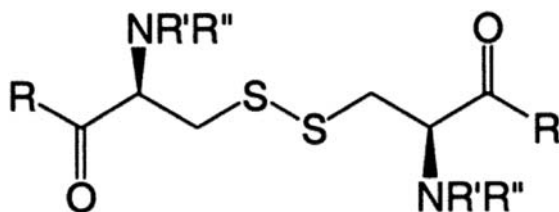
The integrated powder diffraction pattern has been indexed in a monoclinic unit cell and it contains enough information to propose a reasonable packing arrangement for **3** in the fibers. A match between the length of the alkyl ester

chains and the central spacer allows a regular packing of the molecules. In contrast, related molecule **1**, which has a mismatch between the length of the alkyl esters and central chains, should not pack as efficiently. The corresponding diffraction pattern of a concentrated, mature gel of **1** (fully hydrated) was observed with similar properties, but with lower intensities and less orientation of the rings than from the dry fibers of **2** (Figure 12b).



Anatomy of a Gel

On the basis of suggestive X-ray data, 14 aryl L-cystine derivatives were designed, synthesized, and examined for their ability to gelate water [21]. Several members of this amino acid family are remarkably effective hydrogelators. A few of the analogues separate from water as crystals, indicating a close relationship between gelation and crystallization. All effective gelators self-assemble into SAFINs that entrain the solvent in the capillary spaces among them. Hydrogen-bonding sites on the compounds that might stabilize the fibers are identified from specific substitutions that replace a hydrogen donor with a methyl group, enhance the hydrogen-accepting ability of a carbonyl oxygen, or promote the hydrogen-donating ability of an amide proton.



3 ($R=OH$, $R'=H$, $R''=p$ -nitrobenzoyl)

The structural variations are characterized via minimal gelation concentrations and times, X-ray crystallography (Figure 13), light and electron microscopy, rheology and calorimetry. The multiple techniques applied to the

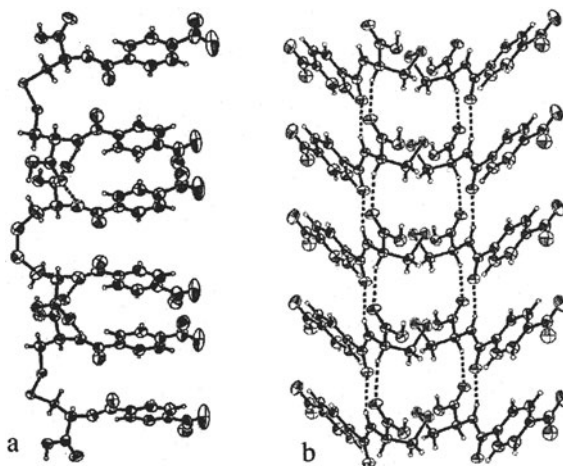


Figure 13. ORTEP patterns of recrystallized an L-cystine derivative **3** (from diethyl ether), demonstrating the polymorphic nature of the structure. (a) Neat crystals arranged with a cross-hydrogen-bonding pattern between the acid carbonyl and the amide proton. (b) Alternative crystalline molecular organization, incorporating one equivalent of ether. (Reprinted with permission from [21]. Copyright (2000) American Chemical Society.)

diverse compounds allowed an extensive search into the basis of gelation. It was concluded, for example, that the compound requiring the lowest minimum concentration and time for gelation also makes one of the weakest hydrogels. This is attributed to kinetic effects that perturb the length of the fibers.

Polymorphism also plays a role. Rheological studies at different temperatures show that certain gels are stable to a 1-Hz, 3-Pa oscillating shear stress at temperatures as high as 90°C. Other gels suffer a catastrophic break at lower temperatures. Calorimetric data indicate a smooth transition from gel to sol phases as the temperature is increased (see Chapter 8).

7. Conclusions

X-ray diffraction is a very powerful technique for elucidating the numerous complex structures of poorly organized systems, and more specifically, molecular gels. Along with a condensed presentation of the crystallographic methods, some examples have been given in order to show how their inherent possibilities make the crystallographic methods an essential tool for investigations in various domains, even in partially disordered phases. Furthermore, the development of synchrotron radiation sources is rapidly increasing the potential of the science of crystallography, and it should facilitate the detailed study of SAFIN structures.

References

- [1] Ladd, M.F.C.; Palmer, R.A. In *Structure Determination by X-ray Crystallography*, New York: Plenum Press, **1977**.
- [2] Stout, G.H.; Jensen, L.H. In *X-ray Structure Determination, a practical guide*, New York: John Wiley & Sons, **1989**.
- [3] Woolfson, M.M. In *Computational Crystallography*, D. Sayre, Ed., Oxford: Clarendon Press, **1982**.
- [4] Shankland, K.; David, W.I.F.; Csoka, T. *Z. Krist.*, **1997**, 212, 550.
- [5] Roisnel, T.; Rodriguez-Carvajal, J. In *Proceedings of the 7-th European Conference on Powder Diffraction (EPDIC7)*, Barcelona, **2000**.
- [6] Lucas, A.; Harris, J.R. In *Ancient Egyptian materials and industries*, Edwards Arnold Ltd., London, **1963**.
- [7] Walter, Ph.; Martinetto, P.; Tsoucaris, G.; Bréniaux, R.; Lefebvre, M.A.; Richard, G.; Talabot, J.; Dooryhée, E. *Nature*, **1999**, 397, 483.
- [8] Rodriguez-Carvajal, J. *Collected Abstracts of Powder Diffraction Meeting*, Toulouse, France, **1990**, 127.
- [9] Martinetto, P.; Anne, M.; Dooryhée, E.; Walter, Ph. *Proceedings of EPDIC-6*, Budapest, August **1998**.
- [10] Ungar, T.; Martinetto, P.; Ribarik, G.; Dooryhée, E.; Walter, Ph.; Anne, M.; *J. Appl. Phys.*, **2002**, 91, 2455.
- [11] Baltenneck, F.; Bernard, B.A.; Garson, J.C.; Engstroem, P.; Riekel, C.; Leroy, F.; Franbourg, A.; Doucet, J. *Cellular and Molecular Biology*, **2000**, 46, 1017.
- [12] Böcskei, Z.; Simon, K.; Rao, R.; Caron, A.; Rodger, C.A.; Bauer, M. *Acta Cryst*, **1998**, C54, 808.
- [13] Terech, P. In *Specialist Surfactants*, I.D. Robb Ed., London: Chapman & Hall, **1997**.
- [14] Terech, P.; Ramasseul, R.; Volino, F. *J. Phys. France*, **1985**, 46, 895.
- [15] Wade, R.H.; Terech, P.; Hewat, E.A.; Ramasseul, R.; Volino, F. *J. Colloid Interface Sci.*, **1986**, 114, 442.
- [16] Grand, D.; Terech, P.; Ramassuel, R.; *Unpublished results*.
- [17] van Esch, J.; Schoonbeek, F.; de Loos, M.; Kooijman, H.; Spek, A.L.; Kellogg, R.M.; Feringa, B.L. *Chem. Eur. J.*, **1999**, 5, 937.
- [18] Ostuni, E.; Kamaras, P.; Weiss, R.G. *Angew. Chem. Int. Ed. Engl.*, **1996**, 35, 1324.
- [19] Terech, P.; Ostuni, E.; Weiss, R.G. *J. Phys. Chem.*, **1996**, 100, 3759.
- [20] Estroff, L.A.; Leiserowitz, L.; Addadi, L.; Weiner, S.; Hamilton, A.D. *Adv. Mater.*, **2003**, 15, 38.
- [21] Menger, F.M.; Caran, K.L. *J. Am. Chem. Soc.*, **2000**, 122, 11679.

Chapter 12

OPTICAL SPECTROSCOPIC METHODS AS TOOLS TO INVESTIGATE GEL STRUCTURES

Henri Bouas-Laurent and Jean-Pierre Desvergne

Laboratoire de Chimie Organique et Organométallique, UMR 5802, CNRS Université Bordeaux I, 33405 TALENCE Cedex, France

1. Introduction	363
2. Electronic Absorption and Emission Spectroscopy	364
2.1. General Considerations Concerning UV-vis and Fluorescence Spectroscopy	364
3. Infrared Spectroscopy	407
3.1. General Considerations	407
3.2. Selected Examples Illustrating the Application of Infrared Spectroscopy to the Study of Gel Structures	409
3.3. IR Absorption Spectroscopy of 2,3-Di- <i>n</i> -decyloxyanthracene (DDOA). Assignment of Vibration Bands and Dichroic Absorption	419
4. Conclusions and Perspectives for the Future	425

1. Introduction

Although UV-vis and fluorescence spectra are not sufficient to characterize molecular gel phases that are self-assembled, supramolecular systems [1–5], they can reveal unique features of intermolecular interactions that are not detectable by other analytical tools. Many gels show *characteristic absorption and emission properties* arising from their *specific aggregation modes*. The utility of these spectroscopic methods is illustrated by some salient examples mostly from the recent literature. A brief account of the principles and general considerations of electronic absorption and emission spectroscopy is given as an introduction to the field and some special aspects are further developed in Section 2.2.

Moreover, IR spectra, whose group frequencies are characteristic of intermolecular interactions should be particularly sensitive to the phase changes as sols or solutions become gels. Section 3 will be devoted to the use of IR spectroscopy to investigate gel structures.

2. Electronic Absorption and Emission Spectroscopy

2.1. General Considerations Concerning UV-vis and Fluorescence Spectroscopy

Detailed explanations of the principles of electronic absorption and emission spectroscopy can be found in many textbooks [6–12]. Here, some aspects related to the influence of environment (particularly molecular aggregation) on the molecules responsible for the absorption and emission spectra are stressed.

Ideally, the electronic transitions from the ground state S_0 to the first electronic state S_1 are represented by the energy diagram in Figure 1 a where the electronic levels are modulated by vibrational (vibronic) levels. The diagram shows excitation or emission from the lowest energy vibronic levels of S_0 or S_1 , respectively, but several can be involved in a transition. No rotational levels are shown although they lead to line broadening. Rotational motions can be hindered especially in the solid state.

The corresponding absorption and emission spectra are displayed in Figure 1b; they are nicely structured as found for rigid conjugated molecules such as aromatic hydrocarbons in solution. As expected, from Figure 1 a, the maximum of the longest wavelength vibronic band in absorption is expected to be at the same wavelength as the highest energy fluorescence band; this

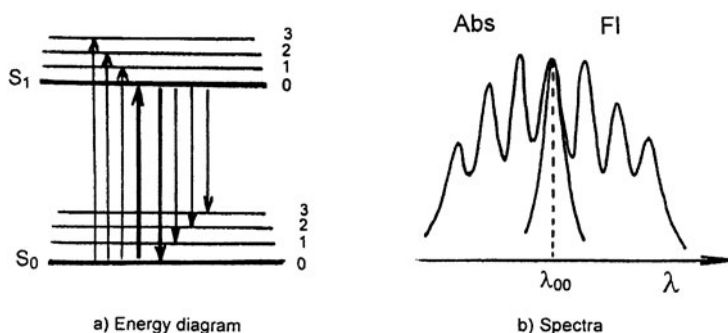


Figure 1. (a) A typical diagram for the first electronic absorption band modulated by the S_1 vibronic levels and the fluorescence modulated by the S_0 vibronic levels. (b) Representation of the corresponding normalized absorption and fluorescence spectra of an aromatic hydrocarbon in solution (e.g., cyclohexane); λ_{00} corresponds to the 0-0 transition.

wavelength corresponds to the 0-0 transition. Such spectra reflect the so-called *mirror-image symmetry*. However, most spectra are not so well resolved: because of the participation of several vibrational modes and interactions with the environment (solvent, matrices), the vibronic levels are not discrete, resulting in attenuation or loss of the fine structure [11]. Moreover, the lowest energy absorption band (ν_a) and the highest energy fluorescence band (ν_f) may be offset from each other: $\Delta\nu = \nu_a - \nu_f$ is called *Stokes shift* and is due to the rearrangement of nuclear configurations between the ground state and the relaxed excited state (Figure 2). The magnitude of this shift can be influenced by solvent polarity (solvatochromism) due to a clear difference of polarity between S_0 and S_1 [12]. Complex molecules and aggregates of molecules may exhibit spectra like those in Figure 2.

An important property of absorption is that the absorbance (A) of a transition is proportional to the concentration of the solute as described by the *Beer-Lambert law*:

$$A = \log I_0/I = \varepsilon_\lambda cl$$

where I_0 and I are the light intensities of the beam entering and leaving the absorption medium respectively, ε_λ is the molar absorption coefficient ($\text{L} \cdot \text{mol}^{-1} \cdot \text{cm}^{-1}$), “ c ” the concentration ($\text{mol} \cdot \text{L}^{-1}$), and “ l ” the absorption pathlength (cm).

One of the limitations of the Beer-Lambert law regards the concentration range over which it applies: ε_λ at each wavelength λ is characteristic of the chemical species. However, if the absorbing molecule is dissociated by solvent or if it forms *aggregates*, the law is no longer obeyed. The latter is the case for gels. The absorption spectra are thus strongly dependent on the nature of the solvent, whether it is a fluid solution or an inhomogeneous matrix. As the *local* concentration of molecules increases (as in gels), their proximity increases and if the transition dipoles of highly allowed transitions for the neighbors are parallel, they interact and split into two levels (one blue-shifted and the other red-shifted). This is called “*exciton splitting*” (or Davydov splitting) [11–13].

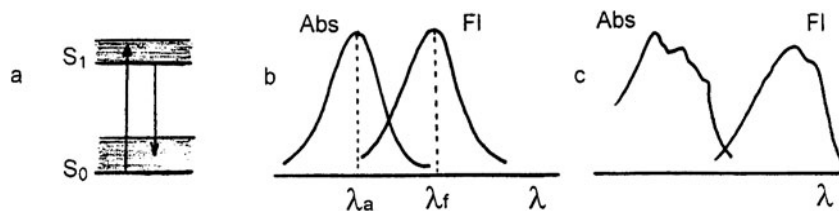


Figure 2. Effect of increased vibronic and rotational level density and environmental influence (a) on the structure of absorption and fluorescence spectra (b). Here, the Stokes shift is defined as $\Delta\nu = \nu_a - \nu_f$. Aggregates may exhibit ill-structured spectra where the mirror symmetry is absent (c).

The same phenomenon, but in a more complex way, is observed when more than two molecules aggregate (see Sections 2.2.2 and 2.2.3).

Excitation spectra

A spectrofluorimeter has a monochromator for selecting the excitation wavelength (M_1) and another for selecting the wavelength of the emitted radiation (M_2). To record a fluorescence spectrum, M_1 is set at fixed wavelength (λ_{exc}) and M_2 is scanned to record the fluorescence intensity as a function of emission wavelength (λ_{em}) (Figure 3a). Conversely, because the fluorescence intensity is proportional to the absorbance A (*vide infra*), the emission monochromator M_2 can be set at a fixed emission wavelength (λ_{em}) and M_1 rotated to scan the excitation spectrum (Figure 3b).

The fluorescence intensity is known [12] to be proportional to the absorption intensity according to Eq. (1).

$$I_F = k_{\phi_F} I_a \quad (1)$$

k is a constant related to the apparatus and recording conditions and ϕ_F is the fluorescence quantum yield. Eq. (1) can be rewritten as Eq. (2) at a given absorption wavelength λ_{exc} .

$$I_F = k_{\phi_F} I_0 (1 - 10^{-A}) \quad (2)$$

If the absorbance A is very low, Eq. (2) can be approximated [12] as Eq. (3)

$$I_F = k_{\phi_F} I_0 A \quad (3)$$

In practice, A should be < 0.1 . The excitation and absorption spectra should be superimposable when normalized for intensity – this is often a test of purity – but they may differ when molecular aggregates, such as those of gels, are present. *Excitation spectra therefore should be recorded to complement fluorescence spectra.*

Correction of fluorescence spectra

The spectrofluorimeter must be corrected for emission and excitation responses because of wavelength-dependent variations of (1) the intensity of

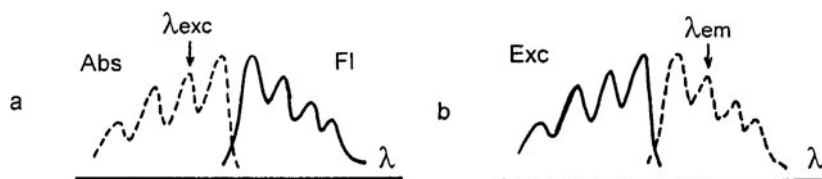


Figure 3. Scheme for recording a fluorescence spectrum (a —) and an excitation spectrum (b —).

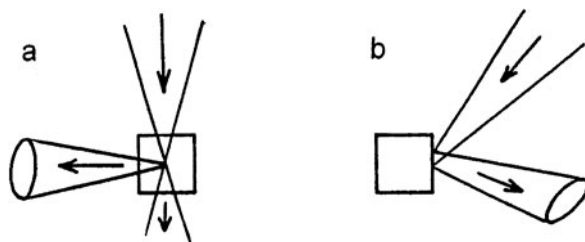


Figure 4. (a) Right-angle observation and (b) front-face illumination.

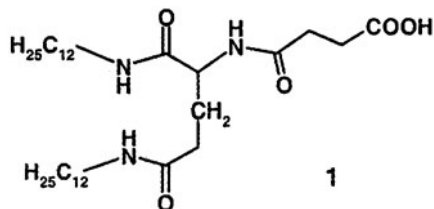
the exciting light, (2) the transmission efficiency of the excitation and emission monochromators, (3) the spectral response of the detection system [12].

Geometric arrangements for the fluorescence observation

For dilute solutions, the incident beam is transmitted through a cuvette and the emitted light is collected at a right-angle (Figure 4a). However, when the fluorescence intensity is very weak, the absorbance must be increased, with the result that the excitation light is absorbed within a thin layer of the sample near its surface. To compensate for the lack of excited species in the region of the sample where detection efficiency is greatest in Figure 4a, the emitted light is collected on the same side as excitation (Figure 4b). This arrangement can lead to some additional complications (see Section 2.2.3).

2.1.1. Pre-aggregation

Before completing the networks that result in macroscopic gelation, especially amphiphilic gelators assemble into smaller aggregates (see Chapters 1 and 4) that can escape several methods of detection. Ihara and co-workers [14a] were able to use absorption spectroscopy to evaluate critical aggregation concentrations (cac) for compound **1**, a lipid-like molecule that forms organogels in several liquids at higher concentrations (0.1–1 mM).



The authors added NK 77, a cyanine dye that is very sensitive to its microenvironment, to a benzene solution of **1**. As shown in Figure 5, the apparent value

of ε_{570} decreases significantly at concentrations of **1** higher than 0.03 mM. At these concentrations, **1** does not produce a gelled state. Therefore, the variation of ε_{570} is attributed to the micro-environmental changes effected by initial aggregation of **1**. In benzene, the cac was thus estimated at 0.025 mM whereas gelation occurred at >0.1 mM. Figure 6 shows plots of ε_{570} for *toluene* and *THF*. In toluene the cac was found to be 0.08 mM whereas a gel formed at

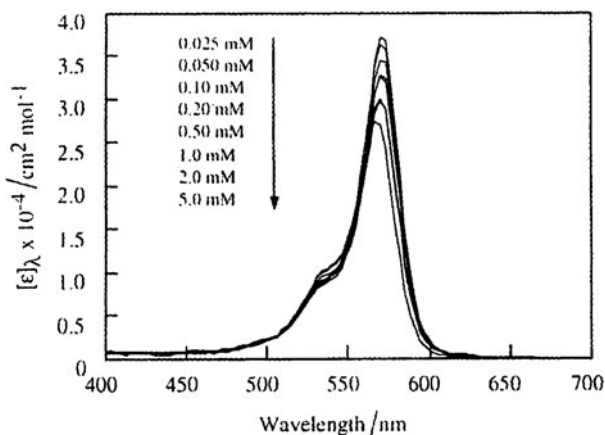


Figure 5. Effect of concentration of **1** on the visible absorption spectrum of 0.025 mM NK-77 (a cyanine dye) at 25°C in benzene solution. (Reproduced by permission from [14a], Taylor and Francis, Ltd.)

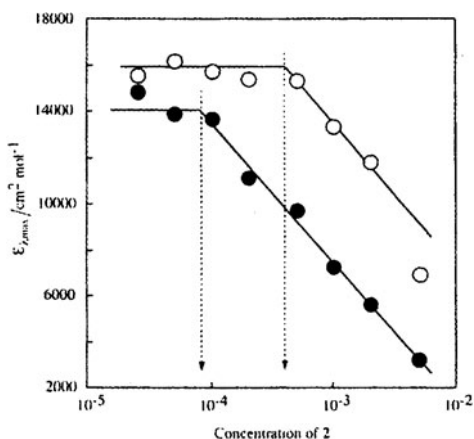
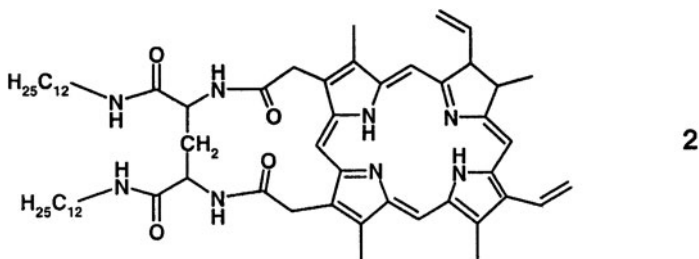


Figure 6. Plot of $\varepsilon_{570 \text{ nm}}$ of 0.025 mM NK-77 versus concentration of **1**: in toluene (\bullet), cac = 0.08 mM; in THF, (\circ) cac = 0.6 mM. (Reproduced by permission from [14a], Taylor and Francis, Ltd.)

1 mM. In THF, the cac was evaluated at 0.6 mM but no gel was detected in this solvent [14a].

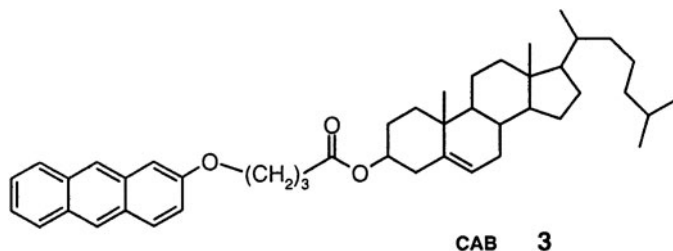


The same method was recently applied [14b] to compound 2, related structurally to 1, but connected to a protoporphyrin that acts as an internal probe of aggregation. Absorption spectra of more concentrated solutions (sols) of 2 at 25° C in benzene show a Soret peak at 436 nm which is blue-shifted from 460 nm, the wavelength maximum of monomeric 2. The blue shift implies that the porphyrin rings are stacked according to the H-aggregation mode [15]. Plots of ϵ_{436} versus the concentration of 2 show a sharp decrease above 1.0 mM, considered to be the cac because no gelation of benzene was observed below 5.0 mM at 25° C [14b].

2.1.2. Circular dichroism

The theoretical background and technical information on circular dichroism (CD) are the subject of Chapter 13. Here, we report other examples of circular dichroism characteristics of some gels that should be useful for practical work.

2.1.2.1. Anthracene-linked steroids. One of the early observations of an enhancement of CD intensity was made by Weiss and co-workers [16] for the gelation of dodecane with a member of the ALS (Aromatic-Linked-Steroids) class of gelators, CAB (cholesteryl 4-(2-anthryloxy)butanoate; 3).



The CD spectrum of the anthracenyl group ($310 < \lambda < 410$ nm) was shown to be distinctly more intense at 18° C (gel phase) than at 63° C (isotropic solution) (Figure 7). According to the authors, the gel spectrum of Figure 7 is reminiscent

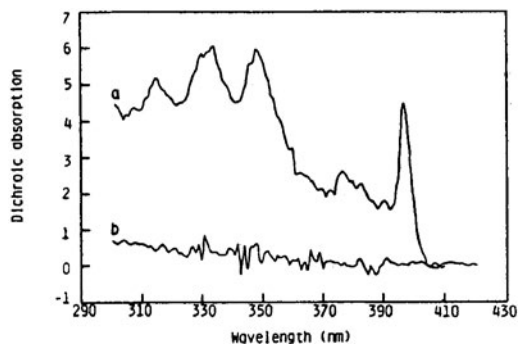
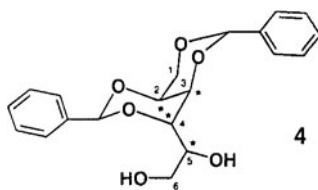


Figure 7. Circular dichroism spectra of CAB (0.72 wt% in dodecane) in the gel (a, 18°C) and isotropic (b, 63°C) phases. (Reprinted with permission from [16]. Copyright (1989) American Chemical Society.)

of liquid-crystal induced CD, which is a consequence of the chiral array of aggregated molecules and the “appearance of a strong CD spectrum is evidence that the CAB molecules are helically stacked” [17]. The virtual absence of CD intensity from the isotropic phase shows that the anthracenyl group of an individual CAB molecule does not experience strongly, at that intramolecular distance, the chirality of the cholesteryl group to which it is linked. The authors also used the variation of CD differential absorption to follow the gelation process [16].

2.1.2.2. Dibenzylidene sorbitol (DBS). Some of the earliest known low molar-mass organic gelators (LMOGs), benzylidene-D-sorbitols were discovered [18] in 1942 to form gels in alcoholic solvents, such as ethanol and ethylene glycol (EG). The UV and CD spectroscopy used by Yamasaki and co-workers [19] to study 1,3:2,4-di-O-benzylidene-D-Sorbitol (D-DBS, **4**) in EG is reported below.



4 = (D) – DBS; the four stereogenic centers are marked with an asterisk. **4** and its (S) enantiomer gelate alcohols and other organic liquids such as acetonitrile; no gel was observed with the racemate.

Macroscopic characterization was obtained by visual and optical microscopic inspection as well as by measurements of light transmittance *versus*

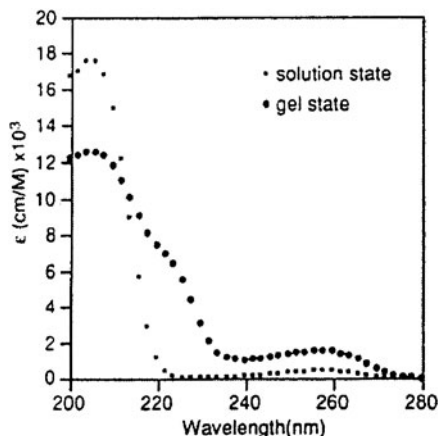
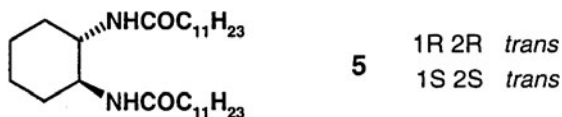


Figure 8. Electronic absorption spectra of D-DBS in EG (ambient temperature) in the gel (●, ≈ 15 mM) and isotropic (■, < 10 mM) states. (Reproduced with permission from [19]. Copyright (1994) The Chemical Society of Japan.)

concentration. In EG at ambient temperature, the solution to gel phase transition was found to occur *at ca.* 10 mM where a gel of spherulitic texture was formed; *at ca.* 30 mM, and above, the spherical domains were believed to overlap as evidenced by a continuous drop in transmittance. Figure 8 shows the UV spectra of **4** in solution and in the gel state. The absorption near 206 nm, associated with a transition moment along the long axis of the benzene chromophore is split in the gel, giving rise to a new red-shifted band at 225 nm.

It is consistent with a clear enhancement of the CD intensity at 225 nm (Figure 9). In addition, one observes that the 255 nm forbidden absorption (polarized along the short axis) as well as the CD intensity are increased, as a result of some stacking interaction of the benzene rings; however, the precise mutual orientation is difficult to assess and these intensity effects vary with concentration (10–70 mM) and temperature (27–93°C), reflecting changes of geometry in the gel phase [19] (see also Section 3.2.1).

2.1.2.3. A simple chiral dialkylamide system. Another interesting example was developed by Hanabusa and co-workers [20] who designed a simple low mass ($M = 478$) chiral dialkylamide system (**5**) which proved to be an efficient gelator for a wide variety of organic fluids (from hydrocarbons to aprotic polar solvents and silicone oil; even methanol and ethanol could be gelled despite their ability to form hydrogen bonds with amides).



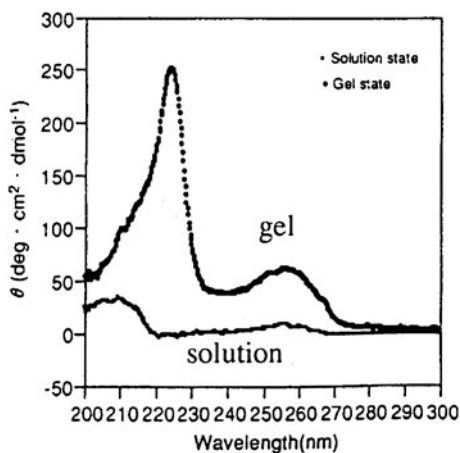


Figure 9. CD spectra of D-DBS in EG at ambient temperature. Solution conc. < 10 mM; gel conc. \approx 15 mM. (Reproduced with permission from [19]. Copyright (1994) The Chemical Society of Japan.)

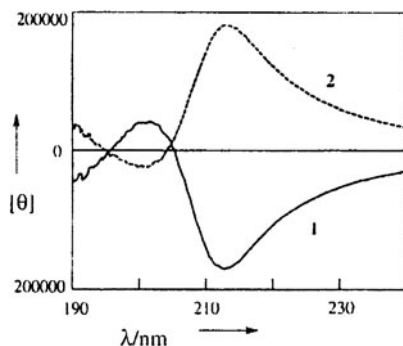


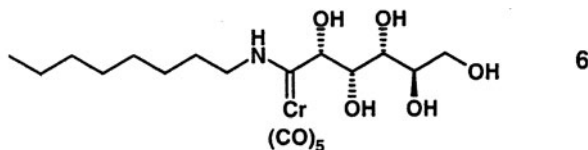
Figure 10. CD spectra of 5_{RR} (1 in the figure) and 5_{SS} (2 in the figure) in acetonitrile (1.0 mM) at 20°C. $[\theta]$ units are degree $\text{cm}^2 \text{dmol}^{-1}$. (Reproduced with permission from [20]. Copyright (1996) Wiley-VCH.)

The *cis* stereoisomer was found not to form gels with any of the liquids and the racemate formed an unstable gel which converted to co-crystals after several hours. The two enantiomers of the *trans* stereoisomers 5_{RR} and 5_{SS} showed the same gelation behavior. The CD spectra of these enantiomers in acetonitrile are shown in Figure 10 in the far UV (190–230 nm). Despite the experimental difficulties encountered in that region, the spectra show clearly CD splitting and intensity enhancement for the RR and SS enantiomers with extrema at 201 and 213 nm.

The peaks intensity decreased with increasing temperature and vanished at 50°C when the gel was transformed into a solution. From these data, coupled

with other observations, the authors inferred that the aggregates formed by **5** are cooperatively organized for helical stacking.

2.1.2.4. Metal-carbene carbohydrate amphiphile. The CD spectroscopy technique was used to get a better insight into a gel formed from a metal-carbene carbohydrate amphiphile (**6**) as reported recently by Dötz and co-workers [21].



Pentacarbonyl [D-gluco-hex(N-n-octylamino)-1-ylidene] chromium

The CD spectra (Figure 11) show the expected intensity enhancement as compared with that of the solution (at 50°C); of special interest is the structural changes with temperature, revealed after heating and cooling. The absorption bands, observed in the UV spectrum could be assigned to the *organometallic chromophore* as follows: 350 nm (metal-to-ligand charge transfer), 320 nm (ligand field transition) and 270–260 nm (ligand to metal charge transfer).

Although the UV spectra showed no significant temperature dependence, the 270–260 nm transition (LMCT) (and not the other ones) exhibited an inversion

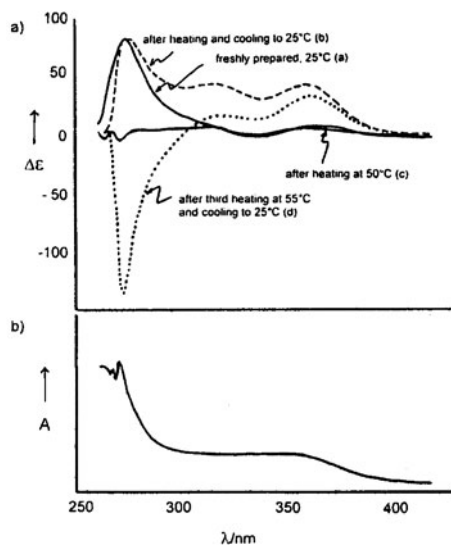


Figure 11. a) CD spectra of **6** in CHCl_3 (4 mM). b) UV spectrum of **6** in isotropic solution. (Reproduced with permission from [21]. Copyright (2003) Wiley-VCH.)

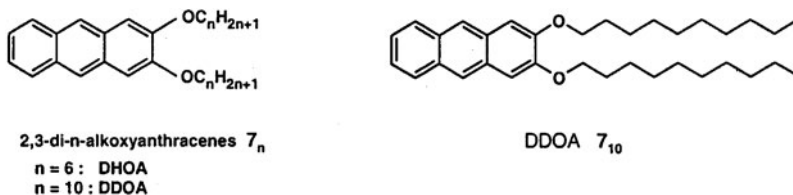
of the CD sign after the third heating-cooling cycle, suggesting that the gel has kinetic and thermodynamic states. Such an observation had been made earlier on another system [22].

2.1.2.5. Other examples of application of circular dichroism. The CD technique has been applied in a number of other cases. It was particularly useful in the elegant study by Feringa and co-workers [23] of the chiral recognition through cooperative interactions between aggregates and gels of bis(ureido)-cyclohexane derivatives and a coaggregating guest. Maitra and co-workers [24] observed exalted and red shifted CD spectra at 10° C for gels formed from a chiral 1-pyrene gelator in cyclohexane supporting the formation of helical stacking. *Vancomycin hydrogels* showed also a large enhancement of the 220 nm peptidal backbone CD spectra, a precious structural information reported by Xu and co-workers [25]. For an other interesting example, see Section 2.2.3.4.

2.1.3. π - π stacking; UV and fluorescence spectra

One of the main driving forces of gel formation originates in the attractive interaction between aromatic or heteroaromatic and generally highly conjugated groups, often termed π - π stacking. Among the chromophores encountered in the recent literature are substituted benzenes, anthracenes, triphenylenes, pyrenes and azobenzenes, porphyrines, tetrathiofulvalenes (TTF). Some of them were arbitrarily selected to illustrate (*vide infra*) the application of UV and fluorescence spectroscopy to the inter chromophoric interactions in the five following subsections.

2.1.3.1. The 2,3-di-*n*-alkoxy anthracene family (the anthracene chromophore). 2,3-di-*n*-decyloxyanthracene (DDOA, **7₁₀**) was shown to be a gelating agent of a variety of organic liquids, especially alcohols (preferably methanol and ethanol) and alkanes [26–29].



This property was discovered by chance and independently of that of other anthryl derivatives of the ALS (Aromatics Linked Steroids) family [30] which

were published earlier. As the structure and spectra of DDOA are less complex than those of ALS, they are described first. Because it can gelate methanol, at ambient temperature, at conc $\simeq 0.6$ mM (0.04 wt%) (and acetonitrile at conc $\simeq 1$ mM), DDOA can be qualified as supergelator. Exploration of the gelation ability as a function of the number (n) of carbons of the aliphatic linear chain has shown that n should be ≥ 6 and that the maximum efficiency is reached for $n = 10$ and 11 [29]. Therefore DDOA is a very good representative of the family.

The absorption, fluorescence and excitation spectra were studied in methanol, methylcyclohexane and acetonitrile in the $10^{-5} - 10^{-3}$ M concentration range at various temperatures.

The absorption spectra of DDOA in methanol (Figure 12) show that the long axis polarized 1B_b band in the isotropic phase (with λ_{\max} at 260 nm) is of much lower intensity in the gel phase; this feature reflects an exciton splitting, suggesting that there is an important mutual interaction between the anthracene group along the long axis. The change of the short axis polarized 1L_a spectrum (300–400 nm) from a badly defined vibronic structure (isotropic phase) into a well defined red shifted vibronic structure was surprising as one expects a lack of structure for aggregates. The well defined vibronic maxima points to an ordered structure of the anthracene groups in the aggregate and a loss of freedom of orientation as in a solid. Therefore, the lowest energy absorption in the gel, at 385 nm, presumably corresponds to the 0-0 transition.

However, as ordered as they are, the DDOA molecules do not experience perfectly similar environments; this is reflected (Figure 13) in the fluorescence spectrum, red shifted as expected for aggregates and exhibiting a fine structure

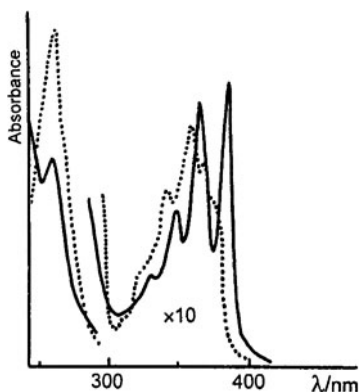


Figure 12. Isotropic (•••••, 26° C) and gel phase (—, -15° C) absorption spectra of DDOA (ca 10^{-3} M) in methanol. Quartz cell thickness 10 mm. (Reproduced by permission of The Royal Society of Chemistry (RSC) on behalf of the Centre National de la Recherche Scientifique (CNRS), [29].)

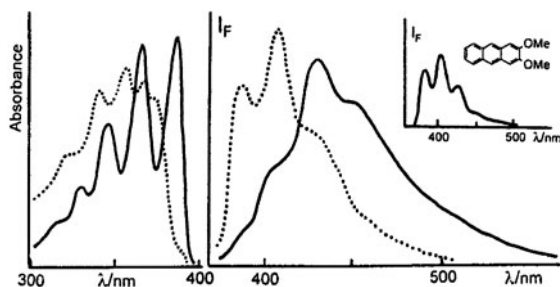


Figure 13. Fluorescence and excitation spectra (arbitrary scale) of DDOA (10^{-4} M) in degassed methanol (fluorescence $\lambda_{\text{exc}} = 370$ nm; excitation $\lambda_{\text{em}} = 435$ nm): isotropic (•••••, 25°C), gel (—, -70°C) phases. Insert is the fluorescence spectrum of 2,3-dimethoxyanthracene (3×10^{-5} M) in degassed ethanol at -65°C ($\lambda_{\text{exc}} = 365$ nm for comparison). (Reproduced by permission of The Royal Society of Chemistry (RSC) on behalf of the Centre National de la Recherche Scientifique (CNRS) [29].)

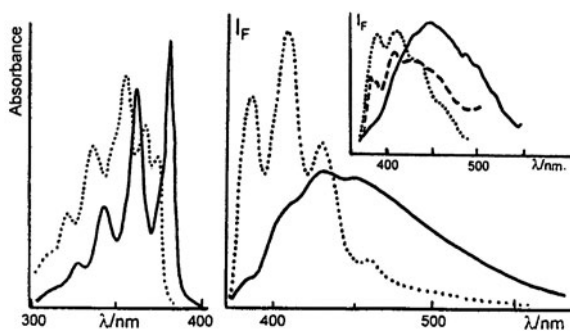


Figure 14. Excitation spectra (left: $\lambda_{\text{em}} = 410$ nm at 20°C and 480 nm at -100°C) and right-angle fluorescence spectra (right: $\lambda_{\text{exc}} = 370$ nm) of DDOA (10^{-5} M) in degassed methylcyclohexane (MCH): isotropic (•••••, 20°C) and gel (—, -100°C) phases. Inset shows time-resolved fluorescence spectra in MCH at 20°C and 0 ns delay (•••••), -104°C and 0 ns delay (- - -), and -104°C and 40 ns delay (—). The population of emitting aggregates changes with time. (Reproduced by permission of The Royal Society of Chemistry (RSC) on behalf of the Centre National de la Recherche Scientifique (CNRS) [29].)

in agreement with the presence of excited complexes (but not true excimers). In addition, kinetic analysis of the fluorescence decay [29] suggests the presence of different excited species displaying slightly different emission spectra (as is observed in some Langmuir-Blodgett films) [31].

The excitation spectra are superimposable on the absorption spectra (isotropic and gel phases, respectively). In MCH, the fluorescence spectrum of the gel (Figure 14) is more red-shifted than in methanol, although the absorption

spectra do not seem significantly different. It is possible that the emitting centers are defects occupying different sites in methanol and MCH. This hypothesis is supported by the time-resolved fluorescence spectra (Figure 14, inset), showing a growing in of a long wavelength emission component.

Interestingly, the UV spectrum of a methanolic gel resembles that of solid DDOA recorded in KBr pellet (Figure 15). This suggests that the mutual arrangement of the anthracene groups in the gel are similar to those in the solid.

The fluorescence spectra represented above were all recorded using a right-angle optical arrangement. Front-face illumination [27] and emission of DDOA (10^{-3} M in methanol), using a 1 mm thickness quartz cell, gave different fluorescence and excitation spectra (Figure 16).

The fluorescence decays were fitted to biexponential functions, but they are clearly different from those obtained at right-angle. These spectra attest to a mixture of single molecules and microfibrinous aggregates developed at the

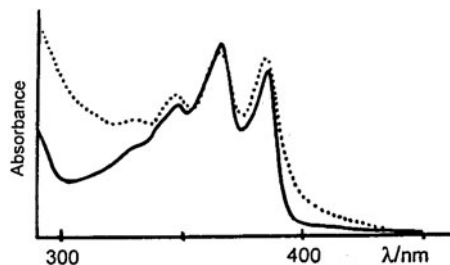


Figure 15. UV absorption spectra of DDOA in a KBr pellet (•••••) and its methanolic gel (—) at ambient temperature. The scattered light is stronger in KBr. (Reproduced by permission of The Royal Society of Chemistry (RSC) on behalf of the Centre National de la Recherche Scientifique (CNRS) [29].)

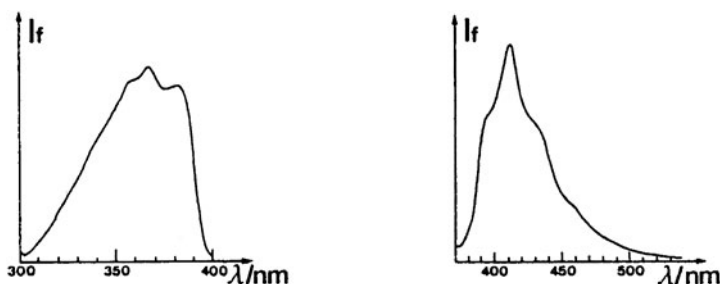
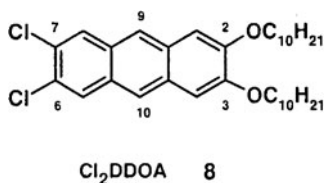


Figure 16. Front-face fluorescence ($\lambda_{exc} = 350$ nm, right) and excitation ($\lambda_{em} = 410$ nm, left) spectra of a DDOA (10^{-3} M) gel in methanol at ambient temperature. Quartz cell thickness 1 mm. Taken from [27].

gel/quartz interface. Such observations may be more common than are currently recognized. It is advised that both right-angle and front-face geometries be employed when measuring emission spectra of gels and that physically thin samples be employed whenever possible.

In order to increase π - π stacking, the authors designed a dichloro derivative of DDOA (**8**) because chlorine atoms on aromatic compounds are known to interact favorably in crystals [28].



The increased dipole moment was also expected to favor mutual attraction through dipole-dipole interactions. Gels were formed in nitriles and alcohols, but they were thermodynamically less stable than those of DDOA and their fibrillar structure was found to be dependent on the solvent nature [28]. Their UV and fluorescence spectra showed features similar to those of DDOA. UV and excitation spectra of Cl₂DDOA are represented as a function of temperature in Figure 17. Despite the effects of scattered light (because the aggregate dimensions are of the same order of magnitude as the incident light), one observes nice isosbestic points, suggesting a clear

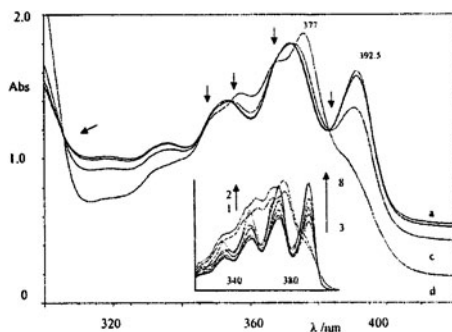


Figure 17. Electronic absorption spectra of Cl₂DDOA (1.95×10^{-3} M, cell 0.1 cm) in butyronitrile in the temperature range 273–280.8 K (a–d). In the domain 273–277.5 K (a–c), the substance is in its gel state; the solution/sol phase is at 280.8 K (d). Several isosbestic points (marked with arrows) and diffused light effects are present. The ¹B_b transition band (not shown) was the same in the two phases. *Inset:* Excitation spectra of Cl₂DDOA in butyronitrile (λ_{em} 432 nm) as gels at 260 K (1) and 238 K (2) and solutions/sols at 221 K (3), 211 K (4), 202 K (5), 187 K (6), 173 K (7) and 171 K (8). (Reprinted from [28]. Copyright (2003) with permission from Elsevier.)

transformation from the free molecules in solution into a solid-like gel; see the red-shifted structured excitation spectrum.

2.1.3.2. The aromatic linked steroids (ALS); the anthryloxy chromophore. Weiss and co-workers [16, 30, 32] have examined the process leading to the formation of thermally-reversible gels with CAB (**3**) as gelator in dodecane as well as in hexadecane, 1-octanol or their mixtures as the liquid component, using electronic absorption and emission spectroscopies, and CD spectroscopy (in dodecane); the latter gave evidence that the CAB molecules are helically stacked (see Section 2.2.2.1). The chiral cholesteryl skeleton has a strong influence on the gel structure and, therefore, on the spectroscopic properties of the anthracene group. The spectra proved to be different from and more complex to analyze than those of DDOA (see Section 2.2.3.1).

The absorption, fluorescence and excitations spectra of CAB (0.72 wt%) in dodecane are represented in Figure 18.

As expressed by the authors, the spectral changes observed for the gel must be related to the aggregation of CAB molecules. The fluorescence spectral width of the gel is smaller than that of the solution but the maximum wavelength of the higher vibronic band in the gel is red-shifted (417 to 422 nm, $\Delta\nu \approx -290\text{ cm}^{-1}$) and the apparent intensity is increased by an order of magnitude.

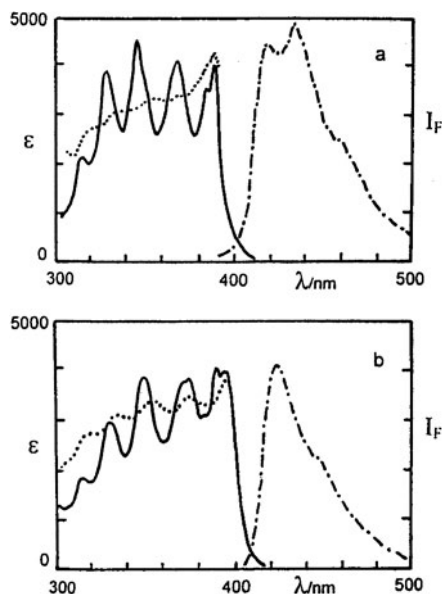


Figure 18. — absorption, - - - fluorescence (λ_{exc} 346 nm) and excitation (λ_{em} 433 nm (a) and 422 nm (b)) spectra of CAB 0.72 wt% in dodecane. a) Macroscopically isotropic solution at 67° C; b) gel phase at 23° C. (Reprinted with permission from [16]. Copyright (1989) American Chemical Society.)

The absence of excimer-like emission suggests that there is no parallel, face-to-face overlap between the anthryloxy subunits. In the absorption spectrum, the short axis polarized 1L_a vibronic band peaks at 390 and 370 nm and the long axis polarized 1B_b at ≈ 258 nm (not shown) in the solution, whereas in the gel phase two new bands appear at 396 and 376 nm; the latter could be ascribed to dipole coupling between anthracenyl groups *stacked along the short axis but with the long axes non-parallel* because the 1B_b absorption was found not to change in the gel phase. More complex functions were required to obtain acceptable fits to gel phase *fluorescence decay histograms* than those from the isotropic phase. Interestingly, the decay curve from the isotropic phase (69°C) of 0.8 wt% CAB in hexadecane could be fit satisfactorily by a biexponential decay function with decay constants of 8 and 13 ns, in keeping with the presence of aggregates also in this phase (see excitation spectra in Figure 18).

The fluorescence intensity enhancement in the gel phase was used to follow the gel formation on cooling and gel melting on heating, as illustrated in Figure 19: the gelation point was taken as the temperature at which the onset of emission intensity increase is observed during a cooling cycle of an isotropic solution [30]. The operation should be repeated at several concentrations to establish a phase transition diagram in a given solvent. This is a *mild technique* to determine T_{gel} .

In another investigation to examine the factors influencing gel formation [32], absorption, fluorescence and excitation spectra were recorded in hexadecane, 1-octanol and their mixtures and compared to those in a non-gelated solvent (e.g., benzene; Figure 20).

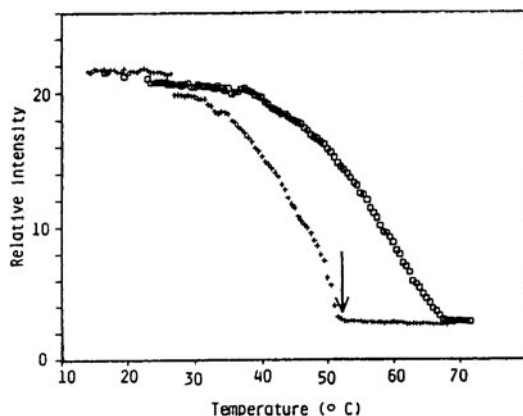


Figure 19. Relative fluorescence intensity at 422 nm (λ_{exc} 355 nm) of 1.43 wt% CAB in dodecane versus temperature. The arrow indicates the gelation temperature. (Reprinted with permission from [30]. Copyright (1987) American Chemical Society.)

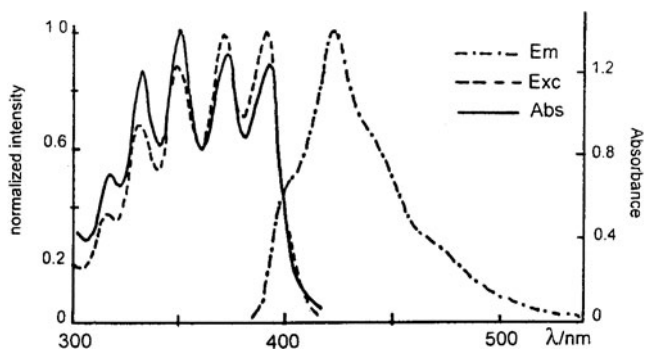


Figure 20. Absorption, fluorescence (λ_{exc} 346 nm) and excitation (λ_{em} 440 nm) spectra of 0.7 wt% CAB in benzene; cell thickness = 0.4 mm. (Reprinted with permission from [32]. Copyright (1993) American Chemical Society.)

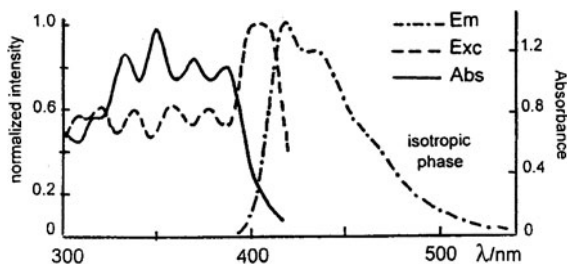


Figure 21. Fluorescence (λ_{exc} 346 nm) and excitation (λ_{em} 440 nm) spectra of 1.5 wt% CAB and absorption spectra of 0.6 wt% CAB in 1-octanol at 85° C (isotropic phase). Cell thickness 0.4 mm. (Reprinted with permission from [32]. Copyright (1993) American Chemical Society.)

The spectra in 1-octanol are represented in Figure 21 (85° C, isotropic phase) and Figure 22 (23° C, gel phase); similar spectra in hexadecane, differing slightly mainly in maximum wavelengths, are not given here.

The spectra in 1-octanol differ clearly from those in benzene, showing those of a true solution. Conversely, as proposed by the authors, the excitation spectra of the macroscopically isotropic phase in 1-octanol reflect the presence of aggregates in the medium: the maxima match the minima of the absorption spectrum and a new large vibronic band appears at 400–415 nm; the authors assigned the spectral features to a distribution of aggregates of different sizes and geometries that generate a wide fluorescence spectrum; in this microscopically heterogeneous solution, the aggregates should be the main emitting centers. In comparison, in the gel phase (Figure 22), the corresponding vibronic band at λ_{max} ca. 415 nm is much narrower (consistent with a narrower fluorescence spectrum), reflecting a more homogeneous environment.

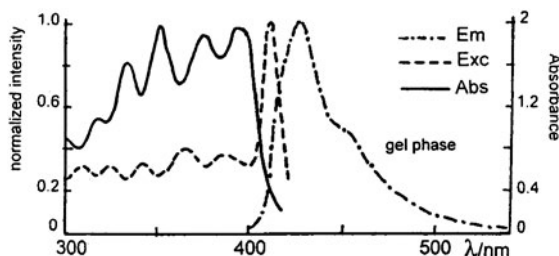
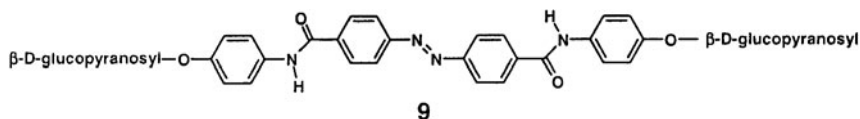


Figure 22. Fluorescence (λ_{exc} 346 nm) and excitation (λ_{em} 440 nm) spectra of 1.5 wt% CAB and absorption spectra of 0.6 wt% CAB in 1-octanol at 23°C (gel phase). Cell thickness = 0.4 mm. (Reprinted with permission from [32]. Copyright (1993) American Chemical Society.)

In addition, the authors showed how the gels can be significantly affected by the hexadecane/1-octanol composition and the thickness (0.4 to 0.05 mm) of the quartz cuvette; particularly striking was the demonstration of the possibility of *inhibiting gel formation or forcing a less kinetically-favored gel* to develop when micro-dimensional constraints do not allow the colloidal aggregates to reach their normal size [32].

2.1.3.3. Azobenzene-based sugar derivatives. The combination of an aromatic (phenyl) group and a water soluble sugar was shown by Shinkai and co-workers [33, 34] to lead to a number of remarkable gelators of *water* or organic solvents or both (see Chapter 15). The same group designed more sophisticated, bola amphiphilic azobenzene-based sugar derivatives including a diamide function [35], e.g. **9**, the di- β -D-glucopyranosyl derivative.



Compound **9** is a *super-gelator for water* (at ambient temperature, gelation was found to occur at conc. ≤ 0.1 wt%). The authors believe that π - π stacking is indispensable for the formation of oriented aggregates in water. Gelation was observed also in DMSO/H₂O mixtures. The UV-vis spectroscopy and CD measurements (not shown) allowed an insight into the aggregation mode.

The UV spectrum of the solution shows a maximum at 347 nm for the azobenzene chromophore (Figure 23); this maximum is flattened and blue shifted by 20 nm in the gel; such hypsochromic and hypochromic shifts are due to the formation of H-type aggregates [15] where the azobenzene entities are stacked on each other.

When the DMSO/H₂O mixture is varied from 100% to 20% DMSO, the λ_{max} undergoes a continued variation. This result supports the interpretation of

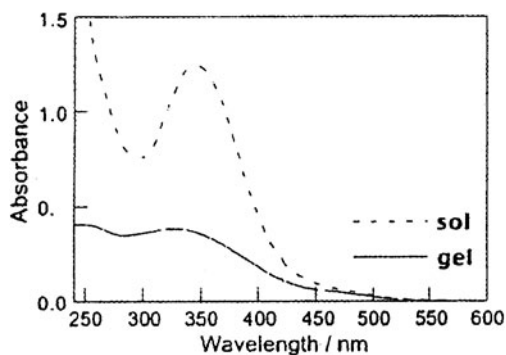
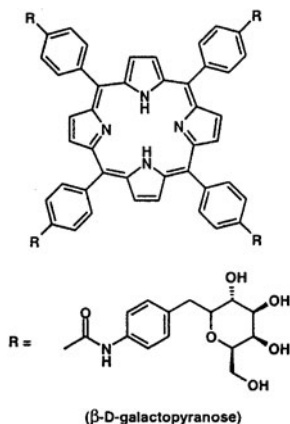


Figure 23. UV absorption spectra of a 0.8 wt% gel of **9** in water and of a solution sample of **10** in DMSO. (Reprinted with permission from [35]. Copyright (2002) American Chemical Society.)

an increase of azobenzene $\pi-\pi$ stacking as the solution becomes more water rich (DMSO is known to efficiently solvate aromatic groups).

2.1.3.4. Sugar appended porphyrin gelator. Porphyrins and phthalocyanines are known to align in one-dimensional aggregates to generate supramolecular architectures whose major-driving force is considered to be $\pi-\pi$ stacking interaction (see Chapter 18). Modification of the porphyrin periphery with saccharide groups, was expected to result in robust organogelators, in analogy to phenyl glucopyranose, a typical representative of sugar gelators [36]. Owing to the strong $\pi-\pi$ stacking ability of the porphyrin core, the new compound (**10**) proved to form a robust gel in DMF-PhCH₂OH mixtures. Direct evidence of the aggregation was obtained from the UV and CD spectra (Figure 24).



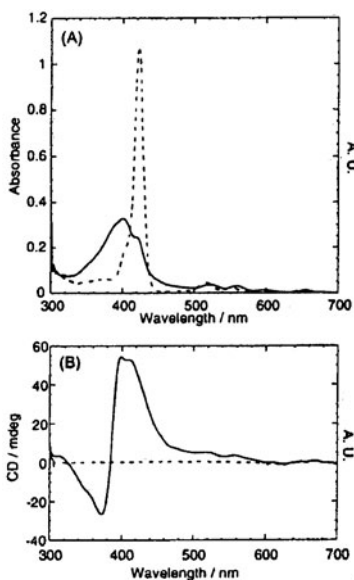


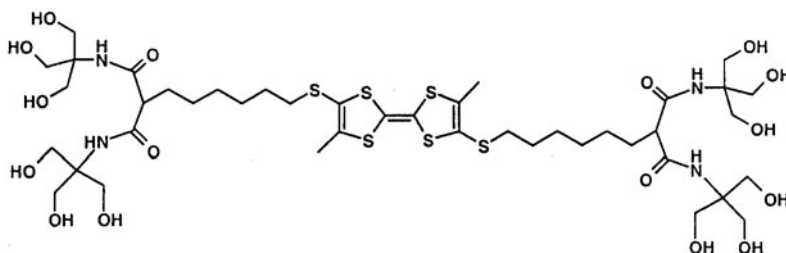
Figure 24. (A) UV-vis absorption spectra at 25° C of **10** in DMF/PhCH₂OH (1/2, v/v): homogeneous solution, 2.3×10^{-6} M (---); gel phase, 16.6×10^{-3} M (—). (B) CD spectra of **10** at 25° C in DMF/PhCH₂OH (1/2, v/v): homogeneous solution, 2.3×10^{-6} M (---); gel phase, 5.5×10^{-4} M (—). (Reprinted with permission from [36]. Copyright (2001) American Chemical Society.)

The Soret band, at 422.5 nm in homogeneous solution shifts to 401 nm in the gel (with a shoulder at 420 nm); this blue shift is characteristic of a *stacked aggregate*, as well as the red shift undergone by the Q-bands in the visible region. The CD spectrum (see Section 2.2.2) of the gel exhibits a positive exciton splitting (the CD spectrum of the homogeneous solution contains no peaks of consequence) indicating that the porphyrin column is helically twisted by the chiral peripheral saccharide groups. Another porphyrin-based gelator, reinforced by peripheral urea groups, displays similar UV spectra [37].

2.1.3.5. Bis-arborol-tetrafulvalene gelator. In an attempt to prepare a molecular wire, Jorgensen and Bechgaard [38] synthesized bis-arborol tetrafulvalene (**11**) which proved to behave as a gelator of ethanol/water or DMF/water (1/3: v/v) mixtures.

From the UV-vis-NIR spectra of **11** compared to those of non-gelating analogs, the authors showed that the gel, in the presence of iodine, exhibits a wide absorption tailing in the near infrared with a band at 874 nm, characteristic

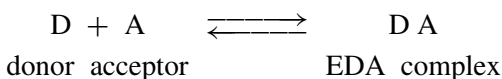
of TTF cation radicals in oligomers or stacks of TTF salts in the crystalline state, whereas the solution does not show such spectral features.



TTF-bisarborol 11

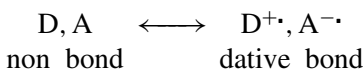
2.1.4. Charge transfer complexes

2.1.4.1. Intermolecular donor-acceptor complexes definition and general considerations. Electron donor-acceptor (EDA) complex is used to describe a group of two (or more) chemical species (atoms, molecules, ions, radicals, etc.) which are bound together [39–43]; one species is an electron donor (D) and the other an electron acceptor (A). In general, the complex is reversible in vapour phase and in solution:



In this section, we are mainly concerned with molecular complexes formed between neutral aromatic molecules, a category of π complexes because the bonding involves an overlap of their π electrons.

In many cases, an EDA complex is colored, displaying characteristic absorption bands, which have no counterpart in either the separate donor or acceptor. The red-shift is due to a stronger stabilization of the excited state energy of $(\text{DA})^*$ vs D^* or A^* than in the ground state (DA). Mulliken [40, 41] first used the valence bond theory to describe the EDA complexes as an hybrid between the “no bond” state and the “dative bond” state.



The ground state is thus described by the wave function ψ_0 and the singlet excited state by ψ_1 , which are mixed states.

$$\begin{array}{ll} \psi_0 = a_0\psi(\text{D, A}) + b_0\psi(\text{D}^+, \text{A}^-) & \text{with } a_0 > b_0 \\ \psi_1 = a_1\psi(\text{D}^+, \text{A}^-) - b_1\psi(\text{D, A}) & \text{with } a_1 > b_1 \end{array}$$

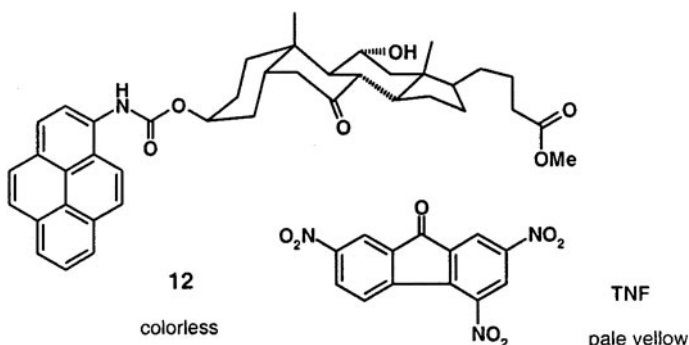
In solution, the weight of the “no bond” state is higher in the ground state and that of the “dative bond” dominates in the excited state.

The electronic transition $\psi_0 \rightarrow \psi_1$ is therefore accompanied by the transfer of almost one electron from D to A. The absorption band associated with their transition is called the charge transfer (CT) band. CT refers essentially to an electronic transition [40].

In the solid state, these π complexes are most often formed from stacks favored by flat aromatic molecules; the stacks are alternating (D,A,D,A,D,A) for neutral D and A that are weakly overlapping neutral molecular constituents or segregated (D,D,D,D... , A,A,A,A...), such as in TTF, TCNQ, for strong complexes. In the latter case, $b_o \approx a_o$ and the Mulliken model is no longer valid [41–44]. Although ionic interaction is an important contribution, a fairly large part of the binding energy probably comes from the dispersion terms (especially for arenes). These crystals are formed by cooperative aggregation and a similar process is anticipated to occur in gel formation. There is another large family of CT complexes including transition metals [44, 45] (not examined here) which might also be involved in new gel formation (see LMCT complex in Ref. [21]).

Based on these results, we suggest that strong π - π stacking of the type found in solid molecular complexes may be a feature to be incorporated into the design of new robust gels.

2.1.4.2. Pyrene derived two-component organogelators. Maitra and co-workers [46] discovered in 1999 that bile acid derivatives functionalized at the 3-position with an aromatic group formed gels in some organic solvents (alcohols, CHCl_3) in the presence of an electron acceptor molecule, 2,4,7-trinitrofluorenone (TNF). For instance, the bile acid below with a 1-pyrenyl carbamate substituent (**12**) is not a gelator in the absence of TNF.



The authors showed that the most effective gelation is a 1/1 **12**/TNF stoichiometry. The gels formed from colorless **12** and pale yellow TNF appeared colored as a result of a CT band. The intensity of this band changes substantially during

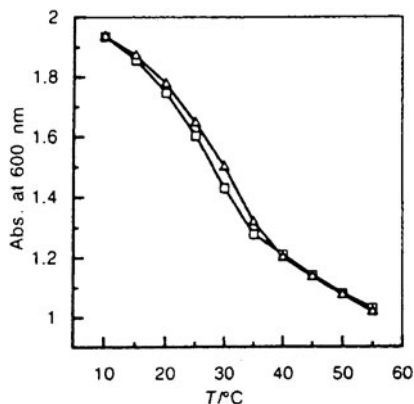
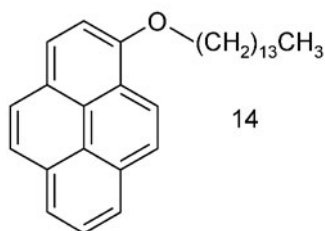
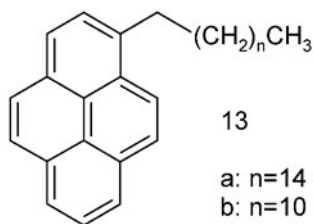


Figure 25. Plot of absorbance at 600 nm (1mm cuvette) versus temperature upon (\diamond) cooling and (\triangle) heating a gel from **12** and TNF (62 mmol each; this corresponds to 2.8 wt% of **12**) in CHCl_3 . (Reproduced by permission of The Royal Chemical Society (RCS) [46].)

the gelation; the process is believed to be associated with a stronger donor-acceptor interaction around T_{gel} (35°C as shown in Figure 25 for **12**/TNF in CHCl_3). The gel phase must favor D-A π - π stacking.

The same group has reported that the bile acid skeleton is not necessary and showed that simple derivatives of pyrene such as **13** and **14** have the ability to gelate a number of organic solvents in the presence of TNF [47].



In alcohols (cyclohexanol, *n*-butanol, *n*-octanol, etc.) or alkanes (*n*-hexane, *n*-dodecane, etc.), **13**/TNF and **14**/TNF form robust gels (at 20 mM, T_{gel} was

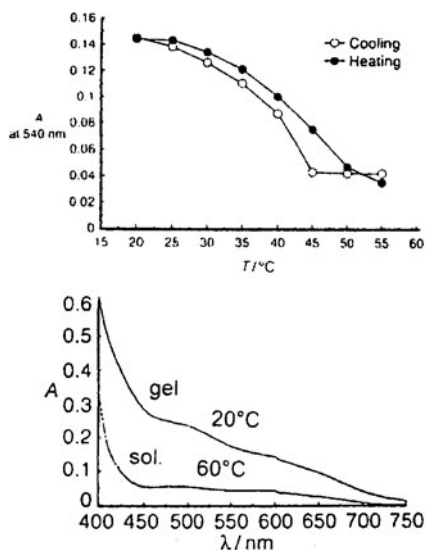
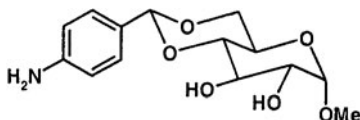


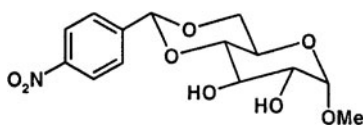
Figure 26. Absorbance of the charge-transfer band at 540 nm of an *n*-dodecane gel of **13a**/TNF (4.7 mmol of **13a**, 0.4 wt%) as a function of temperature in a 1 mm cell (top). Absorption spectra of **13a**/TNF at 20 °C (gel) and 60 °C (solution) (bottom). (Reproduced with permission from [47]. Copyright (2003) Wiley-VCH.)

found to be in the 61–79 °C range) with high temporal stability at ambient temperature. In hydrocarbon solvents, the gels are red and in hydroxylic solvents, they are black. This suggests stronger CT interactions with a substantial polar character. Figure 26 (top) shows an absorbance enhancement in the gel phase of **13a** at 540 nm and Figure 26 (bottom) shows the UV spectra at 20 °C (gel phase) and 60 °C (isotropic phase).

2.1.4.3. Charge-Transfer complex in dual-component sugar based gels.

Shinkai, Reinhoudt and co-workers [48] reported a profound influence on the gel properties of an EDA complex formed by mixing a donor molecule (**15**) and an acceptor molecule (**16**) which are independently good gelators. They showed that gels of the mixtures are more stable thermally than the gels made from the individual gelators and that the degree of stabilization was dependent on the solvent and on the ratio of the two gelators.





16

Using transmission electron microscopy (TEM), the authors discovered for **15** + **16** in diphenylether, an organogel structure with a helical motif, differing greatly from that of the single-component gels in the same solvent. Figure 27 shows the UV-vis features of the CT spectral enhancement of the dual-component gel in 1-octanol. No CT spectrum was observed in solution.

These examples illustrate the ability of EDA complexes to induce gelation or to manipulate the properties of a family of known gelators. There is little doubt that this manner of modulating π - π interactions will lead to the designing of new gelators with enhanced gel stabilities.

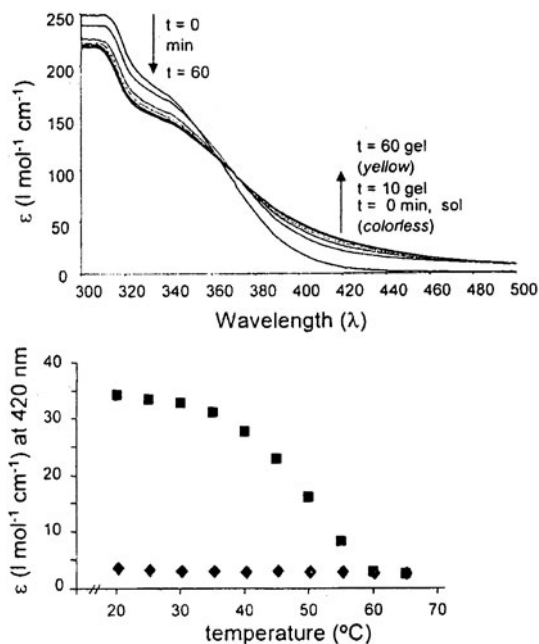
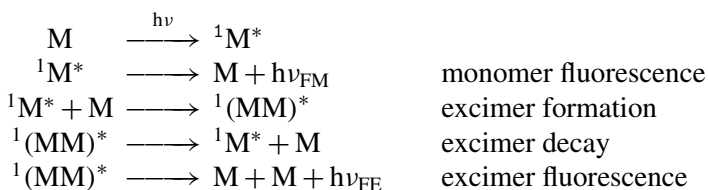


Figure 27. (top) Absorption spectra of a 2 wt% sample of **15** and **16** in a 1 : 1 molar ratio in octanol. At $t = 0$, the sample is a sol; at $t = 10$ min, it is a gel, and between $t = 10$ and $t = 60$ min. The yellow color of the gel strongly increases; (bottom) apparent ϵ_{420} of **15** and **16** (1 : 1 molar ratio) in octanol as a function of temperature: 3 wt% (■) and 1 wt% (◆). (Reprinted with permission from [48]. Copyright (2002) American Chemical Society.)

2.1.5. Excimer fluorescence

2.1.5.1. Excimers (definition and general aspects). An excimer is a 1 : 1 excited state complex between two identical molecules that is dissociative in the ground state [12, 49–52]. Excimers exist in gas phase (noble gas excimers), solution and solid state (e.g., crystalline pyrene [51]). The phenomenon discovered by Förster [50] in 1954 for pyrene in solution is common to most aromatic hydrocarbons. Förster observed that the structured fluorescence spectrum (λ_{\max} ca. 395 nm) is gradually transformed into a broad, structureless emission with a maximum at 480 nm as the concentration of pyrene in cyclohexane solution is increased; it was proposed that this broad spectrum is from a bound complex containing two pyrene molecules, one in its first electronically excited state and the other in the ground state (according to the simplified kinetic scheme below).



This is illustrated by the simple potential energy diagram shown in Figure 28.

The word “excimer” was coined by Stevens [54] from “*excited dimer*” to distinguish this species from an excited complex (whose fluorescence spectrum

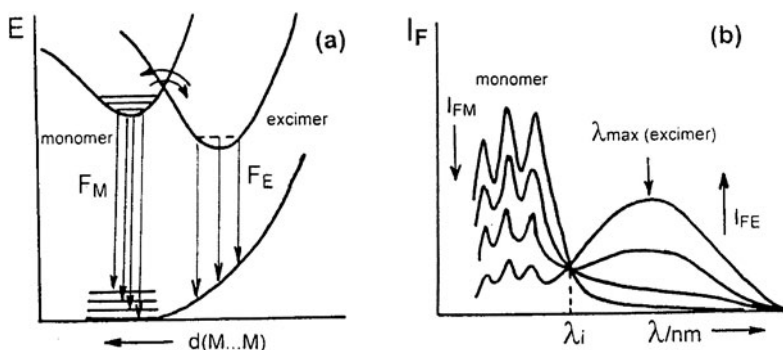


Figure 28. (a) Potential energy diagram illustrating the difference between monomer (structured spectrum) and excimer (no fine structure) fluorescence. In the excimer, the distance between the monomers is smaller than the van der Waals distance. Therefore, the corresponding ground state is repulsive and the emission spectrum is red-shifted and unstructured. (b) Typical fluorescence spectra of monomer (vibrational structure at $\leq 10^{-5}$ M) and excimer (broad structureless at conc. up to 10^{-3} – 10^{-2} M). Note the presence of an isolampsic point at λ_i [53].

is also red-shifted and more or less structured) formed from some kind of ground state aggregate.

In fluid solution, the criteria for the presence of an excimer in a fluorescence spectrum are the following [51]:

- i) broad, structureless, and red-shifted spectrum (as compared to the structured monomer emission).
- ii) the excitation spectra scanned at the wavelengths of monomer and excimer emissions, respectively, are both superimposable to the absorption spectrum.
- iii) kinetic analysis of the fluorescence decay is expressed as follows:

$$i_M(t) = a \cdot \exp(-\lambda_1 t) + b \cdot \exp(-\lambda_2 t) \quad (\text{monomer (M) intensity decay})$$

$$i_E(t) = c[\exp(-\lambda_2 t) - \exp(-\lambda_1 t)] \quad (\text{excimer (E) intensity decay})$$

The excimer decay displays a negative component and equal pre-exponential factors [12, 51]. In non-fluid media such as polymers, matrices, crystals ... or gels, a lumophoric group of one molecule or polymer chain may be close to another lumophore or form an aggregate of several lumophores in the ground state. If so, formation of an aggregated excited species may occur very quickly after a small displacement. These excited state species should be named “excimer-like” or “preformed excimers [12]” or “static excimers” [55]. The rise-time corresponding to their formation may not be detected with standard equipment (time resolution = a few picoseconds). Then the fluorescence decay kinetics at the excimer region is expressed by the following equation:

$$i_E(t) = c \cdot \exp(-\lambda_2 t) + d \cdot \exp(-\lambda_1 t)$$

But in many cases, because the spectra of excimer-like species resemble those of true excimers, the term excimer is often misused.

The wavenumber maxima and shapes of the excimer fluorescence spectra of pyrene in fluid solution, in rigid matrices, and in the crystal state are approximately the same; this strongly suggests that the excimer adopts a fairly rigid structure irrespective of environmental changes [51, 52]. A slightly staggered sandwich structure is supported by the emission from bispyrenophane excimers [56].

In a similar way, in the crystalline state, bis-9,10-anthracenyl crown ether (AAO₅O₅) displayed typical monomer (free ligand) fluorescence whereas the disodium inclusion complex (λ_{max} 580 nm) showed excimer (maximum overlap, slightly staggered sandwich) fluorescence [57] (Figure 29). In solution, the fluorescence spectrum shows monomer and excimer features, the latter with a maximum wavelength at 570 nm in presence of a large excess of sodium cations [57]. The same type of anthracene excimer fluorescence has been reported by

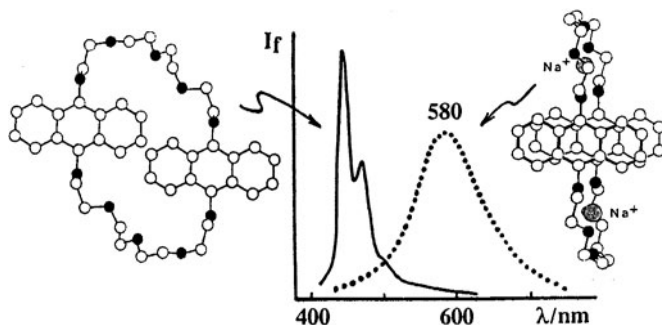
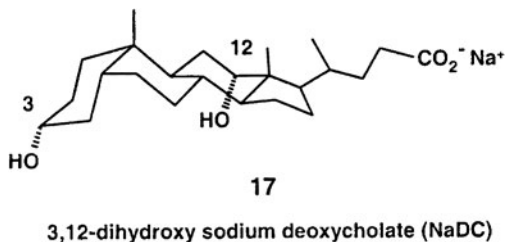


Figure 29. Corrected fluorescence spectra of crystalline AAO_5O_5 (monomer; see text) (—) and of its disodium inclusion complex (.....) (excimer-like at λ_{max} 580 nm). The molecular conformation in the crystal is shown. (Reprinted with permission from [57]. Copyright (1992) International Union of Pure and Applied Chemistry.)

Ferguson from bis-9-anthryl-1,2-ethane in a matrix at very low temperature (10 K) [58].

2.1.5.2. Pyrene “excimer” formation as a probe in sodium deoxycholate gelation. Bile salts are known to form aggregates in aqueous solutions. Among those, sodium deoxycholate **17** (NaDC), a 3,12-dihydroxy bile salt, exhibits special properties, such as the gelation of water at pH values close to neutrality [59].



To study the gelation process, as distinct from micelles and other aggregates formation, steady-state and lifetime fluorescence measurements were applied, using pyrene as a probe [59]. Gelation of water buffered with a phosphate salt, occurs slowly at 20°C , after dissolving NaDC ($\cong 36 \times 10^{-3}\text{M}$) and pyrene ($\cong 10^{-6}\text{M}$). The gelation process could thus be followed by recording the fluorescence spectra and the fluorescence decay kinetics as a function of time between 0 and 40 mins. Figure 30 shows the decrease of the pyrene monomer fluorescence intensity concomitant with the growing of a structureless emission (with λ_{max} 480 nm) characteristic of the pyrene excimer; one observes an isolampsic point [53] at 450 nm. When the fluorescence intensities for both

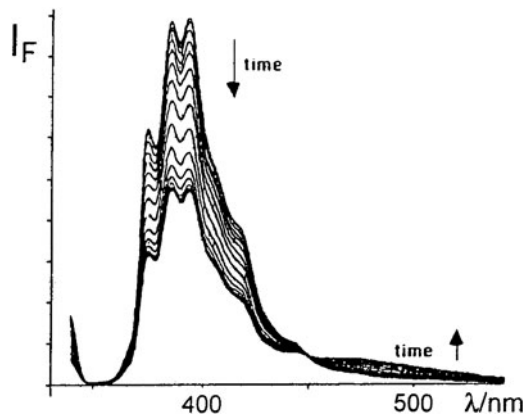


Figure 30. Fluorescence spectral changes from pyrene with time during gelation ($\lambda_{\text{exc}} = 338 \text{ nm}$). $[\text{17}] = 3.62 \times 10^{-2} \text{ M}$; $[\text{pyrene}] = 1.24 \times 10^{-6} \text{ M}$; $[\text{NaH}_2\text{PO}_4] = 0.02 \text{ M}$; pH 6.8. Spectra were recorded every 5 min. $T = 20^\circ \text{ C}$. Note an isolampsic point at 450 nm. (Reprinted with permission from [59]. Copyright (1996) American Chemical Society.)

monomer and “excimer” remain constant, it is evidence that the gel is completely formed (30 mins. in the present case).

The excitation spectra (Figure 31) are different when scanned at 382 nm where only the monomer emits (then it is superimposable to the absorption spectrum of the isolated molecule) or at 480 nm where the emission is essentially that of the “excimer”; in the latter case, there is a bathochromic displacement of the vibronic peaks of pyrene, indicating some mutual interaction of pyrene molecules in the ground state (presumably loosely bound dimers) accompanying the gelation process. The fluorescence spectrum as shown in Figure 31 depends on the excitation wavelength (337 nm or 345 nm), the excimer intensity being higher when the ground state loose complex is excited.

The assumptions are borne out by a transient kinetic analysis as a function of the gelation process. At the beginning, a perfect fit of the data to a single exponential was observed but as the gel was being formed, two exponentials were found to be necessary to fit the experimental results. The fluorescence intensity $I(t)$ is then given by the following equation:

$$I(t) = a \cdot \exp(-t/\tau_1) + b \cdot \exp(-t/\tau_2)$$

τ_1 remained approximately constant over the process within experimental errors (351 to 400 ns) and should be attributed to the pyrene monomer, but the pre-exponential factor ‘ a ’ decreased from 1525 (2 min.) to 355 (105 min.) whereas τ_2 and ‘ b ’ increased during the same period. That both pre-exponential factors are positive (regardless of the wavelength of analysis) indicates that the “excimer” is formed from two molecules previously associated in the

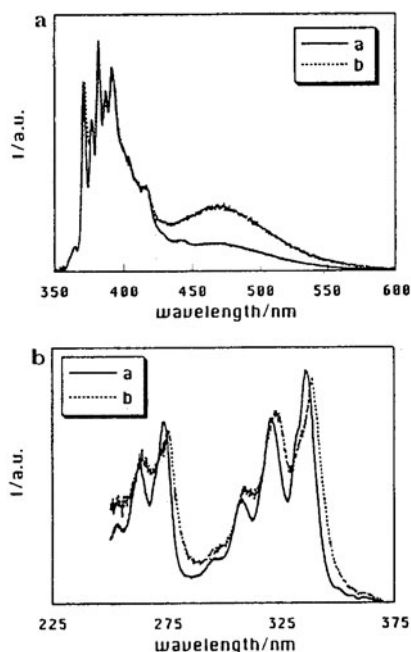


Figure 31. (Top) Emission spectra of pyrene at λ_{exc} 337 nm (a) and 345 nm (b) at the end of gelation process. (Bottom) Excitation spectra of pyrene at λ_{em} 382 nm (a) and 388 nm (b). Experimental conditions are as in Figure 30 except that $T = 25^\circ\text{C}$. (Reprinted with permission from [59]. Copyright (1996) American Chemical Society.)

ground state. Moreover, the “lifetime” $\tau_2 \simeq 119\text{ns}$ observed when the gel was complete, can be compared with the excimer-type fluorescence of pyrene crystals [51] ($\tau \simeq 108\text{ns}$ at 296 K).

All these results (and others given in reference 59) support the following interpretation: the probe environment in bile salts is more rigid than in classical surfactant micelles. In the gel, the pyrene molecules exist in two different environments: as isolated monomers and near to a second pyrene molecule; as the probability of forming a ground state dimer is very low at that concentration (10^{-6}M) in solution, it is greatly favored by the gelation process; the structure of the gel should be solid-like as suggested by the excimer-like complex lifetime.

2.1.5.3. Pyrene “excimer” as a monitor of the formation of vancomycin hydrogel. Vancomycin (Van) polysaccharide, is very well known for its important antibiotic properties. For biomedical applications, Xu and co-workers [60], designed a new hydrogelator (**18**) by introducing a pyrene group on the C-terminal of the backbone of Van (Figure 32).

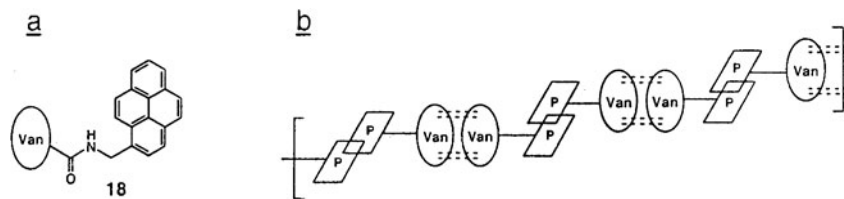


Figure 32. (a) Cartoon representation of the vancomycin (Van)-pyrene monomer (**18**). (b) Proposed polymer of Van-pyrene; two vancomycin subunits can be linked by multiple H-bonds (---) and two pyrene subunits (P) by π - π stacking.

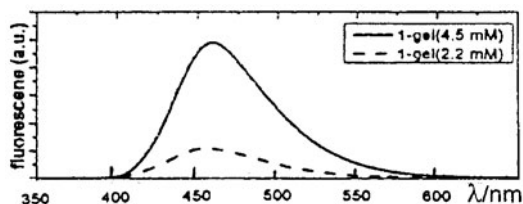
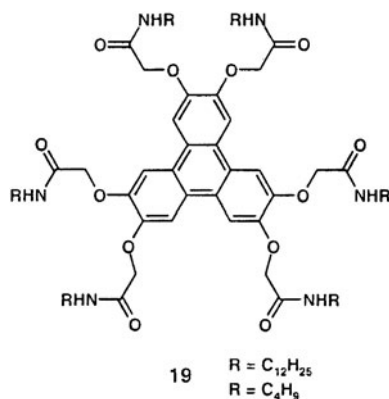


Figure 33. Fluorescence spectra (λ_{exc} 330 nm) of Van-pyrene hydrogels : (—) 4.5 and (- - -) 2.2 mM. (Reprinted with permission from [60]. Copyright (2002) American Chemical Society.)

The resulting molecule was found to gelate water at ≈ 0.36 wt% (2.02 mM) at ambient temperature. Rapid evidence of the polymerisation is given by the pyrene “static excimer” fluorescence observation (λ_{max} : 460 nm, Figure 33); compare λ_{max} at 480 nm for free pyrene. As in the preceding section, the “static excimer” must be formed from a loose ground state dimer. The above proposal for the structure of the Van-pyrene polymer is supported by circular dichroism and electron microscopy [60].

2.1.5.4. “Excimer” emission as compelling evidence of an “eclipsed” overlap of triphenylene chromophores in a gel phase.

Shinkai and co-workers [61] reasoned that they could take advantage of the trend of the triphenylene substrate to form stacked aggregates (the hexasubstituted triphenylenes are known to possess discotic liquid crystal properties) to design new organogelators. To that end, they prepared compound **19-C₁₂** incorporating six amide groups as hydrogen-bonding sites to strengthen the π - π stacking and six long alkyl chains as tail groups to prevent crystallization. For comparison, they also synthesized compound **19-C₄** with shorter chains.



Compound **19-C₁₂** (10 mM) was found to gelate some hydrocarbon solvents such as *n*-hexane, *n*-octane, cyclohexane and *p*-xylene. Among other techniques, fluorescence provided important insight into the supramolecular organization. The fluorescence spectra of **19-C₁₂** in solution and in the gel phase are represented in Figure 34. In general, triphenylene derivatives spectra in the LC phase are shifted to longer wavelengths and such is the case for the cyclohexane gel (partial gel) of **19-C₄** (not represented). But the noteworthy difference exhibited by **19-C₁₂** is a strong new broad structureless emission, centered at 525 nm (Figure 34); this unique emission is that of a “static excimer” formed from stacked aggregates in which the aromatic molecules must be quasi “eclipsed” (corresponding to what has been termed “slightly staggered” in Section 2.2.5.1). Transient kinetic analysis indicates that whereas the monomer (in CHCl₃ solution) has a lifetime of ca. 7 ns, the spectrum formed after 18 ns is mainly related to the emission around 525 nm. The excitation spectra of the cyclohexane gel of **19-C₁₂** (Figure 35) are clearly different when scanned at 389 nm (“monomer” emission) or 525 nm (excimer-like emission). Here also,

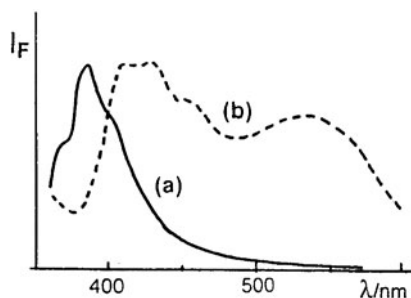


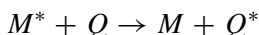
Figure 34. Fluorescence spectra (λ_{exc} 350 nm) of **19-C₁₂**: (a) chloroform solution (5×10^{-5} M); (b) cyclohexane gel (5×10^{-3} M). (Reproduced by permission of The Royal Chemical Society (RSC) [61].)

the broad emission culminating at 525 nm is that of an excited aggregate and should be qualified as “excimer-like”.

2.1.6. Energy transfer

2.1.6.1. Electronic Excitation Energy Transfer: General considerations.

Excitation energy transfer is a process that can suppress molecular emission. It involves the transfer of energy from one molecule in an electronically excited state (M^*) to another molecule initially in its ground state (Q) [12, 43, 49, 62, 63]:



This process, called ‘hetero-transfer’ or photosensitization, is very useful in photochemistry. A necessary condition for the transfer to occur is that the energy level of Q^* must not be higher than that of M^* . Another requirement is that there be some overlap between the normalized emission spectrum of M and the normalized absorption spectrum of Q , as pictured in Figure 36.

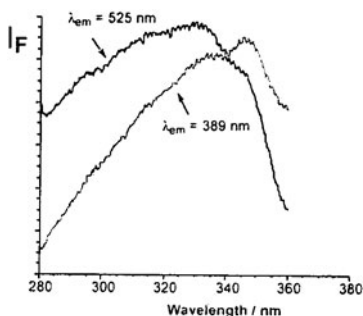


Figure 35. Excitation spectra of 19-C_{12} (5×10^{-3} M) cyclohexane gel. Material kindly supplied by the authors [61].

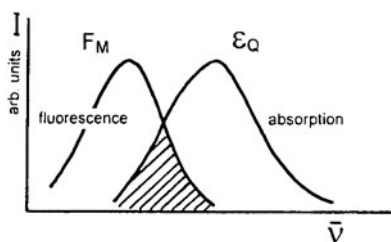
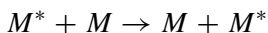


Figure 36. Typical normalized absorption and fluorescence spectra of Q and M , respectively, and the corresponding overlap.

An excitation energy transfer between identical molecules is named “homo-transfer”



If the process occurs over several molecules it is termed energy migration (or hopping) or excitation transport. The energy transfers are classified according to the initial spin multiplicity of M^* and the final spin multiplicity of Q^* . Here, we are primarily concerned with the singlet-singlet transfer:



Different energy transfer processes may be distinguished:

- *Radiative energy transfer*

It is often referred to as “trivial”. The photon emitted by M^* is absorbed by Q in a fashion identical to the direct excitation of Q . It does not require specific interactions between donor and acceptor. Radiative transfer results in a decrease of the donor fluorescence intensity in the region of spectral overlap. The resulting deformation of the fluorescence spectrum is called the “inner filter effect” [12].

- *Non-radiative energy transfer*

Non radiative mechanisms involve the mutual perturbation of the electronic structures of M^* and Q . As several vibronic transitions in the donor have practically the same energy as the corresponding transitions in the acceptor, they are coupled or “in resonance”. For this reason the term Resonance Energy Transfer (RET) is often used as equivalent to excitation energy transfer or electronic energy transfer (EET). But the acronym FRET (Fluorescence Resonance Energy Transfer) sometimes used in the literature, is not correct [12] and should be discarded. Non-radiative energy transfers involve two different processes: coulombic energy transfer and electron-exchange transfer [12, 43, 49, 62, 63].

- *Coulombic energy transfer* (long-range)

According to the theory developed by Förster [12, 51, 52], it does not involve a physical interaction between donor and acceptor but depends on electrostatic interactions (multipole-multipole, *mainly dipole-dipole*) which exert their influence at different intermolecular distances (generally 20–100 Å); such multipole-multipole interactions allow energy transfer hopping between identical chromophores. The coulombic energy transfer is also dependent on an orientation factor. It is emphasized that, in this mode, the electrons which are resident on M^* remain on the de-excited M at the end of the transfer. This is in contrast with the following mode.

- *Electron-exchange transfer* (short-range)

It requires closer contact between M^* and Q for mutual orbital overlap, involving a transfer from the excited electron on M^* to the lowest unoccupied

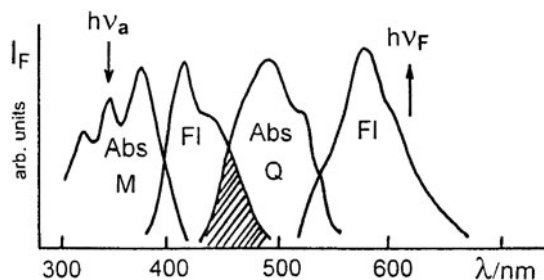


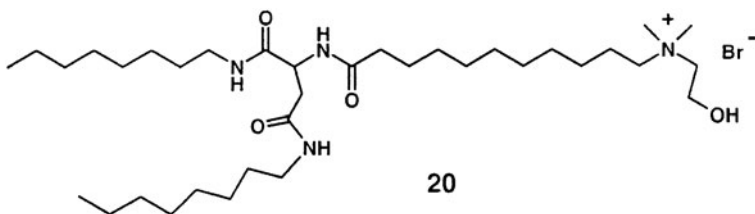
Figure 37. Singlet-singlet energy transfer. Sketch of normalized absorption and fluorescence spectra of M and Q , respectively. Note the overlap area. Absorption in the UV results in emission in the far visible region.

molecular orbital (LUMO) of Q with a simultaneous transfer of an electron from the highest occupied molecular orbital (HOMO) of Q into the corresponding orbital on M . This process may take place at distances 6–20 Å between M^* and Q . The theory has been developed by Dexter [12, 51, 52].

Whatever the mechanism, the singlet-singlet transfer can be described as in Figure 37. In the following examples (Sections 2.2.6.2, 2.2.6.3 and 2.2.6.4) the mechanism involved is a singlet-singlet coulombic energy transfer.

The physical phenomenon of energy transfer depends on the concentrations of M and Q , the average distance $\langle r \rangle$ between them, and, in some cases, their mutual orientation. It can be favored in matrices; in that regard, some gels can act as special (and complex) matrices. In such cases, the existence of electronic energy transfer may reveal interesting features of the gel networks.

2.1.6.2. Light harvesting supramolecular hydrogels. Inspired by Kunitake's work on bilayer-forming amphiphiles (e.g., ammonium glutamate bilayers), Nakashima and Kimizuka [64] designed and prepared **20** in order to form hydrogels for mimicking the mesoscale organization in the photosynthetic membrane. The authors anticipated that the hydrogen bonds formed between the amide linkages would provide sufficient association energy to compensate for the poor hydrophobic interaction among the short octyl chains and therefore allow the generation of fibrous bilayers; the latter were indeed observed in aqueous dispersions.



But to reduce the electrostatic repulsion between the fibrous assemblies, the formation of hydrophobic ion-pairs was required; therefore organic anions (less solvated by water) such as naphthalene sulfonate (NpSO_3^-) were introduced. Upon the addition of an equimolar amount of 5 mM sodium naphthalene sulfonate aqueous solution to an aqueous dispersion of **20** (5 mM) a transparent hydrogel was formed in a few minutes at ambient temperature. The salient and remarkable feature is the enhancement of energy-transfer after light harvesting in the gel phase (bundles of nanofibers crosslinked between each other) as compared to the aqueous fibrous bilayers. The results are shown in the fluorescence spectra in Figure 38. The fluorescence spectrum of aqueous NpSO_3^- (without **20**) displays structured emission spectrum at ca 340 nm, whereas the aqueous mixture of **20**/ NpSO_3^- (0.1 mM) shows a little decrease of fluorescence

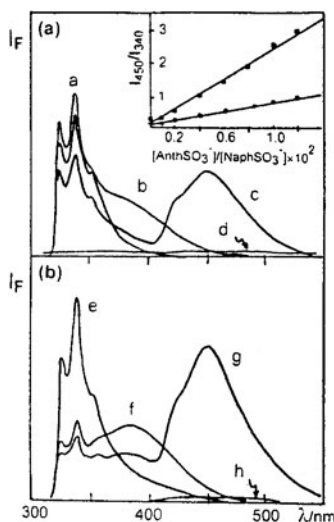


Figure 38. Fluorescence spectra: (a) of a) an aqueous solution of 1.0×10^{-4} M NaphSO_3^- ; b) an aqueous bilayer dispersion of **20**/ NaphSO_3^- ($[\mathbf{20}] = [\text{NaphSO}_3^-] = 1.0 \times 10^{-4}$ M); c) an aqueous bilayer dispersion of **20**/ NaphSO_3^- containing 1 mol-% AnthSO_3^- ($[\mathbf{20}] = [\text{NaphSO}_3^-] = 1.0 \times 10^{-4}$ M, $[\text{AnthSO}_3^-] = 1.0 \times 10^{-4}$ M); d) an aqueous bilayer dispersion of **20** containing AnthSO_3^- ($[\mathbf{20}] = 1.0 \times 10^{-4}$ M, $[\text{NaphSO}_3^-] = 1.0 \times 10^{-6}$ M). (b) e) an aqueous solution of 5.0×10^{-3} M NaphSO_3^- ; f) hydrogel of **20**/ NaphSO_3^- ($[\mathbf{20}] = [\text{NaphSO}_3^-] = 5 \times 10^{-3}$ M); g) hydrogel of **20**/ NaphSO_3^- containing 1 mol-% AnthSO_3^- ($[\mathbf{20}] = [\text{NaphSO}_3^-] = 5 \times 10^{-3}$ M, $[\text{AnthSO}_3^-] = 5.0 \times 10^{-5}$ M); h) hydrogel of **20** containing AnthSO_3^- ($[\mathbf{20}] = 5.0 \times 10^{-3}$ M, $[\text{AnthSO}_3^-] = 5.0 \times 10^{-5}$ M). Excitation wavelength = 290 nm, 18°C. (a) Inset is the dependence of relative fluorescence intensity, I_{450}/I_{340} , versus the molar ratio of $[\text{AnthSO}_3^-]/[\text{NaphSO}_3^-]$. Upper line is for hydrogels ($[\mathbf{20}] = [\text{NaphSO}_3^-] = 5 \times 10^{-3}$ M); lower line is for aqueous bilayers ($[\mathbf{20}] = [\text{NaphSO}_3^-] = 0.1 \times 10^{-3}$ M). (Reproduced with permission from [64]. Copyright (2002) Wiley-VCH.)

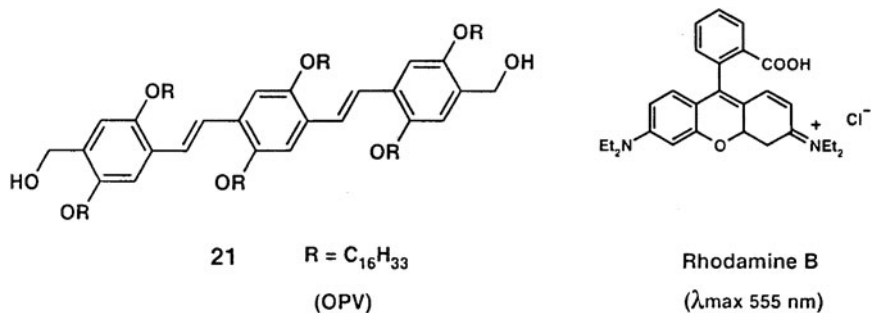
intensity at 340 nm and an excimer component at 380 nm (as a result of the binding of NpSO_3^- to the bilayer of **20**). Doping the latter with 1% (conc = 1×10^{-6} M) of 9,10-dimethoxy-2-anthrylsulfonate (ASO_3^-) quenches NpSO_3^- emission and results in a strong fluorescence emission with a λ_{max} at 450 nm. Without the presence of the naphthalene chromophore, the ASO_3^- shows only weak fluorescence. The authors concluded to the occurrence of energy hopping between the naphthalene molecules followed by energy transfer to the anthracene chromophore.

In another hydrogel phase **20**/ NpSO_3^- containing a higher NpSO_3^- concentration (5 mM) one observes an enhancement of naphthalene quenching and anthracene fluorescence; the relative fluorescence intensity of ASO_3^- and NpSO_3^- I_{450}/I_{340} (see inset of Figure 38) is a measure of the energy transfer efficiency. It is clearly greater in the gel phase.

To account for these results, the authors propose that an ordered organization of NpSO_3^- at the surface of fibrous nano-assemblies allows efficient crosslinking into a light harvesting supramolecular gel network.

2.1.6.3. Gelation assisted light harvesting by selective energy transfer.

Among a number of donor acceptor systems, oligo (phenylenevinylene)s (OPVs) and organic dyes are interesting for their potential use in light-emitting devices. Ajayagosh and co-workers [65] selected OPV derivative **21** known to generate gels in cyclohexane : chloroform (16 : 1) as the donor and Rhodamine B as the acceptor as its absorption (λ_{max} 555 nm) matches the fluorescence spectrum of the self-assembled **21** (λ_{em} 527 and 560 nm) as exhibited by their individual respective spectra (Figure 39), a necessary condition for energy transfer to occur.



An absorption spectrum of a mixture of **21** and Rhodamine B (in excess) showed no indication of any ground state interaction between them. In cyclohexane-chloroform (16 : 1), the same mixture (**21**: 1.01×10^{-5} M and Rhodamine B: 8×10^{-5} M) shows selective quenching of fluorescence excited at λ : 380 nm) between 500 and 650 nm corresponding to the self-assembled OPV gel with the concomitant emission of Rhodamine B at 620 nm (Figure 40);

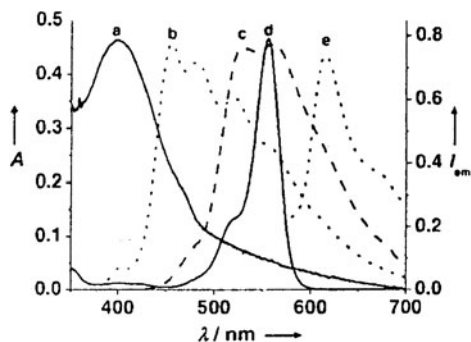


Figure 39. Absorption and emission spectra of **21** and Rhodamine B in cyclohexane: chloroform (16 : 1): a) absorption of **21**; b) emission of monomeric **21** ($\lambda_{\text{exc}} = 380 \text{ nm}$); c) emission of self-assembled **21** gel ($\lambda_{\text{exc}} 470 \text{ nm}$); d) absorption of Rhodamine B; e) emission of Rhodamine B ($\lambda_{\text{em}} 535 \text{ nm}$). (Reproduced with permission from [65]. Copyright (2003) Wiley-VCH.)

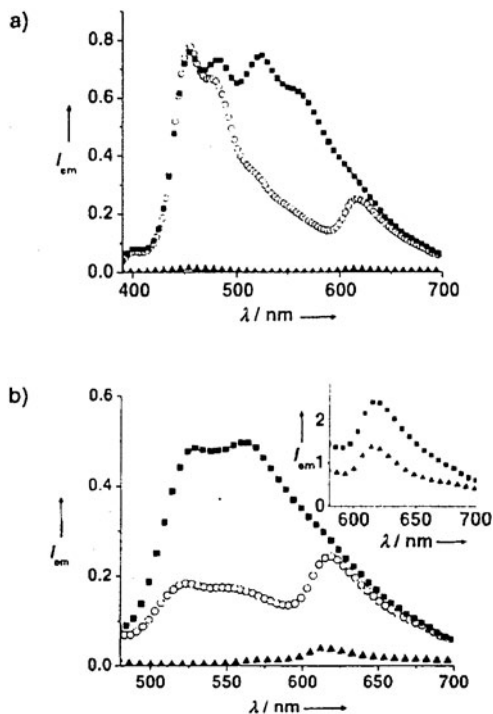


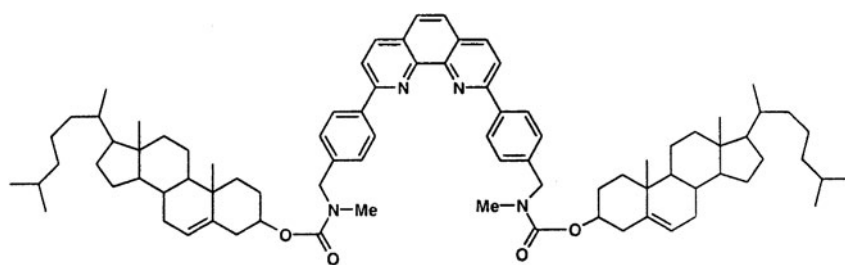
Figure 40. Energy transfer quenching of the fluorescence of **21** ($1.01 \times 10^{-5} \text{ M}$) in cyclohexane: chloroform (16 : 1) in the presence of Rhodamine B ($8 \times 10^{-5} \text{ M}$); $\lambda_{\text{exc}} = 380 \text{ nm}$ (a) and 470 nm (b). (■) fluorescence of **21**; (○) fluorescence of **21** + Rhodamine B; (▲) fluorescence of Rhodamine B. Inset is emission of the dye at $\lambda_{\text{exc}} 470 \text{ nm}$ on indirect excitation (■) and 535 nm on direct excitation (▲) showing the enhanced emission by the energy transfer. (Reproduced with permission from [65]. Copyright (2003) Wiley-VCH.)

interestingly, the 400–480 nm fluorescence corresponding to the dissolved **21** monomer was virtually unaffected; when the medium was excited at 470 nm (absorption of the self-assembled species), the quenching of the 500–650 nm fluorescence was significant and an emission at 620 nm (Rhodamine B) occurred (Figure 40). Moreover, a direct excitation at 380 and 470 nm of the dye without **21** produced no significant emission.

All these facts are a clear indication that the dye emission occurs as a result of energy transfer from the self-assembled gel. This amplified emission implies an efficient energy hopping in the supramolecular aggregate and favorable transfer to the dye which must be immobilized within the *gel network*. The authors also demonstrated that an efficient light harvesting and energy transfer occur in solid xerogel films where a lesser amount of dye could be used as a majority of the dye molecules are trapped in the xerogel [65].

2.1.6.4. Energy transfer in proton-sensitive fluorescent organogels.

The cholesterol substrate was used as a basis for generating new proton sensitive fluorescent organogelators (**22**) by Shinkai and co-workers [66].



22

The fluorescent properties of the 1,3-phenanthroline component change by protonation and aggregation [67]. Compound **22** forms gels in a variety of solvents, particularly 1-propanol (critical gel concentration: 0.2 wt%, 1.6 mM).

The fluorescence spectra in 1-propanol shown in Figure 41 are clearly different in isotropic solution (λ_{\max} 386 nm), in the neutral gel phase (λ_{\max} 396 nm) and in the gel phase of acetic acid (λ_{\max} 522 nm). It is known that because the lowest $\pi\pi^*$ level is stabilized by protonation, the emission maximum observed for 1,10-phenanthroline is red shifted.

In the gel phase (Figure 42), when only 2 equivalents of trifluoroacetic acid (TFA) (with respects to **22**) were added, the 396 nm peak characteristic of neutral **22**^{*} entirely disappeared and the emission from (**22** – H⁺)^{*} appeared at 530 nm. The emission spectrum from the corresponding isotropic solution displays two maxima at different maximum wavelengths. In 1-propanol, even

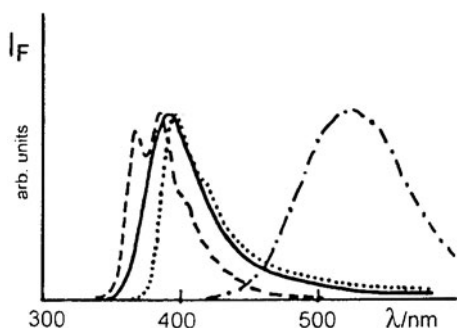


Figure 41. Fluorescence spectra of **22** in 1-propanol as (i) solution (1.6×10^{-5} M) (---) and (ii) gel (2.4×10^{-3} M) (.....); (iii) a solution of non-cholesteric phenanthroline in 1-propanol (2.4×10^{-3} M) (—); (iv) **22** in gelled acetic acid (8×10^{-3} M) (•-•-•). λ_{exc} 285 nm. (Reproduced by permission of the Royal Society of Chemistry (RSC) [66].)

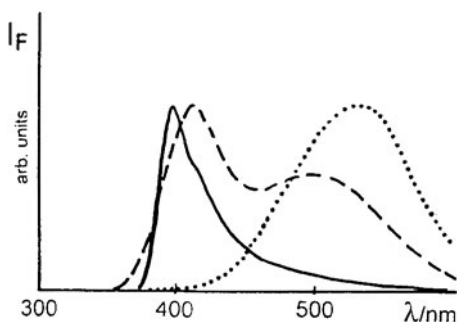
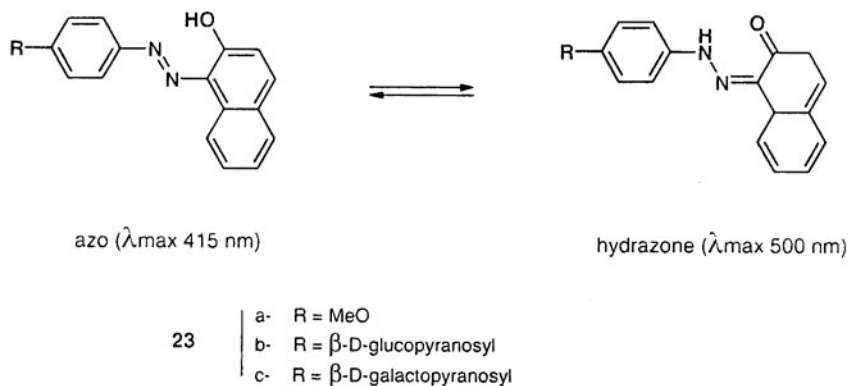


Figure 42. Fluorescence spectra of **22** in 1-propanol (2.4×10^{-3} M): (i) in the gel phase at 25°C without TFA (—) and with 2 equivalents of TFA (.....); (ii) in the solution phase at 90°C with 2 equivalents of TFA (---). (Reproduced by permission of the Royal Society of Chemistry (RSC) [66].)

in the presence of 15 equivalents of TFA, **22** is not completely protonated. Moreover, the fluorescence spectrum of **22** and the excitation spectrum of **22** – H^+ overlap in the 350–400 nm region. The above results show that by exciting **22** at 285 nm, in the presence of TFA (where **22** and **22** – H^+ are present), the fluorescence observed is only that of **22** – H^+ at 530 nm (that of **22** being completely quenched). This is explained by energy transfer from **22*** to **22** – H^+ , which is particularly efficient in the gel phase where the chromophores are presumably stacked. Other experiments by the authors support the conclusion [66].

2.1.7. Miscellaneous

2.1.7.1. UV-vis spectroscopy as a tool to determine the micropolarity of aqueous gels. In extending the family of sugar-integrated gelators, Shinkai and co-workers [68] introduced azoderivatives such as **23b-c** as a probe to detect the micropolarity of the gel aggregates [69]. Gels were found to be formed in water/EtOH mixtures.



The spectral variation of **23c** in various water/EtOH mixed solvents is shown in Figure 43, the spectral features of **23a** (reference compound) and **23c** are almost the same, indicating that the sugar structure does not affect the absorption spectra in homogeneous solutions; the λ_{\max} 415 nm peak characteristic of

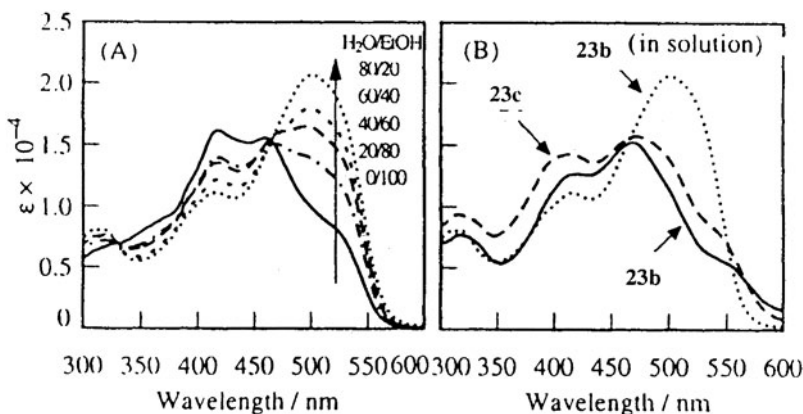
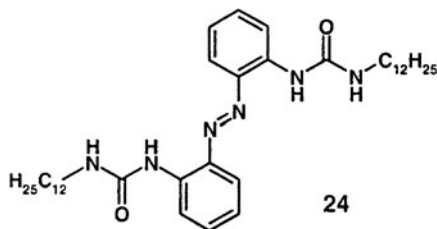


Figure 43. (A) Absorption spectra of **23c** (2×10^{-5} M) at various water/EtOH solvent mixtures. (B) Absorption spectra of **23b** in solution (....., 2×10^{-5} M) and of 2×10^{-3} M **23b** (—) or **23c** (- - -) in the gel phase at water/EtOH: 80/20 (v/v). (Reproduced with permission from [68]. Copyright (2001) The Chemical Society of Japan.)

the azo form increases in EtOH-rich (less polar) solvents whereas the peak at λ_{\max} 500 nm (characteristic of the hydrazobenzene form), increases with the water content.

As observed in Figure 43 the gel phase favors the azo-form. The authors plotted $\varepsilon_{500}/\varepsilon_{415}$ (ratio of absorptivity at 500 and 415 nm) vs EtOH % and found a good linear relationship. From this calibration curve, they deduced that, whereas the overall water content in the gels of **23b** and **23c** is 80%, the micropolarities (around the probe) correspond to ca. 14 and 23% water, respectively. Thus, it was shown that the micropolarity in the gelator aggregates is much lower than that of the gelation media [68].

2.1.7.2. UV-vis spectroscopy as a tool to detect and characterize polymorphism in gels. Compounds that contain one urea and especially two urea groups have been reported to be versatile gelating agents for a wide range of organic solvents. With the purpose of forming photoresponsive gels (see Chapter 24), van Esch, Feringa and co-workers [70] have synthesized new azobenzene bis-urea molecules such as **24**, which were found to be excellent gelators for a variety of solvents, even at very low concentration (0.2 to 30 mM). Spectroscopic (UV-vis and IR) and small-angle X-ray scattering investigations indicate that, two types of aggregates, referred to as type I and type II, are formed in the gel phase.



The electronic absorption spectrum of a 1,2-dichloroethane solution of **24** (0.1 mM, well under the critical gel concentration) is shown in Figure 44; the band at 419 nm and shoulder at 470 nm are interpreted as the $\pi\pi^*$ and $n\pi^*$ transitions, respectively, of the azobenzene. One observes different patterns for the gels: in more polar solvents (ethanol, ethyl acetate, 1,2-dichloroethane) the absorption at 419 nm (solution) has shifted to 400 nm (1,2-dichloroethane gel (1.85 mM)); this blue shift can be attributed to exciton (Davydov) splitting [13] between stacked azobenzene chromophores within the aggregates (termed type I by the authors). In apolar solvents like cyclohexane (2.37 mM) gelation induces a red shift of the $\pi\pi^*$ absorption (λ_{\max} 433 nm, Figure 44) and an enhancement of fine structure corresponding to another gel structure (type II).

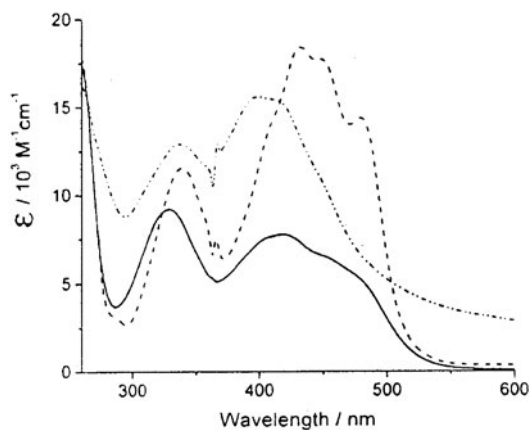


Figure 44. Absorption spectra of a solution of **24** in 1,2-dichloroethane (0.1 mM, —) and of a gel in 1,2-dichloroethane (1.85 mM, -•-•-•-•-, type I) and in cyclohexane (2.37 mM, - - -, type II). (Reprinted with permission from [70]. Copyright (2002) American Chemical Society.)

The authors took advantage of these distinct spectroscopic changes to investigate the mechanism of gelation. Cooling a heated toluene solution of **24** to ambient temperature, induces the formation of a spectrum characteristic of type II gels in the first minutes; within the following 10–60 minutes (depending on the concentration), the spectrum was observed to turn into another spectrum typical of type I aggregates. These results strongly suggest that **24** first assembles in the kinetically favored type II aggregates which slowly transform into the thermodynamically favored type I aggregates (in toluene).

The authors underline that this is an interesting case of observation of two morphs of gels via distinct spectroscopic changes [70]. These results are to be compared with those of other authors [16, 21, 22, 32].

3. Infrared Spectroscopy

3.1. General Considerations

In addition to other physical methods, *infrared spectroscopy*, together with the complementary Raman spectroscopy, is used for the determination of chemical structures and identification of compounds. The technique involves simple handling for routine analysis at ambient temperature. Common Fourier Transform Infra Red (FTIR) spectrometers allow very fast recording of spectra of small size and low concentration samples in gaseous, liquid or solid state, in the 4000–200 cm^{-1} region.

The principles of IR spectroscopy can be found in many textbooks [71–74]. Here, the features of IR spectroscopy related to the study and characterization of gel structures are emphasized. Because organic or organometallic gelators are organized in *molecular aggregates* [5], molecular vibrations are considered in the following. A vibrational mode is active in the IR region when there is a change in the dipole moment during the vibration (in contrast with the Raman spectroscopy which involves a change of polarizability). Asymmetric vibrational modes and vibrations due to polar groups are more likely to exhibit prominent IR absorption, while a symmetrical mode often leads to strong absorption in Raman.

The terms “*group frequencies*” is used to describe the IR bands that are common for molecules containing the same functional groups of atoms and appear in the same spectral region (these vibrations are strongly decoupled while others are significantly coupled together). These group frequencies can be divided into three types [75]:

- 1) those that have a rather constant position regardless of their environment;
- 2) those that change according to their molecular environment in a somewhat predictable manner;
- 3) those that have unpredictable positions or intensities.

The second type is very useful for gel investigations. Among them, the stretching vibrations along the bond linking the atoms or groups of atoms (symbol ν) are often strongly affected by intermolecular interactions (especially hydrogen bonding frequently involved in gels) have been often studied. Other modes such as bending vibrations are also affected by local constraints or structural changes, but to a lesser extent and have been rarely considered (but see DDOA gels in Section 3.3).

The following stretching vibrations: ν_{OH} , ν_{NH} , $\nu_{\text{C=O}}$ were found to be sensitive to their environment. Hydrogen-bonds (subject to concentration and temperature) induce enlargement of the vibronic bands and shift to lower energy of the signals.

The groups frequencies and intensities [76] are dependent on several factors such as the physical state of the sample (in solids, the group frequencies are lowered) and the molecular environment. Therefore it is recommended to examine the fluid solution in comparison with the gel spectra at different concentrations and temperatures.

Dichroic Absorption

Because the absorption of IR radiation originates in the interaction of the electric field vector (E) of the incident radiation with the transition moment vector (M) of a particular vibrational mode (A , absorbance, is proportional to $(ME)^2$), the IR absorption of an oriented sample is therefore sensitive to the state of polarization of the incident radiation with respect to a reference

direction; the latter could be given by the direction of the constraints that have produced the sample anisotropy or could correspond to the main axis of a fiber, the elemental sub-unit of the organogel 3D network (*vide infra*).

The anisotropic optical absorption of oriented samples, so-called dichroism [77], is determined by using successively light parallel (*//*) and perpendicular (\perp) to the fixed reference direction. A parameter commonly used to characterize the degree of anisotropy is the dichroic ratio *R*,

$$R = A(//)/A(\perp)$$

where *A* is the integrated absorbance of the investigated band. It is sometimes converted into the orientation factor *K_i* [78]:

$$K_i = \langle \cos^2 \alpha \rangle = R_i / (R_i + 2)$$

where α is the angle between the transition moment (*M*) of vibration ‘*i*’ with the reference direction (taken as *Z* in the case of DDOA, *vide infra*). A major advantage of the technique is that it can be used to selectively determine the orientation of specific chemical groups in organogels (see Section 3.3).

3.2. Selected Examples Illustrating the Application of Infrared Spectroscopy to the Study of Gel Structures

As indicated in the preceding section, IR spectroscopy is most useful in the study of molecular aggregates, particularly to detect and characterize hydrogen bonding, a major driving force in the formation of gels. Among a large number of reports, only a few examples have been selected, suitable to illustrate the standard technique.

3.2.1. Intermolecular H-bonding of 1,3: 2,4-di-O-benzylidene-D-Sorbitol (DBS) in the gel formation

The gelation of organic solvents (ethanol, ethylene glycol, acetonitrile etc.) by derivatives of sorbitol such as DBS has been known for a long time [78]. DBS (**4**) gels have found commercial applications [79] and have been extensively investigated. It was shown by Yamasaki *et al.* [80] that the racemate (DL-DBS) is unable to form gels; the racemate form platelet-like crystals and show OH stretching bands at 3350–3450 cm^{-1} whereas the enantiomers (xerogels) form rope-like helical nanofibrils and exhibit more intense OH stretching vibrations at 3250 and 3350 cm^{-1} (Figure 45); the vibrations at lower wavenumbers are indicative of stronger hydrogen bonding; it was concluded that the vectors corresponding to the C–O and O–H stretching modes become more linearly

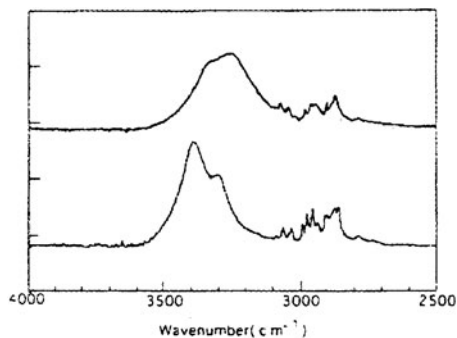


Figure 45. IR spectra of DBS. Upper is xerogel of (D) enantiomer; lower is crystal of racemate. (Reproduced with permission from [80]. Copyright (1995) The Chemical Society of Japan.)

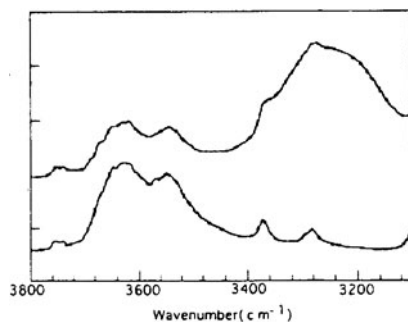


Figure 46. IR spectra of (D)-DBS in acetonitrile. Upper is gel state and lower is solution. (Reproduced with permission from [80]. Copyright (1995) The Chemical Society of Japan.)

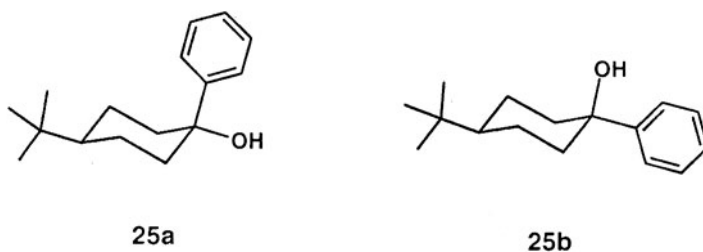
ordered in the enantiomers than in the racemate. In *acetonitrile*, ν_{OH} is observed at ca. 3600 cm^{-1} whereas upon gelation, a new and intense stretch band appears at about 3270 cm^{-1} , which is attributable to intermolecular DBS-DBS interactions (Figure 46).

These observations are in line with other results obtained from UV and CD spectroscopy (see Section 2.2.2).

3.2.2. Organogels of 4-*tert*-butyl-1-arylcylohexanol derivatives (BACOI) IR spectra in the OH stretching region

The following cyclohexanol derivatives provide another example of gelators without a long aliphatic chain [81]. In this case, only one diastereoisomer (**25a**), with an axial phenyl in the most stable conformation, exhibits gelating

ability for a variety of solvents such as heptane, CCl_4 , CH_2Cl_2 , ether, toluene, the equatorial isomer (**25b**) was not found to lead to gels under the same conditions.



The authors showed that IR spectroscopy reveals the aggregation of the BACO1 molecules. Figure 47 exhibits the ν_{OH} region of **25a** in CCl_4 .

In the gel phase, the narrow O–H stretching vibration at 3603 cm^{-1} is that of BACO1 monomers while the broad band with maxima at 3280 and 3189 cm^{-1} is characteristic of oligomers and the absorption at 3450 cm^{-1} strongly suggests

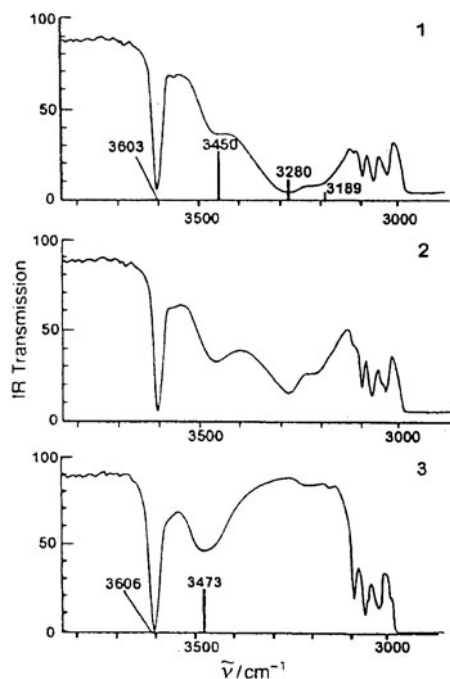


Figure 47. IR spectra of BACO1 (**25a**) in CCl_4 ($c = 4\text{ wt}\%$) at increasing temperatures: 1) $T = 29^\circ\text{ C}$, gel phase; 2) $T = 40^\circ\text{ C}$, intermediate state; 3) $T = 80^\circ\text{ C}$, liquid phase. The absorption in the 3000 cm^{-1} region is due to C–H stretching vibrations. (Reproduced by permission of the Royal Society of Chemistry (RSC) [81].)

the presence of dimers or mixture of dimers and trimers. Indeed, at 80° C (i.e., isotropic phase), the only absorptions left are those of the monomer (3606 cm⁻¹) and the dimer (3473 cm⁻¹); the latter must be solvated by CCl₄ and appears at higher frequency than in the gel where the environment is more solid-like. It was argued that H-bonding is not the unique driving force for aggregation [81], but its contribution is the dominant one.

3.2.3. H-bonding in long chain substituted L-alanine

Peptides and α -aminoacids are known to be gelators of organic solvents [82, 83]. The presence of NH-CO, NH₂ and COOH groups makes these compounds particularly suitable to IR spectroscopy investigations of their gels.



For instance, some long chain substituted L-alanine (e.g., **26a**) were found to gelate [84] a number of organic fluids, even at low concentration (ca. 2.5 × 10⁻² M), but **26b** or **26c** possess aliphatic chains too short or too long to reach the adequate hydrophilic-lipophilic balance. FT-IR spectra for the CCl₄ gel and CHCl₃ solution of **26a** are shown in Figure 48.

The gel spectra exhibit bands characteristic of intermolecular H bonds: ν_{NH} : 3349 cm⁻¹, $\nu_{\text{C=O}}$ of CO₂H; 1704 cm⁻¹, $\nu_{\text{C=O}}$ of amide: 1640 cm⁻¹ whereas the isotropic solution displays absorptions at 3450 cm⁻¹ (ν_{NH}), 1740 ($\nu_{\text{C=O}}$ of COOH) and 1660 cm⁻¹ ($\nu_{\text{C=O}}$ of amide) indicative of non H-bonding stretching vibrations. Interestingly, the authors showed that the spectrum (of the neat gelator in a KBr pellet matrix) is similar to that of the gel [84], suggesting that the hydrogen-bonding pattern of the gel and the crystal are close to each other. Moreover, the presence in the gel spectrum of a sharp band at 1704 cm⁻¹ characteristic of acid dimer supports the formation of an intermolecular H-bond network. These results combined with those of TEM and X-ray diffraction allowed the authors to propose that the gel aggregates consist of repeating bilayer units [84].

3.2.4. Intermolecular H-bonds in the hydrogels of L-lysine derivatives. FT-IR spectra in D₂O

In contrast to organogels, there are a limited number of hydrogels known to be formed by low molar mass gelators (LMOGs). One of them, an L-lysine derivative (**27**) is able to form a transparent gel [85] with water at

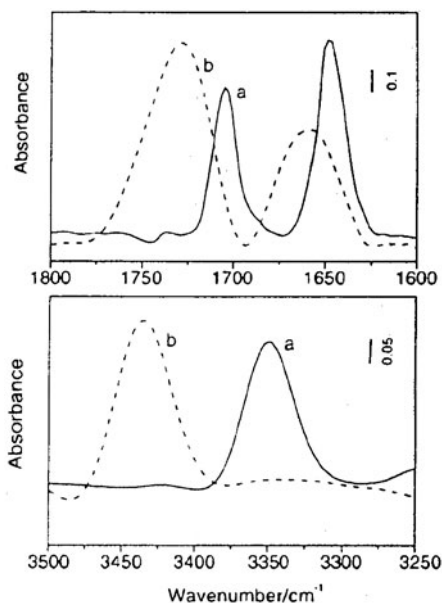
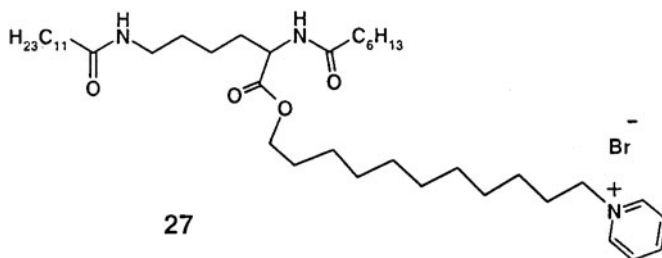


Figure 48. FT-IR spectra of **26a**. Upper: (a) gel in CCl_4 (2.5×10^{-2} M), ν_{max} 1704 and 1640 cm^{-1} ; (b) solution in CHCl_3 ν_{max} 1740 and 1660 cm^{-1} . Lower: (a) gel in CCl_4 (2.5×10^{-5} M) ν_{max} 3349 cm^{-1} ; (b) solution in CHCl_3 ν_{max} 3450 cm^{-1} . (Reproduced by permission of the Royal Society of Chemistry (RSC) [84].)

a concentration of ca. 1.33×10^{-3} M, at ambient temperature (this corresponds to an average of 41,000 molecules of water entrapped by each gelator molecule).



The FT-IR spectra of **27** in CHCl_3 (no gel formed) and in D_2O (gel) are represented in Figure 49.

The spectrum in chloroform, in which no self-assembly occurs, exhibits absorption bands at 1658 and 1514 cm^{-1} due to $\nu_{\text{C=O}}$ (amide I) and δ_{NH} (amide II) respectively. The gel spectrum in D_2O is characterized by bands at 1632 ($\nu_{\text{C=O}}$, amide I) and 1543 (δ_{NH} , amide II) cm^{-1} , assigned to hydrogen-bonded amide groups; the intensity of these bands were found to vary quasi-linearly with the concentration of **27**. These observations indicate that **27** forms intermolecular H-bonds in the gel. The ν_{NH} vibration region was not described

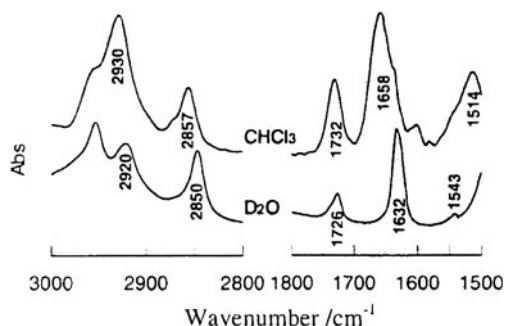


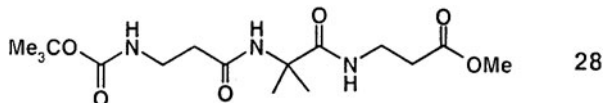
Figure 49. FT-IR spectra of 2×10^{-2} M **27** in CHCl_3 and D_2O . (Reproduced by permission of the Royal Society of Chemistry (RSC) on behalf of the Centre National de la Recherche Scientifique (CNRS) [85].)

but the authors made the interesting remark that the anti-symmetric (ν_{as}) and symmetric (ν_{s}) $_{\text{CH}_2}$ stretching modes in D_2O shift to lower wave numbers ($2930 \rightarrow 2920 \text{ cm}^{-1}$ and $2857 \rightarrow 2850 \text{ cm}^{-1}$); this was attributed to the decrease in the chain fluidity induced by hydrophobic interactions between alkyl groups.

The present case is an interesting example where it could be inferred by other techniques that compound **27** forms first spherical micelles (below the critical gel concentration) through hydrophobic interactions; these micelles then aggregate upon cooperative formation of hydrogen bonds, leading ultimately to a 3D network (SAFIN) structure [85].

3.2.5. Organogel of a synthetic tripeptide; the formation of intermolecular hydrogen bonds

Nandi and co-workers [86] designed a terminally protected tripeptide with noncoded amino acids, combining a conformationally restricted nature and a flexible structure, in order to create a network structure through intermolecular aggregation in organic solvents as a result of intermolecular hydrogen bonds between amide linkages: the molecule **28** is Boc- β -Ala-Aib- β -Ala-OMe.



The authors found that **28** generates thermoreversible gels in 1,2-dichlorobenzene (DCB) at 30°C . The FT-IR spectra of **28** in DCB and in the solid state are shown in Figure 50. One observes that the spectra of solvent subtracted gel (a) and the pure (b) are almost identical; however the solvent

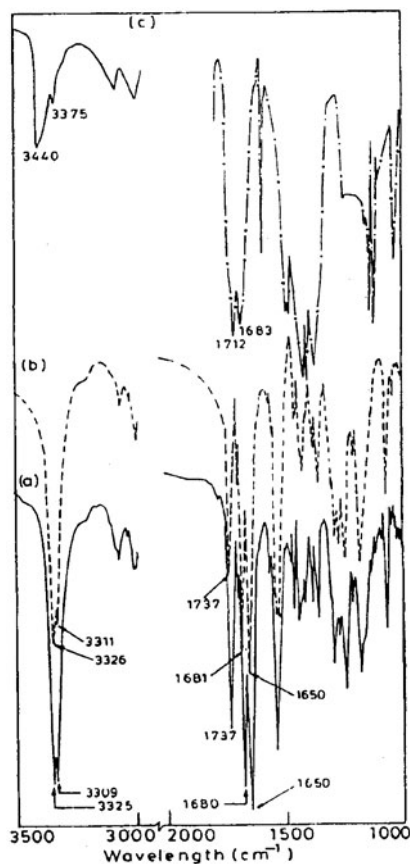


Figure 50. FT-IR spectra of **28**: (a) solvent subtracted tripeptide gel in *o*-dichlorobenzene (10% w/v); (b) neat tripeptide; (c) tripeptide solution in *o*-dichlorobenzene (0.3% w/v). (Reproduced by permission of the Royal Society of Chemistry (RSC) [86].)

subtracted spectrum of the solution is clearly different: the ν_{NH} peak at 3440 (free NH) and 3375 (intramolecular H-bonded) cm^{-1} . In the gel these bands are absent and replaced by peaks at lower frequencies as expected for intermolecular H-bonds (presumably of different geometries).

The $\nu_{\text{C=O}}$ bands are also affected by intermolecular H-bonding: the peak at 1712 cm^{-1} in solution (ester) is shifted to higher wave number (1737 cm^{-1}) as observed elsewhere [87] and the amide $\nu_{\text{C=O}}$ absorbs at lower wave numbers (1680 and 1650 cm^{-1}). In the 3600–3200 cm^{-1} window the authors observed the kinetics of gel formation (Figure 51) after making the solution homogeneous at 100° C and recording the spectra at different time intervals after cooling to 25° C. It shows the growing in of the gel peaks at 3325 and 3309 cm^{-1} and the gradual decrease of the free N-H absorption [86].

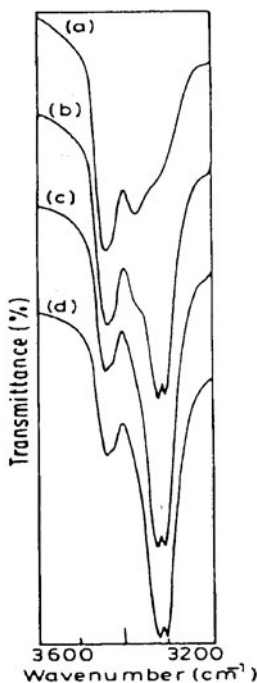
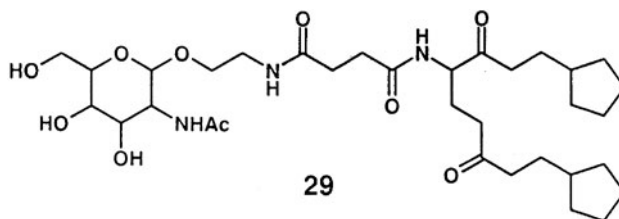


Figure 51. FT-IR spectra of 1% (w/v) solution of **28** in *o*-dichlorobenzene at different times: (a) immediately after preparation; (b) after 15 min; (c) after 1 hour; (d) after 2 hours. (Reproduced by permission of the Royal Society of Chemistry (RSC) [86].)

3.2.6. LMOGs of organic and aqueous media based on glycosylated amino acid derivatives. IR contribution to structural analysis of the gels

Some glycosylated amino acid derivatives were shown to have the remarkable ability to form gels with a broad spectrum of organic solvents *and* also with water [87]. These gels have potential applications as biocompatible materials. The authors have demonstrated that efficient hydrogen-bonding networks are crucial for the gelation [87]. Selected infrared spectra are displayed in Figure 52 for one of them, an N-acetyl-galactosamine appended amino acid derivative **29**.



GalNAc-suc-glu(O-methylcyclopentyl)₂

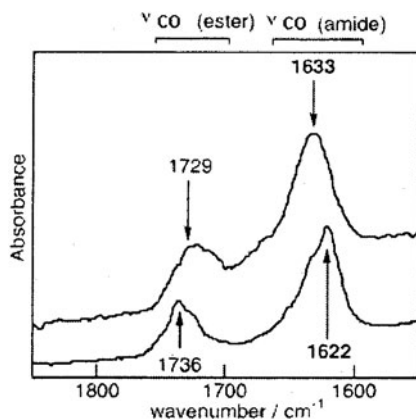


Figure 52. FT-IR spectra of an aqueous solution of GalNac-suc-glu(O-butyl)₂ (upper) and of a hydrogel of 32 mM **29** (lower) at ambient temperature. (Reproduced with permission from [87]. Copyright (2003) Wiley-VCH.)

The spectrum of **29** in D₂O displays a peak at 1622 cm⁻¹ due to the amide carbonyl stretching and another at 1736 cm⁻¹ for the ester carbonyl stretching. The first band is comparable to that due to the H-bonding network of β -sheet in natural proteins and close to that of the amorphous solid state (1624 cm⁻¹, spectrum not shown). The same vibration appears at 1633 cm⁻¹ in the homogeneous aqueous solution in which the H-bonds are formed between the amide carbonyl and the solvent. Thus, the intermolecular H-bonding network in the gel induces a larger down shift. Regarding the ester absorption, it undergoes a shift to higher wavenumber (from 1729 to 1736 cm⁻¹) in the gel aggregate (see also reference 86); this result is not easy to interpret and was not discussed by the authors [86, 87].

3.2.7. A transition metal-carbene carbohydrate amphiphile as organometallic gelator; the carbonyl vibrator

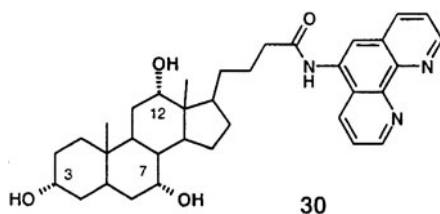
Upon heating to 70–75° C followed by cooling to ambient temperature compound **6**, a metal carbene, was found to form thermoreversible gels within a few minutes, in chloroform, dichloromethane, benzene, toluene and mixtures of these solvents [21].

The $\nu_{C=O}$ region of the IR spectra is rich of information. The spectra in methanol solution, show three bands at 2053, 1968 and 1930–1920 cm⁻¹ that are characteristic for amino-carbene pentacarbonyl chromium complexes of local C_{4v} symmetry. In the IR spectra of chloroform gels (1.0 wt% conc.), two additional strong absorption were observed at 1889 and 1878 cm⁻¹, whereas the

other bands were shifted to 2055, 1976 cm^{-1} and the broad band sharpened at 1926 cm^{-1} . Decreasing the concentration or increasing the temperature (55°C) induces a decrease of the new bands (1889 and 1878 cm^{-1}) and reappearance of the bands observed in solution. These results may reflect the hindered rotation around the metal-carbene bond, reducing the local C_{4v} symmetry and the formation of absorption bands at lower energy is ascribable to intermolecular hydrogen bonding between one or several CO ligands and OH groups. There is little doubt that the IR spectrum of **6** in the solid state resembles that of the gel (for CD spectra of **6**, see Section 2.2.2.4).

3.2.8. A cholic amide-phenanthroline derivative as an LMOG for methanol-water mixtures

Drasar and co-workers [88] have found that a cholic-amide-phenanthroline derivative (**30**) is a very efficient gelator for methanol/water mixtures (especially in a 1/1 ratio).



The structure of the gel has been investigated using several techniques. The IR spectroscopy showed that the self-assembled structure is mainly due to multiple hydrogen-bonding, involving O–H...N interactions between the OH groups on C₃ and C₁₂ and the heterocyclic nitrogens; the third OH (on C₇) interacts with the carbonyl of the amide group { $\nu_{\text{OH}} \approx 3325 \text{ cm}^{-1}$ (broad band) and $\nu_{\text{C=O}}$ at 1689 cm^{-1} (broad band)}.

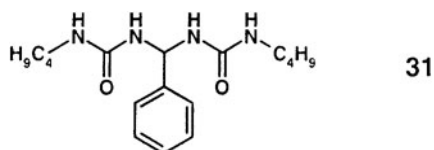
The gelating properties of **30** are strongly affected by the presence of Zn^{II} . In a (4:3) mixture of methanol:chloroform used to dissolve **30** and $\text{ZnSO}_4 \cdot 7\text{H}_2\text{O}$, Zn^{II} is linked to the nitrogens of two phenanthroline units. The IR spectra show strong absorptions at 1525 and 1431 cm^{-1} , associated with the complex. But no further analysis was performed [88].

3.2.9. Bis-urea compounds as gelators for organic solvents; multiple intermolecular hydrogen bonds

Hanabusa and co-workers [20] and van Esch, Feringa and co-workers [89] demonstrated independently the exceptional ability of bis-urea compounds to

form gels in organic solvents. The main driving force in the formation of one-dimensional aggregates appeared to be the multiple intermolecular hydrogen bonds [90].

Evidence for these links rests on FT-IR spectra, since the N-H stretching vibration and the amide I and amide II bands of ureas are known to exhibit large shifts upon the formation of H-bonds. An illustration is given here for compound **31** [91].



At a low concentration (4.4 mM) of compound **31** in 1,2-dichloroethane, a homogeneous solution is obtained. It displays absorptions at 3436 (ν_{NH}) 1690 (amide I) and 1512 (amide II) cm^{-1} , which are characteristic of non H-bonded urea groups. At higher concentration (26.8 mM) a gel is formed, showing bands at 3306 (-130), 1634 (-56) and 1562 ($+50$) cm^{-1} , characteristic of H-bonded urea groups. The absorptions for solid **31** (Nujol mull) (3343, 1632, 1561 cm^{-1}) are closer to that of the gel than those of the homogeneous solution. Molecular modelling and NMR studies were also used for a deeper insight into the gel structure [91].

3.3. IR Absorption Spectroscopy of 2,3-Di-*n*-decyloxanthracene (DDOA). Assignment of Vibration Bands and Dichroic Absorption

2,3-Di-*n*-decyloxanthracene (DDOA) was shown to form gels, at very low concentration, with a large variety of organic liquids [26–29] and other fluids, such as liquid crystals [92] and supercritical CO_2 [93]. The UV-visible absorption and fluorescence spectra have been described and discussed in Section 2.1.3.1.

They reveal that DDOA molecules are strongly associated by intermolecular π - π interactions, involving the aromatic groups; but they do not address the aliphatic chain structure as the chains do not absorb in that region. Moreover, the pure samples were not shown to display any Bragg diffraction patterns in the form of gels, xerogels or aerogels. However, a detailed study of the IR spectra allowed a deeper insight into the gel structure at the molecular level, including that of the chain [94].

3.3.1. Band assignments

The IR spectra of DDOA in CCl_4 solution, in the gel phase and in the solid state (xerogel) are represented in Figure 53. The IR spectrum is sensitive to the sol-gel transition. Assignment of a majority of the vibrational bands was established in order to identify the groups involved in the phase transition and completed by DFT calculation to confirm the assignments and determine the transition moments. The spectra of 2,3-dimethoxyanthracene (DMOA) and 2,3-di-*n*-dihexyloanthracene (DHOA) were also recorded (Figure 53).

The $1000\text{--}400\text{ cm}^{-1}$ region shows the anthracene skeleton out-of-plane vibrations which are little sensitive to the length of the alkoxy chains. In the $1350\text{--}1000\text{ cm}^{-1}$ range, appear the COC groups stretching bands; some of them were found to be coupled to specific in plane motions of the anthracene group. The CH_2 groups were well characterized by the in-phase rocking mode (ν_{CH_2}) at 721 cm^{-1} and the stretching vibrations of the methylene and methyl groups have been well identified at $3000\text{--}2800\text{ cm}^{-1}$. That the aliphatic chains adopt

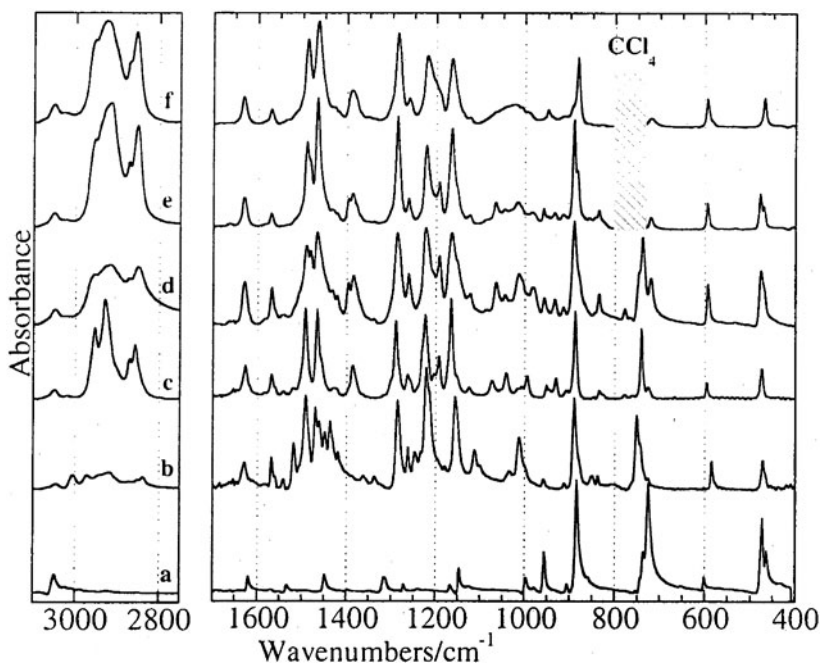


Figure 53. FT-IR spectra of anthracene (a), DMOA (b), DHOA (c), DDOA xerogel (d), DDOA gel (e) and DDOA solution (f). Spectra a-d are recorded in KBr pellets and spectra (e) and (f) are 0.1 M carbon tetrachloride solutions at 0° C (e) or 25° C (f). The cross-hatched area indicates the spectral range where intense CCl_4 absorptions cannot be subtracted. (Reprinted with permission from [94]. Copyright (2003) American Chemical Society.)

an *all-trans* conformation is supported by the presence of a series of weak bands between 1100 and 900 cm^{-1} in the gel (and the solid) which appear as a broad envelop in the isotropic solution (CCl_4) and by the similarity of the frequencies of the methylene stretching vibrations and those expected for the all trans chains [95].

Interestingly, some vibrational modes are split in the gel phase (as well as in the solid), one component being characteristic of the solid, the other of the isotropic solution (Figure 54): thus, the out-of plane anthracene mode (τ_{CCCC} peaking at 469 cm^{-1} in the isotropic solution) is smoothly replaced during the gelation process by a band at 478 cm^{-1} which is characteristic of the solid state. Similar observations can be made for the ε_{CH} out-of-plane mode (882 cm^{-1} in solution, 890 cm^{-1} in the gel).

As shown for DDOA in Figure 53, the spectra of the solid phases (xerogel, microcrystals) and of the gel are similar to each other and different to that of the fluid solution. Moreover, DHOA, which is able to form gel and single crystals [96], behaves as DDOA. These facts indicate that the microscopic organization of these two molecules (DHOA and DDOA) is reminiscent of that found in the crystal.

3.3.2. Dichroic absorption

The IR spectrum of aerogel fibers (produced from supercritical CO_2) which are solvent free, reflects the genuine molecular arrangement of the aggregates;

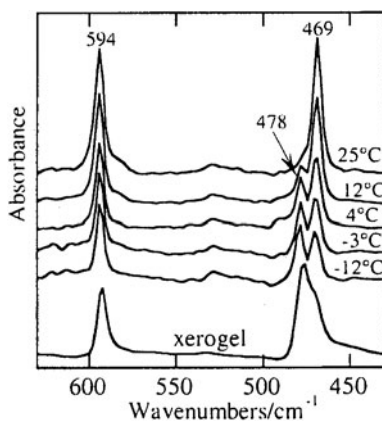


Figure 54. Comparison of IR spectra in the region of the $\alpha(\text{CCC})$ and $\tau(\text{CCCC})$ vibrations for DDOA in its xerogel (KBr pellet) and in a heptane solution (1.2×10^{-2} M) at various temperatures. The sol-gel transition occurs at 22° C. (Reprinted with permission from [94]. Copyright (2003) American Chemical Society.)

the aerogel fibers are therefore ideally suited for probing the molecular organization, using polarized spectroscopy.

Polarized spectra recorded on oriented fibers, reveal strong intensity variations for several bands (see Figure 61; *vide infra*) indicating that DDOA adopts specific orientations inside the fibers. Figure 55 shows that $A_{i\parallel}$ are much smaller than $A_{i\perp}$ for the out-of-plane vibrations of the aromatic group in the 1000–700 cm^{-1} range. Because the transition moments (determined by theoretical calculations) of these vibrations are perpendicular to the anthracene group, it can be deduced that this direction has a larger component perpendicular to the Z axis. Similar considerations for other vibronic bands allowed the evaluation of the orientation factors for the three orthogonal directions K_i from which the α_i -angles could be deduced (Table 1).

It follows that the DDOA molecules are oriented inside the fibers of aerogels as proposed in Figure 56 in which the anthracene long axis (Y_a) is uniaxially directed along Z and the two other axes (X_a and Z_a) display a non cylindrical orientation around the same axis Z . Such an orientation is borne out by linear dichroism studies on the fluorescence spectra [102].

Taking into account the model proposed in Figure 56, the theoretical dichroic ratio for the three kinds of vibrations of the anthracene molecular structure are given by the following equations which, after introduction of the experimental R_i values lead to the unique solution $\theta = 41^\circ$ and $\psi = 28^\circ$.

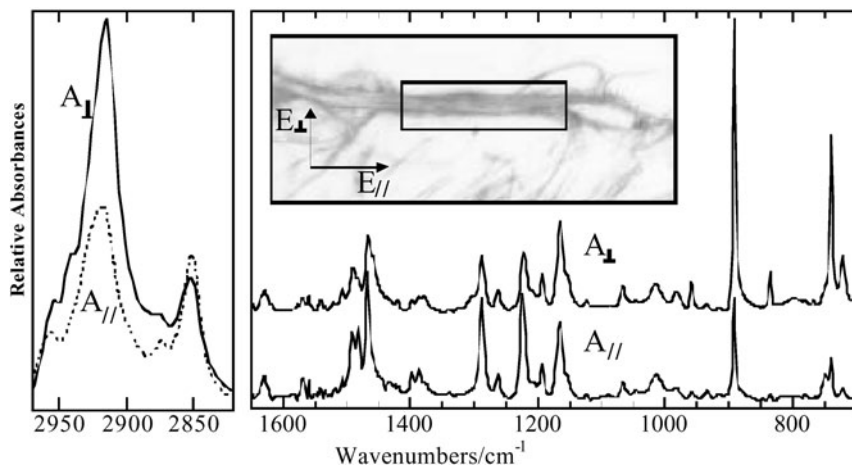


Figure 55. IR spectra of DDOA aerogel fibers recorded with the incident electric vector parallel (bottom) or perpendicular (top) to the fiber axis. A video image of the investigated bundles of aerogel fibers is given in the inset. The size of the inner rectangle is $50 \times 150 \mu\text{m}$. The rectangle was selected through an optical microscope to measure the parallel (A_{\parallel}) and perpendicular (A_{\perp}) polarized spectra relative to the main fiber axis Z . (Reprinted with permission from [94]. Copyright (2003) American Chemical Society.)

Table 1. Orientation factors of DDOA in the aerogel fibers. $\sum K_i$ is equal to 1 within experimental errors.

	Orientation factor			
	K_{XA}	K_{YA}	K_{ZA}	$\sum K_i$
	0.0095	0.51	0.33	0.94
DDOA/aerogel	± 0.012	± 0.05	± 0.02	± 0.08

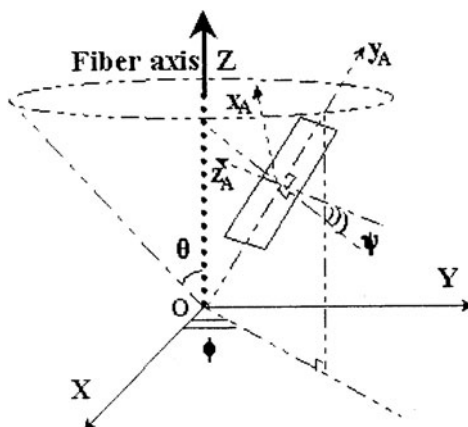


Figure 56. Model of the uniaxial orientation of the Y_A long axis and noncylindrical orientation of the X_A and Z_A axes around the fiber axis Z . The anthracene plane is represented by a rectangle. (Reprinted with permission from [94]. Copyright (2003) American Chemical Society.)

A simple calculation shows that the molecular axes X_A , Y_A and Z_A make angles of 72° , 41° and 55° respectively with the fiber axis.

$$\begin{aligned}
 R_{XA} &= 2A \cdot B / (C + B \cdot D) & A &= \sin^2 \theta \\
 R_{YA} &= 2D / A & B &= \sin^2 \psi \\
 R_{ZA} &= 2A \cdot C / (B + C \cdot D) & C &= \cos^2 \psi \\
 & & D &= \cos^2 \theta
 \end{aligned}$$

The angles obtained from the anthracene vibration modes are similar to those resulting from measurements performed on the aliphatic chains which were found to be in the alignment of the anthracene group.

From the mean orientation of DDOA with respect to the fiber axis and the spectral similarity of the gel and the solid (IR, UV and DHOA single crystals), the authors have modeled the molecular arrangements within the fibers (MM studies, AMBER program). The optimized structure (Figure 57) of clusters of 18 DDOA molecules shows little change compared to the crystal structure of DHOA [96].

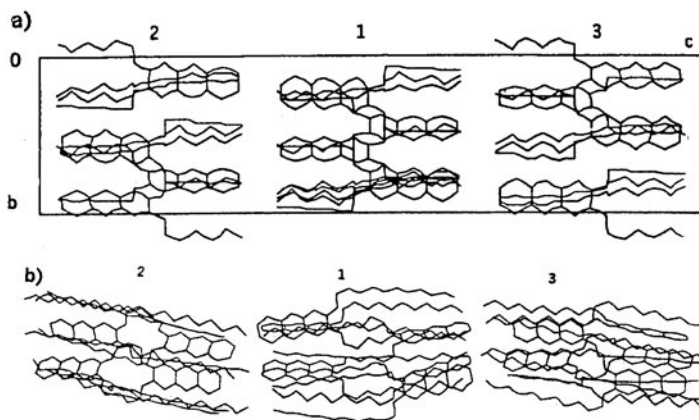


Figure 57. a) Projection of the DHOA unit cell along the a axis. The cell includes 3 blocks (numbered 1–3) that contain 2 triads each. b) Amber-optimized cluster of 18 DDOA molecules displaying an organization similar to that of the DHOA unit cell. (Reprinted with permission from [94]. Copyright (2003) American Chemical Society.)

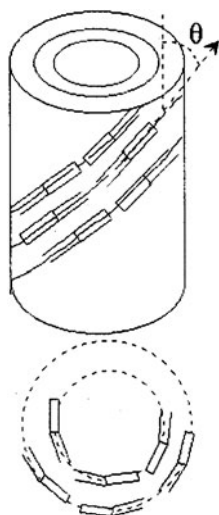


Figure 58. Proposed arrangement of DDOA in the aerogel fiber. (Reprinted with permission from [94]. Copyright (2003) American Chemical Society.)

In the gel, the transversal molecular interactions are reduced, inducing truncations along the A and B directions. It also appears that the aliphatic chains adopt an angular orientation with respect to the anthracene group. The misalignment of the blocks building the gel induces a curved one-dimensional stacking on concentric cylinders (Figure 58) [94].

4. Conclusions and Perspectives for the Future

The wide variety of spectroscopic investigations described in this chapter illustrates the scope and usefulness of UV-vis and IR spectroscopies in the studies of low molar organic gelators (LMOGs). In many cases, these tools are indispensable to characterize a gel phase, and even different types of aggregates inside a gel phase. They provide information not only on gel structure (N.B., stacking, helicoidal organisation, H-bond networks, etc.) but also on the formation process (N. B., critical aggregation concentration, critical gelator concentration, temperature of gelation, etc.). From these investigations, several aspects of gelator structures and gels themselves emerge, as well as propitious avenues for future explorations:

1. π - π stacked aggregates can be a driving force for gel formation and molecules that allow π - π stacking may lead to new, robust LMOGs.
2. Some electron donor-acceptor (charge-transfer, CT) complexes show strong gelating ability, indicating that gelators that form transition metal charge-transfer (LMCT) complexes should be pursued in the future.
3. Gel structures can act as matrices for energy transfer between donor and acceptor species; see Chapter 23 for details. The specific properties of the energy transfer can reveal details of gel structures that are very difficult to obtain using other methods.
4. Other spectroscopic techniques, such as *phosphorescence* [97] or *Raman* coupled with IR spectroscopy, have been exploited to a very limited extent in the investigation of gels, thus far. The information they can provide complements the data from other methods but is not always duplicated by them. Therefore, more attention to these techniques is warranted for the characterization of appropriate gels.
5. Within the last several years, considerable progress has been made to develop spectroscopic tools for the investigation of gels. Nevertheless, there are very few detailed physical chemical investigations that include complete assignment of electronic and vibration transitions of gel structures and that are coupled with theoretical calculations [94]. Many more are needed if the field of molecular gels is to grow and develop.

References

- [1] Lehn, J.-M. *Supramolecular Chemistry, Concepts and Perspectives*, Weinheim: VCH, **1995**.
- [2] Hoffmann, H.; Ebert, G. *Angew. Chem. Int. Ed. Engl.*, **1988**, *27*, 902.
- [3] Guenet, J.-M. *Thermoreversible Gelation of Polymers and Biopolymers*, London: Acad. Press, **1992**.
- [4] Daniel, C.; Dammer, C.; Guenet, J.-M. *Polymer*, **1994**, *35*, 4243.

- [5] a) Terech, P.; Weiss, R.G. *Chem. Rev.*, **1997**, *97*, 3133; b) Terech, P. *Ber. Bunsenges. Phys. Chem.*, **1998**, *102*, 1630.
- [6] Jaffé, H.H.; Orchin, M. *Theory and Applications of Ultraviolet Spectroscopy*, New York: J. Wiley, **1965**.
- [7] Williams, D.H.; Fleming, I. *Spectroscopic Methods in Organic Chemistry*, London: McGraw-Hill, **1966**, Chap 2.
- [8] Stern, E.S.; Timmons, C.J. *Introduction to Electronic Absorption Spectroscopy in Organic Chemistry*, London: Edward Arnold Ltd, **1970**.
- [9] Barrow, G.M. *Molecular Spectroscopy*, New York: McGraw Hill, **1962**, Chaps. 10 and 11.
- [10] Gilbert, A.; Baggott, J. *Essentials of Molecular Photochemistry*, Oxford: Blackwell Scientific Publications, **1991**.
- [11] Mataga, N.; Kubota, T. *Molecular Interactions and Electronic States*, New York: M. Dekker Inc., **1970**, Chaps. 2 and 3.
- [12] Valeur, B. *Molecular Fluorescence, Principles and Applications*, Weinheim: Wiley-VCH, **2002**, Chap. 2 (Absorption of UV-visible light).
- [13] a) Davydov, A.S. *Theory of Molecular Excitons*, M. Kasha, M. Oppenheimer Jr. translators, New York: McGraw Hill, **1962**. b) Kauzman, W.J.; Walter, J.E.; Eyring, H. *Chem. Rev.*, **1940**, *26*, 339.
- [14] a) Ihara, H.; Yoshitake, M.; Takafuji, M.; Yamada, T.; Sagawa, T.; Hirayama, C.; Hachisado, H. *Liq. Cryst.*, **1999**, *26*, 1021. b) Sagawa, T.; Fukugawa, S.; Yamada, T.; Ihara, H. *Langmuir*, **2002**, *18*, 7223.
- [15] a) McRae, E.G.; Kasha, M. "H-aggregates", *J. Chem. Phys.*, **1958**, *28*, 721. b) Kasha, M.; Rawls, H.R.; El Bayoumi, M.A.E. "H-aggregates", *Pure Appl. Chem.*, **1965**, *11*, 371. c) Kunisawa, T.; Sato, T.; Yonezawa, Y.; Popova, G.V. "H-aggregates", *Thin Solid Films*, **1997**, *311*, 267. d) Kobayashi, T. Ed., *J-aggregates*: Singapore: World Scientific, **1996**.
- [16] Lin, Y.C.; Kachar, B.; Weiss, R.G. *J. Am. Chem. Soc.*, **1989**, *111*, 5542.
- [17] Saeva, F.D.; Wysocki, J.-J. *J. Am. Chem. Soc.*, **1971**, *93*, 5928.
- [18] Yamamoto, S. *Kogyo Kagaku Zasshi*, **1942**, *45*, 695.
- [19] Yamasaki, S.; Tsutsumi, H. *Bull. Chem. Soc. Jpn*, **1994**, *67*, 2053 and **1996**, *69*, 561.
- [20] Hanabusa, K.; Yamada, M.; Kimura, M.; Shirai, H. *Angew. Chem. Int. Ed. Engl.*, **1996**, *35*, 1949.
- [21] Bühler, G.; Feiters, M.C.; Nolte, R.J.M.; Dötz, K.H. *Angew. Chem. Int. Ed.*, **2003**, *42*, 2494.
- [22] Murata, K.; Aoki, M.; Suzuki, T.; Harada, T.; Kawabata, H.; Komori, T.; Ohseto, F.; Veda, K.; Shinkai, S. *J. Am. Chem. Soc.*, **1994**, *116*, 6664.
- [23] de Loos, M.; Van Esch, J.; Kellogg, R.M.; Feringa, B.L. *Angew. Chem. Int. Ed.*, **2001**, *40*, 613.
- [24] Maitra, U.; Potluri, V.K.; Sangeetha, N.M.; Babu, P.; Raju, A.R. *Tetrahedron Asymmetry*, **2001**, *12*, 477.
- [25] Xing, B.; Yu, C.W.; Chow, K.H.; Ho, P.L.; Fu, D.; Xu, B. *J. Am. Chem. Soc.*, **2002**, *124*, 14846.
- [26] Brotin, T.; Utermöhlen, R.; Fages, F.; Bouas-Laurent, H.; Desvergne, J.-P. *J. Chem. Soc. Chem. Commun.*, **1991**, 416.
- [27] Brotin, T. Thèse, Université Bordeaux I, Talence, France, **1990**.
- [28] Terech, P.; Meerschaut, D.; Desvergne, J.-P.; Colomes, M.; Bouas-Laurent, H. *J. Colloid Interf. Sci.*, **2003**, *261*, 441.
- [29] Desvergne, J.-P.; Brotin, T.; Meerschaut, D.; Clavier, G.; Placin, F.; Pozzo, J.-L.; Bouas-Laurent, H. *New J. Chem.*, **2004**, in press.

- [30] Lin, Y.C.; Weiss, R.G. *Macromolecules*, **1987**, *20*, 414.
- [31] van der Auweraer, M.; Biesmans, G.; de Schryver, F.C. *Chem. Phys.*, **1988**, *119*, 355.
- [32] Furman, I.; Weiss, R.G. *Langmuir*, **1993**, *9*, 2084.
- [33] Yoza, K.; Amanokura, N.; Ono, Y.; Akao, T.; Shinmori, H.; Takenchi, M.; Shinkai, S.; Reinhoudt, D.N. *Chem. Eur. J.*, **1999**, *5*, 2722.
- [34] Gronwald, O.; Snip, E.; Shinkai, S. *Current Opinion in Colloid and Interface Science*, **2002**, *7*, 148.
- [35] Kobayashi, H.; Friggeri, A.; Koumoto, K.; Amaike, M.; Shinkai, S.; Reinhoudt, D.N. *Org. Lett.*, **2002**, *4*, 1423.
- [36] Tamaru, S.; Nakamura, M.; Takeuchi, M.; Shinkai, S. *Org. Lett.*, **2001**, *3*, 3631.
- [37] Tamaru, S.; Uchino, S.; Takeuchi, M.; Ikeder, M.; Hatano, T.; Shinkai, S. *Tetrahedron Lett.*, **2002**, *43*, 3751.
- [38] Jorgensen, M.; Bechgaard, K. *J. Org. Chem.*, **1994**, *59*, 5877.
- [39] Jaffé, H.H.; Orchin, M. *Theory and Applications of Ultraviolet Spectroscopy*, New York: J. Wiley and Sons, **1965**, pp. 270–273.
- [40] Murrel, J.N.; Kettle, S.F.A.; Tedder, J.M. *Valence Theory*, London: J. Wiley and Sons, **1965**, Chap. 18.
- [41] Mataga, N.; Kubota, T. *Molecular Interactions and Electronic Spectra*, New York: M. Dekker, **1970**, Chap. 6, pp. 201–291.
- [42] Davis, K.M.C. *Molecular Association*, R. Foster, Ed., London: Academic Press, **1975**, *1*, Chap. 3, pp. 151–213.
- [43] Barltrop, J.A.; Coyle, J.D. *Excited States in Organic Chemistry*, London: J. Wiley, **1975**.
- [44] Soos, Z.G.; Klein, D.J. *Charge-Transfer in Solid-State Complexes in Molecular Association*, R. Foster, Ed., London: Academic Press, **1975**, *1*, Chap. 1, pp. 2–109.
- [45] Astruc, D. *Chimie Organométallique*, Les Ulis: EDP Sciences, **2000**.
- [46] Maitra, U.; Vijaykumar, P.; Chandra, N.; D'Souza, L.J.; Prasanna, M.D.; Raju, A.R. *Chem. Commun.*, **1999**, 595–596.
- [47] Babu, P.; Sangeetha, N.M.; Vijaykumar, P.; Maitra, U.; Rissanen, K.; Raju, A.R. *Chem. Eur. J.*, **2003**, *9*, 1922.
- [48] Friggeri, A.; Gronwald, O.; van Bommel, K.J.C.; Shinkai, S.; Reinhoudt, D.N. *J. Am. Chem. Soc.*, **2002**, *124*, 10754.
- [49] Gilbert, A.; Baggott, J. *Essentials of Molecular Photochemistry*, Oxford: Blackwell Scientific Publication, **1991**, Chap. 5, pp. 168–181.
- [50] Förster, Th.; Kasper, K.Z. *Phys. Chem. N. F.*, **1954**, *1*, 275; *Z. Electrochem.*, **1955**, *59*, 976.
- [51] Birks, J.B. *Photophysics of Aromatic Molecules*, New York: J. Wiley, **1970**.
- [52] Mataga, N.; Kubota, T. *Molecular Interactions and Electronic Spectra*, New York: M. Dekker Inc., **1970**, Chap. 9, pp. 411–484.
- [53] Bouas-Laurent, H.; Lapouyade, R.; Castellan, R.; Nourmamode, A.; Chandross, E.A. *Z. Phys. Chem. N. F.*, **1976**, *101*, 39.
- [54] Stevens, B.; Hutton, E. *Nature*, **1960**, *186*, 1045.
- [55] Winnik, F.M. *Chem. Rev.*, **1993**, *93*, 587.
- [56] Staab, H.A.; Sauer, M. *Liebigs Ann. Chem.*, **1984**, 742 and references therein.
- [57] a) Desvergne, J.-P.; Fages, F.; Bouas-Laurent, H.; Marsau, P. *Pure Appl. Chem.*, **1992**, *64*, 1231. b) Marsau, P.; Bouas-Laurent, H.; Desvergne, J.-P.; Fages, F.; Lamotte, M.; Hirschberger, J. *Mol. Cryst. Liq. Cryst. Nonlin. Opt.*, **1988**, *156*, 383. c) Bouas-Laurent, H.; Castellan, A.; Daney, M.; Desvergne, J.-P.; Guinand, G.; Marsau, P.; Riffaud, M.H. *J. Am. Chem. Soc.*, **1986**, *108*, 315.

- [58] a) Ferguson, J.; Morita, H.; Puza, M. *Chem. Phys. Lett.*, **1976**, *42*, 288. b) Ferguson, J. *Chem. Rev.*, **1986**, *86*, 957.
- [59] Jover, A.; Mejjide, F.; Rodriguez Núñez, E.; Vázquez Tato, J.; Mosquera, M.; Rodriguez Prieto, F. *Langmuir*, **1996**, *12*, 1789.
- [60] Xing, B.; Yu, C.-W.; Chow, K.-H.; Ho, P.-L.; Fu, D.; Xu, B. *J. Am. Chem. Soc.*, **2002**, *124*, 14846.
- [61] Ikeda, M.; Takeuchi, M.; Shinkai, S. *Chem. Commun.*, **2003**, 1354.
- [62] Mataga, N.; Kubota, T. *Molecular Interactions and Electronic Spectra*, New York: M. Dekker Inc., **1970**, Chap. 5, pp. 171–200.
- [63] Turro, N.J. *Modern Molecular Photochemistry*, CA: Benjamin/Cummins, Menlo Park, **1978**.
- [64] Nakashima, T.; Kimizuka, N. *Adv. Mater.*, **2002**, *14*, 1113.
- [65] Ajayaghosh, A.; George, S.J.; Praveen, V.K. *Angew. Chem. Int. Ed.*, **2003**, *42*, 332, see also: *J. Am. Chem. Soc.*, **2001**, *123*, 5148.
- [66] Sugiyasu, K.; Fujita, N.; Takeuchi, M.; Yamada, S.; Shinkai, S. *Org. Biomol. Chem.*, **2003**, *1*, 895.
- [67] Armaroli, N.; de Cola, L.; Balzani, V.; Sauvage, J.P.; Dietrich-Buchecker, C.O.; Kern, J.-M. *J. Chem. Soc. Faraday Trans.*, **1992**, 553.
- [68] Amaike, M.; Kobayashi, H.; Shinkai, S. *Chem. Lett.*, **2001**, 620.
- [69] Reichardt, C. *Solvents and Solvent Effects in Organic Chemistry*, Weinheim: VCH, **1990**.
- [70] van der Laan, S.; Feringa, B.L.; Kellog, R.M.; van Esch, J. *Langmuir*, **2002**, *18*, 7136.
- [71] Dyer, J.B. *Applications of Absorption Spectroscopy of Organic Compounds*, NJ: Prentice-Hall Englewood Cliffs, **1965**, Chap. 3.
- [72] Nakanishi, K. *Infrared Absorption Spectroscopy*, San Francisco: Practical-Holden-Day, **1964**.
- [73] Banwell, C.N. *Fundamentals of Molecular Spectroscopy*, London: McGraw-Hill, **1972**.
- [74] Bellamy, L.J. *The Infrared spectra of Complex Molecules*, 3rd ed., Chapman and Hall, **1975**.
- [75] Smith, A.L. *Appl. Spectroscopy*, **1987**, *41*, 1101.
- [76] *Handbook of Vibrational Spectroscopy, Vol 1*, J.M. Chalmers and P.R. Griffiths, Eds., New York: John Wiley & Sons Ltd, **2002**, pp. 693–740.
- [77] Bower, D.J. “Infrared dichroism, polarized fluorescence and Raman spectroscopy”, In *Structure and Properties of oriented Polymers*, I.M. Ward, Ed., London: Chapman Hall, **1997**, Chap. 4, pp. 181–231.
- [78] Wilder, E.A.; Hall, C.K.; Khan, S.A.; Spontak, R.J. *Recent Res. Develop. Mat. Sci.*, **2002**, *3*, 93.
- [79] a) Roehl, E.L.; Tan, H.B. *US Patent*, **1979**, *4*, 154, 816. b) Fernandez, J.A. *US Patent*, **1980**, *4*, 187, 072. c) Nahir, T.M.; Quiu, Y.-J.; Williams, J.L. *Electroanalysis*, **1994**, *6*, 972. d) Isogawa, H.; Anraku, H. *US Patent*, **1996**, *5*, 510, 237. e) Ishiwatari, T.; Tsushima, K. *US Patent*, **1996**, *5*, 554, 649. f) Kasat, R.B.; Lee, W.; McCarthy, D.R.; Telyan, N.G. *US Patent*, **1996**, *5*, 490, 979. g) Kato, T.; Kondo, G.; Hanabusa, K.; Kutsuna, T.; Ukon, M. *US Patent*, **2000**, *6*, 074, 710. h) Bhatt, D.; Rizvi, R.; Galleguillos, R. *US Patent*, **2000**, *6*, 132, 704. i) Acuna, G.; Frater, G.; Gygax, P. *US Patent*, **2000**, *6*, 150, 542.
- [80] Yamasaki, S.; Ohashi, Y.; Tsutsumi, H.; Tsuju, K. *Bull. Chem. Soc. Jpn.*, **1995**, *68*, 146.
- [81] Garner, C.M.; Terech, P.; Allegrand, J.J.; Mistrot, B.; Nguyen, P.; de Geyer, A.; Riviera, D. *J. Chem. Soc. Faraday Trans.*, **1998**, *94*, 2173.

- [82] Hanabusa, K.; Tange, J.; Taguchi, Y.; Koyama, T.; Shirai, H. *J. Chem. Soc. Chem. Commun.*, **1993**, 390.
- [83] Hanabusa, K.; Naka, Y.; Koyama, T.; Shirai, H. *J. Chem. Soc. Chem. Commun.*, **1994**, 2683.
- [84] Luo, X.; Liu, B.; Liang, Y. *Chem. Commun.*, **2001**, 1556.
- [85] Suzuki, M.; Yumoto, M.; Kimura, M.; Shirai, H.; Hanabusa, K. *New J. Chem.*, **2002**, 26, 817.
- [86] Malik, S.; Maji, S.K.; Banerjee, A.; Nandi, A.K. *J. Chem. Soc. Perkin Trans.*, **2002**, 2, 1177.
- [87] Kiyonaka, S.; Shinkai, S.; Hamachi, I. *Chem. Eur. J.*, **2003**, 9, 976.
- [88] Dukh, M.; Šaman, D.; Kroulík, J.; Cerný, I.; Pouzar, V.; Král, V.; Drašar, P. *Tetrahedron*, **2003**, 59, 4069.
- [89] van Esch, J.; Kellogg, R.M.; Feringa, B.L. *Tetrahedron Lett.*, **1997**, 38, 281.
- [90] van Esch, J.; Schoonbeek, F.; de Loos, M.; Kooijman, H.; Spek, A.L.; Kellogg, R.M.; Feringa, B.L. *Chem. Eur. J.*, **1999**, 5, 937.
- [91] Schoonbeek, F.; van Esch, J.; Hulst, R.; Kellogg, R.M.; Feringa, B.L. *Chem. Eur. J.*, **2000**, 6, 2633.
- [92] Kato, T.; Kutsuna, T.; Yabuuchi, K.; Mizoshita, N. *Langmuir*, **2002**, 18, 7086.
- [93] Placin, F.; Desvergne, J.-P.; Cansell, F. *J. Mater. Chem.*, **2000**, 10, 2147.
- [94] Placin, F.; Desvergne, J.-P.; Belin, C.; Buffeteau, T.; Desbat, B.; Ducasse, L.; Lassègues, J.-C. *Langmuir*, **2003**, 19, 4563.
- [95] Ricard, L.; Abbate, S.; Zerbi, G. *J. Phys. Chem.*, **1985**, 89, 4793.
- [96] Pozzo, J.-L.; Desvergne, J.-P.; Clavier, G.M.; Bouas-Laurent, H.; Jones, P.G.; Perlstein, J. *J. Chem. Soc. Perkin Trans.*, **2001**, 2, 824.
- [97] Itoh, T.; Katsoulis, D.E.; Mita, I. *J. Mater. Chem.*, **1993**, 3, 1303. The phosphorescence spectra of poly(dimethylsiloxane) (PDMS) gels of cholesteryl anthraquinone-2-carboxylate (CAQ) were investigated at 77K. This is particularly useful for substrates having a low fluorescence quantum yield.

Chapter 13

CIRCULAR DICHROISM FOR STUDYING GEL-LIKE PHASES

Giovanni Gottarelli¹, Gian Piero Spada¹ and Ettore Castiglioni²

¹*Alma Mater Studiorum – Università di Bologna, Dipartimento di Chimica Organica “A. Mangini”, via San Giacomo II-40126 Bologna, Italy*

²*JASCO EUROPE srl, via Confalonieri 25, 23894 Cremella, Italy*

1. Introduction	431
2. Technique	432
2.1. How to Obtain CD Spectra	433
2.2. Experimental Problems	434
3. Applications to the Study of Gel-Like Phases	435
4. Conclusions and Perspectives for the Future	445

1. Introduction

Chiroptical spectroscopies, optical rotatory dispersion (ORD) and circular dichroism (CD) [1], were developed in the 1960s to study mainly steroidal ketones [2] and octahedral metal complexes [3]. Subsequently, several different chromophores were investigated by CD using different theoretical analyses [4]; the exciton approach, in particular, has been very successful for studying molecular systems containing two or more absorbing chromophores, for example, biaryls [4, 5] and proteins [6]. At the present time, the outstanding sensitivity of CD is employed mainly to study biological macromolecules and their perturbations by external factors. In the field of supramolecular chemistry, CD has several interesting applications. In particular, assembly processes leading to the formation of helical superstructures can be investigated [7]. In those cases where gels are formed by chiral monomers through self-assembly processes, it seems natural to use CD to monitor the progress of the process and, hopefully, to obtain information on the assembled structures that complements that from other techniques (see Chapters 10–12).

2. Technique

The basic principles of CD spectroscopy can be found in several specialized books [1, 4, 5]. A CD spectrometer measures the different absorption of left and right circularly polarized light by a chiral sample as a function of wavelength; standard instruments cover the UV-VIS region, while more specialized models extend to the vacuum-UV or the near-IR and IR ranges. Figure 1 is a diagram of a modern CD spectrometer in which circularly polarized light is generated by an optical modulator [8].

The layout of a spectrometer is practically very similar to a conventional, single beam, UV-VIS spectrophotometer. The strong white light emission of the Xe source necessitates the use of a double monochromator to reduce stray light; moreover, prisms rather than gratings are used as dispersive elements. Prisms perform better in the far-UV where most of CD spectra are run and prisms generate linearly polarized light without any additional optical component.

Inserting a chiral absorbing sample into the compartment, the photomultiplier tube detector will output a signal with two components:

- i) a DC one, proportional also to the regular absorption of the sample;
- ii) an AC one (at 50 kHz), whose intensity and phase will be related to the CD of the sample.

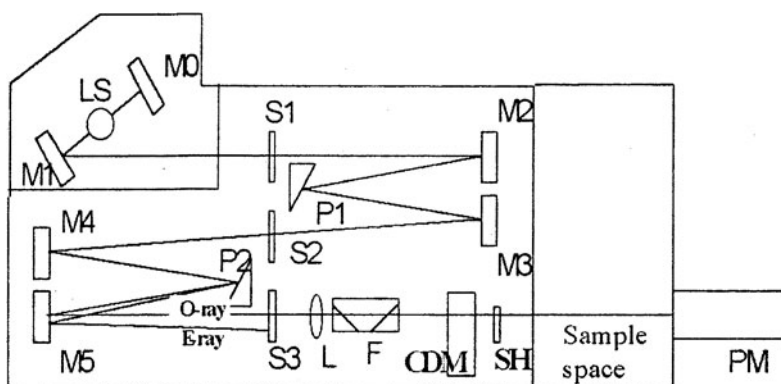


Figure 1. Diagram of a modern CD spectrometer. LS: light source, typically a 150 W Xe lamp, with quartz envelope (it emits a strong continuous spectrum in the 180–900 nm range); M_1 : elliptical mirror to focus radiation on the entrance slit (S_1) of the monochromator; M_0 : spherical mirror to collect back-emitted radiation of the source; S_1 , S_2 , S_3 : entrance, intermediate and exit slit of the double monochromator; M_2 – 4 : spherical collimating mirrors of the monochromator; P_1 , P_2 : quartz prisms, used to disperse radiation and to generate a linearly polarized output (E-ray, the crossed polarization light will not get out of monochromator since trapped by exit slit); L: quartz lens to get a parallel beam through sample compartment; F: series of 45° quartz plates to clean further the polarization; CDM: photoelastic modulator, acting as an achromatic quarter wave plate generating left and right circularly polarized radiation at its oscillation frequency (50 kHz); SH: mechanical shutter to remove, when needed, light on the sample; PM: photomultiplier tube detector.

The correct CD is actually the ratio of the AC versus the DC components, so practically the instruments measure only the AC component (with a lock-in amplifier), while the DC part is kept constant by dynode feedback (i.e., changing automatically the voltage applied to the PM tube).

Using this approach it might seem that the information on the sample transmittance given by the DC level will be lost. This is not the case since single beam sample transmittance (and absorbance) may be extracted from the high voltage applied to the PM tube. Thus, from a single scan, both CD and absorption spectra of the sample can be extracted.

CD is measured either as ellipticity Θ or as differential absorption ΔA ; the following relation correlates the two values:

$$\Delta A = \Theta/32980$$

where ΔA is in absorbance units and Θ in mdeg.

Literature data are typically reported as molar ellipticity,

$$[\Theta] = \Theta/(10Cl) = \Theta M_w/(cl10000)$$

where Θ is the ellipticity (in mdeg), C is the molar concentration (mol/L), c is the w/v concentration (g/mL), M_w is the molecular weight and l is the cell path (in cm). Alternatively, the molar circular dichroism is:

$$\Delta\varepsilon = \varepsilon_L - \varepsilon_R = \Delta A/(Cl)$$

It is related to molar ellipticity by the relation:

$$[\Theta] = 3298\Delta\varepsilon$$

In a few cases, another scale, the anisotropy factor, is used:

$$g = \Delta\varepsilon/\varepsilon = \Delta A/A$$

It is independent of concentration and linearly related to the enantiomeric excess. Note that ΔA , Θ , $\Delta\varepsilon$, and g take on different values at each wavelength, λ .

2.1. How to Obtain CD Spectra

The operations of a CD are very similar to those required for a conventional UV-VIS spectrophotometer. Sampling cells and optimal sample concentration are the same as for UV-VIS spectroscopy. One typically runs the sample first, optimizing parameters to improve results, and later collects the baseline spectrum (typically, the solvent in the same sample cell as employed for the solution) under the same conditions.

However, the technique is much more limited with regard to signal-to-noise (s/n) than UV-VIS spectroscopy. Because practical g factors of many chiral samples are in the 10^{-3} – 10^{-4} range, spectral measurements may require the use of a long time constant to reduce the noise. A common alternative practice is to average multiple scans automatically, improving in this way the s/n by the square root of the number of accumulations.

2.2. Experimental Problems

The CD technique is typically suitable for samples measured in isotropic solution (or more rarely in the gas phase). Factors such as sample turbidity, birefringence and linear dichroism (caused for example by macroscopic anisotropies) may seriously affect the data [9]. Solid sampling may be difficult or may call for dedicated accessories/special hardware [10].

The limitations are many. The main one originates in the optical properties of the photoelastic modulator whose residual static birefringence may distort data. Furthermore, any optical imperfection of the various components (for example, the photomultiplier tube surface) may cause artifacts when working with weakly dichroic samples [11]. The lock-in detection technique, which measures the signal only at the modulation frequency of the photoelastic modulator crystal, is also prone to errors. Signals at double frequency (like those generated by sample linear dichroism) are impossible to remove completely and may distort the final data. For these and other reasons, the *observed* CD spectra may be different from the real ones, and ways to compensate for or correct the spectra are not easy. Thus, several data in the literature are known to be questionable or even incorrect, since no care has been taken to prevent or correct for artifacts.

As a general rule, simultaneous measurement of the linear dichroism (LD) spectra may give clear warnings that the CD spectra are not correct. Simultaneous LD measurement is an easy task. It requires only the addition of a second lock-in amplifier operating at double frequency. Measurement of sample birefringence may help, too. This is a rather more complex task because the unit must be equipped with an extra polarizer in front of the detector.

On the other hand, these sources of potential errors are also the basis for obtaining additional information about the sample. The reasons for the difference between an *observed* and *real* CD may provide additional, valuable information on the sample [12] which is not strictly related to chirality, such as data on the optical homogeneity of multi-layered structures [13].

Although relatively little attention has been paid to these effects in the past, more recent literature provides a deeper understanding of these effects and the use of experimental methods to control them [14].

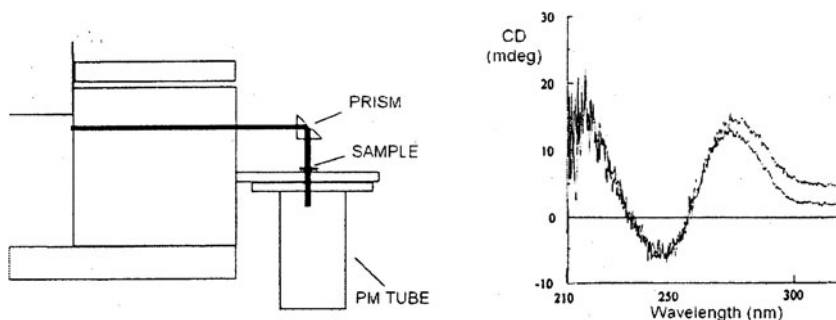


Figure 2. An apparatus for semi-solid samples (left). The sampling beam is deflected 90° to allow horizontal measurements on a soft sample deposited on a quartz plate. The plate itself is thermostatted. At high temperatures, horizontal mounting is the only practical way to avoid sample flow if viscosity decreases. Beam deflection is achieved using a 90° quartz prism, since the use of a simple mirror is not suitable (a 45° mirror would induce strong LD components, masking the CD data). The reliability of the device has been tested measuring a DNA solution in normal sampling position and in the horizontal set-up (right). The overlay is quite acceptable.

Other difficulties originate from the nature of the sample itself. Samples which scatter light will significantly reduce the number of photons reaching the detector; in such cases, the usual approach is to place the sample as close as possible to the photomultiplier tube surface to increase solid angle collection; more sophisticated approaches, such as employing a *fluoroscatter* cell [15], have been proposed, but rarely used. Alternatively, simple accessories can be arranged to measure separately the regularly transmitted and the scattered components, but the effects of scattering on polarized light are rather complex and would call for complicated data treatment [16]. Dealing with semi-solids may be problematic also because the sample may not be kept in the usual vertical position. Figure 2 shows a set-up designed to accommodate semi-solids.

3. Applications to the Study of Gel-Like Phases

In general, for standard solutions, there is a direct correlation between the regions of absorption and CD. In the case of non-coupled chromophores, the shapes of the two spectra are similar (Figure 3), although the vibrational fine structure can be different. If two or more strongly absorbing chromophores are oriented chirally with respect to each other, an exciton spectrum is observed and the λ_{\max} in absorption corresponds, or nearly corresponds, to *zero* CD intensity (Figure 4).

The latter case is rather frequent during the formation of helical aggregates which are the common basis of gel formation by chiral gelators. During self-assembly processes leading to gel formation, the CD spectrum undergoes

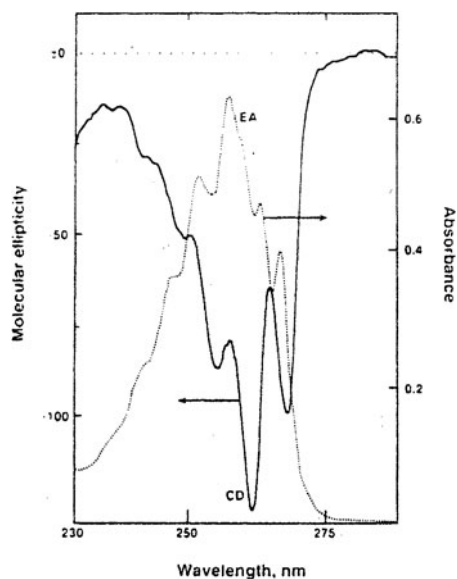
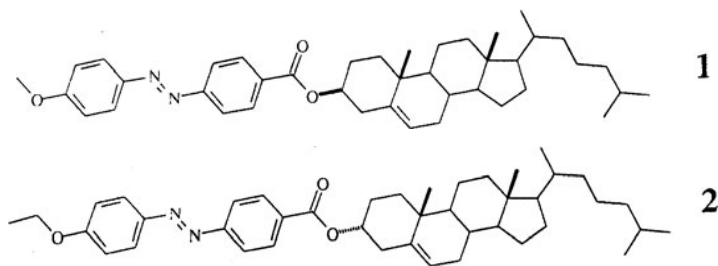


Figure 3. CD and UV spectra of (*R*)-2-amino-1-phenylpropane hydrochloride in 0.1 M KOH in methanol (for the UV spectrum: $c = 3.3$ mM). Adapted with permission from [17]. Copyright (1996) American Chemical Society.

dramatic modifications: the intensity of some bands may increase considerably with respect to those of the unaggregated molecules while other bands may disappear. For example, the spectrum of an unaggregated molecule (like that of Figure 3) may have low intensity. During self-assembly, a new shape begins to appear and the overall intensity eventually becomes much higher (See, for example, Figure 5) [18]. The CD at high temperatures will eventually lead to the spectrum of the isolated molecules if aggregation is reversible, and the melting temperature (T_m) of the system can be inferred from a plot of the variation of intensity at selected wavelengths as a function of temperature (Figure 6) [19].

Also, solvent effects can be readily studied by comparing CD spectra. In particular, a comparison of the spectrum in an H-bonding solvent (e.g., methanol) with that in a less polar solvent provides insights about the importance of H-bonds in the formation of the aggregate.



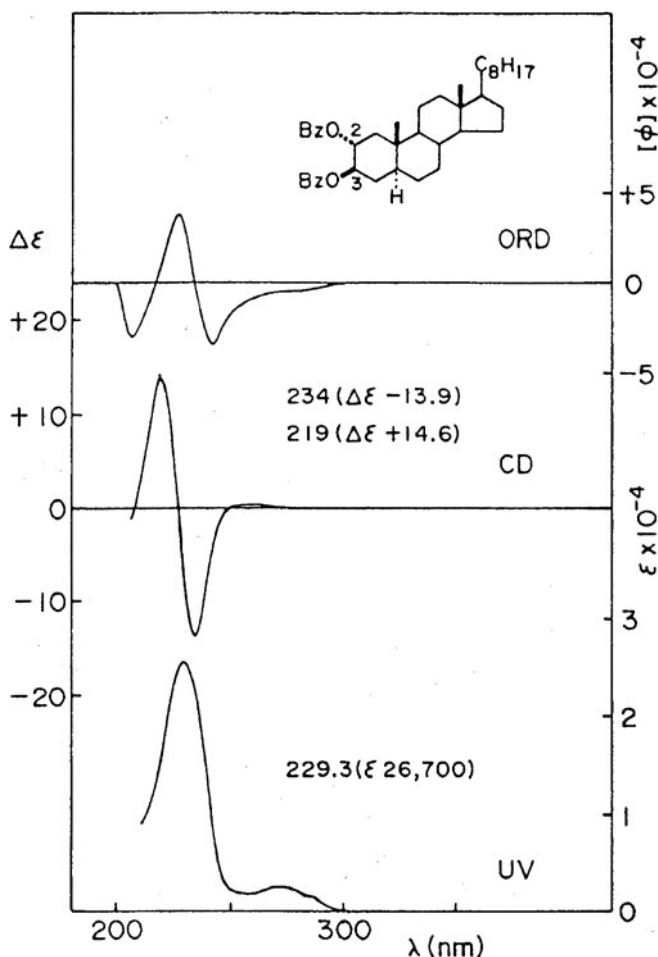


Figure 4. ORD, CD and UV spectra of 5α -cholestane- $2\alpha,3\beta$ -diol dibenzoate in dioxane/ethanol. Adapted with permission from [5]. Copyright (1983) University Science Books.

The presence of an exciton spectrum may be observed during the self-assembly of molecules which show non-coupled spectra (such as that in Figure 3) in the isolated state. This indicates that in the aggregate, the chromophores are arranged in a chiral array, often helicoidal. This allows one to hypothesize several possible assembled structures [20]. However, in order to obtain more precise information on the structure of the assembled species from an exciton spectrum, it is necessary to know the direction of the transition moments of the chromophores involved. The coupling of these moments in a possible model can be calculated, and comparison between the theoretical results and the experimental data can refine the hypotheses. In general, it is not easy to obtain structural information from CD spectra alone, and other

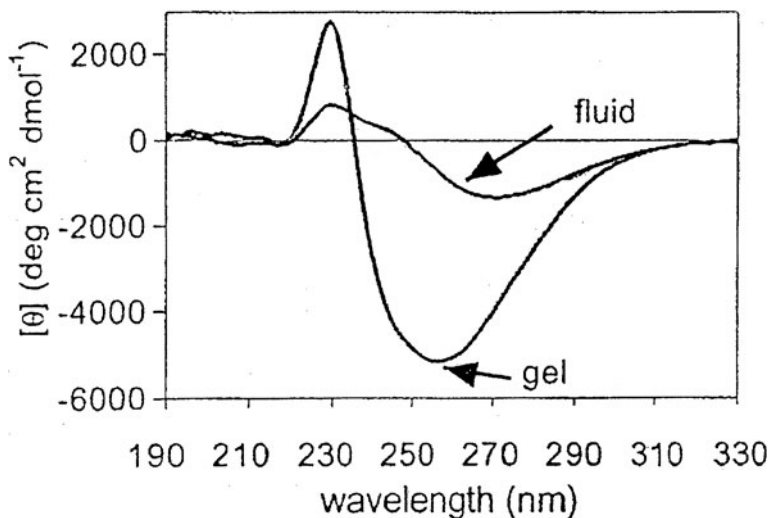


Figure 5. CD spectra of the disulfide form of glutathione GSSG 1mM in 90% methanol as a function of temperature (sample in the gel phase at $T = -10^{\circ}\text{C}$ and in the fluid phase at $T = 20^{\circ}\text{C}$). Adapted with permission from [18]. Copyright (2001) American Chemical Society.

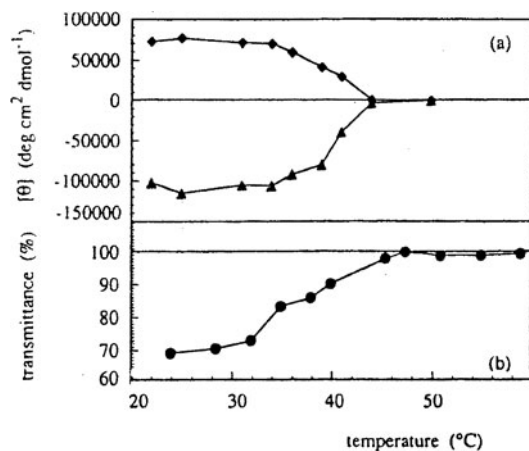


Figure 6. Temperature dependence of CD at two wavelengths (the two maxima of the exciton coupling around 305 nm) and of transmittance in a region out-of-electronic absorptions of 0.2% (w/w) 4-methoxy-4'-((cholesteryloxy)carbonyl)azobenzene (**1**) in 1-butanol; CD and transmittance intensities change synchronously around 40°C . Adapted with permission from [19]. Copyright (1994) American Chemical Society.

complementary techniques should also be employed [21, 22]. For example, the structure of the guanosine assembled species which is responsible for the formation of guanosine gels [23, 24], or, more precisely, liquid crystals, has been deduced using data from both fiber X-ray and CD calculations [25]. The columnar structure based on the piling of G-quartets was later confirmed by single-crystal X-ray work on a G-rich oligonucleotide (Figure 7) [26]. In this case, CD calculations were carried out on a minimal structure (two piled quartets) mimicking the columnar aggregate, but even in this simplified case, the calculations are not easy and require sophisticated treatments.

Instructive examples of the appearance of exciton spectra during gelation have been reported by Shinkai *et al.* [19]. Before gelation (in the sol state), the spectra in the region of the azo chromophore absorptions are flat; after gelation, an exciton pattern appears (Figure 8; the LMOG is the cholesterol derivative **2**). From the temperature dependence of the CD at a single wavelength, the T_g of the gel was estimated. It agrees well with that obtained on the basis of a mechanical test.

In another paper [27], the influence of [60]fullerene on the gelling properties of zinc-porphyrin-appended cholesterol derivatives (e.g., **3**) was studied. In particular, CD spectra corresponding to the porphyrin Soret band show a clear exciton pattern in the gel phase obtained only in the presence of fullerene, which seems to impose a left-handed arrangement of the porphyrins through the formation of sandwich-like complexes (Figure 9). This structure was deduced from CD spectra using the known direction of the effective transition moment of the substituted porphyrin chromophore in the framework of the exciton theory. The authors were very careful during the CD measurements in the gel phase and recorded also the LD spectra as advised in Section 2.2. In fact, it is rather dangerous to attribute CD spectra from anisotropic phases without

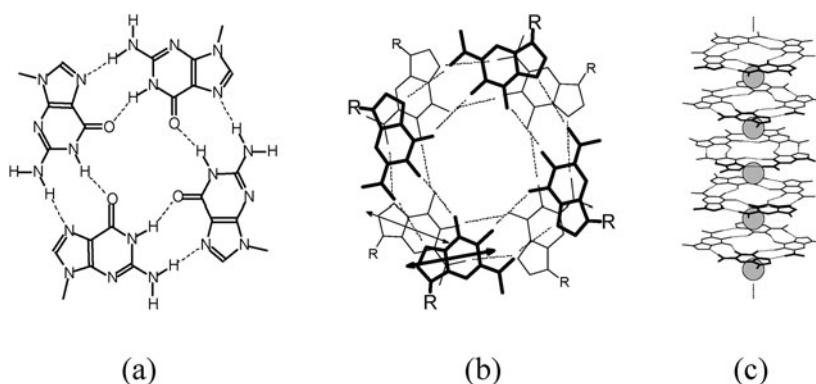


Figure 7. The G-quartet motif (a) originated by guanine with the head-to-tail right-handed stacking of two G-quartets and the clockwise relationship between the transition moments (b) connected to the positive exciton observed in right-handed columnar G-rich oligonucleotides (c).

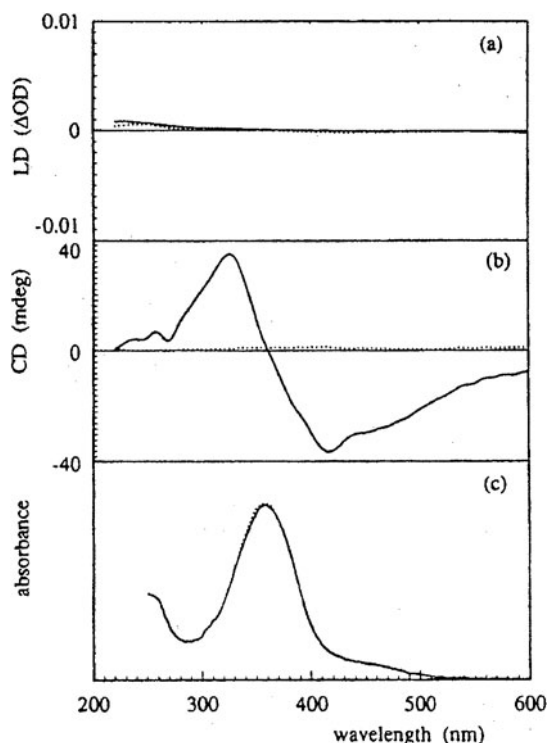
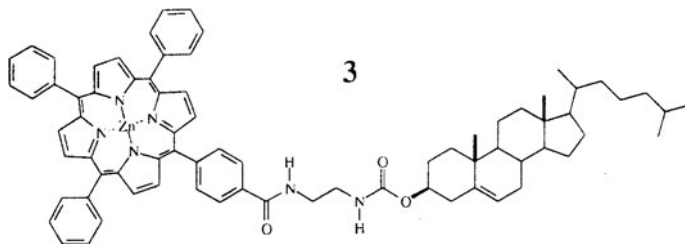


Figure 8. LD, CD and UV spectra of 0.4% (w/w) 4-ethoxy-4'-(cholesteryloxy)carbonyl azobenzene (**2**) in methanol in the gel (full line, $T = 25^\circ\text{C}$) and isotropic (dotted line, $T = 65^\circ\text{C}$) phases. Adapted with permission from [19]. Copyright (1994) American Chemical Society.

assessing the importance of the LD (that may be much stronger than the CD) [9, 28]. If the CD spectrometer cannot measure LD, it has been recommended to repeat the measurements several times after successive rotation of the cell. If drastic changes of the spectra are caused by rotation, the measurements are meaningless with regard to CD because they are strongly influenced by LD [29] and LB (linear birefringence). Figure 10, the “apparent” CD spectra of a hemoglobin gel recorded with different orientations of the cell, is an example of what is found when a sample has high LD (and/or LB) intensity [30].



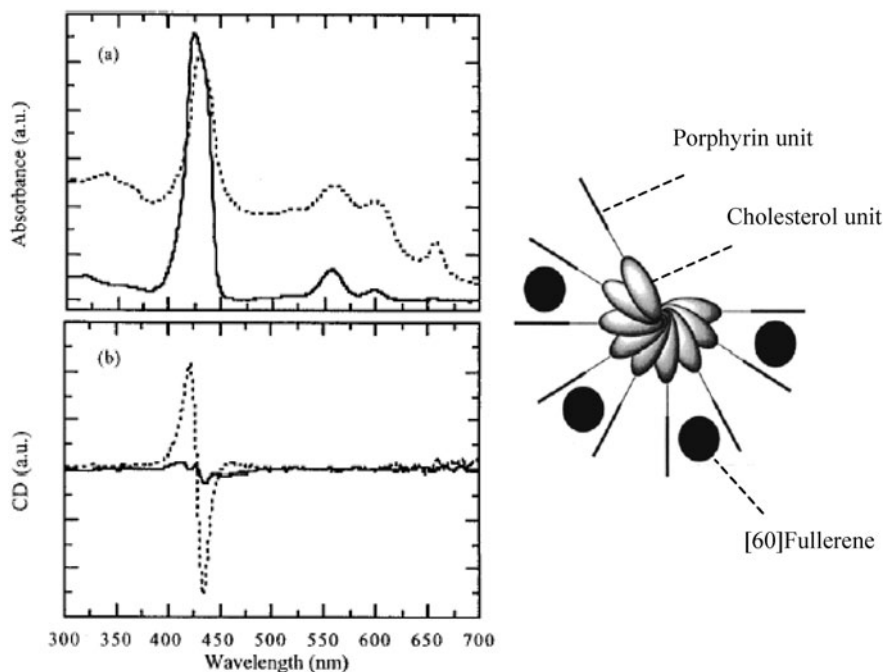


Figure 9. Left side: CD and UV spectra of **3** (full line) and **3**/[60]fullerene 2/1 complex (dotted line) in toluene (2.55×10^{-2} M for **3**) at 20°C. Right side: a model of the aggregate in the gel phase. Adapted with permission from [27]. Copyright (2001) American Chemical Society.

Scattering effects (Section 2.2) or formation of liquid-crystalline phases (cholesteric or chiral smectic C) can give rise to CD signals outside the chromophoric absorption region. Typically, a cholesteric phase has a total reflection CD band that is unrelated to chromophoric absorption and can appear at wavelengths far from the chromophore absorption region. The theory of the origin of this reflection band can be found in specialized texts [31]. The wavelength of the reflection band is related to the pitch p of the cholesteric helix by the relation, $\lambda = n \cdot p$, where n is the average refractive index of the mesophase and p is the distance between parallel molecules in the helix.

Cholesteric phases show CD bands that correspond to molecular absorptions, as well. It should be emphasized that these CD bands are not generated by exciton couplings, but by the linear dichroism of the individual molecules composing the phase [32]. For these reasons, special care must be taken when recording CD spectra of cholesteric phases. The sample must have a planar texture (i.e., the cholesteric helix axis should be perpendicular to the cell walls) and the light beam must also be normal to the cell walls (i.e., parallel to the cholesteric helix axis) [33].

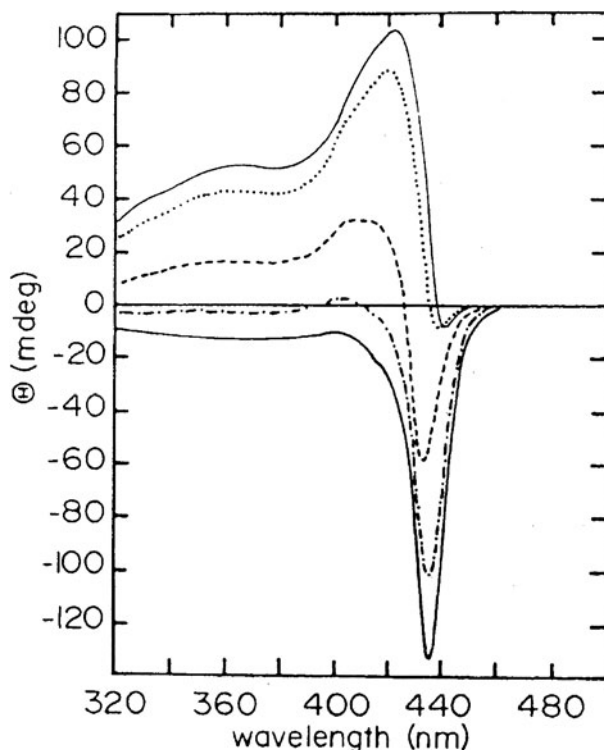


Figure 10. Apparent CD spectra of the Soret band of a sickle-cell deoxyhemoglobin gel in a phosphate buffer (at 24°C). Different curves refer to different orientations of the cell, rotated about an axis defined by the light beam. Adapted with permission from [30]. Copyright (1986) John Wiley & Sons.

Enantiomerically pure 12-hydroxyoctadecanoic acid in CCl_4 and benzene are classic examples of formation of chiral liquid-crystalline gels [34]. In the solid state, this molecule is assembled in helical fibrillar structures with the handedness determined by the enantiomer of the molecule. The gel in CCl_4 displays a CD spectrum characterized by a broad band at ca. 350 nm, in a wavelength range far from the chromophoric absorption, ca. 230 nm (Figure 11).

This band is interpreted as a reflection band of a chiral mesophase, tentatively a smectic one. In this example, CD does not provide information about the helical fibrils whose formation depends on the nature of the solvent. That information was gleaned from electron microscopy.

N-Lauroylglutamic acid forms gel-like cholesteric phases in organic solvents that are characterized by a strong reflection band in the visible region (i.e., well outside the chromophoric absorption region) (Figure 12) [35].

Very often, the reflection band is in the IR region and is not accessible by commercial CD spectrometers. However, some information can be deduced

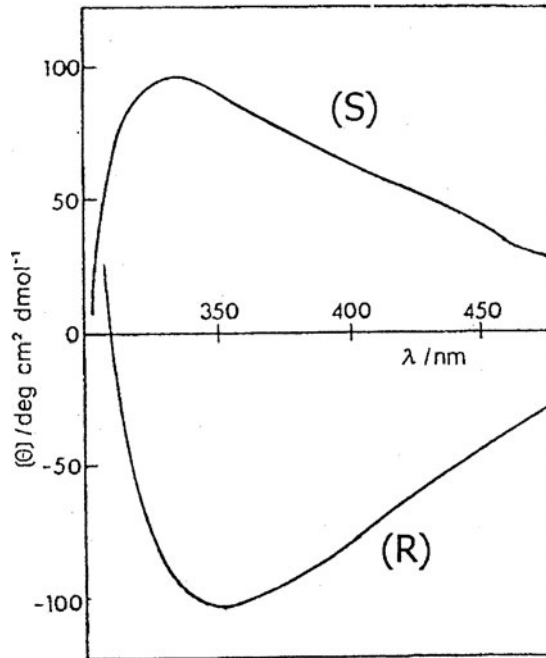


Figure 11. CD spectra of the (*R*) and (*S*) enantiomers of 25–35 mM 12-hydroxyoctadecanoic acid in CCl_4 in the gel state at room temperature. Adapted with permission from [34]. Copyright (1979) Nature Publishing Group.

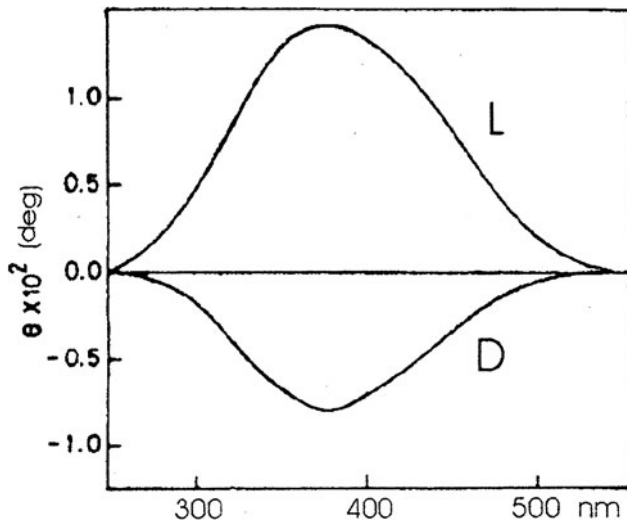


Figure 12. CD spectra of suspensions of L and D *N*-lauroylglutamic acids in benzene ($T = 15^\circ\text{C}$, path length 0.5 mm). Adapted with permission from [34]. Copyright (1978) American Chemical Society.

from the chromophoric absorption region. In the case of guanosine gels, the formation of the cholesteric phase, characterized by pitches of ca. $20\ \mu\text{m}$ (as determined by optical microscopy) that are well outside the ranges of commercial CD spectrometers, can still be detected by CD in the chromophoric absorption region. The spectrum gradually changes from the exciton shape, characteristic of the assembled helical species in isotropic solution, to a much stronger monosignate spectrum whose shape is very similar to the absorption (Figure 13). The latter spectrum is due to the cholesteric phase whose presence was independently verified by optical microscopy. This CD spectrum allows the assignment of the handedness of the cholesteric phase. Cholesteric phases of guanosine derivatives have been detected by CD in aqueous [36, 37] (e.g., Figure 13) and hydrocarbon solutions [38]. Furthermore, the effects of temperature and added salts on the formation of the cholesteric phase can be easily investigated using very small samples.

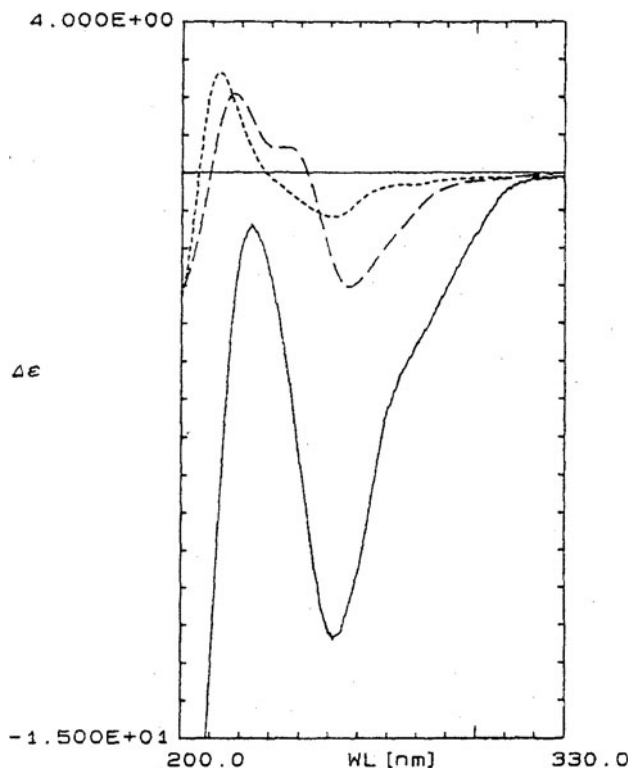


Figure 13. CD spectra of 4% (w/w) ammonium 2'-deoxyguanosine-3'-phosphate in water in the cholesteric (full line, $T = 1^\circ\text{C}$), isotropic assembled (long-dashed line, $T = 5^\circ\text{C}$) and isotropic disassembled (short-dashed line, $T = 30^\circ\text{C}$) states. Adapted with permission from [36]. Copyright (1996) Taylor and Francis.

4. Conclusions and Perspectives for the Future

Until a few years ago, vibrational CD (VCD) was a technique used only by specialized research groups. Today, a few commercial instruments are available and the use of VCD seems promising for studying self-assembly processes and gel formation; one can expect to obtain more detailed information about the functional groups involved in the chiral aggregations from VCD than UV-Vis CD. In a recent example, the self-assembly and gel formation of brucine-porphyrin conjugates were followed studying the VCD in the $\nu_{C=O}$ at ca. 1655 cm^{-1} [39].

The use of simultaneous measurements of circular and linear dichroism seems to be a practice which should be followed more often in order to avoid situations like that exemplified in Figure 10. The use of CD on gel-like or solid samples is a delicate matter, and confusing real spectra with artifacts can lead to extremely unpleasant consequences.

In recent years, calculations of CD spectra and optical rotations have improved greatly, but are currently restricted to relatively small molecules [40]. If it becomes possible to extend the calculations to larger systems, including self-assembled structures, even more detailed structural data on gel formation and structure should be available from CD spectroscopy.

References

- [1] *Circular Dichroism: Principles and Applications*, 2nd edition, N. Berova, K. Nakanishi and R.W. Woody, Eds., New York: Wiley-VCH, **2000**.
- [2] Djerassi, C. *Optical Rotatory Dispersion and its Applications to Organic Chemistry*, New York: McGraw-Hill, **1960**; Crabbé, P. *Optical Rotatory Dispersion and Circular Dichroism in Organic Chemistry*, San Francisco: Holden-Day, **1965**.
- [3] See, for example: Mason, S.F. *Inorg. Chim. Acta Rev.*, **1968**, 2, 89.
- [4] Mason, S.F. *Molecular Optical Activity and the Chiral Discriminations*, Cambridge: Cambridge University Press, **1982**.
- [5] Harada, N.; Nakanishi, K. *Circular Dichroic Spectroscopy: Exciton Coupling in Organic Stereochemistry*, Sausalito, CA: University Science Books, **1983**.
- [6] *Circular Dichroism and the Conformational Analysis of Biomolecules*, G.D. Fasman, Ed., New York: Plenum Press, **1996**.
- [7] See, for example: de Loos, M.; van Esch, J.; Kellogg, R.M.; Feringa, B.L. *Angew. Chem. Int. Ed.*, **2001**, 40, 613; Hanabusa, K.; Yamada, M.; Kimura, M.; Shirai, H. *Angew. Chem. Int. Ed.*, **1996**, 35, 1949.
- [8] Grosjean, M.; Legrand, M. *Compt. Rend. Acad. Sci. (Paris)*, **1960**, 251, 2150.
- [9] Shindo, Y. *Opt. Engin.*, **1995**, 34, 12, 3369.
- [10] Kuroda, R.; Harada, T.; Shindo, Y. *Rev. Sci. Instrum.*, **2001**, 72, 3802.
- [11] Milner, V.A.; Milner, A.A. In *Advances in Magneto-Optics II, Proc. 2nd Int. Symp. Magneto-Optics, Fiz. Nizk. Temp.*, **1992**, 18, 389.
- [12] Kuball, H.G. *private communication*
- [13] Shindo, Y.; Kani, K.; Horinaka, J.; Kuroda, R.; Harada, T. *J. Plastic Film & Sheeting*, **2001**, 17, 164.

- [14] Spector, M.S.; Prasad, S.K.; Weslowski, B.T.; Kamien, R.D.; Selinger, J.V.; Ratna, B.R.; Shashidhar, R. *Phys. Rev. E*, **2000**, *61*, 3977.
- [15] Dorman, B.P.; Hearst, J.E.; Maestre, M.F. In *Methods in Enzymology*, C.H.W. Hirs, S.N. Timasheff, Eds., New York: Academic Press, **1973**, *27*, 767.
- [16] Vitkin, A.; Hoskinson, E. *Opt. Eng.*, **2000**, *39*, 353; Kokhanovsky, A.A. *J. Opt. A: Pure Appl. Opt.*, **2002**, *4*, 288; Kokhanovsky, A.A. *Int. J. Electron. Commun. (AEU)*, **2001**, *55*, 240.
- [17] Smith, H.E.; Neergaard, J.R. *J. Am. Chem. Soc.*, **1996**, *118*, 7694.
- [18] Lyon, R.P.; Atkins, W.M. *J. Am. Chem. Soc.*, **2001**, *123*, 4408.
- [19] Murata, K.; Aoki, M.; Suzuki, T.; Hatada, T.; Kawabata, H.; Komori, T.; Ohseto, F.; Ueda, K.; Shinkai, S. *J. Am. Chem. Soc.*, **1994**, *116*, 6664.
- [20] Wang, R.; Geiger, C.; Chen, L.; Swanson, B.; Whitten, D.G. *J. Am. Chem. Soc.*, **2000**, *122*, 2399.
- [21] See, for example: Bonazzi, S.; Capobianco, M.; De Morais, M.M.; Garbesi, A.; Gottarelli, G.; Mariani, P.; Ponzi Bossi, M.G.; Spada, G.P.; Tondelli, L. *J. Am. Chem. Soc.*, **1991**, *113*, 5809.
- [22] Chantot, J.-F.; Haertle, T.; Guschlbauer, W. *Chimie*, **1974**, *56*, 501.
- [23] Gottarelli, G.; Spada, G.P.; Garbesi, A. In *Comprehensive Supramolecular Chemistry – Vol. 9 – Templating, Self-Assembly and Self-Organization*, J.-P. Sauvage, M.W. Hosseini, Eds., Oxford: Pergamon Press, **1996**, pp. 483–506.
- [24] Guschlbauer, W.; Chantot, J.-F.; Thiele, D. *J. Biomol. Struct. Dyn.*, **1990**, *8*, 491.
- [25] Gottarelli, G.; Palmieri, P.; Spada, G.P. *Gazz. Chim. (It.)*, **1990**, *120*, 101; Gottarelli, G.; Masiero, S.; Spada, G.P. *Enantiomer*, **1998**, *3*, 429.
- [26] Laughlan, G.; Murchie, A.I.H.; Norman, D.G.; Moore, M.H.; Moody, P.C.E.; Lilley, D.M.J.; Luisi, B. *Science*, **1994**, *265*, 520.
- [27] Ishi-i, T.; Iguchi, R.; Snip, E.; Ikeda, M.; Shinkai, S. *Langmuir*, **2001**, *17*, 5825.
- [28] Shindo, Y.; Nishio, M. *Biopolymers*, **1990**, *30*, 25, and references therein.
- [29] Tunis-Schneider, M.J.B.; Maestre, M.F. *J. Mol. Biol.*, **1970**, *52*, 521.
- [30] Hjelm, R.P.; Thiyagarajan, P.; Johnson, M.E. *Biopolymers*, **1986**, *25*, 1359.
- [31] See, for example: Collings, P.J.; Hird, M. *Introduction to Liquid Crystals: Chemistry and Physics*, London: Taylor and Francis, **1977**; McDonnell, D.G. In *Thermotropic Liquid Crystals*, G.W. Gray, Ed., Chichester: Wiley, **1987**.
- [32] Dudley, R.J.; Mason, S.F.; Peacock, R.D. *J. Chem. Soc. Faraday Trans.*, **1975**, *2*, 997.
- [33] Gottarelli, G.; Spada, G.P. In *Circular Dichroism: Principles and Applications*, 2nd edition, N. Berova, K. Nakanishi and R.W. Woody, Eds., New York: Wiley-VCH, **2000**.
- [34] Tachibana, T.; Mori, T.; Hori, K. *Nature*, **1979**, *278*, 578.
- [35] Sakamoto, K.; Yoshida, R.; Hatano, M.; Tachibana, T. *J. Am. Chem. Soc.*, **1978**, *100*, 6898.
- [36] Gottarelli, G.; Proni, G.; Spada, G.P. *Enantiomer*, **1996**, *1*, 201.
- [37] Spada, G.P.; Bonazzi, S.; Garbesi, A.; Zanella, S.; Ciuchi, F.; Mariani, P. *Liq. Cryst.*, **1997**, *22*, 341; Gottarelli, G.; Proni, G.; Spada, G.P. *Liq. Cryst.*, **1997**, *22*, 563; Proni, G.; Spada, G.P.; Gottarelli, G.; Ciuchi, F.; Mariani, P. *Chirality*, **1998**, *10*, 734.
- [38] Pieraccini, S.; Gottarelli, G.; Mariani, P.; Masiero, S.; Saturni, L.; Spada, G.P. *Chirality*, **2001**, *13*, 7.
- [39] Setnička, V.; Urbanová, M.; Pataridis, S.; Král, V.; Volka, K. *Tetrahedron: Asymmetry*, **2002**, *13*, 2661.
- [40] See, for example: Giorgio, E.; Minichino, C.; Viglione, R.G.; Zanasi, R.; Rosini, C. *J. Org. Chem.*, **2003**, *68*, 5186, and references therein.

SYSTEMS – ORGANOGELS

Chapter 14

LOW MOLECULAR-MASS ORGANIC GELATORS

Analyses of the natures of LMOGs and liquids for efficient gelation

Mathew George and Richard G. Weiss

Department of Chemistry, Georgetown University, Washington, D. C., 20057–1227, USA

1. Introduction	449
2. Classification of Organic Gelators	450
2.1. Alkane Gelators	451
2.2. Organic Gelators with One Heteroatom	451
2.3. Organic Gelators with Two Heteroatoms	470
2.4. Organic Gelators Containing Three Heteroatom Types	498
2.5. Polymerizable Organic Gelators	500
2.6. Two Component Organic Gelators	503
2.7. Inorganic and Organometallic Gelators	513
2.8. Liquid-Crystalline Gels	514
2.9. “Latent” Gelators	519
2.10. Microemulsion-based Gelators	521
2.11. Miscellaneous Organic Gelators	523
3. The Role of Liquid in Gelation by LMOGs	527
4. Conclusions and Perspectives for the Future	535

1. Introduction

Several reviews describe the various types of *low molecular-mass organic gelators* (*i.e.*, LMOGs, gelators that are primarily organic in composition and whose molecular mass is usually less than 2000 Da) and their structural features [1–15]. In this chapter, we provide an in depth survey of organogels, comprised of an organic liquid and low concentrations (typically <2 wt.%) of an LMOG.

The LMOGs are separated into “classes” according to criteria based on molecular structure. The properties of the LMOG networks and, when available, information about the nature of their intermolecular interactions both with other gelator molecules and with those of the liquid, are presented. The intent of this chapter is to demonstrate the versatility of the molecular structures that self-aggregate into 3-dimensional fibrillar networks (SAFINs) as well as the properties of the liquid components that promote or inhibit gel formation. In many examples, the properties of the gelators and their liquids are correlated with micro- and macro-properties of their gels. Other aspects of several of the gel systems within this chapter are discussed in greater detail in other chapters. Also, the gelation properties of LMOGs leading to hydrogels and those gelators based on carbohydrates, steroids, and porphyrins are not included here for the most part because they are described in Chapters 15 and 18.

LMOG organogels are usually prepared by warming a macroscopically phase-separated gelator in an organic liquid until the mixture becomes a solution or sol, and then cooling the solution/sol to below a characteristic gelation transition temperature, T_g . Empirically, T_g is the temperature below which flow no longer is discernible over long periods. It depends on the concentration of the gelator, the properties of the liquid, and, in some cases, the protocol for cooling the solution/sol. For a more rigorous rheological definition of a gel and T_g , see Chapters 5 and 8.

Unlike many chemical gels, such as cross-linked polymers where the network is maintained through covalent bonds that must be broken if the system is to revert to a sol or solution, most physical gels of LMOGs are thermally reversible. The forces responsible for the formation of their immobilizing networks can be London dispersion interactions, hydrogen bonding, aromatic (π - π) interactions, ionic or organometallic coordination bonding, or (almost always) a combination of these. The interconversion between the gel and solution/sol phases depends only on the disassembly and assembly of the constituent molecules; in both phases, the chemical composition is unchanged unless disassembly is concurrent with a form of chemical equilibrium, as in the case of coordination bonding.

2. Classification of Organic Gelators

It is not yet possible to select *a priori* a molecule that can gel definitively a selected liquid. Many discoveries of organic gelators have been fortuitous, usually occurring as a result of observations during the workup of a reaction mixture. As an aid to defining strategies for the molecular design of new organic gelators, examples of known LMOGs are grouped by structure, starting from the simplest and increasing in complexity.

2.1. Alkane Gelators

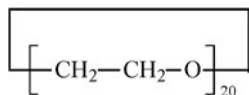
Interactions that are more specific and stronger than London dispersion forces are usually necessary for molecules to self assemble into 3-dimensional gel networks [1, 8]. However, long *n*-alkanes alone can gelate shorter *n*-alkanes as well as other liquids [16–18]. Relatively low concentrations of *n*-tetracosane (**1**, H(CH₂)₂₄H), *n*-octacosane (**2**, H(CH₂)₂₈H), and *n*-hexatriacontane (**3**, H(CH₂)₃₆H) gelate a variety of hydrocarbon liquids, alcohols, halogenated liquids and a silicone oil (tetramethyltetraphenyltrisiloxane). The gelation efficiency of the alkane gelators at one LMOG concentration, as defined by the temperature at which a gel in a sealed tube starts to flow when heated in a water bath (T_g ; the inverse flow method [19]), the diversity of liquids gelated, and the duration of the period that a gel persists in a sealed tube at room temperature without macroscopic phase separation or perceptual flow when inverted (temporal stability), increases with increasing alkane chain length. Within its gels, gelator **3** is packed in a lamellar, orthorhombic (B_o) fashion [18], with individual molecules in extended (*all-transoid*) conformation as shown in Figure 1. The chains of **3** are perpendicular to the lamellar planes and two molecules define the repeat distance. Unlike most other LMOGs whose 3-dimensional networks are comprised of long fibrils, the basic aggregate units of **3** are platelets that interlock [18].

Both T_g and heats of melting (ΔH_g) increase with increasing concentration of alkane gelators. This is illustrated by gels of **3** in silicone oil and *n*-dodecane in Figure 2 [20]. In the plateau regions, the supramolecular networks of the gels become more intricate, but their basic structure and interactions are not changed.

2.2. Organic Gelators with One Heteroatom

Organic gelators that are *n*-alkanes with one heteroatom are also known. The nature of their intermolecular interactions depends on the heteroatom and its placement along the carbon chain. However, London dispersion forces still must play a prominent role to bind the aggregates.

2.2.1. Ethers and thioethers as organic gelators



4

$$M_n = M_w = 880 \text{ g/mol}$$

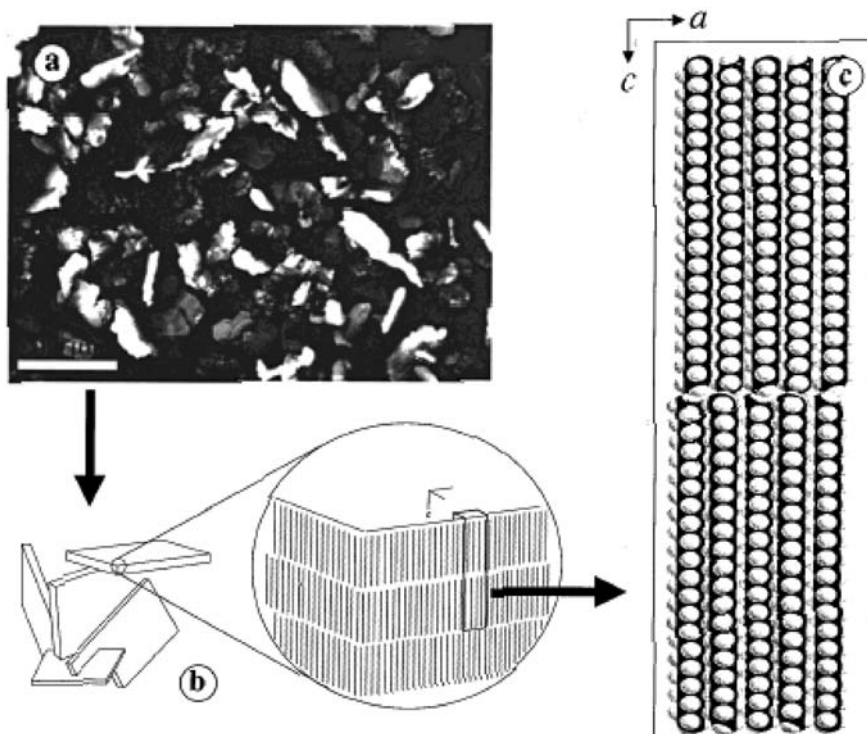


Figure 1. Optical micrograph of a 4 wt.% **3**/1-octanol gel viewed through crossed polars (a), a cartoon representation of the microplatelets in (a) showing the orientations of the long molecular axes of **3** molecules with respect to the major plane of the platelet units (b), and the molecular packing of **3** in its B_O [12b] phase viewed from the b -axis (c). The distance bar in (a) is $100\ \mu\text{m}$. (Reprinted with permission from [18]. Copyright (2000) The American Chemical Society.)

Marand and co-workers investigated thermoreversible gelation of 60-crown-20-macrocyclic **4** in liquids such as CCl_4 and acetone [21]. From kinetic studies, the critical gelation concentration (cgc; i.e., the minimum concentration required for gelation at ambient temperature) of **4** in CCl_4 is estimated to be 3.5 wt.%. Wide-angle X-ray diffraction (WAXD) data indicate that the morphology of the gelator aggregates in dried gels and in neat crystals of **4** are the same.

Thioether **5** ($\text{H}(\text{CH}_2)_{14}\text{S}(\text{CH}_2)_{14}\text{H}$) gels aliphatic alcohols. Its gels consist of large plate-like crystalline domains (like those of the n -alkanes [18]) and are very heterogeneous. The aggregates are stabilized by London dispersion forces from alkyl chain interactions and other weak forces.

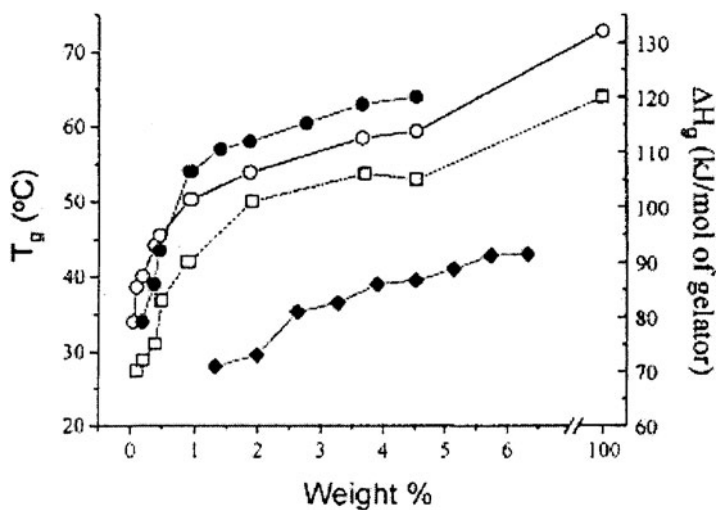
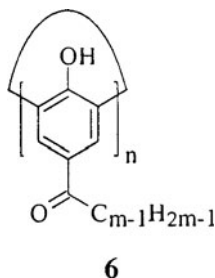


Figure 2. Gel transition temperatures (T_g ; ○, ●, ◆) and molar transition enthalpies (ΔH_g , □) vs weight % of **3** in silicone oil (○, ●, □) and dodecane (◆) by DSC derived measurements based on the average of the first heating and cooling scans (□) or the onsets of the heating and cooling curves (○) and the falling drop method (●, ◆). (Reprinted with permission from [17]. Copyright (2000) The American Chemical Society.)

2.2.2. Calixarene-based gelators



Certain calixarene derivatives possessing long acyl groups at the *para*-positions of the aromatic rings (**6**) form stable gels in organic liquids such as alkanes, alcohols, CS_2 , CCl_4 , and aromatic liquids [23–25]. Interestingly, calixarenes with long alkyl chains at the *p*-positions do not gelate common organic liquids. A major driving force for aggregate formation, intermolecular H-bonding between the carbonyl and OH groups, was confirmed by comparison of IR spectra of the gel and neat solid samples.

2.2.3. Substituted fatty acids

Long chain saturated fatty acids, their salts with alkali metals, alcohols, and esters are known to form hardened materials from organic liquids [26–30]. Among these, 12-hydroxyoctadecanoic acid (**7**) is of special interest because it can gelate a variety of organic liquids. Tachibana *et al.* have reported formation of thermo-reversible jellies of enantiomerically pure **7** in aromatic liquids (>33 mmol/L) and chlorinated solvents (>25 mmol/L) [31, 32]. However, racemic **7** crystallizes from solutions of the same liquids upon cooling. A similar influence of stereo configuration on gelation ability has been observed during gelation studies with gluconamides (see Section 2.3.1) [33]. Jellies of enantiopure **7** exhibit a circular dichroism (CD) absorption band around 370 nm that is attributed to a chiral helical arrangement of the gelator molecules in their fibrillar networks [31] that is manifested in the handedness of the twist of the individual fibrils [34]. X-ray diffraction studies indicate the same lamellar packing within the gel networks and the neat powder. Multiple intermolecular H-bonds control the aggregation mode [35].

By contrast, Terech and co-workers found no difference in the gelating ability, appearance of the gels, variety of liquids that can be gelated, or the concentration needed for gelation by racemic and chiral **7** [33, 37]. The molecules of racemic **7** pack in a monoclinic, head-to-head fashion (Figure 3). Their organization is sensitive to the liquid type employed for gelation as well as the thermal and mechanical histories of the gel.

Gels made from <5 wt.% racemic and chiral **7** and nematic liquid crystal mixtures [38] show interesting electro-optical properties [39, 40] when cast into a shock-resistant, light-reflecting, planar texture by heating to a temperature between the sol-gel and nematic-isotropic transition temperatures. The viscoelasticity of the neat liquid crystal was enhanced by gelation without reduction of its reflectivity or electro-optic response. A significant broadening of the reflection bands and enhanced stability of the focal conic texture was observed for the liquid crystal in the gels.

2.2.4. Alkoxyaryl molecules

Low concentrations of the *trans* isomer of the arylcyclohexanol **8a** gelates a variety of organic liquids through H-bonding [41–43]. The *cis* isomer **8b** does not form gels in any of the liquids examined. As shown by WAXD measurements, bimolecular association of **8a** is present in the gel networks ($d = 14.3$ Å) [42]. However, a xerogel prepared from a cyclohexane gel exhibited 76 Å repeat units, indicating that removal of the liquid involved a morphological change of **8a**.

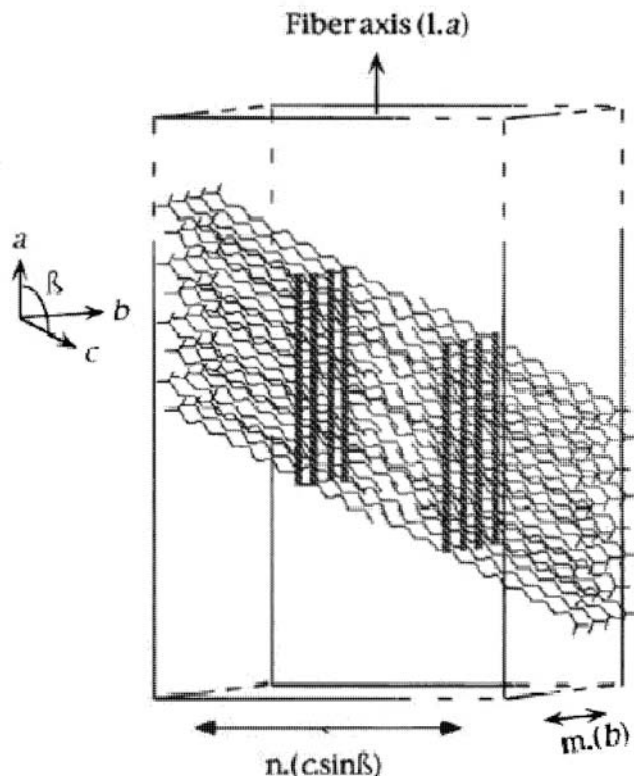


Figure 3. Structural model of fibrillar or ribbon-like aggregates of racemic **7** as formed in gelled organic liquids. The crystallographic axis (monoclinic symmetry) and the fiber geometry are indicated. The dimensions are proportional to the crystallographic cell parameters, as shown. The thick lines represent H-bond sequences connecting the hydroxyl groups at C₁₂ and the spheres are carboxylic end groups. (Reprinted with permission from [36]. Copyright (1994) The American Chemical Society.)

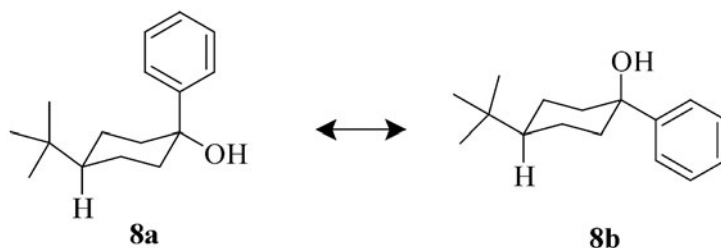


Figure 4i contains scanning electron microscopy (SEM) images of fractured xerogels from **8a**/cyclohexane gels. The brittle gelator network collapses during evaporation of the liquid component. Three different types of aggregates

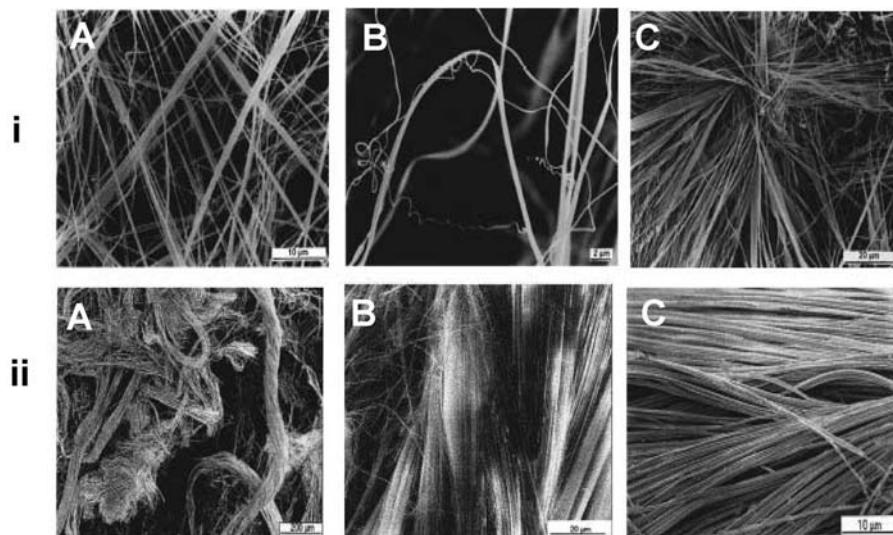


Figure 4. Scanning electron microscope images of (i) fractured xerogels from **8a**/cyclohexane gels, and (ii) phase-separated solid obtained from a **8a**/heptane gel. A, B, and C in Figures i and ii represent different types of gelator aggregators (see text). The space bars correspond to: $10\ \mu\text{m}$ (iA and iiC, $2\ \mu\text{m}$ (iB), $20\ \mu\text{m}$ (iC and iiB), and $200\ \mu\text{m}$ (iiA). (Reprinted with permission from [43]. Copyright (1998) The American Chemical Society.)

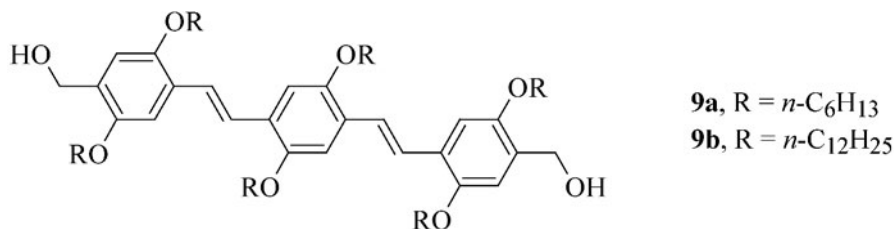
are observed in the SEM: very long and rigid fibers with variable thicknesses ($0.1\text{--}2\ \mu\text{m}$) that are entangled in a porous matrix (Figure 4i-A), thinner fibrils ($0.05\ \mu\text{m}$) with moderate flexibility (Figure 4i-B), and where fibers are emanating from a central point (Figure 4i-C).

Typically, solid-liquid phase separation within **8a**/hydrocarbon gels takes place over periods of months as fibers collapse into oriented bundles like those in Figure 4ii. The major structural difference between the xerogel and the phase separated solid lies in the degree of orientation and the distribution of the patchwork of microdomains of fibers.

When incorporated into a **8a**/mineral oil gel, photochromic spirocyan derivatives exhibit surprising thermal stability [44]. For instance, a 300-fold increase in the lifetime was observed in the gel phase for a merocyanine containing a succinyl group. This effect is attributed to a specific interaction between the 3D gel networks and the succinyl group of the spirocyan molecules involving an intercalation of the succinyl appendages within phenyl-phenyl stacks of the gelator molecules.

All-trans-phenylenevinylenes (**9a,b**) form gels in solvents such as alkanes and aromatic liquids [45]. Structurally related compounds with aldehyde or alkoxide functionality in place of the benzylic OH are not gelators, indicating the key role of intermolecular H-bonding to stabilize the aggregates of these

classes of LMOGs. Other contributing interactions are π -stacking and van der Waals forces of the alkoxy chains.



The existence of aggregates of **9b** in hexane solution at room temperature has been ascertained from absorption and emission spectra (Figure 5). At 25 °C, the absorption spectrum of hexane solutions of <7 mM **9b** resemble that of a sheared gel film (>7 mM). At 50 °C, the absorption spectrum is similar to that in a 18 mM chloroform solution (Figure 5a). Emission spectra of **9b** in hexane at room temperature indicate the presence of both monomeric (λ_{em} ca. 450 nm) and aggregated (λ_{em} > 500 nm) species (Figure 5b). Xerogels consisting of **9b** and an organic dye, such as Rhodamine B (2:1 mol ratio), undergo photoinduced energy transfer about 1.5 times more efficiently than their solution [46].

Many alkoxyanthracene derivatives linked to steroids (**10**) gelate liquids such as alkanes, alcohols, silicone fluids, etc. [47–49]. Spectroscopic and X-ray diffraction studies indicate a stacked, helical arrangement of the gelator molecules with a partial overlap of anthracenyl groups. The forces responsible for gelation in these types of LMOGs are weak van der Waals interactions. Mono- and di-substituted anthraquinone derivatives (**11** and **12**) also gelate

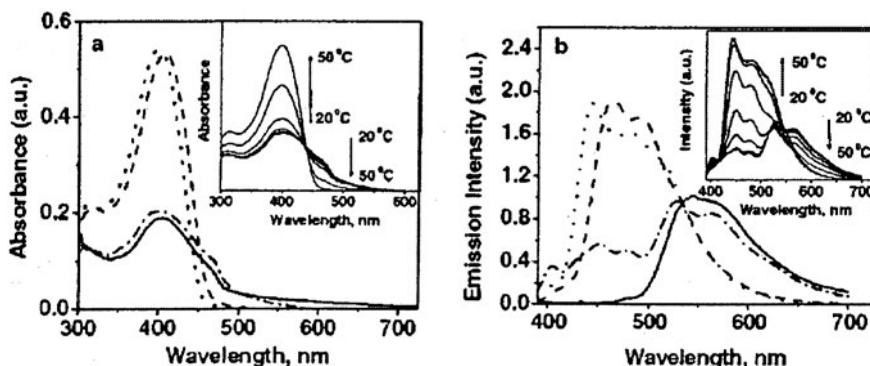
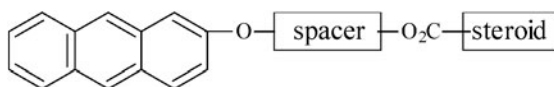
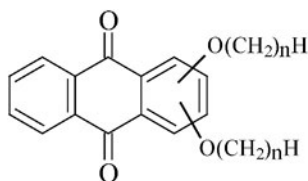
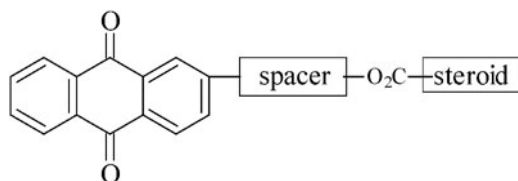
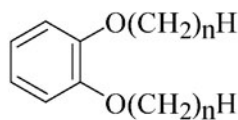
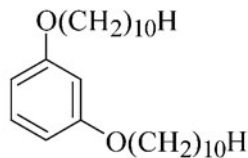
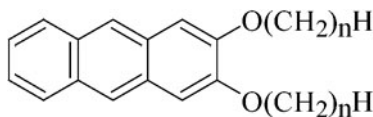


Figure 5. Absorption (a) and emission (b) spectra of **9b** in chloroform at 25 °C (---), hexane at 25 (· - · - ·) and 50 °C (····), and as a sheared film (—). Insets show changes in absorption and emission spectra with temperature (excitation at 380 nm). (Reprinted with permission from [45]. Copyright (2001) The American Chemical Society.)

several types of liquids [50, 51]. The gelation efficiency is maximized when the alkoxy groups are at the 2- and 3-positions of the anthracene rings and there are between 9 and 12 methylene units in the chains.

Symmetrically substituted di-*n*-alkoxybenzenes (**13**) and 2,3-bis-*n*-alkoxyanthracenes (**14**) are better LMOGs of polar liquids than nonpolar ones [52–57]. Because H-bonding between these molecules is not possible, their principal driving force for gel formation may be π - π stacking of the aromatic units and van der Waals interactions of the alkyl chains. Evidence for the former is found in absorption and fluorescence spectra of **14** with $n = 6$ (whose single crystal X-ray structure has been determined) and $n = 10$ in solutions and gel phases [53] as well as comparisons between UV and IR data in their neat and gel phases [58, 59].

**10****11****12****13a****13b****14**

Gels obtained from **14** ($n = 10$) could be used for the templated growth of inorganic fibers [60, 61]. LMOG **14** with $n = 10$ forms gels even in propylene carbonate (PC) and PC/tetraalkylammonium salt solutions [62]. Electrochemical studies of the organogel with electrolytes showed that **14** ($n = 10$) is protected from oxidation and reduction within the gel fibers. Gels of **13** have been exploited to construct porous silica materials with

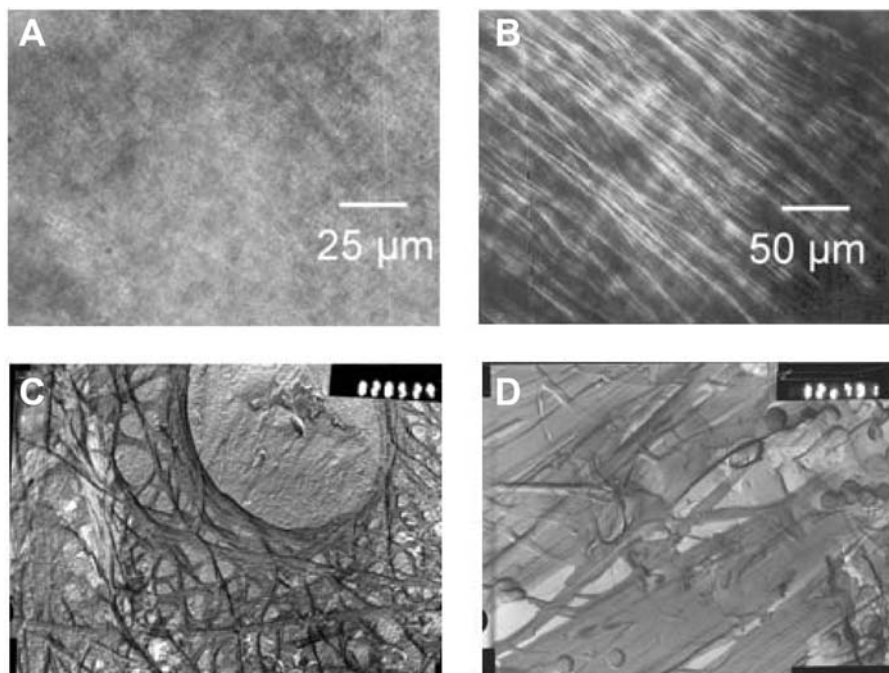
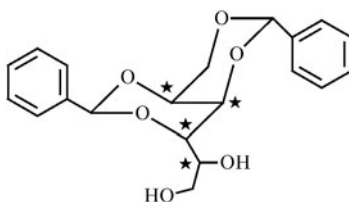


Figure 6. POM (A, B) and TEM images (C, D) at room temperature of a **14** ($n = 10$)/DMF gel made without (A, C) and with (B, D) shear stress. C and D are magnified 8000 \times . (Reprinted with permission from [64]. Copyright (2002) The American Chemical Society.)

different length scales and aerogels prepared from supercritical fluids [54, 63]. Long-range orientation of the fibrils of a **14** gel in DMF has been achieved by applying a mechanical shear stress during cooling of the isotropic solution (sol) [64]. Figure 6 shows POM and TEM images of a 5×10^{-2} M **14**/DMF gel before and after applying shear stress.

2.2.5. Sorbitol derivatives as LMOGs



15

Gels of the chiral molecule, 1,3:2,4-di-*O*-benzylidene sorbitol (**15**; asterisks are at chiral centers intrinsic to sorbitol; the two benzylic centers are not

marked), have been studied extensively [65] since the first report in 1926 [66]. LMOG **15** can gelate both organic liquids [67–73] and polymer melts [74, 75]. The two phenyl rings of **15** make it easier to be dissolved in organic liquids while the hydroxyl groups induce intermolecular H-bonding that leads to aggregation and, finally, gelation. Gels of **15** are important industrially and are found in cosmetics, biomedical materials, and electronic devices. Some of these uses will be discussed in the section of the book dealing with *Applications* and others can be found in [2] of the Introductory chapter.

Figures 7 and 8 are SEM images of gels comprised of **15** in octamethylcyclotetrasiloxane and polydimethylsiloxane (PDS), respectively. Vacuum treated gels of **15** and octamethylcyclotetrasiloxane consist of an opaque region with ribbon-like, flexible, elongated fibers whose widths are in the range of 0.1–3 μm (Figure 7a) and a clear region composed of dense, intertwined microscopic fibers (Figure 7b).

Networks of **15** formed in PDS are inhomogeneous, consisting of loosely-connected, long fibrils and their bundles, as shown in Figures 8a and b. The hairpin and twists in Figures 8c and d suggest that fibrils in the aggregates are somewhat flexible.

Gelation properties of **15** in poly(ethylene glycol) (PEG), poly(propylene glycol) (PPG), and PPG-*b*PEG-*b*PPG triblock copolymers have been investigated [76–78]. The diameters of individual nanofibrils of **15** range from 10 to 70 nm in PEG. Both the gelator concentration and medium polarity determine the rheological properties of the gels (Figure 9). In a polar medium (N. B., hydroxy end-capped PEG), gelation is slower than in the methoxy end-capped analogs of PEG at constant concentrations of **15**. Time/temperature superposition analysis of **14**/PEG gels show that the activation energy for gelator network evolution increases linearly with decreasing gelator concentration when the liquid polarity is kept constant or when the matrix polarity increases at constant concentration of **15** [76].

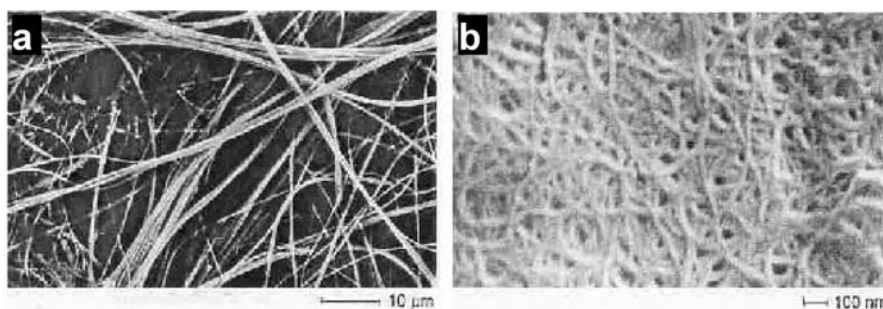


Figure 7. SEM of (a) opaque and (b) clear regions within a 1 wt.% **15**/octamethylcyclotetrasiloxane gel. (Reprinted with permission from [71]. Copyright (1995) The Royal Society of Chemistry.)

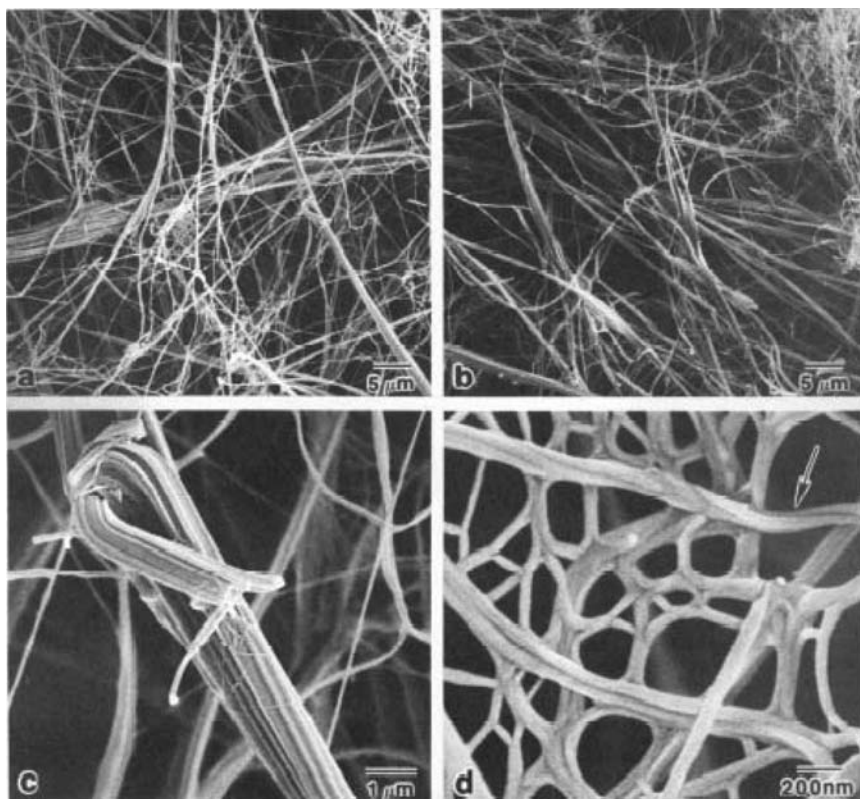


Figure 8. SEM photographs of **15** networks in a PDS homopolymer at different magnifications. (Reprinted with permission from [75]. Copyright (1995) The American Chemical Society.)

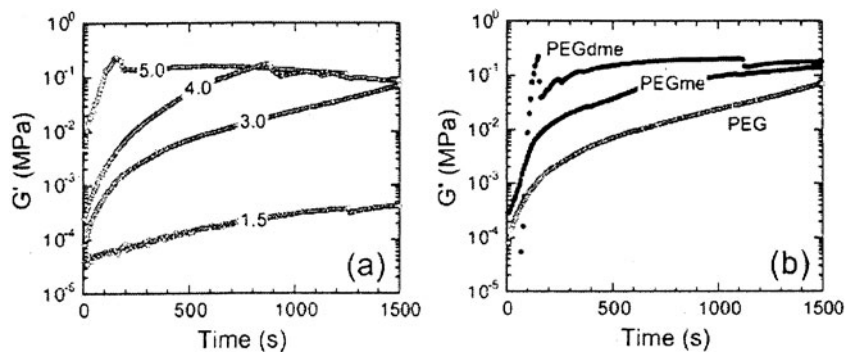
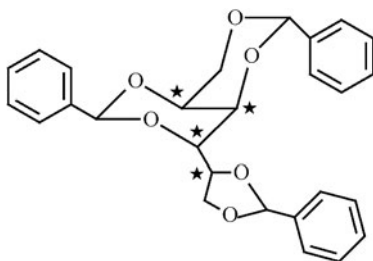


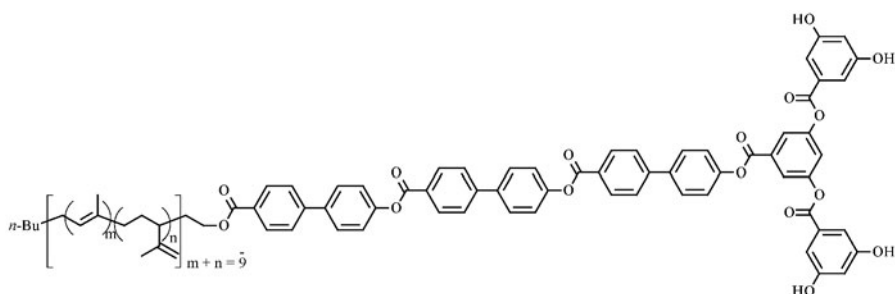
Figure 9. Time-dependent evolution of the dynamic elastic modulus (G') for (a) organogels in PEG at varying concentration (wt.%) of **15** and (b) organogels with 3 wt.% **15** in PEG homopolymers with different chain capping groups (identified in the figure). The strain amplitude and frequency are 1.5% and 10 rad/s, respectively. (Reprinted with permission from [76]. Copyright (2003) The American Chemical Society.)

Compound **15** also gels PPG-*b*-PEG-*b*-PPG triblock copolymers thermoreversibly. Both gel dissolution (T_d) and formation (T_f) temperatures tend to increase with increasing gelator concentration or the PPG fraction in the triblock, and their difference decreases with increasing PPG fraction [77]. However, the magnitude of the dynamic elastic modulus is not affected by the copolymer composition at ca. 1 wt.% concentrations of **15** (corresponding to saturation of the gel networks).

**16**

The fluorescence of **15** and its benzylidene derivative (**16**) in alcoholic liquids has been used to follow molecular association steps [79]. For instance, aggregation of **15** and **16** in ethylene glycol, as indicated by small red shifts in the fluorescence spectra as concentration is increased (Figure 10), was observed even in the pre-gel state. Intramolecular interactions of phenyl groups in molecules of **16** were also detected. The fluorescence of gelators and their gels is discussed in greater detail in Chapters 12 and 24.

2.2.6. Phenyl esters

**17**

Very low concentrations (ca. 0.2 wt.%) of biphenyl ester derivatives (**17**) undergo spontaneous gelation when mixed with organic liquids [80, 81]. These molecules contain coil-like, rodlike, and dendritic segments. The bulk geometry of the dendritic segment relative to the rest of the molecule prevents

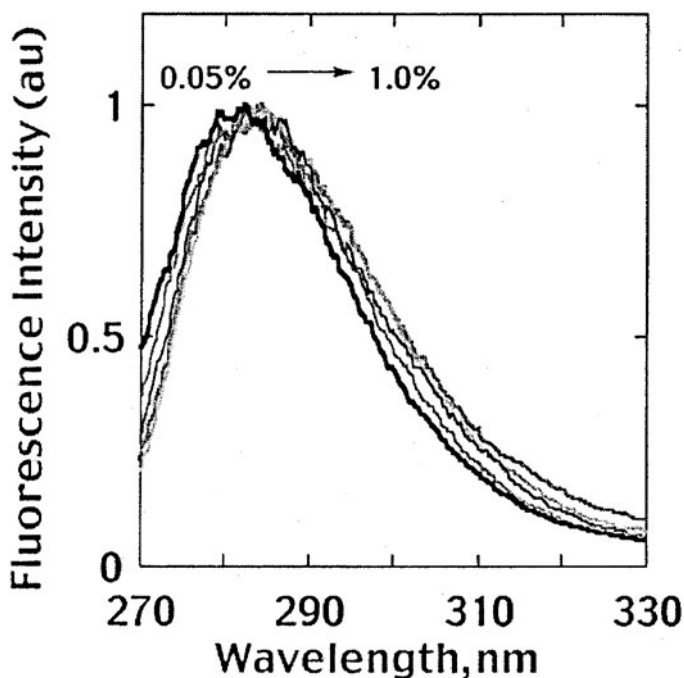


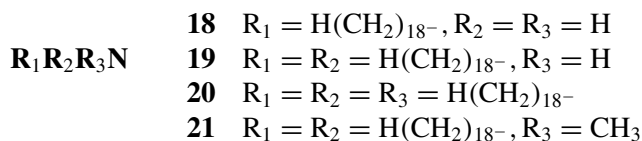
Figure 10. Normalized fluorescence spectra ($\lambda_{\text{exc}} = 259 \text{ nm}$) of 0.05 (black bold line), 0.1, 0.3, 0.5, and 1 wt.% (gray bold line) **15** in ethylene glycol at room temperature. The concentrations increase from bottom to top at 320nm. (Reprinted with permission from [79]. Copyright (1999) The American Chemical Society.)

the formation of two-dimensional aggregates. However, formation of one-dimensional aggregates followed by gelation is possible through H-bonding of hydroxy groups in the periphery of the dendron moiety and π - π stacking of the biphenyl units. Compounds structurally similar to **17**, but with either two or no OH groups, were not LMOGs of the same liquids gelated by **17**. No gelation occurred when molecules contained only one biphenyl group and weak gels (N.B., low gelation temperatures) formed when two biphenyl units were present. The length of the aliphatic chain also influences the gelating properties of molecules similar to **17**. With two long chains, the molecules remained dissolved in liquids gelated by **17**, whereas with no long chains, the molecules precipitated when their solutions were cooled.

2.2.7. Aliphatic amines

The gelating abilities of completely saturated alkyl amines (**18–21**) have been described [22, 82]. Among these, **20** and **21** are tertiary amines so that

their nitrogen atoms can only act as H-bond acceptors. As a result, potential H-bonding interactions like those available among molecules of **18** or **19** are not possible within the gelator assemblies, and **20** and **21** form weaker gels than those of **19** with the same liquids and at the same concentrations. Although intermolecular H-bonding can be prevalent among molecules of the linear primary amine, **18**, its gelation efficiency is much poorer than those of **19–21**. The molecular packing arrangement within its crystalline phase may not be as appropriate to form the fibrillar structures usually requisite for gelation. In addition, at comparable weight percent concentrations, the linear secondary amine, **19**, forms stable gels in several liquids with better temporal stabilities (> 1 year) and higher T_g values than those of the tertiary amines, **20** or **21**. The added stability is attributed to the aforementioned ability of **19** to be both a hydrogen bond donor and acceptor [83]. Turbid gels are formed from the gelators in all liquids examined, and the degree of turbidity was dependent on the rate of cooling of their sol phases. At concentrations slightly above the critical gelator concentration (cgc; the lowest concentration of gelator at which a gel is formed at room temperature), fast cooling resulted in more transparent gels. Figure 11 shows the polarized optical micrographs (POM) of 0.02 M **19**-styrene gels after different cooling protocols. As is clear from the figure, the size of solid domains increases significantly as the rate of cooling decreases.



The positions and appearances of the IR absorption bands of the N-H stretch are the same for **19** in the silicone oil gel and its neat solid phase. Based on this observation, the morphology of **19** in its neat solid phase and silicone oil gel may be the same [84]. However, many organic gelators are polymorphous and it is dangerous to assume that the molecular organizations are the same within the gel and bulk solid phase without much better evidence [85]. X-ray diffraction studies of neat **19** and its 5 wt.% gel in silicone oil (Figure 12) show that the morphology is same within the gel and neat powder [86]. The calculated extended length of **19** (49.3 Å) is comparable to that of the lamellar spacings obtained from the lowest angle peaks in the X-ray diffraction patterns of **19** (Figure 12) [86]. This indicates that the molecules of **19** adopt an extended conformation in the neat solid phase as well as gel aggregates in silicone oil.

Cholestanyldioctadecylamine (**22**), another completely saturated tertiary amine, forms gels in several liquids [82]. The stereochemistry at C3 of the steroidal unit and, therefore, the projection of the dioctadecyl chains with respect to the steroidal skeleton, affect LMOG efficiency. For instance, at

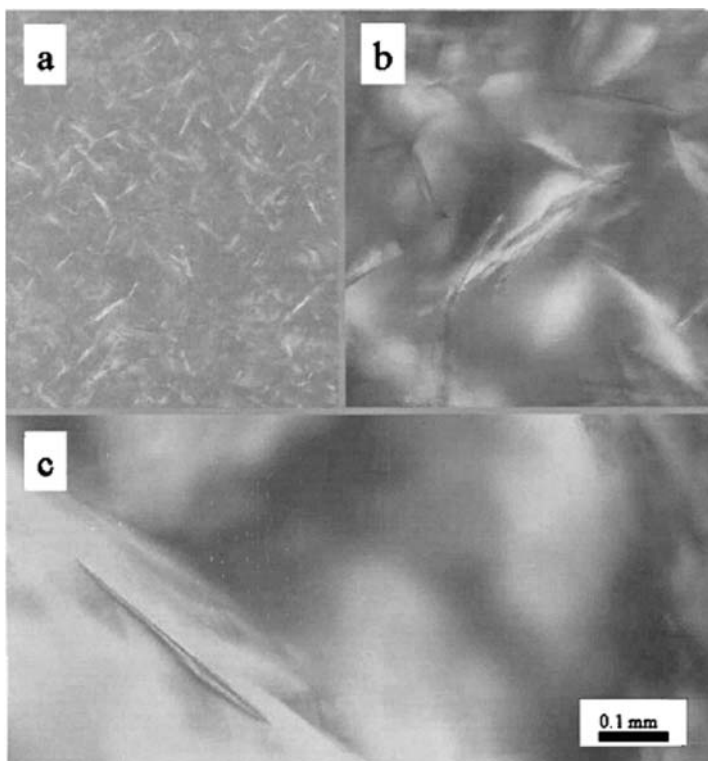
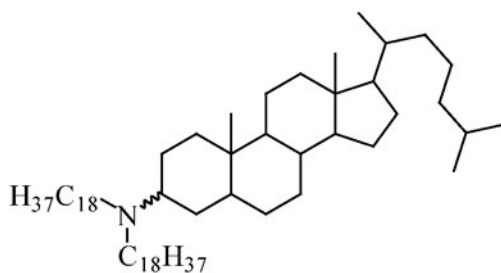


Figure 11. Polarizing optical micrographs of a 0.02 M **19**/styrene gel after (a) fast (sol immersed in a water bath at 5° C), (b) moderate (sol cooled in air), and (c) slow cooling (sol left on the hot stage of a microscope while the block returned slowly to room temperature). The space bar is common to the three POMs. (Reprinted with permission from [22]. Copyright (1999) The American Chemical Society.)

2.5 wt.% and room temperature, the β -anomer gels silicone oil or 1-pentanol while the α -anomer remains dissolved.



22

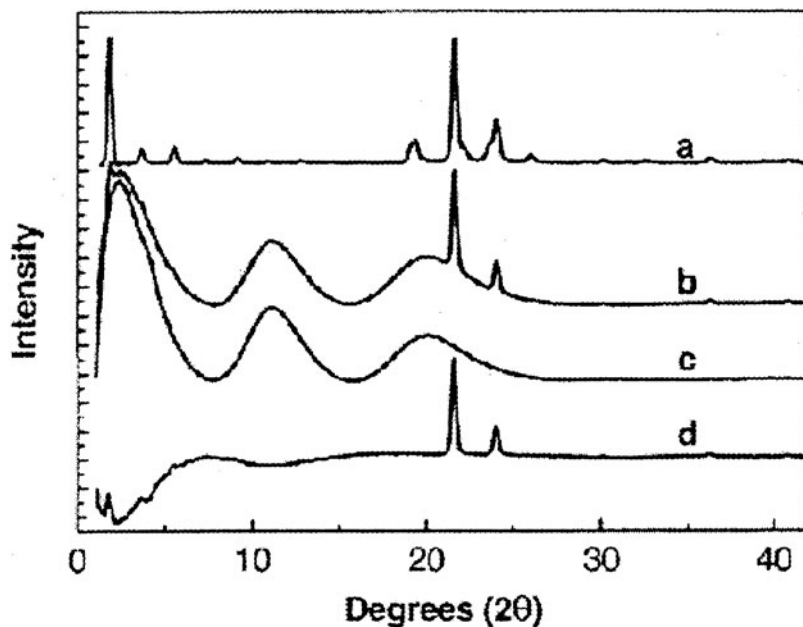


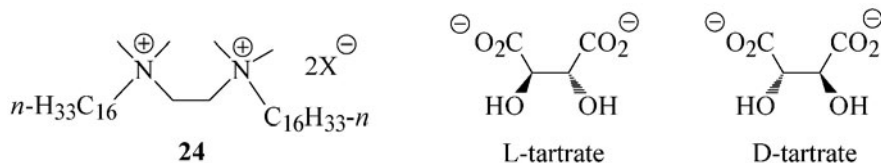
Figure 12. X-ray diffraction patterns (room temperature) of **19**: (a) powder; (b) 5 wt.% gel in silicone oil; (c) neat silicone oil; (d) diffractogram b subtracted from diffractogram c. (Reprinted with permission from [86]. Copyright (2002) The American Chemical Society.)

2.2.8. Ammonium and phosphonium salts

The gelation properties of tetra-*n*-alkylammonium and phosphonium salts, with chloride, bromide, iodide, and perchlorate as anions and alkyl chain lengths ≤ 18 carbon atoms have been investigated [82, 87]. Gelation efficiency increases with increasing alkyl chain length (due to increased van der Waals interactions), and nitrogen cationic centers produce more stable gels than the phosphorous analogs (due to stronger N^+ than P^+ electrostatic interactions with a common anion). Hence, tetra-*n*-octadecylammonium salts ($(H(CH_2)_{18})_4N^+X^-$) (**23**) are the best gelators of the series. Based on X-ray diffraction data [88, 89], the substructure of the gel fibrils are lamellae in which the ionic head groups and their counterions are arrayed in rough planes separated at regular intervals by the alkyl chains.

Gemini surfactants, consisting of dimers of cetyltrimethylammonium ions (**24**, $2X^- = L\text{- and } D\text{-tartrate}$), gelate chlorinated liquids [90]. Gelation was not observed when the counterion was *meso*-tartrate, L-malate, or bromide. Both chirality and H-bonding are important factors in gelation efficiency. Anhydrous halogenated liquids are not gelated; trace amounts of water are necessary to

solvate partially the polar moieties of the gelator. TEM micrographs of **24** gels consist of strongly entangled, long helical fibers.



2.2.9. Perfluoroalkylalkanes and related molecules

There are no reports of successful gelation of any liquid by a fully fluorinated *n*-alkane ($\text{CF}_3(\text{CF}_2)_n\text{CF}_3$). Liquid perfluoroalkanes are “poor” solvents and only slightly miscible with most other liquids [91, 92]. However, when the fluorocarbon and hydrocarbon segments are covalently attached, phase separation is inhibited and interesting organizational phenomena in the neat as well as solution phases occur.

Perfluoroalkylalkanes, in which the fluorocarbon and hydrocarbon segments are covalently linked ($\text{F}(\text{CF}_2)_n(\text{CH}_2)_m\text{H}$, abbreviated as $\mathbf{F}_n\mathbf{H}_m$) are another class of LMOG whose aggregates are stabilized primarily by London dispersion forces [93]. Molecular structures of these LMOGs contain “incompatible” segments [94–96]: molecules of fluorocarbons and hydrocarbons are immiscible below temperatures characteristic of the components [94]. As a result, the perfluoroalkyl and alkyl portions of $\mathbf{F}_n\mathbf{H}_m$ attempt to remain segregated in the lamellae of their gel assemblies. In addition, the mismatch between the cross-sectional areas of the $(\text{CH}_2)_m$ and $(\text{CF}_2)_n$ segments, 18.5 and 28.3 Å², respectively [97, 98], places additional constraints on packing.

2.2.9.1. Linear perfluoroalkylalkane gelators. Formation of gels has been observed when warm isotropic solutions of an $\mathbf{F}_n\mathbf{H}_m$ and a hydrocarbon liquid are cooled to room temperature [99, 100]. The concentrations of the $\mathbf{F}_n\mathbf{H}_m$ necessary for gelation are typically significantly higher than with other LMOGs, including long *n*-alkanes (see Section 2.1). Within the series of $\mathbf{F}_n\mathbf{H}_m$ (where $n = 10, 12$; $m = 0\text{--}20$), some gelate hydrocarbon liquids ($n = 12$; $m = 6\text{--}20$) [99, 101–103] and one ($n = 12$; $m = 10$) can gelate perfluorodecalin [100]. In a particular liquid, the properties of the gels depend strongly on the chain length of the alkyl portion of the gelator. Phase diagrams of binary mixtures of $\mathbf{F}_{10}\mathbf{H}_{12}$ and different hydrocarbon liquids are shown in Figure 13. Based on it, the interaction of the perfluoroalkane is suggested to be sensitive to the shape of the hydrocarbon liquid, and the structure of the $\mathbf{F}_{10}\mathbf{H}_{12}$ aggregates in the gels differs considerably from that of the neat gelator solid [99].

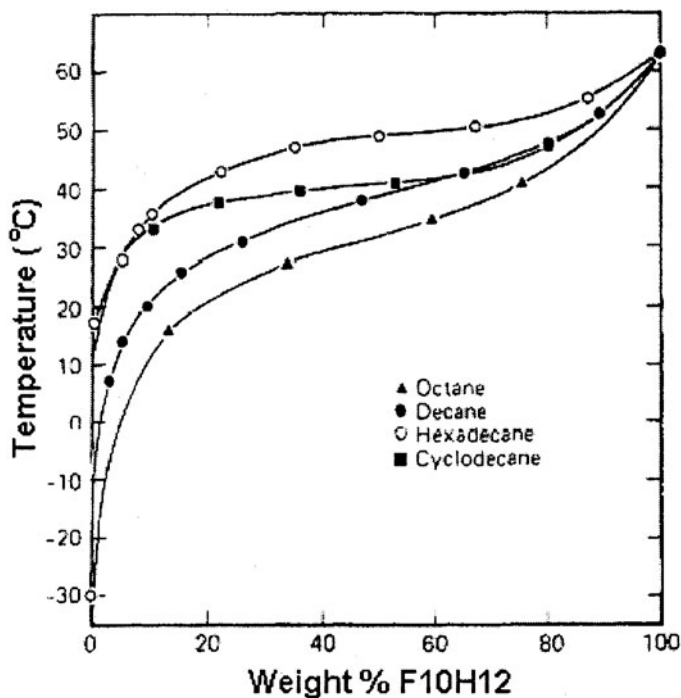


Figure 13. Phase diagrams of $F_{10}H_{12}$ in saturated alkanes. T_g corresponds to the onset of DSC endotherms of the gel samples in sealed pans. (Reprinted with permission from [99]. Copyright (1985) The American Chemical Society.)

Lang *et al.* investigated the structure of F_nH_m aggregates in hydrocarbon gels by POM and small angle X-ray scattering [104]. Keeping the perfluoroalkyl part perfluorododecyl ($F_{12}H_m$), they studied the periods of stability of 5 wt.% gels in dodecane as a function of alkyl chain length. Relatively unstable, turbid gels are formed with $m \leq 6$; more stable but turbid gels are formed when $m = 8-12$. Very stable and transparent gels are formed by $F_{12}H_m$ with $m > 12$. The T_g of these gels also increases with increasing hydrocarbon chain length until m reaches 12 and is almost constant thereafter. The differences among these gel types are exemplified by the POM images in Figure 14. Platelike crystallites are formed when the $F_{12}H_m$ have short alkyl chains, threadlike particles are observed with intermediate alkyl chain lengths, and dendritic structures are observed when m is large.

Somewhat surprisingly [99], the SAXS diffraction patterns of neat $F_{12}H_m$ powders and their 5 wt.% gels in dodecane (Figure 15) are the same [104].

The shorter analog $F_{12}H_6$ packs in lamellae whose thickness, 2.1 nm, [104] is about 80% of the length of an extended molecule (2.7 nm) [105]. This disparity indicates that the lamellae consist of monolayers of fully-extended, tilted

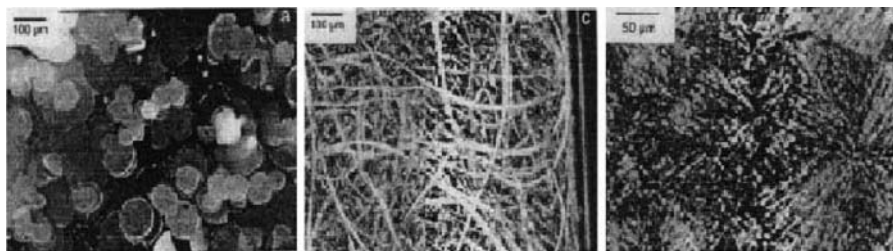


Figure 14. POM images of gels of 5 wt.% (a) $F_{12}H_6$, (b) $F_{12}H_{10}$, and (c) $F_{12}H_{20}$ in toluene. (Reprinted with permission from [104]. Copyright (1998) Wiley-VCH Verlag, GmbH.)

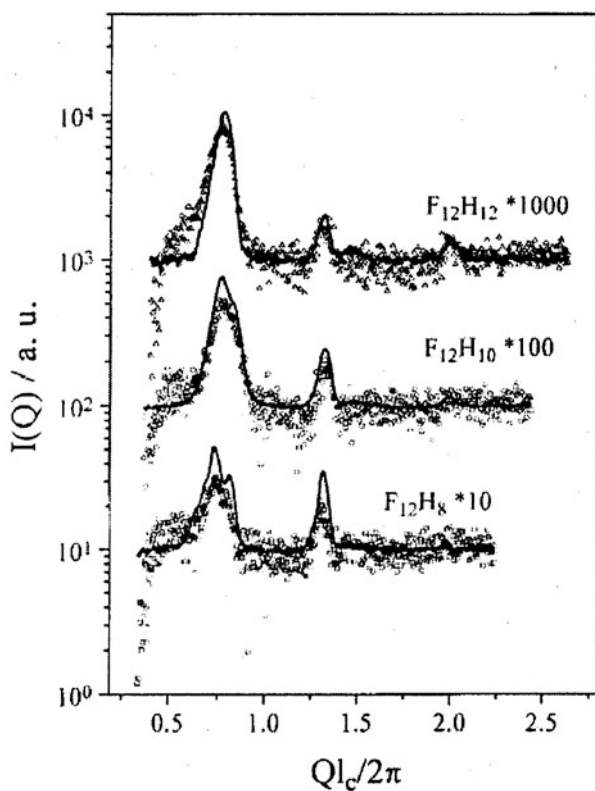


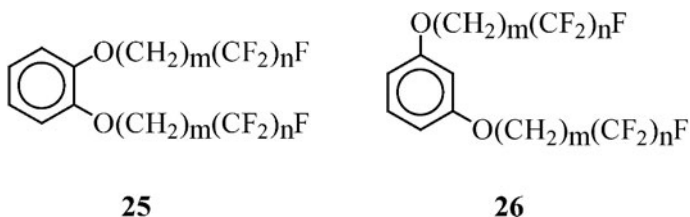
Figure 15. Comparison of the SAXS diffraction patterns from neat $F_{12}H_m$ powders (full lines) and 5 wt.% gels in dodecane (unfilled symbols). For clarity, the data have been offset on the ordinate by appropriate factors. (Reprinted with permission from [104]. Copyright (1998) Wiley-VCH Verlag, GmbH.)

$\mathbf{F}_{12}\mathbf{H}_6$ molecules (tilt angle $\approx 36^\circ$) or that the alkyl chains contain gauche bends. More complex diffraction patterns are observed for $\mathbf{F}_{12}\mathbf{H}_m$ when $8 \leq m \leq 12$ [104, 105]. The lattice spacings of these gelators are much larger than their extended theoretical lengths, suggesting that they adopt a tilted double-layered structure with interdigitating hydrocarbon chains [104, 106, 107].

2.2.9.2. Perfluoroalkanes bearing an additional functional group.

2.2.9.2.1. Perfluoroalkylalkyl chains linked to a dioxybenzene ring.

Pugh and co-workers [103] have reported that 1,2- and 1,3-dioxybenzenes with (perfluoroalkyl)alkyl chains (**25** and **26**), LMOGs with two types of heteroatoms, gelate *n*-alkanes when their heated sols are cooled. From DSC measurements, the melting *entropy* of neat **26** is higher than that of **25**. These data suggest a more ordered packing arrangement for **26** [103].



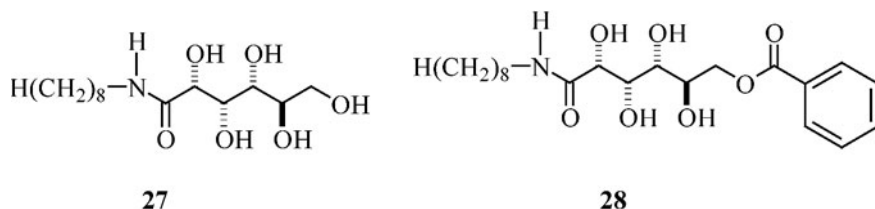
2.3. Organic Gelators with Two Heteroatoms

Primary and secondary amide and related groups (such as ureas, carbamates, and thioureas), another molecular class with two different types of heteroatoms, can act as both H-bond acceptors and donors [108] to form highly oriented aggregates. Many LMOGs have been designed to exploit the directional biases of these groups.

2.3.1. *n*-Alkanamides

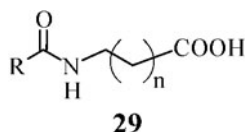
Fibrous aggregates in water can be formed from alkanamides linked to a carbohydrate head group [109–111]. A typical example is *N*-*n*-octyl-D-gluconamide (**27**), which also forms unstable gels in *o*-xylene [112, 113]. Improved gelation characteristics are observed when one or two of the hydroxyl groups of **27** are substituted with other moieties [114]. Quite interestingly, the T_g [19] of some gels of 1 wt.%/vol.% **28** are higher than the boiling points of the corresponding liquids (such as chloroform, dichloromethane, and benzene)

and the gels are stable morphologically for several months in sealed containers [114].



TEM images of a gel of 1 wt.%/vol.% **28** in chloroform ($T_g = 66^\circ\text{C}$; Figure 16) demonstrate that the gelator aggregates are finely meshed fibrils.

Taravel and Pffannemüller have followed the gelation of **27** in aqueous media by ^{13}C NMR [115]. A dimeric form of **27** was detected at 64°C , $2\text{--}4^\circ\text{C}$ above T_g found on cooling an aqueous solution (0.7 g/100 mL). Partial hydrolysis of the amide functionality of **27** also occurs at this temperature. Sols kept at 64°C for longer period (ca. 3 h) are transformed to mixtures of free and aggregated **27** and its ammonium salt. As expected if the onset of gelation involves aggregation and a corresponding loss of molecular mobility, the relaxation times (t_1) of the sugar carbons of **27** decrease as temperature is lowered to 64°C .



Vögtle *et al.* [116] have synthesized **29** ($n = 4, 6, 9,$ and 11), a gelator somewhat similar to 12-hydroxyoctadecanoic acid (**7**) in that both molecules

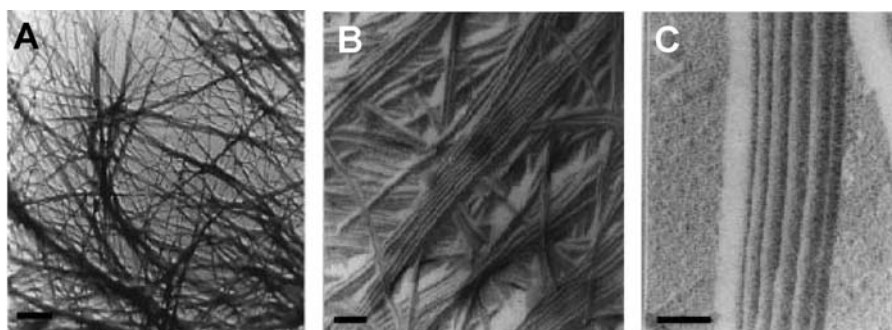


Figure 16. TEM pictures of a gel of **28** in chloroform (Pt shadowing). (A) Network of fibers; bar is $1.6\ \mu\text{m}$. (B) Bundles of whisker-type fibers; bar is $268\ \text{nm}$. (C) Intertwined bundles of fibers; bar is $200\ \text{nm}$. (Reprinted with permission from [114]. Copyright (1999) The American Chemical Society.)

have a carboxylic group and a second potentially interacting group separated by a long polymethylene chain. The gelation efficiency of **29** is dependent on the nature of the pendant N-acyl group, the amino acid chain length, and the ionization state of the carboxylic moiety. The T_g values and periods of stability of gels with acid LMOGs are lower and shorter, respectively, than those of their Na-salts (stabilities >1 year in many cases). Both coordination of the sodium cation by the carboxylate and hydrogen bond formation among amide groups probably dictate the formation of aggregates as shown schematically in Figure 17. When the R group in **29** is a photochromic naphthopyran moiety, gelation/de-gelation could be effected by sequential irradiation and heating treatments (see Chapters 24 and 26) [117].

Several types of bisamides and oligoamides gelate a wide variety of liquids [118–123] due to enhanced directional H-bonding as well as van der Waals interactions. Intermolecular H-bonding of linear α,ω -bisamides can be parallel or antiparallel depending on the number of separating methylene units (Figure 18) [124]. In fact, the gelation efficiency of these bisamides depends more on whether the number of methylene units is even or odd than on the length of the R group. For instance, more **30a**, with an even number of methylene spacers, is required to gelate mesitylene than is **30b**, with an odd number of methylene spacers [124].

The structural differences between the aggregates of **30a** (mp 156–157° C; 6 CH₂ groups in the spacer) and **30b** (mp 134–135° C; 9 CH₂ groups in the spacer) both with R = CH₃(CH₂)₁₀-, illustrated in Figure 18, are manifested

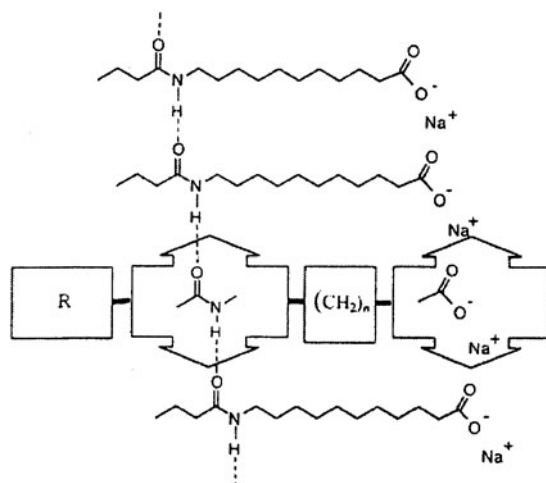


Figure 17. Illustration of one-dimensional self-aggregation in sodium salts of **29** where R is an aliphatic chain or an aromatic group. (Reprinted with permission from [116]. Copyright (2001) Wiley-VCH Verlag GmbH.)

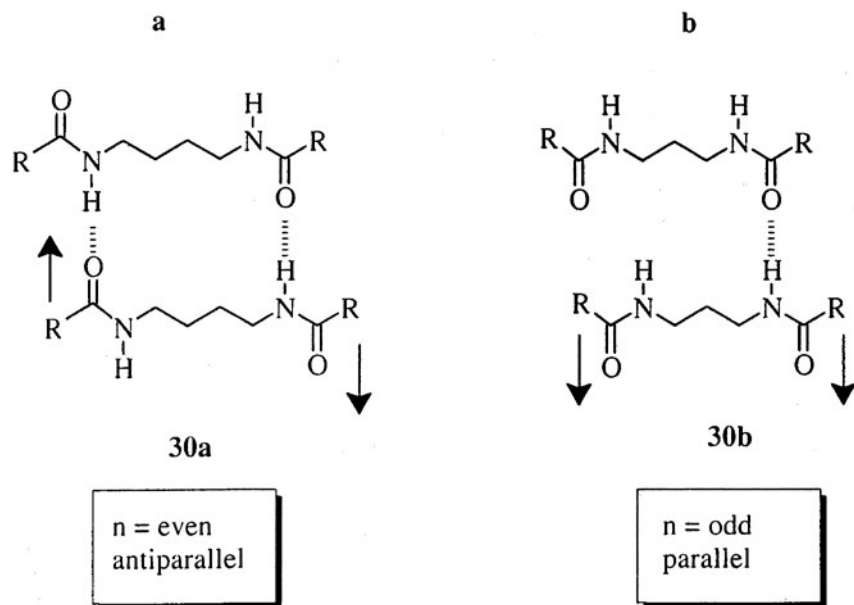
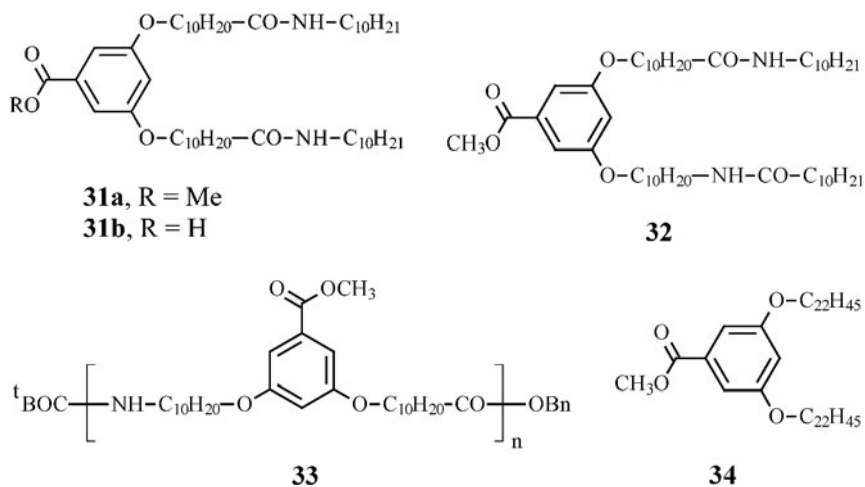


Figure 18. Illustration of antiparallel (a) and parallel (b) interactions between molecules of **30a** (4 CH₂ groups in the spacer) or **30b** (3 CH₂ groups in the spacer). (Reprinted with permission from [124]. Copyright (2001) The American Chemical Society.)

in the very different melting temperatures of the neat solids and consistent with the shapes of their gel aggregates (Figure 19).



Mésini and co-workers have studied the gelating properties of bis- and oligo-amides connected to or through an aromatic unit (**31–33**) [125–127].

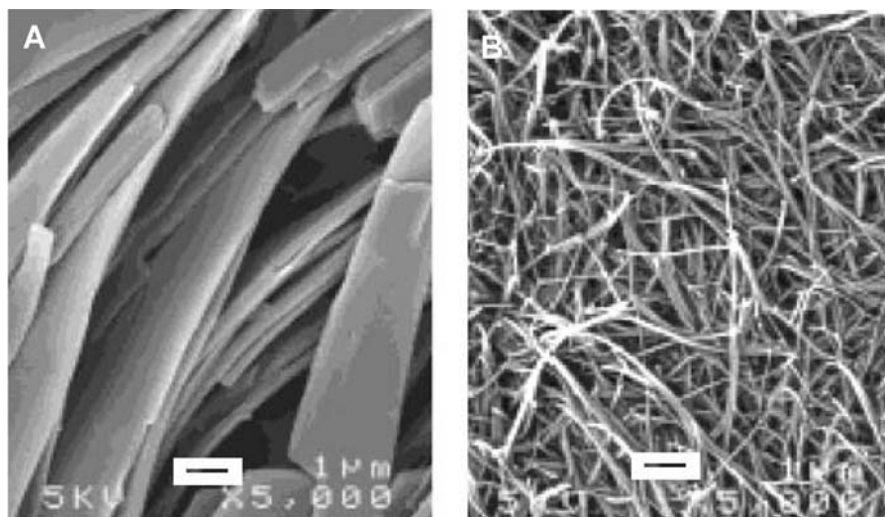
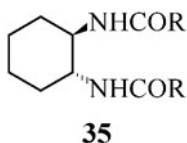


Figure 19. SEM images of xerogels (from mesitylene) of **30a** (A) and **30b** (B). See text for details concerning the specific molecular structures. The space bars correspond to 1 μm . (Reprinted with permission from [124]. Copyright (2001) The American Chemical Society.)

At 3 wt.%, compounds **31**, **32**, and **33** ($n = 3,4$) gelate aromatic liquids like benzene, toluene and *p*-xylene, but the simple ether analogous to **32,34**, remained dissolved in these liquids [127]; the amide groups along the long chains are requisite to molecules with *this* substitution pattern being LMOGs of aromatic liquids. Pozzo *et al.* have determined that 1,2- and 1,3-di-*n*-alkoxybenzenes (i.e., molecules like **34** but with shorter alkyl chains and lacking its methoxycarbonyl group) are LMOGs of polar liquids such as acetonitrile, propylene carbonate, dimethylformamide (DMF), dimethylacrylamide, methanol, and ethanol [52]. The combination of these results suggests that the presence of the carboxy and carbomethoxy groups of **31–33** may be deleterious to packing in a fibrillar network.



The gelation properties of 1,2-diamidocyclohexanes (**35**) have been studied by several groups. Many of the enantio-pure *trans* isomers are able to gelate a wide variety of liquids, including hydrocarbons, alcohols, ketones, esters, ethers, polar aprotic solvents, mineral oils, and edible oils [128]. Intermolecular H-bonding between the amide groups of adjacent molecules, van der Waals

interactions of the long alkyl chains, and the projection angle between the alkyl chains off the cyclohexane platform are principal determinants of the packing within the aggregates of **35**. Thus, no gels are observed when the *n*-alkyl tails of enantiomers of *trans*-**35** contain less than six methylene units. Under these circumstances, chain-chain interactions are not strong enough to maintain fibrillar aggregates. In addition, the (*meso*) *cis* isomer of **35** does not form gels in any of the liquids gelled by the enantiomers of the *trans* isomer. Finally, the importance of projection angles for efficient *intermolecular* interactions and packing is reinforced by observations that racemic mixtures of *trans*-**35** produce much less stable gels than the pure enantiomers [128]. Acetonitrile gels of **35** (with R = H(CH₂)₁₁-) have been used as a matrix for gel electrophoresis [129]. After separation of a mixture of dansylated amino acids, the gels were liquefied so that the individual amino acids could be injected *in situ* into an electrospray mass spectrometer for identification. This approach has clear advantages over polymer gel matrices that require additional preparative steps prior to injection.

When R contains a polymerizable group such as acrylate or conjugated diyne and the fibrillar structure is polymerized, the thermal and temporal stabilities of the gels are enhanced [130, 131].

CD spectra of gels of enantiomers of *trans*-**35** demonstrate that the molecular chirality is manifested in the fibrillar packing. As discussed in Chapter 13, large amplifications of CD signals from aggregates of chiral LMOGs in gels has been observed in other systems as well [47, 48]. Figure 20 includes

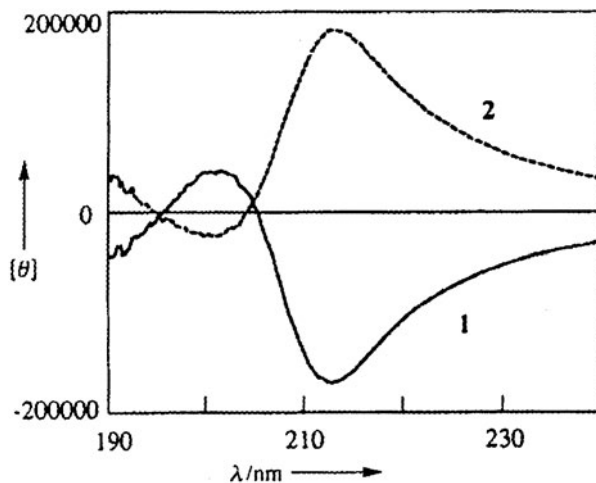


Figure 20. CD spectra at 20° C of gels of 1.0 mM (1*R*, 2*R*)-**35** (1) and (1*S*, 2*S*)-**35** (2) in acetonitrile. The molar ellipticity $[\theta]$ is in $\text{deg}\cdot\text{cm}^2\cdot\text{dmol}^{-1}$. (Reprinted with permission from [128]. Copyright (1996) Wiley-VCH Verlag GmbH.)

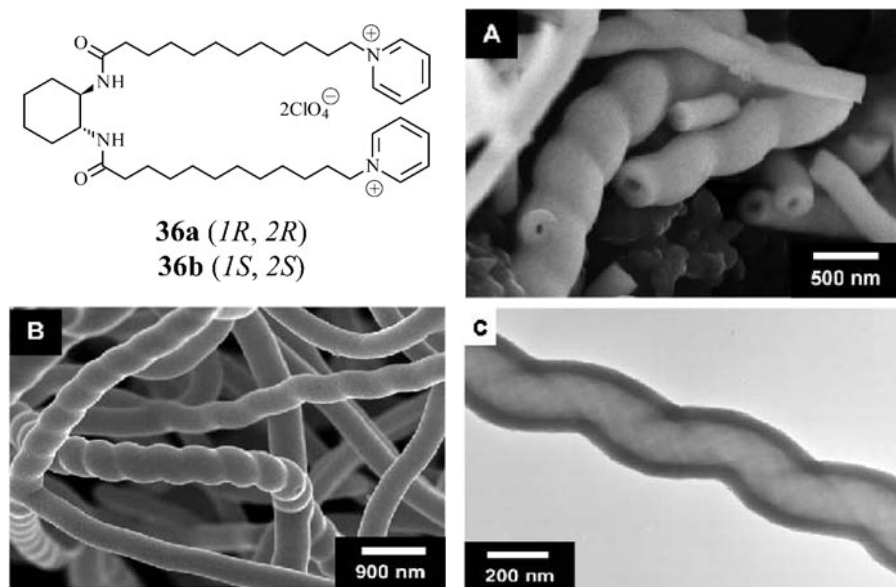
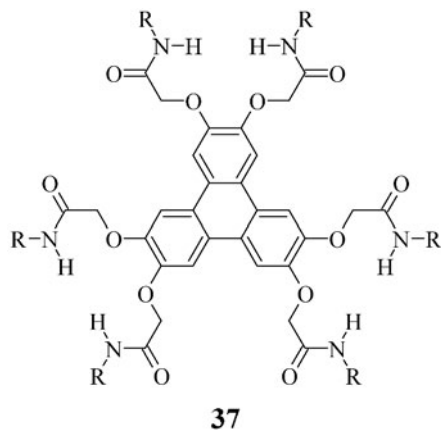


Figure 21. SEM images of tantalum oxide fibers obtained from (A) the (*R, R*)-enantiomer **36a** and (B) the (*S, S*)-enantiomer **36b**, and (C) TEM image of a left-handed helical fiber of tantalum oxide obtained from **36a**. (Reprinted with permission from [133]. Copyright (2002) The American Chemical Society.)

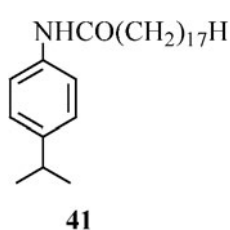
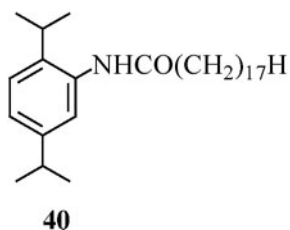
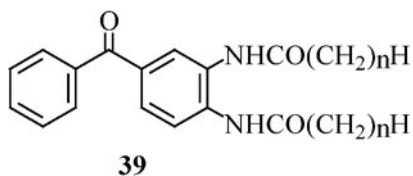
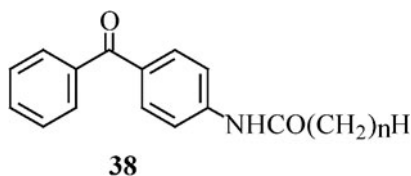
representative CD spectra of gels of (*1R, 2R*) and (*1S, 2S*) *trans*-**35** with $R = n\text{-C}_{11}\text{H}_{23}$ in acetonitrile [128].

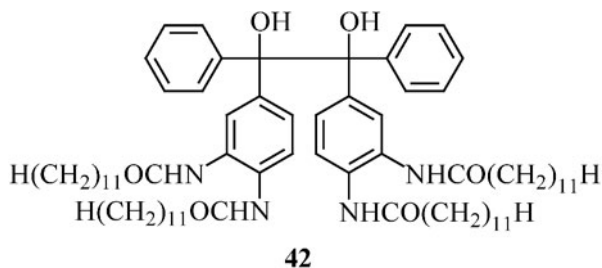
The macroscopically chiral, helical fibrillar structures can be transcribed into silica or transition metal (Ti, Ta, V) oxides by sol-gel polycondensations [132–135]. Figure 21 shows the SEM (**36a,b**) and TEM (**36a**) images of tantalum oxide fibers obtained from the polycondensation of **36a,b** gels in Ta(OC₂H₅)₅. The transcribed objects are helical structures with an outer diameter of 100–600 nm and a maximum length of ca. 30 μm [134]. Mirror-image helical silica structures have been made from 1:1 (wt.%) mixtures of (*1R, 2R*)-**36** and (*1S, 2S*)-**36** with $R = n\text{-C}_{11}\text{H}_{23}$ and $R = \text{C}_{10}\text{H}_{20}\text{N}(\text{CH}_3)_3\text{Br}$ as the gelators [132, 133]. Helical aggregates are known to form in gel phases employing very different classes of LMOGs, including steroid derivatives [4, 136–140], phospholipid-nucleosides [141], porphyrin derivatives [142], substituted helicenes [143], 12-hydroxyoctadecanoic acid salts [144], boronic-acid-appended chiral diols [145], and conjugated diacetylene derivatives [146, 147]. A detailed description of these classes of LMOGs is reported in Chapter 25.



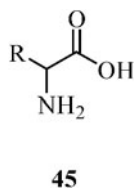
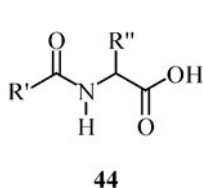
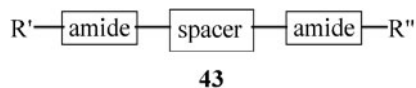
Triphenylene-based LMOGs (**37**) gelate hydrocarbon liquids [148]. LMOGs **37** with longer-alkyl chains ($R = n\text{-C}_{12}\text{H}_{25}$) are more efficient gelators than those with shorter chains ($R = n\text{-C}_4\text{H}_9$). LMOG **37** exhibits unusual optical emission properties from excimer formation [148] in cyclohexane gels.

Koshima and co-workers have converted gels prepared from photoreactive LMOGs (**38–41**) to sols by irradiating them [149]. For example, irradiation of a gel comprised of **39** ($n = 11$; 70 g/L) in 2-propanol for 55 h at 15°C with the output from a high-pressure mercury lamp transformed the gel into a mixture of a yellow liquid and some phase-separated solid. The photoinduced loss of **39** is more rapid in solution than in the gel. The major photoproduct, 20% yield of the pinacol (**42**), was obtained as a 1:1 diastereomeric mixture. Moreover, the photoreaction was significantly slower in the gel phase than in solution.

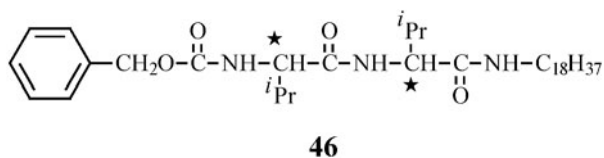




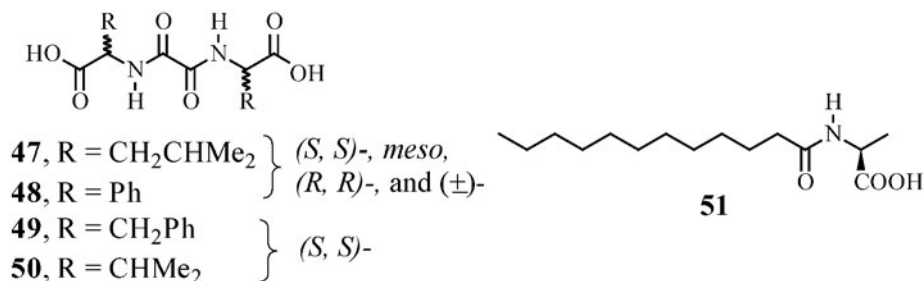
2.3.2. Amino acid derivatives



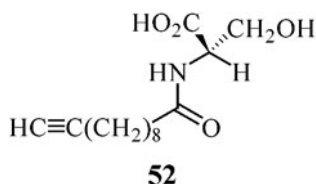
Some amino acid derivatives in which the nitrogen atom is part of an amide moiety, as in molecules with the general structures **43** or **44**, and in which the nitrogen atom is part of a pendant amine group **45**, are gelators of both aqueous and organic liquids. The different functional groups present in these LMOGs allow formation of aggregates through intermolecular H-bonding, dipole–dipole, and other van der Waals interactions. The gelation efficiency of this class of LMOGs differs widely with the nature of the substituent [150–159]. In general, the gelation ability strongly depends on the structure of the amino acid residue: racemic residues are not gelators in most cases and gelation efficiency increases when more than one peptide unit is present in one molecule. Another factor that affects gelation efficiency is the balance between the hydrophobicity of the alkyl substituent and hydrophilicity of the amide moiety. *N*-benzyloxycarbonyl-L-valyl-L-valine *n*-octadecylamide (**46**) is a very efficient gelator. It can gelate a wide variety of organic liquids, including alkanes, alcohols, esters, ketones, aromatic molecules, mineral oils and edible oils [160].



The gelation efficiency of amino acid derivatives can be “tuned” to some extent by structural variations [161]. For instance, the eight H-bonding sites present in LMOGs **47** and **48** allow formation of strong aggregates in water and polar organic liquids (such as ethanol, 1,4-dioxane, THF, ethyl acetate and acetone). The structurally similar compounds **49** and **50** were able to gelate all of the liquids that were gelated by **47** and **48**.



Phase selective gelation of an organic liquid from an aqueous solution containing the gelator **51** has been observed [162]. Although two H-bond donating sites are present in **51**, its alkyl chain exerts a hydrophobic effect [163] to exclude water. As with other LMOGs, there must be a structural component that allows phase separation from the liquid as the sol (solution) is cooled from above T_g .



The L-serine derivative **52** forms “firm solid gels” in CHCl₃, CH₂Cl₂, or CCl₄ at concentrations above 6 mM [164]. A UV-Vis absorption spectrum of 0.2 mM **52** in CHCl₃ indicated intermolecular H-bonding (i.e., an amide absorption band centered at 240 nm), which is stronger than and red-shifted with respect to the band in basic aqueous media (at 213 nm). Three different microstructures are observed in a **52**/CHCl₃ gel (Figure 22): multilamellar spheres (a), tubules up to 3 mm in length and 5–20 μ m in diameter (b), and right-handed helical ribbons of 15–30 μ m width (c). The spherical morphology is unstable and collapses into helical ribbons or tubules with time. The intertwining and entangling of the long tubules and intermolecular H-bonding

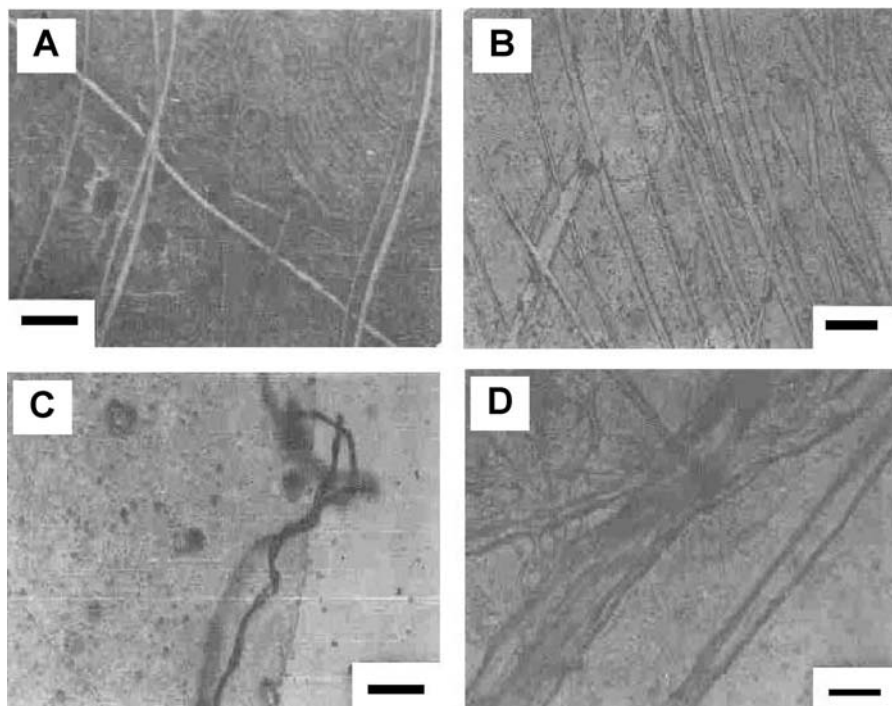
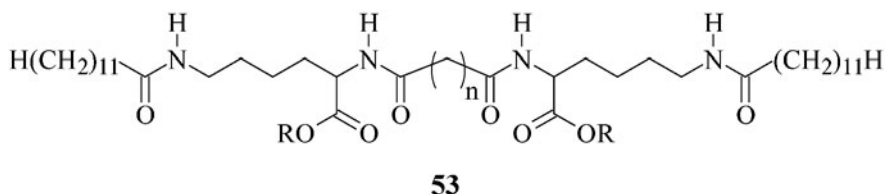


Figure 22. Optical micrographs of a **52**/ CHCl_3 gel: (a) spherical structures and intertwined tubules, (b) tubules, (c) helical ribbons, and (d) precipitated tubules obtained by the addition of petroleum ether to the gel. The scale bars in (a)–(c) correspond to $100\ \mu\text{m}$ and that in (d) is $40\ \mu\text{m}$. (Reprinted with permission from [164]. Copyright (1995) Elsevier Science Ireland Ltd.)

interactions lead to the formation of gels. Addition of a small amount of petroleum ether resulted in the precipitation of intertwined and entangled tubules as shown in Figure 22d. Tubule formation starts with strips separated by sharp domain walls, followed by break-up of the strips along the domain walls to form ribbons. Then, twisting of the ribbons results in helical structures that fuse into tubules (see Chapter 3 for additional information) [165–167]. Examples of structurally-related chiral molecules whose nanotubules organize further into 3-dimensional networks, leading to gels, have been reported by Shimizu and co-workers [168, 169], and several of these gels have been employed in sol-gel transcription (see Chapter 25 for additional information) [170, 171].

Gelation by gemini LMOGs in which two L-lysine derivatives are linked through a polymethylene spacer (**53**) has been observed for diverse organic liquids (e.g., low-polarity cyclohexane and more polar methanol) [172, 173]. Gelation efficiency decreases with increasing oligomethylene spacer length due

to the increasing solvophilicity. The oxalyl amide derivatives ($n = 0$) gelate alcohols, cyclic ethers, aromatic liquids and acetonitrile.



^1H NMR and FT-IR spectra indicate the presence of inter- and intramolecular H-bonds in the gel phase of **53** [172]. The proposed mechanism of gelation is illustrated in Figure 23. In a non-gelled liquid, such as CHCl_3 , the gelator molecules do not self-assemble and possess both free and intramolecular H-bonded amide groups. In the gelled state (such as in CCl_4), molecules of **53** form intermolecular H-bonds and eventually three-dimensional networks.

Žinić and co-workers reported irreversible photoinduced gelation by bis(phenylalanine)maleic acid (**54**) in water [174]. Irradiation of an aqueous solution of **54**, in the presence of trace amounts of bromine, using a high-pressure Hg lamp ($\lambda > 330\text{ nm}$, glass filter), leads to almost instantaneous gelation as a result of formation of the fumarate isomer (**55**).

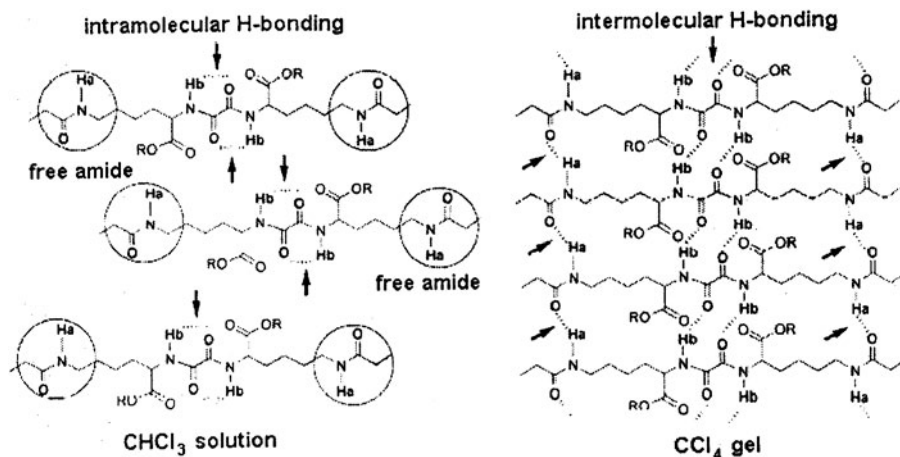


Figure 23. Proposed mechanism for formation of organogel networks by **53** based principally on intermolecular H-bonds. (Reprinted with permission from [172]. Copyright (2003) Royal Society of Chemistry.)

Powder X-ray diffraction and IR spectra of xerogels of **58** are different from those of the recrystallized powder [180]. The major diffraction peaks observed for the xerogels are at $2\theta = 2.86^\circ$ (30.7 Å) and 21.64° (4.10 Å). The powder sample showed peaks at $2\theta = 3.40^\circ$ (26.7 Å) and 21.46° (4.24 Å). The NH stretching frequency of the amide bond in the IR spectra was observed at 3288 cm^{-1} in the xerogel and 3298 cm^{-1} in the recrystallized powder. From these data and related NMR studies, a model with a single-layer structure and tighter packing than in the powder was derived for the xerogel aggregates. The driving force for aggregation is intermolecular H-bonding involving the three amide groups: addition of trifluoroacetic acid (equimolar to **58**) prevents gelation.

Supramolecules and supramolecular assemblies, such as aqueous lipid bilayer membranes and α -helical poly(amino acids), possess highly oriented microenvironments in which nonchiral dyes may reside [181, 182]. In a similar way, aggregates of glutamate in gels also can be oriented structures that have remarkable enhancement of optical activity [176, 177, 183]. These gels have been shown to interact with nonchiral cyanine dyes such as **59a,b** and induce their chirality (Figure 25). The binding ability of the dyes varies with the nature of the substitution on the glutamate chain. The anionic cyanine dye **59a** binds efficiently when the glutamide LMOG contains a pyridinium cation, producing chiral dimers with extremely strong exciton coupling [184, 185]. In a benzene gel of **58**, the binding efficiency of **59a** was much weaker than that of the cationic cyanine dye (**59b**) (Figure 25a). This difference has been attributed to the stronger electrostatic interactions between the cationic dye and the gelator aggregates [177].

When chromophores are attached to a glutamide LMOG, the aggregation phenomena can be monitored by photophysical techniques even at low concentrations [186, 187]. For instance, transparent gels of $2.0 \times 10^{-2}\text{ M}$ spiropyran **60** in benzene could be isomerized photochemically (high pressure mercury lamp; $\lambda = 330\text{--}380\text{ nm}$) to the merocyanine form. The kinetics of the thermal isomerization of the merocyanine-appended **60** was then followed (Figure 26) [188]. The shift of the absorption maxima, from 585 to 560 nm, is ascribed to the presence of H-like (head-to-head) aggregates of merocyanine species [189].

2.3.3. Peptides

Substituted linear and cyclopeptides are known to gelate a wide variety of organic liquids and water [190–192]. The gelation ability of this class of LMOGs is attributed to multiple H-bonding sites in each molecule as well as kinetically-controlled (perhaps random) alignment of the peptides in their aggregates that prevents crystallization. The first gelation of a cyclopeptide

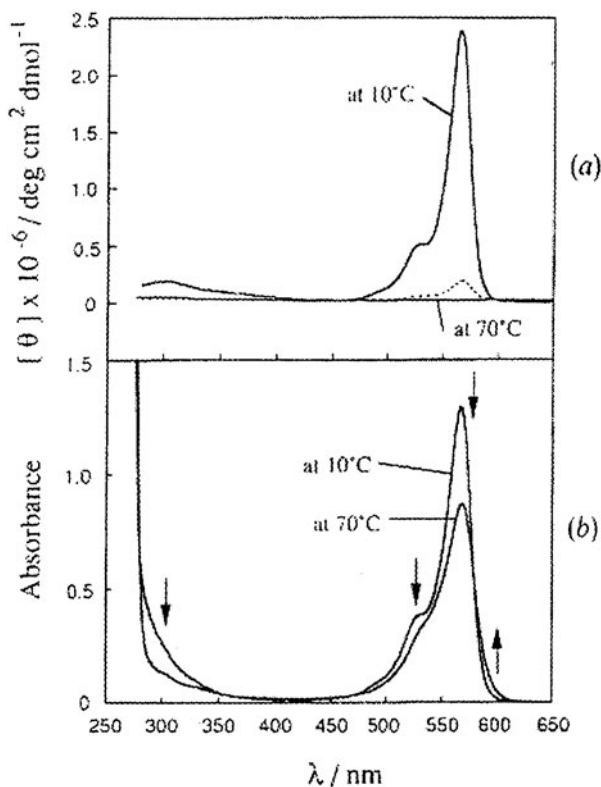
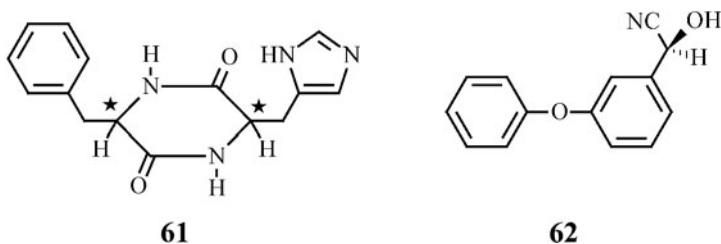


Figure 25. CD (a) and UV-Vis (b) spectra of **59a** (dotted line) and **59b** (solid line) in benzene gels of 5.0×10^{-3} mol/L **58**. $[\mathbf{59a}] = [\mathbf{59b}] = 1.0 \times 10^{-5}$ mol/L. (Reprinted with permission from [177]. Copyright (1995) Taylor & Francis Ltd.)

was reported in 1991 when Danda and co-workers observed gelation of a 1: 0.8 mixture of cyclo[(*R*)-phenylalanyl-(*R*)-histidyl] (**61**) and (*S*)-2-hydroxy-2-(3-phenoxyphenyl)acetonitrile (**62**) in toluene during the course of an asymmetric reaction [193].



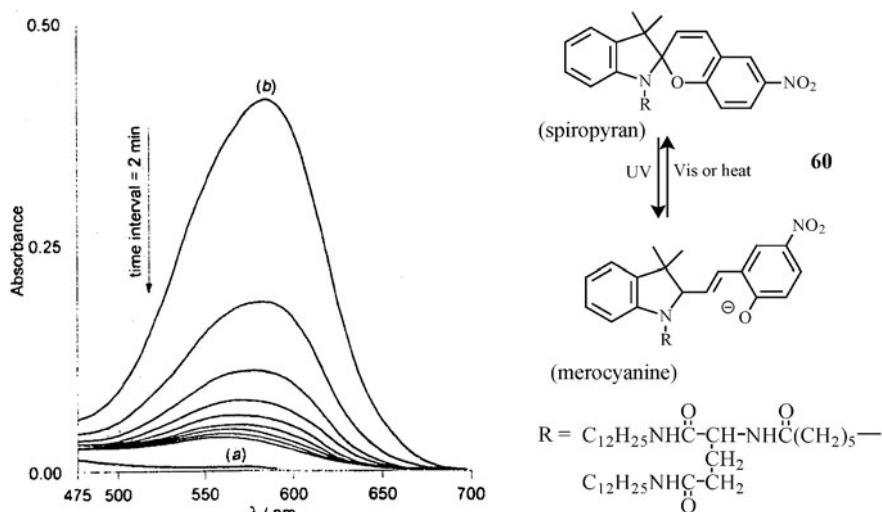
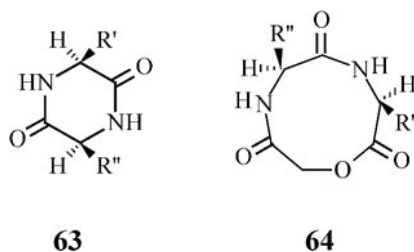


Figure 26. Absorption spectra of an irradiated 2×10^{-2} M **60** in benzene gel in a 0.1 mm path length cell at 20° C: (a) before and (b) immediately after 5 min. irradiation; the intermediate spectra are taken at 2 min. intervals after the excitation. (Reprinted with permission from [188]. Copyright (1997) Royal Society of Chemistry.)

Several substituted cyclodipeptides **63** and **64** can gelate a variety of liquids [151, 192, 194]. Aggregation is driven mainly by intermolecular H-bonding because a long alkyl chain substituent at R' or R'' has no adverse effect on the gelation ability.



Non-polar liquids such as alkanes are gelled by sugar-based guanosine (**65**) and thymidine (**66**) derivatives [195–198]. A structural hierarchy is indicated by atomic force micrographs of **65**/dodecane gels. Mesoscopic-scale, sheet-like assemblies formed via H-bonds between nanometer-scale width tape motifs are seen (Figure 27). The tape motifs are formed by *intra*-tape H-bonds and the sheet-like structure by *inter*-tape H-bonds [195]. Splitting and stitching of these sheet assemblies results in networks and gelation.

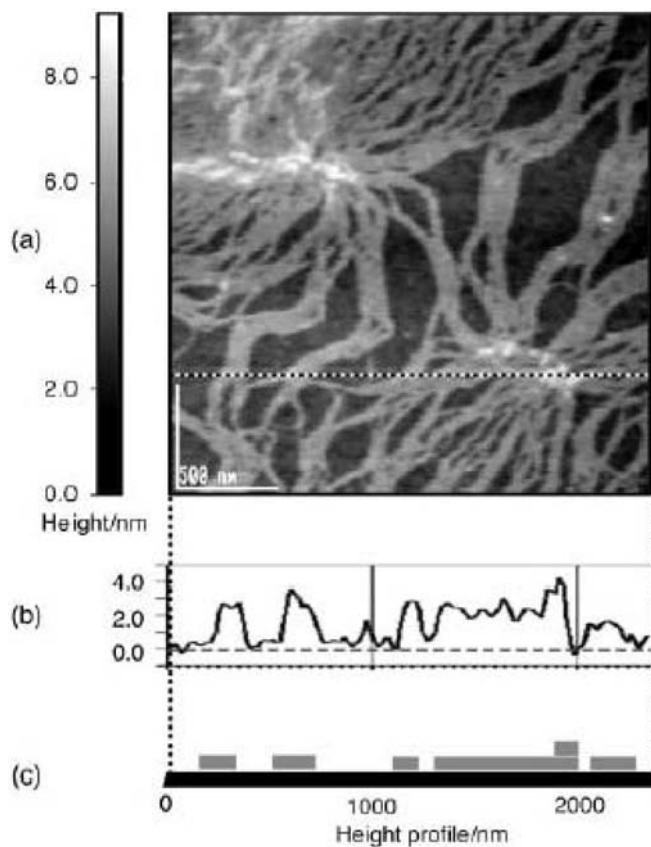
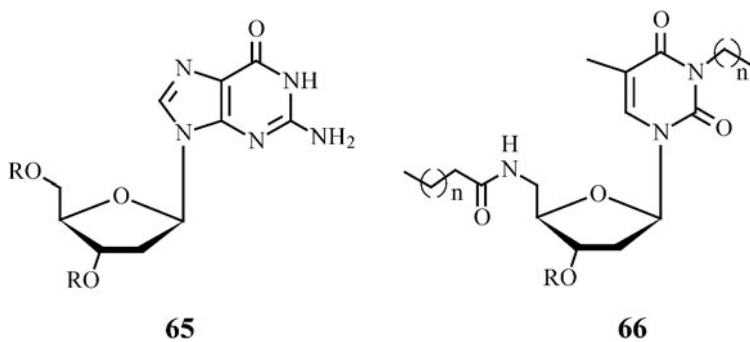


Figure 27. (a) AFM micrographs of a 5 wt.% **65**/dodecane gel. (b) Depth profile along the line in the image. The height from the silicone surface is shown in nm. (c) Schematic view of the depth profile. (Reprinted with permission from [195]. Copyright (2001) Royal Society of Chemistry.)



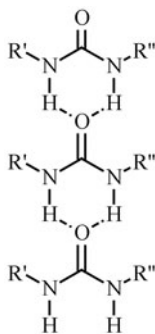
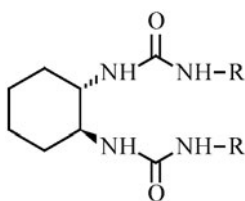


Figure 28. α -Networks formed by N,N' -disubstituted urea derivatives.

2.3.4. Urea derivatives

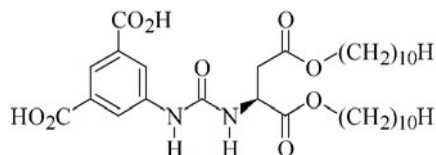
Urea and thiourea are known to aggregate in helical lattices, held in place by intermolecular H-bonding, when molecules like straight-chain hydrocarbons act as templates [199–203]. Their aggregation behavior has been studied extensively [204, 205]. N,N' -Disubstituted ureas can form α -networks (i.e., with one degree of translational symmetry [206]) (Figure 28) [206–208], and some of these have been known for decades to become gels. For example, N -phenyl- N' -(alkoxycarbonyl)phenyl ureas, UV light protecting agents in cosmetics, gelate paraffins [209] and urea and substituted ureas gelate biological fluids such as milk [210], proteins [211–217], and hemoglobin [218]. Several urea derivatives also gelate water [219, 220].

Only a few examples of mono urea and thiourea derivatives as LMOGs for organic liquids are known [221, 222]. These include N,N' -dimethylurea (M_w 88), the lowest molecular mass LMOG currently known [222b]. Clearly, intermolecular H-bonding and, therefore, the strength of intermolecular interactions increase when more than one urea moiety is part of a molecule. Several cyclohexane appended *bis*-urea gelators (**67**) have been studied [130, 132, 223–226]. Their IR spectra in solution and in xerogels demonstrate that strong H-bonding occurs in the gels.

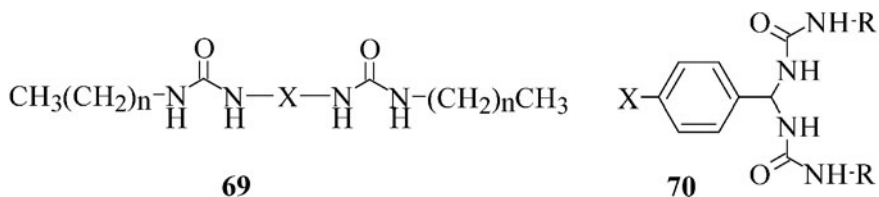
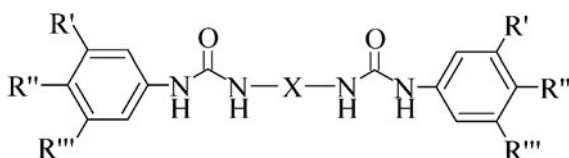


67

As low as 0.5 wt.% of the isophthalic acid appended urea derivative **68** gels chloroform and tetrachloroethane [227]. Investigations with structurally related compounds indicate that the two carboxylic acid and the urea groups are necessary structural features of this variety of gelator.

**68**

Bis-urea LMOGs **69-71** are also known to gelate several liquids [228–231]. The gelation ability of **69** depends strongly on the nature of the X linker: gelation is facilitated more by linear methylene chain X groups than by aromatic groups [223, 232]. When X is an azobenzene moiety, the gelator aggregates are polymorphic [233]. Also, a 4, 4'-disubstituted azobenzene X group results in weaker gelators than its 2,2' analog (**69a**).

**69****70****71**

UV-Vis absorption spectra show that the supramolecular aggregates formed in the gels of **69a** depend on the type of liquid present (Figures 29 and 30). Spectra of gels in polar solvents such as 1,2-dichloroethane are hypsochromically shifted with respect to solutions due to exciton coupling between azobenzene chromophores [234–236]; a face-to-face type aggregate is present in polar solvents [237]. In gels with nonpolar solvents such as cyclohexane, bathochromically shifted spectra with vibronic structural features are observed. Spectra of toluene gels are different still in that they are time-dependent (Figure 30). Apparently, kinetically favored aggregates form

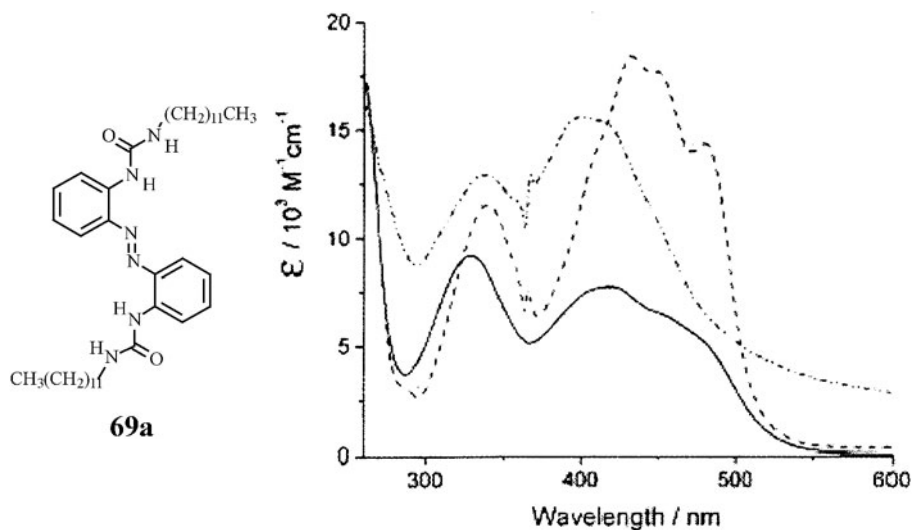


Figure 29. UV-Vis absorption spectra at 25° C of a solution of 0.1 mM **69a** ($n = 11$) (—) and of a gel (1.85 mM) in 1,2-dichloroethane (- - -) and of a gel (2.37 mM) in cyclohexane (- · - ·). (Reprinted with permission from [233]. Copyright (2002) The American Chemical Society.)

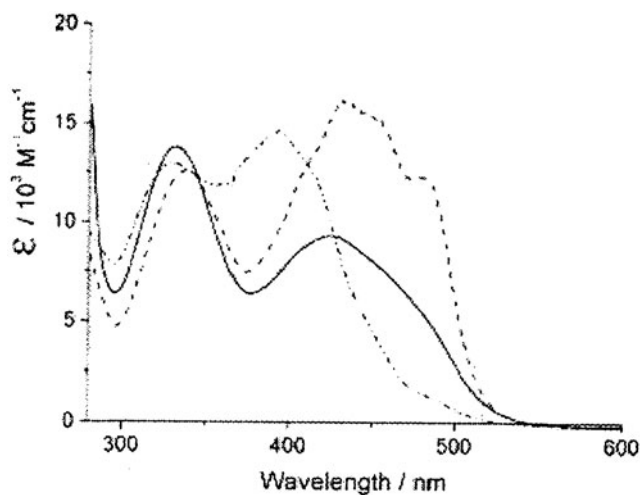


Figure 30. UV-Vis absorption spectra of a solution of 1.26 mM **69a** ($n = 11$) in toluene at 70° C (—) and of the gel obtained immediately after cooling to 25° C (—) and after 30 min (- · - ·). (Reprinted with permission from [233]. Copyright (2002) The American Chemical Society.)

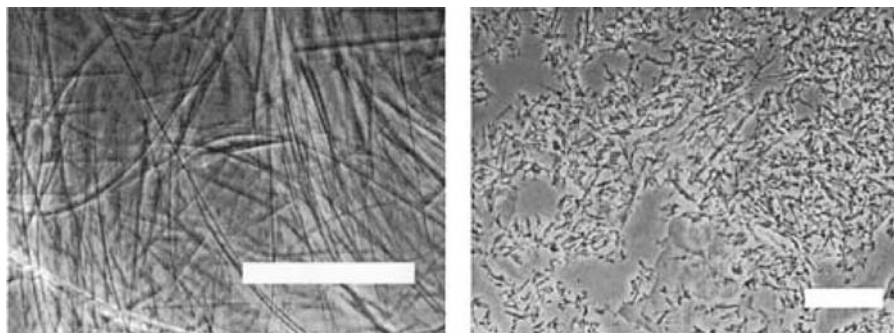
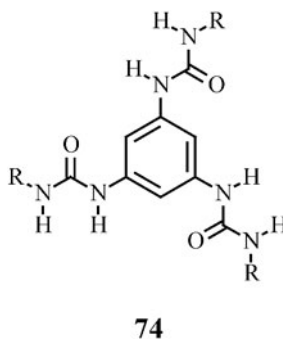
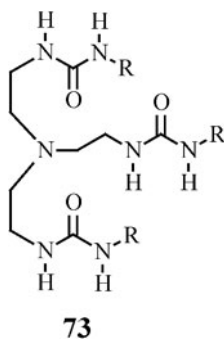
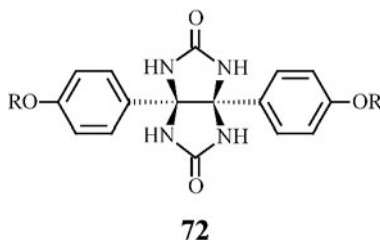
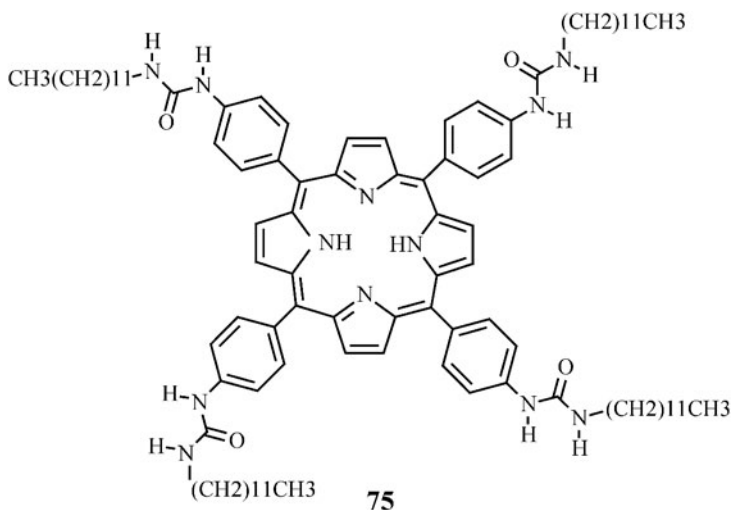


Figure 31. Optical micrographs of benzyl alcohol gels of **72** (a) R = PhCH₂—(scale bar 60 μm) and (b) *n*-C₁₅H₃₁— (scale bar 60 μm). (Reprinted with permission from [239]. Copyright (2001) The American Chemical Society.)

initially in toluene and then transform into thermodynamically more favored one(s) as the gels age.

Menger *et al.* have studied the gelation of benzyl alcohol by ≥ 40 mM bicyclobisureas (**72**) [238, 239]. The nature of aggregates depends on the structure of the substituent R. Long, flexible aggregates form when R is benzyl and small, loosely-assembled microcrystals are observed when R is *n*-C₁₅H₃₁— (Figure 31).

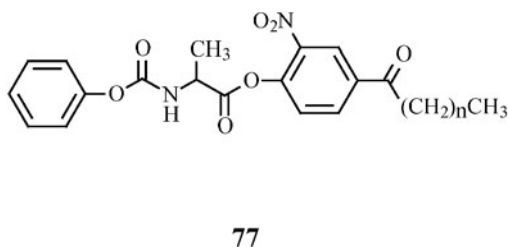
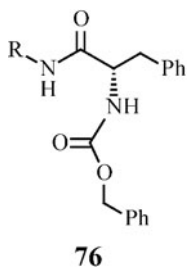




Several *tris*-urea derivatives (**73–75**) are LMOGs for a variety of organic liquids [123, 240, 241]. These LMOGs are not significantly more efficient than analogs *bis*-ureas. *Intramolecular* H-bonding, that negates the possibility of stronger *intermolecular* interactions, may become important in the *tris*-ureas. The C_3 -symmetrical discotics (**74**) form helical, elongated, columnar aggregates. Organogels of the urea-appended porphyrin **75** consist of one-dimensional aggregates, a packing arrangement not encountered frequently with LMOGs [242].

2.3.5. Urethanes

Urethanes (carbamates), like amides and ureas, aggregate through intermolecular H-bonds, π - π and dipolar interactions, and van der Waals forces. Urethanes derived from L-alanine and L-phenylalanine (**76**, **77**) gelate liquids such as *n*-alkanes, aromatics, halogenated solvents, ethers, and short chain alcohols [154, 243, 244]. Urethanes attached to pyrene (**78**) also are LMOGs for organic liquids [245]. Helical aggregates form when a chiral group is present, as in **78b** (Figure 32).



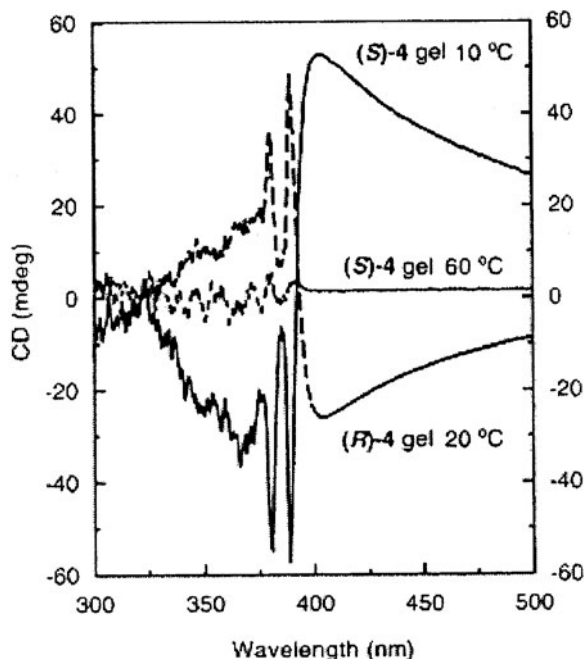
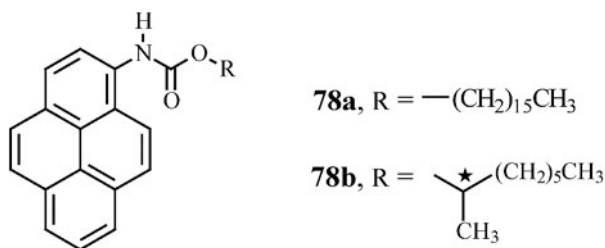
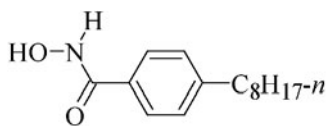


Figure 32. CD spectra of gels derived from (*R*)-**78b** and (*S*)-**78b** in cyclohexane at the temperatures indicated. (Reprinted with permission from [245]. Copyright (2001) Elsevier Science Ltd.)



2.3.6. Miscellaneous two-heteroatom gelators

Terech and co-workers have investigated the gelation and structural properties of 4-octylbenzohydroxamic acid (**79**) in several organic liquids by SAXS and SANS techniques [246, 247]. The aggregates of **79** are stabilized by H-bonding of the head groups and van der Waals interactions of the aliphatic chains. At low (ca. 0.1 wt.%) concentrations of **79**, circular (r , the cross-sectional radius, ca. 58 Å) or slightly rectangular (ca. 70 × 150 Å) shaped rigid fibers are formed [246]. At higher concentrations, flat ribbon or lamellar like particles appear.

**79**

The chiral azobenzene containing a cyclic *syn*-carbonate moiety (*R,R*)-(+)-**80** gels alcohols, alkanes and hexafluorobenzene [248]. Aggregation to make fibrous networks (Figure 33) is driven by dipolar interactions between the chiral carbonate moieties. No gelation was observed by the racemate of **80** in these liquids. IR frequencies of the C=O stretching of (*R,R*)-(+)-**80** in the sol (1720 cm^{-1}) and gel (1708 cm^{-1}) states in dodecane indicate intermolecular interactions between the *syn*-chiral carbonate moieties in the gel state [248].

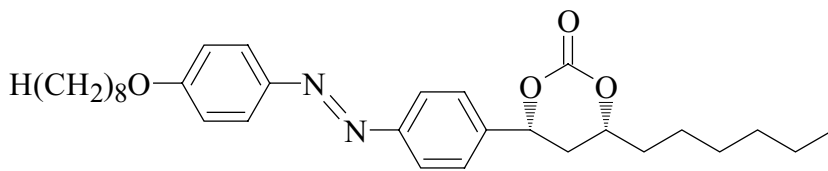
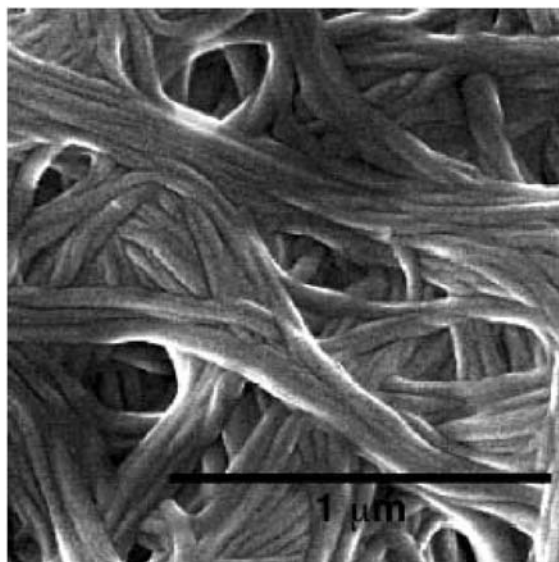
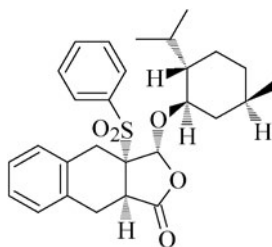
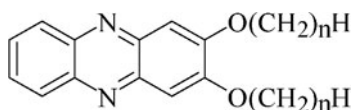
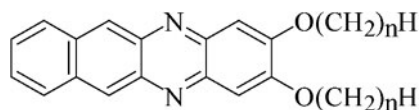
**80**

Figure 33. SEM image of self-assembled fibers prepared from an (*R,R*)-(+)-**80**/2-propanol gel. Scale bar = $1\ \mu\text{m}$. (Reprinted with permission from [248]. Copyright (2002) Royal Society of Chemistry.)

Very low concentrations (e.g., 1:800 (mol:mol) in *n*-hexane) of the γ -alkoxybutyrolactone annulated tetraline derivative (**81**) gels nonpolar organic liquids [249]. However, polar liquids (with the exception of 2-propanol) and others containing π -electrons) are not gelled by **81**. The aggregates consist of highly ordered three-dimensional networks of entangled fibers. The sizes of the domains depend on the concentration of the gelator and the type of liquid. For example, the network of the 2-propanol gel is more rigid than that of the hexane gel at the same gelator concentration [249].

**81**

Azapolycyclic arenes (**82** and **83**) form orange colored, translucent gels with alcohols, propylene carbonate, and acetone that are stable for several weeks [250]. Some principal driving forces for aggregation in these LMOGs are π - π stacking, dipole-dipole and other van der Waals interactions. The gelation abilities of **82** and its non-aza analog **14** (Section 2.2.4) should be compared.

**82****83**

The ease of aggregation and T_g values of **82a** ($n = 9$) and **82b** ($n = 11$) are increased considerably by the addition of trace amounts of a strong acid such as trifluoroacetic acid (TFA) (Figure 34). As expected, gelation also is dependent on the acidity of the liquid component [251]. TEM images of **82b** gels in acetonitrile with and without TFA (Figure 35) consist of elongated, fiber-like aggregates without nodes. Upon addition of TFA, the gelator molecules become more efficiently packed as shown in Figure 35b.

Pyrene-appended aliphatic amides, urethanes, and urea derivatives (**84**, with $n > 8$) gelate hydrocarbons, alcohols, and halogenated liquids. Their aggregation seems to be promoted by π - π stacking and H-bonding interactions [252]. Gelation ability of these compounds depends on the length of the alkyl chain and nature of the aromatic unit. Homologs whose alkyl chain lengths are < 8 carbon atoms or when pyrene is replaced with naphthyl moiety are not gelators of

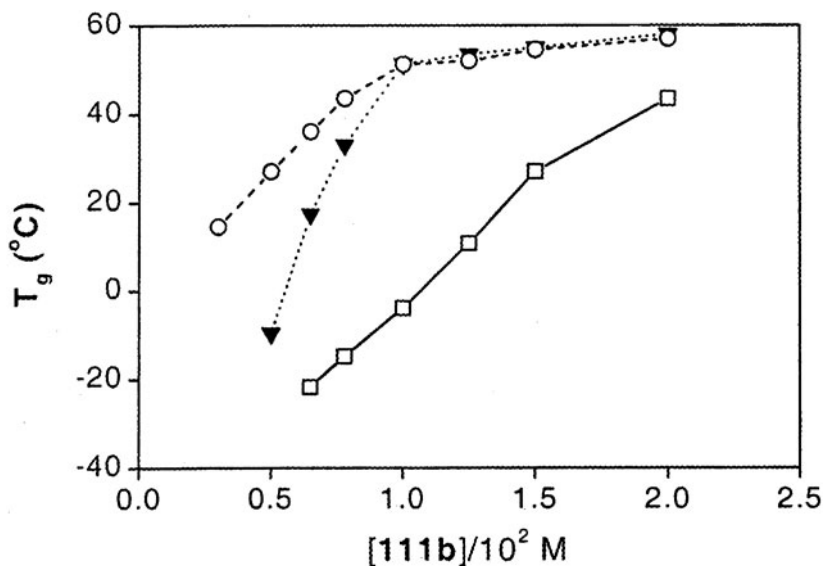


Figure 34. T_g of gels of **82b** in acetonitrile as a function of concentration in the absence (\square) or the presence of 10^{-2} M TFA (\circ) or $[\text{TFA}] = [\mathbf{82b}]$ (\blacktriangledown). (Reprinted with permission from [251]. Copyright (1998) Royal Society of Chemistry.)

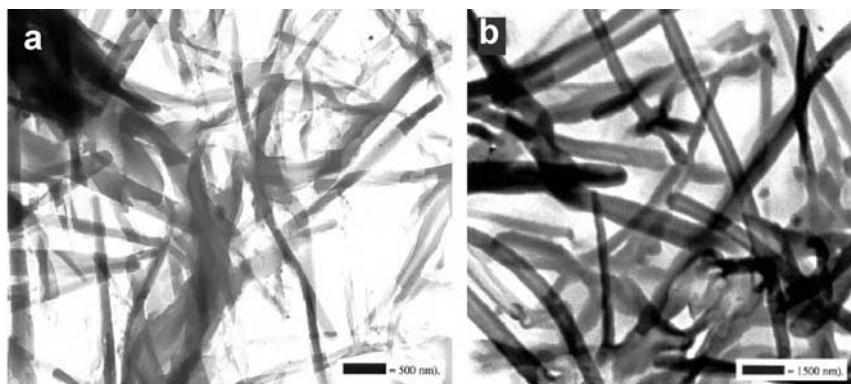
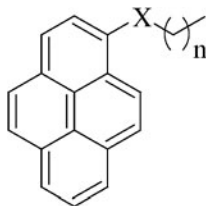


Figure 35. TEM images of xerogels from 10^{-2} M **82b** in acetonitrile in the absence (a) and presence (b) of 10^{-2} M TFA. The black scale bar in (a) corresponds to 500 nm and that in (b) is 1500 nm. (Reprinted with permission from [251]. Copyright (1998) Royal Society of Chemistry.)

the liquids examined. The existence of stacked aromatic units in the gel phase is supported by the temperature dependence of absorption and fluorescence spectra. Pronounced hyperchromism (sudden increase of absorbance on heating) and decreases in the intensities of the monomer and excimer fluorescence

bands were observed upon increasing the temperature due to destacking of the aromatic moieties during melting of the gel [252].

**84**

Optically active *myo*-inositol derivatives possessing a hydrophobic alkylsilyl group (**85** and **86**), but not their racemate, gelate hydrophobic liquids such as alkanes and aromatic solvents [253]. The gelator network is stabilized by intermolecular hydrogen bonds between the OH groups. Temperature dependent NMR studies indicate that the OH groups attached to positions 1 and 6 of the inositol ring play the most important role in the aggregation leading to gelation (Figure 36); the protons at these positions suffer an enormous downfield shift as temperature is reduced (and aggregation increases). The absence

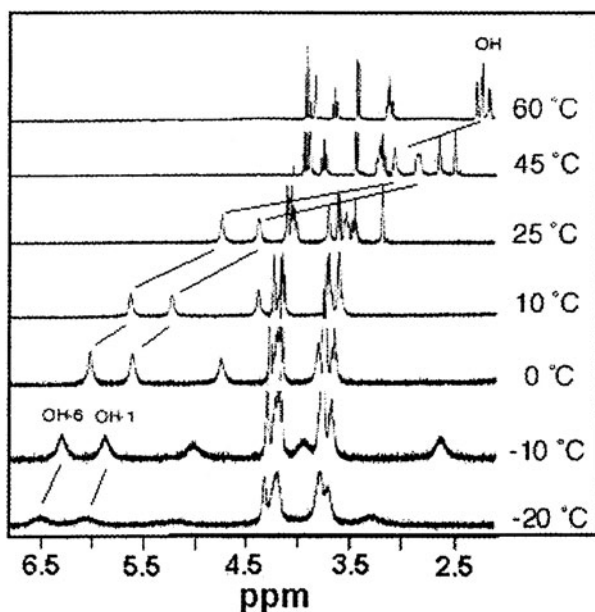
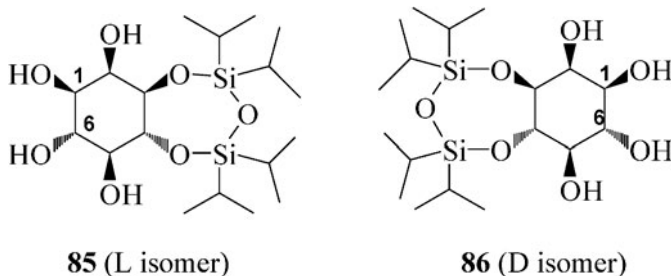


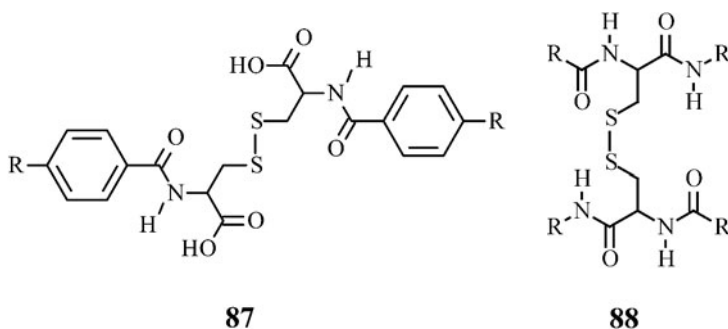
Figure 36. Temperature-dependent ^1H NMR spectra of 10 mM **85** in toluene- d_8 . (Reprinted with permission from [252]. Copyright (2003) The Chemical Society of Japan.)

of gels from the racemic mixture supports the need for carefully controlled directionality of the intermolecular interactions in order to form fibrils.



2.4. Organic Gelators Containing Three Heteroatom Types

In many of the reported cases, two heteroatom types are within an amide, urea, carbamate, etc. functionality and the third atom type of the LMOG is fluorine or sulfur appended elsewhere. The added polarity of some of these LMOGs allows them to gelate aqueous mixtures. For instance, **87** gelates water/ethanol mixtures [190, 254, 255]. The gelation ability of **87** is lost when the S-S linkage is replaced by $\text{CH}_2\text{-CH}_2$ or CH=CH , the acid groups are esterified, or the liquid is made basic.



The oxidized disulfide form of glutathione and its derivatives with **88** as the core structure produce transparent thermoreversible gels with polar organic liquids such as DMF, dimethylsulfoxide (DMSO), and methanol [256]. As with several peptides [257, 258], aggregates of molecules like **88** are extended networks of β -sheet-like structures that lead to gelation. CD spectra of such gels include a strong band near 240 nm [256, 259, 260], as noted in Figure 37 for the tripeptide **89** in methanol. The bands at 212 and 270 nm are assigned to the disulfide transitions and the one at 230 nm to the peptide unit. The positive weak

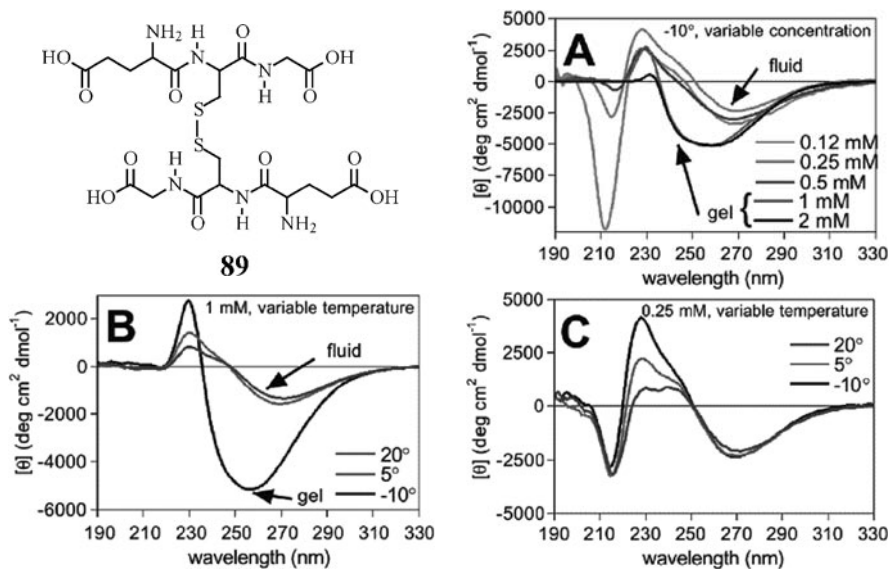
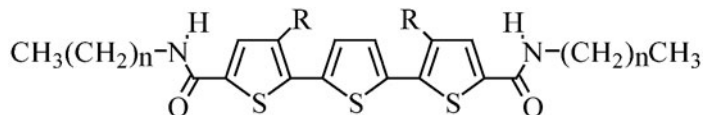


Figure 37. Circular dichroism spectra of **89** in 90/10 methanol/water as a function of temperature and concentration: (A) different concentrations at -10°C (only the 1 and 2 mM samples are in the gel phase); (B) variable temperature measurements at 1 mM (only the -10°C sample is in the gel phase); and (C) variable temperature measurements at 0.25 mM (all samples are fluids). (Reprinted with permission from [256]. Copyright (2001) The American Chemical Society.)

band at 230 nm is changed to a strong negative peak upon gelation, suggesting an alteration in the local structure.

Cyclic *bis*-amide and *bis*-urea derivatives bearing perfluoroalkyl chains and thiophene rings gelate several organic liquids [226, 261]. The *bis*-amide **90b** gelates *n*-alkanes and alcohols. The structurally similar **90a** (lacking the *n*-octyl groups) did not gelate these liquids. The gels of **90b** contain three-dimensional networks of fibrous bundles. They are a result of a combination of hydrophobic interactions and intermolecular H-bonding.

The effect of alkyl chain length on T_g of gels of a series of linear perfluoroalkyl alkanamides ($\text{CF}_3(\text{CF}_2)_{10}\text{CONH}(\text{CH}_2)_n\text{H}$, **91**) in silicone oil and DMSO has been studied (Figure 38) [263]. Both T_g and gelation ability increase first and then decrease with increasingly longer alkyl chains.



90a, R = H

90b, R = *n*-C₈H₁₇

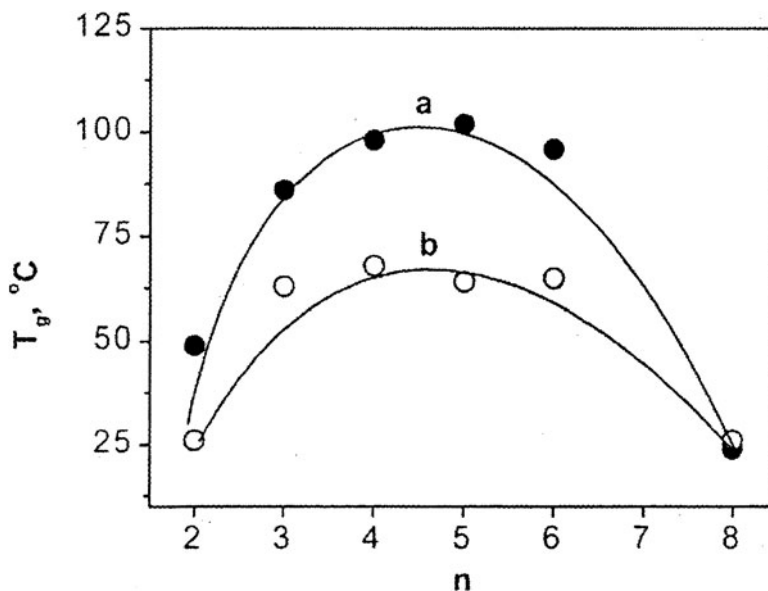
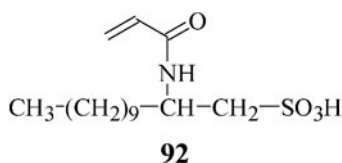


Figure 38. T_g values ($^{\circ}\text{C}$) of 2 wt.% **91** versus n , the number of carbon atoms in the aliphatic chain in (a, ●) silicone oil and (b, ○) DMSO gels. (Reprinted with permission from [263]. Copyright (2003) The American Chemical Society.)

Racemic 2-acryloylamide-dodecane-1-sulfonic acid (**92**) gels chloroform and tetrahydrofuran [264]. Because both right- and left-handed helices of **92** were formed during the gelation process, it is possible that each is comprised of one enantiomer by processes analogous to those discovered by Pasteur during his separation of tartrate crystals [265]. However, additional experimentation will be required to test this hypothesis. Regardless, these results should be compared with several others in which racemic mixtures do not gelate liquids that are gelled efficiently by the individual enantiomers (see, for example, **85** and **86** [253]). The gel networks of **92** have been used as templates to create both right- and left-handed silver nanohelices [264].

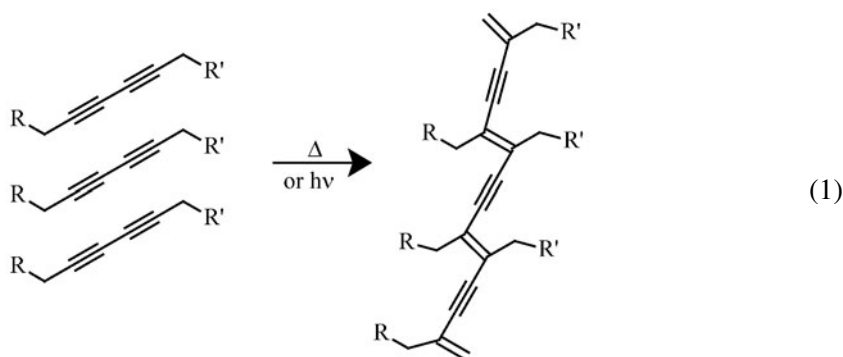


2.5. Polymerizable Organic Gelators

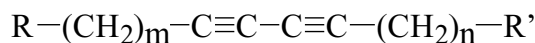
Polymerization of aggregates normally increases the thermal and temporal stabilities of the gels in which they reside. For instance, polymerization of

gels with amide and urea gelators containing acrylate groups has led to significant increases in T_g values while maintaining the same morphology before polymerization [130, 221, 266, 267].

Several LMOGs with conjugated diacetylene groups are known. Diacetylenes can undergo solid-state polymerization reactions by 1,4-additions when the monomer units are aligned appropriately (Eq. (1)) [268, 269]. As with methacrylate-containing LMOGs, polymerization of diacetylenic LMOGs within a gel need not affect the network morphology, and usually increases thermal stability of the gel. Due to their properties, several of these LMOGs are of industrial importance [270–273]. Most polymerized diacetylenes are very insoluble in common organic liquids and undergo a reversible color change from blue to red in response to temperature increases, pH changes, or exposure to some solvents [274–281].



Phospholipid mixtures of 1,2-*bis*(tricoso-10,12-diynoyl)*sn*-glycero-3-phosphocholine (**93**) and 1,2-*bis*(dininyl)*sn*-glycero-3-phosphocholine (**94**) gelate aqueous liquids [282]. Addition of some **94** “spacer” molecules increases the polymerization efficiency of the diacetylenic lipid **93** [283].



95

Amides and ester derivatives containing conjugated diyne units (**95**) gelate several organic liquids [131, 147, 155, 284–286]. The amides are more efficient gelators, in terms of the variety of liquids gelled and the thermal and temporal stabilities of gels, than the ester analogs [147]. The amide groups can both donate and accept H-bonds, but the esters can only accept them. When a chiral group is attached as a part of R in **95** (N.B., **96**), helical aggregates are formed in the gels as evidenced by their CD spectra (Figure 39). X-ray diffraction of the gels indicates that the gelator morphology is unchanged after polymerization (Figure 40).

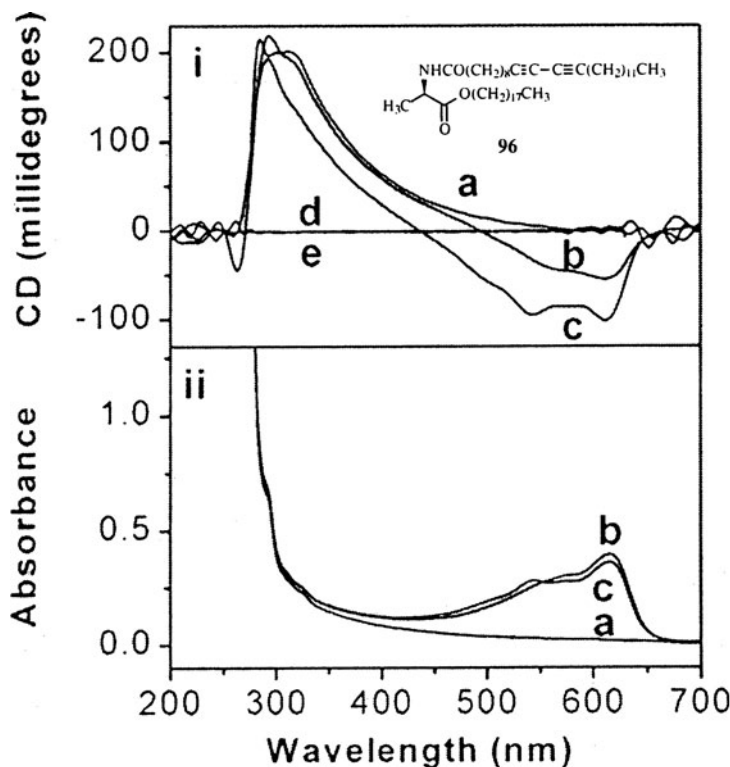
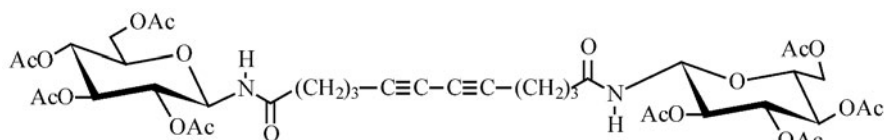


Figure 39. CD (i) and absorption (ii) spectra of a 1 wt.% **96**/silicone oil gel (a) before irradiation, (b) after irradiation for 1 min, and (c) after heating the irradiated gel to ca. 70°C for ca. 2 min. CD spectra of a solution of 1 wt.% **96** in chloroform (d) and of neat silicone oil (e) are also included in (i). The CD data in (i) below ca. 300 nm are not correct because of the very high optical densities at these wavelengths. (Reprinted with permission from [147]. Copyright (2003) The American Chemical Society.)

Evidence for polymerization of the gelator aggregates of **97** is provided in Figure 41. After 40 min irradiation, the average mol. wt. (M_w) of the polymer was in the range $1.6 \times 10^3 - 3.3 \times 10^4$ [285]. Further irradiation induced an increase in molecular weight and a color change from red to orange.



97

Figure 42 shows TEM images of aggregates of **97** in a 1:9 (v:v) ethyl acetate: hexane gel before and after polymerization. The fibrous morphology

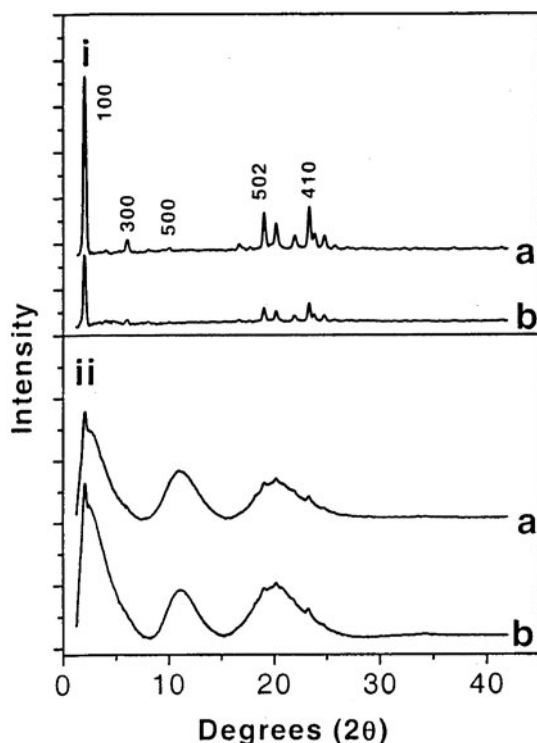


Figure 40. X-ray diffraction patterns (room temperature) of neat **96** (i) and (ii) of a 2 wt.% in silicone oil gel (a) before and (b) after irradiation for 10 min. The diffractogram of silicone oil has been subtracted from that of the gels in **ii**. The indices of diffraction peaks of unirradiated powder in **ia** are also indicated. (Reprinted with permission from [147]. Copyright (2003) The American Chemical Society.)

is maintained after polymerization, indicating that the polymerization occurred within individual nanofibers [286]. IR spectroscopic studies of gelated **97** indicate that intermolecular H-bonding of amide groups directs self-assembly of the LMOGs. The packing order and hence the molecular weight of the polymer formed depends on the substitution pattern on the sugar rings; when the acetate groups in **97** are replaced by hydrogen atoms, better packing and higher molecular weights of the polymers are observed [286].

2.6. Two Component Organic Gelators

John *et al.* have studied extensively the gelation properties of the anionic surfactant, *bis*(2-ethylhexyl) sodium sulfosuccinate (AOT, **98**) and a variety of

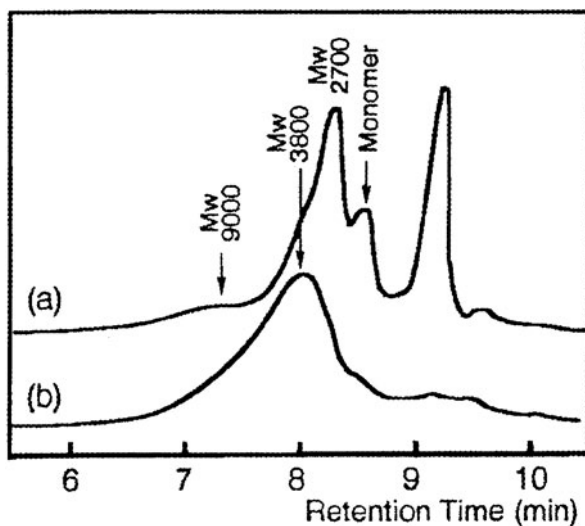
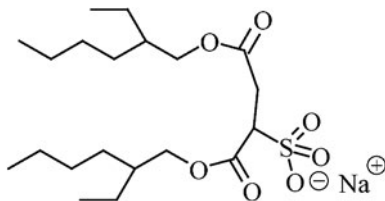


Figure 41. GPC profiles in chloroform for UV-irradiated fibers of **97** after (a) 40 min and (b) 4 h irradiation with a low-pressure Hg lamp. Absorbance was monitored at 250 nm. (Reprinted with permission from [285]. Copyright (1998) The American Chemical Society.)

phenols in nonpolar, aprotic media [287–291]. IR spectral studies of a **98**/phenol gel in isooctane provided evidence for intermolecular H-bonding between phenolic OH groups and the carbonyl groups of **98** [287]. Figure 43a illustrates the phase changes induced by varying the concentrations of **98**/*p*-ethylphenol in isooctane. When all of the carbonyl groups of **98** are H-bonded by phenolic OH groups, the system reverts from a gel to a liquid (Figure 43b). The two carbonyl peak-patterns in the IR spectra of the gel (Figure 43b (b)) are an inherent feature of this kind of gels. The higher frequency vibrations at ca. 1737 cm^{-1} are due to free C=O and the lower frequency vibrations (ca. 1724 cm^{-1}) ascribed to H-bonded carbonyls.



98

The aggregates of **98**/phenol gels consist of strands of stacked and motionally restricted phenol molecules, with the surfactants adsorbed externally

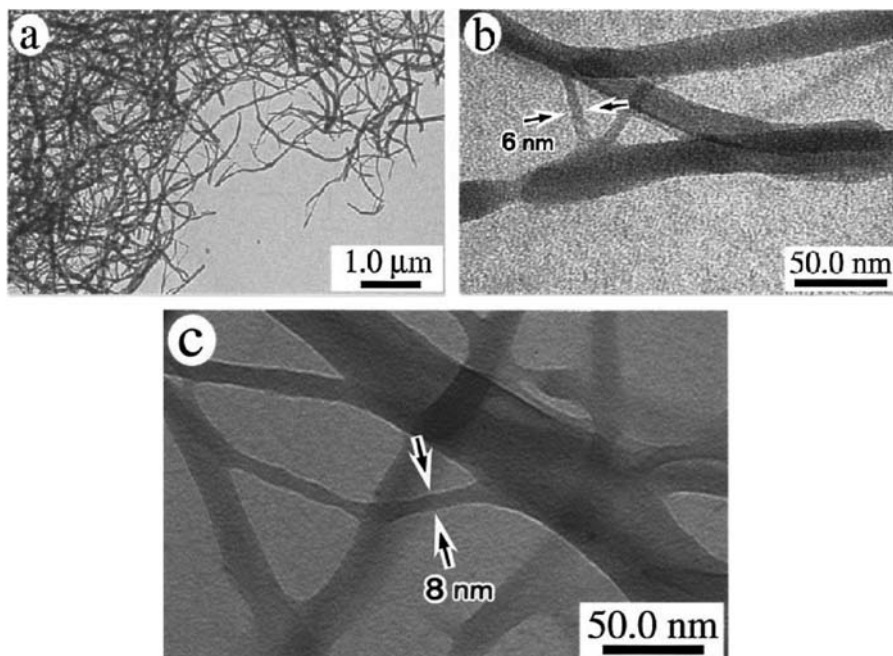


Figure 42. EF-TEM images of (a, b) self-assembled nanofibers (dried and unstained) from a gel of **97** in 1:9 (v:v) EtOAc:*n*-hexane and (c) the polymerized nanofibers following 40 min UV irradiation. (Reprinted with permission from [286]. Copyright (2000) The American Chemical Society.)

(Figure 44). Molecules of **98** are shown as twin-tailed spheres. Black heads are **98** molecules in the back side. The shadowed region represents the hydrophilic shell that envelops the aromatic ring stack, the phenol hydroxyls and the head groups of **98** molecules. When a second species is added to these gels, they stack into the gel matrix by “intercalating” into the motionally restricted regions of the aromatic strand.

NMR spectra of **98**/phenol mixtures are very dependent on the phase. The resonances associated with **98** and solvent molecules remain well resolved in the gel phase while those of the phenolic protons are broadened dramatically (Figure 45) [288]. The phenolic protons are sharp and well-resolved when the gelator network is destroyed by heating or adding a trace of water. These results support the model for the gel indicated in Figure 44. Motions of the phenolic group in the gel phase are highly restricted on the NMR time scale while **98** and solvent molecules can rotate much more freely.

When a second species, such as a cresol, benzoic acid, or cholesterol, is added to these gels, it is intercalated into the gel matrix to a degree that depends on its shape and acidity [289]. The process can be followed by the broadening

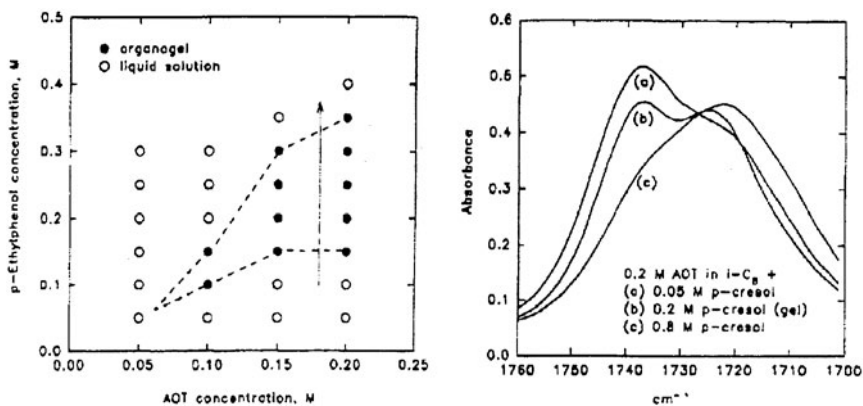


Figure 43. (a) Phase behavior of **98** and *p*-ethylphenol in isooctane. The filled circles represent compositions at which the organogel is formed. (b) IR spectra of the C=O vibrations in **98** at different *p*-cresol concentrations. (Reprinted with permission from [287]. Copyright (1993) The American Chemical Society.)

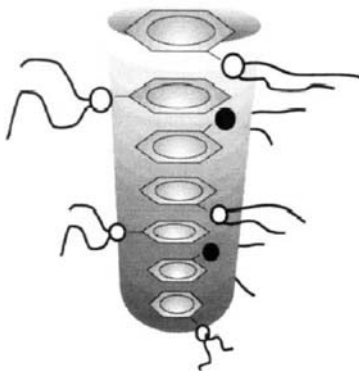


Figure 44. Illustration of the proposed gel structure from the **98**/phenol system. (See text for details.) (Reprinted with permission from [289]. Copyright (1994) The American Chemical Society.)

of peaks of the added species in the ^1H NMR spectra (Figure 46). Less acidic molecules of similar shape, benzyl alcohol, naphthalene, and 4-ethylaniline, are not intercalated into the gel strands. Using similar procedures, nanoparticles can be incorporated into **98**/phenolic gelator aggregates [292, 293].

The lengths of **98**/phenolic-doped strands in the gel phases were determined from SAXS experiments and found to be independent of the concentration of phenolic molecules and dependent on the nature of the phenolic group [294].

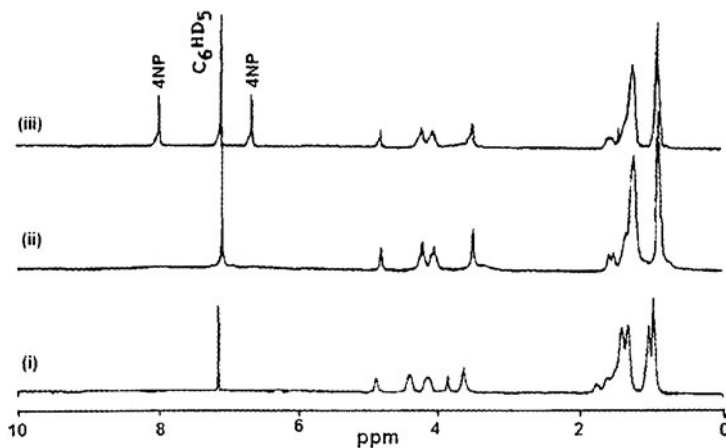
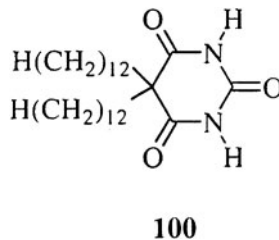
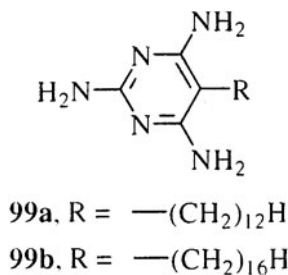


Figure 45. ^1H NMR spectra of (i) a 0.2 M solution of **98** in C_6D_6 , (ii) a **98**/4-nitrophenol (0.15 M each) gel in C_6D_6 , and (iii) the gel in ii after exposure to ambient air (i.e., moisture) at 20°C . 4NP represents 4-nitrophenol protons. The other peaks are from **98** and residual protons from the deuterated benzene. (Reprinted with permission from [288]. Copyright (1994) The American Chemical Society.)

AFM images of the gels show fiber-bundle assemblies with diameters on the order of 20–100 nm (Figure 47). Taken together, the SAXS, NMR, and AFM data indicate three levels of organization present in the organogels. Individual **98**/phenol strands of ca. 2 nm diameter aggregate into fibers of ca. 10 nm diameter that finally form bundles of fibers (Figure 48).

Supramolecular structures based on molecular recognition and self-assembly through non-covalent interactions have been studied extensively for many years [295–297]. Molecules within such assemblies can act as LMOGs in some cases. For instance, a 1:1 (mol:mol) mixture of 2,4,6-triamino-5-hexadecylpyrimidine (**99a**) and 2,2-didodecylbarbituric acid (**100**) gelate organic liquids such as DMF, chloroform, carbon tetrachloride, and cyclohexane at concentrations $\geq 0.04\text{ mol/dm}^3$ [298].



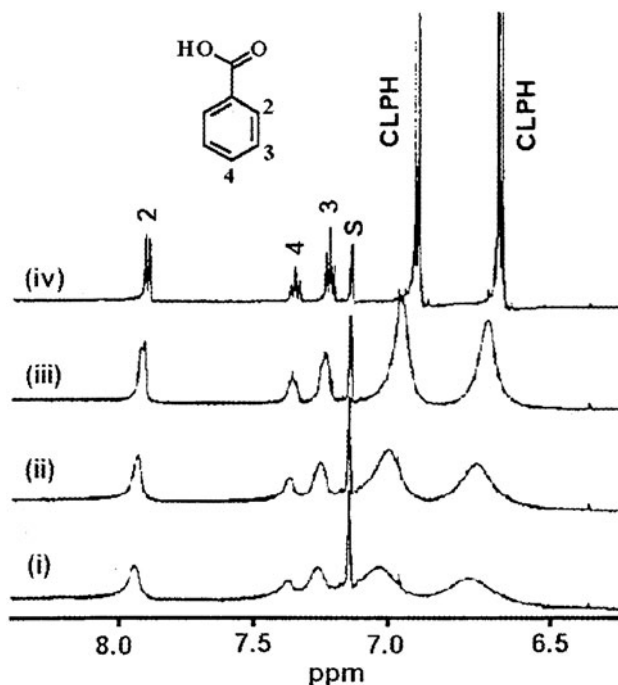


Figure 46. ^1H NMR spectra (aromatic region) of a gel composed of 4-chlorophenol (0.1 M; CLPH), **98** (0.1 M) and 5/95 (v/v) benzene/ CCl_4 and doped with 0.02 M benzoic acid: (i) 20°C, (ii) 25°C, (iii) 30°C, and (iv) 35°C. The benzoic acid peaks are labeled according to the numbering scheme shown. (Reprinted with permission from [289]. Copyright (1994) The American Chemical Society.)

The gelation efficiency is very dependent on the length of the alkyl chains in both components. At different chain lengths, co-crystals or solutions have been observed in the same liquids [298]. Intermolecular H-bonding in the 1:1 gelator aggregates and co-crystals is evident from comparisons of their FTIR spectra and those of pure **99** and **100**. A possible arrangement of 1:1 **99b:100** in its gelator aggregates, from analyses of powder X-ray diffractograms of the xerogel and co-crystal [298, 299], is shown in Figure 49. Layered structures with lamellar spacings of 19.2 (xerogel) and 27.6 Å (co-crystal) were found. In the xerogel, the alkyl chains are randomly folded and bent.

Two component gels consisting of phosphoric acid esters and aluminum *sec*-butoxide are also known [300, 301]. They are used in the hydraulic fracturing of oil formations [302]. The viscosity of such gels depends mainly on the structure of the phosphoric acid ester. It decreases as the gelator mixture becomes more hydrophilic and less lipophilic [303].

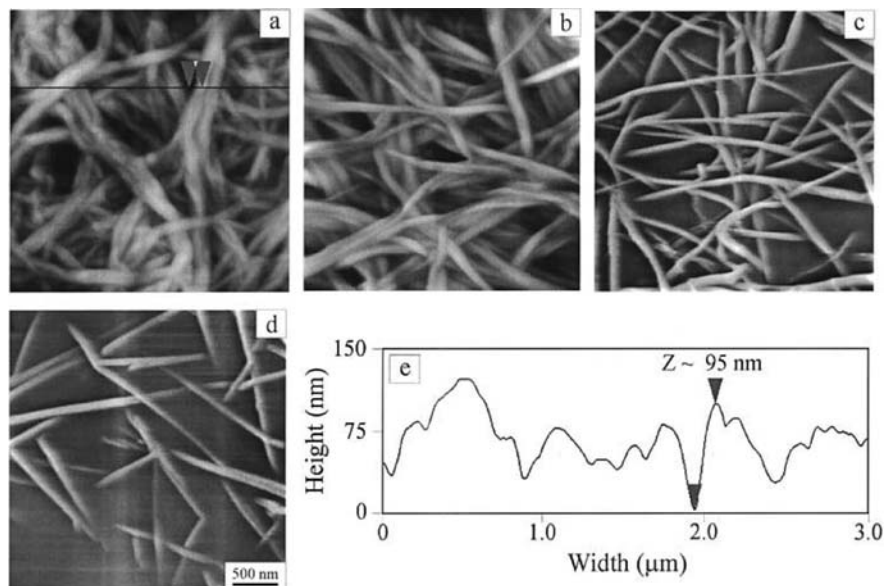
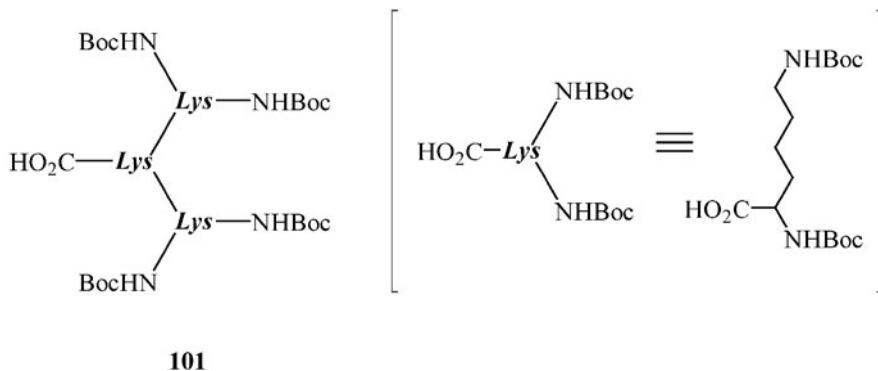


Figure 47. Height AFM images of 0.2 M **98**/0.2 M *p*-chlorophenol organogels in (a) isooctane, (b) decane, (c) tetradecane, and (d) 2,6,10,14-tetramethylpentadecane. All images are $3.0\ \mu\text{m} \times 3.0\ \mu\text{m}$. A cross-sectional cut of (a) is displayed in (e). (Reprinted with permission from [294]. Copyright (2001) The American Chemical Society.)

Mixtures of dialkylamines and dendritic peptides with a free carboxylic acid group at the focal point of the branched structure (**101**) gelate liquids such as toluene, acetonitrile and dichloromethane [304, 305].



Bile acids in combination with a derivative of barbituric acid, fluorenone, an alkylamine, a cyclic urea, or a bicyclic carbohydrate (isomannide or isosorbide) gelate a variety of polar and nonpolar liquids [306–309]. Aggregates of some of these mixtures are worm-like inverted micelles [310] and, as such, their gels may be considered to be a kind of microemulsion [14, 309].

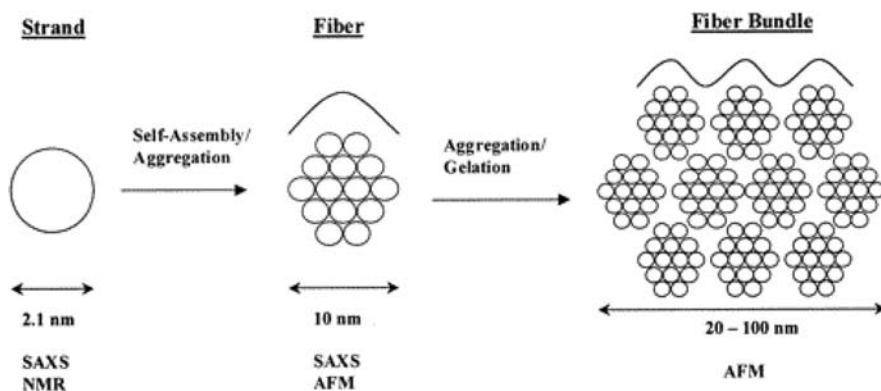


Figure 48. Cartoon representation of the three levels of organization present in **98**/phenolic gels. (Reprinted with permission from [294]. Copyright (2001) The American Chemical Society.)

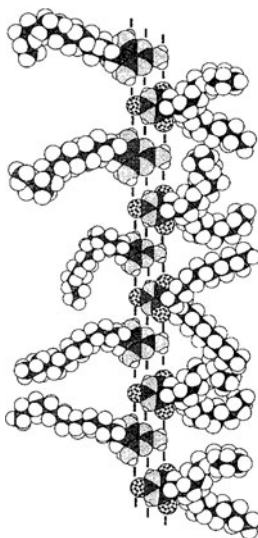


Figure 49. Proposed packing arrangement within gelator aggregates of 1:1 **99b**:**100**. (Reprinted with permission from [298]. Copyright (1993) Royal Society of Chemistry.)

Addition of very small amounts of a polymeric material can facilitate interconnection of aggregates of some two-component gels. For example, an opaque paste of non-branched needle-like fibers was obtained by dissolving a 10 wt.% mixture of a 56:44 (mol:mol) ratio lanosta-8,24-dien-3 β -ol (**102**) and 24,25-dihydrolanosterol (**103**) in diisooctyl phthalate and cooling the hot solution to room temperature [311]. A clear, strong gel was obtained as the fibers were interlinked permanently upon introduction of a small amount of ethylene-vinyl

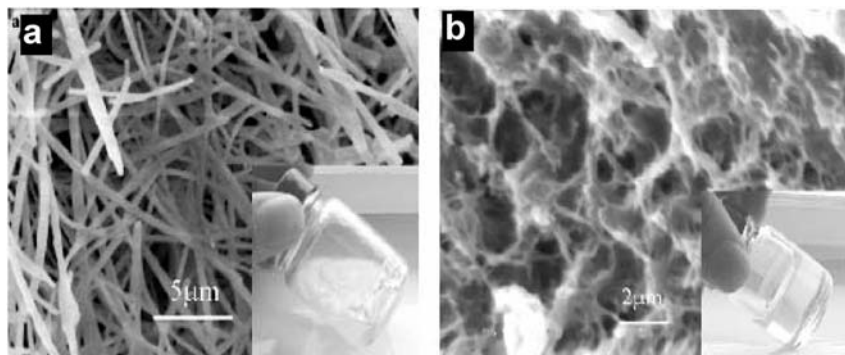
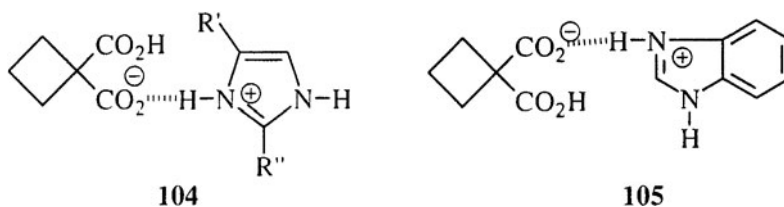


Figure 50. SEM images of (a) separate fibers of a 10 wt.% **102/103** in diisooctyl phthalate gel (an opaque paste; see inset) and (b) interconnected fiber networks after adding a small amount of ethylene-vinyl acetate copolymer to the sample in (a) after reheating and cooling (a clear, strong gel; see inset). (Reprinted with permission from [311]. Copyright (2002) Wiley-VCH Verlag, GmbH.)

acetate copolymer ($M_W = \text{ca. } 100\,000$, 40% in vinyl acetate) (Figure 50). The copolymer is thought to induce a crystallographic mismatch branching within the fibers that leads to their interconnection [119, 178].

Gelation properties of organic salts obtained from imidazole derivatives and cyclobutane-1,1-dicarboxylic acid (**104**, **105**) have been studied by Dastidar and co-workers [312]. The temporal (several months) and thermal ($T_g = 66^\circ\text{C}$) stabilities of gels comprised of nitrobenzene and 0.137 wt.% **104** ($R' = R'' = \text{H}$) are much higher than that of the dicarboxylate with no free carboxylic groups.



Aggregates of **104** in nitrobenzene gels consist of several hundred micrometer long, flexible, intertwined fibers in a network. The fibers are stabilized by intermolecular H-bonding. FTIR spectra of neat **104** and its xerogel are indistinguishable, indicating that molecular packing in the two phases is the same. Single-crystal X-ray diffraction of **104** shows polymeric, one-dimensional, $-\text{COO}^- \cdots \text{H}-\text{N}=\text{H}$ -bonds (Figure 51). These layered structures connect to each other through additional $-\text{COO}^- \cdots \text{HOOC}-\text{H}$ -bonds, making a 3-D network.

As expected from the FTIR results, virtually superimposable powder diffraction patterns were obtained for **104** under various conditions (Figure 52),

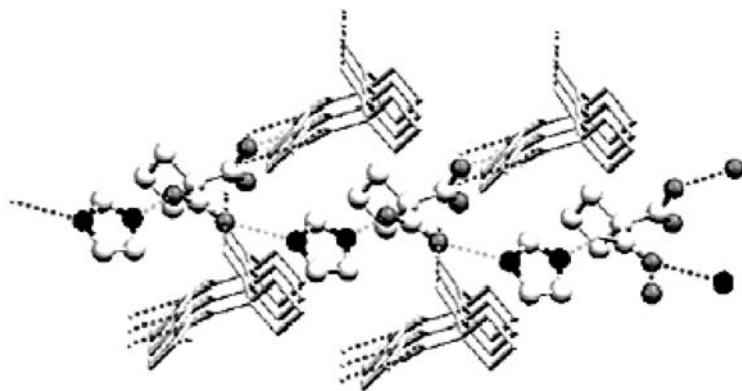


Figure 51. 3-D hydrogen-bonded network in a single-crystal of **104**. The infinite chains involving 1-D hydrogen-bonded imidazolium cyclobutane-1,1-dicarboxylate moieties is shown in a ball-and-stick model. The chains are interconnected via nearly orthogonal COOH...⁻OOC hydrogen bonds (represented in ball-and-stick form). Hydrogen atoms are not shown for the sake of clarity. (Reprinted with permission from [312]. Copyright (2003) The American Chemical Society.)

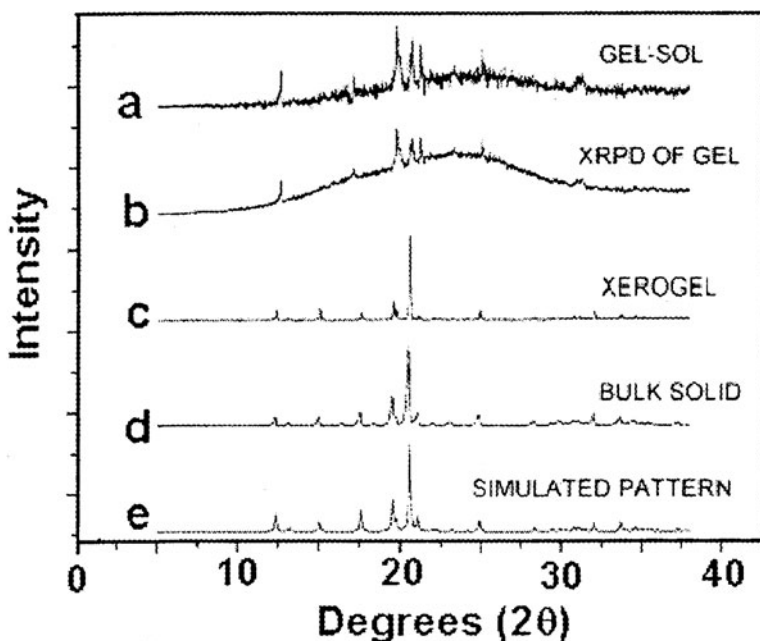
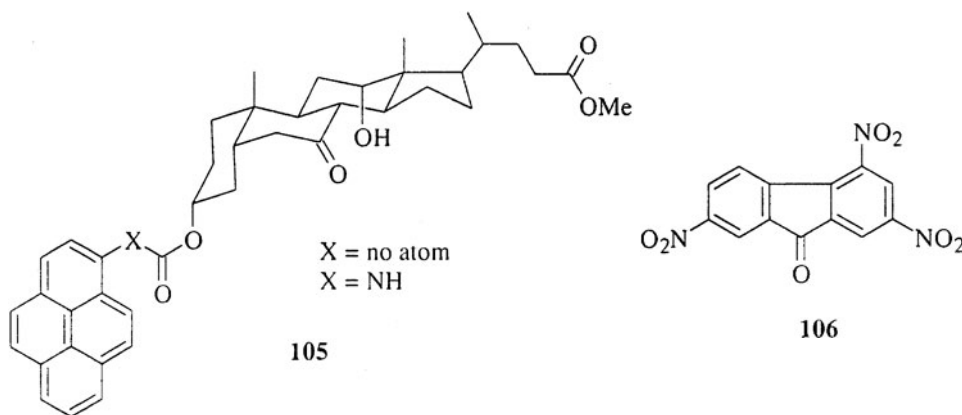


Figure 52. X-ray diffraction patterns of **104** under various conditions. The liquid used in (a) and (b) is nitrobenzene and the concentration of the gelator is ≤ 1 wt.%. The simulated pattern in (e) was generated from single-crystal diffraction data. (Reprinted with permission from [312]. Copyright (2003) The American Chemical Society.)

but not in the gel phase (diffractograms a and b). This result suggests that the xerogel and gel packing of **104** are different. It also demonstrates again [85] the potential danger of assuming that the morphs of the gelator in the gel and in either its xerogel or bulk crystalline phase are the same; many LMOGs are polymorphous, and when that is the case, the gel form can be the less thermodynamically stable one.

Pyrene derivatives (**84** and **105**) are LMOGs of alcoholic or hydrocarbon liquids in the presence of the strong electron acceptor molecule, 2,4,7-trinitrofluorenone (**106**) [252]. Spectroscopic evidence, in the form of new visible absorption bands when one of the pyrene derivatives is mixed with **106**, indicates that the added intermolecular attraction from charge-transfer complexation stabilizes the gel networks here.



Two-component gelators consisting of a mixture of cellulose nitrate and copper bronze gelate anhydrous ethanol/benzene mixtures [313]. The deep-colored gels are produced upon a complexation reaction between copper and the nitrate groups of the cellulose esters that results in elongated gelator strands.

2.7. Inorganic and Organometallic Gelators

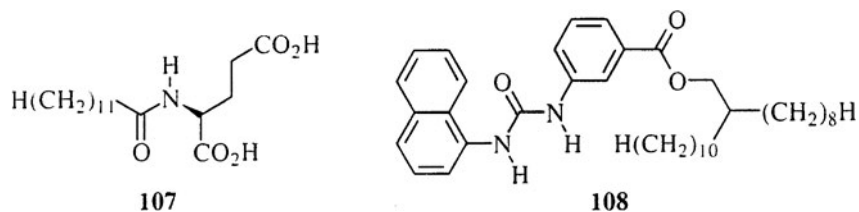
Gelation of colloidal inorganic particles [314] such as V_2O_5 fibrils and rod-like $Fe(OH)_3$ [315–317] usually leads to structures with a low solid content. Very low volume fractions of dispersed aluminum compounds such as imogolite ($Al_2SiO_3(OH)_4$) and boehmite ($AlO(OH)$) rods form space-filling, transparent gels that are stable at room temperature for very long periods [318–320].

Mononuclear and binuclear copper complexes of alkoxyphenylenes and alkanooates gelate hydrocarbon liquids [321–323]. Metalloporphyrins with

four long chain alkyl benzoate ester substituents are also reported to form gel-like materials in hydrocarbon liquids [324–326]. Finally, gold thiolates form supramolecular aggregates in alkylnitrile/alcohol mixtures [327].

2.8. Liquid-Crystalline Gels

In some cases, organogels can also have at least some of the properties of liquid crystals. Applications of these gels are discussed in Chapter 22. For example, amorphous powdered *N*-lauroyl-L-glutamic acid (**107**) becomes birefringent and exhibits a positive CD band in the 300–400 nm region [328] due to the formation of a lyotropic cholesteric liquid crystal phase when it is soaked in an aromatic solvent such as benzene or toluene [329]. If the mixture is heated to its isotropic phase and cooled to ambient temperature, a birefringent organogel is formed [329]. The color of the original suspension, a result of the difference between the optical dispersions of the solvent and the suspended aggregates of **107** (i.e., the Christiansen effect [330]), is reduced in intensity upon gelation.



Nematic gels have been formed from either nematic gelators [331–333] or non-mesogenic gelators in a nematic liquid. Examples of the latter are more common. An example of the former type is lyotropic nematic gels formed by 3–5 wt.% **108** in decane [331]. At these gelator concentrations, T_g (from DSC measurements) is slightly higher than the nematic-to-isotropic (T_{NI}) transition temperature observed by POM. Interestingly, electric or magnetic fields were unable to orient the gelled nematic phase until the temperature reached T_g , at which point the turbulence was induced electrohydrodynamically [331].

Amides and amino acid derivatives with *n*-alkyl substituents form anisotropic gels with cyanobiphenyl nematic liquid crystals [334]. Gelation of cyanobiphenyls (**109**), cyclohexylbenzyl derivatives (**110**), and 4-(methoxy)benzylidene-4'-(butyl)aniline (**111**) by chiral 1,2-bis(alkanoylamino)cyclohexane (**35**) has been studied in detail [335–339]. Some of these mixtures exhibit more than one thermally reversible phase transition within the gel state; cooling the isotropic liquid produces a *normal* gel that transforms to an *anisotropic* gel on further cooling [335]. FTIR spectra indicate that the NH and CO groups of

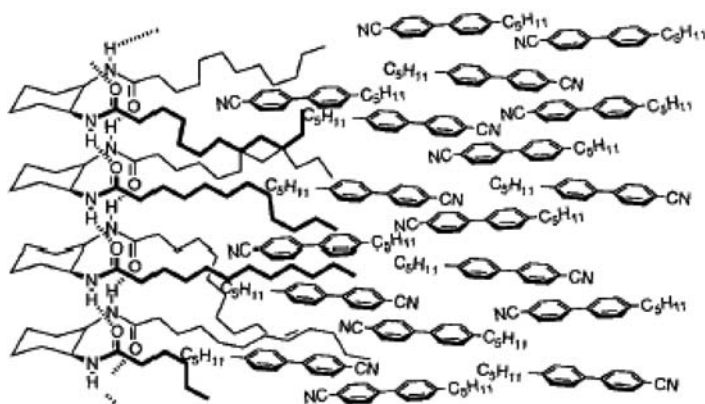
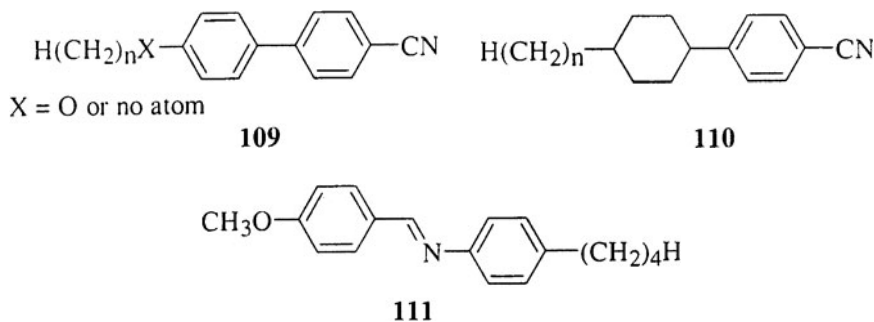
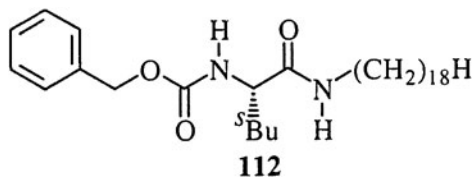


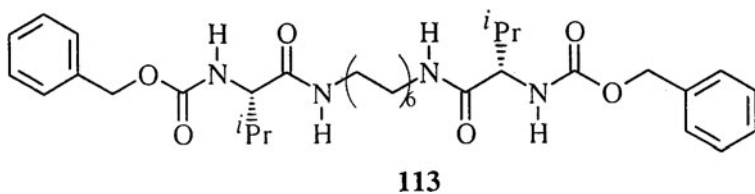
Figure 53. Representation of the structure of the nematic gel formed by 1 mol % **35** ($R = \text{---}(\text{CH}_2)_{10}\text{CH}_3$) and **109**. (Reprinted with permission from [335]. Copyright (1998) Wiley-VCH Verlag, GmbH.)

35 are hydrogen-bonded, suggesting the gelator and liquid organization shown in Figure 53 [335].



Amino acid derivatives **112** and **113** gelate nematic liquids **110** and **111** through H-bonded networks of NH and CO groups [338–343]. Two gel states, a normal (isotropic) gel at higher temperatures and a liquid-crystalline gel at lower temperatures, have been observed in these systems. The higher gel-sol transition temperatures in **113**-based gels are attributed to the larger number of H-bonding sites in **113** than in **112** [340].





The liquid-crystalline **112**-based gel in 4-cyano-4'-pentylbiphenyl **109**, $n = 5$, X = no atom) showed a twisted nematic (i.e., cholesteric-like) character and an electrooptic response (Figure 54), whereas the **113**-based gel exhibited no twist or electrooptical response over the concentration range examined [340]. The optical switching contrast decreases with increasing the concentration of **112** (Figure 54a). At room temperature, the liquid-crystalline **112**-based gel responded significantly faster to an alternating electric field than did neat **109** (Figure 54b). In fact, the response time depends very much on the nature of the LMOG: for instance, the response time of 0.5 mol% **35** (R = $-(\text{CH}_2)_{11}\text{H}$) in **109** (X = no atom, $n = 5$) is 19 ms [335] while the response time of the 0.25 mol% **112/109** gel, 6 ms [340], is twice that of neat **109** (12 ms).

The *N*-octyl gluconamide **114** aggregates via H-bonding and London dispersion interactions to gelate several nematic liquids [344]. Depending on the temperature, three thermoreversible states – isotropic liquid, “normal” (isotropic) gel, and liquid-crystalline gel – could be formed. As demonstrated in Figure 55, the assembly of **114** molecules within gels of **109** (X = no atom, $n = 5$) consists of interconnected, randomly oriented fibers (0.2 – 1.0 μm diameter) that appear to bundle.

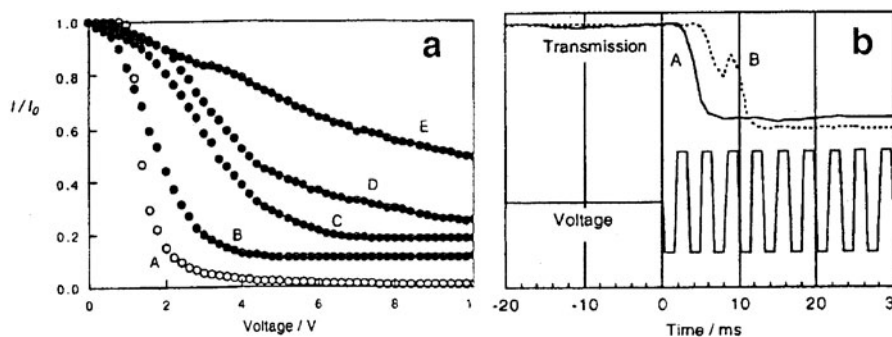


Figure 54. (a) Relationship between transmittance and applied voltage for liquid-crystalline gels of **112** and **109** (X = no atom, $n = 5$) at room temperature in a “twisted nematic” cell (i.e., a cell with parallel transparent conducting plates separated by a precisely-defined gap; the applied electric field can “twist” the nematic phase): (A) 0, (B) 0.25, (C) 0.33, (D) 0.50, and (E) 1.00 mol% **112**. (b) Comparison of the response of (A) a 0.25 mol% **112** gel and (B) neat **109** to an alternating electric field. (Reprinted with permission from [340]. Copyright (1999) Wiley-VCH Verlag, GmbH.)

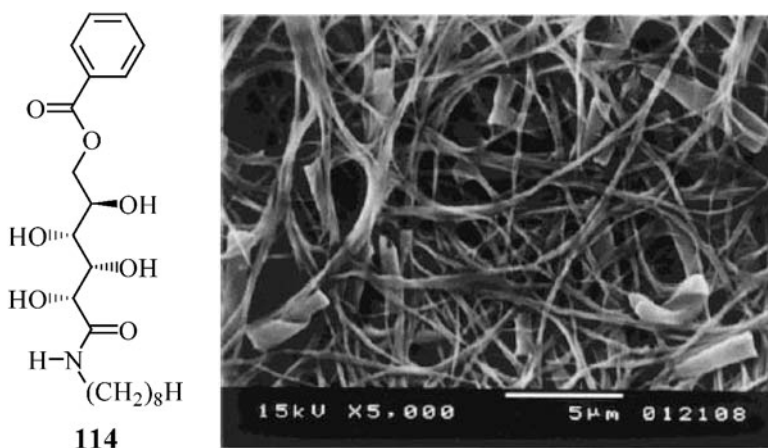


Figure 55. SEM image of fibrous aggregates of **114** assembled in **109**. (Reprinted with permission from [344]. Copyright (2000) The American Chemical Society.)

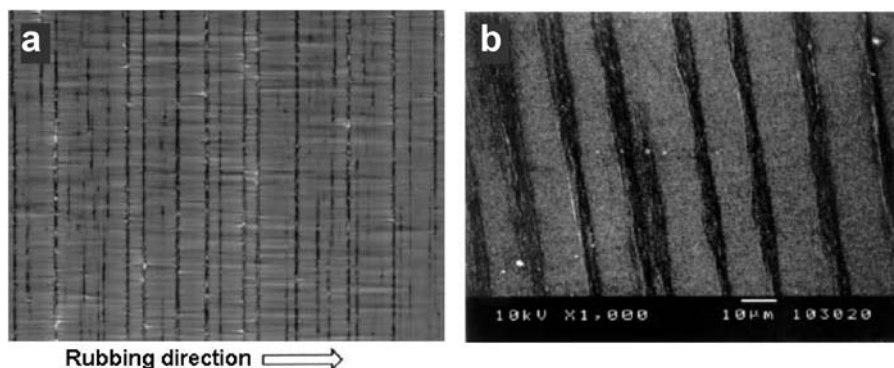


Figure 56. (a) POM images of a mixture of SCE8 and 1 wt.% **112** at 60° C in a parallel rubbed cell and (b) SEM image of oriented fibers made from **112** gel in SCE8 (after extraction of SCE8). (Reprinted with permission from [345]. Copyright (1999) Royal Society of Chemistry.)

Smectic liquid crystals possess higher molecular order than do nematics. Therefore, the sol-gel phase transition in the smectic phase of a mixture of commercially available ferroelectric liquid crystal SCE8 (Hoechst) and the amino acid derivative **112** resulted in the formation of oriented gelator aggregates as shown in Figure 56 [345]. The mixture for POM was sandwiched between two polyimide-coated glass substrates rubbed in the same direction.

The sol-gel phase transition temperature is concentration dependent, and usually increases with increasing gelator concentration [1]. This property has been exploited to modify the relationship between T_{NI} and T_g of gels containing a nematic liquid **109** [346] and the LMOG **115** [347]. When **109** has a high

T_{NI} , gelation can occur either in the isotropic or the nematic phase (depending on the gelator concentration), and the aggregation/isotropic-to-nematic phase transition depends principally on the concentration of the LMOG. As a result of their low concentrations and low solubilities within the liquid (a fundamental condition for gelation in any binary mixture), gelator molecules have almost no effect on the phase transition temperatures of the liquid crystal in the gel [347, 348]. Aggregation can be made to occur at temperatures below T_{NI} at low concentrations of gelator; at higher LMOG concentrations, aggregation and gelation take place at temperatures above T_{NI} . As shown in Figure 57, the morphology of the gelator aggregates can be different in these two cases

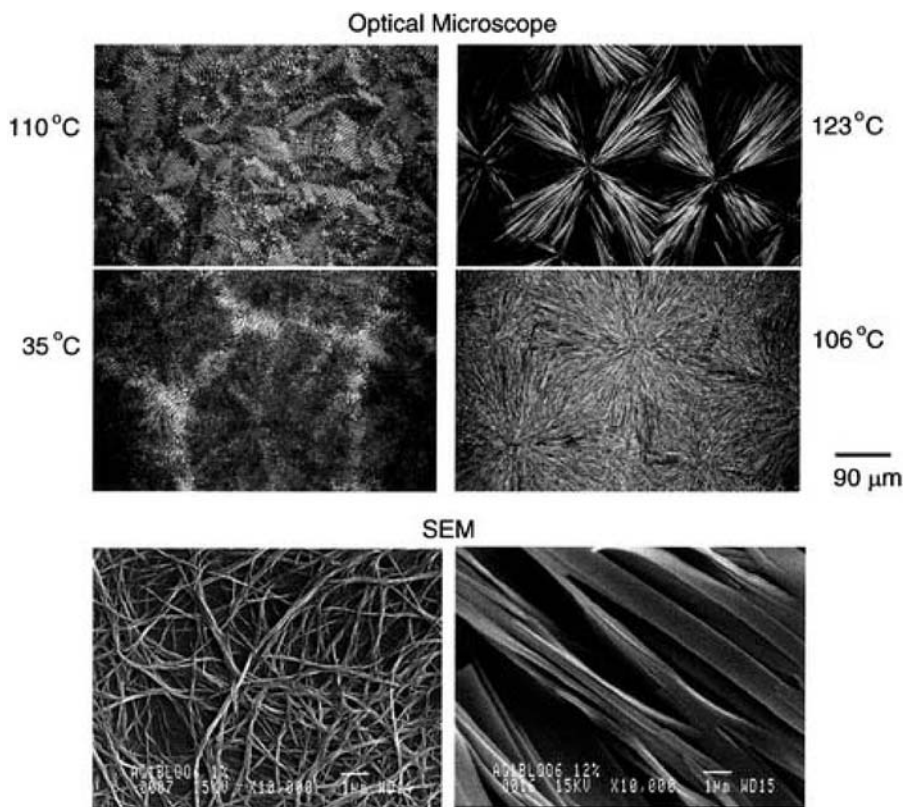


Figure 57. POM and SEM pictures (top view) of two **115/109** mixtures. The optical micrographs at 110 and 35°C (1 wt.% **115**) show the chiral nematic phase of **109** before and after aggregation of **115**; the optical micrographs of 12 wt.% **115** show the aggregation of **115** in the isotropic (123°C) and nematic (106°C) phases of **109**. The SEM pictures are of the fibrous aggregates of **115** formed in the chiral nematic phase (1 wt.% **115**) and in the isotropic phase of **109** (12 wt.% **115**); the scale bars in the SEM pictures are 1 μm. (Reprinted with permission from [347]. Copyright (2001) Royal Society of Chemistry.)

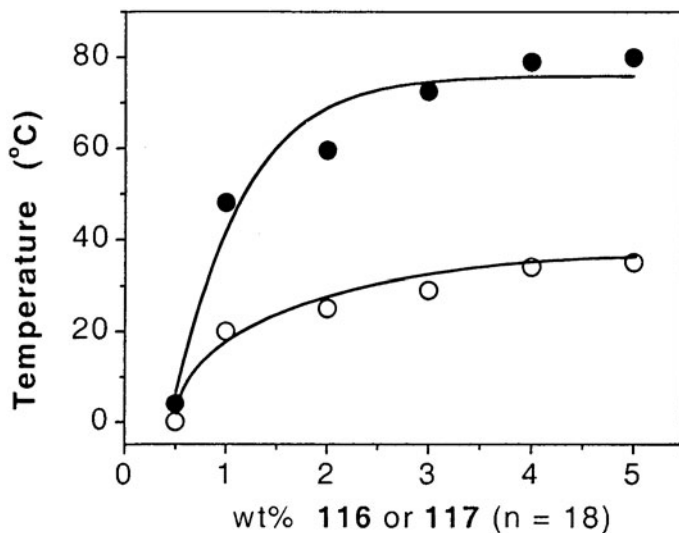


Figure 58. T_g values of gels with silicone oil (tetramethyltetraphenyltrisiloxane) as the liquid as a function of gelator concentration: **116** ($n = 18$) (○) and its ammonium carbamate **117** (●). (Reprinted with permission from [86]. Copyright (2002) The American Chemical Society.)

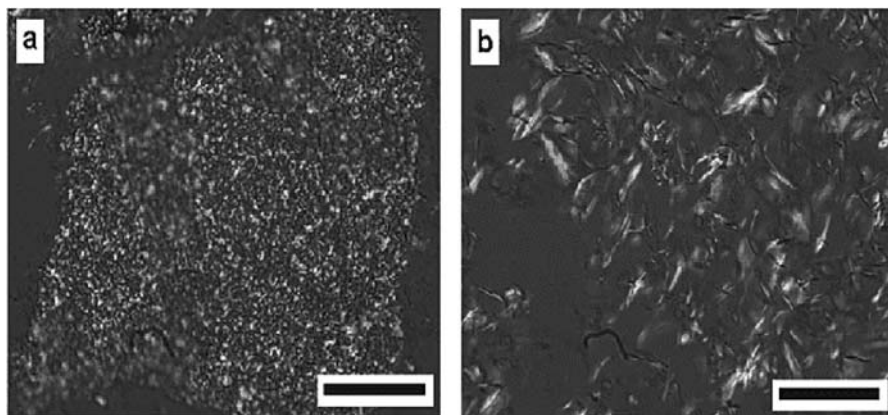


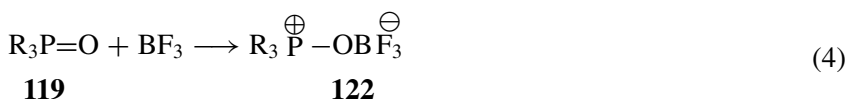
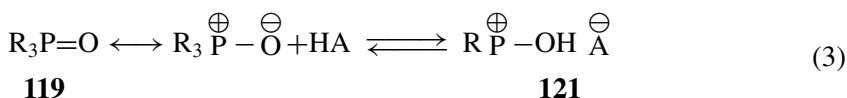
Figure 59. Polarizing optical micrographs (room temperature) of 2 wt.% (a) **116** ($n = 18$) and (b) **117** ($n = 18$) gels in silicone oil. Black space bars are $100\ \mu\text{m}$. The images were taken with a full-wave plate. (Reprinted with permission from [86]. Copyright (2002) The American Chemical Society.) [A color version of this figure may be found on page 941.]

and reduce the solubility of the gelators, especially in liquids of low polarity [366]. In support of this hypothesis, the aggregates formed by **117** ($n = 18$) in a silicone oil (tetramethyltetraphenyltrisiloxane) gel are more elongated and strand-like than those of **116** ($n = 18$) before addition of CO_2 (Figure 59).

When a polymeric amine is the latent gelator, introduction of carbamate and ammonium groups upon addition of CO₂ “cross-links” the chains and eventually causes gelation of some liquids. Examples are the gelation of methanol, longer-chained alcohols, and 1-methyl-2-pyrrolidinone by polyallylamine and CO₂ [367]. Some of these gels have been shown to be effective cleaning agents for oil paintings [368]; see Chapter 27 for additional information.

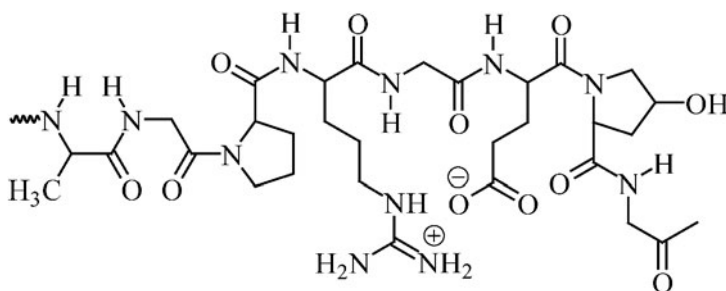
Tri-*n*-alkylphosphine oxides (**119**; R₃P=O) and phosphines (**120**; R₃P, R = *n*-alkyl chains from decyl to octadecyl) are another class of latent gelators [369]. They are converted from uncharged species to salts (**121**) upon reaction with strong Brønsted acids or to zwitterions (**122** and **123**) upon reaction with BF₃ (Eq. 3–5). Both the phosphine oxides and zwitterions are less efficient gelators than the corresponding hydroxyphosphonium salts.

Additional examples and more detailed descriptions of “latent” gelators are found in Chapter 26.

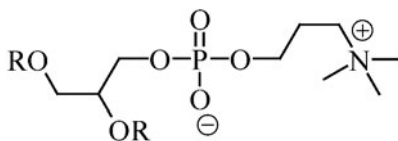


2.10. Microemulsion-based Gelators

Three types of compounds, *bis*(2-ethylhexyl) sodium sulfosuccinate (**98**), gelatin (**124**) and lecithin (**125**), are the most often reported microemulsion-based gels.



124



125

The gelation properties of the anionic surfactant **98** are described in Section 2.6. Gelatin (**124**) is a natural protein that contains a large number of glycine, proline and 4-hydroxyproline residues. Lecithin (**125**) is a mixture of phospholipids that is obtained from soybeans and other natural sources, such as egg yolks and fish.

Transparent, thermoreversible, elastic gels are obtained from **124** on cooling its aqueous solutions below 35° C. They can be formulated with flavoring or medicinal compounds to give materials that “melt in the mouth” [370]. One-component gels in water and water/alcohol mixtures [371, 372], as well as in reverse micelles (i.e., containing water and **98**) [373–375], can be obtained from **124**. The gelator networks contain three-dimensional tubular aggregates of gelatin fibers connecting the water pools with each other (Figure 60).

In non-aqueous media in the presence of small amounts of water, glycerol or formamide, lecithin (**125**) self-assembles into jelly-like micellar aggregates with viscoelastic properties [376, 377]. Organogels of **124** have been studied intensively by rheology [378–381], NMR [382, 383], IR [379–385], SANS [386–389], and other techniques [390–392]. Both **124** and **125** are biocompatible materials and, hence, their gels are used in pharmaceutical [393–400] and other applications [401–403].

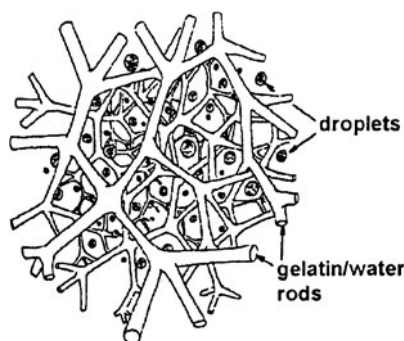
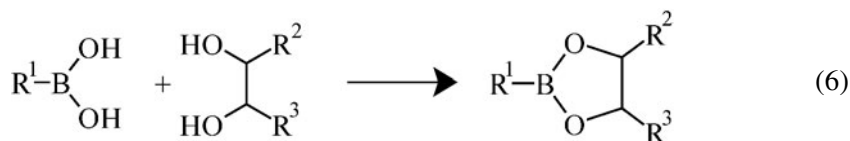


Figure 60. Representation of aggregates formed from **124** gels in reverse micelles. (Reprinted with permission from [374]. Copyright (1989) Royal Society of Chemistry.)

2.11. Miscellaneous Organic Gelators

2.11.1. Boronic acid-appended LMOGs

Shinkai *et al.* have investigated gelation effected by substituted boronate esters, synthesized from a boronic acid and a molecule containing at least two *vic*-hydroxyl groups (Eq. (6)) [404–407].



(D)- and (L)-Enantiomers of some monosaccharides can be differentiated by the phases made by their 1:2 complexes with cholesterylphenylboronic acid. In CCl_4 for example, L-lyxose, L-mannose, and D-xylose result in gels and the complexes of the (D)-enantiomers precipitate [404]. In some cases, complexes of both the (D)- and (L)-enantiomers lead to gels whose stabilities differ.

Bolaamphiphiles bearing two boronate ester groups prepared from chiral *vic*-diols (**126**) create gels [407, 408] whose aggregates are extended one-dimensional H-bonded networks in which the molecules are almost perpendicular to the chain axis (Figure 61). This type of molecular organization is typical of α, ω -diamides separated by a polymethylene chain [409–411].

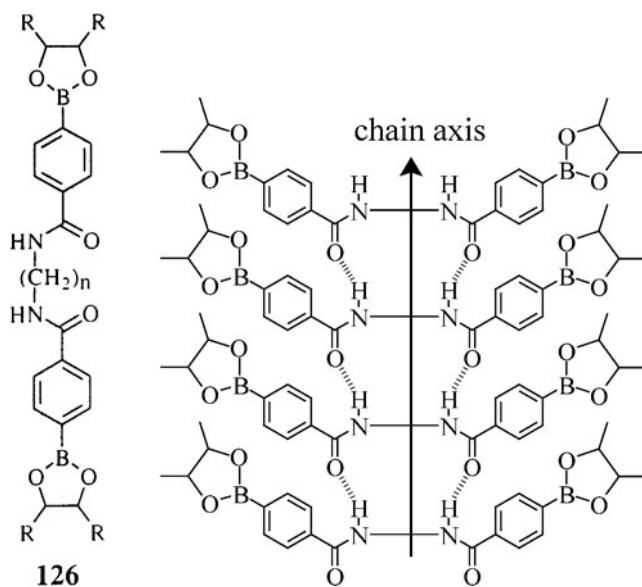


Figure 61. Proposed H-bonded stacks of molecules of **126** in their gel aggregates.

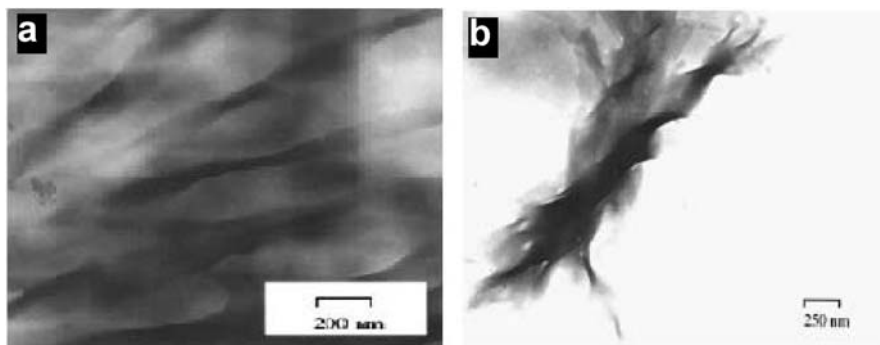


Figure 62. TEM images of **126** gels in toluene: (a) (*R,R*) enantiomer (100 mmol/dm³) and (b) (*S,S*) enantiomer (10 mmol/dm³). The scale bar in (a) is 200 nm and that in (b) is 250 nm. (Reprinted with permission from [406]. Copyright (2001) IOP Publishing Ltd.)

In several cases, the gelator networks display helical higher order structures that reflect the chirality of the terminal diol. Figure 62 presents TEM images of toluene gels obtained from enantiomers of **126** ($R = \text{methyl}, n = 12$). The (*R,R*) fibers have a left-handed helical tape structure and 100–200 nm diameters. The (*S,S*) enantiomer has a right-handed helical tape structure with 100–160 nm diameters. The configuration of these terminal groups attached to boronic acid directs the helicity of the gelator fiber network.

2.11.2. Gelation in supercritical fluids

Porous materials and aerogels, prepared by supercritical fluid extraction techniques, are industrially important [412–418]. Supercritical fluid extraction allows the liquid part of gels to be removed without disturbing the gelator network [75]. Figure 63 compares SEM images of a 2,3-bis-*n*-decyloxyanthracene (**14**; $n = 10$) xerogel (removal of liquid under reduced pressure) and aerogel (supercritical extraction of the liquid) [63]. The superior porosity and lower volume density of the aerogel are obvious. Aggregates of several other LMOGs in alcohol and halogenated liquid gels have been separated from the liquid component by this method [63, 178, 419–421].

In most cases, the LMOGs are insoluble in supercritical CO₂. As a result, direct gelation of supercritical CO₂ must be done in the presence of a co-solvent such as an alcohol or halogenated liquid in which the LMOG is soluble at room or elevated temperatures. If an LMOG can be dissolved in neat supercritical CO₂ and is insoluble at lower CO₂ pressures, very low-density aerogels can be obtained [63, 422, 423].

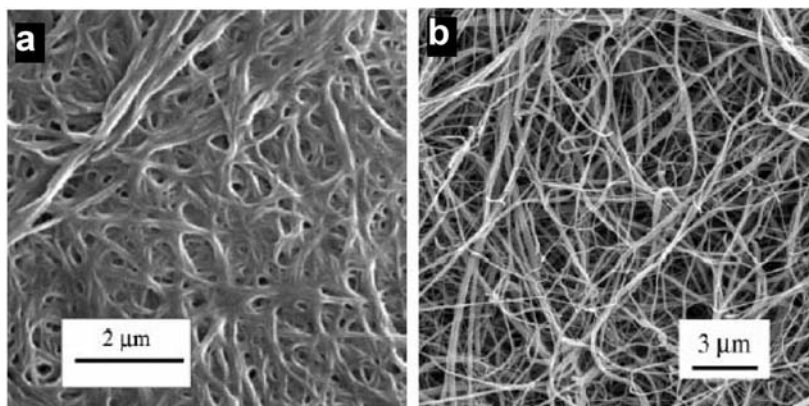
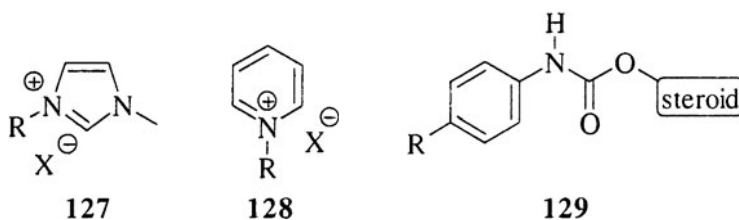
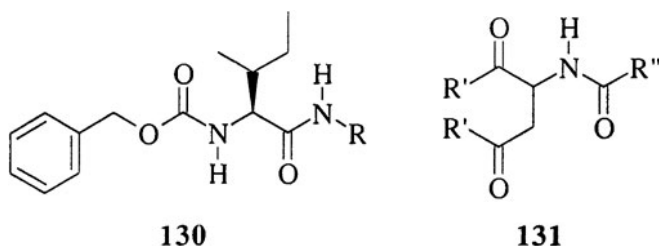


Figure 63. SEM images of **14** ($n = 10$) aggregates from ethanol gels: (a) xerogel (desolvated under low pressure) and (b) aerogel (desolvated by supercritical CO_2 extraction). (Reprinted with permission from [63]. Copyright (2000) Royal Society of Chemistry.)

2.11.3. Gelation of ionic liquids

Ionic liquids are salts whose melting temperatures usually range from sub-ambient to 100°C . Ionic liquids with organic groups (typically in the cationic part), the subject of this section, are employed increasingly in place of traditional organic solvents in chemical reactions, as electrolytes in solar cells, and for a variety of industrial applications [424–426] because of their negligible vapor pressures under most application conditions and potential recyclability. Some of the problems associated with liquid electrolytes in solar cells, such as evaporation, penetration of air and water, etc., have been resolved by gelating ionic liquids with organic [427–433], polymeric [434–439], or nanoparticle [440] gelators or by incorporating them in inorganic sol-gel lattices [441, 442]. For instance, ionic liquids based on 1-alkyl-3-methylimidazolium (**127**) or *N*-alkylpyridinium ions (**128**) have been gelated by the amide or urethane LMOGs **129–131**.





Lyotropic liquid-crystalline gels have been formed by adding 5–40 wt.% water to **127** ($R = n$ -decyl; $X = \text{Br}$) [443]. Figure 64 shows the X-ray diffraction and optical micrograms of the neat ionic liquid and its gel with 16 wt.% water. The diffraction pattern of dry **127** contains a broad Bragg peak, indicative of significant lattice and orientational disorder. The hydrated gel exhibits a strong anisotropic pattern along the equatorial axis (Figure 64D), featuring two diffraction peaks at $Q = 0.22$ and 0.44 \AA^{-1} (Figure 64E). The anisotropy of the X-ray diffraction and presence of additional peaks in the small angle region indicate that the mesogens are well ordered in the gel phase and that they are arranged in lamellae with a layer spacing of 28.6 \AA [443].

Gelation of ionic liquids with a dye-sensitizer in a solar cell improves high temperature durability without decreasing efficiency [431]. Conductivity measurements reveal that gelation does not affect the conductivity of the electrolyte and conductivity increases as iodine is added to both the gel and liquid electrolytes [430]. Aspects of these effects are developed in detail in Chapters 22 and 23.

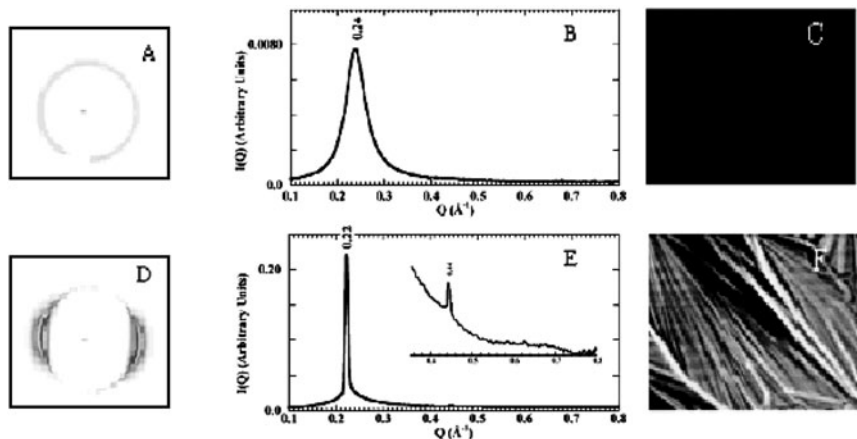


Figure 64. Small-angle X-ray scattering patterns (A, D), azimuthally averaged intensities as a function of scattering vector (B, E), and POM images (C, F) of neat **127** ($R = n$ -decyl; $X = \text{Br}$) (A–C) and its gel with 16 wt.% H_2O (D–F) at 23°C . (Reprinted with permission from [443]. Copyright (2002) The American Chemical Society.)

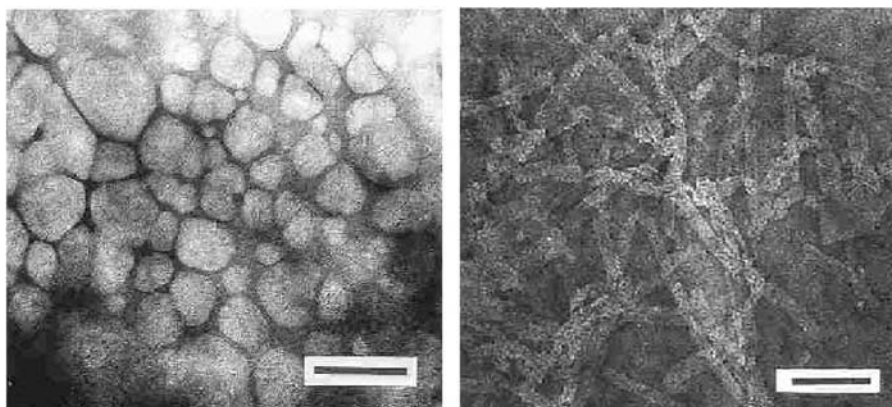
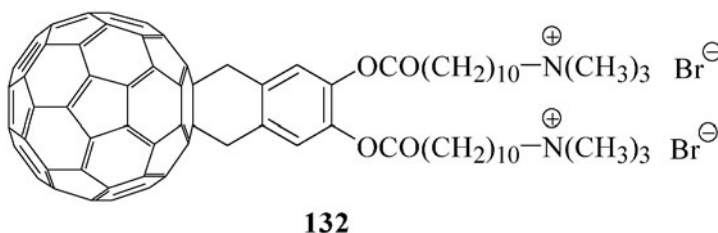


Figure 65. TEM images of 10 mmol dm⁻³ **132** in methanol: (a) solution; (b) gel. The samples were prepared by staining with uranyl acetate solution. The space bars represent 200 nm in (a) and 100 nm in (b). (Reprinted with permission from [446]. Copyright (1999) The Chemical Society of Japan.)

2.11.4. Fullerene derivatives as organic gelators

[60]Fullerene is known to stabilize gels with porphyrin derivatives as the LMOGs [444, 445]. When long amphiphilic groups are attached to [60]fullerene, as in **132**, gels were formed from 10–20 mmol dm⁻³ methanolic solutions that were left at room temperature for a few days [446]. The initial globular aggregates (Figure 65a) transform into numerous fibers and gelation occurs (Figure 65b). The fibers are well-ordered structures with a repeating unit distance of 2.24 nm, as observed by powder X-ray diffraction [446].



3. The Role of Liquid in Gelation by LMOGs

The importance of the liquid component to the stability of LMOG gels and to their SAFIN structures has been demonstrated throughout this chapter and the specific properties of two types of fluids have been emphasized in Sections 2.11.2 and 2.11.3. However, no *general* liquid-gelator interaction has

been identified during the transformation of sols to gels. However, whether general or specific, such interactions must occur because gelation involves a competition between phase separation (i.e., nucleation, aggregation, and precipitation) and dissolution of the gelator molecules. Despite the difficulties associated with identifying how these interactions operate and affect the eventual phase obtained, they can be postulated based on molecular structures and functional group contents, and they should be considered when designing an LMOG to gel a specific liquid. Although much more research will be needed in the future to place the design criteria on firm physical bases, some empirical trends are known and they will be discussed here.

A model of the probable crucial steps in one type of gelation [8] (Figure 66) begins with formation of one-dimensional aggregates that join to form a three-dimensional network by secondary interactions. When the secondary interactions are very strong, precipitation or crystallization of the gelator may take place. It is evident from Figure 66 that the solvent must play an important role in controlling these interactions.

$$\ln \chi_g = \frac{\Delta H_{\text{fus}}}{RT_g} + \frac{\Delta H_{\text{fus}}}{RT_{\text{fus}}} \quad (7)$$

Analyses of the thermochemical properties of gels by the Schröder-van-Laar equation (equation 7) [447–450] can be informative despite the fact that

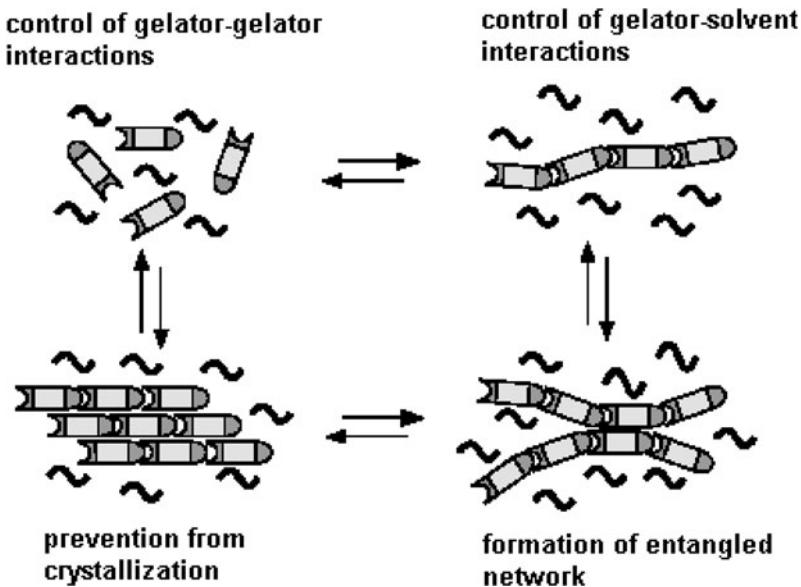


Figure 66. Crucial steps in the formation of gels. (Reprinted with permission from [8]. Copyright (1999) Kluwer Academic Publishers, Boston.)

the gel phases and the sol phases they provide when heated above T_g do not fit the conditions for this analysis – for one, the sols are not ideal solutions and the equation is predicated on the “melted” phase being ideal. In this equation, χ_g is the mole fraction of the gelator and ΔH_{fus} and T_{fus} are the enthalpy of melting of the gel strands and the melting temperature of the neat gelator, respectively. One interesting trend that can be explored is the effect of the liquid on T_g . The Schröder-van-Laar analysis compares ΔH_{fus} of the neat gelator (from DSC measurements) and the heats of melting of the gels as a function of their composition and T_g values at several compositions [17, 22, 51, 86, 136, 250, 263]. This allows the nature of the gel \leftrightarrow sol transition to be analyzed in greater detail. For example, Figure 67 presents a Schröder-van-Laar plot of gels of **20** in silicone oil [22].

The calculated melting enthalpy of neat **20** from the slope (139 kJ/mol) or intercept (137 kJ/mol) of Figure 67 is slightly larger than the experimental value (134 kJ/mol), but all are the same within the limits of experimental error. Higher ΔH_{fus} values from equation 7 than from DSC measurements has also been reported for *n*-alkane gels in silicone oil [17] and cholesterol-based gels in different organic liquids [136]. The higher values are possibly due to the heat of dissolution during the melting of gelator strands that is not present when the neat gelator is melted. In general, the nearer the two values, the smaller the influence of the liquid component on the dissolution of the gelator network at T_g .

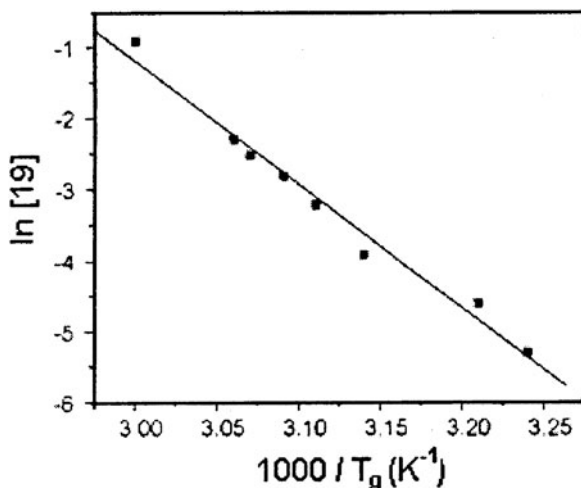


Figure 67. Semilog plot of the molar concentration of **20** in silicone oil vs the inverse of gelation temperature. (Reprinted with permission from [22]. Copyright (1999) The American Chemical Society.)

Systematic studies of the effect of the liquid component on the properties of a series of gels with steroid gelators (**133**, **134**) have been performed [47–50, 451–455]. The results indicate that the polarity of the liquid, its molecular structure, and the extent to which it can dissolve the gelator at different temperatures are three of the most important factors influencing gelation and the nature of the gelator aggregates. The temporal stability of the gels from **133a** ($W = \text{CH}$, $X = \text{O}$, $Y = \text{no atom}$, $Z = \text{H}$, $n = 3$) depends upon both the concentration of the gelator and the nature of the liquid. In *n*-dodecane, unstable gels are formed whereas with 1-heptanol or heptanal, gels stable for more than one year were obtained [47]. The molecular shape of the liquid also plays an important role in stabilizing the gel phase. For example, the temporal stability of **133a** gels decreases considerably when the liquid is changed from *n*-alkanes to cycloalkanes [48]. From electron micrographs of gels of **133a**, it was found that the nearly monodisperse cross-sectional dimensions of the fibrils are somewhat larger in *n*-dodecane (2.2 wt.%) than in 1-octanol (1.9 wt.%); both were near $10 \text{ nm} \times 20 \text{ nm}$ but those of the 1-octanol gel also were twisted (Figure 68; pitch ca. 119 nm) [48, 455].

Absorption and emission spectra and measurements of T_g of gels of **133a** demonstrated some very interesting morphological dependencies on the composition of 1-octanol/*n*-hexadecane liquid mixtures [451]: bulk polarity is more

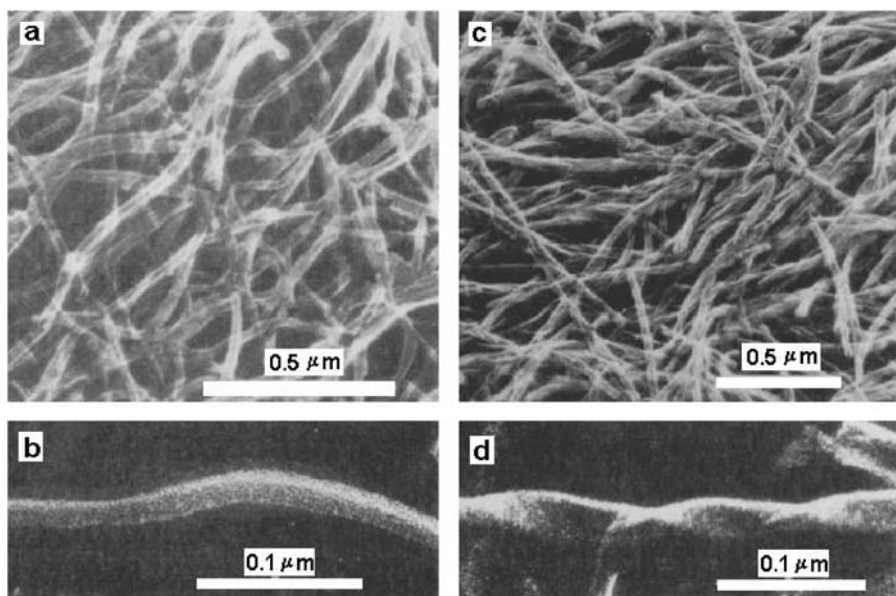
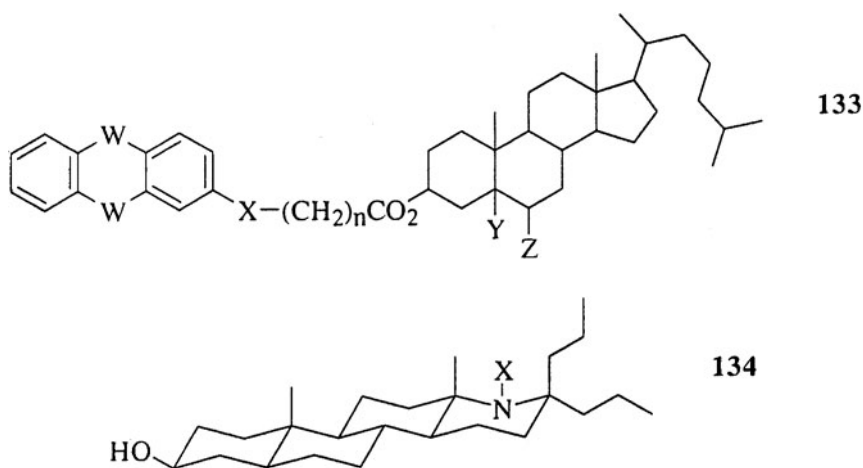


Figure 68. Freeze-fracture electron micrographs of **133a** gels in (a, b) *n*-dodecane (2.2 wt.%) and (c, d) 1-octanol (1.9 wt.%) etched at -60°C and 10^{-7} Torr for 1 h. (Reprinted with permission from [48]. Copyright (1989) The American Chemical Society.)

important than specific solvent-solute interactions in controlling the mode of gelation. When the composition of the liquid mixture was in the 80-85/20-15 range (so that there are many times more alcohol molecules than those of the gelator), the morph of the gelator network could be changed at will from pure alcohol-like networks to pure alkane-like networks by altering the rate of cooling from the sol phase. At compositions richer in alcohol, the morph of **133a** was always that of the neat alcohol, regardless of the cooling rate from the sol phase; at compositions with less than 80% 1-octanol, the morph was always that of the alkane regardless of the cooling rate. Were specific liquid-gelator molecular interactions the more important factor, the transition between the 2 morphs would have occurred at much lower concentration of the alcohol component. Furthermore, the fibrils of gels with 1-alkanols whose chains contain ≥ 10 carbon atoms resemble those of the *n*-alkane gels rather than those of gels with shorter alcohols as the liquid. These results indicate that the bulk polarity sensed by the molecules of **133a** as they aggregate determines their mode of packing.



Gelation studies of a series of anthraquinone-steroid LMOGs also demonstrate the importance of bulk polarity of the liquid on T_g [50, 453]. For instance, gelation of **133b** ($W = C=O$, $X = O$, $Y = \text{no atom}$, $Z = H$, $n = 3$), the anthraquinone analog of **133a**, is most effective in long chain alkanes and alcohols in which the necessary balance between solubility and insolubility is attained [8]. Figure 69 shows the variation of T_g of **133b** in 1-alkanols as a function of the solvent polarity function (Δf) [456] and the number of carbon atoms in the alcohol molecules (n). Especially at 1.0 wt.%, the T_g values in alcohols with $n = 5-10$ are virtually invariant. The higher T_g value of 1.0 wt.% gel than the 1.5 wt.% gel in 1-propanol is not understood at this time; it may

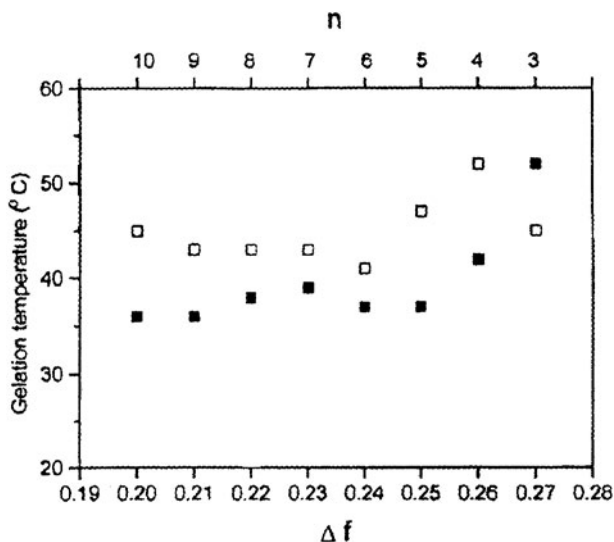


Figure 69. Gelation temperatures for 1.0 (■) and 1.5 wt.% (□) of **133b** in 1-alkanols versus Δf and n . (Reprinted with permission from [453]. Copyright (1996) The American Chemical Society.)

be related to the degree to which liquid molecules are incorporated into the gelator strands, especially at junction zones [455].

Larger polarity changes than those spanned by the data in Figure 69 can have a more drastic influence on T_g is considerably higher in *n*-dodecane ($\Delta f = -0.0013$) [457] gels than that in 1-alkanol gels at comparable concentrations of **133b** [453]. By contrast, the T_g values of **134a** are much lower in alkane gels than in alcohol gels [451]. Clearly, these results indicate that the degree to which a liquid can solubilize an LMOG as the gel is heated will play a major role in determining T_g : **133a** is less soluble in alcohols than is **133b**, but it is more soluble in alkanes. Bulk polarity changes of the liquids also found to influence the T_g values of quaternary ammonium salts of **134a** ($X = H$) formed from alkyl halides [452].

A strong liquid dependence on the size of **134b** ($X = O$) domains has been reported for its hydrocarbon gels. SANS and SAXS data demonstrate that the diameters of rod-like aggregates in the gels of ca. $2 \times 10^{-2} \text{ g cm}^{-3}$ **134b** increase from 105 Å in cyclohexane to 157 Å in methylcyclohexane [458].

Solvent-dependent gelation properties have also been observed for bis-urea-based LMOGs [224, 226, 232, 233]. A bis-urea gelator containing a 2,2'-disubstituted azobenzene moiety has been shown to form fibers in one of two morphs, depending on liquid polarity and kinetic factors related to the rate of transformation of one type of gelator aggregate to the other [233].

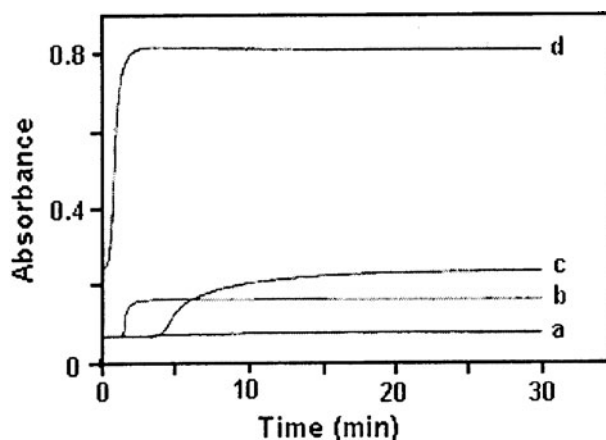


Figure 70. Variation of the opacity at 550 nm during the gelation of 1.77% volume fraction **7** in (a) toluene, (b) dodecane, (c) nitrobenzene, and (d) hexafluorobenzene (optical path = 1 mm). (Reprinted with permission from [37]. Copyright (2000) The American Chemical Society.)

Terech and co-workers have studied the changes in the optical, rheology, kinetic, and thermodynamic properties of gels of **7** in toluene, *n*-dodecane, and nitrobenzene [37]. The optical opacity of the gels varied considerably depending on the nature of the liquid (Figure 70). A very turbid gel is obtained in hexafluorobenzene (trace d) compared to the almost transparent gel in toluene (trace a). The opacity of the gels is related to size of the aggregate crystallites. The sequence of opacity for gels of **7** is toluene < *n*-dodecane < nitrobenzene < perfluorobenzene.

The rheological behavior of gels from 0.88% (volume fraction) **7** in three different liquids is compared in Figure 71. The G' versus γ profiles define the mechanical threshold between the linear and nonlinear regimes of deformations. The linear domain (defined as the region where the dynamic moduli are independent of the strain amplitude (in the frequency range)), is restricted to small levels of strain ($\gamma < 0.01$). Except for the nitrobenzene gel, the linear domains are comparable and the sequence of elasticity based on the data in Figure 71 is toluene < *n*-dodecane < nitrobenzene (at $\nu = 1$ Hz). The same trend has been observed for yield stress values of these gels [37]. Additional discussions about rheological behavior of gels are found in Chapters 5 and 8.

As demonstrated in Chapter 10, SANS studies of molecular gels allow one to characterize the structures of self-assembled networks [459]. SANS data analyses of **7** gels in hydrocarbon liquids showed that fiber aggregates of **7** are formed during gelation (Figure 72) [460]. The unidirectionality of the aggregates is characterized by a Q^{-1} intensity decay at low angles (a plateau in QI vs Q plots). The cross-sectional shape, contrast homogeneity, and monodispersity

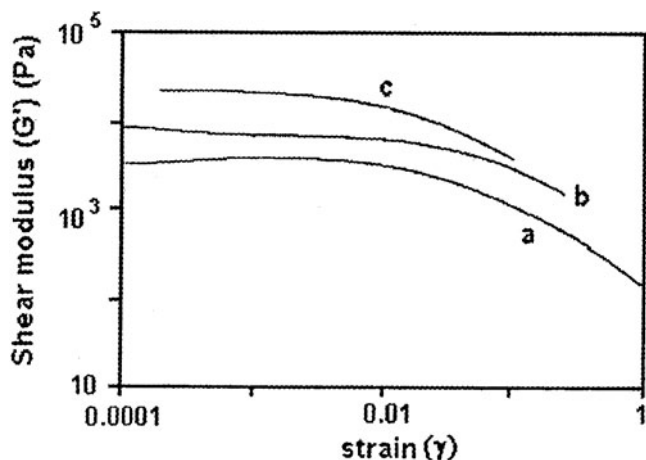


Figure 71. Linear viscoelastic domains of 0.88% (volume fraction) **7** organogels at 1 Hz in (a) toluene, (b) dodecane, and (c) nitrobenzene. (Reprinted with permission from [37]. Copyright (2000) The American Chemical Society.)

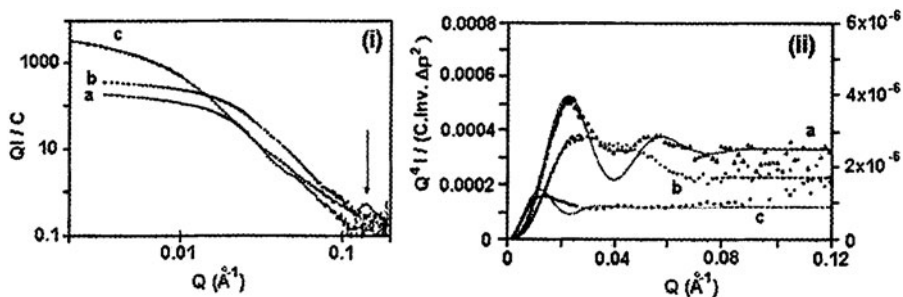
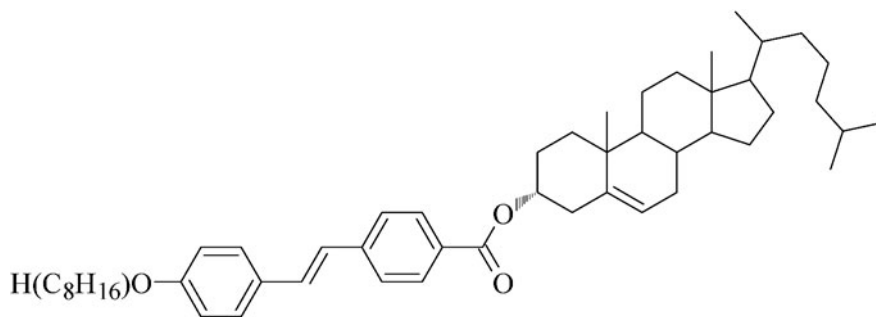


Figure 72. Neutron scattering curves of **7** organogels in (a) benzene- d_6 (0.014 g cm^{-3}), (b) cyclohexane- d_{12} (0.013 g cm^{-3}), and (c) nitrobenzene- d_5 (0.012 g cm^{-3}). (i) Concentration normalized cross-sectional intensity QI vs Q . The vertical arrow points to a Bragg peak at $Q \approx 0.14 \text{ \AA}^{-1}$. (ii) Interfacial scattering Q^4I intensities normalized by concentration, contrast, and scattering invariant versus Q . Dotted horizontal segments indicate the asymptotic large angle limits. Full lines are indicative adjustments for the extreme situations: cylindrical fibers with 180 \AA cross-sections in toluene and ribbons with 300 \AA thicknesses and short-axis cross-sectional distance ca. 1500 \AA in nitrobenzene. The scale for the nitrobenzene gel is the right ordinate axis. (Reprinted with permission from [37]. Copyright (2000) The American Chemical Society.)

could be obtained from Q^4I vs Q plot (Figure 72(ii)) [461, 462]. The fibers of **7** exhibit square cross-sectional shapes (side $s \approx 200 \text{ \AA}$) in benzene and toluene, a slightly rectangular shape in cyclohexane, and a ribbon-like shape with a thickness ca. 300 \AA in nitrobenzene [36, 37].

**135**

Solvent effects on the gelation of monomers have been treated theoretically [463, 464]. The formation and molecular mobility of polymeric gels also are dependent on the nature of the liquid component [465–470]. The sequence of phases (lamellar, hexagonal, isotropic, or gel-like) obtained from binary mixtures of potassium salts of fatty acids in ethylene glycol and butylene glycol or water depend on the nature of the liquid as well as other factors [471]. For instance, the potassium salt of stearic acid ($\text{CH}_3(\text{CH}_2)_{16}\text{CO}_2\text{K}$) or potassium behenate ($\text{CH}_3(\text{CH}_2)_{20}\text{CO}_2\text{K}$) makes hexagonally-packed phases in ethylene glycol and lamellar phases in butylene glycol [471]. Potassium alkanolate salts with <18 carbon atoms form only lamellar phases in the alkanediols examined [471].

Whitten *et al.* have examined the dependence of the type of liquid on the gelation of a cholesterol tethered *trans*-stilbene derivative **135** [472] by AFM [473].

Figure 73 shows a series of time-transient AFM images of a **135** gel (1.6 wt.%) in 1-octanol. Dewetting of the solution from the hydrophobic graphite surface takes place during the gelation process (Figure 73b), indicating that the gelator-liquid interaction is enhanced during the gelation process. Further studies indicate that approximately 30% of the composition of the fibrous bundles formed eventually consists of liquid molecules that cannot be replaced by a second liquid [473]. Alternatively, the liquid molecules may be physically trapped inside the bundles if they are really tubules [165]. Formation of tubules from LMOGs containing cholesteric groups is well documented [136, 140].

4. Conclusions and Perspectives for the Future

Representative examples of different classes of organic gelators have been discussed here. They include a broad spectrum of molecular structures, from simple molecules such as long *n*-alkanes to complex molecules and two component systems and gelators that respond to external stimuli. Different secondary

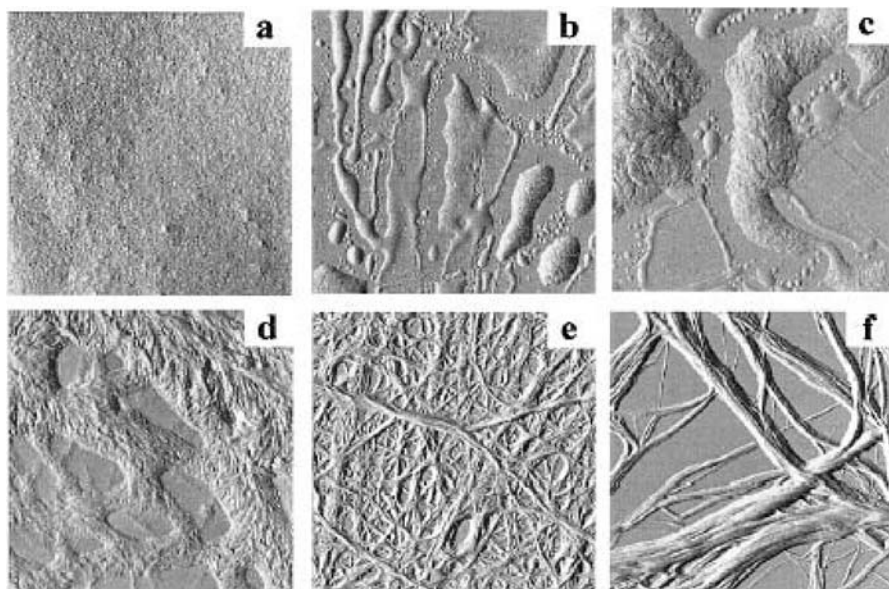


Figure 73. Time-transient AFM images (in amplitude mode) of the sol-gel phase transition occurring as a heated sol (solution) of 1.6 wt.% **135** in 1-butanol was cooled to room temperature for (a) 0, (b) 10, (c) 15, (d) 18, (e) 21, and (f) 31 min. The scale of the images is $12 \times 12 \mu\text{m}$. (Reprinted with permission from [473]. Copyright (2000) The American Chemical Society.)

interactions such as van der Waals, H-bonding, electrostatic, etc. or their combinations are the main non-covalent forces responsible for aggregation by these gelators. Although many types of gelator molecules and interactions responsible for gelation have been studied intensely in recent years, there are no generally applicable recipes to correlate gel stability with molecular structure/properties of the LMOGs. We predict that significant efforts will be devoted to the investigation of the mechanism(s) of organogelation and the formulation of predictive tools for organogelation in the next several years.

The speed with which the area of research called “molecular gels” is able to mature will depend on developments within the more general field of self-assembly. Specifically, it will be necessary to understand the factors that lead to various types of self-assembly and to accelerated (or decelerated) growth of fibers along selected axes. This implies much deeper insights than currently exist into how nucleation of crystals occurs, how liquids interact with growing crystal surfaces, and how fibers interact to form networks. Data already in hand, largely from the research of the Weizmann Institute [474–478], indicate that there may be multiple answers to each of these. In that regard, recent studies have provided a blueprint for understanding the links between the rates of construction of SAFINs and the rheological and structural properties of their

gels [479]. Additionally, new methods to induce gelation via subtle, *in situ*, structural perturbations of LMOGs continue to be discovered [480]. Yet, a blueprint for the *a priori* design of 3-dimensional fibrous networks that has its roots at the level of intermolecular interactions *must* emerge if we are to be able to design low molecular-mass organic gelators for gelation of specific liquids and whose gels have predetermined rheological and thermodynamic properties.

That is the challenge for the future. The vast body of data currently available, as represented by this chapter, awaits those who are able to see the underlying commonalities and express them to us as formulas and recipes.

Acknowledgments

The authors gratefully acknowledge the U.S. National Science Foundation for continued financial support and the many talented graduate students and postdocs from the Georgetown laboratory for their ideas and efforts which permeate this chapter.

References

- [1] Terech, P.; Weiss R.G. *Chem. Rev.* **1997**, *97*, 3133.
- [2] Terech, P.; Weiss, R.G. In *Surface Characterization Methods*, A.J. Milling, Ed., New York: Marcel Dekker, **1999**, p. 286.
- [3] Melendez, R.E.; Carr, A.J.; Linton, B.R.; Hamilton, A.D. In *Structure and Bonding*, M. Fujita, Ed., Berlin: Springer, **2000**, *96*, p. 31.
- [4] Murata, K.; Aoki, M.; Suzuki, T.; Harada, T.; Kawabata, H.; Komori, T.; Ohseto, F.; Ueda, K.; Shinkai, S. *DIC Tech. Rev.*, **1996**, *2*, 39.
- [5] Terech, P. *Ber. Bunsenges. Phys. Chem.*, **1998**, *102*, 1630.
- [6] Terech, P. In *Specialist Surfactants*, I.D. Robb, Ed., London: Chapman and Hall, **1997**.
- [7] Shinkai, S.; Murata, K. *J. Mater. Chem.*, **1998**, *102*, 1630.
- [8] van Esch, J.; Schoonbeek, F.; De Loos, M.; Veen, E. M.; Kellog, R.M.; Feringa, B.L. In *Supramolecular Science: Where It Is and Where It Is Going*, U. Rocco and D. Enrico, Eds., *NATO ASI Ser. E; Math. Phys. Sci.*, Boston: Kluwer, **1999**, *527*, p. 233.
- [9] Abdallah, D.J.; Weiss, R.G. *Adv. Mater.*, **2000**, *12*, 1237.
- [10] Jung, J.H.; Shinkai, S. *J. Incl. Phenom. Macrocycl. Chem.*, **2001**, *41*, 53.
- [11] Yang, Y.J.; Cui, W.J. *Chinese J. Org. Chem.*, **2001**, *21*, 632.
- [12] Shchipunov, Y.A. *Colloid Surface A: Physiochem. Eng. Asp.*, **2001**, *183*, 541.
- [13] Abdallah, D.J.; Weiss, R.G. *J. Brazil. Chem. Soc.*, **2000**, *11*, 209.
- [14] Rees, G.D.; Robinson, B.H. *Adv. Mater.*, **1993**, *5*, 608.
- [15] Gronwald, O.; Snip, E.; Shinkai, S. *Curr. Opin. Colloid. Interface Sci.*, **2002**, *7*, 148.
- [16] Srivastava, S.P.; Saxena, A.K.; Tandon, R.S.; Shekher, V. *Fuel* **1997**, *76*, 625 and references cited therein.
- [17] Abdallah, D.J.; Weiss, R.G. *Langmuir*, **2000**, *16*, 352.
- [18] Abdallah, D.J.; Sirchio, S.A.; Weiss, R.G. *Langmuir*, **2000**, *16*, 7558.
- [19] Eldridge, J.E.; Ferry, J.D. *J. Phys. Chem.*, **1954**, *58*, 992.

- [20] Tetramethyltetraphenylsiloxane, Dow silicone oil 704.
- [21] Prasad, A.; Marand, H.; Bheda, M.; Gibson, H.W. *Polym. Prep.*, **1991**, 32, 469.
- [22] Abdallah, D.J.; Lu, L.; Weiss, R.G. *Chem. Mater.*, **1999**, 11, 2907.
- [23] Aoki, M.; Murata, K.; Shinkai, S. *Chem. Letters*, **1991**, 1715.
- [24] Aoki, M.; Nakashima, K.; Kawabata, H.; Tsutsui, S.; Shinkai, S. *J. Chem. Soc. Perkin Trans 2*, **1993**, 347.
- [25] Xing, B.; Choi, M.-F.; Xu, B. *Chem. Commun.*, **2002**, 362.
- [26] (a) Smith, G.H.; McBain, J.W. *J. Phys. Colloid Chem.* **1947**, 51, 1189. (b) Daniel, J.; Rajasekharan, R. *J. Am. Oil Chem. Soc.*, **2003**, 80, 417.
- [27] Yamakita, I. *Rev. Phys. Chem. Japan*, **1940**, 14, 146.
- [28] Polishuk, A.T. *J. Am. Soc. Lubn. Eng.* **1977**, 33, 133.
- [29] Uzu, Y. *J. Jpn. Oil Chem. Soc.*, **1975**, 24, 261.
- [30] Stephens, J.S. *J. Pharm. Pharmacol.*, **1971**, 23, 774.
- [31] Tachibana, T.; Mori, T.; Hori, K. *Bull. Chem. Soc. Jpn.*, **1980**, 53, 1714.
- [32] Tachibana, T.; Mori, T.; Hori, K. *Bull. Chem. Soc. Jpn.*, **1981**, 54, 73.
- [33] Fuhrhop, J.-H.; Schnieder, P.; Rosenberg, J.; Boekema, E. *J. Am. Chem. Soc.*, **1987**, 109, 3387.
- [34] (a) Hotten, B.W.; Birdsall, D.H. *J. Colloid Sci.*, **1952**, 7, 284. (b) Tachibana, T.; Kambara, H. *J. Am. Chem. Soc.*, **1965**, 87, 3015.
- [35] Tachibana, T.; Yoshizumi, T.; Hori, K. *Bull. Chem. Soc. Jpn.*, **1979**, 52, 34.
- [36] Terech, P.; Rodriguez, V.; Barnes, J.D.; McKenna, G.B. *Langmuir*, **1994**, 10, 3406.
- [37] Terech, P.; Pasquier, D.; Bordas, V.; Rossat, C. *Langmuir*, **2000**, 16, 4485.
- [38] Liquid crystal mixtures from Merck were used: (i) LC-TL213, a multicomponent mixture ($T_{N/I} = 87^\circ \text{C}$, $\varepsilon_{||} = 10$ and $\varepsilon_{\perp} = 5.3$, $\Delta n = 0.234$) and (ii) a chiral nematic material ($84^\circ < T_{N-/I} < 105^\circ \text{C}$, $\Delta n = 0.20$, $\Delta\varepsilon = 28$, $\lambda_{\text{max}} = 495 \text{ nm}$).
- [39] Janssen, R.H.C.; Stümpflen, V.; Bastiaansen, C.W.M.; Broer, D.J.; Tervoort, T.A.; Smith, P. *Jpn. J. Appl. Phys.*, **2000**, 39, 2721.
- [40] Janssen, R.H.C.; Teunissen, J.-P.; Picken, S.J.; Bastiaansen, C.W.M.; Broer, D.J.; Tervoort, T.A.; Smith, P. *Jpn. J. Appl. Phys.*, **2001**, 40, 2372.
- [41] Garner, C.M.; Mistrot, M. *Proc. 221 ACS National Meetings: Div. Org. Chem.*, **1996**, Orgn 099.
- [42] Garner, C.M.; Terech, P.; Allegraud, J.J.; Mistrot, B.; Nguyen, P.; de Geyer, A.; Rivera, D. *J. Chem. Soc., Faraday Trans.*, **1998**, 94, 2173.
- [43] Terech, P.; Allegraud, J.J.; Garner, C.M. *Langmuir*, **1998**, 14, 3991.
- [44] Shumburo, A.; Biewer, M.C. *Chem. Mater.*, **2002**, 14, 3745.
- [45] Ajayaghosh, A.; George, S.J. *J. Am. Chem. Soc.*, **2001**, 123, 5148.
- [46] Ajayaghosh, A.; George, S.J.; Praveen, V.K. *Angew. Chem. Int. Ed.*, **2003**, 42, 332.
- [47] Lin, Y.-C.; Weiss, R.G. *Macromol.*, **1987**, 20, 414.
- [48] Lin, Y.-C.; Kachar, B.; Weiss, R.G. *J. Am. Chem. Soc.*, **1989**, 111, 5542.
- [49] Bujanowski, V.J.; Katsoulis, D.E.; Ziemelis, M.J. *J. Mater. Chem.*, **1994**, 4, 1181.
- [50] Mukkamala, R.; Weiss, R.G. *J. Chem. Soc., Chem. Commun.*, **1995**, 375.
- [51] Clavier, G.M.; Brugger, J.-F.; Bouas-Laurent, H.; Pozzo, J.-L. *J. Chem. Soc., Perkin Trans. 2*, **1998**, 2527.
- [52] Clavier, G.; Mistry, M.; Fages, F.; Pozzo, J.-L. *Tetrahedron Lett.*, **1999**, 40, 9021.
- [53] Brotin, T.; Utermöhlen, R.; Fages, F.; Bouas-Laurent, H.; Desvergne, J.-P. *J. Chem. Soc., Chem. Commun.*, **1991**, 416.
- [54] Pozzo, J.-L.; Clavier, G.; Colomes, M.; Bouas-Laurent, H. *Tetrahedron*, **1997**, 53, 6377.
- [55] Placin, F.; Colomes, M.; Desvergne, J.-P. *Tetrahedron Lett.*, **1997**, 38, 2665.

- [56] Clavier, G.M.; Pozzo, J.-L.; Bouas-Laurent, H.; Liere, C.; Roux, C.; Sanchez, C. *J. Mater. Chem.*, **2000**, *10*, 1725.
- [57] Terech, P.; Bouas-Laurent, H.; Desvergne, J.-P. *J. Colloid Interface Sci.*, **1995**, *174*, 258.
- [58] Pozzo, J.-L.; Desvergne, J.-P.; Clavier, G.M.; Bouas-Laurent, H.; Jones, P.G.; Perlstein, J. *J. Chem. Soc., Perkin Trans. 2*, **2001**, 824.
- [59] Placin, F.; Desvergne, J.-P.; Belin, C.; Buffeteau, T.; Desbat, B.; Ducasse, L.; Lassègues, J.-C. *Langmuir*, **2003**, *19*, 4563.
- [60] Llusar, M.; Pidol, L.; Roux, C.; Pozzo, J.-L.; Sanchez, C. *Chem. Mater.*, **2002**, *14*, 5124.
- [61] Llusar, M.; Roux, C.; Pozzo, J.-L.; Sanchez, C. *J. Mater. Chem.*, **2003**, *13*, 442.
- [62] Lescanne, M.; Colin, A.; Mondain-Monval, O.; Fages, F.; Pozzo, J.-L. *Langmuir*, **2003**, *19*, 2013.
- [63] Placin, F.; Desvergne, J.-P.; Cansell, F. *J. Mater. Chem.*, **2000**, *10*, 2147.
- [64] Lescanne, M.; Colin, A.; Mondain-Monval, O.; Heuzé, K.; Fages, F.; Pozzo, J.-L. *Langmuir*, **2002**, *18*, 7151.
- [65] Wilder, E.A.; Hall, C.K.; Khan, S.A.; Spontak, R.J. *Recent Res. Devel. Mat. Sci.*, **2002**, *3*, 93.
- [66] Thomas, P.; Sibi, M. *Compt. Rend.*, **1926**, *183*, 282.
- [67] Yamamoto, S.i. *J. Soc. Chem. Ind. Japan*, **1943**, *46*, 279.
- [68] McKenna, G.; Kern, F.; Candau, S.J. *Polym. Prep. (Div. Polym. Chem. Am. Chem. Soc)* **1991**, *32*, 455.
- [69] Yamasaki, S.; Tsutsumi, H. *Bull. Chem. Soc. Jpn.*, **1994**, *67*, 906.
- [70] Yamasaki, S.; Tsutsumi, H. *Bull. Chem. Soc. Jpn.*, **1995**, *68*, 123.
- [71] Smith, J.M.; Katsoulis, D.E. *J. Mater. Chem.*, **1995**, *5*, 1899.
- [72] Watase, M.; Itagaki, H. *Bull. Chem. Soc. Jpn.*, **1998**, *71*, 1457.
- [73] Beginn, U.; Keinath, S.; Möller, M. *Macromol. Chem. Phys.*, **1998**, *199*, 2379.
- [74] Thierry, A.; Straupé, C.; Lotz, B.; Wittmann, J. C. *Polym. Commun.*, **1990**, *31*, 299.
- [75] Ilzhoefer, J.R.; Spontak, R.J. *Langmuir*, **1995**, *11*, 3288.
- [76] Wilder, E.A.; Hall, C.K.; Khan, S.A.; Spontak, R.J. *Langmuir*, **2003**, *19*, 6004.
- [77] Mercurio, D.J.; Khan, S.J.; Spontak, R.J. *Rheol. Acta*, **2001**, *40*, 30.
- [78] Wilder, E.A.; Hall, C.K.; Spontak, R.J. *J. Colloid Interface Sci.*, **2003**, *267*, 509.
- [79] Watase, M.; Nakatani, Y.; Itagaki, H. *J. Phys. Chem. B*, **1999**, *103*, 2366.
- [80] Zubarev, E.R.; Pralle, M.U.; Sone, E. D.; Stupp, S. I. *J. Am. Chem. Soc.*, **2001**, *123*, 4105.
- [81] Zubarev, E.R.; Pralle, M.U.; Sone, E.D.; Stupp, S.I. *Adv. Mater.*, **2002**, *14*, 198.
- [82] Lu, L.; Weiss, R.G. *Chem. Commun.*, **1996**, 2029.
- [83] Malpass, J.R. In *Comprehensive Organic Chemistry; The Synthesis and Reactions of Organic Compounds*, D.H.R. Barton and W.D. Ollis, Eds., 2, New York: Pergamon, **1979**.
- [84] Hanabusa, K.; Kawakami, A.; Kimura, M.; Shirai, H. *Chem. Lett.*, **1997**, 191.
- [85] Ostuni, E.; Kamaras, P.; Weiss, R.G. *Angew. Chem. Int. Ed.*, **1996**, *35*, 1324.
- [86] George, M.; Weiss, R.G. *Langmuir*, **2002**, *18*, 7124.
- [87] Abdallah, D.J.; Weiss, R.G. *Chem. Mater.*, **2000**, *12*, 406.
- [88] Abdallah, D.J.; Robertson, A.; Hsu, H.-F.; Weiss, R.G. *J. Am. Chem. Soc.*, **2000**, *122*, 3053.
- [89] Abdallah, D.J. Bachman, R.E.; Perlstein, J.; Weiss, R.G. *J. Phys. Chem. B*, **1999**, *103*, 9269.
- [90] Oda, R.; Huc, I.; Candau, S.J. *Angew. Chem. Int. Ed.*, **1998**, *37*, 2689.

- [91] *Solubility of Nonelectrolytes*, 3rd edition, J.H. Hildebrand and R.L. Scott, Eds., New York: Reinhold Publ. Corp., **1950**.
- [92] *Regular and Related Solutions*, J.H. Hildebrand, J.M. Prausnitz and R.L. Scott, Eds., New York: Van Nostrand-Reinhold, **1970**.
- [93] Höpken, J. *Fluorocarbon-Hydrocarbon Molecules*, Ph.D. Thesis, University of Twente, The Netherlands, **1991**.
- [94] Bedford, R.G.; Dunlap, R.D. *J. Am. Chem. Soc.*, **1958**, *80*, 282.
- [95] Kadi, M. Hansson, P.; Almgren, M. *Langmuir*, **2002**, *18*, 9243.
- [96] Ku, C.-Y.; Nostro, P.L.; Chen, S.-H. *J. Phys. Chem. B*, **1997**, *101*, 908.
- [97] Nostro, P.L.; Ku, C.Y.; Chen, S.H.; Lin, J.S. *J. Phys. Chem.*, **1995**, *99*, 10858.
- [98] Nostro, P.L. *Adv. Colloids Interface Sci.*, **1995**, *56*, 245.
- [99] Twieg, R.J.; Russell, T.P.; Siemens, R.L.; Rabolt, J.F. *Macromolecules*, **1985**, *18*, 1361.
- [100] Höpken, J.; Pugh, C.; Richtering, W.; Möller, M. *Makromol. Chem.* **1988**, *189*, 911.
- [101] Gelation of alkane liquids with partially fluorinated alkanes has been observed by Walter Mahler, (Central Research & Development Department, E.I. DuPont de Nemours & Company, Wilmington, Delaware 19898, USA) as well (private communication dated Oct. 28, 1985).
- [102] Rabolt, J.F.; Russell, T.P.; Siemens, R.; Twieg, R.J.; Farmer, B. *Polym. Prep.*, **1986**, *27*, 223.
- [103] Pugh, C.; Höpken, J.; Möller, M. *Polym. Prep.*, **1988**, *29*, 460.
- [104] Lang, P.; Marczuk, P.; Lermann, E.; Möller, M. *Ber. Bunsenges. Phys. Chem.*, **1998**, *102*, 1644.
- [105] Marczuk, P.; Lang, P.; Möller, M. *Colloids and Surfaces A: Physiochem. Eng. Aspects*, **2000**, *163*, 103.
- [106] Rabolt, J.F.; Russell, T.P.; Twieg, R.J. *Macromolecules*, **1984**, *17*, 2786.
- [107] Russell, T.P.; Rabolt, J.F.; Twieg, R.J.; Siemens, R.L.; Farmer, B.L. *Macromolecules*, **1986**, *19*, 1135.
- [108] Challis, B.C.; Challis, J.A. In *ref.* 83, 2, p. 957.
- [109] Pfannemüller, B.; Welte, W. *Chem. Phys. Lipids*, **1985**, *37*, 227.
- [110] Fuhrhop, J.-H.; Helfrich, W. *Chem. Rev.*, **1993**, *93*, 1565.
- [111] Hafkamp, R.J.H.; Feiters, M.C.; Nolte, R.J. M. *Angew. Chem. Int. Ed.*, **1994**, *33*, 986.
- [112] Fuhrhop, J.-H.; Schnieder, P.; Boekema, E.; Helfrich, W. *J. Am. Chem. Soc.*, **1988**, *110*, 2861.
- [113] Köning, J.; Boettcher, C.; Winkler, H.; Zeitler, E.; Talmon, Y.; Fuhrhop, J.-H. *J. Am. Chem. Soc.*, **1993**, *115*, 693.
- [114] Hafkamp, R.J.H.; Feiters, M.C.; Nolte, R.J. M. *J. Org. Chem.*, **1999**, *64*, 412.
- [115] Taravel, F.R.; Pfannemüller, B. *Makromol. Chem.* **1990**, *191*, 3097.
- [116] Mieden-Gundert, G.; Klein, L.; Fischer, M.; Vögtle, F.; Heuzé, K.; Pozzo, J.-L.; Vallier, M.; Fages, F. *Angew. Chem. Int. Ed.*, **2001**, *40*, 3164.
- [117] Ahmed, S.A.; Sallenave, X.; Fages, F.; Mieden-Gundert, G.; Müller, W.M.; Müller, U.; Vögtle, F.; Pozzo, J.-L. *Langmuir*, **2002**, *18*, 7096.
- [118] Luo, X.; Li, C.; Liang, Y. *Chem. Commun.*, **2000**, 2091.
- [119] Liu, X.Y.; Sawant, P.D. *Adv. Mater.*, **2002**, *14*, 421.
- [120] Jung, J.H.; Shinkai, S.; Shimizu, T. *Chem. Eur.J.*, **2002**, *8*, 2684.
- [121] Beginn U; Sheiko S; Moller M. *Macromol. Chem. Phys.*, **2000**, *201*, 1008.
- [122] Yasuda, Y.; Iishi, E.; Inada, H.; Shirota, Y. *Chem. Lett.*, **1996**, 575.
- [123] van Gorp, J.J.; Vekemans, J.A. J.M.; Meijer, E.W. *J. Am. Chem. Soc.*, **2002**, *124*, 14759.

- [124] Tomioka, K.; Sumiyoshi, T.; Narui, S.; Nagaoka, Y.; Iida, A.; Miwa, Y.; Taga, T.; Nakano, M.; Handa, T. *J. Am. Chem. Soc.*, **2001**, *123*, 11817.
- [125] Schmidt, R.; Schmutz, M.; Michel, M.; Decher, G.; Mésini, P.J. *Langmuir*, **2002**, *18*, 5668.
- [126] Schmidt, R.; Schmutz, M.; Mathis, A.; Decher, G.; Rawiso, M.; Mésini, P.J. *Langmuir*, **2002**, *18*, 7167.
- [127] Schmidt, R.; Adam, F.B.; Michel, M.; Schmutz, M.; Decher, G.; Mésini, P.J. *Tetrahedron Lett.*, **2003**, *44*, 3171.
- [128] Hanabusa, K.; Manabu, Y.; Kimura, M.; Shirai, H. *Angew. Chem. Int. Ed.*, **1996**, *35*, 1949.
- [129] Mizrahi, S.; Gun, J.; Kipervaser, Z.G.; Lev, O. *Anal. Chem.*, **2004**, *76*, 5399.
- [130] de Loos, M.; van Esch, J.; Stokroos, I.; Kellogg, R.M.; Feringa, B.L. *J. Am. Chem. Soc.*, **1997**, *119*, 12675.
- [131] Inoue, K.; Ono, Y.; Kanekiyo, Y.; Hanabusa, K.; Shinkai, S. *Chem. Lett.*, **1999**, 429.
- [132] Jung, J.H.; Ono, Y.; Shinkai, S. *Chem. Eur. J.*, **2000**, *6*, 4552.
- [133] Jung, J.H.; Ono, Y.; Hanabusa, K.; Shinkai, S. *J. Am. Chem. Soc.*, **2000**, *122*, 5008.
- [134] Kobayashi, S.; Hamasaki, N.; Suzuki, M.; Kimura, M.; Shirai, H.; Hanabusa, K. *J. Am. Chem. Soc.*, **2002**, *124*, 6550.
- [135] Kobayashi, S.; Hanabusa, K.; Hamasaki, N.; Kimura, M.; Shirai, H. *Chem. Mater.*, **2000**, *12*, 1523.
- [136] Murata, K.; Aoki, M.; Suzuki, T.; Harada, T.; Kawabata, H.; Komori, T.; Ohseto, F.; Ueda, K.; Shinkai, S. *J. Am. Chem. Soc.*, **1994**, *116*, 6664.
- [137] Shinkai, S.; Murata, K. *J. Mater. Chem.*, **1998**, *8*, 485.
- [138] Jung, J.H.; Ono, Y.; Shinkai, S. *Angew. Chem. Int. Ed.*, **2000**, *39*, 1862.
- [139] Jung, J.H.; Ono, Y.; Shinkai, S. *Langmuir*, **2000**, *16*, 1643.
- [140] Jung, J.H.; Kobayashi, H.; Masuda, M.; Shimizu, T.; Shinkai, S. *J. Am. Chem. Soc.*, **2001**, *123*, 8785.
- [141] Yanagawa, H.; Ogawa, Y.; Furuta, H.; Tsuno, K. *J. Am. Chem. Soc.*, **1989**, *111*, 4567.
- [142] Fuhrhop, J.-H.; Bindig, U.; Siggel, U. *J. Am. Chem. Soc.*, **1993**, *115*, 11036.
- [143] Nuckolls, C.; Katz, T.J.; Castellanos, L. *J. Am. Chem. Soc.*, **1996**, *118*, 3767.
- [144] Tachibana, T.; Kayama, K.; Takeno, H. *Bull. Chem. Soc. Jpn.*, **1972**, *45*, 415.
- [145] Koumoto, K.; Yamashita, T.; Kimura, T.; Luboradzki, R.; Shinkai, S. *Nanotechnol.*, **2001**, *12*, 25.
- [146] Svenson, S.; Messersmith, P.B. *Langmuir*, **1999**, *15*, 4464.
- [147] George, M.; Weiss, R.G. *Chem. Mater.*, **2003**, *15*, 2879.
- [148] Ikeda, M.; Takeuchi, M.; Shinkai, S. *Chem. Commun.*, **2003**, 1354.
- [149] Koshima, H.; Matsusaka, W.; Yu, H. *J. Photochem. Photobiol. A: Chem.*, **2003**, *156*, 83.
- [150] Hanabusa, K.; Okui, K.; Karaki, K.; Koyama, T.; Shirai, H. *J. Chem. Soc., Chem. Commun.*, **1992**, 1371.
- [151] de Vries, E.J.; Kellogg, R.M. *J. Chem. Soc., Chem. Commun.*, **1993**, 238.
- [152] Hanabusa, K.; Matsumoto, Y.; Miki, T.; Koyama, T.; Shirai, H. *J. Chem. Soc., Chem. Commun.*, **1994**, 1401.
- [153] Suzuki, M.; Yumoto, M.; Kimura, M.; Shirai, H.; Hanabusa, K. *Chem. Commun.*, **2002**, 884.
- [154] Makarević, J.; Jokić, M.; Frkanec, L.; Katalenić, D.; Žinić, M. *Chem. Commun.*, **2002**, 2238.
- [155] Bhattacharya, S.; Acharya, S.N. *Chem. Mater.*, **1999**, *11*, 3121.
- [156] Suzuki, M.; Yumoto, M.; Kimura, M.; Shirai, H.; Hanabusa, K. *Chem. Eur. J.*, **2003**, *9*, 348.

- [157] Luo, X.; Liu, B.; Liang, Y. *Chem. Commun.*, **2001**, 1556.
- [158] Willemen, H.M.; Vermonden, T.; Marcelis, A.T.M.; Sudhölter, E.J.R. *Eur. J. Org. Chem.*, **2001**, 2329.
- [159] Makarević, J.; Jokić, M.; Perić, B.; Tomišić, V.; Kojić-Prodić, B.; Žinić, M. *Chem. Eur. J.*, **2001**, 7, 3328
- [160] Hanabusa, K.; Tange, J.; Taguchi, Y.; Koyama, T.; Shirai, H. *J. Chem. Soc., Chem. Commun.*, **1993**, 390.
- [161] Jokić, M.; Makarević, J.; Žinić, M. *J. Chem. Soc., Chem. Commun.*, **1995**, 1723.
- [162] Bhattacharyya, S.; Krishna-Ghosh, Y. *Chem. Commun.*, **2001**, 185.
- [163] *The Hydrophobic Effect: Formation of Micelles and Biological Membranes*, C. Tanford, Ed., New York: Wiley, **1980**.
- [164] Ragunathan, K.G.; Bhattacharya, S. *Chem. Phys. Lipids*, **1995**, 77, 13.
- [165] Selinger, J.V.; Spector, M.S.; Schnur, J.M. *J. Phys. Chem. B*, **2001**, 105, 7157.
- [166] Spector, M.S.; Selinger, J.V.; Schnur, J.M. In *Materials-Chirality (Topics in Stereochemistry, vol 24)*, M.M. Green, R.J.M. Nolte and E.W. Meijer, Eds., Hoboken: Wiley & Sons, **2003**, pp. 281–372, and refs cited therein.
- [167] Helfrich, W.; Prost, J. *Phys. Rev. Lett.*, **1993**, 71, 4091.
- [168] John, G.; Masuda, M.; Okada, Y.; Yase, K.; Shimizu, T. *Adv. Mater.*, **2001**, 13, 715.
- [169] Shimizu, T.; Masuda, M. *J. Am. Chem. Soc.*, **1997**, 119, 2812.
- [170] Ji, Q.; Iwaura, R.; Kogiso, M.; Jung, J.H.; Yoshida, K.; Shimizu, T. *Chem. Mater.*, **2004**, 16, 250.
- [171] Jung, J.H.; Lee, S.H.; Yoo, J.S.; Yoshida, K.; Shimizu, T.; Shinkai, S. *Chem. Eur. J.*, **2003**, 9, 5307.
- [172] Suzuki, M.; Nigawara, T.; Yumoto, M.; Kimura, M.; Shirai, H.; Hanabusa, K. *Org. Biomol. Chem.*, **2003**, 1, 4124.
- [173] Suzuki, M.; Nakajima, Y.; Yumoto, M.; Kimura, M.; Shirai, H.; Hanabusa, K. *Langmuir*, **2003**, 19, 8622.
- [174] Frkanec, L.; Jokić, M.; Makarević, J.; Wolsperger, K.; Žinić, M. *J. Am. Chem. Soc.*, **2002**, 124, 9716.
- [175] Vassilev, V.P.; Simanek, E.E.; Wood, M.R.; Wong, C.-H. *Chem. Commun.*, **1998**, 1865.
- [176] Ihara, H.; Hachisako, H.; Hirayama, C.; Yamada, K. *J. Chem. Soc., Chem. Commun.*, **1992**, 1244.
- [177] Takafuji, M.; Ihara, H.; Hirayama, C.; Hachisako, H.; Yamada, K. *Liq. Crystals*, **1995**, 18, 97.
- [178] Liu, X.Y.; Sawant, P.D. *Appl. Phys. Lett.*, **2001**, 79, 3518.
- [179] Nakashima, T.; Kimizuka, N. *Adv. Mater.* **2002**, 14, 1113.
- [180] Ihara, H.; Yoshitake, M.; Takafuji, M.; Yamada, T.; Sagawa, T.; Hirayama, C. *Liq. Crystals*, **1999**, 26, 1021.
- [181] Ihara, H.; Takafuji, M.; Hirayama, C.; O'Brien, D.F. *Langmuir*, **1992**, 8, 1548.
- [182] Kunitake, T.; Nakashima, N.; Kunitake, M. *Macromolecules*, **1989**, 22, 3544.
- [183] Kimizuka, N.; Shimizu, M.; Fujikawa, S.; Fujimura, K.; Sano, M.; Kunitake, T. *Chem. Lett.*, **1998**, 967.
- [184] Arimura, T.; Shibata, M.; Ihara, H.; Hirayama, C. *Analyt. Sci.*, **1993**, 9, 401.
- [185] Ihara, H.; Shudo, K.; Hirayama, C.; Hachisako, H.; Yamada, K. *Liq. Crystals*, **1996**, 20, 807.
- [186] Ihara, H.; Sakurai, T.; Yamada, T.; Hashimoto, T.; Takafuji, M.; Sagawa, T.; Hachisako, H. *Langmuir*, **2002**, 18, 7120.
- [187] Sagawa, T.; Fukugawa, S.; Yamada, T.; Ihara, H. *Langmuir*, **2002**, 18, 7223.

- [188] Hachisako, H.; Ihara, H.; Kamiya, T.; Hirayama, C.; Yamada, K. *Chem. Commun.*, **1997**, 19.
- [189] Herz, A.H. *Adv. Colloid Interface Sci.*, **1977**, 8, 237.
- [190] Niece, K.L.; Hartgerink, J.D.; Donners, J.J. J.M.; Stupp, S.I. *J. Am. Chem. Soc.*, **2003**, 125, 7146.
- [191] Malik, S.; Maji, S.K.; Banerjee, A.; Nandi, A.K. *J. Chem. Soc., Perkin Trans. 2*, **2002**, 1177.
- [192] Hanabusa, K.; Matsumoto, M.; Kimura, M.; Kakehi, A.; Shirai, H. *J. Colloid Interface Sci.*, **2000**, 224, 231.
- [193] Danda, H.; Nishikawa, H.; Otaka, K. *J. Org. Chem.*, **1991**, 56, 6740.
- [194] Hanabusa, K.; Matsumoto, Y.; Miki, T.; Koyama, T.; Shirai, H. *J. Chem. Soc., Chem. Commun.*, **1994**, 1401.
- [195] Sato, T.; Seko, M.; Takasawa, R.; Yoshikawa, I.; Araki, K. *J. Mater. Chem.*, **2001**, 11, 3018.
- [196] Yun, Y.J.; Park, S.M.; Kim, B.H. *Chem. Commun.*, **2003**, 254.
- [197] Chakraborty, T.K.; Jayaprakash, S.; Srinivasu, P.; Madhavendra, S.S.; Sankar, A.R.; Kunwar, A.C. *Tetrahedron*, **2002**, 58, 2853.
- [198] Giorgi, T.; Grepioni, F.; Manet, I.; Mariani, P.; Masiero, S.; Mezzina, M.; Pieraccini, S.; Saturni, L.; Spada, G.P.; Gottarelli, G. *Chem. Eur. J.*, **2002**, 9, 2143.
- [199] Schlenk Jr, W. *Ann.*, **1949**, 565, 204.
- [200] Schiessler, R.W.; Flitter, D. *J. Am. Chem. Soc.*, **1952**, 74, 1720.
- [201] Smith, A.E. *J. Chem. Phys.*, **1950**, 18, 150.
- [202] Angla, B. *Compt. Rend.*, **1947**, 224, 402.
- [203] Angla, B. *Ann. Chim.*, **1949**, 4, 639.
- [204] Zafar, A.; Geib, S.J.; Hamuro, Y.; Hamilton, A.D. *New J. Chem.*, **1998**, 137.
- [205] Zafar, A.; Geib, S.J.; Hamuro, Y.; Carr, A.J.; Hamilton, A.D. *Tetrahedron*, **2000**, 56, 8419.
- [206] Lauher, J.W.; Chang, Y.-L.; Fowler, F.W., *Mol. Cryst. Liq. Cryst.*, **1992**, 211, 99.
- [207] Zhao, X.; Chang, Y.-L.; Fowler, F.W.; Lauher, J.W. *J. Am. Chem. Soc.*, **1990**, 112, 6627.
- [208] Chang, Y.-L.; West, M.-A.; Fowler, F.W.; Lauher, J.W. *J. Am. Chem. Soc.*, **1993**, 115, 5991.
- [209] Hoppe, U. *Ger. Offen.*, 2 143 671 **1973**. *CA*, **1973**, 78, P147616z.
- [210] Niki, R.; Motoshima, H.; Tsukasaki, F.; Ito, T. *Animal Sci. J.*, **2000**, 71, J347.
- [211] Kaminishi, Y.; Kunitomo, M.; Miki, H.; Nishimoto, J.-I. *Fisheries Sci.*, **1998**, 64, 776.
- [212] Katsuta, K.; Hatakeyama, M.; Hiraki, J. *Food Hydrocolloids*, **1997**, 11, 367.
- [213] Xiong, Y.L.; Kinsella, J.E. *Food Hydrocolloids*, **1990**, 4, 245.
- [214] Katsuta, K.; Kinsella, J.E. *Agri. Biol. Chem.*, **1990**, 54, 2423.
- [215] Kella, N.K. D. *Int.J. Biol. Macromol.*, **1987**, 9, 238.
- [216] McKenzie, H.A.; Smith, M.B.; Wake, R.G. *Biochim. Biophys. Acta*, **1963**, 69, 222.
- [217] Frensdorf, H.K.; Watson, M.T.; Kauzmann, W. *J. Am. Chem. Soc.*, **1953**, 75, 5157.
- [218] Poillon, W.N. *Biochem.*, **1980**, 19, 3194.
- [219] Estroff, L.A.; Hamilton, A.D. *Angew. Chem. Int. Ed.*, **2000**, 39, 3447.
- [220] Wang, G.; Hamilton, A.D. *Chem. Commun.*, **2003**, 310.
- [221] Wang, G.; Hamilton, A.D. *Chem. Eur. J.*, **2002**, 8, 1954.
- [222] (a) George, M.; Weiss, R.G. *Langmuir*, **2003**, 19, 1017. (b) George, M.; Tan, G.; John, V.T.; Weiss, R.G. *Chem. Euro. J.* **2005**, 11, 3243.
- [223] Hanabusa, K.; Shimura, K.; Hirose, K.; Kimura, M.; Shirai, H. *Chem. Lett.*, **1996**, 885.
- [224] Brinksman, J.; Feringa, B.L.; Kellogg, R.M.; Vreeker, R.; van Esch, J. *Langmuir*, **2000**, 16, 9249.

- [225] de Loos, M.; van Esch, J.; Kellogg, R.M.; Feringa, B.L. *Angew. Chem. Int. Ed.*, **2001**, *40*, 613.
- [226] van Esch, J.; Schoonbeek, F.; de Loos, M.; Kooijman, H.; Spek, A.L.; Kellogg, R.M.; Feringa, B.L. *Chem. Eur. J.*, **1999**, *5*, 937.
- [227] Potluri, V.K.; Hamilton, A.D. *J. Supramol. Chem.*, **2002**, *2*, 321.
- [228] Carr, A.J.; Melendez, R.; Geib, S.J.; Hamilton, A.D. *Tetrahedron Lett.*, **1998**, *39*, 7447.
- [229] van Esch, J.; Kellogg, R.M.; Feringa, B.L. *Tetrahedron Lett.*, **1997**, *38*, 281.
- [230] Beginn, U.; Tartsch, B. *Chem. Commun.*, **2001**, 1924.
- [231] Schoonbeek, F.S.; van Esch, J.; Hulst, R.; Kellogg, R.M.; Feringa, B.L. *Chem. Eur. J.*, **2000**, *6*, 2633.
- [232] van Esch, J.; Feyter, S.D.; Kellogg, R.M.; Schryver, F.D.; Feringa, B.L. *Chem. Eur. J.*, **1997**, *3*, 1238.
- [233] van der Laan, S.; Feringa, B.L.; Kellogg, R.M.; van Esch, J. *Langmuir*, **2002**, *18*, 7136.
- [234] Heesemann, J. *J. Am. Chem. Soc.*, **1980**, *102*, 2167.
- [235] Kunitake, T. *Angew. Chem., Int. Ed.*, **1992**, *31*, 709.
- [236] Song, X.; Perlstein, J.; Whitten, D.G. *J. Am. Chem. Soc.*, **1997**, *119*, 9144.
- [237] Kasha, M.; Rawls, H.R.; El-Bayoumi, M. *Pure Appl. Chem.*, **1965**, *11*, 371.
- [238] Kölbel, M.; Menger, F.M. *Adv. Mater.*, **2001**, *13*, 1115.
- [239] Kölbel, M.; Menger, F.M. *Langmuir*, **2001**, *17*, 4490.
- [240] de Loos, M.; Ligtenbarg, A.G.J.; van Esch, J.; Kooijman, H.; Spek, A.L.; Hage, R.; Kellogg, R.M.; Feringa, B.L. *Eur. J. Org. Chem.*, **2000**, 3675.
- [241] Tamaru, S.-i.; Uchino, S.-y.; Takeuchi, M.; Ikeda, M.; Hatano, T.; Shinkai, S. *Tetrahedron Lett.*, **2002**, *43*, 3751.
- [242] Tamaru, S.-i.; Nakamura, M.; Takeuchi, M.; Shinkai, S. *Org. Lett.*, **2001**, *3*, 3631.
- [243] Bhattacharya, S.; Acharya, S.N.G.; Raju, A.R. *Chem. Commun.* **1996**, 2101.
- [244] Hanabusa, K.; Okui, K.; Karaki, K.; Kimura, M.; Shirai, H. *J. Colloid Interface Sci.*, **1997**, *195*, 86.
- [245] Maitra, U.; Potluri, V.K.; Sangeetha, N.M.; Babu, P.; Raju, A.R. *Tetrahedron: Asymmetry*, **2001**, *12*, 477.
- [246] Terech, P.; Coutin, A.; Giroud-Godquin, A.M. *J. Phys. Chem. B*, **1997**, *101*, 6810.
- [247] Terech, P. In *Wiley Polymer Network Group Review Series, Vol. 1* (Chemical and Physical Networks), K. te Nijenhuis and W. Mijs, Eds., Sussex, UK: John Wiley & Sons, Inc., **1998**, p. 147.
- [248] Mamiya, J.-i.; Kanie, K.; Hiyama, T.; Ikeda, T.; Kato, T. *Chem. Commun.*, **2002**, 1870.
- [249] Snijder, C.S.; de Jong, J.C.; Meetsma, A.; van Bolhuis, F.; Feringa, B.L. *Chem. Eur. J.*, **1995**, *1*, 594.
- [250] Placin, F.; Clavier, G.; Najera, F.; Desvergne, J.P.; Pozzo, J.L. *Polycycl. Aromatic Compds.*, **2000**, *19*, 107.
- [251] Pozzo, J.-L.; Clavier, G.M.; Desvergne, J.-P. *J. Mater. Chem.*, **1998**, *8*, 2575.
- [252] Babu, P.; Sangeetha, N.M.; Vijayakumar, P.; Maitra, U.; Rissanen, K.; Raju, A.R. *Chem. Eur. J.*, **2003**, *9*, 1922.
- [253] Hosoda, A.; Miyake, Y.; Nomura, E.; Taniguchi, H. *Chem. Letters*, **2003**, *32*, 1042.
- [254] Hartgerink, J.D.; Beniash, E.; Stupp, S.I. *Proced. Natl. Acad. Sci., USA*, **2002**, *99*, 5133.
- [255] Menger, F.M.; Yamasaki, Y.; Catlin, K.K.; Nishimi, T. *Angew. Chem. Int. Ed.*, **1995**, *34*, 585.
- [256] Lyon, R.P.; Atkins, W.M. *J. Am. Chem. Soc.*, **2001**, *123*, 4408.

- [257] Aggeli, A.; Bell, M.; Boden, N.; Keen, J.N.; McLeish, T.C.B.; Nyrkova, I.; Radford, S.E.; Semenov, A. *J. Mater. Chem.*, **1997**, *7*, 1135.
- [258] Aggelli, A.; Bell, M.; Boden, N.; Keen, J.N.; Knowles, P.F.; McLeish, T.C.B.; Pitkeathly, M.; Radford, S.E. *Nature*, **1997**, *386*, 259.
- [259] Coleman, D.L.; Blout, E.R. *J. Am. Chem. Soc.*, **1968**, *90*, 2405.
- [260] Otnad, M.; Otnad, C.; Hartter, P.; Jung, G. In *Glutathione: Proceedings of the 16th Conference of the German Society of Biological Chemistry*, L. Flohe, H. Benohr, H. Ch., Sies, H.D. Waller and A. Wendel, Eds., Stuttgart: Georg Thieme Verlag, **1973**, p. 20.
- [261] Loiseau, J.; Lescanne, M.; Colin, A.; Fages, F.; Verlhac, J.-B.; Vincent, J.-M. *Tetrahedron*, **2002**, *58*, 4049.
- [262] Liu, P.; Shirota, Y.; Osada, Y. *Polym. Adv. Technol.*, **2000**, *11*, 512.
- [263] George, M.; Snyder, S.L.; Terech, P.; Glinka, C. J.; Weiss, R.G. *J. Am. Chem. Soc.*, **2003**, *125*, 10275.
- [264] Zhan, C.; Wang, J.; Yuan, J.; Gong, H.; Liu, Y.; Liu, M. *Langmuir*, **2003**, *19*, 9440.
- [265] Pasteur, L. "Two lectures delivered before the Soci t  Chimique de France, Jan. 20 and Feb. 03", 1860. [265a,b] (a) *The Foundation of Stereochemistry*, G.M. Richardson, Ed., New York: American Book Co., **1901**. (b) *Selected Papers on Natural Optical Activity*, A. Lakhtakia, Ed.; SPIE Milestone Series Volume MS 15 **1990**, p. 45.
- [266] Kuckling, D.; Vo, C.D.; Wohlrab, S.E. *Langmuir*, **2002**, *18*, 4263.
- [267] Li, J.; Cui, W.J.; Wang, L.; Yang, Y.J. *Ch. J. Org. Chem.*, **2002**, *22*, 651.
- [268] Wegner, G. *Z. Naturforsch.*, **1969**, *24*, 824. Wegner, G. *Makromol. Chem.* **1971**, *145*, 85.
- [269] Wegner, G. *Makromol. Chem.*, **1971**, *145*, 85.
- [270] Zuilhof, H.; Barentsen, H.M.; van Dijk, M.; Sudh lter, E.J.R.; Hoofman, R.J.O.M.; Siebbeles, L.D.A.; de Haas, M.P.; Warman, J.M. In *Supramolecular Photosensitive and Electroactive Materials*, Nalwa, H.S., Ed., New York: Academic Press, **2001**, Chapter 4.
- [271] Polydiacetylenes; Bloor, D.; Chance, R.R., Eds.; *NATO ASI Series E, Applied Sciences*, Dordrecht: Martinus Nijhoff, **1985**.
- [272] H.-J. Cantow, Ed., *Advances in Polymer Science*, New York: Springer-Verlag, **1984**, *63*.
- [273] Spector, M.S.; Price, R.R.; Schnur, J.M. *Adv. Mater.*, **1999**, *11*, 337.
- [274] Patel, G.N. *Polymer Prep., Am. Chem. Soc. Div. Polym. Chem.*, **1978**, *19*, 154.
- [275] Tripathy, S.K.; Kim, W.H.; Masse, C.; Jiang, X.L.; Kumar, J. *Nonlinear Opt.*, **1996**, *15*, 111.
- [276] Chance, R.R.; Patel, G.N.; Witt, J.D. *J. Chem. Phys.*, **1979**, *71*, 206.
- [277] Rubner, M.F.; Sandman, D.J.; Velazquez, C. *Macromolecules*, **1987**, *20*, 1296.
- [278] Wenzel, M.; Atkinson, G.H. *J. Am. Chem. Soc.*, **1989**, *111*, 6123.
- [279] Mino, N.; Tamura, H.; Ogawa, K. *Langmuir*, **1992**, *8*, 594.
- [280] Chance, R.R. *Macromolecules*, **1980**, *13*, 396.
- [281] Nava, A.D.; Thakur, M.; Tonelli, A.E. *Macromolecules*, **1990**, *23*, 3055.
- [282] Markowitz, M.A.; Singh, A.; Chang, E.L. *Biochem. Biophys. Res. Commun.*, **1994**, *203*, 296.
- [283] Rhodes, D.G.; Singh, A. *Chem. Phys. Lipids*, **1991**, *59*, 215.
- [284] Tamaoki, M.; Shimada, S.; Okada, Y.; Belaissaoui, A.; Kruk, G.; Yase, K.; Matsuda, H. *Langmuir*, **2000**, *16*, 7545.
- [285] Masuda, M.; Hanada, T.; Yase, K.; Shimizu, T. *Macromolecules*, **1998**, *31*, 9403.

- [286] Masuda, M.; Hanada, T.; Okada, Y.; Yase, K.; Shimizu, T. *Macromolecules*, **2000**, *33*, 9233.
- [287] Xu, X.; Ayyagari, M.; Tata, M.; John, V.T.; McPherson, G.L. *J. Phys. Chem.*, **1993**, *97*, 11350.
- [288] Tata, M.; John, V.T.; Waguespack, Y.Y.; McPherson, G.L. *J. Phys. Chem.*, **1994**, *98*, 3809.
- [289] Tata, M.; John, V.T.; Waguespack, Y.Y.; McPherson, G.L. *J. Am. Chem. Soc.*, **1994**, *116*, 9464.
- [290] Tata, M.; John, V.T.; Waguespack, Y.Y.; McPherson, G.L. *J. Mol. Liquids*, **1997**, *72*, 121.
- [291] Waguespack, Y.Y.; Banerjee, S.; Ramannair, P.; Irvin, G.C.; John, V.T.; McPherson, G.L. *Langmuir*, **2000**, *16*, 3036.
- [292] Li, S.; John, V.T.; Irvin, G.C.; Rachakonda, S.H.; McPherson, G.L.; O'Connor, C.J. *J. Appl. Phys.*, **1999**, *85*, 5965.
- [293] Simmons, B.; Li, S.; John, V.T.; McPherson, G.L.; Taylor, C.; Schwartz, D.K.; Maskos, K. *Nano Lett.*, **2002**, *2*, 1037.
- [294] Simmons, B.A.; Taylor, C.E.; Landis, F.A.; John, V.T.; McPherson, G.L.; Schwartz, D.K.; Moore, R. *J. Am. Chem. Soc.*, **2001**, *123*, 2414.
- [295] Lehn, J.-M. *Angew. Chem. Int. Ed.*, **1990**, *29*, 1304.
- [296] F. Vögtle, Ed., *Supramolecular Chemistry*, Chichester: Wiley, **1991**.
- [297] Gulik-Krzywicki, T.; Fouquey, C.; Lehn, J.-M. *Proc. Natl. Acad. Sci. USA*, **1993**, *90*, 163.
- [298] Hanabusa, K.; Miki, T.; Taguchi, Y.; Koyama, T.; Shirai, H. *J. Chem. Soc., Chem. Commun.*, **1993**, 1382.
- [299] Lehn, J.-M.; Mascal, M.; DeCian, A.; Fisher, J. *J. Chem. Soc., Chem. Commun.*, **1990**, 479.
- [300] Pilpel, N. *Chem. Rev.*, **1963**, *63*, 221.
- [301] Fukasawa, J-I; Tsutsumi, H.J. *Colloid Interface Sci.*, **1991**, *143(1)*, 69.
- [302] Taylor, R.S.; Funkhouser, G.P. *US Patent 6 511 944 B2*, **2003**.
- [303] Kim, V.; Bazhenov, A.V.; Kienskaya, K.I. *Colloid J.*, **1997**, *59*, 455.
- [304] Partridge, K.S.; Smith, D.K.; Dykes, G.M.; McGrail, P.T. *Chem. Commun.*, **2001**, 319.
- [305] Hirst, A.R.; Smith, D.K.; Feiters, M.C.; Geurts, H.P.M.; Wright, A.C. *J. Am. Chem. Soc.*, **2003**, *125*, 9010.
- [306] Inoue, K.; Ono, Y.; Kanekiyo, Y.; Ishi-i, T.; Yoshihara, K.; Shinkai, S. *J. Org. Chem.*, **1999**, *64*, 2933.
- [307] Maitra, U.; Kumar, P.V.; Chandra, N.; D'Souza, L.J.; Prasanna, M.D.; Raju, A.R. *Chem. Commun.*, **1999**, 595.
- [308] Nakano, K.; Hishikawa, Y.; Sada, K.; Miyata, M.; Hanabusa, K. *Chem. Lett.*, **2000**, 1170.
- [309] Willemen, H.M.; Vermonden, T.; Marcelis, T.M.; Sudhölter, E.J. R. *Langmuir*, **2002**, *18*, 7106.
- [310] Lequeux, F.; Candau, S.J. In *Theoretical Challenges in the Dynamics of Complex Fluids*, T. McLeish, Ed., NATO ASI Series, Series E, 339; Dordrecht, The Netherlands: Kluwer Academic, **1997**, p. 181.
- [311] Liu, X.Y.; Sawant, P.D. *Angew. Chem. Int. Ed.*, **2002**, *41*, 3641.
- [312] Ballabh, A.; Trivedi, D.R.; Dastidar, P. *Chem. Mater.*, **2003**, *15*, 2136.
- [313] Gloor, W.E.; Spurlin, H.M. *J. Am. Chem. Soc.*, **1936**, *58*, 854.
- [314] For a review on colloidal phase transitions, see: Anderson, V.J.; Lekkerkerker, H.N. W. *Nature*, **2002**, *416*, 811.

- [315] Hermans, P.H. Gels. In *Colloid Science*, H.R. Kruyt, Ed., Amsterdam: Elsevier, **1949**, 2.
- [316] Haas, W.; Zrinyi, M.; Kilian, H.G.; Heise, B. *Colloid Polym. Sci.*, **1993**, 271, 1024.
- [317] Philipse, A.P.; Wierenga, A.M. *Langmuir*, **1998**, 14, 49.
- [318] Marzán, L.L.; Philipse, A.P. *Colloids Surf. A: Physicochem. Eng. Aspects*, **1994**, 90, 95.
- [319] Wierenga, A.M.; Philipse, A.P.; Lekkerkerker, H.N.W.; Boger, D.V. *Langmuir*, **1998**, 14, 55.
- [320] van Bruggen, M.P.B.; Lekkerkerker, H.N. W. *Langmuir*, **2002**, 18, 7141.
- [321] Terech, P.; Chachaty, C.; Gaillard, J.; Godquin-Giroud, A.M. *J. Phys. Fr.*, **1987**, 48, 663.
- [322] Terech, P.; Schaffhauser, V.; Maldivi, P.; Guenet, J.M. *Langmuir*, **1992**, 8, 2104.
- [323] Terech, P.; Schaffhauser, V.; Maldivi, P.; Guenet, J.M. *Europhys. Lett.*, **1992**, 17, 515.
- [324] Terech, P.; Gebel, G.; Ramasseul, R., *Langmuir*, **1996**, 12, 4321.
- [325] Terech, P.; Scherer, C.; Demé, B.; Ramasseul, R. *Langmuir*, **2003**, 19, 10641.
- [326] Terech, P.; Scherer, C.; Lindner, P.; Ramasseul, R. *Langmuir*, **2003**, 19, 10648.
- [327] Bachman, R.E.; Bodolosky-Bettis, S.A.; Glennon, S.C.; Sirchio, S.A. *J. Am. Chem. Soc.*, **2000**, 122, 7146.
- [328] Sakamoto, K.; Yoshida, R.; Hatano, M. *Chem. Lett.*, **1976**, 1401.
- [329] Sakamoto, K.; Yoshida, R.; Hatano, M.; Tachibana, T. *J. Am. Chem. Soc.*, **1978**, 100, 6898.
- [330] Christiansen, C. *Justus Liebigs Ann. Chem.*, **1884**, 23, 289.
- [331] Campbell, J.; Kuzma, M.; Labes, M.M. *Mol. Cryst. Liq. Cryst.*, **1983**, 95, 45.
- [332] Hoppe, U. *J. Soc. Cosmetic Chem.* **1973**, 24, 317.
- [333] Urayama, K.; Okuno, Y.; Kawamura, T.; Kohjiya, S. *Macromolecules* **2002**, 35, 4567.
- [334] Kelly, S.M. *Liq. Cryst.*, **1998**, 24, 71.
- [335] Kato, T.; Kutsuna, T.; Hanabusa, K.; Ukon, M. *Adv. Mater.*, **1998**, 10, 606.
- [336] Kato, T.; Kondo, G.; Hanabusa, K. *Chem. Lett.*, **1998**, 193.
- [337] Kato, T.; Kutsuna, T.; Hanabusa, K.; *Mol. Cryst. Liq. Cryst.*, **1999**, 332, 377.
- [338] Mizoshita, N.; Kutsuna, T.; Hanabusa, K.; Kato, T. *Proc. SPIE*, **2000**, 4107, 108.
- [339] Kato, T.; Mizoshita, N.; Kutsuna, T.; Kondo, G. *Macromol. Symp.*, **2000**, 154, 15.
- [340] Mizoshita, N.; Hanabusa, K.; Kato, T. *Adv. Mater.*, **1999**, 11, 392.
- [341] Mizoshita, N.; Kutsuna, T.; Hanabusa, K.; Kato, T. *J. Photopolym. Sci. Technol.*, **2000**, 13, 307.
- [342] Mizoshita, N.; Hanabusa, K.; Kato, T. *Displays*, **2001**, 22, 33.
- [343] Hanabusa, K.; Tanaka, R.; Suzuki, M.; Kimura, M.; Shirai, H. *Adv. Mater.*, **1997**, 9, 1095.
- [344] Yabuuchi, K.; Rowan, A.E.; Nolte, R. J.M.; Kato, T. *Chem. Mater.*, **2000**, 12, 440.
- [345] Mizoshita, N.; Kutsuna, T.; Hanabusa, K.; Kato, T. *Chem. Commun.*, **1999**, 781.
- [346] The nematic liquid crystal employed was BL006 (EM Science), a mixture of cyanobiphenyl compounds.
- [347] Guan, L.; Zhao, Y. *J. Mater. Chem.*, **2001**, 11, 1339.
- [348] Guan, L.; Zhao, Y. *Chem. Mater.*, **2000**, 12, 3667.
- [349] Mizoshita, N.; Monobe, H.; Inoue, M.; Ukon, M.; Watanabe, T.; Shimizu, Y.; Hanabusa, K.; Kato, T. *Chem. Commun.*, **2002**, 428.
- [350] Tong, X.; Zhao, Y. *J. Mater. Chem.*, **2003**, 13, 1491.
- [351] Zhao, Y.; Tong, X. *Adv. Mater.*, **2003**, 15, 1431.
- [352] Hoerr, C.W.; Harwood, H.J.; Ralston, A.W. *J. Org. Chem.*, **1944**, 9, 201.
- [353] Leibnitz von, E.; Hager, W.; Gipp, S.; Bornemann, P. *J. Prakt. Chem.*, **1959**, 9, 217.
- [354] Lallau, J.-P.; Masson, J.; Guerin, H. *Bull. Soc. Chim. Fr.*, **1972**, 3111.

- [355] Nakamura, N.; Okada, M.; Okada, Y.; Suita, K. *Mol. Cryst. Liq. Cryst.*, **1985**, *116*, 181.
- [356] Mathes, R.A. *Inorg. Synth.*, **1950**, *3*, 48.
- [357] Chanon, M.; Metzger, J. *Bull. Soc. Chim. Fr.*, **1968**, 2842.
- [358] Datta, K.; Roussel, C.; Metzger, J. *Bull. Soc. Chim. Fr.*, **1974**, 2135.
- [359] George, M.; Weiss, R.G. *J. Am. Chem. Soc.*, **2001**, *123*, 10393.
- [360] Bannister, W.W.; Pennance, J.R.; Curby, W.A. *U.S. Patent 3 684 733*, (Aug. 15, **1972**).
- [361] Schroeder, D.C. *Chem. Rev.*, **1955**, *55*, 181.
- [362] Williams, A.; Ibrahim, I.T. *J. Am. Chem. Soc.*, **1981**, *103*, 7090.
- [363] Foye, W.E.; Lasala, E.F.; Georgiadis, M.; Meyer, W.L. *J. Pharm. Sci.*, **1965**, *54*, 557.
- [364] Erickson, J.G. *J. Org. Chem.*, **1956**, *21*, 483.
- [365] George, M.; Tan, G.; John, V.T.; Weiss, R.G. *Chem. Eur. J.*, **2005**, *11*, 3243.
- [366] George, M. Weiss, R.G. *Langmuir*, **2003**, *19*, 8168.
- [367] Carretti, E.; Dei, L.; Baglioni, P.; Weiss, R.G. *J. Am. Chem. Soc.*, **2003**, *125*, 5121.
- [368] Carretti, E. *Ph.D. Thesis 2003*, Department of Chemistry and Consortium CSGI, University of Florence, Italy.
- [369] Wang, C.; Robertson, A.; Weiss, R.G. *Langmuir*, **2003**, *19*, 1036.
- [370] Ledward, D.A. In *Functional properties of food macromolecules*, J.R. Mitchell and D.A. Ledward, Eds., London: Elsevier Applied Science, **1986**, pp171–201.
- [371] *The Macromolecular Chemistry of Gelatin*, A. Veis, Ed., New York: Academic, **1964**.
- [372] Joly-Duhamel, C.; Hellio, D.; Djabourov, M. *Langmuir*, **2002**, *18*, 7208.
- [373] Haering, G.; Luisi, P.L. *J. Phys. Chem.*, **1986**, *90*, 5892.
- [374] Atkinson, P.J.; Grimson, M.J.; Heenan, R.K.; Howe, A.M.; Robinson, B.H. *J. Chem. Soc., Chem. Commun.*, **1989**, 1807.
- [375] Atkinson, P.J.; Robinson, B.H.; Howe, A.M.; Heenan, R.K. *J. Chem. Soc. Faraday Trans.*, **1991**, *87*, 3389.
- [376] Scartazzini, R.; Luisi, P.L. *J. Phys. Chem.*, **1988**, *92*, 829.
- [377] Shchipunov, Y.A. *Colloids and Surfaces A: Physiochem. Eng. Aspects*, **2001**, *183–185*, 541.
- [378] Shchipunov, Y.A.; Hoffmann, H. *Langmuir*, **1998**, *14*, 6350.
- [379] Shchipunov, Y.A.; Shumilina, E.V.; Hoffmann, H. *Colloid Polym. Sci.*, **1998**, *276*, 368.
- [380] Shchipunov, Y.A.; Shumilina, E.V.; Ulbricht, W.; Hoffmann, H. *J. Colloid Interface Sci.*, **1999**, *211*, 81.
- [381] Shchipunov, Y.A.; Dürrschmidt, T.; Hoffmann, H. *J. Colloid Interface Sci.*, **1999**, *212*, 390.
- [382] Capitani, D.; Rossi, E.; Segre, A.L. *Langmuir*, **1993**, *9*, 685.
- [383] Capitani, D.; Segre, A.L.; Dreher, F.; Walde, P.; Luisi, P.L. *J. Phys. Chem.*, **1996**, *100*, 15211.
- [384] Cavallaro, G.; Manna, G.L.; Liveri, V.T.; Aliotta, F.; Fontanella, M.E. *J. Colloid Interface Sci.*, **1995**, *176*, 281.
- [385] Shumilina, E.V.; Khromova, Y.L.; Shchipunov, Y.A. *Russ.J. Phys. Chem.*, **2000**, *74*, 1083.
- [386] Shurtenberger, P.; Magid, L.J.; King, S.M.; Linder, P. *J. Phys. Chem.*, **1991**, *95*, 4173.
- [387] Simmons, B.A.; Irvin, G.C.; Agarwal, V.; Bose, A.; John, V.T.; McPherson, G.L.; Balsara, N.P. *Langmuir*, **2002**, *18*, 624.
- [388] Simmons, B.A.; Agarwal, V.; McPherson, G.L.; John, V.T.; Bose, A. *Langmuir*, **2002**, *18*, 8345.

- [389] Aliotta, F.; Fontanella, M.E.; Sacchi, M.; Vasi, C.; LaManna, G.; TurcoLiveri, V. *J. Mol. Struct.*, **1996**, 383, 99.
- [390] Aliotta, F.; Fontanella, M.E.; Galli, G.; Lanza, M.; Migliardo, P.; Salvato, G. *J. Phys. Chem.*, **1993**, 97, 733.
- [391] Shchipunov, Y.A.; Schmiedel, P. *Langmuir*, **1996**, 12, 6443.
- [392] Shchipunov, Y.A.; Dürrschmidt, T.; Hoffmann, H. *Langmuir*, **2000**, 16, 297.
- [393] Anand, B.; Pisal, S.S.; Paradkar, A.R.; Mahadik, K.R. *J. Sci. Ind. Res.*, **2001**, 60, 311.
- [394] Fadnavis, N.W.; Koteswar, K. *Biotechnol. Prog.*, **1999**, 15, 98.
- [395] Schuleit, M.; Luisi, P.L. *Biotechnol. Bioeng.*, **2001**, 72, 250.
- [396] Hedström, G.; Backlund, S.; Eriksson, F. *J. Colloid Interface Sci.*, **2001**, 239, 190.
- [397] Dreher, F.; Walde, P.; Walther, P.; Wehrli, E. *J. Controlled Release*, **1997**, 45, 131.
- [398] Dreher, F.; Walde, P.; Luisi, P.L.; Elsner, P. *Skin Pharmacol.*, **1996**, 9, 124.
- [399] Nastruzzi, C.; Gambari, R. *J. Controlled Release*, **1994**, 29, 53.
- [400] Willmann, H.; Walde, P.; Luisi, P.L.; Gazzaniga, A.; Stroppolo, F. *J. Pharm. Sci.*, **1992**, 81, 871.
- [401] Hinze, W.L.; Isamu, U.; Dai, F.; Braun, J.M. *Curr. Opin. Colloid Interface Sci.*, **1996**, 1, 502.
- [402] Velasco-García, N.; Valencia-González, M.J.; Diaz Garcia, M.E. *Analyst*, **1997**, 122, 1405.
- [403] Choi, M.M. F.; Shuang, S. *Analyst*, **2000**, 125, 301.
- [404] James, T.D.; Murata, K.; Harada, T.; Ueda, K.; Shinkai, S. *Chem. Lett.*, **1994**, 273.
- [405] Kimura, T.; Takeuchi, M.; Shinkai, S. *Bull. Chem. Soc. Jpn.*, **1998**, 71, 2197.
- [406] Kimura, T.; Shinkai, S. *Chem. Lett.*, **1998**, 1035.
- [407] Kimura, T.; Yamashita, T.; Koumoto, K.; Shinkai, S. *Tetrahedron Lett.*, **1999**, 40, 6631.
- [408] Koumoto, K.; Yamashita, T.; Kimura, T.; Luboradzki, R.; Shinkai, S. *Nanotechnol.*, **2001**, 12, 25.
- [409] Liu, Q.; Zhang, S.-W.; Wei, Y.G.; Shao, M.-C. *Acta Crystallogr. C*, **1996**, 52, 2260.
- [410] Jansen, L.H.; *Acta Crystallogr.*, **1962**, 15, 433.
- [411] Pineaut, C.; Brisse, F. *Acta Crystallogr. C*, **1983**, 39, 1434.
- [412] Barton, T.J.; Bull, L.M.; Klemperer, W.G.; Loy, D.A.; McEnaney, B.; Misono, M.; Monson, P. A.; Pez, G.; Scherer, G.W.; Vartuli, J.C.; Yaghi, O.M. *Chem. Mater.*, **1999**, 11, 2633.
- [413] Cooper, A.I.; Wood, C.D.; Holmes, A.B. *Ind. Eng. Chem. Res.*, **2000**, 39, 4741.
- [414] Selvam, P.; Bhatia, S.; Sonwane, C.G. *Ind. Eng. Chem. Res.*, **2001**, 40, 3237.
- [415] Shea, K.J.; Loy, D.A.; *Chem. Mater.*, **2001**, 13, 3306.
- [416] Sawant, P.D.; Liu, X.-Y. *Chem. Mater.*, **2002**, 14, 3793.
- [417] Pierre, A.C.; Pajonk, G.M. *Chem. Rev.*, **2002**, 102, 4243.
- [418] Leventis, N.; Sotiriou-Leventi, C.; Zhang, G.; Rawashdel, A.-M.M. *Nano Lett.*, **2002**, 2, 957.
- [419] Mercurio, D.J.; Spontak, R.J. *J. Phys. Chem. B*, **2001**, 105, 2091.
- [420] Gullapalli, P.; Tsau, J.-S.; Heller, J.P. *Proced. Int. Symp. Oilfield Chem.*, Richardson, Texas: Society of Petroleum Engineers, **1995**, 349.
- [421] Lee, K.-N.; Lee, H.-J.; Lee, J.-Y.; Kim, J.-H. *J. Disp. Sci. Technol.*, **2001**, 22, 79.
- [422] Shi, C.; Huang, Z.; Kilic, S.; Xu, J.; Enrick, R.M.; Beckman, E.J.; Carr, A.J.; Melendez, R.E.; Hamilton, A.D. *Science*, **1999**, 286, 1540.
- [423] Shi, C.; Huang, Z.; Beckman, E.J.; Enrick, R.M.; Kim, S.-Y.; Curran, D.P. *Ind. Eng. Chem. Res.*, **2001**, 40, 908.
- [424] *Ionic Liquids: Industrial Applications to Green Chemistry*, (Am. Chem. Soc. Symp. Ser 818); R.D. Rogers and K.R. Seddon, Eds., Washington, DC: American Chemical Society, **2002**.

- [425] Wasserscheid, P.; Keim, W. *Angew. Chem. Int. Ed.*, **2000**, *39*, 3772.
- [426] Welton, T. *Chem. Rev.*, **1999**, *99*, 2071.
- [427] Yanagida, S.; Kambe, S.; Kubo, W.; Murakoshi, K.; Wada, Y.; Kitamura, A. *Z. Phys. Chem.*, **1999**, *212*, 31.
- [428] Kimizuka, N.; Nakashima, T. *Langmuir*, **2001**, *17*, 6759.
- [429] Ikeda, A.; Sonoda, K.; Ayabe, M.; Tamaru, S.-i.; Nakashima, T.; Kimizuka, N.; Shinkai, S. *Chem. Lett.*, **2001**, 1154.
- [430] Kubo, W.; Murakoshi, K.; Kitamura, T.; Yoshida, S.; Haruki, M.; Hanabusa, K.; Shirai, H.; Wada, Y.; Yanagida, S. *J. Phys. Chem. B*, **2001**, *105*, 12809.
- [431] Kubo, W.; Kitamura, T.; Hanabusa, K.; Wada, Y.; Yanagida, S. *Chem. Commun.*, **2002**, 374.
- [432] Kubo, W.; Kambe, S.; Nakade, S.; Kitamura, T.; Hanabusa, K.; Wada, Y.; Yanagida, S. *J. Phys. Chem. B*, **2003**, *107*, 4374.
- [433] Murai, S.; Mikoshiba, S.; Sumino, H.; Kato, T.; Hayase, S. *Chem. Commun.*, **2003**, 1534.
- [434] Carlin, R.T.; Fuller, J. *Chem. Commun.*, **1997**, 1345.
- [435] Sutto, T.E.; De Long, H.C.; Trulove, P.C. *Z. Naturforsch.*, **2002**, *57a*, 839
- [436] Ieperuma, O.A.; Dissanayake, M.A. K.L.; Somasundaram, S. *Electrochim. Acta*, **2002**, *47*, 2801.
- [437] Fuller, J.; Breda, A.C.; Carlin, R.T. *J. Electroanal. Chem.*, **1998**, *459*, 29.
- [438] Wang, P.; Zakeerruddin, S.M.; Exnar, I.; Grätzel, M. *Chem. Commun.*, **2002**, 2972.
- [439] Noda, A.; Watanabe, W. *Electrochim. Acta*, **2000**, *45*, 1265.
- [440] Wang, P.; Zakeerruddin, S.M.; Comte, P.; Exnar, I.; Grätzel, M. *J. Am. Chem. Soc.*, **2003**, *125*, 1166.
- [441] Stathatos, E.; Lianos, P.; Lavrencic-Stangar, U.; Orel, B. *Adv. Mater.*, **2002**, *14*, 354.
- [442] Stathatos, E.; Lianos, P.; Zakeerruddin, S.M.; Liska, P.; Grätzel, M. *Chem. Mater.*, **2003**, *15*, 1825.
- [443] Firestone, M.A.; Dzielawa, J.A.; Zapol, P.; Curtiss, L.A.; Seifert, S.; Dietz, M.L. *Langmuir*, **2002**, *18*, 7258.
- [444] Ishi-I, T.; Iguchi, R.; Snip, E.; Ikeda, M.; Shinkai, S. *Langmuir*, **2001**, *17*, 5825.
- [445] Shirakawa, M.; Fujita, N.; Shinkai, S. *J. Am. Chem. Soc.*, **2003**, *125*, 9902.
- [446] Oishi, K.; Ishi-I, T.; Sano, M.; Shinkai, S. *Chem. Letters*, **1999**, 1089.
- [447] Schröder, L. *Z. Phys. Chem.*, **1893**, *11*, 449.
- [448] van Laar, J. *Z. Phys. Chem.*, **1908**, *63*, 216.
- [449] Atkins, P.W. *Physical Chemistry*, 5th edition, New York: Freeman, **1994**, p. 227.
- [450] Moore, W.J. *Physical Chemistry*, 4th edition, Englewood Cliffs, NJ: Prentice Hall, **1972**, p. 249.
- [451] Furman, I.; Weiss, R.G. *Langmuir*, **1993**, *9*, 2084.
- [452] Lu, L.; Weiss, R.G. *Langmuir*, **1995**, *11*, 3630.
- [453] Mukkamala, R.; Weiss, R.G. *Langmuir*, **1996**, *12*, 1474.
- [454] Terech, P.; Furman, I.; Weiss, R.G.; Bouas-Laurent, H.; Desvergne, J.P.; Ramasseul, R. *Faraday Discuss.*, **1995**, *101*, 345.
- [455] Terech, P.; Furman, I.; Weiss, R.G. *J. Phys. Chem.*, **1995**, *99*, 9558.
- [456] $\Delta f = \{[(\epsilon - 1)/(2\epsilon + 1)] - [(n^2 - 1)/(2n^2 + 1)]\}$ where ϵ is the dielectric constant and n is the refractive index. [456a](a) Rohatgi-Mukherjee, K. K. *Fundamentals of Photochemistry*, New Delhi, India: Wiley Eastern Limited, **1978**, p. 105.
- [457] Calculated from the Lippert-Mataga equation, $\Delta f = [(\epsilon - 1)/(2\epsilon + 1)] - [(n^2 - 1)/(2n^2 + 1)]$, where ϵ and n for dodecane are 2.01 and 1.4216, respectively, at 20° C. [457a] (a) Dean, J.A. *Lange's Handbook of Chemistry*, New York: McGraw-Hill, 14th edition, **1992**, pp. 1.197 and 5.105).

- [458] Terech, P. *Progr. Colloid Polym. Sci.*, **1990**, *82*, 263.
- [459] Terech, P.; Volino, F.; Ramasseul, R. *J. Physique*, **1985**, *46*, 895–903.
- [460] See Chapter 10 for a detailed description of the application of SANS to analyzing SAFIN networks of gels.
- [461] Glatter, O.; Kratky, O. *Small-Angle X-ray Scattering*, London: Academic Press, **1982**.
- [462] Guinier, A.; Fournet, G. *Small Angle Scattering of X-rays*, New York: Wiley, **1955**.
- [463] Plischke, M.; Vernon, D.C.; Joós, B. *Phys. Rev. E*, **2003**, *67*, 011401.
- [464] Matthews-Morgan, D.; Landau, D.P.; Herrmann, H.J. *Phys. Rev. B*, **1984**, *29*, 6328.
- [465] Guenft, J.-M. *Wiley Polym. Networks Group Rev. Ser.*, **1998**, *1*, 51.
- [466] Hong, P.-D.; Huang, H.-T. *Polym. J.*, **2000**, *32*, 789.
- [467] Ramakrishnan, S.; Prud'homme, R.K. *J. Rheol.*, **2000**, *44*, 885.
- [468] Hong, P.-D.; Chen, J.-H.; Wu, H.-L. *J. Appl. Polym. Sci.*, **1998**, *69*, 2477.
- [469] Itagaki, H.; Nakatani, Y. *Macromolecules*, **1997**, *30*, 7793.
- [470] Nakamura, K.; Kiriya, M.; Takada, A.; Maeda, H.; Nemoto, N. *Rheol. Acta*, **1997**, *36*, 252.
- [471] Dörfler, H.-D.; Knape, M. *Tenside Surf. Det.*, **1993**, *30*, 359.
- [472] Geiger, C.; Stanescu, M.; Chen, L.H.; Whitten, D.G. *Langmuir*, **1999**, *15*, 2241.
- [473] Wang, R.; Geiger, C.; Chen, L.; Swanson, B.; Whitten, D.G. *J. Am. Chem. Soc.*, **2000**, *122*, 2399.
- [474] Weissbuch, I.; Lahav, M.; Leiserowitz, L. *Cryst. Growth Des.*, **2003**, *3*, 125.
- [475] Kuzmenko, I.; Rapaport, H.; Kjaer, K.; Als-Nielsen, J.; Weissbuch, I.; Lahav, M.; Leiserowitz, L. *Chem. Rev.*, **2001**, *101*, 1659.
- [476] Lahav, M.; Leiserowitz, L. *Chem. Eng. Sci.*, **2001**, *56*, 2245.
- [477] Weinbach, Sp.; Kjaer, K.; Bouwman, Wg.; Grubel, G.; Legrand, Jf.; Alsnielsen, J.; Lahav, M.; Leiserowitz, L. *Science*, **1994**, *264*, 1566.
- [478] Lahav, M.; Leiserowitz, L. *J. Phys. D-Appl. Phys.*, **1993**, *26*, B22.
- [479] Huang, X.; Terech, P.; Raghavan, S.R.; Weiss, R.G. *J. Am. Chem. Soc.*, **2005**, *127*, 4336.
- [480] Naota, T.; Koori, H. *J. Am. Chem. Soc.*, **2005**, *127*, 9324.

Chapter 15

DESIGN AND FUNCTION OF LOW MOLECULAR-MASS ORGANIC GELATORS (LMOGs) BEARING STEROID AND SUGAR GROUPS

Norifumi Fujita and Seiji Shinkai

*Department of Chemistry & Biochemistry, Graduate School of Engineering,
Kyushu University, Fukuoka 812-8581, Japan*

1. Introduction	553
2. Steroid Derivatives for Gelating Organic Liquids	554
2.1. Introduction	554
2.2. Structural Variations of Steroid-Based Gelators and their Analyses	554
2.3. Functional Applications of Cholesterol-Based LMOGs	557
2.4. Conclusions	563
3. Sugar Derivatives for Gelating Liquids	564
3.1. Introduction	564
3.2. Structural Variations of Sugar-Based Gelators	564
3.3. Dual-Component Gelators Based on Charge-Transfer Phenomena	567
3.4. Combinatorial Approaches for Finding Gelators and Building Integrated Systems Utilizing a Sugar Library	567
3.5. Conclusions	569
4. Other Related LMOGs	570
4.1. Nucleobase Gelators	570
4.2. Vancomycin Gelator	573
5. Perspectives for the Future	574

1. Introduction

Steroids and sugars are well-known examples of low molecular-mass organic gelators (LMOGs). Although, they have been used and investigated

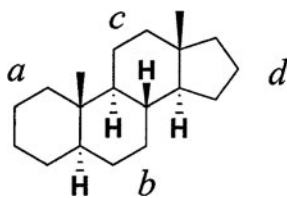


Figure 1. Molecular skeleton of a steroid.

as naturally occurring molecules for many years, the discovery that some are LMOGs was made serendipitously and only a couple of decades ago. Since that time, chemists have designed many LMOGs and have transformed some of their gels into functional materials. The most important objectives of this chapter are: (1) to present the historical development of the above two series of gelators from the standpoint of the relationship between their molecular structures and their aggregate structures in gels and (2) to indicate some of the functions and applications of these gelators that arise, in part, because of the biocompatibility of sugars and steroids.

2. Steroid Derivatives for Gelating Organic Liquids

2.1. Introduction

Steroids are a class of naturally occurring molecules that are lipids. They exist in all plants and animals and play important roles to control biochemical activities associated with life. The molecular structures of steroids are composed of a complicated tetracyclic androstane skeleton (with A, B, C and D rings) which defines the characteristics of steroids. The connective carbon atoms of the fused ring systems generate *cis* or *trans* configurations at each stereocenter. All-*trans* isomers of plural fused rings are most commonly found. They result in somewhat planar and rigid structures. Thus, derivatives of the common steroid, cholesterol, tend to form mesophases in which steroid-steroid stacking, mainly from van der Waals interactions, results in long-range, one-dimensional (1-D), helical structures. 1-D aggregate growth is a prerequisite for the gelation to occur in most known cases.

2.2. Structural Variations of Steroid-Based Gelators and their Analyses

In the early 1960s, some steroidal derivatives (such as deoxycholic, cholic, apocholeic, and lithocholic acids, as well as their salts) were found

to thicken aqueous salt solutions [1a,b]. The first steroid-based LMOG for organic liquids was discovered in 1979 during the course of the synthesis of a D-homosteroidal nitroxide free radical, D-3 β -hydroxy-17,17-dipropyl-17a-azahomoandrostanyl-17a-oxy (**1**) and its amino analogue (**2**) from isoandrosterone derivatives [1c].

Using these molecules and their aggregates, several fundamental technical methods for obtaining structural information about organogels were developed. They include the use of small-angle neutron scattering and appropriate TEM protocols to determine the structures of gel networks *in situ*, the application of strong magnetic fields and shearing stresses to orient or phase separate fibers in a network, the use of complementary techniques (IR, neutron scattering, EPR) to correlate the aggregation features in kinetic experiments at different length scales, and the use of EPR to extract a phase diagram. They provide information for different crystallographic organizations between single crystal, powder, and gel fiber networks, as well as the sensitivity of the gelation behavior to minor chemical structure changes on the steroid organogelator, and the use of CD to extract aggregate information [2].

Later, 1–10 wt. % of dihydrolanosterol (**3**) [3] was found to gelate various oils. In 1987, Weiss *et al.* discovered that anthracene appended cholesterol derivatives (**4** and **5**) [4] can gelate a wide range of organic liquids, from low polarity liquids such as hydrocarbons to polar ones such as alcohols and amines. Moreover, in some cases, less than 1 wt. % of **4** can gelate the liquid. LMOGs capable of creating gels at such low concentrations are now called

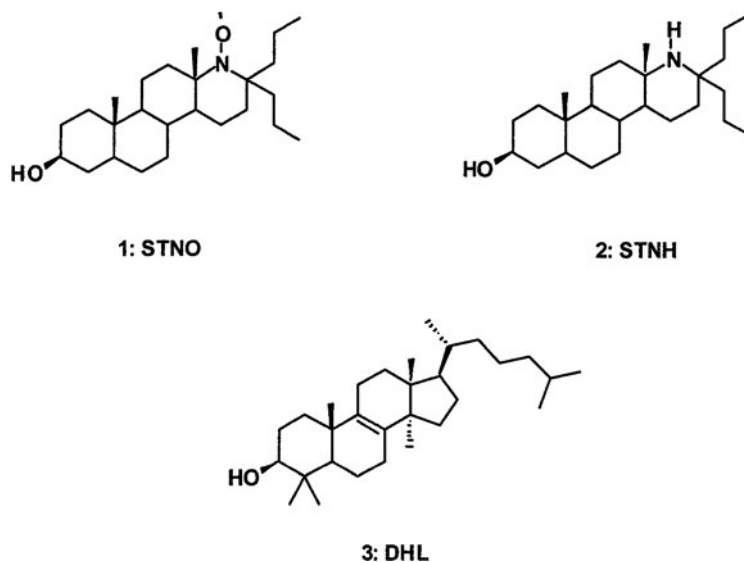


Figure 2. Molecular structures of STNO (**1**), STNH (**2**) and DHL (**3**).

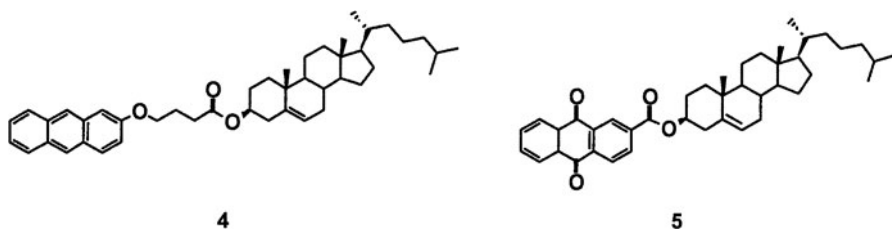


Figure 3. Molecular structures of **4** and **5**.

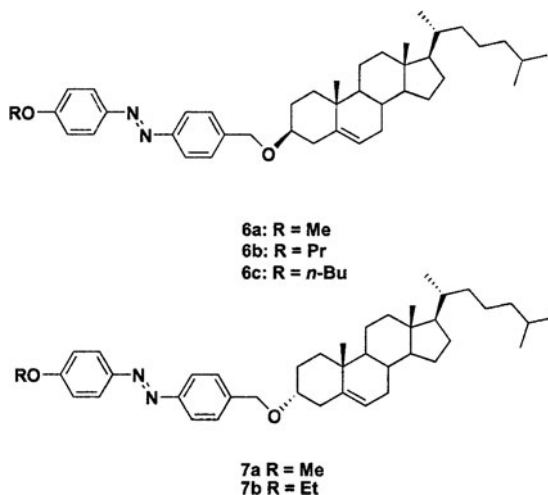


Figure 4. Molecular structures of azobenzene-appended cholesterol: note that **6** and **7** are C-3 epimers.

“supergelators”. After this discovery, a number of structural analogues of **4** and **5** (N.B., anthraquinone-appended cholesterol gelators) were synthesized [5, 6].

Circular dichroism (CD), fluorescence spectroscopy, scanning electron microscopy (SEM), and transmission electron microscopy (TEM) are frequently used to evaluate the nature of 1-D aggregates composed of optically active gelator molecules. On the other hand, the utilization of nuclear magnetic resonance (NMR) spectroscopy is less developed because of the line broadening inevitably occurring in the gel phase. Fluorescence spectroscopic studies on anthracene-containing cholesterol gelators are discussed in detail in Chapter 12 and circular dichroism is the subject of Chapter 13.

The first comprehensive application of CD to evaluate molecular ordering in a cholesteric SAFIN was in 1994 [7]. The authors synthesized nineteen molecules in which an azobenzene moiety is attached at the C-3 position of cholesterol. Reaction between an acid chloride and cholesterol results in

esterification of the latter at the 3-OH group and the products possess the natural (*S*)-configuration at C-3. When Mitsunobu's esterification method is applied, the resultant products possess the non-natural, inverted (*R*)-configuration. Both anomers can gelate many polar and low polarity organic liquids. Interestingly, the seemingly small structural difference at C-3 causes critical differences in the natures of the gel networks. The azobenzene chromophoric group, having an electronic absorption in the visible region, generates convenient CD signals. For instance, the **6a**-1-butanol gel showed a positive exciton coupling band of (*R*)-chirality whereas the **7b**-methanol gel gave a negative exciton coupling band of (*S*)-chirality. These observations mean that the transition dipoles in the azobenzene groups are oriented in a clockwise ((*R*)-chirality) or anticlockwise ((*S*)-chirality) direction, respectively, when they interact. Strangely, **6b** and **6c** gels were found to change the sign of their CD bands depending on the preparation procedures. After careful examination, it was found that inversion occurs when the cooling speed from the sol to the gel is fast. As a result of kinetic influences, a less stable structure is generated preferentially and immobilized in the gel phase. Both the left-handed and right-handed gel networks could be prepared from the same sol solution by slow and fast cooling, respectively, as observed by scanning electron microscopy (SEM).

The influence of the absolute configuration at C-3 of the steroid on the gelation properties was also examined in detail. The *p*-alkoxy-substituted azobenzene-cholesterol derivatives are excellent thermally-reversible LMOGs for various organic liquids. However, it was found that **6a** (with (*S*)-chirality) is a good gelating agent, but the corresponding gelating agent **7a** (with (*R*)-chirality) is not. This chirality influence can be understood by the structural differences between the (*R*)- and the (*S*)-isomers indicated from energy minimization computations. As seen in Figure 5, **6a** adopts an extended linear conformation which enables it to stack efficiently into a 1-D structure, whereas **7a** is in an L-shaped (bent) conformation in which 1-D stack formation is energetically more difficult. This difference may also be partly responsible for why (*S*)-chirality at C-3 of the cholesterol skeleton is much more prevalent in nature.

In summary, it is clear that appending a chromophoric group in different ways to the optically active cholesterol skeleton allows one to obtain detailed information about the modes of molecular aggregation in SAFINs.

2.3. Functional Applications of Cholesterol-Based LMOGs

2.3.1. Fluorescent gels

The fluorescence from cholesterol-based gelators containing an anthracene group were first used as a probe for acquiring information on the local environment of the gelator molecules in their 1-D aggregates [8, 9]. In this case,

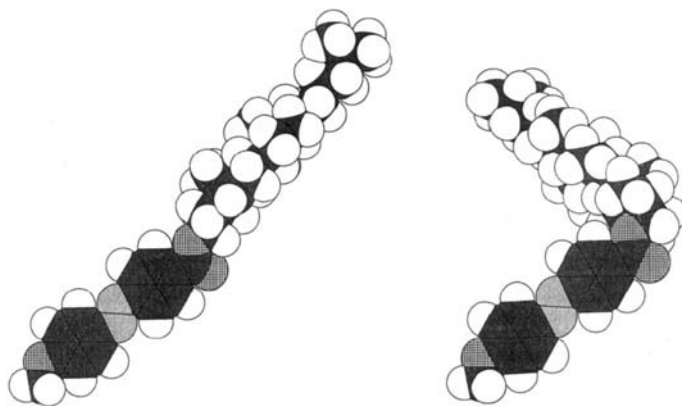


Figure 5. Energy-minimized structures of **6a** (left) and **7a** (right). (Reprinted with permission from [7]. Copyright (1994) American Chemical Society.)

the lowest excitation energy bands are assigned to excitation dipole coupling between the anthryl groups stacked in a face-to-face manner in the molecular aggregates. Furthermore, **4** shows no emission ascribable to an excimer upon irradiation. This means that the geometric arrangements within the gelator networks are inappropriate for **4** to form such species.

A 1,10-phenanthroline-appended cholesterol-based gelator (**8**) emits strong green fluorescence in the gel phase in the presence of protons [10]. In the 1-propanol gel of **8**, the fluorescence at $\lambda_{\max} = 396\text{ nm}$, which is assigned to the emission from neutral **8**, disappears in the presence of only 0.2 equiv of trifluoroacetic acid and is accompanied by the appearance of strong fluorescence at $\lambda_{\max} = 560\text{ nm}$ which is assigned to the emission from $\mathbf{8} \cdot \text{H}^+$. The fluorescence of $\mathbf{8} \cdot \text{H}^+$ becomes particularly intense in the gel phase, presumably because of energy transfer from neutral $\mathbf{8}^*$ to protonated $\mathbf{8} \cdot \text{H}^+$ and restrictions of $\mathbf{8} \cdot \text{H}^+$ molecular motion. The findings demonstrate the feasibility of using gels as new proton-sensitive fluorescence detection systems and as a medium for promoting electronic energy transfer.

In the course of the study, the luminescent properties of cholesterol-appended perylene derivatives (**9**) in their gel and solution phases was investigated [11]. Perylenes are known to be stable to light and to exhibit excellent chemical stability. They have high photoluminescence yields and emit over a wide range of wavelengths in the visible region that can be tuned by choice of substituents into the bay positions (**9b-9d**). Utilizing the 1-D aggregation of gel networks, a “visible” light harvesting system was designed. The gel system is composed of four different perylene-containing gelators, the absorption bands of which cover the width of white light. Excited state energy is transferred from one group to another, eventually ending at the gelator bearing

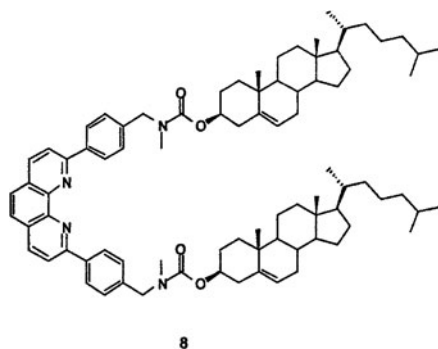


Figure 6. Molecular structure of cholesterol-based 1,10-phenanthroline gelator (**8**). The 2-carbon centers in the alkyl chains are racemic.

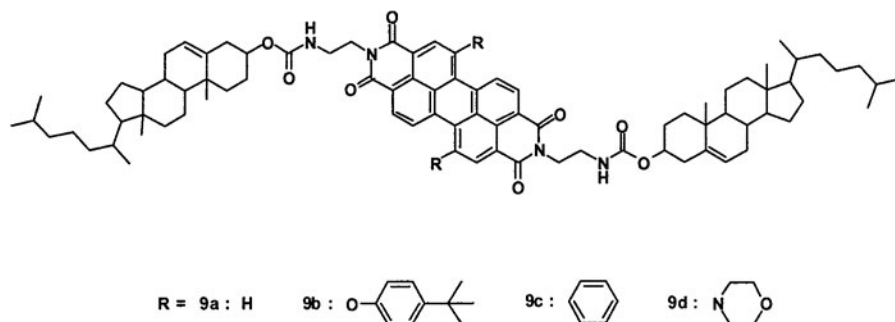


Figure 7. Molecular structure of a cholesterol-based perylene gelator (**9a**) and its energy acceptors (**9b-9d**).

the lowest excited singlet state energy. One can regard this gel system as a sort of “color filter”.

2.3.2. Photo-responsive gels

A more detailed account of photoresponsive gels that includes a broader range of LMOG structures may be found in Chapter 24.

A photoinduced sol-gel phase transition was found when a 1-butanol gel of **6a** was irradiated at 330–380 nm [7]. The absorption maximum at 365 nm (*trans-6a*) gradually disappeared and the proportion of the *cis*-isomer at the photostationary state was estimated to be 38%. As shown in Figure 8, the transmittance of 0.1 wt. % **6a** in 1-butanol is changed reversibly upon alternate UV and visible light irradiation. The photoinduced sol-gel phase transition was also monitored by CD spectroscopy.

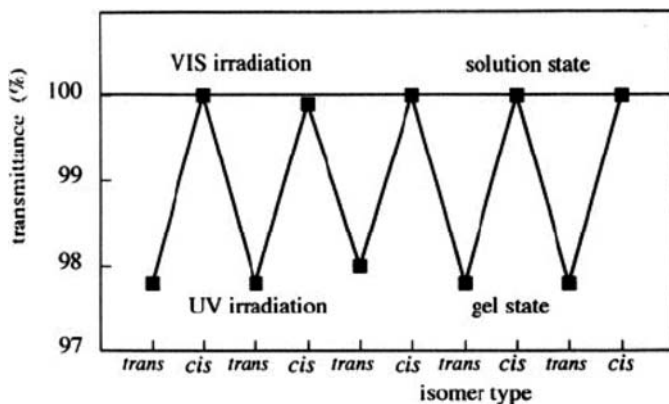


Figure 8. Photocontrol of the sol-gel phase transition for 0.1 wt. % **6a** in 1-butanol measured at 25°C. UV denotes irradiation at 330–380 nm and VIS denotes irradiation at $\lambda > 460$ nm. (Reprinted with permission from [7]. Copyright (1994) American Chemical Society.)

2.3.3. Crown ether-appended cholesterol gelators with chemical responsiveness

As mentioned, most gel networks are based on 1-D assemblies of LMOGs, so that one can expect their stability to be sensitive to complexation by additives which can interact with the gelator molecules. In this approach [12], the gelator molecules should be composed of a gel-induction part (e.g., cholesterol) and a guest-binding part (e.g., a crown ether). The specific effect of the added guest (a diamine in the case to be discussed) on the gelation properties is apparent in cyclohexane and hexane as the liquid components. Although **10** is insoluble or forms a partial gel in cyclohexane and hexane, samples prepared in the presence of ethylenediamine, (*R*)-cyclohexanediamine, or (*S*)-cyclohexanediamine form translucent gels. This phase change is attributed to intermolecular hydrogen-bonding interactions between one diamine and two azacrown rings, and the resultant bridging stabilizes the organogel state. Another interesting feature is the influence of (*R*)-cyclohexanediamine or (*S*)-cyclohexanediamine on the gel-to-sol phase transition temperature (T_g) of the cyclohexanol gels of **10**. The T_g value for (*S*)-cyclohexanediamine is higher than that for (*R*)-cyclohexanediamine in all guest concentration regions. These results indicate that this organogel system can be enantioselectively reinforced by chiral amine additives.

The 24-membered crown-ether ring of the cholesterol-appended benzo-24-crown-8 gelator (**11**) tends to adopt a folded conformation. As noted above, a diamine guest can induce a significant conformational change from a folded to an extended ring conformation that can also trigger a phase transition

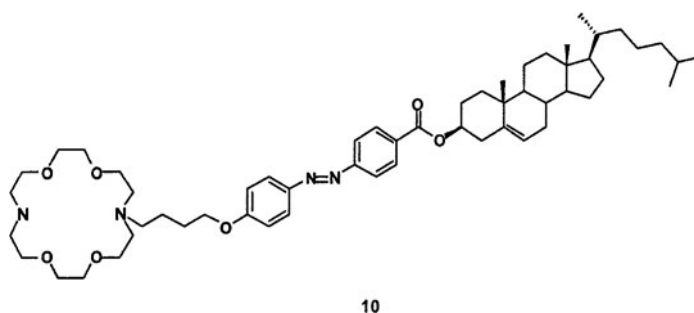


Figure 9. Molecular structure of the cholesterol-based azobenzene gelator **10**.

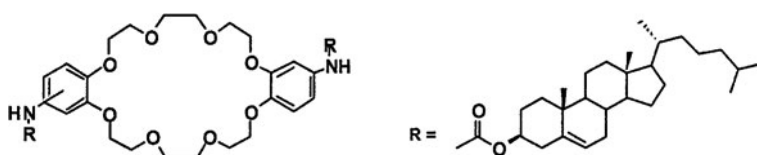


Figure 10. Molecular Structure of **11**.

of the system. In the absence of a diamine, **11** shows only limited ability to gelate cyclohexane, methylcyclohexane and diphenylether [13]. Its gelation efficiency is improved dramatically upon addition of *N,N'*-dimethylpropanediamine to solutions in benzene, toluene and *p*-xylene. **11** forms 1:2 complexes with diamine guests. Evidence for a concurrent conformational change from the folded to extended shapes of the crown part is strongly indicated by T_g , IR, and ^1H NMR spectral measurements; the pseudo-rotaxane-type interactions facilitate strongly gelation and gel stability.

This host-guest interaction also influences the mesoscopic morphologies of the aggregate network of **11** in benzene. SEM images of the xerogel from benzene gels of **11** in the presence of diamine show a well-developed network structure of fibrils with 50–250 nm diameters. Micrographs of the benzene sol of **11** in the absence of diamine show a dahlia flower-like structure. This example demonstrates that the specific host-guest interactions can control gelation. Alkali metal ions, another candidate as guests for crown ether-containing gelators, will be discussed elsewhere.

Two approaches have been examined to exploit the effects of additives. The first enhances some mechanical properties, as in an above-mentioned example, and the second “cuts” the network into rod-like species that are less polydispersed. Since molecules which show the second character do not contain a sugar or steroidal backbone, they will not be discussed here.

2.3.4. Molecular imprinting with LMOGs

One of the extensive applications of host-guest chemistry of gel systems is molecular imprinting using xerogels. From thermodynamic and spectral studies, it has been established that the vast majority of SAFINs comprised of LMOGs are crystal-like and are wetted negligibly by liquid molecules. As a result, xerogel fibers of an LMOG such as **12** may be hosts for guest recognition [14]. If the guest can be removed from the fibers without destroying the xerogel structure, the “porous xerogel” may retain a memory of the size and shape of the guests.

The first example based on this intriguing concept was demonstrated in 1998 [14]. In this work, benzene gels of D- or L-xylose·**12**₂ complexes were chosen for evaluation of the selective saccharide re-binding because their benzene solutions were readily gelled and frozen samples could be conveniently dried. In the first stage of the process, a hot solution of 5.0 wt. % **12** in benzene was gelled by cooling and the xerogel was obtained by freeze-drying. Then, the xerogel was washed sequentially for protracted periods with aqueous 15 vol.% acetic acid and then water-methanol (1:1 wt/wt) at room temperature. The content of the residual xylose in the “porous xerogel” was determined by ¹H NMR spectroscopy. Thereafter, the “porous xerogel” was finely powdered and dispersed in a water-methanol (1:1 wt:wt) solution containing the re-binding saccharide. Neither **12** nor L-xylose·**12**₂ is solubilized into the liquid media by these treatments. After stirring at room temperature, the xerogel was recovered by filtration and the amount of the re-bound saccharide was determined by ¹H NMR spectroscopy.

Even in the **12** gel prepared in the absence of saccharides, L-xylose is bound more efficiently than D-xylose. This implies that the boronic acid groups are

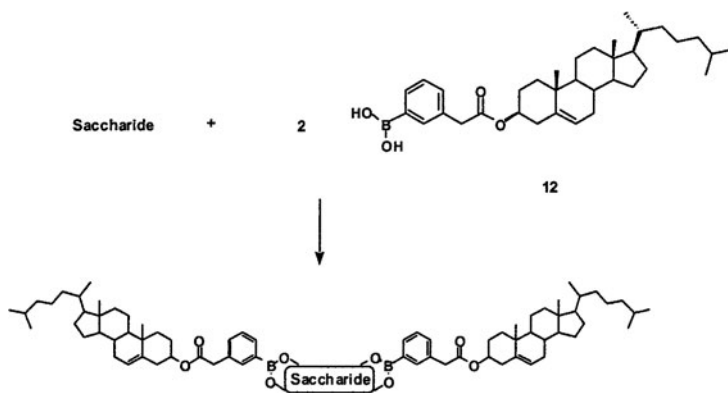


Figure 11. 1:2 complexation mode of a saccharide with cholesterylphenylboronic acid.

in a chiral array within the gel fibers of **12** and that they have the ability to differentiate molecules on the basis of chirality. Secondly, the re-binding ability of the mixture gels is largely dependent upon the enantiomer of the original xylose. When the original xylose is the D-enantiomer, the amounts of the re-bound D- and L- forms are similar. However, when the original xylose is the L-enantiomer, L-xylose is re-bound 4 times more efficiently than D-xylose. The results indicate that D-xylose disorders the chiral gel structure to a greater extent and loses its own “memory” whereas L-xylose makes an oriented structure that is more conducive to its re-binding. Thirdly, the “porous xerogel” prepared only from D-xylose·**12**₂ shows slightly higher affinity for L-xylose than D-xylose. Thus, L-xylose·**12**₂ (used as a mixture with **12**) can provide well-ordered gel structures that can differentiate the L- and D-enantiomers.

The re-binding selectivity of the “porous xerogel” was tested with 6 different monosaccharides. D-enantiomers were used as the re-bound saccharide form except in the case of xylose. In previous studies, these complexes were characterized by their reflectance wavelength in cholesteric liquid crystals (N.B., mixtures of cholesteryl nonanoate and cholesteryl chloride). Reflectance wavelengths for the complexes of D-mannose, L-xylose, D-fructose, D-galactose and D-lyxose caused a blue shift, indicating that their structures are complementary to the cholesterol helical groove. Complexes of D-glucose and D-xylose caused red shifts, indicating that their structures are not complementary to it. The re-binding results agree well with this trend: the former saccharides are preferentially bound. The chiral discrimination of xerogels prepared from **12** and xylose originates from the crystal-like aggregation of the gelators. The “memory” imprinted in the gel fibers should be readily erased by the gel-to-sol phase transition.

2.4. Conclusions

Steroidal derivatives, mainly cholesterol derivatives as investigated thus far, are versatile building-blocks for LMOGs. Several aspects of this diversity have been shown in Section 2 of this chapter:

- (i) cholesterol derivatives can provide chiral and moderately rigid platforms for molecular orientation and molecular recognition.
- (ii) although the aggregation modes of the cholesteric groups are restricted by boundary conditions inherent to each phase, many correlations among different phases dealing with guest selectivity, cohesivity, phase transition temperatures, spectroscopic properties, etc. can be found.
- (iii) small changes in the cholesterol structure can lead to large changes in the aggregation properties of these LMOGs.

One can propose, therefore, that cholesterol-based molecular assemblies can be further extended for applications based on chiral molecular recognition, molecular switches, controlled electron or energy transfer, membrane separations, etc.

3. Sugar Derivatives for Gelating Liquids

3.1. Introduction

In general, the driving forces for 1-D molecular aggregation of gelator molecules can be placed into two categories: hydrogen-bonding interactions [15, 16] and other van der Waals interactions such as London dispersion forces and electrostatic interactions. The cholesterol derivatives discussed in Section 2 are examples that emphasize the latter category, whereas aliphatic amides (such as those presented in Chapters 12 and 14) and saccharide-containing gelators [17–20] stress H-bonding interactions.

Some general guidelines for the design of LMOGs are emerging. They include: i) the presence of strong self-complementary and unidirectional interactions to enforce 1-D self-assembly; ii) control of the fiber-liquid interfacial energy to control solubility and to prevent bulk crystallization; and iii) some factors to induce fiber cross-linking for network formation [21]. Despite recent attempts to elucidate at the molecular level the prerequisites for successful gel formation, the ability to control the course of aggregation is still a goal that has not been attained. Sugars have unique and well-defined molecular architectures and they exist in a wide variety of structures, each of which can be obtained as a single enantiomer. As a result, they allow systematic studies to connect monomer structure with gelation ability. No other class of LMOGs discovered so far have this range of structural diversity.

3.2. Structural Variations of Sugar-Based Gelators

More than 50 years after the discovery by Meunier in 1891 that 1,3:2,4-di-*O*-benzyliden-D-sorbitol (**13**) is an LMOG [22], Yamamoto reported the gelation properties of **13** for about 70 different liquids [23]. Most did form gels in the presence of a few wt. % of **13** and, in some cases, as little as 0.4 wt. %. The elasticity of these gels was noted to be different from that of polymer gels; in some cases, the gels have the consistency of jelly and, in others, they are like solids. The sol-gel phase transitions were thermally reversible and the phase transition temperature depended on the gelator concentration. Also, the

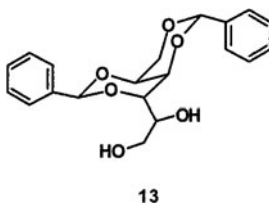


Figure 12. Chemical structure of 1,3:2,4-di-*O*-benzylidene-D-sorbitol (**13**).

gels exhibited a critical gelation concentration (cgc) at room temperature. It is rather amazing that so many of the characteristics found in LMOG-based gels today were identified so long ago.

Shinkai *et al.* have studied the gelation efficiencies of methyl glycosides of 4,6-*O*-benzylidene monosaccharides (**14–18**) [17–20]. Among them, only the gluco and manno molecules in the α -series and methyl 4,6-*O*-benzylidene- β -D-mannopyranoside (**14b**) are efficient gelators. Judging from the T_g values and the variety of liquids gelled, the gelation efficiency with organic liquids decreases in the order of **14b** > **14a** > **15a**. Comparison of the gelation properties of α - and β -mannopyranosides confirms a conclusion derived from a study of D-galactose derivatives [18] that the β anomer is more efficient than the α anomer. Thus, among ten investigated 4,6-*O*-benzylidene monosaccharides, only D-mannose, D-galactose derivatives and methyl 4,6-*O*-benzylidene- α -D-glucopyranoside (**15a**) served as gelators. The inability of the others to gelate a variety of organic liquids can be explained by their inability to form 1-D aggregates in which both hydroxyl groups participate [24]. For instance, methyl 4,6-*O*-benzylidene- α -D-allopyranoside (**17a**) and methyl 4,6-*O*-benzylidene- α -D-allopyranoside (**18**) cannot serve as efficient gelators because of possible strong intramolecular 3-OH-1-OMe interactions between their axially orientated groups [25]. In addition, gelation depends on the gelator's ability to assemble into fiber-like aggregates. Although the β -anomers show a strong tendency to form fibers (as indicated by SEM micrographs of their xerogels), **15b**, **16** and **17b** do not meet the requirements to gelate organic liquids concerning the direction of OH groups.

To gain insight into the packing mode of **15a**, a single crystal was grown from ethyl acetate and its packing was ascertained from X-ray diffraction measurements. The same packing arrangement was found in crystals grown in gelling liquids, but their diffracting quality was worse. **15a** forms 1-D zig-zag chains in which molecules are connected by two hydrogen bonds using the 2-OH and 3-OH groups. This packing arrangement satisfies the hypothetical requirements for a successful gelator.

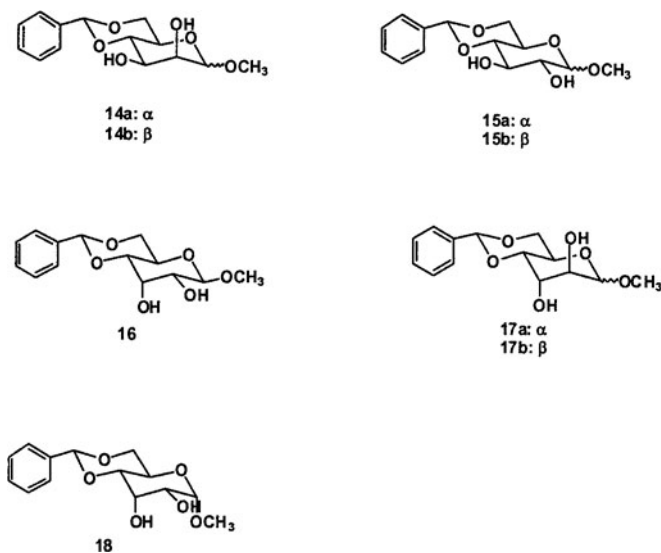


Figure 13. Chemical structures of some sugar-based gelators.

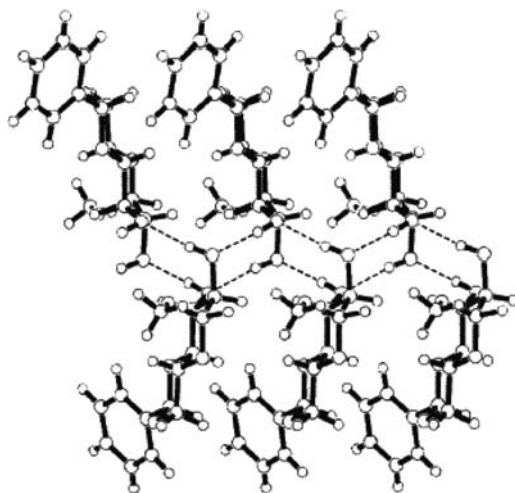


Figure 14. Crystal structure of **15a**. (Reprinted with permission from [15d]. Copyright (2000) Elsevier Science Ltd.)

Recent experiments have extended the range of media gelled by **13** to macromolecules and mesomorphous molecules. For instance, isotactic polypropylene, poly(propylene glycol), silicone fluids (including block copolymers), and liquid crystals have been “gelled” by **13** [26, 27]. Some

beneficial mechanical properties of the polymers occur when the gelator is added. In **13**-poly(ethylene glycol) (PEG) systems, TEM images reveal individual **13** nanofibrils of about 10 to 70 nm in diameter, with a primary nanofibrillar diameter of about 10 nm. Dynamic rheological measurements indicate that the rate of increase of the elastic modulus during gelation, the temperature corresponding to gel formation and dissolution, and the magnitude of the elastic modulus are sensitive to the concentration of **13** and the matrix polarity. At constant **13** mass concentrations, hydroxy-end-capped PEGs are gelled more slowly, but dissolve faster, than their methoxy end-capped analogues. The elastic modulus, however, is less dependent on matrix polarity and scales as the concentration of **13** to the 1.8 power over the range of concentrations examined. Time-temperature superposition analysis provides a direct measure of the activation energy of network evolution. It increases linearly with (i) decreasing mass concentration at constant matrix polarity and (ii) increasing matrix polarity at constant mass concentration.

3.3. Dual-Component Gelators Based on Charge-Transfer Phenomena

A dual-component gelator system consisting of two saccharide-based molecules, one bearing an electron-donor group and the other an electron-acceptor group (**19a** and **19b**) has been investigated in a variety of organic liquids and water and at different compositions [28]. In samples with octanol and diphenyl ether as the liquids, a change from colorless to yellow was observed upon cooling from the hot sol to the gel phase at room-temperature. UV-visible spectroscopy revealed the presence of a charge-transfer band in the octanol gel phase, but not in the sol phase. Also, the T_g at one total gelator concentration was highest at 1:1 **19a:19b**. TEM images of the single-component gels in diphenyl ether revealed fibrous networks (Figure 15) while the dual-component gel exhibited a novel, helical, fibrous-bundle structure whose origin can be ascribed to the charge-transfer interactions.

3.4. Combinatorial Approaches for Finding Gelators and Building Integrated Systems Utilizing a Sugar Library

The wide variety of sugars provides an easily accessible library for searching for new functional materials. Thus, an efficient screening and optimization of low molecular-mass organo- and hydro-gelators was carried out utilizing the combinatorial solid-phase synthesis of glycosylated amino acetates [29]. It was found that *N*-acetyl-galactosamine-appended amino acid esters (GalNAc-aa)

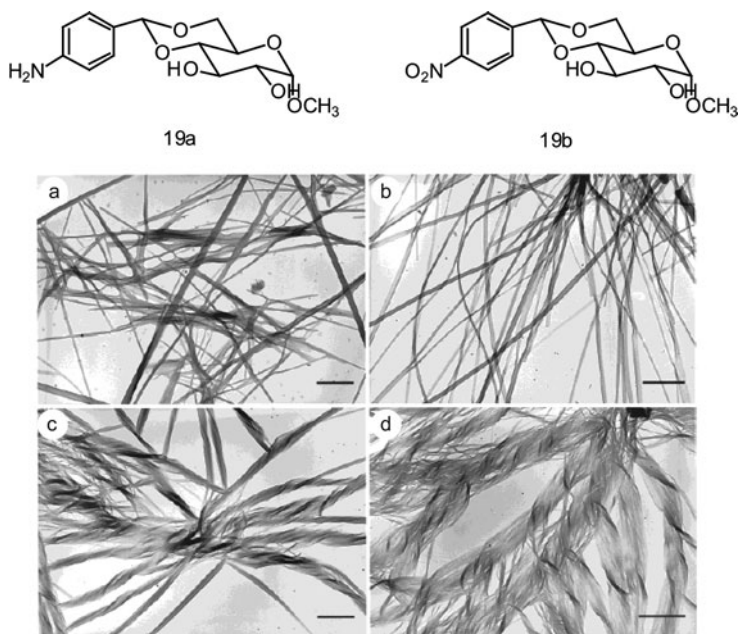


Figure 15. Chemical structures of **19a** and **19b** and TEM images of 3 wt. % gels in diphenyl ether: **19a** (a), **19b** (b), and **19a** and **19b** in a 1:1 molar ratio (c and d). Scale bars show 1.00 μm. (Reprinted with permission from [28]. Copyright (2002) American Chemical Society.)

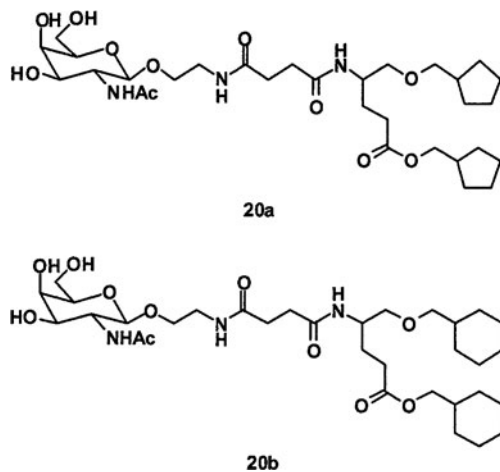


Figure 16. Chemical structures of **20a** and **20b**.

efficiently gelate a wide range of organic liquids. More interestingly, some GalNAc-aa derivatives display excellent hydrogelation capability. TEM, SEM, confocal laser scanning microscopy, and FT-IR data indicate the presence of supramolecular fibers supported by strong hydrogen-bonding networks. In addition, the supramolecular hydrogel consisting of GalNAc-suc-glu (*O*-methyl-cyc-pentyl) **20a** is stable even in the presence of high salt concentrations, probably due to its nonionic character. As a result, even a native protein has been successfully entrapped without denaturation in the **20a** gel matrix [30].

Spontaneous gel-formation and amphiphilic properties of the cyclohexyl analogue of the hydrogel of **20b** have been applied to develop a new type of peptide/protein gel array that is compatible with enzyme assays [30]. Aqueous cavities in the gel matrix can serve as a semi-wet reaction medium for enzymes, whereas the hydrophobic domains of the fibers are sites for monitoring the enzymatic reactions in the assay. The gel array overcomes several drawbacks of conventional protein chips, and, thus, can have potential applications to pharmaceutical research and diagnosis.

A variety of sugar skeletons leads to a variety of aggregate structures. Sugar-appended porphyrins (**21a-21e**) with monosaccharide groups at their periphery have been designed as a new class of gelating reagents [31]. CD spectra of the organogels from anomeric **21a** and **21b** exhibit an almost symmetric pattern, whereas the gel from **21c** gives a completely different pattern. This implies that the gel fibrils wind themselves in a right- or left-handed fashion that reflects the chirality of the specific molecular structure of the gelator; gel fibrils from **21a** and **21b** wind themselves with left-handed and right-handed helicities, respectively. In this way, macroscopic helical morphology reflects structure at a molecular level.

Successful transcription of the organic helical fibrils by a sol-gel process has yielded helical-silica structures which copy the organic morphology. A unimolecular porphyrin-stacking array has also been transcribed into silica fibers when the optimized sol-gel reaction conditions are as shown in Figure 17d. The sugar-based organic-fiber library in porphyrinic gels thus provides a variety of inorganic materials through sol-gel transcription processes.

3.5. Conclusions

Sugar-integrated gelators are valuable molecular tools for the discovery and design of new gelators. The saccharide library provided by nature affords many opportunities for future exploitation to design molecular assemblies, such as macrocycles, DNA mimics, monolayers, bilayer membranes, and liquid crystals. Some of these have been investigated already, but the possibilities are almost endless.

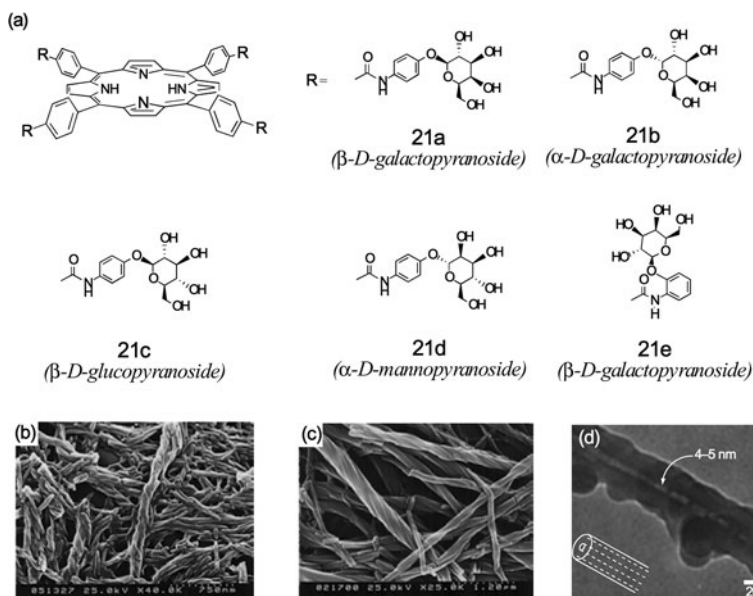


Figure 17. (a) Molecular structures of the sugar appended porphyrins, SEM images of (b) **21a** and (c) **21b** gel, and (d) TEM image of the one-dimensional assembly obtained from **21a**. Copyright (2004). Wiley-VCH.

4. Other Related LMOGs

4.1. Nucleobase Gelators

An example of a LMOG in which nucleobases are attached to a cholesterol group (**22**) was reported in 2001 [32]. The intent was to arrange nucleobases in a 1-D fashion utilizing orientational restrictions imposed by cholesterol stacking. In this way, the 1-D array comprised of nucleobases created by molecular self-assembly may mimic some of the properties of DNA, such as allowing the intercalation of planar polycyclic aromatic molecules such as porphyrins.

For example, when **22**-based gels were formed in the presence of a porphyrin-appended cholesterol, an induced CD signal in the Soret region of the latter was observed, suggesting that the porphyrin moiety is incorporated into the gel fiber [26]. A SEM image of the xerogel prepared from cyclohexane gel of **22** shows a well-developed network of fibrils with diameters of 20–40 nm. At several positions, the fibrils show an apparently right-handed helical structure, which may be related to the strong CD intensity of **22** in the gel phase.

Kim *et al.* reported thymidine-based and 2'-deoxyuridine-based gelators for organic liquids and water (**23**) [33]. Numata and Shinkai examined the complexation of a uracil-appended cholesterol gelator with polyadenylic acid (poly(A)) with the expectation that the complementary pairing would lead to new hybrid supramolecular structures [34]. The combination of **23** and poly(A) forms a gel in below the critical gelation concentration of **23** alone. The superstructure of uracil-appended cholesterol also shows a morphological transition from spheres to well-developed fibrous networks upon the introduction of (and interaction with) poly(A).

Shimizu *et al.* reported the self-assembling behavior of nucleotide-appended bolaamphiphiles **24a-24d**, in which two 3'-phosphorylated thymidine moieties are connected to both ends of a long oligomethylene spacer, in aqueous solutions [35]. The longer homologues, **24f** and **24g**, with C₁₈ and C₂₀ oligomethylene spacers, respectively, gelled water very effectively through formation of fibrous networks. Gelation behavior of both bolaamphiphiles strongly depends on pH and temperature. XRD data from a freeze-dried hydrogel from **24g** suggests the presence of a lamellar organization, consisting of monolayer sheets, within the fibers. Hydrogen bonds involving the 5'-hydroxyl group of the deoxyribose moiety, hydrophobic interactions between the long oligomethylene chains, and π - π stacking of the thymine residues are the factors most responsible for the effective hydrogel formation. By templating the thymidine-based bolaamphiphile assembly, double-helical nanofibers edged by poly(A) were developed [36]. ESI-FTICR-MS provided evidence for 1:1 and 1:2 complex formation in **24g**/d(A)₂ (d(A)_n: oligoadenylic acid with repeating *n* adenylic acid) mixtures, and IR measurements indicate that the thymidine bolaamphiphile **24g** forms a complementary complex with d(A)₁₀ at both ends through hydrogen-bonded A-T base pairs. Interestingly, TEM images reveal that when the chain length of the template is increased (*n* = 10, 20 and 40), discrete helical nanofibers whose width and length are 7–8 nm and several hundreds of nanometers, respectively, become evident in the hydrogel; the helical pitch was estimated to be 20 nm. The fibers of the **24g**/d(A)₄₀ aggregates

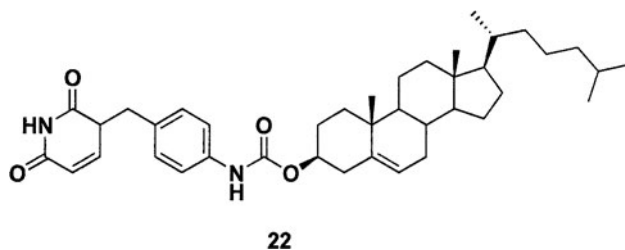


Figure 18. Chemical structure of a nucleobase-bearing cholesteric gelator.

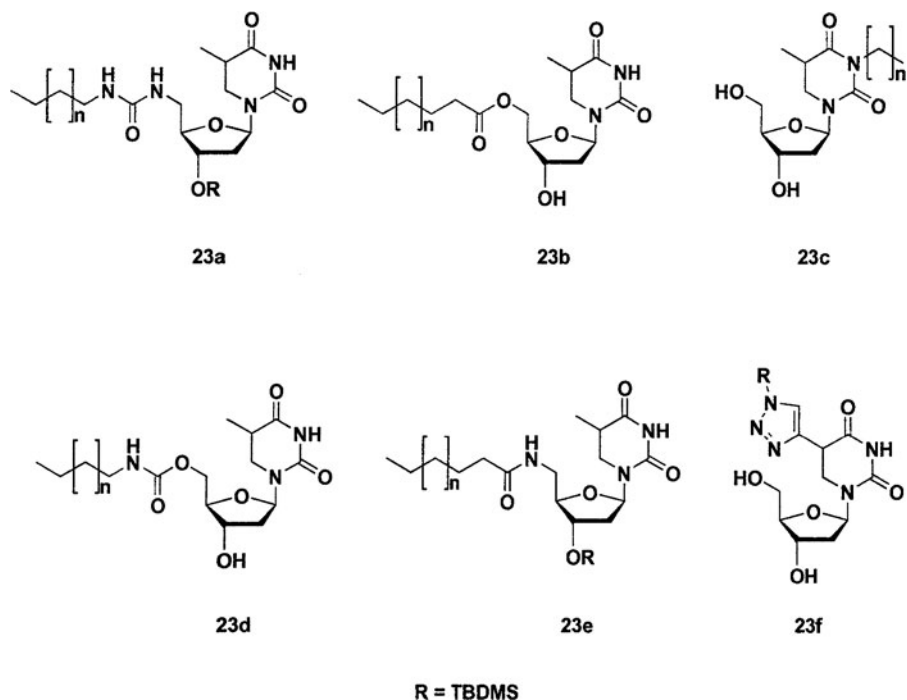


Figure 19. Thymidine-based and deoxyuridine-based LMOGs ($n = 5 \sim 15$).

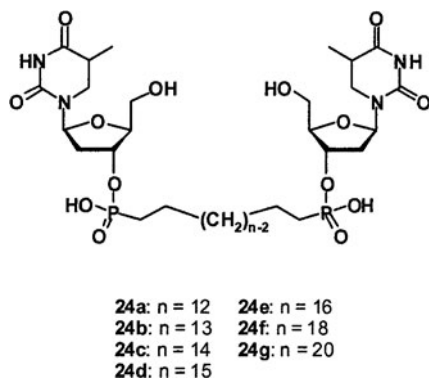


Figure 20. Chemical structures of nucleotide bolaamphiphiles.

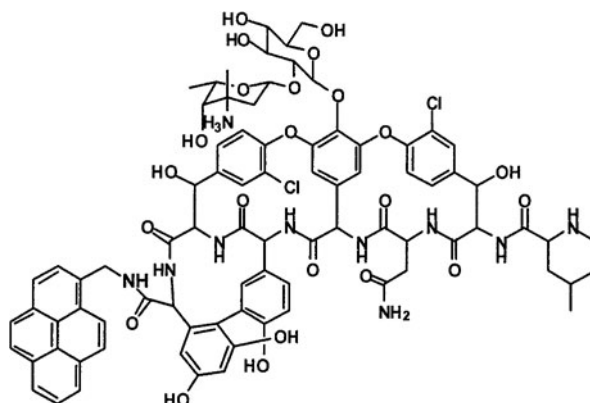
extend to $>1 \mu\text{m}$, lengths much longer than those of the **24g**/d(A)₂₀ assembly (150–700 nm). Thus, the length of the nanofibers increase with n in d(A) _{n} , and helical structures are formed for the templates with $n \geq 10$. Analyses of CD and IR spectroscopic data lead to the conclusion that the artificial double helices

are structurally similar to B-DNA, a species considered to form a right-handed helical structure.

Lipophilic guanosine derivatives are self-assembled into ribbon-like aggregates, both in the crystal state and in solution [37]. The structure of the ribbons has been characterized by single-crystal X-ray diffraction and, in solution, by NMR and ESI-MS. Two different ribbons with different patterns of hydrogen bonds are present in the solid state and in chloroform solution. The gel-like phases obtained in hexadecane, toluene and chloroform have been investigated by optical microscopy and small-angle X-ray diffraction: the type of phase observed is related to the molecular structure of the compounds and depends dramatically on the solvent. The structures of the phases are discussed, with the presence of the two different ribbons being taken into account.

4.2. Vancomycin Gelator

Xu *et al.* found that the pyrene-modified vancomycin (**25**) is an exceedingly efficient hydrogelator; 0.36 wt. % gels water [38]. A CD spectrum of the hydrogel contains a relatively strong band at around 460 nm that is absent in the sol. This band is attributed to the presence of stacked pyrene pairs in the gel aggregates as a result of attempts by **25** to balance hydrophobic and hydrophilic interactions. The same balance leads to formation of 1-D arrays whose stability is aided by the multiple hydrogen bonds among the peptide groups. Remarkably, **25** exhibits an 8- to 11-fold higher activity than Vancomycin itself against Vancomycin resistant Enterococci. The authors conjectured that “*the strong tendency to polymerize and the unexpected potency of 25 also lead us*



25

Figure 21. Chemical structure of a Vancomycin hydrogelator.

to speculate that **25** might aggregate into polymer-like structures at the cell surface when its local concentration is high". This concept is very similar to that proposed for nucleobase gelators showing DNA-mimetic properties.

5. Perspectives for the Future

Research dealing with steroid- and sugar-based LMOGs has progressed very quickly. These LMOGs are attractive candidates for study by physicists, chemists, and biologists due to their clearly defined molecular-ordering tendencies and their compatibility with bioactive molecules that can be used for assays. In addition, because they are synthetically derived, their ease of structural modification and accessibility mark them as important materials in future nano-biotechnology applications. Although some of these applications have been realized, many others in areas of pharmaceutical research and biocompatible gels based on LMOGs with steroid and sugar skeletons will surely be forthcoming.

References

- [1] (a) Klyne, W. *The Chemistry of Steroids*, New York: Wiley, **1960**. (b) Ramanathan, N.; Currie, A.L.; Ross Colvin, J. *Nature*, **1961**, 4778, 779. (c) Martin-Borret, O.; Ramasseul, R.; Rassat, R. *Bull. Soc. Chim. Fr.*, **1979**, 7–8, II–401.
- [2] (a) de Gennes, P. *Comptes Rendus de l'Academie des Sciences Paris*, **1981**. (b) Terech, P.; Ramasseul, R.; Volino, F. *J. Colloid Interface Sci.*, **1983**, 91(1), 280. (c) Terech, P. *J. Colloid Interface Sci.*, **1985**, 107, 244. (d) Terech, P.; Ramasseul, R.; Volino, F. *J. Phys. Fr.*, **1985**, 46, 895. (e) Wade, R.H.; Terech, P.; Hewat, E.A.; Ramasseul, R.; Volino, F. *J. Colloid Interface Sci.*, **1986**, 114, 442. (f) Terech, P. *Reversible Polymeric Gels and Related Systems*, P.S. Russo, Ed., ACS Symposium Series 350; Washington, DC: American Chemical Society, **1987**, Ch. 9. (g) Terech, P. "The living cell in four dimensions", *American Institute of Physics Conference Proceedings*, G. Paillotin, Ed., **1991**, 226, 518. (h) Pfannemüller, B.; Welte, W. *Chem. Phys. Lipids*, **1985**, 37, 227. (i) Terech, P.; Berthet, C.J. *Phys. Chem.*, **1988**, 92, 4269. (j) Terech, P. *J. Surface Sci. Technol.*, **1989**, 5, 163. (k) Terech, P. *Mol. Cryst. Liq. Cryst.*, **1989**, 166, 29. (l) Terech, P.; Rodriguez, V. *Progr. Colloid Polym. Sci.*, **1994**, 97, 151.
- [3] Technical Bulletin from Nikko Chemicals Co., Ltd., 1-4-8 Nihonbashi-Bakurocho, Japan, **1989**.
- [4] Lin, Y.-c.; Weiss, R.G. *Macromolecules*, **1987**, 20, 414–417.
- [5] Mukkamala, R.; Weiss, R.G. *J. Chem. Soc., Chem. Commun.*, **1995**, 375.
- [6] Mukkamala, R.; Weiss, R.G. *Langmuir*, **1996**, 12, 1474.
- [7] Murata, K.; Aoki, M.; Suzuki, T.; Harada, T.; Kawabata, H.; Komori, T.; Ohseto, F.; Ueda, K.; Shinkai, S. *J. Am. Chem. Soc.*, **1994**, 116, 6664.
- [8] Lin, Y.-c.; Kachar, B.; Weiss, R.G. *J. Am. Chem. Soc.*, **1989**, 111, 5542.
- [9] Furman, I.; Weiss, R.G. *Langmuir*, **1993**, 9, 2084.
- [10] Sugiyasu, K.; Fujita, N.; Takeuchi, M.; Yamada, S.; Shinkai, S. *Org. Biomol. Chem.*, **2003**, 1, 895.

- [11] Sugiyasu, K.; Fujita, N.; Shinkai, S. *Angew. Chem. Int. Ed.*, **2004**, *43*, 1229.
- [12] Jung, J.H.; Ono, Y.; Shinkai, S. *Tetrahedron Lett.*, **1999**, *40*, 8395.
- [13] Kawano, S.-i.; Fujita, N.; Shinkai, S. *Chem. Commun.*, **2003**, 1352.
- [14] Inoue, K.; Ono, Y.; Kanekiyo, Y.; Ishi-I, T.; Yoshihara, K.; Shinkai, S. *Tetrahedron Lett.*, **1998**, *39*, 2981.
- [15] (a) Hanabusa, K.; Okui, K.; Karaki, K.; Shirai, H. *J. Chem. Soc., Chem. Commun.*, **1992**, 1371 and references cited therein. (b) Hanabusa, K.; Yamada, Y.; Kimura, M.; Shirai, H. *Angew. Chem. Int. Ed.*, **1996**, *35*, 1949.
- [16] van Esch, J.; De Feyter, S.; Kellogg, R.M.; De Schryver, F.; Feringa, B.L. *Chem. Eur. J.*, **1997**, *3*, 1238.
- [17] James, T.D.; Murata, K.; Harada, T.; Ueda, K.; Shinkai, S. *Chem. Lett.*, **1994**, 273.
- [18] Yamasaki, S.; Tsutsumi, H. *Bull. Chem. Soc. Jpn.*, **1996**, *69*, 561.
- [19] (a) Amanokura, N.; Yoza, K.; Shinmori, H.; Shinkai, S. *J. Chem. Soc. Perkin Trans.*, **1998**, *2*, 2585–2591. (b) Amanokura, N.; Kanekiyo, Y.; Shinkai, S.; Reinhoudt, D.N. *J. Chem. Soc. Perkin Trans.*, **1999**, *2*, 1995.
- [20] (a) Yoza, K.; Ono, Y.; Yoshihara, K.; Akao, T.; Shinmori, H.; Takeuchi, M.; Shinkai, S.; Reinhoudt, D.N. *J. Chem. Soc., Chem. Commun.*, **1998**, 907. (b) Yoza, K.; Amanokura, N.; Ono, Y.; Akao, T.; Shinmori, H.; Takeuchi, M.; Shinkai, S.; Reinhoudt, D.N. *Chem. Eur. J.*, **1999**, *5*, 2722. (c) Luboradzki, R.; Gronwald, O.; Ikeda, A.; Shinkai, S. *Chem. Lett.*, **2000**, 1148. (d) Luboradzki, R.; Gronwald, O.; Ikeda, A.; Shinkai, S.; Reinhoudt, D.N. *Tetrahedron*, **2000**, *56*, 8697. (e) Gronwald, O.; Sakurai, K.; Luboradzki, R.; Kimura, T.; Shinkai, S. *Carbohydr. Res.*, **2001**, *331*, 307.
- [21] van Esch, J.H.; Feringa, B.L. *Angew. Chem. Int. Ed.*, **2000**, *39*, 2263.
- [22] Meunier, M.J. *Ann. Chim. Phys.*, **1891**, *22*, 412.
- [23] (a) Yamamoto, S. *Kogyokagakuzasshi*, **1942**, *45*, 695. (b) Yamamoto, S. *Kogyokagakuzasshi*, **1943**, *46*, 779.
- [24] Luboradzki, R.; Gronwald, O.; Ikeda, A.; Shinkai, S.; Reinhoudt, D.N. *Tetrahedron*, **2000**, *56*, 9595.
- [25] Muddasani, P.R.; Bernet, B.; Vasella, A. *Helv. Chim. Acta*, **1994**, *77*, 334.
- [26] Wilder, E.A.; Hall, C.K.; Spontak, R.J. *J. Colloid Interface Sci.*, **2003**, *267*, 509.
- [27] Wilder, E.A.; Hall, C.K.; Khan, S.A.; Spontak, R.J. *Langmuir*, **2003**, *19*, 6004.
- [28] Friggeri, A.; Gronwald, O.; van Bommel, K.J.C.; Shinkai, S.; Reinhoudt, D.N. *J. Am. Chem. Soc.*, **2002**, *124*, 10754.
- [29] (a) Kiyonaka, S.; Sugiyasu, K.; Shinkai, S.; Hamachi, I. *J. Am. Chem. Soc.*, **2002**, *124*, 10954. (b) Kiyonaka, S.K.; Shinkai, S.; Hamachi, I. *Chem. Eur. J.*, **2003**, *9*, 976.
- [30] Kiyonaka, S.; Sada, K.; Yoshimura, I.; Shinkai, S.; Kato, N.; Hamachi, I. *Nature Mater.*, **2004**, *3*, 58.
- [31] Kawano, S.-i.; Tamaru, S.-i.; Fujita, N.; Shinkai, S. *Chem. Eur. J.*, **2004**, *10*, 343.
- [32] Snip, E.; Shinkai, S.; Reinhoudt, D.N. *Tetrahedron Lett.*, **2001**, *42*, 2153.
- [33] (a) Yun, Y.J.; Park, S.M.; Kim, B.H. *Chem. Commun.*, **2003**, 254. (b) Park, S.M.; Lee, Y.S.; Kim, B.H. *Chem. Commun.*, **2003**, 2912.
- [34] Numata, M.; Shinkai, S. *Chem. Lett.*, **2003**, *32*, 308.
- [35] Iwaura, R.; Yoshida, K.; Masuda, M.; Yase, K.; Shimizu, T. *Chem. Mater.*, **2002**, *14*, 3047.
- [36] Iwaura, R.; Yoshida, K.; Masuda, M.; Ohnishi-Kameyama, M.; Yoshida, M.; Shimizu, T. *Angew. Chem. Int. Ed.*, **2003**, *42*, 1009.
- [37] Giorgi, T.; Grepioni, F.; Manet, I.; Mariani, P.; Masiero, S.; Mezzina, E.; Pieraccini, S.; Saturni, L.; Spada, G.P.; Gottarelli, G. *Chem. Eur. J.*, **2002**, *8*, 2143–2152.
- [38] Xing, B.; Yu, C.-W.; Chow, K.-H.; Ho, P.-L.; Fu, D.; Xu, B. *J. Am. Chem. Soc.*, **2002**, *124*, 14846–14847.

Chapter 16

SAFIN GELS WITH AMPHIPHILIC MOLECULES

Reiko Oda

Institut Européen de Chimie et Biologie, UMR-CNRS 5144 Molécules, Biomolécules et Objets Supramoléculaires (MOBIOS), 2 rue Robert Escarpit - 33607 PESSAC Cedex, France

1. Introduction	577
2. Amphiphilic Molecules	578
2.1. Amphiphilicity	578
2.2. Amphiphilic Molecules	578
3. Gels with Amphiphilic Molecules	581
3.1. Characteristics of SAFIN Gel with Amphiphilic Molecules	582
3.2. Amphiphilic Molecules which Form SAFIN Gels	584
3.3. Chiral Supramolecular Structures	588
4. Gemini Amphiphilic Molecules	591
4.1. Definitions	591
4.2. Particularities of Gemini Molecules	592
4.3. What Kind of Gemini Molecules Form Gels?	593
5. Conclusions and Perspectives for the Future	599

1. Introduction

Among the many *low molecular mass organic gelators* (LMOGs) is a family of amphiphilic molecules. Amphiphilic molecules such as lipids, detergents, surface active agents or surfactants, whose molecular weights are a few hundred Daltons, are undoubtedly one of the most common groups of molecules in our daily lives for their capacities to form nano to sub-millimeter scale aggregates with defined morphologies in solution. In this chapter, we will first classify different types of amphiphilic molecules by their molecular structures. Then, we will discuss the physico-chemical properties of the SAFIN (Self-Assembled Fibrillar Network) gels of amphiphilic molecules.

Many amphiphilic gelators are chiral, and such molecules can self-assemble into nanometer to micrometer scale chiral fibrillar structures (see Chapter 18). Finally, we will examine a particular family of amphiphilic molecules, gemini (or dimeric) amphiphiles. These molecules have dissymmetric molecular shapes and can easily self-assemble into elongated aggregates; these characteristics can be important factors for designing amphiphilic LMOG gelators.

2. Amphiphilic Molecules

2.1. Amphiphilicity

Molecular amphiphilicity (amphi: from Greek amphi-: on both sides: of both kinds, phile: from Greek -philos -philous: lover: one having an affinity for or a strong attraction to, (Merriam-Webster's Collegiate[®] Dictionary, Tenth Edition.)) can be defined as a character of molecules to have two or more parts with each part having different affinities for solvents that do not mix with each other. This character is the origin of many molecular aggregates. Here, we limit the amphiphilic molecules treated in this chapter to those which are hydrophilic and hydrophobic at the same time; amphiphilicity is defined with respect to water. Additional examples are covered in Chapters 17 and 18. We will deal only with the cases in which hydrophilicity and hydrophobicity differences are large (e.g., hydrocarbon chains with at least 6 carbon atoms). The hydrophilic head groups can be either charged or neutral. While most of the charged head groups can be considered to be hydrophilic, the hydrophilicity of the neutral head groups is more difficult to define. In this chapter, we will mainly focus on molecules having head groups sufficiently hydrophilic to be soluble in aqueous media under certain conditions. Such species may be sugars, hydrophilic peptides or oxyethylene groups.

2.2. Amphiphilic Molecules

2.2.1. *Aggregate morphologies of amphiphiles*

Amphiphilic molecules (lipids, surfactants, amphipatic peptides or copolymers) form aggregates in aqueous solution, and the molecular structure as well as various physico-chemical parameters are closely related to the aggregate morphology [1, 2]. These aggregates are held together principally by weak and non-directional hydrophobic effects, and small variations in such parameters can easily induce significant morphology changes. Other than the

most commonly observed structures such as spherical micelles (highly curved structures) and vesicles or lamellar phases (mean curvature is zero), various structures such as d micelles, ribbons, tubules, hexagonal, cubic phases, etc. are observed [3, 4]. Due to their amphiphilicity, sometimes they can form reversed phases such as inverted micelles or lamellar phases in organic solvents containing a trace of water.

One of the most important parameters that has an effect on the morphology of amphiphilic aggregates is the packing parameter, $p = v/a_0l$ (a_0 is the area per head group, l is the effective length of the hydrophobic chain(s), and v is the volume of the hydrophobic chain(s)) introduced by Israelachvili [1, 5]. With a very simple approximation, one can approximate v/l as the area per hydrophobic chain. Therefore, p is the ratio of area per chain over area per head. As shown schematically in Figure 1, the value of p is closely related to the morphologies of the amphiphile aggregates.

Although this parameter depends largely on the molecular structure, it also depends on the environment: it is a result of a complex mixture of external parameters such as temperature, pH, molecular concentrations and salinity. Also, this parameter is based on the assumption that the molecules exist with a symmetric shape. Therefore, it is much more difficult to use this parameter to correlate aggregate morphologies in which the molecular components have dissymmetric shapes, such as two-chained lipids or molecules which organize with orientational order.

While this parameter is conceptually useful for describing why a given family of molecules assembles to certain morphology of aggregates, it is still very difficult to predict the morphology of aggregates that a particular molecule will form in solution.

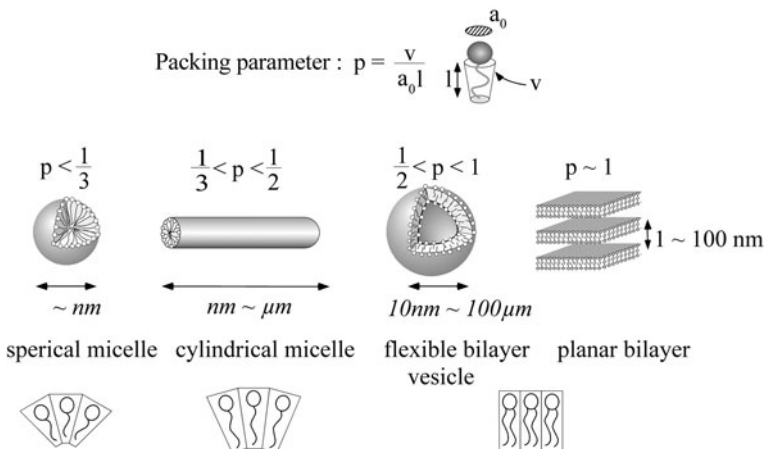


Figure 1. Packing parameter of amphiphilic molecules as defined by Israelachvili, showing different morphologies of amphiphilic aggregates.

2.2.2. Structures of amphiphilic molecules

The head groups of amphiphilic molecules can be charged (cationic or anionic) or neutral (non-ionic or zwitterionic). Non-ionic head groups can be polar, such as a sugar, an oxyethylene, etc. although smaller groups such as hydroxyl or amino moieties are also polar. In the context of this chapter, we will only mention molecules which have head groups with higher hydrophilicity. The most common hydrophobic chains are unbranched saturated or unsaturated hydrocarbons with 5–22 carbon atoms. Chains shorter than 5 carbon atoms do not form defined aggregate structures, and most of the one-head/one-tail amphiphiles are not soluble in water at room temperature when the chain is saturated and its length exceeds 22 carbon atoms. Many studies on fluorinated amphiphilic molecules have been reported where a part of the hydrocarbon chain is replaced by a fluorocarbon segment. The interest in such molecules is based mainly on the immiscibility between hydrocarbon and fluorocarbon chains [6–11] as well as the higher hydrophobicity of fluorocarbon chains compared to their hydrocarbon counterparts [12]. Hydrophobic groups that include aromatic groups (such as azobenzene [13, 14] or stilbene [15]), peptide groups, various dyes or steroid groups [16–18] have been reported.

Amphiphilic molecules can be classified into several families by their molecular structures (Figure 2). The most common (classical) structures are monomeric amphiphiles which have one hydrophilic head group connected to one hydrophobic tail (Figure 2a).

A large majority of amphiphilic lipids has one hydrophilic head group and two hydrophobic chains (Figure 2b). This is closely related to the fact that they are important structural components of biological membranes, and having two hydrophobic chains increases the packing parameter, thus favoring the formation of bilayer structures. Kunitake *et al.* first used this idea to develop artificial membranes with didodecyldimethylammonium bromide [19], a molecule with two hydrophobic chains and one quaternary ammonium head group. Since then, many derivatives of two-chain amphiphiles have been reported. In the case of charged molecules, the counter ions are usually highly water-soluble.

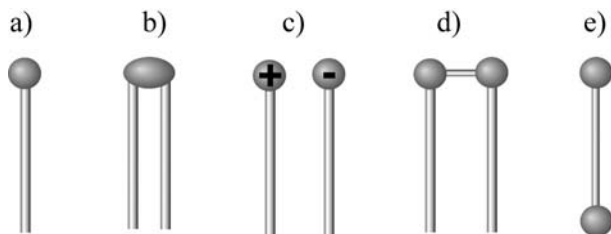


Figure 2. Different structures of amphiphilic molecules: (a) monomeric, (b) lipid-like, (c) catanionic, (d) gemini, (e) bola-amphiphile.

A derivative of such a molecule can be catanionic, where not only charged amphiphilic molecules but also counter ions have hydrophobic tails (Figure 2c). For such molecules, the counter ions are therefore confined to the aggregate interface and, in general, they decrease the curvature of the interface [20–25]. The variation of the interfacial curvature depends on the counter ions. For example, a few percent by weight of the cationic amphiphile, cetyltrimethylammonium forms spheroidal micelles ($p \sim 1/3$) in water when bromide is the counter ion; with salicylate or alkylsulphonate (C6 and C7) as the counter ion, entangled cylindrical micelles ($p \sim 1/2$) are formed in the same concentration range [26]. As the hydrophobicity of the counter ion is increased further, using hydroxynaphthalenecarboxylate or octylsulphonate (C8), vesicles ($p \sim 1$) are formed [27]. In catanionic systems, the interface often becomes quite rigid because of the insertion of hydrophobic tails of counter ions in the bilayer and the phase transition temperature of the membrane decreases [28, 29].

There are also oligomeric amphiphiles (Figure 2d). Most common among them are dimeric (gemini) molecules which will be treated later in this chapter. In such molecules, spacers connect two or more head groups, each carrying a hydrophobic tail.

A final class of amphiphilic molecules called bola-amphiphiles have two head groups, one on each side of a hydrophobic group (2e). They derive their name from the similarity of their shapes to that of a primitive weapon that was used by both the Eskimos and South American Indians. The presence of two head groups makes bola-amphiphiles much more water soluble than their one head counterparts. The two head groups can be symmetrical or non-symmetrical, and the hydrophobic group can contain one or two saturated or unsaturated hydrocarbons. Such structures have been extensively studied by Fuhrhop *et al.* [3] (see Chapter 18). The most common aggregates of such molecules are vesicles [30–32]. However, there are quite a few examples of fibrous, micellar structures or tubular structures [33, 34]. Various bolaamphiphiles containing nucleotide, sugar, or peptide head groups are also known [35–38]. Many of these molecules self-assemble into helical fibrous structures due to the chirality of the head groups.

3. Gels with Amphiphilic Molecules

The term “gel” is used extensively when describing the aggregates of amphiphilic molecules, although the number of these SAFIN gels is *relatively* small to date. Very often “gel” is used as a phenomenological definition when the solution is viscous and/or elastic. The viscosity of such systems is such that the solution does not flow perceptibly when the container is inverted (see Chapter 8). Besides SAFIN gels, concentrated lamellar phases, discoidal assemblies (bicelles) or emulsions display such characteristics. In fact, due

to inter-supramolecular-aggregate interactions, beyond certain concentrations, most of the structures exhibit high viscosity, and are often described as “gel” in the literature.

However, except for a few examples, only SAFIN LMOGs are able to gelate solvents at a few percent concentrations (w/w). In this chapter, we will concentrate mainly on SAFIN systems where solvent gelation is due to three-dimensional networks of fibrous structures, such as tapes, rods, filaments, sheets, tubes, or cylinders, held together by weak interactions between the fibers. Most of the time, the fibers have well-ordered non-symmetrical molecular organizations.

For most SAFIN gels, the driving force for gel formation is a delicate balance between “phile” properties and the “phobe” properties of the gelating agent with the solvent, where the “phile” properties allow the molecule to be solvated without precipitation, but the “phobe” properties assure the aggregation behavior. In this context, most gelating agents can be considered to be amphiphilic. However, we restrict our coverage here to systems that are strongly hydrophilic and hydrophobic, as mentioned in Section 2.1.

3.1. Characteristics of SAFIN Gels with Amphiphilic Molecules

3.1.1. “Metastable” states

Most of the currently known physical gels formed by amphiphilic LMOGs seem to be accepted as metastable states. While gels are generally observed below their Krafft temperature, they do not form directly below the Krafft temperature. That is, if the amphiphiles are dispersed in the solvent without going through the solution state beforehand, they will remain as a precipitate. To form a gel, the amphiphilic molecules must be first solubilized, for example by heating, and then cooling to below the Krafft temperature. Another method often used is dissolution in a solvent in which the molecule is soluble, then adding another solvent in which the molecule is not soluble. Once gels are formed and kept under controlled conditions, they can remain for a long time, in some cases more than ten years. On the other hand, there are cases that amphiphilic gels transform to a precipitate after a certain time. Often, such processes start with nucleation of precipitates in the gel, and grows until it includes the entire gel. Such observations indicate that these gels are not formed under thermodynamic equilibria, but rather exist in metastable states. An exception among SAFIN gels is solutions of entangled cylindrical micelles which form “gels” in thermodynamic equilibrium (see Chapter 19). Such systems show very particular rheological behaviors [39] since their visco-elasticity is assured mainly by the dynamic entanglement processes of cylindrical micelles which can dissociate

and associate rapidly. These gels are thermally and mechanically reversible, and form only below the Krafft temperature. Due to the small diameter of the elongated micelles, ca. twice the molecular lengths (a few nanometers), such gels are transparent. Although the majority of reported micellar structures are in aqueous phases, there are several reports of inverted cylindrical micelles formed in non-aqueous solvents [40].

3.1.2. Thermal and mechanical properties

A majority of SAFIN gels with amphiphilic LMOGs are reported to be thermally reversible; they “melt” to form fluid solutions when they are heated, and form again when the solutions are cooled down. Kinetic aspects of this phase transition are treated in Chapter 4. On the other hand, these gels are, *in general*, mechanically irreversible; once broken either by shaking or mixing, most of the gels do not ‘heal’. This is probably because the junction points of these 3D networks of fibers are static points in most cases, with attractive interactions between fibers (such as hydrogen bonds, ionic interactions or hydrophobic effects). Once broken, such junctions do not reform as can those of worm-like micellar networks which are held together by dynamic entanglements (see Figure 3).

Some systems that are not micellar solutions do display mechanical reversibility. They are thixotropic: the viscosity of the gels decreases under stress, but after removal of the stress, the viscous and elastic moduli of the sample gradually return to their initial values. Most examples of thixotropic gels (except for worm-like micellar solutions) are organogels [41, 42], and

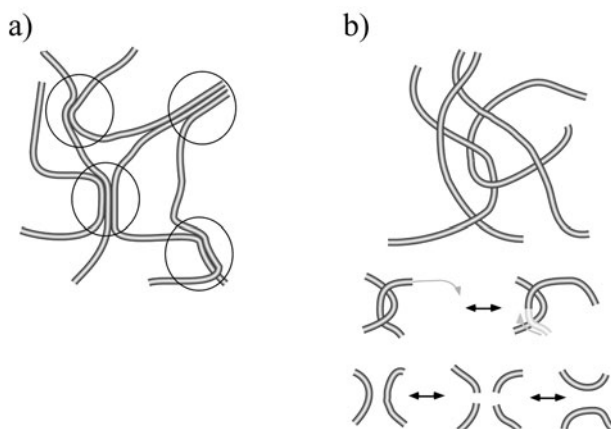


Figure 3. Three-dimensional network of a SAFIN gel with (a) static junction points and (b) dynamic entanglements showing reptation and scission-recombination.

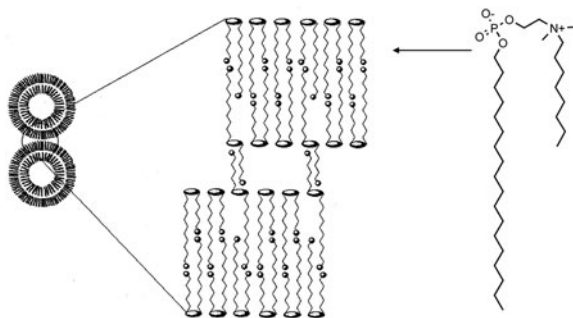


Figure 4. The proposed mechanism of vesicles connected to each other like in a necklace with the phosphocholine derived gemini **1**. The adhesion is assured by the gemini molecular shape. (Reprinted with permission from [43]. Copyright (2003) American Chemical Society.)

these gelators are not amphiphilic. An example of a thixotropic amphiphilic hydrogel contains phosphocholine-derived zwitterionic surfactants **1** [43]. In aqueous solution, this molecule forms “strings of vesicles” where vesicles are connected to each other like pearls in a necklace (Figure 4). The elongated structures of pseudo-linearly aggregated vesicles seem to constitute the gelator network. Another amphiphilic organic gelator **2** that organizes into an aggregate of vesicles has two cholesterol and azobenzene moieties as the hydrophobic part and one aza-crown moiety as a polar head group [44]. It is interesting to note that both vesicular string systems are made with gemini type molecules. It has been suggested that the vesicular aggregation may be due to interactions of the two hydrophobic chains with another chain from the bilayer of another vesicle. Therefore the gemini molecules serve as a bridge between vesicles [45].

The hydrogels with gemini **1** are observed both below and above the melting temperature of the hydrophobic chains. However, mechanical reversibility is observed only above the transition temperature (i.e., when the gel is at thermodynamic equilibrium). The organogel with gelator **2** is not mechanically reversible, probably due to the rigid structure of the hydrophobic part of the molecule that does not “melt”.

3.2. Amphiphilic Molecules which Form SAFIN Gels

3.2.1. Hydrogel, organogel and ambidextrous gels

As mentioned in the Section 2.1, it is difficult to define precisely what amphiphilic molecules are, and we have chosen representative amphiphilic gelators as having both strong hydrophilic and hydrophobic parts. Apart from

some exceptions, such as gelators of supercritical CO₂, most amphiphilic organic gelators can be classified either as forming gels with aqueous or organic liquid media. We will refer to the former as “hydrogelators” and the latter as “organogelators” in this chapter.

Most known hydrogelators are amphiphilic molecules in which the assembling force is mainly due to hydrophobic effects of alkyl or perfluoroalkyl chain segments. Some hydrogelators do not have classical amphiphilic structures, such as cysteine based gelators [46, 47], methyl 4, 6-benzylidene mannose derivatives [48], triazole ring-appended deoxyuridine gelators or bis(amino acid) oxalamide derivatives [50–52]. These molecules do not have hydrophobic chains; instead they have one or two aromatic groups which serve as the aggregation-driving units.

Besides those afforded by hydrophobic groups, additional interactions are assured by hydrogen bonds [53–63] and/or π - π stacking [64–66]. Molecules in the fibrous structures of these gels have pseudo-crystalline organizations that are determined by such directional interactions. Another types of interaction can be induced by hydrophobic counter ions. Especially for worm-like micellar solutions, hydrophobic counter ions tend to “stick” to the aggregate interface and reinforce the interactions [67] of head groups [68–70].

There are also many amphiphilic gelators of organic solvents [71, 72]. Similar intermolecular interactions drive gel formation in aqueous and organic solvents; for instance, hydrogen bonds occur in amino acid, urea, or sugar derivatives [73–80], and π - π stacking is found in steroidal [81, 82], and nucleobase derivatives [83]. Complexation with metal ions can also lead to gel

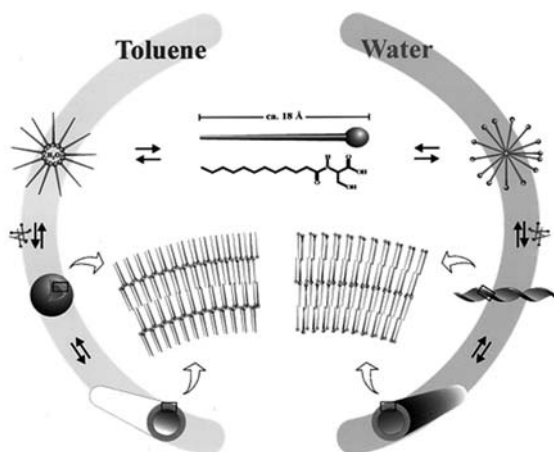


Figure 5. In water, the stacked bilayer structure can expose polar head groups to water whereas in organic solvent, hydrophobic tails are exposed to solvent. (Reprinted with permission from [87]. Copyright (2001) American Chemical Society.)

formation [84]. Selective gelation of organic solvents from mixtures of organic solvents and water can be observed [85].

Due to the amphiphilic character of the molecules, some form gels both in aqueous and organic solvents; they are ‘ambidexterous’. Some (oligo) peptidic lipids, sugar based amphiphiles, and cationic gemini surfactants (detailed below) with chiral counter ions show ambidexterity [86–90]. Most of the ambidextrous gels have bilayer structures (Figure 5).

3.2.2. Towards more robust structures

3.2.2.1. Polymerization. Defined structures with controllable domain sizes that are easily obtained with assemblies of amphiphilic molecules can be useful as templates or reaction media. On the other hand, these assemblies driven by weak interactions transform to other structures or break up when parameters such as temperature or solvent composition are changed and, in the case of SAFIN gels, they are also, in general, mechanically unstable. Therefore, there has been considerable effort to stabilize the assemblies. There are two main approaches for stabilizing SAFIN gels. The first stabilization method involves polymerization of the gelators in their fibrous state (see Chapters 22 and 23). There is a vast literature on the polymerization of the aggregates of amphiphilic molecules [91, 92], and it is not within the scope of this chapter to go into the details. Briefly, various polymerizable groups are incorporated into the amphiphilic molecules, where the most commonly used groups are, styryl, vinyl, dienyl, dienoyl, thiol, methacryloyl, acryloyl, and diacetylenyl groups (Figure 6). They can be hydrophobic or hydrophilic, and can be attached to the head groups, to the hydrophobic chains (near the head, middle, or the end of

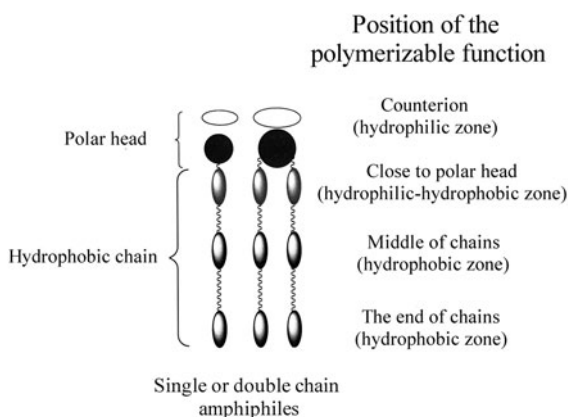


Figure 6. Positions of polymerizable groups [94].

the chains), or to the counter ions. Their positions have a large influence on the mechanism of polymerization and on the aggregate morphologies [93, 94].

Among the structures which were successfully polymerized are micelles [95, 96], cylindrical micelles [97], vesicles (probably the most studied structures) [98–102], cubic phases [103, 104], and hexagonal phases [105]. In spite of the many examples of gels in the literature, relatively few involve polymerization to stabilize the SAFIN gel structures [76, 94, 106–112]. At this time, all known polymerized gels are organogels, although many other polymerized aggregates are in the aqueous phase. This is probably because the polymerizable groups of such gelators have been introduced within the hydrophobic chains. Thus, they are expected to perturb molecular organization in the aggregate of hydrogels more than those of organogels. Moreover, most gel formation requires a delicate equilibrium, at the limit of precipitation, where molecules are organized with pseudo crystalline order, and a slight variation in the molecular structure may induce a drastic change in aggregation behavior. For hydrogels, the hydrophobic chains are usually central to the gelating behavior, and introduction of polymerizable groups along the chains leads to greater loss of the molecular organization needed for fiber formation [94]. The polymerization of the solvent component, methyl methacrylate or styrene, surrounding the aggregates of amphiphilic molecules has been exploited as well to create “reverse gels” [113, 114].

3.2.2.2. Sol-gel transcription. The second method for stabilizing SAFIN gels is to use the assembly of amphiphilic molecules as a scaffold to make inorganic structures by sol-gel transcription [115–117]. This method has been used to obtain inorganic structures with a rich variety of morphologies using amphiphiles aggregates as templates, including chiral structures (Figure 7). Since this topic is treated in Chapter 25, it will be mentioned very briefly

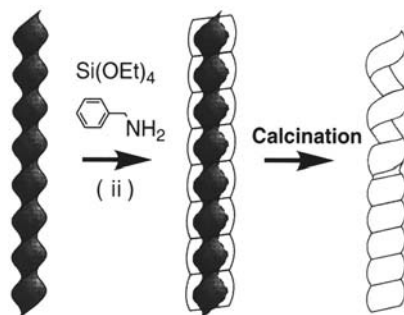


Figure 7. Mechanism of sol-gel transcription. TEOS undergoes polycondensation around the organic self-assembled structure and then the entire complex is calcinated to form inorganic imprinting of the structure.

here. The majority of the sol-gel transcriptions of SAFIN gel have employed organogels using solutions of tetraethylorthosilicate (TEOS) [44, 118–123] as the precursor. The organogels that have been successfully transcribed include LMOGs containing cholesterol, crown ethers, amines, ureas, and sugars. The condensation of TEOS is induced by several mechanisms, as described in Chapter 25.

3.3. Chiral Supramolecular Structures

3.3.1. *To gel or not to gel...*

Since gel formation is often a consequence of inhibited crystallization or precipitation, gel formation can be a history-dependent procedure. The sol can form a precipitate or a gel depending on how it is treated. It is frequently assumed that the local supramolecular organizations in SAFIN gels and SAFIN precipitates are very similar. In this context, there are many reports of elongated or fibrous aggregates without mention of gelation [124–132].

3.3.1.1. Chiral and non chiral aggregates. Many of the fibrous aggregates are chiral structures (hierarchical helices) [133] with various sizes of fibers, single or multiple twisted helical ribbons, or nano/microtubes whose diameters and chiral pitches range from ~ 10 nm to $10\ \mu\text{m}$ [55–57]. Supramolecular chirality of aggregates of amphiphilics was first reported with natural lipids such as sodium deoxycholate [134] and deoxycholic acid [135]. Furthermore, the relationship between molecular chirality and the helicity of the helical aggregates has been first established using D- and L-hydroxyalkyl salts as well as the corresponding acids [131, 132]. Many helical or twisted structures have been also reported from assemblies of a family of lipids derived chiral gelators [124, 125]. Various molecular designs have been made to control the morphologies of the chiral features. Several factors have been indicated as necessary for designing molecules that can be arranged efficiently in the aggregates [2]. They include flexible hydrophobic chains, a hydrophilic head groups and an additional interacting group and/or the presence of rigid segments in the chain. Their inclusion has led to the construction of several molecules that form chiral aggregates successfully [136–140]. Various small changes in molecular structure have been shown to induce significant changes in aggregate morphology. Introduction of amide bond linkages to the phospholipids induces additional lateral intermolecular hydrogen bonding sites, and helical ribbons and tubular aggregates are obtained; ester linkages result in multi-lamellar vesicles with fluid membranes [141]. In the case of tubular structures observed with diacetylenic lipids, various molecular structure variations and solvent effects on the morphology of the tubules have been explored [126, 127]. The diameters

of the tubules can be decreased by a factor of 10 by adding short-chain phospholipids to the diacetylenes [142].

The length of the hydrophobic chain is also an important factor determining fiber morphology [143–145]. For bolaamphiphiles, it was shown that the aggregation behavior is different if the spacer has an odd or even number of carbon atoms in the alkyl groups. Also, the speed of cooling of the sols to the gel phases affects the aggregates morphologies [146–148]. Some of these chiral molecules form gels with fibers that are not macroscopically chiral even when they are in a crystalline state and are arranged in a chiral fashion according to spectroscopic measurements [149–151]. When the macroscopic chirality of the fibrils can be clearly assigned, the relations between molecular chirality and supramolecular chirality are not easily understood. In general, the handedness of a chiral fiber is directly related to the molecular chirality of the building block (e.g., if one enantiomer forms right-handed helices, the other enantiomer forms left-handed helices). However, in some cases, racemic [152, 153] or achiral [154–162] molecules form chiral aggregates (within one fibril). Conversely, a pure enantiomer can give mixture of right- and left-handed helices [163–167].

3.3.2. *Molecular chirality to supramolecular chirality*

3.3.2.1. Molecular organization in chiral SAFIN gel fibers. Typically, the pitch of the helicity of chiral ribbons from amphiphilic molecules ranges from tens of nanometers to microns. This means that between hundreds to tens of thousands of molecules are needed to make one turn of a helix. In other words, from one molecule to its neighbor along the chiral fibrils, there will be a twist of the order of a degree at most. The origin of this chirality transfer is not easily understood. The nature of the molecular organization within the aggregates is very important in determining why chirality is or is not transferred from individual molecules to their aggregate structures, but such data are not always available. To date, most of the studies on molecular organization in the aggregates (chiral or not) have been performed on the desolvated gels; because of the pseudo-crystalline state of SAFIN gel fibers, their molecular organization is often assumed to be unchanged when the gels are converted to xerogels and the fibers are dehydrated. This assumption is necessary (although its validity must be questioned in each case) when, as is frequently found, the gel itself is not amenable to detailed determination of molecular packing. Thus wide-angle X-ray powder diffraction or wide-angle X-ray scattering (WAXS) as well as infrared spectroscopy and solid-state NMR were performed on dehydrated fibers to extrapolate to the gel structure [35, 48, 168–171]. Another somewhat risky extrapolation is that the packing within the gel fibers and in single crystals of the gelators (when they can be grown) are the same. Then, the single-crystal structures provide information about molecular packing in the

gels [169, 170, 172–175]. While this approach has been validated by a comparison of single crystal morph and powder diffractions for some cases [176, 177], it has not been in most cases. Furthermore, even with such information at molecular level, it still is not easy to understand precisely how local molecular packing can be reflected in the supramolecular chirality (i.e., to understand what controls the supramolecular chirality where the rotation per molecule is of the order of one degree (or less)).

3.3.2.2. Theoretical models. Among the various chiral fibrillar structures, chiral bilayer ribbons have intrigued theoreticians most. A variety of models have been proposed to explain the formation of these high-curvature structures (as summarized in articles and reviews and as detailed in Chapters 2 and 3 [178, 179]). Probably the most accepted theory at present assumes that chiral molecules do not pack parallel to their neighbors, but rather at a slight angle with respect to them. Using the continuum elastic theory and by introducing chirality as a global parameter, it can be shown that chirality enhances certain terms in the free energy that favor membrane curvature. Various models develop this concept in different ways, by making different assumptions about the membrane anisotropy or about the possible variations in the molecular tilt direction [179].

3.3.2.3. Helical and twisted ribbons. Among the variety of chiral fibers, the most commonly described in the literature can be classified into two different morphologies: helical and twisted shapes. The distinction between helical ribbons and twisted ribbons is shown in Figure 8. Helical ribbons have cylindrical curvature and can be precursors of tubules. By comparison, twisted ribbons have Gaussian or saddle-like curvature. A theoretical model treating the energy differences between the two types of curvatures has been introduced [179, 180].

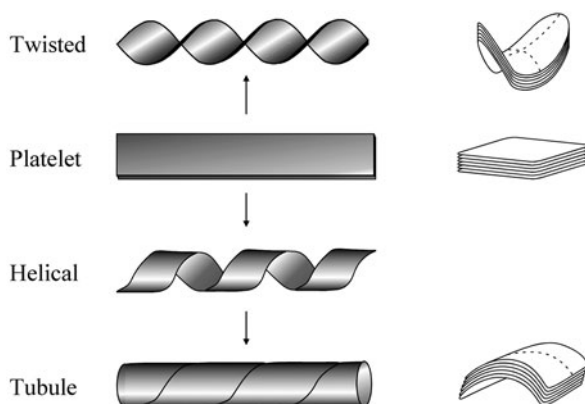


Figure 8. Schematic representation of helical and twisted ribbons.

Both types of bilayer ribbons have been reported in the literature. However, examples where the two morphologies are clearly distinguished are rare. Also, understanding why a given molecule forms ribbons with cylindrical or saddle-like curvature is not straightforward. Transition from twisted ribbons to helical ribbons has been observed from mixtures of cardanyl glucoside with saturated and mono-ene derivatives; twisted ribbons become helical ribbons when the relative concentration of the saturated derivatives is increased [181].

Morphology evolution with time has been also reported for tubules from a mixture of the diacetylenic phospholipids, 1,2-bis-(tricoso-10,12-diyonoyl)-*sn*-glycero-3-phosphocholine (DC8,9-PC), and the short chain lipid, 1,2-dinonanoyl-*sn*-glycero-3-phosphocholine (DNPC) [182]. A gradual transformation of the nanotubules into a lipid gel phase consisting of interconnected “helical” ribbons (i.e., twisted ribbons as defined here) was observed at room temperature. Twisted fibers were obtained from a long-chain glutamate lipid with an oligopeptide headgroup and lipids with an oligosarcosine (N-methyl glycine) head group, whereas the lipids with an oligoproline head group form helical ribbons [183]. Bilayer curvature is sensitive to the head group conformation and chirality of the amphiphiles.

4. Gemini Amphiphilic Molecules

4.1. Definitions

Since the early 90's, there has been a marked, increasing interest in “exotic” surfactants of the gemini or dimeric surfactant type [184–190]. They show unusual phase behaviors and their aggregates in solution often exhibit unexpected physical properties. There have been many reviews on the family of gemini surfactants that describe their general properties. The first three of the five properties of gemini surfactant molecules below (from Ref. [184]) probably define them best.

- (1) They possess at least two hydrophobic chains and two ionic or polar head groups.
- (2) The polar groups are connected by a spacer that can be either short or long (2 carbon to 20 carbon atoms are reported), either rigid or flexible, and either polar or apolar.
- (3) The polar groups can be positively or negatively charged or nonionic.
- (4) The vast majority of geminis have identical head groups and hydrophobic chains, but some unsymmetric geminis are known [191, 192].
- (5) “Geminis” with three or more polar groups or tails have been reported [193–199].

Because the subunits and spacers may be varied independently, it is possible to access more structural variations from geminis than from their monomeric counterparts. For example, varying the two chain lengths with n and m carbon numbers independently already gives $n(n + 1)/2$ instead of n potential variants for the monomer.

4.2. Particularities of Gemini Molecules

The physico-chemical properties of gemini surfactants are quite different from those of their monomeric counterparts [185].

- (1) Geminis have critical micellization concentrations (cmc) that are one to two orders of magnitude lower than for their corresponding monomer surfactants.
- (2) They decrease the surface tension of water much more efficiently than do the corresponding monomeric surfactants.
- (3) Aqueous solutions of some dimeric surfactants with short spacers can have very high viscosities at relatively low surfactant concentrations where viscosities of solutions of the corresponding monomers remain low.
- (4) Gemini surfactants increase wetting, promote emulsification of oil in water, enhance dispersion of solids, and make highly stable foams [200].
- (5) They also show better solubilizing properties, stronger tolerance to multivalent metal ions, and are stronger antimicrobials.

The third characteristics listed above can be related to the specificity of aggregation behavior of gemini molecules because, in terms of aggregate morphology, the gemini molecules are reported to behave quite differently from monomer molecules. The effect of the spacer length on the morphology of the aggregates for a series of cationic gemini molecules has been shown to be important especially when the spacers are much shorter or longer than the average distance between the head groups of monomeric molecules at the aggregate surface (Figure 9) [201–203]. This effect can be understood in terms of the variation of the packing parameter introduced at the beginning of this chapter; the connections between two (or more) head groups changes the distances between them and influences the manner the molecules can pack with each other.

Probably the most well documented class of gemini amphiphiles are cationic bis-quaternary ammonium surfactants, denoted as n - s - m (Scheme 1) [185, 192].

For this group of surfactants, the effects of the length and the nature of the spacer chain on the cmc, the molecular areas, the behavior at a air-water interface, and the morphology of their aggregates have been reported

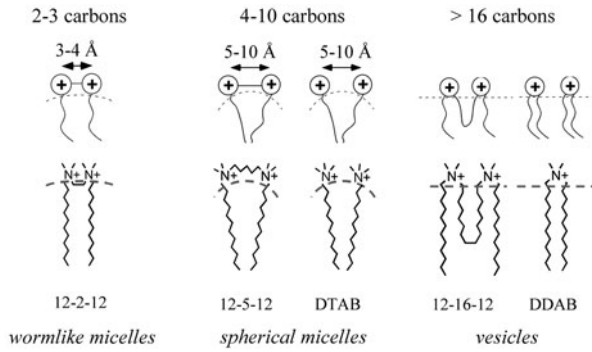
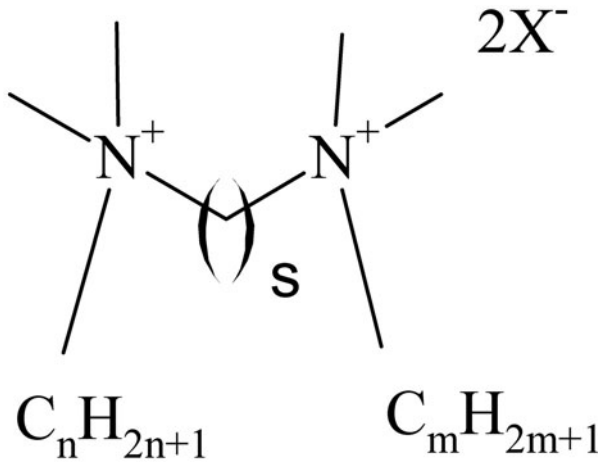


Figure 9. Effect of gemini spacer length on the morphologies of aggregates.



Scheme 1: Cationic bis-quaternary ammonium surfactants, n-2-m.

[199, 201, 203–205]. The effect of the nature of counter ions [206, 207], as well as the physico-chemical properties of the equivalent trimers and tetramers have been also reported [197]. These cationic geminis are capable of forming worm-like micelles without addition of salt or hydrophobic counterions at concentrations as low as a few percent. Such conditions are usually necessary to obtain worm-like micelles from monomeric amphiphiles.

4.3. What Kind of Gemini Molecules Form Gels?

Despite the large number of gemini molecules that have been investigated, examples that serve as SAFIN LMOGs are relatively rare. In fact, a majority

of the studies of gemini aggregate morphology has been done above the Krafft temperature for ionic gemini molecules (and, therefore, above the melting temperature of the gels) on the molecular or supramolecular properties of the systems at thermodynamic equilibrium.

The Krafft temperatures of gemini molecules are well documented [185]. For anionic gemini molecules, the effect of the length of the spacer group on the Krafft temperature is reported for hydrophilic ethylene oxide units. It is higher than for the corresponding monomeric counterparts, and decreases as the spacer length is increased. In the case of cationic gemini molecules, the effect of the spacer length seems to be much more complex [208]. While the Krafft temperature shows a monotonic decrease with the increase of spacer length comprised of the ethylene oxide units, the Krafft temperature does not show a monotonic variation as a function of the spacer length when methylene units are the spacer. However, there seems to be a general tendency that for short spacers (C_n , $n < 5$), the Krafft temperature increases with a decrease of spacer length. This was recently also observed with polymerizable cationic geminis containing bis-phosphonium head groups and various spacer lengths [209]. It is probably for this reason that the majority of studies of the morphology of gemini aggregates are performed with relatively long spacers ($\geq C_4$) with which solutions at thermodynamic equilibrium at room temperature are formed. In parallel, it was shown that some gemini molecules with short spacers can organize into fibrous or elongated aggregations (i.e., the fundamental structures to form SAFIN gels) without head groups or counter ions capable of forming intermolecular interactions [210]. The short spacers between head groups behave as the intermolecular cohesion elements.

A family of bis-urea dicarboxylic acids having hydrogen bonding sites in the head group form aqueous gels [168, 211] and anionic gemini molecules with very short spacers (one oxygen) form fibrous structures [212]. As mentioned previously, gel formation of zwitterionic gemini molecules seems to proceed through a different mechanism [213–215].

4.3.1. Dissymmetric shapes of gemini molecules and elongated shapes of their aggregates

Let us consider the correlation between the molecular shape of a gemini and the elongated shape of its fibrillar aggregate. Because gemini molecules have dissymmetric shapes, if their aggregates exhibit anisotropic molecular orientational order (nematic type order), a difference in line tension (increased energy of the exposed edges of the aggregates) in the directions parallel and perpendicular to the molecular orientation and elongation of aggregates (Figure 10) may be induced. Would there be such orientation?

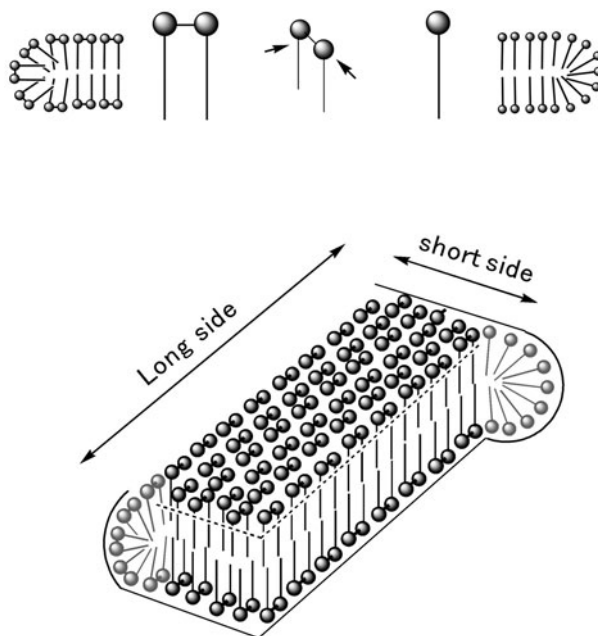


Figure 10. The difference of line tension for directions parallel and perpendicular to the orientation of gemini molecules.

This question pertains again to the general question concerning molecular organization in the aggregates. As discussed in Section 3.3.2.1, the answer is far from being trivial. It is, again, crucial to understand the relationship between gemini molecular organization (on the Angstrom scale) and supramolecular structure (on the micron scale). In the case of dynamic structures, such as worm-like micelles, it is essential that such information be obtained in the aggregates in their solvated state.

To correlate information at the two distance scales, it should be obtained simultaneously: it is necessary to know the orientation of the gemini molecules within the fiber; it is in general very difficult to obtain information about molecular orientation in aggregates. Although XRD data can provide information about molecular organization at pseudo Angstrom resolution if (and only if) the molecules have crystalline order, it is difficult to link that data and the orientations of molecules within an individual fiber. Moreover, XRD experiments on solvated aggregates are not easy to perform [216]. Similar measurements on the aggregates of molecules without crystalline order cannot be made using these techniques (see Chapter 11). The best method would allow simultaneous observation of the molecular conformations and positions in the inner structure of single fibers. However, the general techniques which

would be most suitable (i.e., electron microscopy and AFM) do not yet have the necessary resolution (see Chapter 9). This is because of (1) the very labile structures of the aggregates, (2) the high mobility of the molecules which are poorly organized in a solvated state (especially when there is no other driving force for molecular assembly besides the hydrophobic effect which imposes little directional constraint and allows a high degree of conformational freedom) or (3) the simple resolution problem at a given condition inherent to the techniques.

Another approach is to determine the fiber orientation by one technique first, then observe the molecular orientation by another. In most gels, the fibers of a gel are at or below the limit of detection by optical microscopy, and they are isotropically oriented. Therefore it is not easy to investigate the properties of one fiber. This has been accomplished in very few cases and only under special circumstances where the fibrous structure was observable with optical (wave length at visual domains) microscopy and morphology of molecular packing within a strand could be identified from single crystal structures [216] or by infrared spectroscopy [170].

A more attractive alternative to isolating one fiber is to apply an external force or field that induces the aggregates to orient at the moment of their formation. There are many examples of such orientation induction of elongated supra/macro molecular structures in the literature. Electric fields are often used for aligning elongated structures such as worm-like micelles, polymers in solutions, and DNA strands [217–223]. Magnetic fields can also be used if the molecule has a high magnetic susceptibility. Alignment of disk-like aggregates or tubules have been reported [224–226]. Another very commonly used technique for aligning elongated aggregates in solution is to apply a shear field. Polymers, lipidic tubules [227] and worm-like micelles (in the semi-dilute regime) in solution align in the direction of shear (see Chapters 6 and 19) above a certain shear rate. However, a majority of these examples are aimed at alignment of elongated structures without necessarily studying molecular orientation of the aggregates. In the investigation of gemini orientation in fibrous structures, a series of polarization modulation infrared linear dichroism (PM-IRLD) experiments were performed on aligned worm-like micellar solutions under shear and compared with molecular dynamics simulation results [228]. Both results indicated that the long axis of the gemini head group adopts a preferred orientation of ca. 30–50° with respect to the micelle cylinder axis instead of the expected 0°. This observation was explained to be a result of the competition between charge repulsion between head groups, which favors an orientation of the molecules perpendicular to the cylinder axis (high curvature), and the steric repulsion between hydrophobic tails, which favors an orientation of the molecules parallel to the cylinder axis (zero curvature). Such experiments have not been performed to date on worm-like micellar solutions of nonionic gemini surfactants.

4.3.2. SAFIN gels observed in gemini *n*-2-*n*/tartrate systems

Cationic bis-quaternary ammonium gemini (shown in Section 4.2) with tartrate as counter ions are ambidexterous gelators, forming gels both in water

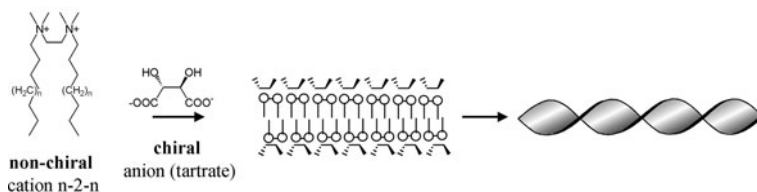


Figure 11. Chiral anions confined at the bilayer surface of non-chiral cationic gemini: formation of twisted bilayer ribbons.

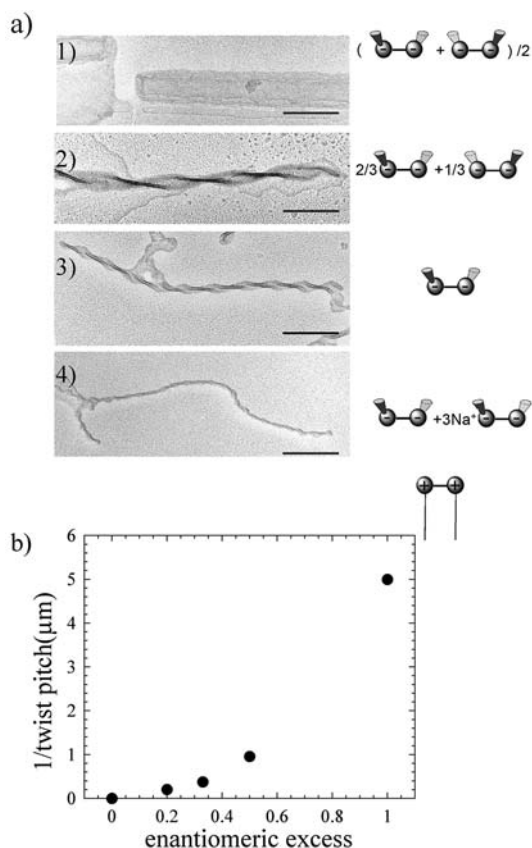


Figure 12. (a) TEM images of gemini (16-2-16)-tartrate ribbons at 0.1% in water for different *e.e.* values: (1) 0 (racemate); (2) 0.5; (3) 1 (pure L); (4) 1 (pure L) in the presence of 1 equiv. of sodium L-tartrate. Bar = 200 nm, (b) 1/twist pitch as a function of *e.e.*

and aromatic or chlorinated solvents [118, 229, 230]. From TEM, neutron and X-ray scattering measurements (see Chapter 10), the fibers in both aqueous and organic media were found to consist of an extended network of multilamellar chiral ribbons with right handed helices for (L)-tartrate and left handed helices for (D)-tartrate (Figure 11).

The reason for the similarity of the fiber structures in the different media has been discussed in Section 3.3.1. In water, the aggregation mechanism is assured by hydrophobic tails and, in organic solvents, hydrogen-bond interactions between tartrates are the driving force.

There are some unique features of this system. For one, the chirality of the system is due to the counter ion rather than the amphiphile. Induction of supramolecular chirality in the aggregates of non-chiral amphiphiles relies upon their interactions with the chiral counter ions. As a result, studies in which the enantiomeric excess (*e.e.*) of the anion is varied can be conducted easily. It was observed that varying the *e.e.* from 0 to 1 changes the pitch of the chiral ribbons continuously; they varied from infinite pitch (flat ribbons) to about 200 nm [231]. Furthermore, upon addition of increasing amounts of sodium (L)-tartrate to the solution of gemini (L)-tartrate (*e.e.* = 1), the twist pitch continued to decrease until it reached a minimum value of about 100 nm (Figure 12). This behavior contrasts with the previously observed helical ribbons composed of mixtures of enantiomers of DC8,9-PC which form separate right-handed and left-handed helices, with the number of each reflecting the *e.e.* [232, 233].

4.3.2.1. From chiral counter ions to twisted membranes. How do chiral structures form from non chiral amphiphiles? To answer this question, one must examine the interactions in the gel assemblies at the molecular level because the mechanism of formation of chiral bilayer membranes strongly depends on the structure of the amphiphile. If a bi-cation gemini is replaced by a non-gemini type amphiphile or a gemini with a longer spacer, the ammonium tartrate does not form chiral bilayers. Conversely, when the tartrate (bi-anion) is replaced by another carboxylate bi-anion with a longer spacer (e.g., gluconate) or a counter ion with fewer hydrogen-bonding sites (e.g., malate) or mono-anions (e.g., glucarate), no chiral bilayers are formed as well [230].

Therefore, formation of the twisted bilayers requires both tartrate and n-2-n type gemini, suggesting a specific association between the two. A qualitative indication of anion-cation recognition is observed from ^1H NMR experiments (Figure 13); diastereotopic patterns are observed with the n-2-n cationic head group in the presence of tartrate. The non-equivalence of some protons of the cation in the presence of a chiral anion in solution demonstrates the existence of the chiral conformers of the cation characterized in the solid state [229].

The hypothesis of a inter-molecular recognition mechanism is further reinforced by vibrational CD (VCD) measurements. VCD performed in

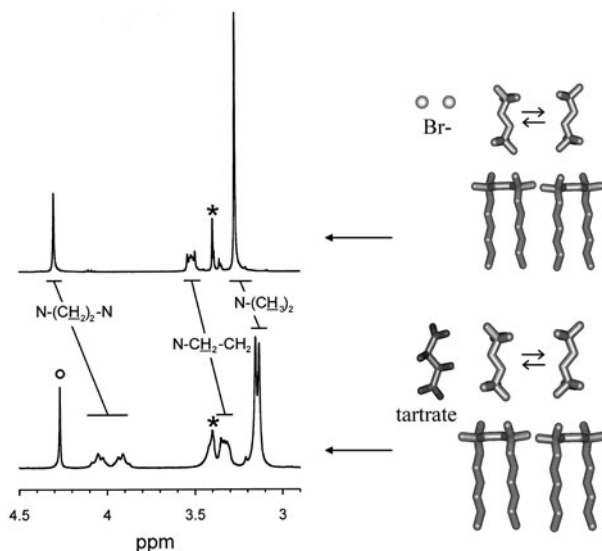


Figure 13. Part of the 400 MHz ^1H NMR spectra of 18–2–18 gemini with Br⁻ counterions (top) and with tartrate counter ions (bottom). The asterisks indicate the methanol residual solvent peak (CHD_2OD). The circle indicates the CHOH signal of the tartrate counter ion. (Reprinted with permission from [229]. Copyright (2002) American Chemical Society.)

the gels of 16–2–16 tartrate clearly shows CD signals in the absorption region of vibration belonging to the hydrocarbon chains ($2800\text{--}2950\text{ cm}^{-1}$) of the cationic amphiphiles (Figure 14a) while such signals are not observed with a fluid micellar solution of cetyltrimethyl ammonium (CTA)-tartrate (Figure 14b).

These results demonstrate that the non-chiral molecules adopt chiral conformations in the bilayers induced by tartrate counter anions. They provide a clear example of membrane chirality, controlled and tuned by chiral counter ions.

5. Conclusions and Perspectives for the Future

In this chapter, we have discussed the aggregate properties of a variety of small amphiphilic LMOGs whose molecular weights vary from a few hundred to about a thousand Daltons. The majority of the amphiphilic molecules have one or two hydrophobic alkyl chains and one or two polar head groups. The structures of amphiphilic molecules can be classified in five families: (1) one head group and one hydrophobic chain; (2) one head group and two chains, (3) a pair of oppositely charged monomeric amphiphiles (catanionic); (4) two head groups with two chains connected to each other at head groups

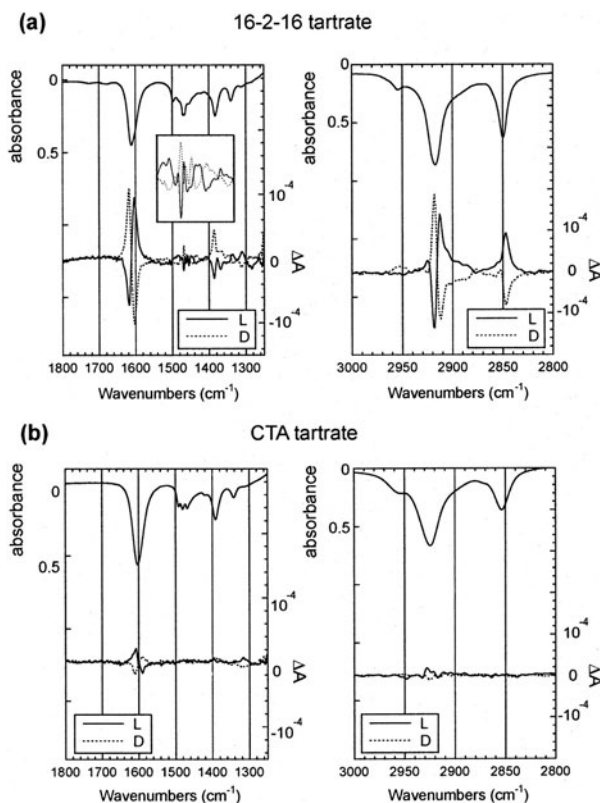


Figure 14. IR absorption and CD spectra of 16–2–16 L- and D-tartrate (a) and CTA L- and D-tartrate (b) and absorption spectra of sodium tartrate and of 16-2-16 with bromide counterions (c). The inset of part (a) shows the region 1400–1500 cm⁻¹ of the VCD spectra. (Reprinted with permission from [229]. Copyright (2002) American Chemical Society.)

(gemini), (5) two head groups at the end of one hydrophobic chain (bolaamphiphile). The polar head groups can be positively or negatively charged or can be neutral or zwitterionic. A minor variation in molecular structure of such molecules, as well as external parameters such as temperature, concentration, addition of salt, etc., can provoke drastic morphology changes of their aggregates that can be qualitatively described by the packing parameter p . A variety of amphiphilic gelators can be found in the literature, and some of them are gelators of both organic and aqueous liquid (i.e., they are ambidextrous).

The SAFIN gels formed with these LMOGs have several common characteristics. Most are metastable and are formed below their Krafft temperature, and molecules within the fibrillar structures that constitute the network are in crystalline-like arrangements; but an exception is the wormlike micelles. The specific nature of these gels frequently depends on their history.

Several features seem necessary for the design of amphiphilic gelators. They usually incorporate a delicate balance between “solvophobic” moieties which assure aggregation formation, and “solvophilic” moieties which assure the solvation necessary to avoid bulk precipitation. Often these molecules have additional interacting groups such as hydrogen bonding sites or π - π stacking sites which allow attractive and directional intermolecular interactions. Such interactions favor non-uniform growth of aggregates and formation of fibrous structures.

Chiral amphiphilic gelators can form chiral fibrillar structures. Such aggregates can be twisted or helical bilayer ribbons or inter-wound micellar fibers. However, the relationship between molecular chirality and supramolecular chirality is not straightforward. Some pure enantiomers give a mixture of right- and left-handed helices. As a corollary, racemic or achiral amphiphilic gelators can form chiral fibers by crystallization in chiral space groups. Of course, both chiral types of aggregates are present even in such cases. Also, gels of some chiral amphiphilic gelators have macroscopically achiral structures; in such cases, the molecules often are arranged locally in a chiral manner within their fibrils.

To date, it is still difficult to design amphiphilic molecules so that they will self-assemble to predefined structures. To do so requires understanding the relationship between molecular organization and conformation in the aggregates. This is extremely difficult for the cases where the assemblies are dynamic structures and are at equilibrium, but less so for the gels, which are quite often in their metastable state upon precipitation or crystallization. Several groups have already demonstrated the correlation between molecular organization and supramolecular structures. Such an approach will certainly be a key to designing gels with given aggregate morphologies in the future.

As is the case for most of SAFIN gels formed with LMOGs (whether amphiphilic or not), a large majority of the gels formed with amphiphilic molecules are thermally reversible and many are mechanically irreversible (that is, not thixotropic). The non-thixotropy of gels limits their potential applications; however, polymerization or sol-gel transcription of such gels can be used to increase the rigidity of their fragile SAFIN structures.

Finally, newly introduced gemini-type amphiphilic gelators with short spacers are able to self-assemble into aggregates with particular morphologies. The dissymmetric shape of gemini molecules seems to promote formation of fibrillar aggregates even without interacting groups. This attribute provides insights into the factors necessary to design new types of gelators.

Acknowledgment

I would like to thank all the colleagues with whom I had the opportunity to work with on gemini surfactant systems, first of all, I. Huc, who has been my

precious collaborator on the gemini systems, and who always has pertinent suggestions upon designing new molecules. Many thanks to D. Berthier, T. Labrot and A. Brizard, without whom we would not have obtained the results presented above. I also warmly thank S. J. Candau, F. C. Mackintosh, M. Schmutz, J.-C. Homo, F. Kern, F. Lequeux, E. Mendes, B. Desbat, T. Buffeteau, M. Laguerre. I had stimulating discussions with R. Zana, F. Menger, S. Shinkai, S. Bhattacharya, T. Shimizu, T. Ihara, J. Schnur, J. V. Selinger, and M. Spector. I also thank L. Cuccia and R. Blatchly for numerous suggestions on the manuscript. The research described in this chapter was funded by Centre National de la Recherche Scientifique, French Ministry of Research, the University of Bordeaux I, the University Louis Pasteur, and Rhône-Poulenc.

References

- [1] Israelachvili, J. *Intermolecular & Surface Forces*, 2nd edition, London: Academic Press, **1992**, Part III.
- [2] Kunitake, T.; Okahata, Y.; Shimomura, M.; Yasunami, S.; Takarabe, K. *J. Am. Chem. Soc.*, **1981**, *103*, 5401.
- [3] Fuhrhop, J.-H.; Köning, J. *Membranes and Molecular Assemblies: The Syntkinetic Approach*, London: Royal Society of Chemistry, **1994**.
- [4] Fuhrhop, J.-H.; Rosengarten, B. *Synlett*, **1997**, 1017.
- [5] According to this definition, the packing parameter of a molecule which forms spherical micelles is of the order of $1/3$; as the parameter increase towards $1/2$, cylindrical micelles are observed; vesicles or flexible bilayers are observed with the parameter $1/2 \sim 1$; bilayers are observed with the parameter equal to 1.
- [6] Asakawa, T.; Hisamatsu, H.; Miyagishi, S. *Langmuir*, **1996**, *12*, 7687.
- [7] Funasaki, N.; Hada, S. *J. Phys. Chem.*, **1980**, *84*, 736.
- [8] Mukerjee, P.; Yang, A.Y.S. *J. Phys. Chem.*, **1976**, *80*, 13881.
- [9] Elbert, R.; Folda, T.; Ringsdorf, H. *J. Am. Chem. Soc.*, **1984**, *106*, 7687.
- [10] Tamori, K.; Ishikawa, A.; Kihara, K.; Ishii, Y.; Esumi, K. *Colloids and Surfaces*, **1992**, *67*, 1.
- [11] Riess, J.G.; Frézard, F.; Greiner, J.; Krafft, M.P.; Santaella, C.; Vierling, P.; Zarif, L. *Handbook on Non-medical Applications of Liposomes*, Y. Barenholz and D.D. Lasic, Eds., FL: CRC Press, Boca Raton, **1996**, *III*, Ch. 8.
- [12] Mukerjee, P.; Mysels, K.J. *ACS Symp. Ser.*, **1975**, *9*, 239.
- [13] Kunitake, T.; Nakashima, N.; Shimomura, M.; Okahata, Y.; Kano, K.; Ogawa, T. *J. Am. Chem. Soc.*, **1980**, *102*, 6642.
- [14] Okahata, Y.; Ihara, H.; Shimomura, M.; Kunitake, T.; Tawaki, S. *Chem. Lett.*, **1980**, 1169.
- [15] Shimomura, M.; Hashimoto, H.; Kunitake, T. *Langmuir*, **1989**, *5*, 174.
- [16] Carey, J.C.; Montet, J.C.; Phillips, M.C.; Armstrong, M.J.; Mazer, N.A. *Biochemistry*, **1981**, *20*, 3637.
- [17] Roda, A.; Hofman, A.F.; Mysels, K.J. *J. Biol. Chem.*, **1983**, *258*, 6362.
- [18] Leibfritz, D.; Roberts, J.D. *Am. Chem. Soc.*, **1973**, *95*, 4996.
- [19] Kunitake, T.; Okahata, Y. *J. Am. Chem. Soc.*, **1977**, *99*, 3860.
- [20] Tondre, C.; Caillet, C. *Adv. Colloid Interface Sci.*, **2001**, *93*, 115.

- [21] Dubois, M.; Deme, B.; Gulik-Krzywicki, T.; Dedieu, J.C.; Vautrin, C.; Desert, S.; Perez, E.; Zemb, T. *Nature*, **2001**, *411*, 672.
- [22] Kihara, K.; Tamori, K.; Esumi, K.; Meguro, K.J. *Jpn. Oil Chem. Soc.*, **1993**, *42*, 140.
- [23] Regev, O.; Khan, A. *J. Colloid Interface Sci.*, **1996**, *182*, 95.
- [24] Blanzat, M.; Perez, E.; Rico-Lattes, I.; Prome, D.; Prome, J.C.; Lattes, A. *Langmuir*, **1999**, *15*, 6163.
- [25] Blanzat, M.; Perez, E.; Rico-Lattes, I.; Lattes, A. *New. J. Chem.*, **1999**, *23*, 1063.
- [26] Oda, R.; Narayanan, J.; Salkar, R.A.; Kern, F.; Manohar, C.; Candau, S.J. *Langmuir*, **1998**, *16*, 4364.
- [27] Hassan, P.A.; Narayanan, J.; Menon, S.V.G.; Salkar, R.A.; Samant, S.D.; Manohar, C. *Colloid Surf. A*, **1996**, *117*, 89.
- [28] Dubois, M.; Belloni, L.; Zemb, T.; Demé, B. Gulik-Krzywicki, Th. *Prog. Colloid Polym*, **2000**, *115*, 238.
- [29] Zemb, T.; Dubois, M.; Demé, B.; Gulik-Krzywicki, Th. *Science*, **1999**, *283*, 816.
- [30] Lasic, D.D. *Liposomes*, Elsevier: Amsterdam, **1993**.
- [31] Fuhrhop, J.-H.; Mathieu, J. *Angew. Chem. Int. Ed.*, **1984**, *23*, 100.
- [32] Fuhrhop, J.-H.; Fritsch, *Acc. Chem. Res.*, **1986**, *19*, 130.
- [33] Fuhrhop, J.-H.; Spiroski, D.; Böttcher, C. *J. Am. Chem. Soc.*, **1993**, *115*, 1600.
- [34] Newkome, G.R.; Barker, G.R.; Arai, S.; Saunders, M.J.; Russo, P.S.; Theriot, K.J.; Moorefield, C.N.; Rogers, L.E.; Miller, J.E.; Lieux, T.R.; Murray, M.R.; Phillips, B.; Pascal, L. *J. Am. Chem. Soc.*, **1990**, *112*, 8458.
- [35] Shimizu, T.; Masuda, M. *J. Am. Chem. Soc.*, **1997**, *119*, 2812.
- [36] Nakazawa, I.; Masuda, M.; Okada, Y.; Hanada, T.; Yase, K.; Shimizu, T. *Langmuir*, **1999**, *15*, 4757
- [37] Shimizu, T. Iwaura, R.; Masuda, M.; Hanada, T.; Yase, K. *J. Am. Chem. Soc.*, **2001**, *123*, 5947.
- [38] Kogiso, M.; Ohnishi, S.; Yase, K.; Masuda, M.; Shimizu, T. *Langmuir*, **1998**, *14*, 4978.
- [39] Cates, M.E.; Candau, S.J. *J. Phys. Condens. Matter*, **1990**, *2*, 6869.
- [40] (a) Garkins, F.H.; Brodnyan, J.G.; Philippoff, W. *Trans. Soc. Rheol.*, **1969**, *13*, 17;
(b) Leibler, L.; Rubinstein, M.; Colby, R.H. *Macromolecules*, **1991**, *24*, 4701;
(c) Cates, M.E. *Macromolecules*, **1987**, *20*, 2289.
- [41] Brinksma, J.; Feringa, B.L.; Kellog, R.M.; Vreeker, R.; Van Esch, J. *Langmuir*, **2000**, *16*, 9249.
- [42] Lescanne, M.; Grondin, P.; d'Aléo, A.; Fages, F.; Pozzo, J.-L.; Mondain Monval, O.; Reinheimer, P.; Colin, A. *Langmuir*, **2004**, *20*, 3032.
- [43] Menger, F.M.; Peresykin, A.V. *J. Am. Chem. Soc.*, **2003**, *125*, 5340.
- [44] Jung, J.H.; Ono, Y.; Sakurai, K.; Sano, M.; Shinkai, S. *J. Am. Chem. Soc.*, **2000**, *122*, 8648.
- [45] It is also believed that the asymmetry of the molecules is important for the cohesion of vesicles since interdigitation is a factor to solidify the bilayer. The organogelator consisting of two cholesterol and azobenzene moieties are not asymmetric, however the azobenzene and cholesterol can serve as a cohesion parts.
- [46] Menger, F.M.; Caran, K.L. *J. Am. Chem. Soc.*, **2000**, *122*, 11679.
- [47] Kölbel, M.; Menger, F.M. *Langmuir*, **2001**, *17*, 4490.
- [48] Gronwald, O.; Shinkai, S. *Chem. Eur. J.*, **2001**, *7*, 4328.
- [49] Park, S.M.; Lee, Y.S.; Kim, B.H. *Chem. Commun.*, **2003**, 2912.
- [50] Makarevic, J.; Jokic, M.; Peric, B.; Tomosoc, V.; Kojic-Prodic, B.; Zinic, M. *Chem. Eur. J.*, **2001**, *7*, 3328.
- [51] Jokic, M.; Makarevic, J.; Zinic, M. *Chem. Commun*, **1995**, 1723.

- [52] Frkanec, L.; Jokic, M.; Makarevic; Wolsperger, K.J.; Zinic, M. *J. Am. Chem. Soc.*, **2002**, *124*, 9716.
- [53] Fuhrhop, J.; Schnieder, P.; Rosenberg, J.; Boekema, E. *J. Am. Chem. Soc.*, **1987**, *109*, 3387.
- [54] Pfannemüller, B.; Welte, W. *Chem. Phys. Lipids*, **1985**, *37*, 227.
- [55] Svenson, S.; Köning, J.; Fuhrhop, J.-H. *J. Phys. Chem.*, **1994**, *98*, 1022.
- [56] König, J.; Boettcher, C.; Winkler, H.; Zeitler, E.; Talmon, Y.; Fuhrhop, J. *J. Am. Chem. Soc.*, **1993**, *115*, 693.
- [57] Imae, T.; Takahashi, Y.; Muramatsu, H. *J. Am. Chem. Soc.*, **1992**, *114*, 3414.
- [58] Imae, T.; Hayashi, N.; Matsumoto, T.; Tada, T.; Furusaka, M. *J. Colloid Interface Sci.*, **2000**, *225*, 285.
- [59] Hafkamp, R.J.H.; Heiters, M.C.; Nolte, R.J.M. *Angew. Chem. Int. Ed. Engl.*, **1994**, *33*, 986.
- [60] Jung, J.H.; John, G.; Masuda, M.; Yoshida, K.; Shinkai, S.; Shimizu, T. *Langmuir*, **2002**, *17*, 7229.
- [61] Estroff, L.; Hamilton, A.D. *Angew. Chem. Int. Ed.*, **2000**, *39*, 3447.
- [62] Imae, T.; Takahashi, Y.; Muramatsu, H. *J. Am. Chem. Soc.*, **1992**, *114*, 3414.
- [63] In water, hydrogen bonds are less efficient than in organic solvent due to the competition between inter-amphiphiles and inter amphiphile-water hydrogen bonds. In general, to observe strong hydrogen bonding among amphiphiles in water, it is necessary to have many hydrogen bonding sites in a cooperative manner or to have them coupled with hydrophobic effect.
- [64] Yanagawa, H.; Ogawa, Y.; Furuta, H.; Tsuno, K. *J. Am. Chem. Soc.*, **1989**, *111*, 4567.
- [65] Hanabura, K.; Hirata, T.; Inoue, D.; Kimura, M.; Shirai, H. *Colloids and Surfaces, A*, **2000**, *169*, 307.
- [66] Wang, G.; Hamilton, A.D. *Chem. Commun*, **2003**, 310.
- [67] Hofmeister, F. *Arch. Exp. Pathol. Pharmacol.*, **1888**, *24*, 247.
- [68] Hoffmann, H. In *Structure and Flow in Surfactant Solutions*, C. Herb, R. Prud'homme, Eds.; ACS Symposium Series No. 578; American Chemical Society, Washington, DC, **1994**, Chapter 1.
- [69] Hassan, P.A.; Narayanan, J.; Menon, S.V.G.; Salkar, R.A.; Samant, S.D.; Manohar, C. *Colloid Surf. A*, **1996**, *117*, 89.
- [70] Oda, R.; Narayanan, J.; Hassan, P.A.; Manohar, C.; Salkar, R.A. *Langmuir*, **1998**, *14*, 4364.
- [71] Terech, P.; Weiss, R.G. *Chem. Rev.*, **1997**, *97*, 3133.
- [72] van Esch, J.H.; Feringa, B.L. *Angew. Chem. Int. Ed.*, **2000**, *39*, 2263.
- [73] Hofkamp, R.J.H.; Feiters, M.C.; Nolte, R.J.M. *J. Org. Chem.*, **1999**, *64*, 412.
- [74] Li, G.; Fudickar, W.; Skupin, M.; Klyszcz, A.; Draeger, C.; Lauer, M.; Fuhrhop, J.-H. *Angew. Chem. Int. Ed.*, **2002**, *41*, 1828.
- [75] Ihara, H.; Hachisako, H.; Hirayama, C.; Yamada, K. *Chem. Commun.*, **1992**, 1244.
- [76] Bhattacharya, S.; Acharya, S.N. *Chem. Mater*, **1999**, *11*, 3121.
- [77] van Esch, J.H.; Schoonbeek, F.; de Loos, M.; Kooijman, H.; Spek, A.L.; Kellogg, R.M.; Feringa, B.L. *Chem. Eur. J.*, **1999**, *5*, 937.
- [78] Fuhrhop, J.-H.; Schnieder, P.; Boekema, E.; Helfrich, W. *J. Am. Chem. Soc.*, **1988**, *110*, 2861.
- [79] Tachibana, T.; Mori, T.; Hori, K. *Bull. Chem. Soc. Jpn.*, **1980**, *53*, 1714.
- [80] Terech, P. *Colloid Polym. Sci.*, **1991**, *269*, 490.
- [81] Nakashima, T.; Kimizuka, N. *Adv. Mater.*, **2002**, *14*, 1113.
- [82] Terech, P.; Ramasseul, R.; Volino, F. *J. Phys. (France)*, **1985**, *46*, 895.
- [83] Yun, Y.J.; Park, S.M.; Kim, B.H. *Chem. Commun*, **2003**, 254.

- [84] Pilpel, N. *Chem. Rev.*, **1963**, 63, 221.
- [85] Bhattacharya, S.; Krishnan-Ghosh, Y.I. *Chem. Commun.*, **2001**, 185.
- [86] Jung, J.H.; Yoshida, K.; Shimizu, T. *Langmuir*, **2002**, 18, 8724.
- [87] Boettcher, C.; Schade, B.; Fuhrhop, J.-H. *Langmuir*, **2001**, 17, 873.
- [88] Yamada, N.; Matsubara, K.; Narumi, K.; Sato, Y.; Koyama, E.; Ariga, K. *Colloids and Surfaces A.*, **2000**, 169, 271.
- [89] Gronwald, O.; Shinkai, S. *J. Chem. Soc. Perkin Trans.*, **2001**, 2, 1933.
- [90] Oda, R.; Huc, I.; Candau, S.J. *Angew. Chem. Int. Ed.*, **1998**, 37, 2689.
- [91] Mueller, A.; O'Brien, D.F. *Chem. Rev.*, **2002**, 102, 727.
- [92] Tajima, K.; Aida, T. *Chem. Commun.*, **2000**, 2399.
- [93] Akimoto, A.; Dorn, K.; Gros, L.; Ringsdorf, H.; Schupp, H. *Angew. Chem. Int. Ed.*, **1981**, 20, 90.
- [94] Berthier, D. PhD Thesis, Bordeaux University I, **2000**.
- [95] Paleos, C.; M.; Malliaris, A. *J. Macromol. Chem. - Rev. Macromol. Chem. Phys.*, **1988**, C28 384, 403.
- [96] Summers, M.; Eastoe, J.; Davis, S.; Du, Z.; Richardson, R. M.; Heenan, R.K.; Steytler, D.; Grillo, I. *Langmuir*, **2001**, 17, 5388.
- [97] Kline, S.R. *Langmuir*, **1999**, 15, 2726.
- [98] Stupp, S.I.; Osenar, P. *Materials Science and Technology*, **1999**, 513.
- [99] Regen, S.L.; Czech, B.; Singh, A. *J. Am. Chem. Soc.*, **1980**, 102, 6638.
- [100] Fukuda, H.; Kawata, K.; Okuda, H.; Regen, S.L. *J. Am. Chem. Soc.*, **1990**, 112, 1635.
- [101] Lee, Y.-S.; O'Brien, E.F. *J. polymer. Sci. Part A: Polym. Chem.*, **1994**, 32, 1437.
- [102] Paleos, C.N. *J. Macromol. Sci.*, **1991**, c30, 379.
- [103] Lee, Y.-S.; Yang, J.-Z.; Sisson, T.M.; Frankel, D.A.; Gleeson, J.T.; Aksay, E.; Keller, S.L.; Gruner, S.M.; O'Brien, D.E. *J. Am. Chem. Soc.*, **1995**, 117, 5573.
- [104] Pindzola, B.A.; Hoag, B.P.; Gin, D.L. *J. Am. Chem. Soc.*, **2001**, 123, 4617.
- [105] Srisiri, W.; Sisson, T.M.; O'Brien, D.F.; McGrath, K.M.; Han, Y.; Gruner, S.M. *J. Am. Chem. Soc.*, **1997**, 119, 4866.
- [106] Wang, G.; Hamilton, A.D. *Chem. Eur. J.*, **2002**, 8, 1954.
- [107] Masuda, M.; Hanada, T.; Yase, K.; Shimizu, T. *Macromolecules*, **1998**, 31, 9403.
- [108] Masuda, M.; Hanada, T.; Okada, Y.; Yase, K.; Shimizu, T. *Macromolecules*, **2000**, 33, 9233.
- [109] Tamaoki, M.; Shimada, S.; Okada, Y.; Belaisaoui, A.; Kruk, G.; Yase, K.; Matsuda, H. *Langmuir*, **2000**, 16, 7545.
- [110] de Loos, Maaik, Esch, J.V.; Stokroos, I.; Kellogg, R.M.; Feringa, B.L. *J. Am. Chem. Soc.*, **1997**, 119, 12675.
- [111] Beginn, U.; Zipp, G.; Möller, M. *Chem. Eur. J.*, **2000**, 6, 2016.
- [112] Ihara, H.; Takafuji, M.; Hyrayama, C. *Langmuir*, **1992**, 8, 1548.
- [113] Gu, W.; Lu, L.; Chapman, G.B.; Weiss, R.G. *Chem. Commun.*, **1997**, 543.
- [114] Takafuji, M.; Ishiodori, A.; Sakurai, T.; Ihara, H. *Chem. Commun.*, **2004**, 1122.
- [115] Mann, S.; Ed. *Biomimetic Materials, Chemistry*, New York: VCH, **1996**.
- [116] Burkett, S.L.; Mann, S. *Chem. Commun.*, **1996**, 321.
- [117] van Bommel, K.J.C.; Friggeri, A.; Shinkai, S. *Angew. Chem. Int. Ed.*, **2003**, 42, 980.
- [118] Ono, Y.; Nakashima, K.; Sano, M.; Kanekiyo, Y.; Inoue, K.; Hojo, J.; Shinkai, S. *Chem. Commun.*, **1998**, 1477.
- [119] Jung, J. H.; Kobayashi, H.; Masuda, M.; Shimizu, T.; Shinkai, S. *J. Am. Chem. Soc.*, **2001**, 123, 8785.
- [120] Sugiyasu, K.; Tamaru, S.; Takeuchi, M.; Berthier, D.; Huc, I.; Oda, R.; Shinkai S. *Chem. Commun.*, **2002**, 1212.

- [121] Jung, J.H.; Yoshida, K.; Shimizu, T. *Langmuir*, **2002**, *18*, 8724.
- [122] El Rassy, H.; Buisson, P.; Bouali, B.; Perrard, A.; Pierre, A.C. *Langmuir*, **2003**, *19*, 358.
- [123] Friggeri, A.; Gronwald, O.; van Bommel, K.J.C.; Shinkai, S.; Reinhoudt, D.N. *Chem. Commun.*, **2001**, 2434.
- [124] Yager, P.; Schoen, P.E. *Mol. Cryst. Liq. Cryst.*, **1984**, *106*, 371.
- [125] Yager, P.; Schoen, P.E.; Davies, C.; Price, R.; Singh, A. *Biophys. J.*, **1985**, *48*, 899.
- [126] Georger, J.H.; Singh, A.; Price, R.R.; Schnur, J.M.; Yager, P.; Schoen, P.E. *J. Am. Chem. Soc.*, **1987**, *109*, 6175.
- [127] Schnur, J.M. *Science*, **1993**, *262*, 1669.
- [128] Yamada, K.; Ihara, H.; Ide, T.; Fukumoto, T.; Hirayama, C. *Chemistry Letters.*, **1984**, 1713.
- [129] Kulkarni, V.S.; Boggs, J.M.; Brown, R.E. *Biophys. J.*, **1999**, *77*, 319.
- [130] Sommerdijk, N.A.J.M.; Lambermon, M.H.L.; Feiters, M.C.; Nolte, R.J.M.; Zwanenburg, B. *Chem. Commun.*, **1997**, 1423.
- [131] Tachibana, T.; Kambara, H. *J. Am. Chem. Soc.*, **1965**, *87*, 3015.
- [132] Tachibana, T.; Kambara, H. *Bull. Chem. Soc. Jpn.*, **1969**, *42*, 3422.
- [133] Schnur, J.M.; Ratna, B.R.; Selinger, J.V.; Singh, A.; Jyothi, G.; Easwaran, K.R.K. *Science*, **1994**, *264*, 945.
- [134] McCrea, J.F.; Angerer, S. *Biochem. Biophys. Acta*, **1960**, *42*, 357.
- [135] Ramanathan, N.; Currie, A.L.; Colvin, J.R. *Nature*, **1961**, *190*, 779.
- [136] Kunitake, T.; Yamada, N. *Chem. Commun.*, **1986**, 655.
- [137] Yamada, N.; Sasaki, T.; Murata, H.; Kunitake, T. *Chem. Lett.*, **1989**, 205.
- [138] Kunitake, T.; Kim, J.-M.; Ishikawa, Y. *J. Chem. Soc. Perkin Trans.*, **2**, **1991**, 885.
- [139] Nakashima, N.; Asakuma, S.; Kim, J.-M.; Kunitake, T. *Chemistry Letters.*, **1984**, 1709.
- [140] Nakashima, N.; Asakuma, S.; Kunitake, T. *J. Am. Chem. Soc.*, **1985**, *107*, 509.
- [141] Ihara, H.; Fukumoto, N.; Hirayama, C.; Yamada, K. *Nippon Kagakukaishi*, **1987**, *3*, 543.
- [142] Svenson, S.; Messersmith, P.B. *Langmuir*, **1999**, *15*, 4464.
- [143] Murata, K.; Aoki, K.; Suzuki, T.; Harada, T.; Kawabata, H.; Komori, T.; Ohseto, F.; Ueda, K.; Shinkai, S. *J. Am. Chem. Soc.*, **1994**, *116*, 6664.
- [144] Becerril, J.; Burguete, M.I.; Escuder, B.; Luis, S.V.; Miravet, J.F.; Querl, M. *Chem. Commun.* **2002**, 738.
- [145] Hanabusa, K.; Maesaka, Y.; Kimura, M.; Shirai, H.; *Tetrahedron. Lett.* **1999**, *40*, 2385.
- [146] Shimizu, T.; Masuda, M.; Kogiso, M.; Asakawa, M. *J. of the National Institute of Materials and Chem. Research*, **1998**, *6*, 235.
- [147] Shimizu, T.; Masuda, M. *J. Am. Chem. Soc.*, **1997**, *119*, 2812.
- [148] Thomas, B.; Safinya, C. R.; Plano, R.J.; Clark, N.A. *Science*, **1995**, *267*, 1635.
- [149] Ihara, H.; Yoshitake, M.; Takafuji, M.; Yamada, T.; Sagawa, T.; Hirayama, C. *Liquid Cryst.*, **1999**, *26*, 1021.
- [150] Takafuji, M.; Ihara, H.; Hirayama, C.; Hachisako, H.; Yamada, K. *Liq. Cryst.*, **1995**, *18*, 97.
- [151] Nakashima, N.; Asakuma, S.; Kunitake, T. *J. Am. Chem. Soc.*, **1985**, *107*, 509.
- [152] Singh, A.; Burke, T.G.; Calvert, J.M.; Georger, J.H.; Herendeen, B.; Price, R.R.; Schoen, P.E.; Yager, P. *Chem. Phys. Lipids*, **1988**, *47*, 135.
- [153] Spector, M.S.; Selinger, J.V.; Singh, A.; Rodrigues, J.M.; Price, R.R.; Schnur, J.M. *Langmuir*, **1998**, *14*, 3493.

- [154] Pakhomov, S.; Hammer, R.P.; Mishra, B.K.; Thomas, B.N. *Proc. Natl. Acad. Sci., USA*, **2003**, *100*, 3040.
- [155] Yang, W.; Chai, X.; Chi, L.; Liu, X.; Cao, Y.; Lu, R.; Jiang, Y.; Tang, X.; Fuchs, H.; Li, T. *Chem. Eur. J.* **1999**, *5*, 1144.
- [156] Lindsell, W.E.; Preston, P.N.; Seddon, J.M.; Rosair, G.M.; Woodman, T.A.J. *Chem. Mater.* **2000**, *12*, 1572.
- [157] von Berlepsch, H.; Kirstein, S.; Böttcher, C. *J. Phys. Chem. B* **2003**, *107*, 9646.
- [158] von Berlepsch, H.; Böttcher, C.; Ouart, A.; Regenbrecht, M.; Akari, S.; Keiderling, U.; Schnablegger, H.; Dähne, S.; Kirstein, S. *Langmuir*, **2000**, *16*, 5908.
- [159] Giuleri, F.; Krafft, M.-P.; Riess, J.G. *Angew. Chem. Int. Ed. Engl.*, **1994**, *33*, 1514.
- [160] Giuleri, F.; Guillod, F.; Greiner, J.; Krafft, M.-P.; Riess, J.G. *Chem. Eur. J.*, **1995**, *2*, 1335.
- [161] Matsui, H.; Pan, S.; Gologan, B.; Jonas, S.H. *J. Phys. Chem. B*, **2000**, *104*, 9576.
- [162] Shimizu, T.; Iwaura, R.; Masuda, M.; Handada, T.; Yase, K. *J. Am. Chem. Soc.*, **2001**, *123*, 5947.
- [163] Zastavker, Y.V.; Asherie, N.; Lomakin, A.; Pande, J.; Donovan, J.; M.; Schnur, J.; M.; Benedek, G.B. *Proc. Natl. Acad. Sci. USA*, **1999**, *96*, 7883.
- [164] Thomas, B.N.; Corcoran, R.C.; Cotant, C.L.; Lindemann, C.M.; Kirsch, J.E.; Persichini, P.J. *J. Am. Chem. Soc.*, **1998**, *120*, 12178.
- [165] Thomas, B.N.; Lindemann, C.M.; Clark, N.A. *Phys. Rev. E*, **1999**, *59*, 3040–3047.
- [166] Thomas, B.N.; Lindemann, C.M.; Corcoran, R.C.; Cotant, C.L.; Kirsch, J.E.; Persichini, P.J. *J. Am. Chem. Soc.*, **2002**, *124*, 1227.
- [167] Lin, Y.-C.; Kachar, B.; Weiss, R.G. *J. Am. Chem. Soc.*, **1989**, *111*, 5542.
- [168] Estroff, L.A.; Leiserowitz, L.; Addadi, L.; Weiner, S.; Hamilton, A.D. *Adv. Mater.*, **2003**, *15*, 39.
- [169] Shirakawa, M.; Kawano, S.; Fujita, N.; Sada, K.; Shinkai, S. *J. Org. Chem.*, **2003**, *68*, 5037.
- [170] Placin, F.; Desvergne, J.-P.; Belin, C.; Buffeteau, T.; Desbat, B.; Ducasse, L.; Lasségués, J.-C. *Langmuir*, **2003**, *19*, 4563.
- [171] Svenson, S.; Kirste, B.; Fuhrkop, J.-H. *J. Am. Chem. Soc.*, **1994**, *116*, 11969.
- [172] Mamiya, J.; Kanie, K.; Hiyama, T.; Ikeda, T.; Kato, T. *Chem Commun*, **2002**, 1870.
- [173] Nakano, K.; Hishikawa, Y.; Sada, K.; Miyata, M.; Hanabusa, K. *Chem. Lett.*, **2000**, 1170.
- [174] Sada, K.; Shiomi, N.; Miyata, M. *J. Am. Chem. Soc.*, **1998**, *120*, 10543.
- [175] Masuda, M.; Shimizu, T. *Chem. Commun.*, **1996**, 1057.
- [176] Terech, P.; Rodriguez, V.; Barnes, J.D.; McKenna, G.B. *Langmuir*, **1994**, *10*, 3406.
- [177] Ostuni, E.; Kamaras, P.; Weiss, R.G. *Angew. Chem. Int. Ed.*, **1996**, *35*, 1324.
- [178] Selinger, J.; V.; MacKintosh, F.C.; Schnur, J. M. *Phys. Rev. E.*, **1996**, *53*, 3804.
- [179] Selinger, J.V.; Spector, M.S.; Schnur, J.M. *J. Phys. Chem. B.*, **2001**, *105*, 7158.
- [180] Oda, R.; Huc.; I.; Schmutz, M.; Candau, S.J.; MacIntosh, F.C. *Nature*, **1999**, *399*, 566.
- [181] John, G.; Jung, J.H.; Minamikawa, H.; Yoshida, K.; Shimizu, T. *Chem. Eur. J.*, **2002**, *8*, 5494.
- [182] Svenson, S.; Messersmith, P.B. *Langmuir*, **1999**, *15*, 4464.
- [183] Shimizu, T.; Hato, M. *Biochim. Biophys. Acta*, **1993**, *1147*, 50.
- [184] Menger, F.M.; Keiper, J.S. *Angew. Chem. Int. Ed.*, **2000**, *39*, 1906.
- [185] Zana, R. *Gemini Surfactants*, New York: Marcel Dekker, **2004**.
- [186] Rosen, M.J. *J. Surf. Deterg.*, **1998**, *1*, 547.
- [187] Fiscaro, E.; Compari, C.; Rozycka-Roszak, B.; Viscardi, G.; Quagliotto, P.L. *Curr. Top. Colloid Interface Sci.*, **1997**, *2*, 53.

- [188] Alami, E.-O.; Holmberg, K. *Adv. Colloids Interface Sci.*, **2003**, 100-102, 13.
- [189] Menger, F.M.; Littau, C. A. *J. Am. Chem. Soc.*, **1991**, 113, 1451.
- [190] Zana, R.; Benraou, M.; Rueff, R. *Langmuir*, **1991**, 7, 1072.
- [191] Renouf, P.; Mioscowski, C.; Lebeau, L.; Hebrault, D.; Desmurs, J.-R. *Tetrahedron Lett.*, **1998**, 39, 1357.
- [192] Oda, R.; Huc, I.; Candau S. *J. Chem. Commun.*, **1997**, 2105.
- [193] Zana, R.; Levy, H.; Papoutsi, D.; Beinert, G. *Langmuir*, **1995**, 11, 3694.
- [194] Zana, R.; In, M. *Uzbek J. Phys.* **1999**, 24.
- [195] Rosen, M.J.; Gao, T.; Nakatsuji, Y.; Masuyama, A. *Colloids Surf. A*, **1994**, 88, 1.
- [196] Esumi, K.; Goino, M.; Koide, Y. *Colloid Interface Sci.*, **1996**, 183, 539.
- [197] In, M.; Bec, V.; Aguerre-Chariol, O.; Zana, R. *Langmuir*, **2000**, 16, 141.
- [198] Danino, D.; Talmon, Y.; Zana, R.; Levy, H.; Beinert, G. *Science*, **1995**, 269, 1420.
- [199] Kim, T.-S.; Kida, T.; Nakatsuji, Y.; Ikeda, I. *Langmuir*, **1996**, 12, 6304.
- [200] Rosen, M.J. *Chem. Technol.*, **1993**, 30.
- [201] Danino, D.; Talmon, Y.; Zana, R. *Langmuir*, **1995**, 11, 1448.
- [202] Frindi, M.; Michels, B.; Levy, H.; Zana, R. *Langmuir*, **1994**, 10, 1140.
- [203] Alami, E.; Levy, H.; Zana, R.; Skoulios, A. *Langmuir*, **1993**, 9, 940.
- [204] De, S. Aswal, V.; K.; Goyal, P. S.; Bhattacharya, S. *J. Phys. Chem. B*, **102**, 6152.
- [205] Rosen, M.; Song, L.D. *J. Colloid Interface Sci.*, **1996**, 179, 261.
- [206] Oda, R.; Huc, I.; Candau, S.J. *Angew. Chem. Int. Ed.*, **1998**, 37, 2689.
- [207] Bhattacharya, S.; De, S. *Langmuir*, **1999**, 15, 3400.
- [208] Zana, R. *J. Colloid Interface Sci.*, **2002**, 252, 259.
- [209] Pinzola, B. A.; Jin, J.; Gin, D.L. *J. Am. Chem. Soc.*, **2003**, 123, 2940.
- [210] Oda, R.; Huc, I.; Homo, J.-C.; Heinrich, B.; Schmutz, M.; Candau, S.J. *Langmuir*, **1999**, 15, 2384.
- [211] Estroff, L.A.; Hamilton, A.D. *Angew. Chem. Int. Ed.*, **2000**, 39, 19.
- [212] Jaeger, D.A.; Wang, Y. Pennington, R.L. *Langmuir*, **2002**, 18, 9259.
- [213] Menger, F.M.; Peresykin, A.V. *J. Am. Chem. Soc.*, **2001**, 123, 5614.
- [214] Menger, F.M.; Sereyuk, C.A.; Apkarian, R.P.; Write, E.R. *J. Am. Chem. Soc.*, **2002**, 124, 12408.
- [215] Menger, F.M.; Peresykin, A.V. *J. Am. Chem. Soc.*, **2003**, 125, 5340.
- [216] Abdallah, D.J.; Sirchio, S.A. Weiss, R.G. *Langmuir*, **2000**, 16, 7558.
- [217] Hoffmann, H.; Krämer, U.; Thurn, H. *J. Phys. Chem.*, **1990**, 92, 2027.
- [218] van der Schoot, P.; Cates, M.E. *J. Chem. Phys.*, **1994**, 101, 5040.
- [219] Lachenmayer, K.; Oppermann, W. *J. Chem. Phys.*, **2002**, 116, 392.
- [220] Hong, M.K.; Narayan, O.; Goldstein, R.E.; Shyamsunder, E.; Austin, R.H.; Fisher, D.S.; Hogan, M. *Phys. Rev. Lett.*, **1992**, 68, 1430.
- [221] Oizumi, J.; Kimura, Y.; Ito, K.; Hayakawa, R. *J. Chem. Phys.*, **1996**, 104, 9137.
- [222] Oda, R.; Lequeux, F.; Mendes, E. *Journal de Phys. II (France)*, **1996**, 6, 1429.
- [223] Maier, B.; Seifert, U.; Rädler, J.O. *Europhys. Lett.*, **2002**, 60, 622.
- [224] Prosser, S.R.; Hunt, S.A.; DiNatale, J.A.; Vold, R.R. *J. Am. Chem. Soc.*, **1996**, 118, 269.
- [225] Katsaras, J.; Donaberger, R.L.; Swainson, I.P.; Tennant, D.C.; Tun, Z.; Vold, R.R.; Prosser, R. S. *Phys. Rev. Lett.*, **1997**, 78, 899.
- [226] Rosenblatt, C.; Yager, P.; Schoen, P. *Biophys. J.*, **1987**, 52, 295.
- [227] Terech, P.; de Geyer, A.; Struth, B.; Talmon, Y. *Adv. Mat.*, **2002**, 14, 495.
- [228] Oda, R.; Laguerre, M.; Huc, I.; Desbat, B. *Langmuir*, **2002**, 18, 9659.
- [229] Berthier, D.; Buffeteau, T.; Léger, J.-M.; Oda, R. Huc, I. *J. Am. Chem. Soc.*, **2002**, 124, 13486.
- [230] Oda, R. Huc, I.; Candau, S. *J. Angew. Chem. Int. Ed.*, **1998**, 37, 2689.

- [231] Oda, R. Huc, I.; Schmutz, M.; Candau, S.J.; MacKintosh, F. *Nature*, **1999**, *339*, 566.
- [232] Singh, A.; Burke, T.G.; Calvert, J.M.; Georger, J.H.; Herendeen, B.; Price, R.R.; Schoen, P.E.; Yager, P. *Chemistry and Physics of Lipids*, **1988**, *47*, 135.
- [233] Spector, M.S.; Selinger, J.V.; Singh, A.; Rodriguez, J.M.; Price, R.R.; Schnur, J.M. *Langmuir*, **1998**, *14*, 3493.

SYSTEMS – HYDROGELS

Chapter 17

ADVANCES IN MOLECULAR HYDROGELS

Santanu Bhattacharya^{1,2}, Uday Maitra^{1,2}, Samrat Mukhopadhyay¹,
and Aasheesh Srivastava¹

¹Department of Organic Chemistry, Indian Institute of Science, Bangalore 560 012, India

²The Chemical Biology Unit, Jawaharlal Nehru Centre for Advanced Scientific Research,
Bangalore 560 064, India

1. Introduction	613
2. Historical Perspectives	615
3. Amino Acid and Oligopeptide Based Hydrogelators	616
4. β -Peptide Based Hydrogelators	625
5. Carbohydrate Based Gelators	628
6. Hydrogelators from Bola-amphiphiles and Gemini Surfactants	631
7. Miscellaneous Hydrogelators	634
8. Bile Acid Based Hydrogelators	636
9. Structural and Dynamic Aspects of Hydrogels	640
10. Application of Hydrogels in Materials Science	642
11. Perspectives for the Future	643

1. Introduction

Gel formation in water (hydrogels) has been well documented with polymeric substances either from natural or synthetic origin [1]. Gelation with gelators of water (e.g., gelatin) is believed to occur by chemical and/or physical cross-linking of polymeric chains, leading to the formation of highly entangled three-dimensional networks which trap water molecules presumably through a combination of surface forces and hydrogen bonding interactions. When the driving forces for the gelation involve only non-covalent interactions (physical), the resulting hydrogels (*molecular gels*) are found to

be thermo-reversible. For instance, polymers based on polyacrylic and polymethacrylic backbones show this behavior. On the other hand, the gels formed by chemical cross-linking (e.g., polyesters, polyamides etc.) generally do not display thermo-reversible behavior.

Hydrogels are important materials for biomedical applications, for example, in tissue engineering, drug delivery systems and medical implants [2]. The importance of hydrogels in drug action has recently been highlighted [3]. Problems associated with conventional non-degradable polymeric gels have also been discussed. Only a few biodegradable polymers are available, and these are not suitable for hydrogel formation. Therefore, non-polymeric hydrogelators (i.e., low molecular mass organic gelators (LMOGs) of aqueous liquids) are promising candidates as alternatives to polymeric hydrogelators. Non-polymeric (molecular) gels are formed solely due to the self-assembly of small molecules through non-covalent interactions like hydrogen bonding, π - π stacking, van der Waals forces, and hydrophobic and electrostatic interactions. The number of reports on molecular hydrogelators is far fewer than that of organogelators (i.e., LMOGs of organic liquids), but has increased rapidly in recent times (Figure 1). This chapter will be concerned with the concepts, strategies and accomplishments in the area of molecular hydrogelators; a list of abbreviations is provided on page 644.

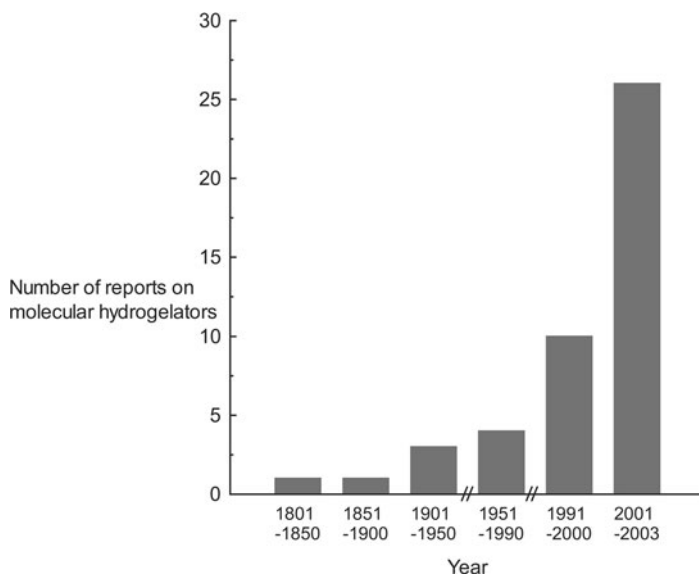


Figure 1. The number of reports on novel molecular hydrogelators has increased sharply in the last three years (taken from the reference section).

2. Historical Perspectives

For a more general history of gels, see the Introduction. LMOG hydrogelators were discovered more than a century ago. However, such findings went unnoticed perhaps because of the lack of appropriate terminology and semantics. In 1841, Lipowitz discovered the formation of a gelatinous mass from uric acid in aqueous media while studying its solubility properties in the presence of lithium carbonate (Figure 2) [4]. To the best of our knowledge, this is the first document published on a hydrogelator, uric acid (Figure 3a). At that

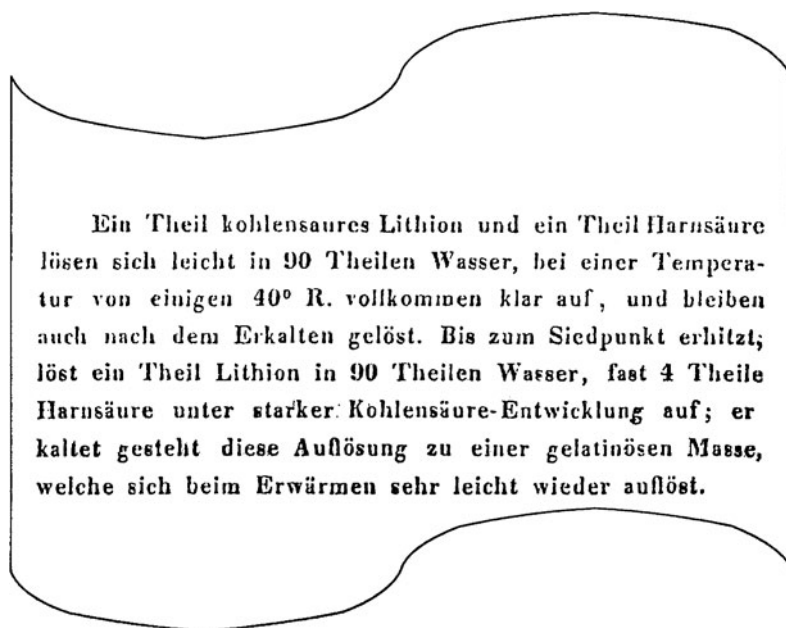


Figure 2. Lipowitz's description in *Ann. Chem. Pharm.*, **1841**, 38, 352.

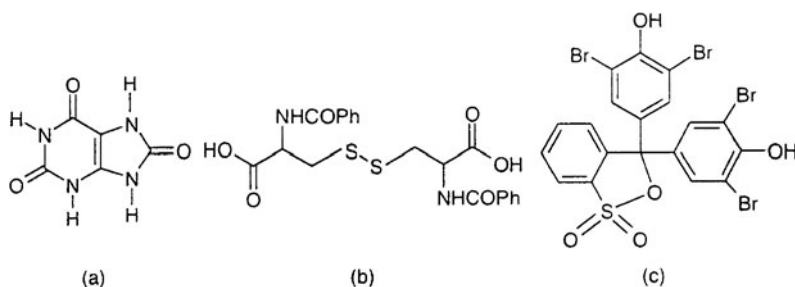


Figure 3. (a): Uric acid. (b): dibenzoyl cystine. (c): bromophenol blue.

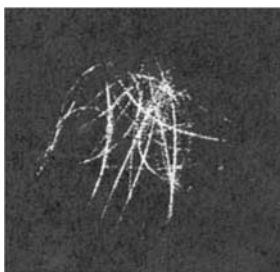


Figure 4. “Ultramicroscopic” image of 10% sodium-oleate jelly (140 X) obtained in 1912. Adapted from [8].

time, due to lack of microscopic facilities, it was not possible to obtain details about the physical organization of the gel. In 1879, Nageli addressed the issue pertinent to the structural aspects of micelles and gels, in general [5]. Gels were proposed to be composed of aggregated micelles, creating meshes, which are responsible for immobilizing water molecules in the interstitial spaces. Brenzinger first reported gelation of aqueous solutions of dibenzoyl cysteine in 1892 (Figure 3b) [6]. This was re-investigated by Gortner and Hoffman in 1921 [7]. Menger and Caran have recently evaluated detailed structure-property relationship of this class of molecules (Section 3). In 1912, ultramicroscopic studies were made on soap solutions and gelatin to get insights into the physical nature of such organizations [8]. Sodium-palmitate, -oleate and -stearate were shown to form jellies in aqueous media. Ultramicroscopic images revealed the self-assembled fibrillar networks (SAFINS) of the aggregates (Figure 4). Another interesting report appeared in 1939 on the gelation of aqueous solution of bromophenol blue (Figure 3c) [9]. Upon acidification, an alkaline solution of bromophenol blue became progressively more viscous and finally formed a clear lemon colored gel. These gels were stable for only a few hours, and eventually formed brown crystals, presumably due to the formation of the acid form of the dye. Aqueous gels from another class of molecules – bile salts – were first discovered in 1913, which will be discussed in Section 8 in detail.

3. Amino Acid and Oligopeptide Based Hydrogelators

This class of molecules has concurrent actions of hydrophobic effects (from amino acid side-chains) and hydrogen bonding (from amide linkages and hydrophilic side-chains). Hence they constitute one of the largest groups of hydrogelators. Self-assembling behavior of amino acid based surfactants were undertaken by Imae *et al.* [10]. It was observed that *N*-dodecyl-*L*-glutamic acid (Figure 5a) formed gels at low temperature and at low pH (<4.9). Surfactants

based on aspartic acid also resulted in gel-like materials at low pH. Lysine based unsymmetrical bola-amphiphiles (Figures 5b and 5c) were shown to form gels by Fuhrhop *et al.* [11].

“Bola-amphiphiles” (see Chapter 16) containing a long poly-methylene chain and two amino acids at the level of head groups gelated water (Figure 6). The Histidine derivative could gelate water at a lower concentration than the alanine derivative. However, these gels were found to be thermally unstable above 25° C [12].

Aroyl *L*-cystine derivatives were shown to rigidify water in the presence of co-solvents [5, 6]. Menger and Caran reinvestigated the gelation property of aroyl *L*-cystine derivatives [13]. The carboxamide derivatives were better gelators than the corresponding carboxylic acids (Figure 7). Carboxamide derivatives exhibited faster gelation, better rigidifying ability, and smaller influence of substitution elsewhere in the molecule as compared to the carboxylic acid derivatives. Enhanced hydrogen-bonding ability of the carboxamide group has been suggested to be responsible for the self-association. The disulfide linkage has been found to be critical for gelation, possibly due to the conformational

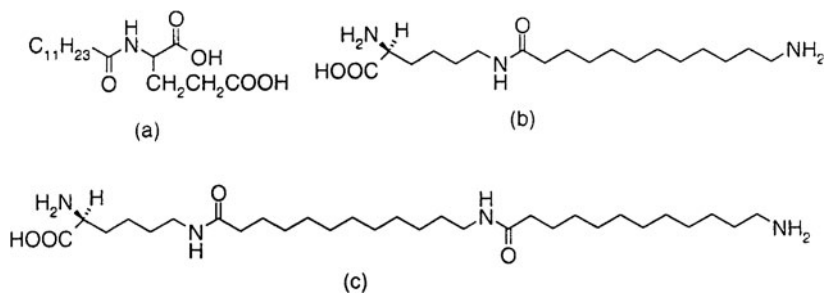


Figure 5. Amino acid based surfactants as hydrogelators.

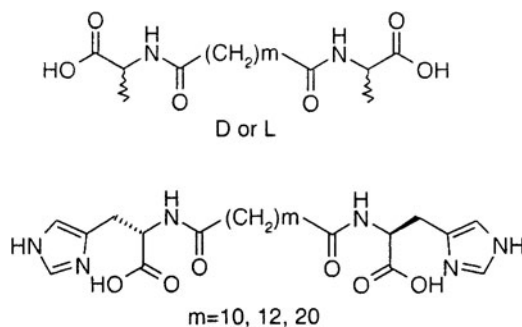


Figure 6. Bola-amphiphilic amino acid hydrogelators.

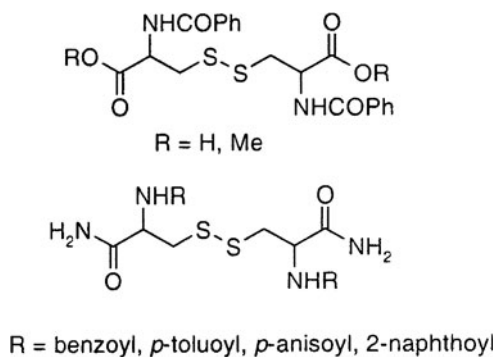


Figure 7. Aroyl *L*-cystine derived hydrogelators.

rigidity of the S-S bond that effectively directs the groups for hydrogen bonding. The best gelator had a naphthoyl amide group and a carboxamide moiety, underlining the importance of hydrophobic moieties in the efficient gelation of water. The relationship between gelation and crystallization was also addressed. According to this report, gelation could be favored if the solubility of a compound is decreased by the functional groups responsible for the intermolecular association. However, if the intermolecular forces are too strong, crystallization or precipitation prevails instead of gelation.

Dynamic mechanical analyses of gels provide quantitative information on the viscoelastic and rheological properties of materials by measuring the mechanical response of the samples as they are deformed under periodic stress (see Chapters 5 and 8). Menger and Caran have demonstrated the dominant elastic behavior ($G' > G''$) as a function of imposed stress (σ) for various *L*-cystine based gels using a 1-Hz oscillatory stress [13]. At the “yield stress” (σ_y) gels break under the applied force and begin to flow. Each gel has its characteristic σ_y according to its mechanical strength. The gel \rightarrow sol phase transition temperature was demonstrated by temperature-sweep oscillation rheology. The plot of G' and G'' vs. temperature showed a crossover point (from $G' > G''$ to $G' < G''$) suggesting a change from “solid like” to “liquid like” material.

Several other amino acid derivatives showed efficient hydrogelation ability. For example, Jokić *et al.* demonstrated that bis(amino acid)oxalyl amides were *ambidextrous* gelators, since they gelled both water and organic solvents (Figure 8) [14]. Concentration dependent UV and fluorescence studies suggested the formation of π - π stacked associates. Similarly, temperature-dependent NMR spectra indicated the dissociation of π - π stacked assemblies upon heating. It was proposed that the inter-molecular hydrophobic and π - π stacking interactions favor the formation of primary assemblies which were further stabilized by inter-molecular hydrogen-bonding interactions.

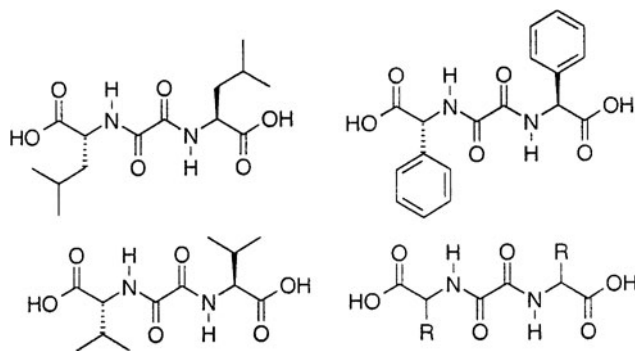


Figure 8. Bis(amino acid)oxalyl amide gelators.

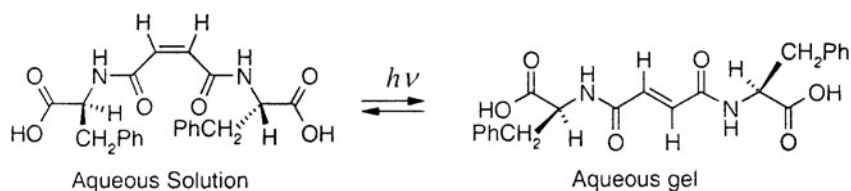


Figure 9. Photoisomerization driven gelation.

An interesting extension of this work was achieved by the exploitation of bis(phenylalanine)-maleic and fumaric acid derivatives for gelation (Figure 9) [15]. Only the (*trans*) fumaric acid derivative resulted in the hydrogel formation. Photoisomerization was shown to trigger a morphological transition at the supramolecular level (see Chapter 24). Thus, irradiating an aqueous solution of maleic amide resulted in gelation in <30 sec. Microscopic examination indicated that the initial microsphere morphology (solution) was converted to entangled fibrous structures (gel). ^1H NMR of the sample showed the formation of fumaric amide derivative upon irradiation with only traces of maleic amide. Gelation was not observed even in mixtures of maleic and fumaric amides. This is one example where hydrogelation is controlled by external stimuli (see Chapter 26).

Cyclohexane-*cis*-1,3,5-tricarboxamides derived from amino acids yielded potent gelators of water (Figure 10) [16]. Hydrogen bonding (from amides) and hydrophobic effects (from hydrophobic amino acids like methionine and phenylalanine) are important for gelation. The gelation process was found to be unaffected upon micelle formation when surfactants such as SDS, CTAB and OG were added.

A Sodium 11-aminoundecanoate unit appended to amino acids forms a new class of *ambidextrous* gelators [17]. Valine and α -phenylglycine derivatives

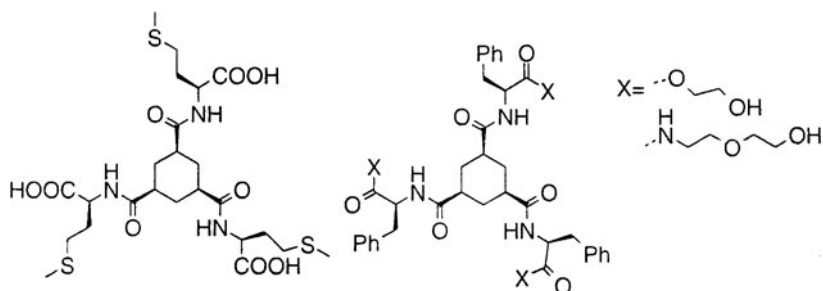


Figure 10. Cyclohexane-*cis*-1,3,5-tricarboxamides derived gelators.

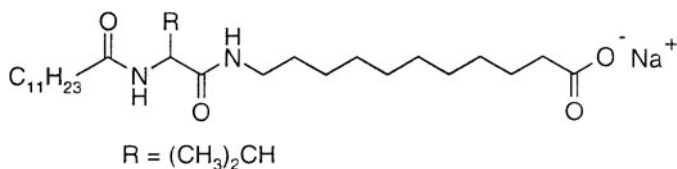


Figure 11. 11-Aminoundecanoate conjugated with amino acids.

gelled water (Figure 11). Pure enantiomers, as well as the racemates, showed gelation ability. In several cases reported earlier gelation was possible only with the pure enantiomers and not with the racemates [33, 44]. The gelation property could be tuned by (a) adjusting the ionization-state of the terminal carboxylic acid functionality, (b) introducing additional amide groups for hydrogen bonding, and (c) incorporating a chiral amino acid fragment.

A novel antibiotic-gelator that has triggered interest amongst some biologists is the vancomycin-pyrene conjugate (Figure 12) developed by Xing *et al.* that gels water at 0.36 wt.% [18]. In other words, immobilization of $\approx 23,000$ water molecules per gelator molecule was achieved. In the gel, pyrene units aggregated via π - π stacking as evidenced by an excimer-type band in the fluorescence spectrum. CD studies showed that in the gel-state, the peptide backbones are associated in a head-to-tail fashion, possibly by four hydrogen bonds.

Using aliphatic quaternary ammonium derivatives of *L*-glutamate, Nakashima and Kimizuka demonstrated the requirement for an aromatic surface to enhance aggregation in water (Figure 13) [19]. These cationic amphiphiles showed hydrogelation *only* when ion-paired with aromatic sulfonate anions, viz. naphthalene or anthracene sulfonates (NaphSO_3^- or AnthSO_3^-). A delicate balance between hydrophobicity and hydrophilicity was found to be important for gelation. Another significant observation was that fluorescence resonance energy transfer (FRET) from NaphSO_3^- to AnthSO_3^- was more efficient in the gel-state, than in the pre-gel state. This was ascribed to

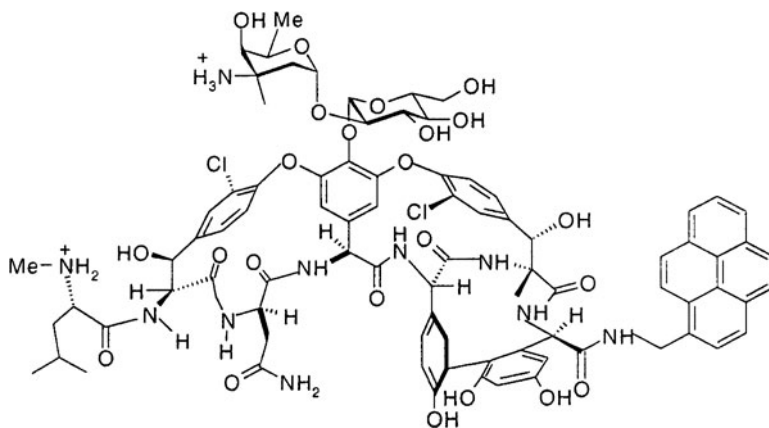


Figure 12. A gelator from vancomycin-pyrene conjugate.

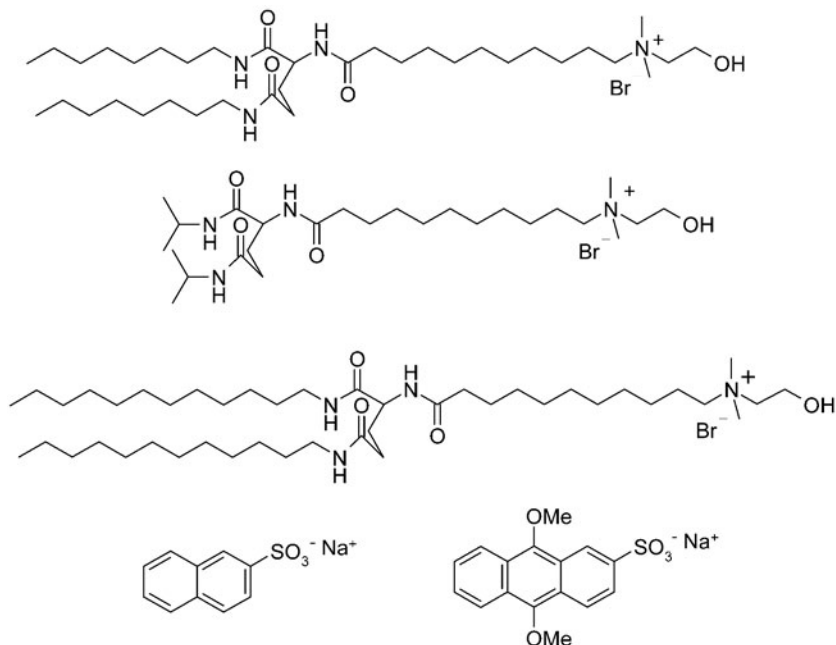


Figure 13. Light harvesting hydrogel-system.

the accumulation of NaphSO_3^- chromophores on the fibrous nano-assemblies, which makes them light harvesting supra-molecular networks.

Other strategies were also utilized for gelation to attain a requisite balance between hydrophobicity and hydrophilicity. The work of Suzuki *et al.*

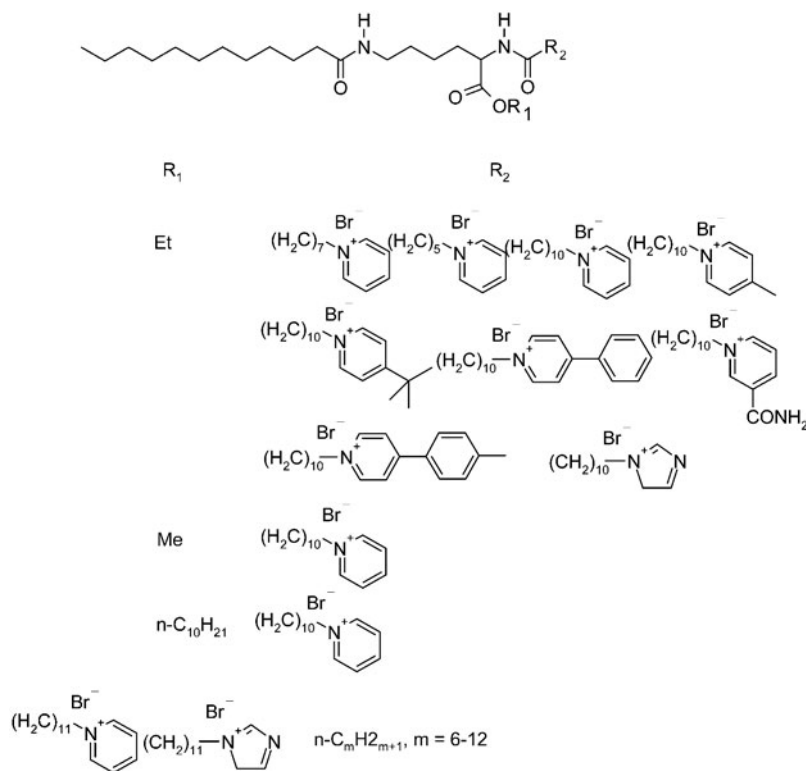


Figure 14. Hydrogelators based on quaternary ammonium derivatives of lysine.

reveals that the quaternary ammonium derivatives of amino-acid esters are very potent gelators [20]. These gelators are long-chain cationic derivatives of *L*-Lysine esters wherein the quaternary ammonium group provides water solubility (Figure 14). Here too, aromatic ammonium derivatives could gelate water much better than the aliphatic ammonium groups, probably because of π - π stacking interactions. The critical gelator concentration (cgc) in some cases was as low as 0.2 wt.%. 1H NMR and UV-vis studies indicated that in addition to intermolecular hydrogen bonding, π - π stacking is another driving force for gelation here. Variation of location of the quaternary ammonium group did not influence the gelation ability significantly. Thus, charge on either the ester side-chain or the amide side-chain resulted in efficient hydrogelation.

Urea derivatives of amino acids represent another class of low molecular weight hydrogelators. Estroff and Hamilton have demonstrated the gelation ability of *bis*-urea-glutamate esters in water in the presence of co-solvents with MGC in the range of <0.3 wt.% [21]. Buffers and solutions of high ionic strength were also gelated by these *bis*-urea derivatives (Figure 15).

Interestingly, these compounds formed vesicles at low pH. Upon increasing the pH, the solubility increased and gelation ensued. The efficiency of these gelators was increased through subtle structural modifications. Thus, mono-urea serine esters were used as gelators of *pure* water by Wuang and Hamilton (Figure 16) [22]. These molecules have molecular weights of <250 Da and hence constitute one of the smallest LMOGs of water. Structural analysis showed that aromatic esters were better gelators than their aliphatic counterparts, with lowest MGC of ~1% (w/v). The mono-urea derivatives had some advantages over their *bis*-urea counterparts: (a) easier synthesis; (b) lower molecular weights; (c) co-solvents were not needed for gelation.

Boettcher *et al.* reported gelation of water by *N*-dodecanoyl-serine (Figure 17) [23]. According to their observation the gelation was pH sensitive. Helical ribbons and tubules were observed between pH 4.9 and 6.4. In this pH range, hydrogen-bonding interaction arising from amide as well as $\text{COO}^- \dots \text{HOOC}$ interactions could be the driving force for aggregation. Aggregates in water had higher curvature (i.e., smaller pitch) than those in toluene, probably due to greater hydration force provided by water.

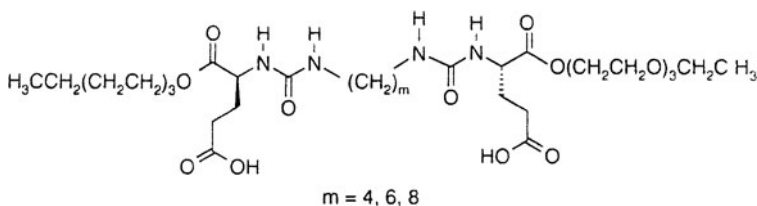


Figure 15. Bis-urea hydrogelator.

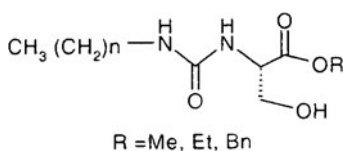


Figure 16. Mono-urea gelators.

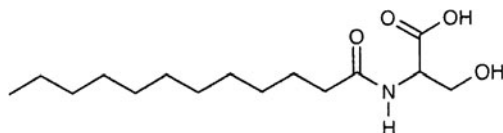


Figure 17. *N*-dodecanoyl-serine gelator.

Oligopeptide gelators are another important class of hydrogelators. They hold promise in applications as biocompatible hydrogels. An example of this class of gelator is the cyclic peptide (depsipeptide) cyclo[CH₂-CO-L-Leucyl-L-Leucine], prepared by de Vries *et al.* [24]. The 9-membered cyclic compound is an organo-gelator whereas one of the 18-membered analogs was found to be a hydrogelator in the presence of a small quantity of DMSO (Figure 18).

Another class of peptide amphiphile gelators has also been characterized (Figure 19) [25]. They combine the advantages of peptide backbone with those of amphiphiles that are known to self-assemble into various structures. The influence of the type of amino acid and the type of alkyl tail on gelation were investigated. Self-assembly could be triggered by changes in pH, the presence of a divalent cation and an increase in concentration. The presence of four consecutive cysteine residues allowed the formation of high molecular weight fibrous polymers upon (potentially reversible) oxidation of the thiol to disulfide. The thiol functionality was found to be important for gelation to occur. The intra-molecular disulfide bond formation suppressed self-assembly due

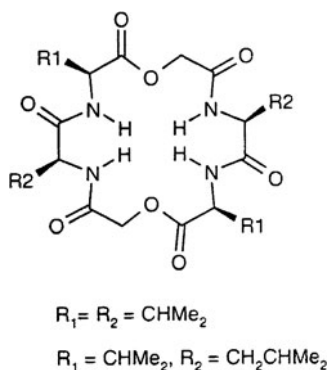


Figure 18. 18-Membered depsipeptide hydrogelator.

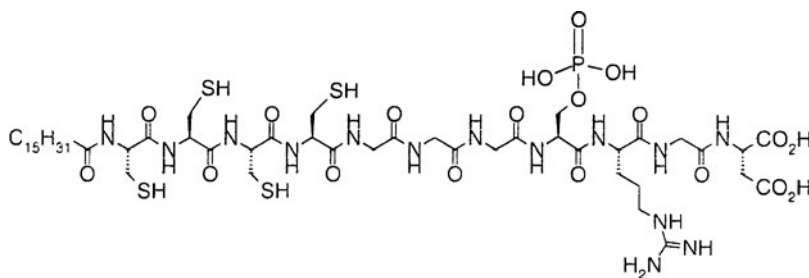


Figure 19. Peptide amphiphile.

to conformational changes. The gelation process remained unaffected by the replacement of tetra-cysteine with tetra-alanine. Gelation took place only in acidic conditions. As little as 0.25 wt.% of peptide was sufficient to form a self-supporting gel. Though nanofibres were formed at low initial concentrations, their organization into flat, parallel bundles occurred only beyond a critical concentration. The addition of Ca^{2+} ions led to immediate gelation, whereas the addition of K^{+} ions did not yield a gel.

4. β -Peptide Based Hydrogelators

Aggregation behavior of β -sheet peptides is of considerable interest due to their pathological implications [26]. Under certain conditions, some β -peptides aggregate to form thermoreversible gels. Also, their gelation can be controlled by various physical and chemical stimuli. Though these are *not* low molecular weight species *per se*, they still lead to “molecular gels” in that the networks are formed by supramolecular self-assembly of individual polypeptide molecules.

Radford and co-workers have designed a biological motif utilizing a β -sheet peptide sequence (**$\text{CH}_3\text{CO-Gln-Gln-Arg-Phe-Gln-Trp-Gln-Phe-Glu-Gln-Gln-NH}_2$**), which undergoes pronounced gelation in water [27]. Hydrophobic effects, π - π stacking, hydrogen bonding and coulombic interactions were suggested to be important contributors to the gelation of this β -sheet forming peptide.

Collier *et al.* found that a 16-amino acid peptide (FEK 16) consisting of alternating hydrophobic and hydrophilic residues, [**$\text{H}_2\text{N-(FEFEFKFK)}_2\text{-COOH}$**], self-assembled into β -sheet structure, which led to the formation of stable hydrogels in the presence of NaCl, KCl or CaCl_2 . The β -sheet structure is favored by the disposition of alternating hydrophobic and hydrophilic amino acid residues [28]. The same authors also showed that gelation could be thermally and photochemically triggered by utilizing stimuli-responsive liposomes designed to release salts such as CaCl_2 at a specific temperature or in response to near infrared (NIR) light exposure. Temperature and light-activated gelation of FEK 16/liposome system was detected using oscillating rheometry [28]. The light-sensitive system remained fluid in the dark, whereas it gelled rapidly upon irradiation by NIR light, as indicated by increase of dynamic storage modulus (G') by 2-3 orders of magnitude. Similar results were obtained for temperature-triggered gelation. Such an approach may be useful in biomedical applications. See Chapters 24 and 26 for other gel systems that respond to external stimuli.

Other examples of this class of molecules consist of unsymmetrical peptide bola-amphiphiles (see Chapter 16) [29]. These molecules contain head-groups formed by (*L*-glutamyl)₃glycine and tetraethylene glycol separated by a hydrophobic segment covalently conjugated using β -alanine, *p*-aminobenzoic

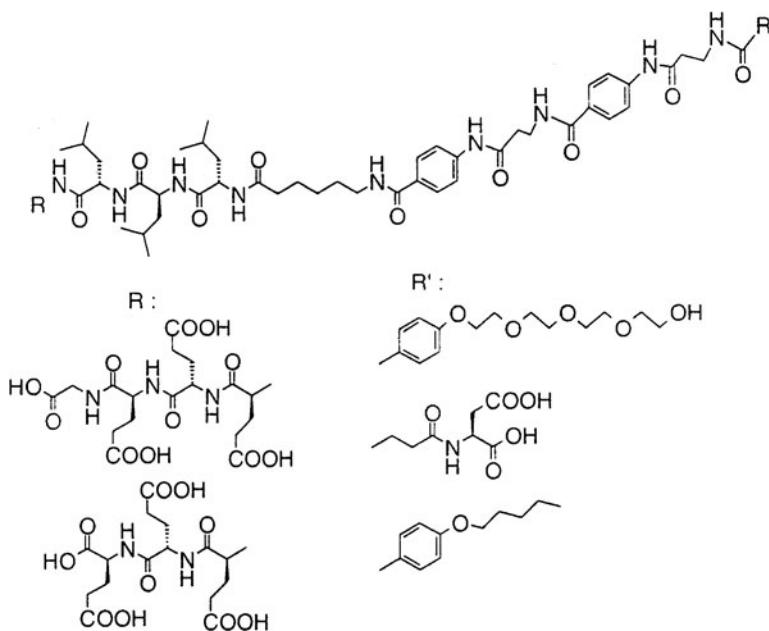


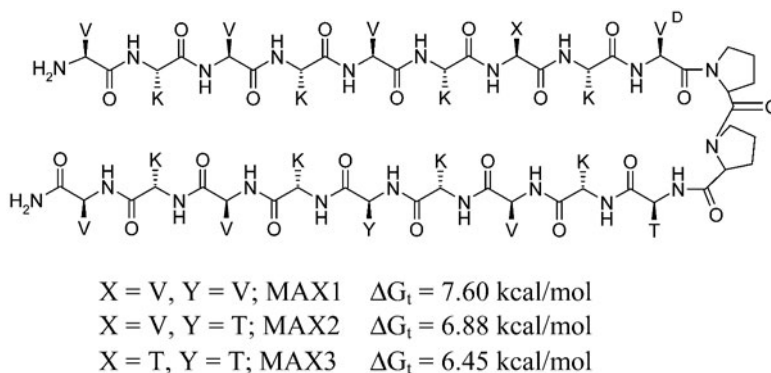
Figure 20. Unsymmetrical peptide bola-amphiphiles.

acid, 6-aminohexanoic acid and *L*-leucine (Figure 20). Exposure of an alkaline solution of peptide to HCl vapor led to self-assembly and subsequent gelation. The gels were translucent, birefringent and self-supporting. The formation of β -sheets was found to be essential for gelation, as evidenced by FTIR studies. Gelation occurred by the aggregation of cylindrical micelles formed by these peptides.

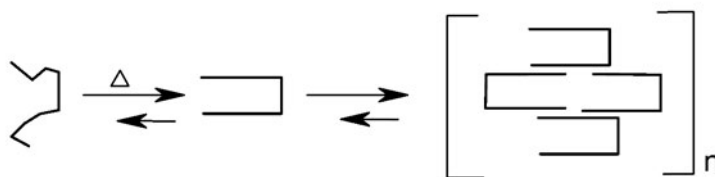
Schneider *et al.* reported pH-dependent intramolecular folding of a β -sheet hairpin peptide (MAX1, Figure 21) which self-assembled into hydrogels [30]. CD and FTIR spectral studies revealed that at low pH, the peptides are “unstructured” and their solutions are not viscous. An intra-molecular folding took place under basic conditions, leading to the formation of amphiphilic β -hairpins that assembled in an intermolecular fashion.

The kinetics for the gelation of β -hairpin peptide was measured using a time-sweep experiment at constant strain and frequency [30]. An increase in the storage modulus (G') was observed from ~ 1 Pa to > 1 kPa upon gelation. Rheological studies at lower peptide concentrations indicated that the crossover concentration from $G' < G''$ (liquid like) to $G' > G''$ (solid like) is ca. 1 wt.% (minimum gelling concentration).

Gels formed by β -peptides (Figure 21a) responded to both chemical stimuli (pH) and physical stimuli (temperature) [31]. It is interesting to note



(a)



(b)

Figure 21. (a): Structures of MAX1, MAX2 and MAX3 with their calculated free energies of transfer (ΔG_t) of unfolded peptide from octanol into water at 25°C. V, T and K are side-chains of valine, threonine and lysine, respectively. (b): Plausible scheme for thermally triggered folding and self-assembly.

that gelation was observed at *elevated* temperatures, and they became low-viscous solutions at lower temperatures. Heating causes the unimolecular folding of the peptide from random coil to amphiphilic β -hairpin by a mechanism similar to hydrophobic collapse. Eventually, folded polypeptide molecules self-assemble into a gel-network (Figure 21b). The β -sheet formation is enhanced by the presence of alternating hydrophilic/hydrophobic residues in the form of lysine and valine (an amino acid known to form β -sheet structures with high propensity) [31]. This process of folding followed by self-assembly could be modulated by varying the hydrophobic character of the peptide. The replacement of Val7 with Thr resulted in a less-hydrophobic peptide (see ΔG_t values in Figure 21) whose solutions led to self-assembly at a higher temperature ($\approx 60^\circ\text{C}$) than those of the peptide containing Val ($\approx 40^\circ\text{C}$). A similar peptide ($^D\text{Pro}10$ replaced by ^LPro) that is devoid of the propensity to form β -sheet structures, did not form a gel. This result establishes that folding of the peptide into a β -sheet structure is a key to gelation.

5. Carbohydrate Based Gelators

Several reports describe gelators of sugar derivatives (see Chapter 15). The first sugar based hydrogel was described by Pfannemuller and Welte, who examined the gelation behavior of gluconamides in aqueous solutions (Figure 22) [32]. All compounds that contained *one* non methylated linkage gave rise to gels whose structure consisted of rope-like fibrillar structures with right-handed helical twists. Compounds containing two non-methylated amide linkages formed gels consisting of flat ribbons devoid of twist. All compounds, containing amide groups formed gels at low concentrations and high temperatures, whereas the corresponding substances with *N*-methylated amide linkages were readily soluble in water. It was suggested that molecules self-assemble by hydrogen bonds, affording one-dimensional, quasi-crystalline, aggregates that led to the fibrils observed by microscopic studies.

Furhopp *et al.* described the gelation behavior of octyl (*L*- and *D*-) gluconamides in water (Figure 23) (see Chapter 18). Gelation occurred in the concentration range of 0.5–50% (w/v) [33]. The *L*-enantiomer produced left-handed helical fibers while the *D*-enantiomer produced right-handed fibrous assemblies. High-resolution electron microscopy showed “bulgy helices” formed by inter-twinning of the fibers. Differential scanning calorimetric (DSC) studies showed a sharp exothermic peak at 339 K on cooling associated with the gel-to-sol transition. This process was found to be reproducible and independent of concentration. Racemic mixtures yielded precipitates.

Bhattacharya and Acharya have reported that some long alkyl chain derivatives of lactosylamine and maltosylamine are potent gelators of water in

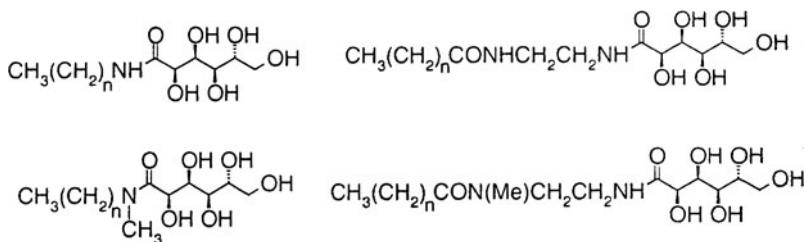


Figure 22. Long chain gluconamides that gel water.

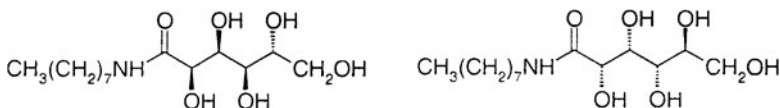


Figure 23. *D*- and *L*-Gluconamides.

the presence of a small amount of co-solvent (Figure 24). Mono-hexadecyl lactosylamine was found to be a more efficient gelator than its dihexadecyl analogue. The corresponding maltosylamine also displayed similar behavior. However, the reduced sugar form hexadecylamino-deoxylactitol, did not gelate water [34]. The addition of divalent cations in such systems afforded giant vesicles [35].

Sugar-based hydrogelators containing an azobenzene moiety linked to the saccharides via amide bridges were designed by Shinkai and co-workers (Figure 25) [36]. Gels were formed at concentrations as low as 0.05 wt.%. UV-vis studies indicated that aromatic π - π stacking of azobenzene moieties was probably the principal driving force. CD spectral studies indicated that the azobenzene moieties were stacked in a clockwise direction, confirming the right-handed helical growth of the gel fibers. SEM observations of the gel fibers show that this molecular scale helicity is also manifested in the handedness

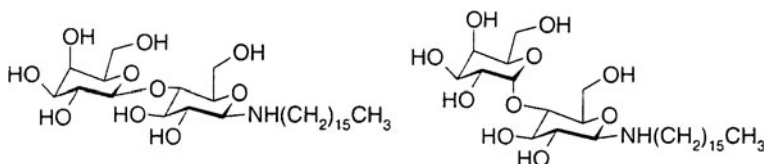


Figure 24. Glycosylamine-based hydrogelators.

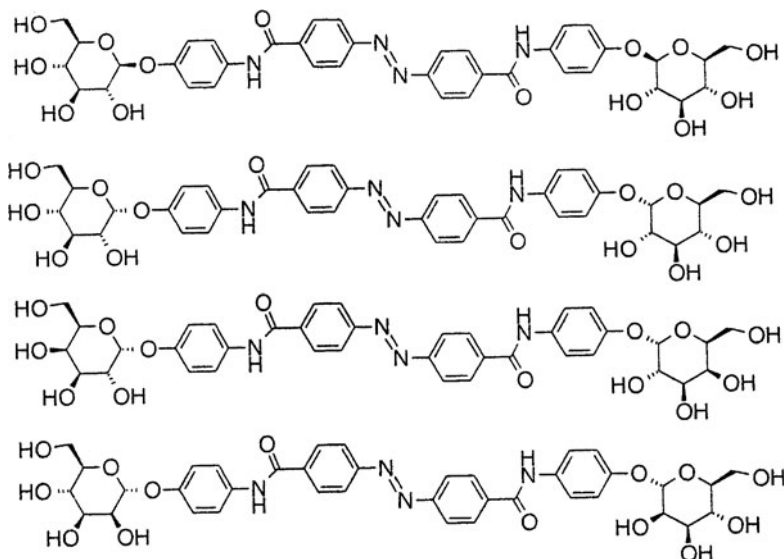


Figure 25. Azobenzene-sugar conjugates.

observed at the nanometer to micrometer scales as well. The presence of the glucose moiety was surmised to be the reason of this helicity. Planarity of the gelator molecules was found to be essential for their proper packing in the assemblies.

Combinatorial syntheses of glycodendrimers were also undertaken by McWatt and Boons (Figure 26), and some derivatives were found to gelate water [37]. These molecules are homologous compounds differing only in the length of intervening alkyl chains. Eight saccharide units were incorporated per molecule. Except compound **f** (Figure 26) all other compounds led to hydrogelation. Observed variations in T_{gel} resulted from the differences in the innermost tier length, n^1 . The replacement of peripheral melibiose moieties with galactoside units resulted in water-insoluble glycodendrons.

Gelators having an aldopyranose moiety, an aminophenyl group and a long alkyl chain in as a “double head group”, exhibited enhanced hydrogelation properties compared to the corresponding “single head group” form

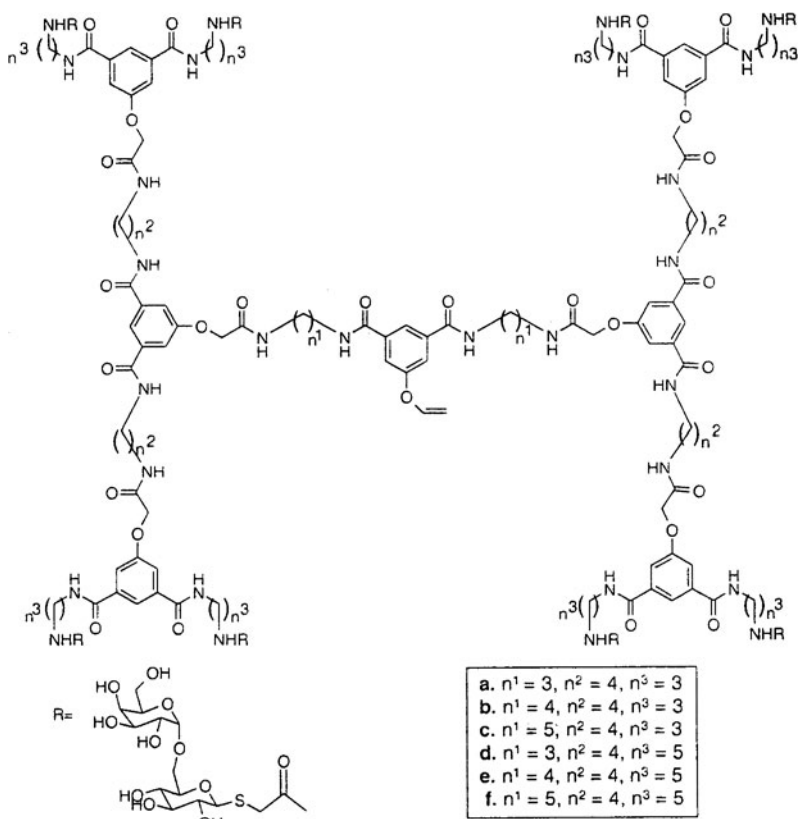


Figure 26. Glycodendrimer gelators.

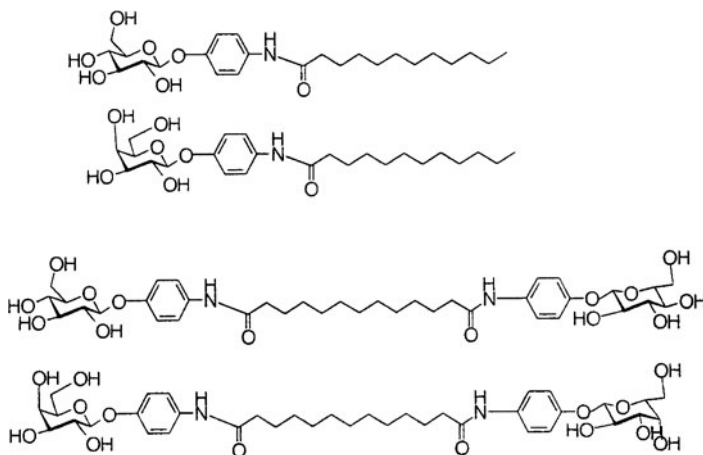


Figure 27. Aldopyranose bola-amphiphiles and their “monoamphiphile” analogues.

(Figure 27) [38]. The presence of two aldopyranose groups per molecule increased water solubility as well as hydrogen bonding. Other groups present in the molecule may promote hydrogen-bonding, π - π stacking interactions and interdigitations. These multiple stabilizing interactions resulted in very efficient gelation abilities at 0.05–5.0 wt.% of gelator. There are other advantages of a “bola-amphiphilic” molecular structure. While monovalent amphiphiles produced opaque gels that could be destroyed by mechanical agitation, aqueous suspensions of bola-amphiphiles resulted in the formation of transparent and more robust gels. Also, the bola-amphiphiles were able to gelate water without co-solvent, and their gels exhibited an ordered chiral structure.

In recent times, a combinatorial approach, using solid phase synthesis protocols, has been invoked by Kiyonaka *et al.* to synthesize numerous compounds based on glycosylated derivatives of amino acids [39]. Some of these derivatives were observed to be hydrogelators. The gels were stable between 0–250 mM NaCl and pH from 5 to 8. One of the gels was able to trap oxymyoglobin in its active form with low leakage into the liquid part.

6. Hydrogelators from Bola-amphiphiles and Gemini Surfactants

Bola-amphiphiles and gemini surfactants together form a class of hydrogelators. Amino acid, peptide and sugar based bola-amphiphiles and gemini surfactants have already been discussed in previous sections. Newkome *et al.* have shown that polyhydroxy dendritic bola-amphiphiles

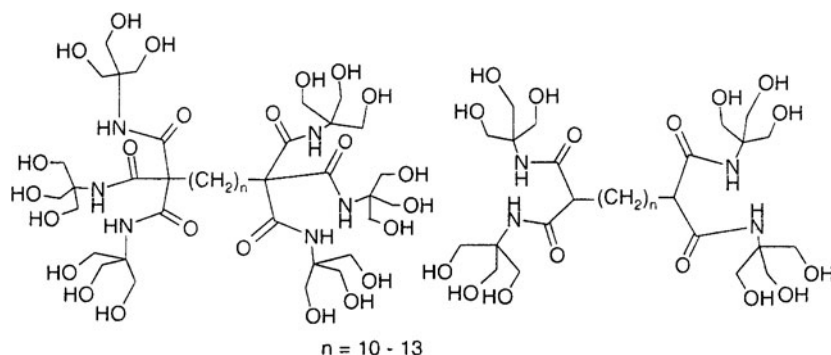


Figure 28. Arborols as hydrogelators.

arborols (*arborous*: relating to or formed by trees), form thermoreversible, thixotropic gels in aqueous media (Figure 28) [40]. Compounds with either six or nine hydroxyl groups on the termini and spacer chain lengths of ten to thirteen $-(CH_2)_n$ units formed gels at gelator concentrations of 2–10 wt.% over a wide range of pH (2–12) in buffered aqueous solutions of varying ionic strengths. These gels were investigated using viscometry and optical, electron, and fluorescence microscopies. Fluorescence microscopy, using a hydrophobic dye, chlorotetracycline as the reporter, was performed to identify the region of dye intercalation in the gel network. Since the dye is practically non-fluorescent in water, it was inferred from the strong fluorescence in the gel that the dye resides in regions that are hydrophobic.

In a few cases, gemini surfactants have been shown to act as potent gelators of aqueous fluids (see Chapter 16). Gemini surfactants are composed of two surfactant units that are covalently connected via charged head groups. These surfactants show aggregation properties markedly different from their “monomeric” counterparts [41–43]. Oda and co-workers have carried out interesting investigations on the aggregation properties of gemini surfactants [44]. For instance, they found that when *bis*-(hexadecyldimethylammonium)ethane was ion-paired with different tartrates, gelation of chlorinated and other polarizable liquids, including water, occurred (Figure 29). The use of *meso*-tartrate as counterion did not lead to gelation. Notably, the monomeric form of this “dimeric” surfactant, $(CTA)_2$ -*L*-tartrate, did not form gels. Headgroup connections, possibly the reciprocal bridging of bis-anions and bis-cations in this case, is a prerequisite to assembly of a non-covalent polymeric material. *L*-tartrate gave exclusively right-handed helices and *D*-tartrate resulted in left-handed helices. In water, a mixture of *D*- and *L*-tartrates gave more viscous and less fragile gels than either enantiomer alone. This exemplified the importance of the orientation of the hydroxyl groups for efficient gelation.

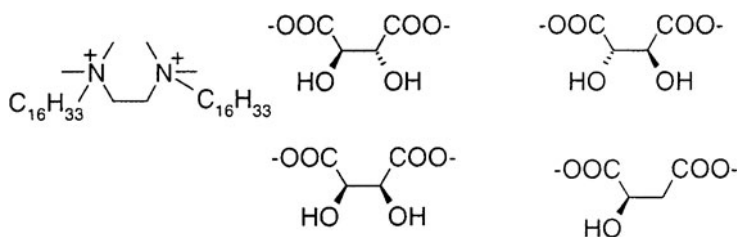


Figure 29. Gemini surfactant tartrates with counterions.

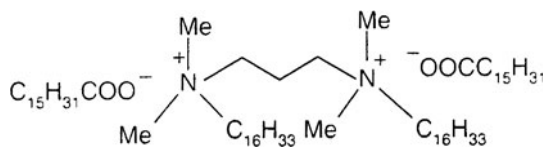


Figure 30. Gemini surfactant with palmitate as counterions.

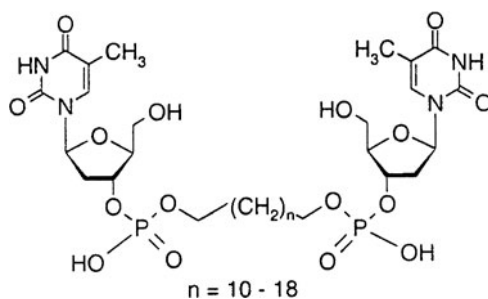


Figure 31. Nucleotide bola-amphiphiles.

Bhattacharya and De have independently examined the gelation behavior of *bis*-(hexadecyldimethylammonium)propane in an aqueous medium in the presence of palmitate as the counterion (Figure 30) [45]. Optical microscopy indicated the presence of tubular aggregates in such gels.

Gelation of water by a nucleotide bola-amphiphile was reported by Iwaura *et al.* [46]. It was found that nucleotide bola-amphiphiles were very efficient gelators, being able to entrap >25000 water molecules per gelator molecule. The strong influence of pH and the length of the polymethylene spacer on gelation behavior were evaluated for this class of molecules. Compounds with $n = 10 - 12$ gave solutions in alkaline buffers while vesicles and gels were formed by the longer homologues with $n = 14, 16$ and $n = 20$, respectively.

The aggregation behavior of asymmetric zwitterionic gemini surfactants having the general sequential structures, long chain/phosphate/2-carbon

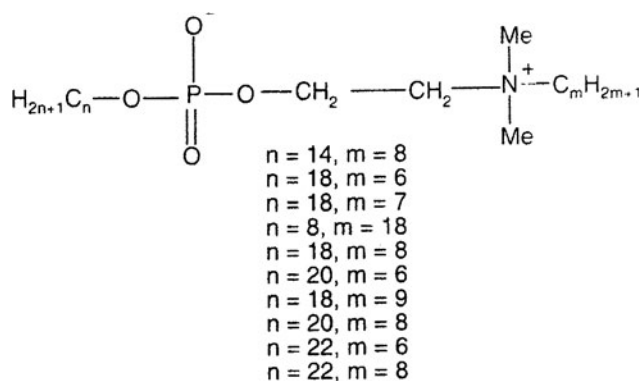


Figure 32. Asymmetric zwitterionic gemini surfactants.

spacer/quaternary nitrogen/short chain (Figure 32), have been reported by Menger and Peresykin [47]. These surfactants aggregate in water to form vesicles. Owing to the zwitterionic character of the surfactants used and the protrusion of short chains from the vesicle surfaces, these vesicles further self-assembled in a “pearls on a string” morphology. This complex networking of the vesicles caused gelation of pure water.

Self-assembly of bipolar phosphocholine leading to gelation in water has been reported recently [48]. The authors note that the rheological behavior for this gel-system is complicated and in some way related to the behavior of other association colloids such as wormlike micelles.

7. Miscellaneous Hydrogelators

Several other types of molecules have recently been shown to gelate aqueous media. Fuhrhop *et al.* have been able to produce hydrogels from sodium and potassium salts of tartaric amide monocarboxylates (Figure 33) [49]. Gelation occurred in a pH range of 4.1–4.9. It appears that aggregation was promoted by hydrogen-bond formation between carboxylate and the partially protonated (acid) present at this pH range.

A resorc[4]arene (Figure 34) was shown to form aqueous solutions when the pH was lowered below 2.5 [50]. Raising the pH reversed the gelation and and this cycle could be repeated until the concentration fell below the minimum gelation concentration. The gel forming ability was completely suppressed in the presence of two equivalents of Cu^{2+} ions.

Certain water-soluble polycationic organophosphorous dendrimers are powerful gelators for aqueous media over a wide range of pH (2–9) (Figure 35) [51]. The gelation time (time for gel to form) was shortened by

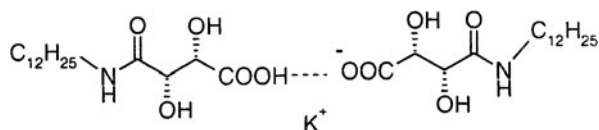


Figure 33. Tartaric amide monocarboxylates.

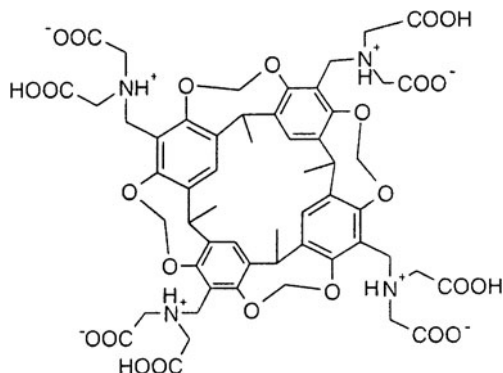


Figure 34. Resorc[4]arene based hydrogelator.

polar component additives (10–30%) such as TRIS buffer, metal salts (Ni, Y, Er acetates), acids (citric, ascorbic, lactic, *L*-tartaric etc.), dithioerythritol, and EDTA. It is surprising that these gels do not display thermo-reversibility despite being physical gels.

Earlier studies have shown that the presence of electrolytes such as potassium bromide or sodium salicylate in micellar solutions of cetyl trimethyl ammonium salts lead to a marked increase in the viscoelasticity of the resulting solutions and eventual formation of hydrogels [52]. These additives reduced the repulsion between the amphiphile head-groups of the micellar aggregate and led to the growth of micelles. The morphology of the micelles also changed from spherical to rod-like [53]. A number of surfactant micelles have been examined for such gelation. This observation was found to be true only for single-headed amphiphiles (Figure 36). The analogous double- and triple-headed surfactants did not lead to a viscoelastic mass, strongly suggesting the importance of charge balance in such processes [54].

A number of benzyl derivatives of triazole-appended 2'-deoxyuridine gelate pure water (Figure 37) [55]. The triazole units increase the hydrophilicity and the benzyl units increase both the hydrophobic and π - π stacking interactions. Among the seven hydrogelators investigated, the *p*-ethylbenzyl derivative had the lowest MGC (0.2 wt.%). FTIR studies indicate that 3'- and 5'-OH groups are involved in hydrogen-bonding interactions in the gel phase.

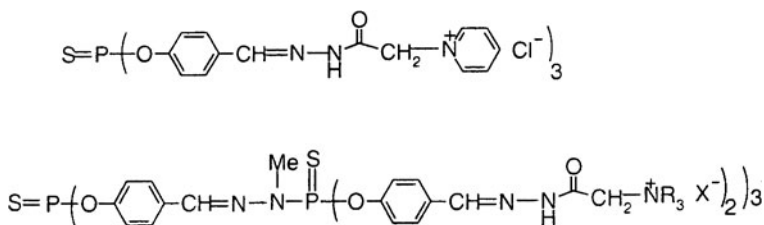


Figure 35. Polycationic organophosphorus dendrimers.

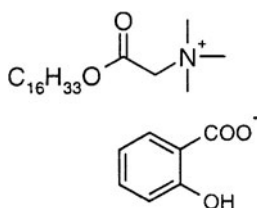


Figure 36. Single-headed amphiphile/salicylate hydrogel system.

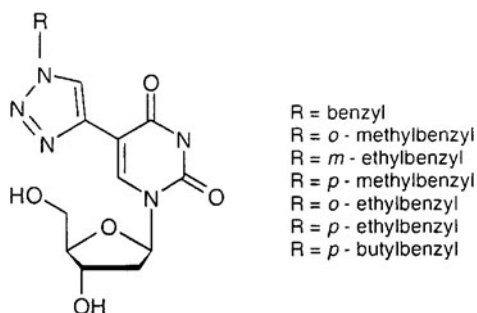


Figure 37. 2'-Deoxyuridine based gelators.

8. Bile Acid Based Hydrogelators

The aggregation behavior of bile salts has been under intense scrutiny for the past several decades, since this class of molecules plays a pivotal role in fat and cholesterol solubilization in the form of mixed micelles with lipids (Figure 38) [56]. Unlike conventional surfactant molecules, bile acids possess a rigid steroid backbone and polar hydroxyl groups on the concave α -face and methyl groups on the convex β -face (Figure 39). This arrangement creates a strikingly unique *facial amphiphilicity* for this class of molecules, enabling them to aggregate in aqueous media in a distinctive manner. The aggregation

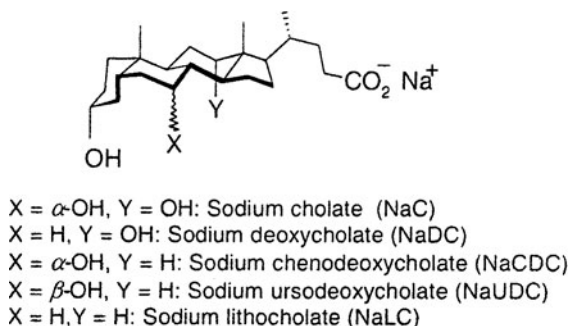


Figure 38. Naturally occurring bile salts.

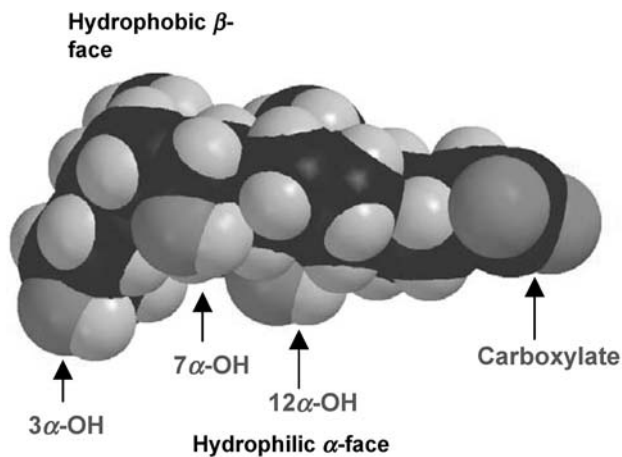


Figure 39. Space-filling computer generated model of cholate. [A color version of this figure may be found on page 942.]

of bile salts in aqueous media is largely driven by hydrophobic association of the apolar β -faces of the steroid backbones, while further aggregation occurs through hydrogen bonding interactions. The gelation of aqueous solutions of sodium deoxycholate (3α , 7α -dihydroxy) was first observed by E. Graf von Schönborn and was communicated to the Biochemical Society in May 1913 [62a]. This observation remained unnoticed until 1958 when Sobotka and Czczowiczka serendipitously rediscovered the gelation phenomenon while working on bile salts in bacteriological media [57]. The gelation was found to be pH dependent (optimal at pH ~ 7), and this gel was thixotropic in nature. Lithocholic acid ($3\alpha\text{-OH}$, monohydroxy) has a stronger tendency to form gels, even at pH 12. Glycodeoxycholate was also found to form gels at lower pH, and the

gelation phenomenon was attributed to the incipient hydrolysis of glycodeoxycholic acid to deoxycholic acid. X-ray diffraction studies performed by Rich and Blow on NaDC (sodium deoxycholate) gel revealed that the (supra) molecular complex formed a helical structure with 36 Å diameter [58]. The complex formation (gelation) was favored at lower pH and higher ionic strength.

Results from equilibrium ultracentrifugation and light scattering studies suggest that all trihydroxy bile salts form very small micelles with aggregation numbers (N) between 2–10, whereas dihydroxy bile salts form small micelles at low concentration ($N < 10$) and large micelles (N 12–100) at higher concentrations [59]. It was suggested that the small micelles are formed primarily due to hydrophobic packing of β -faces of steroid units, while the larger micelles are formed by the aggregation of small micelles through hydrogen bonding of hydroxyl groups, which leads to gelation. The NaDC gel-system has been studied using capillary flow [60a], pressures dependence on sol-gel transition [60b], steady-state and time-resolved fluorescence [60c], small angle X-ray scattering, small angle neutron scattering and quasi-elastic light scattering [60d]. All of the data indicate the growth of the spherical micelle (secondary aggregation process) along the rod (fiber) axis, leading to gelation.

Sodium deoxycholate NaDC gel was also investigated by rheometry. Experiments were carried out in the linear viscoelastic region while varying the pH, ionic strength (NaCl) and the bile salt concentration [61]. The $G \propto f^n$ relationship, the creep-recovery experiment, and the frequency-temperature superposition principle revealed that the interactions in the gels are physical in nature and that its mechanical behavior can be explained by a simple relaxation mechanism. Hydrogen bonds are the main forces involved in the formation, relaxation and strength of this gel.

On the contrary, the sodium salt of cholic acid (3α , 7α , 12α -trihydroxy) did not form a gel under any condition as attempted by several research groups. It was hypothesized that the lack of gelation is because sodium cholate is more water-soluble, and thus less prone to aggregation, than mono- and dihydroxy bile salts. This was further substantiated by the aggregation number data. However, sodium cholate was shown to form a gel in the presence of calcium ion by Schryver in 1913 while investigating “clot” formation using sodium cholate [62]. He had found a striking similarity between certain vital activities of cells and the behavior of the cholate gel. These significant observations/conclusions appear to have been unnoticed so far by subsequent researchers in this area.

It is interesting to note that gelation of aqueous media is quite common among dihydroxy bile salts (NaDC, NaGDC, NaCDC, NaUDC), while the trihydroxy bile salt (NaC) forms gels only under carefully controlled conditions in the presence of calcium ions. However, Maitra *et al.* have demonstrated efficient gelation of predominantly aqueous fluids by a *cholic acid* trimer (tripodal cholamide; Figure 40) [63]. These gels were formed at remarkably low gelator concentrations (0.02% w/v, 0.15 mM) One gelator molecule immobilizes 10^5

water molecules. The formation of hydrophobic “pockets” during gelation was inferred using ANS as a polarity sensitive probe. A thermochromic gel was developed using bromophenol blue as a dye. The ANS-binding study has been found to be useful to determine MGC for several other molecular hydrogels by other researchers [20].

Simpler monomeric cationic and neutral analogs of dihydroxy bile salts were subsequently shown to gelate aqueous fluids (Figure 41) [64]. Gelation was enhanced in the presence of NaCl, suggesting the importance of the hydrophobic effect in gelation. Recently rheological experiments were performed on gels derived from cationic and neutral analog of bile acids [65]. In the frequency sweep experiments, the elastic modulus G' was predominant, and

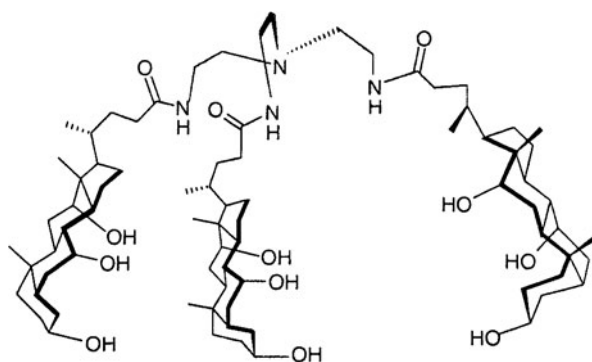


Figure 40. The tripodal cholamide gelator.

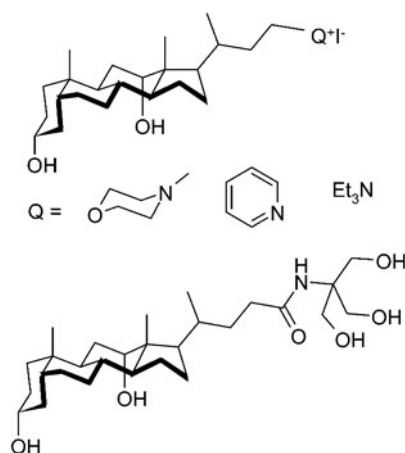


Figure 41. Cationic and neutral analogs of bile acids.

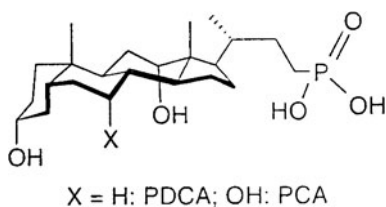


Figure 42. Phosphonobile acids.

an order of magnitude higher than the loss modulus G'' , which is a characteristic behavior of viscoelastic soft solids.

Gelation behavior of phosphonobile acids (where CO_2H of the steroid is replaced by a PO_3H_2 , Figure 42) in acidic pH has also been observed recently. Better gelation by these phosphonobile acids than the corresponding natural bile acids at comparable concentrations, may be explained by the lower critical aggregation concentrations for these phosphonobile acids [66].

9. Structural and Dynamic Aspects of Hydrogels

Structure and dynamics together form the basis of the properties and functions for all biomolecules [67]. Structure and dynamics should govern the physical properties of materials such as gels. Gels are very interesting materials owing to the coexistence of solid and liquid phases. The networked fibrous structure (solid) of a gel restrains the solvent molecules (liquid) from flowing macroscopically. Therefore, both structure and dynamics govern the properties of a gel. Gels derived from LMOGs are outstanding media to study supramolecular organization. Since gels don't lend themselves to studies at atomic resolution, structural analyses are not straightforward. However, by using a variety of techniques it has been possible to get insights into the gel structure. Both optical and electronic microscopic studies have revealed that gels are composed of networked fibrous organization, a SAFIN. Scanning and transmission electron microscopic studies on gels have indicated that the diameters of these fibers in many cases are fairly uniform and range from a few of nanometers to microns. Newkome *et al.* have compared the cryo-TEM image (Figure 43) of a gel obtained from the tripodal cholamide shows entangled fibers of ≈ 10 nm in diameter [68]. In some cases, the dimensions of these fibers have been rationalized using molecular modeling studies on the aggregates. Newkome *et al.* have compared the diameter of the fibers based on TEM (34–36 Å) with the calculated end-to-end distance of the gelator molecule (ca. 29 Å) [40]. The difference was attributed to some degree of hydration of the cylindrical aggregate and the stain used for the TEM studies. In some cases, X-ray crystal

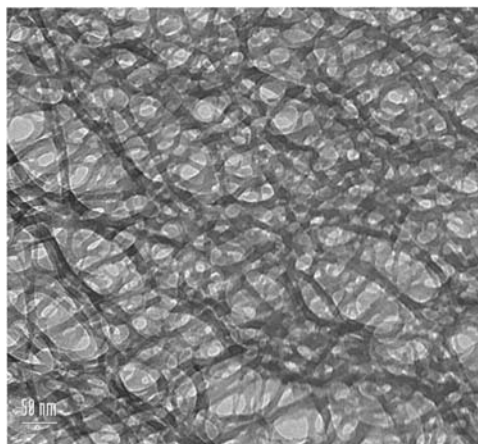


Figure 43. A cryo-TEM picture of the gel derived from the tripodal cholamide in Figure 40.

structure of a molecule, closely related to the gelator molecule has been used as a model to describe the approximate structure of the aggregate in the gel phase [13]. Small angle X-ray scattering (SAXS) and small angle neutron scattering (SANS) experiments can provide information about the long-range structural organization in the gel phase [30]. For instance, sodium lithocholate gels were investigated by SAXS and SANS, which revealed that the diameter of the rod-like structure is ca. 650 Å [69]. IR, NMR, CD and fluorescence spectra also provide information in selected cases. For example, comparative IR and NMR data in the gel and sol phases have indicated the extent of hydrogen bonding in the aggregate [13, 20, 28, 30, 40, 54]. Chirality amplification (e.g., from helical organizations) in the gel phase have been confirmed by CD experiments [18, 28, 36, 65]. Results from the fluorescence experiments are useful to establish the role of π - π stacking in molecules having large aromatic surfaces [18, 19]. Therefore, using a combination of several techniques, it is now possible to describe the structure of a gel with some degree of accuracy.

During the gelation process both the viscosity and the aggregate sizes change significantly. Hence information on dynamics in the gel phase would be of considerable interest. Mukhopadhyay *et al.* have studied the dynamics of fluorescent dyes in the gel phase (see Chapter 24) derived from the tripodal cholamide (Figure 40) using picosecond time-resolved fluorescence technique [70]. The time-resolved decay of the fluorescence anisotropy (r) of a probe molecule is directly related to the reorientation dynamics of excited molecules, and hence, it is best suited for the investigation of the local molecular dynamics near the binding site (Eqs. (1) and (2)).

$$r(t) = r_0 \sum \alpha_i \exp(-t/\varphi_i) \quad (1)$$

$[r(t)$ is the fluorescence anisotropy at any time t , r_0 is the initial anisotropy (i.e. at $t = 0$), and α_i is the amplitude associated with the i^{th} rotational correlation time (φ_i)].

$$\varphi = \eta V / kT \quad (\text{Stokes-Einstein's equation}) \quad (2)$$

[η is the viscosity and V is the volume of the rotating molecular system].

In an aqueous solution (viscosity ca. 1 cP), a fluorescent probe (small organic molecule) rotates very fast, having a very short rotational correlation time (φ) ranging from 0.1 to 0.2 ns. Binding of the probe to hosts/aggregates/macromolecules dampens the rotational motion by several fold. Thus the observed rotational correlation time increases depending on the size (V) of the host/aggregate/macromolecule and the micro-viscosity (η) felt by the probe in a binding pocket. A water-soluble fluorescent probe such as ANS has a rotational correlation time of 90 ps (≈ 0.1 ns) in an aqueous medium. The time-resolved decay of the anisotropy of ANS fluorescence in the gel from the tripodal cholamide consisted of two rotational correlation time components for ANS: 13.2 ns (bound to the gel) and 1.0 ns (“free” aqueous ANS). The longer component is believed to be associated both with the size of the aggregate and the enhanced microviscosity of the binding pocket in the gel phase. It is interesting to note that “free” ANS also showed slower rotational motion than in an aqueous solution. It was suggested that these ANS molecules are associated with the water molecules ordered (rigidified) around the entangled gel network. The partial immobilization of solvent molecules (increase in the viscosity/order/structure) around a gel network was experimentally demonstrated by probing the dynamics of a water-soluble polarity sensitive dye. A water insoluble fluorescent dye, DPH showed only one component (4.8 ns), characterized as the probe solubilized in the hydrophobic core of the gel network.

10. Application of Hydrogels in Materials Science

A more comprehensive description of potential applications of gels is presented in Chapters 22–27, especially. This section focuses on hydrogels. Hydrogels can act as templates to direct the structure of inorganic materials. There are numerous examples of applications of the sol-gel technique in materials science [72]. Shinkai and co-workers utilized sol-gel chemistry with organo-gels (see Chapter 25) to obtain meso-porous silica [73]. Hydrogels from aldehydes have also been used as templates to form silica nano-structures. Tubular silica was successfully transcribed by utilizing hydrogen-bonding interactions between the amino group of a gelator and tetraethyl orthosilicate. Hollow spherical silica has also been templated by a gel [38].

The use of a hydrogel as a template has the intrinsic advantage that water-soluble metals salts can be used as precursors. The hydrogel derived from

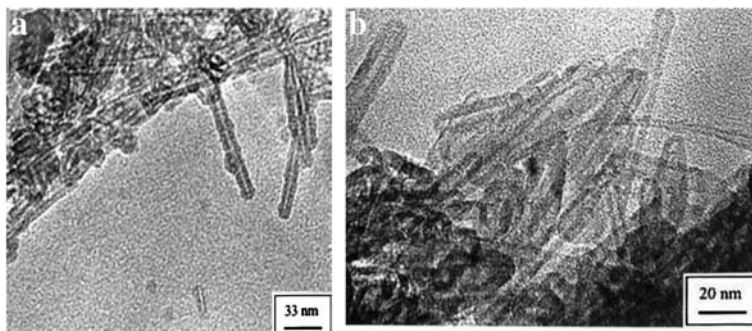


Figure 44. Nanotubes of titania (TiO_2) (a) and ZnSO_4 (b) Reproduced from [74] by permission of The Royal Society of Chemistry.

the tripodal choline (Figure 40) contains well-defined fibers with diameters between 8 and 10 nm and lengths extending to a few hundred nanometers as revealed by TEM (see Figure 43). Using these gel fibers as templates, Gundiah *et al.* synthesized nanotubes of oxides such as SiO_2 , TiO_2 , ZrO_2 , WO_3 , ZnO and nanotubes of sulfates such as BaSO_4 as well as of water-soluble ZnSO_4 (Figure 44). ZnO has been extensively investigated as a potential inorganic material for applications in opto-electronics. There has been only one synthesis (hydrothermal route) of ZnO nanotubes by Zhang *et al.* [75], and they had inner diameters of ca. 250 nm. In contrast, the nanotubes obtained by Gundiah *et al.* were much smaller in diameter (<20 nm) due to their genesis from sol-gel templated chemistry. These results demonstrated the utility of water-soluble metal salts in sol-gel chemistry. Metal alkoxides need not be the precursors of nanotubes with organogel templates.

11. Perspectives for the Future

Molecular hydrogels are promising materials for biomedical applications. Unlike polymeric gels, molecular hydrogels should be biocompatible in many cases, particularly those derived from amino acids, carbohydrates, peptides, nucleotides or bile acids. It would be useful to have more gel systems of this sort, which could be switched by external stimuli (chemical or physical). For potential biological applications, it is important to develop hydrogels, which remain unperturbed in biological systems in the presence of ions, lipids or other biomolecules. The optimal gels for biomedical applications, (a) should form in the absence of any co-solvents (b) their gelation should be triggered by external stimuli (c) the gelator molecules should be biocompatible and (d) their gelation properties should be unaffected in the presence of electrolytes and

biomolecules. Additionally, for an ideal drug delivery system, the gel melting temperature should be around physiological temperature (37°C). One of the major limitations associated with many low molecular mass hydrogels is that their formation is strongly dependent on factors related to the protocol for their preparation, and slight changes often lead to inhibition of the gelation process. We hope that the concepts and strategies described in this chapter will be useful in the coming years to develop advanced gel systems for unforeseen applications.

Abbreviations

ANS:	8-anilinonaphthalene-1-sulfonic acid
CD:	circular dichroism
CTAB:	cetyltrimethylammonium bromide
DPH:	1,6-diphenylhexatriene
EDTA:	ethylenediaminetetraacetic acid
FRET:	fluorescence resonance energy transfer
FT:	Fourier transform
IR:	infrared
MGC:	minimum gel concentration
NMR:	nuclear magnetic resonance
OG:	<i>n</i> -octyl- β - <i>D</i> -glucopyranoside
SEM:	scanning electron microscope
TEM:	transmission electron microscope
TRIS:	tris(hydroxymethyl)-aminomethane
UV:	ultra-violet

Acknowledgments

Part of the work presented herein has been supported by grants from the Department of Science & Technology (Swarnajayanti Fellowship to SB), and from the Council of Scientific & Industrial Research and the Indo-French Centre for the Promotion of Advanced Research (UM). AS and SM acknowledge the CSIR and the IISc, respectively, for senior research fellowships.

References

- [1] (a) Terech, P. In *Encyclopedia of Surface and Colloid Science*, New York: Marcel Dekker, Inc., **2002**, pp. 2299–2319; (b) Osada, Y.; Kajiwara, K. Eds., Fushimi, T.; Hirasa, O.; Hirokawa, Y.; Matsunaga, T.; Shimomura, T.; Wang, L. Assoc. Eds., Ishida, H. (translator) In *Gels Handbook, Vol. 1, The Fundamentals*, San Diego: Academic Press, **2001**; (c) Guenet, J.M. In *Thermoreversible Gelation of Polymers and Biopolymers*, New York: Academic Press, **1992**.

- [2] (a) Lee, K.Y.; Moony, D.J. *Chem. Rev.*, **2001**, *101*, 1869; (b) Miyata, T.; Uragami, T.; Nakamae, K. *Adv. Drug Delivery Rev.*, **2002**, *54*, 79.
- [3] Tiller, J.C. *Angew Chem. Int. Ed.*, **2003**, *42*, 3072.
- [4] Lipowitz, von A. *Ann. Chem. Pharm.*, **1841**, *38*, 348.
- [5] Nägeli, K.v. *Theorie der Gärung*, (München), **1879**, 102.
- [6] Brezinger, Z. *Physiol. Chem.*, **1892**, *16*, 537.
- [7] Gortner, R.A.; Hoffman, W.F. *J. Am. Chem. Soc.*, **1921**, *43*, 2199.
- [8] (a) Zsigmondy, R.; Bachmann, W.; Bachmann, v.W. *Kolloid-Zeitschrift*, **1912**, *11*, 145; (b) <http://www.nobel.se/chemistry/laureates/1925/zsigmondy-lecture.pdf>.
- [9] Amis, E.S.; Lamer, V.K. *Science*, **1939**, *90*, 90.
- [10] Imae, T.; Takahashi, Y.; Muramatsu, H. *J. Am. Chem. Soc.*, **1992**, *114*, 3414.
- [11] Fuhrhop, J.-H.; Spiroski, D.; Boettcher, C. *J. Am. Chem. Soc.*, **1993**, *115*, 1600.
- [12] Franceschi, S.; de Viguier, N.; Riviere, M.; Lattes, A. *New J. Chem.*, **1999**, *23*, 447.
- [13] Menger, F.M.; Caran, K.L. *J. Am. Chem. Soc.*, **2000**, *122*, 11679.
- [14] (a) Jokić, M.; Makarević, J.; Žinić, M. *Chem. Commun.*, **1995**, 1723; (b) Makarević, J.; Jokić, M.; Perić, B.; Tomišić, V.; Kojić-Prodić, B.; Žinić, M. *Chem. Eur. J.*, **2001**, *7*, 3328; (c) Makarević, J.; Jokić, M.; Frkanec, L.; Katalenić, D.; Žinić, M. *Chem. Commun.*, **2002**, 2238.
- [15] Frkanec, L.; Jokić, M.; Makarević, J.; Wolsperger, K.; Žinić, M. *J. Am. Chem. Soc.*, **2002**, *124*, 9716.
- [16] Heeres, A.; van der Pol, C.; Stuart, M.; Friggeri, A.; Feringa, B.L.; van Esch, J. *J. Am. Chem. Soc.*, **2003**, *125*, 14252.
- [17] D'Aléo, A.; Pozzo, J.-L.; Fages, F.; Schmutz, M.; Mieden-Gundert, G.; Vögtle, F.; Caplar, V.; Žinić, M. *Chem. Commun.*, **2004**, 190.
- [18] Xing, B.; Yu, C.-W.; Chow, K.-H.; Ho, P.-L.; Fu, D.; Xu, B. *J. Am. Chem. Soc.*, **2002**, *124*, 14846.
- [19] Nakashima T.; Kimizuka, N. *Adv. Mater.*, **2002**, *14*, 1113.
- [20] (a) Suzuki, M.; Yumoto, M.; Kimura, M.; Shirai, H.; Hanabusa, K. *Chem. Eur. J.*, **2003**, *9*, 348; (b) Suzuki, M.; Yumoto, M.; Kimura, M.; Shirai, H.; Hanabusa, K. *Chem. Commun.*, **2002**, 884; (c) Suzuki, M.; Yumoto, M.; Kimura, M.; Shirai, H.; Hanabusa, K. *New J. Chem.*, **2002**, *26*, 817.
- [21] Estroff L.A.; Hamilton, A.D. *Angew. Chem. Int. Ed.*, **2000**, *39*, 3447.
- [22] Wuang, G.; Hamilton, A.D. *Chem. Commun.*, **2003**, 310.
- [23] Boettcher, C.; Schade, B.; Furhorp, J.-H. *Langmuir*, **2001**, *17*, 873.
- [24] de Vries, E.J.; Kellogg, R.M. *J. Chem. Soc. Chem. Commun.*, **1993**, 238.
- [25] Hartgerink, J.D.; Beniash, E.; Stupp, S.I. *Proc. Natl. Acad. Sci. (USA)*, **2002**, *99*, 5133.
- [26] Nyrkova, I.A.; Semenov, A.M.; Joanny, J.F.; Khokhlov, A.R. *J. Phys. II.*, **1996**, *6*, 1411.
- [27] Aggeli, A.; Bell, M.; Boden, N.; Keen, J.N.; Knowles, P.F.; McLeish, T.C.B.; Pitkeathly, M.; Radford, S.E. *Nature*, **1997**, *386*, 259.
- [28] Collier, J.H.; Hu, B.-H.; Ruberti, J.W.; Zhang, J.; Shum, P.; Thompson, D.H.; Messersmith, P.B. *J. Am. Chem. Soc.*, **2001**, *123*, 9463.
- [29] Claussen, R.C.; Rabatic, B.M.; Stupp, S.I. *J. Am. Chem. Soc.*, **2003**, *125*, 12680.
- [30] Schneider, J.P.; Pochan, D.J.; Ozbas, B.; Rajagopal, K.; Pakstis, L.; Kretsinger, J. *J. Am. Chem. Soc.*, **2002**, *124*, 15030.
- [31] Pochan, D.J.; Schneider, J.P.; Kretsinger, J.; Ozbas, B.; Rajagopal, K.; Haines, L. *J. Am. Chem. Soc.*, **2003**, *125*, 11802.
- [32] Pfannemuller, B.; Welte, W. *Chem. Phys. Lipids*, **1985**, *37*, 227.
- [33] Furhorp, J.-H.; Schnieder, P.; Rosenberg, J.; Boekema, E. *J. Am. Chem. Soc.*, **1987**, *109*, 3387.

- [34] Bhattacharya S.; Acharya, S.N.G. *Chem. Mater.*, **1999**, *11*, 3504.
- [35] Bhattacharya S.; Acharya, S.N.G. *Langmuir*, **2000**, *16*, 87.
- [36] Kobayashi, H.; Friggeri, A.; Koumoto, K.; Amaike, M.; Shinkai, S.; Reinhoudt, D.N. *Org. Lett.*, **2002**, *4*, 1423.
- [37] McWatt, M.; Boons, G.-J. *Eur. J. Org. Chem.*, **2001**, 2535.
- [38] Jung, J.H.; Shinkai, S.; Shimizu, T.; *Chem. Eur. J.*, **2002**, *8*, 2684.
- [39] Kiyonaka, S.; Shinkai, S.; Hamachi, I. *Chem. Eur. J.*, **2003**, *9*, 976.
- [40] Newkome, G.R.; Baker, G.R.; Arai, S.; Saunders, M.J.; Russo, P.S.; Theriot, K.J.; Moorefield, C.N.; Rogers, L.E.; Miller, J.E.; Lieux, T.R.; Murray, M.E.; Phillips, B.; Pascal, L. *J. Am. Chem. Soc.*, **1990**, *112*, 8458.
- [41] Menger, F.M.; Keiper, J.S. *Angew. Chem. Int. Ed.*, **2000**, *39*, 1907.
- [42] Zana, R.; Talmon, Y. *Nature*, **1993**, *362*, 228.
- [43] (a) De, S.; Aswal, V.K.; Goyal, P.S.; Bhattacharya, S. *J. Phys. Chem.*, **1996**, *100*, 11664; (b) De, S.; Aswal, V.K.; Goyal, P.S.; Bhattacharya, S. *J. Phys. Chem. B*, **1997**, *101*, 5639.
- [44] Oda, R.; Huc, I.; Candau, S.J. *Angew. Chem. Int. Ed.*, **1998**, *37*, 2689.
- [45] Bhattacharya S.; De, S. *Langmuir*, **1999**, *15*, 3400.
- [46] Iwaura, R.; Yoshida, K.; Masuda, M.; Yase, K.; Shimizu, T. *Chem. Mater.*, **2002**, *14*, 3047.
- [47] Menger, F.M.; Peresyphkin, A. *J. Am. Chem. Soc.*, **2003**, *125*, 5340.
- [48] Köhler, K.; Förster, G.; Hauser, A.; Dobner, B.; Heiser, U.F.; Ziethe, F.; Richter, W.; Steiniger, F.; Drechsler, M.; Stettin, H.; Blume, A. *Angew. Chem. Int. Ed.*, **2004**, *43*, 245.
- [49] Fuhrhop, J.-H.; Demoulin, C.; Rosenberg, J.; Boettcher, C. *J. Am. Chem. Soc.*, **1990**, *112*, 2827.
- [50] Haines, S.R.; Harrison, R.G. *Chem. Commun.*, **2002**, 2846.
- [51] Marmillon, C.; Gauffre, F.; Gulik-Krzywicki, T.; Loup, C.; Caminade, A.-M.; Majoral, J.-P.; Vors, J.-P.; Rump, E. *Angew. Chem. Int. Ed.*, **2001**, *40*, 2626.
- [52] Manohar, C.; Rao, U.R.K.; Valaulikar, B.S.; Iyer, R.M. *J. Chem. Soc. Chem. Commun.*, **1986**, 379.
- [53] Aswal, V.K.; Goyal, P.S.; Thiyagarajan, P. *J. Phys. Chem. B*, **1998**, *102*, 2469.
- [54] (a) Haldar, J.; Aswal, V.K.; Goyal, P.S.; Bhattacharya, S. *Angew. Chem. Int. Ed.*, **2001**, *40*, 1228; (b) Haldar, J.; Aswal, V.K.; Goyal, P.S.; Bhattacharya, S. *J. Phys. Chem. B*, **2001**, *105*, 12803.
- [55] Park, S.M.; Lee, Y.S.; Kim, B.H. *Chem. Commun.*, **2003**, 2912.
- [56] (a) Small, D.M. *Proc. Natl. Acad. Sci. (USA)*, **2003**, *100*, 4; (b) Hofmann, A.F. In *Bile Acids and Hepatobiliary Disease*, T. Northfield, P.L. Zentler-Munro, R.P. Jazrawi, Eds., Boston: Kluwer Academic Publishers, **1999**, pp. 303–332 and references therein; (c) Small, D.M. In *The Bile Acids: Chemistry, Physiology and Metabolism*, P.P. Nair, D. Kritchevsky, Eds., New York: Plenum Press, **1971**, vol. 1, pp. 249–356.
- [57] Sobotka, H.; Czeczowiczka, N. *J. Colloid Sc.*, **1958**, *13*, 188.
- [58] (a) Rich, A.; Blow, D.M. *Nature*, **1958**, *182*, 423; (b) Blow, D.M.; Rich, A. *J. Am. Chem. Soc.*, **1960**, *82*, 3566.
- [59] Small, D.M. *Adv. Chem. Ser.*, **1968**, *84*, 31.
- [60] (a) Sugihara, G.; Tanaka, M.; Matura, R. *Bull. Chem. Soc. Jpn.*, **1977**, *50*, 2542; (b) Sugihara, G.; Ueda, T.; Kaneshina, S.; Tanaka, M. *Bull. Chem. Soc. Jpn.*, **1977**, *50*, 604; (c) Jover, A.; Meijide, F.; Núñez, E.R.; Tato, J.V. *Langmuir*, **1996**, *12*, 1789; (d) Lopez, F.; Samseth, J.; Mortensen, K.; Rosenqvist, E.; Rouch, J. *Langmuir*, **1996**, *12*, 6188.
- [61] Jover, A.; Meijide, F.; Núñez, E.R.; Tato, J.V. *Langmuir*, **2002**, *18*, 987.

- [62] (a) Schryver, S.B. *Roy. Soc. Proc. B*, **1914**, 87, 366; (b) Schryver, S.B. *Roy. Soc. Proc. B*, **1916**, 89, 176; (c) Schryver, S.B. *Roy. Soc. Proc. B*, **1916**, 89, 361.
- [63] Maitra, U.; Mukhopadhyay, S.; Sarkar, A.; Rao, P.; Indi, S.S. *Angew. Chem. Int. Ed.*, **2001**, 40, 2281.
- [64] Sangeetha, N.M.; Balasubramanian, R.; Maitra, U.; Ghosh, S.; Raju, A.R. *Langmuir*, **2002**, 18, 7154.
- [65] Sangeetha, N.M.; Terech, P.; Maitra, U. Unpublished results.
- [66] Maitra, U.; Babu, P. *Steroids*, **2003**, 68, 459.
- [67] Frauenfelder, H.; Sligar, G.; Wolynes, P.G. *Science*, **1991**, 254, 1598.
- [68] Schmidt, J.; Talmon, I.; Mukhopadhyay, S.; Maitra, U. Unpublished results.
- [69] Terech, P.; Smith, W.G.; Weiss, R.G. *J. Chem. Soc. Faraday Trans.*, **1996**, 92, 3157.
- [70] Mukhopadhyay, S.; Ira, Krishnamoorthy, G.; Maitra, U. *J. Phys. Chem. B*, **2003**, 107, 2189.
- [71] Lakowicz, J.R. In *Principles of Fluorescence Spectroscopy*, New York: Plenum Press, **1999**.
- [72] (a) Langer, F.F. *Science*, **1996**, 273, 903 and references therein; (b) Nakamura, M.; Matsui, Y. *J. Am. Chem. Soc.*, **1995**, 117, 2651; (c) Kasuga, T.; Hiramatsu, M.; Hason, A.; Sekino, T.; Niihara, K. *Langmuir*, **1998**, 14, 3160.
- [73] (a) Ono, Y.; Nakashima, K.; Sano, M.; Kanekiyo, Y.; Inoue, K.; Hojo, J.; Shinkai, S. *Chem. Commun.*, **1998**, 1477; (b) Jung, J.H.; Ono, Y.; Shinkai, S. *Angew. Chem., Int. Ed.*, **2000**, 39, 1862; (c) Jung, J.H.; Kobayashi, H.; Masuda, M.; Shimizu, T.; Shinkai, S. *J. Am. Chem. Soc.*, **2001**, 123, 8785; (d) Jung, J.H.; Ono, Y.; Hanabusa, K.; Shinkai, S. *J. Am. Chem. Soc.*, **2000**, 122, 5008; (e) Jung, J.H.; Amaike, M.; Nakashima, K.; Shinkai, S. *J. Chem. Soc. Perkin Trans.*, **2001**, 2, 1938.
- [74] Gundiah, G.; Mukhopadhyay, S.; Tumkurkar, U.G.; Govindaraj, A.; Maitra, U.; Rao, C.N.R. *J. Mater. Chem.*, **2003**, 13, 2118.
- [75] Zhang, J.; Sun, L.; Liao C.; Yan, C. *Chem. Commun.*, **2002**, 262.

Chapter 18

AQUEOUS GELS MADE OF CHIRAL LIPID- AND PORPHYRIN-AMPHIPHILES

Jürgen-Hinrich Fuhrhop, Tianyu Wang, Sheshanath Bhosale,
Sidhanath Bhosale and Matthias Lauer

Freie Universität Berlin, FB Biologie, Chemie, Pharmazie, Institut für Chemie/Organische Chemie, Takustr. 3, D-14195 Berlin, Germany

1. Introduction	649
2. Electron Microscopy in Water and Toluene	649
3. The Effect of Charge Repulsion in Water	651
4. Stereochemistry and the Chiral Bilayer Effect	653
5. Viscoelastic Gels in Water	660
6. Bolaamphiphiles	661
7. Conclusions	661

1. Introduction

Water is the most powerful solvent to separate polar molecules and ions from each other as well as to stabilize ultrathin molecular assemblies. The high dielectricity constant ($\epsilon = 81$), which expresses this unique capability in a single number, is caused by the formation of tetrahedral water pentamers which form a diamond-shaped crystal in hexagonal ice and extended clusters in the fluid state up to 40° C. These clusters not only separate cations and anions, but also form clouds of solvent around the head groups of extended fibers of mono- or bimolecular thickness, which would otherwise stick together in bundles or rearrange to form multilayered scrolls or thick and broad ribbons. Such assemblies are invariably found in organic solvents, but can be avoided in water.

2. Electron Microscopy in Water and Toluene

High resolution cryo electron microscopy (see Chapter 9) yields images of micellar fibers in gels, which clearly reflect stereochemical differences imposed

by the medium. A typical example is the simple L-serine-dodecylamide bilayer, which produces multilayered tubules in toluene and bilayered helical ribbons in water [1]. Cryo transmission electron microscopy (Cryo-TEM) also shows a pronounced tendency of the assembly in toluene to form aggregates, whereas most of the ribbons in water appear individually (Figure 1).

The latter effect is, however, pH-dependent. Twisted ribbons and isolated tubules only appeared in the pH-range between 4.9 and 6.4, where amide

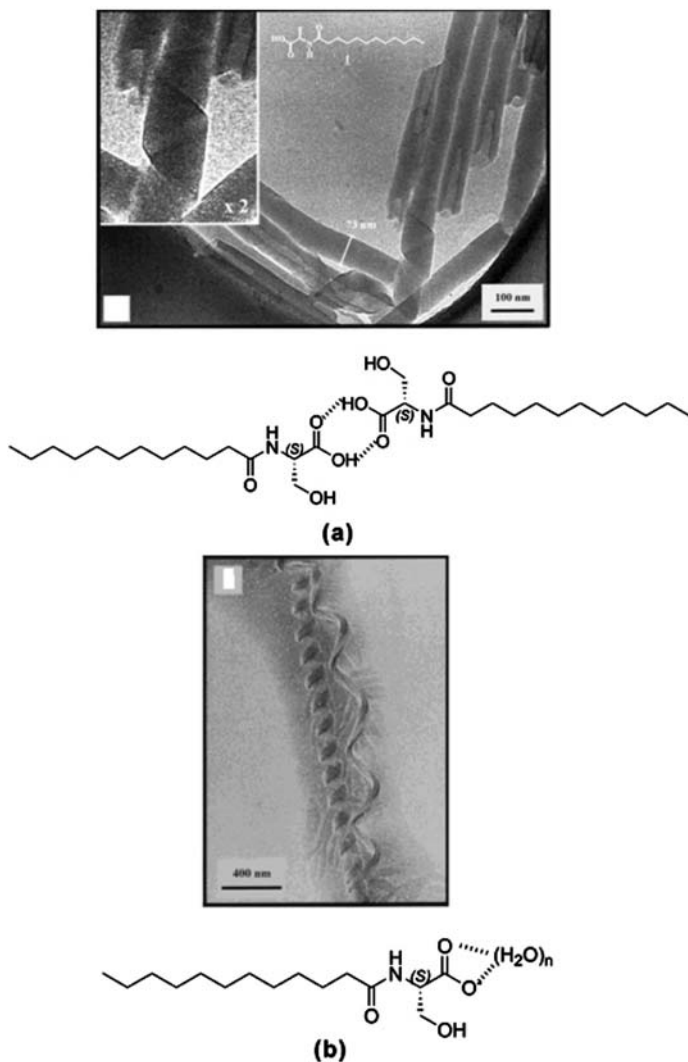


Figure 1. Typical appearance of fibers (a) in organic solvents (toluene) and (b) in water. Here: serine-dodecylamide. (Reprinted from [1] with permission. Copyright (2001) American Chemical Society.)

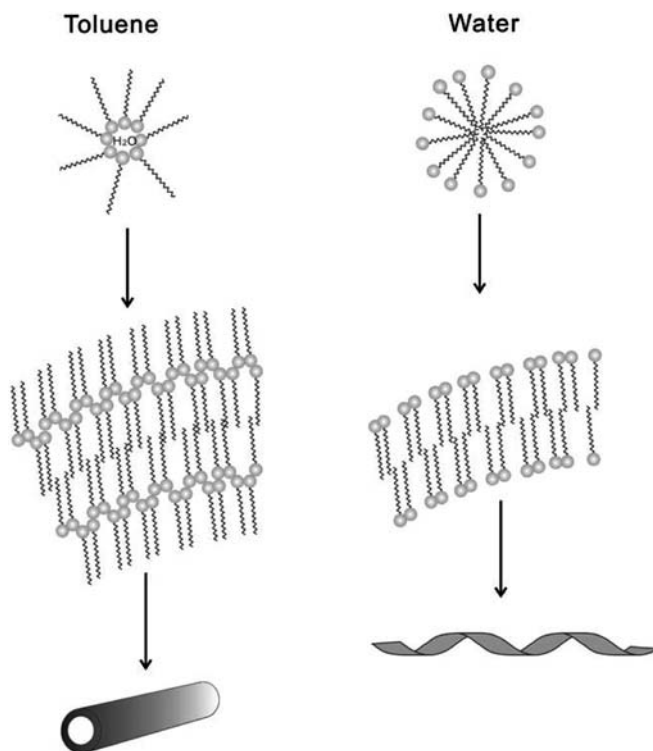


Figure 2. Model of inverted bilayer micelles in solvents of low polarity and of micellar fibers in water. The first leads quickly to multilayered tubules; only bilayers with polar surfaces may be seen in TEM as single helices or twisted ribbons. (Reprinted with permission from [1]. Copyright (2001) American Chemical Society.)

and $\text{COO}^{\ominus}\cdots\text{HOOC}$ hydrogen bonds occur simultaneously. Two chains of hydrogen bonds presumably stabilize micellar ribbons and tubules in water, and hydration water enforces curvature. If there is only one hydrogen bond, the fiber dissolves or forms three-dimensional crystals. In toluene, the same chains of hydrogen bonds are not solvated; only the alkyl chain regions swell and intercalate. As a result, multilayered tubules are formed. The polar head group regions assemble in toluene, whereas they remain separated in water (Figure 2).

3. The Effect of Charge Repulsion in Water

If, however, the head groups are charged, strong repulsive forces will remain between them. Lithium- and potassium salts of chiral fatty acids, for example, form beautiful chiral ribbons, whereas only spherical, short-lived micelles occur in water (Figure 3) [2]. In this case the two ions form polar

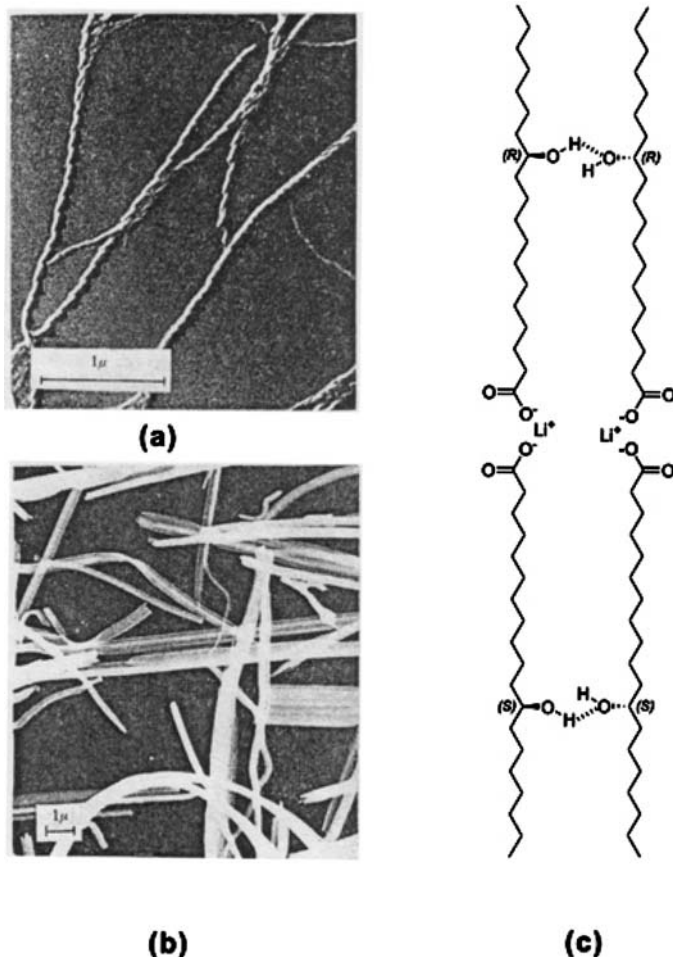


Figure 3. TEM of fibers of (a) 12-L-hydroxystearic acid and (b) its lithium salt from toluene (c) shows the racemate of the lithium salt. (Reprinted with permission from [2]. Copyright (1969) The Chemical Society of Japan.)

pairs in the organic solvent and the formation of crystal planes of low curvature is not favorable [2, 3].

The most famous of all chiral compounds, tartaric acid, has also been converted to a fatty acid amide which forms micellar fibers. It is very similar to the serine amide depicted first and it also carries a C₁₂-chain. It is, however, negatively-charged at the head group. Electrostatic repulsion is strong between head groups, and highly-curved micellar strands are formed. These micellar strands are 4 nm thick and are made of simple bilayers. In water, however, thousands of these strands assemble to form stocking-like formed cloths,

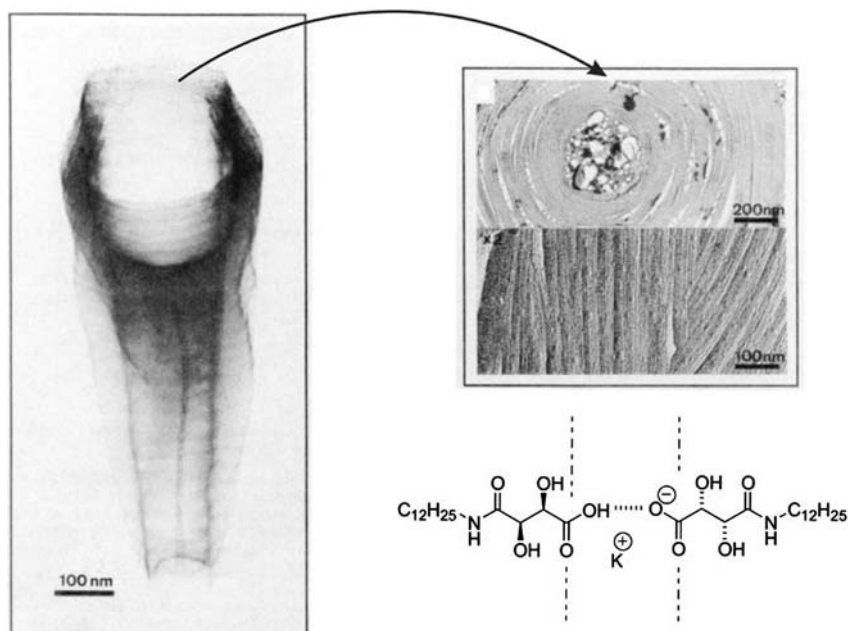


Figure 4. A multilayered cloth “woven” with chiral micellar fibers made of potassium tartaric dodecylamide. (Reprinted with permission from [4]. Copyright (1990) American Chemical Society.)

in which the single threads are fully visible in TEM upon negative staining (Figure 4). The size of these assemblies approaches that of biological cells [4].

4. Stereochemistry and the Chiral Bilayer Effect

The curved fibers are stable only if their amphiphiles are pure enantiomers. Racemates crystallize from both water and toluene as platelets. This phenomenon is observed quite often and is called the “chiral bilayer effect”.

The chiral bilayer effect has been studied in exhaustive detail with *N*-octyl- and *N*-dodecyl-glyconamides, in particular with the glucon-diastereomer. It forms bilayer helices in water with a thickness of 4.0 nm. The surface energy of these helices of ultimate bilayer thinness, however, is too large even after the formation of hydration spheres around the open-chain sugar head groups.

Four-helices therefore wind into each other and a quadruple helix of virtually infinite length is formed (Figure 5) [6–11]. Upon heating to 72° C, these quadruple helices melt because the amide hydrogen bond chains are broken co-operatively (Figure 6).

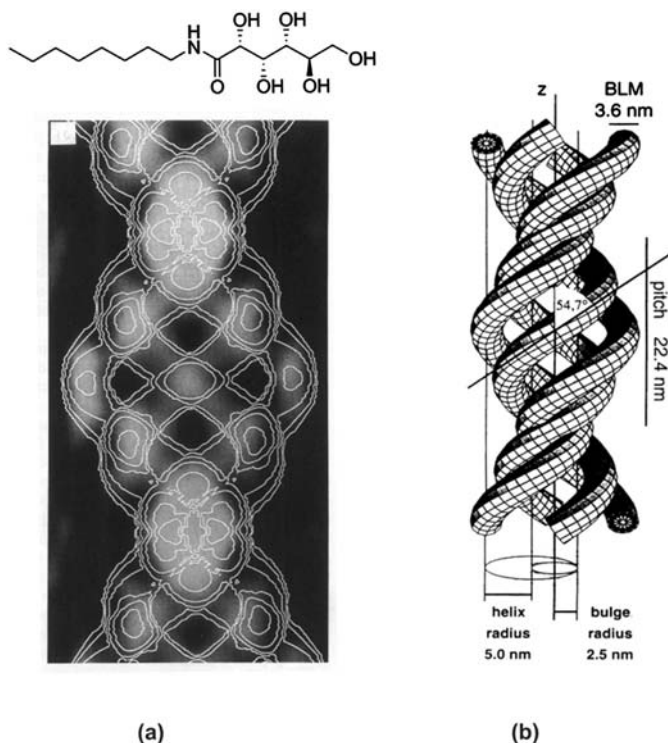


Figure 5. (a) The calculated contour line diagram of the N-octyl-D-gluconamide fiber isolated from water. Underneath the original TEM image is shown. (b) Computer model of the quadruple helix. (Reprinted with permission from [9]. Copyright (1993) American Chemical Society.)

Head-to-tail oriented crystals (see below) melt at about 150° C. Upon cooling, the fibers are formed within a few seconds and a slightly turbid gel is formed. Crystallization takes several days to weeks at room temperature, whereas addition of small amounts of sodium dodecyl sulphate (SDS) prevents it for years. Presumably the mixed SDS-gluconamide micelles dissolve any crystallite which separates from the fibers [6, 11].

The same kind of helices also will form for a short period of time if L-octyl-gluconamide is mixed with D-dodecyl-gluconamide. Left- and right-handed helices form next to each other (Figure 7) and the usual gel is formed. After a few minutes, however, the curved structure disappears and is replaced by a network of planar crystallites. The gel is also destroyed, because the platelets precipitate rapidly (Figure 7) [6].

If one mixes D- and L-gluconamides with hydrophobic chains of the same length, immediate crystallization occurs. No gel formation is observed. The explanation of the chiral bilayer effect is of the utmost simplicity.

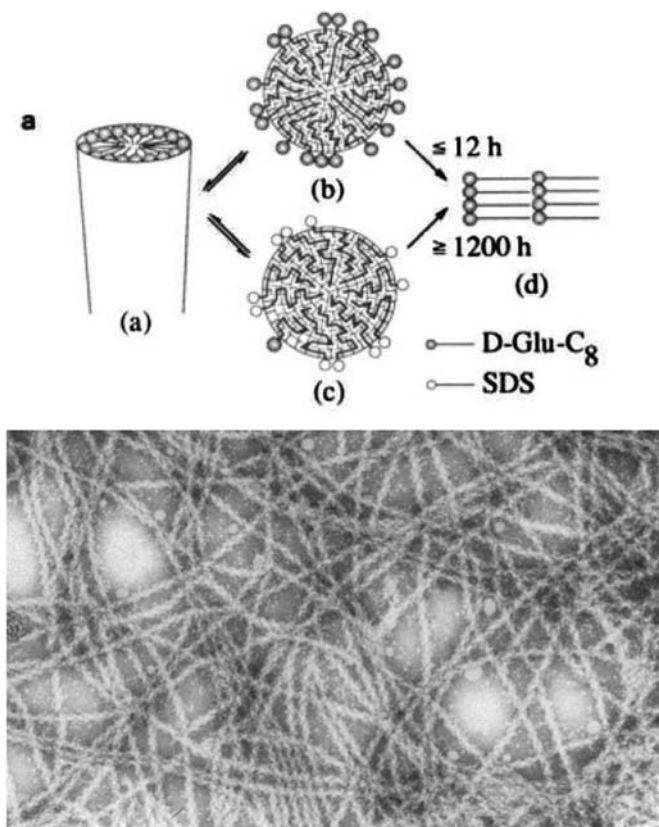


Figure 6. Single D-gluconamide molecules split off from micellar fibers and lead to (a) slow formation of crystals. The gel decomposes. This may be prevented for years, when SDS-micelles, which dissolve crystallites, are added to the gel [5]. The TEM shows such a gel after 2 months. (Reprinted with permission from [6]. Copyright (1990) American Chemical Society.)

Crystallization of chiral amphiphiles often occurs in planes, where all molecules are oriented in the same direction. This is particularly true for chiral zig-zag chains, and often less pronounced when chirality occurs in cyclic parts of the molecules (e.g., furanoses or pyranoses). In order to achieve the same orientation of chiral centers, the amphiphile must crystallize head-to-tail. This arrangement is, however, highly unlikely in water, where micellar tail-to-tail arrangements are lowest in energy. It is also unlikely for salts in toluene, where the charges concentrate in thin bilayers and do not tend to separate from each other. An example of a head-to-tail crystal, N-octyl-D-gluconamide, is given below. The straight conformation is stabilized by a homodromic hydrogen bond cycle (Figure 8).

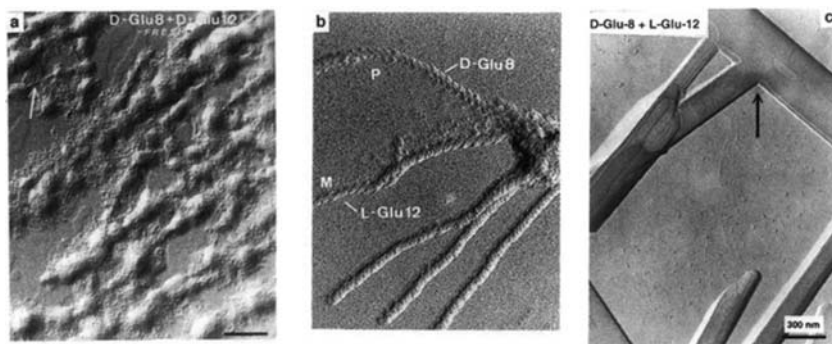


Figure 7. TEM of a mixture of D-octyl- and L-dodecyl-gluconamides (a) immediately after dissolution in hot water and drying on carbon grids; (b) after 10 minutes, (c) after 30 minutes; (a) shows micellar lumps, (b) separated M- and P-helices, (c) pseudo-racemic crystals. (Reprinted with permission from [12]. Copyright (1990) American Chemical Society.)

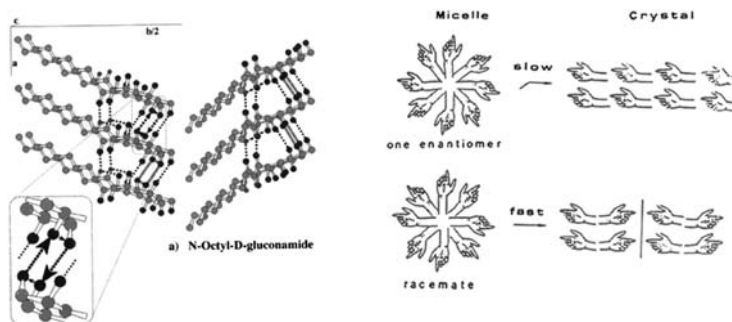


Figure 8. (a) Crystal structure of N-dodecyl-D-gluconamide; (b) model of the chiral bilayer effect. (Reprinted with permission from [5]. Copyright (1987) American Chemical Society.)

The corresponding racemate gave only small crystallites for which the expected tail-to-tail bilayer could be demonstrated in X-ray powder diffraction diagrams [8–10].

The conformation of the gluconamide head group in isolated, dry fibers was evaluated by solid state ^{13}C -NMR spectroscopy. This was not possible directly because there were no coupling constants between neighboring atoms; only chemical shift values were available. Nevertheless, comparison of several ^{13}C -NMR spectra of glyconamides in solution and in crystalline form combined with comparisons of crystal structures allowed clear assignments: there is a single *gauche*-bend in the glucon head group which is strongly hydrated (Figure 9). The bend is caused by 1,3-repulsive OH-interactions.

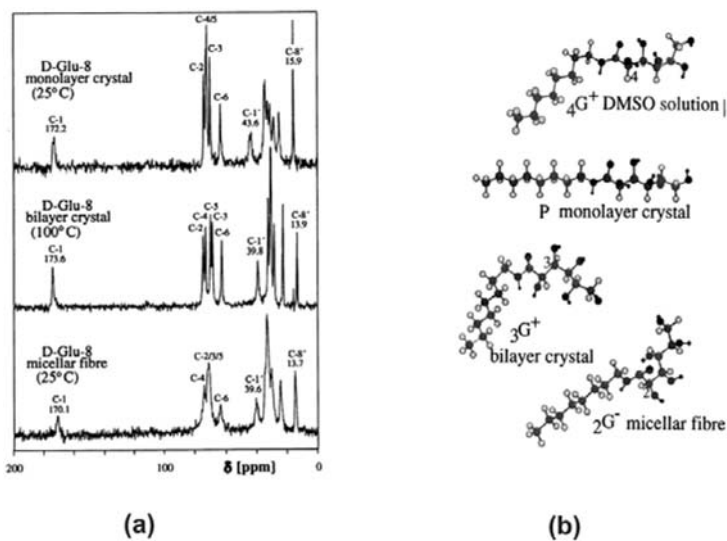


Figure 9. (a) Solid state NMR spectra of monocrystalline D-gluconamide material, microcrystalline D,L-gluconamide and isolated fibers. The chemical shift patterns were assigned to conformers with the aid of crystal structures and solution ^1H -NMR and ^{13}C -NMR spectra. (b) Models of the conformers. (Reprinted with permission from [8, 10]. Copyright (1994) American Chemical Society.)

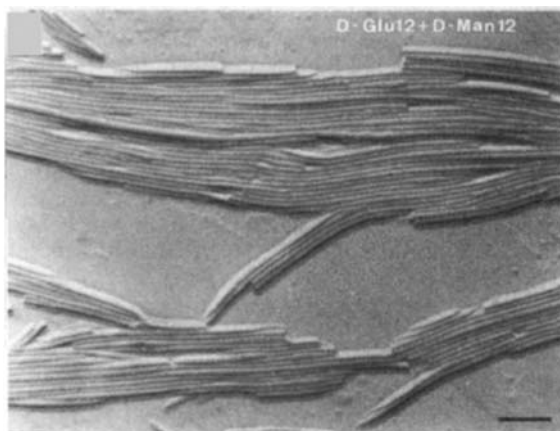


Figure 10. Uniform tubules are formed in water if equimolar amounts of dodecylamides of mannonic and gluconic acids are mixed in a 1:1 ratio. (Reprinted with permission from [12]. Copyright (1990) American Chemical Society.)

This bend is straightened out when the gluconamide is mixed with an equal amount of N-octyl-D-galactonamide, where no repulsive 1,3-OH interactions occur. Narrow tubules are formed from this mixture (Figure 9), whereas the mannonamide alone forms scrolls of up-rolled sheets only [12].

All of the glyconamide structures depend on water. In organic solvents, short multilayered tubules are observed exclusively.

The alkyl chains in the chiral amphiphiles have been replaced by protoporphyrin, which is a major chromophore in reactive biopolymers. Protoporphyrin itself is also amphiphilic: it has hydrophobic eastern, western and northern edges and a hydrophobic southern edge carrying two propionic acid side-chains. This amphiphile has never been crystallized although thousands of other porphyrin crystal structures are known. Porphyrin forms fibers instead [13, 14]. If the amphiphilic character is removed, (e.g., by esterification of the propionate side-chains), crystallization will occur immediately from saturated solutions. If the porphyrin carries propylamino groups instead of propionic acids, stable gels and fibers are obtained (Figure 11) [15]. Uniform, but relatively short tubules are formed in water. Their length increases considerably upon breaking hydrogen bonds with DMSO, and a rearrangement to rods is also observed.

Chiral gluconamide groups at the porphyrin's southern edge also produce long and stable fibers (Figure 12) and gels, but the large porphyrin plane does not aggregate to form twisted fibers. They rather assemble to step-like ribbons. The interaction of the porphyrin π -system then produces strong exciton effects (see Chapters 12 and 13): the 400 nm Soret band splits into a 350 and a 450 nm band, indicating strong dipole-dipole interaction between excited states in the fibers [14].

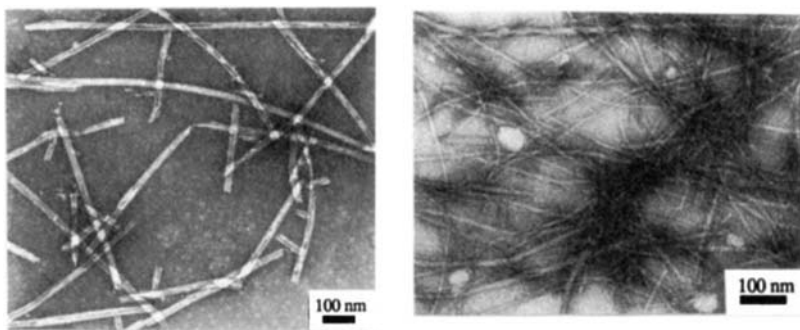


Figure 11. Protoporphyrin with two propionic acid side-chains forms short, ill-defined fibers in water (not shown) and does not crystallize. The corresponding diamine (COOH replaced by NH_2), however, gave uniform tubules, stabilized by stiff $\text{NH}_2\text{-NH}_3$ hydrogen bond chains (left) which rearranged to much longer, more flexible rods upon addition of DMSO (right). (Reprinted with permission from [15]. Copyright (1993) American Chemical Society.)

Chiral porphyrin fibers have also been obtained when chiral lactate counterions were used together with cyanate as ligands in tin(IV)-porphyrins. The cyanate binds strongly to the tin(IV)-ions and the lactate forms the bridges in the spiral staircase (Figure 13) [16]. The fibers are broadened by interactions between the carboxyl groups, but the CD-effect of the chiral ligand is, nevertheless, strong ($\Theta \approx 10^6$ deg cm²/mol).

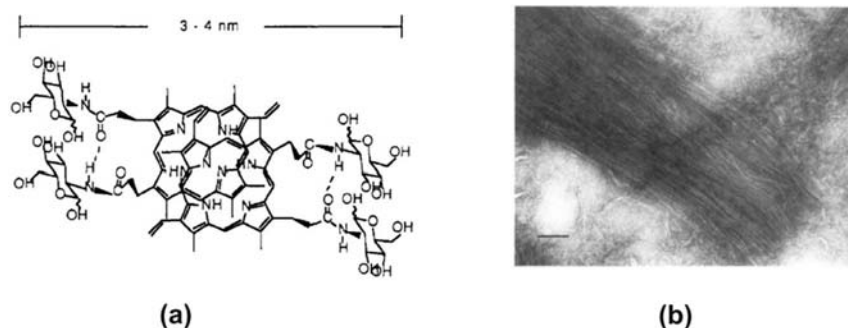


Figure 12. TEM (b) and model of a bundle of bis-2-amino-gluconamide protoporphyrin fibers obtained in water (a). (Reprinted with permission from [14]. Copyright (1992) American Chemical Society.)

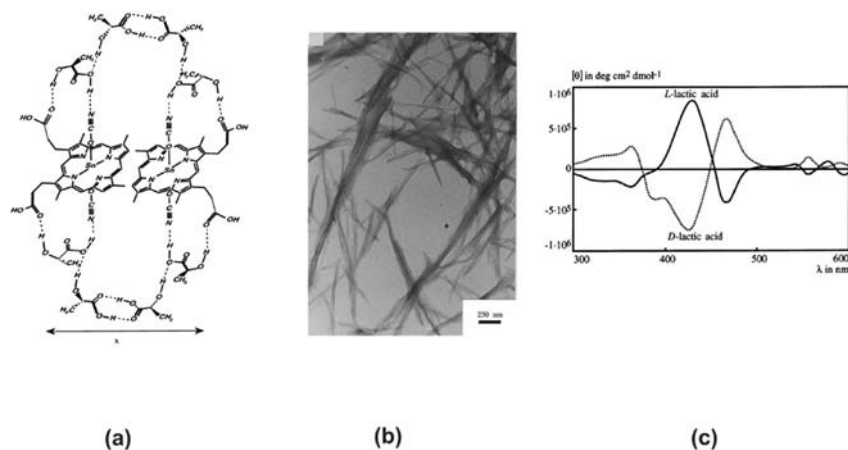


Figure 13. TEM (b) and model of cyanate-L-lactate-tin(IV)-protoporphyrin fibers. (a) They are ill-defined, because the propionic acid chains favor lateral aggregation. CD-spectra (c) show, however, strong effects caused by the chiral lactate linker combined with the strong cyanate ligand. (Reprinted with permission from [16]. Copyright (1998) Society of Porphyrins and pthalocyanina.)

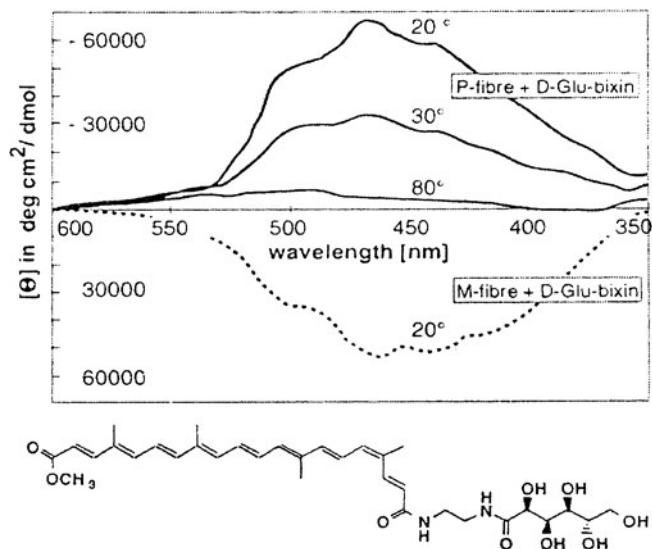


Figure 14. The CD effect of bixingluconamide, which is integrated into D-gluconamide fibers (see Figure 5) only depends on the chirality of the colorless helices. The stiff bixin core is not able to form stable helices. Reprinted with permission from [17]. Copyright (1990) American Chemical Society.

Bixin, a carotenoid bolaamphiphile with carboxylate and carbomethoxyl head groups, was amidated with gluconhydrazide and integrated into D- and L-configured N-octyl-gluconamide fibers. The bixin was thus non-covalently integrated into the alkyl chains of the quadruple helix (see Figure 5) and CD-spectra of medium intensity appeared upon helix formation and vanished upon melting the fibers (Figure 14) [17].

5. Viscoelastic Gels in Water

Only micellar fibers which do not form large assemblies are able to form “viscoelastic” gels. These gels are slightly opaque and reflect rotating air bubbles when the gel is stopped after rotation. Ephedrinium myristate produces networks of single 4 nm fibers which are difficult to detect and characterize by cryo TEM [18]. The benzene ring of ephedrine plunges into the fiber, and the polar amino and alcohol substituents separate the fibers from each other. Weak CD-bands of dissolved magnesium porphyrins ($\Theta = 30,000\text{--}60,000 \text{ deg cm}^2/\text{mol}$) indicate chiral organization of the counterions; $^1\text{H-NMR}$ spectra of the ephedrinium and pseudo-ephedrinium counterions show uniform conformers (Figure 15).

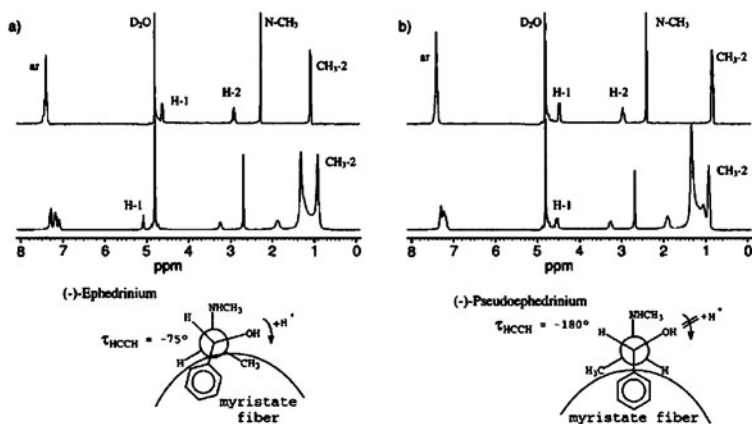


Figure 15. ^1H -NMR spectra of ephedrinium and pseudoephedrinium ions in viscoelastic myristine fibers. The chiral counterions are integrated into the fiber in a uniform conformation (synclinal for ephedrinium, anti for pseudoephedrinium). (Reprinted with permission from [18]. Copyright (1997) American Chemical Society.)

6. Bolaamphiphiles

A final remark concerns bolaamphiphiles (see Chapters 16 and 17). These amphiphiles carry two head groups on both ends of a hydrophobic skeleton. They also aggregate to form a large variety of fibers made of molecular monolayers or assemblies. The subject has been reviewed by us recently [19]. It turned out, however, that bolaamphiphilic assemblies with amino acid, carbohydrate and base head groups produce similar ribbons and wide tubules, such as described in Section 2 for fibers in organic media. High curvature and great lengths are seldom obtained. Fibers and resulting gels are, however, produced at particularly low concentrations; often ten times less bolas than single-headed amphiphiles are needed to form a gel. Bolaamphiphiles are most useful to functionalize and protect planar surfaces.

7. Conclusions

Curvature and chirality are closely related in covalent and non-covalent fibers. Short-pitch helices are only obtained if the helix diameter is small. In the α -helix of proteins, the width of the inner part of the helix is about 1.0 nm and the pitch is 1.6 nm. The structure of this helix is simply determined by the bond angles, which allow one turn after 3.6 amino acids. Stabilization occurs by four parallel-running hydrogen bond chains. The double helix of B-DNA has a diameter of 2 nm and a pitch of 3.4 nm. It is stabilized by hydrogen bonds

and hydrophobic effects between the base pairs in the center. F-Actin forms a long-pitch helix with a width of about 9 nm and a pitch of 78 nm.

Non-covalent helices in water are uniformly stabilized at first by the hydrophobic effect. A low polarity core made, for example, of alkyl chains or porphyrins is surrounded by chiral head groups or the core contains chiral centers itself (e.g., hydroxy fatty acids or steroids). The hydrophobic core increases the diameter of the fibers to at least 3–4 nm. This would allow for a pitch of 2 nm, such as observed in DNA. This has, however, never been achieved. Long pitches in the order of 25–150 nm are invariably found. The number of amphiphiles per turn lies typically around 20–30 nm.

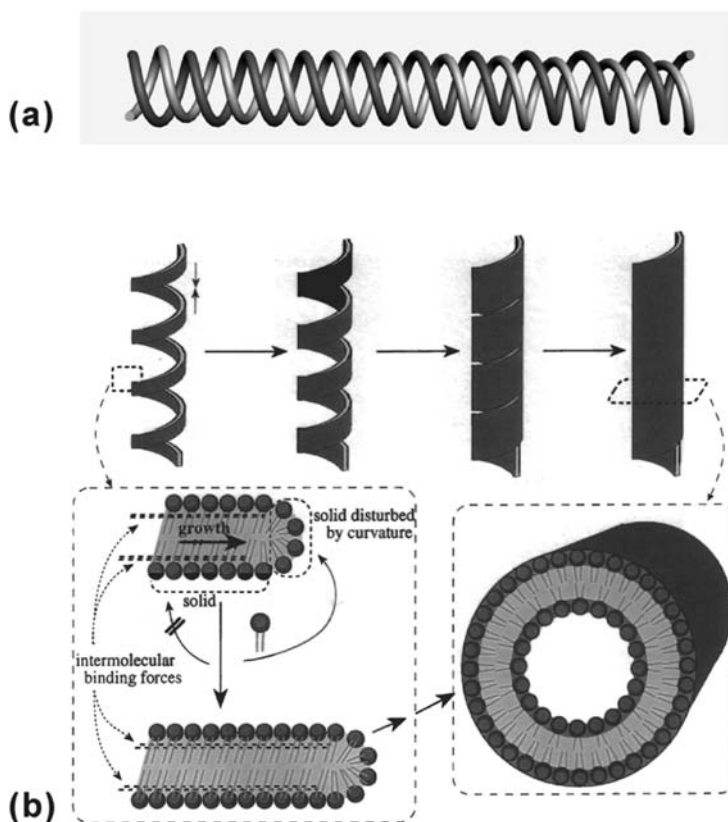


Figure 16. (a) Solid helical bilayer rods, which may be bent and assemble to form multiple helices. Such assemblies have so far only been observed in water. The most impressive example is the gluconamide quadruple helix (see Figure 4) with a circular diameter in each of the single fibers. (b) In organic solvents flat ribbons are formed and very often they are twisted. Such solid bilayer ribbons may add material and finally form tubules and assemblies of tubules. Such assemblies are also observed in water, when the high-curvature tubules merge after extended periods.

Even the lithium or potassium salts of 12-D-hydroxystearic acid in mineral oil do not appear as simple bilayer helices, but as multilayered twisted ribbons. The gluconamide micellar helix in water is the only known amphiphilic assembly of bimolecular thickness and radius without a charged surface. However, it appears as a quadruple helix with a width of 9 nm and a pitch of 28 nm. Tartaric acid micellar fibers are, surprisingly, not helical and form gigantic rings which assemble to multilayers without merging. This effect is certainly caused by the charged surface and connection by counterions. The lack of helicity probably points to a totally linear conformation of the R,R-tartaric acid head group. No OH–OH repulsion occurs and the *all-anti* conformer is presumably stabilized by OH \cdots OC hydrogen bridges to the neighboring carboxyl groups.

The ultimate thinness of the fibers corresponding to a molecular bilayer can thus be achieved in water, but the fibers assemble to complex multiple fibers or large objects. The only exceptions are the ultrathin fibers in the stiff “viscoelastic” gel which carry α -ammonium- β -alcohols as integrated chiral head groups (see Section 5).

The helical micellar fibers with a defined pitch may be treated as crystalline bilayers and physically described by the bending energy. They may be as flexible as fluid membranes and chiral spontaneous curvature can bend the micellar rods. The bending energy is proportional to the square of curvature $1/r^2$, where r is the radius of the fiber. It has a minimum when the angle of the helix against optical axes is 45° . The geometrically meaningful angle of the helical rise against the helical axis is often close to the magic angle of 54.7° . Here the dipole of the amphiphilic monomers is minimized. The helical pitch is thus first enlarged by steep angles of helix winding ($\geq 45^\circ$) and becomes even larger when the cylindrical bilayer is replaced by a broad bilayer ribbon. Such ribbons do not assemble to form multiple helices, but tend to add material at their edges, which finally leads to tubules. Their inner diameter is usually larger than 30 nm, again caused by the size and stiffness of hydrophobic bilayer structures (Figure 16) [20–22].

References

- [1] N-Dodecanoyl-(D- and L-) Serine-Assemblies in Vitreous Toluene and Water. Boettcher, C.; Schade, B.; Fuhrhop, J.-H. “Comparative cryo-electron microscopy of non-covalent”, *Langmuir*, **2001**, *17*, 873–877.
- [2] Tachibana, T.; Kambara, H. “Studies of helical aggregates of molecules. I. enantiomorphism in the helical aggregates of optically active 12-hydroxystearic acid and its lithium salt”, *Bull. Chem. Soc. Jpn.*, **1969**, *42*, 3422–3424.
- [3] Tachibana, T.; Yoshizumi, T.; Hori, K. “Monolayer studies of chiral and racemic 12-hydroxyoctadecanoic acids”, *Bull. Chem. Soc. Jpn.*, **1979**, *52*, 34–41.

- [4] Fuhrhop, J.-H.; Demoulin, C.; Rosenberg, J.; Boettcher, C. "Cloth-like aggregates of micellar fibers made of n-dodecyltartaric acid monoamides", *J. Am. Chem. Soc.*, **1990**, *112*, 2827–2829.
- [5] Fuhrhop, J.-H.; Schnieder, P.; Rosenberg, J.; Boekema, E. "The chiral bilayer effect stabilizes micellar fibers", *J. Am. Chem. Soc.*, **1987**, *109*, 3387–3390.
- [6] Fuhrhop, J.-H.; Svenson, S.; Boettcher, C.; Roessler, E.; Vieth, H.-M. "Long-lived micellar n-alkylaldonamide fiber gels. solid-state NMR and electron microscopic studies", *J. Am. Chem. Soc.*, **1990**, *112*, 4307–4312.
- [7] Mueller-Fahrnow, A.; Saenger, W.; Fritsch, D.; Schnieder, P.; Fuhrhop, J.-H. "Molecular and crystal structure of the bolaamphiphile octamethylene-N,N'-D-gluconamide", *Carbohydr. Res.*, **1993**, *242*, 11–20.
- [8] Svenson, S.; Koenig, J.; Fuhrhop, J.-H. "Crystalline order in probably hollow micellar fibers of n-octyl-d-gluconamide", *J. Phys. Chem.*, **1994**, *98*, 1022–1028.
- [9] Koenig, J.; Boettcher, C.; Winkler, H.; Zeitler, E.; Talmon, Y.; Fuhrhop, J.-H. "Magic angle (54.7°) gradient and minimal surfaces in quadruple micellar helices", *J. Am. Chem. Soc.*, **1993**, *115*, 693–700.
- [10] Svenson, S.; Kirste, B.; Fuhrhop, J.-H. "A CPMAS ¹³CNMR procedure based on single-crystal structures to determine molecular conformations and disorder in microcrystals and supramolecular assemblies", *J. Am. Chem. Soc.*, **1994**, *116*, 11969–11975.
- [11] Fuhrhop, J.-H.; Krull, M. "Self-assembling lipid membranes – from planar bilayer sheets to cloth-like aggregates of micellar fibers", In *Modern Trends in Supramolecular Chemistry*, H.-J. Schneider and H. Duerr, Eds., Weinheim: VCH, **1991**, pp. 223–249.
- [12] Fuhrhop, J.-H.; Boettcher, C., "Stereochemistry and curvature effects in supramolecular organization and separation processes of micellar n-alkylaldonamide mixtures", *J. Am. Chem. Soc.*, **1990**, *112*, 1768–1776.
- [13] Inamura, I.; Uchida, K. "Association behavior of protoporphyrin IX in water and aqueous poly(N-vinylpyrrolidone) solutions. Interaction between protoporphyrin IX and poly(N-vinylpyrrolidone)", *Bull. Chem. Soc. Jpn.*, **1991**, *64*, 2005–2007.
- [14] Fuhrhop, J.-H.; Demoulin, C.; Boettcher, C.; Koenig, J.; Siggel, U. "Chiral micellar porphyrin fibers with 2-aminoglycosamide head groups", *J. Am. Chem. Soc.*, **1992**, *114*, 4159–4165.
- [15] Fuhrhop, J.-H.; Bindig, U.; Siggel, U. "Micellar rods and vesicular tubules made of 14', 16'-diaminoporphyrins", *J. Am. Chem. Soc.*, **1993**, *115*, 11036–11037.
- [16] Rosengarten, B.; Böttcher, C.; Schulz, A.; Fuhrhop, J.-H.; Siggel, U. "Lateral, chiral tin(IV) porphyrin assemblies", *J. Porphyrins Phthalocyanines*, **1998**, *2*, 273–284.
- [17] Fuhrhop, J.-H.; Krull, M.; Schulz, A.; Moebius, D. "Bolaform amphiphiles with a rigid hydrophobic bixin core in surface monolayers and lipid membranes", *Langmuir*, **1990**, *6*, 497–505.
- [18] Traeger, O.; Sowade, S.; Boettcher, C.; Fuhrhop, J.-H. "Fluid and chiral eqhedrinium myristate micellar fibers", *J. Am. Chem. Soc.*, **1997**, *119*, 9120–9124.
- [19] Fuhrhop J.-H.; Wang T. Bolaamphiphiles. *Chem. Rev.*, **2004**, *104*, 2901–2938.
- [20] Fuhrhop, J.-H.; Helfrich, W. "Fluid and solid fibers made of lipid molecular bilayers", *Chem. Rev.*, **1993**, *93*, 1565–1582.
- [21] Helfrich, W. J.; Prost, J. "Intrinsic bending force in anisotropic membranes made of chiral molecules", *Phys. Rev. A*, **1988**, *38*, 3065–3068.
- [22] Helfrich, W. J. "Elastic theory of helical fibers", *Langmuir*, **1991**, *7*, 567–568.

ANALYSES OF SPECIFIC SYSTEMS

Chapter 19

RHEOLOGY OF WORMLIKE MICELLES: EQUILIBRIUM PROPERTIES AND SHEAR BANDING TRANSITIONS

Jean-François Berret

*Matière et Systèmes Complexes, UMR CNRS n° 7057,
Université Denis Diderot, 140 rue de Lourmel, 75015 Paris, France*

1. Introduction	667
2. Equilibrium Properties	669
2.1. Theoretical Background	669
2.2. Physical Chemistry of Wormlike Micelles and Related Systems	670
2.3. Flexibility of Wormlike Micelles	674
2.4. Phase Behavior	678
2.5. Linear Rheology and Scaling	680
2.6. Concluding Remarks on the Equilibrium Properties	685
3. Shear Banding Transition in Concentrated and Semi-Dilute Regimes	686
3.1. Isotropic-to-Nematic Transition in the Concentrated Regime	687
3.2. Shear Banding in Semi-Dilute Regime	696
3.3. Theories and Interpretations	702
4. Conclusions and perspectives for the Future	706

1. Introduction

Wormlike micelles are elongated and semi-flexible aggregates resulting from the self-assembly of surfactant molecules in aqueous solutions. In the general context of complex fluids, wormlike micelles have received considerable attention from theoreticians and experimentalists during the past decade

[1–8]. One reason for this interest is due to their remarkable rheological properties. When micelles grow and become wormlike, the aggregates are much like polymers, and as polymers they entangle above a critical concentration. The aqueous solutions then become viscoelastic. Quantitative rheological measurements show that this viscoelasticity is characterized by a single relaxation time, a property which is rather unusual for fluids with complex microstructures [9]. This rule is indeed so general that it is now accepted that a single relaxation time in the linear mechanical response is a strong indication of the wormlike character of self-assembled structures. This property has prompted several groups to use wormlike micelles as reference systems for the testing of new experimental techniques [10–13]. Wormlike micelles are also considered as models for polymers because of their nonlinear rheological properties. When submitted to steady shear, these viscoelastic fluids undergo a shear banding transition, which is associated with a plateau in the stress *versus* shear rate curve. The shear banding transition is a transition between a homogeneous and a non-homogeneous state of flow, the latter being characterized by a “separation” of the fluid into macroscopic regions (bands) of different shear rates. This type of transition is thought to be analogous in nature to the instability found in extrusion of polymer melts at high temperature. Since the first reports on shear banding in micellar solutions [14–16], non-homogeneous flows have been observed in many other complex systems. A final, but also an important reason to study wormlike micelles, is the widespread range of their applications in today’s life. Viscoelastic surfactant phases are already used in oil fields as fracturing fluids, in hydrodynamic engineering as drag reducing agents, and in many home and personal care products [8, 17].

In the first part of this chapter, we investigate the equilibrium properties and emphasize three properties that are crucial for the rheology: the dynamics of growth of the aggregates, the role of the flexibility on the phase behavior, and the relaxation dynamic in the viscoelastic regime. Each aspect is illustrated by data and references taken from the recent literature. We also provide several results that have not yet been published, for instance on the determination of the persistence length. Scaling laws express the specific dependences of some physical quantities, such as the viscosity or the scattering with the concentration. A critical analysis of the scaling properties found in wormlike micelles is proposed. The second part of the review deals with nonlinear rheological properties of semi-dilute and concentrated phases of wormlike micelles. Based on a broad bibliographic survey, our approach appears to demonstrate the existence of a “standard” behavior for all these systems. The characteristics of the “standard” behavior are a Maxwellian behavior of the linear viscoelasticity and a shear banding transition in the nonlinear response. We explore the diversity of the features of shear banding in micelles and show that for concentrated systems the instability is associated with a thermodynamic transition between an isotropic and a nematic state.

2. Equilibrium Properties

2.1. Theoretical Background

Wormlike micelles are elongated and semi-flexible aggregates resulting from the self-assembly of surfactant molecules in aqueous solutions. The growth and stability of micellar aggregates are, in general, described in terms of packing of the surfactant molecules, or equivalently in terms of the curvature of the water/hydrocarbon interface. Above the critical micellar concentration (cmc), spherical micelles form spontaneously and their size is related to that of the amphiphilic molecules. The kinetics of the micelle formation and breakdown above the cmc is based multiple equilibria, in which the micelles grow or shrink by stepwise incorporations or dissociations of monomers. This equilibrium has been known for some time and its description can be found in reviews [18–20] and textbooks [4, 21, 22]. Several parameters can be adjusted in order to modify the curvature of the water/hydrocarbon interface and to favor a change of morphology. These parameters are the surfactant concentration, the ionic strength, the temperature, etc. For a surfactant showing preferentially the cylindrical aggregation, the end-cap energy E denotes the excess in packing energy (between a spherical and a cylindrical environment) for the molecules located in the two hemispherical end-caps. In the following, we derive the growth laws for neutral and polyelectrolyte micelles.

Neutral Micelles: The end-cap energy E is here equivalent to the scission energy necessary to create two new chain ends. For a dispersion of micelles of length L and molecular weight distribution $c(L)$, the minimization of a free energy that takes into account the end-cap energy and the translational entropy yields for the average micellar length [4, 22, 23] is given by Eq. (1), where n_0 is the number of surfactants per unit length of the linear aggregate and n_0 (in \AA^{-1}) is of the order of unity.

$$\bar{L} = \frac{2}{n_0} c^{1/2} \exp\left(\frac{E}{2k_B T}\right) \quad (1)$$

End-cap energies have been determined from temperature jump measurements and they are in the range 20–30 $k_B T$ [1, 24]. Note that the same type of reasoning for two-dimensional aggregation leads to the conclusion that disc-like aggregates can only exist as infinite bilayers. The distribution in length $c(L)$ is broad and given by Eq. (2). $c(L)dL$ denotes the number density of chains of length comprised between L and $L + dL$. The exponential distribution in Eq. (2) corresponds to an index of polydispersity of 2.

$$c(L) = \frac{c}{\bar{L}^2} \exp\left(-\frac{L}{\bar{L}}\right) \quad (2)$$

Polyelectrolyte Micelles: Electrostatically charged micelles are made from ionic surfactants and the solutions are prepared with no added salt. For these aggregates, point charges located at the hydrocarbon/water interface modify the micellar growth and length distribution. This effective charge of the aggregate arises actually from the incomplete compensation of the surfactant charges by the counterions. MacKintosh and coworkers have proposed a model to demonstrate that the electrostatic interactions reduce the scission energy and favor the breaking of micelles [25, 26]. For polyelectrolyte micelles, the end-cap energy is not equivalent to the scission energy. The electrostatic contribution to the free energy results in a broad dilute regime. There, the micelles are rather monodisperse and their length is only very slowly increasing with concentration. The overlap concentration c^* between the dilute and semi-dilute regimes depends on the effective linear charge density, noted ν , through Eq. (3) where ℓ_B is the Bjerrum length ($\ell_B = 7.15 \text{ \AA}$ in water) and R_C is the radius of the cylinder.

$$c^* = \left(\frac{k_B T \ell_B R_C \nu^2}{E} \right)^2 \quad (3)$$

Above the overlap threshold, which also corresponds to the screening of the electrostatic interactions by the counterions, the micelles grow more rapidly according to:

$$\bar{L} = \frac{2}{n_0} c^{1/2} \exp \left(\frac{E}{2k_B T} \left[1 - (c^*/c)^{1/2} \right] \right) \quad (4)$$

Figure 1 displays the growth laws for neutral and charged micelles, according to Eq. (1) and Eq. (4), respectively. In Figure 1, the ratio \bar{L}/R_C is plotted as function of c , the surfactant concentration and using parameters indicated in the caption [25, 26]. The predictions for the dynamics of growth of neutral and polyelectrolyte micelles agree qualitatively with experiments. For instance, it is known that the addition of salt to a solution of polyelectrolyte micelles can result in a strong increase of viscosity, the solution passing from a viscous fluid to a viscoelastic gel. In Figure 1, this change corresponds to a transition at a fixed concentration from the bottom curve (polyelectrolyte, dilute regime) to the top curve (neutral, semi-dilute regime). Quantitatively, however, and except for few systems [27], the analytic forms of the growth laws for neutral and polyelectrolyte micelles have not been found systematically. This issue will be discussed at the end of the first part of this chapter.

2.2. Physical Chemistry of Wormlike Micelles and Related Systems

Wormlike micelles can form spontaneously at ambient temperature using cationic surfactants with 16 carbon atoms, for example, in the aliphatic chain.

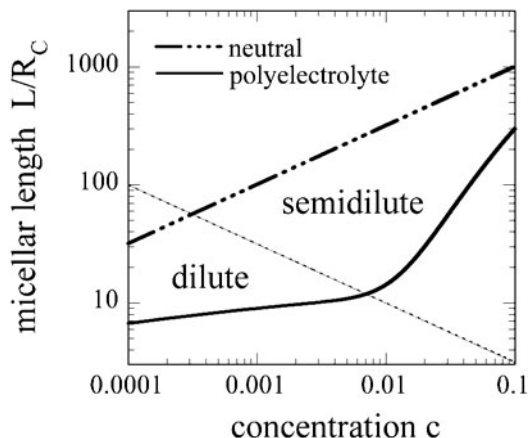


Figure 1. Predictions for the average micellar length of neutral and polyelectrolyte wormlike micelles as a function of the surfactant concentration (as a volume fraction). The dash-dotted and continuous lines are calculated according to Eqs. (1) and (4), respectively, with parameters taken from [25, 26]: $E = 20 k_B T$, $\ell_B R_C v^2 = 1$, and $n_0 = 1/2$. (Reprinted with permission from [26]. Copyright (1990) EDP Sciences.)

This is the case for cetyltrimethylammonium bromide (CTAB) [28–30] and cetylpyridinium bromide (CPBr) [31]. As seen previously, because of electrostatics the transition between spherical to cylindrical aggregates occurs at relatively high surfactant concentrations (Figure 1). The growth of the aggregates can be promoted however if co-surfactants or other low molecular weight additives are incorporated into the solutions. These additives are short chained alcohols, strongly binding counterions, oppositely charged surfactants, etc. We review below the different classes of surfactants and co-surfactants/additives which form such structures. A list of the most common surfactants and counterions known to form wormlike micelles is given in Table 1. Table 1 also provides the chemical formulas of these molecules and their abbreviations. During the last decade, a number of other low molecular weight molecules have been found to associate in solutions into elongated structures (see also Chapters 16–18). Because in many cases their rheology is similar to that of the surfactant micelles, we have included them in the listing below.

A–Surfactant and simple salt. The addition of simple salts, such as sodium chloride (NaCl) or potassium bromide (KBr), to ionic surfactant solutions results in the screening of the electrostatic interactions between the charges, and thus in the growth of the aggregates. The archetype system of class **A** is CTAB with KBr [5, 20, 24, 32–35]. Other well-known examples are sodium dodecyl sulfate (SDS) with monovalent [27, 36–41] or multivalent counterions [42, 43].

Table 1. Common surfactants and counterions known to form wormlike micelles in water. The counterions in the third column with formulas $\text{OH}-(\text{C}_6\text{H}_4)-\text{COO}^-$, $\text{CH}_3-(\text{C}_6\text{H}_4)-\text{SO}_3^-$ and $\text{Cl}-(\text{C}_6\text{H}_4)-\text{COO}^-$ are salicylate (Sal), toluenesulfonate (or tosylate, abbreviated as T or Tos) and chlorobenzoate (ClBz), respectively.

Surfactant name	Formula	Counterion	Abbr.
Decyl sulfate	$(\text{C}_{10}\text{H}_{21})-\text{SO}_3^-$	Na^+	SdS
Dodecyl-trimethylammonium	$(\text{C}_{12}\text{H}_{25})-\text{N}^+(\text{CH}_3)_3$	Br^-	DTAB
Dodecyl sulfate	$(\text{C}_{12}\text{H}_{25})-\text{SO}_3^-$	Na^+	SDS
tetradecyl-trimethylammonium	$(\text{C}_{14}\text{H}_{29})-\text{N}^+(\text{CH}_3)_3$	Br^-	TTAB
Cetyl-trimethylammonium	$(\text{C}_{16}\text{H}_{33})-\text{N}^+(\text{CH}_3)_3$	Br^-	CTAB
		Cl^-	CTAC
		$\text{CH}_3-(\text{C}_6\text{H}_4)-\text{SO}_3^-$	CTAT
		$\text{Cl}-(\text{C}_6\text{H}_4)-\text{COO}^-$	CTACIBz
Cetylpyridinium	$(\text{C}_{16}\text{H}_{33})-(\text{C}_5\text{H}_5)-\text{N}^+$	Br^-	CPBr
		Cl^-	CPCI
		ClO_3^-	CPClO ₃
		$\text{OH}-(\text{C}_6\text{H}_4)-\text{COO}^-$	CPSal
Dodecyl-benzenesulfonate	$(\text{C}_{12}\text{H}_{25})-(\text{C}_6\text{H}_4)-\text{SO}_3^-$	Na^+	SDBS
Tetradecyl-dimethylamine oxide	$(\text{C}_{14}\text{H}_{29})-\text{N}^+(\text{CH}_3)_2-\text{OH}$	Cl^-	C14DMAO
Hexadecyloctyl-dimethylammonium	$(\text{C}_{16}\text{H}_{33})-(\text{C}_8\text{H}_{17})-\text{N}^+(\text{CH}_3)_2$	Br^-	C18-C8DAB

B – Surfactant and co-surfactant. where the co-surfactant is a short alcohol chain. Classical examples are the ternary systems, sodium alkylsulfate-decanol-water (SdS-Dec [44–47] and SDS-Dec [48–50], see Table 1) and cetylpyridinium chloride-hexanol-brine (CPCI-Hex) [51–55]. In these systems, the ratio between the alcohol and surfactant concentrations controls the polymorphism of the self-assembly. The theoretical arguments developed in Section 2.1 for neutral chains should apply to this class, namely those for which the cylindrical aggregates are intermediate structures between spheres and bilayers.

C – Surfactant and strongly binding counterion. Strongly binding counterions are small molecules of opposite charge with respect to that of the surfactant. They are sometimes called hydrotopes. Well-known examples of hydrotopes are salicylate, tosylate and chlorobenzoate counterions, which all contain an aromatic phenyl group (see Table 1). CTAB and CPCI with sodium salicylate (NaSal) have been probably the most studied micellar systems during the last two decades [3, 56–70]. Contrary to simple salts (class A), a large

proportion of these counterions ($\sim 80\%$) is assumed to be incorporated into the micelles. It was found that in CPCI-NaSal, long wormlike micelles are immediately formed at the cmc (0.04 wt. %), without passing through an intermediate spherical morphology [68, 69, 71].

D – Amphoteric surfactant. Amphoteric surfactants are surface active molecules that contain positive and negative charges in the head group. Betaine-type molecules with quaternary ammonium and carboxylate groups are the representatives of this class. They associate at low concentrations and aqueous solutions exhibit strong gel-like properties. These properties are attributed to the existence of an entangled network of micelles [72, 73].

E – Gemini surfactants and surfactant oligomers. The covalent linking of amphiphilic moieties at the level of the head group yields to gemini surfactants and surfactant oligomers; see [74] for a review and Chapters 16 and 17 for gemini-based gels. In aqueous solutions, these molecules present a broad polymorphism of aggregation [75–79]. Gemini surfactants are one of the rare examples for which cylindrical micelles close on themselves spontaneously, forming loops or rings. This property has been attributed to large end-cap energies [80].

F – Cationic and anionic mixtures. Oppositely charged surfactants have shown synergistic enhancements of rheological properties, and notably through the formation of mixed wormlike micelles. The growth of the micelles is assumed to arise from the charge neutralization of the surface potential (as in C) and from the related increase of the ionic strength (as in A). Recent examples studied are the mixtures of sodium dodecylsulfate (SDS) and dodecyltrimethylammonium bromide (DTAB) [81, 82], or the mixtures made from cetyltrimethylammonium tosilate and sodium dodecyl benzenesulfonate [83, 84].

G – Reverse micelles in organic solvent. Lecithin is a phospholipid that is a major component in the lipid matrix of biological membranes. When dissolved in a nonpolar solvent (an alkane), reverse spherical micelles are formed. The addition of small amount of water triggers the growth of aggregates. The rheology of these solutions was shown to be similar to that of direct wormlike micellar solutions [85–88].

H – Metallic salts in organic solvent. In apolar solvent, some metallic salts such as a bicopper tetracarboxylate complex associate into elongated wires. The wires are built with only one molecule in the cross-section. As in surfactant micelles, the aggregation number can be very large and the wires are described as long and semiflexible colloids. With increasing concentrations, solutions become viscoelastic with the same signatures as those of surfactant systems [89, 87–91].

I – Block copolymers. Cylindrical self-assembly has also been reported in aqueous solutions of low molecular weight block copolymers [92–94]. The system investigated in [92, 93] is poly(ethylene oxide)-poly(butadiene) with

a weight fraction around 50% for the first block. “Giant” micelles have been found by cryo-transmission electron microscopy and the cylindrical morphology of the poly(butadiene) core was confirmed by neutron scattering.

2.3. Flexibility of Wormlike Micelles

2.3.1. Persistence length

The persistent character of the micellar chains is a fundamental feature of wormlike micelles. The flexibility of the chains determines the equilibrium conformations in a good solvent, as well as the phase behavior of the solutions at high concentrations. Figure 2 shows the segment of a cylindrical micelle that is uniformly bent. The vector $\mathbf{u}(s)$ is tangent to the micellar axis and s denotes the curvilinear length. The bending free energy per unit of s is proportional to the product κC^2 , where κ is the bending modulus of the chain and C its curvature. For surfactants, Ben-Shaul and coworkers have shown that this free energy has a molecular origin [95]. Contributions arising from the repulsions between head groups, from the hydrocarbon-water interfacial energy and from the conformations of the aliphatic chains in the core should be taken into account in the calculation of κ .

From a geometrical point of view, the persistence length, b , measures the decay length of the angular correlation along the micellar axis and can be defined through the equality in Eq. (5) where the brackets denote the average over the orientational distribution of micellar segments.

$$\langle \mathbf{u}(0) \cdot \mathbf{u}(s) \rangle = \exp(-s/b) \quad (5)$$

From a thermodynamical point of view, b is associated to the bending modulus through the relationship, $b = \kappa / k_B T$. b is the length over which the thermal fluctuations are able to cancel the orientational coherence of the chain. The first experimental determination of the persistence length in wormlike micellar solutions was carried out in 1980 by Porte and co-workers [96], combining

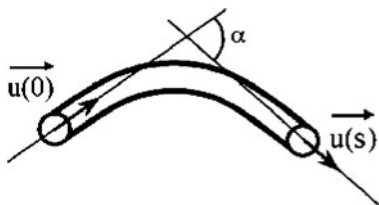


Figure 2. Representation of a segment of a wormlike micelle. The angular correlation function of the vectors $\mathbf{u}(s)$ tangent to the micellar axis is used to define the persistence length b of the polymer-like aggregate (Eq. (5)). For wormlike micelles, b is of the order of 400 Å.

dynamic light scattering and magnetic birefringence experiments. The system investigated was cetylpyridinium bromide (CPBr) with sodium bromide (class A) [96, 97]. For this system, the saturation of the magnetic field-induced birefringence observed with increasing surfactant concentration (and in a range where the hydrodynamic radius was still growing) was interpreted as evidence of the independent alignment of segments of length b . b was estimated to be on the order of 200 Å [53, 98, 99]. It has been recognized since then that elongated cylindrical micelles of surfactants must be described as semi-flexible chains. In this section, we show how scattering techniques and, in particular, small-angle neutron scattering can be used to determine the persistence length of wormlike micelles.

2.3.2. Scattering function of a persistent micellar chain

Small-angle neutron scattering (SANS) is an ideal tool for studying surfactant polymorphism because of the large scattering contrast resulting from the use of hydrogenated surfactants and deuterated water as a solvent (see Chapter 10). For wormlike micelles, SANS presents a second advantage. The radius R_C and the persistence length b fall in the wave-vector range covered by this technique ($q = 10^{-3} \text{ \AA}^{-1} - 0.4 \text{ \AA}^{-1}$) and their respective signatures are well separated. The average length of micelles can also be obtained, but the wave-vector limitations restrict this determination to values below $\sim 1000 \text{ \AA}$ [27, 41, 81]. Light scattering [100] and ultra small-angle neutron scattering are then useful complementary techniques. Our goal here is to derive the scattering function of a persistent chain as function of the wave-vector q and to show how it compares to experimental data on one example. The scattering cross-section of semiflexible chains is usually derived from asymptotic behaviors [101]. The two wave-vector ranges relevant for SANS are $qb < 1$ and $qb > 1$. In the following, we referred to them as low and high wave-vectors ranges, respectively. We assume furthermore the inequality $R_C < b < \bar{L}$.

$qb > 1$ (high q -range): In this range, micelles appear to neutrons as dispersed and disordered rods of lengths shorter than b , and the scattering cross-section $d\sigma(q)/d\Omega$ is given by Eq. (6) where J_1 denotes the first-order Bessel function and $\Delta\rho$ is the difference in scattering length densities between the aggregates and the solvent.

$$\frac{d\sigma}{d\Omega}(q, qb > 1) = 4\pi^3 \Delta\rho^2 \mathcal{L} R_C^4 \frac{1}{q} \left(\frac{J_1(qR_C)}{qR_C} \right)^2 \quad (6)$$

For surfactant micelles with core radius R_C of 20 Å, the range of validity of Eq. (6) goes from 0.01 to 0.4 Å⁻¹. Note that the average micellar length \bar{L}

does not enter Eq. (6) explicitly. Instead, the total micellar length per unit volume \mathcal{L} is in the prefactor. For a solution prepared at concentration c with a surfactant of molecular weight M_W , the ratio $c\mathcal{N}_A/M_W\mathcal{L}$ is the number of surfactants per unit length of micelles, noted n_0 in Eqs. (1) and (4). This ratio can thus be determined accurately by SANS and it is of the order of $n_0 = 2$ molecules/Å [41, 102, 103]. For $qR_C < 1$, the expression in parenthesis in Eq. (6) approaches 1/2 and the scattering function varies as q^{-1} .

$qb < 1$ (low q -range): At low wave-vectors, the scattering probes the self-avoiding random walk configuration of the chains. The intensity decreases with a power law with an exponent of -2 for Gaussian chains and $-5/3$ for chains in good solvent. The flexibility of micellar aggregates manifests itself as a cross-over between a q^{-1} and a q^{-2} (or $q^{-5/3}$) behavior; this cross-over occurs in the range $q \sim 1/b$. This reasoning is also valid for the semi-dilute regime if the curvilinear length L_e between entanglements is much larger than the persistence length b . L_e is related to the mesh size ξ of the network through the equation $L_e \sim \xi^{5/3}b^{-2/3}$ [104].

These ideas are illustrated in Figure 3. Here, the form factor of a single chain is shown as function of the wave-vector. The calculation is made using the analytical expressions provided by Brûlet *et al.* and by Pedersen and Schurtenberger without excluded volume interactions [105, 106]. In the inset of Figure 3, the transition between the q^{-1} and a q^{-2} regimes is emphasized. This transition is smooth and continuous.

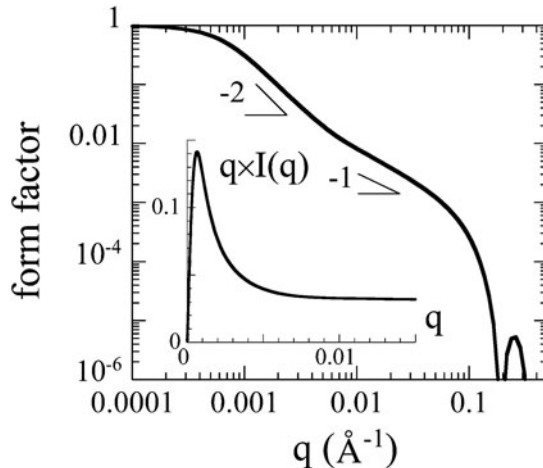


Figure 3. Scattering form factor of a wormlike micellar aggregate of total curvilinear length $L = 4 \mu\text{m}$, of persistence length $b = 400 \text{ \AA}$, and of radius $R_C = 20 \text{ \AA}$. Calculations were made using the Pedersen and Schurtenberger model [106]. The cross-over between the q^{-1} and q^{-2} regimes is emphasized in the inset (Holtzer representation, $q \times I(q)$ versus q).

2.3.3. Comparison with small-angle neutron scattering

Figure 4 displays data obtained on several CTAB solutions prepared at $c = 0.2$ wt.% and using increasing amounts of sodium salicylate (NaSal). In this figure, the parameter R denotes the molar ratio between the two components: $R = [\text{Sal}^-]/[\text{CTA}^+]$. At $R = 0$ (i.e., for pure CTAB solution), the scattering cross-section $d\sigma(q)/d\Omega$ is low and indicative of interacting spherical micelles. At $R = 0.36$, the neutron spectrum is modified and exhibits an increase in scattering at low q . At $R = 1.46$ and above, all sets of data display the q^{-1} behavior characteristic of elongated aggregates. Neutron scattering thus provides a clear illustration of the micellar growth by addition of strongly binding counterions. At this concentration and values of R , the CTAB-NaSal solutions are in the slightly entangled regime and the curvilinear length between entanglements is much larger than the persistence length. We have compared these data to the predicted cross-section for semi-flexible aggregates [105, 106]. In Figure 5, the product $q \times d\sigma(q)/d\Omega$ is shown in double logarithmic scales for the system CTAB-NaSal at molar ratios 7.3 and 36.4. This representation, also called the Holtzer representation, emphasizes the transition between the q^{-1} and q^{-2} asymptotic regimes. The data are those of Figure 4. The continuous lines through the data are calculated using $b = 380$ Å and $b = 360$ Å, respectively. Persistence lengths of the order of 400 Å are typical for neutral wormlike micelles, and have been found repeatedly in the recent literature [27, 53, 98, 100, 102, 107]. For polyelectrolyte micelles, the

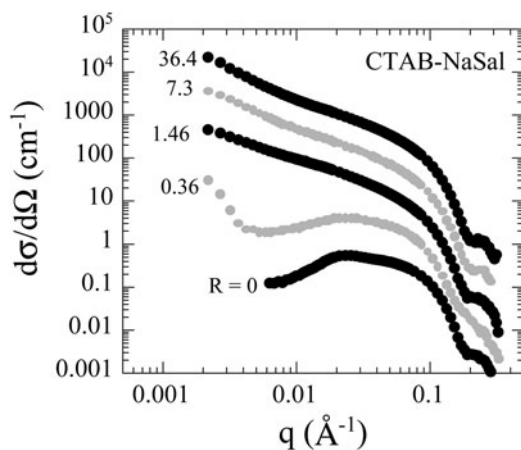


Figure 4. Neutron scattering cross-section $d\sigma(q)/d\Omega$ versus q for CTAB-Sal micelles for molar ratios, $R = [\text{Sal}^-]/[\text{CTA}^+]$, between $R = 0$ and $R = 36.4$. The CTAB concentration is $c = 0.2$ wt.% (5.5 mmol/l) for all solutions. The scattering curves have been shifted by a factor 5 with respect to each other. The increase of the scattering at low q with increasing R is interpreted as evidence of the micellar growth.

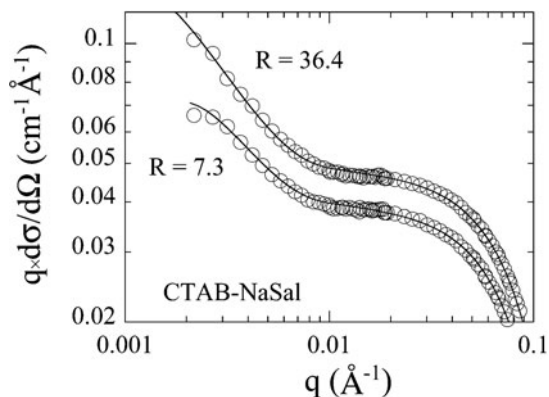


Figure 5. $q \times d\sigma(q)/d\Omega$ versus q for CTAB-NaSal wormlike micelles at surfactant concentration $c = 0.2$ wt.% and molar ratios $R = 7.3$ and $R = 36.4$. The experimental data are those of Figure 4. The continuous lines are calculated according to the model described by Pedersen and Schutenberger [106]. The adjustable parameters are the micellar radius R_C , the persistence length b and the average micellar length between entanglements. For $R = 7.3$, $b = 380$ Å and $L/b = 15$ and for $R = 36.4$, $b = 360$ Å and $L/b = 40$ (with $R_C = 20$ Å for both). The intensity for $R = 36.4$ has been shifted by a factor 1.3.

total persistence length can be larger than the above characteristic values [108, 109]. In conclusion, the persistence length of micellar aggregates is of the order of 400 Å, a value that is between that of synthetic polymers [104] and that of biological molecules, such as DNA, actin and tubulin [110, 111].

2.4. Phase Behavior

At high surfactant concentration, the average contour length of wormlike micelles can be of the order of microns (i.e., much larger than the persistence length b : $L \gg b \gg R_C$). Semenov and Kokhlov have shown that for semi-flexible chains obeying the last inequalities, long-range orientational order appears with increasing volume fraction as a result of a first-order phase transition [112–114]. The transition is between an isotropic disordered phase and an orientationally ordered nematic phase. Based on the approach developed for stiff chains [115], and assuming only steric interactions between chains, the values of the phase boundaries between the ordered and disordered states, as well as the order parameter of the nematic phase, were predicted. These boundaries are denoted c_{I-N} and c_N and are defined as follows: for $c < c_{I-N}$, the solutions are isotropic; at $c > c_N$ they are nematic; for $c_{I-N} < c < c_N$, they separate into an isotropic and a nematic phase. For semi-flexible chains, Semenov and Khokhlov have found:

$$c_{I-N} = 10.48 \frac{R_C}{b}, \quad c_N = 11.39 \frac{R_C}{b} \quad \text{and} \quad w = \frac{c_N}{c_{I-N}} - 1 = 0.09 \quad (7)$$

The important result in Eq. (7) is that the phase boundaries depend only on the ratio between the radius and the persistence length. For rigid rods, the same type of equations was obtained, the persistence length being replaced by the average length of the rods. For rods, the prefactors are also different from those in Eq. (7) [112, 114, 115].

Experimentally, nematic phases of wormlike micelles have been found systematically at high surfactant concentrations, between 20 and 50 wt. % [44, 46–48, 50, 52, 71, 116–120]. Examples of phase diagrams reported recently in the literature are shown in Figure 6. Three ternary systems are presented: cetylpyridinium chloride-hexanol-water (at 0.2 M NaCl) [52, 119, 121], cetylpyridinium chloride-sodium salicylate-water (at 0.5 M NaCl) [122] and

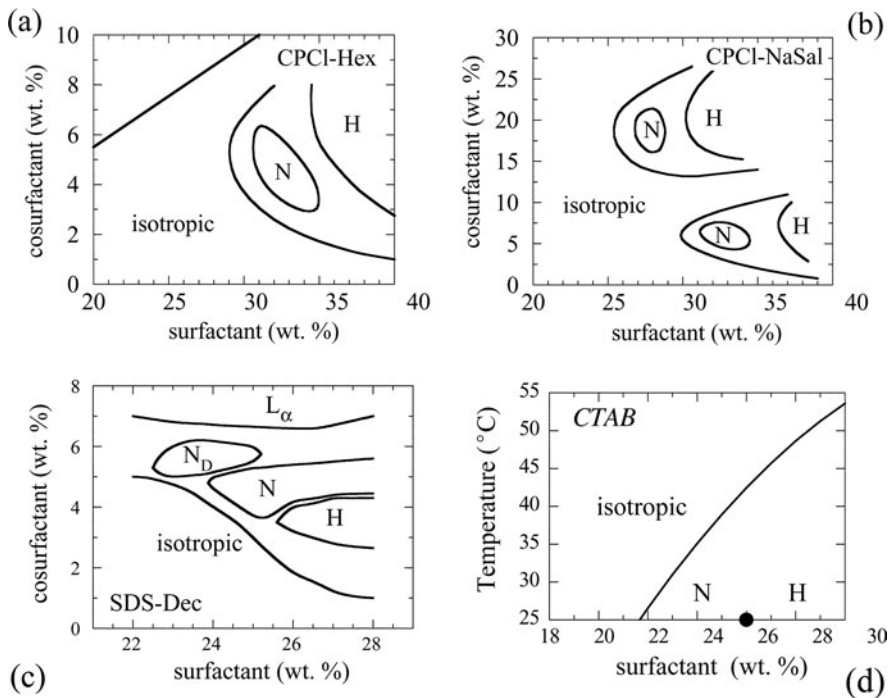


Figure 6. Phase diagrams of four wormlike micellar systems: (a) cetylpyridinium chloride, hexanol and water (0.2 M NaCl) [121]; (b) Cetylpyridinium chloride, sodium salicylate and water (0.5 M NaCl) [122]; (c) sodium dodecylsulfate, decanol and water [49, 50, 120]; (d) cetyltrimethylammonium bromide and water [30, 124]. For the diagrams (a), (b) and (c), the cosurfactant concentration is in the ordinate. For diagram (d), temperature is in the ordinate. The phase boundary between the nematic and hexagonal phases in CTAB-H₂O is not known. According to Fontell *et al.*, the transition occurs at $c = 26$ wt.% at room temperature ($T = 25^\circ\text{C}$) [30]. At fixed cosurfactant/surfactant ratios or fixed temperature, similar sequences of phases are observed with increasing concentrations: isotropic (entangled), nematic (N) and hexagonal (H). N_D and L_α denote nematic discotic and lamellar, respectively. (Reprinted with permission from [121]. Copyright (1994) EDP Sciences.)

sodium dodecyl sulfate-decanol-water [49, 50, 120]. In Figure 6d, the binary system cetyltrimethylammonium bromide-water is shown and the phases are displayed in a temperature-concentration diagram [30, 117, 123]. Note for CPCI-Sal the presence of two nematic “islands”, one at salicylate concentration around 5 wt.% and one around 20 wt.%. All four systems show that at constant ratio with respect to the alcohol or hydrotope content, there is the same sequence of thermodynamically stable phases: isotropic, nematic, and hexagonal. Thus, the packing of semi-flexible cylinders leads to mesophases with orientational and translational order. For the four systems, the limits of phases c_{I-N} and c_N (varying between 20 and 45 wt.%) compare well with the theoretical values predicted for semi-flexible chains with radius 20 Å and persistence length 400 Å (as previously determined). Eq. (7) gives values for c_{I-N} and c_N around 50 wt.%. The deviations observed for SDS-Dec and CTAB are the largest, and they could be due to additional electrostatic interactions.

2.5. Linear Rheology and Scaling

Several authors noticed as early as the 1950's that surfactant solutions can be strongly viscoelastic (see also Chapter 6). Nash, for instance, identified the role of additives such as naphthalene derivatives in the onset of viscoelasticity in CTAB solutions [56]. One intriguing result was that the viscoelasticity of the solution began to increase well below the cmc of the surfactant. Some years later, Gravsholt and coworkers recognized that other types of additives, such as salicylate or chlorobenzoate counterions, are actually solubilized by the micelles, lowering the cmc of the surfactant [59, 125]. It was suggested by the same authors that the viscoelasticity had the same physical origin as that of polymer solutions and melts, namely entanglements and reptation [104]. The picture proposed in late 1970's was that of a network of entangled rod-like micelles.

Maxwellian Behavior: An advancement in the description of micellar dynamics was made by the first quantitative measurements of the linear mechanical response of these solutions by Rehage, Hoffmann [3, 126, 127], Shikata [63, 128–130], and Candau [1, 131, 132] and their co-workers. Rehage and Hoffmann used rheology to demonstrate that micellar growth results in an increase of the fluid viscosity. Figure 7 displays the static viscosity data for cetylpyridinium chloride at 3.6 wt.% (100 mmol) as function of sodium salicylate content [3, 126, 127]. The steep increase seen at molar ratio $R \sim 0.3$ is interpreted as a transition between spherical and wormlike micelles. Similar viscosity behavior was observed with CTAB and NaSal [63, 64, 133]. Note in

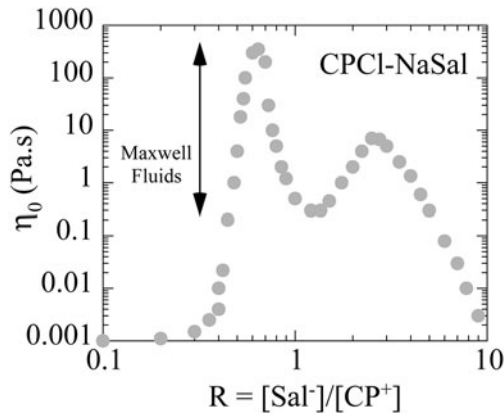


Figure 7. Static viscosity η_0 for cetylpyridinium chloride-sodium salicylate solutions as a function of $R(=[\text{Sal}^-]/[\text{CP}^+])$. The CPCI concentration is $c = 3.6$ wt.% (100 mmol). Data are taken from Rehage and Hoffmann [3]. Solutions with viscosity larger than $0.2 \text{ Pa} \cdot \text{s}$ are entangled and exhibit a Maxwellian behavior (Eqs. (8) and (9)). (Reprinted with permission from [127]. Copyright (1988) American Chemical Society.)

Figure 7 the presence of a secondary maximum around $R \sim 2.5$. It is interesting to note here that the two maxima in viscosity correspond to molar ratios at which a nematic phase is observed at higher concentrations (Figure 6b). The correlation between a high viscosity in the semi-dilute regime (indicating the formation of very long micelles) and the presence of a nematic phase was recognized by Göbel and Hilltrop [71].

A fascinating result from the work of Rehage, Hoffmann, Shikata and Candau and their co-workers is that the viscoelasticity of these surfactant solutions can be characterized by a single exponential response function. A stress relaxation function $G(t)$ of the form in Eq. (8) was found.

$$G(t) = G_0 \exp(-t/\tau_R) \quad (8)$$

G_0 denotes the elastic modulus extrapolated to $t \rightarrow 0$ (equivalent to the storage modulus at infinite frequency G'_∞) and τ_R is the relaxation time. Equation (8) describes the behavior of a Maxwell fluid for which the static viscosity η_0 is the product of $G_0\tau_R$. Rheological experiments are classically performed as a function of the angular frequency, and the response function is then the dynamical elastic moduli $G^*(\omega)$. $G^*(\omega) = G'(\omega) + iG''(\omega)$ is the Fourier transform of $G(t)$. $G'(\omega)$ and $G''(\omega)$ denote the storage and loss moduli, respectively:

$$G'(\omega) = G_0 \frac{\omega^2 \tau_R^2}{1 + \omega^2 \tau_R^2} \quad \text{and} \quad G''(\omega) = G_0 \frac{\omega \tau_R}{1 + \omega^2 \tau_R^2} \quad (9)$$

Eqs. (8) and (9) have been found to apply repeatedly in viscoelastic micellar systems. They are so general that it is now commonly accepted that a Maxwellian behavior is a strong indication of wormlike character of self-assembled structures. Figure 8 shows one example of Maxwellian behavior obtained for the CPCI-NaSal system at different temperatures [123]. The storage and loss moduli are displayed in reduced units (G'/G_0 and G''/G_0 versus $\omega\tau_R$) and superposition is obtained over the whole temperature range. The continuous lines are calculated according to Eq. (9). Typical C16 wormlike micellar solutions such as the ones based on CPCI or CTAB surfactants have elastic moduli in the range 1–1000 Pa·s and relaxation times τ_R between 1 ms (the lowest relaxation time detectable with rotational rheometers) and several seconds at room temperature. For longer hydrophobic chains, such as for a C22 mono-unsaturated cationic surfactant recently studied, Maxwellian behavior with relaxation times as long as 1000 seconds has been reported at room temperature [72, 134, 135].

The theoretical challenge is to account for the unique relaxation time of the mechanical response. This was accomplished by Cates and co-workers in the 1980's using the reptation-reaction kinetics model [1, 23, 136–139]. The reptation-reaction kinetics model is based on the assumption that in the viscoelastic regime, wormlike micelles form an entangled network analogous to that of polymers. The micelle-polymer structural analogy was demonstrated

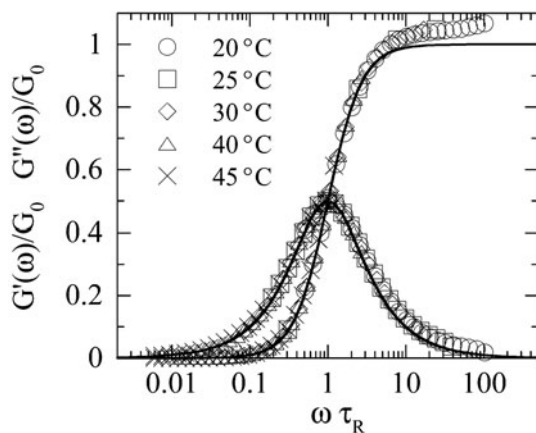


Figure 8. Elastic moduli G' and G'' as a function of the angular frequency for temperatures between 20°C and 45°C. G' and G'' are divided by the elastic modulus G_0 and the angular frequency ω is normalized by the relaxation time τ_R of the fluid. Data are for the CPCI-NaSal wormlike micelles in water (0.5 M NaCl) at $c = 12$ wt.% [123]. The solid lines correspond to Maxwellian viscoelastic behavior (Eq. (9)). (Reprinted with permission from [123]. Copyright (1997) American Physical Society.)

by means of static and dynamic light scattering during the same period [20, 24, 34, 35, 140, 141]. Cates suggested that the breaking and recombination events of the chains are coupled to the reptation [104] and accelerate the overall relaxation of the stress [23, 136]. In the fast breaking limit, a given micelle undergoes several scission and recombination reactions on the time scale of the reptation. Thus, all initial deformations of the tube segments relax at one rate that is driven by the reversible scission. Because of the breaking and recombination dynamics, wormlike micelles are often described as equilibrium or living polymers. Other relaxation mechanisms were also explored, such as bond and end interchange processes between micelles [139]. In the reptation-reaction kinetics model, the rheological time τ_R is given by Eq. (10), where τ_{break} and τ_{rept} are the characteristic times for breaking/recombination and reptation, respectively.

$$\tau_R \sim \sqrt{\tau_{\text{break}} \tau_{\text{rept}}} \quad (10)$$

In wormlike micellar systems, typical breaking times are of the order of milliseconds [24] and Eq. (10) was found to be in qualitative agreement with experimental data [142]. Experimentally, however, it has been difficult to determine τ_{break} and τ_{rept} separately and to confirm the validity of Eq. (10). Another way to test the predictions of the reptation-reaction kinetics model is to study the scaling properties (as a function of the concentration) for some structural and rheological quantities describing the micellar entangled state.

Scaling Laws: In the entangled regime, the properties of wormlike micelles depend on the micellar volume fraction (i.e., the surfactant concentration) and not on the properties of individual micelles, such as their average length or their length distribution. By analogy with polymers, Cates suggested that wormlike micelles should follow scaling laws [1, 23]. These scaling behaviors have the form of power laws, with scaling exponents that can be compared to those found in experiments. The scaling exponents of some representative quantities related to the structure and rheology of wormlike micelles are given in Table 2. These quantities are the elastic modulus G_0 , the relaxation time τ_R , the static viscosity η_0 , the mesh size ξ , the Rayleigh ratio extrapolated at zero wave-vector $\mathcal{R}(q \rightarrow 0)$, and the self-diffusion coefficient D_S . Here, $\mathcal{R}(q \rightarrow 0)$ is determined from static light scattering experiments and D_S is the diffusion coefficient of the surfactant molecules. The theoretical exponents are given within the mean-field Gaussian approximation. The reptation-reaction kinetics model predicts, for instance, that the static viscosity above c^* scales as $\eta_0 \sim c^{7/2}$ and the elastic modulus as $G_0 \sim c^{9/4}$. Figure 9 illustrates such behavior for the system CPCl-NaSal in 0.5 M NaCl brine [122, 143]. In this figure, power laws

Table 2. Experimental and theoretical exponents of some relevant quantities in the semi-dilute regime of wormlike micelles.

	Scaling exponents (theory)	Scaling exponents (experiment)	Refs.
Elastic modulus G_0	+2.25	1.8...2.4	<i>a</i>
Relaxation time τ_R	+1.25	> 0 and/or < 0	<i>a</i>
Static viscosity η_0	+3.5	1...4	<i>a</i>
Mesh size ξ	-0.75	-(0.5...1)	<i>b</i>
Rayleigh ratio $\mathcal{R}(q \rightarrow 0)$	-0.25	-(0.3...0.4)	<i>b</i>
Self-diffusion constant	-1.58	-(1...4)	<i>c</i>

(a): [1, 6, 84, 85, 87, 89, 122, 126, 127, 131, 132, 134, 143, 146-149];

(b): [1, 20, 34, 35, 65, 87, 134, 141, 143, 144, 150];

(c): [1, 140, 144, 151, 152].

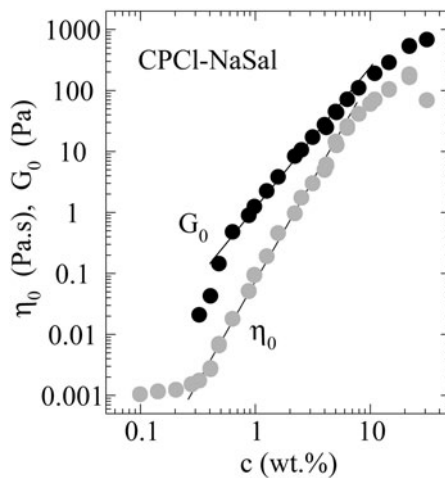


Figure 9. Concentration dependence of the static viscosity η_0 and of the elastic modulus G_0 for the CPCI-NaSal system. In the semi-dilute regime ($c^* \sim 0.3$ wt.%), both quantities exhibit scaling laws as a function of the concentration [143]. The exponents are here 2.2 and 3.3, in good agreement with the predictions (see Table 2). (Reprinted with permission from [122]. Copyright (1990) EDP Sciences.)

are observed over more than a decade in concentration range and the exponents are close to the predicted ones.

In Table 2, we also summarize the results of a survey of 15 different surfactant systems and provide the experimental exponents for neutral micelles as a comparison. The elastic modulus G_0 is in agreement with theory for most (if not all) of the systems. Scaling exponents are between 1.8 and 2.4. As far as the structure of the network is concerned and although fewer measurements were

done, the mesh size ξ and the Rayleigh ratio $\mathcal{R}(q \rightarrow 0)$ also agree with theory. The best examples are CTAC [1, 20, 34, 35, 65] and CPClO₃ [141, 144]. The exponent associated with the self-diffusion constant has a broader variation, between -1 and -4 , whereas theory predicts -1.58 [145]. In contrast, for the viscosity and for the relaxation time, the predicted exponents are observed in a few systems only, as for instance CPCl-NaSal in brine (0.5M NaCl) [121, 143], CTAB with 0.25 M KBr [1], CTAB-NaSal in brine (0.1M NaCl) [1], lecithin reverse micelles [87] and metallic salts in organic solvents [89]. For the majority of wormlike micelles, however, the scaling exponents for η_0 and τ_R are not in agreement with the model. As a function of the concentration, τ_R can either increase or decrease, or even pass through a maximum [1, 3, 6, 84, 126, 127, 131, 134, 146]. Some authors have ascribed these discrepancies to the existence of micellar branching [5].

We propose here an alternative explanation. In the reptation-reaction kinetics model, both the reptation and the breaking times depend on the average micellar length \bar{L} . The scaling are: $\tau_{\text{break}} \sim \bar{L}^{-1}c^0$ and $\tau_{\text{rept}} \sim \bar{L}^3c^{3/2}$ [23, 136]. So, both τ_R and η_0 will depend on \bar{L} . This is not the case for ξ and G_0 . We suggest that the failure to observe the correct scaling for the viscosity and relaxation times is due to the fact that, for these systems, the average micellar length does not follow the predicted $c^{1/2}$ dependence (Eq. (1)). We suggest also that the theory developed in Section 2.1 for neutral and polyelectrolyte micelles does not strictly apply to surfactant systems with strongly binding counterions, such as CPCl-NaSal and CTAB-NaSal (class C) or for cationic and anionic mixtures (class F). In these systems, complexation between oppositely charged species might be a more appropriate description for the growth law of micelles.

2.6. Concluding Remarks on the Equilibrium Properties

In this part of the chapter, three main aspects of the equilibrium properties of wormlike micelles have been addressed: the self-assembling properties and the dynamics of growth of linear aggregates, the role of flexibility on the phase behavior, and the relaxation dynamic in the viscoelastic regime. In the semi-dilute regime, wormlike micelles entangle and form a transient network. The solutions appear to be “gels” but quantitative measurements reveal a Maxwellian behavior for most systems. The relaxation times are between 1 ms–1000 s, depending on the surfactant chain length. We have also noted that Maxwellian behavior extends well beyond the surfactant phases reviewed here. It has been observed on for a wide variety of low molecular weight molecules that are known to self-assemble, as surfactants, into linear, semi-flexible and reversible aggregates.

In the concentrated regime, the mesh size of the network is shorter than the persistence length b , and orientational correlations start to appear. We have

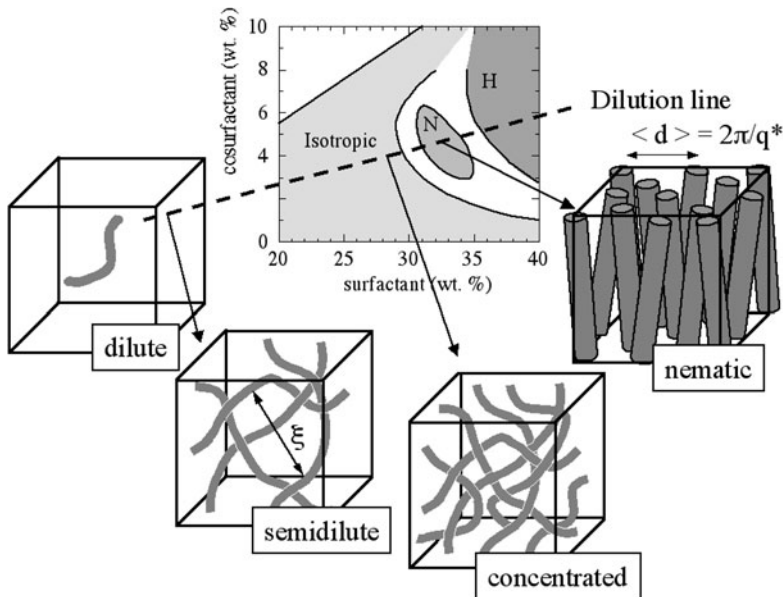


Figure 10. Schematic illustrations of the different phases encountered in wormlike micellar solutions, from dilute solutions to concentrated mesophases. The phase diagram shown is that of CPCI-Hex (Figure 6a). $\langle d \rangle$ denotes the average distance between colinear micelles in the concentrated isotropic and nematic phases. ξ is the mesh size of the entangled network in the semi-dilute regime.

cited several examples of surfactant systems, including systems with screened and unscreened electrostatics, for which an increase in concentration yields a succession of thermodynamically stable mesophases, such as nematic and hexagonal ones. This sequence of phases is illustrated in Figure 10, together with a representation of the local environments for the aggregates. This picture is in relatively good agreement with the theories that describe the phase behavior of linear and semi-flexible aggregates [26, 114, 136]. Two features, the Maxwellian viscoelasticity and the presence of long-range orientational order at high concentration, play a crucial role in the nonlinear rheology of wormlike micelles and in the shear banding transition.

3. Shear Banding Transition in Concentrated and Semi-Dilute Regimes

When submitted to a steady shear, wormlike micelles generally do not change their local morphology. The aggregates remain cylindrical, with an average length and distribution that might eventually depend on the shear rate

[153, 154]. A number of publications suggest that the solutions undergo a transition of shear banding. The shear banding transition is a transition between an homogeneous and a non-homogeneous state of flow, the latter being characterized by a demixing of the fluid into macroscopic regions of high and low shear rates. Shear banding has been identified unambiguously in wormlike micelles using flow birefringence [14] and NMR velocimetry [15, 16] measurements. Since the first reports on micellar fluids, non-homogeneous flows were observed in many other complex fluids, such as cubic phases of soft colloids [155], electro- and magneto-rheological fluids [156], transient networks of associative polymers [157] and soft glassy materials [158]. Shear banding is in general an abrupt transition that occurs at a critical shear rate, noted $\dot{\gamma}_1$. In some cases, it is appropriate to introduce a second characteristic shear rate, $\dot{\gamma}_2$, which corresponds to the onset of a second homogeneous flow at higher shear rates. In the following, we review the phenomenology of shear banding in concentrated and semi-dilute wormlike micelles. The first step consists of defining the rheological signatures.

3.1. Isotropic-to-Nematic Transition in the Concentrated Regime

3.1.1. Steady-state and transient rheology

By analogy with polymer solutions, the concentrated regime of wormlike micelles is defined for entangled networks with mesh sizes of the order or shorter than the persistence length (i.e., $\xi < b$) [143]. In the surfactant systems cited in the first part of this chapter, this inequality corresponds to weight concentrations between ~ 10 wt.% and c_{I-N} , the isotropic-to-nematic phase boundary. In this section, we illustrate the rheology of concentrated wormlike micelles by focusing on a solution made from cetylpyridinium chloride/hexanol. This CPCI-Hex solution is isotropic, but close to the isotropic-to-nematic boundary (Figure 10). The steady-state shear stress shown in Figure 11 as a function of the shear rate $\dot{\gamma}$ has been obtained by conventional rheometry using a cone-and-plate geometry. The flow curve of the CPCI-Hex solution exhibits a discontinuity of slope at the critical value $\dot{\gamma}_1$, followed by a stress plateau that stretches over more than a decade in shear rates. We call σ_P the value of the stress at the discontinuity. At high shear rates, there is a further increase of the stress. Various shear histories have been applied to the solution in order to ensure the reproducibility and robustness of the plateau. The data in Figure 11 can thus be considered as steady-state values.

In some concentrated wormlike systems, the plateau is not totally flat, but exhibits a slight increase as a function of the shear rate. This increase is described, in general, by a power law, $\sigma(\dot{\gamma}) \sim \dot{\gamma}^\alpha$ where $\alpha = 0.1 - 0.3$.

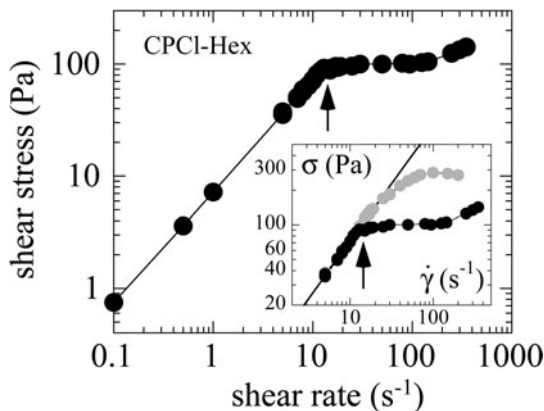


Figure 11. Steady state response of a concentrated cetylpyridinium chloride / hexanol (CPCI-Hex) micellar solution. Concentrations are $c_{\text{CPCI}} = 28.0$ wt.% and $c_{\text{Hex}} = 3.9$ wt.%. Experiments are made using a rotational rheometer using a cone-and-plate geometry. The onset of the stress plateau is at the critical shear rate $\dot{\gamma}_1 = 14 \text{ s}^{-1}$. The static viscosity of this micellar fluid is $7.2 \text{ Pa}\cdot\text{s}$ [148, 159]. Inset: Zoom of the plateau region, showing the initial (open symbols) and the steady-state (closed symbols) values of the stress, as obtained from start-up experiments in which the shear rate is increased progressively from an initial rest state.

Stress plateaus or pseudo-plateaus in concentrated wormlike micelles were reported for the first time in CPClO_3 [116] and CPCI-Hex [121, 159] systems. They have been found for other surfactants, such as CPCI-NaSal [123, 148], CTAB [117, 124, 160], CTAB-KBr [161], and CTAT [162]. Stress plateaus are the central feature in the nonlinear rheology of wormlike micelles.

The transient stress responses at different shear rates, below the critical rate $\dot{\gamma}_1$ (Figure 12a) and in the plateau region (Figures 12b and 12c), are displayed in Figure 12. These transients were obtained. Below $\dot{\gamma}_1$, the stress grows rapidly (at times < 1 s) up to a stationary value and remains constant. Above $\dot{\gamma}_1$, the transient stress exhibits the same rapid increase at short times and a slow relaxation at longer times. The stress kinetics in the plateau region is described by Eq. (11) [122, 148, 163] where the initial and steady state stresses, $\sigma(t \rightarrow 0)$ and σ_{ST} , as well as the characteristic time of the relaxation, τ_N , depend on $\dot{\gamma}$.

$$\sigma(t) = \sigma_{\text{ST}} + (\sigma(t \rightarrow 0) - \sigma_{\text{ST}}) \exp[-(t/\tau_N)^n] \quad (11)$$

For flat plateaus, $\sigma_{\text{ST}} = \sigma_P$. In the inset of Figure 11, $\sigma(t \rightarrow 0)$ and σ_{ST} are shown by open and closed symbols. Note that the stress overshoot, $\sigma(t \rightarrow 0) - \sigma_{\text{ST}}$, at its maximum is much larger than the stationary value of the stress itself, suggesting a rather profound transformation of the fluid in this regime. The slow kinetics of the shear stress in the plateau region was originally assumed to coincide with the nucleation and growth of shear bands [122, 148]. The

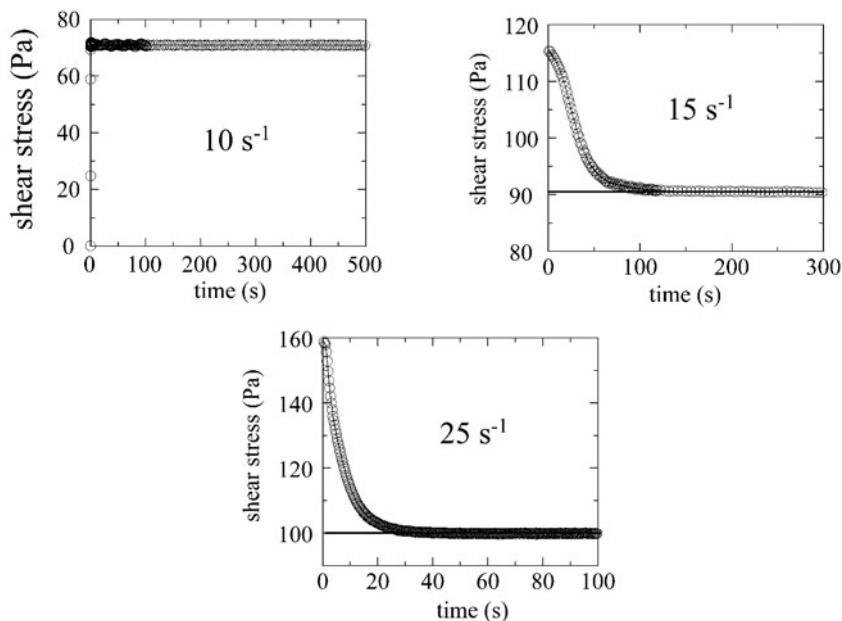


Figure 12. Transient shear stress as determined from start-up experiments for the solution shown in Figure 11. Data are taken below and in the plateau region. The characteristic time of the initial stress decrease at 15 and 25 s^{-1} is much larger than the Maxwell relaxation time ($\tau_R = 0.02$ s). The slow kinetics corresponds to the formation of shear bands.

coefficient n in Eq. (11) has been found to be in the range 1–3, depending on the system and on the shear rate [164]. Note finally that in the systems showing stress plateaus and slow kinetics, the characteristic time τ_N in Eq. (11) is always much larger than the Maxwell relaxation time τ_R derived from the linear response. For the CPCl-Hex solution studied here, $\tau_R = 20$ ms whereas τ_N varies between 1 and 100 s depending on the shear rates [164].

The data presented in Figures 11 and 12 were obtained in controlled strain rheometry (i.e., in an experiment where the strain rate is held fixed and where the stress is deduced from the torque transmitted by the fluid). Rotational rheometry also allows control of the stress and simultaneously recording of the angular velocity of the mobile part. Semi-dilute and concentrated wormlike micelles have been extensively studied using controlled stress rheometry [14, 42, 84, 117, 132, 134, 161, 165, 166]. The generic behavior for this type of experiment is summarized in Figure 13. For a CTAB- D_2O concentrated solution ($c = 18$ wt.%, $T = 32^\circ\text{C}$), the shear stress measured at steady state exhibits two stable branches at low and high shear rates. These two branches are separated by a stress plateau which coincides exactly with that of a strain controlled experiment.

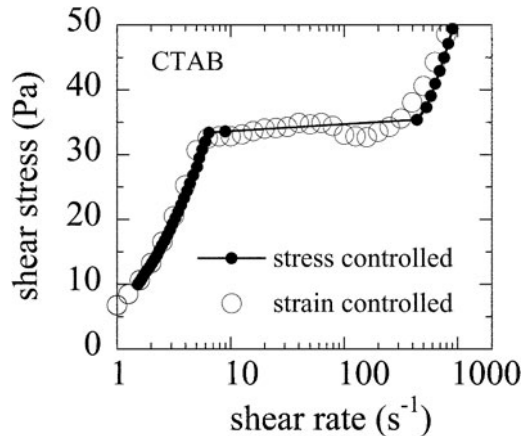


Figure 13. Comparison between the steady state shear stress results obtained from controlled strain and controlled stress rheometry in the plateau region. The data are for CTAB-D₂O wormlike micelles at $c = 18$ wt.% and $T = 32^\circ\text{C}$. When stress is applied, the sheared solution jumps from the low shear to the high shear branch of the flow curve. In the lower branch, the stress increases linearly with a static viscosity $\eta_0 = 6.7$ Pa·s. (Reprinted with permission from [124]. Copyright (1997) American Physical Society.)

The interesting feature here is that no steady state can be set up in the plateau region when the stress is controlled. Instead, there is a jump in shear rate; the shear rate switches rather abruptly from $\dot{\gamma}_1$ to $\dot{\gamma}_2$. The present results reinforce the idea of a shear-induced phase separation, where the stress or strain rate is the intensive or extensive variable, respectively.

3.1.2. Flow birefringence

Flow birefringence experiments have been carried out during the past decades to investigate the orientation properties of polymer solutions and melts [167, 168]. More recently, rheo-optical techniques were applied with success to the study of wormlike micelles [2, 14, 117, 161, 169–172]. Experimental set-ups designed for studying complex fluids generally utilize a Couette cell as a shearing device (Figure 14). For flow birefringence, the cell has a narrow gap and the polarized light is sent along the vorticity direction. The velocity (\mathbf{v}), velocity gradient ($\nabla\mathbf{v}$) and vorticity ($\boldsymbol{\omega} = \mathbf{v} \times \nabla\mathbf{v}$) directions are indicated in Figure 14 for the Couette geometry. The two physical quantities determined in this type of experiments are the birefringence intensity, Δn , and the extinction angle χ . Δn is the difference between the indices of the ordinary and extraordinary directions and χ is the angle of the refractive index tensor with respect to the flow velocity. For an isotropic fluid, $\Delta n = 0$ and $\chi = 45^\circ$.

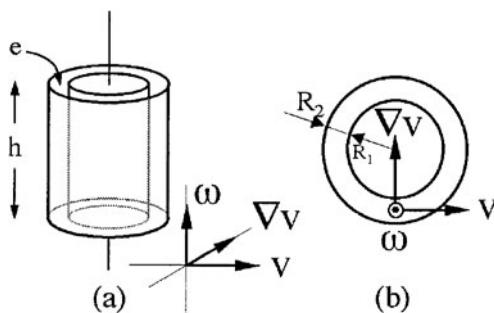


Figure 14. Representation of a Couette cell used in investigations of the structure of wormlike micelles under shear. The fluid is introduced between the two concentric cylinders (a). The value of the gap, $e = R_2 - R_1$, is small compared to the overall size of the cell. The motion of the outer cylinder (the inner one being immobile) produces a velocity gradient in the gap. The three directions characterizing simple shear are shown: the velocity \mathbf{v} , the velocity gradient $\nabla\mathbf{v}$ and the vorticity $\boldsymbol{\omega}$. Data from flow birefringence, small-angle neutron scattering and nuclear magnetic resonance have been obtained with this type of device. In flow birefringence, the incident and polarized light beam propagates along the vorticity direction. In SANS, the incident beam passes through the Couette along $\nabla\mathbf{v}$ (radial configuration) and passes twice through the moving fluid.

The device in Figure 14 can also be used for direct visualization of the solution under shear. The transmitted light is recorded on a digital camera with a spatial resolution of the order of microns. This was the configuration that was chosen to show the phenomenon of shear banding transition in wormlike micelles [14, 161, 173]. Figure 15 shows six photographs of a 1mm-gap containing a concentrated CPCI-Hex solution under steady shear before the onset of stress plateau (A), in the plateau region (B–E), and after the upturn at high shear rate (F). We note that in Figures 15A and 15F, corresponding to the lower and upper branches of flow curve, the birefringence and the micellar orientations are homogeneous throughout the gap. For intermediate $\dot{\gamma}$, there is a coexistence between a bright and a dark band. The dark and bright bands in Figure 15 have birefringences Δn of the order of -10^{-5} and -10^{-3} , respectively. The negative sign of Δn arises from the anisotropy of the polarizability tensor that describes a monomer in the micellar chain [170, 171]. The dark band in Figures 15A–15E results from the adjustment between the angle made by the polarizer and χ . In the plateau regime, the bright band broadens as the shear rate increases. The growth of the strongly birefringent phase from the inner cylinder is generally explained in terms of curvature effect of the Couette cell. For concentric cylinders, the shear rate is a weakly varying function of the spatial coordinate and its largest value is reached at the inner wall [174, 175]. The shear banding is initiated where the fluid first reaches σ_p , at the inner wall.

In order to demonstrate that the shear-induced bright band corresponds to a nematic phase, we compare in Figure 16 the flow birefringence of an

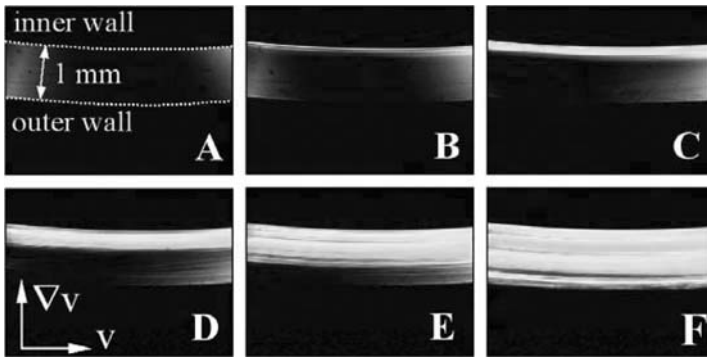


Figure 15. Photographs showing the gap of a Couette cell containing a CPCI-Hex solution at concentrations $c_{\text{CPCI}} = 28.0 \text{ wt.}\%$ and $c_{\text{Hex}} = 3.9 \text{ wt.}\%$ (see Figures 11 and 12 for the rheology). The letters correspond to increasing shear rates. Photographs (A) and (F) are taken in the Newtonian regime and in the high shear rate branch, respectively. Photographs (B) to (E) are taken in the plateau region. Typical exposure times are of the order of milliseconds. The polarizer and analyzer are oriented so that the band close to the outer cylinder appears dark. With increasing shear rates, the bright nematic band fills up the gap progressively. [A color version of this figure may be found on page 942.]

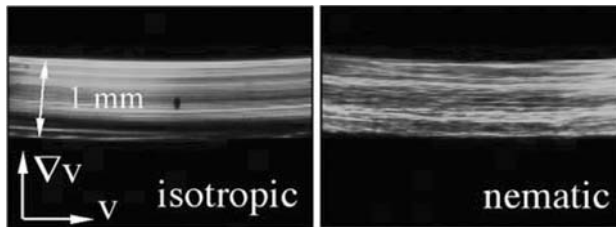


Figure 16. Comparison between the flow birefringence of two CPCI-Hex solutions under shear. The solution on the left is isotropic at rest (same concentration as in Figure 15) and the photograph is taken at a shear rate of 220 s^{-1} . This corresponds to the high shear rate branch of the flow curve. The solution on the right is nematic at rest ($c_{\text{CPCI}} = 29.1 \text{ wt.}\%$ and $c_{\text{Hex}} = 4.1 \text{ wt.}\%$) and the photograph represents the fluid sheared at 8.9 s^{-1} . In order to reduce the transmitted intensity, a green filter has been placed in the optical path before the solution. [A color version of this figure may be found on page 943.]

isotropic solution at high shear rate and a nematic solution under moderate steady shear. The two fluids are made from the same micelles and the nematic liquid crystal is slightly more concentrated than the isotropic one. Figure 16 shows that the transmitted light, and thus the birefringence Δn are the same for the two experiments. The extinction angles in both solutions are also close to 0° , as expected for an oriented nematic. The textures observed for the nematic solution vanish if $\dot{\gamma}$ is increased further.

3.1.3. Neutron scattering under shear

As discussed in the first part of this chapter, SANS is generally used to probe the translational degrees of freedom of microstructures on a 10 \AA – 1000 \AA length scale. Using a two-dimensional detector, SANS can also probe the orientational degrees of freedom of a micellar fluid subjected to flow (see Chapter 10). A set-up similar to that for flow birefringence is utilized in a typical SANS experiment (Figure 14). In the radial (or tangential) scattering configuration, the incident beam passes through the Couette along the gradient (or velocity) direction. Figures 17a–17c show two-dimensional scattering patterns obtained for a CPCI-Hex solution at a concentration close to isotropic-to-nematic transition. The shear rates correspond to the three different branches of the flow curve. In the first stable branch, at low shear rate, the scattering is isotropic and exhibits a broad maximum at $q^* \sim 0.1 \text{ \AA}^{-1}$. This maximum results from strong translational correlations between the micellar threads. An estimate of the distance between micelles (i.e., between their axis of symmetry) yields $\langle d \rangle = 2\pi/q^* \sim 60 \text{ \AA}$. In the plateau regime, some anisotropy arises in the scattering function, which manifests itself by symmetric

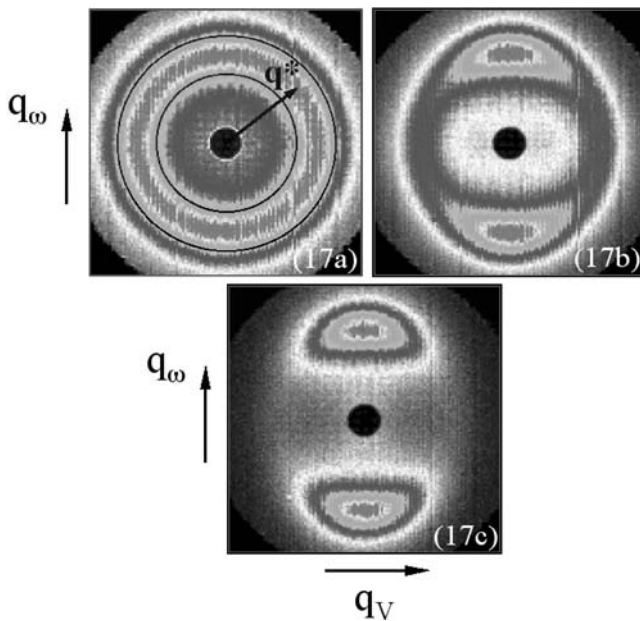


Figure 17. Neutron scattering intensities obtained from a concentrated micellar solution under shear [121, 159]. Shear rates are $\dot{\gamma} = 0$ (a), 64 (b) and 213 s^{-1} (c). The data are recorded in the velocity-vorticity plane, corresponding to the wave-vectors \mathbf{q}_V and \mathbf{q}_ω . The maximum scattering at $q^* = 0.0996 \text{ \AA}^{-1}$ arises from steric interactions between micelles. [A color version of this figure may be found on page 943.]

crescent-like peaks in the vorticity direction \mathbf{q}_ω . At still higher shear rates, the ring-like structure vanishes and the scattering is dominated by the anisotropic pattern (Figure 17c). This latter pattern is qualitatively analogous to the one obtained from a micellar solution which is nematic at rest and subjected to a moderate shearing. The scattering signature of a nematic phase of micelles is shown in Figure 18 for comparison. Similar results have been reported on various other surfactant systems close to the I-N transition [116, 124, 148, 159].

Neutron data have been analyzed quantitatively in terms of orientational degrees of freedom. The proportions of isotropic and nematic phases under shear, as well as the order parameter of the shear-induced nematic, can thus be derived. The two-dimensional spectra of Figures 17 and 18 are first converted into vectors representing the angular distribution of the scattered intensity $I(\psi)$, where ψ is the azimuthal angle. ψ is defined as the angle between the wave-vector \mathbf{q} and the vorticity direction \mathbf{q}_ω . For isotropic patterns, $I(\psi)$ is constant, whereas for anisotropic patterns it is a maximum at $\psi = 0^\circ$ and $\psi = 180^\circ$. The azimuthal intensity is then fitted using the phenomenological relation in Eq. (12) where $I_I(\dot{\gamma})$ is the contribution of the isotropic phase and $I_N(\dot{\gamma})$ is the prefactor of the nematic component.

$$I(\psi, \dot{\gamma}) = I_I(\dot{\gamma}) + I_N(\dot{\gamma}) \sinh(m \cos^2 \psi) \quad (12)$$

The ψ -dependence of the nematic contribution is periodic, and it is characterized by a unique parameter m . This parameter determines the order parameter of the oriented phase. Knowledge of $I_I(\dot{\gamma})$ and $I_N(\dot{\gamma})$ on the other hand allows derivation of the proportion of each phase at different shear rates. These results are discussed in Section 3.1.4 and are compared with data from flow birefringence and nuclear magnetic resonance.

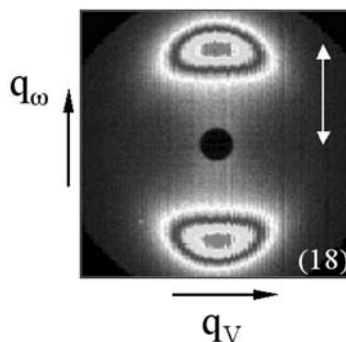


Figure 18. Neutron scattering intensity obtained from nematic wormlike micelles under shear [119, 176] at the shear rate $\dot{\gamma} = 100 \text{ s}^{-1}$. As in Figure 17, the data are recorded in the velocity-vorticity plane. The scale for Figures 17 and 18 is given by the double-headed arrow which represents 0.1 \AA^{-1} . [A color version of this figure may be found on page 944.]

The shear-induced phase is characterized by the orientational distribution of the micellar threads, or equivalently by the moments of this distribution. P_2 , the second moment of the distribution, represents the order parameter of the phase:

$$P_2 = \langle (3 \cos^2 \beta - 1)/2 \rangle \quad (13)$$

Here, the average $\langle \dots \rangle$ is performed over all micellar orientations and β is the angle made by the cylindrical micelles with the flow velocity. Using analytical expressions to relate the n^{th} -order moment of the distribution to the experimental intensity $I(\psi, \dot{\gamma})$ [177], we found a constant value for $P_2(\dot{\gamma})$ in the plateau region, $P_2 = 0.65 \pm 0.03$ [159]. This value agrees well with that of a nematic monodomain made from the same micelles, $P_2 = 0.70 \pm 0.04$ [118, 176] and is slightly higher than the order parameter predicted for persistent chains, $P_2 = 0.49$ [114]. It can be concluded that the shear-induced phase is strongly oriented and nematic. Due to its excellent alignment, director instabilities within the new phase, such as tumbling or wagging, can be ruled out [118, 178].

3.1.4. Nuclear magnetic resonance under shear

For the wormlike micelles, nuclear magnetic resonance (NMR) was used primarily to determine the velocity field in the banded regime [15, 16, 160, 179–184]. With NMR, it is also possible to resolve spatially (i.e., within the gap of the shearing cell) the spectral splitting associated with the quadrupole interactions of the deuteron nucleus with the local electric-field gradient. This splitting is actually proportional to the order parameter of the phase that is initiated. Should this splitting be zero, the phase is disordered; should it be non-zero, the phase is nematic. The splitting is actually due to the fact that in an oriented nematic of micelles, the D_2O molecules of the solvent inherit the alignment of the cylindrical structures [50]. The NMR technique allows measurement of velocity fields and spectral splitting with a spatial resolution on the order of 10–50 μm and needs, in general, long acquisition times. This technique was applied to a CTAB- D_2O solution ($c = 20 \text{ wt.}\%$, $T = 41^\circ\text{C}$), one that compares well with that of Figure 13. The shear banding transition observed by neutron and flow birefringence was confirmed by NMR under shear. Furthermore, the proportions of isotropic and nematic phases in the plateau regime were calculated [160] and they were found to be in excellent agreement with the SANS results (Figure 19). NMR velocimetry profiles performed simultaneously on the same solution show also that the birefringent band visualized by rheo-optics does not correspond necessarily to a high shear band. This intriguing result was interpreted as arising from a nematic phase of high viscosity, possibly associated with mesoscale ordering. Since the first results on micelles, NMR has been applied to other complex fluids for velocity field imaging [158].

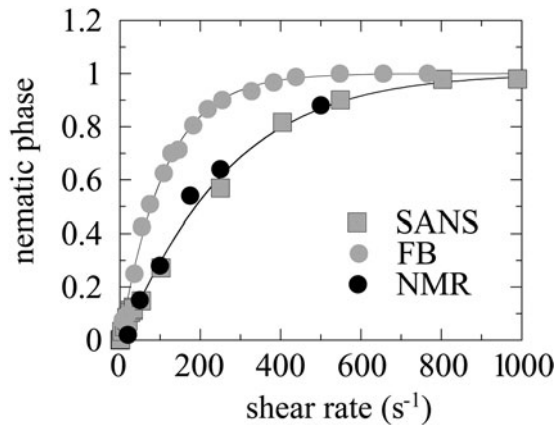


Figure 19. Percentage of the nematic phase induced by shearing obtained from flow birefringence [124], small-angle neutron scattering [124] and deuterium NMR [160]. Experiments were performed on a CTAB-D₂O concentrated solution close to the I-N transition. The data from SANS and NMR are in good agreement. (Reprinted with permission from [161]. Copyright (2001) American Physical Society.)

A list of concentrated wormlike micelles showing stress plateaus and shear banding have been collected from the recent literature (Table 3). Conclusions from this table will be made at the end of Section 3.2.

3.2. Shear Banding in Semi-Dilute Regime

In the semi-dilute wormlike micelles (i.e., for concentrations comprised of 0.1 wt.% to 10 wt.% (or, equivalently, 0.003 mol/L to 0.3 mol/L) for a C16 surfactant), the structural and rheological properties are qualitatively analogous to those found for concentrated solutions. Stress plateaus and shear banding are still the main features of these solutions in response to shear flow. There are differences however that depend on the concentration:

- (i) Unlike to the concentrated regime, the rheology of semi-dilute solutions exhibits more than one behavior. The nonlinear mechanical response can be either shear-thinning or shear-thickening. In the shear-thinning class, the flow curves and shear banding characteristics can differ from one system to the other.
- (ii) Because of this broad diversity in rheological behaviors, experimental data in the semi-dilute regime are often incomplete. Few systems have been investigated using several different techniques.
- (iii) The last point concerns electrostatics. Diluting micellar phases (and keeping the solutions free of additional salt) increases the range of the

Table 3. Wormlike micellar systems known to exhibit stress plateaus or quasi plateaus in steady state rheology. Systems for which the shear banding has been observed by structural methods are indicated. The abbreviations are: “sd” for semi-dilute and “c” for concentrated. Abbreviations of techniques used to show shear banding: “SANS” for small-angle neutron scattering, “FB” for flow birefringence, “NMR” for nuclear magnetic resonance and “DLS” for dynamic light scattering.

Surfactant	Additive	Salt	Conc.regime	Shear banding and technique	Refs.
CPCI	NaSal		sd	NMR	<i>a</i>
CTAB	NaSal		sd	—	<i>b</i>
CTAB		KBr	sd/c	FB	<i>c</i>
CPClO ₃		NaClO ₃	c	SANS	<i>d</i>
CPCI	Hexanol	NaCl	c	SANS, FB	<i>e</i>
CPCI	NaSal	NaCl	sd/c	FB,DLS	<i>f</i>
CTAC	NaSal		sd	FB	<i>g</i>
CTAB			c	SANS,FB,NMR	<i>h</i>
CTAHNC			sd	—	<i>i</i>
CTAB		NaNO ₃	sd/c	FB	<i>j</i>
CTAT			sd/c	—	<i>k</i>
CTAT	SDBS		sd	—	<i>l</i>
SDES		AgCl ₃	sd	—	<i>m</i>
EHAC	NaSal		sd	—	<i>n</i>

(*a*): [3, 15, 16, 127, 181, 182, 187–189]; (*b*): [64, 132, 190]; (*c*): [132, 161, 191, 192]; (*d*): [116]; (*e*): [122, 159, 164]; (*f*): [122, 123, 148, 163, 183, 189, 193]; (*g*): [14, 172]; (*h*): [117, 124, 160, 173]; (*i*): [194, 195]; (*j*): [165, 196–198]; (*k*): [146, 199–203]; (*l*): [84]; (*m*): [42]; (*n*): [134].

electrostatic interactions between micelles. This may have considerable effects on the stability and equilibrium properties of the phases [185, 186]. However, in the concentrated regime, the ionic strength is always large (of the order of 1 M) and electrostatics has a minor effect. In the following section, emphasis will be placed on shear-thinning systems with screened electrostatic interactions.

3.2.1. Generalized “flow phase diagram” and standard behavior

Cetylpyridinium chloride with sodium salicylate is the system for which the most extensive set of rheological data in the nonlinear regime is available [15, 60, 122, 123, 126, 127, 143, 163, 183, 188, 189, 204]. To our knowledge, it is also the first system for which a stress plateau has been reported [3]. When electrostatics is screened by addition of sodium chloride, CPCI-Sal has been shown to exhibit the right scaling exponent for the concentration dependence of the viscosity (Figure 9) and the micellar fluids prepared between 1 wt.%

to 30 wt.% reveal a clear Maxwellian behavior. The steady-state shear stress has been measured as function of the shear rate, temperature, and concentration, and the temperature-concentration superposition principle has been used to derive the generalized flow phase diagram [123]. The steady shear stress normalized by the elastic modulus G_0 is shown in Figure 20 as function of the normalized shear rate $\dot{\gamma}\tau_R$, for c between 2 wt.% and 21 wt.%. The flow curve at $c = 21$ wt.% makes the link with the concentrated regime. There, a quasi-plateau is observed and the findings are in line with the data of Figures 11 and 13. As concentration decreases, stress plateaus are still observed, but the normalized stress and shear rate at which the discontinuity occurs are shifted to larger values.

At $c = 6$ wt.% and above, the transition is much smoother and the stress levels off without discontinuity. According to Figure 20, stress plateaus are found in semi-dilute wormlike micelles for stress and rates below the following critical conditions [123]:

$$\sigma_P/G_0 = 0.9 \quad \text{and} \quad \dot{\gamma}\tau_R = 3 \pm 0.5 \quad (14)$$

Assuming the relationship, $G_0 \sim k_B T/\xi^3$, between the modulus and the mesh size ξ of the network, σ_P/G_0 can be viewed as the mechanical energy dissipated at the scale of the mesh in units of thermal energy. The product $\dot{\gamma}\tau_R$ represents

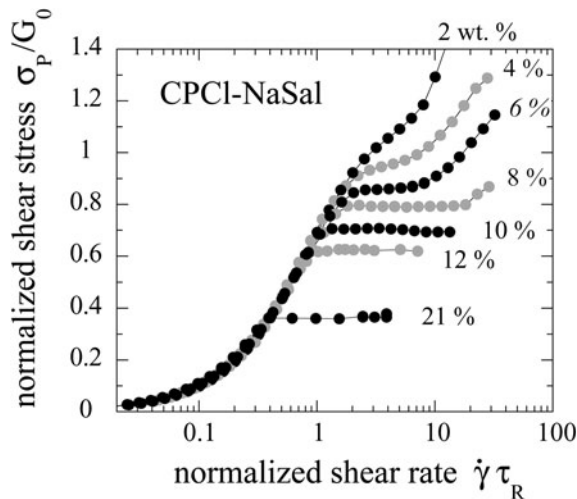


Figure 20. Generalized “flow phase diagram” obtained for CPCI-NaSal wormlike micelles. The shear stress normalized by the elastic modulus σ_P/G_0 is plotted against the reduced shear rate $\dot{\gamma}\tau_R$. The diagram is obtained using the invariance property of the flow curves under temperature and concentration changes. No stress plateau is observed for the critical conditions $\sigma_P/G_0 > 0.9$ and $\dot{\gamma}\tau_R > 3$. (Reprinted with permission from [123]. Copyright (1997) American Physical Society.)

the shear rate in the time scale unit of the fluid. The analogy of Figure 20 with the phase diagram of an equilibrium system undergoing a phase separation (such as the liquid-gas transition) is striking. This analogy is strengthened by two observations. First, the ratio σ_P/G_0 decreases linearly with the concentration and extrapolates at the concentration c_{I-N} at which the system at rest undergoes the isotropic-to-nematic transition ($c_{I-N} = 36$ wt.%, Figure 21). The critical conditions quoted in Eq. (14) also suggest that by choosing the concentration, temperature or salt content adequately, it is possible to find a stress plateau between $\sigma_P/G_0 \sim 0$ and 0.9, and of onset between $\dot{\gamma}\tau_R \sim 0$ and 3. Second, the flow curves with stress plateaus all exhibit the slow transient kinetics and sigmoidal relaxations described by the concentrated regime. The coefficient n in Eq. (11) was found between 1 and 3 [122, 148, 188, 197]. In CPCI-NaSal, the stretched coefficient $n = 2$ was interpreted as an indication of a one-dimensional nucleation and growth process [121, 123, 163]. Semi-dilute wormlike micelles showing stress plateaus similar to those of Figure 20 have been included in the list in Table 3. This collection of systems, all sharing the same rheological properties, demonstrates that the behavior described here is actually representative for this class of materials. In the following section, Maxwellian linear behaviors and shear banding transitions associated with non-linear stress plateaus will define the “standard behavior” in wormlike micelles.

3.2.2. Structure of the shear bands in the semi-dilute regime

Flow Birefringence: Decruppe and co-workers have shown the existence of shear bands in several micellar systems (e.g., in CTAC-NaSal [14, 172],

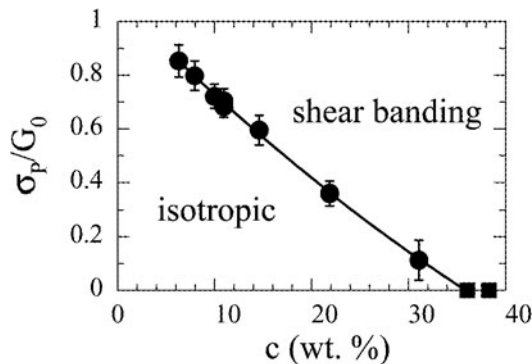


Figure 21. Concentration dependence of the reduced stress (closed circles) at the plateau for the CPCI-NaSal system. At high concentrations, the values of σ_P/G_0 extrapolate to c_{I-N} , the isotropic-to-nematic concentration (closed squares, $c_{I-N} = 0.356$). At concentrations below 6 wt.%, stress plateaus are not observed. (Reprinted with permission from [122]. Copyright (1994) EDP Sciences.)

in CTAB-KBr [161, 191, 192] and in CTAB-NaNO₃ [197, 198]). From their work, two main behavior types have been identified. The CTAB-KBr system shows strongly birefringent shear bands starting at the inner wall of the cell and progressively filling the gap as the shear rate is increased. In the concentrated systems, shear banding was found to correlate with the onset of a stress plateau at $\dot{\gamma}_1$. In the nematic phase, a bright band with an extinction angle $\chi \sim 0^\circ$ was found. The kinetics of band destabilization of reconstruction and travel of the interface of this system was re-examined recently [192]. CTAB-KBr behaves like the micellar systems, showing a shear-induced isotropic-to-nematic phase transition [161]. For semi-dilute solutions in general, a complete transformation of the micellar fluid into a nematic phase requires very high shear rates which are not attainable with the instrumentation currently available.

The second type of behavior was found in CTAB-NaNO₃ [197, 198] and CPCI-NaSal [123]. In both cases, the electrostatic interactions were screened. CTAB-NaNO₃ is interesting for several reasons. In the semi-dilute regime, for a concentration of 10.9 wt.% with $[\text{NaNO}_3] = 1.79 \text{ M}$, the linear and nonlinear rheology and even the short-time flow birefringence are in agreement with the “standard” behavior outlined in Section 3.2.1. The long time flow birefringence however shows some striking features. As time evolves, the shear band splits into several finely striated sub-bands of few microns in thickness. These striations can occupy half of the gap at the steady-state and show unstable fluctuations of position and width. This type of band structure is clearly different from that of concentrated solutions and, therefore, may not easily be attributed to a shear-induced I–N transition.

Nuclear Magnetic Resonance: For the concentrated solutions, NMR has been used as an imaging technique to determine the velocity field in the banded regime. The micellar solution studied was 100 mM cetylpyridinium and 60 mM sodium salicylate in pure water. This solution is semi-dilute and is considered to be representative of the wormlike micelles class [3, 188, 204]. NMR was performed using different flow geometries, such as Couette [15, 16, 205], cone-and-plate [179, 180, 182], and Poiseuille [15, 181, 183]. Shear banding was found in all three types of geometries. With the Couette cell, a high-velocity and very thin band was detected near the inner cylinder. The cone-and-plate geometry has a more uniform distribution of shear rate than the Couette, and it displayed slightly different results. The high shear rate band now appears at the center of the sheared solution. Two interfaces with the adjacent low shear regions are visible in the NMR-plots [15, 189]. With pipe flow, the increase of the flow rate from the Newtonian to the plateau regime corresponds to the transition between parabolic and almost flat velocity profiles. For the latter, the shear rate is localized close to the walls as in a plug flow. Finally, velocity field measurements using dynamic light scattering in heterodyne mode have been performed recently. The spatial resolution of this new technique is comparable to that of NMR ($\sim 50 \mu\text{m}$). The data obtained on a CPCI-Sal semi-dilute

solution at $c = 6$ wt.% (whose flow curve is shown in Figure 20) confirm the coexistence of two macroscopic shear bands in the plateau region [193].

In conclusion, the shear banding in the semi-dilute regime of wormlike micelles shows more complex features than in the concentrated regime. The NMR velocimetry measurements provide evidence for the role of flow geometry on the band structures. We have completed Table 3 by adding comments and references for every system that displays shear banding whether observed by flow birefringence, by NMR, or by SANS.

3.2.3. Non-standard behaviors

As already mentioned, not all semi-dilute systems provide “standard behavior”. There are few exceptions, and it is instructive to describe some of them in order to illustrate the diversity of rheological behaviors. One is a binary solution of hexadecyloctyldimethylammonium bromide (C18-C8DAB, see Table 1) in water at $c = 2.3$ wt.%. This micellar solution was investigated by Hoffmann and co-workers by SANS at rest and under shear. Above a threshold shear rate, the solution undergoes an isotropic-to-hexagonal transition. The long range hexagonal order was characterized by a strong anisotropy perpendicular to the velocity direction (as in Figure 17), with clearly identified a first and a second Bragg peaks. The data were interpreted in terms of coexistence of two types of cylindrical micelles of different lengths, the short ones contributing to the ring-like pattern and the long ones being responsible for the hexagonal phase. Although the data resemble those of the I-N transition in the concentrated regime, to our knowledge neither shear banding nor stress plateaus have been reported.

A second system showing a non-standard behavior is an equimolar 40 mM solution of cetylpyridinium chloride and sodium salicylate ($c = 2.1$ wt.%). At this concentration, CPCI-NaSal is Maxwellian and has a relaxation time around 10 ms. With increasing shear rate, the solution first shear-thins, the stress reaching continuously a plateau regime. The solution then undergoes an abrupt and strong shear-thickening. This instability occurs at reduced shear rate $\dot{\gamma}\tau_R$ around 3 and is associated with the appearance of clear and turbid bands stacked perpendicular to the vorticity direction. At steady state, the bands oscillate. This double transition, shear-thinning and then shear-thickening, as well as the simultaneous occurrence of bands along the vorticity, is a unique feature of wormlike micelles. This instability has received much attention during the last years [206].

Wunderlich *et al.* and Pine and co-workers have also studied the flow behavior of equimolar solutions of CTAB-NaSal [207, 208] and of tris(2-hydroxyethyl)-tallowalkyl ammonium acetate (TTAA)-NaSal solutions [209–212]. The weight concentrations, between 0.1 and 1 wt.%, are slightly

lower than the previous case. Wunderlich and Brunn had first noticed the existence of anomalously long transients at the thickening transition, as well as a striking dependence of the viscosity as a function of the gap of their Couette cells. At concentrations between 1–10 mM, the micellar network is hardly entangled and the static viscosity is larger than that of the solvent only by a factor of 10–100. As shear is increased, there is first a modest shear thinning and then an abrupt shear thickening at the critical stress. This behavior resembles, in some respects, that of the CPCI-NaSal solution at 40 mM studied in Wheeler *et al.* [166]. In addition, the shear-thickening transition occurs simultaneously to the growth of a shear-induced structure, starting at the inner cylinder of the Couette (as in the shear banding transition). Because the apparent viscosity is an increasing function of $\dot{\gamma}$, the shear-induced structures in CTAB-NaSal and TTAA-NaSal solutions were described as gel phases. No connection with the phenomenology of the I–N transition was made in these systems. Other observations, such as homogeneous nucleation, fracture, and re-entrant flow curves were also described for these systems [208–212].

In conclusion, although the nonlinear rheology of semi-dilute wormlike micelles is dominated by stress plateaus and shear banding, non-standard behavior may be found. Exotic rheologies are encountered essentially at low concentrations and for systems with binding counterions and unscreened electrostatics; see also [213–216] for additional examples of non-standard behavior.

3.3. Theories and Interpretations

The interest of theoreticians in the rheology of wormlike micelles has come from two different sides. One group has focused on the investigation of the mechanical signature of shear banding. This includes the regimes of stress plateaus or quasi-plateaus and the slow kinetics of the stress. The mechanical theories establish a formal analogy between the instability shown by wormlike micelles and that observed in polymer melts in extrusion, the so-called “spurt” effect [15]. McLeish and Ball suggested in 1987 that the “spurt” instability in polymer melts would be the consequence of a multi-valued non-monotonic flow curve (Figure 22) [217]. In Figure 22, the stress increases linearly with increasing $\dot{\gamma}$, passes through a maximum (A) and then through a minimum (B) before increasing further. Two branches, one at low and one at high shear rates are separated by a mechanically unstable regime (AB), characterized by a negative slope for $d\sigma/d\dot{\gamma}$. If a controlled strain experiment is performed in the unstable region, the system will demix into two macroscopic bands of low ($\dot{\gamma}_1$) and high shear rate ($\dot{\gamma}_2$). Figure 23 displays schematically the demixing between an isotropic and a nematic phase. This scheme mimics the photographs of the gap obtained by flow birefringence. In a simple shear experiment, mechanical

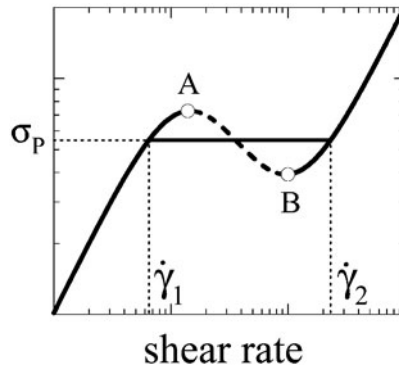


Figure 22. Non-monotonic constitutive equation assumed for wormlike micelles. The two stable branches at low and high shear rates are separated by an unstable portion [AB]. In the plateau region, the micellar solution demixes in bands of shear rate $\dot{\gamma}_1$ and $\dot{\gamma}_2$.

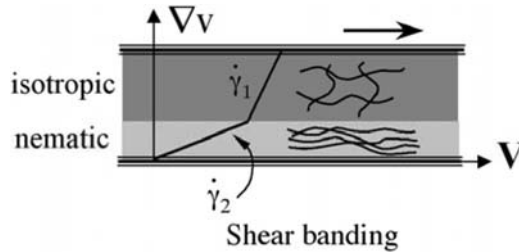


Figure 23. Schematic representation of the shear banding for a system undergoing a shear-induced isotropic-to-nematic transition.

stability requires that the shear stress be constant throughout the fluid. In the plateau region, this stress is σ_p and so Eq. (15) applies.

$$\begin{aligned} \sigma_p &= \eta_1 \dot{\gamma}_1 = \eta_2 \dot{\gamma}_2 = \text{cste} \\ \dot{\gamma} &= (1 - x) \dot{\gamma}_1 + x \dot{\gamma}_2 \end{aligned} \tag{15}$$

Here, η_1 and η_2 are the viscosities in each band ($\eta_1 > \eta_2$) and x is the proportion of the solution that has been transformed. Cates and co-workers have used the reptation-reaction model developed for the linear rheology to derive a constitutive equation, and they have found a non-monotonic behavior similar to that in Figure 22 [218]. This model predicts the occurrence of a stress plateau at $\sigma_p = 2G_0/3$ and reduced rate $\dot{\gamma} \tau_R = 2.6$, values that are in qualitative agreement with experiment. The main difficulty of the early models by McLeish, Ball, Cates and co-workers on polymer melts and on semi-dilute micelles was to find the mechanism for the selection of the stress which the system demixes

[174, 217–219]. In the unstable region, these models usually predict hysteresis and values of stress which depend on the shear scenarios.

The second theoretical approach is based on thermodynamical arguments. It consists in studying the non-equilibrium phase behavior of an isotropic fluid in the vicinity of the isotropic-to-nematic transition. The scheme followed by Hess, Olmsted, Dhont and co-workers started with a dispersion of rigid rods [220–225], either in the melt form or in solution using an Onsager-type formalism for determining the interactions between particles [115]. For thermotropics, the temperature is the control parameter and for lyotropics it is the concentration. Imposing a shear flow to the disordered phase modified the interaction potential between rods (essentially through alignment) and triggered the transition to a nematic long-range orientational state at lower temperature or concentration. The early applications predicted the flow velocity-temperature phase diagram and quantified the influence of a shear rate on the transition [223]. The thermodynamic approach underlines an important issue which does not appear in the mechanical theories, but matches more closely the data on wormlike micelles [225–227]. Above the upturn at high shear rate ($\dot{\gamma} > \dot{\gamma}_2$), the stable branch in the $\sigma(\dot{\gamma})$ -curve is that of a nematic phase [117]. A major difficulty in this type of approach concerns the validity of equilibrium thermodynamic concepts for non-equilibrium or forced transitions; see [224, 225, 228] for discussions. There is also a conceptual difficulty in generalizing results obtained on dispersions of rods to entangled meshes of extremely long micelles. In the previous sections dedicated to experiments, shear banding was interpreted either in terms of a mechanical instability or in terms of a shear-induced transition, depending for instance on whether the solution belongs to the semi-dilute or the concentrated regime. Theories face the same duality. This duality in the interpretations of shear banding (i.e., mechanical instability *versus* shear-induced transition) has been a major focus of research on micelles during the past decade.

All the theoretical approaches have tried to account for at least two experimental observations:

- (i) the existence and robustness of the stress plateau or quasi-plateaus. As shown in many systems, there is no hysteresis in the steady-state values of the stress.
- (ii) the coexistence of macroscopic bands of different shear rates and orientations. As in an equilibrium phase transition, the proportions of the bands vary as the shear rate is changed in the plateau region.

Other interesting issues related to the shear banding transition have been treated theoretically. They include the role of the flow geometry on the banding structure [174, 175], the hypothesis of a stress-concentration coupling component [228–232], and the difference of nonlinear response between stress and strain controlled rheology [189, 224, 228, 230–233]. A major improvement in the

theoretical description was achieved by taking into account explicitly in the conservation equations an additional stress generated at the interface between bands [175, 219, 226, 228, 234–236]. This is a diffusion term which corrects the stress anomaly at the interface. For this purpose, we follow the reasoning of Dhont [224]. Assume that, as a result of the non-monotonic constitutive equation, the micellar fluid demixes into two bands when it is sheared in the unstable region. The shear rate $\dot{\gamma}(y, t)$ as well as the local viscosity $\eta(y, t)$ will then vary as function of the coordinate y along the velocity gradient direction. Even at steady state, these local quantities can also be functions of the time. A generalization of Eq. (15) at steady state (and still without the diffusion term) gives:

$$\sigma_P = \eta[\dot{\gamma}(y, t)]\dot{\gamma}(y, t) = \text{cste} \tag{16a}$$

$$\dot{\gamma} = \int_0^e \dot{\gamma}(y, t) dy. \tag{16b}$$

In the case of the non-monotonic stress-rate relationship, the equality in Eq. (16a) cannot be fulfilled. An example of a two band state is given in Figure 24. It shows that at the interface the stress exhibits strong spatial variations. This is due to the fact that at the interface the shear rate explores the instability region AB of the flow curve. Several authors [224, 234, 235] have suggested to re-write Eq. (16a) as:

$$\sigma_P = \eta(\dot{\gamma}(y, t))\dot{\gamma}(y, t) - D(\dot{\gamma}(y, t)) \frac{\partial^2 \dot{\gamma}(y, t)}{\partial y^2} = \text{cste} \tag{17}$$

A convenient choice of the diffusion coefficient $D(\dot{\gamma}(y, t))$ allows one to recover the constancy of the stress throughout the gap. Once the diffusion

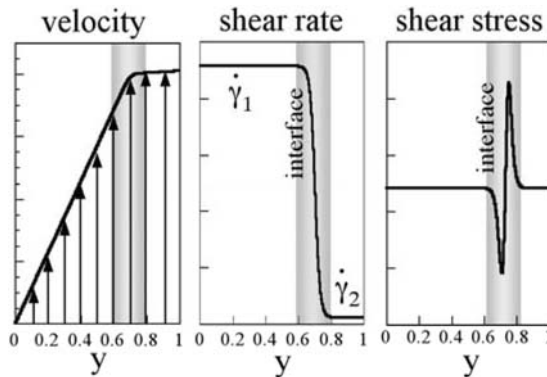


Figure 24. Velocity, shear rate, and shear stress profiles calculated under the assumptions of shear banding and of non monotonic flow curve. In order to remove the spurious oscillations in the shear stress, a gradient term is needed (Eq. (17)). (Reprinted with permission from [224]. Copyright (1999) American Physical Society.)

term is introduced in the conservation equation, it is possible to demonstrate that the stress selection rule at the plateau is robust and without hysteresis. This approach was carried out by several authors using different computing and simulation techniques. It seems globally equivalent here to consider a non-local term with a second derivative of the stress or of the shear rate [175, 227, 228, 232]. Dhont suggests finally the shear banding transition can be assimilated into a hydrodynamic instability. The thermodynamic character of this instability results from a formal analogy between the Navier-Stokes equation and a Cahn-Hilliard equation of motion for the density in unstable systems [224, 228].

4. Conclusions and Perspectives for the Future

In this chapter, we have explored the experimental and, to a lesser extent, the theoretical results accumulated during the last decade on the structure and on the rheology of wormlike micelles. The systems considered are aqueous solutions of surfactants, but some results are clearly generalized to other self-assembled phases of anisotropic structures [85, 86, 89, 90, 92, 93, 237–240]. Our approach has been to show the existence of a common rheological behavior shared by most semi-dilute and concentrated wormlike micellar solutions. Our conclusions are summarized below.

(i) The local morphology of the cylindrical aggregates, such as their ability to break and recombine, and their flexibility, plays a very important role in determining the structure and rheology. Wormlike micelles are analogues of polymers as far as their structural properties are concerned. Their dynamical properties however are very specific and mainly dictated by the reversible breaking mechanisms. A correlation between the existence of nematic phases at high concentrations and the semi-flexibility of the aggregates has been established experimentally.

(ii) Based on a review of the surfactants and counterions that self-assemble into wormlike colloids, a “standard” rheological behavior can be defined. The features of this common behavior can be formulated as follows. Semi-dilute and concentrated solutions are viscoelastic fluids characterized by a single relaxation time. They are, to a good approximation, Maxwellian fluids. In steady shear, the fluids undergo a shear banding transition associated with a plateau in the stress *versus* shear rate curves. For concentrated solutions, the new phase exhibits long range orientational order of nematic type. Because of this unique behavior, wormlike micelles are often considered as a reference system among complex fluids. Several viscoelastic systems show stress plateaus closely resembling those of micelles, such as dispersions of F-actin microtubules [237] or solutions of entangled DNA molecules [238]. For synthetic

polymers, we cite side-chains liquid crystals [239, 240] and block copolymer microemulsions [241]. Note that except in the early work by Buxbaum *et al.* [237], explicit comparisons with surfactant micelles were made in discussions of these systems.

(iii) Reliable models for the linear and nonlinear rheology of wormlike micelles now exist. For the linear rheology, the reptation-reaction kinetics model takes into account the two major relaxation modes shown by these colloids. For the shear banding transition, we have followed a recent approach that identifies the transition to a hydrodynamic instability. This instability takes place because there is a non-monotonic stress *versus* shear rate relationship that describes the mechanical response of the fluid (such as in Figure 22). It is also suggested that the non-monotonic flow curve originates from the existence of a nematic phase at high concentration. In this respect, the hydrodynamic instability and the shear-induced isotropic-to-nematic transition are intertwined phenomena.

(iv) Although the rheology of entangled wormlike micelles is dominated by stress plateaus and shear banding, a number of systems do not display such behavior. Transitions and instabilities with features different from that of shear banding are found at low concentrations and for charged systems with strongly binding counterions, such as in CPCI-NaSal and CTAB-NaSal. This raises the question of the appropriateness of the existing models for these fluids.

Our point here is to outline the need for further theoretical treatments in such surfactants and other low-molecular weight systems. We think that the remarkable behavior revealed in the nonlinear rheology (although the linear response is Maxwellian) is an indication of the existence of relaxation modes other than reptation and reversible breaking.

Acknowledgments

I would like to thank all my colleagues with whom I have worked during these years. It is a pleasure to acknowledge J. Appell, W. Burghardt, J.-P. Decruppe, R. Gamez-Corrales, S. Lerouge, F. Molino, P. Olmsted, G. Porte, O. Radulescu, D.C. Roux, C. Schmidt, T. Thiele and L. Walker for the fruitful and exciting discussions we had on this topic. I would like to thank also all those with whom I had the opportunity to discuss about the rheology of micelles. I am personally grateful to Sandra Lerouge for having read the first draft of the manuscript and for her suggestions. The Laboratoire Léon Brillouin (Saclay, France), the Institute Laue-Langevin and the European Synchrotron Radiation Facilities (Grenoble, France) are also acknowledged for their technical and financial supports. I have benefited from the stimulating environment provided by the Groupement de Recherche 1081 "Rhéophysique des Colloïdes et

Suspensions” (CNRS funding). The research described in this review is funded in most part by the Centre National de la Recherche Scientifique in France, and in part by the European TMR-Network “Rheology of Liquid Crystals”, contract number FMRX-CT96-0003 (DG 12 - ORGS).

References

- [1] Cates, M.E.; Candau, S.J. “Statics and dynamics of wormlike surfactant micelles”, *J. Phys.: Condens. Matter*, **1990**, *2*, 6869–6892.
- [2] Hofmann, S.; Rauscher, A.; Hoffmann, H. “Shear induced micellar structures”, *Ber. Bunsenges. Phys. Chem.*, **1991**, *95*, 153–164.
- [3] Rehage, H.; Hoffmann, H. “Viscoelastic surfactant solutions: model systems for rheological research”, *Mol. Phys.*, **1991**, *74*, 933–973.
- [4] Gelbart, W.M.; Ben-Shaul, A.; Roux, D. *Micelles, Membranes, Microemulsions and Monolayers*. New York: Springer, **1994**.
- [5] Lequeux, F.; Candau, S.J. In *Structure and Flow in Surfactant Solutions (ACS Symposium Series 578)*, C.A. Herb and R.K. Prud’homme, Eds., Washington D.C.: American Chemical Society, **1994**.
- [6] Candau, S.J.; Oda, R. “Linear viscoelasticity of salt-free wormlike micellar solutions”, *Colloids Surfaces A*, **2001**, *183–185*, 5–14.
- [7] Walker, L.M. “Rheology and structure of wormlike micelles”, *Curr. Opin. Colloid Interface Sci.*, **2001**, *6*, 451–456.
- [8] Yang, J. “Viscoelastic wormlike micelles and their applications”, *Curr. Opin. Colloid Interface Sci.*, **2002**, *7*, 276–281.
- [9] Larson, R.G. *The Structure and Rheology of Complex Fluids*. New York: Oxford University Press, **1999**.
- [10] Zanten, J.H.v.; Rufener, K.P. “Brownian motion in a single relaxation time maxwell fluid”, *Phys. Rev. E*, **2000**, *62*, 5389–5396.
- [11] Bellour, M.; Skouri, M.; Munch, J.-P.; Hébraud, P. “Brownian motion of particles embedded in a solution of giant micelles”, *Eur. Phys. J. E*, **2002**, *8*, 431–436.
- [12] Cardinaux, F.; Cipelletti, L.; Scheffold, F.; Schutenberger, P. “Microrheology of giant-micelle solutions”, *Europhys. Lett.*, **2002**, *57*, 738–744.
- [13] Belmonte, A. “Self-oscillations of a cusped bubble rising through a micellar solution”, *Rheol. Acta*, **2000**, *39*, 554–559.
- [14] Makhloufi, R.; Decruppe, J.-P.; Aït-Ali, A.; Cressely, R. “Rheo-optical study of wormlike micelles undergoing a shear banding flow”, *Europhys. Lett.*, **1995**, *32*, 253–258.
- [15] Callaghan, P.T.; Cates, M.E.; Rofe, C.J.; Smeulders, J.B.A.F. “A study of the ‘spurt effect’ in wormlike micelles using nuclear magnetic resonance microscopy”, *J. Phys. II France*, **1996**, *6*.
- [16] Mair, R.W.; Callaghan, P.T. “Observation of shear banding in wormlike micelles by NMR velocity imaging”, *Europhys. Lett.*, **1996**, *36*, 719–724.
- [17] Rosen, M.J.; Dahanayake, M. *Industrial Utilization of Surfactants: Principle and Practice*. Champaign: Illinois, AOCS Press, **2000**.
- [18] Aniansson, E.A.G.; Wall, S.N.; Almgren, M.; Hoffmann, H.; Kielmann, I.; Ulbricht, W.; Zana, R.; Lang, J.; Tondre, C. “Theory of the kinetics of micellar equilibria and quantitative interpretation of the chemical relaxation studies of micellar solutions of ionic surfactant”, *J. Phys. Chem.*, **1976**, *80*, 905–922.

- [19] Zana, R. *Surfactant Solutions: New Methods of Investigation*. New York: Marcel Dekker, Inc., **1987**.
- [20] Candau, S.J.; Hirsch, E.; Zana, R.; Adam, M. "Network properties of semi-dilute KBr solutions of cetyltrimethylammonium bromide", *J. Colloid Interface Sci.*, **1988**, *122*, 430–440.
- [21] Tandford, C. *The Hydrophobic Effect: Formation of Micelles and Biological Membranes*. New York: Wiley & Sons, **1980**.
- [22] Israelachvili, J.N. *Intermolecular and Surface Forces*. London: Academic Press, **1992**.
- [23] Cates, M.E. "Dynamics of living polymers and flexible surfactant micelles: scaling laws for dilution", *J. Phys. France*, **1988**, *49*, 1593–1600.
- [24] Candau, S.J.; Merikhi, F.; Waton, G.; Lemaréchal, P. "Temperature-jump study of elongated micelles of cetyltrimethylammonium bromide", *J. Phys. France*, **1990**, *51*, 977–989.
- [25] Safran, S.A.; Pincus, P.A.; Cates, M.E.; MacKintosh, F.C. "Growth of charged micelles", *J. Phys. France*, **1990**, *51*, 503–510.
- [26] MacKintosh, F.C.; Safran, S.A.; Pincus, P.A. "Self-assembly of linear aggregates: the effect on electrostatics on growth", *Europhys. Lett.*, **1990**, *12*, 697–702.
- [27] Arleth, L.; Bergström, M.; Pedersen, J.S. "Small-angle neutron scattering study of the growth behavior, flexibility, and intermicellar interactions of wormlike SDS micelles in NaBr solutions", *Langmuir*, **2002**, *18*, 5343–5353.
- [28] Reiss-Husson, F.; Luzzati, V. "The structure of micellar solutions of some amphiphilic compounds in pure water as determined by absolute small-angle X-ray scattering experiments", *J. Phys. Chem.*, **1964**, *68*, 3504–3511.
- [29] Ekwall, P.; Mandell, L.; Solyom, P. "The aqueous cetyl trimethylammonium bromide solutions", *J. Colloid Interface Sci.*, **1971**, *35*, 519–527.
- [30] Fontell, K.; Khan, A.; Lindström, B.; Maciejewska, D.; Puang-Ngern, S. "Phase equilibria and structures in ternary systems of a cationic surfactant ($C_{16}TABr$ or $(C_{16}TA)_2SO_4$), alcohol and water", *Colloid Polym. Sci.*, **1991**, *269*, 727–742.
- [31] Porte, G.; Poggi, Y.; Appell, J.; Maret, G. "Large micelles in concentrated solutions. The second critical micellar concentration", *J. Phys. Chem.*, **1984**, *88*, 5713–5720.
- [32] Debye, P.; Anacker, E.W. "Micelle shape from dissymmetry measurements", *J. Phys. Chem.*, **1950**, *55*, 644–655.
- [33] Quirion, F.; Magid, L.J. "Growth and counterion binding of cetyltrimethylammonium bromide aggregates at 25°C: a neutron scattering study", *J. Phys. Chem.*, **1986**, *90*, 5435–5441.
- [34] Candau, S.J.; Hirsch, E.; Zana, R. "New aspects of the behaviour of alkyltrimethylammonium bromide micelles: light scattering and viscometric studies", *J. Physique*, **1984**, *45*, 1263–1270.
- [35] Candau, S.J.; Hirsch, E.; Zana, R. "Light scattering investigations of the behavior of semi-dilute aqueous micellar solutions of cetyltrimethylammonium bromide: analogy with semi-dilute polymer solutions", *J. Colloid Interface Sci.*, **1985**, *105*, 521–528.
- [36] Emerson, M.F.; Holtzer, A. "On the ionic strength dependence of micelle number", *J. Phys. Chem.*, **1967**, *71*, 1898–1907.
- [37] Mazer, N.A.; Benedeck, G.B.; Carrey, M.C. "An investigation of the micellar phase of sodium dodecylsulfate in aqueous sodium chloride solutions using quasielastic light scattering spectroscopy", *J. Phys. Chem.*, **1976**, *80*, 1075–1085.
- [38] Young, C.Y.; Missel, P.J.; Mazer, N.A.; Benedeck, G.B.; Carrey, M.C. "Deduction of micellar shape from angular dissymmetry measurements of light scattered from

- aqueous sodium dodecylsulfate solutions at high sodium chloride concentrations”, *J. Phys. Chem.*, **1978**, *82*, 1375–1378.
- [39] Missel, P.J.; Mazer, N.A.; Benedeck, G.B.; Young, C.Y.; Carrey, M.C. “Thermodynamic analysis of the growth of sodium dodecyl sulfate micelles”, *J. Phys. Chem.*, **1980**, *84*, 1044–1057.
- [40] Missel, P.J.; Mazer, N.A.; Benedeck, G.B.; Carrey, M.C. “Influence of chain length on the sphere-to-rod transition in alkyl sulfate micelles”, *J. Phys. Chem.*, **1983**, *87*, 1264–1277.
- [41] Magid, L.J.; Li, Z.; Butler, P.D. “Flexibility of elongated sodium dodecyl sulfate micelles in aqueous sodium chloride: a small-angle neutron scattering study”, *Langmuir*, **2000**, *16*, 100280–10036.
- [42] Mu, J.-H.; Li, G.-Z.; Jia, X.-L.; Wang, H.-X.; Zhang, G.-Y. “Rheological properties and microstructures of anionic micellar solutions in the presence of different inorganic salts”, *J. Phys. Chem. B*, **2002**, *106*, 11685–11693.
- [43] Mu, J.-H.; Li, G.-Z.; Wang, H.-X. “Effect of surfactant concentration on the formation and viscoelasticity of anionic wormlike micelle by the methods of rheology and freeze-fracture TEM”, *Rheol. Acta*, **2002**, *41*, 493–499.
- [44] Lawson, K.D.; Flautt, T.J. “Magnetically oriented lyotropic liquid crystalline phase”, *J. Am. Chem. Soc.*, **1967**, *89*, 5489–5491.
- [45] Yu, L.J.; Saupe, A. “Observation of a biaxial nematic phase in potassium laurate-1-decanol mixtures”, *Phys. Rev. Lett.*, **1980**, *45*, 1000–1003.
- [46] Hendriks, Y.; Charvolin, J. “Structural relations between lyotropic phases in the vicinity of the nematic phases”, *J. Physique*, **1981**, *42*, 1427–1440.
- [47] Hendriks, Y.; Charvolin, J.; Rawiso, M.; Liébert, L.; Holmes, M.C. “Anisotropic aggregates of amphiphilic molecules in lyotropic nematic phases”, *J. Phys. Chem.*, **1983**, *87*, 3991–3999.
- [48] Amaral, L.Q.; Helene, M.E.M. “Nematic domain in the sodium lauryl sulfate/water/decanol system”, *J. Phys. Chem.*, **1988**, *92*, 6094–6098.
- [49] Quist, P.O.; Halle, B.; Furo, I. “Micelle size and order in lyotropic nematic phases from nuclear spin relaxation”, *J. Chem. Phys.*, **1992**, *96*, 3875–3891.
- [50] Thiele, T.; Berret, J.-F.; Muller, S.; Schmidt, C. “Rheology and NMR measurements under shear of sodium dodecyl sulfate/decanol/water nematics”, *J. Rheol.*, **2001**, *45*, 29–48.
- [51] Porte, G.; Gomati, R.; Haitamy, O.E.; Appell, J.; Marignan, J. “Morphological transformations of the primary surfactant structures in brine-rich mixtures of ternary systems (surfactant/alcohol/brine)”, *J. Phys. Chem.*, **1986**, *90*, 5746–5751.
- [52] Gomati, R.; Appell, J.; Bassereau, P.; Marignan, J.; Porte, G. “Influence of the nature of the counterion and of hexanol on the phase behavior of the dilute ternary systems: cetylpyridinium bromide or chloride-hexanol-brine”, *J. Phys. Chem.*, **1987**, *91*, 6203–6210.
- [53] Porte, G.; Marignan, J.; Bassereau, P.; May, R. “Shape transformation of the aggregates in dilute surfactant solutions: a small-angle neutron scattering study”, *J. Phys. France*, **1988**, *49*, 511–519.
- [54] Marignan, J.; Appell, J.; Bassereau, P.; Porte, G.; May, R. “Local structures of the surfactant aggregates in dilute solutions deduced from small angle neutron scattering patterns”, *J. Phys. France*, **1989**, *50*, 3553–3566.
- [55] Nastishin, Y.A. “Brine-rich corner of the phase diagram of the ternary system cetylpyridinium chloride-hexanol-brine”, *Langmuir*, **1996**, *11*, 5011–5015.
- [56] Nash, T. “The interaction of some naphthalene derivatives with a cationic soap below the critical micelle concentration”, *J. Colloid Sci.*, **1958**, *13*, 134–139.

- [57] Larsen, J.W.; Magid, L.J.; Payton, V. "A highly specific effect of organic solutes at low concentrations on the structure of CTAB micelles", *Tetrahedron Lett.*, **1973**, *29*, 2663–2666.
- [58] Hyde, A.J.; Johnstone, D.W.M. "The effect of anorganic additives on paraffin chain electrolyte solutions", *J. Colloid Interface Sci.*, **1975**, *53*, 349–357.
- [59] Ulmius, J.; Wennerström, H.; Johansson, L.B.-Å.; Lindblom, G.; Gravsholt, S. "Viscoelasticity in surfactant solutions. Characteristics of the micellar aggregates and the formation of periodic structures", *J. Phys. Chem.*, **1979**, *83*, 2232–2236.
- [60] Hoffmann, H.; Platz, G.; Rehage, H.; Schorr, W.; Ulbricht, W. "Viskoelastische Tensidlösungen", *Ber. Bunsenges. Phys. Chem.*, **1981**, *85*, 255–266.
- [61] Hoffmann, H.; Platz, G.; Rehage, H.; Schorr, W. "The influence of counter-Ion concentration on the aggregation behaviour of viscoelastic detergents", *Ber. Bunsenges. Phys. Chem.*, **1981**, *85*, 877–882.
- [62] Underwood, A.L.; Anacker, E.W. "Organic counterions and micellar parameters: methyl-, chloro-, and phenyl-substituted acetates", *J. Colloid Interface Sci.*, **1984**, *100*, 128–135.
- [63] Shikata, T.; Hirata, K.; Kotaka, T. "Micelle formation of detergent molecules in aqueous media: viscoelastic properties of aqueous cetyltrimethylammonium bromide solutions", *Langmuir*, **1987**, *3*, 1081–1086.
- [64] Shikata, T.; Hirata, K.; Takatori, E.; Osaki, K. "Nonlinear viscoelastic behavior of aqueous detergent solutions", *J. Non-Newtonian Fluid Mech.*, **1988**, *28*, 171–182.
- [65] Makhloufi, R.; Hirsch, E.; Candau, S.J.; Binana-Limbele, W.; Zana, R. "Fluorescence quenching and elastic and quasi-elastic light scattering studies of elongated micelles in solutions of cetyltrimethylammonium chloride in the presence of sodium salicylate", *J. Phys. Chem.*, **1989**, *93*, 8095–8101.
- [66] Imae, T. "Light scattering of spinnable, viscoelastic solutions of hexadecyltrimethylammonium salicylate", *J. Phys. Chem.*, **1990**, *94*, 5953–5959.
- [67] Clausen, T.M.; Vinson, P.K.; Minter, J.R.; Davis, H.T.; Talmon, Y.; Miller, W.G. "Viscoelastic micellar solutions: microscopy and rheology", *J. Phys. Chem.*, **1992**, *96*, 474–484.
- [68] Bijma, K.; Engberts, J.B.F.N. "Effect of counterions and headgroup hydrophobicity on properties of micelles formed by alkylpyridinium surfactants. 1. Conductometry and ¹H-NMR chemical shifts", *Langmuir*, **1997**, *13*, 4843–4849.
- [69] Bijma, K.; Bandamer, M.J.; Engberts, J.B.F.N. "Effect of counterions and headgroup hydrophobicity on properties of micelles formed by alkylpyridinium surfactants. 2. microcalorimetry", *Langmuir*, **1998**, *14*, 79–83.
- [70] Harwigsson, I.; Söderman, O.; Regev, O. "Diffusion and cryo-transmission electron microscopy studies in bicontinuous micellar solutions", *Langmuir*, **1994**, *10*, 4731–4734.
- [71] Göbel, S.; Hiltrop, K. "Influence of organic counterions on the structure of lyotropic mesophases", *Progr. Colloid Polym. Sci.*, **1991**, *84*, 241–242.
- [72] Fischer, P.; Rehage, H.; Grüning, B. "Rheological properties of dimeric acid betaine solutions", *Tenside Surf. Det.*, **1994**, *31*, 99–108.
- [73] Fischer, P.; Rehage, H.; Grüning, B. "Linear flow properties of dimer acid betaine solutions with and without changed ionic strength", *J. Phys. Chem. B*, **2002**, *106*, 11041–11046.
- [74] In, M. In *Reactions and Synthesis in Surfactant Systems*, J. Texter, Ed., New York: Marcel Dekker Inc., **2001**.

- [75] Buhler, E.; Mendes, E.; Boltenhagen, P.; Munch, J.-P.; Zana, R.; Candau, S.J. "Phase behavior of aqueous solutions of a dimeric surfactant", *Langmuir*, **1997**, *13*, 3096–3102.
- [76] Oda, R.; Panizza, P.; Schmutz, M.; Lequeux, F. "Direct evidence of the shear-induced structure of wormlike micelles: Gemini 12-2-12", *Langmuir*, **1997**, *13*, 6407–6412.
- [77] Oda, R.; Huc, I.; Homo, J.-C.; Heinrich, B.; Schmutz, M.; Candau, S. "Elongated aggregates formed by cationic gemini surfactants", *Langmuir*, **1999**, *15*, 2383–2390.
- [78] In, M.; Warr, G.G.; Zana, R. "Dynamics of branched threadlike micelles", *Phys. Rev. Lett.*, **2001**, *83*, 2278–2281.
- [79] Oelschlaeger, C.; Buhler, E.; Waton, G.; Candau, S.J. "Synergistic effects in mixed wormlike micelles of dimeric and single-chain cationic surfactants at high ionic strength", *Eur. Phys. J. E*, **2003**, *11*, 7–20.
- [80] In, M.; Aguerre-Chariol, O.; Zana, R. "Closed-looped micelles in surfactant tetramer solutions", *J. Phys. Chem. B*, **1999**, *103*, 7747–7750.
- [81] Bergström, M.; Pedersen, J.S. "Formation of tablet-shaped and ribbonlike micelles in mixtures of an anionic and a cationic surfactant", *Langmuir*, **1999**, *15*, 2250–2253.
- [82] Yin, H.; Mao, M.; Huang, J.; Fu, H. "Two-phase region in the DTAB/SL mixed surfactant system", *Langmuir*, **2002**, *18*, 9198–9203.
- [83] Kaler, E.W.; Herrington, K.L.; Murthy, A.K.; Zasadzinski, J.A.N. "Phase behavior and structures of mixtures in anionic and cationic surfactants", *J. Phys. Chem.*, **1992**, *96*, 6698–6707.
- [84] Koehler, R.D.; Raghavan, S.R.; Kaler, E.W. "Microstructure and dynamics of wormlike micellar solutions formed by mixing cationic and anionic surfactants", *J. Phys. Chem. B*, **2000**, *104*, 11035–11044.
- [85] Schurtenberger, P.; Scartazzini, R.; Luisi, P.L. "Viscoelastic properties of polymerlike reverse micelles", *Rheol. Acta*, **1989**, *28*, 372–381.
- [86] Schurtenberger, P.; Scartazzini, R.; Magid, L.J.; Leser, M.E.; Luisi, P.L. "Structure and dynamic properties of polymer-like reverse micelles", *J. Phys. Chem.*, **1990**, *94*, 3695–3701.
- [87] Shchipunov, Y.A.; Hoffmann, H. "Growth, branching, and local ordering of lecithin polymer-like micelles", *Langmuir*, **1998**, *14*, 6350–6360.
- [88] Shchipunov, Y.A.; Hoffmann, H. "Thinning and thickening effects induced by shearing in lecithin solutions of polymer-like micelles", *Rheol. Acta*, **2000**, *39*, 542–553.
- [89] Terech, P.; Maldivi, P.; Dammer, C. "Living polymers in organic solvents: stress relaxation in bicopper tetracarboxylate/tert-butyl cyclohexane solutions", *J. Phys. II France*, **1994**, *4*, 1799–1811.
- [90] Terech, P.; Weiss, R.G. "Low molecular mass gelators of organic liquids and the properties of their gels", *Chem. Rev.*, **1997**, *97*, 3133–3159.
- [91] Terech, P.; Coutin, A. "Structure of a transient network made up of entangled monomolecular organometallic wires in organic liquids. Effects of an endcapping molecule", *Langmuir*, **1999**, *15*, 5513–5525.
- [92] Won, Y.-Y.; Davis, H.T.; Bates, F.S. "Giant wormlike rubber micelles", *Science*, **1999**, *283*, 960–963.
- [93] Won, Y.-Y.; Paso, K.; Davis, H.T.; Bates, F.S. "Comparison of original and cross-linked wormlike micelles of poly(ethylene oxide-*b*-butadiene) in water: rheological properties and effects of poly(ethylene oxide) addition", *J. Phys. Chem. B*, **2001**, *105*, 8302–8311.
- [94] Hamley, I.W.; Pedersen, J.S.; Booth, C.; Nace, V.M. "A small-angle neutron scattering study of spherical and wormlike micelles formed by poly(oxyethylene)-based diblocks copolymers", *Langmuir*, **17**, 6386–6388.

- [95] May, S.; Bohbot, Y.; Ben-Shaul, A. "Molecular theory of bending elasticity and branching of cylindrical micelles", *J. Phys. Chem. B*, **1997**, *101*, 8648–8657.
- [96] Porte, G.; Appell, J.; Poggi, Y. "Experimental investigations on the flexibility of elongated cetylpyridinium bromide micelles", *J. Phys. Chem.*, **1980**, *84*, 3105–3110.
- [97] Porte, G.; Appell, J. "Growth and size distributions of cetylpyridinium bromide micelles in high ionic strength aqueous solutions", *J. Phys. Chem.*, **1981**, *85*, 2511–2519.
- [98] Appell, J.; Bassereau, P.; Marignan, J.; Porte, G. "Polymorphism in dilute surfactant solutions: a neutron scattering study", *Prog. Colloid Polym. Sci.*, **1990**, *81*, 13–18.
- [99] Appell, J.; Marignan, J. "Structure of giant micelles: a small-angle neutron scattering study", *J. Phys. II France*, **1991**, *1*, 1447–1454.
- [100] Butler, P.D.; Magid, L.J.; Hayter, J.B. In *Structure and Flow in Surfactant Solutions (ACS Symposium Series 578)*, C.A. Herb and R.K. Prud'homme, Eds., Washington: D.C., **1994**.
- [101] Sharp, P.; Bloomfield, V.A. "Light scattering from wormlike chains with excluded volume effects", *Biopolym.*, **1968**, *6*, 1201–1211.
- [102] Gamez-Corrales, R.; Berret, J.-F.; Walker, L.M.; Oberdisse, J. "Shear-thickening dilute surfactant solutions: the equilibrium structure as studied by small-angle neutron scattering", *Langmuir*, **1999**, *15*, 6755–6763.
- [103] Magid, L.J.; Han, Z.; Li, Z.; Butler, P.D. "Tuning of microstructure of cationic micelles on multiple length scales: The role of electrostatics and specific ion binding", *Langmuir*, **2000**, *16*, 149–156.
- [104] Doi, M.; Edwards, S.F. *The Theory of Polymer Dynamics*. Oxford: Clarendon Press, **1986**.
- [105] Brûlet, A.; Boué, F.; Cotton, J.P. "About the experimental determination of the persistence length of wormlike chains of polystyrene", *J. Phys. II France*, **1996**, *6*, 885–891.
- [106] Pedersen, J.S.; Schurtenberger, P. "Scattering functions of semiflexible polymers with and without excluded volume effects", *Macromolecules*, **1996**, *29*, 7602–7612.
- [107] Magid, L.J. "The surfactant-polyelectrolyte analogy", *J. Phys. Chem. B*, **1998**, *102*, 4064–4074.
- [108] Sommer, C.; Pedersen, J.S.; Egelhaaf, S.; Cannavacciuolo, L.; Kohlbrecher, J.; Schurtenberger, P. "Wormlike micelles as "equilibrium polyelectrolytes": light and neutron scattering experiments", *Langmuir*, **2002**, *18*, 2495–2505.
- [109] Cannavacciuolo, L.; Pedersen, J.S.; Schurtenberger, P. "Monte carlo simulations study of concentration effects and scattering functions for polyelectrolyte wormlike micelles", *Langmuir*, **2002**, *18*, 2922–2932.
- [110] Gittes, F.; Mickey, B.; Nettleton, J.; Howard, J. "Flexural rigidity of microtubules and actin filaments measured from thermal fluctuations in shape", *J. Cell Biol.*, **1993**, *120*, 923–934.
- [111] Smith, S.B.; Cui, Y.; Bustamante, C. "Overstretching B-DNA: The elastic response of individual double-stranded and single-stranded DNA molecules", *Science*, **1996**, *271*, 795–799.
- [112] Khokhlov, A.R.; Semenov, A.N. "Liquid-crystalline ordering in the solution of long persistent chains", *Physica A*, **1981**, *108*, 546–556.
- [113] Khokhlov, A.R.; Semenov, A.N. "Liquid-crystalline ordering in the solution of partially flexible macromolecules", *Physica A*, **1982**, *112*, 605–614.
- [114] Semenov, A.N.; Khokhlov, A.R. "Statistical physics of liquid-crystalline polymers", *Sov. Phys. Usp.*, **1988**, *31*, 988–1014.
- [115] Onsager, L. "The effects of shape on the interaction of colloidal particles", *Ann. N.Y. Acad. Sci.*, **1949**, *51*, 627–649.

- [116] Schmitt, V.; Lequeux, F.; Pousse, A.; Roux, D. "Flow behavior and shear induced transition near an isotropic/nematic transition in equilibrium polymers", *Langmuir*, **1994**, *10*, 955–961.
- [117] Cappelaere, E.; Cressely, R.; Decruppe, J.P. "Linear and non-linear rheological behaviour of salt-free aqueous CTAB solutions", *Colloids Surfaces A*, **1995**, *104*, 353–374.
- [118] Berret, J.-F.; Roux, D.C.; Porte, G.; Lindner, P. "Tumbling behavior of nematic wormlike micelles under shear Flow", *Europhys. Lett.*, **1995**, *32*, 137–142.
- [119] Berret, J.-F.; Roux, D.C. "Rheology of nematic wormlike micelles", *J. Rheol.*, **1995**, *39*, 725–741.
- [120] Furo, I.; Halle, B. "Micelle size and orientational order across the nematic-isotropic transition: a field-dependent nuclear spin relaxation study", *Phys. Rev. E*, **1995**, *51*, 466–477.
- [121] Berret, J.-F.; Roux, D.C.; Porte, G.; Lindner, P. "Shear-induced isotropic-to-nematic phase transition in equilibrium polymers", *Europhys. Lett.*, **1994**, *25*, 521–526.
- [122] Berret, J.-F.; Roux, D.C.; Porte, G. "Isotropic-to-nematic transition in wormlike micelles under shear", *J. Phys. II France*, **1994**, *4*, 1261–1279.
- [123] Berret, J.-F.; Porte, G.; Decruppe, J.-P. "Inhomogeneous shear flows of wormlike micelles: A master dynamic phase diagram", *Phys. Rev. E*, **1997**, *55*, 1668–1675.
- [124] Cappelaere, E.; Berret, J.-F.; Decruppe, J.P.; Cressely, R.; Lindner, P. "Rheology, birefringence, and small-angle neutron scattering in a charged micellar system: evidence of a shear-induced phase transition", *Phys. Rev. E*, **1997**, *56*, 1869–1878.
- [125] Gravsholt, S. "Viscoelasticity in highly dilute aqueous solutions of pure cationic detergents", *J. Colloid Interface Sci.*, **1979**, *57*, 575–577.
- [126] Hoffmann, H.; Löbl, H.; Rehage, H.; Wunderlich, I. "Rheology of surfactant solutions", *Tenside Detergents*, **1985**, *22*, 290–298.
- [127] Rehage, H.; Hoffmann, H. "Rheological properties of viscoelastic surfactant systems", *J. Phys. Chem.*, **1988**, *92*, 4712–4719.
- [128] Shikata, T.; Hirata, K.; Kotaka, T. "Micelle formation of detergent molecules in aqueous media. 2. Role of free salicylate ions on viscoelastic properties of aqueous cetyltrimethylammonium bromide-sodium salicylate solutions", *Langmuir*, **1988**, *4*, 354–359.
- [129] Shikata, T.; Hirata, K.; Kotaka, T. "Micelle formation of detergent molecules in aqueous media. 3. Viscoelastic properties of aqueous cetyltrimethylammonium bromide-salicylic acid solutions", *Langmuir*, **1989**, *5*, 398–405.
- [130] Shikata, T.; Hirata, K.; Kotaka, T. "Micelle formation of detergent molecules in aqueous media. 4. Electrostatic features and phase behavior of cetyltrimethylammonium bromide: salicylic acid micellar solutions", *J. Phys. Chem.*, **1990**, *94*, 3702–3706.
- [131] Kern, F.; Zana, R.; Candau, S.J. "Rheological properties of semi-dilute and concentrated aqueous solutions of cetyltrimethylammonium chloride in the presence of sodium salicylate and sodium chloride", *Langmuir*, **1991**, *7*, 1344–1351.
- [132] Khatory, A.; Lequeux, F.; Kern, F.; Candau, S.J. "Linear and nonlinear viscoelasticity of semi-dilute solutions of wormlike micelles at high salt content", *Langmuir*, **1993**, *9*, 1456–1464.
- [133] Hartmann, V.; Cressely, R. "Occurrence of shear-thickening in aqueous micellar solutions of CTAB with some added organic counterions", *Colloid Polym. Sci.*, **1998**, *276*, 169–175.
- [134] Raghavan, S.R.; Kaler, E.W. "Highly viscoelastic wormlike micellar solutions formed by cationic surfactants with long unsaturated chains", *Langmuir*, **2001**, *17*, 300–306.

- [135] Croce, V.; Cosgrove, T.; Maitland, G.; Hughes, T.; Karlsson, G. "Rheology, cryogenic transmission electron spectroscopy, and small-angle neutron scattering of highly viscoelastic wormlike micellar solutions", *Langmuir*, **2003**, *19*, 8536–8541.
- [136] Cates, M.E. "Reptation of living polymers: dynamics of entangled polymers in the presence of reversible chain-scission reactions", *Macromolecules*, **1987**, *20*, 2289–2296.
- [137] Drye, T.J.; Cates, M.E. "Living networks: the role of cross-links in entangled surfactant solutions", *J. Chem. Phys.*, **1992**, *96*, 1367–1375.
- [138] Graneck, R.; Cates, M.E. "Stress relaxation in living polymers: results from a poisson renewal model", *J. Chem. Phys.*, **1992**, *96*, 4758–4767.
- [139] Turner, M.S.; Cates, M.E. "Linear viscoelasticity of wormlike micelles: a comparison of micellar reaction kinetics", *J. Phys. II France*, **1992**, *2*, 503–519.
- [140] Messenger, R.; Ott, A.; Chatenay, D.; Urbach, W.; Langevin, D. "Are giant micelles living polymers", *Phys. Rev. Lett.*, **1988**, *60*, 1410–1413.
- [141] Porte, G.; Appell, J. "Polymerlike behaviour of giant micelles", *Europhys. Lett.*, **1990**, *12*, 185–190.
- [142] Turner, M.S.; Cates, M.E. "Linear viscoelasticity of living polymers: a quantitative probe of chemical relaxation times", *Langmuir*, **1991**, *7*, 1590–1594.
- [143] Berret, J.-F.; Appell, J.; Porte, G. "Linear rheology of entangled wormlike micelles", *Langmuir*, **1993**, *9*, 2851–2854.
- [144] Khatory, A.; Kern, F.; Lequeux, F.; Appell, J.; Porte, G.; Morie, N.; Ott, A.; Urbach, W. "Entangled versus multiconnected network of wormlike micelles", *Langmuir*, **1993**, *9*, 933–939.
- [145] Schmitt, V.; Lequeux, F. "Surfactant self-diffusion in wormlike micelles", *Langmuir*, **1998**, *14*, 283–287.
- [146] Soltero, J.F.A.; Puig, J.E.; Manero, O. "Rheology of the cetyltrimethylammonium tosilate water system. 2. Linear viscoelastic regime", *Langmuir*, **1996**, *12*, 2654–2662.
- [147] Hoffmann, H. In *Organized Solutions, Surfactant in Science and Technology*, S.E. Friberg and B. Lindmann, Eds., New York: Marcel Dekker Inc., **1992**.
- [148] Berret, J.-F.; Roux, D.C.; Porte, G. "Dynamics of the isotropic-to-nematic phase transition induced by shear in equilibrium polymers", In *Fourth European Rheology Conference*, Spain: Sevilla, **1994**.
- [149] Massiera, G.; Ramos, L.; Ligoure, C. "Role of the size distribution in the elasticity of entangled living polymer solutions", *Europhys. Lett.*, **2002**, *57*, 127–133.
- [150] Buhler, E.; Munch, J.-P.; Candau, S.J. "Dynamic light scattering study of abnormally fluid semi-dilute solutions of wormlike micelles", *Europhys. Lett.*, **1996**, *34*, 251–255.
- [151] Ott, A.; Urbach, W.; Langevin, D.; Schurtenberger, P.; Scartazzini, R.; Luisi, P.L. "A self-diffusion study of polymer-like micelles", *J. Phys.: Condens. Matter*, **1990**, *2*, 5907–5912.
- [152] Morie, N.; Urbach, W.; Langevin, D. "Self-diffusion in networks of CPClO₃ wormlike micelles", *Phys. Rev. E*, **1995**, *51*, 2150–2156.
- [153] Kröger, M.; Makhloufi, R. "Wormlike micelles under shear flow: a microscopic model studied by nonequilibrium-molecular-dynamics computer simulations", *Phys. Rev. E*, **1996**, *53*, 2531–2536.
- [154] Carl, W.; Kröger, M.; Makhloufi, R. "On the shape and rheology of linear micelles in dilute solutions", *J. Phys. II France*, **1997**, *7*, 931–946.
- [155] Eiser, E.; Molino, F.; Porte, G.; Diat, O. "Nonhomogeneous textures and banded flow in a soft cubic phase under shear", *Phys. Rev. E*, **2000**, *61*, 6759–6764.

- [156] Volkova, O.; Cutillas, S.; Bossis, G. "Shear banded flows and nematic-to-isotropic transition in ER and MR fluids", *Phys. Rev. Lett.*, **1999**, *82*, 233–236.
- [157] Berret, J.-F.; S  r  ro, Y. "Evidence of shear-induced fluid fracture in telechelic polymer networks", *Phys. Rev. Lett.*, **2001**, *87*, 0483031–0483034.
- [158] Coussot, P.; Raynaud, J.S.; Bertrand, F.; Moucheron, P.; Guilbaud, J.P.; Huynh, H.T.; Jarny, S.; Lesueur, D. "Coexistence of liquid and solid phases in flowing soft-galssy materials", *Phys. Rev. Lett.*, **2002**, *88*, 2183011–2183014.
- [159] Berret, J.-F.; Roux, D.C.; Lindner, P. "Structure and rheology of concentrated wormlike micelles at the shear-induced isotropic-to-nematic transition", *Eur. Phys. J. B*, **1998**, *5*, 67–77.
- [160] Fisher, E.; Callaghan, P.T. "Shear banding and the isotropic-to-nematic transition in wormlike micelles", *Phys. Rev. E*, **2001**, *64*, 0115011–0115014.
- [161] Decruppe, J.P.; Cappelaere, E.; Cressely, R. "Optical and rheological properties of a semi-diluted equimolar solution of cetyltrimethylammonium bromide and potassium bromide", *J. Phys. II France*, **1997**, *7*, 1–8.
- [162] Soltero, J.F.A.; Bautista, F.; Puig, J.E.; Manero, O. "Rheology of cetyltrimethylammonium p-toluenesulfonate-water system. 3. Nonlinear viscoelasticity", *Langmuir*, **1999**, *15*, 1604–1612.
- [163] Berret, J.-F. "Transient rheology of wormlike micelles", *Langmuir*, **1997**, *13*, 2227–2234.
- [164] Berret, J.-F.; Porte, G. "Metastable versus instable transients at the onset of a shear-induced phase transition", *Phys. Rev. E*, **1999**, *60*, 4268–4271.
- [165] Cappelaere, E.; Cressely, R. "Shear banding structure in viscoelastic micellar solutions", *Colloid Polym. Sci.*, **1997**, *275*, 407–418.
- [166] Wheeler, E.K.; Fischer, P.; Fuller, G.G. "Time-periodic flow induced structures and instabilities in a viscoelastic surfactant solution", *J. Non-Newtonian Fluid Mech.*, **1998**, *75*, 193–208.
- [167] Jerrard, H.G. "Theory of streaming double refraction", *Chem. Rev.*, **1959**, *59*.
- [168] Fuller, G.G. *Optical Rheometry of Complex Fluids*. New York: Oxford University Press, **1995**.
- [169] Wunderlich, I.; Hoffmann, H.; Rehage, H. "Flow birefringence and rheological measurements on shear induced micellar structures", *Rheol. Acta*, **1987**, *26*, 532–542.
- [170] Shikata, T.; Dahman, S.J.; Pearson, D.S. "Rheo-optical behavior of wormlike micelles", *Langmuir*, **1994**, *10*, 3470–3476.
- [171] Humbert, C.; Decruppe, J.P. "Flow birefringence and stress optical law of viscoelastic solutions of cationic surfactants and sodium salicylate", *Eur. Phys. J. B*, **1998**, *6*, 511–518.
- [172] Decruppe, J.P.; Ponton, A. "Flow birefringence, stress optical rule and rheology of four micellar solutions with the same low shear viscosity", *Eur. Phys. J. E*, **2003**, *10*, 201–207.
- [173] Decruppe, J.P.; Cressely, R.; Makhouloufi, R.; Cappelaere, E. "Flow birefringence experiments showing a shear-banding structure in a CTAB solution", *Colloid Polym. Sci.*, **1995**, *273*, 346–351.
- [174] Greco, F.; Ball, R.C. "Shear-band formation in a non-newtonian fluid model with a constitutive instability", *J. Non-Newtonian Fluid Mech.*, **1997**, *69*, 195–206.
- [175] Olmsted, P.D.; Radulescu, O.; Lu, C.-Y.D. "Johnson-segalman model with a diffusion term in cylindrical couette flow", *J. Rheol.*, **2000**, *44*, 257–275.
- [176] Roux, D.C.; Berret, J.-F.; Porte, G.; Peuvrel-Disdier, E.; Lindner, P. "Shear induced orientations and textures of nematic wormlike micelles", *Macromolecules*, **1995**, *28*, 1681–1687.

- [177] Deutsch, M. "Orientational order determination in liquid crystals by X-ray diffraction", *Phys. Rev. A*, **1991**, *44*, 8264–8270.
- [178] Larson, R.G. "Arrested tumbling in shearing flows of liquid-crystal polymers", *Macromolecules*, **1991**, *23*, 3983–3992.
- [179] Britton, M.M.; Callaghan, P.T. "Two-phase shear band structures at uniform stress", *Phys. Rev. Lett.*, **1997**, *78*, 4930–4933.
- [180] Britton, M.M.; Callaghan, P.T. "Nuclear magnetic resonance visualization of anomalous flow in cone-and-plate rheometry", *J. Rheol.*, **1997**, *41*, 1365–1386.
- [181] Mair, R.W.; Callaghan, P.T. "Shear flow of wormlike micelles in pipe and cylindrical geometries as studied by nuclear magnetic resonance microscopy", *J. Rheol.*, **1997**, *41*, 901–924.
- [182] Britton, M.M.; Callaghan, P.T. "Shear band instability in wormlike micellar solutions", *Eur. Phys. J. B*, **1999**, *7*, 237–249.
- [183] Britton, M.M.; Mair, R.W.; Lambert, R.K.; Callaghan, P.T. "Transition to shear banding in pipe and couette flow of wormlike micellar solutions", *J. Rheol.*, **1999**, *43*, 897–909.
- [184] Fisher, E.; Callaghan, P.T. "Is a birefringence band a shear band?", *Europhys. Lett.*, **2000**, *50*, 803–809.
- [185] Bellour, M.; Knaebel, A.; Munch, J.-P.; Candau, S.J. "Scattering properties of salt-free wormlike micellar solutions", *Eur. Phys. J. E*, **2000**, *3*, 111–121.
- [186] Berret, J.-F.; Gamez-Corrales, R.; Lerouge, S.; Decruppe, J.P. "Shear-thickening transition in surfactant solutions: new experimental features from rheology and flow birefringence", *Eur. Phys. J. E*, **2000**, *2*, 343–350.
- [187] Hoffmann, H.; Kalus, J.; Thurn, H.; Ibel, K. "Small angle neutron scattering studies on viscoelastic detergents", *Ber. Bunsenges. Phys. Chem.*, **1983**, *87*, 1120–1129.
- [188] Grand, C.; Arrault, J.; Cates, M.E. "Slow transients and metastability in wormlike micelle rheology", *J. Phys. II France*, **1996**, *7*, 1071–1086.
- [189] Porte, G.; Berret, J.-F.; Harden, J.L. "Inhomogeneous flows of complex fluids: mechanical instability versus non-equilibrium phase transition", *J. Phys. II France*, **1997**, *7*, 459–472.
- [190] Shikata, T.; Pearson, D.S. "Phase transitions in entanglement networks of wormlike micelles", *Langmuir*, **1994**, *10*, 4027–4030.
- [191] Humbert, C.; Decruppe, J.P. "Stress optical coefficient of viscoelastic solutions of cetyltrimethylammonium bromide and potassium bromide", *Colloid Polym. Sci.*, **1998**, *276*, 160–168.
- [192] Radulescu, O.; Olmsted, P.D.; Decruppe, J.P.; Lerouge, S.; Berret, J.-F.; Porte, G. "Time scales in shear banding of wormlike micelles", *Europhys. Lett.*, **2003**, *62*, 230–236.
- [193] Salmon, J.B.; Colin, A.; Manneville, S.; Molino, F. "Velocity profiles in shear banding wormlike micelles", *Phys. Rev. Lett.*, **2003**, *90*, 2283031–2283034.
- [194] Hassan, P.A.; Valaulikar, B.S.; Manohar, C.; Kern, F.; Bourdieu, L.; Candau, S.J. "Vesicle to micelle transition: rheological investigations", *Langmuir*, **1996**, *12*, 4350–4357.
- [195] Oda, R.; Narayanan, J.; Hassan, P.A.; Manohar, C.; Salkar, R.A.; Kern, F.; Candau, S.J. "Effect of the lipophilicity of the counterion on the viscoelasticity of micellar solutions of cationic surfactant", *Langmuir*, **1998**, *14*, 4364–4372.
- [196] Cappelaere, E.; Cressely, R. "Rheological behavior of an elongated micellar solution at low and high salt concentrations", *Colloid Polym. Sci.*, **1998**, *276*, 1050–1056.

- [197] Lerouge, S.; Decruppe, J.P.; Berret, J.-F. "Correlations between rheological and optical properties of a micellar solution under shear banding flow", *Langmuir*, **2000**, *16*, 6464–6474.
- [198] Decruppe, J.P.; Lerouge, S.; Berret, J.-F. "Insight in shear banding under transient flow", *Phys. Rev. E*, **2001**, *63*, 0225011–0225014.
- [199] Soltero, J.F.A.; Puig, J.E.; Manero, O.; Schulz, P.C. "Rheology of cetyltrimethylammonium tosilate-water system. 1. Relation to phase behavior", *Langmuir*, **1995**, *11*, 3337–3346.
- [200] Hernandez-Acosta, S.; Gonzalez-Alvarez, A.; Manero, O.; Mendez-Sanchez, A.F.; Perez-Gonzalez, J.; Vargas, L.d. "Capillary rheometry of micellar aqueous solutions", *J. Non-Newtonian Fluid Mech.*, **1999**, *85*, 229–247.
- [201] Bandyopadhyay, R.; Basappa, G.; Sood, A.K. "Observation of chaotic dynamics in dilute sheared aqueous solutions of CTAT", *Phys. Rev. Lett.*, **2000**, *84*, 2022–2025.
- [202] Bautista, F.; Soltero, J.F.A.; Macias, E.R.; Puig, J.E.; Manero, O. "Irreversible thermodynamics approach and modelling of shear-banding flow of wormlike micelles", *J. Phys. Chem. B*, **2002**, *106*, 13018–13026.
- [203] Bandyopadhyay, R.; Sood, A.K. "Effect of screening of intermicellar interactions on the linear and nonlinear rheology of a viscoelastic gel", *Langmuir*, **2003**, *19*, 3121–3127.
- [204] Mendez-Sanchez, A.F.; Lopez-Gonzalez, M.R.; Rolon-Garrido, V.H.; Perez-Gonzalez, J.; Vargas, L.d. "Instabilities of micellar systems under homogeneous and non-homogeneous flow conditions", *Rheol. Acta*, **2003**, *42*, 56–63.
- [205] Holmes, W.M.; Lopez-Gonzalez, M.R.; Callaghan, P.T. "Fluctuations in shear-banded flow seen by NMR velocimetry", *Europhys. Lett.*, **2003**, *64*, 274–280.
- [206] Fischer, P.; Wheeler, E.K.; Fuller, G.G. "Shear-banding structure orientated in the vorticity direction observed for equimolar micellar solution", *Rheol. Acta*, **2002**, *41*, 35–44.
- [207] Wunderlich, A.M.; Brunn, P.O. "The complex rheological behavior of an aqueous cationic surfactant solution investigated in a couette-type viscosimeter", *Colloid Polym. Sci.*, **1989**, *267*, 627–636.
- [208] Liu, C.-H.; Pine, D.J. "Shear-induced gelation and fracture in micellar solutions", *Phys. Rev. Lett.*, **1996**, *77*, 2121–2124.
- [209] Boltenhagen, P.; Hu, Y.; Matthys, E.F.; Pine, D.J. "Observation of bulk phase separation and coexistence in a sheared micellar solution", *Phys. Rev. Lett.*, **1997**, *79*, 2359–2362.
- [210] Boltenhagen, P.; Hu, Y.; Matthys, E.F.; Pine, D.J. "Inhomogeneous structure formation and shear-thickening in wormlike micellar solutions", *Europhys. Lett.*, **1997**, *38*, 389–394.
- [211] Hu, H.T.; Boltenhagen, P.; Pine, D.J. "Shear thickening in low-concentration solutions of wormlike micelles: I. Direct visualisation of transient behavior and phase transitions", *J. Rheol.*, **1998**, *42*, 1185–1208.
- [212] Hu, Y.T.; Boltenhagen, P.; Matthys, E.; Pine, D.J. "Shear thickening in low-concentration solutions of wormlike micelles. II. Slip, fracture, and stability of the shear-induced phase", *J. Rheol.*, **1998**, *42*, 1209–1226.
- [213] Kadoma, I.A.; Egmond, J.W.v. "Tuliplike scattering patterns in wormlike micelles under shear flow", *Phys. Rev. Lett.*, **1996**, *76*, 4432–4435.
- [214] Kadoma, I.A.; Egmond, J.W.v. "Shear-enhanced orientation and concentration fluctuations in wormlike micelles: effect of salt", *Langmuir*, **1997**, *13*, 4551–4561.
- [215] Kadoma, I.A.; Egmond, J.W.v. "Flow-induced nematic string phase in semi-dilute wormlike micelles", *Phys. Rev. Lett.*, **1998**, *80*, 5679–5682.

- [216] Lerouge, S.; Decruppe, J.P.; Humbert, C. "Shear banding in a micellar solution under transient flow", *Phys. Rev. Lett.*, **1998**, *24*, 5457–5460.
- [217] McLeish, T.C.B.; Ball, R.C. "A molecular approach of the spurt effect in polymer melt flow", *J. Polym. Sci. Polym. Phys.*, **1986**, *24*, 1735–1745.
- [218] Spenley, N.A.; Cates, M.E.; McLeish, T.C.B. "Nonlinear rheology of wormlike micelles", *Phys. Rev. Lett.*, **1993**, *71*, 939–942.
- [219] Spenley, N.A.; Yuan, X.F.; Cates, M.E. "Nonmonotonic constitutive laws and the formation of shear banded flows", *J. Phys. II France*, **1996**, *6*, 551–571.
- [220] Hess, S. "Pre- and post-transitional behavior of the flow alignment and flow-induced phase transition in liquid crystals", *Z. Naturforsch.*, **1976**, *31a*, 1507.
- [221] Olmsted, P.D.; Goldbart, P.M. "Theory of nonequilibrium phase transition for nematic liquid crystals under shear flow", *Phys. Rev. A*, **1990**, *41*, 4578–4581.
- [222] See, H.; Doi, M.; Larson, R. "The effect of steady flow fields on the isotropic-nematic phase transition of rigid rod-like polymers", *J. Chem. Phys.*, **1990**, *92*, 792–800.
- [223] Olmsted, P.D.; Goldbart, P.M. "Isotropic-nematic transition in shear flow: state selection, coexistence, phase transitions, and critical behavior", *Phys. Rev. A*, **1992**, *46*, 4966–4993.
- [224] Dhont, J.K.G. "A constitutive relation describing the shear-banding transition", *Phys. Rev. E*, **1999**, *60*, 4534–4544.
- [225] Lenstra, T.A.J.; Dogic, Z.; Dhont, J.K.G. "Shear-induced displacement of isotropic-nematic spinodals", *J. Chem. Phys.*, **2001**, *114*, 10151–10162.
- [226] Olmsted, P.D.; Lu, C.-Y.D. "Phase coexistence of complex fluids in shear flow", *Faraday Discuss.*, **1999**, *112*, 183–194.
- [227] Olmsted, P.D.; Lu, C.-Y.D. "Phase separation of rigid-rod suspensions in shear flow", *Phys. Rev. E*, **1999**, *60*, 4397–4415.
- [228] Fielding, S.; Olmsted, P.D. "Flow phase diagrams for concentration-coupled shear-banding", *Eur. Phys. J. B*, **2003**, *11*, 65–83.
- [229] Schmitt, V.; Marques, C.M.; Lequeux, F. "Shear-induced phase separation of complex fluids: the role of the flow-concentration coupling", *Phys. Rev. E*, **1995**, *52*, 4009–4015.
- [230] Olmsted, P.D. "Two-state shear diagrams for complex fluids in shear flow", *Europhys. Lett.*, **1999**, *48*, 339–345.
- [231] Goveas, J.L.; Olmsted, P.D. "A minimal model for vorticity and gradient banding in complex fluids", *Eur. Phys. J. E*, **2001**, *6*, 79–89.
- [232] Fielding, S.; Olmsted, P.D. "Early stage in the unified model of shear-induced demixing and mechanical shear banding instabilities", *Phys. Rev. Lett.*, **2003**, *90*, 2245011–2245014.
- [233] Ajdari, A. "Rheological behavior of a solution of particles aggregating on the containing walls", *Phys. Rev. E*, **1998**, *58*, 6294–6298.
- [234] Yuan, X.-F. "Interfacial dynamics of viscoelastic fluid flows", *Phys. Chem. Chem. Phys.*, **1999**, *1*, 2177–2182.
- [235] Yuan, X.-F. "Dynamics of a mechanical interface in shear-banded flow", *Europhys. Lett.*, **1999**, *46*, 542–548.
- [236] Lu, C.-Y.D.; Olmsted, P.D.; Ball, R.C. "Effects of nonlocal stress on the determination of shear banding flow", *Phys. Rev. Lett.*, **2000**, *84*, 642–645.
- [237] Buxbaum, R.E.; Dennerll, T.; Weiss, S.; Heidemann, S.R. "F-actin and microtubule suspensions as intermediate fluids", *Science*, **1987**, *235*, 1511–1514.
- [238] Jary, D.; Sikorav, J.-L.; Lairez, D. "Nonlinear viscoelasticity of entangled DNA molecules", *Europhys. Lett.*, **1999**, *46*, 251–255.

- [239] Pujolle-Robic, C.; Noirez, L. "Observation of shear-induced nematic-isotropic transition in side-chain liquid crystal polymers", *Nature*, **2001**, *409*, 167–171.
- [240] Pujolle-Robic, C.; Olmsted, P.D.; Noirez, L. "Transient and stationary flow behaviour of side-chain liquid crystalline polymers: evidence of shear-induced isotropic-to-nematic phase transition", *Europhys. Lett.*, **2002**, *59*, 364–369.
- [241] Krishnan, K.; Almdal, K.; Burghardt, W.R.; Lodge, T.P.; Bates, F.S. "Shear-induced nano-macro structural transition in a polymeric bicontinuous microemulsion", *Phys. Rev. Lett.*, **2001**, *87*, 0983011–0983014.

Chapter 20

CRYO-TEM, X-RAY DIFFRACTION AND MODELING OF AN ORGANIC HYDROGEL

Lara A. Estroff and Andrew D. Hamilton

*Department of Chemistry, Yale University, PO Box 208107,
New Haven, CT 06520-8107, USA*

1. Introduction	721
2. Techniques	722
3. Modeling Gel Structure	723
3.1. Molecular Structure	724
3.2. Nanometer Structure	724
3.3. Micrometer Structure	728
4. A Case Study	729
4.1. Cryo-Transmission Electron Microscopy	731
4.2. X-Ray Diffraction	732
4.3. Modeling	734
5. Perspectives for the Future	737

1. Introduction

A more detailed picture of the molecular organization in a molecular gel will assist in efforts to rationally design low molecular mass organic gelators (LMOGs) of both organic and aqueous solvents. There is also increasing interest in being able to control the morphology of the resulting self-assembled fibrillar network (SAFIN) which will only be possible when we understand the connection between the molecular and the nano/micro structure of a given gelator [1]. The molecular recognition events leading to gelation are still poorly understood

and there is a paucity of techniques with molecular level resolution that are adaptable to the analysis of gels. This chapter discusses how experimental data from complementary techniques can be used to develop models of gel structure at several levels of resolution. Using a case study of an organic hydrogelator [2, 3], we demonstrate how data obtained from vitrified ice cryo-transmission electron microscopy (cryo-TEM) (see Chapter 9) and X-ray diffraction (XRD) (see Chapter 11) can be used to develop a model of the molecular assembly processes that lead ultimately to gelation by small organic molecules.

2. Techniques

Approaches traditionally used to evaluate molecular assembly are not necessarily applicable to disordered, colloidal gels [4]. Microscopic techniques, including light, scanning probe [5–7], and scanning (SEM) and transmission (TEM) electron [8, 9], provide insights into gel structure with various levels of resolution. Under standard operating conditions (high vacuum), electron microscopy requires complete dehydration of the sample leading to artifacts for gel systems usually composed of >90% solvent [10]. The visualization of thin vitrified films containing organic assemblies by TEM allows visualization in what is essentially a solvated environment [11]. The high viscosity of gel systems also makes it difficult to form a film containing well-formed aggregates that is sufficiently thin for complete vitrification. Nevertheless, several groups have successfully used cryo-TEM to visualize the structures of organic gels [2, 8, 9, 12, 13].

Likewise, various diffraction techniques can provide information about the molecular structure of organogels [14–19]. Yet, much of this work has been on dried samples, making it difficult to draw direct conclusions about the structure of the gel in its native state. Crystal structures of related molecules can also provide information about the molecular organization leading to gelation [14–20]. If crystal structures of all possible polymorphs of the gelator molecule itself can be obtained, then they can be compared to the powder diffraction pattern of the gelled material. The closest match is chosen as the structure of the gel [14, 15]. This only is possible for a small number of gelators since many do not form X-ray quality crystals. More often, the crystal structures of related molecules are used as a comparison for the XRD of the gel and from them possible models of the molecular packing in the gel are developed [17, 19]. When this is the case, it must be remembered that polymorphism is common among gelling molecules and that the very fact that one molecule gels and the other crystallizes points to a difference in molecular assembly. Finally, if no single crystal structures are available, it is possible to use good quality powder diffraction data (of the gel and/or related molecules) [2, 21–25], complemented by modeling to obtain a molecular level representation of a gel.

3. Modeling Gel Structure

None of these techniques, with the exception of single crystal diffraction combined with polymorph identification, provides information that can be directly translated into a molecular model with atomic scale resolution. The combined data from several techniques, however, can be used to intelligently model the gel system. Modeling can be done at several levels of resolution, all important to understanding how and why a given molecule gels a certain solvent. One way of understanding a gel is to break it down into having a primary, secondary and tertiary structure, much like a protein (Figure 1). Recognition at the molecular level generates the primary structure (Å to nanometer scale) by driving one and/or two dimensional aggregation of the gelator molecules (see Chapters 1–3). For example, ureas and other functional groups capable of hydrogen bonding are often used in gelator design to promote 1-D assembly (Figure 1a) [2, 3, 17, 18, 26–33]. The morphology of the aggregates (i.e., micelles, vesicles, fibers, ribbons, sheets) constitutes the secondary structure (nano- to micro-meter scale) and is directly influenced by the molecular structure (Figure 1b). Finally, the tertiary structure (micro- to milli-meter scale) involves the interaction of individual aggregates and ultimately determines whether a SAFIN leading to a gel is formed or instead fibers (or other aggregates) precipitate from solution rather than entrap it (Figure 1c).

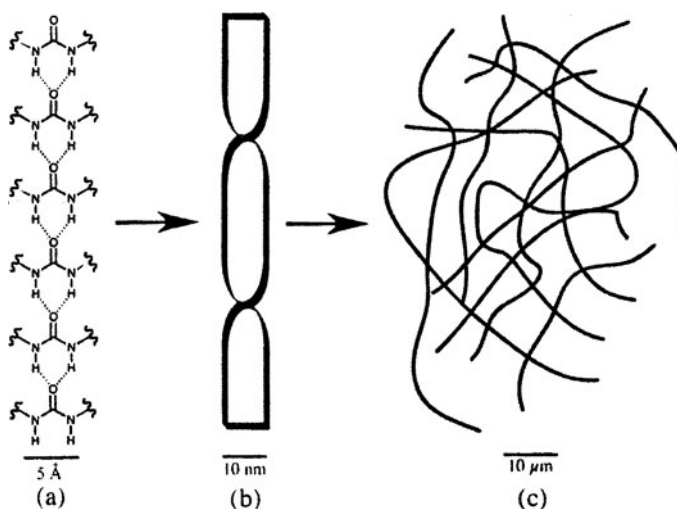


Figure 1. Schematic representations of examples of the primary (a), secondary (b), and tertiary (c) structure of a self-assembled physical gel. Adapted with permission from [40]. Copyright (2004) American Chemical Society.

This view of a gel, while helpful in understanding the recognition events at several scales, ignores the structure and role of solvent molecules in gel formation, which will eventually have to be accounted for in the models. Recently, several groups, using small-angle X-ray and neutron scattering (SAXS and SANS, respectively) data (see Chapters 10 and 11), have begun this process by adding solvent molecules into their models of gel structure [7, 34–36]. This chapter, however, focuses on understanding how branched, fibrous networks are formed by LMOGs since it is generally accepted that such structures are best able to trap solvent, immobilizing and thus gelating it [4]. In the following sections, examples of how modeling can be used to understand the structure of gels at each level (Figure 1) are presented.

3.1. Molecular Structure

The primary structure of gels has been modeled using energy minimization and molecular dynamic calculations to identify possible modes of aggregation for gelators of both aqueous [37–40] and organic solvents [17, 27, 30, 41, 42]. There have been many reports of organogelators that have hydrogen bond donors and acceptors to promote aggregation and subsequent fiber formation (Figure 1a) [43–45]. The attachment of long alkyl chains onto the hydrogen-bonded core enhances solubility in organic solvents and promotes association among the fibers through van der Waals forces, eventually leading to gel formation.

Feringa and co-workers have modeled the aggregation of bis-urea organogelators [17, 30]. They have shown that for 1,2-bis-(N-methylureido)cyclohexane, the preferred sites of interaction for the three lowest energy conformers are above and below the two urea groups (Figure 2.I) [17]. Such anisotropic tendencies mean that aggregation in one direction is highly favored, which is a common characteristic among gelator molecules. Next, they take the monomers and use symmetry to construct one-dimensional aggregates and optimize their geometry (Figure 2.II). The final step is to extend the modeling on the truncated molecule to the actual gelator and use experimental data, such as powder X-ray diffraction, to propose a structure of the aggregates (Figure 2.III).

3.2. Nanometer Structure

Due to the strongly anisotropic driving forces for aggregation among gelator molecules, the most common morphologies observed at the nano- and micrometer scale for gels are elongated aggregates such as ribbons, fibers and tubules

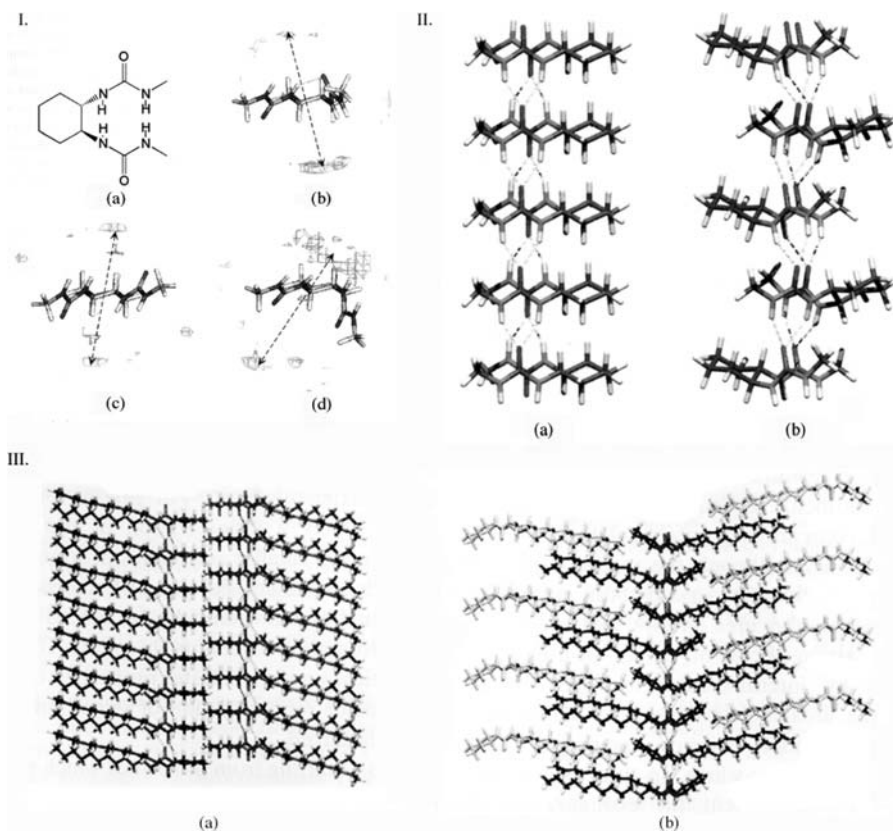


Figure 2. I. (a) Structure of *trans*-1,2-bis-(N-methylureido)cyclohexane and the energy-minimized conformations with (b) an intramolecular hydrogen bond, (c) antiparallel urea groups and (d) parallel urea groups. The contour levels for an interaction energy of -80 kJ mol^{-1} with a second molecule of *trans*-1,2-bis-(N-methylureido)cyclohexane are shown as well. II. Two possible hydrogen-bonded aggregates of *trans*-1,2-bis-(N-methylureido)cyclohexane: (a) translation aggregate with urea groups antiparallel, and (b) screw axis aggregate with urea groups parallel. III. Tentative arrangements of the bis-urea gelator in (a) a double layer structure constructed from translational aggregates and (b) a structure constructed via a screw axis with the urea groups parallel. (Reprinted with permission from [17]. Copyright (1999) Wiley-VCH.)

(Figure 1b) [40, 43, 46]. Understanding the finer details of the morphology (twisted vs. helical, flat vs. tubular) requires another level of modeling. For example, Boden and co-workers have used chiral, rod-like monomers to model the formation of helical and twisted ribbons by peptide β -sheets [47, 48].

In other work, Oda, Huc and co-workers have extensively studied a series of gemini surfactants with chiral counterions that gel water via the formation of twisted ribbons (Figure 3) (see Chapter 16) [49–52]. They developed a structural model for the origin of the twist in these systems using

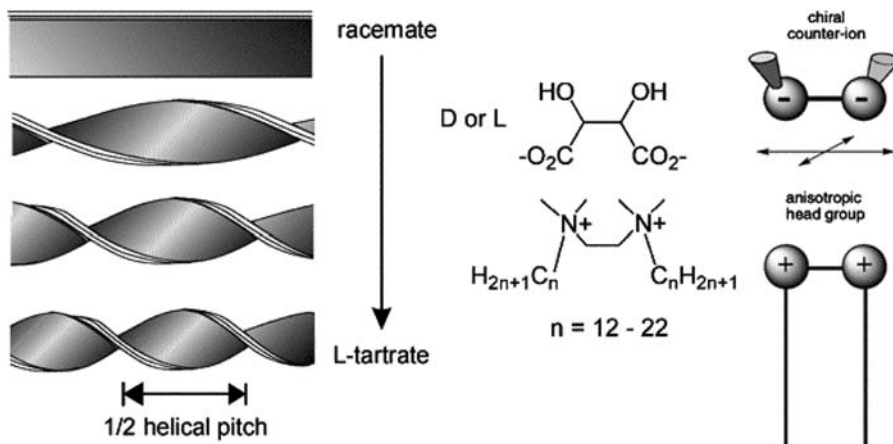


Figure 3. Structure of the n -2- n dimeric amphiphiles having tartrate counterions and schematic representation of the multi-bilayer ribbons they form in water. The pitch of the ribbons can be tuned upon varying the enantiomeric excess (ee) of the anion. Adapted with permission from [49]. Copyright (2002) American Chemical Society and from [52] with permission from the authors and *Nature*. Copyright (1999) Macmillan Magazines Ltd.

a range of techniques, including TEM, single crystal XRD, NMR, UV/CD and VCD (vibrational circular dichroism). The degree of twist varies with the enantiomeric excess (ee) present in the design. The trend begins with flat ribbons formed by the racemate and extends to a twisted ribbon with pure enantiomer of tartrate, with the direction of the twist reflecting its configuration [49, 52]. The key structural control questions concern the origin of the morphology of the twist and the extent to which it can be tuned by varying the ee of the monomer. The shape of the twist appears to have a geometrical origin. In particular, there is extensive hydrogen bonding between the tartrate counterions in consecutive layers [50]. Interlayer coordination favors saddle-like (Gaussian) curvature and maintains equal contact between all layers. Cylindrical curvature, in which the outer layers have less contact than the inner ones, is less favored (Figure 4).

The tunability of the twist is less easily explained. Achiral counterions, such as bromide, cause the formation of flat ribbons, similar to those formed in the presence of the racemate. This, in addition to the ability of D- and L-tartrate to give opposite handed twists, suggests that the twisting is a molecular level phenomenon. The n -2- n family of gemini surfactants can adopt any of seven conformers by rotation about the bonds linking the nitrogens to the spacer carbons (Figure 5). These seven are made up of three sets of enantiomers and one symmetrical conformer. The A/A' conformers appear to be the most likely candidates for bilayer formation since they are the only ones in which both alkyl chains lie on the same face of the molecules without additional gauche

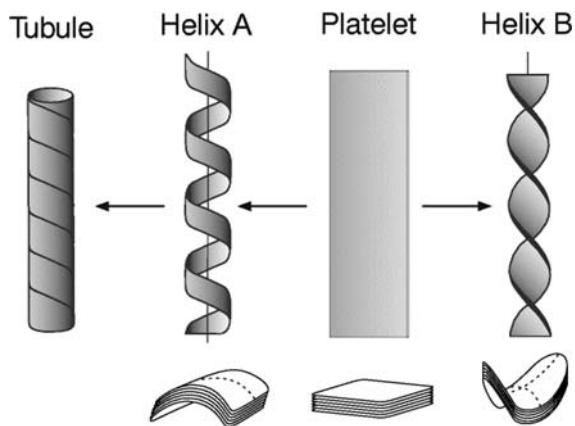


Figure 4. Different types of ribbons showing cylindrical (Helix A) and Gaussian (Helix B) type curvature. The side views show the difference in contact between multiple layers in the two geometries. (Reproduced from [52] with permission from the authors and *Nature*. Copyright (1999) Macmillan Magazines Ltd.)

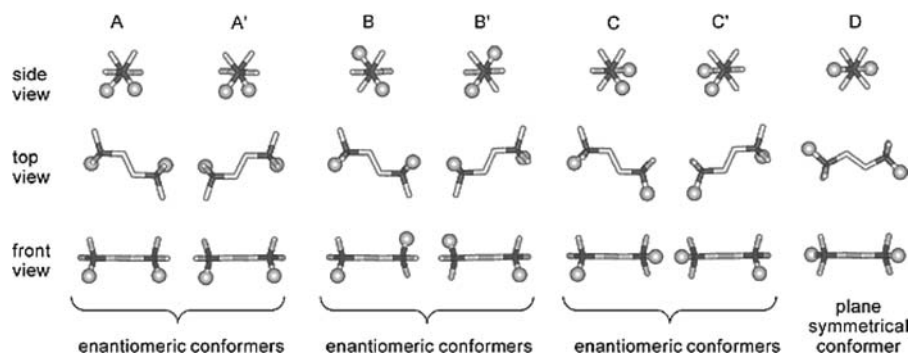


Figure 5. Stick representations of the seven conformers of an n -2- n dimeric amphiphile head-group generated by 120° rotations about the bonds linking nitrogens (in dark grey) to the spacer carbons. The alkyl chains are schematized by balls. (Reprinted with permission from [49]. Copyright (2002) American Chemical Society.)

or 1,3-diaxial interactions. In addition, the single crystal X-ray structure of a related surfactant (dioctadecyl-dimethylammonium bromide monohydrate) is a mixture of two enantiomeric conformers which correspond to the A/A' forms. Achiral counterions should not discriminate between the enantiomers. Using ^1H NMR, Berthier showed that the dications and chiral anions interact directly with each other, suggesting that chiral induction by the chiral anion can occur, causing the whole system to behave as a chiral amphiphile [49].

The chirality of the dication is intrinsically dynamic suggesting that lowering the *ee* of the anion will lead to a decrease in the efficiency of the chiral induction by the tartrate ions. Previous examples of chiral amphiphiles have been shown to express supramolecular chirality in their aggregates [53–55]. The link between the *ee* of the tartrate anions and the degree of twisting, in contrast to enantiomeric resolution or precipitation of racemate [12], is not yet understood.

3.3. Micrometer Structure

After understanding the origins of the morphology of the gelator aggregates, it is desirable to understand how these aggregates form a suprastructure (i.e., a SAFIN) that causes gelation. The property of gelation is generally thought to arise from the self-assembled fibers, such as those from polymer gels [56], entangling and trapping solvent (Figure 1c) [4]. Liu, Sawant and co-workers have proposed an intriguing hypothesis about the origins of gelation in fibrous networks [57–59]. They found that the SEM images of gels compared to viscous liquids formed by (lanosta-8,24-dien-3 β -ol:24,25-dihydrolanosterol, 56:44 molar ratio) in diisooctylphthalate (DIOP) in the presence and absence of additive, EVACP (ethylene/vinyl acetate copolymer), had one striking difference: the gels showed interconnected networks of long, thin fibers while the viscous liquids had separate, thicker, and shorter fibers (Figure 6) [57, 58].

Physically, the long, thin, flexible fibers are better able than the shorter fibers to trap solvent, leading to gelation [4]. The powder X-ray diffraction patterns of both materials are identical, indicating that the long range order in each is the same despite the differences in morphology [57, 58]. Liu *et al.* attribute the differences to the additive molecule preferentially adsorbing onto the tips

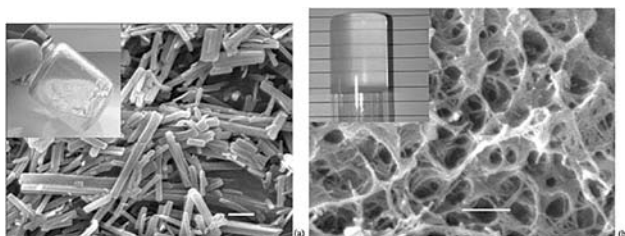


Figure 6. (a) Separate fibers occurring in the 10 wt. % L-DHL/DIOP system. This system gives rise to a viscous solution as shown in the upper right corner. (b) Interconnected fiber networks in 10 wt. % L-DHL/DIOP system after adding 0.004 wt. % EVACP. This system is a gel as shown in the upper right corner. Scale bars: 1 μ m. (Reprinted with permission from [57]. Copyright (2002) American Chemical Society.)

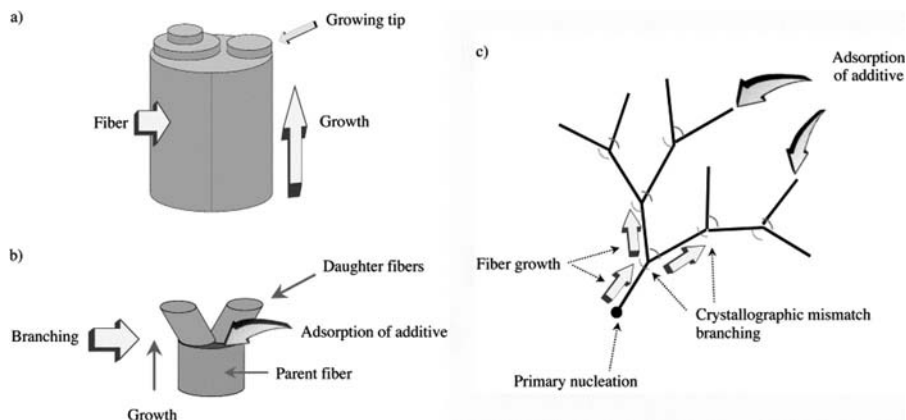


Figure 7. (a) Growth of L-DHL fibrils controlled by the birth-and-spread two-dimensional nucleation mechanism in which the structure of the new layers exactly matches that of the crystal surface. (b) The adsorption of EVACP causes mismatch nucleation at the tip of the growing fibril, which leads to a crystallographic mismatch. (c) The formation of extended, interconnected fiber networks via repeated adsorption of EVACP and branching events. (Reproduced with permission from [58]. Copyright (2002) Wiley-VCH.)

of the growing fibers and forcing a branching event due to a crystallographic mismatch (Figure 7). This results in a highly branched network of thin, long fibers. In the absence of additive, fiber growth progresses smoothly in one direction, resulting in the thicker fibers observed in the viscous liquid. In another system, they demonstrated that in the absence of a “branch-promoting” additive, the same effect can be achieved by varying gelation temperature and thus the rate of nucleation and growth events, with an increasing number of branching events at higher temperatures [59].

The previous three sections demonstrate how thorough experimental analysis, using a variety of complementary techniques, and modeling can be used to evaluate a gel system. All of them provide fresh insight into the connection between aggregate morphology and molecular structure as well as suggesting mechanisms that lead to gel formation by a given class of molecules. In the next section, a case study is used to demonstrate how high quality cryo-TEM and X-ray powder diffraction data can be combined to model the molecular structure of an organic hydrogel.

4. A Case Study

The bis-urea dicarboxylic acid hydrogelators (**2**, **3a-d**) [3] described here were originally designed as a modification of the known organogelator **1**

(Figure 8) [18, 26]. The self-assembling bis-urea motif was retained and free carboxylic acids were added for solubility in water and the ability to trigger gelation via pH and cation control. To promote aggregation in an aqueous environment, the long alkyl chains were retained in the design. This series of compounds shows aggregation in aqueous base that displays a strong pH and ionic strength dependence [3]. The gelation of water by **2** and related gelators at concentrations <0.3 wt. % corresponds to $>17,000$ molecules of water per gelator molecule and occurs over a narrow pH range that varies according to molecular weight. For example, **2** forms a gel from slightly basic (pH 8-9) aqueous solutions with a strong dependence on both the nature and concentration of the cation in solution. Standard gelation conditions are 3.2 mM of **2**, 3 mM CaCl_2 , and 50 mM tris(hydroxymethyl)aminomethane (Tris) buffer, pH 8.8. In addition, **3a** precipitates as fibers under similar conditions (Tris, pH 8.8) while at pH 5.9 (0.2 M phosphate buffer), it forms a gel, suggesting that its molecular aggregation is related to **2** [3].

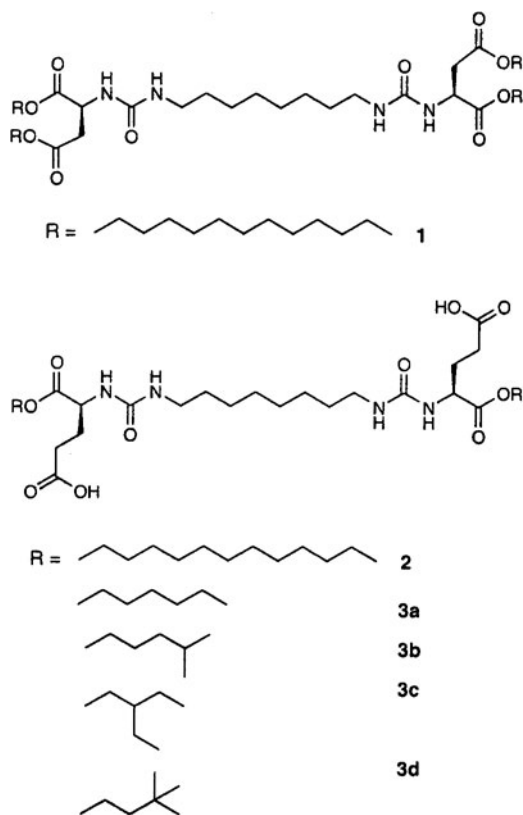


Figure 8. Structures of the gelators, **1**, **2**, and **3a-d**, discussed in the text.

4.1. Cryo-Transmission Electron Microscopy

Scanning electron micrographs of the dried and rinsed gel of **2** indicate a fibrous structure (Figure 9). Such images, however, suffer from possible artifacts due to dehydration [3]. Therefore, cryo-TEM, a high resolution microscopic technique (see Chapter 9), was employed to image the gels in their native, hydrated state. The high viscosity of the matured gel from **2** made it attractive to study the early stages of gel formation by cryo-TEM. After several attempts in which too thick (unvitrified), torn or empty grids were formed, we found that in order to form thin, vitrified, intact, films it was necessary to load the grids with dilute, warm gelator solution that had not yet gelled. The solution was then allowed to cool slightly, beginning the gelation process, on the grid before blotting and plunging. In this way we were able to capture the initial aggregation before complete gelation made it impossible to form thin films. The use of glow-charged grids (a process that increases the hydrophilicity of the grids) was found to facilitate the formation of uniformly thin, well-formed films [60].

Images of the twisted ribbons (as opposed to helical/coiled ribbons – see Figure 4) [52] observed in the vitrified samples of the gel state of **2** (0.8 mM **2**, 1.8 mM CaCl₂, 50 mM Tris, pH 9) are shown in Figure 10. It is likely that these ribbons are responsible for gel formation by becoming entangled and as a result, trapping solvent [4]. The ribbons are 15 nm to 40 nm in width with a periodicity of the twisting that varies from 120 nm to 330 nm. The narrowest portions of the twists were used to estimate the ribbon thickness with the minimum measured value being 3 nm. The ribbons that have untwisted portions exhibit steps of approximately 5 nm. Earlier work has pointed to the twisting of ribbons as being due to the chiral elastic properties of membranes formed by chiral molecules [8, 46, 52, 61–64]. The saddle-like curvature of the ribbons

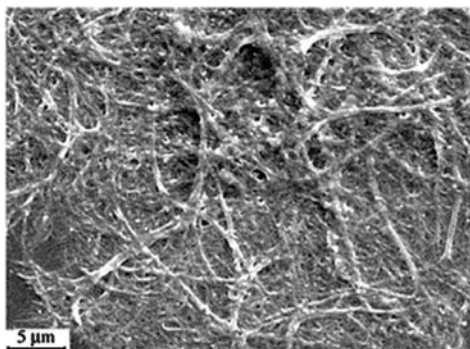


Figure 9. Scanning electron micrograph the dried hydrogel formed by **2** in pH 7.9 phosphate buffer (0.2 M, $l = 1.0$ m). See [3] for additional SEM images of the same system.

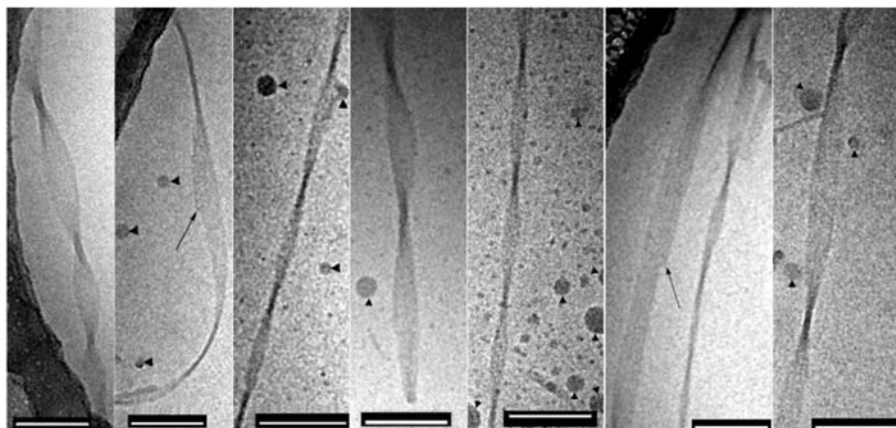


Figure 10. Cryo-TEM images of a gel of **2** (0.8 mM **2**, 1.8 mM CaCl₂, 50 mM Tris). Round dark circles (marked by arrow heads) are ice crystals. The long arrows indicate steps in untwisted portions of the ribbon. Scale bars: 100 nm. For other cryo-TEM images of the same system see [2].

is different from the cylindrical curvature of helical/coiled ribbons that are common in gels [65]. As discussed in Section 3.2, in multi-layered system, Gaussian-type curvature is favored when there is interaction between the layers, consistent with our results (see Figure 4) [52].

4.2. X-ray Diffraction

Cryo-TEM provided insight into the secondary (nanoscale) structure (Figure 1b) of the hydrogel formed by **2**. Another technique with higher resolution such as X-ray diffraction was required to develop a model of the primary (molecular-scale) structure (Figure 1c). The mature, hydrated gel of **2**, however, did not diffract well, even at high concentrations (8 mM **2**, 8 mM CaCl₂, 50 mM Tris, pH 9). Only three oriented bands (33.5 Å, 11 Å and 4.5 Å) were observed from the diffraction of the bulk gel, drawn into a 1.5 mm capillary (Figure 11). This information alone is not enough to develop a model of the molecular structure of the gelled state of **2**.

The pH of gelation in this family of bis-urea dicarboxylic acids depends strongly on the hydrophobic surface area. As the molecular weight of the derivatives decreases, instead of gel formation, fibrous precipitates are observed at high pH values [3]. In particular, the derivative with straight-chain hexyl esters, **3a**, forms fibers in the presence of cations that show birefringence between cross-polarizers, indicating that they have a large degree of long range order (see Ref. [3] for light microscope images of the fibers).

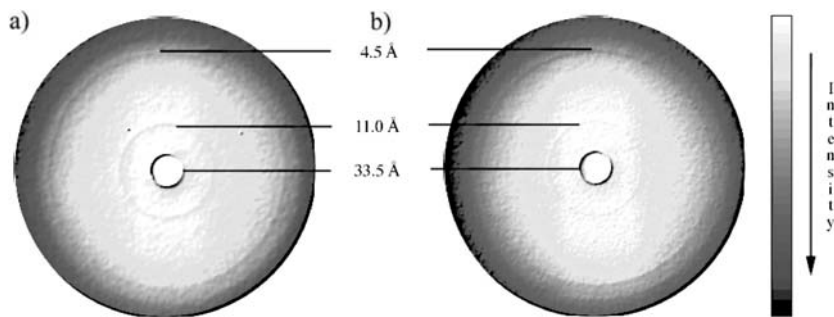


Figure 11. X-ray image plates of (a) 8 mM **2**, 8 mM CaCl₂, 50 mM Tris, pH 9, unoriented pattern. (b) 8 mM **2**, 8 mM CaCl₂, 50 mM Tris, pH 9, oriented pattern [2]. [A color version of this figure may be found on page 944.]

The two-dimensional diffraction pattern of a powdered sample of fibers of **3a**·Ca²⁺ (precipitated from a solution of 3 mM **3a**, 3 mM CaCl₂, 50 mM Tris, pH 9) has 19 sharp rings (Table 1). An oriented pattern, with fewer reflections (16), could be obtained by packing uncrushed fibers into a capillary that served to orient them (Figure 12). Three inner reflections were observed with spacings of 27.30 Å, 13.65 Å, 9.12 Å (1, 1/2, 1/3). These indicate a lamellar packing with a long repeat of 27.3 Å that is somewhat shorter than **3a** when it adopts an extended conformation. Interdigitation of the alkyl ester tails probably leads to this difference in observed length (Figure 13). These results allow us to interpret the *d* spacings with respect to the fibril long axis and to propose explanations for the orientation of the aggregated molecules within the fibers. The program TREOR90 [66], part of Cerius2 (Accelrys Software), was used to index the integrated powder diffraction pattern (of the unoriented sample) to a monoclinic unit cell with the following dimensions: *a* = 27.35 Å, *b* = 9.43 Å, *c* = 7.80 Å; $\alpha = 90.00^\circ$; $\beta = 93.53^\circ$; $\gamma = 90.0^\circ$ (Table 1).

The packing arrangement of **3a** in the fibers was further probed by analyzing the diffraction data [21–25]. The observed and calculated *d* spacings (Table 1) showed an excellent fit ($< \pm 0.2\%$). Furthermore, the unit cell dimensions are compatible with the shape and length of **3a**: *b* = 9.4 Å is consistent with hydrogen bonding between the urea groups along a two-fold screw axis [17, 30, 67] (Figure 13b) and *c* = 7.8 Å is appropriate for the stacking of sheets held together by bis-carboxylate-calcium interactions. The intermolecular distance between the urea groups fits well with half the *a* axis which in turn corresponds to the distance between neighboring 2-fold screw axes (Figure 13d) [68]. The calculated volume is 2001 Å³ [3], which gives a density of 1.46 g/cm³ for two molecules of **3a** and two Ca²⁺ cations per unit cell. The density of the fibers was determined experimentally to be between 1.6 and 1.3 g/cm³.

Table 1. The $\{hkl\}$ assignments for the diffraction pattern of fibers of $3\mathbf{a} \cdot \text{Ca}^{2+}$ calculated by TREOR90 [66]. The calculated and observed d spacings are listed together with the observed orientation of the bands.

$\{hkl\}$	d (obs)	d (calc)	Orientation ^[a]
100	27.30	27.30	Equatorial
200	13.65	13.65	Equatorial
300	9.12	9.10	Equatorial
001	7.80	7.79	weak axial
20 $\bar{1}$	6.94	6.94	weak equatorial
201	6.61	6.60	weak equatorial
20 $\bar{1}$	6.10	6.10	weak equatorial
301	5.76	5.76	weak equatorial
500	5.46	5.46	Equatorial
120	4.65	4.65	Axial
220	4.47	4.46	absent ^[b]
411	4.41	4.41	weak equatorial
320	4.18	4.19	absent ^[b]
51 $\bar{1}$	4.13	4.13	weak equatorial
021	4.03	4.03	absent ^[b]
002	3.89	3.90	Axial
102	3.83	3.83	Axial
202	3.69	3.69	Weak
42 $\bar{1}$	3.52	3.52	Weak

^[a]The orientation is given in reference to Figure 12 as either equatorial or axial.

^[b]Peaks marked absent were only observed in the X-ray pattern of a powdered sample (randomly oriented) of $3\mathbf{a} \cdot \text{Ca}^{2+}$.

Based on the dimensions of the unit cell and the symmetry of $3\mathbf{a}$, the unit cell was assigned to the $P2_1$ space group, with the unique, two-fold screw axis along b , in the same direction as the hydrogen bonding chain of the ureas [17, 30]. The space group and $\{hkl\}$ assignments were further supported by the intensities and orientations of the observed reflections. Applying Lorentz-polarization corrections [69] gave the strongest peaks as $\{002\}$ and $\{102\}$, consistent with $P2_1$. In addition, the $\{h00\}$ reflections are aligned orthogonal while the $\{00l\}$ are aligned parallel to the capillary (see inset in Figure 12).

4.3. Modeling

The cryoTEM and XRD results can be combined to develop a model for the structure of the fibers in three dimensions involving several motifs that

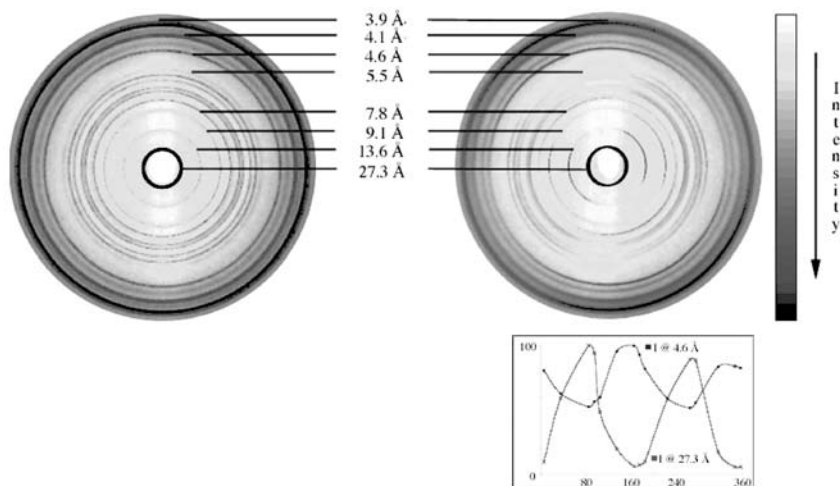


Figure 12. X-ray image plates of powdered fibers of $3\mathbf{a} \cdot \text{Ca}^{2+}$ (left) and uncrushed fibers of $3\mathbf{a} \cdot \text{Ca}^{2+}$ (right). Inset: Graph of intensity variation with orientation of the diffraction bands at 27.3 Å and 4.6 Å [2]. [A color version of this figure may be found on page 945.]

contribute to the packing of the molecules (Figure 13). First, molecules of $3\mathbf{a}$ lie with their long axis along the a axis, which is perpendicular to the long fiber axis (the c axis). Growth along the c axis is enhanced by the alkyl ester tails making hydrophobic contact with each other and by the carboxylate groups coordinating the Ca^{2+} across the two-fold screw axis (Figure 13). The urea groups must hydrogen bond to each other along the 9.4 Å two-fold screw axis (b axis), which is equivalent to the fiber thickness (Figure 13). The similarity of the alkyl ester chain length and that of the central spacer allows a regular packing of the molecules *via* interdigitation of the alkyl ester chains (Figure 13c) [68].

To explore further this hypothesis, several derivatives with branched alkyl ester chains ($3\mathbf{b-d}$) were synthesized to determine if interdigitation played a key role in fiber formation. All three of these branched derivatives were soluble in hot buffer (Tris, pH 8.8) but showed no fiber formation upon cation addition and cooling. This result further strengthens the proposed model involving intercalation of the alkyl ester tails in fiber formation by $3\mathbf{a}$.

Combining the X-ray data of 2 and $3\mathbf{a}$ with the cryo-TEM results, a model of the organization of 2 emerges which further gives insight into the tendency of 2 to gel rather than crystallize. Based on a parallel fibril orientation in the capillary for the dry fibers of $3\mathbf{a}$ and the solvated ribbons of 2 , the diffraction data of the dry fibers of $3\mathbf{a}$ can be used to derive a picture of the molecular organization of the gel ribbons. The bands common to the diffraction patterns of both

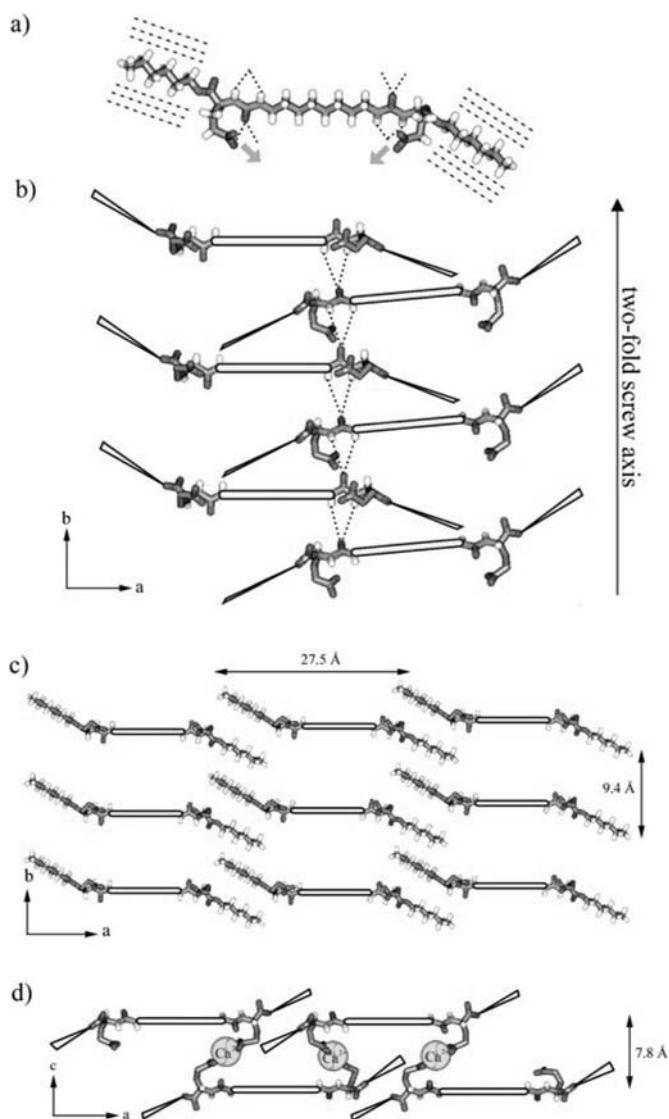


Figure 13. (a) A molecular model of **3a** showing the different structural motifs leading to aggregation: hydrophobic interactions of the alkyl ester chains, hydrogen bonding of the ureas and calcium-carboxylate coordination. (b) The hydrogen bonding motif between molecules related by the two-fold screw axis, *b*. (c) The stacking between the alkyl ester side chains of molecules related by translation. (d) The packing along the *c* axis through Ca²⁺-bis-carboxylate interactions, which are located on a two-fold screw axis. (Reproduced with permission from [2]. Copyright (2003) Wiley-VCH.)

2 and **3a** are the primary long d spacings (33.5 Å and 27 Å, respectively), oriented perpendicular to the capillary and the 4.5 Å ring, oriented parallel. These results suggest that the molecules of **2** are arranged in an extended conformation (33.5 Å), with an orientation that is perpendicular to the growth direction of the gel ribbons (Figure 13). The 4.5 Å band probably arises from diffraction by the well-packed alkyl chains. As discussed above, interdigitation of the alkyl ester tails and a match between the length of the central spacer and alkyl ester tails is essential for fiber formation. The gelator, **2**, has a mismatch between the length of the alkyl esters and central chains and therefore cannot pack as efficiently in three dimensions. The bands observed in the gel diffraction pattern derive from the molecular arrangement in two dimensions. The disorder in the third dimension is caused by the mismatch of distances and may explain why **2** aggregates to form gels in water rather than precipitates as fibers, like **3a**. Earlier analysis of the gelation of certain peptides has exploited similar mechanisms whereby gelation derives from the interspersions of zones of crystallinity and disorder [70]. Another hypothesis for gelation by different agents (Section 3.3) involves a crystallographic mismatch resulting in branched fiber formation [57, 59].

5. Perspectives for the Future

The inherent disorder of gel systems makes complete characterization (culminating in a molecular level model) difficult. As the field progresses, the ability to rationally design and manipulate gel structures will become increasingly important. There is currently interest in the development of small-molecule hydrogels for biological applications such as the controlled release of drugs, the formation of protein arrays and the growth of inorganic crystals [71–74]. Designing such systems will require an understanding of how the gel structure interacts with the trapped materials (drugs, proteins, crystals, etc.). As discussed in this chapter, several complementary techniques can be coupled with modeling to provide a better understanding of all levels of gel structure. The next challenge in the field will be to include solvent in the models. Several reports have been recently published on the behavior of water in small, confined, hydrophobic spaces [75–78]. The results of these studies suggest that for hydrogels the structure of the water molecules trapped by the fibers may differ from bulk solvent. Understanding the role of solvent in gel formation will shed light on the unique properties of gels such as slowed diffusion rates, altered ion activities and trapping of larger molecules. Controlled manipulation of these characteristics will lead to gels with applications in multiple fields including biology, medicine and materials science.

Acknowledgments

We thank Professors Lia Addadi, Steve Weiner and Leslie Leiserowitz (Weizmann Institute of Science, Rehovot, ISRAEL) for a stimulating and fruitful collaboration that led to the experiments and models presented in this chapter. We also thank Talmon Arad, Weizmann Institute of Science, for valuable assistance with the cryo-TEM and Dr. Linda Shimon, Weizmann Institute of Science, for assistance with the X-ray diffraction. In addition we thank Jessica Huang, Yale University, for synthesizing of some of the derivatives discussed. Finally, we thank NSF (CHE0131477) and the Yale-Weizmann exchange fund for financial support of this work.

References

- [1] John, G.; Jung, J.H.; Minamikawa, H.; Yoshida, K.; Shimizu, T. "Morphological control of helical solid bilayers in high-axial-ratio nanostructures through binary self-assembly", *Chem. Eur. J.*, **2002**, *8*, 5494–5500.
- [2] Estroff, L.A.; Leiserowitz, L.; Addadi, L.; Weiner, S.; Hamilton, A.D. "Characterization of an organic hydrogel: a cryo-transmission electron microscopy and X-ray diffraction study", *Adv. Mater.*, **2003**, *15*, 38–42.
- [3] Estroff, L.A.; Hamilton, A.D. "Effective gelation of water using a series of bis-urea dicarboxylic acids", *Angew. Chem. Int. Ed. Engl.*, **2000**, *39*, 3447–3450.
- [4] Flory, P.J., "Introductory Lecture: gels and gelling processes", *Faraday Discuss.*, **1974**, *57*, 7–18.
- [5] Geiger, C.; Stanescu, M.; Chen, L.H.; Whitten, D.G. "Organogels resulting from competing self-assembly units in the gelator: structure, dynamics, and photophysical behavior of gels formed from cholesterol-stilbene and cholesterol-squaraine gelators", *Langmuir*, **1999**, *15*, 2241–2245.
- [6] Wang, R.; Geiger, C.; Chen, L.; Swanson, B.; Whitten, D.G. "Direct Observation of sol-gel conversion: the role of the solvent in organogel formation", *J. Am. Chem. Soc.*, **2000**, *122*, 2399–2400.
- [7] Simmons, B.A.; Taylor, C.E.; Landis, F.A.; John, V.T.; McPherson, G.L.; Schwartz, D.K.; Moore, R. "Microstructure determination of AOT + phenol organogels utilizing small-angle X-ray scattering and atomic force microscopy", *J. Am. Chem. Soc.*, **2001**, *123*, 2414–2421.
- [8] Boettcher, C.; Schade, B.; Fuhrhop, J.H. "Comparative cryo-electron microscopy of noncovalent N-dodecanoyl-(D- and L-) serine assemblies in vitreous toluene and water", *Langmuir*, **2001**, *17*, 873–877.
- [9] Hartgerink, J.D.; Beniash, E.; Stupp, S.I. "Self-assembly and mineralization of peptide-amphiphile nanofibers", *Science*, **2001**, *294*, 1684–1688.
- [10] Kolbel, M.; Menger, F.M. "Hierarchical structure of a self-assembled xerogel", *Chem. Commun.*, **2001**, 275–276.
- [11] Adrian, M.; Dubochet, J.; Lepault, J.; McDowell, A.W. "Cryo-electron microscopy of viruses", *Nature*, **1984**, *308*, 32–36.
- [12] Fuhrhop, J.H.; Schnieder, P.; Rosenberg, J.; Boekema, E. "The chiral bilayer effect stabilizes micellar fibers", *J. Am. Chem. Soc.*, **1987**, *109*, 3387–3390.

- [13] Lambert, O.; Levy, D.; Ranck, J.L.; Leblanc, G.; Rigaud, J.L. "A new 'gel-like' phase in dodecyl maltoside-lipid mixtures: implications in solubilization and reconstitution studies", *Biophys. J.*, **1998**, *74*, 918–930.
- [14] Abdallah, D.J.; Sirchio, S.A.; Weiss, R.G. "Hexatriacontane organogels. The first determination of the conformation and molecular packing of a low-molecular-mass organogelator in its gelled state", *Langmuir*, **2000**, *16*, 7558–7561.
- [15] Ostuni, E.; Kamaras, P.; Weiss, R.G. "Novel X-ray method for in situ determination of gelator strand structure: polymorphism of cholesteryl anthraquinone-2-carboxylate", *Angew. Chem. Int. Ed. Engl.*, **1996**, *35*, 1324–1326.
- [16] Menger, F.M.; Yamasaki, Y.; Catlin, K.K.; Nishimi, T. "X-ray structure of a self-assembled gelating fiber", *Angew. Chem. Int. Ed. Engl.*, **1995**, *34*, 585–586.
- [17] van Esch, J.; Schoonbeek, F.; de Loos, M.; Kooijman, H.; Spek, A.L.; Kellogg, R.M.; Feringa, B.L. "Cyclic bis-urea compounds as gelators for organic solvents", *Chem. Eur. J.*, **1999**, *5*, 937–950.
- [18] Carr, A.J.; Melendez, R.; Geib, S.J.; Hamilton, A.D. "The design of organic gelators: Solution and solid state properties of a family of bis-ureas", *Tetrahedron Lett.*, **1998**, *39*, 7447–7450.
- [19] Hanabusa, K.; Matsumoto, M.; Kimura, M.; Kakehi, A.; Shirai, H. "Low molecular weight gelators for organic fluids: Gelation using a family of cyclo(dipeptide)s", *J. Colloid Interface Sci.*, **2000**, *224*, 231–244.
- [20] Menger, F.M.; Caran, K.L. "Anatomy of a gel. Amino acid derivatives that rigidify water at submillimolar concentrations", *J. Am. Chem. Soc.*, **2000**, *122*, 11679–11691.
- [21] Harris, K.D.M.; Tremayne, M.; Kariuki, B.M. "Contemporary advances in the use of powder X-ray diffraction for structure determination", *Angew. Chem. Int. Ed. Engl.*, **2001**, *40*, 1626–1651.
- [22] Prest, P.J.; Prince, R.B.; Moore, J.S. "Supramolecular organization of oligo (m-phenylene ethynylene)s in the solid-state", *J. Am. Chem. Soc.*, **1999**, *121*, 5933–5939.
- [23] Struijk, C.W.; Sieval, A.B.; Dakhorst, J.E.J.; van Dijk, M.; Kimkes, P.; Koehorst, R.B.M.; Donker, H.; Schaafsma, T.J.; Picken, S.J.; van de Craats, A.M.; Warman, J.M.; Zuilhof, H.; Sudholter, E.J.R. "Liquid crystalline perylene diimides: architecture and charge carrier mobilities", *J. Am. Chem. Soc.*, **2000**, *122*, 11057–11066.
- [24] Ito, S.; Wehmeier, M.; Brand, J.D.; Kubel, C.; Epsch, R.; Rabe, J.P.; Mullen, K. "Synthesis and self-assembly of functionalized hexa-peri-hexabenzocoronenes", *Chem. Eur. J.*, **2000**, *6*, 4327–4342.
- [25] Amato, M.E.; Caminiti, R.; Carriedo, G.A.; Garcia-Alonso, E.J.; Garcia-Alvarez, J.L.; Lombardo, G.M.; Pappalardo, G.C. "Structural features and molecular assembly of amorphous phosphazenic materials in the bulk-combined theoretical and experimental techniques: tris-(2,2'-dioxy-1,1'-binaphthyl)cyclotriphosphazene", *Chem. Eur. J.*, **2001**, *7*, 1486–1494.
- [26] Shi, C.; Huang, Z.; Kilic, S.; Xu, J.; Enick, R.M.; Beckman, E.J.; Carr, A.J.; Melendez, R.E.; Hamilton, A.D. "The gelation of CO₂: a sustainable route to the creation of microcellular materials", *Science*, **1999**, *286*, 1540–1543.
- [27] van Esch, J.; DeFeyter, S.; Kellogg, R.M.; DeSchryver, F.; Feringa, B.L. "Self-assembly of bis-urea compounds in organic solvents and on solid substrates", *Chem. Eur. J.*, **1997**, *3*, 1238–1243.
- [28] van der Laan, S.; Feringa, B.L.; Kellogg, R.M.; van Esch, J. "Remarkable polymorphism in gels of new azobenzene bis-urea gelators", *Langmuir*, **2002**, *18*, 7136–7140.

- [29] van Esch, J.; Kellogg, R.M.; Feringa, B.L. "Di-urea compounds as gelators for organic solvents", *Tetrahedron Lett.*, **1997**, *38*, 281–284.
- [30] Schoonbeek, F.S.; van Esch, J.H.; Hulst, R.; Kellogg, R.M.; Feringa, B.L. "Geminal bis-ureas as gelators for organic solvents: gelation properties and structural studies in solution and in the gel state", *Chem. Eur. J.*, **2000**, *6*, 2633–2643.
- [31] Lortie, F.; Boileau, S.; Bouteiller, L.; Chassenieux, C.; Deme, B.; Ducouret, G.; Jalabert, M.; Laupretre, F.; Terech, P. "Structural and rheological study of a bis-urea based reversible polymer in an apolar solvent", *Langmuir*, **2002**, *18*, 7218–7222.
- [32] Brinksma, J.; Feringa, B.L.; Kellogg, R.M.; Vreeker, R.; van Esch, J. "Rheology and thermotropic properties of bis-urea-based organogels in various primary alcohols", *Langmuir*, **2000**, *16*, 9249–9255.
- [33] de Loos, M.; van Esch, J.; Kellogg, R.M.; Feringa, B.L. "Chiral recognition in bis-urea-based aggregates and organogels through cooperative interactions", *Angew. Chem. Int. Ed. Engl.*, **2001**, *40*, 613–616.
- [34] Sakurai, K.; Jeong, Y.; Koumoto, K.; Friggeri, A.; Gronwald, O.; Sakurai, K.; Okamoto, S.; Inoue, K.; Shinkai, S. "Supramolecular structure of a sugar-appended organogelator explored with synchrotron X-ray small-angle scattering", *Langmuir*, **2003**, *19*, 8211–8217.
- [35] Sakurai, K.; Kimura, T.; Gronwald, O.; Inoue, K.; Shinkai, S. "A hexagonally organized elemental supramolecular structure of a sugar-appended organogelator observed by synchrotron X-ray source (Spring-8)", *Chem. Lett.*, **2001**, 746–747.
- [36] Sakurai, K.; Ono, Y.; Jung, J.H.; Okamoto, S.; Sakurai, S.; Shinkai, S. "Synchrotron small angle X-ray scattering from organogels. Part I. Changes in molecular assemblies of cholesterol gelators during gel-sol transition", *J. Chem. Soc., Perkin Trans.*, **2001**, *2*, 108–112.
- [37] Bhattacharya, S.; Acharya, S.N.G. "Pronounced hydrogel formation by the self-assembled aggregates of N-alkyl disaccharide amphiphiles", *Chem. Mater.*, **1999**, *11*, 3504–3511.
- [38] Mikami, M.; Matsuzaki, T.; Masuda, M.; Shimizu, T.; Tanabe, K. "Molecular dynamics simulation for the crystal structure of synthetic sugar-based bolaamphiphiles", *Comp. Mater. Sci.*, **1999**, *14*, 267–276.
- [39] Makarevic, J.; Jokic, M.; Peric, B.; Tomisic, V.; Kojic-Prodic, B.; Zinic, M. "Bis(amino acid) oxalyl amides as ambidextrous gelators of water and organic solvents: supramolecular gels with temperature dependent assembly/dissolution equilibrium", *Chem. Eur. J.*, **2001**, *7*, 3328–3341.
- [40] Estroff, L.A.; Hamilton, A.D. "Water gelation by small organic molecules", *Chem. Rev.*, **2004**, *104*, 1201–1218.
- [41] Malik, S.; Maji, S.K.; Banerjee, A.; Nandi, A.K. "A synthetic tripeptide as organogelator: elucidation of gelation mechanism", *J. Chem. Soc., Perkin Trans.*, **2002**, *2*, 1177–1186.
- [42] Bhattacharya, S.; Acharya, S.N.G. "Impressive gelation in organic solvents by synthetic, low molecular mass, self-organizing urethane amides of L-phenylalanine", *Chem. Mater.*, **1999**, *11*, 3121–3132.
- [43] Terech, P.; Weiss, R.G. "Low molecular mass gelators of organic liquids and the properties of their gels", *Chem. Rev.*, **1997**, *97*, 3133–3159.
- [44] Abdallah, D.J.; Weiss, R.G. "Organogels and low molecular mass organic gelators", *Adv. Mater.*, **2000**, *12*, 1237–1247.
- [45] van Esch, J.H.; Feringa, B.L. "New functional materials based on self-assembling organogels: From serendipity towards design", *Angew. Chem. Int. Ed. Engl.*, **2000**, *39*, 2263–2266.

- [46] Fuhrhop, J.H.; Helfrich, W. "Fluid and solid fibers made of lipid molecular bilayers", *Chem. Rev.*, **1993**, *93*, 1565–1582.
- [47] Fishwick, C.W.G.; Beevers, A.J.; Carrick, L.M.; Whitehouse, C.D.; Aggeli, A.; Boden, N. "Structures of helical β -tapes and twisted ribbons: the role of side-chain interactions on twist and bend behavior", *Nano Lett.*, **2003**, *3*, 1475–1479.
- [48] Aggeli, A.; Nyrkova, I.A.; Bell, M.; Harding, R.; Carrick, L.; McLeish, T.C.B.; Semenov, A.N.; Boden, N. "Hierarchical self-assembly of chiral rod-like molecules as a model for peptide beta-sheet tapes, ribbons, fibrils, and fibers", *Proc. Natl. Acad. Sci. U.S.A.*, **2001**, *98*, 11857–11862.
- [49] Berthier, D.; Buffeteau, T.; Leger, J.-M.; Oda, R.; Huc, I. "From chiral counterions to twisted membranes", *J. Am. Chem. Soc.*, **2002**, *124*, 13486.
- [50] Oda, R.; Huc, I.; Candau, S.J. "Gemini surfactants as new, low molecular weight gelators of organic solvents and water", *Angew. Chem. Int. Ed. Engl.*, **1998**, *37*, 2689–2691.
- [51] Oda, R.; Huc, I.; Homo, J.C.; Heinrich, B.; Schmutz, M.; Candau, S. "Elongated aggregates formed by cationic gemini surfactants", *Langmuir*, **1999**, *15*, 2384–2390.
- [52] Oda, R.; Huc, I.; Schmutz, M.; Candau, S.J.; MacKintosh, F.C. "Tuning bilayer twist using chiral counterions", *Nature*, **1999**, *399*, 566–569.
- [53] Fuhrhop, J.H.; Koning, J. *Membranes and Molecular Assemblies: The Synkinetic Approach*. Cambridge, UK: Royal Society of Chemistry, **1994**.
- [54] Spector, M.S.; Price, R.R.; Schnur, J.M. "Chiral lipid tubules", *Adv. Mater.*, **1999**, *11*, 337–340.
- [55] Tachibana, T.; Kambara, H. "Enantiomorphism in the helical aggregate of lithium 12-hydroxystearate", *J. Am. Chem. Soc.*, **1965**, *87*, 3015–3016.
- [56] Keller, A. "Introductory lecture: aspects of polymer gels", *Faraday Discuss.*, **1995**, *101*, 1–49.
- [57] Liu, X.Y.; Sawant, P.D.; Tan, W.B.; Noor, I.B.M.; Pramesti, C.; Chen, B.H. "Creating new supramolecular materials by architecture of three-dimensional nanocrystal fiber networks", *J. Am. Chem. Soc.*, **2002**, *124*, 15055–15063.
- [58] Liu, X.Y.; Sawant, P.D. "Micro/nanoengineering of the self-organized three-dimensional fibrous structure of functional materials", *Angew. Chem. Int. Ed. Engl.*, **2002**, *41*, 3641–3645.
- [59] Liu, X.Y.; Sawant, P.D. "Mechanism of the formation of self-organized microstructures in soft functional materials", *Adv. Mater.*, **2002**, *14*, 421–426.
- [60] Dubochet, J.; Groom, M.; Mueller-Neuteboom, S. "The mounting of macromolecules for electron microscopy with particular reference to surface phenomena and the treatment of support films by glow discharge", In *Advances in Optical and Electron Microscopy*, R. Barer and V.E. Cosslett, Eds., New York: Academic Press, **1982**, *8*, pp. 107–135.
- [61] Zubarev, E.R.; Pralle, M.U.; Sone, E.D.; Stupp, S.I. "Scaffolding of polymers by supramolecular nanoribbons", *Adv. Mater.*, **2002**, *14*, 198–203.
- [62] Selinger, J.V.; Spector, M.S.; Schnur, J.M. "Theory of self-assembled tubules and helical ribbons", *J. Phys. Chem. B*, **2001**, *105*, 7157–7169.
- [63] Nakazawa, I.; Masuda, M.; Okada, Y.; Hanada, T.; Yase, K.; Asai, M.; Shimizu, T. "Spontaneous formation of helically twisted fibers from 2-glucosamide bolaamphiphiles: energy-filtering transmission electron microscopic observation and even-odd effect of connecting bridge", *Langmuir*, **1999**, *15*, 4757–4764.
- [64] Terech, P.; de Geyer, A.; Struth, B.; Talmon, Y. "Self-assembled monodisperse steroid nanotubes in water", *Adv. Mater.*, **2002**, *14*, 495–498.

- [65] Jung, J.H.; Kobayashi, H.; Masuda, M.; Shimizu, T.; Shinkai, S. "Helical ribbon aggregate composed of a crown-appended cholesterol derivative which acts as an amphiphilic gelator of organic solvents and as a template for chiral silica transcription", *J. Am. Chem. Soc.*, **2001**, *123*, 8785–8789.
- [66] Werner, P.E.; Eriksson, L.; Westdahl, M. "TREOR, a Semi-Exhaustive Trial-and-Error Powder Indexing Program for All Symmetries", *J. Appl. Crystallogr.*, **1985**, *18*, 367–370.
- [67] Leiserowitz, L.; Hagler, A.T. "The generation of possible crystal-structures of primary amides", *Proc. R. Soc. London Ser. A-Math. Phys. Eng. Sci.*, **1983**, *388*, 133–175.
- [68] Bernstein, J.; Etter, M.C.; Leiserowitz, L. "The role of hydrogen bonding in molecular assemblies", In *Structure Correlation*; H.-B. Burgi and J.D. Dunitz, Eds., New York: VCH, **1994**, *2*, pp. 431–507.
- [69] Stout, G.H.; Jensen, L.H. *X-ray Structure Determination – A Practical Guide*. Second edition, New York: John Wiley & Sons, **1989**.
- [70] Kennedy, S.B.; deAzevedo, E.R.; Petka, W.A.; Russell, T.P.; Tirrell, D.A.; Hong, M. "Dynamic structure of a protein hydrogel: a solid-state NMR study", *Macromolecules*, **2001**, *34*, 8675–8685.
- [71] Kiyonaka, S.; Sada, K.; Yoshimura, I.; Shinkai, S.; Kato, N.; Hamachi, I. "Semi-wet peptide/protein array using supramolecular hydrogel", *Nature Materials*, **2004**, *3*, 58–64.
- [72] Xing, B.; Yu, C.W.; Chow, K.H.; Ho, P.L.; Fu, D.; Xu, B. "Hydrophobic interaction and hydrogen bonding cooperatively confer a vancomycin hydrogel: a potential candidate for biomaterials", *J. Am. Chem. Soc.*, **2002**, *124*, 14846–14847.
- [73] van Bommel, K.J.C.; van der Pol, C.; Muizebelt, I.; Friggeri, A.; Heeres, A.; Meetsma, A.; Feringa, B.L.; van Esch, J. "Responsive cyclohexane-based low-molecular-weight hydrogelators with modular architecture", *Angew. Chem. Int. Ed. Engl.*, **2004**, *43*, 1663–1667.
- [74] Estroff, L.A.; Addadi, L.; Weiner, S.; Hamilton, A.D. "An organic hydrogel as a matrix for the growth of calcite crystals", *Org. Biomol. Chem.*, **2004**, 137–141.
- [75] Beckstein, O.; Sansom, M.S.P. "Liquid-vapor oscillations of water in hydrophobic nanopores", *Proc. Natl. Acad. Sci. U.S.A.*, **2003**, *100*, 7063–7068.
- [76] Mashl, R.J.; Joseph, S.; Aluru, N.R.; Jakobsson, E. "Anomalously immobilized water: a new water phase induced by confinement in nanotubes", *Nano Lett.*, **2003**, *3*, 589–592.
- [77] Ball, P. "How to keep water dry", *Nature*, **2003**, *423*, 25–26.
- [78] Ohba, T.; Kanoh, H.; Kaneko, K. "Affinity transformation from hydrophilicity to hydrophobicity of water molecules on the basis of adsorption of water in graphitic nanopores", *J. Am. Chem. Soc.*, **2004**, *126*, 1560–1562.

Chapter 21

GELATION OF A LIQUID-CRYSTALLINE L_{α} PHASE INDUCED BY THE PROLIFERATION OF TOPOLOGICAL DEFECTS

The gelating power of PEG-lipids

Patrick Davidson

Laboratoire de Physique des Solides, Bât. 510, UMR 8502 CNRS, Université Paris-Sud, 91405 Orsay cedex, France

1. Introduction	744
1.1. Basic Definitions	744
1.2. Topological Defects in an Organized Phase Can Induce Gelation	747
1.3. Scope and Outline of the Chapter	747
2. Gelation of a Lamellar L_{α} Phase by Addition of Peg-Lipids	748
2.1. Description of the System and its Components	748
2.2. Phase Diagram and Gelation	749
2.3. Observations of Samples in Polarized Light	751
2.4. Electron Microscopy	752
2.5. X-Ray Scattering	753
2.6. Rheology	755
2.7. Model and Discussion	757
3. A New Class of Gels	759
3.1. Extensive Chemical Modification of PEG-lipids Does not Affect Their Gelating Power	759
3.2. Double-End-Anchored PEG-Surfactants also Induce Gelation	761
4. Generalization	765
4.1. Gelation of a Lamellar Phase by Addition of Particles	765

4.2. Gelation of Other Mesophases	765
4.3. “Ringing Gels”	766
5. Conclusions and Perspectives for the Future	767

1. Introduction

Usual physical gels are based either on networks of large polymers or on the self-assembly of low molecular-mass gelators (especially low molecular-mass organic gelators (LMOGs)). The focus of this book is the latter. Quite often, but not always, molecular gels form isotropic phases that have no long-range order. In this chapter, we consider anisotropic liquid-crystalline phases that show positional long-range order in at least one dimension. Like crystals, liquid-crystalline phases have topological defects. We describe here how addition of minute amounts of amphiphilic molecules that stabilize topological defects can gelate the liquid-crystalline phase. This phenomenon was observed in a dozen different systems and does not seem to rely acutely on molecular details. This defect-induced gelation mechanism may be fairly general and could lead to a new class of gels.

1.1. Basic Definitions

In this section, we recall several definitions about gels and liquid crystals, probably known by many readers, that will be necessary to understand this chapter.

Giving an accurate definition of a physical gel is a difficult task that will surely be better dealt with by some other contributors to this book (see Introduction) [1]. Nevertheless, we shall use here the following definitions and conventions. From an experimental point of view, we can call a gel a two-component (at least) viscoelastic system, comprised of a solvent and a gelator, that displays two distinct mechanical properties: (i) the system does not flow under mechanical stress (imposed, in principle, for a very long time) smaller than a limit value, called the “yield stress”, σ_y ; (ii) The system must be more elastic than viscous.

These mechanical properties can be qualitatively assessed by very simple (but sometimes misleading) experimental tests. For instance, turning a test-tube upside-down and watching whether the sample will flow under its own weight is a commonly used procedure (see Chapter 8). However, depending on how long the sample is observed, a very viscous liquid could be wrongly qualified as a gel or a gel with a very small yield stress could be considered a sol.

Another, perhaps more sensitive procedure, consists in injecting small air bubbles inside the material and watching whether they rise to the surface or remain trapped.

More sophisticated rheology techniques are required to characterize a gel rigorously (see Chapter 5) [2]. The use of rheometers allows one to record the sample “flow curve” that relates its deformation (or deformation rate) to its mechanical stress. In principle, this curve gives access to σ_y , even though the procedure can be hampered in practice by the non-linear flow behavior of many gels. Dynamic measurements in the oscillatory mode give access to the elastic and viscous contributions that are defined by the dynamic elastic and loss moduli, G' and G'' , respectively. These two moduli are usually measured as a function of oscillation frequency and a viscoelastic material will be labeled a gel if G' is larger than G'' by roughly an order of magnitude over a large frequency range (several decades) centered around frequencies of practical interest (typically 1 Hz). The results given by test-tube inversion and rheology were recently compared in the case of molecular organogels [3]. Small discrepancies between the two techniques were found and it seems that, according to the former technique, a weak gel would be wrongly assigned as a fluid sample, which results in a small shift of the sol/gel transition line in the phase diagram. The same trend was observed for the gels described in this chapter.

From a theoretical point of view, gelation is usually associated with a percolation transition that can be, in some way, related to the modern theories of phase transitions (see Chapter 1) [4]. Such an approach involves the identification of a component (the gelator) that will form a 3-dimensional network (i.e., a SAFIN) in the material, depending on its association probability and the nature of the network (site percolation or bond percolation). Identification of the percolating component can be rather easy for polymer-based gels or for LMOGs. Sometimes, the percolating component can be very difficult to identify, as illustrated by the case of laponite clay gels [5].

Let us now turn to liquid crystals that are much easier to define in spite of their rather paradoxical name [6, 7]. We shall define liquid-crystal as a phase of matter that shows both fluidity and anisotropy. The phase should not have 3-dimensional long-range positional order (at least, at the molecular level) in order to be fluid, but it should have long-range orientational order to ensure phase anisotropy. A material will be called a liquid-crystal if it shows one or several liquid-crystalline phases that are stable in a given range of thermodynamic parameters such as temperature, pressure, concentration, etc.

There are two kinds of liquid crystals. Thermotropic liquid crystals are pure compounds (or possibly mixtures of liquid-crystalline compounds) that display liquid-crystalline phases, depending mostly on temperature. Lyotropic liquid crystals are multi-component systems, usually comprised of a solvent and a solute (at least) for which the concentrations are the most relevant

parameters. Although this classification can be somewhat fuzzy, it corresponds in practice to very different kinds of materials. Thermotropic liquid crystals are extensively used in displays and electro-optic applications whereas lyotropic liquid-crystals are commonly used in the cosmetic and detergent industries. We shall be concerned only with the second kind of liquid crystals.

Amphiphilic molecules (also called surfactants), that form a very important class of lyotropic liquid crystals, will be the focus of this chapter. They are generally comprised of a hydrophilic part and a hydrophobic part. For instance, soap molecules bear an ionic headgroup covalently linked to an aliphatic chain. At low concentrations, these surface-active molecules adsorb at the air-water interface. Beyond a well-defined concentration, called the cmc (critical micellar concentration), they form aggregates (micelles) that can be spherical, cylindrical or lamellar, depending on concentration and molecular geometry. These supramolecular aggregates may then self-assemble into liquid-crystalline phases. Note also that some of these amphiphilic molecules actually have gelating properties, and the structures of the cross-linking areas that they form in gels are highly reminiscent of the organizations of lyotropic liquid-crystalline phases [8].

There are many different types of liquid-crystalline phases that differ by the symmetry and dimensionality of their long-range orders. We are here mostly concerned with the lamellar L_α phase (also called smectic A for thermotropic liquid crystals) that has positional long-range order in one dimension only and long-range orientational order. This phase is classically depicted as a regular stack of fluid membranes (Figure 1) with a period, d , of the order of 1–100 nm. The phase easily flows in the plane of the membranes but resists deformation

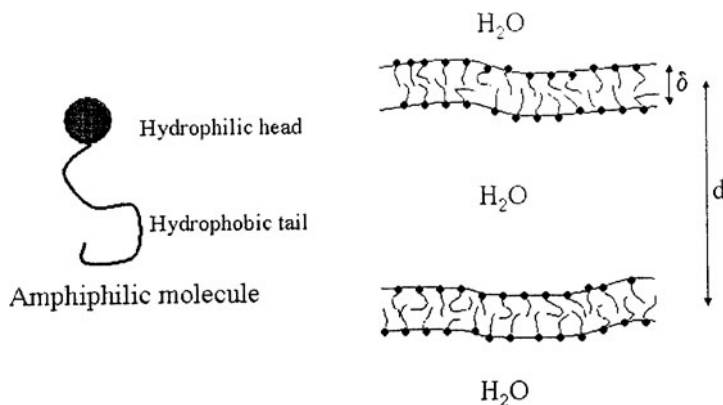


Figure 1. Schematic of a lyotropic liquid-crystalline lamellar L_α phase comprised of stacked membranes of surfactants. d is the lamellar period, δ is the membrane thickness, and $d_w = d - \delta$ is the thickness of the aqueous medium. The phase is called “swollen” when $d \gg \delta$.

(and therefore flow), with an elastic compression modulus B , in the direction perpendicular to the membranes. The phase also resists shear applied in the direction perpendicular to the layers to avoid layer tilting [9]. The L_α phase is usually found with amphiphilic molecules whose shape obeys the steric criterion, $1/2 < V/la < 1$, (where V , l , and a are the molecular volume, length, and head-group cross-sectional area, respectively) [10].

1.2. Topological Defects in an Organized Phase Can Induce Gelation

The molecular organization of the L_α phase shown in Figure 1 is an ideal defect-free single domain. However, in practice, samples of the L_α phase are usually multi-domains and also display topological defects. These defects, somewhat similar to the domain walls and the dislocation lines observed in crystals, may slowly anneal with time or can even vanish if a single domain is formed by applying a magnetic field or a shear flow. The defects may also persist if their free energy is not too high or if they are even stable from a thermodynamic point of view. This is, for instance, the case of the L_α phase, close to its limit of stability where quite large screw-dislocation densities have been observed [11]. Then, the mechanical properties of the liquid-crystalline phase can be largely altered by the contributions of the defects.

If topological defects, involving membrane curvature and folding, start proliferating in the L_α phase, then this provides a gelation mechanism by which membranes will percolate throughout the sample in all directions and orientations on the micron length scale. Because membranes are then found in all orientations, the sample will resist macroscopic deformation and flow, and will appear elastic [12].

This gelation phenomenon was observed several years ago by doping a classical L_α phase with small amounts of a special surfactant molecule that acts as a gelator and that induces thermodynamically stable curvature defects due to its special molecular geometry [13]. This molecule has a quite bulky hydrophilic headgroup so that its steric parameter V/la is smaller than $1/2$.

1.3. Scope and Outline of the Chapter

The remainder of this chapter is organized as follows: Section 2 describes in detail the first example of gelation of a lyotropic L_α phase through proliferation of topological defects. In Section 3, the chemical structure of the gelator is systematically varied in order to test the robustness of this new gelation mechanism. In Section 4, we describe rather similar effects observed in related

systems, speculate about how this new type of gelation could be achieved in other phases, and give a short conclusion.

2. Gelation of a Lamellar L_α Phase by Addition of Peg-Lipids

2.1. Description of the System and its Components

A lamellar L_α phase comprised of very flexible surfactant membranes is found in the (dimyristoyl phosphatidyl choline (DMPC), pentanol, water) system [14]. This phase can be highly “swollen”, which means that it can incorporate as much as $\sim 90\%$ water and it can reach a period $d \sim 250 \text{ \AA}$. DMPC is a double-chain phospholipid surfactant that is very common in biological membranes. Its headgroup is zwitterionic (i.e., it bears a positive charge and a negative one separated by a few \AA). Consequently, the surfactant headgroup has no overall charge and electrostatic interactions can be neglected. Pentanol is a co-surfactant (i.e., it is a small molecule that would not form a liquid-crystalline phase by itself) added to the system in a fixed ratio (pentanol/lipid = 4:1). Its role is to ensure the fluidity of the membranes and to decrease their bend elastic constant so that the phase stability at high dilution arises from the Helfrich entropic interactions that involve membrane undulations [15]. Wide-angle X-ray scattering experiments in the L_α phase have indeed shown that the two chains of DMPC are in the molten state. The dependence of the lamellar period with composition, $d = \delta/\phi_m$, where ϕ_m is the membrane volume fraction, gives the membrane thickness $\delta = 28 \text{ \AA}$.

PEG-lipid molecules are comprised of a phospholipid moiety (dimyristoyl phosphatidyl ethanolamine, DMPE) covalently bonded to a short PEG chain. These gelators are commercially available in various molecular weights. The phospholipid part inserts into the surfactant membrane and therefore acts as an anchor. The PEG chain adopts a mushroom conformation in the aqueous medium, with a gyration radius comparable to the membrane thickness (Figure 2). The PEG-lipid molecules are free to diffuse inside the membrane because it is in a fluid state. The size of these gelators is not actually much larger than that of DMPC because the PEG chains used here are rather small ($M_w = 2000$) and have a gyration radius of about 3 nm, compared to the DMPC size of about 1.5 nm.

In these studies, small PEG chains were used as water soluble moieties because of eventual biomedical applications. Indeed, chemically bonding proteins with PEG chains are known to increase their blood circulation times [16]. Moreover, PEG-coated liposomes were reported to show enhanced biocompatibility, which makes them suitable as drug-delivery systems [17].

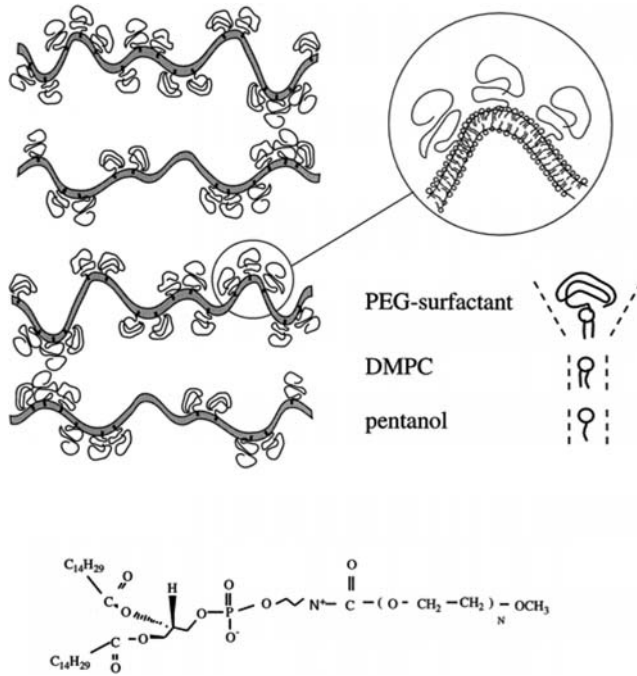


Figure 2. Schematic of a swollen L_α phase doped with small amounts of PEG-lipid gelators. In the upper right blow-up, the PEG-lipids are shown to induce a non-zero spontaneous membrane curvature. The chemical formula of PEG-DMPE is represented below.

2.2. Phase Diagram and Gelation

The incorporation of the PEG-lipid molecules into the (DMPC, pentanol, water) system does not always lead to monophasic mixtures. In fact, biphasic samples are observed both at high and low water contents. We will see that the reasons for this is that the PEG chains cannot insert between the membranes at low water content and that the phase cannot incorporate more than a given amount of water (high dilution limit). A homogeneous L_α phase is observed between these two biphasic domains. Doping this lamellar and fluid phase with PEG-lipid molecules changes dramatically its viscoelastic properties. This is illustrated in Figure 3 that displays a series of test-tubes holding samples of increasing water weight fraction, Φ_w , and constant PEG-lipid fraction, c_{PEG} , compared to total lipid. Strangely enough, adding water to the system induces gelation. This observation is strongly counter-intuitive and in sharp contrast with the analogous behavior of gels. Of course, gelation also occurs upon increasing PEG-lipid concentration at fixed water content.

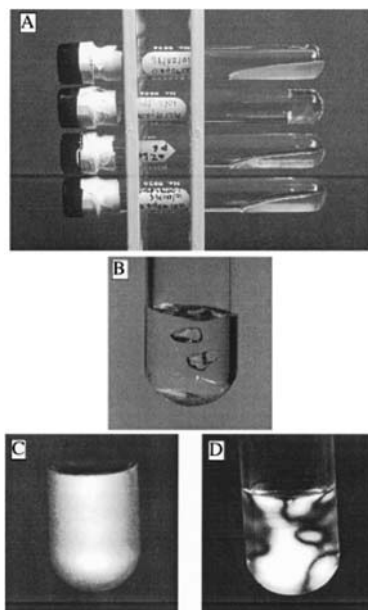


Figure 3. (A) Series of samples, with the water fraction increasing from bottom to top, at fixed PEG-lipid concentration. The first two bottom samples are in the fluid L_{α} phase, the third sample is in the gel L_{α} phase and the top sample, that is fluid again, belongs to a biphasic region. (B) A gel sample that shows distorted bubbles permanently trapped. Viewed in polarized light, a fluid lamellar sample (C) displays a plain featureless birefringence whereas a gel lamellar sample (D) displays a Schlieren nematic-like texture.

The gels formed by addition of PEG-lipids to the fluid L_{α} phase are fairly stiff. They can trap non-spherical bubbles (created with a pipette) for years. Moreover, gelation is observed whatever the conditions of preparation of the samples. Because dilution of the mixture makes it biphasic and fluid again, chemical cross-linking is not occurring.

The conclusions from observations of hundreds of such test-tubes are most conveniently summarized in a phase diagram (Figure 4), represented as a function of PEG-lipid and water content. A very large domain of the L_{α} lamellar phase appears and is bordered by two biphasic areas at low and high water contents, respectively. The lamellar phase is itself divided into two regions by a sol/gel transition line whose orientation is quite surprising; this line is not very sharp, as expected experimentally for this kind of phenomenon. Indeed, the amount of PEG-lipid required to achieve gelation is a decreasing function of the water content. Note also that gelation takes place in mixtures containing as little as 0.5 wt.% gelator molecules, which illustrates the excellent gelating power of PEG-lipid molecules.

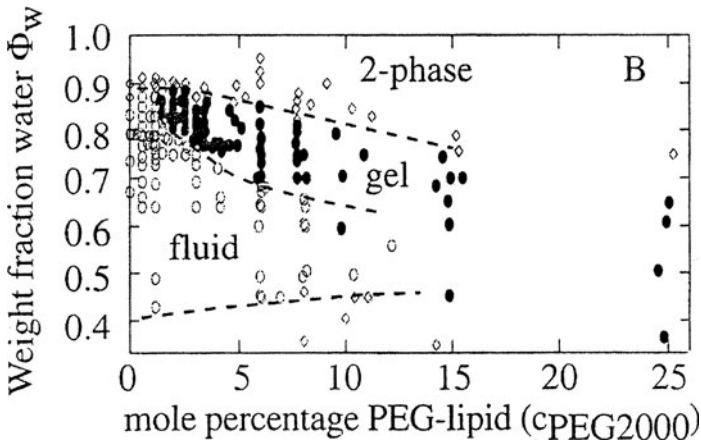


Figure 4. Phase diagram of the L_α phase doped with PEG-DMPE, as a function of water fraction and PEG-lipid concentration (compared to total surfactant). “Fluid” and “gel” refer to fluid L_α phase and gel L_α phase (filled symbols), respectively.

2.3. Observations of Samples in Polarized Light

Samples held in test-tubes appear birefringent when observed with the naked eye between crossed polarizers (Figure 3). The fluid L_α phase looks bright and featureless. By contrast, the gel phase shows a typical birefringence pattern that is sometimes called a Schlieren texture in the field of liquid crystals. This type of texture is more frequent for nematic phases than for lamellar ones but X-ray scattering experiments demonstrate the lamellar nature of the phase (*wide infra*).

In fact, liquid-crystalline textures are better examined by optical microscopy in polarized light. For this purpose, samples are held in flat glass optical capillaries, flame-sealed at both ends, that can be kept for years. A series of such capillaries filled with samples of increasing PEG concentration (c_{PEG}) is shown in Figure 5. The first sample, taken from a fluid L_α phase, has a texture showing bright streaks on a dark background. This “oily streak” texture is typical of lamellar phases. The dark areas are regions where the layers lie parallel to the flat glass walls; they are called homeotropic. The bright streaks, called oily streaks, are defect regions that connect adjacent homeotropic areas differing by the number of layers. Detailed studies have been reported that give a complete description of these defects in terms of pairs of parallel dislocation lines [18].

Samples of mixtures at compositions near the sol-gel transition show a different texture, designated as “wispy” because of the presence of many very thin birefringent lines on a dark background. These lines, that spontaneously nucleate in the sample, look like tiny oily streaks when observed at very high

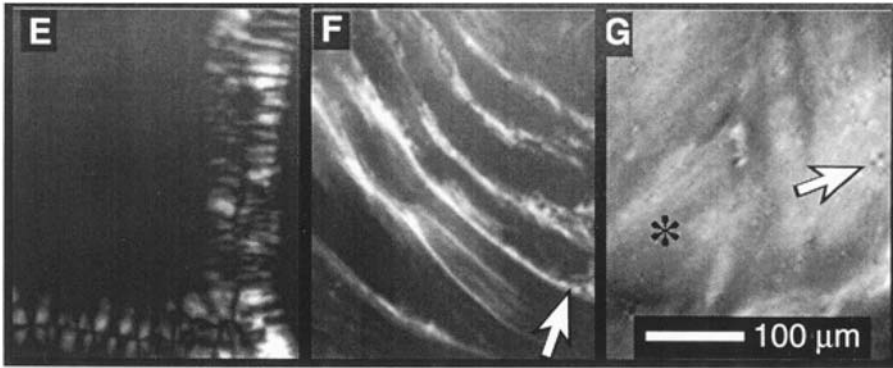


Figure 5. Textures of samples held in sealed flat glass capillaries and observed by polarized light microscopy. Left image: the fluid L_α phase displays a homeotropic texture broken by occasional oily streaks; center image: a sample from the sol/gel transition region displays many more thin linear defects (arrow); the gel L_α phase displays a highly defected texture with hardly resolved tiny linear defects and a few spherulites (arrow).

magnification. They do not vanish with time and cannot be temperature- or shear-annealed.

Finally, the optical textures of samples taken from deep in the gel region are reminiscent of the Schlieren texture, but with a less uniform and more grayish background. By using a good resolution microscope, very thin defect lines could sometimes be observed; they are locally parallel and seem to display a nematic order. This orientational order of topological defect lines, at the 1–10 microns length scale, probably explains the appearance of the nematic Schlieren texture.

2.4. Electron Microscopy

Freeze-fracture electron microscopy experiments (see Chapter 9) have been performed in an attempt to visualize the topological defects barely resolved by optical microscopy [19]. Figure 6 shows electron microscopy images of samples taken from the fluid L_α phase, the sol/gel transition region, the gel L_α phase, and an “onion” phase [20] for the sake of comparison. As expected, the fluid sample shows large areas of periodically stacked membranes with a few topological defects. Overall, the electron microscopy images are highly reminiscent of the homeotropic texture observed in polarized light microscopy. The transitional sample shows many more curvature defects and their average size is smaller. The sample of gel L_α phase displays a large density of small defects that possibly look more like spherulites (often anisotropic) and dislocation loops than like simple dislocation lines. Moreover, single

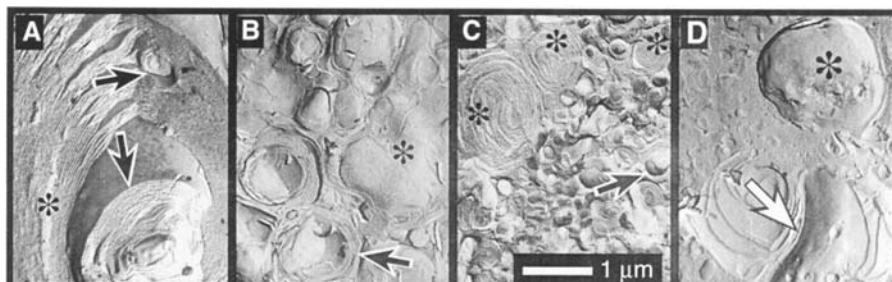


Figure 6. Freeze-fracture electron microscopy images of a fluid L_α sample (A) that shows large well-ordered stacks of membranes bounded by a few defects (arrows); (B) a sample from the sol/gel transition region shows curvature defects (arrow); (C) highly defected texture of the gel L_α phase with spherical (arrow) and highly distorted (stars) spherulites tethered together by membranes. For comparison, an image of multilamellar vesicles from the DDAB system is shown (D).

membranes percolating throughout the whole region examined could also be clearly observed. Thus, the electron microscopy images evidence curvature defects tethered together by shared membranes. Such membranes are completely missing in the so-called onion phase that is produced by strongly shearing a swollen lamellar phase and that is not a gel. Altogether, this electron microscopy investigation fully supports the interpretation that the PEG-lipids induce gelation through the proliferation of topological defects comprising highly curved membranes.

2.5. X-Ray Scattering

Small angle X-ray scattering (SAXS) experiments can be performed to probe the molecular organizations of materials on length scales ranging from 1 to 500 nm (see Chapter 10). This technique is used with a rotating anode X-ray generator or at synchrotron radiation facilities on dedicated beamlines. For this purpose, samples are usually held in Lindemann glass cylindrical capillaries of about 1 mm diameter. Due care must be taken to ensure a “powder-like” distribution of domains, so that domains of all orientations are found in the X-ray beam with equal probabilities. If the structure of a material shows any positional long-range order with a period d , it will result in sharp diffraction rings located at $q = 2\pi/d$ (and possibly also at its harmonics; q is the scattering vector modulus equal to $4\pi \sin \theta/\lambda$ where 2θ is the scattering angle and λ is the wavelength). If there is only liquid-like positional short-range order, then weak diffuse rings will be observed.

Figure 7 shows a series of X-ray scattering scans from samples of increasing water content but constant PEG-lipid concentration. Several sharp diffraction

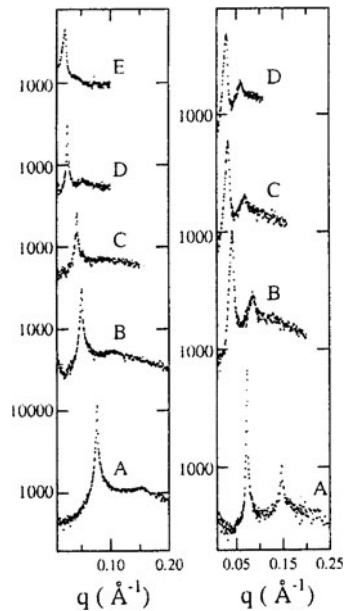


Figure 7. SAXS powder scans of the scattered intensity versus scattering vector modulus of two series of samples of increasing water fractions from bottom to top (left scans: $c_{\text{PEG}} = 0.5\%$, right scans: $c_{\text{PEG}} = 3\%$). The lamellar period increases with dilution so that the diffraction peaks move to smaller q values. Although the samples span both the fluid and gel lamellar regions, no particular change occurs at the gel transition.

lines are observed that can be indexed with a 1-dimensional lattice. They are the X-ray scattering signature of the liquid-crystalline lamellar L_α phase. As the water content increases, the positions of these peaks gradually shift to smaller angles, which reflects the increase of the lamellar period with phase dilution. However, the number and shape of these peaks do not change very much. In particular, there is no sudden change of any kind between the X-ray scans of samples taken on both sides of the gelation line inside the L_α phase region of the phase diagram. Therefore, the gelation does not seem to be related to a structural change of the liquid-crystalline phase.

The X-ray scattering scans from samples of increasing PEG-lipid concentration, but constant water fraction, behave slightly differently (Figure 8). The number of lamellar diffraction peaks increases progressively although the peaks keep roughly the same shape. Without going into details, the number of diffraction peaks is a function of the phase elastic constants [21]. Therefore, an increasing number of diffraction peaks, upon increasing c_{PEG} , is the sign of phase “stiffening”, which is confirmed by a careful analysis of the peak profiles. However, here again, there is no sudden change when crossing the gelation line. Nevertheless, the same profile analysis shows that domain size

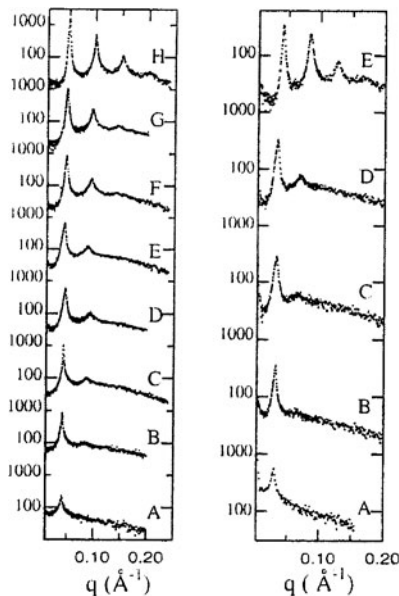


Figure 8. SAXS powder scans of the scattered intensity versus scattering vector modulus of two series of samples of increasing c_{PEG} from bottom to top (left scans: $\Phi_w = 75\%$, right scans: $\Phi_w = 82\%$). The number of lamellar peaks increases upon doping with increasing amounts of PEG-lipid but no discontinuous change occurs at the gel transition.

is much smaller in the gel lamellar phase than in the fluid one, which is also consistent with the notion of defect proliferation.

Wide angle X-ray scattering experiments were also performed to understand the organization of the phase at the 0.1–1 nm length scale (Figure 9). These X-ray scans only showed the diffuse rings due to water and to the molten state of the paraffinic chains of the surfactants. Such experiments demonstrate that the sol/gel transition induced by the PEG-lipid molecules has nothing to do with the so-called “gel” $L_{\beta'}$ lamellar phases in which the surfactant chains are not molten but crystallized.

2.6. Rheology

Two methods were used to try to assess the mechanical properties of the sol or gel mixtures: The “tube inversion” test was used for all the samples (see Chapter 8). Some samples have been kept upside-down for years without flowing. This simple test proves the existence of a yield stress. In addition, dynamic mechanical analysis was also performed for some selected samples. This technique consists in submitting the sample to an oscillatory stress at a constant frequency and recording the in-phase and the 90° out of phase deformation

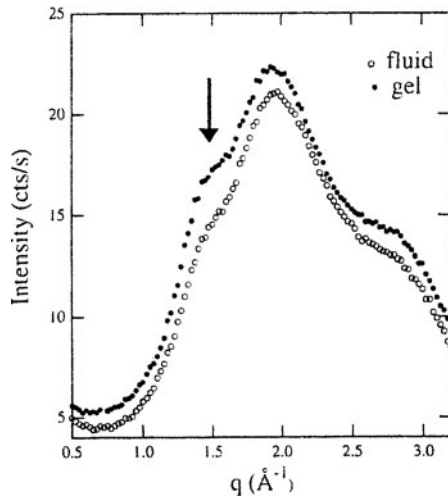


Figure 9. Typical WAXS data for fluid and gel liquid-crystalline lamellar samples. In both phases, the lipid chains are in a fluid state (arrow). The peaks at 2 and 2.7 \AA^{-1} are due to water.

responses. The corresponding G' and G'' moduli are then plotted versus frequency.

Figure 10 shows the evolution of G' and G'' for a series of samples of increasing water contents. At low dilution, in the L_α phase, the values of G' and G'' are comparable. Moreover, the measurements are not really reproducible from one sample to another or even for the same sample. In fact, this is hardly surprising because the rheology of liquid crystals is complicated by the fact that the texture (i.e., the distribution of domains in which the liquid-crystalline order prevails) must be carefully controlled. When a liquid-crystal is inserted and then studied in a rheometer, its texture could be random but it is more often partially aligned due to flow during cell filling. In particular, this is usually the case of the lamellar L_α phase that is fluid enough to exhibit such a behavior. Specific and delicate treatments, such as surface anchoring or directional growth, must then be used to obtain meaningful rheology data [22].

In contrast, rheology measurements of the gel L_α phase proved highly reproducible even though no particular caution was taken to control the liquid-crystalline texture. This is most probably due to the fact that the texture should be close to “powder-like” (i.e., an isotropic distribution of lamellar liquid-crystalline domains) because of defect proliferation. Interestingly enough, the rheology data of the gel phase was not affected by a strong shear prior to the experiment. Figure 10 shows the increase of both viscoelastic moduli upon gelation but the increase of G' is clearly larger than that of G'' . As a result, in the gel L_α phase, G' is larger than G'' by an order of magnitude over the whole range of frequencies used. The values of G' measured ($G' \sim 5000$ Pa)

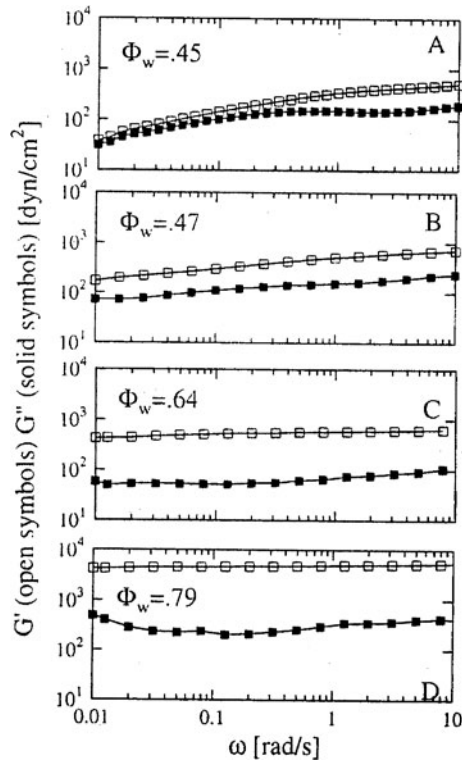


Figure 10. Rheological behavior of a series of samples of increasing water fraction (Φ_w) but constant PEG-lipid concentration ($c_{\text{PEG}} = 6\%$). (G' : open symbols; G'' : filled symbols)

correspond to a fairly stiff gel. It should be noted here that the gelation lines determined by rheology and by the tube inversion test are approximately the same. The rheology data are quite reminiscent of that of a chemical gel but the sol/gel transition is reversible, which proves the physical nature of the gel.

2.7. Model and Discussion

In this section, we introduce a very simple model to describe the gelation of the swollen L_α phase induced by addition of PEG-lipids. Even though this model is a bit naive and crude, it still accounts for the two very important counter-intuitive features related to this gelation: (i) the sol/gel transition occurs upon water addition at constant gelator concentration; (ii) less PEG-lipid is required to achieve gelation when the water content increases.

We assume here that the addition of PEG-lipids promotes the proliferation of line defects due to the high membrane spontaneous curvature induced by

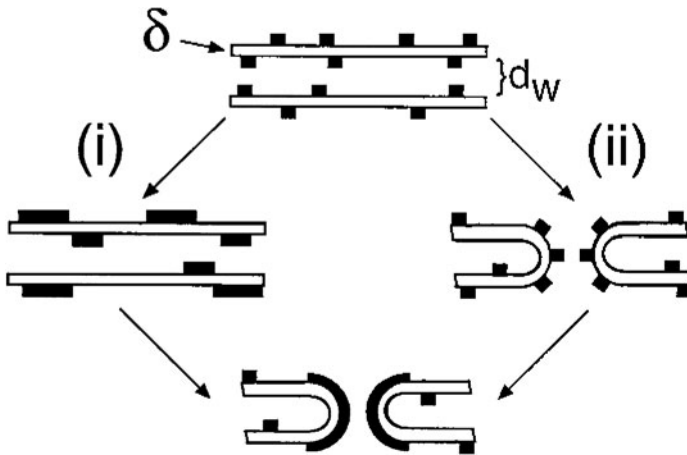


Figure 11. Schematic illustrating two possible paths for the creation of curvature defects: Along path (i), PEG-lipids first laterally segregate within the membranes that become unstable versus formation of curved regions due to local spontaneous curvature; along path (ii), curvature defects first spontaneously nucleate and then attract the PEG-lipids that energetically stabilize them.

these very asymmetric molecules. There are two schematic ways of creating line defects (Figure 11). In the first, the PEG-lipid molecules that are free to diffuse within the membranes segregate in distinct regions; these regions then nucleate curvature defects in which the PEG-lipids are less frustrated than in the flat bilayers. Along the second, curvature defects spontaneously nucleate and are then stabilized by their PEG-lipids coatings.

Whichever path is the correct one, we now consider the simple defect geometry shown in Figure 11 that corresponds to a channel between two next neighbor water layers. The thermodynamic energy of such line defects can be expressed by using the Helfrich free-energy of the lamellar L_α phase [23]:

$$E = \frac{1}{2}\kappa \int [(C_1 - C_0) + (C_2 - C_0)]^2 dS$$

where C_0 is the spontaneous curvature of the membrane, κ is its bend elastic constant ($\kappa \approx k_B T$), and C_1 and C_2 are the principal membrane curvatures. We consider a line defect of length L with curvatures $C_1 = 2/d$ and $C_2 = 0$, which leads to an elastic cost:

$$E = \frac{1}{2}\kappa \left(\frac{2}{d} - C_0 \right)^2 \pi L d$$

The defect has a persistence length ξ_p given by $\xi_p = \frac{\pi d \kappa}{k_B T}$, which gives an entropic gain in free energy:

$$TS = \frac{(k_B T)^2 L}{\pi d \kappa}$$

The line defects will proliferate when their elastic cost will be equal to their entropic gain, which yields a relation between the lamellar period at the gelation point, d_{gel} , and the spontaneous curvature, $C_{0\text{gel}}$:

$$d_{\text{gel}} = \frac{1}{C_{0\text{gel}}} \left(2 - \frac{\sqrt{2} k_B T}{\pi \kappa} \right)$$

Moreover, we assume that C_0 is proportional to the PEG-lipid concentration (DMPC and pentanol do not induce any membrane spontaneous curvature) at low c_{PEG} , and since d is proportional to the water amount (Φ_w), an inverse relationship between Φ_w and c_{PEG} is derived.

Qualitatively, larger water fractions correspond to larger lamellar periods and, therefore, to smaller curvatures. This relationship explains why less PEG-lipid is needed to reach the sol/gel transition as the water content increases and why gelation is observed upon water addition. This model should obviously be refined [24], for instance by considering the defect loops suggested by the electron microscopy images discussed above. However, this minimal model already captures the salient features of the system. In fact, any model based on curvature defect proliferation should also show these main trends.

At this stage, the existence of a biphasic region at low water content still needs to be explained. It is mostly due to the fact that a minimum lamellar period d is required for the PEG chains to insert into the aqueous medium between the surfactant membranes. As long as the aqueous medium thickness, $d_w = d - \delta$, is much smaller than the gyration radius of the PEG chains, they cannot fit between the membranes and the PEG-lipid molecules are expelled from the fluid L_α phase. This interpretation is strongly supported by a comparison between the phase diagrams obtained with various PEG-lipid molecules differing by the length of their PEG chains (as shown in Section 3).

3. A New Class of Gels

3.1. Extensive Chemical Modification of PEG-lipids Does not Affect Their Gelating Power

The phenomenon described in the previous part is not restricted to a particular PEG-lipid molecule. In fact, both the PEG chain length and the nature of the surfactant part could be varied without loss of the gelating power [25, 26].

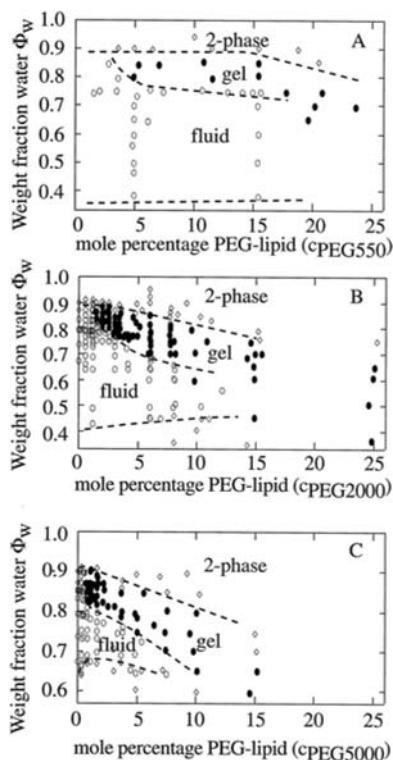


Figure 12. Phase diagrams of the L_α phase doped with PEG-DMPE of three different chain lengths: (A) PEG550, (B) PEG2000, (C) PEG5000, as a function of water fraction and PEG-lipid concentration (compared to total surfactant). “Fluid” and “gel” refer to fluid L_α phase and gel L_α phase, respectively.

First, the influence of the PEG chain length is examined. PEG550, PEG 2000, and PEG 5000 were used to promote gelation of the L_α phase of the (DMPC, pentanol, water) system. The topologies of the phase diagrams obtained with the two gelators are very similar (Figure 12). However, upon close inspection, two main differences can be seen in the two diagrams. Firstly, the lower stability limit of the fluid L_α phase occurs at higher water content in the case of the PEG-lipid comprised of the PEG 5000 chain. This is clearly due to the fact that a thicker aqueous medium is necessary to accommodate the larger gyration radius of the PEG 5000 chain ($R_g \sim 62 \text{ \AA}$ for PEG5000; $R_g \sim 35 \text{ \AA}$ for PEG2000; $R_g \sim 15 \text{ \AA}$ for PEG550). Secondly, the gelation line is shifted to smaller PEG-lipid concentrations as the PEG chain increases. This is actually the behavior predicted by the crude model introduced in the previous section because it predicts that $d_{\text{gel}} \sim N^{-1/3}$ where N is the PEG chain polymerization degree. Qualitatively, this means that PEG-lipids of larger PEG chains

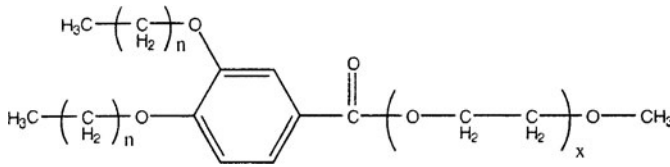


Figure 13. Chemical formula of the synthetic PEG-surfactants (x is the polymerisation degree of the PEG chain and n defines the hydrophobic chain length) to be compared with PEG-lipids (see Figure 2).

are more asymmetric moieties and are more efficient at stabilizing defected curved regions.

The lipid part of the gelator was also severely modified by chemically grafting a PEG chain onto a synthetic surfactant moiety that is completely different from a phospholipid molecule (Figure 13). Strikingly, these new PEG-surfactant molecules still have the ability to induce gelation of the fluid L_α phase. The phase diagrams obtained by doping the L_α phase of the DMPC/pentanol/water system with these new PEG-surfactants superimpose quite well onto those described previously. Optical micrographs illustrate the proliferation of tethered topological defects, consistent with SAXS investigations that demonstrate the decrease in domain size. Even though these systems have been investigated in great detail, no additional specific features were observed. Consequently, they will not be considered further.

These studies, in which the chemical structure of the PEG-lipid molecule was systematically explored, show that the chemical details of these gelator structures are unimportant, and demonstrate the generality of the defect-induced gelation mechanism. In the next section, the gelator architecture is changed even more drastically without losing the gelation properties.

3.2. Double-End-Anchored PEG-Surfactants also Induce Gelation

The PEG-surfactant molecules that we have considered so far have an anchor at one end of a PEG chain; they are “single-end-anchored” (SEA) PEG-surfactants. It is of course tempting to try to substitute the two ends of a PEG chain with a surfactant moiety, yielding “double-end-anchored” (DEA) PEG-surfactants [27, 28]. These molecules will insert each of their two extremities inside the (DMPC, pentanol) membranes and each end will be free to diffuse within the fluid bilayers.

Two very different conformations can be expected for a DEA-PEG-surfactant (Figure 14). In the “loop” conformation, both anchors are inserted inside the same membrane. The PEG coil may lie flattened on the membrane or fairly extended, depending on its affinity with the membrane. In the “bridge” conformation, the two anchors are inserted inside adjacent membranes, effectively connecting them, which may *a priori* give rise to a different gelation mechanism. The loop conformations, giving rise to repulsive interactions between membranes, are usually considered to be more probable than the bridge ones that would induce attractive interactions [29].

The phase diagrams obtained by doping the fluid L_α phase with small amounts of DEA-PEG-surfactants (Figure 14) are slightly more complicated than those obtained with the SEA-PEG-surfactants. However, some general features are still retained: the L_α phase is preserved in a large region of the phase diagram and this region is still divided by a sol/gel transition line that has roughly the same shape as described previously. Therefore, DEA-PEG-surfactants can also gelate the fluid lamellar L_α phase; gels could be obtained with very small amounts of gelator and less gelator was required as the water amount increased. In fact, most of the features associated with gelation observed with the SEA-PEG-surfactants were also present in this new system. Microscopic observations of textures in polarized light reveal the proliferation of tiny line defects that connect the membranes in a 3-dimensional fashion. Wide-angle X-ray scattering demonstrates that the membranes are still in a fluid state, and small-angle X-ray scattering from samples taken in the L_α phase always display the equidistant sharp reflections typical of long-range 1-dimensional positional order. Consequently, it seems that the gelation phenomenon brought about by the DEA-PEG-surfactants is of the same nature as that observed with single-end-anchored gelators.

Nevertheless, these new systems are somewhat different from the previous ones. The most obvious difference is that there appears a new biphasic area close to the usual stability domain of the L_α phase on the low-dilution side. Moreover, the stability domain of the lamellar phase is much narrower as a function of Φ_w , especially for short PEG chains. The swelling limit at high dilution now depends on the PEG molecular weight and decreases with c_{PEG} , at low c_{PEG} .

The origin of the new biphasic area is addressed first. The structures of the coexisting phases can be understood from SAXS data (Figure 15). The SAXS scans correspond to the superposition of two sets of equidistant peaks that arise from two lamellar phases of different periods. The evolutions with PEG-surfactant concentration of the periods of these two phases are not the same. The first one, called L_α has a period that increases with c_{PEG} , a phenomenon already observed with the SEA-PEG-surfactants due to the volume increase of the aqueous sublayers. The second one, called $L_{\alpha'}$, has a period that decreases slightly with c_{PEG} (Figure 15). This strongly suggests that the L_α phase is a loop-rich lamellar phase whereas the $L_{\alpha'}$ phase is a bridge-rich lamellar phase.

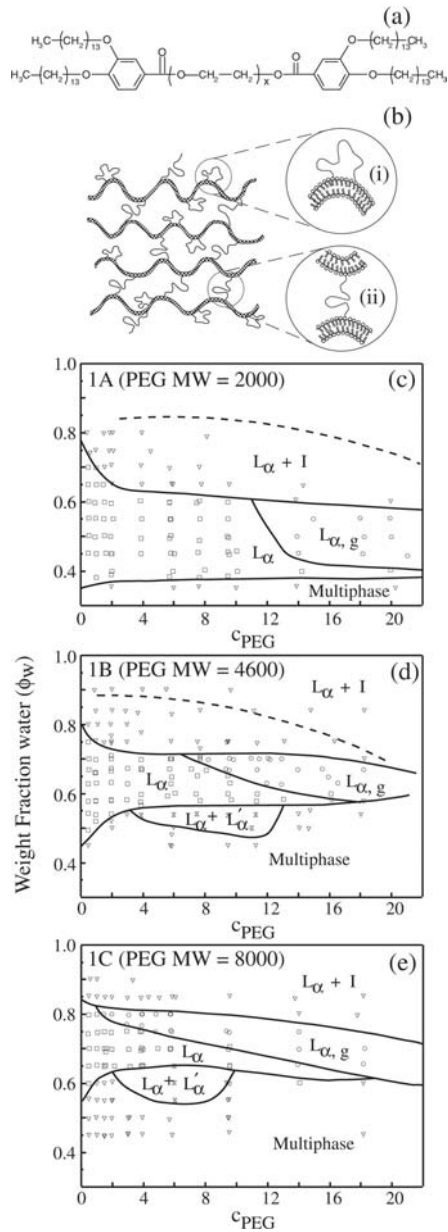


Figure 14. (a) Chemical formula of double-end-anchored PEG-surfactants. (b) Schematic of the loop- (i) and bridge- (ii) conformations of DEA-PEG-surfactants inserted in the swollen L_α phase. (c-e) phase diagrams of the L_α phase doped with DEA-PEG-surfactants of PEG M_w 2000, 4600, and 8000, respectively. ($L_{\alpha, g}$ is the gel L_α phase.) Compare the previous phase diagrams in Figure 12 and note the occurrence in (d) and (e) of a region of coexistence of two fluid lamellar phases, L_α and $L_{\alpha'}$. Note also that the upper 2-phase boundary now strongly depends on PEG molecular weight; the dashed line is the upper 2-phase boundary observed with SEA-PEG-surfactants of equivalent length.

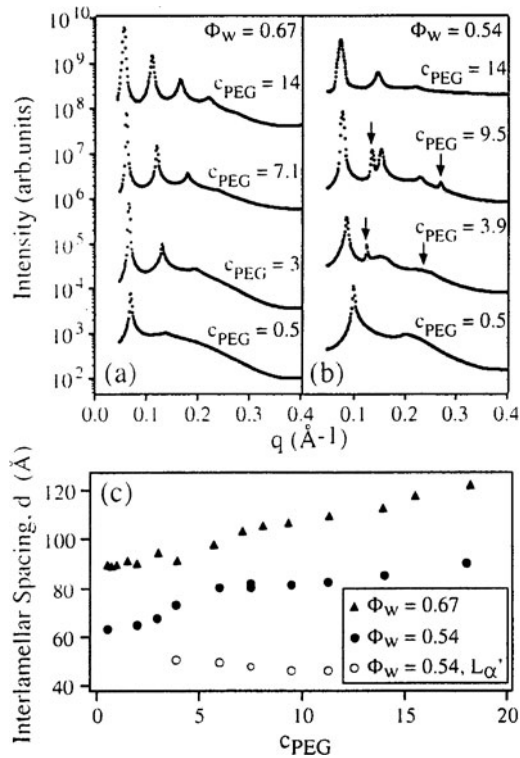


Figure 15. SAXS scans from samples of increasing c_{PEG} and fixed water volume fractions. The first series (a) of samples only span the L_{α} phase including the sol/gel transition. The second series (b) includes samples taken from the $L_{\alpha}/L_{\alpha'}$ coexistence region (the arrows point to the diffraction peaks of the $L_{\alpha'}$ phase). (c) Evolution of the periods of the L_{α} and $L_{\alpha'}$ phases with c_{PEG} .

However, from the point of view of gelation, the bridging conformations do not seem to be as efficient as the curvature topological defects since the gel is not observed in the coexistence region of the two lamellar phases except, as before, in the high dilution limit of the L_{α} phase.

The stability limit of the L_{α} phase at high dilution is now considered. The strong dependence of this limit on the PEG molecular weight at low c_{PEG} is a new feature, typical of the DEA-PEG-surfactants. It was interpreted as the influence of bridging conformations in the loop-rich L_{α} phase. A numerical study of the chain conformations can account for the dependence of the high dilution limit on c_{PEG} and on PEG molecular weight. The number of bridging conformations strongly decreases as the membrane separation increases. This is the most salient effect of the bridging conformations on the gel L_{α} phase, whose origin still lies in the proliferation of curvature defects.

4. Generalization

4.1. Gelation of a Lamellar Phase by Addition of Particles

A quite similar defect-induced gelation phenomenon was recently reported [30]. The fluid L_α phase of a commercial anionic surfactant was doped with polymer spheres of $10\ \mu\text{m}$ diameter which stabilized an oily streak defect network. This defect-ridden L_α phase displayed gel-like behavior and its rheological properties could be explained by a model describing the elasticity of the oily streak network. Although the influence of the particle diameter was not investigated, it is likely that smaller particles would have stabilized smaller line-defects. The same idea could be extrapolated to the nanometric length scale by doping the phase with hydrophobically coated spherical nanoparticles. Alternatively, one could also consider doping with hydrophobic molecules of a structure very different from the surfactant used. Being hydrophobic, such molecules would be located within the membranes. Moreover, they could also segregate within the membranes and self-assemble into inclusions of nanometric size that would stabilize the defects and lead to gelation.

4.2. Gelation of Other Mesophases

Even though they are not the main focus of this book, thermotropic liquid crystals that display a very similar defect-induced sol/gel transition [31, 32] will be discussed briefly. Doping the nematic phase of rod-like liquid-crystals with chiral molecules brings about a helical organization. It is called “cholesteric” because it was first observed with cholesterol derivatives. Like the nematic phase, the cholesteric phase has long-range orientational order but no long-range positional order of the molecules; however, the latter phase also has a helical pitch that can be on the μm length scale and creates a layered-like structure. As a result, the cholesteric phase can have the same topological defects as the L_α phase. Adding small spherical inclusions to the cholesteric phase resulted in the stabilization of oily streak networks and gave rise to enhanced 3-dimensional elasticity. Moreover, a detailed rheological model of the defect network was devised in this work to account for the values of the viscoelastic moduli.

Lyotropic phases of hexagonal symmetry form another very important class of liquid crystals. These phases, called H_α , may also be found in the phase diagrams of amphiphilic molecules if their packing parameter obeys $1/3 < V/la < 1/2$. Then, the surfactants self-assemble into very long cylindrical micelles that organize on a long-range 2-dimensional lattice. In principle, a single domain of the H_α phase should flow easily along the hexagonal symmetry axis and should not have gel properties. However, the H_α phase also has

specific curvature line and wall defects that can give an elastic contribution to the phase mechanical properties. Indeed, the H_α phase of surfactants is usually quite stiff and does not flow under its own weight, which makes it different from the L_α phase. The hexagonal (and cubic phases) of block copolymer systems also show a similar behavior [33]. Topological defects can be suppressed by applying a shear-flow followed by slow annealing, resulting in very well aligned samples [34]. Nevertheless, topological defects can also be thermodynamically stable and proliferate close to a phase transition. For instance, large densities of connections between cylinders have been detected in the H_α phase close to the isotropic phase [35]. One can then speculate that doping the H_α phase with molecules of different packing parameter may also stabilize connection defects between cylinder micelles and thus promote gelation. Unfortunately, unlike the fluid L_α phase, the H_α phase of surfactants cannot usually be swollen to a large extent. The highest swelling solvent concentration reported so far is 75% [36]. This means that a fair amount of surfactant must still be used to achieve gelation, in contrast with the gel swollen lamellar phase described in the previous sections where the water volume fraction can be as large as 90%. Moreover, at high surfactant concentrations, the phase elastic constants will still be quite large, probably precluding the thermodynamic proliferation of defects.

4.3. “Ringing Gels”

The topic of this chapter is reminiscent of the so-called “ringing gels” that were reported by Hoffmann in the phase diagrams of surfactants [37, 38]. These materials vibrate and give a ringing sound when the vial they are held in is gently tapped. They can sustain sound propagation with little damping and probably even establish standing waves. It seems that, in most cases, these phases have a liquid-crystalline cubic structure (Note, however, that samples of some hexagonal phases also vibrate when held in vials of the right size.) and appear when small amounts of hydrocarbons are added to the surfactant/water system. The elastic constants of these gels can reach values on the order of 10^5 Pa, but the precise gelation mechanism is still unclear. A possible explanation is that the cubic phase is made of densely packed spherical micelles, which would give a percolation mechanism. Here again, the volume fraction of water is rather small ($\sim 40\%$) and the gelating power is of limited practical interest.

However, a highly swollen cubic liquid-crystalline phase has been reported in a complex 5-component phase diagram [39]. The cubic lattice parameter reached values of 220 nm at high dilution: little surfactant and co-surfactant are required to form the phase. It should be interesting to study the rheological behavior of this phase and determine whether it is a gel. If any 3-dimensional elastic properties are found (which is likely in a cubic phase), it would then be

interesting to determine whether they arise from intrinsic structural elements (such as minimal surfaces) or from topological defects that can be stabilized at high dilution.

5. Conclusions and Perspectives for the Future

The new systems described here are very dilute hydrogels formed by doping phospholipid membranes with minute amounts of biocompatible gelators. This suggests that they may be useful for biomedical applications. Indeed, hydrogels are often employed to produce convenient pharmaceutical formulations. The fluid membranes of these new gels could incorporate membrane proteins, to confer them with well-designed biological activity. In addition, one could exploit the generality of the defect-induced gelation mechanism by replacing the PEG chain with another short water soluble chain molecule that could either be a polypeptide or even a polysaccharide used for cell signaling. Also, the membrane composition may be varied by considering different lipids or mixtures of lipids. In particular, the choice of pentanol as a co-surfactant may not be the best one for biomedical applications, and other similar small molecules should be investigated. The robustness of the defect-induced gelation provides the opportunity to explore many combinations of lipids and polymer-lipids in the future. More fundamentally, this gelation mechanism of a liquid-crystalline phase introduces a new concept to be tested in a variety of situations.

Acknowledgments

This chapter describes a research project, initiated and organized by Prof. C.R. Safinya (University of California at Santa Barbara, USA), that took place between 1994 and 2001. The work reported here has been the subject of the PhD theses of H.E. Warriner and N.L. Slack. This project also results from a wide interdisciplinary collaboration between American and European scientists, namely: M.A. Chibbaro, P. Eiselt, S.H.J. Idziak, C. Jeppesen, S.L. Keller, P. Pincus, M. Schellhorn, U. Schulze, H.W. Schmidt, J.A. Zasadzinski. The author is deeply indebted to all of them.

References

- [1] It seems that a standard, widely accepted, definition of a physical gel still remains to be reached. See, for instance: J. Brandrug, E.H. Immergut and E.A. Grulke, Eds. *Polymer Handbook*, New York: John Wiley & Sons, 1999, p. VII-765.

- [2] See, for instance: J.E. Glass, Ed. *Polymers in Aqueous Media*, Advances in Chemistry Series, 223, Washington, DC: American Chemical Society, 1989.
- [3] Terech, P.; Rossat, C.; Volino, F. *J. Coll. Int. Sci.*, **2000**, 227, 363.
- [4] De Gennes, P.G. *Scaling Concepts in Polymer Physics*, Ithaca, NY: Cornell University Press, 1979.
- [5] Mourchid, A.; Delville, A.; Lambard, J.; Lécolier, E.; Levitz, P. *Langmuir*, **1995**, 11, 1942.
- [6] De Gennes, P.G.; Prost, J. *The Physics of Liquid Crystals*, Oxford: Clarendon Press, 1993.
- [7] Collings, P.J. *Liquid Crystals*, Princeton, NJ: Princeton University Press, 1990.
- [8] Terech, P.; Weiss, R.G. *Chem. Rev.*, **1997**, 97, 3133.
- [9] Safinya, C.R.; Sirota, E.B.; Bruinsma, R.F.; Jeppesen, C.; Plano, R.J.; Wenzel, L.J. *Science*, **1993**, 261, 588.
- [10] Israelachvili, J.N. *Intermolecular and Surface Forces*, London: Academic Press, 1995.
- [11] Allain, M.; Kléman, M. *J. de Physique*, **1987**, 48, 1799.
- [12] Kawasaki, K.; Onuki, A. *Phys. Rev A*, **1990**, 42, 3664.
- [13] Warriner, H.E.; Idziak, S.H.J.; Slack, N.L.; Davidson, P.; Safinya, C.R. *Science*, **1996**, 271, 969.
- [14] Safinya, C.R.; Sirota, E.B.; Roux, D.; Smith, G.S. *Phys. Rev. Lett.*, **1989**, 62, 1134.
- [15] Helfrich, W. *Z. Naturforsch. A*, **1978**, 33, 305; idem, *Z. Naturforsch. C*, **1973**, 28, 693.
- [16] V.H.L. Lee, Ed. *Peptide and Protein Drug Delivery*, New York: Dekker, **1991**.
- [17] D.D. Lasic and F.J. Martin, Eds. *Stealth Liposomes*, Boca Raton, Florida: CRC Press, 1995.
- [18] Boltenhagen, P.; Kléman, M.; Lavrentovich, O. *J. de Physique II*, **1994**, 4, 1439.
- [19] Keller, S.L.; Warriner, H.E.; Safinya, C.R.; Zasadzinski, J.A.N. *Phys. Rev. Lett.*, **1997**, 78, 4781.
- [20] Diat, O.; Roux, D. *J. de Physique II*, **1993**, 3, 9.
- [21] Safinya, C.R.; Roux, D.; Smith, G.S.; Sinha, S.K.; Dimon, P.; Clark, N.A.; Bellocq, A.M. *Phys. Rev. Lett.*, **1986**, 57, 2718.
- [22] See for instance, a) Bartolino, R.; Durand, G. *Phys. Rev. Lett.*, **1977**, 39, 1346. b) Cagnon, M.; Durand, G. *Phys. Rev. Lett.*, **1980**, 45, 1418. c) Oswald, P. *J. de Physique*, **1985**, 46, 1255.
- [23] Helfrich, W. *Z. Naturforsch. A*, **1978**, 33, 305.
- [24] Kohyama, T. *Physica A*, **1998**, 248, 323.
- [25] Warriner, H.E.; Davidson, P.; Slack, N.L.; Schellhorn, M.; Eiselt, P.; Idziak, S.H.J.; Schmidt, H.W.; Safinya, C.R. *J. Chem. Phys.*, **1997**, 107, 3707.
- [26] Warriner, H.E.; Keller, S.L.; Idziak, S.H.J.; Slack, N.L.; Davidson, P.; Zasadzinski, J.A.N.; Safinya, C.R. *Biophys. J.*, **1998**, 75, 272.
- [27] Slack, N.L.; Schellhorn, M.; Eiselt, P.; Chibbaro, M.A.; Schulze, U.; Warriner, H.E.; Davidson, P.; Schmidt, H.W.; Safinya, C.R. *Macromolecules*, **1998**, 31, 8503.
- [28] Slack, N.L.; Davidson, P.; Chibbaro, M.A.; Jeppesen, C.; Eiselt, P.; Warriner, H.E.; Schmidt, H.W.; Pincus, P.; Safinya, C.R. *J. Chem. Phys.*, **2001**, 115, 6252.
- [29] a) Lipowsky, R. *Phys. Rev. Lett.*, **1996**, 77, 1652. b) Lipowsky, R. *Colloids Surf. A*, **1997**, 128, 255.
- [30] Basappa, G.; Suneel, Kumaran, V.; Nott, P.R.; Ramaswamy, S.; Naik, V.M.; Rout, D. *Eur. Phys. J. B*, **1999**, 12, 269.
- [31] The gelation of thermotropic liquid-crystalline phases is presently the focus of intense studies. See, for instance, Chapters 14 and 22 as well as: Kato, T. *Science*, **2002**, 295, 2414.

- [32] Zapotocky, M.; Ramos, L.; Poulin, P.; Lubensky, T.C.; Weitz, D.A. *Science*, **1999**, 283, 209.
- [33] Hamley, I.W. *The Physics of Block Copolymers*, Oxford: Oxford University Press, 1998.
- [34] Impéror-Clerc, M.; Davidson, P. *Eur. Phys. J. B*, **1999**, 9, 93.
- [35] Constantin, D.; Oswald, P.; Impéror-Clerc, M.; Davidson, P.; Sotta, P. *J. Phys. Chem. B*, **2001**, 105, 668.
- [36] Ramos, L.; Fabre, P. *Langmuir*, **1997**, 13, 682.
- [37] Oetter, G.; Hoffmann, H. *Colloids and Surfaces*, **1989**, 38, 225.
- [38] Gradzielski, M.; Hoffmann, H.; Oetter, G. *Colloid and Polymer Science*, **1990**, 268, 167.
- [39] Peter, U.; König, S.; Roux, D.; Bellocq, A.M. *Phys. Rev. Lett.*, **1996**, 76, 3866.

APPLICATIONS

Chapter 22

GELS OF LIQUID CRYSTALS AND ION-CONDUCTING FLUIDS

Rifat A.M Hikmet

Philips Research, Prof. Holstlaan 4, 5656 AA, Eindhoven, The Netherlands

1. Introduction	773
2. Liquid Crystal and Ion Conducting Gels for Electro Optical Devices	774
2.1. Gels with Chemically Cross-Linked Networks	774
2.2. Photopolymerization of Acrylates	774
2.3. Liquid Crystal Gels	775
2.4. Ion Conducting Gels	781

1. Introduction

Gels can be found in many products we use in our daily lives (see Introduction) [1]. They are used in massive quantities in foodstuff, packaging, photographic film, sanitary products, such as diapers, and in the cosmetic industries. In construction industries, they are used to make soil slurries which can be transported in pipes. Gels are also used in agriculture and oil industries. Various medical applications of gels such as soft contact lenses and artificial skin have also been described. They are also used in oral, transdermal, and implantation drug delivery where the rate of release of the drug is carefully adjusted by the gel. Gels are also widely used in tissue culture and biotechnologies. They are used in separations based on size selectivity, selective adsorption or ion exchange. In the electronic industry, gels play a crucial role in the production of various components such cathode ray tubes.

This chapter will focus on applications of gels in electro-optical and electronic devices.

2. Liquid Crystal and Ion Conducting Gels for Electro Optical Devices

2.1. Gels with Chemically Cross-Linked Networks

In this section, production of liquid crystal and ion conducting gels based on chemically cross-linked networks and applications of these gels will be described. The gels are produced by *in-situ* photo-polymerization of acrylate monomers in the presence of non-reactive molecules. In this way, a chemically cross-linked network swollen by a non-reactive medium (gel) is obtained. In the coming sections various kinds of gels and their applications will be described. In these gels, as gelation is isothermally induced by photo-initiated polymerization, various ways using light intensity modulations to create patterned gels will also be described. However, before describing liquid crystal and ionic gels, we first will consider the photo-induced polymerization of acrylates.

2.2. Photopolymerization of Acrylates

A schematic representation of a radical initiated photo-polymerization process involving reactive acrylate molecules and a frequently used photo-initiator, $\alpha\alpha$ -dimethoxy- α -phenylacetophenone, is shown in Figure 1.

Under UV radiation ($\lambda < 380$ nm), the cleavage of the photo-initiator occurs. Free radicals are very reactive and attack the double bonds of the acrylate groups inducing a chain reaction until the reaction is terminated by the recombination of two radicals. However, the reaction within the system continues as long as the system is irradiated with UV light, whilst the mobility within the system is retained. In the bulk, the decrease in the polymerization rate is usually caused

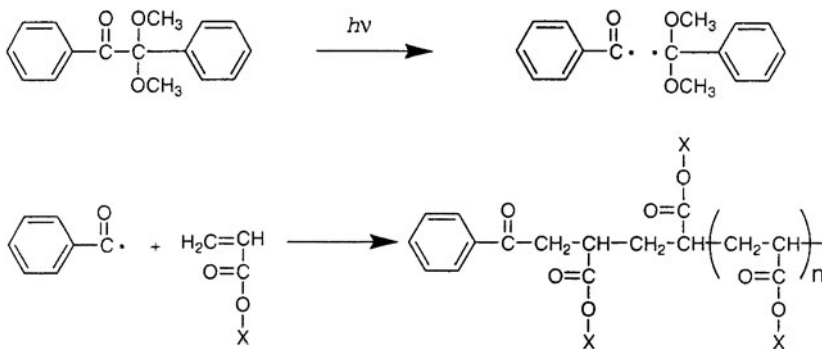


Figure 1. Schematic representation of radical initiated acrylate polymerization.

by the reduced mobility. In the case of gels, where the acrylate molecules are polymerized in the presence of a large amount of solvent, the decrease in the polymerization rate is due to the depletion of the reactive molecules within the system [2]. In these gels, the conversion of the reactive groups is almost complete except for those containing low concentrations of acrylate network.

2.3. Liquid Crystal Gels

2.3.1. Liquid crystallinity

Liquid crystals flow like a liquid while showing crystal-like properties such as birefringence [3]. In the case of rod-like thermotropics, the liquid crystal (LC) phase is usually observed as an intermediate phase between the isotropic transition point and the melting or the glass transition temperature. Figure 2 shows schematically the temperature sequence for the observation of various phases in thermotropic LC systems.

In systems showing nematic and smectic phases, the smectic phase is observed at temperatures below the nematic phase. In the nematic phase, the molecules on average tend to align with their long axis parallel to a common axis called the director (n). There is no long-range correlation between the centers of gravity of the molecules, and there is no macroscopic polarization. In the smectic phase, in addition to the orientational order, there is also a degree of lateral order and the centers of the molecules are confined to planes. As in the case of the nematic phase, smectics do not possess macroscopic polarization. In the smectic phase (S_c) where the molecules are tilted with respect to the planes, the symmetry can be broken if a molecule which is not the same as its mirror image (chiral molecule) and which has a lateral dipole, is used and ferroelectricity is induced.

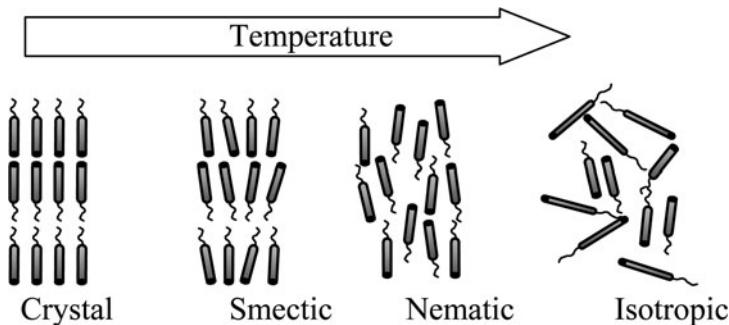


Figure 2. Schematic representations of LC sequences.

A special case of the nematic phase is the cholesteric (chiral nematic) phase. The cholesteric liquid crystal phase is obtained when a nematic phase is doped with chiral molecules. In the cholesteric phase, the director rotates about a helix with an axis perpendicular to the director. Due to the helical structure in the cholesteric phase, a band of circularly polarized light with the same sense as the cholesteric helix is reflected. This gives the colorful appearance to the cholesteric phase.

In the coming sections, various gels that can be used in obtaining various effects will be described. The effects can be used in applications such as electrically induced scattering for fast shutters, as well as switchable mirrors, and for optical elements such as gratings.

2.3.2. Types of liquid crystal gels

The most common way of inducing macroscopic orientation of LC molecules is to place them on surfaces containing uniaxially rubbed polymer layers. Cells provided with such surfaces can be filled with the monomeric LC mixture where a macroscopic orientation is induced. Another way to align LC molecules is under electric fields. After inducing macroscopic alignment, liquid crystal gels are obtained by photo-polymerization of the reactive LC in a mixture of non-reactive LC molecules. In this way, anisotropic networks containing liquid crystal molecules are produced. Various kinds of LC molecules that can be used in gel formation are shown in Figure 3.

Depending on the composition of the reactive molecules used in the production of gels, various types of gels that can be used in various applications have been demonstrated [4, 5]. Broadly, the gels can be divided into two categories: A) densely cross-linked gels; B) lightly cross-linked gels. These gels will be described before considering in detail gels obtained in various phases and the applications of these gels.

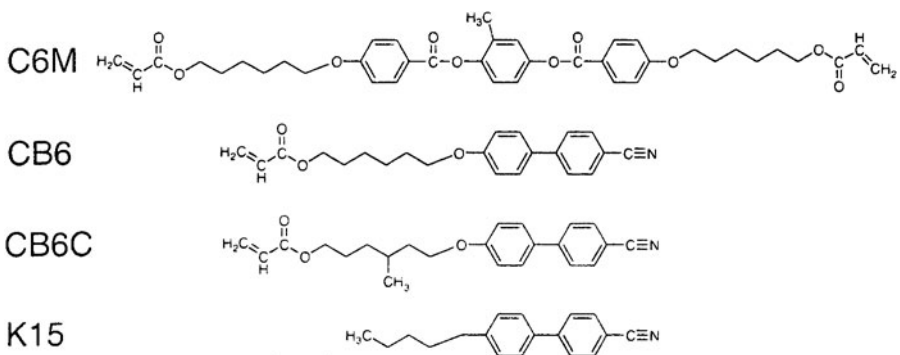


Figure 3. Some examples of reactive acrylates and a structurally related liquid crystal.

2.3.2.1. Densely cross-linked gels. Densely cross-linked gels are obtained using bifunctional reactive groups (C6M) as shown in Figure 3. Extensive studies of gels revealed that in general two types of densely cross-linked gels exist [6]. The first type of gel is considered to consist of channels of polymer networks elongated in the direction of the long axis of the network molecules. The conventional LC molecules are confined within the walls of the network. On the other hand, the second type consists of fibrillar polymer networks dispersed within the non-reactive liquid crystal. In gels of type 1, the network determines largely the behavior of the LC molecules. In this type of gel, two populations of the LC molecules, which are not chemically bonded to the network, were identified. One of the populations of LC remained ordered even above their isotropic transition temperature, while the other population behaved as in the bulk.

2.3.2.2. Lightly cross-linked gels. In display applications where high switching speeds are required, low molar mass LC molecules are used. In most display applications, the orientation of the LC from the rest state is altered by the application of an electric field. However, in some displays, the influence of the cell surfaces is not always sufficient to obtain the desired optical effects [7, 8]. In order to take over the function of the surfaces into the liquid crystal layer, lightly cross-linked gels have been developed [9]. These gels are made up of three components: conventional non-reactive LC; reactive LC of a single reactive group (monoacrylate); reactive LCs with two reactive groups (diacrylate). Figure 4 shows a schematic drawing of gel formation.

After polymerization, the mono-functional molecules become part of the network and can be switched under the influence of an electric field together

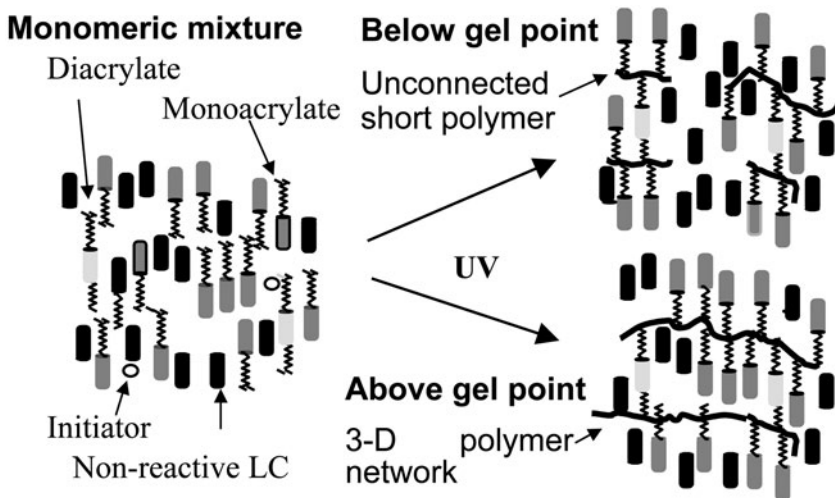


Figure 4. Schematic representation lightly cross-linked gel formation.

with low viscous non-reactive molecules. The diacrylate molecules serve as X-link points providing the system with memory and enable the rapid reversion to the initial state. In short, the network in such a gel has four functions: it provides the system with a memory and ensures that the molecules revert to the initial orientation state when the electric field is removed; transient switching states can be stabilized and various modes of switching can be obtained; it preserves the polymer structure obtained during polymerization and prevents the diffusion of the polymer; it permanently fixes the configuration of the molecules so that temperature dependence effects are removed. These gels are mainly used in the production of patterned gels for switchable gratings and cholesteric gels described below.

2.3.3. Gels obtained in various phases

2.3.3.1. Nematic gels. The electrical switching behavior of the non-reactive molecules in gels of type-1 was influenced to a larger extent than in gels of type-2. This influence of the network on the LC molecules is used in producing various effects, such as electrically induced light scattering [10, 11]. In the case of electrically induced light scattering, the presence of the network causes the LC molecules to orient in various ways in different domains upon application of an electric field, leading to large scale fluctuation in the refractive index, and hence scattering of light. In the case of uniaxially oriented planar gels, scattering of one of the polarization direction is induced. These gels are therefore suitable for switchable polarizers. However, when the gels are homeotropically (perpendicular to the cell surfaces) oriented and LC molecules with a negative dielectric anisotropy are used, very fast switching polarization independent shutters can be produced. Such shutters can have applications, such as in camera modules where artifacts due to the presence of an intense light spot can be eliminated using such fast shutters.

Gels can also be used in the replication process of various structures such as lenses and gratings. Such gels show good matching of the refractive indices of a liquid crystal and its temperature dependence. Thus, such gels are suited in the manufacture of switchable gratings and lenses [12].

2.3.3.2. Cholesteric gels. The presence of the helical arrangement of molecules leads to optical effects unique to the cholesteric phase [3]. For example, extreme optical rotary dispersion is observed as a band of circularly polarized light having the same sense as the cholesteric helix is reflected at the normal, while the band with the opposite sense is transmitted. The upper (λ_{\max}) and lower (λ_{\min}) boundaries of the reflected band are $\lambda_{\max} = p * n_e$ and $\lambda_{\min} = p * n_o$, respectively, where p is the cholesteric pitch corresponding to the length over which the director rotates 360° , and n_e and n_o are the

extraordinary and the ordinary refractive indices of a uniaxially oriented phase, respectively. The pitch is determined by the concentration of the chiral component and decreases with an increasing chiral fraction. These properties of cholesterics make them suitable for use in switchable optical components, such as reflectors, polarizers and band-pass and notch filters [13]. However, reversible switching of cholesterics between defect-free reflecting (Grandjean texture) and transparent homeotropic textures is difficult to attain. In a uniform planar orientation (Grandjean texture) between two substrates, a short-pitch cholesteric phase can show specular reflection in the visible wavelength range. Application of an electric field across such a layer causes the rotation of the cholesteric helix to lie in the cell plane and assume a light-scattering planar conical state. Further increase in the voltage leads to a homeotropic alignment. Reducing the electric field slowly leads to a light scattering focal-conic texture. Fast removal of the electric field can, however, lead to the recovery of the Grandjean texture with defects. Using the lightly cross-linked gels described in Section 2.3.2.2, cholesteric gels, which can switch fast between transparent and specularly reflecting states have been demonstrated [14, 15]. In these gels the lightly cross-linked network performs a memory function. Using this property of the gels, a simple display containing pixels reflecting various colors has also been demonstrated [16]. Furthermore, a memory effect was also applied in order to create a pitch gradient along the cell and gels reflecting white light were produced [9].

2.3.3.3. Patterned gels. In the gels described above, the network determines the switching behavior, configuration of the molecules, and their orientation. During the production of gels, photo-induced polymerization can be used to structure the gels in various ways, including lateral directions. The threshold voltage (V_c) of a uniaxially oriented system is given by the equation below.

$$V_c = \pi(K_1/\varepsilon_0\Delta\varepsilon)^{0.5} \quad (1)$$

K_1 is the splay elastic constant, ε_0 is the permittivity of the free space, and $\Delta\varepsilon$ is the dielectric anisotropy of the material. In lightly cross-linked gels, for example, the threshold voltage for switching can be influenced by the network which increases K_1 . It has been demonstrated that the threshold voltage remained constant up to a certain cross-link (diacrylate) concentration, above which the threshold voltage rapidly increased. The fact that the threshold voltage shows an increase above a critical concentration indicated that the elastic constant shows an increase above this concentration, corresponding to the gel-point of the system. At this concentration, the side-chain polymers formed by the monoacrylate molecules cross-linked by the diacrylate molecules create a three-dimensional network. In the schematic representation shown in Figure 4,

it can be seen that the factors influencing the gel-point are the cross-link density and the kinetic chain length of the linear molecule. The cross-link density is determined by the concentration of the diacrylate molecules within the system while the kinetic chain length is determined by various other parameters, such as the concentration of the monoacrylate, initiator concentration, and the intensity of UV light used to initiate polymerization.

Patterned illumination therefore can be used in the production of various switchable optical components such as gratings, zone plates, and lenses without needing to pattern the electrodes. Here, we describe how a switchable grating can be manufactured [17]. For this purpose, cells with transparent electrodes were used and irradiated with UV in two stages. In the first stage, the mixture was irradiated through a mask containing ruled gratings. In the second stage, the mask was removed and the whole cell was exposed to flood radiation. Two effects play a role in this process: 1) in the first step, the gel becomes polymerized in the irradiated areas, causing the diffusion of reactive groups to these areas; 2) in the second step, all of the molecules in the system are polymerized. As the first step is limited by diffusion, the reactive mixture has to be irradiated at a low intensity in the first step and a high intensity in the second step when large structures have to be produced. Figure 5 shows an optical photograph of the grating in “on” and “off” states. The transparent areas of the mask, where polymerization took place during the first stage of UV radiation, led to the formation of a network within the gel with a high threshold voltage. This is the reason why when an electric field was applied across the gel, these areas do not switch, and only the areas that were irradiated during the second stage of UV radiation start to switch. Such gratings can be used in optical storage read out units schematically also shown in Figure 5.

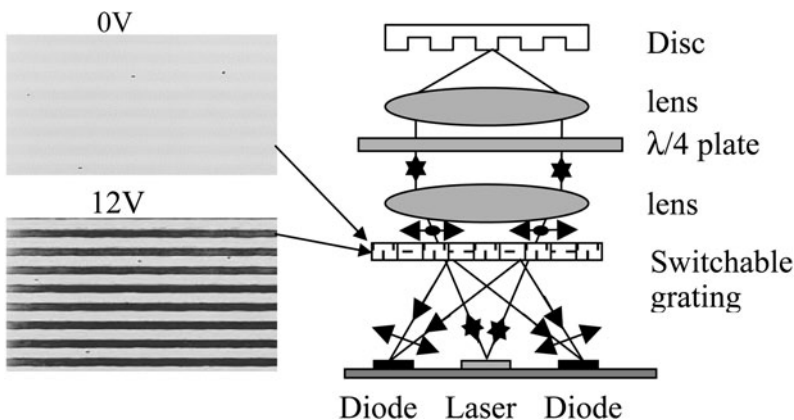


Figure 5. Photographs of patterned gel shown together with the optical unit.

2.4. Ion Conducting Gels

Ion conductors are of great interest because they are used in many applications such as electrochromic devices, fuel cells, photoelectric cells and batteries [18]. In these applications, electrolytes perform essential functions and facilitate the transport of ions. As applications where the ion conductors are used become more complex, ion conductors are required to perform more functions. For example, in applications which are described below, it will become clear that electrolytes should not only be good ion conductors, they also must function as separators as well as adhesives with mechanical integrity.

Some topics related to ion-conducting gels are found in Chapters 23 and 24, also.

2.4.1. Various applications of ion conductors

2.4.1.1. Batteries. In a battery, electrochemical energy is converted into electrical power [19]. The operation of a lithium ion battery is schematically represented in Figure 6. The battery consists of a negative electrode (the anode) and a positive electrode (the cathode), which are traditionally held apart by a microporous separator immersed in a liquid ion conductor (electrolyte). During the charging of the battery, electrons flow outside the battery from the cathode to the anode while the ions move inside the cell. Discharging of the battery occurs when the cell is short-circuited using a load, and the flow directions of the electrons and the ions become reversed.

For fast charging and discharging of batteries, it is important to have low internal resistance. It is therefore necessary to have highly ion conducting

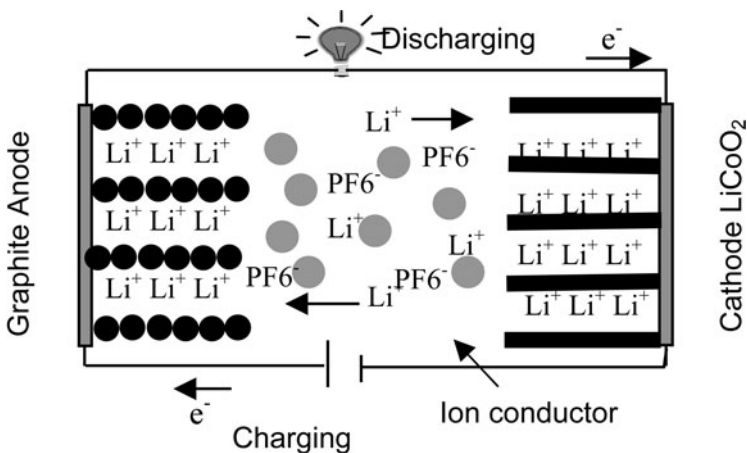


Figure 6. Schematic representation of working of a lithium ion battery.

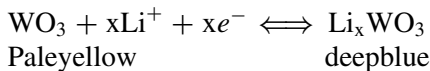
electrolytes. It is also desirable to have a thin separator between the anode and the cathode of the battery. It is for these reasons that there is an intensive search for ion conductors with high ion conductivity as well as good mechanical stability.

Today, there are 3 separator/electrolyte technology options for the Li-ion batteries. In Li-ion batteries in a metal can, a liquid electrolyte is used together with a microporous separator based on polyethylene (PE) or polypropylene (PP). In Li-ion batteries in a soft pack (a PE/Al/PE foil), the separator is in some cases combined with a gelled electrolyte. The advantage of the gelled electrolyte is seen in the low vapor pressure at elevated temperatures and increased overcharge resistance. The mechanical properties of the gel are of limited importance as the separator separates the electrodes. This is the most common application of gelled electrolyte. A third possibility is the applications of gelled electrolytes with sufficient mechanical strength to omit the PE or PP separator.

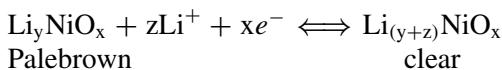
2.4.1.2. Electrochromic devices. Electrochromic materials [20, 21] show color changes during or as a result of an electrochemical reaction. Such materials can be used in the production of devices such as large displays, anti-glare rear-view mirrors, and windows for energy control. In a basic configuration, an electrochromic cell consists of two electrodes separated by an electrolyte and works like a rechargeable battery. Electrochromic materials are either dissolved in the electrolyte or placed on top of the electrodes. Three major categories of materials have been studied for their electrochromic properties. The first class of materials is molecular dyes which can be dissolved in the electrolyte. However, these systems suffer from reversibility and stability. Furthermore, they lack bistability. The second class of materials is metal oxides. They are prepared usually from tungsten, nickel or molybdenum. Conducting polymers such as derivatives of polypyrroles, polyanilines and polythiophenes form the third class of electrochromic materials. Electrochromic devices can work either in the transmissive or reflective modes. In the reflective mode, one of the electrodes needs to be transparent while the other electrode is reflective. In such a configuration, a transparent electrolyte needs to be used. When a highly light scattering electrolyte is used, it is also possible to use an absorbing electrode. Again in the reflective configuration, the redox reaction taking place at the transparent electrode must be between transparent and colored states while when a scattering electrolyte is used, the redox reaction taking place at the counter electrode may take place between any states. It can be the reduction and oxidation of metal ions. In the case of a transmissive electrochemical cell, the electrolyte needs to be clear. Furthermore, complementary reactions need to take place at the electrodes, so that in the colored state of the cell reduction at one of the electrodes leads to decoloration, whereas at the counter electrode

the oxidation reaction should not induce color change in the visible range. Nickel oxide and tungsten oxide are the most common redox couples used in electrochromic devices as described in the schemes shown below.

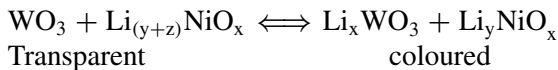
For tungsten oxide, the reversible insertion of lithium ions produces



And lithylated Nickel oxide electrode produces



Which leads to



In electrochromic cells, the speed of switching to a large extent is determined by the conductivity of the electrolyte. Patterned electrolytes are also desirable since they simplify the manufacturing process in display applications where a certain pattern needs to be switched “on” and “off”. In these devices, as explained above, there is also need for electrolytes which scatter light. In the case of flexible electrochromic cells, use of gelled electrolytes enables the lamination of the layers for easy manufacture of such devices.

2.4.1.3. Electrochemical luminescence. Electro-generated chemiluminescence (ECL) involves the production of light by the electron transfer reactions between electro-generated species [22]. Typically the excited states are produced by an electron-transfer reaction between an oxidized species (radical cation) and reduced species (radical anion), both of which are generated at an electrode by an alternative pulsing of the electrode potential. Alternatively the excited state can be produced in a single potential step. In the case of conducting polymers, a blend or a gel is produced using an ion conductor. A mechanism of operation of such a device is illustrated in Figure 7.

Upon initial application of voltage, the anions move towards the anode. At the same time, electrons are removed from the polymer as it becomes oxidized. This results in a p-doped polymer. In the same way, the polymer at the cathode is reduced to give n-type conductor with the cations acting as counter charges. At the interface of n- and p-doped regions, excitons can form leading to emission of light. Highly efficient devices operating at low voltages based on this technology have already been demonstrated. These devices work much like organic light emitting devices. However, as opposed to such devices, the thickness of the layer does not need to be a few hundred nanometers but can be several microns, making the manufacturing process much easier.

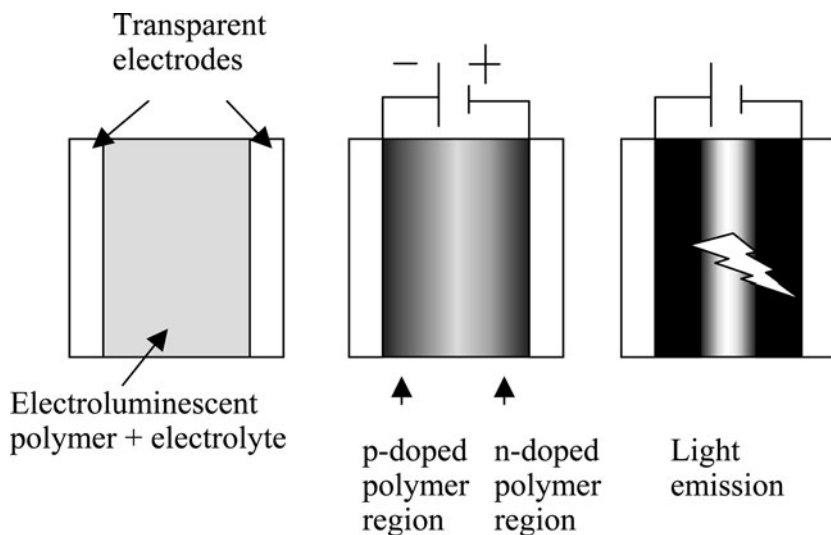


Figure 7. Operation of an electro-chemiluminescent device.

Furthermore as opposed to conventional organic light emitting diodes (OLED) devices where highly moisture-sensitive low-work-function cathodes are used, any metal regardless, of its work function, can be used in ECL cells. In such devices, again, it is important to have ion conductors with high conductivity to obtain fast turn-on times. The morphology of the gel/blend is also very important. Best results have been obtained using fine interpenetrating phases of ion conductor and polymer.

2.4.1.4. Photoelectric devices. Light induced redox reactions in nanocrystalline systems form the basis for the operation of photocells. There is variety of photoelectric cells. Here we consider an example using an electrolyte [23]. A schematic drawing of such a cell is shown in Figure 8.

In this cell, the surface of titanium oxide (TiO_2) nanoparticles is covered by a dye such as a ruthenium complex. Upon excitation with light the electrons are excited to the LUMO level of the dye from where they can be injected into TiO_2 . In the cell, a LiI containing electrolyte, which works as a redox shuttle, is also used. At the TiO_2 electrode, an electron is transferred to the dye as I^- is oxidized to I_3^- and at the counter electrode, I_3^- is reduced to I^- . Highly efficient photocells working on this principle have been demonstrated. However the presence of liquid electrolytes in such systems is considered to be one of the disadvantages. Here again gelled electrolytes with high ion conductivity for drawing high currents from such cells are expected to offer significant improvements.

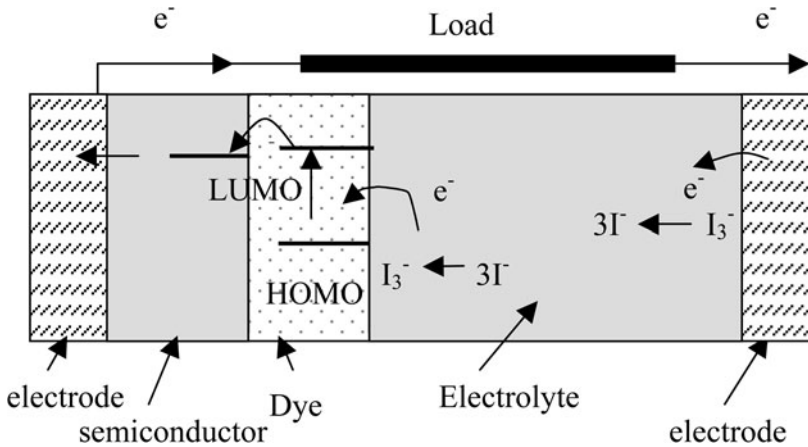


Figure 8. Operation of a photoelectric cell.

2.4.2. Properties of ion conductors

Before describing the properties of such gels, it is important to consider various physical parameters, such as conductivity which is important in the applicability of the ion conductors. Electrolytes are obtained by dissolving salts in organic solvents. The conductivity σ of an electrolyte can be expressed as in Eq. (2):

$$\sigma = \sum_i n_i q_i \mu_i \quad (2)$$

n is the number, q is the charge and μ is the diffusion constant of i type charge carriers; high conductivity requires a high concentration of fully dissociated ions with a high mobility.

Here we first consider the solvation mechanism in electrolytes. A solvent will dissolve an inorganic salt if the total energy of the system (Gibbs free energy) is decreased. The change in the Gibbs free energy (ΔG) can be written as in Eq. (3) where:

$$\Delta G = \Delta H - T \Delta S \quad (3)$$

T is the absolute temperature and ΔH and ΔS are the changes in the enthalpy and the entropy, respectively. Dissolution of the salt increases the entropy of the cation and the anion, but co-ordination of the solvent molecules by the cation decreases the entropy of the solvent. In the case of polymers, cations form pseudo- cross-links and thus reduce the entropy of the system. Therefore, the net change in the entropy upon dissolution of salt molecules in high molecular

weight polymers is usually positive, regardless of the type of salt. The enthalpic change is however very dependent on the type of solvent and the salt interactions. One of the approaches used to promote dissolution is to use large salt molecules with low lattice energies.

Dissolution of the salt molecules does not always lead to the formation of free ions. In poor solvents, extensive ion pairing occurs even in dilute solutions. With increasing solvent quality, ion association occurs at higher ion concentrations. In such systems, fully dissociated (free) ions, neutral ion pairs and ion clusters with a net charge exist. The state of the ions can be determined using various techniques such as infrared and Raman spectroscopy.

The other factor on which the conductivity depends is the mobility of the ions. The mobility is dependent on the size of an ion and the free volume within the system. Einstein's relationship between the mobility of an ion with a charge q and the diffusion coefficient D is given in Eq. (4):

$$\mu = \frac{qD}{kT} \quad (4)$$

k is the Boltzmann constant. In ionic crystals, ions are in an array of energetically equivalent sites which are partially occupied. If the vacancy is in a potential well, the ions need to overcome the potential barrier ΔH during their thermal motion in order to be able to move to another site and the self-diffusion coefficient can be written as in Eq. (5):

$$D = D_0 \exp(-\Delta H/kT). \quad (5)$$

This equation implies that a plot of $\log(D)$ versus $1/T$ should be a straight line. However, in the case of organic electrolytes close to their glass transition temperature, substantially curved lines have been observed. This indicates that the behavior of the organic electrolytes cannot be described in terms of a thermally activated process with a single activation energy. In liquid electrolytes, the motion of the ions is coupled to the movement of the liquid molecules, whereas in polymers the segmental motion of the polymer determines the ionic mobility. For this reason, the viscosity of liquids and the storage modulus of polymers have been considered in attempts to explain the ion conductivity in such systems. The Stokes-Einstein's relation relates the diffusion constant of an atom with a radius r to the viscosity η of a liquid as in Eq. (6):

$$D = \frac{kT}{6\pi\eta r}. \quad (6)$$

By combining Eqs. (4), (5) and (6), the conductivity can be rewritten as in Eq. (7):

$$\sigma = \frac{nq^2}{6\pi\eta r}. \quad (7)$$

The temperature dependence of the viscosity is, in turn, described using free volume theory [24] which relates the viscosity to the free volume vf as in Eq. (8):

$$\eta = A \exp(\gamma vc/vf) = A \exp \left[\frac{\gamma}{\alpha(T - T_o)} \right] \quad (8)$$

A is a constant and γvc is a dimension corresponding roughly to the volume of the diffusing molecule. T_o is the temperature at which the free volume disappears. T_o lies approximately 50°C below the glass transition temperature ($T_o = T_{gl} - 50$). The free volume dependence of the temperature is then given by $vf = v\alpha(T - T_o)$. Using the theory of Choen and Turnbull [24], a modified free volume theory [25] has been established which relates the conductivity to the free volume and the fraction of the components within the system as in Eq. (9):

$$\sigma = BCX \exp(-\gamma vc/vf) \quad (9)$$

B is a constant, C is the concentration of salt molecules and $(1 - X)$ is the fraction of the polymer within the system. This equation is used for mixed systems containing low molar mass solvents as well as polymer. The free volume is then defined as $vf = (v - vg)$, where v is the volume measured at a given temperature and vg is the average volume of the system at its glass transition point (i.e., the temperature at which long-range diffusion within the system vanishes). This volume is related to the van der Waals volume (vw), approximated as $vg = 1.45vw$. This equation has been used successfully to construct master curves relating the conductivity to the free volume within various systems.

Impedance spectroscopy is often used in order to measure average conductivity. However, an important requirement for electrolytes in applications such as batteries, besides high conductivity, is a high transport number for cations such as lithium. The transport number for lithium, defined as $t^+ = D^+ / (D^- + D^+)$ can be estimated from the diffusion coefficients, D^- and D^+ , for anions and cations, respectively. When an ion conductor with a low Li transport number is used, concentration gradients build up during the charge/discharge of a battery. This results in an undesirable internal potential.

2.4.3. Gel electrolytes with chemical cross-links

Gel electrolytes can be obtained easily by mixing liquid electrolytes in polymerizable molecules. Polymerization of such a system results in a three-dimensional network containing liquid electrolyte (gel electrolyte). Depending on the solvent and the type of acrylate used, the gels obtained may be homogeneous (single-phase gels) or phase-separated. It is also possible to produce gels with a concentration gradient along the thickness and also in lateral directions. Various properties of these gels are described below.

2.4.3.1. Single phase gels. In the case of homogeneous gels, the polymer network is homogeneously dispersed. Such gels are highly transparent and, depending on the polymer concentration, can also show high mechanical stabilities [25, 26]. A common monomer used in the production of such gels is polyethylene glycol diacrylate (PEGDA, $\text{CH}_2=\text{CH}-\text{COO}-(\text{CH}_2\text{CH}_2\text{O})_n-\text{CO}-\text{CH}=\text{CH}_2$). Such polymers interact well with the salt and with many polar solvents, giving rise to single-phase gels. In Figure 9, conductivity of mixtures containing various amounts of PEGDA ($n = 9$) in liquid electrolyte (1 mol LiPF_6 in propylene carbonate (PC)) is shown before and after polymerization as function inverse temperature [25].

After polymerization of the acrylates in the mixtures to form gels, conductivity decreases. These decreases can be explained in terms of the free volume theory described above. Using the van der Waals volumes and the measured densities of the samples, σ/CX was plotted as a function of the inverse free volume per unit mass for mixtures before and after polymerization [25] (Figure 10).

The points obtained for the monomer and the polymer lie on a single line for a given concentration. This indeed shows that the reduction in the free volume within the system is responsible for the decrease in the conductivity during polymerization. However, the free volume theory does not take into account the specific interactions within the system such as the preferential co-ordination of Li^+ by polyethers. Because the long-distance movement of polyether chains would be prevented by polymerization, the diffusion of Li^+

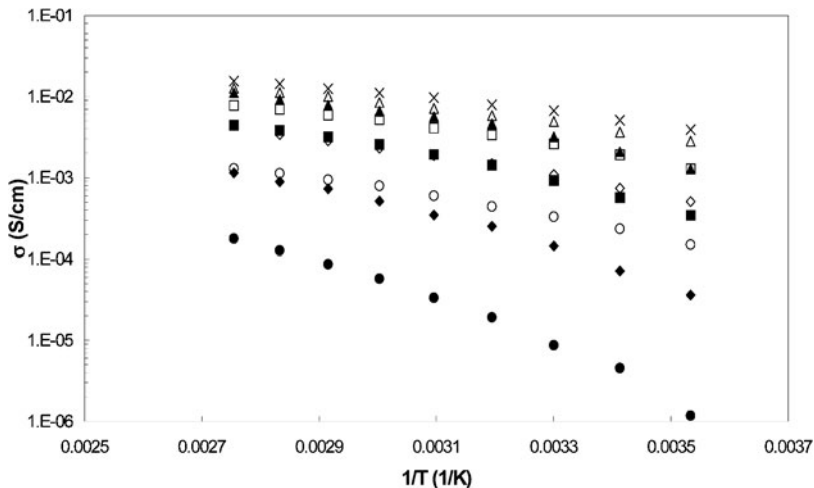


Figure 9. Arrhenius plot of the ionic conductivity for mixtures containing various amounts of PEGDA ($n = 9$) before (open symbols) and after (filled symbols) polymerization. \times = Liquid electrolyte, Δ = 20%, \square = 40%, \diamond = 60%, \circ = 80% by wt.

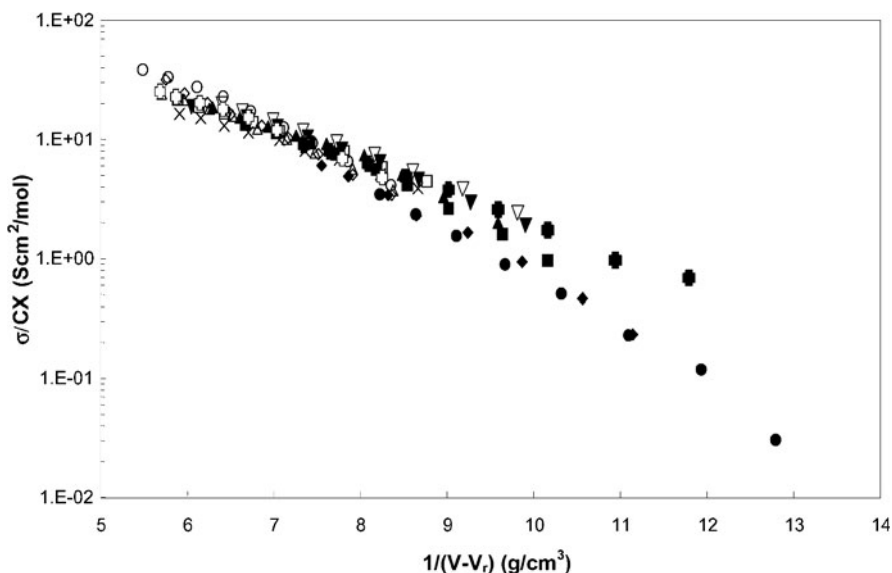


Figure 10. σ/CX as a function of inverse free volume per unit mass for mixtures containing various amounts of PEGDA ($n = 9$) before and after polymerization. \times = Liquid electrolyte, Δ = 20%, \square = 40%, \diamond = 60%, o = 80%, ∇ = 40% PEGDA ($n = 3$), \square = 40% PEGDA ($n = 45$). Open symbols are before polymerization and closed symbols are after polymerization.

would also be expected to decrease accordingly. The points corresponding to the monomeric mixture and the polymer should hence not lie on a single line at a given composition. The fact that they do indicates that the diffusion of lithium is already retarded before polymerization and the mobility of PF_6^- is much higher than that of Li^+ . Diffusion constants of various components in such gels can be determined using pulse field gradient nuclear magnetic resonance [27].

Table 1 shows the results for various gels before and after polymerization.

Li^+ , the smallest particle in the system, has the lowest diffusion coefficient. This is associated with an increased hydrodynamic radius of the Li^+ ion as a result of association with the solvent molecules and/or polyether chains. The diffusion coefficient of Li^+ also decreases with increasing molecular weight of PEGDA, while the diffusion coefficients of PC and PF_6^- remain almost unchanged. This indicates that the lithium ions are to a large extent coordinated by the PEGDA molecules rather than PC. This is even more evident after polymerization where long-range diffusion of the polymer stops and the diffusion coefficient of lithium decreases. On the other hand, the diffusion coefficient of PC is almost the same after polymerization while that of the PF_6^- is lower. This indicates a strong interaction within the PEGDA gels, which influences the motion of the lithium and PF_6^- ions, but the diffusion of PC is retarded to a much smaller extent.

Table 1. Diffusion constants for various components at room temperature of various systems containing 40% acrylate (Mon = monomer; Pol = polymer).

Acrylate	State	$D(\text{Ac})$ (cm^2/s)	$D(\text{PC})$ (cm^2/s)	$D(\text{Li}^+)$ (cm^2/s)	$D(\text{PF6}^-)$ (cm^2/s)	σ mS/cm	t^+
No acrylate	Mon	n.a.	17×10^{-7}	7.5×10^{-7}	15×10^{-7}	5.9	0.34
C10	Mon	8.4×10^{-7}	17×10^{-7}	6.1×10^{-7}	12×10^{-7}	3.59	0.33
C10	Pol	n.d.	4.5×10^{-7}	3.1×10^{-7}	6.1×10^{-7}	1.81	0.34
PEGDA ($n = 9$)	Mon	4.8×10^{-7}	15×10^{-7}	3.5×10^{-7}	11×10^{-7}	2.2	0.07
PEGDA ($n = 9$)	Pol	n.d.	15×10^{-7}	0.09×10^{-7}	2.9×10^{-7}	0.7	0.3

2.4.3.2. Phase-separated gels. Phase-separated gels are formed when a low polarity diacrylate such as decanediol diacrylate (C10, $\text{CH}_2=\text{CH}-\text{COO}-(\text{CH}_2)_{10}-\text{OOC}-\text{CH}=\text{CH}_2$) is used [28]. In the monomeric state, the acrylate is miscible with the electrolyte. Polymerization causes phase separation due to the lowered entropy, and the gels become translucent and gave rise to light scattering.

In two-phase gels, the conductivity is mainly determined by the polymer-poor phase. As in single-phase gels, the conductivity of the phase-separated gels was lower than in the corresponding monomeric state. However, the conductivity change in phase-separated gels is explained more easily by the phase behavior than the free volume theory. In the polymer-poor phase (liquid electrolyte phase) within the gels, the conductivity can be considered the same as the bulk conductivity of the liquid electrolyte. In the polymer-rich phase, electrolyte is also present but the conductivity is reduced. As a result, the net conductivity decreases with increasing polymer concentration.

The main difference between the single-phase and phase-separated gels becomes apparent when the diffusion constants of various components are compared in Table 1. There are only slight changes in the diffusion constants of various components and the diffusion coefficient of lithium, and its transport number remains almost unaltered after polymerization. This is due to a low degree of interaction between the polymer and the lithium ions. In phase-separated gels, the lithium ions are still very mobile making the gels suitable for applications where not only high conductivity but a high transport number for the cation is required.

2.4.3.3. Structured ion-conducting gels. There is a demand for gels with specific internal structures. In the case of electrochromic devices, anisotropic ion conduction is desired. In the case of multiplexed electrochromic displays where electrodes cross each other, it is desired to pattern electrolytes laterally where highly ion conduction domains are separated from each other by low ion conducting walls. In the case of batteries, there is a demand for an electrolyte with a gradient along the thickness of the electrolyte so as to have a thin layer

at one of the sides to suppress so-called dendrite formation, whereas in the rest of the electrolyte, conductivity is very high.

For the purpose of controlling the distribution of the polymer within these gels, the polymerization rate was adjusted to enable the reacting polymer to diffuse. The easiest way of influencing the polymerization rate is by changing the intensity of the UV light, which is used to induce polymerization. The reaction rate decreases with decreasing UV intensity. This dependence of the polymerization rate on the intensity of the UV light can be used to produce systems with a specific polymer distribution. Simply by irradiating a mixture containing reactive molecules through a mask, local variations in the plane of the film can be created [29]. Initiation of polymerization in the irradiated areas causes the depletion of the molecules in these regions. As a result, reactive molecules diffuse into these regions from the areas not exposed to UV light, resulting in higher polymer concentrations in the irradiated regions. The mask is subsequently removed and the system is subjected to flood exposure in order to polymerize all the reactive molecules in the system. In this way an ion-conducting layer consisting of channels with high ion conductivity surrounded by thin walls with lower conductivity was obtained.

References

- [1] K. Kajiwara, Y. Osada, Eds., *Gels Handbook; Vol. 3: Applications*, **2001**; London: Academic Press.
- [2] Kloosterboer, J.G. "Network formation by chain crosslinking photopolymerization and its applications in electronics", *Adv. Polym. Sci.*, **1988**, *84*, 1–61.
- [3] Goodman, L.A. In *Introduction to Liquid Crystals*, E.B. Priesly, P.J. Wojtowicz and P. Sheng, Eds. **1974**, London: Pendulum.
- [4] Hikmet, R.A.M.; Lub, J. "Anisotropic networks and gels obtained by photopolymerization in the liquid crystalline state: synthesis and applications", *Prog. Polym. Sci.*, **1996**, *21*, 1165–1209.
- [5] Hikmet, R.A.M.; Lub, J. Maassen van den Brink, P. "Structure and mobility within anisotropic networks obtained by photopolymerization of liquid crystal molecules", *Macromolecules*, **1992**, *25*, 4194–4199.
- [6] Hikmet, R.A.M. "Anisotropic gels and plasticised networks formed by liquid crystal molecules", *Liq. Cryst.*, **1991**, *9*, 405–416.
- [7] Gerber, P.R.Z. "Voltage-induced cholesteric structure transformation in thin layers", *Naturforsch.*, **1981**, *36a*, 718–726.
- [8] Schadt, M.; Gerber, P. "Dielectric, electrooptical and phase-change properties of liquid crystal guest-host displays", *Mol. Cryst. Liq. Cryst.*, **1981**, *5*, 241–263.
- [9] Hikmet, R.A.M.; Kemperman, H. "Electrically switchable mirrors and optical components made from liquid-crystal gels", *Nature*, **1998**, *392/2*, 476–479.
- [10] Hikmet, R.A.M. "Electrically induced light scattering from anisotropic gels", *J. Appl. Phys.*, **1990**, *68*, 4406–4412.
- [11] Hikmet, R.A.M. "Electrically induced light scattering from anisotropic gels with negative dielectric anisotropy", *Mol. Cryst. Liq. Cryst.*, **1992**, *213*, 117–131.

- [12] Stallinga, S.; Vreken, J.J.; Wals, J.; Stapert, H.; Versteegen, E. "Liquid crystal aberration compensation devices", *Proceedings of SPIE-The International Society for Optical Engineering*, **2000**, 4081, (Optical Storage and Optical Information Processing), 50–59.
- [13] Kelker, H.; Hatz, R. *Handbook of Liquid Crystals*, **1980**, Weinheim: Verlag Chemie.
- [14] Hikmet, R.A.M.; Kemperman, H. "Switchable mirrors of chiral liquid crystal gels", *Liq. Cryst.*, **1999**, 26, 1645–1653.
- [15] Hikmet, R.A.M.; Zwerver, B.H. "Structure of cholesteric gels and their electrically induced light scattering and color changes", *Liq. Cryst.*, **1992**, 12, 319–336.
- [16] Hikmet, R.A.M.; Polesso, R. "Patterned multicolor switchable cholesteric liquid crystal gels", *Adv. Mater.*, **2002**, 14, 502–504.
- [17] Hikmet, R.A.M.; Pools, H.L. "An investigation of patterning anisotropic gels for switchable recordings", *Liq. Cryst.*, **2000**, 27, 17–25.
- [18] Scrosati, B. *Applications of Electroactive Polymers*, **1993**, London: Chapman and Hall.
- [19] Gray, F.M. *Solid Polymer Electrolytes*, **1991**, Weinheim: VCH.
- [20] Monk, P.M.S.; Mortimer, R.J.; Rosseinsky, D.R. *Electrochromism: Fundamentals and Applications*, **1995**, Weinheim: VCH.
- [21] Kurunathan, K.; Murugan, A.V.; Marimuthu, R.; Mulik, U.P.; Amalnerkar, D.P. "Electrochemically synthesized conducting polymeric materials for applications towards technology in electronics, optoelectronics and energy storage devices", *Mater. Chem. Phys.*, **1999**, 61, 173–191.
- [22] Pei, Q.; Yu, G.; Zhang, C.; Yang, Y.; Heeger, A.J. "Polymer light emitting electrochemical cells", *Science*, **1995**, 269, 1086–1088.
- [23] Hagfeld, A.; Gratzel, M. "Light induced redox reactions in nanocrystalline systems", *Chem. Rev.* **1995**, 95, 49–68.
- [24] Cohen, M.H.; Turnbull, D.J. "Molecular transport in liquids and gases", *Chem. Phys.*, **1959**, 31, 1164–69.
- [25] Hikmet, R.A.M.; Peeters, M.P.J. "A study of the effect of the polymer network and the solvent on the ion conductivity in gels", *Solid State Ionics*, **1999**, 126, 25–39.
- [26] Ballard, D.G.H.; Cheshire, P.; Mann, T.S.; Przewoski, J.E. *Macromolecules*, **1990**, 23, 1256–1263.
- [27] Hayamizu, K.; Aihara, Y.; Arai, S.; Price, W.S. Diffusion, conductivity and DSC studies of a polymer gel electrolyte composed of cross-linked PEO, *gamma*-butyrolactone and LiBF₄, *Solid State Ionics*, **1998**, 107, 1–12.
- [28] Hikmet, R.A.M.; Peeters, M.P.J.; Lub, J.; Nijssen, W. "Physical properties and battery performance of novel two-phase ion-conducting gels", *J. Electrochem. Soc.*, **1999**, 146, 2397–2403.
- [29] Hikmet, R.A.M.; Michels, I. "Novel Lithium-ion conducting gels with a tailor-made concentration gradient and their use in secondary lithium metal batteries", *Adv. Mater.*, **2001**, 13, 338–341.

Chapter 23

ELECTRON CONDUCTING AND MAGNETO-SENSITIVE GELS

Frédéric Fages

*GCOM2 UMR CNRS 6114, Université de la Méditerranée, Faculté des Sciences de Luminy,
13288 Marseille Cedex 9, France*

1. Introduction	793
1.1. Electron Conduction in Conducting Polymers	794
1.2. Conducting Gels	798
2. Molecular Gels as Templating Media for Electronic Materials	805
2.1. Polymerizable LMOGs	806
2.2. Templating of Inorganic Structures	806
2.3. Spatial Organization of Semiconductor Nanoparticles	808
3. Magnetosensitive Gels	808
4. Conclusions and Perspectives for the Future	810

1. Introduction

The supramolecular nature of gels from low molecular-mass organic gelators (LMOGs) renders them unique materials for electronic and magnetic applications. The self-recognition and self-assembly processes responsible for gelation provide a means to control the spatial arrangement of individual molecular components within fibrillar aggregates. These are the organizational factors that govern the extent of long-range charge delocalization or magnetic interactions and lead to more efficient materials with enhanced device performance. A few gelator molecules with tailored features that allow access to materials with charge transport properties have been reported. Examples of magnetic molecular gels are even less common. Among the many features of molecular gels, the possibility to host metal nanoparticles or to template the formation of inorganic semiconducting nanostructures represent challenging opportunities to create novel functional materials. In this chapter, we describe some of the

current issues in the field and outline future prospects. The discussion includes polymeric counterparts of LMOGs because the state of the art for long range electron conduction with polymer assemblies is far ahead of those with LMOGs at the time of this writing.

1.1. Electron Conduction in Conducting Polymers

1.1.1. General aspects

Conductive polymers encompass a very broad variety of molecular materials that fall into two main categories. The first consists of redox polymers containing covalently-linked pendant groups that are electrochemically reactive. They allow the formation of polymeric membranes in which chemical or biochemical species (e.g., cofactors, enzymes, proteins, DNA, etc.) can be immobilized. An oversimplified description of the overall charge transport phenomena in redox polymers points to the occurrence of both electron self-exchange between neighboring oxidized and reduced sites and ion motions between the redox membrane and the contacting electrolyte. Under certain conditions, particularly in the absence of conjugation between pendant groups, the dominant factor to account for efficient electrochemical charge transport within the mixed-valence states of the polymer is the segmental mobility of the macromolecular scaffold. The higher the mobility, the higher the rate of collisions between electron donor and acceptor sites that lead to electron-transfers. Redox polymer coated electrodes were first investigated for electrochromic and electrocatalytic applications [1]. The development of biosensors and biofuel cell elements for chemical-to-electrical energy conversion is currently giving a new impetus to the design of additional materials [2].

The second class consists of π -conjugated polymers. They have great scientific and commercial interest, as witnessed by the huge volume of literature on the subject [3]. In contrast to the first class, conjugated polymers possess a highly delocalized π -electron system whose electrical conductivity can be tailored from the semiconducting to the metallic regime by selective doping. Owing also to their low cost and ease of processing and fabrication, these materials are destined to play a crucial role in tomorrow's electronics.

The following summarizes some of the most important characteristics of charge transport phenomena in conjugated polymers and their gels.

1.1.2. Charge transport in conjugated polymers

Electronic properties of conjugated polymers, as quasi one-dimensional systems have been investigated extensively. A large number of theoretical

treatments on the nature of the charge carriers and the mechanisms of transport have appeared [3, 4].

A simple electronic description of conjugated polymers is based on the consideration of two electronic bands, the valence and the conduction bands, provided that the effective conjugation length is “infinite”. The valence band originates from the highest occupied molecular orbitals (HOMOs) of the interacting unsaturated monomeric units; the conduction band is from the lowest unoccupied levels (LUMOs). The band gap, that is the energy difference ΔE between these bands, is an important feature that can explain many of the physical properties. Most conjugated polymers display a large band gap ($\Delta E > 1$ eV) and, as a result, are insulating or, at best, semiconducting. When they undergo redox reactions, the conductivity of conjugated polymers can be drastically increased, reaching metal-like values at high charging levels.

The soliton model involves neutral radicals or charges without spin as charge carriers and it is useful in the low-doping regime. Thus, although it can be applied to polyacetylene, it is not appropriate to describe many other conducting polymers. For most of the latter that display non-degenerate ground-states, the doping process leads to the formation of charged radicals (polarons) or spinless charged states (bipolarons) depending on the extent of charging. Charge injection into the π -chain also leads to a profound change of geometrical structure (affecting bond lengths and torsional angles). This is due to electron-lattice interactions that strongly favor localization of the polarons to a segment defined by a limited number of monomeric subunits. Particularly in one-dimensional systems, the effect of electronic state confinement is enhanced by disordering effects, such as structural and/or conformational inhomogeneities. As a result and as expected in the case of non-crystalline media, charge transport and recombination occur in conjugated polymers via hopping among the localized states.

Solid-state conductivity in doped three-dimensional samples is a macroscopic solid-state property. It depends on the structure of the polymer, the nature of the charge carriers and the amount of doping. The effective conjugation length of a conjugated polymer is an especially important parameter that directly affects the ease of charge transport along a chain. Conductivity also involves charge transfer across neighboring polymer chains. Like the *intrachain* mechanism, the *interchain* hopping transport process is thermally activated. As a result, conductivity increases when temperature is increased. The opposite behavior is observed in the case of well-organized crystalline inorganic materials that behave according to the delocalized band theory. Both intra- and inter-chain charge transport are thus important to describe solid state conductivity. In most conducting polymers, polymer chains are bundled to form densely entangled fibrils in which interchain charge transport is highly controlled by the molecular packing of π -chains. Thus, a third kind of carrier transport process, inter-fibrillar mode of transfer, has to be taken in account in

order to describe fully the solid state behavior. As a consequence, much effort has been devoted to the functionalization of π -conjugated polymers with alkyl or alkoxy groups that increase solubility by creating some packing disorganization, but also induce self-assembly in the solid state. Supramolecular engineering of conjugated polymers still remains a challenging task with far-reaching possible applications in many areas, such as low-cost organic electronics [5].

1.1.3. Oligomers versus polymers

Long-chain, conjugated polymers are structurally inhomogeneous and have broad distributions of chain lengths that depend on the fabrication method. Therefore, the optical and electronic properties reflect the disordered nature of polymers. In particular, the effective conjugation length can be dramatically reduced by the presence of structural defects, such as sp^3 -hybridized carbon centers in the π -chain, as well as local conformational disordering. For example, rotation around the σ -bond between monomeric aromatic units is sufficient to hamper van der Waals stacking between conjugated chains and to reduce the spatial extension of polarons along the polymer chain. The distribution of conformations in conjugated polymers is sensitive to their environment, and this feature explains the reversible spectral changes that are observed as a function of temperature (thermochromism) or solvent nature (solvatochromism) (see Chapter 12).

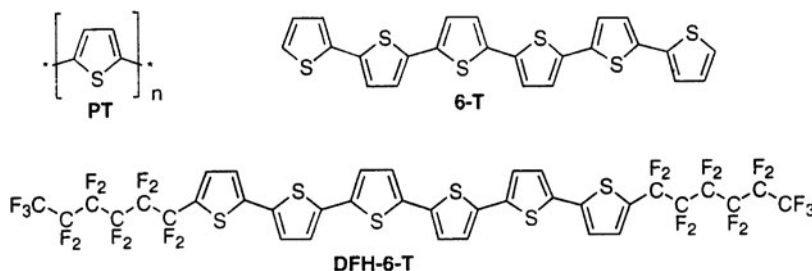
Recently, some conjugated oligomers have been made with attractive features that are superior to those of the parent polymers [6]. They are well-defined chemical systems in which the conjugation chain length can be exactly controlled. They exhibit optical and electronic properties near those of “infinite” polymers owing to the fact that the conjugation length in the finite-sized systems often corresponds to the effective conjugation length in infinite π -chains, and that length is shorter than the oligomer lengths. Depending on their size and substitution patterns, the oligomers are usually more soluble in normal organic solvents and therefore more processable than their much longer homologues. Furthermore, highly crystalline or polycrystalline thin films of conjugated oligomers that contain no more than a small number of defects can be prepared. As a consequence, oligomers form highly organized solid-state materials, usually with high mobilities of charge carriers.

As an example of an advantageous fabrication technique open to oligomers but not to their longer homologues, organic thin film transistors have been made from low molecular weight compounds by sublimation techniques. Vapor deposited organic semi-conductors offer better charge carrier mobility generally. However, solution-processed devices should have lower manufacturing costs. To this end, soluble semiconducting organic molecules are needed that are capable of experiencing the supramolecular interactions obtained by vapor

deposition (i.e., effective π -stacking of the conjugated moieties) when made into films by solution processing. One processing technique that potentially offers both low cost and high operational efficiency is gelation from sol phases.

1.1.4. Oligo- and poly-thiophenes

Since the discovery of highly conducting polyacetylene in 1977 [7], a tremendous amount of research has been devoted to the design and synthesis of conducting polymers consisting of conjugated aromatic rings, such as poly-*p*-phenylene, polyaniline, and poly-*p*-phenylenevinylene, as well as heterocyclic moieties, such as polypyrrole, polyfuran and polythiophene [3]. The electrochemical polymerization of thiophene in 1982 has given birth to one of the most investigated electronic polymers today, conducting polythiophene (**PT**) [8]. This interest stems from the remarkable semiconducting properties of **PTs**, the high stability of conducting and semiconducting polythiophenes, and the ease of their structural modification by using functionalized monomeric building-blocks. The polythiophene backbone is a versatile scaffold on which to base the design of "intelligent" materials that can be used as transducers, sensors, memories, and logic operators [9]. Equally important, oligothiophenes, such as sexithiophene (**6-T**), display many of the remarkable attributes of their polymeric counterparts. A detailed review of the syntheses and properties on oligo- and poly-thiophenes has appeared [10].



Due to their facile oxidation, oligo- and poly-thiophenes and their derivatives give rise to p-type semiconductors. Therefore, holes are the probable principal charge carriers. They are easily generated by exposing a solid sample to iodine vapor as the oxidant. n-Type doping has been investigated to a smaller extent because it requires the use of alkali metal deposition procedures. However, substitution of oligothiophenes with electron-withdrawing groups, such as in the perfluorocarbon chain-substituted derivative (**DFH-6-T**), has been shown recently to allow switching from p-type to n-type character [11].

Characteristic organizational features of the solid state packing of conjugated polythiophenes are relevant to supramolecular organization in gels. In their solid states, chains of polythiophene and oligothiophenes adopt fully extended *s-anti* conformations which allow the systems to be quasi-planar as long as no steric factors give rise to torsional distortions around thiophene-thiophene σ -bonds. In a rigid lattice, the planar chains are packed in a parallel fashion with angles of 40–60° between molecular planes, and, thus, provide a so-called herringbone arrangement that is detrimental to the efficient charge transport properties in the direction normal to the long molecular axis. To circumvent this packing, region-regular, alkyl-substituted polythiophenes have been synthesized that form nearly sandwich-type structures associated with a close packing of the alkyl side chains. These materials exhibit unusually high conductivities, up to 5500 S cm⁻¹ [12].

Therefore, synthetic control of both the planarity and π -overlap of the conjugated backbone is critical to the generation of these materials if they are to be used for electro-optical applications. Planarization of the backbone leads to a reduction of the bandgap. Various synthetic strategies have been reported to control the bandgap in linear conjugated systems [13]. An increase of π -overlap can be achieved by the introduction of self-assembling side units that direct the stacking of the conjugated chains. Thus, insofar as the oligomers are concerned, doping and substitution can be used to force the rod-like molecules to pack in a face-to-face relationship [14].

1.2. Conducting Gels

1.2.1. Polymer gels

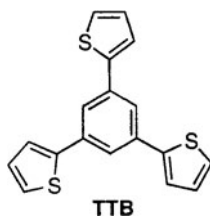
1.2.1.1. Conjugated polymers. Conducting polymer gels have emerged as a fascinating class of materials that present a unique combination of physical properties that include rubbery elasticity (mechanical properties), ability to be swelled by “good” solvents, and specific electron transport due to the existence of a three-dimensional connected network. The theoretical aspects of conduction in gels have been addressed by de Gennes [15].

Synergetic electronic and viscoelastic properties in a gel are expected to lead to electromechanical effects with potential applications as actuators, artificial muscles, electronic switches, optical switches, optical memories, shape memories, etc. [16].

Gelation of organic liquids by several kinds of conjugated polymers, such as polyaniline or polyfluorene-based materials, has been observed [16]. Organogels of **PT** derivatives have been the subject of numerous studies, and organogels have been obtained by chemical or electrochemical polymerization of 3-alkylthiophenes in chloroform [16]. An insoluble fraction of the

polymer displayed the gelating characteristics. The gel content was increased by subjecting the swelled polymer to γ -ray irradiation or treatment with benzoyl peroxide, both of which induce the formation of cross-links between alkyl side chains. Remarkable changes in the absorption (chromism) and photoluminescence spectra were observed in the polymer gels when the temperature or the solvent composition was changed. These effects were attributed to variations in volume of the gels. For example, a gel with chloroform as the swelling liquid was observed to shrink drastically upon addition of ethanol, and the effect was reversed when the ethanol was removed. Remarkably, shrinkage of the gel volume was also observed when the gel was doped with iodine, and the conductivity was enhanced. Because a conducting polymer bimorph, composed of conducting polymer gel and non-gel polymer layers, could be bent upon application of a voltage, it may be useful as an actuator.

In an attempt to synthesize gel networks with controlled and reproducible architectures, branched conjugated polymers were prepared by oxidative copolymerization of 3-*n*-octylthiophene with various trithienylbenzene derivatives, such as **TTB**, acting as the cross-linking units [17]. This strategy allowed the preparation of three-dimensional networks whose specific natures depend on the initial molar ratio of trithienylbenzene to monomer; the resulting polymers have well-defined structures [18].



Conducting properties have been determined mainly with samples of doped dried gels (xerogels). There, conduction is still controlled by hopping – the data are in good agreement with a model of inter-cluster hopping conduction [17, 18]. These clusters may be regarded as ordered and crystalline grains where interchain charge transfer is easier. Consistent with this model, the intrinsic conductivity of the conducting clusters was higher in the copolymer than in linear poly(3-*n*-octylthiophene). Chloroform-swollen gels doped with iodine retained good conductivity but the mechanism for transport has not been addressed thus far [17, 18].

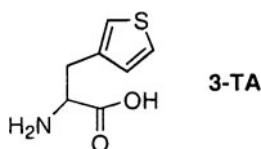
Both organogels and hydrogels have been made from polythiophene-based materials. As an example, a water-swollen gel was synthesized by chemical cross-linking of poly(3-thiophenylacetic acid) with adipoyl dihydrazide as the cross-linking agent [19]. The undoped hydrogel was a much better conductor than in its dry state, due probably to enhanced ionic conduction in the former.

Interestingly, a swollen sample doped with HClO_4 exhibited a high conductivity, ca. $10^{-2} \text{ S cm}^{-1}$, that is only one order of magnitude lower than that of electropolymerized poly(3-alkylthiophene) doped with perchlorate anions. These systems may be useful components of bioelectronic devices for the detection of biomolecules that can be entrapped within the gel network.

In an analogous fashion, a hydrogel from an aqueous solution of the highly conductive polymer PEDOT/PSS, whose trade name is Baytron-P (Bayer AG, Germany), has been used as a component of an enzyme-enhanced electrode apparatus [20]. Owing to their fractal nature, conducting gel networks may also act as network devices whose shape selectivity (for dopant molecules) mimic some functions of neurons [21].

1.2.1.2. Non-conjugated conducting polymers. Hydrogels have been obtained from redox polymers that contain covalently-linked pendant electron-donor and -acceptor groups. Due to their fast transport of electrons and the rapid permeation of water-soluble biological reactants and products, these materials are attractive matrices for the electrical connection between reactions centers of immobilized enzymes and electrodes [22]. Redox hydrogels are thus particularly interesting for the fabrication of biofuel cells [23] and electrochemical sensors [24].

1.2.1.3. Protein-based materials. The organizational principles employed in nature represent a source of inspiration for chemists who need high levels of control in polymer synthesis and architecture. Protein engineering provides an approach toward so-called bio-inspired materials with well-ordered three-dimensional structures [25]. While α -helical peptides have been studied in great detail, model β -sheets have been less investigated [26]. Yet oligopeptides based on the β -sheet motif exhibit a unique propensity to self-assemble into polymeric tapes, giving rise to the formation of hydrogels [27]. This may represent a nice opportunity to create novel conducting materials. A first step toward this direction that is based on the biosynthesis of a thiophene-containing alanine (**3-TA**) has been reported [28].

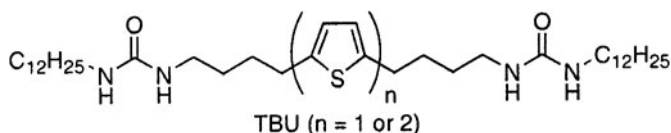


1.2.2. Conducting gels based on LMOGs

As mentioned above, the conducting or semiconducting properties of small molecules, including oligomers, are sometimes better than those of polymers.

Crucial to the performance of materials is the possibility to control precisely the arrangements of π -systems of neighboring molecules (N.B., face-to-face stacking) in the solid state. To this end, the concepts of supramolecular chemistry as applied to gels offer elegant opportunities to create supramolecular electronics [29]. Electron-conducting LMOGs endowed with groups that promote the type of self-assembly that leads to face-to-face stacking of π -systems are thus attractive candidates for the generation of organic charge-transport devices.

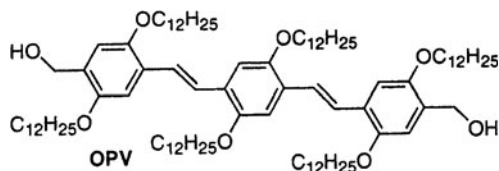
1.2.2.1. LMOGs based on conjugated oligomers. Due to their important role in organic electronics, oligothiophenes have received some attention for the creation of conducting gels. An elegant approach is based on bis(urea) LMOGs [30]. The self-assembling properties of bisurea compounds were exploited to organize spatially thiophene-containing fragments; several (oligo)thiophene-containing bisurea systems (**TBU**) gelate tetralin and 1,2-dichloroethane. Experimental data and modeling studies point to the formation of unidirectional aggregates in which the thiophene units are held near each other and experience extensive stacking along the long fiber axis. This packing arrangement is extremely favorable for efficient charge transport via a hopping mechanism. Charge carrier mobilities, measured by a pulsed-radiolysis, time-resolved microwave conductivity (PR-TRMC) technique, were remarkably high for molecules with such short molecular conjugation; the mobility for the bithiophene compound is close to that of longer oligomers or polymers. LMOGs based on terthiophene-bearing amide units have also been reported [31].



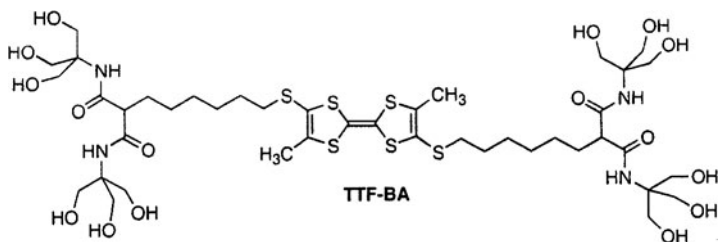
Although sexithiophene derivatives connected at the α, α' -positions to achiral and chiral penta(ethylene glycol) chains are not reported to be gelators, they do form fiber-like assemblies in solution and in the solid state [32]. Structural and spectroscopic studies have revealed that the sexithiophene units are well-organized and excitonically-coupled within their supramolecular structures. This arrangement may be responsible for the observed high conductivity.

Oligo(phenylene vinylene) derivatives represent an additional important class of hole-conducting materials for organic light-emitting diodes (OLEDs) and photovoltaic devices. An oligo(phenylene vinylene)-based gelator (**OPV**) displays remarkable photophysical properties in its toluene gels [33]. Thus,

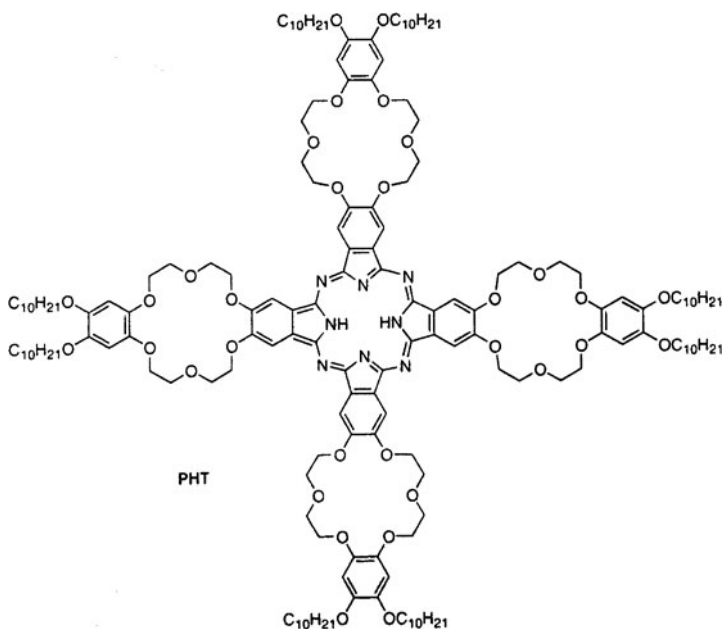
the emission from **OPV** undergoes dramatic changes during gelation that are indicative of significant chromophore aggregation in the self-assemblies.



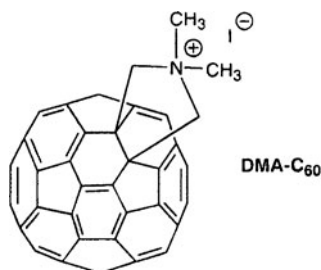
1.2.2.2. Tetrathiafulvalene (TTF) based organogelators. TTF-containing molecules have been important conducting materials historically [34]. Given also the rich diversity of TTF-based molecules, they represent versatile building-blocks for future design of conducting gelators. As of the date of this chapter, only one example of an organogelator incorporating the TTF motif (**TTF-BA**) has been reported [35]. It incorporates Newkome bis-arborol structures and is able to gelate ethanol/water or dimethylformamide/water liquid systems. The gel could be doped with iodine (as oxidizing agent). Absorption spectra of the oxidized gel indicated the formation of TTF stacks through which conduction is anticipated to take place.



1.2.2.3. Porphyrin and phthalocyanine gelators. Porphyrin and phthalocyanine derivatives display a strong propensity to stack into elongated wires prone to propagate electrons. Particularly phthalocyanines have been investigated as p- or n-type semiconductors depending on the nature of the peripheral substituents. Several reports described the gelation properties of properly substituted porphyrin [36] and phthalocyanine [37] derivatives. For example, the phthalocyanine-containing compound **PHT** forms a gel in chloroform in which the self-assembled strands are made of arrays of stacked phthalocyanines. The formation of fibrous assemblies in water was also reported in the case of amphiphilic metallophthalocyanines [38].



1.2.2.4. C₆₀ containing gels. Substituted fullerenes (C₆₀) have emerged as a fascinating class of carbon molecules. C₆₀ are capable of multiple electron reductions, which renders them attractive electron acceptors for the generation of artificial photosynthetic systems. Recently C₆₀ attracted much attention in view of its application in photovoltaic devices [39]. A variety of synthetic procedures is available that allows easy chemical modifications of C₆₀ and thus access to a wide range of functionalized derivatives. The supramolecular self-assembly of C₆₀ into well-organized structures is a challenging task. Recently a derivatized C₆₀ (**DMA-C₆₀**) was shown to self-assemble into nanorods [40].



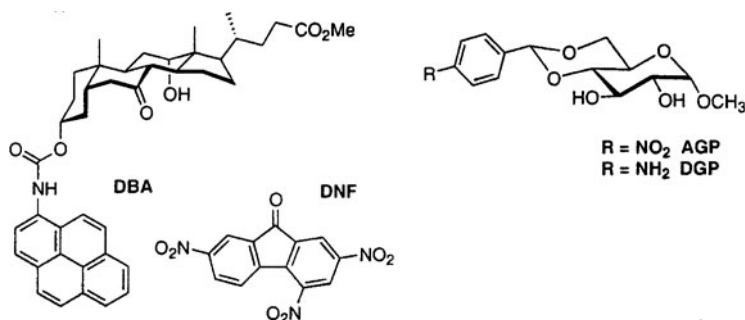
Yet, the use of C₆₀ in molecular gel chemistry has been poorly investigated to date, and there is no report of a C₆₀-containing gelator. Actually the C₆₀-porphyrin interaction has been exploited by Shinkai *et al.* to reinforce the organogel structure of a porphyrin-appended cholesterol derivative [41].

Very recently, the same group proposed an improved version of a porphyrin gelator that bears hydrogen-bonding sites. Self-assembly and gelation resulted from the formation of one-dimensional superstructures encapsulating C_{60} molecules [42]. Given the tremendous potential porphyrin- C_{60} dyads for photovoltaic applications and new electronic devices, these examples represent a first promising approach.

1.2.2.5. Donor/acceptor interaction in dual-component organogels.

Since the discovery of high electrical conductivity of one-dimensional charge-transfer (CT) complexes in 1973 [43], research in the field has expanded enormously. From a structural point of view, donor and acceptor molecules in a CT complex may occur in the solid state either segregated in separated stacks or associated in alternate stacks. In the former case, the resulting material is likely to be conducting. In the latter, the materials are electrically insulating, although they may display interesting magnetic properties. In designing CT complex-based materials, electronic criteria relative to the donor and acceptor fragments need to be met. In addition, control of the geometrical arrangement of the donor and acceptor partners is also critical to the material properties. Careful design of organogelator molecules with properties designed for specific forms of self-assembly may provide a useful approach toward the control of donor and acceptor unit organization within gel fibers, and may be amenable to design of both types of CT interactions.

Currently, few reports of donor-acceptor interactions in organogels have appeared. One describes the effective doping of gels of a donor-substituted bile acid derivative (**DBA**) with trinitrofluorenone (**TNF**) [44]. Another describes gels consisting of mixtures of two saccharide-based gelators, a donor- and an acceptor-containing glucopyranoside, **DGP** and **AGP**, respectively [45]. In both examples, CT complex formation was confirmed by electronic absorption spectroscopy and it was found to promote or enhance gelation.



In these examples, the self-assembled networks are composed of hybrid fibers (i.e., structures containing both donor and acceptor moieties). An

alternative situation is the one where the two components self-assemble independently into two coexisting separate networks to give a hybrid gel. On the basis of this “gel inside a gel” strategy, as proposed by Menger [46], one can thus envision interspersing electron-donor fibers within the network of an electron-acceptor gelator. This would be interesting from the fundamental standpoint of electron transfer phenomena as well as being of practical importance for electroluminescence or photovoltaic purposes. Practically, donor and acceptor molecules that self-assemble via specifically defined interactions to favor homo-recognition over hetero-aggregation would have to be designed. While a few donor gelator systems such as oligothiophenes, TTF, and OPV are available, acceptor counterparts leading to efficient n-type semiconducting materials are not known. To this end, acceptor molecules found in liquid crystal chemistry may serve as models [47].

1.2.3. Outlook for the future

The afore-mentioned examples show the tremendous potential of conducting molecular gels as novel materials for diverse applications. While there is a need for the design and synthesis of new classes of functional gelators, it is also necessary to look beyond the current conceptual approaches. Thus, molecular gels with electronic properties should be used for the fabrication of active devices that are of practical interest for organic electronics. As an example, one can envisage integrating conducting gels or xerogels as the active layer into thin-film field effect transistors (FETs). FETs represent not only important logic devices but also allow the characterization of fundamental properties of semiconducting materials, such as their charge carrier mobility or switching ratio [48]. Other examples of important devices are solar cells and OLEDs.

Moreover, the rheological properties of gels offer important practical advantages over the properties of non-gelated systems. Because fibers can be aligned during organogel formation, oriented materials with anisotropic properties should be possible [49]. They may offer substantial improvements in solution processing techniques of organic semiconductors, such as in ink-jet printing.

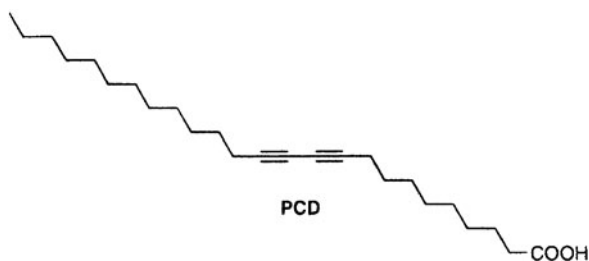
2. Molecular Gels as Templating Media for Electronic Materials

The conducting properties of the gels described in the previous section stem from the presence of an inherently conducting or semiconducting π -conjugated moiety in the LMOG structure. This describes some potential applications of gel systems that are non-conducting but can be indirectly exploited for generation of electronic materials. Two strategies have been used. The first is based on the

entrapment of chemical species within the network cavity. For example, dye-sensitized solar cells with high efficiency which rely on a room-temperature molten salt, iodine, and an LMOG as quasi-solid-state electrolyte have been produced [50]. A similar approach has used a polymer to obtain the gel [51]. The second approach benefits from the well-organized fibrillar structure of the supramolecular assemblies. In this case, polymerization or polycondensation reactions can lead to organic or inorganic functional materials.

2.1. Polymerizable LMOGs

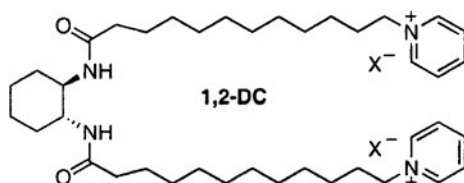
Polymerization of self-assembled LMOG molecules within the fibers of a molecular gel locks in the scaffold-like structures and can make new stable materials. The group of Groningen reported the first case of organogel stabilization by photopolymerization [52]. Irradiation converted a gel of a bis(ureido)cyclohexane derivative containing a methacrylate unit into a highly cross-linked gel displaying remarkably high thermal and temporal stability owing to the formation of covalent linkages. This approach has been further developed by the group of Hamilton [53]. Photopolymerization in the gels of 10,12-pentacosadiynoic acid (**PCD**) and its amide derivatives have been employed to access polymeric networks with potential electrical conductivity [54]. This strategy is based on the known propensity of diacetylenes to undergo topochemical solid-state 1,4-addition reactions leading to conjugated polymers.



2.2. Templating of Inorganic Structures

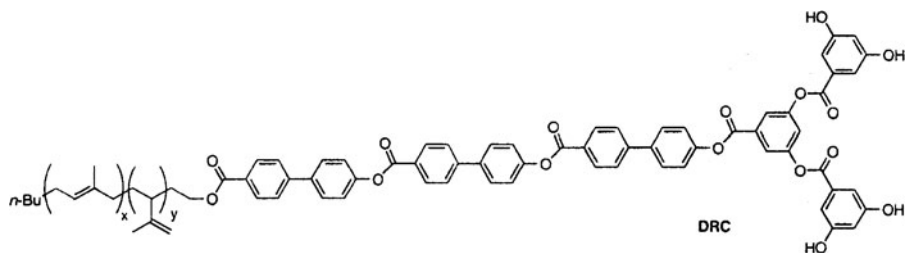
The use of organogels as templates for the generation of inorganic structures and materials has received considerable attention [55]. These concepts are developed further in Chapter 25. Three dimensional networks permit inorganic materials to be arranged on the microscopic level, leading to otherwise unattainable structures. The major advantage of using LMOGs relies on the greater ease with which the template structure can be removed, as compared to inorganic templates or organic polymers. Inorganic nanostructures are obtained

by coating the fibers with the inorganic precursor followed by polycondensation or crystallization, and then calcination to remove the organic template. Remarkably, the process allows hollow fibers, whose morphology and chirality are directly related to that of the templating supramolecular assemblies, to be produced. For example, helical silica fibers have been obtained with a single screw sense [55]. The transcription of organogel superstructures into semiconducting inorganics holds promise for the development of the next-generation of nanostructured materials in electronics. Indeed, replication based on the sol-gel polycondensation of metal (Ti, Ta, V) alkoxides using organogelators as templates has been shown to produce tubular helical fiber materials of transition-metal oxides [56].



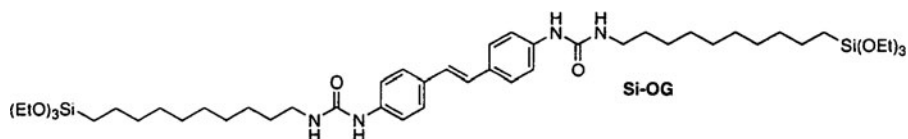
The helices were always left-handed in the sol-gel system of the *R,R*-enantiomer of a *trans*-1,2-diaminocyclohexane derivative (**1,2-DC**) as gelator, and were always right-handed with the *S,S*-enantiomer. These materials may also be useful in optical applications and in chiral- and photo-catalysis.

Cadmium sulfide (CdS) is a non-oxide semiconductor of interest for photovoltaic applications. Its templating on the nanoscale in a helical morphology has been reported [57]. Cadmium nitrate was added to the gel of a “dendron rodcoil” (**DRC**) followed by mineralization with hydrogen sulfide gas. Interestingly, the nanoribbon assemblies did not need to be in the gelled state to produce helical structures of CdS. A dilute suspension of isolated nanoribbons that was subjected to mineralization was also found to act as templates for CdS nanostructure formation. This observation suggests that single, stable, supramolecular, fiber-like objects may be templates [58].



An alternative use of the mineralization process is found in the encapsulation of electron conducting organic fibers made of self-assembling redox components. Here the deposition of an inorganic mantle around the organic

aggregates preserves the morphologies of the flexible organic structures. Carefully controlled sol-gel polycondensation of tetraethoxysilane in the presence of self-assembled metallophthalocyanines columnar stacks produced silica walls that did not alter the long-range ordering [59]. The same kind of approach has been used with the bis(urea) derivative of a conjugated oligomer bearing terminal triethoxysilane functionalities (**Si-OG**) [60].



2.3. Spatial Organization of Semiconductor Nanoparticles

Quantum dots and nano wires with non-oxides, including many semiconductors of interest for optoelectronic applications, are being investigated extensively. Metal nanoparticles have been incorporated into polymeric hydrogels to make functional materials [61]. A current challenge is the synthesis of hierarchically ordered inorganic frameworks with applications in a wide range of materials. To this end, template-directed methods afford access to inorganic materials with higher-order architectures [62]. As of the writing of this chapter, the interplay between metal nanoparticles and organogel networks has received little attention. Recently a method has described the incorporation of semiconducting quantum dots of CdS into an isooctane gel, obtained from p-chlorophenol and sodium bis(2-ethylhexyl) sulfococinate (**AOT**) [63]. The particles spontaneously spatially organized themselves, being compartmentalized into the strands of the gel. These particles should confer rather unique properties to gels, and the thermoreversible nature of the compartmentalization process may open lead to materials with erasable memories. More control of particle interactions with gels fibers is expected if chemically-modified nanoparticles with programmed self-assembling groups are used [64].

3. Magnetosensitive Gels

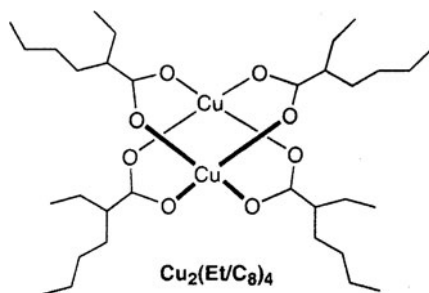
Magnetic nanoparticles are of technological and fundamental scientific importance. Recent advances in the synthesis of various magnetic nanoparticles have been achieved [65], and applications of these materials can be found in magnetic storage devices, contrast enhancement in magnetic resonance imaging, artificial muscles, drug targeting, and catalysis [66]. The use of high-gradient magnetic fields for separation has become widespread in biology and biotechnology [67]. Applications include cell sorting, DNA isolation,

preparation, and sequencing, as well as immunology (immuno-magnetism) and a wide variety of isolation and enrichment techniques for biological entities [68]. Although not explicitly covered here, gels that contain nanoparticles (especially of TiO_2) and respond to electric fields are also of increasing interest [69].

Ferrogels represent an important class of magnetic-field sensitive materials that are based on the incorporation of super paramagnetic nanoparticles, mainly $\gamma\text{-Fe}_2\text{O}_3$ (ferrite) or Fe_3O_4 (magnetite), into polymeric hydrogels. Under a non-uniform magnetic field, the particles undergo motions which, in turn, induce elongation, contraction, or bending of the gels with short response times [70]. The possibility to control quick changes of shape of a material can be used to create a wide range of motions such as those observed in muscles. Ferrogels are an attractive medium to actuate biomechanical and biomimetic motions. Biomimetic valves have been envisioned on this principle, but many other applications, as microsensors, switches, or controlled delivery systems, are anticipated. For instance, these studies have contributed to a better fundamental knowledge of magneto-elastic coupling in polymer networks swollen by a ferrofluid [71]. Hydrogels of polyvinyl alcohol have been investigated [72], but other polymer networks such as polyacrylamides were also used [73].

Very few examples of magneto-sensitive organogels made from LMOGs have been reported. In the first example, ferrites particles were suspended in a AOT-based isooctane gel that became super-paramagnetic at 6 K when the applied field was 1000 G [74]. When exposed to an alternative magnetic field, the super-paramagnetic particles produced heat according to Brown and Néel relaxation effects [75]. This behavior suggests that these gels may be useful as novel hyperthermic materials. Recently, ferrite and CdS particles were compartmentalized into the strands of an organogel [63]; it may be a new magneto-sensitive material.

Aside from the incorporation of magnetic nanoparticles, molecular magnet-based LMOGs may also generate magnetic gels. For instance, a binuclear copper(II) tetracarboxylate complex ($\text{Cu}_2(\text{Et/C}_8)_4$) forms organometallic wires in organic liquids that may behave as spin ladders with unusual magnetic properties [76].



4. Conclusions and Perspectives for the Future

Clearly, many applications of molecular gels from low molecular-mass organic gelators as electronic or magnetosensitive materials can be envisioned. Yet, their potential has not been exploited thus far; the few examples are described in this chapter. Given the recent advances in the systematic synthesis of organogelators, and relying on the creative imagination of chemists, it seems highly probable that the future will witness a large number of new, gel-based materials with exciting applications. Their ability to be cycled reversibly between free-flowing liquids and non-flowing materials is one of the most important of the many exciting attributes of these molecular gels. In this regard, there is a need for viscosity control in inkjet printing processes for the deposition of electronic materials on flexible substrates.

Also, we have mentioned the incorporation of spherical metal nanoparticles into molecular gels. There have been no investigations of the incorporation of particles with high aspect ratios, such as metal or semiconducting nanorods. Such doped gels may open additional fascinating opportunities to assemble nanoscale objects into functional devices.

Acknowledgments

The Université Bordeaux 1 and the Université de la Méditerranée are gratefully acknowledged for their support in the preparation of this chapter. Dr. C. Vidolot-Ackermann is acknowledged for critical discussion.

References

- [1] (a) Daum, P.; Lenhard, J.R.; Rolison, D.; Murray, R.W. "Diffusional charge transport through ultrathin films of radiofrequency plasma polymerized vinylferrocene at low temperature", *J. Am. Chem. Soc.*, **1980**, *102*, 4649–4653. (b) Pickup, P.G.; Kutner, W.; Leidner, C.R.; Murray, R.W. "Redox conduction in single and bilayers films of redox polymer", *J. Am. Chem. Soc.* **1984**, *106*, 1991–1998.
- [2] Willner, I.; Katz, E. "Integration of layered redox proteins and conductive supports for bioelectronic applications", *Angew. Chem. Int. Ed.*, **2000**, *39*, 1180–1218.
- [3] *Handbook of Organic Conductive Molecules and Polymers*, H.S. Nalwa, Ed., Chichester: John Wiley, **1997**, 1–4.
- [4] Baumgarten, M.; Müllen, K. "Radical ions: where organic chemistry meets materials sciences", *Topics in Current Chem.*, **1994**, *169*, 1–103, and references therein.
- [5] Holdcroft, S. "Patterning of π -conjugated polymers", *Adv. Mater.*, **2001**, *13*, 1753–1765.
- [6] *Electronic Materials: the Oligomer Approach*, K. Müllen and G. Wegner, Eds., Weinheim: Wiley-VCH, **1998**.

- [7] Shirakawa, H.; Louis, E.J.; MacDiarmid, A.G.; Chiang, C.K.; Heeger, A.J. "Synthesis of electrically conducting organic polymers: halogen derivatives of polyacetylene (CH)_x", *J. Chem. Soc. Chem. Commun.*, **1977**, 578–580.
- [8] Roncali, J. "Conjugated poly(thiophene)s: synthesis, functionalization, and applications", *Chem. Rev.*, **1992**, 92, 711–738.
- [9] Garnier, F. "Functionalized conducting polymers – towards intelligent materials", *Angew. Chem. Int. Ed. Engl.*, **1989**, 28, 513–517.
- [10] *Handbook of Oligo- and Polythiophenes*, D. Fichou, Ed., Weinheim: Wiley-VCH, **1999**.
- [11] Fachetti, A.; Yoon, M.H.; Stern, C.L.; Katz, H.E.; Marks, T.J. "Building blocks for n-type organic electronics: regiochemically modulated inversion of majority carrier sign in perfluoroarene-modified polythiophene semiconductors", *Angew. Chem. Int. Ed.*, **2003**, 42, 3900–3903.
- [12] McCullough, R.P.; Williams, S.P.; Tristram-Nagle, S.; Jayaraman, M.; Ewbank, P.C.; Miller, L. "The first synthesis and new properties of regioregular, head-to-tail coupled polythiophenes", *Synth. Met.*, **1995**, 69, 279–282.
- [13] Roncali, J. "Synthetic principles for bandgap control in linear π -conjugated systems", *Chem. Rev.*, **1997**, 97, 173–205.
- [14] Fichou, D.; Ziegler, C. "Structure and properties of oligothiophenes in the solid state: single crystals and thin films" in Ref. [10], pp. 183–282.
- [15] de Gennes P.-G. "Solutions de polymères conducteurs. Lois d'échelles. (Scaling laws for solutions of conducting polymers)", *C. R. Acad. Sc. Paris, Série II*, **1986**, 302, 1–5.
- [16] Yoshino, K. "Novel functional gel characteristics of conducting polymer", In *Conjugated Polymers and Related Materials: The Interconnection of Chemical and Electronic Structure, Proceedings of the Eighty-first Nobel symposium*, W. R. Salaneck, I. Lundström and B. Ranby, Eds., Oxford: Oxford University Press, **1993**, 121–138.
- [17] Pépin-Donat, B.; Van-Quynh, A.; Viallat, A. "Mechanisms of deformation in fully conjugated conducting gels. Stretching and swelling", *Macromolecules*, **2000**, 33, 5912–5917.
- [18] Sixou, B.; Pépin-Donat, B.; Nechtschein, M. "The routes towards three-dimensional conducting polymers: 2. Transport properties of fully conjugated gels of poly(3-n-octylthiophene)", *Polymer*, **1997**, 38, 1581–1587.
- [19] Chen, L.; Kim, B.; Nishino, M.; Ping Gong, J.; Osada, Y. "Environmental responses of polythiophene hydrogels", *Macromolecules*, **2000**, 33, 1232–1236.
- [20] Åsberg, D.P.; Inganäs, O. "PEDOT/PSS hydrogel networks as 3-D enzyme electrodes", *Synth. Met.*, **2003**, 137, 1403–1404.
- [21] Fujii, M.; Ihori, H.; Arii, K.; Onoda, M. "Control of weight of network path of neuron-like conducting polymer", *Synth. Met.*, **2001**, 119, 483–484.
- [22] Mao, F.; Mano, N.; Heller, A. "Long tethers binding redox centers to polymer backbones enhance electron transport in enzyme 'wiring' hydrogels", *J. Am. Chem. Soc.*, **2003**, 125, 4951–4957.
- [23] Mano, N.; Mao, F.; Shin, W.; Chen, T.; Heller, A. "A Miniature biofuel cell operating at 0.78 V", *Chem. Commun.*, **2003**, 518–519.
- [24] Sallacan, N.; Zayats, M.; Bourenko, T.; Kharitonov, A.B.; Willner, I. "Imprinting of nucleotide and monosaccharide recognition sites in acrylamidephenylboronic acid-acrylamide copolymer membranes associated with electronic transducers", *Anal. Chem.* **2002**, 74, 702–712.
- [25] van Hest, J.C.M.; Tirrell, D.A. "Protein-based materials, toward a new level of structural control", *Chem. Commun.*, **2001**, 1897–1904.

- [26] Aggeli, A.; Bell, M.; Boden, N.; Keen, J.N.; McLeish, T.C.B.; Nyrkova, I.; Radford, S.E.; Semenov, A. "Engineering of peptide β -sheet nanotapes", *J. Mater. Chem.*, **1997**, 7, 1135–1145.
- [27] Aggeli, A.; Bell, M.; Boden, N.; Keen, J.N.; Knowles, P.F.; McLeish, T.C.B.; Pitkeathly, M.; Radford, S.E. "Responsive gels formed by the spontaneous self-assembly of peptides into polymeric β -sheet tapes", *Nature*, **1997**, 386, 259–262.
- [28] Kothakota, S.; Mason, T.L.; Tirrell, D.A.; Fournier, M.J. "Biosynthesis of a periodic protein containing 3-thienylalanine: a step toward genetically engineered conducting polymers", *J. Am. Chem. Soc.*, **1995**, 117, 536–537.
- [29] El-Ghayoury, A.; Schenning, A.P.H.J.; van Hal, P.A.; van Duren, J.K.J.; Janssen, R.A.J.; Meijer, E.W. "Supramolecular hydrogen-bonded oligo(p-phenylene vinylene) polymers", *Angew. Chem. Int. Ed.*, **2001**, 40, 3660–3663.
- [30] Schoonbeek, F.S.; van Esch, J.H.; Wegewijs, B.; Rep, D.B.A.; de Haas, M.P.; Klapwijk, T.M.; Kellog, R.M.; Feringa, B.L. "Efficient intermolecular charge transport in self-assembled fibers of mono- and bithiophene bisurea compounds", *Angew. Chem. Int. Ed.*, **1999**, 38, 1393–1397.
- [31] Liu, P.; Shirota, Y.; Osada, Y. "A novel class of low-molecular-weight organic gels based on terthiophene", *Polym. Adv. Technol.*, **2000**, 512–517.
- [32] (a) Schenning, A.P.H.J.; Kilbinger, A.F.M.; Biscarini, F.; Cavallini, M.; Cooper, H.J.; Derrick, P.J.; Feast, W.J.; Lazzaroni, R.; Leclère, P.; McDonell, L.A.; Meijer, E.W.; Meskers, S.C.J. "Supramolecular organization of α, α' -disubstituted sexithiophenes", *J. Am. Chem. Soc.*, **2002**, 124, 1269–1275. (b) Sandberg, H.; Henze, O.; Kilbinger, A.F.M.; Sirringhaus, H.; Feast, W.J.; Friend, R.H. "Oligoethyleneoxide sexithiophene organic field effect transistors", *Synth. Metals*, **2003**, 137, 885–886.
- [33] Ajayaghosh, A.; George, S.J. "First phenylenevinylene based organogels: self-assembled nanostructures via cooperative hydrogen bonding and π -stacking", *J. Am. Chem. Soc.*, **2001**, 123, 5148–5149.
- [34] For a recent TTF review, see: Segura, J.L.; Martin, N. "New concepts in tetrathiafulvalene chemistry", *Angew. Chem. Int. Ed.*, **2001**, 40, 1372–1409.
- [35] Jørgensen, M.; Bechgaard, K.; Bjørnholm, T.; Sommer-Larsen, P.; Hansen, L.G.; Schaumburg, K. "Synthesis and structural characterization of a bis-arborol tetrathiafulvalene gel: toward a self-assembling 'molecular' wire", *J. Org. Chem.*, **1994**, 59, 5877–5882.
- [36] (a) Tian, H.J.; Inoue, K.; Ishi-I, T.; Shinkai, S. "New organic gelators bearing a porphyrin group: a new strategy to create ordered porphyrin assemblies", *Chem. Lett.*, **1998**, 871–872. (b) Terech, P.; Gebel, G.; Ramasseul, R. "Molecular rods in a zinc(II) porphyrin/cyclohexane physical gel: neutron and X-ray scattering characterizations", *Langmuir*, **1996**, 12, 4321–4323.
- [37] van Norstrum, C.F.; Picken, S.J.; Schouten, A.J.; Nolte, R.J.M. "Synthesis and supramolecular chemistry of novel liquid crystalline crown ether-substituted phthalocyanines: toward molecular wires and molecular electronics", *J. Am. Chem. Soc.*, **1995**, 117, 9957–9965.
- [38] Kimura, M.; Muto, T.; Takimoto, H.; Wada, K.; Ohta, K.; Hanabusa, K.; Shirai, H.; Kobayashi, N. "Fibrous assemblies made of amphiphilic metallophthalocyanines", *Langmuir*, **2000**, 16, 2078–2082.
- [39] Sariciftici, N.S.; Smilowitz, L.; Heeger, A.J.; Wudl, F. "Photoinduced electron transfer from a conducting polymer to buckminsterfullerene", *Science*, **1992**, 258, 1474–1476.

- [40] Cassell, A.M.; Asplund, C.L.; Tour, J.M. "Self-assembling supramolecular nanostructures from a C₆₀ derivative: nanorods and vesicles", *Angew. Chem. Int. Ed.*, **1999**, *38*, 2403–2405.
- [41] Ishi-I, T.; Iguchi, R.; Snip, E.; Ikeda, M.; Shinkai, S. "[60]Fullerene can reinforce the organogel structure of porphyrin-appended cholesterol derivatives: novel odd-even effect of the (CH₂)_n spacer on the organogel stability", *Langmuir*, **2001**, *17*, 5825–5833.
- [42] Shirakawa, M.; Fujita, N.; Shinkai, S. "[60]Fullerene-motivated organogel formation in a porphyrin derivative bearing programmed hydrogen-bonding sites", *J. Am. Chem. Soc.*, **2003**, *125*, 9902–9903.
- [43] Ferraris, J.; Cowan, D.O.; Walatka, V.V.; Perlstein, J.H. "Electron transfer in a new highly conducting donor-acceptor complex", *J. Am. Chem. Soc.*, **1973**, *95*, 948–949.
- [44] Maitra, U.; Kumar, P.V.; Chandra, N.; D'Souza, L.J.; Prasanna, M.D.; Raju, A.R. "First donor-acceptor interaction promoted gelation of organic fluids", *Chem. Commun.*, **1999**, 595–596.
- [45] Friggeri, A.; Gronwald, O.; van Bommel, K.J.C.; Shinkai, S.; Reinhoudt, D.N. "Charge-transfer phenomena in novel, dual-component, sugar-based organogels", *J. Am. Chem. Soc.*, **2002**, *124*, 10754–10758.
- [46] Kölbl, M.; Menger, F.M. "Molecular recognition among structurally similar component of a self-assembling soft material", *Langmuir*, **2001**, *17*, 4490–4492.
- [47] Pieterse, K.; van Hal, P.A.; Kleppinger, R.; Vekemans, J.A.J.M.; Janssen, R.A.J.; Meijer, E.W. "An electron-deficient discotic liquid-crystalline material", *Chem. Mater.*, **2001**, *13*, 2675–2679.
- [48] Dimitrakopoulos, C.D.; Malenfant, P.R.L. "Organic thin transistors for large area electronics", *Adv. Mater.*, **2002**, *14*, 99–117.
- [49] Lescanne, M.; Colin, A.; Mondain-Monval, O.; Heuzé, K.; Fages, F.; Pozzo, J.L. "Flow-induced alignment of fiberlike supramolecular self-assemblies during organogel formation with various molecular mass organogelator-solvent systems", *Langmuir*, **2002**, *18*, 7151–7153.
- [50] Kubo, W.; Kitamura, T.; Hanabusa, K.; Wada, Y.; Yanagida, S. "Quasi-solid-state dye-sensitized solar cells using room temperature molten salts and a low molecular weight gelator", *Chem. Commun.*, **2002**, 374–375.
- [51] Wang, P.; Zakeeruddin, S.M.; Exnar, I.; Grätzel, M. "High efficiency dye-sensitized nanocrystalline solar cells based on ionic liquid polymer gel electrolyte", *Chem. Commun.*, **2002**, 2972–2973.
- [52] de Loos, M.; van Esch, J.; Stokroos, I.; Kellog, R.M.; Feringa, B.L. "Remarkable stabilization of self-assembled organogels by polymerization", *J. Am. Chem. Soc.*, **1997**, *119*, 12675–12676.
- [53] Wang, C.; Hamilton, A.D. "Synthesis and self-assembly properties of polymerizable organogelators", *Chem. Eur. J.*, **2002**, *8*, 1954–1961.
- [54] George, M.; Weiss, R.G. "Low molecular-mass gelators with diyne functional groups and their unpolymerized and polymerized gel assemblies", *Chem. Mater.*, **2003**, *15*, 2879–2888, and references therein.
- [55] van Bommel, K.J.C.; Friggeri, A.; Shinkai, S. "Organic templates for the generation of inorganic materials", *Angew. Chem. Int. Ed.*, **2003**, *42*, 980–999.
- [56] Kobayashi, S.; Hamasaki, N.; Suzuki, M.; Kimura, M.; Shirai, H.; Hanabusa, K. "Preparation of helical transition-metal oxide tubes using organogelators as structure-directing agents", *J. Am. Chem. Soc.*, **2002**, *124*, 6550–6551.

- [57] Sone, E.D.; Zubarev, E.R.; Stupp, S.I. "Semiconductors nanohelices templated by supramolecular ribbons", *Angew. Chem. Int. Ed.*, **2002**, *41*, 1706–1709.
- [58] (a) Matsui, H.; Pan, S.; Gologan, B.; Jonas, S.H. "Bolaamphiphile nanotube-templated metallized wires", *J. Phys. Chem. B*, **2000**, *104*, 9576–9579. (b) Matsui, H.; Gologan, B.; Pan, S.; Douberly, Jr., G.E. "Controlled immobilization of peptide nanotube-templated metallic wires on Au surfaces", *Eur. Phys. J. D*, **2001**, *16*, 403–406.
- [59] Kimura, M.; Wada, K.; Ohta, K.; Hanabusa, K.; Shirai, H.; Kobayashi, N. "Organic-inorganic composites comprised of ordered stacks of amphiphile molecular disks", *J. Am. Chem. Soc.*, **2001**, *123*, 2438–2439.
- [60] Dautel, O.J.; Lère-Porte, J.P.; Moreau, J.J.E.; Wong Chi Man, M. "Vapour diffusion hydrolysis of a self-assembled silylated organogel, the OG-HG transcription process: a new way to cast and handle fluorescent silsesquioxane", *Chem. Commun.*, **2003**, 2662–2663.
- [61] Shipway, A.N.; Willner, I. "Electronic transduced molecular mechanical and information functions on surfaces", *Acc. Chem. Res.*, **2001**, *34*, 421–432.
- [62] Davis, S.E.; Breulmann, M.; Rhodes, K.H.; Zhang, B.; Mann, S. "Template-directed assembly using nanoparticle building-blocks: a nanotechtonic approach to organized materials", *Chem. Mater.*, **2001**, *13*, 3218–3226.
- [63] Simmons, B.; Li, S.; John, V.T.; McPherson, G.L.; Taylor, C.; Schwartz, D.K.; Maskos, K. "Spatial compartmentalization of nanoparticles into strands of a self-assembled organogel", *Nano Lett.*, **2002**, *2*, 1037–1042.
- [64] Matsui, H.; Pan, S.; Douberly, G.E., Jr. "Fabrication of nanocrystal tube using peptide tubule as template and its application as signal-enhancing cuvette", *J. Phys. Chem. B*, **2001**, *105*, 1683–1686.
- [65] For a recent review: Hyeon, T. "Chemical synthesis of magnetic nanoparticles", *Chem. Commun.* **2003**, 927–934.
- [66] (a) Berkovsky, B. M.; Medvedev, V.F.; Krakov, M.S. *Magnetic Fluids: Engineering Applications*. Oxford: Oxford University Press, **1993**. (b) Weller, D.; Doerner, M.F. "Extremely high-density longitudinal magnetic recording media", *Annu. Rev. Mater. Sci.*, **2000**, *30*, 611–644.
- [67] Dunlop, E.H.; Feiler, W.A.; Mattione, M.J. "Magnetic separation in biotechnology", *Biotech. Adv.*, **1984**, *2*, 63–74.
- [68] Hatch, G.P.; Stelter, R.E. "Magnetic design considerations for devices and particles used for biological high-gradient magnetic separation (HGMS)", *J. Magn. Magn. Mater.*, **2001**, *225*, 262–276.
- [69] (a) Zrinyi, M.; Szabo, D.; Barsi, L. In *Polymer Sensors and Actuators*, Y. Osada and D.E. Rossi, Eds.; Berlin: Springer-Verlag, **1999**, pp. 385–408. (b) Zrinyi, M.; Szabo, D.; Filipcsei, G.; Feher, J. In *Polymer Gels and Networks*, Y., Osada and A. Khokhlov, Eds., New York: Marcel Dekker, **2001**, pp. 309–355.
- [70] Zrinyi, M.; Barsi, L.; Büki, A. "Ferrogel: a new magneto-controlled elastic medium", *Polym. Gels Networks*, **1997**, *5*, 415–427.
- [71] Narita, T.; Knaebel, A.; Munch, J.P.; Candau, S.J.; Zrinyi, M. "Diffusing-wave spectroscopy study of the motion of magnetic particles in chemically cross-linked gels under external magnetic fields", *Macromolecules*, **2003**, *36*, 2985–2989.
- [72] Szabo, D.; Czabo-Nagy, I.; Zrinyi, M.; Vértes, A. "Magnetic an Mössbauer studies of magnetite-loaded polyvinyl alcohol hydrogels", *J. Colloid Interface Sci.*, **2000**, *221*, 166–172.
- [73] (a) Xulu, P.M.; Filipcsei, G.; Zrinyi, M. "Preparation and responsive properties of magnetically soft poly(N-isopropylacrylamide) gels", *Macromolecules*, **2000**,

- 33, 1716–1719. (b) Mayer, C.R.; Cabuil, V.; Lalot, T.; Thouvenot, R. “Magnetic nanoparticles trapped in pH 7 hydrogels as a tool to characterize the properties of the polymeric network”, *Adv. Mater.*, **2000**, *12*, 417–420.
- [74] Li, S.; John, V.T.; Irvin, G.C.; Suguna, S.H.; Rachakonda, H.; McPherson, G.L.; O’Connor, C.J. “Synthesis and magnetic properties of a novel ferrite organogel”, *J. Appl. Phys.*, **1999**, *85*, 5965–5967.
- [75] Babincova, M.; Leszczynska, D.; Sourivong, P.; Cicmanec, P.; Babinec, P. “Superparamagnetic gel as a novel material for electromagnetically induced hyperthermia”, *J. Magn. Magn. Mat.*, **2001**, *225*, 109–112.
- [76] Lopez, D.; Guenet, J.M. “Encapsulation of self-assembled bicopper complex filaments in thermoreversible gel fibrils: effect of the solvent isomer”, *J. Phys. Chem. B*, **2002**, *106*, 2160–2165.

Chapter 24

PHOTORESPONSIVE GELS

André Del Guerzo and Jean-Luc Pozzo

CSBN UMR CNRS 5802, Université Bordeaux I,
351 cours de la Libération, 33405 Talence, France

1. Luminescent Gels	817
1.1. General Considerations	817
1.2. Luminescent Organogels and Energy Transfer	824
2. Phototunable Gels	835
2.1. General Considerations	836
2.2. Systems	837
2.3. Photochromic Gels Based on Polymers	841
2.4. Photochromic Properties Modulated by the Sol-Gel Transitions Using LMOGs	843
2.5. Irreversible, Photo-Induced Phase Transitions Using LMOGs	844
2.6. Reversible, Photo-Induced Phase Transitions Using LMOGs	846
3. Conclusions and Perspectives for the Future	850

1. Luminescent Gels

1.1. General Considerations

1.1.1. *Excited states and luminescence*

1.1.1.1. Fluorescence. Luminescence is a general term used here to describe the transition of an excited state of a molecule to its ground state by a radiative process. More precise terms are fluorescence (when the initial and final states are of the same multiplicity, usually singlet states) and

phosphorescence (when the spin multiplicity of the initial and final states differ; usually, the initial state is a triplet and the final state is a singlet). Changes of luminescence are caused by molecular aggregation during gel formation. We will briefly mention some aspects related to these changes, but additional details can be found in textbooks on the subject and, especially, in Chapter 12.

1.1.1.2. Excimer emission. Emission from excimers can be an important diagnostic for molecules that aggregate. Excimers consist of a monomer (M) that associates with another monomer *in the excited state* (M^*) and in which the ground state is dissociative. Figure 1 shows a typical excimer (“excited dimer”) emission. It differs from the monomer emission in several ways: (i) it appears at lower energies (higher wavelengths); (ii) it is broadened so that there is a loss of vibronic structure; (iii) under pulsed irradiation, the intensity of the excimer emission shows a rise-time or a decay-time identical to the decay-time of the monomer emission. Excimer emission can be observed in many fluorescent aromatic hydrocarbons and often is a consequence of π -stacking. Indeed, excimer emission only occurs when M and M^* are in proximity, thus usually when they stack. Note that an excimer emission differs from the emission of an excited complex formed from the association of monomers in the ground state.

1.1.1.3. Charge-transfer states and energy transfer. Excited states are more easily described in isolated molecules than in condensed phases. When a mixture of compounds is assembled and interacts, several additional aspects of their behavior have to be taken into account. These include charge-transfer states and energy transfer processes. These processes can lead to more complex photophysical properties, and, among others, lead to enhanced Stokes shifts.

Charge transfer. In many cases, an electron donor-acceptor (EDA) complex is colored, displaying characteristic absorption bands which have no

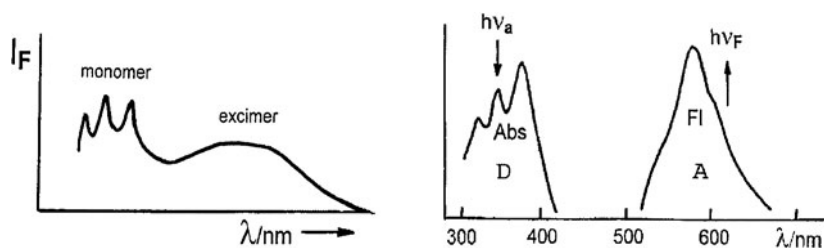


Figure 1. (Left) Typical fluorescence spectra of a monomer (with vibrational structure) and an excimer (broad structureless), when present simultaneously. (Right) Normalized absorption of a donor (D) and fluorescence spectrum of an acceptor (A) showing a large Stokes shift, typically observed if singlet-singlet energy transfer occurs from the D to A (*vide infra*).

counterpart in the separated donor and acceptor. The excited state of such a complex, $(DA)^*$, is often more stable than D^* or A^* alone relative to the ground state (DA) . Thus, $(DA)^*$ represents the lowest energy excited state of multiplicity*. Charge-transfer (CT) states based on organic EDA complexes are often not luminescent due to the intervention of new, non-radiative deactivation processes, whereas some transition metal complexes show luminescent CT states.

Energy transfer. Excitation energy transfer consists of the transfer of energy from a donor molecule in its excited state (D^*) to an acceptor molecule in its ground state (A) while leading to the return of D to its ground state and the promotion of A to an electronically excited state: $D^* + A \rightarrow D + A^*$. This process partially or totally suppresses the emission of (D^*), but can lead to enhanced emission of (A) (see illustration in Figure 1). If (A) is non-emissive, total quenching of the emission can occur.

1.1.2. Possible applications

Even though this chapter will focus on LMOG-based luminescent organogels, it is interesting to compare them with other luminescent materials, some of which have defined applications. For example, the sensitivity of the fluorescence of some materials to their environment can easily be exploited for the detection of analytes. These examples point to future directions in LMOG research.

1.1.2.1. Fluorescent polymers. Interesting examples of fluorescent polymers with potential applications as analyte detectors have been developed by Swager *et al.* [1–7] as well as a number of other research groups [8–12]. The functionality is based on the principle depicted in Figure 2.

In a “traditional” chemosensor, the (spectroscopic) property of the sensor is changed only when an analyte is bound (e.g., goes from grey to white). When the receptors are wired together in such a way that, for example, electronic delocalization occurs between a large number of chromophores, addition of one molecule of analyte can modify the (spectroscopic) property of *all* of sensor units in the “wire”. **SU1-6** (Figure 3) are some sensor units that have been shown to bind analytes [2].

To be effective, the polymer must be highly fluorescent and the different units must be well connected electronically. Conjugation and linearity of the polymer are ensured by an acetylene-phenylene backbone. Low fluorescence quantum yields due to quenching processes can be an important drawback of fluorescent polymers in condensed phases. Indeed, in a condensed phase, colinear aggregation of the polymer chains can occur, inducing deactivating interactions between the parallel transition dipoles. Polymers in which interchain

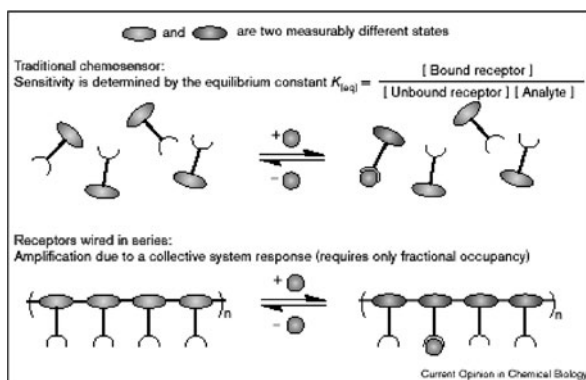


Figure 2. Paradigm for novel chemosensors. (Reprinted with permission from [2]. Copyright (2000) Elsevier.) [A color version of this figure may be found on page 945.]

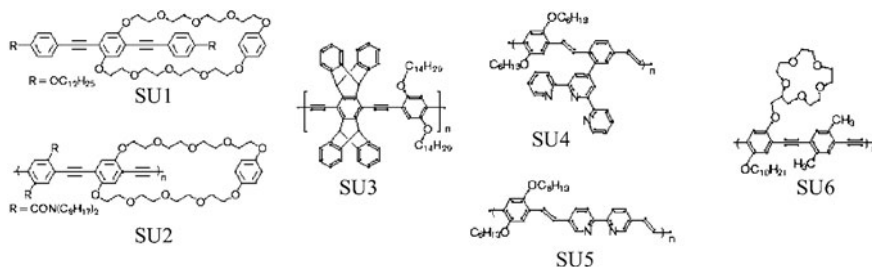


Figure 3. Various examples of conjugated polymer units including a receptor unit. (Reprinted with permission from [2]. Copyright (2000) Elsevier.)

aggregation of chromophore units is inhibited sterically have been made to avoid this problem (Figure 4).

An elegant way to avoid colinear aggregation employs chiral polymers which are forced to aggregate at an oblique angle. As mentioned, they can show much more intense fluorescence than non-interlocked, but colinear aggregated polymers. An example is shown in Figure 5. A femtogram detection limit of these polymers to 2,4,6-trinitrotoluene (TNT) has been demonstrated [4, 6]. They have potential applications for open-air land mine detection.

1.1.2.2. Luminescent doped gels. Prasad *et al.* tested organogels consisting of sodium bis(2-ethyl-hexyl)sulfosuccinate (AOT)-isooctane-water-gelatin mixtures as new media for two photon-pumped lasing [13]. The gel was doped with 4-(dimethyl-amino)-*N*-methylstilbazoliumtosylate (DAST), a second-order non-linear dye. Organogels may avoid a principal limitation shown by polymers, phase separation at high doping levels. These organogels offer

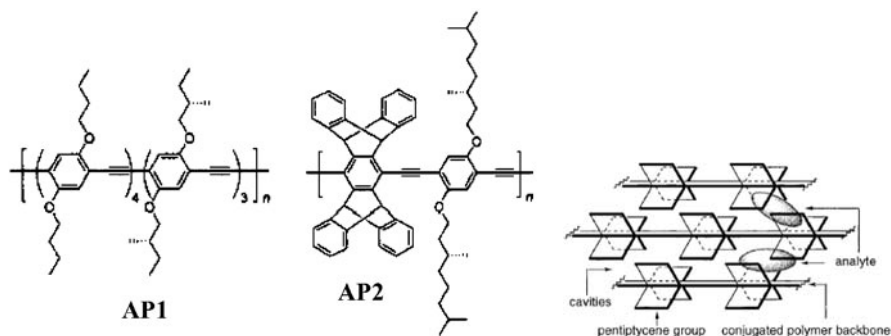


Figure 4. (Left) **AP1**, a chiral acetylene-phenylene monomer unit; **AP2**, a modified unit favoring steric hindrance between chains. (Right) Schematic representation of non-aggregating chromophoric groups on polymer chains and analyte-chromophore association. (Reprinted with permission from [4]. Copyright (2002) Wiley and from [6]. Copyright (1998) American Chemical Society.)

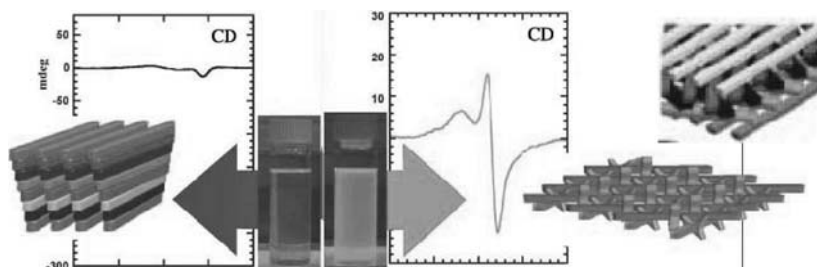


Figure 5. Polymers including chiral monomer units: (left) colinear aggregation of non-interlocking polymer chains (8 layers of **AP1**, see Figure 4) resulting in a small circular dichroism and little fluorescence; (right) angled aggregation of interlocked polymer chains (2 or 5 layers of **AP2**, see Figure 4) resulting in a strong CD signal and a high fluorescence quantum yield. (Reprinted with permission from [4]. Copyright (2002) Wiley.) [A color version of this figure may be found on page 946.]

hydrophilic and hydrophobic domains that are well-separated. Dye inserted in the organogels showed longer optical lifetimes and higher damage thresholds than when inserted in the polymer or glass media tested. Two photon-pumped lasing (in a 1 cm cuvette-cavity) is shown in Figure 6 and compared to one photon fluorescence (the red-shift is due to self-absorption). Figure 6 shows also that the strong non-radiative deactivation of the TICT excited state of DAST is strongly attenuated in the organogel. These results indicate that organogels can be utilized as superior laser pumped optical media because of their ability to accept dopant species and their effects (in some cases, at least) on the photophysical properties of included dyes.

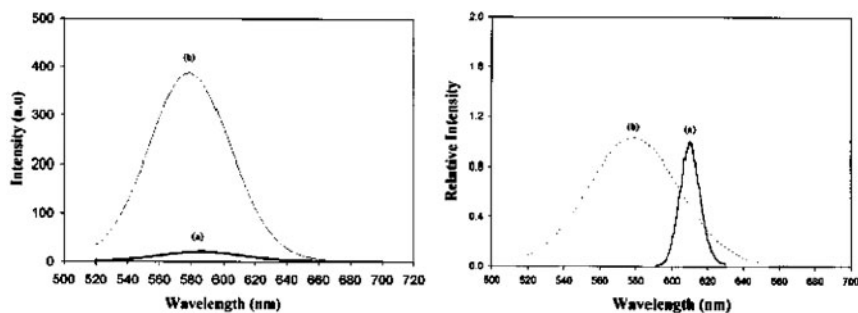


Figure 6. (Left) One-photon induced fluorescence of (a) DAST-doped aqueous gelatin gel and (b) DAST-doped organogel. (Right) (a) Two photon pumped lasing from the DAST-doped organogel and (b) one-photon induced fluorescence. (Reprinted with permission from [13]. Copyright (1999) American Chemical Society.)

Several authors have doped gels with dyes for the development of luminescent sensors. Sato *et al.* studied the emission of SiO_2 and TiO_2 hydrogels, prepared by a sol-gel method, with the luminescent transition metal complex $[\text{Ru}(\text{bpy})_3]^{2+}$ [14]. They showed that the cationic luminescent complex interacts strongly with partially negatively charged SiO_2 units to effect a rigidochromic blue-shift of its emission. In contrast, the luminescence in TiO_2 hydrogels is the same as in aqueous solution. The luminescent compound is assumed to be only trapped in the gel framework but not interacting with the TiO_2 . Electron transfer processes between $[\text{Ru}(\text{bpy})_3]^{2+}$ and methylviologen (MV^{2+}) were also shown to occur in the hydrogel. Sensing of analytes to which cationic dyes are sensitive can thus be envisaged in such gels.

Díaz-García *et al.* gelled reverse micellar solutions using AOT as a surfactant and gelatin [15]. During the gelating process, they included $[\text{Ru}(\text{bpy})_3]^{2+}$ (final concentration = 1.5×10^{-7} M) as a luminescent O_2 sensor and then replaced the organic solvent, isooctane, by an aqueous buffered solution without observing any leaching of the entrapped ruthenium complex. $[\text{Ru}(\text{bpy})_3]^{2+}$ was chosen because its luminescence is known to be quenched very efficiently by O_2 [16]. These gels offer several advantages as sensors. For one, the easily entrapped molecules preserve most of their electronic characteristics and are accessible to external reagents through the pore networks. Also, a thermally and photochemically inert matrix can be chosen. Finally, in contrast to inorganic sol-gel materials, these are not brittle and can be molded into different shapes. Thus, a gel-film has been introduced in a sensing device (shown diagrammatically in Figure 7) and its sensitivity to O_2 has been studied as a function of the organogel properties (N.B., the concentrations of gelatin and AOT). The optimal concentrations were related to gel hardness, accessibility of the luminophore to molecular oxygen, and mechanical properties of the film. They consisted of 2.5% w/v of gelatin and 0.1 M AOT.

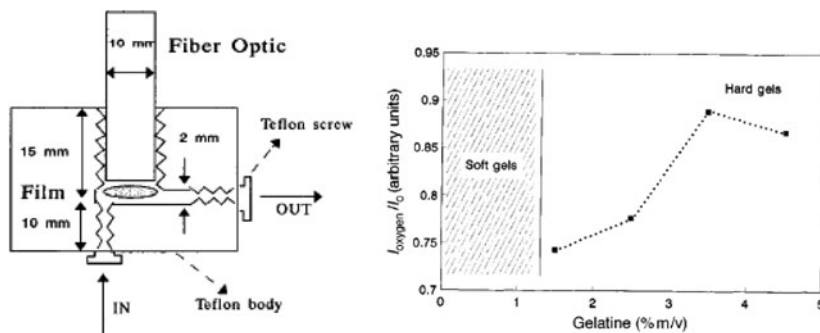


Figure 7. (Left) Sensing device based on an organogel film; (Right) Quenching of included $[\text{Ru}(\text{bpy})_3]^{2+}$ luminescence by molecular oxygen as a function of gelatin concentration. (Reprinted with permission from [15]. Copyright (2002) Wiley.)

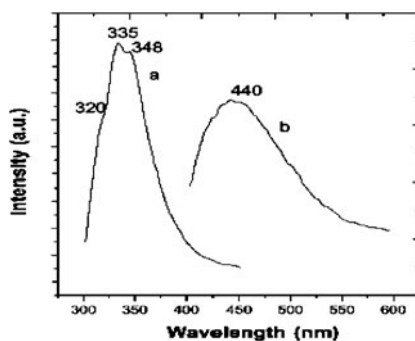


Figure 8. Luminescence of nanoparticles of ZnS in a gel (a; $\lambda_{\text{exc}} = 240 \text{ nm}$) and of neat ZnS (b; $\lambda_{\text{exc}} = 323 \text{ nm}$). (Reprinted with permission from [17]. Copyright (2003) Elsevier.)

Another interesting case consists of the doping of gels by nanoparticles. Hu *et al.* prepared ZnS nanoparticles in a polyacrylamide (PAM) gel using γ -irradiation to initiate crystallization [17]. High resolution electron microscopy shows that the nanoparticles are well-immersed and confined in the PAM network. The particle size is also quite mono-disperse (2–3 nm), showing that PAM inhibits particle aggregating and growth. The emission spectrum of the new material behaves differently from bulk ZnS, showing the quantum confinement effect typically observed in nano-crystallites (Figure 8).

A gel matrix can also be doped with lanthanides. Lin *et al.* prepared organically modified silica xerogels (OMSX) that can trap Eu^{3+} and Tb^{3+} ions (Figure 9) [18]. They observed an intense emission stemming from the lanthanide ions: red for the Eu^{3+} and green for the Tb^{3+} -doped gels. Moreover, an energy transfer occurring from the OMXS matrix to Eu^{3+} and Tb^{3+} , respectively, enhances their emission intensity. The origin of the blue emission of

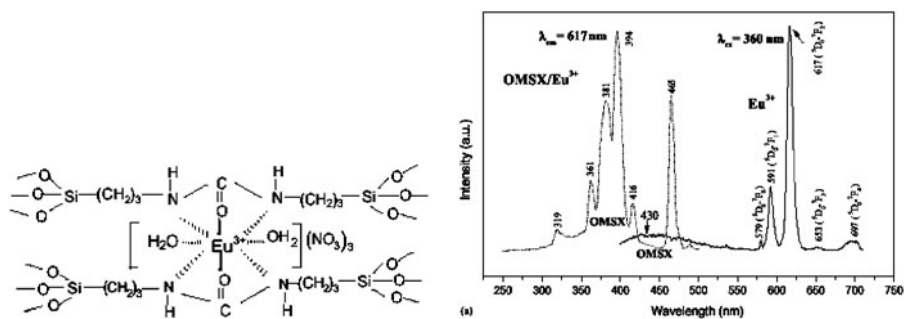


Figure 9. (Left) Structure and (Right) excitation and emission spectra of Eu^{3+} trapped in an OMSX (xerogel). (Reprinted with permission from [18]. Copyright (2003) Elsevier.)

OSMX in the absence of doping agents is not understood well and is attributed to carbon impurities [19].

1.2. Luminescent Organogels and Energy Transfer

A major objective of this chapter is to characterize the luminescence properties of LMOG-based organogels. Indeed, like the polymers and the organogels presented in the earlier sections, some LMOG gels might be efficient analyte detectors or be amenable to other applications requiring a photo-responsive activity. In any application, the luminescence must be very sensitive to the external stimulus, whether this stimulus alters the emission of the organogel by acting directly on the LMOG molecules or by modifying their fibrillar structure. Moreover, large enhancement of the sensitivities or changes of the efficiencies of the luminescence should be induced by self-assembly of the LMOGs. Because relatively few examples, in which addition of an analyte to an LMOG-based organogel results in a strong luminescence response are known, we will focus on the factors that strongly affect the luminescence of LMOGs during their gelation. Thereby, we can identify the characteristics valuable for the development of new and efficient luminescent gels.

Because spectroscopic properties, including luminescence, of gels is presented in Chapter 12, the discussion here will focus on some specific aspects. Changes in luminescence intensity upon gelation can occur due to the appearance, disappearance, or modification of rates of deactivation pathways. In some cases, shape changes or shifts in the wavelengths of emission can occur, leading to color changes. For some cases, both effects can be observed simultaneously. During gelation (and aggregation), changes of LMOG luminescence can be related to the formation of excimers or to increased efficiency of energy transfer processes. As a result of the latter, there is growing interest in exploring the potential of gels for efficient light-harvesting and energy storage.

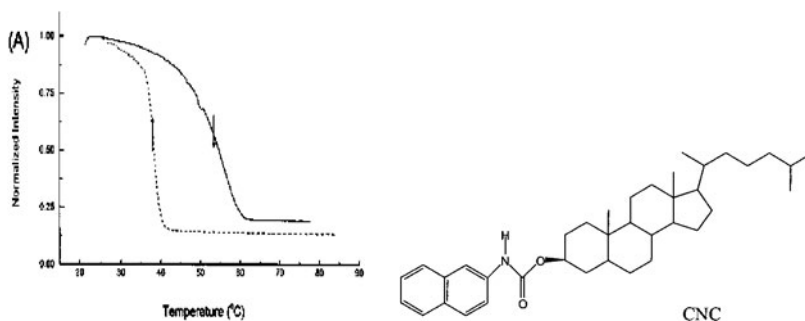


Figure 10. Relative fluorescence intensity at 400 nm ($\lambda_{\text{exc}} = 340$ nm) of 0.9 wt% CNC in *n*-octane vs. temperature. (—) slow-heating and (---) slow-cooling. (Reprinted with permission from [21]. Copyright (2000) American Chemical Society.)

In a second section, we will present some examples of LMOG-based gels that have been doped with luminescent organic compounds or nanoparticles that do not participate to the construction of the fibrillar networks.

1.2.1. Gels based on luminescent LMOGs

1.2.1.1. Phase-induced intensity enhancement and spectral shifts.

Weiss *et al.* studied gelators based on a cholesteryl unit and a fluorophore, naphthalene (CNC) or anthracene (cholesteryl 4-(2-anthryloxy)butanoate; CAB) (Figure 10) [20, 21]. They observed very large emission intensity increases upon gelation with both LMOGs. The intensity changes were accompanied by small shifts of the emission maxima that are ca. 400 nm for CNC and 422 nm for CAB in the gel states. This demonstrates that aggregation of the LMOG molecules within a gel can significantly alter their photophysical properties, and may enhance radiative deactivation pathways.

Other cholesteryl-containing molecules using stilbene or squaraine as the fluorophore have been prepared by Whitten *et al.* [22] Fluorescence studies of the stilbene derivative **CSt** have revealed a 16-fold increase in the intensity of the slightly red-shifted blue emission upon gelation (Figure 11). This increase can be explained by inhibition of a photochemical deactivation process, *cis-trans* isomerization, upon incorporation of the LMOGs into their gel fibers. They also noticed that the intensity increases and wavelength shifts are smaller than the ones observed in Langmuir-Blodgett (LB) films of styrene derivatives, suggesting a weaker association or lower aggregation number for the chromophores in the gel than in the LB films. In contrast, a complete loss of fluorescence intensity is observed upon gelation of the cholesteryl-squaraine derivative **CSq**, indicating strong modification of the electronic properties of

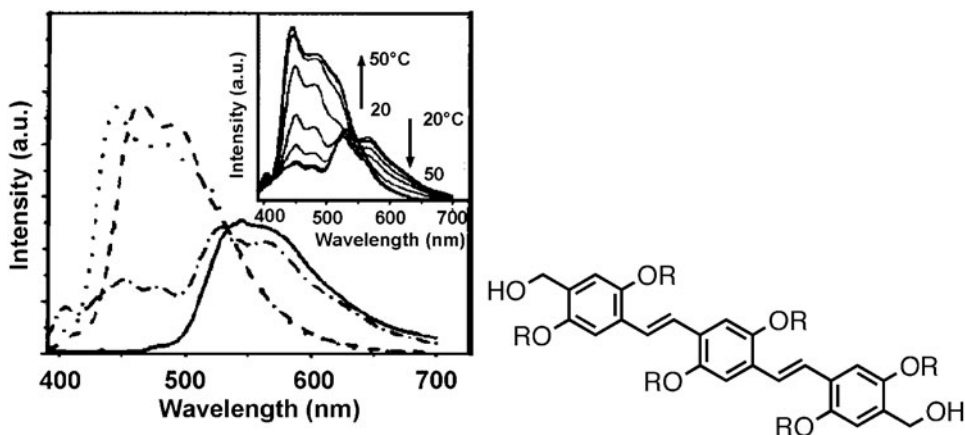


Figure 12. (top) Oligo-phenylene-vinylene (OPV) LMOG ($R=C_{12}H_{25}$). (left) Fluorescence spectra of OPV in chloroform at 25°C (---), hexane at 25°C (·-·) and 50°C (···), and as a sheared film (—). Inset: changes in emission with temperature ($\lambda_{exc} = 380$ nm). (Reprinted with permission from [23]. Copyright (2001) American Chemical Society.)

aggregated and dissolved OPV, can nevertheless limit possible applications. Based on UV-vis-IR spectroscopic and XRD measurements, π -stacking and H-bonding have been suggested to describe the self-assembly [23]. This example suggests that when the lumophore is strongly involved in π -stacking and, thus, in the stabilization of the gel structure, a large change in emission wavelengths (N.B., color) should be expected and may be exploited for various applications.

1.2.1.2. Gel-induced excimer and CT-bands. Up to now, we have presented cases where an enhancement or a shift of the emission band occurs, but strong changes in emission can also be induced by the emergence of new transition bands and the involvement of several excited states. Some of the excited states may lead to emissions, such as from excimers, and others may non-emissive, such as many charge-transfer excited states.

Maitra *et al.* studied LMOGs containing pyrene, a well documented fluorophore. They observed that the rather simple pyrene derivatives, **Pyr1** and **Pyr2** (Figure 13), gelate organic solvents through the formation of strong H-bonds and π -stacking interactions [24, 25]. Gelation is accompanied by interesting changes in the spectroscopic properties, including luminescence. As discussed in the introduction, π -stacking of pyrene can aid the formation of excimers, resulting in the appearance of a supplemental, broad, red-shifted emission. In these cases, the emission of the monomer occurs typically at 407 nm, whereas the excimer emits at 480 nm. The variation of the excimer emission of **Pyr2** and of the monomer emission of **Pyr1** with temperature is

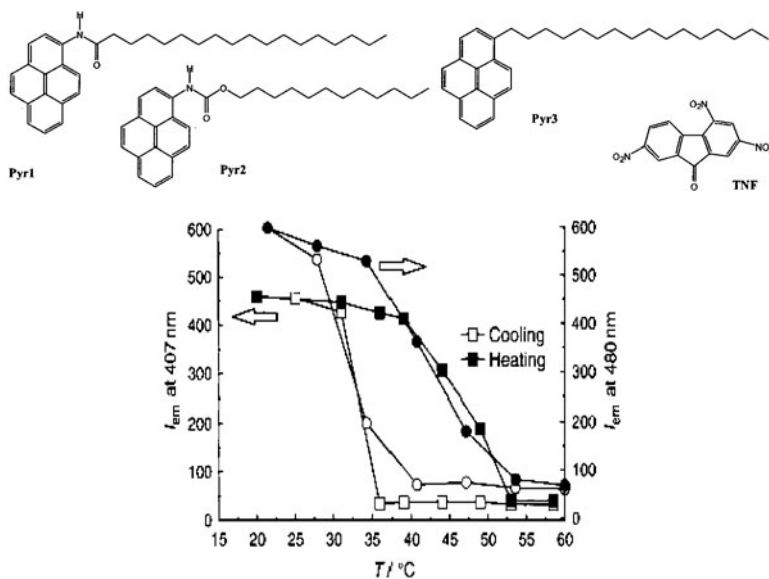


Figure 13. Variable-temperature fluorescence intensities (λ_{exc} 355 nm, λ_{em} 480 nm): **Pyr2** (37.3 mM) in cyclohexane (circles); (λ_{exc} 355 nm, λ_{em} 407 nm): **Pyr1** (10.3 mM) in toluene (squares). (Reprinted with permission [25]. Copyright (2003) Wiley.)

illustrated in Figure 13. In both cases, melting is achieved by heating the gels above 52°C where all emission disappears, whereas gel formation requires cooling below 30°C and re-establishes both excimer and monomer emission.

Another excited state appears in pyrene derivatives such as **Pyr3**, when the co-gelator and electron acceptor, trinitrofluorenone (TNF), is added. In that case, a charge-transfer interaction with the donor pyrene occurs in the ground state. The resultant new CT band has a lower energy than the pyrene-centred transitions. Thus, the non emissive CT-state is probably the lowest-lying excited state. The formation of donor-acceptor pairs can totally quench the emission of pyrene upon gel formation.

Shinkai *et al.* have described another LMOG-based gel that involves complex excited state behavior [26]. The fluorescence of the triphenylene derivatives (TRIPHEN) undergo a strong color change upon gelation (Figure 14). A small red-shift of the emission band around 400 nm is observed, as in the case of some triphenylene derivatives in a sol-liquid crystal transitions [27]. The particularity in the gels is the appearance of a new band at 525 nm, which can be attributed to excimer emission. The same excimer emission, and thus probably a similar structure, is retained in dried, cast films prepared from the gel. It has also been shown by time-resolved emission spectroscopy that the lower energy emission arises on the nanosecond timescale with time-constants identical to that of the higher energy emission decay. This confirms that the emission stems from an excimer, and thus it is

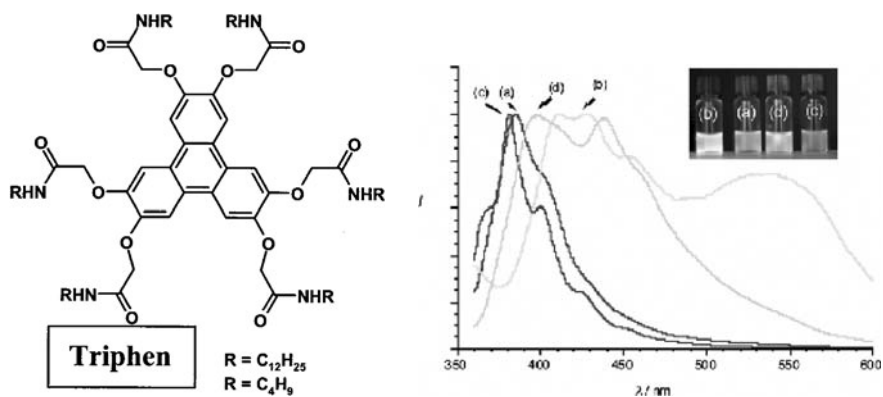


Figure 14. Fluorescence spectra (λ_{exc} 350 nm) of **Triphen-C₁₂**: (a) chloroform solution (5×10^{-5} M); (b) cyclohexane gel (5×10^{-5} M); (c) chloroform solution (5×10^{-3} M); (d) cyclohexane gel (5×10^{-3} M). Inset: photographs of samples at $\lambda_{\text{exc}} = 365$ nm. (Reprinted with permission from [26]. Copyright (2003) Royal Society of Chemistry.) [A color version of this figure may be found on page 946.]

concluded that stacking occurs in the gel fibers. The authors propose that the supramolecular triphenylene derivatives undergo an eclipsed overlap stacking due to the formation of H-bonds of the side-chain, a stacking mode that is different from the one observed in LC-forming triphenylene derivatives [27] (stack by staggered or helical overlap).

Shinkai *et al.* have also induced a strong change in emission of a gel by other means [28]. Fluorescence at 394 nm is observed in some phenanthroline-cholesterol based gels. This purple emission can be changed to a yellow emission by protonating the phenanthroline (*phen*) upon addition of an acid (Figure 15). Full protonation has been achieved in acetic acid, leading to an emission centred at 522 nm. In contrast, in 1-butanol, only partial protonation is achieved by addition of trifluoroacetic acid (TFA), leading thus to an emission with two distinct emission bands, one due to the protonated form and another due to the unprotonated form. This is a rare example of LMOG gels showing a high sensitivity to an external chemical stimulus (in this case, a potential analyte).

1.2.1.3. Gel-mediated energy transfer. In Shinkai's *chol-phen* system [28], the fluorescence data also suggest the presence of energy transfer processes in the gels with partial protonation of the *phen* unit. Energy transfer is favored by the overlap of the absorption spectrum of the protonated phenanthroline and the emission spectrum of the non-protonated *phen* in the 350–400 nm region and is supported by measurements of the fluorescence of a non-gelator phenanthroline derivative as a function of temperature and TFA-concentration. For instance, at concentrations of TFA equal to 0.2 equiv. of phenanthroline, an unexpected total quenching of the non-protonated *phen* and an unexpected high

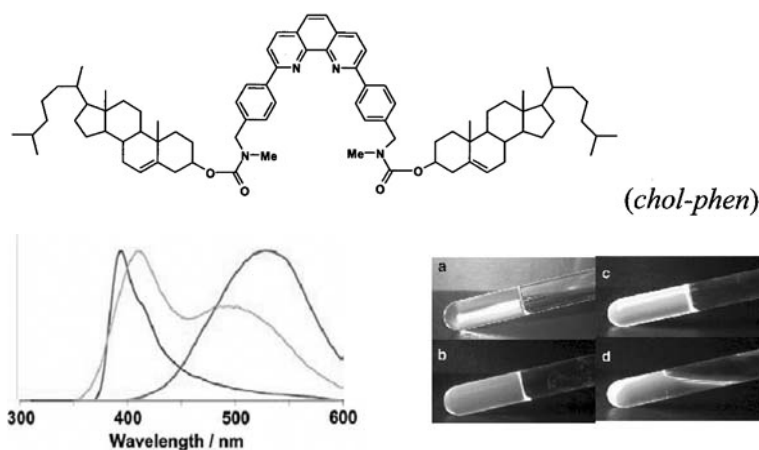


Figure 15. (left) Fluorescence spectra of chol-phen in a 1-propanol gel phase without TFA (blue), in a gel with 2 equiv. TFA (red), in a sol phase with 2 equiv. TFA at 90°C (green); (right) pictures of the same compound as a (a) gel, (b) UV-irradiated gel, (c) as in *b* but with 2 equiv. TFA added, and (d) as in *c* but at 90°C. (Reprinted with permission from [28]. Copyright (2003) Elsevier.) [A color version of this figure may be found on page 947.]

emission intensity of the protonated *phen* was observed and can be rationalized by energy transfer processes.

Energy transfer and, thus, a shift of the emission wavelength is observed in a 3-molecule gelator system [29]. The quaternary amine $N4^+$ (Figure 16) forms hydrogels when it is in equimolar proportions to the counter-anion, naphthalene sulfonate ($NpSO_3^-$). The appearance of a new fluorescence band is observed at lower energy due to excimer formation. In this case, the 40 nm red-shift of the excimer emission relative to that of the monomer emission is not sufficient to completely separate the two bands (Figure 16b). A more significant change in the emission is observed when a 1% molar equiv. of anthracenesulfonate ($AnSO_3^-$) relative to $NpSO_3^-$ is added; energy transfer occurs from the naphthalene excited singlet state to the anthracene, which then emits at 450 nm (as compared to 340 nm for $NpSO_3^-$, Figure 16c). It has to be noticed that the energy transfer occurs also in an aqueous dispersion, but in a lower proportion. This case is more interesting for its light harvesting properties, leading to sensitisation of anthracene, than for its gel-induced emission change.

A perylene-dicholesteryl derivative **Per1** has been shown to gelate *p*-xylene and alcoholic solvent mixtures, whereas **Per2–4** are not gelators (Figure 17) [30]. Nevertheless, **Per1** can incorporate large proportions of **Per2**, **Per3** or **Per4** upon gelation, thus obtaining mixed gels. Under visible radiation, the gel of **Per1** is emissive, even though its intensity is ca. two orders of magnitude lower than in solutions (where its quantum yield is 0.93). When **Per2**, **Per3** or **Per4** is incorporated in the gel, an energy transfer occurs

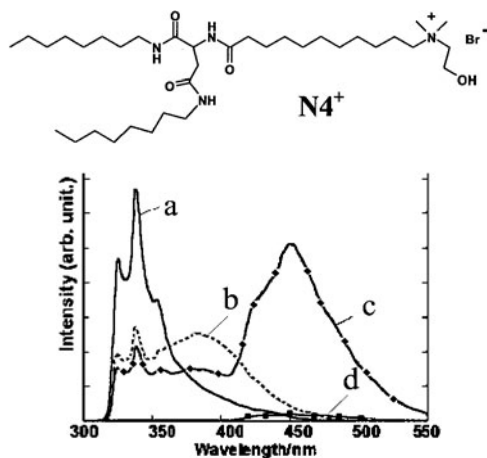


Figure 16. Fluorescence spectra of (a) an aqueous solution of 5.0×10^{-3} M $NaphSO_3^-$, (b) a hydrogel of $N4^+/NaphSO_3^-$ (equimolar, 5×10^{-3} M), (c) the hydrogel in b with addition of 1 mol-% $AnthSO_3^-$; (d) hydrogel of $N4^+$ containing only $AnthSO_3^-$ ($[N4^+] = 5.0 \times 10^{-3}$ M, $[AnthSO_3^-] = 5.0 \times 10^{-5}$ M). Excitation wavelength, 290 nm, 18° C. (Reprinted with permission from [29]. Copyright (2002) Wiley.)

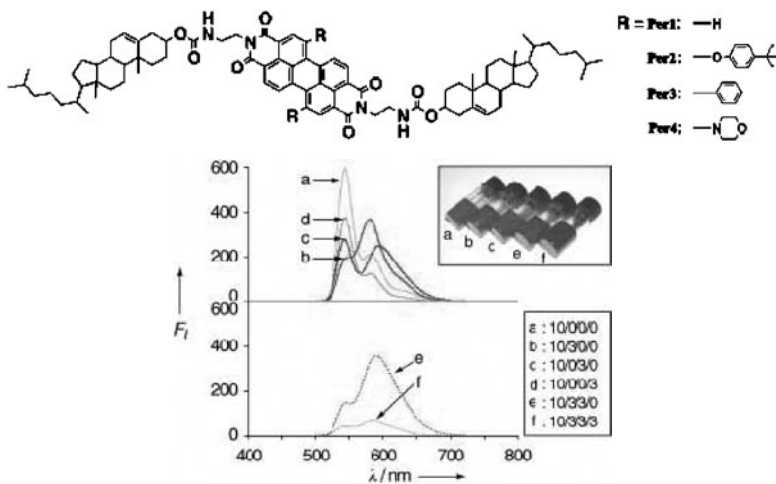


Figure 17. Fluorescence spectra of **Per1/Per2/Per3/Per4** mixed gels in *p*-xylene/1-propanol (3/1 v/v); $\lambda_{ex} = 457$ nm. The numbers in the legend correspond to the molar ratios of **Per1/Per2/Per3/Per4** in the gels a–f. $[Per1] = 0.5$ wt/vol% (3.8 mM), $[Per2-4] = 0$ if denoted 0 in the legend, or 1.3 mM if denoted 3. Inset: a photograph displaying the **Per1/Per2/Per3/Per4** mixed gels (no irradiation). (Reprinted with permission from [30]. Copyright (2004) Wiley.) [A color version of this figure may be found on page 947.]

from **Per1** to the other **Per** derivative. The efficiency is directly related to the spectral overlap of the emission of **Per1** and the absorption of **Per2–4**. In a mixture of **Per1** and **Per2–4**, stepwise energy transfer can occur leading finally to excited singlet states of **Per4**, a very weak emitter. These gel mixtures can thus cover a large spectral range in absorption, and the components act as light-harvesting units leading to the excitation of the derivative with the lowest-lying excited state.

Recently, a two-component mixed gel based on LMOGs prone to intimate intermixing has shown to exhibit an extremely efficient energy transfer process [31]. Indeed, DDOA (2,3-didecyloxyanthracene) acts as a light-harvesting matrix for the sensitisation of DDOT (2,3-didecyloxytetracene, Figure 18) present in very small amounts (<1%). 0.75% of DDOT are sufficient to quench >90% of the emission of DDOA. Figure 18 shows the intense fine structured emission of DDOT that appears upon excitation of the DDOA matrix. An efficient fluorescence colour switching, from blue to turquoise-green, can thus be obtained by the temperature-induced *sol-gel* phase transition. Similar results have been observed with a tetrahydro-DDOA gel containing <1% of DDOA [31]. Indeed, upon formation of the *gel* only the blue emission of DDOA was observed, whereas in the isotropic *sol* phase the tetrahydro-DDOA is the only emitter (emission in the UV spectral range).

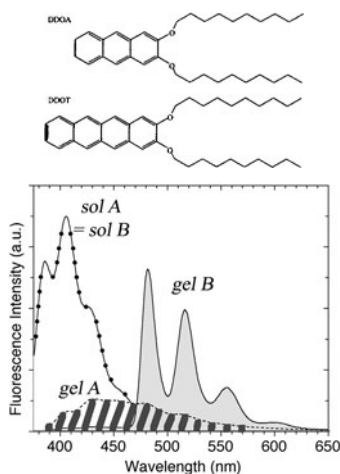


Figure 18. (Top) 2,3-didecyloxyanthracene (DDOA) and 2,3-didecyloxytetracene (DDOT). (bottom) Emission spectra in methylcyclohexane of (A) DDOA and (B) DDOA+DDOT(0.75%): (—●—) *sol* of (A) and *sol* of (B) at 298 K, $\lambda_{\text{exc}} = 366$ nm; (grey surface) *gel* of (A) at 170 K, $\lambda_{\text{exc}} = 382$ nm; (striped surface) *gel* of (B) at 170 K, $\lambda_{\text{exc}} = 382$ nm. [DDOA] = 2×10^{-5} M. Similar results are obtained with [DDOA] = 2×10^{-3} M in DMSO and thus at higher temperatures (*gel* at 298 K and *sol* at 338 K). Unpublished results: J. Reichwagen, H. Hopf (TU-Braunschweig, Germany) A. Del Guerzo, C. Belin, H. Bouas-Laurent, J.-P. Desvergne (Université Bordeaux 1, France).

1.2.2. Doped LMOG-based Gels

The LMOG-based gels designed by Nakashima-Kimizuka [29], Shinkai [30] and Desvergne [31] have been doped with luminescent dyes such as anthracene, perylene or tetracene derivatives. In these cases, the dopant acts as an energy acceptor and appears to be integrated into the fibrillar structure of the organogel. There are few examples in which a luminescent compound that does not participate in the construction of the gel-fiber network has been doped into an LMOG-based gel. Two approaches to using such system in luminescence studies have been advanced: using the gel as a scaffold or using light-absorbing LMOGs to act as light-harvesting scaffolds.

In an example using the LMOG as a scaffold, nanoparticles were incorporated in organogels of AOT and *p*-chlorophenol in isoctane [32]. AFM images of the topography of the gel fibers show 100 nm diameter fibers that consist of parallel fiber bundles (10 nm in size) and ferrite nanoparticles appear as dots on the surfaces of the fibers. Fluorescent CdS nanoparticles (0.44 mM) were also added to the same gel system. Only small changes in the emission spectrum of CdS are induced upon the gelation of the micellar AOT solution: emission intensity increases slightly at lower frequency whereas an attenuation occurs at higher frequency; the emission maximum (540 nm) does not change (Figure 19).

Octanethiol-covered Au nanoparticles, although non-emissive, have been incorporated within an organogel [33] and the system merits discussion here because of the efficient 3D-organization of the nano-particles that was achieved through site exchange. The gel is composed of thiol-terminated compounds that gelate toluene. The organization and aggregation of the particles is evidenced by

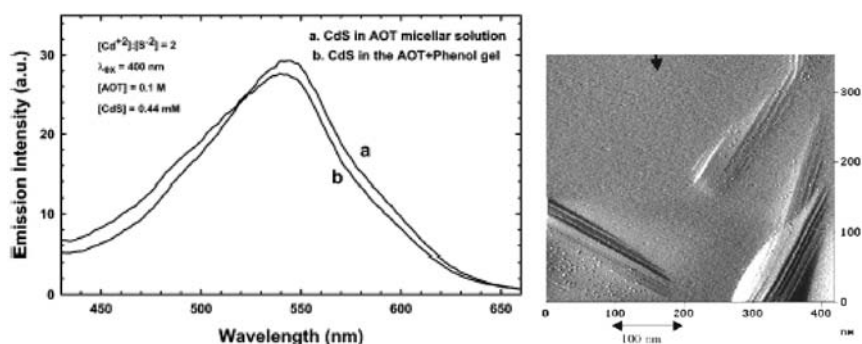


Figure 19. (Left) Fluorescence spectra (λ_{exc} 400 nm) of CdS nanoparticles (a) in an AOT micellar solution and (b) in an AOT+phenol gel; (right) AFM topography image of ferrite nanoparticles on AOT+phenol gel-fibers. (Reprinted with permission from [32]. Copyright (2002) American Chemical Society.)

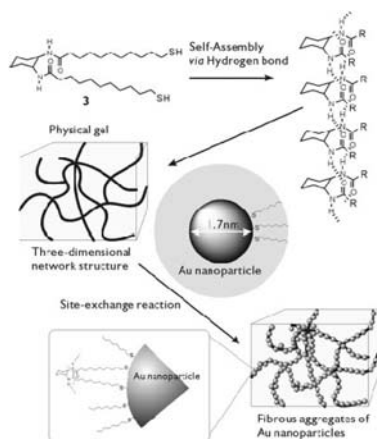


Figure 20. Organization of Au nanoparticles on the organogel. (Reprinted with permission from [33]. Copyright (2004) Wiley.)

SEM micrographs and by the modification of the plasmon resonance absorption band of the nanoparticles at 512 nm. The pertinent information is summarized in Figure 20.

A different behavior is observed when rhodamine B is added to an OPV-based organogel (see Section 1.2.1.1). Energy transfer occurs from OPV to rhodamine upon excitation in the near UV region of the spectrum [34]. This energy transfer is very efficient in a xerogel film. As seen in Figure 21, the emission of condensed OPV centered at 550 nm is almost completely quenched by the rhodamine that then emits intensely at 630 nm. Electron microscopy images of the xerogel show that the rhodamine aggregates and the aggregates become attached to the surface of the gel fibers. These agglomerates act as emitting centers whereas the gel chromophores serve as a scaffold and as light-harvesting antennae. Aggregation is also responsible for the red-shift in the emission of the rhodamine.

A coumarin dye in a solution of 1-butanol has been gelled with the stilbene-derivative **CSt** in order to study the gels by conventional and fluorescence microscopy [22]. It was established that the gelator and solvent occupy the same region of space, the fiber network. The fibers emit intensely under UV irradiation (blue stilbene emission) as well as under visible irradiation (green coumarin emission). Another fluorescent probe, a merocyanine, was also used in order to probe the viscosity of the gel medium [22]. In solution, the lifetime of the probe increases significantly with increasing viscosity. In the gel phase, no change in the emission of the probe is observed, indicating at least that the majority of the solvent stays in a very fluid phase upon gelation.

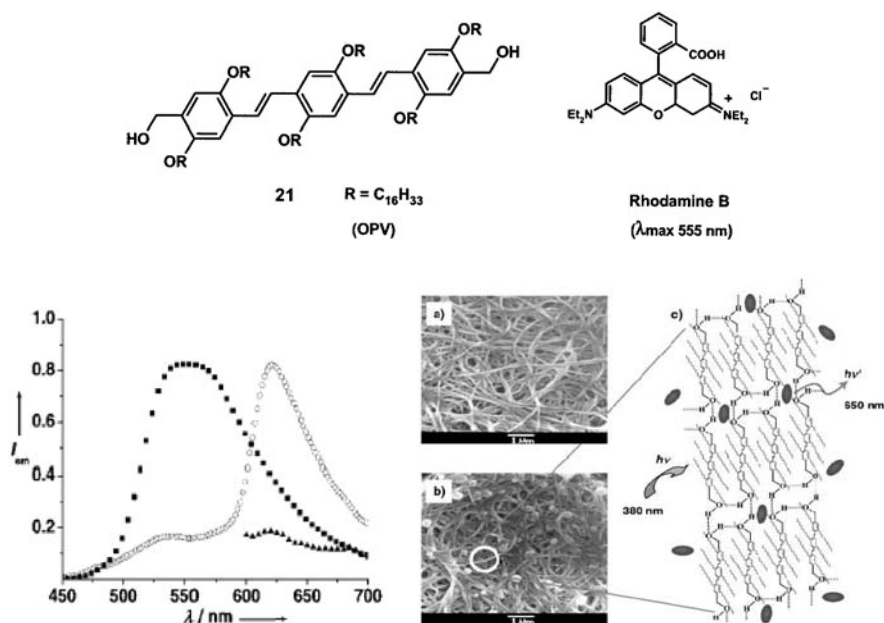


Figure 21. (Left) Fluorescence spectra (λ_{exc} 380 nm) of the xerogel film of OPV (squares) and upon addition of rhodamine B (2:1 mol ratio, circles); the third spectrum is obtained from direct excitation of rhodamine B (λ_{exc} 535 nm, triangle). (right) SEM images of (a) an OPV film, (b) a film with rhodamine B, and a (c) schematic representation of the molecular organization. (Reprinted with permission from [33]. Copyright (2003) Wiley.)

2. Phototunable Gels

A promising approach towards development of smart gels relies on the introduction of an addressable function into the LMOGs. Photochemically active molecules, including photochromic ones, could be addressable in this way. Their excitation and subsequent chemical transformation could modify the self-assembly process of the individual molecules as well as their supramolecular networks. Extensive research has been devoted to the study of molecules whose physical properties can be changed reversibly using light. Although irreversible reactions are more common in photochemistry [35], reversible transformations, especially those that involve photochromism, can be very useful [36]. The focus of this chapter is on the reversible reactions because they can lead to so-called “smart materials”.

A photochromic compound is characterized by its ability to alternate between two different chemical forms having different absorption spectra in response to irradiation of appropriate wavelengths. *Photochromism* is defined as a *light-induced, reversible change of color*. Some chemical species undergo

reversible photochemical reactions that encompass reversible physical phenomena, leading to devices that act as switches [37], optical memories [38], sources of variable electrical current, enhancers of ion transport through membranes, modulators of wettability, etc. Usually, for such purposes, organic photochromic compounds are incorporated into polymers, liquid crystalline materials or other matrices.

The changes in physical or chemical properties can be transferred to the microenvironment or supramolecular structure by photochromic molecules. In fact, supramolecular systems of this sort are photoresponsive materials [39]. In this section, we discuss selected aspects of photochromic molecules confined within gels.

2.1. General Considerations

Consider a molecule whose reversible transformation is induced by electromagnetic radiation between two states, **A** and **B**, having distinguishable absorption spectra. The changes may be induced by IR, visible or UV radiation (Figure 22) The thermodynamically more stable form **A** is transformed by irradiation into form **B**. The reverse reaction can occur thermally (Type T-photochromism) or photochemically (Type-P). Photochemically produced forms **B** need not to be susceptible to thermal reversion to **A** in the dark. Although the former is quite common, those systems which are thermally stable in the form **B** and revert to form **A** only under irradiation have the greatest potential for practical device applications.

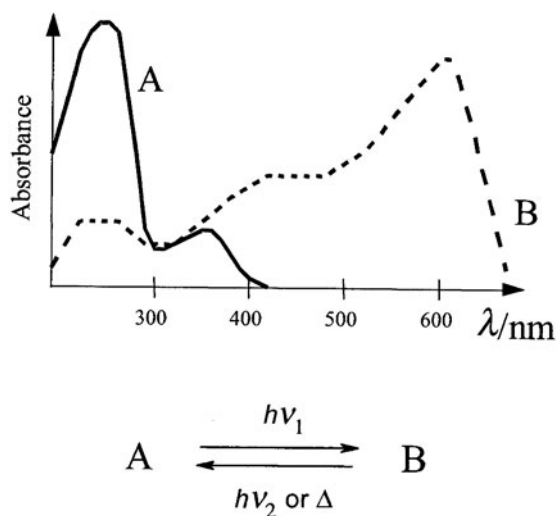


Figure 22. Schematic representation of photochromic equilibrium.

The most common organic photochromic systems involve *unimolecular* reactions of molecules that are colorless or pale yellow in form A and colored in form B (e.g., red or blue).

This phenomenon is referred to as *positive photochromism*. Other systems are *bimolecular*, such as those involving photocycloaddition reactions. When $\lambda_{\max}(A) > \lambda_{\max}(B)$, *photochromism* is said to be *negative or inverse* [39]. The mechanisms responsible for the effects frequently are *cis-trans* isomerizations, tautomerizations, and electrocyclic ring closures or openings.

2.2. Systems

2.2.1. *Cis-trans* isomerization

E (*trans*) \rightleftharpoons Z (*cis*) photochemical isomerizations processes are especially useful. The (usually) less stable (Z) isomer can be made to predominate at photoequilibrium. Because the E- and Z-alkenes usually have very similar absorption spectra, both isomers absorb the radiation. In the absence of secondary reactions, a photostationary state (PSS) is therefore reached.

For example, stilbenes undergo reversible *cis-trans* photoisomerization [40]. Direct excitation leads to isomerization exclusively from singlet excited states. Competing processes include fluorescence from the *trans* isomer and photocyclization from the *cis* isomer (Figure 23) [41].

In highly concentrated solutions, *trans*-stilbene (**TS**) undergoes a [2+2] cycloaddition reaction to form a cyclobutane derivative. *Cis*-stilbene (**CS**) can also undergo a photoinduced, unimolecular 6π -electrocyclization to give the 12π -system, 4a,4b-dihydrophenanthrene, which in turn can be converted irreversibly under oxidizing conditions into phenanthrene. Both are undesirable side products in a photochromic system. For these reasons, stilbenes have seen limited use as reversible photoswitches.

A closely related class of molecules with more favorable photochemical properties are azobenzenes (**AB**; Figure 24) [42]. Many azo compounds are

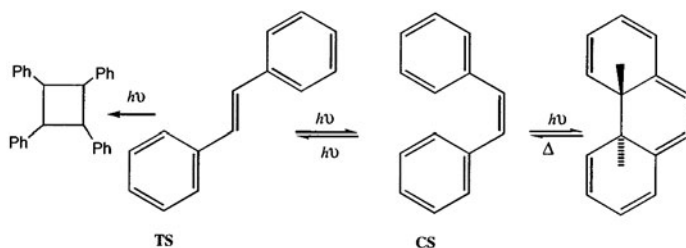


Figure 23. Photochemical behavior of stilbenes.

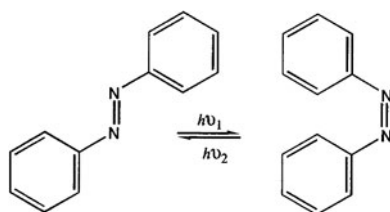


Figure 24. Photochemical behavior of azobenzenes (**AB**).

commercial dyes and their structures are “pseudo stilbenes”. Because they are less prone to side reactions than stilbenes themselves, the azo analogues are used more frequently in supramolecular assemblies to trigger reversible environmental changes in a variety of molecular systems [37]. An additional advantage when azobenzenes are incorporated into supramolecular or rigid systems is that they are often forced into conformations that lead to increased thermal stability.

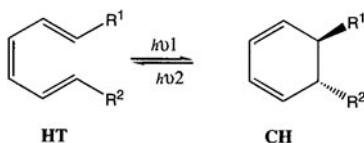


Figure 25. Schematic representation of the electrocyclicization reaction between 1,3,5-hexatriene (**HT**) and 1,3-cyclohexadiene (**CH**).

2.2.2. Electrocyclizations

Another light-induced transformation that molecular switches can undergo is an electrocyclic reaction. The 1,3,5-hexatriene (**HT**)/1,3-cyclohexadiene (**CH**) interconversion depicted on Figure 25, is one of the most important reactions giving rise to photochromic systems [43]. The concerted ring closure is conrotatory for photochemical reactions, resulting in a *trans* positioning of R^1 and R^2 from the *trans,trans* isomer of **HT**. The thermal ring closure is disrotatory resulting in a *cis* arrangement of R^1 and R^2 .

Electrocyclic reactions are encountered with *spiropyrans* **SP**, a family of spiro[azaheterocycle-benzopyrans] [44]. Photochromic spiropyrans are colorless or weakly colored as solids or in solutions. Upon UV irradiation, they become colored due to their merocyanine forms and solutions of them fade *thermally* to the original spiropyran state; in many cases, the merocyanines can also be decolorized by visible light (Figure 26). A few spiropyrans display negative photochromism. They are colored in the dark and *bleached* by UV light.

Many spiropyrans are also *thermochromic* and exhibit spectra in the colored forms which are identical to those produced photochemically. The presence of a nitro group on the 2H-1-benzopyran moiety is a prerequisite for efficient photochromism at ambient temperatures. This induces the formation of a mixture of colored forms (**TC** and **TT**) which possess a pronounced zwitterionic character.

Spiropyrans have some major deficiencies as photochromic molecules. They have low thermal stability in the merocyanine form [45], undergo photooxidation [46] as a side reaction, and exhibit thermochromic behavior [47]. Nevertheless, spiropyrans are widely employed in photochromic polypeptides [48], holographic recording [49], and opto-bioelectronic devices [50].

The development of spiroxazines (**SO**) is modeled after spiropyrans (Figure 27). They have excellent resistance to light-induced degradation [51] due to the photochemical stability of the oxazine molecular framework in the ring-closed and open-ring forms. Their fatigue resistance is an important attribute for applications in photo-responsive eyeglasses [52]. Photochromic behavior of spiroxazines can be affected enormously by the nature of the media in which they reside.

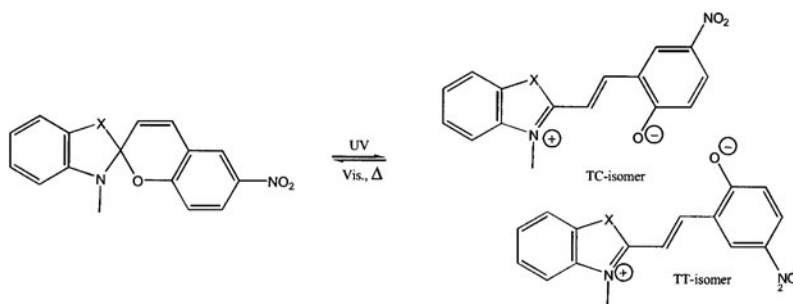


Figure 26. A spiropyran (**SP**) and its open forms (**TC**- and **TT**-isomers).

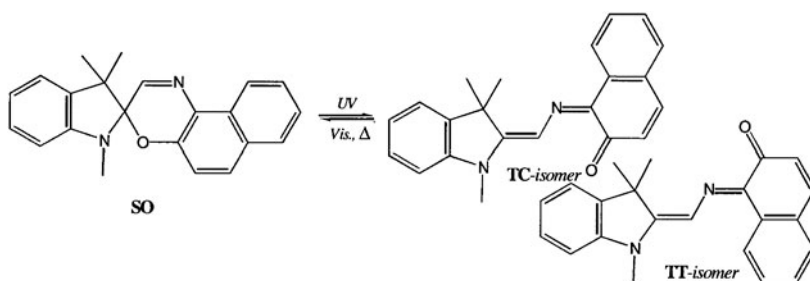


Figure 27. Photochromic equilibrium for a spiroxazine (**SO**).

Recent interest in the photochromism of naphthopyrans, **NP**, (Figure 28) [53] has been sparked by commercialization of photochromic plastic ophthalmic eyewear [54]. Although structurally related to spiropyrans, they behave in a different manner from them. The open forms are exclusively quinonic and the photochromic properties are strongly dependent on the aryl groups tethered to the C-sp³ center. NMR investigations allow the ratio between the **TT**- and **TC**-isomers to be quantified [55].

Last, but certainly not least of the photochromic molecules that will be discussed are the diarylethenes, **DARE** (Figure 29) [55]. Upon irradiation with UV-light the diarylethenes undergo a ring closure to the colored closed form. This closed form is thermally stable and upon irradiation with visible light the system returns to the ring opened form. The most important properties of these compounds are the thermal stability of the closed form and the high fatigue resistance. Of all the photochromic systems, this property is restricted to fulgides [56] and the diarylethenes without the presence of any other chemical partners.

In a supramolecular system, an optical switch must be thermally stable. Furthermore, all properties should be retained after incorporation in a supramolecular system. As previously mentioned, irradiation of *cis*-stilbene **CS** (Figure 23) can lead to the formation of thermally unstable dihydrophenanthrene. The thermal stability of the ring-closed form is controlled by the energy barrier, and five-membered rings, especially thiophenes (**DTE**), are the most appropriate choice.

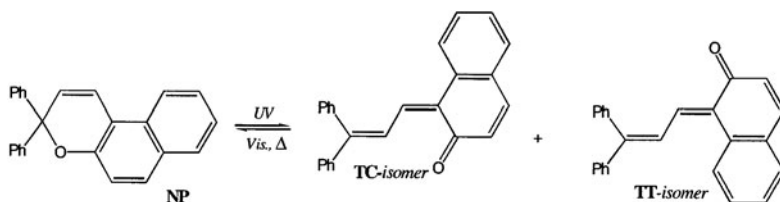


Figure 28. Photochromic equilibrium for a naphthopyran (**NP**).

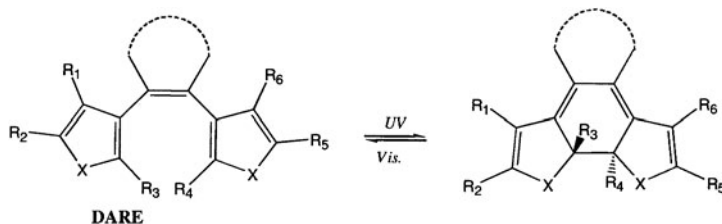


Figure 29. Photochromic equilibrium for diarylethenes (**DARE**).

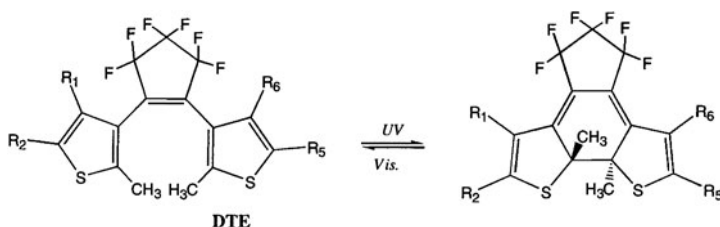


Figure 30. Photochromic equilibrium for 1,2-Bis(thien-3-yl)perfluorocyclopentène (**DTE**).

In order to prevent *cis-trans* isomerization during the photochemically induced ring closing reaction, the alkene bridging unit is part of a cyclic structure, such as maleic anhydride, maleimide or a perfluorocyclopentene-bridge as depicted for DTE (Figure 30).

2.3. Photochromic Gels Based on Polymers

The preparation of various functional photochromic polymers [48, 52] have been used in many photonic applications. Reversible, photoinduced physical and chemical properties can be transferred to the micro-environment by a photochromic molecule incorporated in such systems. For that reason, numerous efforts have been devoted to polymeric gels and/or hydrogels [57]. Their swelling and shrinking behavior has many potential uses in applications such as controlled release of drugs, separations, and construction of actuators [58, 59].

The photoresponsive behavior of poly(*N*-isopropylacrylamide) (PNIPAM), modified with side chains containing azobenzene units that undergo photoisomerization, has been investigated [60]. Thus, 1% aqueous solutions of poly(*N*-isopropylacrylamide) can form thermoreversible gels, and irradiation of pendant azobenzene groups (2.7 mol%) leads to reversible changes of the gelation temperature (Figure 31).

At 750 nm, the solution is transparent, whereas the gel is opaque, as shown in Figure 31. The *cis* form of azobenzene, **AB** maintains a high percent of transmittance between 20 and 26° C ($T_g \approx 30^\circ\text{C}$) whereas the *trans* isomer induces a sol-gel transition temperature around 20° C. These transition temperatures are triggered by light of different wavelengths which triggers *cis-trans* isomerization. In this way, the transmittance can be tuned from 80% to 0% (or 0% to 80%) by irradiation in the 20–26° C temperature range. Irradiation at 350–410 nm solubilizes the polymer and the solution becomes transparent; visible irradiation at $\lambda_1 > 410\text{ nm}$ decreases the solubility and the polymer undergoes phase separation.

swelling in water can be controlled both by the time of irradiation and by the nature of the substitution on the anthracene moieties. The photo-cross-linked PAEI gel reverts to a soluble polymer by cleaving the disulfide bond as shown in Figure 32 upon addition of a reducing agent. In addition, photocleavage of the anthracene dimer has been reported to be efficient at shorter wavelengths.

2.4. Photochromic Properties Modulated by the Sol-Gel Transitions Using LMOGs

To understand how gelation is induced by small organic molecules, it is necessary to understand the relationship between the gelator structure, the gelled solvent properties, and the molecular organization in fibers constituting the three-dimensional gel network. In this regard, attempts have been made to distinguish between the critical gelation and the critical aggregation concentrations.

The lowest concentration at which gelator molecules aggregate in a sol, has been determined using the fading rate of a spiropyran moiety covalently linked to an L-glutamic acid derivative, **SPG** (Figure 33) [63]. The first-order kinetics of the thermal reversion of the merocyanine to the spiropyran form is strongly dependent on the nature of the medium and state of photochrome aggregation. The latter allows determination of the critical aggregation concentrations.

The supramolecular organization of gels have also been used to stabilize photochromic alkylammonium polyoxomolybdates [64]. The inorganic derivatives have been reported to exhibit weak reversibility both in solution and solid states. When incorporated into an organogel based on *trans*-(1R,2R)-1,2-bis(undecylcarbonylamino)cyclohexane [65], the light-induced absorbance is increased significantly.

The colored species are stable for a month whereas the solution is decolorized within several hours. An alkylammonium molybdate complex within a gel may be considered an inorganic photochrome. As such, this example

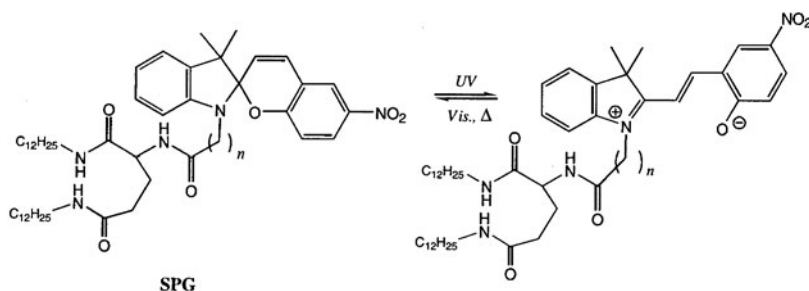


Figure 33. Photochromic equilibrium for **SPG**.

involves color generation and erasing switched by the sol-gel phase transition (Figure 34). A similar stabilization provided by an LMOG gel is known [66].

2.5. Irreversible, Photo-Induced Phase Transitions Using LMOGs

Some gels that undergo sol-gel phase transitions induced by external stimuli other than temperature changes are known. One employs a photochemically-controlled gelation system based on *cis-trans* isomerization of the double bond in maleic acid amides (Figure 35) [67].

Thus, some bis(aminoacid) oxalamides are efficient hydrogelators and their intermolecular lipophilic interactions can be followed by the degree of cooperative, self-complementary H-bonding. The photoisomerization at the molecular level induces a morphological transition at the supramolecular level comprising transformation of microspheres formed by maleic acid amides into fibrous gel network of fumaric acid amides (Figure 36). Instantaneous and irreversible conversion of the maleinamide sol to fumaramide gel is achieved upon irradiation at >330 nm and upon addition of a catalytic amount of bromine.

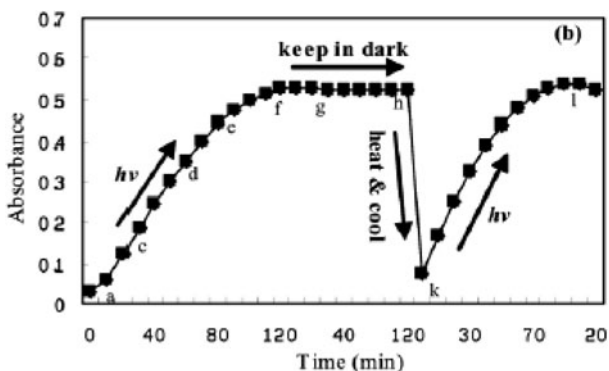


Figure 34. Coloration and fading cycle of alkylammonium molybdate in the gel state. (Reprinted with permission from [65]. Copyright (2002) American Chemical Society.)

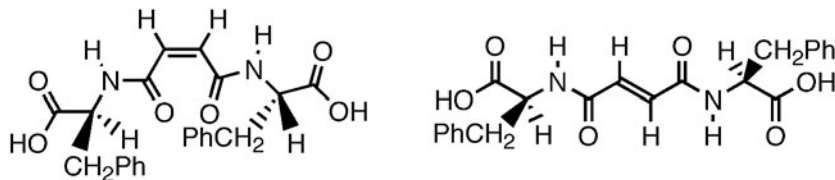


Figure 35. Maleic and fumaric acid derivatives.

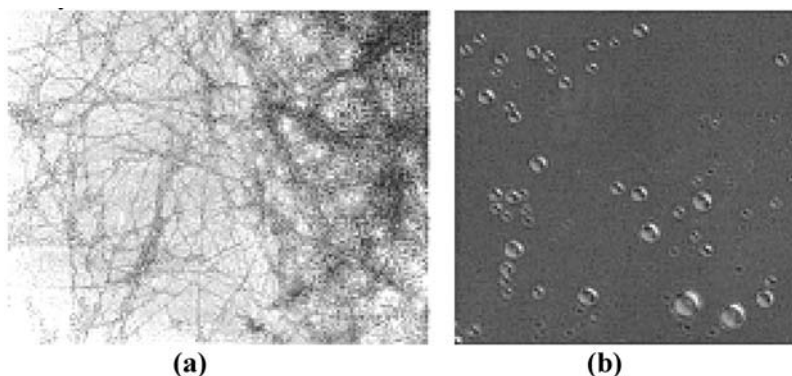


Figure 36. (a) Fibrous gel network formed by fumaric acid derivatives. (b) Microspheres formed by maleic acid derivatives. (Reprinted with permission from [67]. Copyright (2002) American Chemical Society.)

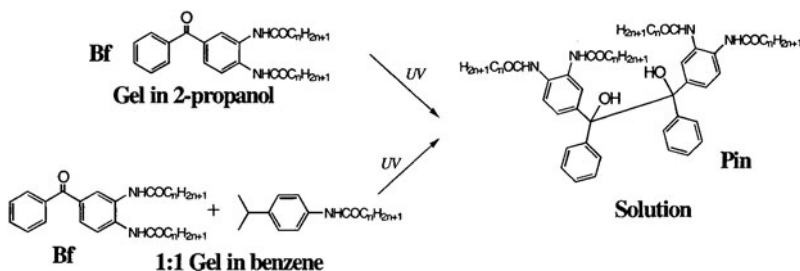


Figure 37. Irreversible transformation of gels into solution under UV-irradiation.

Restricted molecular motion, such as imposed by the crystalline state, can cause specific and highly selective photoreactions [68]. Benzophenones functionalized with two alkylamide side chains have been designed as photoreactive LMOGs [69]. The efficiency of pinacol formation upon irradiation of benzophenone is dependent upon the hydrogen donating ability of a co-reactant, such as an alcohol or isopropylarene. In this case, N-alkylcarbonyl-4-isopropylanilines are the hydrogen-donor/co-gelators. When irradiated, gels of benzophenone linked with alkylamides (**Bf**) in 2-propanol gradually dissolved from the outside to the inside (Figure 37).

After prolonged irradiation, the gel phase was completely lost and pinacol derivatives (**Pin**) were the main products in the solution. Similar results were obtained when a 1:1 mixture of both gelator molecules was irradiated. This is an example of an irreversibly photoinduced gel-to-sol phase transition. It is a prototype for the use of the three-dimensional network of gels as soft, solid matrices to control photochemical reactions.

2.6. Reversible, Photo-Induced Phase Transitions Using LMOGs

Reversible, photochemically-controlled gelation has been accomplished using 4-methoxy-4'-[(cholesteryloxy)carbonyl]azobenzene as the LMOG and 1-butanol as the liquid [70]. The *trans* \rightarrow *cis* photoisomerization (300–380 nm) and subsequent *cis* \rightarrow *trans* isomerization ($\lambda > 450$ nm) was repeated several times in the gel and sol states without any noticeable photodegradation (Figure 38). As indicated by the temperature of gelation values (T_g), the strength of the network was higher when the LMOG was in its *trans* (**AB1t**) configuration than at its pss: at selected concentrations, the *trans*-isomer gels 1-butanol whereas the pss of the *cis-trans* mixture provides a sol.

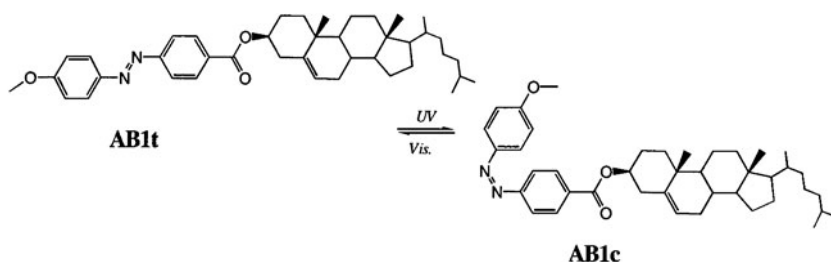


Figure 38. *Cis-trans* photoisomerization of azobenzene-based LMOGs.

Additional examples of gelators incorporating an azobenzene unit have been shown to be photosensitive [71, 72]. Also, an azobenzene co-aggregating guest has been used for chiral recognition [72], and various nematic mesogens have been gelled using azobenzene derivatives [73].

Photochemical control of the self-assembly in supramolecular nanostructures has been demonstrated using LMOGs containing photochromic diarylethene units [74] that lead to thermally bistable systems [55]. Dithienylcyclopentenes undergo reversible electrocyclization and ring opening upon exposure to UV and visible light, respectively. The pronounced change of conformational flexibility between the cyclic and acyclic forms should strongly affect supramolecular self-assembly.

However, only viscous solutions were observed when dithienylcyclopentenes linked to alkylamides (**TAM**) with a long alkyl chain (Figure 39) were examined in a variety of fluids. Compounds possessing a tert-butyl group in place of the alkyl chains did not appear to aggregate at all. Irradiation of 5 mM viscous solutions did lead to the switching process of the photochromic unit that was accompanied by a clear decrease of viscosity; the open-form self-assembles into larger aggregates than the closed-form as described on Figure 40.

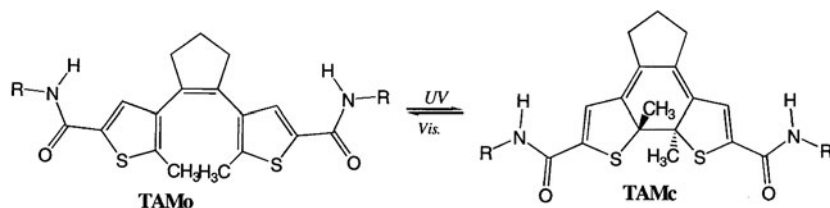


Figure 39. Electrocyclization of diarylethene-based LMOGs (**TAM**).

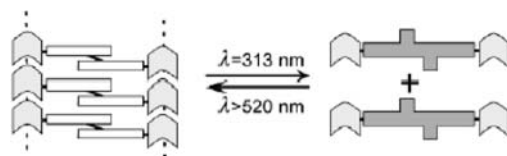


Figure 40. Probable self-assembled structures of **TAMo** (left) and **TAMc** (right); cf Figure 39. (Reprinted with permission from [74]. Copyright (2001) Royal Society of Chemistry.)

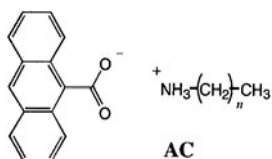


Figure 41. Structural Formula of **AC**.

A photochemically controllable two-component gelator, one being a photoresponsive anion, has been reported. Several alkylammonium cations have been shown to act as efficient solvent hardeners [75]; anthracene-9-carboxylate **AC** (Figure 41) due to its ability to undergo photodimerizations, was selected as the counter-ion.

The concept relies on greater efficiency of the photoreaction in the confinement of the network than in solution [76] and when the photoresponsive component is not covalently linked to the structure-forming component. Under these conditions, the anthracene moiety is able to acquire more space necessary for the photochemical reaction. The linear, primary alkylammonium salts that combine with the anion to make gels have 9 or 10 methylene units. Shorter derivatives lead to precipitates and longer ones to viscous solutions. When subjected to UV irradiation, the gels are converted to sols. Under the reaction conditions, the transformation was complete after 120 s of irradiation. The morphological change was monitored by dark-field microscopy as depicted in Figure 42. Although the change in the superstructure is ascribed to molecular

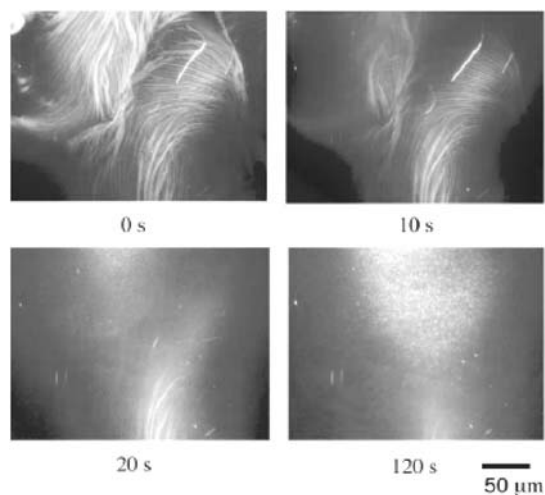


Figure 42. Morphological changes of AC as a function of photoirradiation time. (Reprinted with permission from [75]. Copyright (2003) Royal Society of Chemistry.)

dimerization of the anthracene moieties, the ratios of the different isomers have not been determined and the cause and effect of irradiation on the gel morphology remains unknown.

However, disappearance of the absorption bands of the anthracene group has been noted as the gel is converted to its sol. When the sol is kept in the dark and warmed to 30° C, the anthracene bands reappear, indicating that the photodimers dissociate thermally. The back reaction proceeded to 90% of the initial absorbance and a precipitate formed instead of a gel being regenerated. The authors suspect that by-products within the irradiated binary gelator may not permit the desired regeneration. Regardless, this approach demonstrates that phase changes among a gel, sol, and macroscopic, solid-liquid mixture can be catalyzed by light.

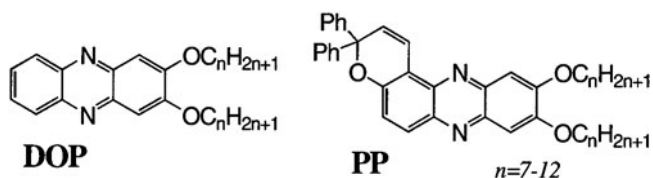


Figure 43. Structural Formulas of DOP and PP.

2,3-Di-*n*-alkoxyphenazines (DOP) are pH-sensitive gelators (Figure 43). They can gelate aqueous solutions upon addition of acid and become solutions upon addition of base [77]. Aggregation is maximized when the basic sites

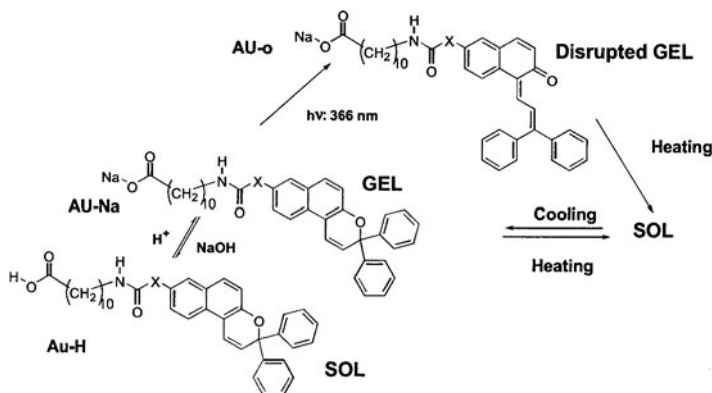


Figure 44. Macroscopic states as a function of molecular structures for **AU** derivatives.

of the phenazines are protonated. Structurally closed photochromes have been developed (**PP**) but they do not act themselves as LMOGs. In mixed gels that incorporate various ratios of both compounds, the coloration and decoloration rates and the variation of the gel-to-sol phase transition temperatures gave strong evidence that the main part of the photochromes are inserted into the supramolecular assembly. The photoinduced ring-opening of the photochromic molecules induces a decrease of the gel strength which triggers the phase transition over a short range of temperatures [78].

The potential diversity of organogelator structures based on *N*-acyl amino acid scaffolds and incorporating segments such as short linear alkyl chains, heterocycles, adamantanes, or aromatic moieties that differ in shape and electronic properties seems limitless [79]. Some examples are known and many others await synthesis. Thus, sterically demanding 3,3-diphenylnaphtho[2,1-*b*]pyrans were covalently linked to sodium *N*-acyl-11-aminoundecanoate (**AU-*Na***) to create effective gelators of DMF and DMSO (Figure 44) [80]. Sodium salts of various *N*-acyl-1, ω -aminoacids are able to gelate polar organic fluids, whereas the neutral carboxylic derivatives make solutions. Formation of intermolecular hydrogen bonds between amide groups and ionic interactions between carboxylate sodium salts and thereafter the supramolecular aggregates, is strongly affected by photoinduced structural changes of the photochromic subunit (**AU-*o***). The ring opening of the chromonic moiety largely diminishes the strength of the supramolecular networks, but does not totally suppress it. Indeed, the deeply colored open forms could act as an internal filter, preventing total conversion. When irradiation ceases, the coloration progressively disappears to yield a colorless viscous solution which does not revert spontaneously into gels. Gelation could be achieved by heating and then cooling. This complete interconversion process among the gel state, viscous liquid, and isotropic

solution can be repeated. Upon addition of sodium hydroxide, the homogeneous solutions of neutral carboxylic species (**AU-H**) in DMF and DMSO are reversibly converted into gels (Figure 44).

Such multi-addressable self-assembling organogelators represent suitable building blocks for the development of functional materials that respond to external stimuli.

3. Conclusions and Perspectives for the Future

Gels arising from low molecular-mass organic gelators have many potential applications as soft functional materials and devices of nanoscale dimensions. We expect that the control of the supramolecular organization ubiquitous in molecular gels can be triggered by external stimuli, since weak intermolecular interactions, such as hydrogen bonding, van der Waals forces and π -stacking, are sensitive to temperature, magnetic fields, electric fields, pH and light. In that regard, photoresponsive molecules such as luminescent, phototunable, or photoswitchable derivatives can initiate a modification of the self-assembly process and the resulting supramolecular network by means of light. Yet, light-induced transformations have been explored relatively little to date; many of the known examples have been described in this chapter.

The use of organogels as confining and/or anisotropic media has also received considerable interest. The use of three-dimensional networks allows one to shape materials on the microscopic level, leading to otherwise unattainable structures that show properties not observed in the unaggregated molecules. Thus, kinetic and topological control of photochemical reactions may be exploited to a greater extent in the future using specifically designed, self-assembling gelators. Additionally, organized gel fibers from the networks (SAFINs) may be exploited as nano-wires for the transport of optical information or for energy storage.

One of the many exciting attributes of physical gels is their ability to be reversibly cycled between free-flowing liquids and non-flowing materials. These gels may serve as media for chemosensors or for the active delivery of chemicals. Introducing a photoreactive center within the three-dimensional network constitutes a new route toward nano-sized architectures, which could be irreversibly or reversibly influenced upon irradiation. An interesting recent example of this is the red-green-blue (RGB) tuned phosphorescence from an organometallic LMOG gel [81]. Combined with pH, redox and/or host-guest units, these systems may allow the elaboration of fascinating smart gels which display on-demand response to various changes of their environment. Finally, light is not a pollutant in the sense one uses the word commonly; it is a powerful and convenient tool to build promising materials, as exemplified by the transcription of SAFINs into chemical gels using photopolymerization [82].

Acknowledgments

The Université Bordeaux 1 is thanked for its continued support of our research in this field. The authors are grateful to Dr. Jiaan Gan for many critical discussions.

References

- [1] Swager, T.M. "The molecular wire approach to sensory signal amplification", *Acc. Chem. Res.*, **1998**, *31*, 201–207.
- [2] Wosnick, J.H.; Swager, T.M. "Molecular photonic and electronic circuitry for ultra-sensitive chemical sensors", *Curr. Opin. in Chem. Biol.*, **2000**, *4*, 715–720.
- [3] McQuade, D.T.; Pullen, A.E.; Swager, T.M. "Conjugated polymer-based chemical sensors", *Chem. Rev.*, **2000**, *100*, 2537–2574.
- [4] Zahn, S.; Swager, T.M. "Three-dimensional electronic delocalization in chiral conjugated polymers", *Angew. Chem. Int. Ed.*, **2002**, *41*, 4225–4230
- [5] McQuade, D.T.; Kim, J.; Swager, T.M. "Two-dimensional conjugated polymer assemblies: interchain spacing for control of photophysics", *J. Am. Chem. Soc.*, **2000**, *122*, 5885–5886.
- [6] Yang, J.-S.; Swager, T.M. "Fluorescent porous polymer films as TNT chemosensors: electronic and structural effects", *J. Am. Chem. Soc.*, **1998**, *120*, 11864–11873.
- [7] Zhang, S.-W.; Swager, T.M. "Fluorescent detection of chemical warfare agents: functional group specific ratiometric chemosensors", *J. Am. Chem. Soc.*, **2003**, *125*, 3420–3421.
- [8] Tirapattur, S.; Belletete, M.; Drolet, N.; Leclerc, M.; Durocher, G. "Steady-state and time-resolved studies of 2,7-carbazole-based conjugated polymers in solution and as thin films: determination of their solid state fluorescence quantum efficiencies", *Chem. Phys. Lett.*, **2003**, *370*, 799–804.
- [9] Gupta, R.; Stevenson, M.; McGehee, M.D.; Dogariu, A.; Srdanov, V.; Park, J.Y.; Heeger, A.J. "Foerster transfer based amplified spontaneous emission in conjugated polymer blends", *Syn. Metals*, **1999**, *102*, 875–876.
- [10] Ego, C.; Grimsdale, A.C.; Uckert, F.; Yu, G.; Srdanov, G.; Mullen, K. "Triphenylamine-substituted polyfluorene—a stable blue-emitter with improved charge injection for light-emitting diodes", *Adv. Mater.*, **2002**, *14*, 809–811.
- [11] Whitten, D.; Jones, R.; Bergstedt, T.; McBranch, D.; Chen, L.; Heeger, P. "From superquenching to biodetection: building sensors based on fluorescent polyelectrolytes", *Molec. Supramolec. Photochem.*, **2001**, *7*, 189–208.
- [12] Bulovic, V.; Baldo, M.A.; Forrest, S.R. "Excitons and energy transfer in doped luminescent molecular organic materials", In *Organic Electronic Materials: Conjugated Polymers and Low Molecular Weight Organic Solids*, Springer Series in Materials Science, **2001**, *41*, R. Farchioni and G. Grosso, Eds., New York: Springer Berlin, 391–441.
- [13] Lal, M.; Pakatchi, S.; He, G.S.; Kim, K.S.; Prasad, P.N. "Dye-doped organogels. A new medium for two-photon pumped lasing and other optical applications", *Chem. Mater.*, **1999**, *11*, 3012–3014.
- [14] Murakata, T.; Sato, K.; Nakamura, I.; Hujishima, K.; Higuchi, T.; Sato, S. "Interaction between gel framework of SiO₂ or TiO₂ hydrogel and incorporated surfactants and Ru(bpy)₃²⁺", *J. Chem. Eng. Jpn.*, **2002**, *35*, 938–943.

- [15] Velasco-Garcia, N.; Valencia-Gonzalez, M.J.; Diaz-Garcia, M.E. "Fluorescent organofilms for oxygen sensing in organic solvents using a fiber optic system", *Analyst*, **1997**, *122*, 1405–1409.
- [16] Demas, J.N.; DeGraff, B.A. *Anal. Chem.*, **1991**, *63*, 829A.
- [17] Hu, Y.; Chen, W.-M.; Chen, J.-F.; Zhang, Z.-C. "Preparation of ZnS nanocrystals in network of hydrogel", *Mater. Lett.*, **2003**, *57*, 1312–1316.
- [18] Han, Y.; Lin, J. "Luminescence and energy transfer of organically modified silica xerogels (OMSX) doped and undoped with Eu^{3+} and Tb^{3+} ", *J. Solid State Chem.*, **2003**, *171*, 396–400.
- [19] Green, W.H.; Le, K.P.; Grey, J.; Au, T.T.; Sailor, M.J. *Science* **1997**, *276*, 1826.
- [20] Terech, P.; Furman, I.; Weiss, R.G. "Structures of organogels based upon cholesteryl 4-(2-anthryloxy)butanoate, a highly efficient luminescing gelator: neutron and X-ray small-angle scattering investigations", *J. Phys. Chem.*, **1995**, *99*, 9558–9566.
- [21] Lu, L.; Cocker, T.M.; Bachman, R.E.; Weiss, R.G. "Gelation of organic liquids by some 5α -cholestan- 3β -yl N-(2-aryl)carbamates and 3β -cholesteryl 4-(2-anthrylamino)butanoates. How important are H-bonding interactions in the gel and neat assemblies of aza aromatic-linker-steroid gelators?", *Langmuir*, **2000**, *16*, 20–34.
- [22] Geiger, C.; Stanescu, M.; Chen, L.; Whitten, D.G. "Organogels resulting from competing self-assembly units in the gelator: structure, dynamics, and photophysical behavior of gels formed from cholesterol-stilbene and cholesterol-squaraine gelators", *Langmuir*, **1999**, *15*, 2241–2245.
- [23] Ajayaghosh, A.; George, S.J. "First phenylenevinylene based organogels: self-assembled nanostructures via cooperative hydrogen bonding and π -stacking", *J. Am. Chem. Soc.*, **2001**, *123*, 5148–5149.
- [24] Maitra, U.; Vijay Kumar, P.; Chandra, N.; D'Souza, L.J.; Prasanna, M.D.; Raju, A.R. "First donor-acceptor interaction promoted gelation of organic fluids", *Chem. Commun.*, **1999**, 595–596.
- [25] Babu, P.; Sangeetha, N.M.; Vijaykumar, P.; Maitra, U.; Rissanen, K.; Raju, A.R. "Pyrene-derived novel one- and two-component organogelators", *Chem. Eur. J.*, **2003**, *9*, 1922–1932.
- [26] Ikeda, M.; Takeuchi, M.; Shinkai, S. "Unusual emission properties of a triphenylene-based organogel system", *Chem. Commun.*, **2003**, 1354–1355.
- [27] Markovitsi, D.; Germain, A.; Millié, P.; Lécuyer, P.; Gallos, L.K.; Argyrakis, P.; Bengs, H.; Ringsdorf, H. *J. Phys. Chem.*, **1995**, *99*, 1005.
- [28] Sugiyasu, K.; Fujita, N.; Takeuchi, M.; Yamada, S.; Shinkai, S. "Proton-sensitive fluorescent organogels", *Org. Biomolec. Chem.*, **2003**, *1*, 895–899.
- [29] Nakashima, T.; Kimizuka, N. *Adv. Mater.*, **2002**, *14*, 1113.
- [30] Sugiyasu, K.; Fujita, N.; Shinkai, S. "Visible-light-harvesting organogel composed of cholesterol-based perylene derivatives", *Angew. Chem. Int. Ed.*, **2004**, *43*, 1229–1233.
- [31] *Unpublished results*: (a) DDOT: J. Reichwagen, H. Hopf, A. Del Guerzo, C. Belin, H. Bouas-Laurent, J.-P. Desvergne. (b) Tetrahydro-DDOA: F. Placin, G. Clavier, H. Bouas-Laurent, J.-P. Desvergne. (c) For spectroscopic properties of DDOA, see J.-P. Desvergne, T. Brotin, D. Meerschaut, G. Clavier, F. Placin, J.-L. Pozzo, H. Bouas-Laurent, Spectroscopic properties and gelling ability of a set of rod-like 2,3-disubstituted anthracenes, *New J. Chem.*, **2004**, *28*, 234–247.
- [32] Simmons, B.; Li, S.; John, V.T.; McPherson, G.L.; Taylor, C.; Schwartz, D.K.; Maskos, K. "Spatial compartmentalization of nanoparticles into strands of a self-assembled organogel", *Nano Letters*, **2002**, *2*, 1037–1042.
- [33] Kimura, M.; Kobayashi, S.; Kuroda, T.; Hanabusa, K.; Shirai, H. "Assembly of gold nanoparticles into Fibrous Aggregates Using Thiol-Terminated Gelators", *Adv. Mater.*, **2004**, *16*, 335–338.

- [34] Ajayaghosh, A.; George, S.J.; Praveen, V.K. "Gelation-assisted light harvesting by selective energy transfer from an oligo(p-phenylenevinylene)-based self-assembly to an organic dye", *Angew. Chem. Int. Ed.*, **2003**, *42*, 332–335.
- [35] *Organic Photochemistry: Principles and Applications*, J. Kagan, San Diego: Academic Press, **1993**.
- [36] a) *Photochromism: Molecules and Systems*, H. Dürr and H. Bouas-Laurent, Eds., Amsterdam: Elsevier, **1990**. b) *Photochromic and Thermochromic Compounds and Systems*, J. Crano and R. Guglielmetti, Eds., Vol. 1&2, New York: Plenum Press, **1999**.
- [37] *Molecular Switches*, B.L. Feringa, Ed., Darmstadt: Wiley-VCH, **2001**.
- [38] Irie, M. "Diarylethenes for memories and switches", *Chem. Rev.*, **2000**, *100*, 1683–1716.
- [39] Bouas-Laurent, H.; Dürr, H. "Organic Photochromism", *Pure Appl. Chem.*, **2001**, *73*, 639–665.
- [40] a) Mitchell, R.H. "The metacyclophanediene-dihydropyrene photochromic Pi switch", *Eur. J. Org. Chem.*, **1999**, *1999(11)*, 2695–2703. b) *Handbook of Organic Photochemistry and Photobiology*, W.M. Horspool, Ed., Boca Raton: CRC Press, **1995**.
- [41] a) Saltiel, J.; Marinari, A.; Chang, D.; Mitchener, J.C.; Megarity, D.D. "Trans-cis photoisomerization of the stilbenes and a reexamination of the positional dependence of the heavy-atom effect", *J. Am. Chem. Soc.*, **1979**, *101*, 2982–2996. b) Meier, H. "Photochemistry of stilbenoid compounds and their role in materials technology", *Angew. Chem. Int. Ed.*, **1992**, *31*, 1399–1407.
- [42] Griffiths, J. "Photochemistry II: photochemistry of azobenzene and its derivatives", *Chem. Soc. Rev.*, **1972**, *1*, 481–493.
- [43] Langhoven, P. Cyclohexadiene-hexatriene electrocyclizations, Chapter 3 in Ref. [36a].
- [44] For a recent review, see: Berkovic, G.; Krongauz, V.; Weiss, V. "Spiropyrans and spirooxazines for memories and switches", *Chem. Rev.*, **2000**, *100*, 1741–1753.
- [45] Zhang, X.Y.; Jin, S.; Ming, Y.F.; Liang, Y.C.; Yu, L.; Fan, M.G.; Luo, J.; Yao, S.D. "Substituent effect on photochromism of indolinospiroxazines", *J. Photochem. Photobiol. A: Chem.*, **1994**, *80*, 221–225.
- [46] Baillet, G.; Giusti, G.; Guglielmetti, R. "Study of the fatigue process and the yellowing of spiroopyrans", *Bull. Chem. Soc. Jpn.*, **1995**, *68*, 1220–1225.
- [47] Day, J.H. *Chem. Rev.*, **1963**, *63*, 65–83.
- [48] Pieroni, O.; Ciardelli, F. "Photoresponsive polymeric materials", *Trends in Polymer Science* **1995**, *3*, 282–287.
- [49] Weiss, V.; Krongauz, V.; Friesem, A.A. "Temporal holographic response in photochromic polymeric films", *Mol. Cryst. Liq. Cryst.*, **1994**, *246*, 367–370.
- [50] Willner, I.; Willner, B. *Photochemical Biomolecular Switches: The Route to Optobioelectronics*, Chapter 6 in Ref. [37].
- [51] Maeda, S. *Spirooxazines*, Chapter 2, pp. 85–110 in Ref. [36b].
- [52] *Applied Photochromic polymer system*, G. Mc Ardle, Ed., London: Blackie, **1992**.
- [53] van Gemert, B. *Benzo and naphthopyrans (chromenes)*, Chapter 3, pp. 111–140 in Ref. [36b].
- [54] Delbaere, S.; Luccioni-Houze, B.; Bochu, C.; Teral, Y.; Campredon, M.; Vermeersch, G. *J. Chem. Soc. Perkin Trans. 1*, **1998**, 1153–1157.
- [55] For a recent review, see: Irie, M. "Photochromism: memories and switches", *Chem. Rev.* **2000**, *100*, 1685–1712.
- [56] Takeda, J.; Tayu, T.; Kurita, S.; Yokoyama, Y.; Kurita, Y.; Kuga, T.; Matsuoka, M. "Radiative and non-radiative decay processes of the excited state of the colored form of furylfulgides", *Chem. Phys. Lett.* **1994**, *220*, 443.
- [57] *Reversible polymeric gels and related systems*, P.S. Russo, Ed., *ACS Symposium Series Vol. 350*, Washington: American Chemical Society, **1987**.

- [58] *Thermoreversible Gelation of Polymers and Biopolymers*, J.M. Guenet, Ed., London: Academic Press, **1992**.
- [59] a) Osada, Y.; Gong, J.; “Stimuli-responsive polymer gels and their application to chemomechanical systems”, *Progress in Polymer Science* **1993**, *18*, 187–226. b) Zheng, Y.; Andreopoulos, F.; Micic, M.; Huo, Q.; Pham, S.; Leblanc, R. “A novel photoscissile PEG-based hydrogel”, *Adv. Funct. Mater.*, **2001**, *11(1)*, 37–40.
- [60] Irie, M. *Adv. Polym. Sci.*, H. Fujita, Ed., Berlin: Springer Verlag, **1990**, pp. 27–67.
- [61] Kang, M.-S.; Gupta, V. “Photochromic cross-links in thermoresponsive hydrogels of poly(N-isopropylacrylamide)”, *J. Phys. Chem. B*, **2002**, *106*, 4127–4132.
- [62] Chujo, Y.; Sada, K.; Nomura, R.; Naka, A.; Saegusa, T. “Photogelation and redox properties of anthracene-disulfided-modified polyoxazolines”, *Macromolecules* **1993**, *26*, 5611–5614.
- [63] Hachisako, H.; Nakayama, H.; Ihara, H. “Determination of critical aggregation concentrations of self-assembling lipids in non polar organic media using spiropyrans as photochromic probes”, *Chem. Lett.*, **1999**, 11165–11166.
- [64] Yi, T.; Sada, K.; Sugiyasu, K.; Kazunori, H.; Hatano, T.; Shinkai S.; Kato, T. “Photoinduced color generation and color erasing switched by the sol-gel phase transition”, *Chem. Commun.*, **2003**, 344–345.
- [65] Hanabusa, K.; Yamada, M.; Kimura, M.; Shirai, H. “Prominent gelation and chiral aggregation of alkylamides derived from 1,2-*trans*-cyclohexane”, *Angew. Chem. Int. Ed.*, **1996**, *35*, 1949–1950.
- [66] Shumburo, A.; Biewer, M.C. “Stabilization of an organic photochromic materials by incorporation in an organogel”, *Chem. Mater.* **2002**, *14*, 3745–3750.
- [67] Frkanec, L.; Jokic, M.; Makarevic, J.; Wolsperger, K.; Zinic, M. “Bis(PheOH) maleic acid amide fumaric acid amide photoisomerization induces microspheres to gel fiber morphological transition: the photoinduced gelation system”, *J. Amer. Chem. Soc.* **2002**, *124*, 9716–9717.
- [68] *Organic solid state reactions*, F. Toda, Ed., Dordrecht: Kluwer Academic Publishers, **2002**.
- [69] Koshima, H.; Matsusaka, W.; Yu, H. “Preparation and photoreaction of organogels based on benzophenone”, *J. Photochem. Photobiol. A: Chem.*, **2003**, *156*, 83–90.
- [70] Murata, K.; Aoki, M.; Suzuki, M.; Harada, T.; Kawabata, H.; Komori, T.; Ohseto, F.; Ueda, K.; Shinkai, S. “Thermal and light control of the sol-gel phase transition in cholesterol-based organic gels. Novel helical aggregation modes as detected by circular dichroism and electron microscopies observation”, *J. Amer. Chem. Soc.*, **1994**, *116*, 6664–6676.
- [71] Mamiya, J.-I.; Kanie, K.; Hiyama, T.; Ikeda, T.; Kato, T. “A rodlike organogelator: fibrous aggregation of azobenzene derivatives with a syn-chiral carbonate moiety”, *Chem. Commun.*, **2002**, 1870–1871.
- [72] a) De Loos, M.; van Esch, J.; Kellogg, R.M.; Feringa, B.L. “Chiral recognition in bis-urea based aggregates and organogels through cooperative interactions”, *Angew. Chem. Int. Ed.*, **2001**, *40*, 613–616. b) van der Laan, S.; Feringa, B.L.; Kellogg, R.M.; van Esch, J. “Remarkable polymorphism in gels of new azobenzene bis-urea gelators”, *Langmuir* **2002**, *18*, 7136–7140.
- [73] a) Zhao, Y.; Tong, X. “Light-induced reorganisation in self-assembled Liquid Crystal gels: electrically switchable diffraction gratings”, *Adv. Mater.*, **2003**, *15*, 1431–1435. b) Mizoshita, N.; Suzuki, Y.; Kishimoto, K.; Hanabusa, K.; Kato, T. “Electrooptical properties of liquid-crystalline physical gels: a new oligo(amino acid) gelator for light scattering”, *J. Mater Chem.*, **2002**, *12*, 2197–2201. c) Moriyama, M.; Mizoshita, N.; Yokota, T.; Kishimoto, K.; Kato, T. “Photoresponsive anisotropic soft solids:

- liquid-crystalline physical gels based on a chiral photochromic gelator”, *Adv. Mater.*, **2003**, *15*, 1335–1338.
- [74] Lucas, L.N.; van Esch, J.; Feringa, B.L.; Kellogg, R.M. “Photocontrolled self-assembly of molecular switches”, *Chem. Commun.*, **2001**, 759–760.
- [75] Ayabe, M.; Kishida, T.; Fujita, N.; Sada, K.; Shinkai, S. “Binary organogelators which show light and temperature responsiveness”, *Org. Biomol. Chem. Comm.*, **2003**, *1*, 2744–2747.
- [76] *Supramolecular Photochemistry*, V. Balzani, Ed., *NATO ASI series, mathematical and physical sciences*, *214*, Dordrecht: D. Reidel, **1987**.
- [77] Pozzo, J.-L.; Clavier, G.; Desvergne, J.P. “Rational design of new acid-sensitive organogelators”, *J. Mater. Chem.*, **1998**, *8*, 2575–2577.
- [78] Pozzo, J.-L.; Clavier, G.; Rustemeyer, F.; Bouas-Laurent, H. “photochromic guests in organogels”, *Mol. Cryst. Liq. Cryst.*, **2000**, *344*, 101–106.
- [79] a) Mieden-Mundert, G.; Klein, L.; Fischer, M.; Vögtle, F.; heuze, K.; Pozzo, J.L.; Vallier, M.; Fages, F. “Rational design of low molecular weight gelators: toward a library of functional *N*-acyl-1 and *w*-amino acid derivatives, *Angew. Chem. Int. Ed.*, **2001**, *40*, 3164–3166. b) D’Aleo, A.; Pozzo, J.L.; Fages, F.; Schmutz, M.; Mieden-Mundert, G.; Vögtle, F.; Caplar, V.; Zinic, M. “11-aminoundecanoic acid: a versatile unit for the generation of low molecular weight gelators for water and organic solvents”, *Chem. Commun.*, **2004**, 190–191.
- [80] Ahmed, S.; Sallenave, X.; Fages, F.; Mieden-Gundert, G.; Müller, W.M.; Müller, U.; Vögtle, F.; Pozzo, J.-L. “Multiaddressable self-assembling organogelators based on 2H-chromene and *N*-1,*w*-acyl-amino acid units”, *Langmuir*, **2002**, *18*, 7096–7101.
- [81] Kishimura, A.; Yamashita, T.; Aida, T. “Phosphorescent organogels via “metal-philic” interactions for reversible RGB-color switching”, *J. Am. Chem. Soc.*, **2005**, *127*, 179–183.
- [82] a) Wang, G.; Hamilton, A.D. “Synthesis and self-assembling properties of polymerizable organogels”, *Chem. Eur. J.*, **2002**, *8*, 1954–1961. b) Masuda, M.; Takeshi, O.; Okada, Y.; Yase, K.; Shimizun, T. “Polymerization in nanometer-sized fibers: molecular packing order and polymerizability”, *Macromolecules*, **2000**, *33*, 9233–9238. c) De Loos, M.; van Esch, J.; Kellogg, R.M.; Feringa, B.L. “Remarkable stabilization of self-assembled organogels by polymerization”, *J. Amer. Chem. Soc.*, **1997**, *119*, 12675–12676. d) George, M.; Weiss, R.G. “Low molecular mass gelators with diyne functional groups and their unpolymerized and polymerized gels”, *Chem. Mater.*, **2003**, *15*, 2879–2888.

Chapter 25

GELS OF LOW MOLECULAR-MASS ORGANIC GELATORS AS TEMPLATES FOR TRANSCRIPTION

Arianna Friggeri¹, Kjeld J.C. van Bommel¹, and Seiji Shinkai²

¹*BiOMaDe Technology Foundation, Nijenborgh 4, 9747 AG Groningen, The Netherlands*

²*Department of Chemistry and Biochemistry, Graduate School of Engineering, Kyushu University, Fukuoka, 812-8581, Japan*

1. Introduction	858
2. The Basics of Sol-Gel Chemistry	860
2.1. Hydrolysis	862
2.2. Condensation	863
3. Transcription of the Gelator Template	864
3.1. Gelators Possessing Covalently Attached, Positively Charged Centers	865
3.2. Gelators Containing Non-Covalently Attached, Positively Charged Centers	868
3.3. Gelators Containing Hydrogen-Bond Donating Amine Groups	870
3.4. Gelators with Different Structural Features	872
3.5. Outlook for the Future	874
4. Shapes of Transcribed Materials	875
4.1. Transcription of Cholesterol-Based Gelators	877
4.2. Transcription of Sugar-Based Gelators	882
4.3. Transcription of Cyclohexane-Based Gelators	886
4.4. Perspectives for the Future	888
5. General Conclusions and Challenges for the Future	888

1. Introduction

Templates can be defined as patterns that are used to reproduce a particular shape accurately. In chemistry, a template can be the structure of a compound that serves for the production of another compound with a complementary shape. Template molecules are used in many areas of chemistry, especially in molecular imprinting [1, 2], in supramolecular chemistry [3] and in the field of catalytic antibodies [4]. In general, molecular imprinting consists of the copolymerization of functional and cross-linking monomers in the presence of a template molecule. Subsequently, the template molecule can be removed, revealing well-defined binding sites in which the arrangement of functional groups is particularly suited for binding the template molecule or other structurally related molecules. The templating step in a molecular imprinting process can be carried out in solution or on surfaces, leading to a great variety of materials with recognition properties [5]. In supramolecular chemistry, templates are generally used as a driving force for bringing together molecular components. Such components may subsequently react and go on to form products in which the template molecule can remain entwined or from which the template can easily be removed. The use of templates in supramolecular chemistry has led to the development of interesting, new receptor molecules, and also to the construction of very complex molecular architectures that would otherwise have been impossible. In the field of catalytic antibodies, template molecules are “injected” into living organisms that are able to produce antibodies capable of specifically binding to the template. Such antibodies can subsequently be employed to catalyze reactions in which the transition state is analogous in structure to the original template molecule.

Although templates are generally thought of as single molecules or ionic species, much larger self-assembled structures, held together by weak forces, such as hydrogen bonding, π - π stacking or van der Waals interactions, can also function in a similar manner. Examples of self-assembled systems that have been used as templates are the self assembled fibrillar network (SAFIN) structures of gels of low molecular-mass organic gelators (LMOGs) [6], vesicles [7, 8], organic crystals [9, 10], and even larger entities such as red blood cells [11] and virus cells [12]. All of these particular systems have been employed as templates for a process known as transcription [6]. With this process the morphology of the organic template can be transferred to an inorganic material, giving rise to otherwise unattainable, microscopically detailed inorganic structures.

The process of transcription consists of several steps (Figure 1). First of all, the organic template is brought into contact with inorganic precursor molecules or small particles of the inorganic material that will ultimately be formed. This step takes place in solution, in the presence of a catalyst, and leads to

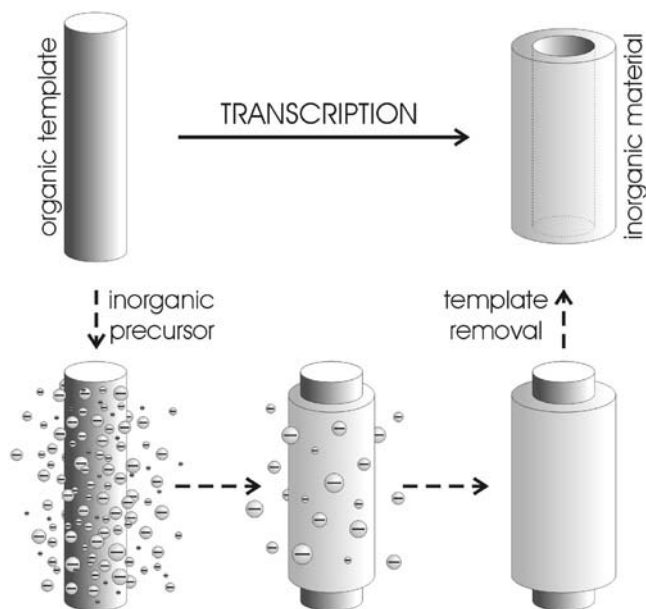


Figure 1. Schematic representation of the transcription process: the organic template (top left) is brought into contact with the inorganic precursor which leads to the deposition of inorganic material on the surface of the template; the latter can subsequently be removed to yield the transcribed inorganic material (top right). (Reprinted from [6] with permission of the publisher, Wiley-VCH.)

the deposition of the inorganic material on the inner or outer surface of the organic template. The material obtained at this point is an organic-inorganic hybrid that may present interesting properties as such or from which the template can be removed, leading to a purely inorganic material whose morphology is directly related to the organic template. Template removal can be achieved by heat treatment [13], microwave irradiation [14], or washing with organic solvents [11, 15]. The procedure of template removal by heat treatment, also known as calcination, is the most common and was first introduced by Kawahashi and Matijević during their search to produce hollow spheres of yttrium compounds [13]. This procedure consists of placing the organic-inorganic hybrid material in a furnace and exposing it to very intense heat (up to 500°C) under aerobic conditions, thereby burning away/decomposing the organic template. Microwave irradiation is a more recent procedure for template removal; it relies on the heat generated by microwave irradiation and is therefore a more rapid process than calcination [14]. Removing the organic template by dissolving it with an appropriate solvent would seem to be the simplest and quickest method for obtaining the transcribed, inorganic

material. However, at times, residues of organic material remain entrapped in the inorganic structures, yielding impure products and making this method of template removal generally unsuitable.

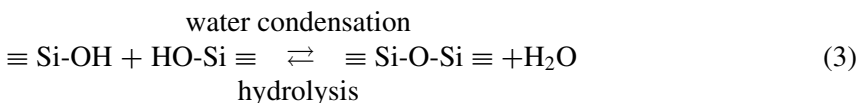
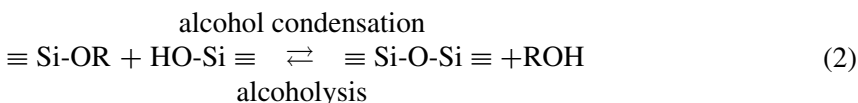
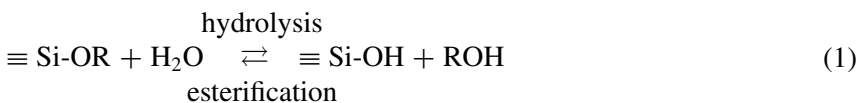
In this chapter, the transcription of LMOG gels into discrete, inorganic structures will be discussed, whereas the formation of continuous structures in which for example templated channels and cavities are present (e.g., macroporous silica or zeolites) will not be considered. Due to the non-covalent nature of the aggregates that constitute LMOG gel templates, they can present a very wide variety of morphologies: fibrous, tubular, ribbon-like, lamellar, and hollow spherical. Similarly, surfactant molecules can also self-assemble into a variety of shapes and, together with organic crystals and biomaterials, they can give rise to interesting transcribable structures. However, it is not the aim of this book to discuss these systems in detail, and relevant reviews can be found in the literature [6, 16]. In Section 2, the chemical reactions involved in the sol-gel chemistry necessary for the transcription process are presented and the interactions between inorganic precursors and various catalysts, mainly with regards to the formation of silica-based products, are described. In Section 3, the important choice of the gelator molecule for successful transcription of the template structure is discussed. The importance of positively charged moieties and hydrogen-bonding groups, covalently attached to the gelator molecule or non-covalently incorporated into the network, is explained. The great variety of inorganic shapes obtained from gel transcription and the relationship between such shapes and the properties of the gelator molecules that generate them will be presented in Section 4. The concepts presented will be illustrated with examples from the recent literature, and the first actual application of a transcribed inorganic structure will be discussed along with future perspectives for these materials in Section 5.

2. The Basics of Sol-Gel Chemistry

In order to understand the transcription of gels of LMOGs into inorganic structures, it is essential first to examine the chemistry involved in sol-gel processes (N.B., sol-gel here refers to the preparation of ceramic, i.e., inorganic materials). It is knowledge of this sol-gel chemistry that will be invaluable for the reader's ability to comprehend the interactions between the organic templates and the precursors that form the inorganic coatings that are vital for the transcription process to occur. However, because a comprehensive overview of sol-gel chemistry would go beyond the scope of this chapter, only those reactions important for the understanding of gel-related transcription will be discussed. Furthermore, as most of the experiments dealing with the transcription of organogel templates into inorganic materials use a silica precursor, this section will mainly focus on the reactions leading to the formation of silica.

However, examples of different inorganic materials will occasionally be discussed as well. For a thorough overview of the science of sol-gel processing, the interested reader is referred to the excellent book, “*Sol-Gel Science, The Physics and Chemistry of Sol-Gel Processing*,” by Brinker and Scherer [17].

The method most frequently used for the formation of silica is the hydrolysis of monomeric, tetraalkoxysilanes using either an acid or base as catalyst, after which a myriad of condensation reactions takes place, leading to the formation of the final polycondensate that is silica. Three reactions can be distinguished when describing the formation of silica (commonly known as the sol-gel process).



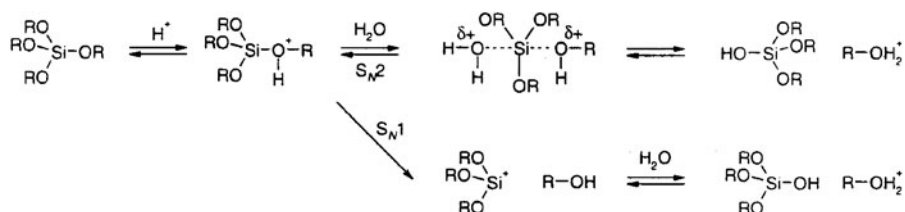
The first reaction to take place is hydrolysis (Eq. (1)) in which alkoxide groups (OR) are replaced by hydroxyl groups (OH). Subsequently, two types of condensation reactions can take place, both leading to the formation of siloxane bonds (Si-O-Si). Firstly, Eq. (2) shows the alcohol condensation reaction in which a silanol group reacts with an alkoxide to give a siloxane bond and the resulting alcohol. Equation (3), on the other hand, shows how a siloxane bond may be formed (as well as a molecule of water) from a reaction between two silanol groups. Generally, the condensation reactions commence before the alkoxide precursor is completely hydrolyzed. Although the speeds of the reactions can differ largely, similar processes can occur when alkoxide precursors of other elements are used (e.g., $\text{Ti}(\text{OiPr})_4$, $\text{Al}(\text{OtBu})_3$, $\text{Zr}(\text{OEt})_4$). The most widely used tetraalkoxysilanes are tetraethoxysilane ($\text{Si}(\text{OEt})_4$) and tetramethoxysilane ($\text{Si}(\text{OMe})_4$), commonly abbreviated as TEOS (tetraethylorthosilicate) and TMOS (tetramethylorthosilicate), respectively. Due to their immiscibility with water, the silica polycondensation reactions are usually carried out in the presence of a common solvent (often alcohols) in order to homogenize the system.

Both the hydrolysis and condensation steps benefit from the addition of a catalyst. Although mineral acids (e.g., HCl) and ammonia are the catalysts most commonly used in ordinary sol-gel chemistry, a variety of other catalysts can

be used. Acetic acid, KOH, amines, KF, HF, titanium alkoxides, and vanadium alkoxides and oxides have been successfully employed. The catalysts most commonly employed for the transcription of LMOG-based template structures are acetic acid and benzylamine, both of which are readily miscible with a variety of organic solvents as well as water.

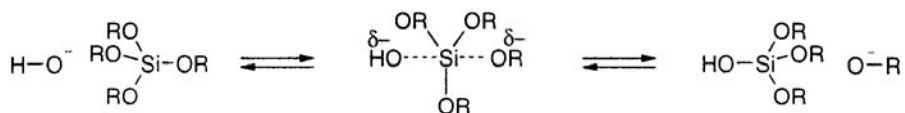
2.1. Hydrolysis

Under acidic conditions, the hydrolysis reaction starts with the rapid protonation of an alkoxide group. However, as of yet, it is unclear whether the reaction proceeds in an S_N1 or S_N2 manner (Scheme 1): does the alcohol leave before or after a water molecule binds to the Si atom? Other mechanisms have been proposed, and even steric effects have been shown to be of influence. However, a full treatise of these theories goes beyond the scope of this chapter.



Scheme 1. Two possible mechanisms for the acid-catalyzed hydrolysis step.

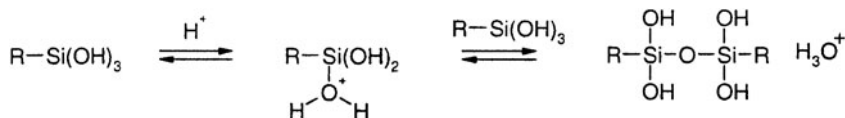
As with the acid-catalyzed hydrolysis, the exact mechanism of the base-catalyzed hydrolysis has not yet been fully clarified. Under basic conditions, however, it is likely that water is dissociated to form hydroxyl ions that, due to their nucleophilic nature, attack the silicon atom. Hydrolysis then occurs by the displacement of the alkoxide anion, a process that may be aided by hydrogen bonding of the alkoxide anion with the solvent (Scheme 2). It is important to realize that concurrent with the hydrolysis steps, transesterification and reesterification reactions will also take place.



Scheme 2. Possible mechanism for the base-catalyzed hydrolysis step.

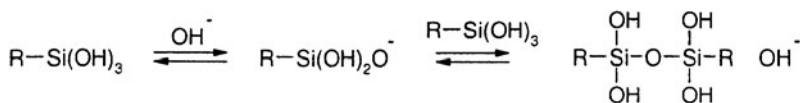
2.2. Condensation

As mentioned, polymerization to form siloxane bonds occurs by either an alcohol-producing condensation reaction (Eq. (2)) or a water-producing condensation reaction (Eq. (3)). However, the mechanisms of both reactions are analogous. Because gelation times in aqueous silicate systems are observed to decrease at pH values below the isoelectric point of silica (generally around 2), it is generally believed that the mechanism for the acid-catalyzed reaction involves a protonated silanol species (Scheme 3). Protonation results in a more electrophilic silicon that is more susceptible to nucleophilic attack. The silanols existing as monomers or weakly branched oligomers are the most basic silanol species, and are the most likely to be protonated. This results in preferential reactions involving condensation between neutral species and protonated silanols situated on monomers, end groups of chains, etc.



Scheme 3. Possible mechanism for the acid-catalyzed condensation step.

The attack of a nucleophilic, deprotonated silanol on a neutral silicate species is the most likely mechanism for the base-catalyzed condensation reaction (Scheme 4). This reaction takes place above the isoelectric point of silica, where surface silanols are deprotonated. Because the acidity of silanols depends on the other substituents on the silicon atom, this isoelectric point may vary from pH 1.5–4.5 depending on the extent of condensation of the silicate species. Replacement of basic OR and OH moieties with OSi moieties reduces the electron density on the Si, thus increasing the acidity of the protons of the remaining silanols. Hence, reactions between larger, more highly condensed species, containing acidic silanols, and smaller, less weakly branched species are favored. The condensation rate is highest near neutral pH, where both species are present in significant concentrations.



Scheme 4. Possible mechanism for the base-catalyzed condensation step.

From these mechanisms, the following deductions can be made. Because TEOS has an isoelectric point of 2, cationic silicate species ($\equiv \text{Si-OH}_2^+$) are

present in solution under strong acidic conditions ($\text{pH} < 2$). Under moderately acidic conditions ($\text{pH} 2\text{--}7$), anionic silica species ($\equiv \text{Si-O}^-$) are present in solution. Naturally, similar conclusions can be reached for other inorganic precursor molecules. However, the pH values at which the different species will be prevalent will not be the same as those for TEOS. For example, the isoelectric point of $\text{Ti}(\text{OiPr})_4$ is ca. 5; cationic species will be prevalent below and anionic species will be dominant above pH 5. The presence of these charged species in both the acid- and base-catalyzed condensation steps is essential for the transcription process to take place successfully. Their roles will be clarified in Section 3.

3. Transcription of the Gelator Template

The employment of networks of LMOG gels as templates for the formation of inorganic structures started with the discovery that certain cholesterol-based gelators (e.g., **1** in Figure 2) are capable of gelling liquid silanol derivatives [18, 19]. The idea arose that if the sol-gel polymerization of these silanol derivatives were carried out in the presence of the organogel fibers, they might act as a template, thus creating voids inside the resulting silica. Several attempts were undertaken to polymerize a TEOS gel of compound **1**. However, the resultant silica did not display any sign of being templated by the organogel fibers. In order to mimic the structure of cationic surfactants, which at that time had already been successfully employed as templates for the formation of mesoporous silica [20], compound **2**, containing a quaternary ammonium cation, was synthesized. A method was developed to obtain a gel of compound **2** in a mixture of acetic acid, TEOS, and water. After a period of 10 days, a solidified material was obtained that, after drying and calcination, was shown to consist of tubular silica (Figure 3) [21]. The realization that the cationic charge caused deposition of the silica onto the gel fibers, was crucial for the development of this field of chemistry. Since this first report, great progress

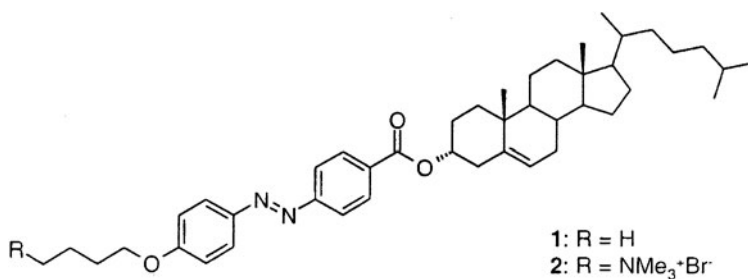


Figure 2. Structure of a neutral and a charged cholesterol-based LMOG.

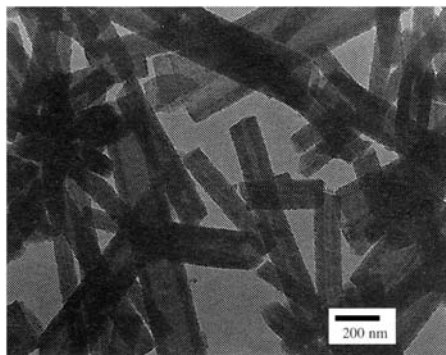


Figure 3. TEM image of tubular silica (after calcination) obtained by transcription of an acetic acid gel of LMOG **2**. (Reprinted from [21] with permission of the publisher. The Royal Society of Chemistry.)

has been made in understanding the requirements for successful transcription. The following sections will discuss the structural moieties that can lead to transcription, when incorporated into the gelator structure.

3.1. Gelators Possessing Covalently Attached, Positively Charged Centers

As shown by the previous example, carrying out the sol-gel polymerization of TEOS in the presence of a gelator possessing quaternary ammonium moieties (**2**) led to transcription, whereas attempted transcription of gels of the non-charged analogue (**1**) only resulted in the formation of granular silica [21]. Clearly, the presence of the cationic charges is vital for successful transcription during the polycondensation reaction of TEOS, but in what way?

In the example discussed above, the transcription was carried out in acetic acid, a solvent that is also an excellent catalyst for the TEOS polycondensation reaction. As discussed in Section 2.2, anionic silica species ($\equiv \text{Si-O}^-$) are present in solution under moderately acidic conditions (pH 2–7). As a result of the high density of positive charges on the gel fibers, the negatively charged silica species are attracted to and adsorbed onto the cationic gelator fibrils. Once this deposition has started, growth of the inorganic material will continue primarily on the surface of the template and, to a lesser extent, through the formation of new inorganic particles in solution. The reason is that species with relatively flat surfaces (i.e., with low radii of curvature) have lower solubilities than materials of the same composition with strongly curved surfaces, hence resulting in the preferential growth of weakly curved surfaces

over strongly curved surfaces [22]. The growth of the inorganic material on the surface of the gel fibers eventually yields fibrous silica with an inner cavity that is filled with the template (i.e., the gel fiber). Removal of the gelator molecules through calcination indeed resulted in the isolation of the hollow silica fibers shown in Figure 3. Subsequently, it was shown that transcription caused by electronic interactions between positively charged gelator fibers and anionic silica species can be blocked by the presence of other cationic charges (e.g., Me_4NCl) [23]. Although at low concentrations (50 mM) of Me_4NCl no disturbing effect was observed, at higher concentrations (2.7 M) only granular silica was obtained even though the positively charged gel fibers were present.

An important step toward understanding the transcription process was made when experiments were carried out in gels consisting of mixtures of compounds **1** and **2** [23]. By varying the molar ratio of (neutral) **1** and (charged) **2**, the influence of cationic charge density at fibril surfaces on the formation of the tubular silica was investigated. At molar composition fractions, $R(=[\mathbf{2}]/([\mathbf{1}] + [\mathbf{2}]))$ as low as 0.25, fibrous, tubular silica was still obtained. Unexpectedly, however, upon lowering R to 0.15, *helical* tubular silica was obtained. TEM micrographs again demonstrated that the organogel had acted as the template for the formation of these helical fibers; they possessed an inner channel whose diameter corresponded to that of the gel fibers. Furthermore, SEM micrographs of the silica showed that *all* the helical fibers were right-handed. Had the helicity been induced by shrinkage during drying or calcination, equal amounts of left- and right-handed helices would have been obtained. Circular dichroism (CD) spectra of organogels of mixtures of **1** containing some **2** demonstrated that the gelator molecules were also oriented in a right-handed helical orientation within the fibers; there was a positive sign for the first Cotton effect [24]. Lowering R even further (to <0.05) resulted in formation of only granular silica (i.e., no templating effect). Clearly, dilution of the cationic charges present in the gel fibers played a decisive role in how accurately the template was transcribed into the inorganic material.

These observations can be explained as follows. A high concentration of cationic charges in the gel fibers results in a rapid and random adsorption of anionic silica precursors or particles, leading to formation of tubular silica that does not display any of the chirality present in the gel fibers. A very low concentration of positive charges, on the other hand, does not result in transcription because the charge density on the fiber surfaces is insufficient to lead to a preferential deposition of silica particles. A moderate concentration of cationic charges, however, results in excellent transcription (i.e., chiral helical silica) because deposition is more controlled due to the tempered driving force for surface adsorption by negatively charged silica precursors. Clearly, transcription speed is directly linked to the accuracy of the transcription process.

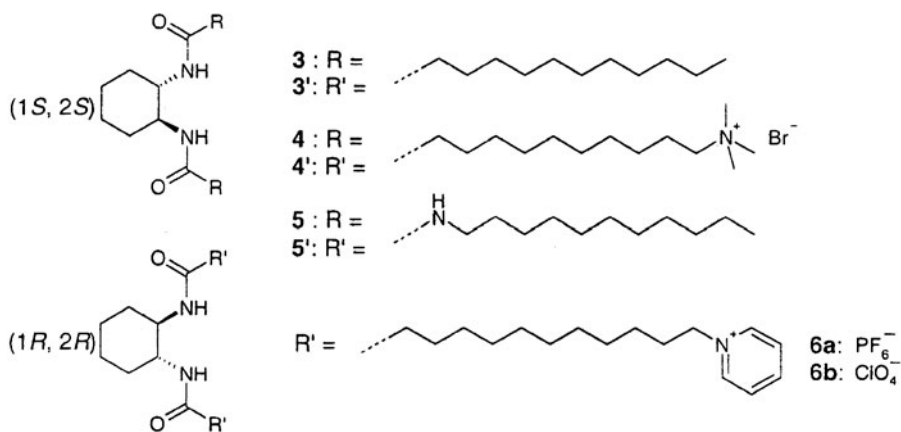


Figure 4. Amide and urea containing cyclohexane-based LMOGs.

Another organogel system in which positively charged compounds were mixed with neutral gelators, involved the cyclohexane-based gelators **3** (**3'**), **4** (**4'**), and **5** (**5'**) (Figure 4) [25, 26]. Again, the effect of the cationic charge density on transcription was apparent. Polycondensation of TEOS in the presence of mixtures of gelators **4** and **5** at $R (= [4]/([5] + [4]))$ between 0.25 and 0.80 led to hollow, helical silica fibers [27]. Lowering R below 0.25 (i.e., lowering the fraction of charged gelator) resulted in the formation of granular silica only. Above $R = 0.80$, gelation was no longer observed and transcription could not be carried out. Other combinations of charged and neutral gelators (e.g., **4'** and **3'**) showed similar trends. Peculiarly, in this system, helical silica was obtained even in samples with relatively high cationic charge density. However, as the two examples discussed above used different solvents, catalysts, amounts of TEOS, and (maybe most importantly) different gelators, it should be no surprise that there are significant differences in transcription results between the two systems. Regardless, as was observed with mixtures of **1** and **2**, a high dilution of cationic charge in the cyclohexane-based systems also eventually results in a loss of transcription.

Another example, illustrating the importance of electrostatic interactions to successful transcription, employs organogelator **6a**, capable of gelating (or, rather, strongly thickening) a mixture of ethanol and $\text{Ti}(\text{OiPr})_4$ [28, 29]. Polycondensation of the titanium alkoxide, conducted with ammonium hydroxide as catalyst, resulted in the formation of hollow, tubular TiO_2 fibers. When the catalyst was 2 M HCl, no fibers were observed. In the presence of ammonium hydroxide, transcription was carried out at basic pH, and the propagating species is considered to be anionic; in the presence of the strongly acidic HCl, cationic titanium species that will not deposit on the positively charged gel fibers are prevalent. In addition, a gel of **6b** was successfully

employed to template tubular Ta₂O₅ and V₂O₅ structures (see also Section 4.3; Figure 23).

3.2. Gelators Containing Non-Covalently Attached, Positively Charged Centers

Shinkai *et al.* demonstrated that positive charges associated with gel fibers in a non-covalent manner can also function as transcription-directing moieties [30]. The benzo-18-crown-6 group of compound **7** is capable of complexing cationic species, in particular K⁺. The benzylamine-catalyzed polycondensation of TEOS in the butanol gel of **7** in the absence of metal salts produced granular silica. Similar results were obtained in the presence of 0.25 molar equivalents (with respect to **7**) of KClO₄, whereas tubular silica was obtained in the presence of 0.5 and 1.0 equivalents. These results demonstrate that positive charges introduced in a non-covalent manner can aid transcription in a manner analogous to covalently-attached cations, and that the surface density of these positive charges, like that of the covalently-attached ones, is crucial to successful transcription. Interestingly, when K⁺ was replaced by Li, Na, Rb, and Cs cations, transcription was not successful due to their low affinity for the crown ether of **7**.

To incorporate different Group I cations into the gels and, thus, the inorganic materials obtained after transcription, several azacrown-containing gelators were synthesized (**8–11** in Figure 5). Analogously to compound **7**, the 1-butanol gels of LMOGs **8**, **9** and **10**, as well as the aniline gel of **11**, were successfully transcribed into silica in the presence of various metal salts: AgNO₃ (**8** and **10**), CsClO₄ (**9** and **10**), Pd(NO₃)₂ (**11**), and KClO₄ (**8** and **9**) [31–34]. Complexation of the metal cations by the (aza)crown ethers introduced positive charges into the LMOG-based templates, allowing transcription to take place. After calcination of the organic-inorganic hybrid material from AgNO₃ impregnated templates, Ag particles could be observed in the spaces previously filled by the gel-template [31] (see also Section 4.1, Figure 14); the presence of Cs or Pd in the calcinated materials obtained from templates containing these ions was demonstrated with an electron probe microanalyzer [32, 34]. Remarkably, 1-butanol gels of **8** and **9** and acetic acid gels of **10** and **11** could be successfully transcribed into silica even in the absence of metal salts. Because it is known that positive charges in the gel fibers can aid transcription, it was postulated that protonation of the nitrogen atoms of the azacrown moieties of **8** and **9** had occurred. In the gels with acetic acid as the solvent and **10** or **11** as the gelator, protonation will obviously occur. In the cases of the 1-butanol gels of **8** and **9**, a small amount of water was added in order to allow polycondensation of TEOS to take place. Some protonation of the nitrogen atoms by water is expected and evidence for it is available [35–37].

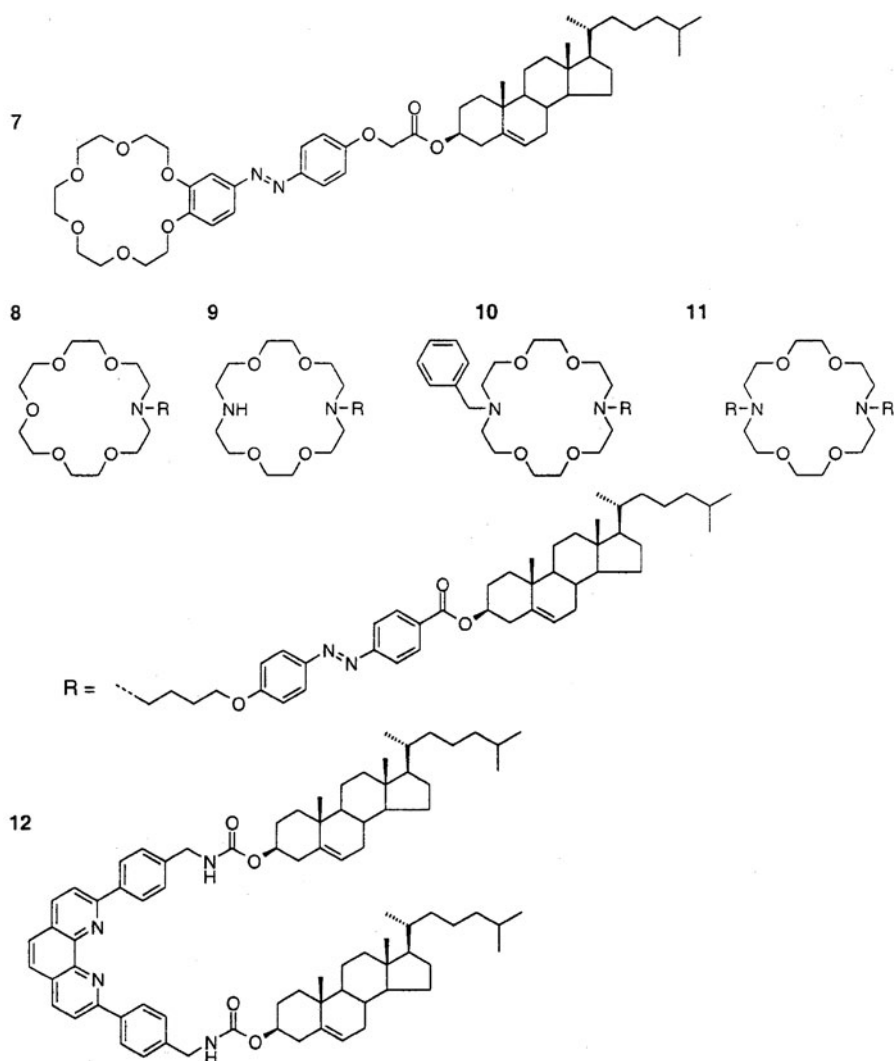


Figure 5. Structures of cholesterol-based LMOGs with metal binding sites.

When a small amount of Et_4NOH was added to the 1-butanol gels of **8** to neutralize the positive charges on the azacrown groups, polycondensation of TEOS resulted only in granular silica. However, polycondensation of TEOS in the 1-butanol gels of **9** in the presence of Et_4NOH still resulted in the formation of tubular silica. The original explanation for this result was based on the differences in pK_a values between monoaza-crown (9.0–10.2) and diaza-crown compounds (10.64), assuming residual protonation even in the presence of Et_4NOH [33]. However, it is more likely that transcription occurred as a result of

hydrogen bonding between the negatively charged silica species in solution and the NH moiety of the azacrown of **9**. The use of such hydrogen-bond donating groups in transcription will be discussed in the next section. The knowledge that protonated amines can also function as transcription-directors allowed hollow, tubular silica to be obtained from an acetic acid gel of a phenanthroline-containing LMOG **12** [38].

3.3. Gelators Containing Hydrogen-Bond Donating Amine Groups

As mentioned in the previous section, networks of gels of LMOG **9** could be transcribed into hollow, tubular silica even in the absence of any apparent positive charges. Although it was not realized at the time, this was the first example of gel transcription enabled by a hydrogen-bond donating moiety. Analogous to the examples discussed in the previous sections, strongly hydrogen-bond donating moieties can interact with negatively charged inorganic species in solution, leading to a deposition of inorganic material and transcription of the template structure. Compounds **13_n** were the first LMOGs especially designed to enable transcription through the action of such hydrogen-bond donating moieties. The molecules combine a gelation-inducing cholesteryl group with an $\text{NH}(\text{CH}_2)_n\text{NH}_2$ moiety, previously used in gemini surfactants where it was found to enable the transcription of vesicles [39]. Indeed, benzylamine-catalyzed transcription of 1-butanol gels of **13_n** yielded either fibrous or lamellar silica, depending on the value of *n* (see Section 4.1, Figure 10) [40].

The diamines **13₂** and **13₃** have been used also to bind and, thus, incorporate metals (Ni or Pd) into the inorganic structures formed after transcription. After calcination, metal particles could be observed in the resultant silica tubes [41]. 1-Butanol gels of a different cholesteryl and amine based LMOG (**14**) have been used for the templated formation of helical ribbons or tubular structures of SiO_2 or TiO_2 (see also Section 4.1 and Figure 15). As was the case for the azacrown compounds discussed previously, transcription continued to occur when Et_4NOH was added; proving that protonated amines could not have caused the transcription and that hence the hydrogen bond donating amines must have been the cause of transcription [42, 43].

The sugar-based LMOGs **15'–18'** (Figure 6) represent another class of molecules frequently used as templates for formation of inorganic materials [44–46]. Although **15–18**, like many other sugar-based compounds [47, 48], are capable of gelating a variety of solvents, they could not be used for templating inorganic materials; only granular silica was obtained from benzylamine-catalyzed polycondensations of TEOS in their gels. Reduction of the nitro groups of **15–18** yielded the amino-containing **15'–18'** that gelate a

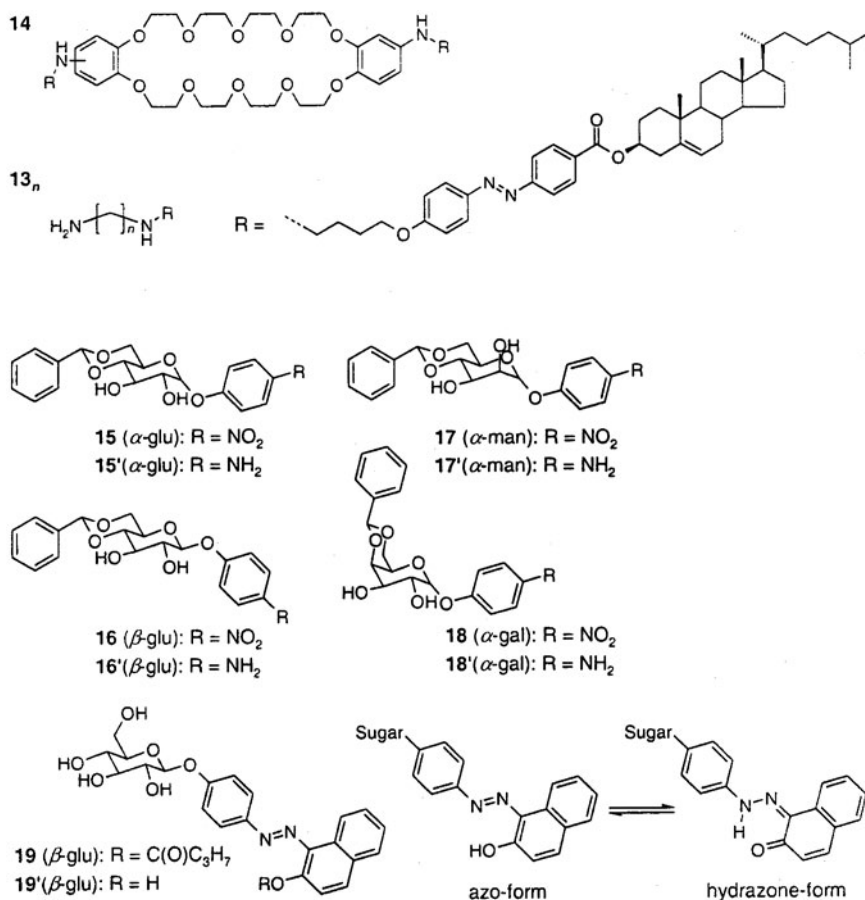


Figure 6. Structures of various cholesteryl- and sugars-based LMOGs.

range of solvents, including water. Unlike their nitro-containing counterparts, gels of **15'**–**18'** were successfully transcribed into silica using benzylamine as a catalyst. Because benzylamine is a much stronger base than **15'**–**18'** [49], protonation of the gelator amine groups cannot be responsible for the successful transcription. It must be due to hydrogen-bonding interactions between negatively charged silica species and the amino groups on the gel fibers. Compounds **19** and **19'** (Figure 6) provide another example of the importance of strong hydrogen bonding in transcription [50]. Although both **19** and **19'** gelate water/ethanol mixtures, only gels of **19'** were successful in transcription (i.e., templated formation of hollow, tubular silica). These results can be explained by realizing that only **19'** can switch between the so-called azo- and hydrazone-forms (Figure 6, bottom right); the relatively strong hydrogen-bond donating ability of the NH part of the azo-form allows transcription to take place.

3.4. Gelators with Different Structural Features

Although some of the gelators that will be discussed here could have been included in previous sections, each contains structural features that make it somewhat unique. For that reason, their transcription will be explained on a case-by-case basis.

The first example uses a “binary gel system” methodology in which a gelator is mixed with a compound that can effect transcription [51]. LMOG **20** (Figure 7) does not possess groups that can interact with an inorganic material intermediate and, hence, its networks cannot effect templated formation. Thus, some of compound **21**, possessing an amine moiety, was added to the structurally similar **20** in hopes of incorporating some strong hydrogen bond donating groups in the gel fibers. Both CD and NMR spectral data indicate that incorporation of some **21** took place, and subsequent benzylamine-catalyzed transcription resulted in the formation of hollow, double helical, tubular silica (see Section 4.2, Figure 21). Again, the concentration of the hydrogen-bonding sites was shown to be of importance; transcription took place only when **21** was present in weight ratios >20% [52].

The use of a transcription-enabling additive, benzylamine, has already been discussed in several previous examples. *p*-Nitrobenzylidene-functionalized monosaccharides are known to possess excellent gelating properties, both in apolar organic solvents and in water [48]. After the initial reports of the gels of these LMOGs, the possibility that their *p*-nitrobenzylidene groups might interact with benzylamine through π - π stacking and additional hydrophobic interactions was explored for the purposes of incorporating such molecules into gel fibers and facilitating transcription [53]. Thus, silica transcription of a hydrogel

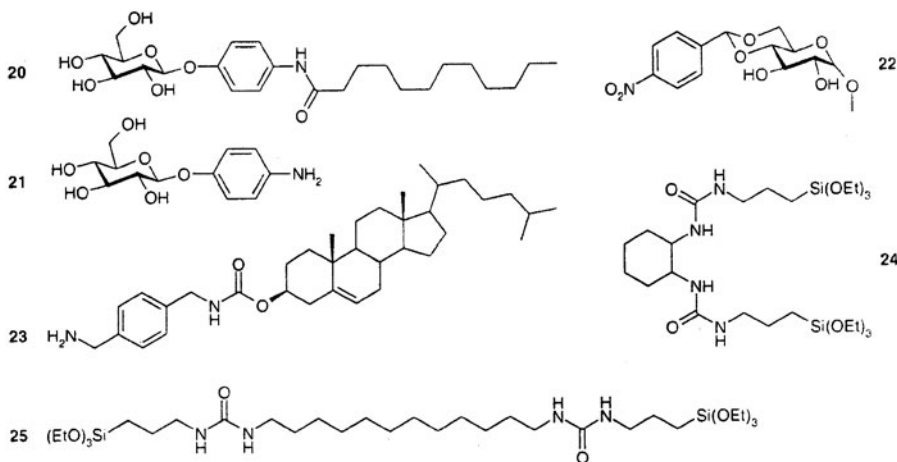


Figure 7. Structures of special LMOGs as well as of some non-gelating additives.

of **22** in the presence of one equivalent of benzylamine resulted in hollow, tubular silica. When a structurally incompatible catalyst, hydrazine, was added in place of benzylamine, only granular silica was obtained.

In the examples above, the catalyst is present initially in the solution/sol phase before gelation, and transcription takes place as a result of catalyzed formation of charged inorganic species in solution that are attracted to the template surface. In compound **23** (Figure 7), capable of gelating a number of solvents, the benzylamine is linked covalently to the gelator scaffold. Performing the transcription of a gel of **23** to silica in the absence of an additional catalyst resulted in the initiated formation and subsequent growth of the inorganic material exclusively on the fiber surface; *only tubular silica was detectable* [54]. In other cases, “transcribed silica” is accompanied by granular silica that forms from nucleation events in the liquid part of a gel.

In another approach, the precursor of the inorganic has been incorporated into gelator-like structures (**24** and **25**) [55]. Although compound **24** (either as the *R,R* or *S,S* enantiomer) gels a number of organic solvents, transcription experiments were carried out in aqueous solutions. In acidic water, inorganic/organic hybrid materials formed that display opposite macroscopic chirality depending on the enantiomer of **24** employed. In ethanol/water mixtures, tubular silica containing many parallel channels was obtained [56]. Although no true gels were used in both cases, the actual template involved stacks of molecules of **24** similar to the stacks present in its gels. Even though compound **25** gels toluene, it was polymerized in the non-gelated solvent, water, and lamellar silica was obtained [57]. These examples, although not employing gels, show that incorporation of the inorganic precursor into a gelator structure is a viable strategy that should be extendable to fibers of true gels.

In all of the previous examples, alkoxides of transition metals and other elements (e.g., $\text{Si}(\text{OEt})_4$, $\text{Ti}(\text{OiPr})_4$) have been used as the inorganic precursors, leading to the formation of polymeric metal oxides or other oxide materials (e.g., TiO_2 , SiO_2 , and V_2O_5). The work of Stupp and co-workers [58] demonstrates that LMOGs can be used for the templated formation of a much wider range of inorganic materials. For instance, LMOG **26** (Figure 8), consisting of five distinct structural parts (A–E), assembles into cylindrical micelles. Its single phosphorylated serine residue (D) strongly interacts with calcium ions, allowing gels of **26** to be templates for formation of $\text{Ca}_{10}(\text{PO}_4)_6(\text{OH})_2$ (i.e., hydroxyapatite (HA)). Thus, gel fibers of **26** were exposed to solutions of CaCl_2 and Na_2HPO_4 , which, upon mixing, with time formed HA on the surface of the gel fibers. In all cases, preferential alignment of the HA crystallographic *c* axis with the long axes of the gel fibers was observed. The crystallization-directing effect of the phosphorylated serine group was demonstrated by showing that mineralization using a non-phosphorylated analogue of **26** results only in amorphous deposits of HA around the fibers.

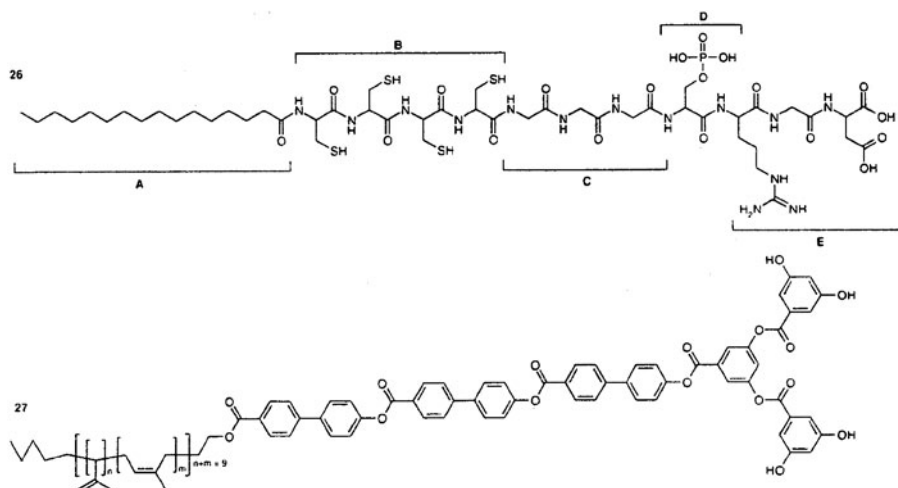


Figure 8. Two LMOGs developed by Stupp *et al.* [58, 59].

A strikingly different transcription system employed LMOG **27** that assembles in organic solvents into helical nanoribbons [59]. The addition of a solution of cadmium nitrate and subsequent exposure of the mixture to H_2S gas led to nanohelices consisting of polycrystalline CdS (as well as significant amounts of untemplated material). The affinity of Cd^{2+} ions for the hydrophilic regions of the ribbons (i.e., the hydroxy-containing parts) was given as the reason for the templating effect. A local supersaturation of Cd^{2+} ions leads to nucleation, growth of the CdS crystals along the fiber surfaces, and, ultimately, formation of helical structures [60].

3.5. Outlook for the Future

Although knowledge about transcription-enabling groups has increased enormously during the last decade, many fundamental issues still need to be investigated. For instance, thus far only amines have been successfully used as hydrogen-bond donating catalysts. Can other moieties be used and what is the minimum $\text{p}K_b$ required in order for hydrogen bond donating moieties to function as transcription-enabling groups? Furthermore, in all transcription experiments carried out thus far, interactions have been between a gelator and *negatively* charged inorganic species. However, analogously, *positively* charged inorganic species may be attracted to oppositely charged gel fiber, allowing the use of gelators containing hydrogen bond accepting moieties as transcribing agents. Carrying out transcription of such gelators at a pH at which the inorganic precursor exists predominantly as positively charged species (e.g., $\text{pH} < 2$ for

TEOS and $\text{pH} < 5$ for $\text{Ti}(\text{OiPr})_4$) should result in formation of inorganic structures analogous to those reported thus far.

Initially, the presence of a cationic charge in the gelator structure was thought to be indispensable for transcription of organogel templates. Now, we know that many other moieties can be utilized. In addition, the examples described in Section 3.4 have suggested that the precursor to the inorganic material may be a part of the gelator. In fact, any of the three essential components in the transcription reaction – the catalyst, the inorganic precursor, and the transcription-directing moiety – may be incorporated into the gelator structure or may be present in solution. Finally, the examples involving **26** and **27** describe systems that are not based on polycondensation reactions. They demonstrate that a wide variety of specific interactions between a gel-based template and an inorganic precursor may be exploitable to give transcription.

All of this flexibility and diversity will allow people working in the area of transcription to make use of a much wider range of templating compounds and reactions, and we predict a vast increase both in the number of hybrid and inorganic structures as well as in the methods used to obtain them.

4. Shapes of Transcribed Materials

Since LMOGs have a general tendency to form fibrous networks, the principal structures obtained from transcription of their gels are of a tubular nature. Upon closer examination, however, a great variety of shapes can be found within this general framework. Paper roll-like assemblies, helices, spirals, and intertwined fibers have successfully been transcribed into inorganic materials. Moreover, LMOGs can also give rise to colloidal-type gels, whose architecture consists of closely packed vesicular or spherical components. These types of gels can also be transcribed into inorganic material. In this section, the relationship between the molecular structure of the gelators and the shape of the inorganic material obtained from transcription of the respective gels will be discussed. Furthermore, an attempt will be made to relate the resulting inorganic shapes to the experimental conditions used for the transcription process, which often vary with respect to the type of catalyst or solvent used, the reaction times, the temperature, the stoichiometry, and the type of polymeric precursor employed.

The wide variety of inorganic shapes obtained thus far from gel transcription has actually arisen by implementing modifications to three basic molecular structures. These basic structures provide the molecules with their gelation ability, while the modifications at their periphery lead to slight variations in their self-assembly mode or in the manner of interaction with the solvent, and, thus, to different transcribable shapes. The three basic units that allow these molecules to self-assemble into one-dimensional aggregates and, therefore, give rise to

gels are: a cholesterol, a sugar (i.e., glucose, galactose or mannose) covalently linked to at least one aromatic moiety, and a 1,2-bis-substituted cyclohexane where the substituents are linked to the cyclohexane via amide or urea groups. In the case of cholesterol, molecular stacks are formed predominantly due to the large hydrophobic interactions between these molecules [61]. For cholesterol-based gelators functionalized with azobenzene moieties, a general model for molecular packing within the gel fibers is shown schematically in Figure 9 [62].

Sugar-based gelators, on the other hand, can self-assemble through hydrogen-bonding interactions, possibly with π - π stacking of any aromatic units (if present) contributing to stabilization of the assembly [63]. Finally, cyclohexane-based gelator molecules are considered to stack due to hydrophobic interactions between the cyclohexyl rings, while the amide or urea substituents in the 1 and 2 positions provide a strong, one-dimensional hydrogen-bonding network [64].

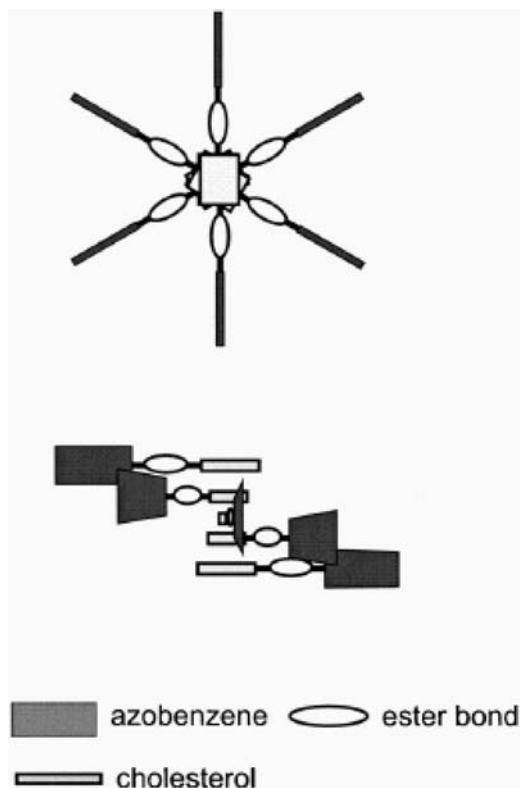


Figure 9. Schematic representation of helically stacked molecular assemblies of cholesterol-azobenzene gelators. (Reprinted from [62] with permission of the publisher, The Royal Society of Chemistry.)

4.1. Transcription of Cholesterol-Based Gelators

Cholesterol-based gelators can be used to obtain transcribed materials with practically any of the previously mentioned shapes, given appropriate substituents and transcription conditions. Using H-bonding as the principal interaction mode between the gelator and TEOS, a series of cholesterol-bearing alkylamine substituents ($\mathbf{13}_n$), with various chain lengths (n) between the amine group and the gelator scaffold, has been prepared and transcribed [40, 41]. Interestingly, a film-like, pseudo-cylindrical structure was observed for the 1-butanol gels of gelators containing either ethylamine or butylamine groups (Figure 10, A and C, respectively), whereas the propyl- and pentylamine functionalized molecules gave a fibrous gel architecture (Figure 10, B and D, respectively). These differences in the gel architecture most probably arise from different molecular packing of the terminal NH_2 groups in gelators with even (ethyl and butyl) and odd (propyl and pentyl) numbers of CH_2 groups.

Gels in acetic acid of gelator $\mathbf{12}$, consisting of two cholesterol moieties functionalizing a bis-aryl phenanthroline group, consist of very fine fibers (5–30 nm in diameter) [38]. Following transcription (using acetic acid also as the catalyst),

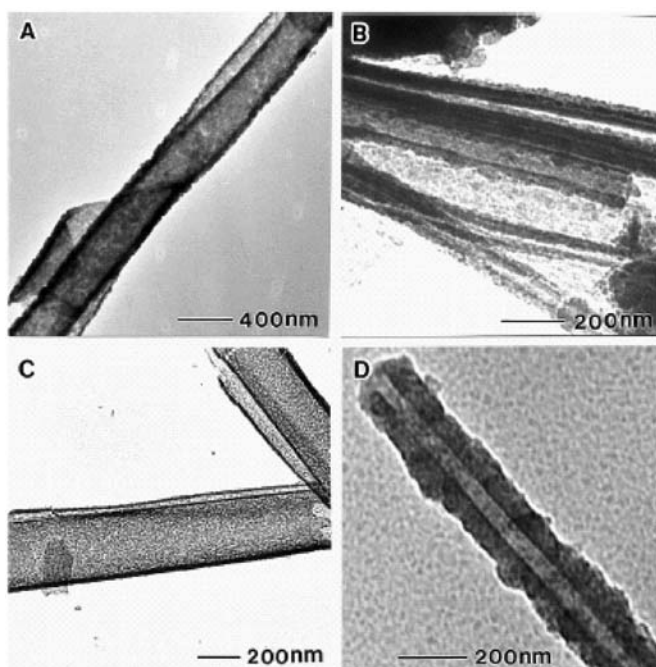


Figure 10. TEM pictures of silica obtained from gels of $\mathbf{13}_n$ in 1-butanol, with $n = 2$ (A), 3 (B), 4 (C), and 5 (D). (Reprinted from [41] with permission of the publisher, The Royal Society of Chemistry.)

thin tubules are obtained with an inner diameter of 4–5 nm, corresponding to the molecular length of **12**. In order to obtain such small inner diameters, the aggregation of the single gel fibers into larger bundles had to be limited, which was achieved by carrying out the transcription at a temperature close to the gelation temperature, T_g (here 23–25° C).

The gelating scaffold comprising cholesterol and azobenzene units has been particularly successful and often used in combination with either “covalently” or “non-covalently” linked charged moieties to facilitate transcription into silica. The “covalently” linked $-(\text{Me})_3\text{N}^+\text{Br}^-$ derivative **2** behaves rather differently under slightly different transcription conditions [21]. The use of acetic acid as the catalyst and the solvent, for example, leads to the formation of silica tubules, whereas the addition of ethanol to this system results in silica fibers without a hollow interior. Since ethanol facilitates TEOS polymerization, the resultant structure in the presence of ethanol becomes denser and tubules cannot be observed. Furthermore, the shape of the transcription product obtained from the gels of **2** can also be manipulated by the addition of a second gelator (**1**), which possesses neither H-bonding nor positively charged groups [23, 24]. As mentioned in Section 3.1, mixtures of **2** and **1** with $R = \mathbf{2}/(\mathbf{2} + \mathbf{1})$ equal to 0.25–1.00 lead to the formation of hollow fibers/tubules. However, at lower R values (0.01–0.10), exclusively right-handed helical silica fibers were observed, and at $R < 0.01$ only granular silica was formed due to the low density of positive charges present in the gel fibers. Careful examination of SEM (Figure 11) and TEM images reveals that the observed right-handed helical silica fibers have a helical pitch of 100–200 nm and an inner diameter of ca. 10 nm with a relatively narrow size distribution. Such observations clearly support the view that the helical fibers are a direct result of templation by the chiral gelator structure.

Other gelators containing the cholesterol-azobenzene scaffold as well as either a crown or aza-crown ether group (located at the periphery or near the

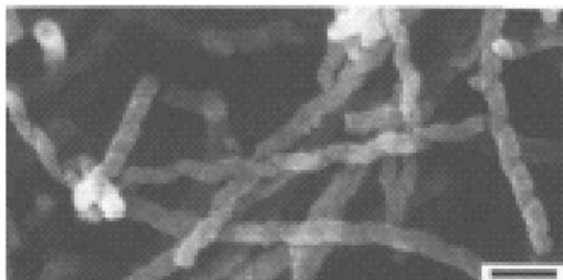


Figure 11. SEM image of silica prepared using a mixed gel of **1** and **2** ($R = 0.10$) as the template. Scale bar = 200 nm. (Reprinted from [23] with permission of the publisher, The Chemical Society of Japan.)

center of the molecule), have also been successfully used for transcription in the presence of complexed cations [30–34]. Transcription of gels of **7** into tubular silica can be achieved by addition of KClO_4 in a 1:1 or 1:2 molar ratio followed by the addition of 1-butanol, TEOS, water and benzylamine. Smaller amounts of KClO_4 led to granular, untemplated silica [30]. A metal salt is not required for transcription of (1-butanol) gels of **8** and **9**. A positive charge on the monoaza-18-crown-6 moiety of **8** and an additional NH group that can function as a H-bonding moiety in **9** (see Section 3.2) are the most probable reasons for the successful transcriptions [33]. In both cases, tubular, paper roll-like structures approximately 400 nm in diameter are formed. Figure 12 shows that the surface of the hollow silica fibers obtained by transcription of gels of **8** (transcription of gels of **9** gave very similar structures) is rather smooth and that the tube walls are quite thin.

Presumably, the TEOS sol-gel polymerizations proceed along the surface of the lamellar gel aggregates, growing further into paper-roll structures. A schematic representation of this process is depicted step-by-step in Figure 13 [33].

Gelator **10** possesses a diaza-18-crown-6 moiety like that of **9**. However, the hydrogen atom of NH has been replaced by a benzyl moiety that no longer allows the amino group to function as a hydrogen-bond donor. Therefore, transcription requires that salts such as AgNO_3 and CsClO_4 be added to the gels. The silica tubules obtained in this way are right-handed spirals with a 25–50 nm inner diameter (Figure 14A); some additional lamellar silica structures are present in the case of CsClO_4 . The right-handed features are a reflection of the chirality of the gel fibers. In them, the cholesterol-azobenzene moieties are

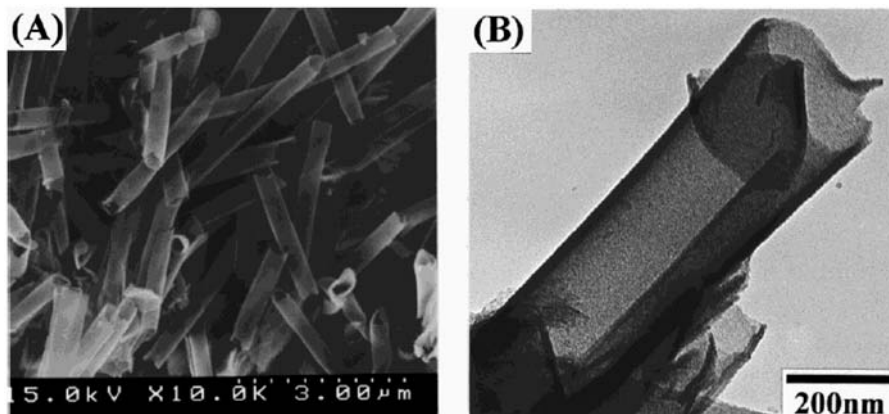


Figure 12. (A) SEM and (B) TEM of hollow silica from the transcription of TEOS/1-butanol gels of **8**. (Reprinted from [33] with permission of the publisher, The American Chemical Society.)

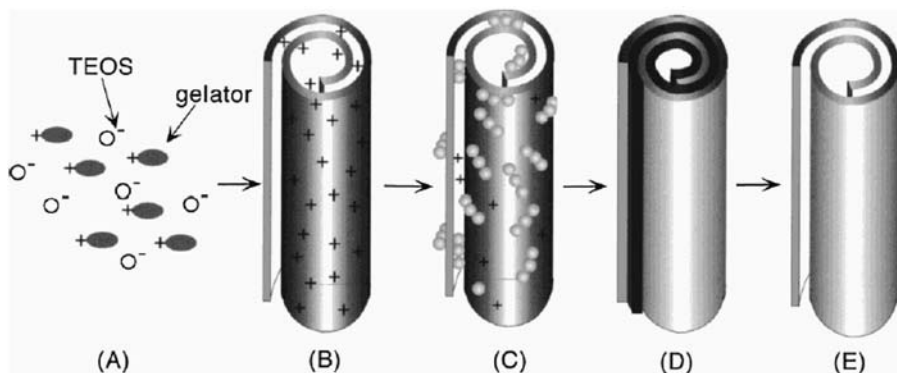


Figure 13. Schematic representation of transcription occurring at the surface of a lamellar gel aggregate: (A) mixture of gelator and TEOS; (B) gelation; (C) sol-gel polymerization of TEOS and adsorption of negatively charged silica particles onto the positively charged gel; (D) organic-inorganic hybrid before calcination; and (E) after calcination. (Reprinted from [33] with permission of the publisher, The American Chemical Society.)

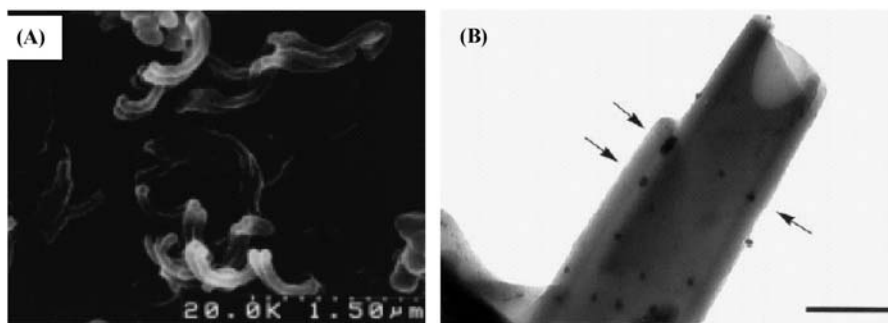


Figure 14. (A) SEM image of spiral silica obtained from a gel of $10 \cdot \text{AgNO}_3$ (1:1 molar ratio). (B) TEM image of the silica obtained from a gel of $8 \cdot \text{AgNO}_3$; arrows indicate positions of metal particles deposited in the interlayer spaces (scale bar = 200 nm). (Reprinted from [32] and [31] with permission of the publishers, Wiley-VCH and The Royal Society of Chemistry.)

oriented in a clockwise fashion [32]. After calcination of the organic-inorganic hybrid material deriving from the transcription of networks of gels of **8** and **10** containing AgNO_3 , Ag particles of ca. 1 nm diameter, as well as some larger (20–55 nm) Ag aggregates could be observed in the spaces previously filled by the gel-template (Figure 14B); azacrown-appended gelators can be used for metal-deposition on the silica matrix [31].

Gelator **14** consists of a central crown ether symmetrically functionalized by two cholesterol-azobenzene groups. Its transcription in gels of 1-butanol or acetic acid using TEOS or $\text{Ti}(\text{OiPr})_4$ as the monomer has yielded particularly

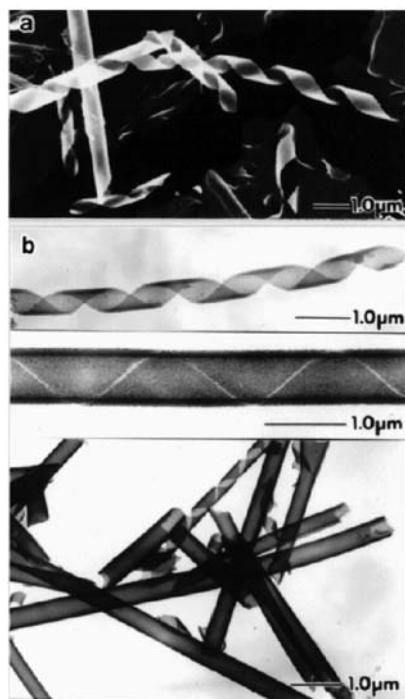


Figure 15. SEM (a) and TEM (b) images of silica obtained after calcination of an acetic acid/TEOS gel of **14**. (Reprinted from [42] with permission of the publisher, The American Chemical Society.)

interesting materials [42]. Figure 15 contains images of both helical ribbons (pitch: 1300–1700 nm) and tubular silica (ca. 560 nm outer diameter) obtained from a gel of **14** in acetic acid. The helical silica structures are right-handed, corresponding to the helicity of the gel structures as determined by CD spectroscopy. In this way, the molecular helicity of the gel is reflected in the nanoscopic structure of the transcribed material.

The tubule walls consist of a double layer of silica with an interlayer distance of 8–9 nm, indicating that TEOS-derived species were adsorbed onto both surfaces of the tubule walls during polycondensation. Similar structures were produced in TiO_2 structures from transcription of fibers of **14** in gels containing acetic acid and $\text{Ti}(\text{OiPr})_4$ as the monomeric precursor [42]. A proposed mechanism for the sol-gel polymerization is presented in Figure 16 (the mechanism should be identical for both TEOS and $\text{Ti}(\text{OiPr})_4$) [42, 43].

Extreme changes in gel architecture and, therefore, of the corresponding transcribed material can be accomplished with another symmetrically functionalized diaza-18-crown-6 molecule (**11**). Networks of gels of **11** in acetic acid consist of spherical, vesicular structures ~ 200 nm in diameter, as well as

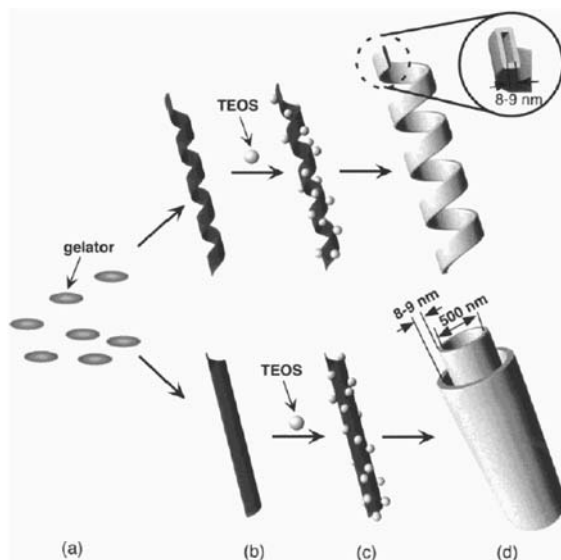


Figure 16. Postulated mechanism for the sol-gel polymerization of TEOS using an acetic acid gel of **14** as template: (a) gelator, (b) gelation, (c) sol-gel polymerization of TEOS and adsorption onto the gel, and (d) hollow helical ribbon (upper) and hollow double-layered nanotube (lower) of TiO_2 formed after calcination. (Reprinted from [43] with permission of the publisher, The American Chemical Society.)

of some larger spheres ~ 2500 nm in diameter (Figure 17) [34]. The smaller vesicles seem to be connected in a pearl necklace-like fashion, which most probably accounts for gelation. Moreover, SEM and TEM images of sections of the gel revealed that the vesicles are multilayered structures with single layer thicknesses of about 5 nm. They correspond quite well to the vesicle wall structure represented in Figure 18 in which **11** adopts a folded conformation. Transcription of these acetic acid gels leads to a faithful reproduction of the template into silica, where multilayered spherical structures with 5 nm lamellar spacings can be observed (Figure 17, B and C).

4.2. Transcription of Sugar-Based Gelators

The wide variety of sugar-based gelators synthesized as of the beginning of 2004 provides many morphologically different superstructures: linear, helical, bundled, multilayered cigar-like and vesicular [47, 48, 65]. However, relatively few sugar-based gels have been transcribed into inorganic materials because introduction of a moderate amount of positive charge in these gelators is not trivial. All sugar-based gelators transcribed thus far are based on H-bonding as the principal source of interaction between the gelator and TEOS. Additionally,

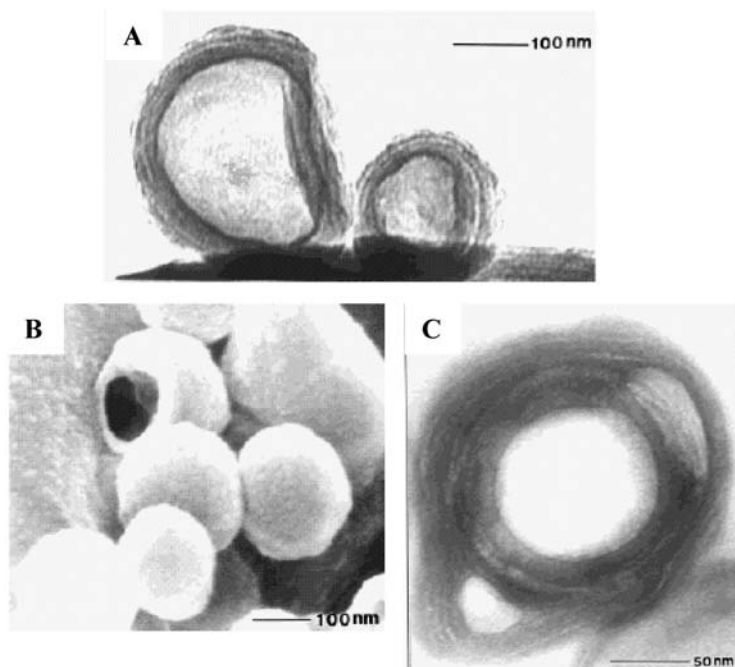


Figure 17. (A) TEM image of the xerogel of **11** obtained from the acetic acid gel (negatively stained with UO_2^{2+}), (B) SEM and TEM (after sectioning) images of silica obtained from an acetic acid gel of **11**. (Reprinted from [34] with permission of the publisher, The American Chemical Society.)

all gelators of this class contain at least one aromatic unit to provide sufficient hydrophobic (intermolecular) interactions to allow formation of a network in a polar solvent.

Sugar-based gelators consisting of a central sugar (α -glucose, β -glucose or α -galactose) functionalized on opposite ends with two aromatic rings (**15'**, **16'**, and **18'** in Figure 6) have been designed to be transcribed efficiently into silica [44–46]. This structural design results in rather flat molecules that are ideal for packing as 1-dimensional aggregates. In addition, they contain H-bonding OH groups in the middle of the structures that are shielded from the sol-gel reaction medium by the two hydrophobic groups that, themselves, provide additional intermolecular interactions via π - π stacking. Furthermore, one of the aromatic units possesses an amino group to promote gelator-TEOS interactions via H-bonding. Whereas the α -glucose based gelator forms narrow (5–20 nm cross-section), frizzled fibrils, fibers of the β -glucose based gelator are straighter and broader (50–150 nm cross-section). These differences are reproduced in the transcribed materials which, for **15'**, consist of thin tubular silica with a 5–10 nm inner diameters (Figure 19a); from gels of **16'**, tubular

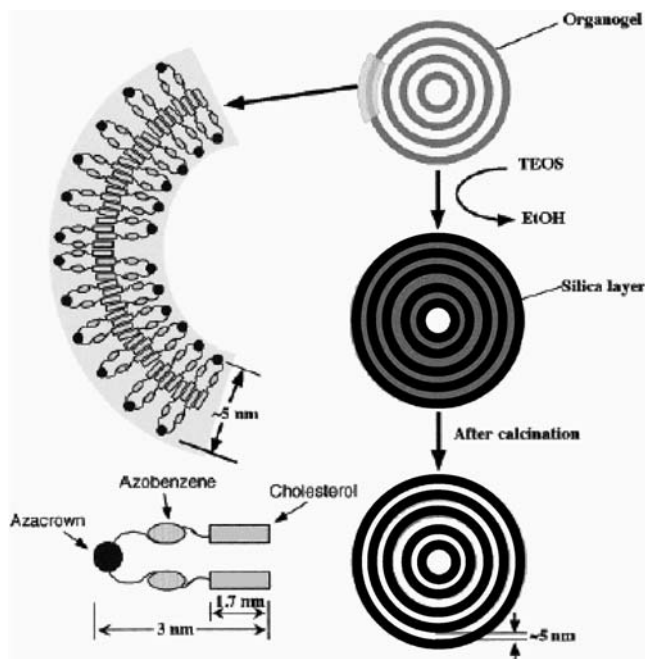


Figure 18. Schematic representation of sol-gel transcription of the multilayered spherical structure in gels of **11**. (Reprinted from [34] with permission of the publisher, The American Chemical Society.)

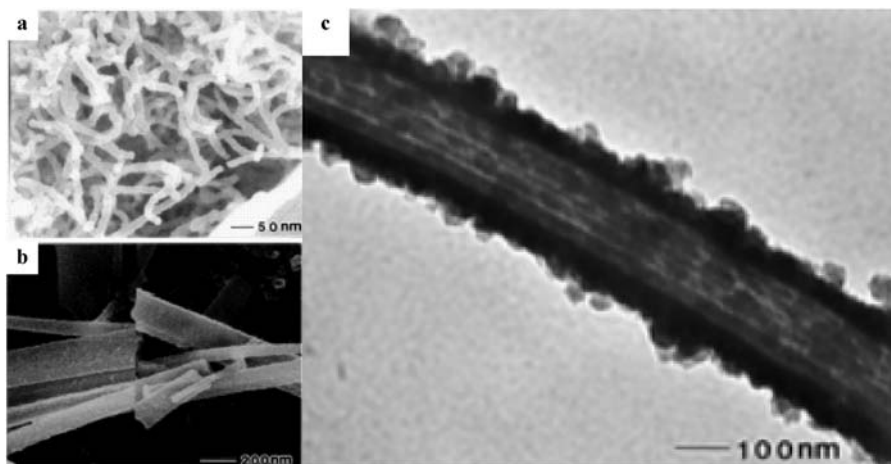


Figure 19. (a) SEM picture of silica obtained after transcription of an ethanol gel of **15'**; (b) SEM and (c) TEM pictures of silica obtained after transcription of an ethanol gel of **16'** (after calcination). (Reprinted from [44] with permission of the publisher, The Royal Society of Chemistry.)

silica with a 50–100 nm inner diameter is obtained (Figure 19b). The larger tubules consist of bundles of smaller tubules (5–10 nm cross-section), similar to a lotus root structure, indicating that transcription of gel fibers within a bundle of fibers had occurred (Figure 19c) [44].

An example of how solvent-gelator interactions can lead to morphological variations is provided by the α -galactose based **18'**. In EtOH gels, fibers of **18'** are like those of **15'** and **16'**, and transcription leads to tubular structures (Figure 20a). In H₂O gels, aggregates of **18'** consist of spherical features, 200–350 nm in diameter, that result in hollow silica spheres after transcription and calcination (Figure 20b). Transcription of aqueous gels of the α -mannose derivative **17'** also leads to hollow silica spheres [45]. It remains unclear why **17'** and **18'** produce hollow spheres and **15'** and **16'** yield only tubular structures.

By varying the temperature at which the transcription of a number of porphyrin-based gelators bearing four sugar moieties as peripheral groups was carried out, it proved possible to influence the morphology of the resultant silica [66]. At high temperatures where TEOS polycondensation proceeds in preference to organogel fiber aggregation, thin tubular silica was formed with an internal diameter corresponding to the size of one gelator molecule. However, when transcription was conducted at a lower temperature where organogel fiber aggregation is more rapid than TEOS polycondensation, the templates were large organogel bundles and the resultant silica consisted of thick helical fibers displaying either right- or left-handedness depending on the peripheral sugar structure.

Some innovative solutions to the transcription problem presented by the sensitivity of sugar-based gelators to positive charges have been discussed in Section 3.4. In this regard, interesting silica structures were obtained when sugar-based gelator **20** was mixed with non-gelator **21** that also contains an amino group [51]. Incorporation of **21** within the fibers of **20** provides sufficient

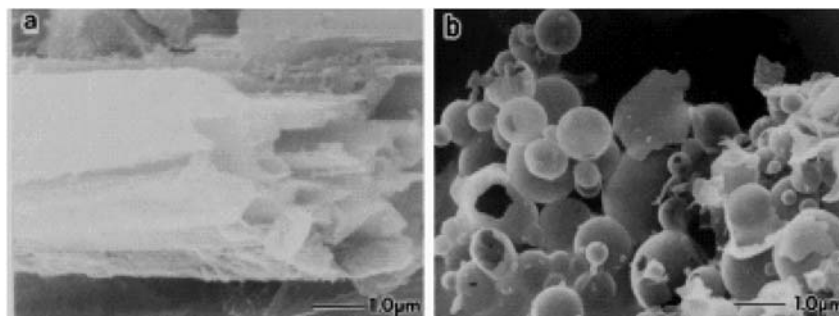


Figure 20. SEM pictures of silica obtained after transcription of (a) an ethanol and (b) a water gel of **18'**. (Reprinted from [45] with permission of the publisher, The Royal Society of Chemistry.)

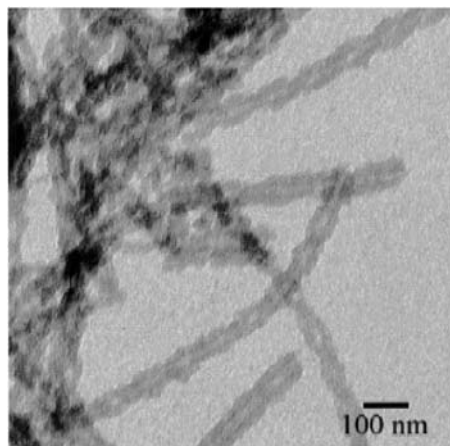


Figure 21. TEM image of double-helical silica nanotubes obtained after transcription of a mixed gel of (1:1 w/w) **20** and **21** in water-methanol (10:1 v/v) (after calcination). (Reprinted from [52] with permission of the publisher, The American Chemical Society.)

H-bonding sites for the transcription process to be successful. A rather unique double-helical silica structure with a 50–80 nm diameter and a 50–100 nm pitch was obtained. The spacing between the two strands of the double helix was ca. 25 nm (Figure 21). As far as could be determined, all of the helical structures were right-handed, reflecting the chirality expressed by the gel fibers [52].

4.3. Transcription of Cyclohexane-Based Gelators

Cyclohexane-based gelators have been synthesized with a variety of charged substituents to facilitate the transcription process. Depending on the nature of these substituents, either tubular or helical structures can be obtained. Thus, transcription of helical gel fibers consisting of mixtures of neutral and charged cyclohexanediamine derivatives (**3/4** and **3'/4'** in Figure 4) gives rise to the corresponding helical silica structures (Figure 22) [25, 26]. Careful examination of the TEM images (Figure 22c, and d) reveals the existence of inner tubules with diameters of 20–70 nm for both right- and left-handed silica structures, indicating that transcription does not occur around a single gel fiber, but more likely around a bundle of fibers.

Similarly, the helicity of gel fiber bundles of cyclohexane derivative **6b**, containing pyridinium perchlorate as the charged species, could also be transcribed into a variety of inorganic materials (i.e., Ti-, Ta- and V-oxides) with helical structures (Figure 23) [28, 29]. For both cyclohexanediamine derivatives, the *R,R* enantiomers resulted in left-handed helical tubules and the *S,S* enantiomers provided the right-handed helical material. Gels of **6a** containing

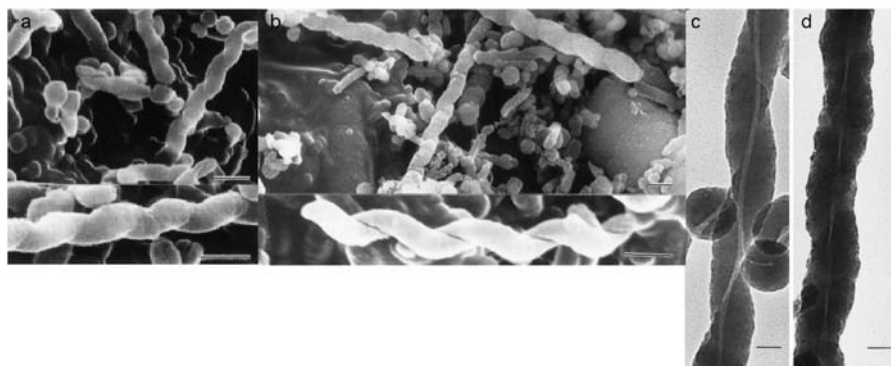


Figure 22. Right-handed (b, SEM; d, TEM) and left-handed (a, SEM; c, TEM) helical silica fibers obtained after transcription of a mixed gel of **3/4** and **3'/4'**, respectively. (Reprinted from [26] with permission of the publisher, Wiley-VCH.)

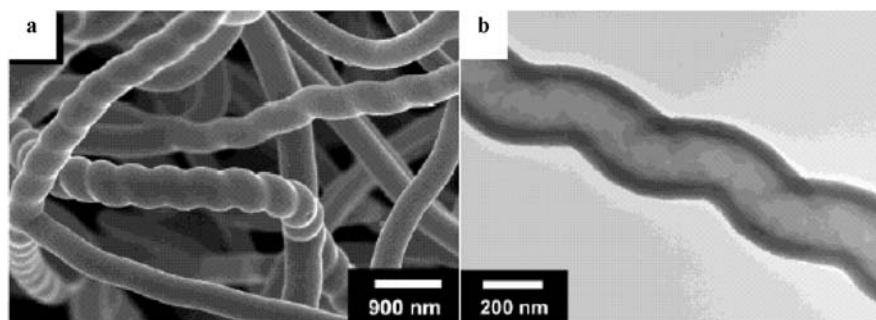


Figure 23. (a) SEM image of tantalum oxide fibers obtained from the *S,S* enantiomer of **6b**; (b) TEM image of a tantalum oxide fiber obtained from the *R,R* enantiomer of **6b** (gel in ethanol). (Reprinted from [29] with permission of the publisher, The American Chemical Society.)

hexafluorophosphate instead of perchlorate as counter-ion, however, gave rise to achiral tubular structures only [29]. This difference may be related to the difference in hydrophilicity of the two counter-ions, however, this aspect of the transcription is yet to be determined definitively.

Recently, interesting helical gel templates have been obtained by using a completely different gelator: 2-acryloylamide-dodecane-1-sulfonic acid (ADSA) [67]. Such ADSA gel ribbons were used for the generation of silver nanohelices (approximately 50–180 nm in diameter) by reducing the silver cations adsorbed onto the gel template with sodium borohydride. Because the racemic mixture of the gelator was used, both right- and left-handed silver helices were obtained. However, by making use of enantiomerically pure gelator, a product with either right- or left-handed helicity should be obtainable

enabling the study of the chiral dependence of electronic or photonic properties of 1D metal nanostructures.

4.4. Perspectives for the Future

Self-assembled, non-covalently linked systems possess the striking ability to yield a wide variety of shapes, perhaps much wider than fully covalent systems. Low molecular mass gelators and their gels are notable examples of such versatile systems. Although synthetic polymers, for example, are practically unrivaled as templates for making hollow spherically shaped materials, and carbon nanotubes are an excellent choice for fabrication of tubular structures, networks of LMOG gels can function as templates not only for these specific shapes, but also for helices, intertwined double-helices, spirals, vesicles, and paper roll-like structures [6]. In particular, helical structures can aid in inducing chirality in the corresponding transcribed inorganic material.

In considering the variety and number of transcribed structures presented in this section, it is noteworthy that they arise from a limited number of gelating scaffolds that are (for the most part) cholesterol-, sugar-, or cyclohexane-based. Moreover, a single gelator may, under different conditions, display different gel morphologies (e.g., fibers in ethanol and spheres in water), leading to several structurally different inorganic materials. These differences in gel morphology are generally induced by changing the solvent or by addition of a specific metal salt to the system. Although in most cases transcription leads to a product with a single morphology (apart from moderate amounts of granular silica), in some cases more than one shape of the inorganic material is present after transcription as a consequence of the kinetic nature of the self-assembled process. Absolute control over this process, as well as avoiding the formation of granular silica remain two of the outstanding challenges that needs to be met in order to obtain morphologically pure products.

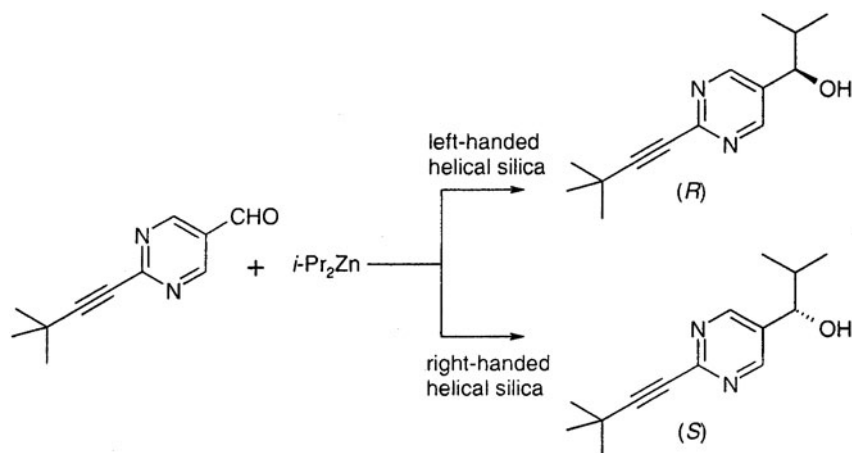
Despite the fact that only a limited number of gelating scaffolds has been used to prepare most of the transcribed materials thus far, a large diversity of inorganic shapes have been found. Clearly, use of other types of gelators will further broaden the variety of interesting materials obtainable. However, with greater gelator (template) diversity comes an additional challenge: being able to predict the outcome of a transcription experiment based on the type of gelator. This challenge is already formidable.

5. General Conclusions and Challenges for the Future

This field of research began when it was demonstrated that introduction of a positive charge onto an existing gelator scaffold can lead to transcription of

organogel fibers into silica [18, 19, 21]. Since then, scientists have increasingly been able to design, make use of, and understand the functioning of LMOG-based template structures for the formation of a variety of inorganic materials. Owing to the non-covalent interactions, which are at the basis of LMOG based gels, a large number of gel and, hence, template morphologies has been available. This has led to a many different shapes and sizes of inorganic materials, generally not obtainable via other fabrication techniques.

As the research into this field continues to develop, the accumulated knowledge will undoubtedly lead to inorganic or hybrid materials with novel shapes, more uniform properties, more exotic compositions. However, what will be the applications of these esthetically pleasing materials?



Scheme 5. Reaction carried out in the presence of chiral, helical silica [68].

Catalysis is one of the areas in which the use of inorganic or hybrid materials with specific nanoscale features can be envisioned. Several examples of templated silica structures with a metal incorporated or bearing metal particles are currently known [31, 33, 34]. However, they have not been applied in catalytic systems thus far. However, an artificially designed chiral inorganic material [25, 26] has been used to direct the stereo course of a reaction between diisopropylzinc and pyrimidine-5-carbaldehyde (Scheme 5) [68]. Use of the left-handed helical silica resulted in the formation of the R-product, whereas use of the right-handed silica yielded S-product with up to 97% ee. At present, it is unclear whether the asymmetric induction is a result of the helicity of the silica fibers or as a result of sites *on* or *in* the silica that are chirally imprinted during transcription of the original organogel template. Regardless, the results outlined in Scheme 5 are a very positive omen for future applications of the inorganic materials described here.

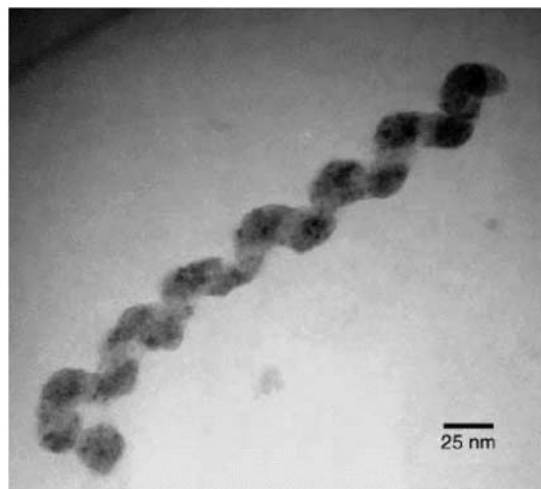


Figure 24. TEM micrograph of a helical nanostructure of CdS with a pitch of 40–50 nm. (Reprinted from [60] with permission of the publisher, Wiley-VCH.)

Undoubtedly, the coming years will bring many stunning examples of novel templated inorganic materials and, as with the advancement of nanotechnology the demands for small functional and well defined materials and devices will undoubtedly increase, this may be the era for templated inorganic materials. The cadmium sulfide helices mentioned previously [60] and shown in Figure 24 should have interesting electronic or photonic semiconductor properties. They are one example of how organic chemistry in general and organogel chemistry in particular can be the *science of choice* for the advancement of several technologies in the 21st century.

References

- [1] Wulff, G. *Angew. Chem. Int. Ed. Engl.*, **1995**, *34*, 1812–1832.
- [2] Haupt, K.; Mosbach, K. *Chem. Rev.*, **2000**, *100*, 2495–2504.
- [3] Chapman, R.G.; Sherman, J.C. *Tetrahedron*, **1997**, *53*, 15911–15945.
- [4] Winter, G.; Milstein, C. *Nature*, **1991**, *349*, 293–299.
- [5] Friggeri, A.; Kobayashi, H.; Shinkai, S.; Reinhoudt, D.N. *Angew. Chem. Int. Ed.*, **2001**, *40*, 4729–4731; and references therein.
- [6] Van Bommel, K.J.C.; Friggeri, A.; Shinkai, S. *Angew. Chem. Int. Ed.*, **2003**, *42*, 980–999.
- [7] Kim, S.S.; Zhang, W.; Pinnavaia, T.J. *Science*, **1998**, *282*, 1302–1305.
- [8] Hubert, D.H.W.; Jung, M.; Frederik, P.M.; Bomans, P.H.H.; Meuldijk, J.; German, A.L. *Adv. Mater.*, **2000**, *12*, 1286–1290.
- [9] Nakamura, H.; Matsui, Y. *J. Am. Chem. Soc.*, **1995**, *117*, 2651–2652.

- [10] Miyaji, F.; Davis, S.A.; Charmant, J.P.H.; Mann, S. *Chem. Mater.*, **1999**, *11*, 3021–3024.
- [11] Caruso, F. *Chem. Eur. J.*, **2000**, *6*, 413–419.
- [12] Shenton, W.; Douglas, T.; Young, M.; Stubbs, G.; Mann, S. *Adv. Mater.*, **1999**, *11*, 253–256.
- [13] Kawahashi, N.; Matijević, E. *J. Colloid Interface Sci.*, **1991**, *143*, 103–110.
- [14] Gallis, K.W.; Landry, C.C. *Adv. Mater.*, **2001**, *13*, 23–26.
- [15] Lu, Y.; Yin, Y.; Xia, Y. *Adv. Mater.*, **2001**, *13*, 271–274.
- [16] For recent reviews see: a) Raman, N.K.; Anderson, M.T.; Brinker, C.J. *Chem. Mater.*, **1996**, *8*, 1682–1701; b) Mann, S.; Burkett, S.L.; Davis, S.A.; Fowler, C.E.; Mendelson, N.H.; Sims, S.D.; Walsh, D.; Whilton, N.T. *Chem. Mater.*, **1997**, *9*, 2300–2310; c) Estroff, L.A.; Hamilton, A.D. *Chem. Mater.*, **2001**, *13*, 3227–3235; d) Davis, S.A.; Breulmann, M.; Rhodes, K.H.; Zhang, B.; Mann, S. *Chem. Mater.*, **2001**, *13*, 3218–3226; e) Caruso, R.A.; Antonietti, M. *Chem. Mater.*, **2001**, *13*, 3272–3282.
- [17] Brinker, C.J.; Scherer, G.W. *Sol-Gel Science*, San Diego: Academic Press, **1990**.
- [18] Murata, K.; Aoki, M.; Suzuki, T.; Harada, T.; Kawabata, H.; Komori, T.; Ohseto, F.; Ueda, K.; Shinkai, S. *J. Am. Chem. Soc.*, **1994**, *116*, 6664–6676.
- [19] Murata, K. *Ph.D. Thesis*, Graduate School of engineering, Kyushu University, **1997**.
- [20] Stein, A.; Melde, B.J.; Schroden, R. *Adv. Mater.*, **2000**, *17*, 1403–1419, and references therein.
- [21] Ono, Y.; Nakashima, K.; Sano, M.; Kanekiyo, Y.; Inoue, K.; Hojo, J.; Shinkai, S. *Chem. Commun.*, **1998**, 1477–1478.
- [22] Reference 17, Chapter 6.
- [23] Ono, Y.; Nakashima, K.; Sano, M.; Hojo, J.; Shinkai, S. *Chem. Lett.*, **1999**, 1119–1120.
- [24] Ono, Y.; Nakashima, K.; Sano, M.; Hojo, J.; Shinkai, S. *J. Mater. Chem.*, **2001**, *11*, 2412–2419.
- [25] Jung, J.H.; Ono, Y.; Hanabusa, K.; Shinkai, S. *J. Am. Chem. Soc.*, **2000**, *122*, 5008–5009.
- [26] Jung, J.H.; Ono, Y.; Shinkai, S. *Chem. Eur. J.*, **2000**, *6*, 4552–4557.
- [27] For comparison reasons, the *R*-values have been adapted from ref 25 to represent molar ratios rather than weight ratios.
- [28] Kobayashi, S.; Hanabusa, K.; Hamasaki, N.; Kimura, M.; Shirai, H.; Shinkai, S. *Chem. Mater.*, **2000**, *12*, 1523–1525.
- [29] Kobayashi, S.; Hamasaki, N.; Suzuki, M.; Kimura, M.; Shirai, H.; Hanabusa, K. *J. Am. Chem. Soc.*, **2002**, *124*, 6550–6551.
- [30] Ono, Y.; Kanekiyo, Y.; Inoue, K.; Hojo, J.; Shinkai, S. *Chem. Lett.*, **1999**, 23–24.
- [31] Jung, J.H.; Ono, Y.; Shinkai, S. *J. Chem. Soc., Perkin Trans. 2*, **1999**, 1289–1291.
- [32] Jung, J.H.; Ono, Y.; Shinkai, S. *Angew. Chem. Int. Ed.*, **2000**, *39*, 1862–1865.
- [33] Jung, J.H.; Ono, Y.; Shinkai, S. *Langmuir*, **2000**, *16*, 1643–1649.
- [34] Jung, J.H.; Ono, Y.; Sakurai, K.; Sano, M.; Shinkai, S. *J. Am. Chem. Soc.*, **2000**, *122*, 8648–8653.
- [35] Sakamoto, H.; Kimura, K.; Matsuo, M.; Shono, T. *J. Org. Chem.*, **1986**, *51*, 4974–4979.
- [36] Shukla, J.P.; Jeon, E.G.; Knudsen, B.E.; Puglia, M.J.; Bradshaw, J.S.; Bartsch, R.A. *Thermochim. Acta*, **1988**, *130*, 103–113.
- [37] Spiess, B.; Arnaud-Neu, F.; Schwing-Weill, M.J. *Helv. Chim. Acta*, **1979**, *62*, 1531–1542.
- [38] Jung, J.H.; Nakashima, K.; Shinkai, S. *Nano Lett.*, **2001**, *1*, 145–148.
- [39] Kim, S.S.; Zhang, W.; Pinnavaia, T.J. *Science*, **1998**, *282*, 1302–1305.

- [40] Jung, J.H.; Ono, Y.; Shinkai, S. *Chem. Lett.*, **2000**, 636–637.
- [41] Jung, J.H.; Shinkai, S. *J. Chem. Soc., Perkin Trans. 2*, **2000**, 2393–2398.
- [42] Jung, J.H.; Kobayashi, H.; Masuda, M.; Shimizu, T.; Shinkai, S. *J. Am. Chem. Soc.*, **2001**, *123*, 8785–8789.
- [43] Jung, J.H.; Kobayashi, H.; van Bommel, K.J.C.; Shinkai, S.; Shimizu, T. *Chem. Mater.*, **2002**, *14*, 1445–1447.
- [44] Jung, J.H.; Amaike, M.; Shinkai, S. *Chem. Commun.*, **2000**, 2343–2344.
- [45] Jung, J.H.; Amaike, M.; Nakashima, K.; Shinkai, S. *J. Chem. Soc., Perkin Trans. 2*, **2001**, 1938–1943.
- [46] Jung, J.H.; Amaike, M.; Shinkai, S. *Trans. Mater. Res. Soc. Jap.*, **2001**, *26*, 527–530.
- [47] Gronwald, O.; Shinkai, S. *Chem. Eur. J.*, **2001**, *7*, 4329–4334.
- [48] Gronwald, O.; Shinkai, S. *J. Chem. Soc., Perkin Trans. 2*, **2001**, 1933–1937.
- [49] The pK_a for benzylamine is 9.34, whereas the pK_a of the gelators should be similar to that of *p*-anisidine, 5.3. *Handbook of Chemistry and Physics*, 49th edition, R.C. Weast, Ed., Cleveland, Ohio: The Chemical Rubber Co., pp. 1968–1969.
- [50] Jung, J.H.; Shinkai, S.; Shimizu, T. *Nano Lett.*, **2002**, *2*, 17–20.
- [51] Jung, J.H.; John, G.; Masuda, M.; Yoshida, K.; Shinkai, S.; Shimizu, T. *Langmuir*, **2001**, *17*, 7229–7232.
- [52] Jung, J.H.; Yoshida, K.; Shimizu, T. *Langmuir*, **2002**, *18*, 8724–8727. Similar double helical silica fibrils have been created by sol-gel transcription of chiral aggregates of gemini surfactants: Sugiyasu, K.; Tamaru, S.; Takeuchi, M.; Berthier, D.; Huc, I.; Oda, R.; Shinkai, S. *Chem. Commun.*, **2002**, 1212–1213.
- [53] Friggeri, A.; Gronwald, O.; van Bommel, K.J.C.; Shinkai, S.; Reinhoudt, D.N. *Chem. Commun.*, **2001**, 2434–2435.
- [54] Van Bommel, K.J.C.; Shinkai, S. *Langmuir*, **2002**, *18*, 4544–4548.
- [55] Moreau, J.J.E.; Vellutini, L.; Man, M.W.C.; Bied, C. *J. Am. Chem. Soc.*, **2001**, *123*, 1509–1510.
- [56] Moreau, J.J.E.; Vellutini, L.; Man, M.W.C.; Bied, C. *Chem. Eur. J.*, **2003**, *9*, 1594–1599.
- [57] Moreau, J.J.E.; Vellutini, L.; Man, M.W.C.; Bied, C.; Bantignies, J.L.; Dieudonne, P.; Sauvajol, J.L. *J. Am. Chem. Soc.*, **2001**, *123*, 7957–7958.
- [58] Hartgerink, J.D.; Beniash, E.; Stupp, S.I. *Science*, **2001**, *294*, 1684–1688.
- [59] Zubarev, E.R.; Pralle, M.U.; Sone, E.D.; Stupp, S.I. *J. Am. Chem. Soc.*, **2001**, *123*, 4105–4106.
- [60] Sone, E.D.; Zubarev, E.R.; Stupp, S.I. *Angew. Chem. Int. Ed.*, **2002**, *41*, 1705–1709.
- [61] Shieh, H.-S.; Hoard, L.G.; Nordman, C.E. *Acta Cryst. B*, **1981**, *37*, 1538–1543.
- [62] Sakurai, K.; Ono, Y.; Jung, J.H.; Okamoto, S.; Sakurai, S.; Shinkai, S. *J. Chem. Soc., Perkin Trans. 2*, **2001**, 108–112.
- [63] Gronwald, O.; Shinkai, S. *Chem. Eur. J.*, **2001**, *7*, 4328–4334; and references therein.
- [64] Hanabusa, K.; Yamada, M.; Kimura, M.; Shirai, H. *Angew. Chem. Int. Ed. Engl.*, **1996**, *35*, 1949–1951.
- [65] a) Yoza, K.; Ono, Y.; Yoshihara, K.; Akao, T.; Shinmori, H.; Takeuchi, M.; Shinkai, S.; Reinhoudt, D.N. *Chem. Commun.*, **1998**, 907–908; b) Amanokura, N.; Yoza, K.; Shinmori, H.; Shinkai, S.; Reinhoudt, D.N. *J. Chem. Soc., Perkin Trans. 2*, **1998**, 2585–2591; c) Yoza, K.; Amanokura, N.; Ono, Y.; Akao, T.; Shinmori, H.; Takeuchi, M.; Shinkai, S.; Reinhoudt, D.N. *Chem. Eur. J.*, **1999**, *5*, 2722–2729; d) Amanokura, N.; Kanekiyo, Y.; Shinkai, S.; Reinhoudt, D.N. *J. Chem. Soc., Perkin Trans. 2*, **1999**, 1995–2000; e) Amaike, M.; Kobayashi, H.; Shinkai, S. *Chem. Lett.*, **2001**, 620–621; f) Kobayashi, H.; Friggeri, A.; Koumoto, K.; Amaike, M.; Shinkai, S.; Reinhoudt, D.N. *Org. Lett.*, **2002**, *4*, 1423–1426.

- [66] a) Tamaru, S.-i.; Takeuchi, M.; Sano, M.; Shinkai, S. *Angew. Chem. Int. Ed.*, **2002**, *41*, 853–856; b) Kawano, S.-i.; Tamaru, S.-i.; Fujita, N.; Shinkai, S. *Chem. Eur. J.*, **2004**, *10*, 343–351.
- [67] Zhan, C.; Wang, J.; Yuan, J.; Gong, H.; Liu, Y.; Liu, M. *Langmuir*, **2003**, *19*, 9440–9445.
- [68] Sato, I.; Kadowaki, K.; Urabe, H.; Jung, J.H.; Ono, Y.; Shinkai, S.; Soai, K. *Tet. Lett.*, **2003**, *44*, 721–724.

Chapter 26

RESPONSIVE MOLECULAR GELS

Jaap J.D. de Jong, Ben L. Feringa, and Jan van Esch

*Laboratory for Organic Chemistry, Stratingh Institute, University of Groningen,
Nijenborgh 4, 9747 AG Groningen, The Netherlands*

1. Introduction	895
1.1. Responsive Chemical Gels	896
1.2. Responsive Physical Gels	897
1.3. Triggering Signals and Expected Responses	897
1.4. Boundaries and Limitations	899
2. Chemo-Responsive Gels	899
2.1. Chemo-Responsive Gels by Host-Guest Complexation	900
2.2. Metal-Ion Responsive Gels	905
2.3. Responsive Gel Systems by Uptake and Release of Gasses	907
2.4. Gel-Sol Phase Transitions Triggered by pH Changes	908
3. Physico-Responsive Gels	914
3.1. An Unusual Temperature Responsive LMOG Gel	914
3.2. Responses to Mechanical Stress	915
3.3. Light-Responsive Gels	917
4. Conclusions and Perspectives for the Future	924

1. Introduction

Responsive materials are characterized by a change in their properties in response to a specific physical or chemical stimulus. Semiconductors, magnetic coatings, and liquid crystals are among the most prominent examples of such materials. Gels represent a completely different class of soft condensed

materials and are ideally suited to be responsive materials because they combine the elastic behavior of solids with the micro-viscous properties of fluids [1].

The archetype responsive gel is the cytoskeleton, which consists of a highly dynamic network of microtubules and actin filaments embedded in a liquid phase. The continuous assembly and disassembly of the microtubules and actin filaments is governed not only by thermodynamics, but is under active kinetic control via mechanisms involving nucleation and enzymatic covalent modification. As a result of these dynamic processes, the function of the cytoskeleton involves much more than just giving a cell its shape and mechanical stability. The kinetic regulation leads to a number of interesting and unusual phenomena, such as polar growth and self-organization. They are essential to many complex functions such as intracellular transport and organization, endo- and exocytosis, cell movement, and cell division.

The cytoskeleton is, without doubt, one of the most sophisticated gel types that is currently around us, and if mankind were able to incorporate even a few of the aspects of its functionality into artificial systems, it would lead to major progress in areas such as drug delivery, separation and catalysis, microfluidics, and actuator and sensor technology.

1.1. Responsive Chemical Gels

The most widely used gels are the chemical (or polymer) in which a three-dimensional network is maintained by cross-linked covalent bonds. The covalent cross-links make these gels robust and tolerant to physical deformation (Figure 1A). Chemical gels have been developed that can react to a physical

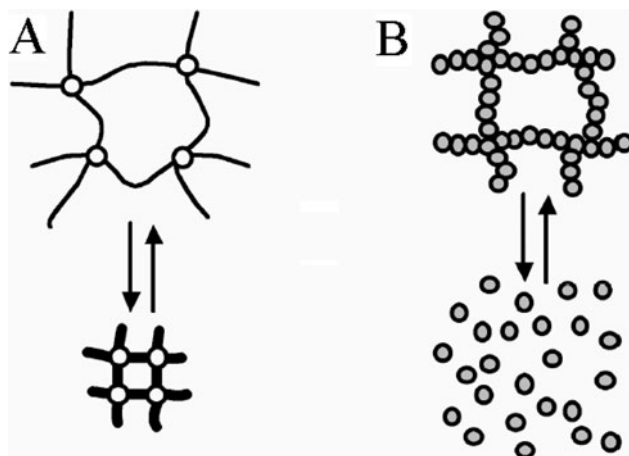


Figure 1. Schematic representation of a chemical gel (A) and a physical gel (B). The chemical gel alters its volume upon temperature changes, whereas the physical gel dissolves and reassembles.

or chemical stimulus by changing their size or shape, their optical, dielectric, or viscoelastic characteristics, and even their chemical properties, such as the affinity for guest molecules, leading to applications in valves, motors, muscles, smart drug release systems, etc. [2]. The responsive behavior of chemical gels depends on their viscoelastic properties as well as on the sensitivity of the interaction potential between the network filaments and/or filament-liquid interactions towards changes of the physical or chemical environment. Responsive chemical gels of this sort are discussed in detail in the references provided.

1.2. Responsive Physical Gels

In contrast to the chemical gels, the network structures of physical gels are built from smaller subunits, which are held together by noncovalent interactions. Many gels formed by polymers, proteins, surfactants, and even mineral clays belong to this class. Despite the differing nature of their constituents, they all exhibit a characteristic thermally reversible gel-sol phase transition at moderate temperatures, because the strengths of the noncovalent interactions responsible for holding the subunits together are comparable to the near ambient thermal energy (Figure 1B). Responsiveness is thus an intrinsic property of physical gels.

A distinct class of physical gels is formed by certain low molecular mass organic compounds (low molecular-mass organic gelators or LMOGs), some of which have the capability to gelate liquids at concentrations well below 1 mass% [3]. Despite the structural diversity among LMOGs, they have the common property that, in solution, they self-assemble into fibers very efficiently. These fibers, in turn, form entangled networks (SAFINs) and, thereby, convert the liquid (sol) into a gel. Most research efforts in recent years have concentrated on structural aspects of organogelation and have led to the successful design of novel gelating agents that form different architectures such as sheets, fibers, cylinders, or tapes, and, hence, to organogelators that are tailor-made for specific liquids, and to functional organic gelators. The viscoelastic and dynamic properties of organogels, on the other hand, have received less attention. This is remarkable because it is precisely these properties that make gels distinct from other materials and that form the basis for most applications. The reversible nature and sensitivity of their properties to minor structural changes of the gelating agents make LMOG gels excellent candidates for novel responsive systems.

1.3. Triggering Signals and Expected Responses

Physical gels, and particularly LMOG gels, have the advantage over cross-linked polymer gels that they can respond to stimuli or trigger signals at different

hierarchical levels (i.e., by a change of the fiber properties, by the formation or breaking of junction zones, by the extent of self-assembly, or changes at the molecular level such as structure and geometry). The type of response depends on the applied stimulus and the mode of interaction between the stimulus and the gel network.

A few common stimuli are intrinsic to all physical gels. First is the temperature dependent association of the components into a fibrous network. For LMOG gels, association is usually enthalpy driven, and hence, an increase in temperature shifts the association equilibrium to the non-aggregated state, causing dissolution of the fibers. At the temperature, T_g , at which the fraction of fibers drops below a critical value (given by the number density and aspect ratio), the fibrous network loses its integrity and a gel-sol phase transition is observed [4]. The second common stimulus is the application of mechanical stress, which will deform or destroy the gels depending on their viscoelastic properties and the magnitude of the applied stress.

The direct relation between the association equilibrium of the gelator molecules and the gel-sol phase transition renders LMOG gels also sensitive to additives, so-called chemical triggers which influence the association equilibrium via non-specific or specific intermolecular interactions with the gelator molecules in solution or in the aggregated state. An almost trivial example of a rather unspecific chemical trigger is a change of the liquid, which can have dramatic effects on T_g . In recent years, however, some examples of gel systems have been reported whose T_g change upon addition of acid or base, metal ions, or reactive gasses, either via specific non-covalent intermolecular interactions or via a reversible chemical reaction between the additive and the LMOG compound.

Temperature changes and mechanical stress are examples of physical stimuli that are commonly used to probe the properties of the gels. In some cases, unusual responses have been observed, such as a reversible shrinking and swelling of an LMOG gel induced by a temperature change, and the reversible transition of a gel to a viscous fluid and vice-versa upon application and relief of mechanical stress, respectively. In principle, it should be possible to employ magnetic or electric fields as triggers as well, provided that the gels display an interaction with these fields, for instance, when paramagnetic species or dipolar components are present. However, examples of such systems have not yet been reported for LMOG gels (at least after their formation). On the other hand, photo-responsive gel systems from LMOGs are known (see Chapter 24). They represent a special case of physically responsive LMOG gels because here a physical stimulus (photons) invokes a photo-chemical reaction which transforms the LMOG compound to a different species with its own characteristic gelation properties.

The external influences described above can trigger a range of responses that seems, almost, unlimited. Unfortunately, the field has not progressed to the

stage where all of these possibilities have been explored, and many challenges remain. The most common response is a transition from solution (sol) to gel (or vice versa), either by dissolution or disruption of the junction zones and/or fibers. Less frequently observed responses of LMOG gels include swelling and shrinking by extension or contraction of the network, or changes in other chemical or physical properties, such as conductivity or color.

1.4. Boundaries and Limitations

This chapter provides an overview of responsive gel systems formed by LMOGs. The range of gels and gelation phenomena is so large that some boundaries are required. First, only responsive gels will be discussed; the gel system should be able to react to external stimuli by a change of at least one physical/chemical property. Second, chemical gels and also physical gels formed by substances other than low molecular-mass organic molecules, although having very interesting properties, will be excluded because there is an overwhelming amount of literature on these topics. Third, only gelators with molecular-masses less than about 1 kDa will be discussed, and the liquid components will be limited to water or an organic liquid. See Chapter 22 for a discussion of gels with liquids that form liquid-crystalline phases.

The topics of this chapter are organized according to the types of “trigger” employed, but intrinsic triggers such as solubility, concentration and temperature effects have not been included explicitly. All gels respond to these factors and, therefore, are “responsive”; we reserve this designation for gels that respond to other stimuli. Two distinct types of LMOG gel systems will be described: those that respond upon the addition of chemical triggers and those that respond to physical perturbations.

2. Chemo-Responsive Gels

In the past decade, several LMOG gel systems have been reported that respond to chemical triggers, either via specific non-covalent intermolecular interactions or via a reversible chemical reaction between the additive and the LMOG compound. Most interestingly, the interaction between the trigger molecule and the gel can take place at different hierarchical levels, leading to different responses, as will be illustrated in the following sections.

Although, the structural characteristics of the LMOGs involved are very different, the responsive gel systems known so far can be conveniently divided in four distinct groups according to the nature of the chemical trigger (i.e., organic host-guest complex formation, metal ion coordination, gas absorption, and pH dependent equilibria). In the following sections we will discuss each

of these groups and will address the major factors that characterize the responsiveness of the gel systems (i.e., the trigger and its interaction with the gel, as well as the nature, kinetics, and reversibility of the response).

2.1. Chemo-Responsive Gels by Host-Guest Complexation

Host-guest complex formation represents a very interesting type of trigger because it relies on complementary intermolecular interactions. Consequently, in some cases, it can lead to selective response of a gel property to a specific trigger species.

Hydrogen bonding groups are particularly useful in the design of selective host-guest interactions because of their strength and directionality. One such two-component gelator system is based on 5,5-dialkylbarbituric acid **1** and 5-alkyl-2,4,6-triaminopyrimidine **2** (Figure 2) [5]. It forms gels with organic liquids when mixed in a precise 1:1 molar ratio. However, when one of the components is in excess, gelation is not observed. This phenomenon has not been investigated in detail, although the clear dependency on the stoichiometry, together with FT-IR, X-ray diffraction and electron microscopy data, strongly suggest that **1** and **2** self-assemble into linear tapes through complementary hydrogen bonding interactions.

Shinkai and co-workers have studied gel formation induced by specific recognition due to hydrogen-bond formation in an elegant system based on Hamilton's receptors **3** and **4** (Figure 3) [6, 7]. If host **3** or **4** binds a guest by complementary hydrogen bonding interactions, a planar host-guest complex is formed and it is likely to form columnar stacks similar to those made by flat

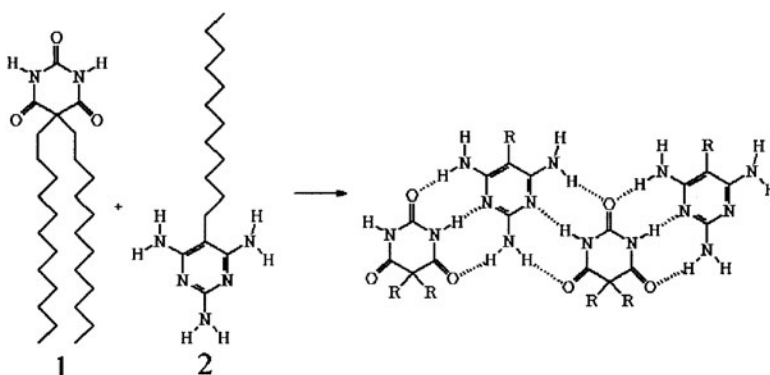


Figure 2. Barbituric acid (**1**) and triaminopyrimidine derivatives (**2**) self-assemble through complimentary hydrogen bonds into linear tapes (taken from [5], reproduced by permission of The Royal Society of Chemistry).

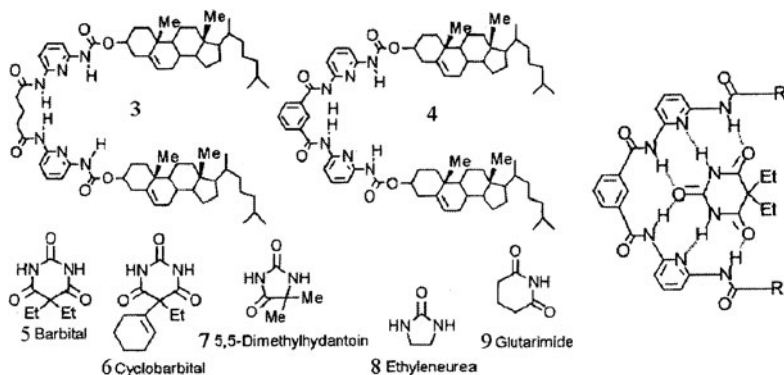


Figure 3. The gelation ability of **3** and **4** for organic liquids is drastically improved by binding of barbituric acid derivatives **5–9** via complementary hydrogen bonding, as is shown on the right. (Reprinted with permission from [7]. Copyright (1999) American Chemical Society.)

aromatic molecules. Compounds **3** and **4** gelate various organic liquids, but in the presence of guests **5–9**, the range of liquids gelated and, most importantly, the thermal stability of the gels increases. In this gel systems, optimal gelation, as indicated by the maximum T_g values, was found for 1:1 molar ratios of host and guest. Similar stabilizing effects have been observed for gels formed by nucleoside derivatives due to complementary hydrogen bonding with added polynucleotides [8, 9].

Donor-acceptor interactions have been used frequently to stabilize host-guest complexes. Aromatic donor-substituted bile acid derivatives **10–12**, by themselves, do not gelate organic liquids, but addition of an electron acceptor, such as trinitrofluorenone **13**, leads to a remarkable induction of gelation behavior for a wide range of organic liquids (Figure 4, top) [10]. Due to a charge-transfer band, the gels become colored, and hence UV/VIS spectroscopy may be used to correlate the gel formation and the charge-transfer complexation. In this case, the gels have maximal strength at a 1:1 molar ratio of gelator components, indicative of specific host-guest interactions. The absence of any gelation capability for **14** and **15**, even in the presence of an acceptor, demonstrated that the gelation ability of host-guest complexes is very sensitive to molecular structure and conformation also, as is well known for ordinary LMOGs. Charge-transfer interactions have also been used to reinforce gels formed by dual-component, sugar-based gelators (see Chapter 15) [11].

The tendency of bile acids to associate in aqueous solutions has been exploited in the tripodal bile acid derivatives **16** and **17**. They are excellent gelators in water, whereas model compound **18** does not show any gelation (Figure 4) [12]. Under acidic conditions, the central nitrogen atom is protonated, leading to the formation of slightly turbid and weak gels in dilute aqueous HCl solutions. In the presence of small amounts of organic co-liquids, such

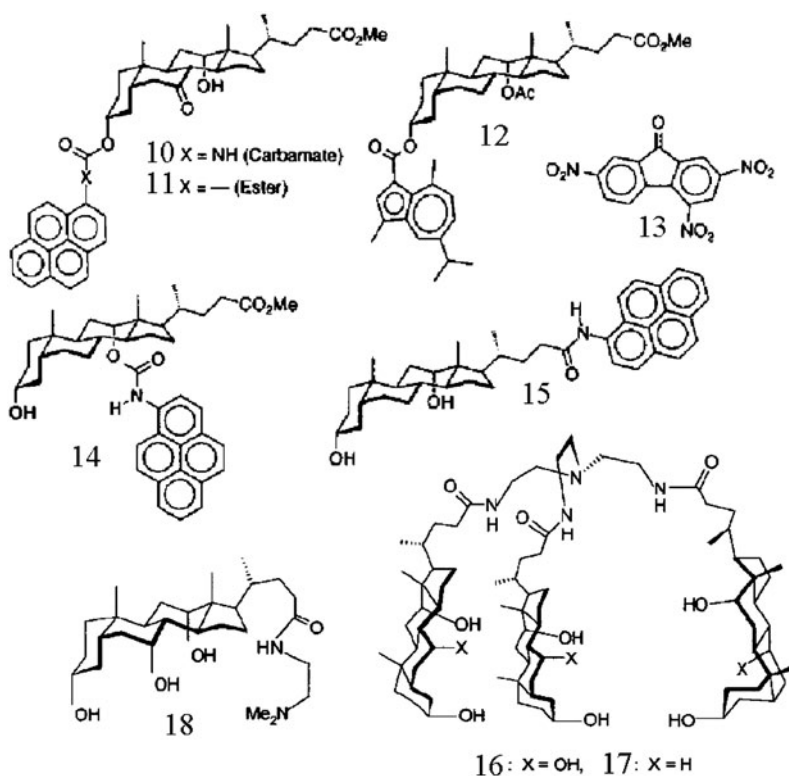


Figure 4. Typical examples of gelators derived from bile-acids. Compounds **10–12** are able to gelate organic liquids after binding of guest **13** via donor-acceptor interactions, but compounds **14** and **15** remain soluble. Compounds **16** and **17** are potent LMOGs for aqueous liquids themselves, which can bind guest molecules in hydrophobic pockets within the gel fibers (top figure taken from [10], reproduced by permission of The Royal Society of Chemistry, bottom figure taken from [12], with permission from Wiley-VCH.)

as acetone and DMSO, hard, transparent gels are formed, probably due to an improved balance between the hydrophobic/hydrophilic environments. Hydrogels formed by **16** and **17** are able to accommodate guest molecules, such as 8-anilino-1-naphthalene-1-sulfonic acid (ANS), in the fibers. The clear shift of the emission maximum of ANS upon binding indicates that ANS is shielded from the aqueous environment and becomes incorporated in hydrophobic pockets in the fibers, presumably between the bile acid side groups. These hydrophobic binding sites are, however, not very selective as witnessed by the fact that other hydrophobic guest molecules, such as bromophenol blue (BPB), are bound.

The use of bile acids in the development of new LMOGs is clearly inspired by the many successful examples of gelator molecules that have exploited the

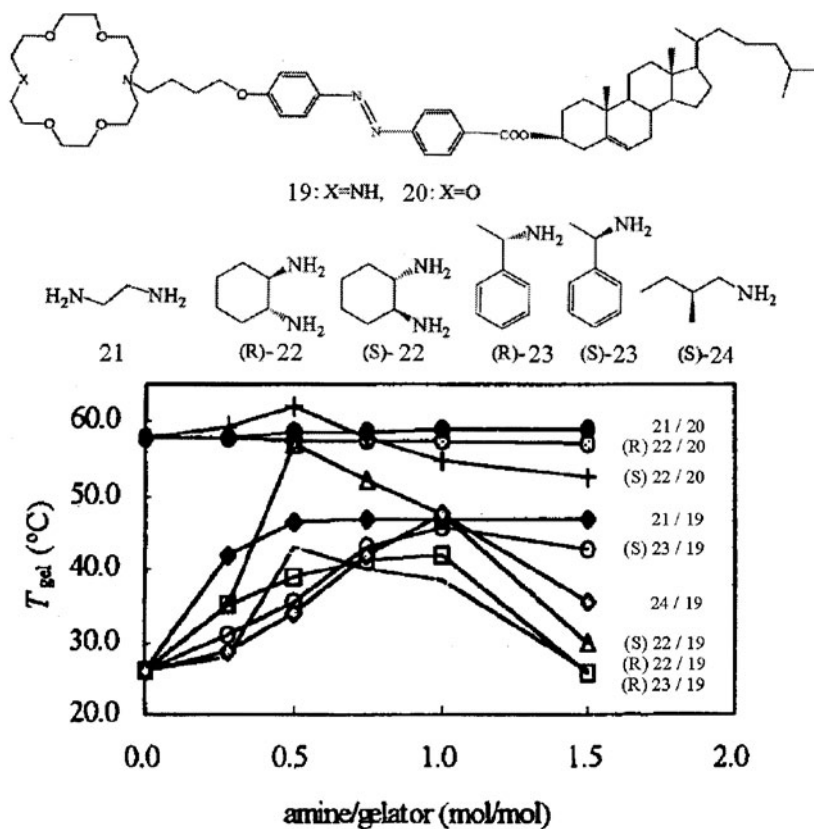


Figure 5. Gelators **19** and **20** are able to bind amines **21**–**24** via specific interactions with the crown-ether moieties, thereby increasing the thermal stability of the gels. (Reprinted from [13], with permission from Elsevier.)

anisotropic association properties of the steroidal skeleton in a self-assembly motif. Gels of aza-crown-appended cholesterol organic gelators **19** and **20** were indeed stabilized by binding of amines in the crown-ether moiety (as noted by an increase of T_g in the presence of amines (Figure 5) [13]. Again, a 1:1 stoichiometry of host and guest leads to the highest melting temperatures of the gels. The use of diamines leads to a further enhancement of the thermal stability of the gels, however with a maximum enhancement at 1:0.5 host/guest molar ratios. Most likely, the diamines are bridged between two gelator molecules, thereby reinforcing the fiber structure. Interestingly, binding of either the *R* or *S* enantiomers of chiral amines **22** and **23** to gels of chiral gelators **19** and **20** lead to significantly different enhancements of the thermal stability, indicating that in these gels, host-guest complexation is also diastereoselective.

Cholesterol units have been combined with porphyrins to give a new class of very potent gelators that includes the versatile functionality of the porphyrin moiety [14]. Compound **25** gels various aromatic liquids, leading to gels with gel-sol phase transitions at ambient temperature. However, the thermal stability of the gels gradually increases with increasing amounts of fullerene[60] up to a 0.5:1 fullerene[60]:**25** molar ratio, where a maximum enhancement of the thermal stability ($T_g = 49^\circ\text{C}$) is reached (Figure 6) [15]. This stabilizing effect has been attributed to the formation of 2:1 sandwich complexes between the zinc-porphyrins and fullerene[60], although the pronounced dependency of the stabilizing effect on the overall concentration of fullerene[60]:**25** shows that this interaction is quite weak.

Azobenzene and cholesterol derivatives can form excellent gelators of aqueous liquids through modification with pendant carbohydrate moieties, such as compounds **26** and **27** (Figure 7) [16, 17]. Gels formed by these compounds can react with poly(L-lysine)boronic acids **28**, due to ester formation between the boronic acid groups and the sugar hydroxyl groups. Because covalent

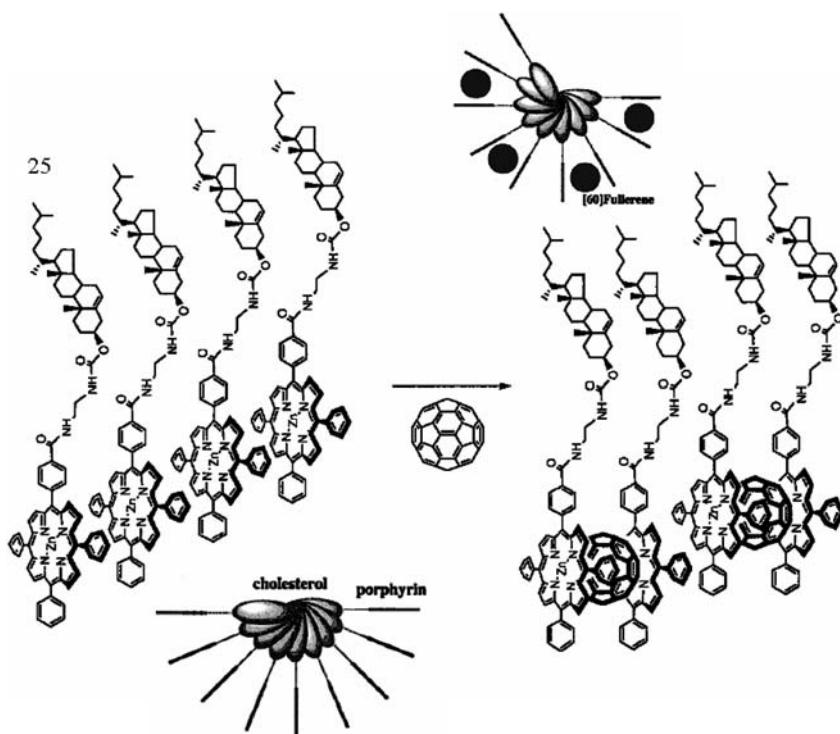


Figure 6. Porphyrin-based gels have been stabilized by binding of fullerene[60] between two porphyrin units in the gel fibers. (Reprinted with permission from [15]. Copyright (2001) American Chemical Society.)

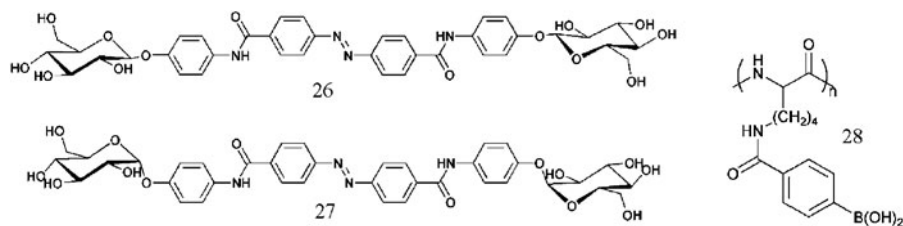


Figure 7. Carbohydrate-based compounds **26** and **27** can gelate water, but ester formation of boronic acid **28** causes a sol-gel transition (taken from [17], reproduced by permission of The Royal Society of Chemistry).

bonds between **27** and **28** are formed, it is formally not a host-guest complex. Nevertheless, the **27–28** conjugate shows a strong resemblance to host-guest complexes because of the selectivity of boronic acids for vicinal dihydroxy moieties and the dynamic character of these particular ester bonds. Contrary to expectations, ester formation between **27** and **28** does not lead to a reinforcement of the gels, but to a gradual decrease of the thermal stability until (above 1:3.0 gelator:boronic acid molar ratios) only solutions were obtained. Transmission electron microscopy reveals that the destabilizing effect of **28** on gels of **27** is due to a morphological transition from a fibrous network of **27** alone, to a vesicular solution formed by **27–28**. This morphological transition could be reversed by the addition of D-fructose (known for its high affinity for boronic acids) due to trans-esterification in which **27** is liberated.

2.2. Metal-Ion Responsive Gels

Metal-ion responsive gels are attractive candidates for responsive materials because of the prominent role of metal ions in many enzymes, catalysts, (molecular) electronic devices etc. The presence of a metal ion in a particular compound may have a large impact on its solubility, conductivity, and spectroscopic properties, for example. Such changes make it easier to examine and study gel behavior. An example of a metal-ion responsive gel is comprised of compound **29** and an organic liquid. The gelation is due to hydrogen bond formation between the amide moieties (Figure 8) [18]. Upon addition of an aqueous solution of $\text{FeCl}_2 \cdot 4\text{H}_2\text{O}$ on top of the gel, the bipyridine moieties form a water-soluble complex with the Fe(II) ions, resulting in transfer of **29** to the aqueous phase and concomitant loss of the gel integrity. Unfortunately, the reversibility of this process has not yet been demonstrated.

Carbohydrate based gelators **30** and **31**, having an amine or nitro group at the R position (Figure 8), can be reinforced by addition of salts such as AgNO_3 ,

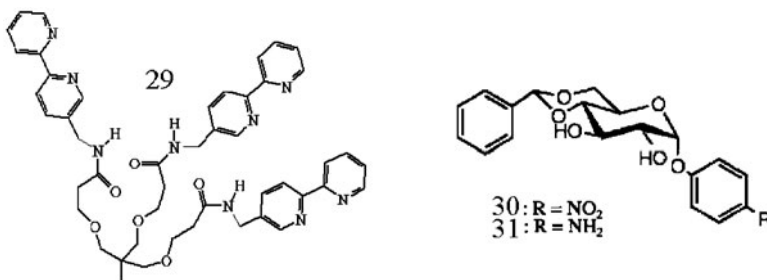


Figure 8. Tris-bipyridine tripodal ligand **29** is able to gelate toluene, but the gel structure is lost upon coordination of Fe(II) to the bipyridine moieties. On the other hand, gels formed by **30** and **31** could be reinforced by coordination of transition metal ions (left figure taken from [18], right figure taken from [19], both reproduced by permission of The Royal Society of Chemistry.)

FeCl₃, CoCl₂, CdCl₂ and CaCl₂ [19]. Compounds **30** and **31** are not able to gelate many liquids alone, nor are the gels very stable thermally. Addition of one equivalent of CoCl₂ and CdCl₂, however, results in an increase of T_g in ethanol from -10°C without metal ions to 71°C with them. Spectroscopic data reveal that the enhancement of thermal stability is due to the formation of coordination complexes between the metal ions and the amino or nitro groups. Thereby, molecules of **30** and **31**, respectively, are bridged, leading to straightening of the fibers.

As reported by Terech and Coutin, Cu(II) ions are an integral part of the long monomolecular fibers that are formed in gels through coordination bond formation with 2-ethylhexanoic acid [20]. The viscoelastic properties of the gels respond to the addition of excess carboxylic acid by a dramatic drop of the elastic modulus, most likely because the carboxylic acid acts as an “end-capping” species.

Metal ion complexation has been used to control the chirality of aggregates formed by **32**, which contain an isoquinoline moiety as a chelating head group (Figure 9) [21]. Compound **32** alone forms extended chiral aggregates at lower temperatures, as evidenced by CD spectral data. The addition of CuCl₂ leads to the formation of square planar coordination complexes with the isoquinoline moieties and concurrent distinct changes in the UV-vis absorption spectrum and an enhancement of the CD intensity. In contrast, addition of CoCl₂ or ZnCl₂ resulted in the formation of octahedral coordination complexes, which do not show discernible circular dichroism; the macro-chiral arrangement is destroyed. These interpretations are supported by TEM measurements that show fragmented globular aggregates for the Co(II) complexes, but tape-like aggregates for the Cu(II) complexes.

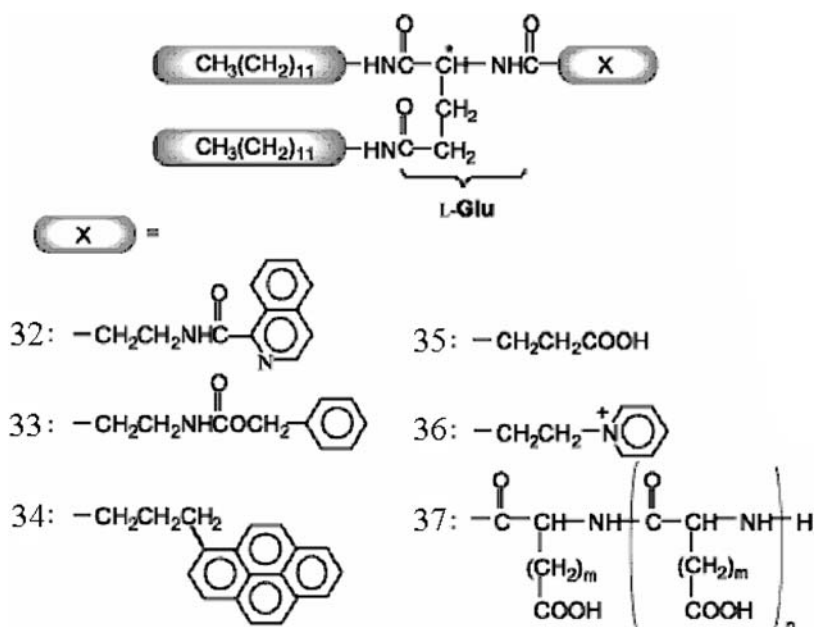


Figure 9. The chirality of aggregates formed by L-glutamic acid-derived lipids **32** could be tuned by coordination of transition metals to the isoquinoline head-group. (Reprinted with permission from [21]. Copyright (2002) American Chemical Society.)

2.3. Responsive Gel Systems by Uptake and Release of Gasses

The use of reactive gases to develop responsive gel systems is an attractive concept, because it allows the addition and withdrawal of reactants via the gas-phase, leaving all other components in the liquid or gel phase. As a result, gas responsive gels are attractive to sensor technology. Moreover, the uptake and release of gaseous substances can be repeated many times without significant dilution of the system. An interesting system of this type involves simple, commercially available primary and secondary amines such as **38ab–i**. These “latent” gelators can be converted almost instantaneously to ammonium carbamates **39ab–i** simply by bubbling CO_2 through a solution of the amine (Figure 10) [22, 23]. These ammonium carbamates are very potent gelators and gels were obtained within 30 seconds after the introduction of CO_2 . Formation of the ammonium carbamate gels is thermally reversible, and their thermal stability is much better than gels obtained from the corresponding amines due to ionic interactions between the carbamates and ammonium groups. Mild heating of the gels reverts the ammonium carbamates to the corresponding amines and CO_2 , thereby demonstrating that the CO_2 -induced gelation is chemically

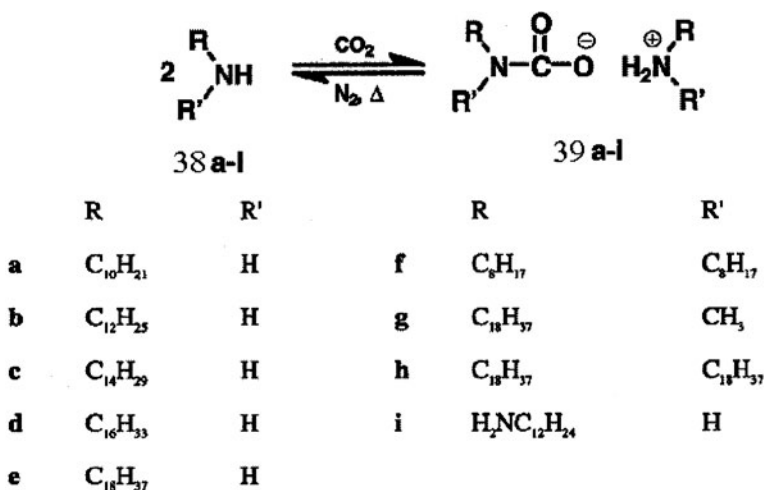


Figure 10. Many amines are “latent” gelators for organic liquids, which form hard gels after ammonium carbamate formation by uptake of CO_2 from the gas phase. (Reprinted with permission from [23]. Copyright (2002) American Chemical Society.)

reversible. Salt formation of amines was also achieved by their reaction with other triatomic gases, such as NO_2 , SO_2 , and CS_2 . Only with CS_2 was gelation generally observed. Moreover, subsequent heating of the NO_2 and SO_2 derived salts led to the formation of complex mixtures of reaction products, indicating that the initial uptake of gas by the amines is chemically irreversible [24]. However, very clean transformations of the CS_2 adducts, ammonium dithiocarbamates, to thioureas (with liberation of H_2S gas) was noted. Interestingly, several of the derived thioureas are also good gelators of organic liquids.

2.4. Gel-Sol Phase Transitions Triggered by pH Changes

The use of pH-sensitive groups to effect gel-to-sol transitions or to modify the surface potential of gel fibers has been addressed only marginally hitherto, despite the importance of electrostatic interactions in aqueous and non-aqueous environments, and their relevance for applications in drug delivery and biomedical systems and devices. An example of a pH-dependent gelating system is comprised of 2,3-di-*n*-alkoxyanthracene or its derivatives as the LMOGs [25]. It was found that van der Waals, dipole-dipole, and π -stacking interactions contribute to self-assembly of these compounds, but the only stimulus that affected gel formation was temperature. Therefore, the anthracene group was replaced by a phenazine moiety (**40**), and the influence of acid on the gelation behavior was investigated. Addition of trifluoroacetic acid to gels of **40** in acetonitrile

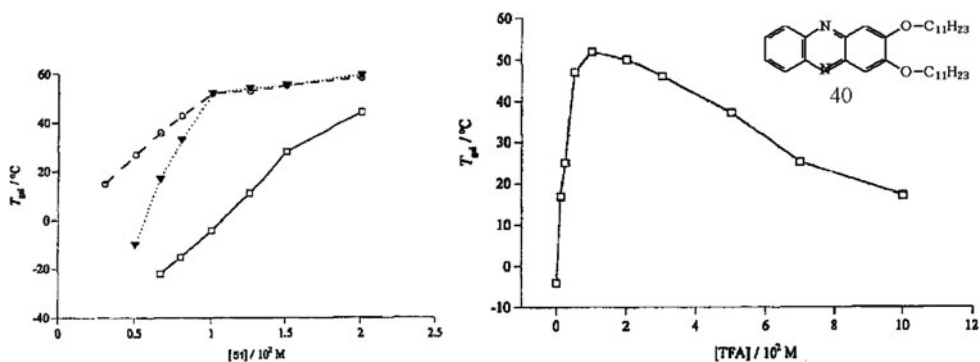


Figure 11. The thermal stability of gels of **40** increases, as usual, with increasing concentration (left), but is also affected markedly by protonation of the phenazine moieties (right) (taken from [25], reproduced by permission of The Royal Society of Chemistry).

led to mono-protonation and an increase of almost 60° C in the T_g (Figure 11). The process could be reversed by bubbling ammonia through the system.

As a result of the many elegant examples of protein aggregates found in nature, there is a lot of interest in exploiting the self-assembly properties of peptides to create novel nano-structures and soft materials. One of the first successful designs of peptide-based gelators exploited one-dimensional self-assembly of peptides to produce elongated β -sheet tapes, which in turn form an entangled network in organic or aqueous liquids (see Chapter 3) [26]. By introducing acidic or basic amino acids into the side chain at regular intervals, control of the self-assembly properties of these peptides via the pH of the liquid was achieved (Figure 12 top) [27]. In arginine and glutamic acid containing peptides, there is a positive charge at pH <5, leading to stable nematic solutions and gels. Upon increasing the pH to >5, the peptide becomes neutral and flocculation of the system is observed. Apparently, a net charge on the fibrils and the resultant electrostatic repulsion between them is necessary to avoid their aggregation. By varying the amino acids that are incorporated, gel systems could be obtained that are stable over a wider pH range, and reversible switching between solutions, gels and flocculated systems could be achieved by addition of small amounts of acid or base. Unfortunately, this reversible switching is limited to 4 cycles of added acid and base, due to the increasing ionic strength which inhibits the system.

pH-sensitive gelation of these peptides has been exploited in a 2-component gelating system consisting of 2 different peptides that are soluble in the pH range 7.2 and 7.4, but have net opposite charges due to the presence of either Glu ($-\text{CH}_2\text{CH}_2\text{COOH}$) or Orn ($-\text{CH}_2\text{CH}_2\text{CH}_2\text{NH}_2$) residues [28]. Upon mixing solutions of these peptides, aggregation and gelation of the aqueous solution occurs due to attractive intermolecular electrostatic interactions (Figure 12 bottom). Gel formation is accompanied by a transition of the random-coiled

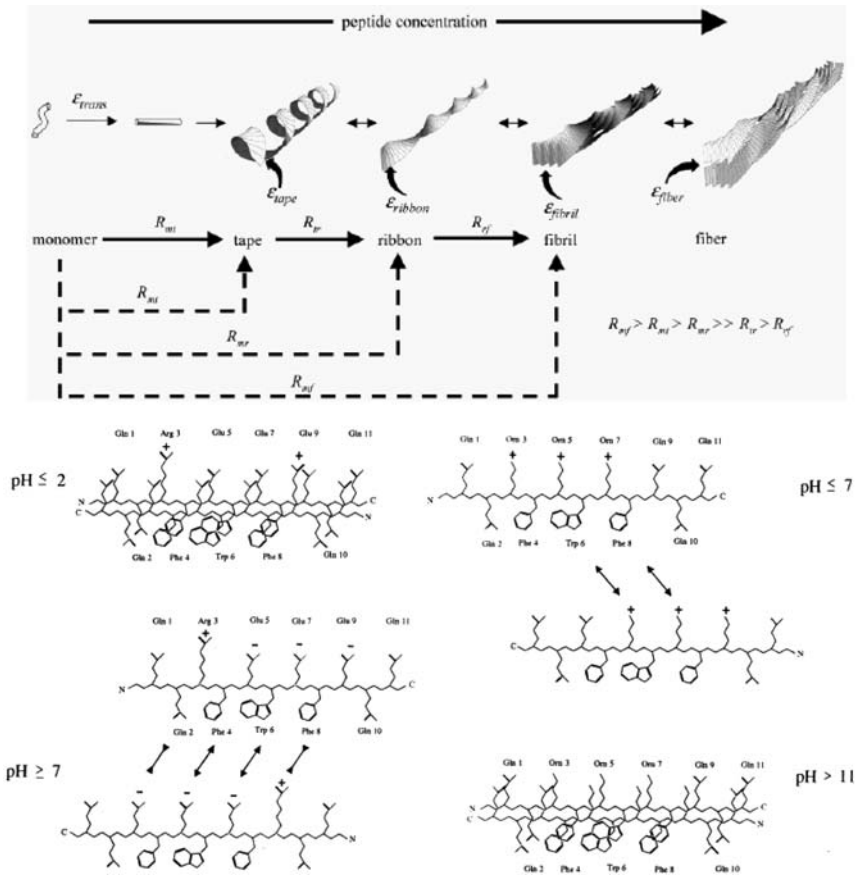


Figure 12. The self-assembly of peptides into fibers proceeds through a hierarchy of supramolecular structures, as shown at the top, and can be directed by tuning the charge on the peptides via the pH of the liquid (bottom). The ϵ_j corresponds to free energy differences whereas R_{ij} symbolizes conversion rates between the different structures. Solid arrows represent dissolution at constant pH and dashed arrows show direct conversions to various configurations from monomer. (Reprinted with permission from [27]. Copyright (2003) American Chemical Society.)

structure of the peptides in solution to an anti-parallel cross- β -sheet within the fibers that are formed after mixing. The β -sheet self-assembly motif has been used by other research groups in the design of peptide-based pH-responsive gelling systems [29].

Another attractive protein self-assembling motif is the leucine-zipper coiled-coil structure, which has been used in a system that showed remarkable sol-gel transitions with change in pH [30]. Although, this example is on the very edge of the definition of LMOG gels given at the beginning of this chapter, it is included because of the elegance of the supramolecular design. Using recombinant DNA techniques, it has been possible to synthesize artificial

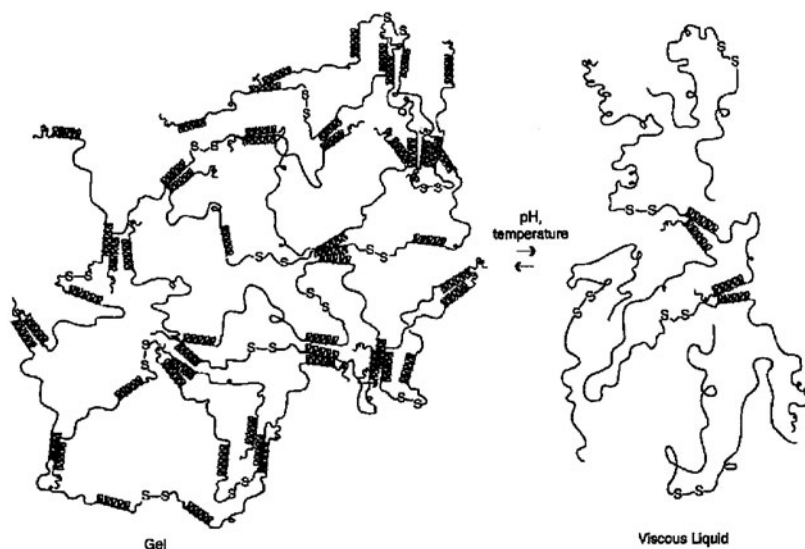


Figure 13. Artificial triblock proteins consisting of a polyelectrolyte segment flanked by two leucine zipper domains can form pH and temperature reversible hydrogels when the leucine zipper domains self-assemble. (Reprinted with permission from [30]. Copyright (1998) American Association for the Advancement of Science.)

tri-block proteins that consist of a central polyelectrolyte block, flanked at either end by leucine zipper domains with acidic residues (Figure 13 left). At $\text{pH} < 9.5$, the leucine zipper forms coil domains that lead to extensive physical cross-linking of the polymer solution, thereby causing gelation of the aqueous liquid. The system undergoes a reversible gel-sol transition by increasing the temperature or raising the pH to > 10 .

Peptide-amphiphiles **41** self-assemble into highly-ordered nanofibers that gelate aqueous phases (Figure 14) [31]. The peptide amphiphiles consist of five distinct parts, each having its own function. Region (A) is a long alkyl chain that gives hydrophobic character to the molecule, region (B) can be polymerized via the sulfur atoms, and region (C) is a flexible linker. The phosphorylated serine residue of region (D) can interact strongly with calcium ions and region (E) enables the system to adhere to cells. These peptide-amphiphiles form birefringent gels in water at concentrations above 2.5 mg/mL due to the formation of a network of elongated fibers with cylindrical cross-sections. Self-assembly of these peptide amphiphiles is pH dependent due to the presence of acidic groups. The fibers and gels are stable to $\text{pH} < 7$, but above pH 7, the peptide amphiphiles become multiply charged due to deprotonation of the acidic moieties and the fibers dissolve. The pH dependent gel-sol phase transition may be inhibited by cross-linking of the peptide amphiphiles through I_2 oxidation of the thiol groups. The crosslinks can be destroyed upon addition of a reducing

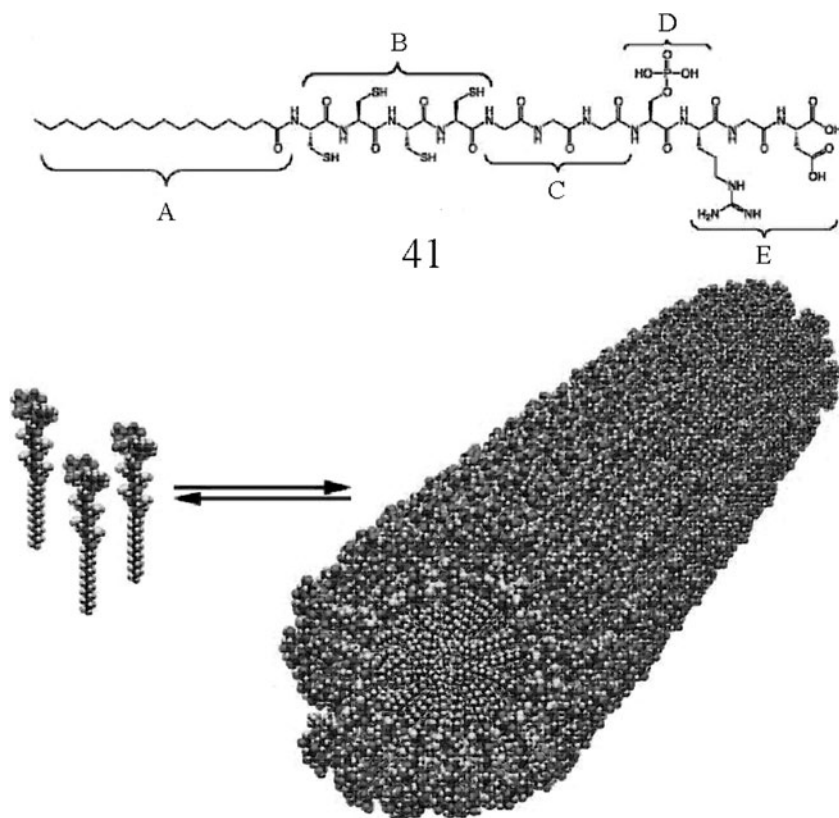


Figure 14. Peptide amphiphiles such as **41** self-assemble into mono-disperse elongated fibrils that form an entangled network in water. The formation of the fibers and stability of their gels can be controlled by pH and redox reactions. (Reprinted with permission from [31] and courtesy of S. I. Stupp, Northwestern University. Copyright (2001) American Association for the Advancement of Science.) [A color version of this figure may be found on page 948.]

agent. Gel-formation by these peptide-amphiphiles is, therefore, both a pH and a redox responsive process.

pH sensitive hydrogelation is not restricted to large peptide-based molecules such as those in the previous examples. For instance, resorcinarene based molecules **42** (Figure 15) can gelate water at certain pH values and concentrations [32]. Under neutral or basic conditions, the molecules dissolve readily, but when the pH drops below 2.5, a transparent gel is formed. Gel formation by **42** is also sensitive to the presence of certain metal ions. The addition of 2 equivalents of Fe²⁺ or Co²⁺ raises the critical gelation concentration (cgc) by a factor of 5, whereas the addition of Cu²⁺ inhibited gelation completely.

By making use of the unidirectional self-assembly properties of tri-amide cyclohexane **43**, it has been possible to accomplish the modular design of

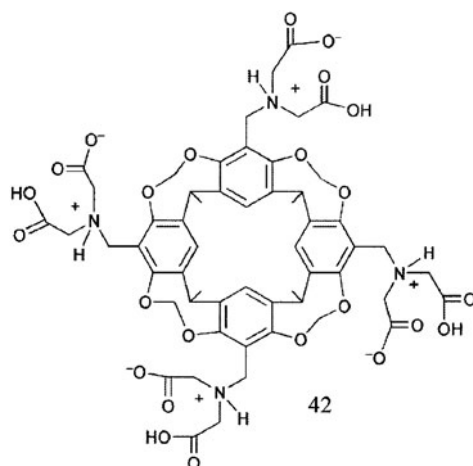


Figure 15. The gelation of water by resorcinarene **42** could be inhibited by complexation of transition metal ions (taken from [32], reproduced by permission of The Royal Society of Chemistry).

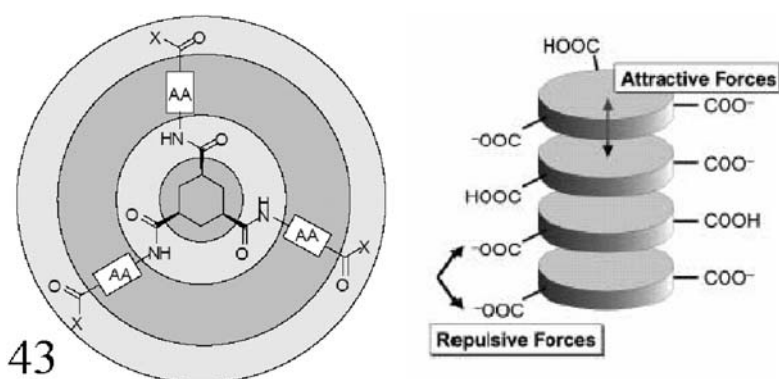


Figure 16. Cyclohexane tris(peptide) compounds self-assemble into elongated fibers due to cooperative effects of hydrogen bonding and hydrophobic interactions. pH-control of self-assembly and gelation appeared to be dependent on the pK_a of the ionizable groups, as well as the strength of the intermolecular interactions which stabilize the fibers. (Reproduced from [33], with permission from Wiley-VCH.)

some pH-responsive LMOGs of aqueous liquids (Figure 16) [33]. The triamide cyclohexane moiety was modified with hydrophobic amino acids to shield the amide groups from competitive interactions with water and, thereby, reinforce the anisotropic self-assembly of the gelator molecules in water by the concurrent action of hydrogen bonding and hydrophobic effects. The modular

architecture allows modification of the gelation properties by attaching different amino acids while preserving the unidirectional self-assembly motif. In this way, a complete set of gelating agents has been obtained that are either insensitive to pH (by attaching neutral substituents) or display a reversible gel-sol phase transition on going from low to high pH or from high to low pH (by attachment of acidic or neutral peripheral substituents, respectively). The pH of the gel-sol phase transition ($\text{pH}_{\text{gel-sol}}$) could be modified by attaching peripheral groups with different pK_a values that, in essence, modify the intermolecular interactions that hold the molecules together. For instance, replacement of the ester groups in **43** with amide groups leads to an increase of the $\text{pH}_{\text{gel-sol}}$ by 1.5 units, although the intrinsic pK_a 's of the carboxylic acids are comparable.

Most interestingly, the simultaneous self-assembly of these 1,3,5-trisamide-cyclohexane-based hydrogelators and various surfactants in water leads to self-assembled fibrillar networks (networks) with encapsulated micelles [34]. This prototypical system is an example of orthogonal self-assembly (i.e., the independent formation of two different supramolecular structures, each with its own characteristics that coexist within a single system).

3. Physico-Responsive Gels

Responsive gel systems that act upon application of a physical trigger are particularly attractive because they can be incorporated easily in many types of devices. For instance, cross-linked polymeric gels that swell, shrink or change their shape under the influence of an electric field have been used to construct microporous valves, actuators, and smart drug release systems [35]. Also LMOG gel systems can be addressed by physical stimuli. For instance, the alignment of steroid gelators in magnetic fields during gel-formation has been reported [36], and the first steps towards magnetic responsive LMOG gels have been made [37] (see Chapter 23). In most cases, only the usual temperature-induced gel-sol phase transition or disintegration of the gel structure, due to mechanical stress is observed. Very few examples have been reported in which LMOG gels respond differently to temperature changes or mechanical stress. We will conclude this section with some examples of photo-responsive gels, which have received much more attention and also show a broader range of responses.

3.1. An Unusual Temperature Responsive LMOG Gel

Most LMOG gels react to temperature changes by a gel-sol phase transition because of the non-covalent nature of the interactions that hold the network

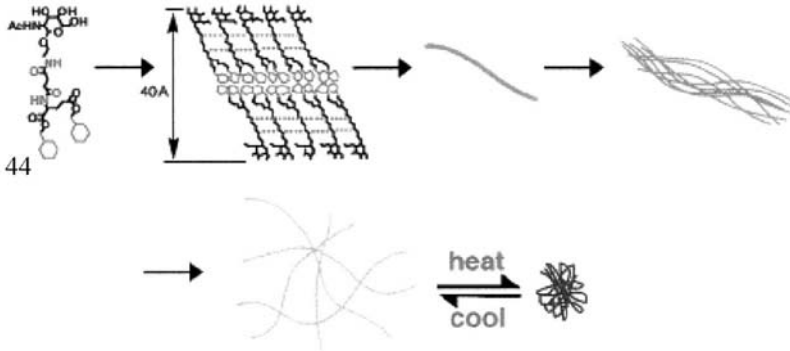


Figure 17. Glycosylated amino acid derivative **44** exhibits a temperature dependent volume-phase transition that is unique for LMOG gels discovered to date. (Reprinted with permission from [38]. Copyright (2002) American Chemical Society.)

together. Other responses, such as reversible volume phase transitions and shape changes, have been considered to be typical for gels composed of covalently cross-linked polymers. However, in 2002, a novel hydro-gelator based on glycosylated amino acid **44** was reported [38]. It shows dramatic shrinking and swelling behavior in response to temperature changes (Figure 17). This behavior is remarkable because the gel is very stable to heating and, instead of undergoing a gel-sol phase transition, the liquid component was expelled and the gel shrank to about 1% of its original volume at the phase transition temperature, 69° C. The process is fully reversible: upon cooling, the gel expanded by re-absorption of the liquid.

Electron microscopy did not reveal any unusual structural features, but from infrared spectroscopic investigations, the hydrogen bonds were shown to remain intact in the shrunken state formed upon heating. Apparently, the degree of aggregation does not change at the volume phase transition. It remains unclear why this gelator behaves so differently from the others prepared thus far. The volume phase transition of these gels has been exploited to control the selective release of substances from its interior. For instance, more than 90% of entrapped DNA was released from the gel at temperatures above the volume phase transition temperature, but hydrophobic substances remained entrapped within the gel.

3.2. Responses to Mechanical Stress

One of the most prominent features of gels is their viscoelastic properties. The solid character of organogels at low stress values, for instance, provides a convenient test for gelation because gels resist gravitational flow. These,

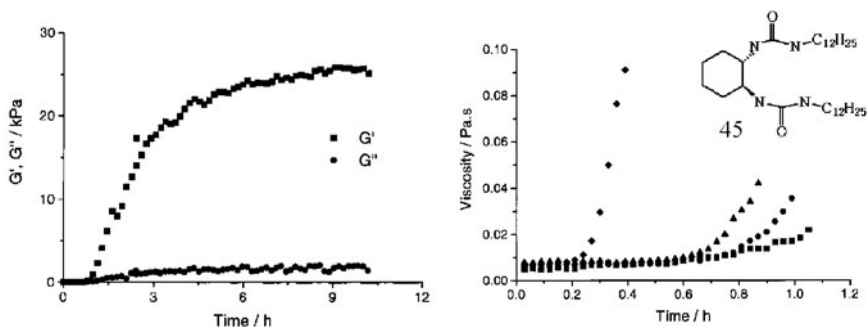


Figure 18. Mechanical agitation leads to irreversible destruction of most LMOG gels, but in the case of bisurea cyclohexane **43**, the gel state is spontaneously restored at room temperature (left, 19 mM of **43** in hexanol), a process which is even accelerated by the application of shear (right shear rates 5 (■), 15(●), 25(▲), and 100(◆) s^{-1}). (Reprinted with permission from [41]. Copyright (2000) American Chemical Society.)

and other viscoelastic properties of organogels are a direct consequence of the presence of a network structure. Pioneering work by Terech demonstrated that most organogels can be classified as “strong” gels, but there are also a few documented examples of “weak” gels [39].

An excellent example of such “weak” LMOG gels is based on copper carboxylate coordination complexes, which form extended monomolecular wires in organic solvents [40]. These weak gels are characterized by a notable frequency dependence of the viscoelastic properties: at short time scales the system behaves as an elastic solid, but at longer timescales it behaves as a viscous fluid. The reason for this behavior is found in the low scission energies of the wires (and hence short lifetimes), due to the fact that the molecular wires are only stabilized by a few coordination interactions between the Cu(II) ions and the carboxylate moieties. In such systems, the relaxation of stress is possible through a mechanism such as chain scission and recombination, and the viscoelastic properties are governed by the lifetimes of these relaxation processes.

Most organogels, on the other hand, consist of much thicker fibers with long lifetimes, and it is no surprise that they can be classified as “strong” gels (i.e., they behave as elastic solids up to a characteristic stress value (yield stress), with little dependence on the time scale of the experiment). If the applied stress (amplitude of the oscillation) exceeds the yield stress, the gel network breaks down to become a viscous fluid, in which, for most systems, the gel state can be restored only by a heating-cooling cycle through the gel-sol-gel phase transitions.

Some of these “strong” LMOG gel systems, however, are thixotropic (i.e., a spontaneous restoration of the gel state occurs if the stress is removed). For

instance, gels of the cyclohexane bisureas **45** in alcohols disintegrate above the yield stress to give a viscous fluid of sub-millimeter gel particles, but the gel state is restored after the stress is removed and the system is left at rest [41]. Even more remarkable is that during steady-shear viscosity measurements, it was found that viscosity increases faster if higher shear rates are applied. Presumably, the shear promotes the aggregation of the fibers into larger structures, but obviously the gel state is only restored when the system is no longer experiencing shear forces. Similar effects have been observed for some peptide gels [26] and with metalloporphyrin rods [42]. Pozzo and co-workers have reported a systematic method for a few different gel systems [43] which allows the fibers of the gel to be oriented by shear forces. These long-range fiber orientations offer interesting future prospects for molecular electronics or optically limiting materials.

3.3. Light-Responsive Gels

Absorption of photons is a very attractive means to change gel properties because it allows a photo-responsive group that has been incorporated in the gel to be addressed selectively. The ultimate response of the gel will depend on several factors, such as the structural level at which the photo-responsive group is incorporated within the gel and the chemical changes that are invoked by the photochemical reaction.

LMOGs with photo-responsive groups have been known for quite a while [44, 45], but they were not reported to undergo a photo-controlled gel-sol phase transition. Gelators **46** and **47**, containing steroid, azobenzene and crown ether parts (Figure 19), respond to either metal complexation or light [46–48]. Numerous liquids have been gelled with only small amounts of **46** or **47**, and irradiation of their gels at 330–380 nm causes photochemical *trans-cis* isomerization of the azobenzene moiety to a photo-stationary state that contains 38% of the *cis* isomer. This relatively small change in overall composition and structure, nevertheless, leads to a significant decrease in T_g . Exposure of a solution of the photo-stationary state mixture to visible radiation at temperatures between its T_g and that of the completely *trans* form led to reformation of the gel phase without going through a typical heat-cool protocol. Gel-formation could be monitored by CD spectroscopy because gels of the *trans*-isomer show a strong positive CD effect, whereas gels of the photostationary state mixture showed no discernible CD. Curiously, CD spectra of gels with an identical composition were sometimes inverted due, apparently, to a kinetic effect; slow cooling from a solution (sol) of the *trans* form to the gel phase led to the usual positive exciton coupling, whereas fast cooling led to a CD spectrum with negative exciton coupling. Electron microscopy revealed that the inversion of the CD spectra was due to an inversion of the helical structure. Related examples

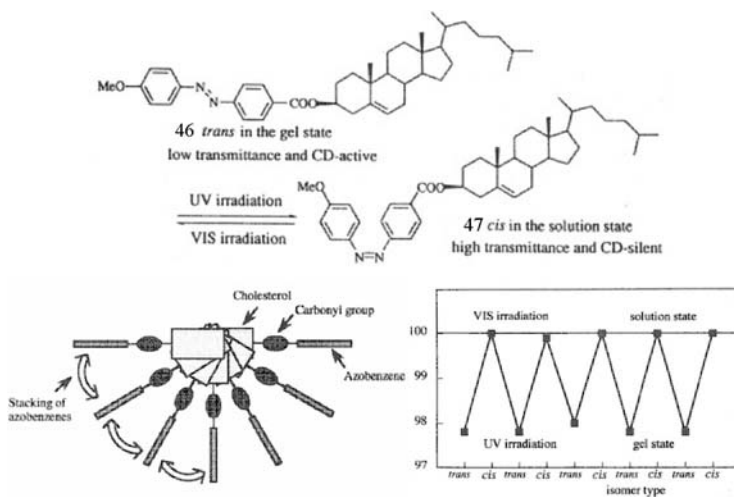


Figure 19. Self-assembly and enhanced gel formation by azobenzene crown ether steroids can be controlled by photochemical *trans-cis* and *cis-trans* isomerizations that are induced by irradiation with UV and visible light, respectively. The process could be repeated many times. (Reprinted with permission from [48]. Copyright (1994) American Chemical Society.)

of morphological changes in gel structures induced by the rate of cooling of solutions have been reported [49].

Incorporation of a photochromic moiety within the LMOG molecule is a very interesting approach to obtaining photo-responsive gel systems. A photochromic molecule within a gel has been co-assembled with a non-photoactive gelator molecule [50]. Photochemical conversion of the photochromic guest molecule led to loss of the gel state. A similar approach has been applied to the photochromic system based on pyrano[3,2-*a*]phenazines that were designed to be incorporated into fibers of 2,3-di-*n*-undecyloxyphenazine [51]. It appeared, however, that the spiro photochromic switches alone are able to gelate polar liquids such as DMF and DMSO at millimolar concentrations. By incorporation of the spiro photochromic moiety and acidic groups into the gelator molecules, the system can be addressed by light and pH changes (Figure 20). Irradiation of **48** induces ring-opening of the spiro moiety, which, in turn, leads to disruption of the gel structure. Although this process is not photochemically reversible, the ring-closed spiro form of **48** was regenerated by a heating/cooling cycle. Gelation by the closed spiro form of **48** was also reversible by pH change and hence the design of multi-responsive systems is feasible.

The incorporation of photochromic guest molecules into an organogel has been used to “write” photochemically, and to erase thermally via the gel-sol phase transition [52]. Gels derived from *trans*-(1*R*,2*R*)-1,2-bis(undecyl-carbonyl-amino)cyclohexane gelators were used as a host for photochromic

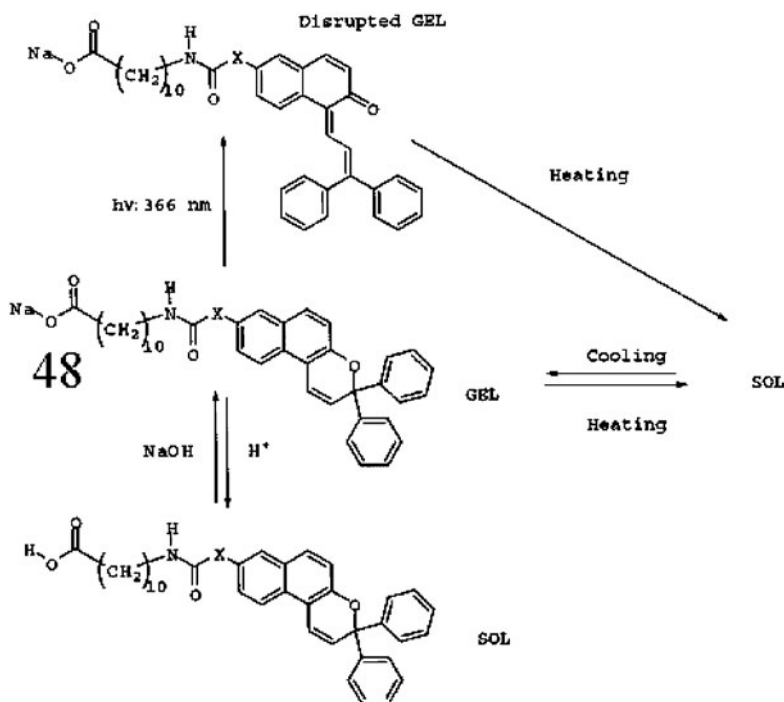


Figure 20. The gelation properties of pyrano[3,2-a]phenazine **48** can be controlled by temperature, pH, and photoisomerization. (Reprinted with permission from [51]. Copyright (2002) American Chemical Society.)

molybdenum complexes. Irradiation with UV light transformed the colorless $[\text{NH}_2(\text{CH}_2\text{CH}_2\text{CH}_2\text{NH}_3)_2]_2 \cdot [\text{Mo}_8\text{O}_{26}(\text{MoO}_4)]$ complex into a blue species due to a photo-redox reaction. Whereas in solution the blue species returns to its colorless state within 5 h, in the gel state, it is stable for more than a week. The colorless state could, however, be regenerated easily by a heating and cooling cycle that includes the gel-sol phase transition (Figure 21).

A very elegant and simple photo-responsive gel system is the 9-anthracenecarboxylic acid-*n*-alkylamine binary gelator system **49/50** (Figure 22) [53]. These salts with alkyl chains of 8–10 carbon atoms in length were able to gelate organic liquids by forming a fibrous network. Irradiation of **49** with UV-light led to dimerization of the anthracene moiety. The dimer **50** does not fit into the lattice of **49**, and a gel-sol phase transition ensues. Again, **49** could not be reformed by irradiation of **50**, but it could be reformed by heating. However, the monomer-dimer conversions occur with side products so that multiple cycles of photo-induced gel-sol phase transitions were not possible.

A different type of irreversible photo-response has been observed for the maleic-amide based compound **51** [54]. The irreversible photo-isomerization

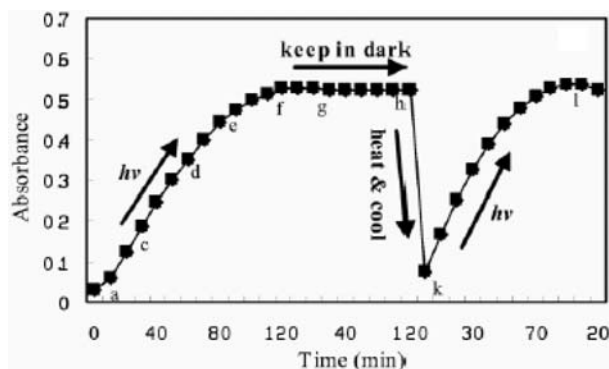


Figure 21. Molybdenum complexes $[\text{NH}_2(\text{CH}_2\text{CH}_2\text{CH}_2\text{NH}_3)_2]_2 \cdot [\text{Mo}_8\text{O}_{26}(\text{MoO}_4)]$ that are incorporated in gels develop a strong blue color upon irradiation with UV light as a result of a photo-redox reaction. The blue color was erased by heating the gel to above the gel-sol phase transition temperature (taken from [52], reproduced by permission of The Royal Society of Chemistry).

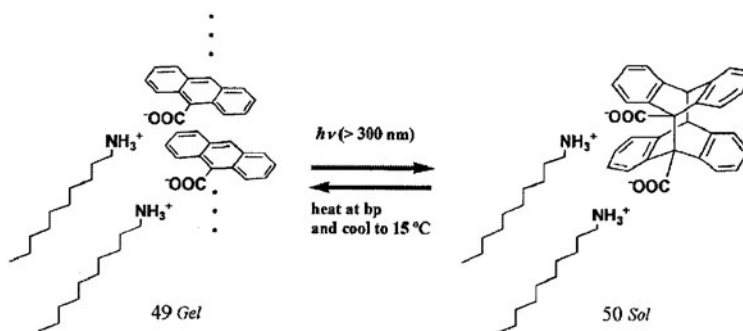


Figure 22. The salts of amines with anthracene carboxylic acid form an elegant gel system in which the gelation ability could be controlled by temperature and photochemical dimerization of the anthracene (taken from [53], reproduced by permission of The Royal Society of Chemistry).

of maleic acid into fumaric acid transforms the non-gelating maleic-amide **51** into the known fumaric amide gelator **52**. **51** (Figure 23) dissolves in water and upon addition of trace amounts of bromine and irradiation ($\lambda > 300 \text{ nm}$), a gel was formed within 30 seconds. Since addition of traces of bromine causes self-assembly of the maleic amide itself into micro-spheres, the photochemically induced gelation involves a morphological transition rather than a sol-gel transition.

Other photo-responsive gels based on spiro-switches **53** and **54** (Figure 24) have been reported [55, 56]. Irradiation of gels formed by these compounds causes color changes, but does not result in gel-sol phase transitions. The

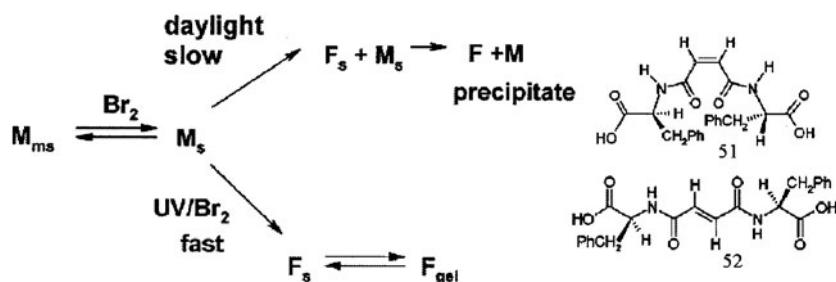


Figure 23. Maleic amide **51** can undergo a rapid acid-assisted photo-isomerization to the fumaric amide **52**, which is accompanied by an almost instantaneous gelation of the aqueous phase (taken from [54], reproduced by permission of The Royal Society of Chemistry.)

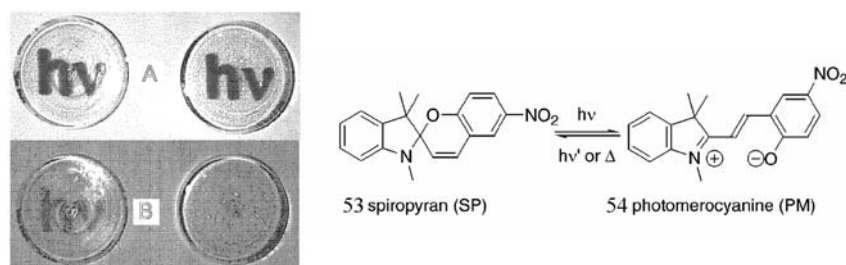


Figure 24. Spiro-switches **53/54** can gelate organic liquids, which could be colored reversibly by photochemical isomerization reactions. (Reprinted with permission from [54]. Copyright (2002) American Chemical Society.)

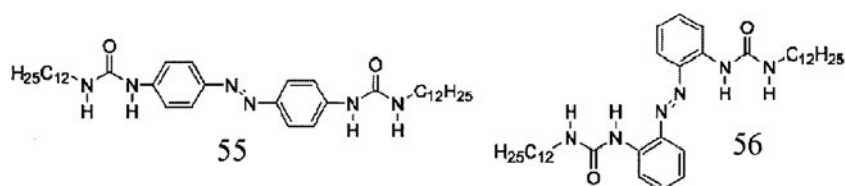


Figure 25. Bis-ureido azobenzenes **55** and **56** gelate organic liquids, but photochemical isomerization of *trans*-**56** to *cis*-**56** in solution inhibits gelation. (Reprinted with permission from [57]. Copyright (2002) American Chemical Society.)

kinetics of the photochemical conversion from **54** to **53** was found to be up to 195 times slower in the gel state than in solution. This observation is ascribed to the conformational constraints imposed by the packing of the molecules in their gel fibers.

Photo-responsive gel systems employing the bis-ureido-azobenzenes **55** and **56** as LMOGs have been investigated as well [57]. The *trans*-isomer of **55** readily forms gels with aromatic liquids, but the photochemical *trans-cis* isomerization is completely blocked in the gel state, most likely because of the conformational constraints imposed on azobenzene moieties by their incorporation in the hydrogen bonded chains that stabilize the gel fibers. Photochemical *trans-cis* isomerization is possible at temperatures above the gel-sol phase transition, but the *cis*-containing mixtures did not gelate their liquids upon cooling to temperatures below T_g of the *trans* isomer. Presumably, the *cis*-isomer blocks the intermolecular hydrogen bonding necessary to form fibers.

The latter examples clearly demonstrate that the success of photochromic LMOGs depends on their ability to undergo photochemical switching *in the gel state*, and that such processes can become difficult because confinement of the molecular geometry in the aggregated state may not be conducive to accommodation of (large) structural changes (such as those that attend photochemical isomerizations). Diarylethene photochromic switches, however, exhibit only small geometrical changes upon photochemical conversion of one isomer to the other, and several examples have been shown to display photochromism even in the confined geometry of molecular crystals [58]. Moreover, and in contrast to azobenzenes, the photochromic states of dithienylethenes do not interconvert thermally, and have excellent fatigue resistance.

We envision that the differences between the electronic properties and, particularly, the conformational flexibility of the open and closed forms of dithienylethenes may be exploited in the design of new photo-responsive gel systems (i.e., in the open form **57**, the two thienyl moieties are not conjugated and can rotate around the bond connecting them with the cyclopentene ring, whereas in the ring-closed form **58**, the conjugation extends throughout the chromophore and rotational freedom is lost) (Figure 26). Thus, a dithienylcyclopentene with amides was investigated in hopes of effecting self-assembly in solution and, eventually, gelation. The derivatives with long alkyl substituents on the amides gave only viscous solutions [59]. However, the presence of aromatic (chiral) substituents on the amide moieties results in LMOGs in low polarity organic liquids [60]. The chiral dithienyl cyclopentene **57** displayed very interesting gelation behavior and stereoselectivity of photochemical ring-closure. In solution, **57** exists in a dynamic equilibrium of M and P helical conformations of the central dithienylcyclopentene core, and photochemical ring-closure leads to equal amounts of the corresponding diastereomers, despite the presence of the chiral side groups. When photochemical ring-closure is carried out in the gelled state, only one diastereomer of **58** is formed. On this basis, it appears that only one of the two dynamic diastereomeric conformations of **57** is selected for incorporation in the aggregates (N.B., fibers).

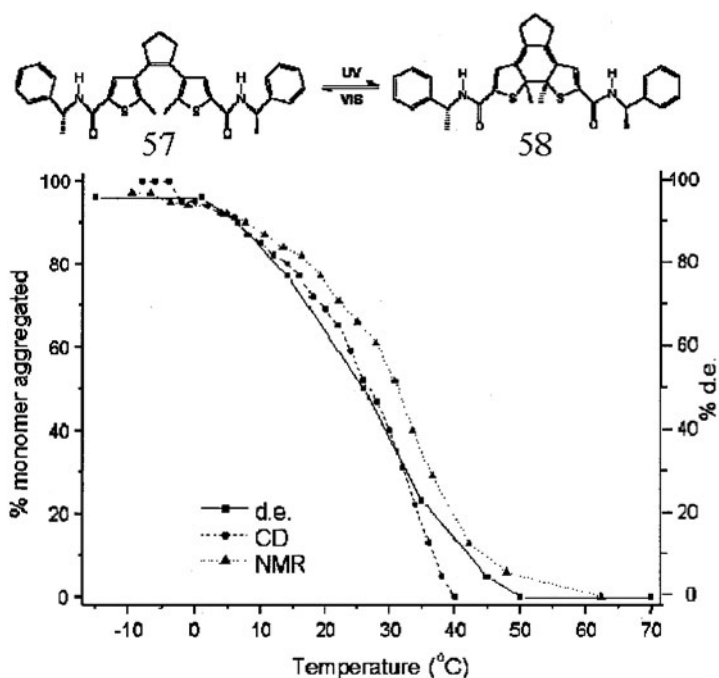


Figure 26. Photochemical ring closure of chiral dithienyl cyclopentene **57** in solution leads to two diastereomers of **58** in equal amounts, but in the gel state only one diastereomer is formed. The diastereomeric excess (right axis) shows an excellent correlation with the fraction of **57** incorporated in the gel state (left axis, from CD and ^1H NMR data). (Reprinted with permission from [60]. Copyright (2004) American Association for the Advancement of Science.)

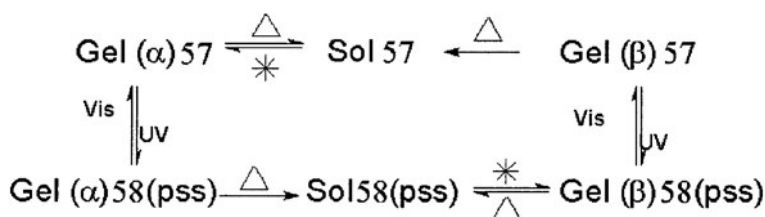


Figure 27. Starting with an isotropic solution of open form **57**, a stable gel (α) **57** (P-helicity) is obtained upon gelation (cooling (= \ast)). Photocyclization results in metastable gel (α) with **58** at its PSS mole fraction (P-helicity) and high diastereoselectivity (96% d.e.); the process is fully reversible. Heating of gel (α) **58** (PSS) leads to an isotropic solution of **58** [sol **58** (PSS)] which, upon cooling, yields a stable gel (β) **58** (PSS) (M-helicity). Irradiation of gel (β) **58** (PSS) with visible light results in metastable gel (β) **57**, which can be reconverted to the stable gel (β) **58** (PSS) by UV irradiation. Finally, a heating-cooling cycle results in the transformation of metastable gel (β) **57** to the original stable gel (α) **57** via an isotropic solution of **57** (sol **57**). (Reprinted with permission from [60]. Copyright (2004) American Association for the Advancement of Science.)

Gel formation and photochemical interconversion between **57** and **58** was studied in more detail by CD spectroscopy, which revealed the presence of two supramolecular aggregation states, α and β for both the open **57** and closed form **58** of the switch. Thus, there are four aggregation states of the switch which could be addressed by light and temperature changes (Figure 27). In the photochemical steps, the supramolecular chirality is preserved. However, photochemical ring-opening or ring-closure changes the rigidity and chirality (fixed or dynamic) of the central unit and, as a consequence, the stability of the chiral aggregate changes. Optical switching between different chiral aggregate states and the interplay of molecular and supramolecular chirality offers attractive new prospects for the development of molecular memory systems and smart functional materials.

4. Conclusions and Perspectives for the Future

Physical low molecular mass “responsive” gelators are interesting molecules with many potential applications in areas such as catalysis, sensor and separation technology, drug delivery, and biomedicine. In a relatively short period, a wide variety of responsive LMOG systems that can be addressed by chemical and physical triggers have been developed.

LMOG systems can be made responsive to a wide variety of chemical triggers, such as host-guest or metal-ion complexation, reactive gases, or pH, by integration of the appropriate functionality into the LMOG compound. As a result, directed design of new chemo-responsive LMOG systems appears to be feasible.

Similar approaches have also led to the successful development of photo-responsive LMOG gel systems. In most of the chemo- or photo-responsive gels, the typical response is a gel-sol or sol-gel transition. Here, the challenge is to develop systems in which a stimulus leads to a different response, such as a volume phase transition or a change of the shape of the bulk gel.

The field of physically-triggered gels has not reached the same level of understanding and design as chemo- or photo-responsive ones. Only a few examples have been reported of LMOG gels that show a temperature-dependent volume phase transition or display thixotropic behavior after application of mechanical stress, and the level of understanding of these systems is poor. Surprisingly, application of other interesting stimuli, such as electric or magnetic fields are almost unexplored, despite these triggers having very widespread application in molecular based devices.

Already, the scope of possible LMOG structures, the triggers, and their responses is impressive, but only a continued expansion of this field will lead to the level of understanding that is necessary for practical application. We foresee during the next decade dramatic improvements in understanding, design,

response time, and the number of applications for LMOGs. There is great promise for these smart low molecular mass gelators if we, as scientists, are sufficiently smart to unlock their secrets.

References

- [1] Tanaka, T. *Sci. Am.*, **1981**, *244*, 110–123.
- [2] (a) Tanaka, T.; Wang, C.N.; Pande, V.; Grosberg, A.Y.; English, A.; Masamune, S.; Gold, H.; Levy, R.; King, K. *Faraday Disc.*, **1995**, *102*, 210–216. (b) van Esch, J.; Schoonbeek, F.; de Loos, M.; Veen, E.M.; Kellogg, R.M.; Feringa, B.L. *Nato ASI. Ser. C*, **1999**, *527*, 237–259. (c) van Esch, J.H.; Feringa, B.L. *Angew. Chem.*, **2000**, *39*, *13*, 2263–2266.
- [3] (a) Terech, P.; Weiss, R.G. *Chemical Reviews*, **1997**, *97*, *8*, 3133–3159. (b) Abdallah, D.J.; Weiss, R.G. *Adv. Mater.*, **2000**, *12*, *17*, 1237–1247.
- [4] Philipse, A.P.; Wieringa, A.M. *Langmuir*, **1998**, *14*, 49–54.
- [5] Hanabusa, K.; Miki, T.; Taguchi, Y.; Koyama, T.; Shirai, H. *J. Chem. Soc., Chem. Commun.*, **1993**, 1382–1384.
- [6] Chang, S.-K.; Hamilton, A.D. *J. Am. Chem. Soc.*, **1988**, *108*, 1318–1319.
- [7] Inoue, K.; Ono, Y.; Kanekiyo, Y.; Ishi-I, T.; Yoshihara, K.; Shinkai, S. *J. Org. Chem.*, **1999**, *64*, 2933–2937.
- [8] Snip, E.; Shinkai, S.; Reinhoudt, D.N. *Tet. Letters*, **2001**, *42*, 2153–2156.
- [9] Numata, M.; Shinkai, S. *Chem. Lett.*, **2003**, *32*, 308–309.
- [10] Maitra, U.; Kumar, P.V.; Chandra, N.; D'Souza, L.J.; Prasanna, M.D.; Raju, A.R. *Chem. Commun.*, **1999**, 595–596.
- [11] Friggeri, A.; Gronwald, O.; van Bommel, K.J.C.; Shinkai, S.; Reinhoudt, D.N. *J. Am. Chem. Soc.*, **2002**, *124*, 10754–10758.
- [12] Maitra, U.; Mukhopadhyay, S.; Sarkar, A.; Rao, P.; Indi, S.S. *Angew. Chem.*, **2001**, *40*, 2281–2283.
- [13] Jung, J.H.; Ono, Y.; Shinkai, S. *Tet. Letters*, **1999**, *40*, 8395–8399.
- [14] Ishi-I, T.; Jong, J.H.; Shinkai, S. *J. Mater. Chem.*, **2000**, *10*, 2238–2240.
- [15] Ishi-I, T.; Iguchi, T.; Snip, E.; Ikeda, M.; Shinkai, S. *Langmuir*, **2001**, *17*, 5825–5833.
- [16] Kobayashi, H.; Amaike, M.; Jung, J.H.; Friggeri, A.; Shinkai, S.; Reinhoudt, D.N. *Chem. Commun.*, **2001**, 1038–1039.
- [17] Kobayashi, H.; Koumoto, K.; Jung, J.H.; Shinkai, S. *J. Chem. Soc., Perkin Trans. 2*, **2002**, 1930–1936.
- [18] Sohna, J.E.S.; Fages, F. *Chem. Commun.*, **1997**, 327–328.
- [19] Amanokura, N.; Kanekiyo, Y.; Shinkai, S.; Reinhoudt, D.N. *J. Chem. Soc., Perkin Trans. 2*, **1999**, 1995–2000.
- [20] Terech, P.; Coutin, A. *J. Phys. Chem. B*, **2001**, *105*, 5670–5676.
- [21] Ihara, H.; Sakurai, T.; Yamada, T.; Hashimoto, T.; Takafuji, M.; Sagawa, T.; Hachisako, H. *Langmuir*, **2002**, *18*, 7120–7123.
- [22] George, M.; Weiss, R.G. *J. Am. Chem. Soc.*, **2001**, *123*, 10393–10394.
- [23] George, M.; Weiss, R.G. *Langmuir*, **2002**, *18*, 7124–7135.
- [24] George, M.; Weiss, R.G. *Langmuir*, **2003**, *19*, 1017–1025.
- [25] Pozzo, J.-L.; Clavier, G.M.; Desvergne, J.-P. *J. Mater. Chem.*, **1998**, *8*, 2575–2577.
- [26] Aggeli, A.; Bell, M.; Boden, N.; Keen, J.N.; Knowles, P.F.; McLeish, T.C.B.; Pitkeathly, M.; Radford, S.E. *Nature*, **1997**, *386*, 259–262.
- [27] Aggeli, A.; Bell, M.; Carrick, L.M.; Fishwic, C.W.G.; Harding, R.; Mawer, P.J.; Radford, S.E.; Strong, A.E.; Boden, N. *J. Am. Chem. Soc.*, **2003**, *125*, *32*, 9619–9628.

- [28] Aggeli, A.; Bell, M.; Boden, N.; Carrick, L.M.; Strong, A.E. *Angew. Chem.*, **2003**, *42*, 5603–5606.
- [29] Schneider, J.P.; Pochan, D.J.; Ozbas, B.; Rajagopal, K.; Pakstis, L.; Kretsinger, J. *J. Am. Chem. Soc.*, **2002**, *124*, *50*, 15030–15037.
- [30] Petka, W.A.; Harden, J.L.; McGrath, K.P.; Wirtz, D.; Tirrell, D.A. *Science*, **1998**, *281*, 389–392.
- [31] Hartgerink, J.D.; Beniash, E.; Stupp, S.I. *Science*, **2001**, *294*, 1684–1688.
- [32] Haines, S.R.; Harrison, R.G. *Chem. Commun.*, **2002**, 2846–2847.
- [33] van Bommel, K.J.C.; van der Pol, C.; Muizebelt, I.; Friggeri, A.; Heeres, A.; Feringa, B.L.; van Esch, J. *Angew. Chem.*, **2004**, *43*, 1663–1667.
- [34] Heeres, A.; van der Pol, C.; Stuart, M.; Friggeri, A.; Feringa, B.L.; van Esch, J. *J. Am. Chem. Soc.*, **2003**, *125*, 14252–14253.
- [35] Galaev, I.Y.; Mattiasson, B. *Trends Biotechnol.*, **1999**, *17*, 335–340.
- [36] Terech, P.; Berthet, C. *J. Phys. Chem.*, **1988**, *92*, 4269–4272.
- [37] (a) Li, G.C.; John, V.T.; Irvin, G.C.; Rachakonda, S.H.; McPherson, G.L.; O’Conner, C.J. *J. Appl. Phys.*, **1999**, *85*, 5965–5967; (b) Simmons, B.; Li, G.C.; John, V.T.; McPherson, G.L.; Taylor, C.; Schwartz, D.K.; Maskos, K. *Nano Lett.*, **2002**, *2*, 1037–1042.
- [38] Kiyonaka, S.; Sugiyasu, K.; Shinkai, S.; Hamachi, I. *J. Am. Chem. Soc.*, **2002**, *124*, 10954–10955.
- [39] Terech, P. *Ber. Bunsenges. Phys. Chem.*, **1998**, *102*, *11*, 1630–1643.
- [40] Terech, P.; Schaffhauser, V.; Maldivi, P.; Guenet, J.M. *Langmuir*, **1992**, *8*, 2104–2106.
- [41] Brinksma, J.; Feringa, B.L.; Kellogg, R.M.; Vreeker, R.; van Esch, J. *Langmuir*, **2000**, *16*, 9249–9255.
- [42] Terech, P.; Scherer, C.; Lindner, P.; Ramasseul R. *Langmuir*, **2003**, *19*, 10648–10653.
- [43] Lescanne, M.; Colin, A.; Mondain-Monval, O.; Heuzé, K.; Fages, F.; Pozzo, J.-L. *Langmuir*, **2002**, *18*, 7151–7153.
- [44] Lin, Y.; Kachar, B.; Weiss, R.G. *J. Am. Chem. Soc.*, **1989**, *111*, 5542–5551.
- [45] Brotin, T.; Utermohlen, R.; Fages, F.; Bouaslaurent, H.; Desvergne, J.P. *J. Chem. Soc., Chem. Commun.*, **1991**, 416–418.
- [46] Murata, K.; Aoki, M.; Nishi, T.; Ikeda, A.; Shinkai, S. *J. Chem. Soc., Chem. Commun.*, **1991**, 1715–1718.
- [47] Murata, K.; Aoki, M.; Shinkai, S. *Chem. Letters*, **1992**, 739–742.
- [48] Murata, K.; Aoki, M.; Suzuki, T.; Harada, T.; Kawabata, H.; Komori, T.; Ohseto, F.; Ueda, K.; Shinkai, S. *J. Am. Chem. Soc.*, **1994**, *116*, 6664–6676.
- [49] Furman, I.; Weiss, R.G. *Langmuir*, **1993**, *9*, 2084–2088.
- [50] Pozzo, J.-L.; Clavier, G.; Rustemeyer, F.; Bouras-Laurent, H. *Mol. Cryst. Liq. Cryst.*, **2000**, *344*, 101–106.
- [51] Ahmed, S.A.; Sallenave, X.; Fages, F.; Mieden-Gundert, G.; Muller, W.M.; Muller, U.; Vogtle, F.; Pozzo, J.-L. *Langmuir*, **2002**, *18*, *19*, 7096–7101.
- [52] Yi, T.; Sada, K.; Sugiyasu, K.; Hatano, T.; Shinkai, S. *Chem. Commun.*, **2003**, 344–345.
- [53] Ayabe, M.; Kishida, T.; Fujita, N.; Sada, K.; Shinkai, S. *Org. Biomol. Chem.*, **2003**, *1*, 2744–2747.
- [54] Frkanec, L.; Jokic, M.; Makarevic, J.; Wolsperger, K.; Zinic, M. *J. Am. Chem. Soc.*, **2002**, *124*, *33*, 9716–9717.
- [55] Hachisako, H.; Ihara, H.; Kamiya, T.; Hirayama, C.; Yamada, K. *Chem. Commun.*, **1997**, 19–20.
- [56] Shumburo, A.; Biewer, M.C. *Chem. Mater.*, **2002**, *14*, 3745–3750.

- [57] van der Laan, S.; Feringa, B.L.; Kellogg, R.M.; van Esch, J. *Langmuir*, **2002**, *18*, 7136–7140.
- [58] Irie, M.; Fukaminato, T.; Sasaki, T.; Tamai, N.; Kawai, T. *Nature*, **2002**, *420*, 759–760.
- [59] Lucas, L.N.; van Esch, J.; Kellogg, R.M.; Feringa, B.L. *Chem. Commun.*, **2001**, 759–760.
- [60] de Jong, J.J.D.; Lucas, L.N.; Kellogg, R.M.; van Esch, J.H.; Feringa, B.L. *Science*, **2004**, *304*, 278–281.

Chapter 27

GELS AS CLEANING AGENTS IN CULTURAL HERITAGE CONSERVATION

Emiliano Carretti and Luigi Dei

*Department of Chemistry and Consortium CSGI, University of Florence, via della
Lastruccia 3, I-50019 Sesto Fiorentino, (Florence) Italy*

1. Introduction	929
2. Polyacrylic Acid-Based Gels in Cultural Heritage Conservation	933
3. Application and Removal of Gels from Painted Surfaces	934
4. Future Perspectives	936

1. Introduction

One of the most widely used techniques to clean easel paintings, when the intent is to remove selectively the components not constituting the original work of art, still involves the application of pure organic solvents. Unfortunately, penetration of the organic solvents into the original paint layers can lead to undesirable swelling and partial leaching as well.

The volume changes of a polymeric varnish layer induced by a solvent have been studied by Stolow [1]. Swelling and leaching processes were studied for new and aged pigmented films; Figure 1a shows that once a maximum swelling is reached, the oil volume and weight decrease. Upon drying, the film appears denser and much more brittle. If the same film is exposed a second time to the solvent, no additional shrinkage due to the leaching effect is observed (Figure 1b) and less swelling is noted.

During cleaning, the degree of leaching is very dependent on the depth of penetration of the solvent (d_s) into the paint layer. The Washburn equation (Eq. (1)) [2] describes the degrees of penetration as a function of time.

$$t = \frac{4L^2\eta}{D\gamma \cos\theta} \quad (1)$$

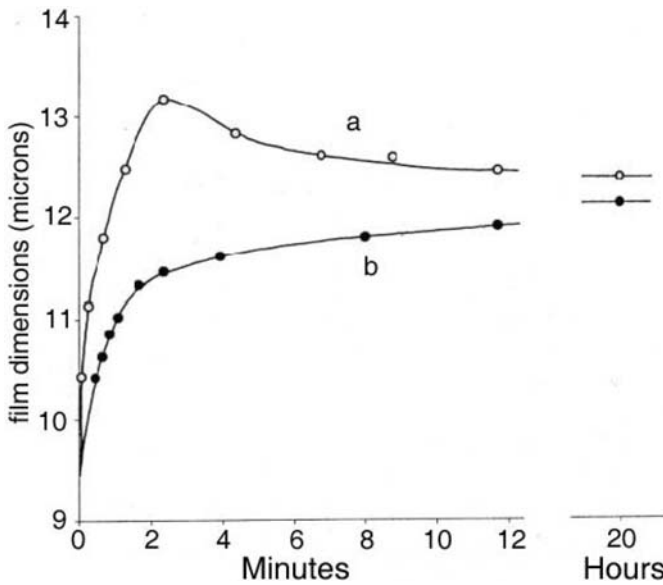


Figure 1. Swelling and leaching (a) of a polymeric binding medium film (linseed oil) and re-swelling of the same film (b). (Reprinted from [1] by permission of International Institute for Conservation of Historic and Artistic Works and the Author.)

D is a variable diffusion coefficient expressed by Crank's curve [3] ($D = D_{\text{dry}} \exp(kC/C_s)$, where D_{dry} is the diffusion coefficient of the dried polymer, C and C_s are the polymer concentrations of the unswollen and swollen polymer, respectively, and k is Stolow's coefficient for the polymer), η is the viscosity of the liquid, γ is the surface tension, θ is the contact angle at the liquid-air interface for the unswelled polymer surface and L is the penetration depth of the swelling liquid. Because the action of the solvent is faster at higher d_s [4], the impact of an active solvent will never be equal to zero during cleaning.

As indicated by Michalski [4], many solvents that are able to solubilize coating varnishes also penetrate rapidly into the paint layer at a rate of about $10 \mu\text{m}/\text{sec}$. This causes swelling of the most common binding media. For example, toluene, acetone, and xylene induce a ca. 30% volume increase of a linseed oil film. Essential fatty acids were commonly used in the past as binding media for easel paintings. The main consequence of swelling and drying of the solvent is at the same time the decreased strength of the paint layer and the change of its surface morphology that appears smoothed. SEM micrographs of a raw sienna oil paint film before (A) and after (B and C) cleaning with a triethanolamine based liquid mixture obtained by Erhardt and Bischoff are reported in Figure 2. Figure 2B clearly shows that the paint layer is completely

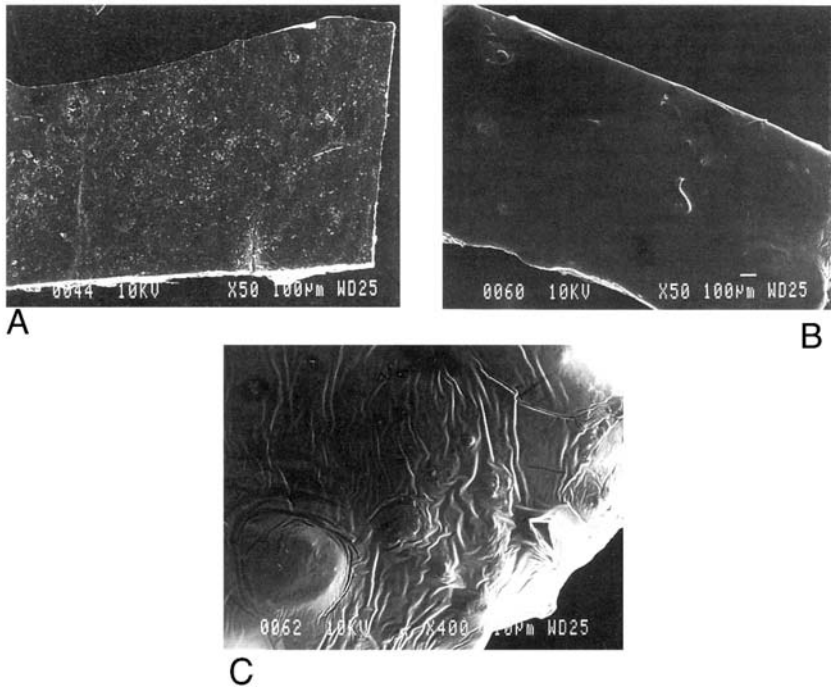


Figure 2. SEM micrographs of raw sienna oil paint film before (A) and after (B and C) treatment with a triethanolamine mixture. Erosion (B) and wrinkling (C) are observed at the paint surface. (Reprinted from [5] by permission of International Institute for Conservation of Historic and Artistic Works and the Authors.)

smoothed and the wrinkling of the paint surface layer occurs too (Figure 2C). Furthermore, treatment with the liquid mixture induces a softening of the paint film not only at the paint surface, but also below this layer [5]. Since triethanolamine is a nonvolatile solvent, its residues are most likely responsible for the observed permanent effects – wrinkling and softening of the paint.

Reductions of the penetration rate and the amount of solvent swelling can be achieved by the use of highly stable viscous condensed systems (Brookfield viscosity values up to 55000 cP) [6] with very high retention powers (such as those found in gels) [7, 8]. Removal of the variegated materials (fatty acids, proteins, waxes, acrylic and vinyl polymers, etc., usually in a degraded form) requires gel solvents having different polarities. Figure 3 shows three SEM micrographs of a sienna oil paint film before (A) and after (B and C) the application of a sodium abietate based gel system (triethanolamine is part of the solvent system) [5]. After application of the gel (Figure 3B) the paint surface looks slightly smoothed. At higher magnification (Figure 3C), the micrograph indicates that no significant changes are observed; in this case the wrinkling

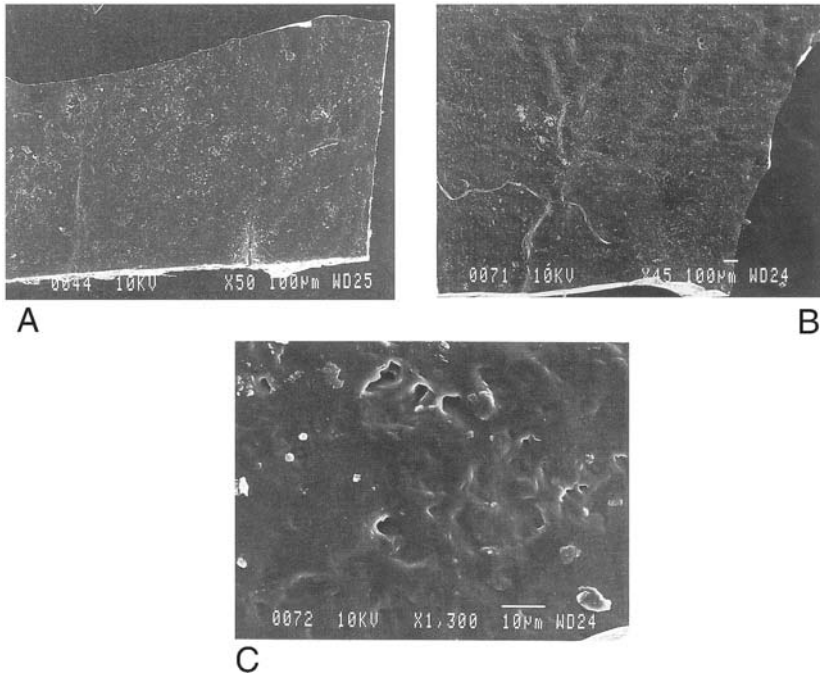


Figure 3. SEM micrographs of raw sienna oil paint film before (A) and after (B and C) the treatment with triethanolamine mixture gelled with sodium abietate (pH = 10). (Reprinted from [5] by permission of International Institute for Conservation of Historic and Artistic Works and the Authors.)

effect is completely absent [5]. Furthermore, residues of gelator remain on the surface, indicating that the cleaning action is more limited than the one typical of pure solvents. In fact, one of the main characteristics of the cleaning methods based on gels is that the application of gels produces both a reduction of the efficacy of the strong solvents or solvent mixtures and an increase of the efficacy of the milder solvents. Many gels can be obtained with solvents covering a very wide range of polarities [8, 10]. This makes the gel-based cleaning technique quite versatile. In addition to organic solvents and water, highly selective cleaning agents such as enzymes or chelating solutions can be gelled. For instance, gelled aqueous solutions of lipases have been used to remove degraded triglycerides [11]. Analogously, proteases and carbohydrases are used for the removal of protein coatings layers and carbohydrate-based polymers [8, 12] not a part of the original work of art. Chelating agents such as EDTA or citric acid are useful for the selective removal of salts. Their action is usually specific to a narrow range of ions, especially metal cations. The chelators preserve the surface to be cleaned from the possible action of ions (both anions and cations) and many of the formulations described here

can clean other surfaces (e.g., glasses [13], metals [14] and feathers) [15, 16]. For these reasons, gels have an enormous number of potential applications for cleaning [17].

2. Polyacrylic Acid-Based Gels in Cultural Heritage Conservation

Most gels for cleaning purposes employ polymeric gelators (i.e., gellants). Commonly, they are highly functionalized, such as polyacrylic acid with high molecular weights (up to 4×10^6 Dalton) [18]. Their gels have been known for many years [19] and were used initially to complex metal ions [20, 21] and in the cement industry [22]. Today, they are being used in many other applications such as in drug delivery [23–25]. Wolbers has introduced polyacrylic acid-based gels as a cleaning tool in cultural heritage conservation; these systems are commonly called *solvent gels* [7]. To obtain gels, the acidic groups of the polymer are treated with a base, yielding carboxylates. Repulsive interactions between the negatively charged groups cause the unfolding of the polymer structure (Figure 4) that allows formation of three-dimensional polymer matrices of intertwining chains and formation of a highly viscous gel.

Deprotonation in organic solvents is usually achieved by addition of a non-ionic surfactant (e.g., Ethomeen C12 or Ethomeen C25, known also as cocoamines) characterized by weakly basic properties. Both C12 and C25 have a long alkyl chain and form salts with carboxyl groups of the polyacrylic acid chains (Figure 5).

Water/polyacrylic acid gels can also be obtained. The main difference between the gels described above and them is related to the nature of the unfolding process. It is induced in this case by the addition of an inorganic base, such as NaOH or NH_3 , usually in 0.1 M concentration. By varying the amount of the added base, it is possible to obtain formulations at different

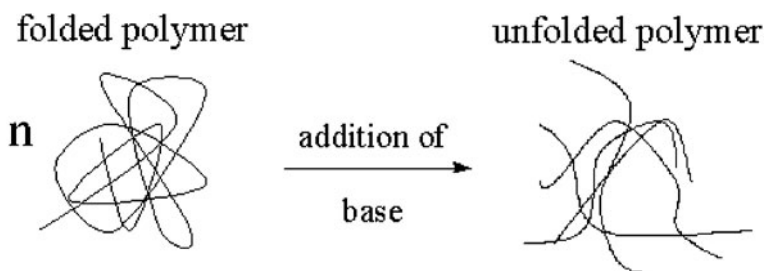


Figure 4. Formation of a three-dimensional network obtained by the unfolding of polymer chains upon addition of a base.

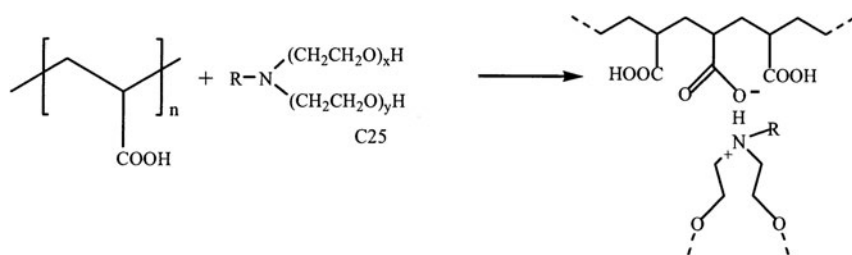


Figure 5. In non-polar organic solvents, the gel properties of polyacrylic acid are related to the alkyl chain length R and to the x and y values of the added surfactant. For Ethomeen C12 (HLB 10; molecular weight 217–385 D), R usually contains between 8 and 20 carbon atoms. Ethomeen C25 (HLB 19; molecular weight 789–957 D) molecules contain more than one hydroxyl group and, for this reason it is useful in the gelation of more polar solvents. Gels are usually prepared by dispersing ca. 1% wt. of polymer into the solvent and then adding 1–2% wt. of the surfactant. Viscosity increases are noted when a small amount of water (up to 1.5%) is added dropwise.

pH values [26]. The rheological Ostwald-De Waele model, typical of many pseudoplastic hydrogels [27, 28], is followed. The viscosity η is expressed by the relationship, $\eta = m(d\gamma/dt)^{n-1}$, where m and n are the consistency and the pseudoplasticity indices, respectively. The increase of the m values with increasing pH (from $2.9 \text{ Pa} \times \text{s}^n$ at pH = 3 to $15.6 \text{ Pa} \times \text{s}^n$ at pH = 12) [26] is due to the increased population of carboxylate groups and, thus, to the increased unfolding of the polymer chains and hydrogen bonding with water molecules.

Other gel formulations, especially those with one polar solvent component only (N.B., alcohols and water) [11] and their solutions containing enzymes and chelating agents, are known. As in many other areas of applied science, art restoration technology takes its tools from other disciplines. Polymers such as cellulose derivatives and agar are commonly employed as gellants [11] in the food industry, for catalysis, for drug delivery technology, etc. [29–32]. However, these gellants are less versatile than the polyacrylic acid based ones due to the limited range of liquids they can gelate.

For all the gels previously indicated, their application to painted surfaces can be carried out mainly in two different ways: application of the gel without any further operation (contact times usually are less than one minute); the use of a brush, implying a mechanical action on the surface of the paint.

3. Application and Removal of Gels from Painted Surfaces

As mentioned above, application of any of the gels described to a painted surface is usually achieved either by putting an aliquot onto a designated area and leaving it there undisturbed for ≤ 1 minute or by brushing the gel onto

the surface in order to initiate a mechanical force. Complete removal after treatment is the principal practical problem associated with the use of gels as cleaning agents for painted surfaces. The effects of residues from gels and other cleaning agents on the surface of works of art over time are still being determined [33]. For instance, Burnstock and Kieslich demonstrated by gas chromatography/mass spectroscopy and scanning electron microscopy analyses that residues of Ethomeen are present both when a gel containing this component is removed mechanically or by solubilization [9]. The gel components are removed most effectively when another agent consisting of the same solvent mixture employed in the gel is applied. Of course, this is not an optimal solution.

A new approach has been recently proposed [33]. In it, the impact of the cleaning action on easel paintings is reduced by using polyallylammonium/polyallylcarbamate (PAA · CO₂) gellants. The gel is obtained by bubbling CO₂ through a solution of polyallylamine (PAA) in a solvent [34], as showed in Figure 6. Then, the gel is applied following the methods previously indicated.

To remove the gel from the painted surface in this case, the chemical reversibility of the system is exploited. PAA is regenerated in its protiated (ammonium) form and the gel structure is destroyed by the addition of few drops of a solution of dilute (0.1 M) acetic acid (i.e., vinegar) to the paint surface. Then, the residual PAA can be removed easily and completely. This approach has been used successfully to remove a post-applied coat of varnish from a XIV century oil-on-wood painting from the National Gallery of Siena in Italy [36] and other superficial layers from sculpted objects [37].

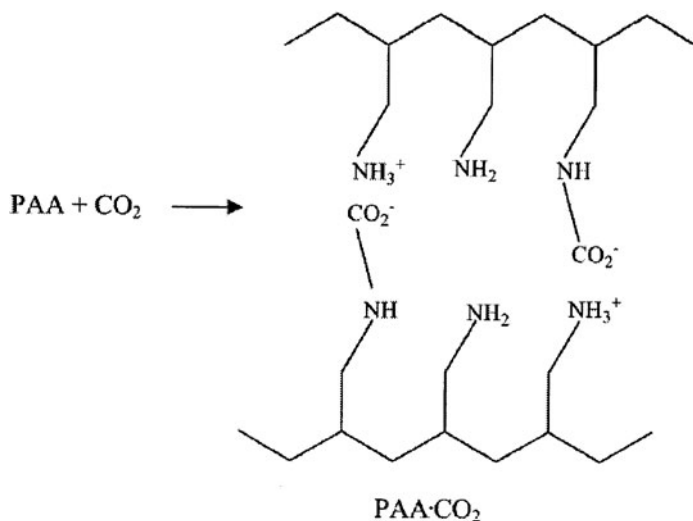


Figure 6. Gelation of a PAA solution by its conversion to PAA·CO₂ upon CO₂ bubbling. (Reprinted with permission from [34]. Copyright (2003) American Chemical Society.)

4. Future Perspectives

The possibility to convert gels chemically into flowing liquid systems (i.e., chemically-induced rheo-reversibility) suggests several practical advantages over traditional gels for cleaning purposes. In these cases, the polymeric gellants can be removed as easily as their neat solvents because the gel network structure is not intact but is present in a latent sense. Then, the rheo-reversibility approach represents a new approach to the cleaning of painted surfaces for art conservation. Furthermore, many others polyamines and their ammonium carbamates should be investigated to increase the range of solvents that can be gelled and to find other useful systems for art conservation cleaning technology.

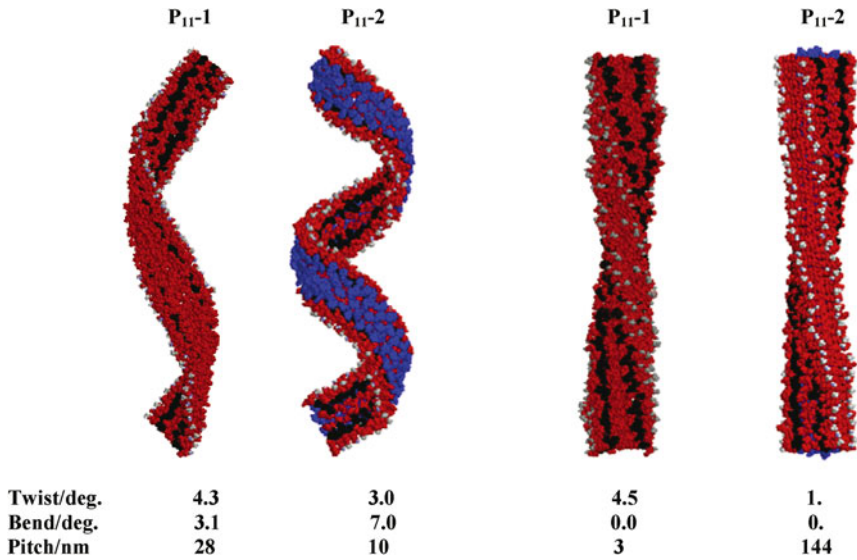
References

- [1] Stolow, N. "The measurement of film thickness and of solvent action on supported films", *Studies in Conservation*, **1957**, 3, 40–44.
- [2] Patton, T.C. *Paint Flow and Pigment Dispersion*, New York: John Wiley and Sons, **1979**.
- [3] Crank, J. *The Mathematics of Diffusion*, Oxford: Clarendon Press, **1975**.
- [4] Michalski, S. "A physical model of the cleaning of oil paint. Proceeding of cleaning, retouching and coatings: technology and practice for easel paintings and polychrome sculpture", *Preprints of the Contributions to the Congress; 1990 September 3–7; Brussels*, London: International Institute for Conservation, **1990**.
- [5] Erhardt, D.; Bishoff, J. J. "The roles of various components of resins soaps, bile acid soaps and gels, and their effects on oil paint films", *Studies in Conservation*, **1994**, 39, 3–27.
- [6] AAVV. "Carbopol, high performance polymers for pharmaceuticals, Bulletin 11, Thickening Properties" (B. F. Goodrich Specialty Chemicals).
- [7] Wolbers, R. C. *Proceeding of Workshop on New Methods in the Cleaning of Paintings and other Decorative Surfaces; 1988; Marina Del Rey, CA*. Ottawa: Canadian Conservation Institute, **1990**.
- [8] Cremonesi, P.; Curti, A.; Fallarini, L.; Raio, S. "Preparation and use of solvent gels, reagents for the cleaning of polychrome works", *Progetto Restauro*, **2000**, 7, 25–33.
- [9] Burnstock, A.; Kieslich, T. "A study of the clearance of solvent gels used for varnish removal from paintings", *Proceeding of ICOM Committee for Conservation, 11th Triennial Meeting in Edinburgh, Scotland; 1996 September 1–6*, London: James & James (Science Publishers), **1996**.
- [10] J.A. Dean, Ed., *Lange's Handbook of Chemistry*, 30th edition, New York: Mc Graw-Hill, **1985**.
- [11] Wolbers, R.C. *Cleaning Painted Surfaces, Aqueous Methods*, London: Archetype Publications, **2000**.
- [12] Butazzoni, N.; Casoli, A.; Cremonesi, P.; Rossi, P. "Preparation and use of enzyme and surface-active gels for the cleaning of polychrome works", *Progetto Restauro*, **200**, 7, 11–19.
- [13] Valentin, N.; Sánchez, A.; Herraes, I. "Analyses of deteriorated spanish glass windows: cleaning methods using gel systems", *Proceeding of ICOM 11th Triennial Meeting; 1996 September 1–6; Paris*, London: James & James, **1996**.

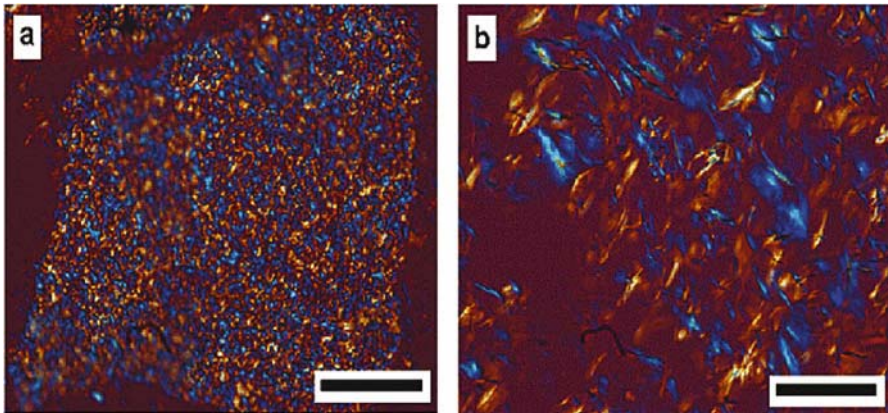
- [14] Tomozei, M.; Balta, Z. "La restauration d'une plaque de corselet (Iran, 17^{ème} siècle)", *Proceeding of International Conference on Metals Conservation; mai 27–29 1998; Figanières*, London: James & James, **1998**.
- [15] Carretti, E.; Salvadori, B.; Mauro, M.; Giovannoni, S.; Bellé, S.; De Santis, P.; Dei, L. Unpublished results.
- [16] Silveira, L. "A note on the poultice cleaning of feathers using Laponite RD gel", *Studies in Conservation*, **1997**, *4*, 11–16.
- [17] Khandekar, N. "A survey of the conservation literature relating to the development of aqueous gel cleaning on painted and varnished surfaces", *Reviews in Conservation*, **2000**, *1*, 10–20.
- [18] Scalisi, L. "Cleaning a painting with solvent gels: experimentation and practice", *Conservation News*, **1998**, *66*, 46–48.
- [19] Chatterjee, A.; Marinsky, J. A. "Dissociation of methacrylic acid resins", *J. Phys. Chem.*, **1963**, *67*, 41–47.
- [20] Gustafson, R. L.; Lirio, J. A. "Interaction of cross-linked polymethacrylic acid with polyvalent metal ions. I", *J. Phys. Chem.*, **1965**, *69*, 2849–2856.
- [21] Gustafson, R. L.; Lirio, J. A. "Binding of divalent metal ions by crosslinked polyacrylic acid", *J. Phys. Chem.*, **1968**, *72*, 1502–1505.
- [22] Wagner, H.B. "Polymer-modified hydraulic cements", *Ind. Engin. Chem. Res., I&EC Proc. Des. Dev.*, **1965**, *4*, 191–196.
- [23] Cheng, H.S.; Park, H.; Kelly, P.; Robinson, J. R. "Bioadhesive polymers as platforms for oral controlled drug delivery. II: synthesis and evaluation of some swelling, water-insoluble bioadhesive polymers", *J. Pharma. Sci.*, **1985**, *74*, 399–405.
- [24] Barry, B. W. "Rheology of dermatological vehicles." In *Dermatological Formulations. Percutaneous Absorption*, B.W. Barry, Ed., New York: Marcel Dekker, **1983**.
- [25] Unlu, N.; Ludwig, A.; Van Ooteghem, M.; Hincal, A. "Formulation of carbopol 940 ophthalmic vehicles, and *in vitro* evaluation of the influence of simulated lacrimal fluid on their physico-chemical properties", *Pharmazie*, **1991**, *46*, 784–788.
- [26] Taberner, T.S.; Villodre, A.M.; Pla-Delfina, J.M.; Herraes, J.V. "Consistency of Carbopol 971-P NF gels and influence of soluble and cross-linked PVP. Intern", *J. Pharma.*, **2002**, *233*, 43–50.
- [27] Chauveau, C.; Maillols, H.; Delonca, H. "Natrosol 250 H: Caractérisation et modélisation du comportement rhéologique", *Pharm. Acta Helv.*, **1986**, *61*, 10–11.
- [28] McNeill, I.C.; Sadeghi, M.T. "Thermal stability and degradation mechanisms of poly(acrylic acid) and its salts: Part 1. Poly(acrylic acid)", *Poly. Deg. Stabil.*, **1990**, *29*, 233–246.
- [29] Sachin, S.; Chaphekar, S.S.; Samant, S.D. "Cyanoethylation of alcohols catalyzed by a novel aqueous agar gel-entrapped NaOH catalyst", *Appl. Catal. A*, **2003**, *242*, 11–15.
- [30] Pietranera, M.S.A.; Narvaiz, P. "Examination of some protective conditions on technological properties of irradiated food grade polysaccharides", *Radia. Phys. Chem.*, **2001**, *60*, 195–201.
- [31] Ogawa, K.; Wang, B.; Kokufuta, E. "Enzyme-regulated microgel collapse for controlled membrane permeability", *Langmuir*, **2001**, *17*, 4704–4707.
- [32] Raksakulthai, R.; Haard, N.F. "Purification and characterization of a carboxypeptidase from squid hepatopancreas (*Illex illecebrosus*)", *J. Agric. Food Chem.*, **2001**, *49*, 5019–5030.
- [33] Stulik, D.; Miller, D.; Khandekar, N.; Wolbers, R.; Carlson, J.; Peterson, W. C. *Solvent Gels for the Cleaning of Works of Art. The Residue Question*, V. Dorge, Ed., Los Angeles: The Getty Conservation Institute, **2004**.

- [34] Carretti, E.; Dei, L.; Baglioni, P.; Weiss, R.G. "Synthesis and characterization of gels from polyallylamine and carbon dioxide as gellant", *J. Am. Chem. Soc.*, **2003**, *125*, 5121–5129.
- [35] George, M.; Weiss, R.G. "Chemically reversible organogels: aliphatic amines as 'Latent' gelators with carbon dioxide", *J. Am. Chem. Soc.*, **2001**, *123*, 10393–10394.
- [36] Carretti, E.; Macherelli, A.; Dei, L.; Weiss, R.G. "Rheo-reversible polymeric organogels: the art of science for art conservation", *Langmuir*, **2004**, *20*, 8114–8118.
- [37] Carretti, E.; Dei, L.; Weiss, R.G. "Soft matter and art conservation: rheo-reversible gels and beyond", *Soft Matter*, **2005**, *1*, 17–22.

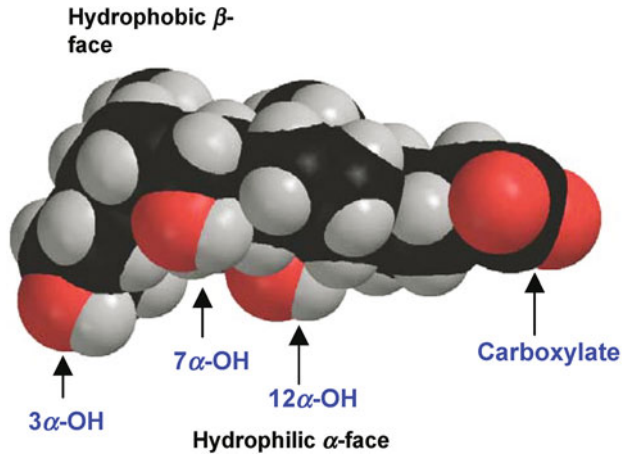
COLOR SECTION



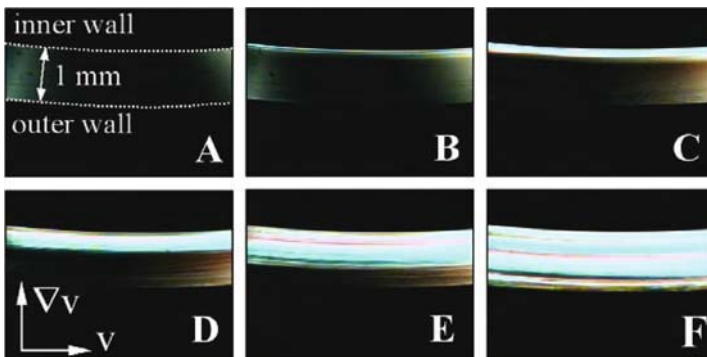
Chapter 3 Figure 8. Molecular dynamics generated structures of tapes (left) and ribbons (right) for peptides P₁₁-1 and P₁₁-2 [9]. (Reprinted in part with permission from [9]. Copyright (2003) American Chemical Society.)



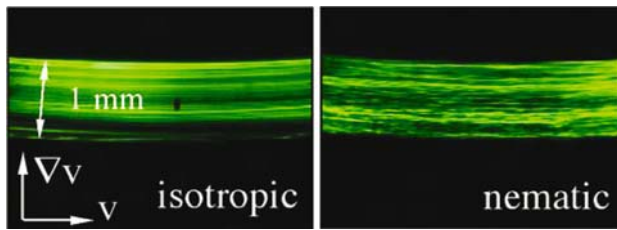
Chapter 14 Figure 59. Polarizing optical micrographs (room temperature) of 2 wt. % (a) **116** ($n = 18$) and (b) **117** ($n = 18$) gels in silicone oil. Black space bars are 100 μm . The images were taken with a full-wave plate. (Reprinted with permission from [86]. Copyright (2002) American Chemical Society.)



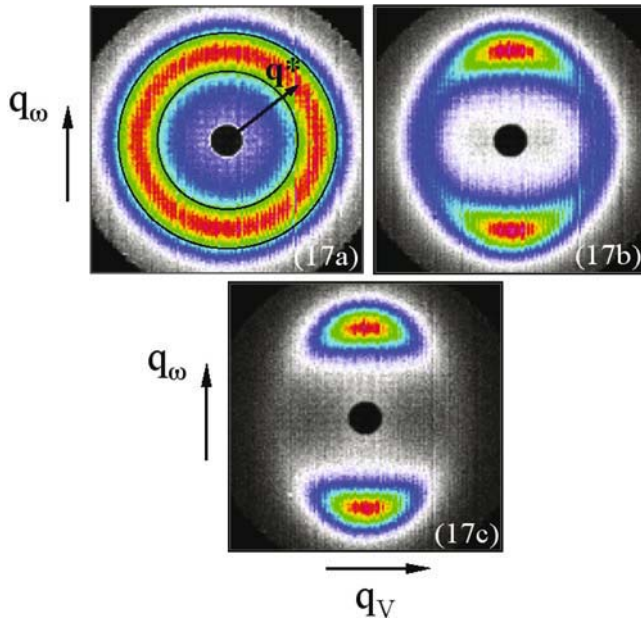
Chapter 17 Figure 39. Space-filling computer generated model of cholate.



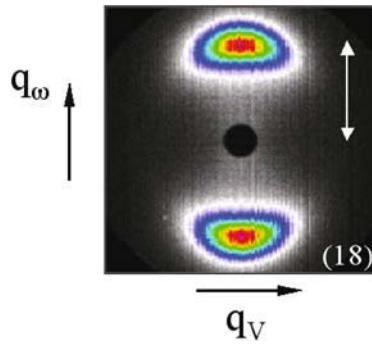
Chapter 19 Figure 15. Photographs showing the gap of a Couette cell containing a CPCI-Hex solution at concentrations $c_{\text{CPCI}} = 28.0 \text{ wt. } \%$ and $c_{\text{Hex}} = 3.9 \text{ wt. } \%$ (see Figures 11 and 12 for the rheology). The letters correspond to increasing shear rates. Photographs (A) and (F) are taken in the Newtonian regime and in the high shear rate branch, respectively. Photographs (B) to (E) are taken in the plateau region. Typical exposure times are of the order of milliseconds. The polarizer and analyzer are oriented so that the band close to the outer cylinder appears dark. With increasing shear rates, the bright nematic band fills up the gap progressively.



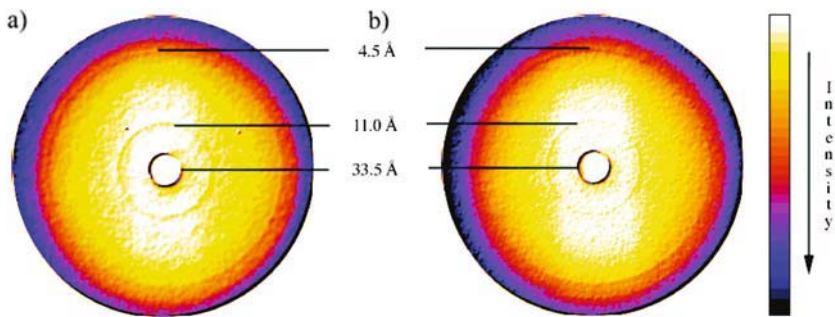
Chapter 19 Figure 16. Comparison between the flow birefringence of two CPCI-Hex solutions under shear. The solution on the left is isotropic at rest (same concentrations as in Figure 15) and the photograph is taken at a shear rate of 220 s^{-1} . This corresponds to the high shear rate branch of the flow curve. The solution on the right is nematic at rest ($c_{\text{CPCI}} = 29.1 \text{ wt. } \%$ and $c_{\text{Hex}} = 4.1 \text{ wt. } \%$) and the photograph represents the fluid sheared at 8.9 s^{-1} . In order to reduce the transmitted intensity, a green filter has been placed in the optical path before the solution.



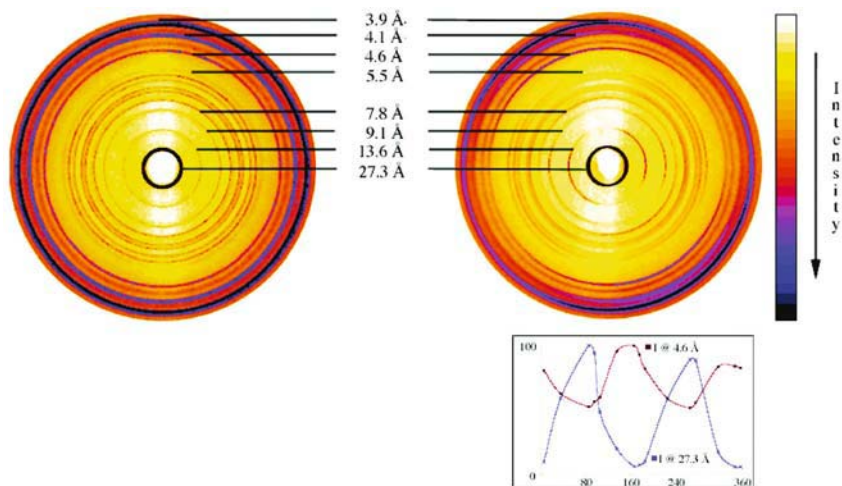
Chapter 19 Figure 17. Neutron scattering intensities obtained from a concentrated micellar solution under shear [121, 159]. Shear rates are $\dot{\gamma} = 0$ (a), 64 (b) and 213 s^{-1} (c). The data are recorded in the velocity-vorticity plane, corresponding to the wave-vectors \mathbf{q}_v and \mathbf{q}_ω . The maximum scattering at $q^* = 0.0996 \text{ \AA}^{-1}$ arises from steric interactions between micelles.



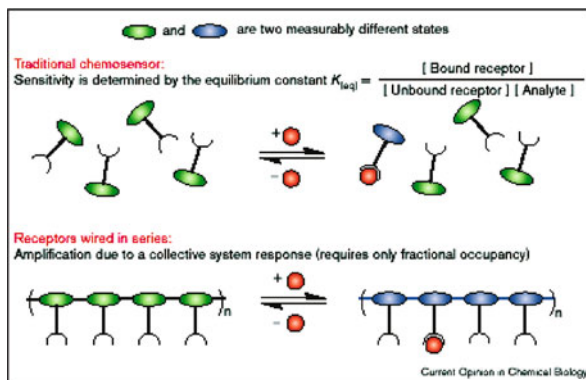
Chapter 19 Figure 18. Neutron scattering intensity obtained from nematic wormlike micelles under shear [119, 176] at the shear rate $\dot{\gamma} = 100 \text{ s}^{-1}$. As in Figure 17, the data are recorded in the velocity-vorticity plane. The scale for Figures 17 and 18 is given by the double-headed arrow which represents 0.1 \AA^{-1} .



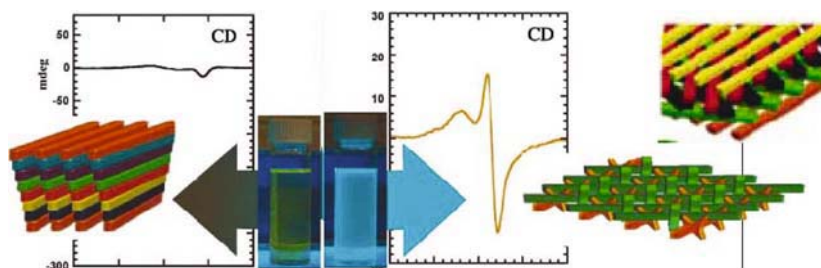
Chapter 20 Figure 11. X-ray image plates of (a) 8 mM **2**, 8 mM CaCl_2 , 50 mM Tris, pH 9, unoriented pattern. (b) 8 mM **2**, 8 mM CaCl_2 , 50 mM Tris, pH 9, oriented pattern [2].



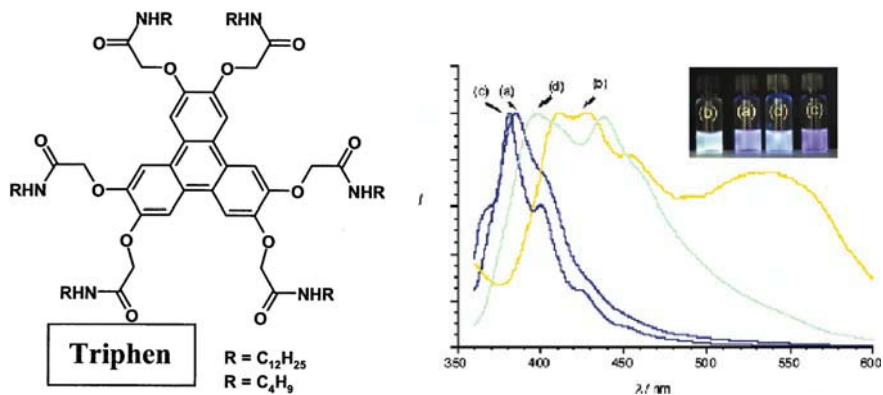
Chapter 20 Figure 12. X-ray image plates of powdered fibers of $3a \cdot Ca^{2+}$ (left) and uncrushed fibers of $3a \cdot Ca^{2+}$ (right). Inset: Graph of intensity variation with orientation of the diffraction bands at 27.3 Å and 4.6 Å [2].



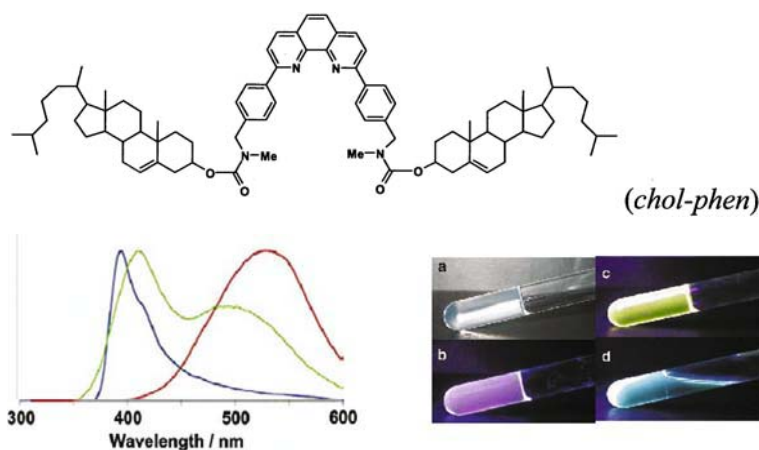
Chapter 24 Figure 2. Paradigm for novel chemosensors. (Reprinted with permission from [2]. Copyright (2000) Elsevier.)



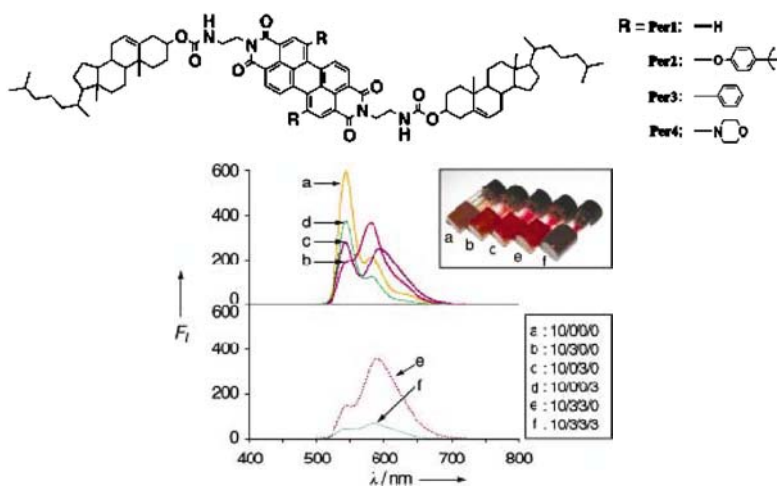
Chapter 24 Figure 5. Polymers including chiral monomer units: (left) colinear aggregation of non-interlocking polymer chains (8 layers of **AP1**, see Figure 4) resulting in a small circular dichroism and little fluorescence; (right) angled aggregation of interlocked polymer chains (2 or 5 layers of **AP2**, see Figure 4) resulting in a strong CD signal and a high fluorescence quantum yield. (Reprinted with permission from [4]. Copyright (2002) Wiley.)



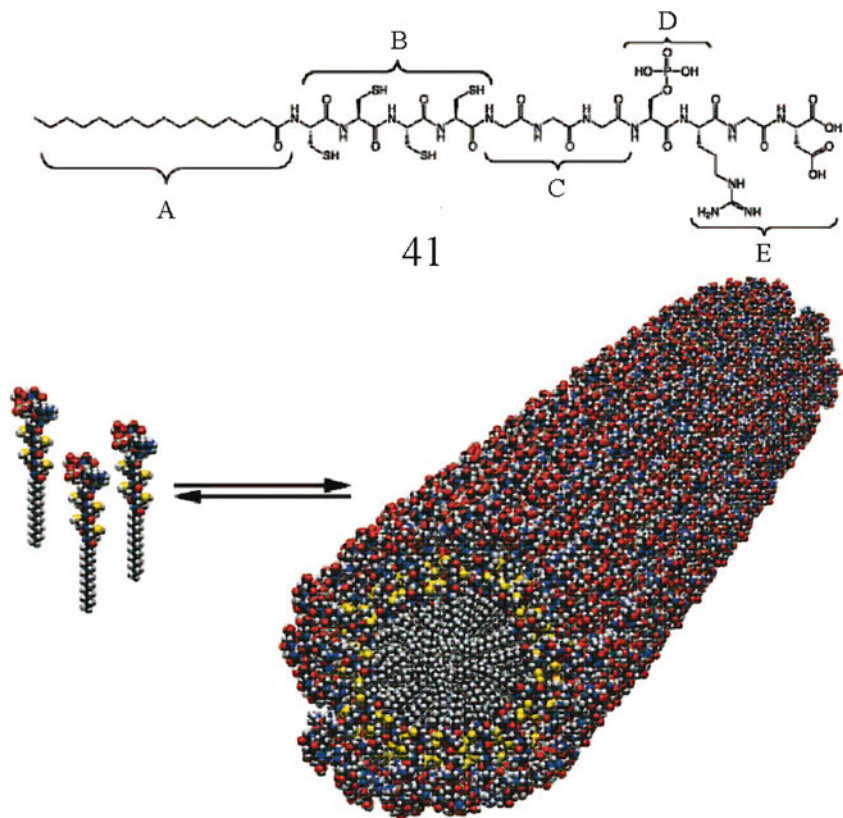
Chapter 24 Figure 14. Fluorescence spectra (λ_{exc} 350 nm) of **Triphen**- C_{12} : (a) chloroform solution (5×10^{-5} M); (b) cyclohexane gel (5×10^{-5} M); (c) chloroform solution (5×10^{-3} M); (d) cyclohexane gel (5×10^{-3} M). Inset: photographs of samples at $\lambda_{\text{exc}} = 365$ nm. (Reprinted with permission from [26]. Copyright (2003) Royal Society of Chemistry.)



Chapter 24 Figure 15. (left) Fluorescence spectra of chol-phen in a 1-propanol gel phase without TFA (blue), in a gel with 2 equiv. TFA (red), in a sol phase with 2 equiv. TFA at 90° C (green); (right) pictures of the same compound as a (a) gel, (b) UV-irradiated gel, (c) as in *b* but with 2 equiv. TFA added, and (d) as in *c* but at 90° C. (Reprinted with permission from [28]. Copyright (2003) Elsevier.)



Chapter 24 Figure 17. Fluorescence spectra of **Per1/Per2/Per3/Per4** mixed gels in *p*-xylene/1-propanol (3/1 v/v); $\lambda_{\text{ex}} = 457 \text{ nm}$. The numbers in the legend correspond to the molar ratios of **Per1/Per2/Per3/Per4** in the gels a-f. [**Per1**] = 0.5 wt/vol% (3.8 mM), [**Per2-4**] = 0 if denoted 0 in the legend, or 1.3 mM if denoted 3. Inset: a photograph displaying the **Per1/Per2/Per3/Per4** mixed gels (no irradiation). (Reprinted with permission from [30]. Copyright (2004) Wiley.)



Chapter 26 Figure 14. Peptide amphiphiles such as **41** self-assemble into mono-disperse elongated fibrils that form an entangled network in water. The formation of the fibers and stability of their gels can be controlled by pH and redox reactions (reprinted with permission from [31] and courtesy of S. I. Stupp, Northwestern University. Copyright (2001) American Association for the Advancement of Science).

INDEX

- ab initio* structure determination, powder
 - x-ray diffraction 338–9
- absolute intensities, small-angle scattering 278–9
- absorption spectroscopy 364–407
- acetic acid gels, templates for silica transcription 882, 883
- acetonitrile gels, 1,2-diamidocyclohexane gelator 475–6
- N*-acetyl-galactosamine-appended amino acid esters, hydrogelation 567–9
- achiral counter ions, twisted ribbon structures 726–7
- acrylate photopolymerization 774–5
 - ion conducting gels 788–91
 - liquid crystal gels 777–8, 780
- 2-acryloylamide-dodecane-1-sulfonic acid (ADSA)
 - racemic mixtures 500
 - transcription, cyclohexane-based gelators 887–8
- N*-acyl-11-aminoundecanoate (Au)
 - derivatives, reversible photo-induced phase transitions 849–50
- adhesion, peptide gel structure 108, 113
- ADSA *see* 2-acryloylamide-dodecane-1-sulfonic acid
- adsorption
 - correlated, side-chain association 36
 - silica onto tubule wall 881–2
- aerogels 6
 - from supercritical fluids 458–9, 524–5
 - IR spectroscopy 421–4
- AFM *see* atomic force microscopes
- ageing
 - kinetics of nucleation 158–60
 - soft glassy rheology 168–70, 176–87
- aggregates
 - conformations, linear self-assembly 83–4
 - discotic monomers model 90
 - ends, self-assembly 86–90
 - formation 436–7
 - interconnection 510–11
 - morphology, amphiphilic molecules 578–9
 - size, liquid component 532
 - solvent effects 650–1
 - structure
 - peptide concentration 103–4, 108–12
 - two component organic gelators 504–7
- aggregation
 - critical concentration 281
 - helical, supramolecular polymers 80–2
 - kinetic studies 317–19
 - modes, spectroscopic analysis 363–425
 - numbers
 - number-average 21
 - weight averages 24
 - secondary, kinetics of nucleation 158–60
- air bubble injection
 - gel assessment 745
 - liquid-crystalline phase gelation 750
- aldopyranose bolaamphiphiles, hydrogelators 630–1
- alignment tensor, nematogenic fluids 203–10
- aliphatic amines, organic gelators 463–6
- aliphatic chain length, gelating properties 463
- aliphatic quaternary ammonium derivatives 620
- n*-alkanamides, properties 470–8
- alkane chain length, gelation efficiency 451
- alkoxyanthracene derivatives, steroid linked 457
- alkoxyaryl molecules 454–9
- γ -alkoxybutyrolactone annulated tetraline derivative 495
- alkyl amines, saturated 463–4
- alkyl chain length
 - F(CF₂)₁₂(CH₂)*m*H 468
 - linear perfluoroalkyl alkanamides 499–500
- alkylammonium alkylcarbamate 519–21

- 1-alkyl-3-methylimidazolium 525–6
N-alkylpyridinium ions, ionic liquids 525–6
 ALS *see* aromatic linked steroids
 aluminum *sec*-butoxide, phosphoric acid esters 508
 Alzheimer's amyloid fibrils 114–15, 116
 AMBER program, anthracene molecular structure 422–4
 ambidextrous gelators
 amphiphilic gelators 584–6, 597–9
 bis(amino acid)oxalyl amides 618–20
 amide derivatives, with diyne units 501–2
 amines, transcription enabling moieties 870–1
 amino acid based, hydrogelators 616–25
 amino acid derivatives
 nematic liquid gelators 515–16
 organic gelators 478–84
 ammonium salts, organic gelators 466–7
 ammonium surfactants, gemini amphiphilic gelators 592–3
 amphiphilic aggregates, packing parameter 579
 amphiphilic molecules
 see also surfactants
 lyotropic liquid-crystals 746
 self-assembled fibrillar networks (SAFINs) 577–602
 amphiphilicity, bile acid hydrogelators 636–7
 amphoteric surfactants 673
 amplification
 chirality 90–1
 factor, spinodal decomposition 155–6
 amyloid fibrils, structure 114–15
 amylopectin, cryogenic-temperature transmission electron microscopy 265
 amylose gelation, cryogenic-temperature transmission electron microscopy 265
 analogs, dihydroxy bile salts 639–40
 analyte detection, fluorescent polymers 819–20
 androstane
 skeleton 554
 x-ray diffraction 353
 8-anilino-naphthalene-1-sulfonic acid (ANS), guest molecule 902
 anionic surfactant
 cationic polyelectrolyte system 267
 two component organic gelators 503–7
 anionic/cationic mixtures, wormlike micelles 673
 anisometric sections, small-angle scattering 293–5
 anisotropy
 aggregation forces 724
 dichroic absorption, IR spectroscopy 409
 annealing, crystal structure 334–5
 ANS *see* 8-anilino-naphthalene-1-sulfonic acid
 anthracene
 appended to cholesterol 555–6
 chromophore 374–9
 dichroic ratio, IR spectroscopy 422–4
 excimer fluorescence spectra 391–2
 linked to steroids 369–70
 anthracene-9-carboxylate, photo-induced phase transitions 847–8
 9-anthracenecarboxylic acid-*n*-alkylamine, light-responsive gels 919
 anthraquinone derivatives 457–8
 anthryloxy chromophore 379–82
 antibiotic-gelator, vancomycin-pyrene conjugate 620, 621
 antiparallel interactions, bisamides 473
 AP *see* associating polymers
 aqueous gels, micropolarity 405–6
 arborols, polyhydroxy dendritic bolaamphiphiles 631–2
 arginine peptides, pH-sensitive gelation 909
 aromatic linked steroids (ALS), UV and fluorescence spectroscopy 379–82
 aromatic units
 alkanamide gelators 473–4
 pyrene-appended 496–7
 shape of template for transcription 883
 aroyl *L*-cystine derivatives
 hydrogelators 617–18
 x-ray diffraction 359–60
 Arrhenius plot, gelation calorimetry 250–2
 art restoration, cleaning agents 929–36
 artifacts, circular dichroism spectroscopy 434
 artificial tri-block proteins, pH-sensitive gelation 910–11
 arylcyclohexanol 454–6
 assays, for enzymes 569
 assembly processes, organic hydrogel modeling 721–37
 associating mixtures, models 18–19
 associating polymers (AP) 58–63
 association constant
 multiple association 62
 pairwise association 49–50
 side chains 37
 thermodynamic theory 27
 associative forces, models 18
 associative molecules 69–73
 asymmetric drop shapes, wetting fibers 227–30

- asymmetric induction, helicity 889
asymmetric zwitterionic, gemini surfactants 633–4
atactic polystyrene in carbon disulfide 56–7
atomic force microscopes (AFM) 271
 guanosine/dodecane gel 487
atomic vectors, x-ray diffraction 332–3
attractive glasses, rheology 162
attractors, wormlike micelles 198
Au *see* *N*-acyl-11-aminoundecanoate derivatives
auto-indexing procedures, x-ray diffraction 340–1
Avrami equation, nucleation 151–3
axisymmetric drop shapes, wetting fibers 226–7
aza-crown appended gelators
 cholesterol complexation 903
 transcription templates 868–70
azapolycyclic arenes 495, 496
azobenzene
 appended cholesterols 556–8, 560–1
 bis-urea, polymorphism 406–7
 crown ether steroids 917–18
 cyclic *syn*-carbonate moiety 494
 photoresponsive gels 846
 sugar conjugates 629–30
 sugar derivatives 382–3
azoderivatives, probes for micropolarity 405–6
- β -hairpin peptides, hydrogels 626–7
 β -sheet complexes, peptide polyelectrolyte 127
BACO1 *see* 4-tert-butyl-1-arylcyclohexanol derivatives
ball test, tabletop rheology 245–6
band assignments, IR absorption spectroscopy 420–1
base treatment, cleaning gels 933–4
baseline spectrum, circular dichroism spectroscopy 433–4
bathochromic displacement, pyrene excitation spectra 393–4
batteries, ion conducting gels 781–2, 787, 790–1
Beer-Lambert law, optical spectroscopy 365
bending energy, chiral bilayer effect 656–7, 663
benzylamine, transcription facilitating 872–3
1,3:2,4-di-*O*-benzylidene-D-sorbitol 564–5, 566–7
4,6-*O*-benzylidene monosaccharides 565
N-benzyloxyxcarbonyl-L-valyl-L-valine *n*-octadecylamide 478–9
Bessel function, rod-like scatterers 283, 299
bicyclobisureas, gelation structures 491
bilayers
 ambidextrous gels 585–6
 chiral effect, stereochemistry 653–60
 chiral and twisted 598–9
 ribbons
 amphiphilic gelators 590–1
 aqueous gels 662–3
bile acids
 based, hydrogelators 636–40
 cryogenic-temperature transmission electron microscopy 261
 host-guest complexation 901–3
 trinitrofluorenone doped gel 804
binary gelator system, transcription templates 872
binary systems
 associating mixtures 19
 light-responsive gels 919
binding free energy
 non-gelling associations 27
 pairwise association 54
Bingham fluid, falling sphere test, tabletop rheology 245–6
binodal curve, thermodynamic concepts 133
binodal line, two-phase equilibrium 26
biocompatible materials
 IR spectroscopy 416–17
 microemulsion-based gelators 522
biomedical applications, hydrogels 614
biomimetics, magnetosensitive gels 809
biopolymers, protoporphyrin 658–9
biphasic regions, liquid-crystalline gels 749–51, 759, 762
biphenyl ester derivatives 462–3
birefringence
 organogels 514
 patterns 750, 751–2
 wormlike micelles 690–2, 696, 699–700
bis-amides, three heteroatoms 499
bis-arborol-tetrafulvalene gelator 384–5
2,3-bis-*n*-alkoxyanthracenes 458–9
2,3-bis-*n*-decyloxyanthracene, supercritical extraction of liquid 524–5
bis-urea cyclohexane, response to stress 916–17
bis-urea dicarboxylic acid
 pH dependence 730, 732
 structural analysis 731–7
bis-urea gelators
 cyclohexane appended 488

- electron conduction 801
- IR spectroscopy 418–19
- ultra violet-visible absorption spectra 489–90
- x-ray diffraction 354–6
- bis-ureido azobenzenes, light-responsive gels 921–2
- 1,2-bis(alkanoylamino)cyclohexane 514–15
- bisamides 472–3
- bis(amino acid)oxalyl amides, ambidextrous gelators 618–19
- bis(2-ethylhexyl) sodium sulfosuccinate 521–2
- bis(phenylalanine)maleic acid 481–2
- bixin, chiral bilayer effect 660
- block copolymers
 - chain, dimer formation 28–9
 - cylindrical self-assembly 673–4
- Boc- β -Ala-Aib- β -Ala-OMe, thermoreversible gel 414–16
- bolaamphiphiles
 - amphiphilic molecules 581
 - aqueous gels 661
 - boronic acid-appended 523–4
 - dendritic hydrogelators 631–2
 - hydrophobic chain length 589
 - nucleotide-appended 571–3
- boronic acid-appended gelators 523–4
- Bose-Einstein condensation 33–4
- bottlebrush, side-chain association 38
- Bragg scattering
 - intensities 341–4
 - reflections 329–30
- branching networks
 - importance in gel formation 729
 - small-angle scattering 304–5
- Bravais lattices, x-ray diffraction 328–9
- bridge conformations, liquid-crystalline gelation 762–4
- bubble rise test, tabletop rheology 246
- bubbling gas gelation 519
- bulk polarity, liquid component 530–2

- C18-C8DAB *see*
 - hexadecyloctyldimethylammonium bromide
- C₆₀ containing gels, electron conduction 803–4
- CAB *see* cholesterol
 - 4(2-anthryloxy)butanoate
- cac *see* critical aggregation concentration
- cadmium sulfide, transcription 874
- calcination, template removal 859
- calibration, tube inversion experiments 245

- calixarene-based gelators 453
- calorimetry, gelation phase diagrams 247–51
- cameras, cryogenic-temperature transmission electron microscopy 258, 271
- capillary length, wetting fibers 223
- capillary tube, liquid penetration 235
- CAQ *see* cholesteryl
 - anthraquinone-2-carboxylate
- carbamates, two heteroatoms 492–3
- carbohydrate based gelators 628–31
 - host-guest complexation 904–5
 - metal ion complexation 905–6
- carbon dioxide, trigger, responsive gels 907–8
- carbonyl stretching, IR spectroscopy 417
- carbonyl vibrator, organometallic gelator 417–18
- cascade theory, multiple association 61
- catalysis, applications 889
- cationic bis-quaternary ammonium surfactants 592–3
- cationic charge, deposition of silica 864, 865–7
- cationic polyelectrolyte system 267
- cationic/anionic mixtures 673
- Cauchy-Hadamard's theorem 45
- Cayley tree, pairwise association 48–9
- CD *see* circular dichroism
- CEP *see* critical endpoint
- cetylpyridinium bromide (CPBr) 671–2, 675
- cetylpyridinium chloride (CPCl) 672, 682, 683–4
- cetylpyridinium chloride sodium salicylate (CPCl-NaSal) 679, 683–4, 697–9, 701–2
- cetylpyridinium chloride-hexanol (CPCl-hex) 672, 679, 687–8, 691–2
- cetyltrimethylammonium bromide (CTAB)
 - cryogenic-temperature transmission electron microscopy 268
 - wormlike micelles 671, 672, 677–8, 679, 680
- cetyltrimethylammonium tosylate (CTAT) 194–200
- CEVS *see* controlled-environment vitrification system
- chains
 - ends, self-assembly 86–90
 - Gaussian, chain/ring formation 33
 - hydrophobic 589
 - length
 - gelating properties 463
 - linear perfluoroalkyl alkanamides 499–500

- open, non-gelling mixtures 32
- chaos
 - rheological 193–200
 - shear flow 195–210
- charge density, transcription 864, 865–7
- charge repulsion, water 651–3
- charge transfer
 - bands of luminescence 827–9
 - dual-component gelators 388–9, 567, 568
 - electron donor/acceptor 804
 - host-guest complexation 901
 - luminescence 818–19
 - spectroscopy 385–9
- charge transport, conjugated polymers 794–6
- chemical potentials
 - pairwise association 53
 - polymer chains 22–3
- chemo-responsive gels 899–914
- chemosensors, fluorescent polymers 819–20
- chimney, miscibility 44
- chiral amphiphiles
 - cryogenic-temperature transmission electron microscopy 262
 - fibrillar structures 601
- chiral anions, twisted ribbons 727–8
- chiral azobenzene, cyclic *syn*-carbonate moiety 494
- chiral bilayer effect, stereochemistry 653–60
- chiral 1,2-bis(alkanoylamino)cyclohexane 514–15
- chiral dialkylamide system 371–3
- chiral dimers, pyridinium cation 484
- chiral lipid-amphiphiles, aqueous gels 649–63
- chiral nematic *see* cholesteric
- chiral ordering, side-chain association 38–9
- chiral organics, structure 115–17
- chiral porphyrin-amphiphiles 649–63
- chiral rod-like units, self-assembly model 100–4
- chiral supramolecular structures 588–91
- chirality
 - amplification 90–1
 - gelation ability, amino acids 482
 - left-handed twisting 102–3
 - metal ion complexation 906–7
 - small-angle scattering 298–300
- chloroform donor, light harvesting 401–3
- chol-phen* *see* phenanthroline-cholesterols
- cholates 637–8
- cholestanyldioctadecyclamine 464–5
- cholesteric liquid crystal gels 778–9
 - (chiral nematic) phase 776
 - circular dichroism spectroscopy 441–4
- cholesterol 4(2-anthryloxy)butanoate (CAB) 369–70, 379–82
- cholesterols
 - azobenzene gelator 560–1
 - host-guest complexation 903
 - influence of liquid component 535
 - perylene gelator 558–9
 - structural diagram 876
 - transcription templates 868–71, 877–9
- cholesteryl anthraquinone-2-carboxylate (CAQ) 357–8
- cholesteryls
 - luminescence 825–6
 - transcription templates 870–1
- cholic acid trimer 638–9, 641
- cholic-amide-phenanthroline, IR spectroscopy 418
- chromophores
 - attachment to glutamide gelators 484
 - exciton spectrum 437–8
- circular dichroism (CD)
 - examples of application 369–74
 - spectroscopy 431–45
- cis-trans* isomerization, photochemical reactions 837–8, 844, 846
- cleaning agents, paintings 929–36
- closed-loop miscibility gap, non-gelling mixtures 39–41
- clusters
 - formation, thermodynamics 134–7
 - macroscopic micellization 45–6
 - phase composition 147–8, 150
 - size and number-average 21
- cmc *see* critical micellar concentration
- co-networks, gelation 69–73
- co-surfactants
 - pentanol 748–9
 - wormlike micelles 671–2
- coarsening, kinetics of nucleation 158–60
- coexistence regions, liquid crystals 43–4
- coherent scattering 279–81
- color filter, cholesterol-based perylene gelator 559
- comb block copolymers
 - non-gelling mixtures 35
 - side-chain association 38
- combinatorial approach, solid phase synthesis 631
- concentrated regimes, shear banding 687–96

- concentration effects
 two component organic gelators 504–7
 visible absorption spectra 367–9
- condensation, transcription 861–2, 863–4
- conducting gels 798–805
see also electron conduction
- conducting polymers 794–8
- conductivity, ion conducting gels 785–7, 788, 789
- conformation, chiral bilayer effect 656–7
- conical fiber, drop behaviour 230–1
- conjugated oligomers
 conducting LMOG gels 801–2
 polymer comparison 796–7
- conjugated polymers
 charge transport 794–6
 conducting gels 798–800
- constitutive properties
 definition 163
 soft glassy rheology (SGR) 173–4
- contrast variation, small-angle scattering 277
- controlled-environment vitrification system (CEVS) 255–7
- cooperativity, helical transition 87–8
- copolypeptides 263
- correction, spectrofluorimeter 366–7
- correction terms, work of critical cluster formation 140
- correlated adsorption, side-chain association 36
- cosmetic powders, x-ray diffraction 348–52
- Couette cells, wormlike micelles 690–2
- coulombic energy transfer 398
- counter ions
 ambidextrous gels 597–9
 wormlike micelles 672–3
- coupling, exciton spectrum 437–8, 441
- covalently attached, transcription facilitation 865–8, 878
- covalently linked, perfluoroalkylalkanes 467
- CP *see* critical point
- CPBr *see* cetylpyridinium bromide
- CPCl *see* cetylpyridinium chloride
- CPCl-hex *see* cetylpyridinium chloride-hexanol
- CPCl-Na-Sal *see* cetylpyridinium chloride sodium salicylate
- creep compliance, rheology 165, 188–9
- critical aggregation concentration (cac)
 absorption spectroscopy 367–9
 organic gelators 843
 small-angle scattering 281
- critical clusters
 basic thermodynamic concepts 134–7
 methods of determination of work 140–51
- critical endpoint (CEP), pairwise association 56
- critical gelation concentration 843
- critical micellar concentration (cmc)
 micellization theory 47–8
 wormlike micelles 669, 680
- critical point (CP)
 closed loops, non-gelling mixtures 39–40
 pairwise association 56
- critical shear rate, wormlike micelles 687–8
- critical solution temperature, non-gelling mixtures 39–40
- critical wave number, spinodal decomposition 156–7
- cross- β -structure, one-dimensional self-assembly 99–100
- cross-linking
 mechanism 56–63
 networks
 acrylate photopolymerization 774–5, 777–8
 ion conducting gels 781–91
 liquid crystal gels 775–80
- cross-section, differential scattering 284–9
- crown ether-appended cholesterol gelators 560–2
- 60-crown-20-macrocycle, ethers as organic gelators 452–3
- cryo-TEM *see* cryogenic-temperature transmission electron microscopy
- cryogen, properties for transmission electron microscopy 255, 257
- cryogenic-temperature transmission electron microscopy (cryo-TEM) 253–71
 structural analysis/modeling 721–2, 731–2, 734–7
- crystal structure
 comparison analysis 722
 x-ray diffraction 325–60
- crystalline gluconamides 656–7
- crystallization
 directing effect 873–4
 kinetics of nucleation 152–3
 steady-state nucleation rate 138–9
- CT *see* charge transfer
- CTAB *see* cetyltrimethylammonium bromide
- CTAT *see* cetyltrimethylammonium tosylate
- curvature
 bilayer ribbons 591

- defects, liquid-crystalline phase gelation 747, 752–3, 758
- surface solubility 865–6
- wetting fibers 225, 226
- curved one-dimensional stacking, IR absorption spectroscopy 424
- cyanate ligand, lactate linker 659
- cyclic bis-urea compounds, x-ray diffraction 354–6
- cyclic peptides, hydrogelators 624
- cyclic *syn*-carbonate moiety, chiral azobenzene 494
- cyclobutane-1,1-dicarboxylic acid 511–13
- cyclodipeptides, two heteroatoms 486
- cyclohexane appended bis-urea gelators, two heteroatoms 488
- cyclohexanes, transcription templates 886–8
- cyclohexanol derivatives, O-H stretching 410–12
- cyclo[(R)-phenylalanyl-(R)-histidyl], two heteroatoms 485
- cylindrical curvature, ribbons 726, 727, 732
- cylindrical symmetry, small-angle scattering 282–5
- L-cystine derivatives, x-ray diffraction 359–60
- cytoskeleton, responsive gel 896

- DARE *see* diarylethenes
- DBS *see* dibenzylidene sorbitol
- DDAB *see* didodecyltrimethylammonium bromide
- DDOA *see* 2,3-di-*n*-decycloxyanthracene
- DEA *see* double-end-anchored
- Debye-Bragg model, random nodes 302–3
- deformation tensor, soft glassy rheology 174
- degree of polymerization (DP)
 - multiple association 61
 - side chains 34
 - thermodynamic theory 24
- dehydration *see* dried samples
- dendritic bolaamphiphiles, hydrogelators 631–2
- dendritic peptides, dialkylamines 509
- densely cross-linked gels, liquid crystals 777
- density-functional approaches, work of critical cluster formation 144–6
- deoxycholic acid, supramolecular chirality 588–9
- 2'-deoxyuridine based, hydrogelators 635–6
- deoxyuridine-based gelators 571, 572
- depletion effects, kinetics of nucleation 153–4
- deposition of silica, cationic charge 864, 865–7
- depsipeptide hydrogelator 624
- design, three-dimensional networks, future research 537
- designer peptides, structure 115
- destacking aromatic moieties 496–7
- detergency, wetting fibers 228
- deterministic chaos, shear flow 195–210
- di- β -D-glucopyranosyl derivative 382–3
- 2,3-di-*n*-alkoxyanthracene, pH-dependent gelation 908–9
- di-*n*-alkoxybenzenes 458–9
- 2,3-di-*n*-decycloxyanthracene (DDOA)
 - fluorescence spectroscopy 374–9
 - IR spectroscopy 419–24
- 1,3:2,4-di-*O*-benzylidene sorbitol 459–62
- diacetylenes
 - electronic applications 806
 - polymerization 501
- diacrylates
 - liquid crystal gels 777–8, 779–80
 - phase-separated gels 790
- 2,3-di-*n*-alkoxyphenazines (DOP), phase transitions 848–9
- dialkylamines, dendritic peptides 509
- 1,2-diamidocyclohexanes, gelation 474–6
- diamines
 - guest, cholesterol gelators 560–2
 - transcription 870–1
- diarylethenes (DARE)
 - photochromism 840
 - reversible photo-induced phase transitions 846
- diastereoselection, host-guest complexation 903
- diastereomers, gelation ability 482
- dibenzoyl cysteine, hydrogelation 616
- dibenzylidene sorbitol (DBS)
 - circular dichroism spectroscopy 370–1, 372
 - differential scanning calorimetry 249–50
 - hydrogen bonding 409–10
- diblock copolymers, dimer formation 28–9
- dications, twisted ribbon structures 727–8
- dichloro derivative,
 - 2,3-di-*n*-decycloxyanthracene (DDOA) 378–9
- dichroic absorption
 - 2,3-di-*n*-decycloxyanthracene (DDOA) 419–24
 - general, IR spectroscopy 408–9

- 2,2-didodecylbarbituric acid,
2,4,6-triamino-5-hexadecylpyrimidine
507–8
- didodecyltrimethylammonium bromide
(DDAB)
amphiphilic molecules 580
cryogenic-temperature transmission
electron microscopy 266
- dielectricity constant, water 649
- differential absorption, circular dichroism
spectroscopy 433
- differential scanning calorimetry (DSC)
247–51
- differential scattering, cross-section,
small-angle scattering 284–5
- diffraction
one-dimensional crystals 311–12
structural analysis 722
x-ray scattering 325–60
- diffuse scattering, x-ray diffraction 327
- diffusion constants, ion conducting gels
789, 790
- dihydroxysterol 555
- dimeric form, *N-n*-octyl-D-gluconamide
471
- dimers
excited, spectroscopy 390–7
formation, thermodynamic theory 28–31
- N,N'*-dimethylpropanediamine,
guest-binding 561
- N,N'*-dimethylurea, two heteroatoms 488
- dimyristoyl phosphatidyl choline (DMPC)
748–64
- dioctadecyldimethylammonium chloride
(DODMAC) 259–60
- dioxybenzene ring, linked to
perfluoroalkylalkyl chains 470
- direct imaging, cryogenic-temperature
transmission electron microscopy 253–7
- direct lattice, x-ray diffraction 329–30
- direct methods, phase calculation 333–4
- director turbulence, nematic liquid crystals
201
- discotics
helical-transition temperature 88–9
self-assembly 82–3
- disorder, gel versus fiber formation 737
- disordered materials, x-ray diffraction 326
- disorientation, dimer formation 29
- dissolution heat, tertiary amines 529
- dissymmetric shapes, gemini aggregates
594–6
- distribution function, aggregates 20–5
- N,N'*-disubstituted ureas, two heteroatoms
488
- dithienylethenes, light-responsive gels
922–3
- diyne units, polymerization 501–2
- DMPC *see* dimyristoyl phosphatidyl choline
- N*-dodecanoyl-(*D*- and *L*-) serine 262
- n*-dodecanoyl-serine 623
- dodecyl maltoside (DOM) 262
- N*-dodecyl-glyconamides, chiral bilayer
effect 653–4
- dodecyltrimethylammonium chloride
(DOTAC) 264, 266–7
- DODMAC *see*
dioctadecyldimethylammonium chloride
- DOM *see* dodecyl maltoside
- domain size, steroid/hydrocarbon gels, effect
of liquid component 532
- donor-acceptor complexes 385–6
- donor-acceptor interactions, host-guest
complexation 901
- DOP *see* 2,3-di-*n*-alkoxyphenazines
- doped gels, luminescence 833–5
- DOTAC *see* dodecyltrimethylammonium
chloride
- double critical point, non-gelling mixtures
39
- double helix, transcribed silica 886
- double-end-anchored PEG-surfactants
(DEA-PEG-surfactants), liquid-crystalline
phase gelation 761–4
- DP *see* degree of polymerization
- dried samples, structural analysis techniques
722, 731
- drop motion, heterogeneous fiber 230–1
- drop shapes, wetting fibers 225–30
- drug delivery systems 265–6
PEG-lipids 748
- drug polymorphism, powder x-ray diffraction
352–3
- DSC *see* differential scanning calorimetry
- dual-component gelators, charge transfer
567, 568
- dual-component organogels 804–5
- dual-component sugar based gels, charge
transfer complexes 388–9
- dyes
luminescent doped organogels 820–2,
833–5
sensitizer, ionic liquids gelation 526
- dynamic entanglements 583
- dynamic mechanical analysis 755–7
- dynamics, gel phase 641–2
- E* *see* end-cap energy
- ECL *see* electro-generated
chemiluminescence

- eclipsed, triphenylene chromophores,
excimer fluorescence 395–7
- ee *see* enantiomeric excess
- efficiency of gelation
n-alkanamides 472
cholestanyldioctadecyclamine 464–5
- elastic modulus, 1,3:2,4-di-*O*-benzylidene
sorbitol 460–2
- elastic scattering 279–81
- elastic turbulence, polymer solution flow
200–1
- elastically effective chains 66–9
- elasticity of organogels, liquid component
533–4
- Eldridge-Ferry method
networks structure 64–5
poly(vinyl alcohol) 67
- electric fields, liquid crystal gels 776–9
- electrical switching behaviour, liquid crystal
gels 777–8
- electrically induced light scattering, liquid
crystal gels 778
- electro optical devices
ion conducting gels 773–5, 781–91
liquid crystal gels 773–80
- electro-generated chemiluminescence (ECL)
783–4
- electrochemical luminescence 783–4
- electrochromic devices 782–3, 790
- electrocyclizations, photochemical reactions
838–41
- electron conduction 793–808, 810
- electron density maps, x-ray diffraction
336–7
- electron donor-acceptor complexes 385–9
- electron donor-acceptor interactions 804–5
- electron microscopy
liquid-crystalline phase gelation 752–3
structural analysis techniques 722
- electron-acceptor molecule 513
- electron-exchange transfer 398–9
- electronic absorption spectroscopy
364–407
- electronic excitation energy transfer 397–9
- electronic materials, templating media
805–8
- electrooptical response, liquid-crystalline
gels 516
- electrophoresis, acetonitrile gels,
1,2-diamidocyclohexanes 475
- electrostatic interactions, transcription
865–7
- electrostatic repulsion, water 651–3
- elliptical cross-sections, small-angle
scattering 294–5, 297
- ellipticity, circular dichroism spectroscopy
433
- elongated aggregates, structural modeling
724–5
- elongational shear, anisotropic scattering
patterns 316
- embedding time delay vectors, wormlike
micelles 198
- emission spectroscopy 364–407
excitation energy transfer 397
- enantiomeric excess (*ee*), twisted ribbons
726
- enantiomers
chiral dialkylamide system 372
circular dichroism spectroscopy 442–3
1,3:2,4-di-*O*-benzylidene-*D*-sorbitol
409–10
- end-cap energy (*E*), wormlike micelles 669
- energy transfer
luminescence 819, 824–35
UV and fluorescence spectroscopy
397–405
- engineering functional hydrogels 119–27
- entanglements, amphiphilic gels 583
- enterococci, vancomycin 573–4
- enthalpy
gelation calorimetry 251–2
melting, tertiary amines 529
- entropy
disorientation, dimer formation 29
Flory-Huggins 20
melting 470
- enzyme assays 569
- ephedrinium counter ions 660–1
- equilibrium constant
aggregates, definition 23
chains, non-gelling mixtures 32
pairwise association 48–9
- equilibrium properties, wormlike micelles
667–86
- ergodicity, soft glassy rheology (SGR) 172
- ester bonds, structural diagram 876
- esterification 556–7
- ethers, organic gelators 451–3
- bis-(2-ethylhexyl) sodium sulfosuccinate
503–7
- eutectic point, dimer formation 31
- Ewald construction, oriented fibers 311–12
- excimers
emission, luminescence 818, 827–9
UV and fluorescence spectroscopy
390–7
- excitation energy transfer 397–9
- excitation spectra, optical spectroscopy 366
- excited states, luminescence 817–19

- exciton coupling, circular dichroism spectroscopy 437–8, 441
- exciton spectrum, circular dichroism spectroscopy 431, 435–45
- exciton splitting, optical spectroscopy 365–6
- experimental tests, physical gels 744–5
- experiments
- self-assembling peptide gels 105–12
 - shear flow, viscoelastic materials 195–201, 218
- extremum, work of critical cluster formation 145, 150
- extrusion of gel test, tabletop rheology 247
- face-to-face stacking, π -systems 798, 801
- facial amphiphilicity, bile acid hydrogelators 636–7
- falling sphere test, tabletop rheology 245–6
- fatty acids
- charge repulsion in water 651–3
 - substituted, organic gelators 454
- $F(\text{CF}_2)_{10}(\text{CH}_2)_{12}\text{H}$, linear perfluoroalkylalkane gelators 467–8
- $F(\text{CF}_2)_n(\text{CH}_2)_m\text{H}$, perfluoroalkylalkanes 467
- ferrogels, magnetic field sensitive materials 809
- FETs *see* field effect transistors
- FFR *see* freeze-fracture-replication
- fibers
- interlinked, two-component gels 510–11
 - morphology, polymerization 502–3
 - wetting 223–36
- fibril orientation, sheer stress 459
- fibrillar systems, structure factor 307–10
- fibrous networks
- bis-urea dicarboxylic acid hydrogelators 732–3, 735–7
 - viscous liquid/gel comparison 728–9
- field effect transistors (FETs), thin-film conducting gels 805
- films
- flow, network of fibers 233–4
 - phenylenevinylenes, organic gelators 457
 - structural analysis techniques 722, 731
- finite clusters, number-average of chains 24
- first-order phase transitions
- kinetics of nucleation 153–4
 - thermodynamics 248
- fixation, cryogenic-temperature transmission electron microscopy 254–5
- fixed multiplicity model 63
- flexibility
- expression, small-angle scattering 293
 - wormlike micelles 674–8
- flip flop shear bands, rheological chaos 203
- flocculation, peptide hydrogels 120–1
- Flory-Huggins, mixing entropy 20, 25
- Flory's χ -parameter 20–1
- renormalization 25
 - supramolecular liquid crystals 43
- Flory's treatment, pairwise association 53–8
- flow
- network of fibers 231–2
 - shear and scattering experiments, small-angle scattering 315–16
- flow birefringence
- wormlike micelles
 - concentrated regime 690–2, 696
 - semi dilute regime 699–700
- flow curve, soft glassy rheology 167–8, 175–6, 187
- flow phase diagrams, wormlike micelles 697–9
- flow-microstructure coupling, shear-banding model 210–11
- fluorescence
- definition 817–18
 - polymers 819–20
- fluorescence spectroscopy 364–407
- fluorescent gels, cholesterol-based gelators 557–9
- fluorescent organogels, proton-sensitive 403–5
- fluorocarbon segment, amphiphilic molecules 580
- fluoroscatter cell, circular dichroism spectroscopy 435
- $F_n H_m \text{see } F(\text{CF}_2)_n(\text{CH}_2)_m\text{H}$
- folding, β -sheet peptides, hydrogelation 626–7
- form-factors
- small-angle scattering
 - disk 300–2
 - rod-like scatterers 282–92
- Fourier series, crystal structure, x-ray diffraction 331–2, 336–7
- Fourier Transform Infra Red (FTIR) spectrometers 407
- fractal dimensions, wormlike micelles 198
- fractal features, networks, small-angle scattering 304–5
- fractured xerogels, arylcyclohexanol 455–6
- free energy
- multiple association 59–60

- orientational, supramolecular liquid
 - crystals 41–2
 - of reaction, thermodynamic theory 20–5
- free enthalpy, spinodal decomposition 154
- free volume theory, conductivity 787, 788, 789
- freeze-fracture electron microscopy 752–3
- freeze-fracture-replication (FFR) 257–8
- front-face illumination
 - 2,3-di-*n*-decyloxyanthracene (DDOA) 377–8
 - optical spectroscopy 367
- FTIR *see* Fourier Transform Infra Red
- fullerenes
 - derivatives, organic gelators 527
 - effect on porphyrins, circular dichroism spectroscopy 439–41
 - electron conduction 803–4
 - host-guest complexation 904
- fumarate isomer, photoinduced gelation, bis(phenylalanine)maleic acid 481–2
- future perspectives, hydrogels 643–4

- G-quartets, guanosine structure 439
- gas bubbling gelation, latent gelators 519
- gases, responsive gel systems 907–8
- gauche-bend, crystalline gluconamides, chiral bilayer effect 656–8
- Gaussian chain, chain/ring formation 33
- Gaussian (saddle-like) curvature, twisted ribbon structures 726, 727, 731–2
- gel
 - anatomy 359–60
 - concentrations 321
 - definitions 242, 744–5
 - diagnostic tests 242–7
 - electrolytes, *see also* ion conducting gels
 - formation
 - aromatic linked steroids 380–2
 - bis-urea dicarboxylic acid 735–7
 - introduction 241–2
 - induction, crown ether-appended cholesterol gelators 560–2
 - mediated energy transfer, luminescence 829–32
 - phase, dynamics of hydrogelators 641–2
 - point, pairwise association 52
 - removal, art cleaning gels 935
 - stability, polymerizable organic gelators 500–3
 - structure, optical spectroscopic methods 363–425
- gelatin
 - microemulsion-based gelators 521–2
 - mixed networks structure 73
- gelation
 - classification 18
 - with co-networks 69–73
 - concentration, junction multiplicity 63–4
 - differential scanning calorimetry (DSC) 248–51
 - efficiency
 - n*-alkanamides 472
 - alkane gelators 451
 - cholestanyldioctadecyclamine, aliphatic amine gelator 464–5
 - inverted, mixed networks 73
 - kinetic studies, small-angle scattering 318–19
 - liquid-crystalline phases 743–67
 - mechanism, L-lysine derivatives 481
 - pairwise association 48–58
 - poly(vinyl alcohol)(PVA) 65–6
 - role of liquid 527–35
 - supercritical fluids 524–5
 - theory, macroscopic clusters 47
- gelators
 - best type, small-angle scattering 320–1
 - general properties 449–537
 - strand structure, x-ray diffraction 357
 - structure, shape of transcribed material 875–88
- gel–sol phase transitions
 - irreversible photoinduction 845
 - reversible photoinduction 846–50
- gemini amphiphile molecules 591–9
- gemini organic gelators, polymethylene spacer, L-serine derivatives 480–1
- gemini surfactants
 - ammonium salts, organic gelators 466–7
 - hydrogelators 632–4
 - wormlike micelles 673
- gemini *n*-2-*n*/tartrate systems, amphiphilic gelators 597–9
- generalized Ostwald's rule of stages, work of critical cluster formation 147–9
- Gibbs free energy, basic thermodynamic concepts 134–7
- Gibb's method
 - non-equilibrium states 150
 - work of critical cluster formation 140–4
- Gibbs–D–hem relation 25
- globular scatterers, fibrillar systems, small-angle scattering 308–9
- glucon-diastereomer, chiral bilayer effect 653–4
- gluconamides
 - chiral bilayer effect 653–5, 663
 - gelation behaviour 628

- glutamate derivatives, xerogel structure 482–4
- glutaric acid peptides, pH-sensitive gelation 909
- glycodendrimers, hydrogelators 630
- glycodeoxycholate, hydrogelators 637–8
- glycosylated amino acid derivatives
 - physico-responsive gels 915
 - spectroscopy 416–17
- gravity, drop shapes on a fiber 228–9
- grid cooling, cryogenic-temperature
 - transmission electron microscopy 257
- group frequencies, IR spectroscopy 408
- growth spurt, helical transition 89
- growth template, inorganic fibers,
 - 2,3-bis-*n*-alkoxyanthracenes 458–9
- guanosine
 - circular dichroism spectroscopy 439, 444
 - derivative/dodecane gel, atomic force micrographs (AFM) 487
 - derivatives, two heteroatoms 486–7
- guest-binding, crown ether-appended
 - cholesterol gelators 560–2
- Guinier plots, small-angle scattering analysis 286, 287, 291–2

- H-bonding, IR spectroscopy 412–24
- Hamilton's receptors, host-guest
 - complexation 900–1
- handedness, chirality amplification 93
- Hankel representation, real space data 316–17
- hard sphere model, small-angle scattering 308–9
- head groups, amphiphilic molecules 580–1
- heat of dissolution, tertiary amines 529
- helical aggregation, supramolecular polymers 80–2
- helical ribbons
 - amphiphilic gelators 590–1
 - curvature types 726, 727, 732
 - microstructure, L-serine derivatives 479–80
- helical self-assembly 94–5
 - supramolecular polymers 79–80
- helical transition, cooperativity 87–9
- helicity
 - asymmetric induction, organogel template 889
 - chirality amplification 91–3
 - reflected in transcribed silica 881
- helix
 - induction, side-chain association 36, 38–9
 - small-angle scattering 298–300
 - structures, aqueous gels 661–3
- hemoglobin gel, circular dichroism spectroscopy 440–2
- hetero-dimerization, thermodynamic theory 28
- hetero-transfer, UV and fluorescence spectroscopy 397–9
- heteroatoms
 - one, organic gelators 451–70
 - three, organic gelators 498–500
 - two, organic gelators 470–98
- heterogeneous fiber, wetting of fibers 230–1
- hexadecyloctyldimethylammonium bromide (C18-C8DAB) 701
- n*-hexatriacontane
 - gel transition temperature 453
 - platelet structure 451, 452
- historical perspectives, molecular hydrogels 615–16
- HMHEC *see* hydrophobically modified hydroxyethyl cellulose
- homo-transfer, UV and fluorescence spectroscopy 398
- homodromic hydrogen bond,
 - N-octyl-D-glyconamide, chiral bilayer effect 655–6
- homogeneous networks, small-angle scattering 303–4
- host-guest complexation, chemo-responsive gels 900–5
- host-guest interaction, cholesterol-based gelators 561
- hourglass, phase diagrams, hydrated polymer solutions 40–1
- hybrid gels, electron-donor/acceptor interactions 805
- hydration, water-soluble polymers 34–5, 39–41
- hydrogelators
 - amphiphilic gelators 585–6
 - molecular 613–44
- hydrogels
 - future perspectives 643–4
 - liquid crystalline phase 743–67
 - material science applications 642–3
 - properties and structure 640–2
 - self-assembling peptide gels 100
- hydrogen bonds
 - dimer formation 31
 - host-guest complexation 900–1
 - intermolecular, calixarene-based gelators 453
 - multiple, bis-urea compounds, IR spectroscopy 418–19

- supramolecular liquid crystals 41–4
- tertiary amines, organic gelators 464
- hydrogen-bond donation, transcription templates 870–1
- hydrolysis, transcription 861–2
- hydrophilic shell, surfactant/phenol gel 504–7
- hydrophilicity
 - self-assembled fibrillar networks 578
 - transcription, cyclohexane-based gelators 887
- hydrophobes, associating polymers 58
- hydrophobic chains
 - amphiphilic molecules 580–1
 - length, amphiphilic gelator morphology 589
- hydrophobic forces, peptide gel structure 108, 113
- hydrophobic interactions, alkyl groups 414
- hydrophobically modified hydroxyethyl cellulose (HMHEC) 266–7
- hydrophobicity
 - gelation efficiency, amino acid derivatives 478–9
 - self-assembled fibrillar networks 578
- 12-hydroxyoctadecanoic acid
 - organic gelators 454
 - structural model 455
- (S)-2-hydroxy-2-(3-phenoxyphenyl)acetonitrile, two heteroatoms 485
- hyperchromism, aromatic units 496–7
- ideally homogeneous networks, small-angle scattering 303–4
- imidazole derivatives,
 - cyclobutane-1,1-dicarboxylic acid, two-component gels 511–13
- imposed strain, soft glassy rheology (SGR) model 176–84
- imposed stress, soft glassy rheology (SGR) model 184–7
- impregnation rate, film flow in network of fibers 234–5
- incident beam angle, x-ray diffraction 329
- incoherent scattering, small-angle scattering 280
- indexing, powder x-ray diffraction 340–1
- induced orientation
 - gemini aggregate morphology 596, 598–600
 - organogels, small-angle scattering 316
- inelastic scattering
 - cryogenic-temperature transmission electron microscopy 254
 - x-ray diffraction 327
- infrared spectroscopy 407–24
 - applications 409–24
- inhomogeneous networks, 1,3:2,4-di-*O*-benzylidene sorbitol gelator 460
- initial conditions, chaotic dynamics 198
- initial states, thermodynamic concepts 133–4
- inorganic gelators 513–14
- inorganic photochromes 843–4
- inorganic structure templating, electronic applications 806–8
- myo*-inositol derivatives 497–8
- instability, wormlike micelles 702
- intensity, measurement in small-angle scattering 279, 284, 297, 319
- interatomic vectors, x-ray diffraction 332
- intercalated species, surfactant/phenol gel 505–7
- interfacial tension
 - wetting of fibers 223–4
 - work of critical cluster formation 148
- intermittency, nematogenic fluids 204, 211
- intermolecular donor-acceptor complexes 385–6
- intermolecular hydrogen bonds
 - calixarene-based gelators 453
 - IR spectroscopy 412–24
- internal clock, soft glassy rheology 174
- internal free energy, cluster 20
- intramolecular hydrogen bonds, two heteroatoms 492
- invasion, network of fibers 231–6
- inverse photochromism *see* negative photochromism
- inverted gelation, mixed networks 73
- ion conducting gels
 - applications 781–4
 - batteries 781–2, 787, 790–1
 - chemical cross-links 787–91
 - electro optical devices 773–5, 781–91
 - electrochemical luminescence 783–4
 - electrochromic devices 782–3
 - phase-separated gels 790
 - photoelectric devices 784
 - properties 785–7
 - single phase gels 788–9
 - structured gels 790–1
- ion mobility, ion conducting gels 786
- ion-pairing, hydrogelation 620
- ionic liquids, gelation 525–7
- ionization states, peptide hydrogels 119–27
- ionomers, fibrillar systems 308–9
- IR *see* infrared
- Irbetsartan, powder x-ray diffraction 353, 354

- irradiation, template removal, transcription 859
- irradiation-induced polymerization 841–2
- irreversible photo-induced phase transitions, LMOGs 844–5
- Ising chain, two-state model 85
- isoandrosterone derivatives, steroid based gelators 555
- isomerization
photochemical 825–7, 841–6, 917–19, 921–2
thermal 484
- isomers, 1,2-diamidocyclohexanes 474–6
- isophthalic acid appended urea derivatives, organic gelators with two heteroatoms 489
- isosbestic points,
2,3-di-*n*-decyloxyanthracene (DDOA) 378
- isothermal gelation
alkylammonium alkylcarbamate 519–21
cryogenic-temperature transmission electron microscopy 264
- isotopic composition, small-angle scattering 277
- isotropic phase
nematic phase transition, wormlike micelles 678–80, 687–96
thermotropic liquid crystals 775
- isotropic-to-nematic phase boundary, wormlike micelles 678–9, 687
- isotropic-to-nematic phase transition
liquid-crystalline gels 518
peptide gels 117–18
peptide hydrogels 122
- jamming, soft glassy rheology (SGR) 190
- junction zones, small-angle scattering 300–7
- junctions
elastically effective chains 67
multiplicity, gelation concentration 63–4
- Kappa-carrageenan (KC),
cryogenic-temperature transmission electron microscopy 264
- KCl concentrations, structural transitions 268
- kinetic studies, small-angle scattering 317–19
- Kolmogorov-Avrami equation, kinetics of nucleation 151–3
- Krafft temperature
amphiphilic gels 582–3
gemini aggregate morphology 594
- L-alanine, H-bonding, IR spectroscopy 412
- L-cystine derivatives, x-ray diffraction 359–60
- L-lysine derivatives
H-bonding, IR spectroscopy 412–14
polymethylene spacer, gemini organic gelators 480–1
- L-serine derivatives, different microstructures 479–80
- lactate linker, cyanate ligand, chiral bilayer effect 659
- lactosylamine, hydrogelators 628–9
- lamella L_{α} phase, lyotropic liquid-crystals 746–65
- lamellar gel aggregates, transcription process 880
- lanthanides, luminescent doped organogels 823–4
- Laplace pressure, wet fiber interface 224–5
- large- Q asymptotic behavior, small-angle scattering 289–90
- latent gelators 519–21
- lattice crystals, x-ray diffraction 328–30
- lattice theory, polymer solutions 19, 20
- laurionite, powder x-ray diffraction 351–2
- N*-lauroyl-L-glutamic acid, liquid-crystalline gels 514
- layering transition, dense lamellar phase 200
- LCA *see* lithocholic acid
- LD *see* linear dichroism
- lecithin, microemulsion-based gelators 521–2
- left-handed twisting, rod-like monomers 102–3
- Leslie-Ericksen theory 205
- leucine-zipper, pH-sensitive gelation 910–11
- library, sugar-based gelators 567–9
- Lifshitz point, dimer formation 31
- light harvesting
gelation assisted, UV and fluorescence spectroscopy 401–3
hydrogel system 620–1
steroid based gelators 558–9
supramolecular hydrogels, UV and fluorescence spectroscopy 399–401
- light scattering, structural studies 276
- light-emitting diodes *see* organic light-emitting diodes
- light-responsive gels 917–24
- lightly cross-linked gels, liquid crystals 777–8, 779
- line defects, thermodynamic energy,
liquid-crystalline phase gelation 758–9

- line tension, gemini aggregate morphology 594–6
- linear amines, gelation efficiency 464
- linear dichroism (LD)
 - birefringence 440
 - circular dichroism spectroscopy 434, 440–1
- linear perfluoroalkyl alkanamides, alkyl chain length 499–500
- linear perfluoroalkylalkanes gelators 467–70
- linear rheological response
 - function 165
 - imposed strain 177–82
 - imposed stress 184–5
 - without ageing 175–6
- linear rheology, wormlike micelles 680–5
- linear self-assembly, supramolecular polymers 83–5
- linear viscoelastic domains 533–4
- linearity, rheology 164
- linked fibers, two-component gels 510–11
- lipid-amphiphiles, aqueous gels 649–63
- lipophilic guanosine derivatives, nucleobase gelators 573
- liquid, role in gelation 527–35
- liquid crystal gels
 - acrylate photopolymerization 774–5, 777–8, 780
 - applications 777–80
 - cholesteric 778–9
 - cross linkage 777–8
 - electro optical devices 773–80
 - nematic 778
 - patterned 779–80
 - thermotropic 775–80
 - types 776–80
- liquid crystals
 - circular dichroism spectroscopy 439–42
 - hydrogen-bonded supramolecular 41–4
 - miscibility chimney 44
- liquid ethane, cryogenic-temperature transmission electron microscopy 255, 257
- liquid molecules, gelator strands 532
- liquid nitrogen, cryogenic-temperature transmission electron microscopy 255, 257
- liquid-crystalline gels 514–19
- liquid-crystalline phases
 - definitions 745–7
 - gelation 743–65
 - lamella L_{α} phase liquid-crystals 746–65
 - topological defects 748–51, 752–3, 757–64
 - wormlike micelles 692
- lithium ion batteries, ion conducting gels 781–2, 787, 790–1
- lithium transport number, ion conducting gels 787, 790
- lithocholate tubes, small-angle scattering 296–8
- lithocholic acid (LCA),
 - cryogenic-temperature transmission electron microscopy 261–2
- living polymers, wormlike micelles 193–200
- LMOGs *see* low molecular-mass organic gelators
- long rod-like scatterers, small-angle scattering 290
- long-range ordering, x-ray diffraction 327–9
- loop conformations 762–4
- low molecular-mass organic gelators (LMOGs)
 - chiral organic 115–17, 128
 - cryogenic-temperature transmission electron microscopy 258–71
 - electron conduction 800–5
 - inorganic structure templating 806–8
 - magnetic applications 809
 - photopolymerization, electronic applications 806
 - phototunable gels 835–50
 - properties 449–537
 - sol–gel phase transitions
 - photo-induced 844–50
 - photochromism 843–4
 - structural modeling 721–37
- low- Q asymptotic behavior, small-angle scattering 285–6
- luminescence
 - applications 819–24
 - cholesterol-appended perylenes 558–9
 - definitions 817–18
 - doped gels 820–4, 833–5
 - energy transfer 829–32
 - eximers/CT-bands 827–9
 - gels 817–35
 - phase-induced intensity enhancement 825–7
- Lyapunov exponent
 - nematic hydrodynamics 217–18
 - wormlike micelles 194, 198–9, 205, 209
- lyotropic lamellar phase, rheological oscillations 200

- lyotropic liquid-crystalline gels,
 - 1-alkyl-3-methylimidazolium, ionic liquids 526
- lyotropic liquid-crystals
 - definition 745–6
 - hexagonal H_α phase 765–6
 - lamella L_α phase 746–65
- lyotropic nematic gels, liquid-crystalline gels 514
- lyotropism, networks, small-angle scattering 307
- lysine based, unsymmetrical bolaamphiphiles 617
- lysozyme, cryogenic-temperature
 - transmission electron microscopy 263–4
- macroscopic clusters, micellization 45–6
- macroscopic properties, work of critical cluster formation 146
- magnetosensitive gels 793, 808–10
- majority effect, non-gelling mixtures 39
- majority-rules, chirality amplification 91
- maleic-amide compound,
 - photo-isomerization 919–21
- maltosylamine, hydrogelators 628–9
- material science applications, hydrogels 642–3
- matrix polarity, 1,3:2,4-di-*O*-benzyliden-D-sorbitol 567
- Maxwellian fluids, wormlike micelles 195–6, 680–3, 701, 706
- mechanical properties, studies of organogels, small-angle scattering 320
- mechanical reversibility, amphiphilic gels 583–4
- mechanical stress
 - physico-responsive gels 915–17
 - responsive molecular gels 898–9
- mechanisms of gelation
 - organogel networks, L-lysine derivatives 481
 - research 536
- melting enthalpy, tertiary amines 529
- melting temperature, circular dichroism spectroscopy 436
- membrane chirality, gemini aggregate morphology 599
- membranes
 - curvature, liquid-crystalline phase gelation 747, 752–3, 757–64
 - lamella L_α phase liquid-crystals 746–65
- memory
 - liquid crystal gels 778
 - porous xerogels, cholesterol-based gelators 562–3
- meniscus, liquid penetration, network of fibers 231
- merocyanine-appended spiropyran, thermal isomerization 484
- mesogenic cores, supramolecular liquid crystals 41–2, 44
- mesoscopic elements, soft glassy materials 170
- metal binding sites, organic gelators, transcription templates 868–70
- metal ion complexation, responsive gels 905–7
- metal-carbene carbohydrate amphiphile
 - circular dichroism spectroscopy 373–4
 - gelator, IR spectroscopy 417–18
- metal-deposition, silica matrix, transcription 879–80
- metallic salts, organic solvents, wormlike micelle comparison 673
- metastability
 - basic thermodynamic concepts 134–7
 - soft glassy rheology 170–6
- metastable phases, supramolecular liquid crystals 43–4
- metastable states, amphiphilic gels 582–3
- methyl 4,6-*O*-benzylidene- α -D-glucopyranoside, sugar-based gelators 565–6
- micelles
 - critical concentration 47
 - helix, gluconamide, aqueous gels 663
 - L-lysine derivatives, IR spectroscopy 414
 - length predictions 670, 671
 - reverse, organic solvents 673
 - wormlike
 - equilibrium properties 667–86
 - rheological chaos 193–200
 - rheology 667–707
 - shear banding transitions 667–8, 686–706
- micellization, theory 44–8
- micro-crystalline gels 64–5
- micro-crystalline junctions, pairwise association 58
- microemulsion, two component organic gelators 509
- microemulsion-based gelators 521–2
- micrographs, cryogenic-temperature
 - transmission electron microscopy 254, 260
- micrometer-scale structures
 - bis-urea dicarboxylic acid hydrogelators 734–7
- modeling 723, 728–9

- microphases
 - dimer formation 31
 - separation transitions (MST) 29–31
 - side-chain association 38
- micropolarity, aqueous gels, UV and fluorescence spectroscopy 405–6
- microscopy
 - fluorescence 632, 826, 834
 - optical 73, 122, 307, 444, 573, 633, 751–2
 - scanning electron 350, 455, 556–7, 935
 - transmission electron 277, 389, 556, 905
 - cryo 253–71, 650, 674, 721–2, 731–2
- microstrain broadening, powder x-ray diffraction 346–7
- microstructures
 - cryogenic-temperature transmission electron microscopy 258
 - powder x-ray diffraction 345–7
- microwave irradiation, template removal, transcription 859
- mineralization, LMOG templating 807–8
- mini-max junction, multiple association 62–3
- mirror-image symmetry, optical spectroscopy 365
- miscibility chimney, liquid crystals 44
- miscibility gap
 - closed loop, non-gelling mixtures 39–41
 - dimer formation 31
- mixed gels, luminescence 830–2
- mixed networks, classification 70–3
- mixing entropy, Flory-Huggins 20
- mobility, soft glassy rheology (SGR) 189
- models
 - aggregated states of discotic monomers 90
 - anthracene molecular structure, IR spectroscopy 422–4
 - associating mixtures 18–19
 - Avrami 151–3
 - Cahn-Hilliard 145–6, 154–7
 - Eldridge-Ferry 64–5
 - gel formation 528
 - Ising chain 85
 - Oosawa-Kasai, helical assembly 80–1, 88
 - organic hydrogel structures 721–37
 - Ostwald-De Woele 934
 - phasing, x-ray diffraction 331–4
 - poly(ethylene glycol), gelation 757–9
 - reptation-reaction, wormlike micelles 195, 203, 682–3, 684
 - ribbon morphology 725–8, 731–2
 - self-assembling chiral rod-like units 100–12
 - shear thickening, rheological chaos 202
 - soft glassy rheology (SGR) 170–6
 - statistical 148
 - structure of hydrogels 641–2
 - structure of 12-hydroxyoctadecanoic acid 455
 - thermodynamic 18–27
 - van der Waals 146, 154
 - Witten-Sander cluster aggregation 159
 - Zimm-Bragg 81, 85
- molecular aggregates, IR spectroscopy 408
- molecular assembly processes, organic hydrogel modeling 722, 728–9
- molecular bottlebrush, side-chain association 38
- molecular chirality, amphiphilicity in gel fibers 589–91
- molecular hydrogels 613–44
- molecular imprinting, cholesterol-based gelators 562–3
- molecular packing, gel versus fiber formation 735–7
- molecular shape, liquid component of gel 530
- molecular-scale structures
 - bis-urea dicarboxylic acid hydrogelators 732–4
 - modeling 723, 724
- monitor, pyrene excimer, formation of vancomycin hydrogel 394–5
- mono-urea derivatives, hydrogelators 623
- monoacrylate, liquid crystal gels 777
- monodispersity, tubular cross-sections, small-angle scattering 296–7
- monomers
 - amphiphilic molecules 580–1
 - concentration, aggregate structure 103–4
 - gelation, influence of liquid component 535
- monosignate spectrum, circular dichroism spectroscopy 444
- morph of gelator network, influence of liquid component 530–4
- morphology
 - aggregates of amphiphilic molecules 578–9
 - linear secondary amine gelators 464, 465, 466
 - x-ray diffraction 325–60
- motion control, magnetosensitive gels 809
- MST *see* microphase separation transitions
- multi-phase patterns, powder x-ray diffraction 344–5

- multilamellar spheres, microstructure,
 - L-serine derivatives 479–80
- multiple association, theory 58–63
- multiple chemical equilibrium conditions 23
- multiple intermolecular hydrogen bonds,
 - bis-urea compounds, IR spectroscopy 418–19
- multiple junctions, networks structure 63–9
- multiple solution, phase calculation, x-ray diffraction 334
- myo*-inositol derivatives, optically-active,
 - organic gelators with two heteroatoms 497–8
- N*-lauroylglutamic acid, circular dichroism spectroscopy 442–4
- nano-biotechnology
 - steroid-based gelators 574
 - sugar-based gelators 574
- nanometer-scale structures
 - bis-urea dicarboxylic acid hydrogelators 731–2
 - modeling 724–8
- nanoparticles
 - luminescent doped organogels 823, 833–4
 - magnetsensitive gels 808
 - semiconductor spatial organization 808
- nanorods, organic gel incorporation 810
- nanostructures 270–1
 - organic gelator templating 807–8
 - small-angle scattering 275–322
- nanotubes
 - lithocholic acid, cryogenic-temperature transmission electron microscopy 261–2
 - wetting of fibers 236
- naphthalene sulfonate, fluorescence spectra 400–1
- naphthopyrans (NP), photochromism 840
- negative photochromism 837, 838
- nematic hydrodynamics, spatio-temporal rheochaos 211–18
- nematic hydrogels, self-assembling peptide gels 100, 117–19
- nematic interaction parameter,
 - supramolecular liquid crystals 42
- nematic liquid crystals
 - director turbulence 201
 - gelators, amino acid derivatives 515–16
 - gels 778
 - phase, wormlike micelles 678–80, 687–96
 - thermotropic phase 775–6
- nematic Schlieren texture, liquid-crystalline phase gelation 750, 752
- nematogenic fluids, temporal chaos 203–10
- net helicity, chirality amplification 91–3
- networks
 - formation, thermodynamic theory 18–27
 - inhomogeneous, 1,3:2,4-di-*O*-benzylidene sorbitol gelator 460
 - liquid penetration 231–6
 - with multiple junctions 63–9
 - small-angle scattering 300–7
 - visco-elastic properties 66–9
- neutral micelles, wormlike micelles 669
- neutron powder diffraction 347–8, 349
- neutron scattering
 - see also* small-angle neutron scattering
 - structural analysis 275–322
 - under shear, wormlike micelles 693–5, 696
- nodes, junction zones, small-angle scattering 302–3
- noise reduction, circular dichroism spectroscopy 434
- noise temperature, soft glassy rheology (SGR) 189
- non-conducting gels, electronic applications 805–8
- non-conjugated polymers, conducting gels 800
- non-covalently attached, charged moieties,
 - transcription facilitation 868–70
- non-equilibrium states, kinetics of nucleation 150
- non-gelling mixtures, thermodynamic theory 27–44
- non-homogeneous flows, wormlike micelles 687
- non-radiative energy transfer 398
- nonlinear rheology
 - imposed strain 182–4
 - imposed stress 186–7
 - wormlike micelles 686
- NP *see* naphthopyrans
- nuclear density maps, crystal structure, x-ray diffraction 336–7
- nuclear magnetic resonance (NMR)
 - wormlike micelles 700–1
 - under shear 695–6
- nucleation
 - basic thermodynamic concepts 134–54
 - helical supramolecular polymers 86–7
- nucleobase gelators 570–3
- nucleotide bolaamphiphiles
 - hydrogelators 633
 - nucleobase gelators 571–3

- number density, rod-like particles, small-angle scattering 317–19
- number-average cluster size, thermodynamic theory 21
- O-H stretching,
 - 4-tert-butyl-1-arylcyclohexanol derivatives, IR spectroscopy 410–12
- N*-octyl gluconamide, structural analysis, liquid-crystalline gels 516–17
- N*-*n*-octyl-*D*-gluconamide, organic gelators 470–1
- N*-octyl-*D*-glyconamides, chiral bilayer effect 653–6
- 4-octylbenzohydroxamic acid, organic gelators with two heteroatoms 493
- oligo (phenylene vinylenes) (OPVs) gelators, photophysical properties 801–2
 - light harvesting, UV and fluorescence spectroscopy 401–3
 - luminescent gels 826–7, 834
- oligomers
 - amphiphilic molecules 581
 - electron conduction 796–8, 801–2
- oligonucleotides, circular dichroism spectroscopy 439
- oligopeptide based, hydrogelators 616–25
- oligothiophenes, electron conduction 797–8, 801–2
- olive oil and monoglyceride gel,
 - nanostructure, cryogenic-temperature transmission electron microscopy 270–1
- on-the-grid cooling, cryogenic-temperature transmission electron microscopy 257
- one-dimensional aggregates
 - n*-alkanamides, organic gelators 472
 - urea-appended porphyrin 492
- one-dimensional crystals, diffraction patterns, small-angle scattering 311–12
- one-dimensional self-assembly 99–100
- one-dimensional stacking,
 - 2,3-di-*n*-decyloxyanthracene (DDOA), IR absorption spectroscopy 424
- Oosawa-Kasai model, helical assembly 80–1, 88
- opacity
 - gel, influence of liquid component 533
 - variation, 1,3:2,4-di-*O*-benzylidene sorbitol gelator 460
- open chains, non-gelling mixtures 32
- optical activity
 - chirality amplification 94
 - oriented structures, glutamate aggregates 484
 - optical microscopy, polarized light observations, liquid-crystalline phase gelation 751–2
 - optical spectroscopic methods 363–425
 - optical switching, light-responsive gels 924
 - optically-active, *myo*-inositol derivatives, organic gelators with two heteroatoms 497–8
 - optimized structure, anthracene molecular model, IR spectroscopy 422–4
 - OPVs *see* oligo (phenylene vinylenes)
 - order-disorder transition, x-ray diffraction 326
 - organic gelators
 - classification 450–527
 - one heteroatom 451–70
 - polymerizable 500–3
 - three heteroatoms 498–500
 - two heteroatoms 470–98
 - organic hydrogels
 - bis-urea dicarboxylic acid hydrogelators 729–37
 - structural analysis techniques 722, 731–4
 - structural modeling 721–37
 - x-ray diffraction 357–9
 - organic light-emitting diodes (OLEDs), oligo (phenylene vinylenes) 801
 - organic solvents
 - art restoration 929–31
 - metallic salts, wormlike micelle comparison 673
 - reverse micelles 673
 - organic thin film transistors, conjugated oligomers 796
 - organogelators, amphiphilic gelators 585–6
 - organogels
 - luminescent doping 820–4
 - network formation, L-lysine derivatives 481
 - orientation effects, small-angle scattering 316
 - properties 449–537
 - self-assembling peptide gels 100
 - organometallic chromophore, circular dichroism spectroscopy 373–4
 - organometallic fibers, small-angle scattering 286–7
 - organometallic gelators 513–14
 - metal-carbene carbohydrate amphiphile, IR spectroscopy 417–18
 - organometallic wires, magnetic properties 809

- orientation
 - correlated domains, networks, small-angle scattering 305–7
 - dichroic absorption, IR spectroscopy 408–9
 - fibers
 - DDOA, IR absorption spectroscopy 422–4
 - gemini aggregate morphology 595–6
 - small-angle scattering 311–16
 - optical activity, glutamate aggregates 484
 - shear stress, 2,3-bis-*n*-alkoxyanthracenes 459
- orientational free energy, supramolecular liquid crystals 41–2
- oscillations
 - rheological, wormlike micelles 194, 200
 - spatio-temporal rheological chaos 210–18
- oscillatory strain, rheological ageing 180–2
- oscillatory stress, rheological ageing 185
- osmotic pressure, polymer solutions 26
- Ostwald ripening 9, 153, 158, 934
- Ostwald-De Woele model 934
- Ostwald's rule of stages, generalized 147–9
- ovalbumin, cryogenic-temperature transmission electron microscopy 263–4
- over-ageing, rheological ageing 182

- P₁ 1-1, self-assembling peptide gel experiments 105–8
- P₁ 1-2, self-assembling peptide gel experiments 108–12
- π - π stacking, UV and fluorescence spectroscopy 374–85
- π -systems, face-to-face stacking 798, 801
- π -conjugated polymers, electron conduction 794, 795–6
- packing parameter, amphiphilic aggregates 579, 600
- paintings, cleaning agents 929–36
- pairwise association, gelation 48–58
- palmitate, counter ions, gemini surfactants 633
- paper, flow through network of fibers 231–6
- parallel interactions, bisamide organic gelators 473
- partially disordered compounds, powder x-ray diffraction 348–53
- particle-size broadening, powder x-ray diffraction 345–7
- partition function, aggregate conformations 84
- pathological amyloid fibrils 114–15
- pattern decomposition, powder x-ray diffraction 342–3
- patterned gels, liquid crystal gels 779–80
- Patterson methods, x-ray diffraction 331–3
- PEG *see* poly(ethylene glycol)
- penetration rates, network of fibers 231–2
- pentanol, liquid-crystalline phase system co-surfactant 748–9
- peptide amphiphiles
 - hydrogelators 624–5
 - pH-sensitive gelation 911–12
- β -peptide based hydrogelators 625–7
- peptide hydrogels, functional properties 119–27
- peptide polyelectrolyte β -sheet complexes 127
- peptide units, gelation efficiency 478
- peptides
 - concentration, aggregate structure 103–4
 - de novo* design, properties 107
 - dialkylamines, two component organic gelators 509
 - nematic hydrogels 117–19
 - organic gelators with two heteroatoms 484–8
 - self-assembling gels 99–130
 - self-assembly, experiments 105–12
- percolation theory, gelation 249
- perfluoroalkyl alkanamides, alkyl chain length 499–500
- perfluoroalkyl alkanes, organic gelators 467
- perfluoroalkylalkyl chains, linked to dioxybenzene ring, organic gelators 470
- persistence length, wormlike micelles 674–5, 677–8
- perylene
 - cholesterol-based gelators 558–9
 - dicholesteryl derivatives, luminescent gels 830–2
- pH dependence, gel formation 730, 732
- pH effects
 - polyacrylic acid-based cleaning gels 933–4
 - L-serine-dodecylamide aggregate formation 650–1
- pH sensitive
 - gelators, photochrome mixtures 848–9
 - responsive gel systems 908–14
- pharmaceutical molecules, powder x-ray diffraction 348–53
- phase anisotropy, liquid-crystals 745
- phase behaviour
 - peptide hydrogels 119–27
 - phase-separated ion conducting gels 790
 - wormlike micelles 678–80

- phase diagrams
 - chiral rod-like units 104
 - hydrated polymer solutions 40–1
 - liquid crystals 43
 - liquid-crystalline phase gelation 750–1
 - mixed networks 72
 - nematogenic fluids 206
 - symmetric blend, associating diblock copolymers 30
 - using calorimetry 247–51
 - using tabletop rheology 242–7
- phase separation
 - ion conducting gels 790
 - thermodynamic theory 26
- phase transition
 - first-order, kinetics of nucleation 153–4
 - isotropic-to-nematic in peptide gels 117–18
 - temperatures, liquid-crystalline gels 517–18
 - thermodynamic concepts 132–4
- phase-induced intensity enhancement, luminescent LMOG-based gels 825–7
- phases, thermotropic liquid crystals 775–6
- phasing models, x-ray diffraction 331–4
- 1,3-phenanthroline, protonation, UV and fluorescence spectroscopy 403
- phenanthroline-cholesterols (*chol-phen*), luminescent LMOG-based gels 829–30
- phenyl esters, organic gelators 462–3
- phenylene vinylenes
 - luminescence 826–7
 - organic gelators 456–7
- phosgenite, powder x-ray diffraction 351–2
- phosphatidylcholine-phosphatidic acid mixtures, cryogenic-temperature transmission electron microscopy 262
- phosphines, latent gelators 521
- phosphocholine-derived zwitterionic surfactants 584
- phospholipid gels, cryogenic-temperature transmission electron microscopy 260–1
- phospholipid membranes 767
 - see also* membranes
- phosphonium salts, organic gelators 466–7
- phosphonobile acids, bile acid based hydrogelators 640
- phosphorescence, definition 817–18
- phosphoric acid esters, aluminum *sec*-butoxide, two component gels 508
- phosphorylated serine 873–4
- photo-induced phase transitions
 - irreversible 844–5
 - reversible 846–50
- photo-responsive gels 917–24
 - cholesterol-based gelators 559–60
- photocells *see* photoelectric devices
- photochemical reactions
 - cis-trans isomerization 837–8
 - electrocyclizations 838–41
 - type P-photochromism 836
- photochemical switching, light-responsive gels 922
- photochromic moiety, light-responsive gels 918–19
- photochromism
 - cis-trans isomerization 837–8
 - definition 835–6
 - electrocyclizations 838–41
 - organic gelators 843–50
 - phototunable gels 835–44
 - polymer gels 841–3
- photocyclization, dithienylethenes, light-responsive gels 923
- photoelectric devices (photocells), ion conducting gels 784
- photoinduced gelation, bis(phenylalanine)maleic acid 481–2
- photoinduced sol-gel transition, cholesterol-based gelators 559–60
- photoisomerization, hydrogelation 619
- photopolymerization
 - acrylates 774–5, 777–8, 780, 791
 - electronic applications 806
- photoreaction, gel transformation, organic gelators 477
- photoresponsive gels 817–50
 - luminescence 817–35
 - photo-induced phase transitions 844–50
 - photochromism 835–44
- photosensitization, UV and fluorescence spectroscopy 397
- phototunable gels 835–50
- photovoltaic devices, C₆₀ containing gels 803–4
- phthalocyanine gelators, electron conduction 802–3
- physical gels, definitions 744–5
- physical triggers, responsive gel systems 914–24
- plain fibers, small-angle scattering 282–92
- platelet structure, *n*-hexatriacontane 451, 452
- platelet-like junction zones, small-angle scattering 300–2
- platforms, molecular orientation, cholesterol-based gelators 554–63
- PM-IRLD *see* polarization modulation infrared linear dichroism

- PNEI *see* poly(N-acetyleneimine)
- PNIPAM *see* poly(N-isopropylacrylamide)
- polarity of liquid component, gelation 530–2
- polarization, dichroic absorption, IR spectroscopy 408–9
- polarization modulation infrared linear dichroism (PM-IRLD), gemini aggregate morphology 596
- polarized light
- circular dichroism spectroscopy 432
 - observations, liquid-crystalline phase gelation 750, 751–2
 - wormlike micelles, concentrated regime 690–2
- polarized spectra,
- 2,3-di-*n*-decyloxyanthracene (DDOA), IR absorption spectroscopy 422–4
- polyallylamine (PAA), art cleaning gels 935
- polycationic organophosphorus dendrimers, hydrogelators 634–5, 636
- polycondensations
- n*-alkanamide gelators 476
 - silica adsorption onto tubule wall 881–2
 - tetraethylorthosilicate, sol-gel transcription 587–8
- polydispersity
- multiple association 58–9
 - polymer mixtures, free energy 20
 - small-angle scattering 286–9
- polyelectrolyte micelles, wormlike micelles 670
- poly(ethylene glycol) diacrylate (PEGDA), ion conducting gels 788–9
- poly(ethylene glycol) (PEG)
- cryogenic-temperature transmission electron microscopy 265
- lipids
- liquid-crystalline phase gelation 748–64
 - chemical modification 759–61
 - double-end-anchored 761–4
 - model 757–9
 - observations 751–7
 - water content effects 749–51
- polyhydroxy dendritic bolamphiphiles, arborols, hydrogelators 631–2
- polymerizable organic gelators 500–3
- electronic applications 806
- polymerization
- amphiphilic gelators 586–7
 - fiber morphology 502–3
 - macroscopic clusters 47
 - thermal line, chain/ring formation 34
- polymers
- conventional lattice view 19
 - elastic turbulence 200–1
 - electron conduction 794–800
 - influence of liquid component in gels 535
 - organic solvent swelling/leaching 929–30
 - photochromic gels 841–3
 - unfolding, polyacrylic acid-based cleaning gels 933
 - wormlike micelle comparison 668, 702
- polymethylene spacer, gemini organic gelators, L-lysine derivatives 480–1
- polymorphism
- pharmaceutical compounds, powder x-ray diffraction 352–3
 - UV-vis spectroscopy 406–7
- poly(N-acetyleneimine) (PNEI), photochromic polymer gels 842–3
- poly(N-isopropylacrylamide) (PNIPAM), photochromic polymer gels 841–2
- polysaccharides, cryogenic-temperature transmission electron microscopy 265
- polythiophenes (PT), electron conduction 797–8
- poly(vinyl alcohol) (PVA)
- Eldridge-Ferry plot 67
 - networks structure 65–6
- poorly organized systems, x-ray diffraction 325–60
- pore filling, film flow in network of fibers 234
- Porod's plot, small-angle scattering 290–1
- porous xerogels, cholesterol-based gelators 562–3
- porphyrin gelator, UV and fluorescence spectroscopy 383–4
- porphyrin gelators, electron conduction 802
- porphyrin-amphiphiles, aqueous gels 649–63
- porphyrin-appended cholesterol, nucleobase gelators 570
- porphyrin-C₆₀ gelators, photovoltaic/electronic devices 803–4
- porphyrins
- chiral bilayer effect 659
 - circular dichroism spectroscopy 439–41
 - fullerene, host-guest complexation 904
- positive photochromism 837, 838
- positively charged centers, organic gelators 865–70
- postgel regime
- pairwise association 52–8
 - thermodynamic theory 19, 20, 24–5

- powders
 - recrystallized, glutamate derivatives 482–4
 - x-ray diffraction 337–47
 - applications 348–53
 - indexing 340–1
- pre-aggregation, absorption spectroscopy 367–9
- precursor
 - incorporation into gelator 873
 - tetralkoxysilanes 861
- preformed excimers, UV and fluorescence spectroscopy 391
- pregel regime
 - pairwise association 51
 - thermodynamic theory 19, 23–4
- primary *n*-alkanamines, latent gelators 519–21
- primary structures
 - see also* molecular-scale structures
 - molecular modeling 723–4, 732
- probability of association, pairwise association 49–50
- probes
 - micropolarity in aqueous gels 405–6
 - pyrene excimer 392–4
 - sodium deoxycholate 392–4
- profile refinement, powder x-ray diffraction 341–5
- protein-based conducting gels 800
- protein-surfactant systems 263–4
- proteins, pH-sensitive gelation 910–11
- proton-sensitive
 - fluorescence detection 558
 - fluorescent organogels 403–5
- protoporphyrin, chiral bilayer effect 658–9
- pseudo-crystalline amphiphilic gelators 585
- pseudo-ephedrinium counter ions 660–1
- PT *see* polythiophene
- pyrene
 - appended, gelators with two heteroatoms 495–7
 - derivatives
 - luminescent gels 827–8
 - two-component organogelators 386–8
 - excimer, fluorescence spectra 391–4
 - vancomycin 394–5, 573–4
- pyridinium cation, chiral dimers 484
- Q*-resolution, small-angle scattering 278
- quadratic potential wells, soft glassy rheology (SGR) 172
- quadruple helix, chiral bilayer effect 653–4, 663
- quaternary ammonium derivatives, hydrogelation 620–2
- quenching
 - naphthalene, UV and fluorescence spectroscopy 401
 - UV and fluorescence spectroscopy 401–3
- racemic
 - 2-acryloylamide-dodecane-1-sulfonic acid 500
 - 1,3:2,4-di-O-benzylidene-D-sorbitol, IR spectroscopy 409–10
 - 12-hydroxyoctadecanoic acid, model structure 455
- radial polydispersity, small-angle scattering 287–9
- radiation, small-angle scattering 275–322
- radiative energy transfer, UV and fluorescence spectroscopy 398
- radius of curvature, solubility, sol-gel chemistry 865–6
- radius of fiber, drop behaviour 229–30
- Raman spectroscopy 407–8
- random nodes, small-angle scattering 302–3
- random phase approximation (RPA), dimer formation 30
- Rayleigh-Plateau instability, wetting of fibers 224–5
- re-binding saccharide, xylose complexes, cholesterol-based gelators 562–3
- real space
 - crystal structure, x-ray diffraction 334–5
 - small-angle scattering 277, 316–17
- reciprocal lattice, x-ray diffraction 329–30
- reciprocal space, small-angle scattering 277
- recrystallized powder, glutamate derivatives 482–4
- rectangular polydisperse fibers, small-angle scattering 289
- rectangular sections, small-angle scattering 294
- red-shifted fluorescence spectrum, 2,3-di-*n*-decyloxyanthracene (DDOA) 376–7
- redox polymers, electron conduction 794
- reference states, work of critical cluster formation 141–4, 147
- refinement stage, crystal structure, x-ray diffraction 335–6, 341–5
- relaxation rates, rheological responses 188
- reptation-reaction models, wormlike micelles 195, 203, 682–3, 684
- repulsive glasses, soft glassy rheology 162
- resorc[4]arene, hydrogelators 634–5

- resorcinarene, pH-sensitive hydrogelation 912–13
- response function, rheology 165
- responsive gels 896–9
- reverse gels, polymerization, amphiphilic gelators 587
- reverse micelles
 microemulsion-based gelators 522
 organic solvents 673
- reversibility, mechanical, amphiphilic gels 583–4
- reversible network formation 19
- reversible reactions
 photo-induced phase transitions 846–50
 photochromism 835–44
- rheo-reversibility, art cleaning gels 936
- rheology
 ageing 176–87
 definitions 163–70
 equilibrium properties 667–86
 liquid-crystalline phase gelation 755–7
 shear banding transitions 667–8, 686–706
 slender-body suspensions 202
 soft glassy 162–90
 spatio-temporal investigations 210–18
 surfactant solutions 194
 wormlike micelles 193–200, 667–707
- rheopexy 8
- Rhodamine B acceptor, light harvesting, UV and fluorescence spectroscopy 401–3
- ribbons
 amphiphilic gelators 590–1
 microstructure, L-serine derivatives 479–80
 morphology, structural modeling 725–8, 731–2
 self-assembling peptide gel experiments 105–12
- Rietveld profile method, powder x-ray diffraction 338–9, 342–5
- right-angle observation
 2,3-di-*n*-decyloxanthracene (DDOA) 377
 optical spectroscopy 367
- right-handed helical ribbons, L-serine derivatives 479–80
- ring closure, light-responsive gels 922–3
- ring formation, non-gelling mixtures 31–4
- ringing gels, liquid-crystal comparison 766–7
- rod-like monomers, self-assembly 100–4
- rod-like scatterers 282–92
- rods, orientation and scattering anisotropy, small-angle scattering 313–15
- RPA *see* random phase approximation
- saccharide library 569
- saccharide-based gelators, electron donors/acceptors 804
- saddle points
 kinetics of nucleation 150
 work of critical cluster formation 145
- saddle-like (Gaussian) curvature, twisted ribbons 726, 727, 731–2
- SAFINs *see* self-assembling fibrillar networks
- salicylate/amphiphile, hydrogelators 635–6
- salt concentrations, structural transitions 267–70
- salts
see also metallic salts
 wormlike micelles 671
- SANS *see* small-angle neutron scattering
- SAS *see* small-angle scattering
- saturated alkyl amines, organic gelators 463–4
- SAXS *see* small angle X-ray scattering
- scaffold, network 262–3
- scaling laws, wormlike micelles 683–5
- scattering
 function, wormlike micelles 675–6
 profiles, small-angle scattering 322
 small-angle, structural analysis 275–322
- schematic representation
 cholesterol-azobenzene gelators 876
 transcription 880, 884
- Schlieren texture, liquid-crystalline phase gelation 750, 751–2
- Schmidt model, helices 299–300
- Schröder-van-Laar equation, thermochemical properties of gels 528–9
- Schultz-Flory's parameter, non-gelling mixtures 27
- screening, sugar library 567–9
- SDS *see* sodium dodecyl sulfate
- SEA *see* single-end-anchored
- second-order phase transitions 248
- secondary aggregation, nucleation 158–60
- secondary structures
see also nanometer-scale structures
 structural modeling 723
- segregation
 in solutions, thermodynamics 132–4
 steady-state nucleation rate 138
- selective energy transfer, light harvesting 401–3
- self-aggregation, *n*-alkanamides 472

- self-assembling fibrillar networks (SAFINs)
 - 114–17, 127
 - properties 449–537
 - structural modeling 721, 723, 728–9
- self-assembly
 - aggregate ends 86–90
 - circular dichroism spectroscopy 435–6
 - future research 536
 - one-dimensional 99–100
 - peptide gels 99–130
 - supramolecular polymers 79–80, 83–5
 - surfactant molecules 667, 669
- semi-rigid fibers, small-angle scattering 292–3
- semiconductors
 - inorganic templating 807–8
 - nanoparticle spatial organization 808
 - spatial organization 808
- sergeants-and-soldiers effect
 - chirality amplification 91–4
 - side-chain association 39
- L-serine-dodecylamide, solvent effect on bilayers 650–1
- sexithiophenes, electron conduction 801
- SGR *see* soft glassy rheology
- shape of transcribed material 875–88
- shear alignment, oriented fibers 312–16
- shear banding
 - flow-microstructure coupling 210–11
 - wormlike micelles 194–6, 667–8, 686–706
- shear flow, deterministic chaos 195–210
- shear stress, nematogenic fluids 206–8
- shear-induced phase (SIP) 199
- shear-induced structures (SIS),
 - cetyltrimethylammonium tosylate (CTAT) 199
- shear-thickening
 - rheological chaos 202
 - soft glassy rheology 176
 - wormlike micelles 199
 - semi-dilute regimes 696
- shear-thinning, semi-dilute regimes 696
- shear-transformation zone (STZ) theory 190
- sheared gel film, phenylenevinylenes 457
- sheared micelles, chaotic dynamics 195–200
- β -sheet peptides, hydrogelators 625
- shift factor, temperature, side-chains 37
- short rods, small-angle scattering 290–2
- shrinking response, physico-responsive gels 915
- sickle-cell deoxyhemoglobin 442
- side-chain association, non-gelling mixtures 34–9
- signal
 - limitation, small-angle scattering 277–8
 - responsive molecular gels 897–9
- silica, adsorption onto tubule wall 881–2
- silver nanohelices 500
- silver-deposition, silica matrix 879–80
- simulated annealing, x-ray diffraction 334–5
- simultaneous growth, nucleation 151–3
- single crystal diffraction 329–37
- single phase gels, ion conducting 788–9
- single-end-anchored PEG-surfactants (SEA-PEG-surfactants) 761–2
- single-headed, amphiphiles 635–6
- singlet-singlet energy transfer 399
- SIP *see* shear-induced phase
- SIS *see* shear-induced structures
- size broadening, powder x-ray diffraction 345–7
- slender-body suspensions, rheological chaos 202
- slow-scan CCD cameras, electron microscopy 258
- slump test, tabletop rheology 247
- small angle X-ray scattering (SAXS),
 - liquid-crystalline phase gelation 753–5
- small-angle neutron scattering (SANS),
 - wormlike micelles 675–8, 693–5, 696
- small-angle scattering (SAS) techniques 275–322
- smart materials, phototunable gels 835
- smectic interaction parameter,
 - supramolecules 42
- smectic liquid crystals 517
- smectic phase, thermotropic liquid crystals 775
- SO *see* spiroxazines
- sodium deoxycholate
 - gelation 392–4
 - hydrogelators 637–8
 - supramolecular chirality 588–9
- sodium dodecyl sulfate (SDS)
 - electron microscopy 263–4, 266–70
 - wormlike micelles 671, 672, 679
- sodium lithocholate
 - structural investigation 641
 - tubes, small-angle scattering 296–8
- sodium naphthalene sulfonate, fluorescence spectra 400–1
- soft glassy rheology (SGR), model 170–6
- sol, volume fractions 19

- sol-gel chemistry
 - phase transitions
 - calorimetry techniques 247–51
 - liquid-crystalline gels 517–18
 - photochromic property modulation 843–4
 - reversible photoinduction 846–50
 - tabletop rheology 242–7
 - thermodynamic theory 24–5
 - polycondensations 476
 - transcription 860–4
 - amphiphilic gelators 587–8
 - schematic representation 884
- solar cell, ionic liquids gelation 526
- solid phase synthesis, combinatorial approach, hydrogelators 631
- solid-state conductivity 795–6
- solubility
 - curvature of surface 865–6
 - gelation calorimetry 250–1
- solvent
 - cleaning agents 929–36
 - effect on bilayers 650–1
 - gel formation role 724, 737
 - polarity, liquid component 530–2
- solvophilicity
 - amphiphilic gelators 601
 - gelation efficiency 480–1
- solvophobic, amphiphilic gelators 601
- sorbitol derivatives (DBS)
 - hydrogen bonding 409–10
 - organic gelators 459–62
- SP *see* spiropyrans
- spacer length
 - gelation efficiency 480–1
 - gemini amphiphile molecules 592–3
- spatial organization, semiconductor nanoparticles 808
- spatio-temporal intermittency (STI), nematic hydrodynamics 215
- spatio-temporal rheological chaos 210–18
- spectral analysis, peptide gels 110
- spectral shifts, luminescence 825–7
- spectrometers
 - circular dichroism 432
 - fluorescence 366–7
 - Fourier Transform Infra Red (FTIR) 407
- spectroscopic methods 363–425
- speed of transcription, accuracy 866
- spheres
 - microstructure 479–80
 - repulsion, fibrillar systems 308–9
 - test, tabletop rheology 245–6
 - transcriptions 884–5
- spherical clusters, nucleation 152
- spherical micelles
 - L-lysine derivatives 414
 - wormlike micelle relationship 669
- spherical scatterers, fibrillar systems 308–9
- spherulitic nodes 302
- spinodal
 - curve 133–4
 - decomposition 134, 154–8
 - line 26, 30
 - work critical clusters 145–6
- spiro-switches, light-responsive gels 920–1
- spiropyran (SP)
 - arylcyclohexanol gel 456
 - photochromism 838–9, 843
 - thermal isomerization 484
- spiroxazines (SO), photochromism 839
- “spurt” effects, wormlike micelles 702
- stability
 - aliphatic amine gelators 464
 - limit 26–7, 30
 - metal ion complexation 905–6
 - molecular shape of liquid component 530
 - polymerizable gelators 500–3
 - spiropyran, arylcyclohexanol gel 456
 - thermodynamic concepts 133–4
- stabilization
 - by polymerization 586–7
 - twist in peptide gels 112–13
- stacked aggregate, porphyrin gelator 384
- stacked aromatic units 496–7
- stacking efficiency, steroids 557
- standard reference state
 - multiple association 59
 - thermodynamic theory 20–2
- startup experiments, rheological ageing 182
- state of the art, small-angle scattering 321–2
- state diagram, chiral rod-like units 103–4
- state parameters, work of critical clusters 142
- static excimers, spectroscopy 391, 395, 396
- steady state nucleation rate 137–40
- steady state response, rheology 167–8
- steady-state shear stress 687–8, 689–90
- step strain
 - response 178–84
 - rheology 164
- step stress, response 184–7
- stereochemistry
 - chiral bilayer effect 653–60
 - cholestanyldioctadecyclamine 464–5
- steroids
 - alkoxyanthracene derivatives 457
 - circular dichroism 369–70

- derivatives 554–64
 - liquid component 530
- STI *see* spatio-temporal intermittency
- stick-slip process, cetyltrimethylammonium tosylate (CTAT) 199
- trans*-stilbene, liquid component 535
- stilbenes, photochromism 837–8, 840–1
- Stockmayer's treatment, pairwise association 54–8
- stoichiometric compounds, pairwise association 58
- Stokes shift, optical spectroscopy 365
- strain
 - broadening 346–7
 - rheological ageing 176–84
- strand size, surfactant/phenol gelator 506–7, 509, 510
- stress
 - physico-responsive gels 915–17
 - plateaus 687–90, 696–9, 704, 706
 - responsive gels 898–9
 - rheological ageing 184–7
- strong gels, response to stress 916
- structural modeling, organic hydrogels 721–37
- structural transitions, electron microscopy 267–70
- structure factor
 - single crystal diffraction 330
 - small-angle scattering 307–10
- structure solution, powder x-ray diffraction 341–4
- STZ *see* shear-transformation zone
- substituted fatty acids 454
- sugar library 567–9
- sugar-based gelators 564–70
 - azobenzene moiety 629–30
 - transcription templates 870–1, 882–6
- super-paramagnetic gels 809
- supercritical extraction of liquid 524–5
- supercritical fluids
 - di-*n*-alkoxybenzene aerogels 458–9
 - gelation 524–5
- supergelators
 - anthracene appended cholesterols 555–6
 - di- β -D-glucopyranosyl derivative 382–3
- supersaturation
 - critical cluster formation 143–4, 149
 - steady-state nucleation rate 137–8
- supramolecular aggregates 489–90
- supramolecular chirality 589–91
- supramolecular excimer fluorescence 396
- supramolecular hydrogels, light harvesting 399–401
- supramolecular polymers 79–95
- surface of tension, work of critical cluster formation 141
- surfactant/phenol strands 506–7, 509, 510
- surfactants
 - cetyltrimethylammonium tosylate (CTAT) 194–200
 - concentration effects 268–70
 - gemini amphiphilic gelators 592–3
 - hydrogelators 632–4
 - lyotropic liquid-crystals 746
 - oligomers 673
 - phase defect inducing 747–64
 - two component 503–7
 - wormlike micelles 667–707
- swelling response, glycosylated amino acid 915
- switchable gratings 778, 780
- switching, light-responsive gels 922
- swollen liquid-crystalline phases 746, 748, 749, 757
- symbolic addition, phase calculation 334
- synchrotron beam
 - powder x-ray diffraction 351
 - small-angle scattering 317
- syneresis 8
- synthetic tripeptide, hydrogen bonds 414–16
- tabletop rheology, gelation phase diagrams 242–7
- tantalum oxide fibers, polycondensations, *n*-alkanamide gelators 476
- tapes, self-assembling peptide gel experiments 105–12
- tartaric acid, charge repulsion in water 651–3
- tartaric amide monocarboxylates 634–5
- n*-2-*n*/tartrate systems 597–9
- TBU *see* thiophene-containing bisurea
- TCP *see* tricritical point
- telechelic polymers, chain/ring formation 31
- temperature
 - critical solution 39–40
 - responsive molecular gels 898–9, 914–15
 - shift factor, side-chains 37
- transcriptions
 - cholesterol-based gelators 878
 - sugar-based gelators 885
- templates
 - definition 858–60
 - growth of inorganic fibers 458–9
 - media, electronic materials 805–8
 - transcription 857–90
- temporal chaos, nematogenic fluids 203–10

- tension, gemini aggregate morphology 594–6
- tensor, nematogenic fluids 203–10
- tensorial model, soft glassy rheology 174–5
- TEOS *see* tetraethylorthosilicate
- ternary systems, associating mixtures 19
- 4-tert-butyl-1-arylcyclohexanol derivatives (BACO1), O-H stretching 410–12
- tertiary amines, hydrogen bonding 464
- tertiary structures
see also micrometer-scale structures
structural modeling 723
- tetracyclic androstane skeleton 554
- tetraethylorthosilicate (TEOS)
precursor, sol-gel chemistry 861, 863–4
transcription 587–8
- tetramethylorthosilicate (TMOS), precursor, sol-gel chemistry 861
- tetrathiafulvalene (TTF), electron conduction 802
- TFA *see* trifluoroacetic acid
- thermal characterization, gelation 247–51
- thermal equilibrium, multiple association 59
- thermal fixation 255
- thermal isomerization, spiropyran 484
- thermal polymerization line, chain/ring formation 34
- thermal reactions, type T-photochromism 836
- thermal reversibility, kinetics 318
- thermal stability
photochromic materials 838, 839, 840
spiropyran 456
- thermochemical properties, gels,
Schröder-van-Laar equation 528–9
- thermochromism, spiropyran 839
- thermodynamics
line defects 758–9
network theory 18–27
shear banding transitions 704
- thermoreversible dimers 30
- thermoreversible gels
Boc- β -Ala-Aib- β -Ala-OMe 414–16
Eldridge-Ferry method 65
- thermoreversible hetero-association 28
- thermoreversible mixed networks 69–73
- thermotropic liquid crystals
definition 745
electro optical devices 775–80
gelation 765
- thin-film conducting gels, field effect transistors 805
- thioethers, organic gelators 451–3
- thiophene-containing bisurea (TBU),
conducting LMOG gels 801
- thixotropy
amphiphilic gels 583–4
gels 8–9, 261, 320, 601, 632
response to mechanical stress 916–7
- three-dimensional networks 19
future research 537
two-component gels 511–13
- threshold switching voltage, liquid crystal gels 779
- thymidine derivatives, two heteroatoms 486–7
- thymidine-based gelators 571–3
- time, tube inversion experiments 244–5
- time delay vectors, wormlike micelles 198
- time series analysis (TISEAN), chaotic data 208–9
- time translational invariance (TTI), rheology 163–70
- time-dependent gels 489–91
- time-resolution, electron microscopy 256
- time-sectioning, electron microscopy 256
- tin(IV)-porphyrins, chiral bilayers 659
- TISEAN *see* time series analysis
- titration behaviour, peptide hydrogels 120, 122
- TMOS *see* tetramethylorthosilicate
- TNF *see* 2, 4, 7-trinitrofluorenone
- toluene gels, bolaamphiphiles 524
- topological defects, liquid-crystalline phase gelation 743–67
- trans-cis* photoisomerization 846
- transcription
accuracy 866
amphiphilic gelators 587–8
lamellar gel aggregates 880
polycondensations 476
steps in process 858–60
sugar-based library 569
temperature
cholesterol-based gelators 878
sugar-based gelators 885
templates 857–90
- transformation, kinetics of nucleation 152–3
- transient shear stress responses 688–90
- transients, time translational invariance (TTI) 169
- transition line, sol/gel 24–5
- transition metal-carbene carbohydrate amphiphile 417–18
- transition moments, exciton spectrum 437–8
- translational degree of freedom 20–1

- transport number, cations 787, 790
- traps
 interrupted 183
 soft glassy rheology (SGR) 172
- tri-amide cyclohexane, pH-sensitive gelation 912–14
- tri-block copolymer gelation 462
- tri-block proteins, pH-sensitive gelation 910–11
- tri-*n*-alkylphosphine oxides, latent gelators 521
- 2,4,6-triamino-5-hexadecylpyrimidine 507–8
- tricritical point (TCP), pairwise association 56
- trifluoroacetic acid (TFA), energy transfer 403–4
- triggers
 physico-responsive gels 914–24
 responsive molecular gels 897–9
- 2,4,7-trinitrofluorenone (TNF) 386–8
 electron-acceptor molecule 513
- tripeptides
 hydrogen bonds 414–16
 three heteroatoms 498–9
- triphenylene chromophores 395–7
- triphenylene derivatives, luminescent gels 828–9
- triphenylene-based, organic gelators 477
- tripodal bile acids
 derivatives 261
 host-guest complexation 901–3
- tripodal cholanide
 hydrogelator 638–9, 641
 small-angle scattering 309–10
- tris-bipyridine tripodal ligand, metal ion complexation 905–6
- tris*-urea derivatives, two heteroatoms 492
- Truesdell function, chain/ring formation 33–4
- TTF *see* tetrathiafulvalene
- TTI *see* time translational invariance
- tube inversion
 gel assessment 744
 liquid-crystalline phase gelation 755
 tabletop rheology 243–5
- tubes
 small-angle scattering 295–8
 plain fibers 288
- tubules, microstructure 479–80
- turbidity, aliphatic amine gelators 464
- twist
 self-assembly 102–3
 stabilization 112–13
- twisted bilayers, gemini amphiphiles 598–9
- twisted nematic character 516
- twisted ribbons
 amphiphilic gelators 590–1
 electron microscopy 731–2
 structural analysis 725–8
- two-chain, amphiphilic molecules 580–1
- two-component organic gelators 503–13
 UV and fluorescence spectroscopy 386–8
- two-state model, Ising chain 85
- ultra violet irradiation
 photochromism 836, 838, 840
 reversible phase transitions 846–7
- ultra violet radiation, acrylate
 photopolymerization 774–5, 780, 791
- ultra violet-visible spectroscopy 364–407
 bis-urea organic gelators 489–90
 polymorphism 406–7
- ultra-small angle diffractometer 277
- unaggregated molecules 436
- unduloidal drops, wetting of fibers 227
- unimers, definition 23
- unit cell 328–9, 340–1
- units, small-angle scattering 281
- unsymmetrical bolaamphiphiles
 hydrogelators 625–6
 lysine based 617
- up-hill diffusion, first-order phase transitions 154–8
- urea derivatives
 amino acids 622–3
 two heteroatoms 488–92
 x-ray diffraction 354–6
- urea-appended porphyrin 492
- bis-urea-glutamate esters 622–3
- urethanes, two heteroatoms 492–3
- UV-vis *see* ultra violet-visible
- vancomycin hydrogels 573–4
 circular dichroism spectroscopy 374
 pyrene conjugate 620, 621
 UV and fluorescence spectroscopy 394–5
- vapour pressure, ionic liquids 525
- varnish, cleaning agents 929–30, 935
- vesicular phospholipid gels 260–1
- vibration bands, IR absorption spectroscopy 419–24
- vibrational circular dichroism spectroscopy 445
- vibrational mode, molecular aggregates 408
- vibronic band, UV and fluorescence spectroscopy 375, 379–81

- viscoelasticity
 - domains, liquid component 533–4
 - gels in water 660–1
 - networks theory 66–9
 - self-assembling peptide gels 118–19
 - shear flow, deterministic chaos 195–210
 - spectra 165–7, 180–2
 - wormlike micelles 193, 668, 680–5
- viscosity
 - Brookfield 931
 - helical supramolecular polymers 82
 - ion conducting gels 787
 - mixed networks 73
 - Newtonian 139
 - phosphoric acid ester/aluminum *sec*-butoxide gels 508
 - static 680–1, 683–4, 688, 690, 702
 - viscous liquids, gel comparison 728–9
 - visible light harvesting 558–9
 - visible ultra violet spectroscopy 364–407
 - vittrification 255
 - voids, flow through fibers 234
 - volume fractions, sols 19
- water content effects, liquid-crystalline gels 749–51, 753–4, 759
- wave number, spinodal decomposition 156–7
- WAXS *see* wide angle X-ray scattering
- weak gels, response to stress 916
- wetting, fibers 223–36
- wicking
 - fibers 231
 - specimen, electron microscopy 256
- wide angle X-ray scattering (WAXS) 755, 756
- Witten-Sander model, clusters 159
- work of critical cluster formation 140–51
- wormlike micelles
 - micellization theory 45, 47
 - rheological chaos 193–200
 - rheology 667–707
- x-ray diffraction (XRD) 325–60
 - image plates 358
 - powders 337–47
 - structural modeling 721–2, 732–7
- x-ray scattering
 - experiments, liquid-crystalline gels 753–5
 - structural analysis 277–9
- xerogels 6, 353–5, 420–1, 508–13, 524–5, 561–3
 - arylcyclohexanol 454–6
 - 1,3:2,4-di-O-benzylidene-D-sorbitol 409–10
 - glutamate derivatives 482–4
 - images 570, 834–5, 883
- XRD *see* x-ray diffraction
- xylose complexes 562–3
- yield energy
 - nonlinear 183, 187
 - soft glassy rheology (SGR) 171–4
- yield stress
 - hydrogelators 618
 - measurement 247
- zig-zag chains
 - chiral bilayer effect 655
 - methyl 4,6-*O*-benzylidene- α -D-glucopyranoside 565–6
- Zimm-Bragg model, helical aggregation 81, 85
- zinc-porphyrins, fullerene, host-guest complexation 904
- zwitterionic surfactants
 - gemini surfactants 633–4
 - thixotropic amphiphilic hydrogel 584